Environmental
Studies
Research
Fund

217

Transmission Loss Modelling of Seismic Airgun Sounds: Predicted Received Levels, with Frequency Weighting, off Atlantic Canada

Modélisation de perte de transmission des bruits sismiques provenant de canons à air : niveaux de réception anticipés avec pondération fréquentielle, au large du Canada atlantique

Canada 2018

Transmission Loss Modelling of Seismic Airgun Sounds

Predicted Received Levels, with Frequency Weighting, off Atlantic Canada

Submitted to:

Environmental Studies Research Fund
Project Identification Code: ESRF 2014-02S

Authors:

Terry J. Deveau
Julien Delarue
Bruce Martin
Klaus Lucke

13 December 2018

P001276-001
Document 01620
Version 2.0

JASCO Applied Sciences (Canada) Ltd
202—32 Troop Avenue
Dartmouth, NS B3B 1Z1 Canada
Tel: +1-902-405-3336
Fax: +1-902-405-3337
www.jasco.com

Suggested citation:

Deveau, T.J., J. Delarue, S.B. Martin, and K. Lucke. 2018. *Transmission Loss Modelling of Seismic Airgun Sounds: Predicted Received Levels, with Frequency Weighting, off Atlantic Canada*. Document Number 01620, Environmental Studies Research Funds Report Number 217, Version 2.0. Technical report by JASCO Applied Sciences for Environmental Studies Research Fund, Dartmouth, NS, Canada. 43 pp + appendices.

Disclaimer:

The results presented herein are relevant within the specific context described in this report. They could be misinterpreted if not considered in the light of all the information contained in this report. Accordingly, if information from this report is used in documents released to the public or to regulatory bodies, such documents must clearly cite the original report, which shall be made readily available to the recipients in integral and unedited form.

Contents

Figures

Tables

Executive Summary

This report is part of the Environmental Studies Research Fund Project 2014-02S final deliverables. The overall project objectives were to provide new results that will inform future environmental assessments of human activities on Canada's East Coast. The project was broken into two major programs: 1) measuring the existing soundscape and the presence of vocalizing marine life; and 2) understanding the effects of the acoustic footprint of seismic surveys in the study area. Measurements of the soundscape were made continuously at 20 sites from Labrador to Nova Scotia over a two-year period. To study of the effects of seismic sound, computer-based acoustic propagation modelling was performed that was validated by field measurements.

The acoustic monitoring program deployed twenty marine acoustic recorders off Canada's east coast between August 2015 and July 2017 (Delarue 2018). The recording protocol was selected to monitor marine mammal acoustic occurrence and to characterize the underwater soundscapes of selected areas. The monitored locations ranged from the Scotian Shelf to the southern Labrador shelf through the Grand Banks of Newfoundland. The choice of monitored locations represents a balance between areas of potential interest for oil and gas development and less-sampled locations that were known or presumed to be important to marine mammals.

The underwater soundscape and its noise contributors were quantified. Drilling platforms contributed significantly to the local soundscape of targeted areas. Seismic survey sounds were detected over wide areas, particularly north of the Flemish Pass. Vessels were detected at all stations, with the highest vessel sound levels measured at stations near shipping lanes or near active drilling platforms.

The study provided unprecedented insight into the occurrence of marine mammals off Eastern Canada. Species richness was consistently higher at deep stations along the continental slope than at nearshore stations or at stations on the continental shelf. Stations in the southern parts of the study area maintained high species richness throughout the year, whereas northern stations saw a decline in winter and spring. The year-round presence of Cuvier's and Sowerby's beaked whales south of the Grand Banks and northern bottlenose whales north of the Flemish Pass and off southern Labrador, represents valuable new information. The year-round presence of sperm whales in the Flemish Pass area contrasts with the seasonal decline in detection rates observed throughout the study area in winter and highlights the area's potential importance for this species. Bearded, grey, and harp seal acoustic detections were associated with male sound production during the breeding season, when these species are most vocally active. Baleen whales showed pronounced seasonal variations in acoustic occurrence, which was attributed to the seasonality of their vocal behaviour, migratory movements, or both. Blue whales occurred nearly year-round in the Cabot Strait, and into January at most stations. In winter, they were common at deep offshore stations east of the Grand Banks. Sustained fin whale acoustic signals from September to March at most stations (excluding those with seasonal ice cover) indicates that this species does not migrate seasonally out of Canadian waters, as was traditionally believed. In summer and fall, sei whales regularly occurred at deep stations ranging from the Flemish Pass to southern Labrador.

This report is the second of two reports dealing with modelling of sound from seismic airguns arrays. Geophysical survey sources, such as seismic airguns, emit high-intensity sounds and have the potential to harm or disturb marine organisms. Sound fields from airguns are typically described in terms of sound pressure, but pressure is often not the most relevant parameter for assessing effects in non-mammalian species. For fish and invertebrates, acoustic particle motion (the motion of an infinitesimal portion of the medium, relative to the medium as a whole) is more appropriate. It is known that all fish are capable of directly sensing the particle motion component of sound, while relatively few fish additionally sense the pressure component. Furthermore, animals such as crustaceans with statocyst-based hearing are thought to only sense particle motion. Because of increasing concern over the effects of anthropogenic sounds on these marine species, more complete descriptions of the sound fields to which animals are exposed are needed. The absence of ground-truthed models for acoustical particle motion from seismic airguns is an important knowledge gap that ESRF Research Study 2014-02S addressed.

The first seismic modelling report (Warner and MacGillivray 2018) contained two chapters. Chapter 1 presented the results of a detailed analysis of the Svein Vaage particle motion measurements made by the JIP in Norway in 2010. Our analysis found several issues with the calibration of the data from the M20

particle motion sensors, particularly with the absolute levels recorded on the accelerometer channels and in the logged positions of the sensors. Thus, we used measurements from several other calibrated hydrophones, which were deployed at the same time as the M20 sensors, to derive corrections for the sensitivities and positions of the M20 sensors. We also used information on the calibrations of the M20 sensors, provided by GTI, to correct the data for their frequency-dependent sensitivity. The results of this analysis were used to correct the identified issues and to obtain calibrated measurements of particle motion that could be used for subsequent airgun model validation.

In Chapter 2, model validation results for pressure and particle acceleration from single airguns using JASCO's Airgun Array Source Model (AASM) were presented. We performed the model validation using the Svein Vaage measurements, after applying correction factors for the M20 particle acceleration channels that we derived in Chapter 1. These results showed that AASM accurately predicted measured particle motion from single airguns, with best agreement between at frequencies below 300 Hz (i.e., where airguns generate most of their acoustic energy). Thus, AASM can be used for accurately modelling exposures of marine organisms to particle motion from seismic airguns at short range, which is particularly important for assessing potential impacts to fish and invertebrates.

The results of the first seismic study were used in this report, which contains the modelled acoustic footprints for hypothetical seismic surveys conducted near each of the monitoring locations and provides the radii to at which the sound levels exceed the NMFS (2018) exposure thresholds for acoustic injury (temporary or permanent hearing threshold shifts). The modelling analysis also compares the results from modelling a generic sand bottom with a bottom whose geo-acoustic properties were computed in Warner and MacGillivray (2018). This report shows that the range at which low-frequency marine mammals may suffer permanent hearing threshold shifts from exposure to seismic surveys varies by location and season. The distance can range from 100 m to almost 10,000 m. The modelling study also concluded that use of local bottom properties is important for obtaining accurate propagation loss values and therefore realistic radii for possible acoustic injury and disturbance to marine life.

Sommaire

Ce rapport est le deuxième de trois rapports finals du projet 2014-02S du Fonds pour l'étude de l'environnement. Les objectifs généraux du projet visaient à fournir de nouveaux résultats afin d'éclairer les évaluations environnementales futures des activités humaines sur la côte est canadienne. Le projet était divisé en deux grands programmes : 1) Mesure de l'environnement acoustique actuel et de la présence de vie marine qui contribue au paysage sonore et 2) Compréhension des effets de l'empreinte acoustique des relevés sismiques dans la zone d'étude. Les mesures de l'environnement acoustique se sont effectuées de façon continue à vingt sites situés entre le Labrador et la Nouvelle-Écosse au cours d'une période de deux ans. Pour étudier les effets des bruits sismiques, un modèle informatisé de la propagation sonore a été réalisé et il a été validé avec des mesures prises sur le terrain.

Le programme de surveillance acoustique a déployé vingt capteurs acoustiques sur la côte est canadienne entre août 2015 et juillet 2017 (Delarue et al. 2018). Le protocole d'enregistrement sélectionné visait à surveiller les activités sonores des mammifères marins et à caractériser l'environnement sonore sous-marin des zones sélectionnées. Les zones contrôlées se situaient entre la plate-forme néo-écossaise et le plateau continental sud du Labrador, en passant par les Grands Bancs de Terre-Neuve. Les choix de zones contrôlées constituent un équilibre entre les zones d'intérêt potentiel pour l'exploitation du pétrole et du gaz et les zones moins bien étudiées qui sont connues ou présumées importantes pour les mammifères marins.

L'environnement sonore sous-marin et les éléments qui y contribuent ont été quantifiés. Les plates-formes de forage ont contribué considérablement à l'environnement sonore local des zones ciblées. Le bruit des relevés sismiques a été détecté sur de vastes étendues, particulièrement au nord de la passe Flamande. Des navires ont été détectés à toutes les stations, et les stations près des routes maritimes ou des plates-formes de forage en opération ont affiché les niveaux sonores les plus élevés.

L'étude a fourni un aperçu sans précédent des activités des mammifères marins au large de la côte est du Canada. La diversité des espèces était toujours plus élevée au large de la pente continentale qu'aux stations littorales ou qu'à celles situées sur le plateau continental. Les stations situées dans les régions sud de la zone d'étude maintenaient une diversité des espèces élevée toute l'année, alors que celle des stations nordiques déclinait en hiver et au printemps. La présence à longueur d'année des baleines à bec de Cuvier et de Sowerby au sud des Grands Bancs et des baleines à bec au nord de la passe Flamande et au large de la côte sud du Labrador constitue de l'information nouvelle et précieuse. La présence à longueur d'année de cachalots dans la région de la passe Flamande contraste avec le déclin saisonnier des taux de détection observés dans l'ensemble de la zone d'étude en hiver et souligne l'importance potentielle de la zone pour ces espèces. Les détections acoustiques des phoques barbus, des phoques gris et phoques du Groenland ont été associées à la production de sons par les mâles pendant la période de reproduction, la période où ces espèces produisent le plus de son. L'activité sonore des baleines à fanons a démontré des variations saisonnières prononcées qui ont été attribuées au cycle saisonnier de leur comportement sonore, de leurs mouvements migratoires ou des deux. L'activité sonore des rorquals bleus a été décelée presque toute l'année dans le détroit de Cabot et jusqu'en janvier à la plupart des stations. En hiver, ils étaient de fréquemment détectés aux stations en mer profonde des Grands Bancs. La présence continue, de septembre à mars, des signaux sonores du rorqual commun à la plupart des stations (sans compter celles comportant une couche de glace saisonnière) indique que l'espèce ne quitte pas les eaux canadiennes de façon saisonnière, contrairement à ce que nous pensions. En été et à l'automne, la présence du rorqual boréal a été régulièrement détectée aux stations profondes de la passe Flamande jusqu'au sud du Labrador.

Ce rapport constitue le deuxième de deux rapports sur la modélisation de l'activité sonore produite par des batteries de canons à air lors de relevés sismiques. Les sources de levés géophysiques, comme les canons à air, émettent des sons à haute intensité et sont susceptibles de nuire aux organismes marins ou de les perturber. Les champs acoustiques produits par les canons à air sont généralement définis selon leur pression sonore, mais la pression n'est souvent pas le paramètre le plus pertinent en ce qui concerne l'évaluation de l'impact sur des espèces autres que les mammifères. Pour les poissons et les invertébrés, le mouvement des particules sonores (le mouvement d'une portion infinitésimale du milieu, relativement à l'ensemble du milieu) est un paramètre plus pertinent. Il est bien connu que tous les poissons ont la capacité de percevoir directement la composante du mouvement des particules d'un son, alors que relativement peu de poissons peuvent, en plus, percevoir la composante de la pression. De plus, on croit que les animaux, tels les crustacés dont l'ouïe repose sur le statocyste, ne perçoivent que le mouvement des particules. En raison des préoccupations croissantes relativement aux effets des sons d'origine anthropique sur ces espèces marines, il est essentiel d'établir des descriptions plus complètes des champs acoustiques auxquels sont exposés les animaux. L'absence de modèles témoins pour le mouvement des particules sonores produites par des canons à air constitue un manque de connaissance important que l'étude de recherche 2014-02S du FEE tente d'aborder.

Le premier rapport sur la modélisation sismique (Warner et MacGillivray 2018) était composé de deux chapitres. Le chapitre 1 présentait les résultats d'une analyse approfondie de la mesure du mouvement des particules de Svein Vaage menée en 2010 par JIP en Norvège. Notre analyse a décelé plusieurs problèmes dans l'étalonnage des données des capteurs de mouvement de particules M20, particulièrement en ce qui concerne les niveaux absolus enregistrés sur les canaux accélérométriques et la position consignée des capteurs. Par conséquent, nous avons utilisé des mesures provenant d'autres hydrophones étalonnés, déployés en même temps que les capteurs M20, en vue de déterminer l'écart de sensibilité et de position des capteurs M20. Nous avons également utilisé l'information sur l'étalonnage des capteurs M20, fournie par GTI, afin de corriger les données de sensibilité qui varient en fonction de la fréquence. Les résultats de cette analyse ont servi à corriger les problèmes décelés et à obtenir des mesures étalonnées du mouvement des particules qui peuvent être utilisées pour vérifier de futurs modèles de canons à air.

Le chapitre 2 présentait les résultats de vérification du modèle pour la pression et l'accélération acoustiques provenant d'un canon à air unique, à l'aide du Modèle d'une batterie de canons à air (AASM – Airgun Array Source Model) de JASCO. Nous avons effectué la vérification de modèle à l'aide des données Svein Vaage, après avoir appliqué les facteurs de correction pour les canaux d'accélération acoustique M20, dérivés au chapitre 1. Ces résultats ont démontré que le modèle AASM a prédit avec exactitude le mouvement de particules mesurées d'un canon à air unique. La meilleure concordance s'est située aux fréquences inférieures à 300 Hz (c.-à-d. aux fréquences où les canons à air produisent la majorité de leur énergie acoustique). Par conséquent, le modèle AASM peut être utilisé pour adéquatement modéliser l'exposition d'organismes marins au mouvement de particule produit par des canons à air de courte portée, ce qui est particulièrement important pour évaluer les impacts potentiels sur les poissons et les invertébrés.

Les résultats du premier relevé sismique ont été utilisés dans ce rapport qui comporte les empreintes acoustiques modélisées des relevés sismiques hypothétiques menés à proximité de chacun des sites de surveillance et qui indique le rayon où les niveaux acoustiques excèdent les seuils d'exposition (NMFS 2018) susceptibles d'endommager l'ouïe (variations temporaires ou permanents du seuil auditif). L'étude théorique compare également les résultats de modélisation d'un plancher océanique sablonneux avec un plancher dont les propriétés géoacoustiques ont été calculées selon Warner et MacGillivray (2018). Ce rapport démontre que la plage de basse fréquence, à laquelle les mammifères marins sont susceptibles de souffrir de variations du seuil auditif dû à l'exposition aux relevés sismiques, varie selon la position et les saisons. La distance varie de 100 m à près de 10 000 m. L'étude de modélisation a également démontré l'importance de tenir compte des propriétés du plancher océanique pour obtenir des valeurs d'affaiblissement de propagation précises et donc, des valeurs de rayons réalistes en ce qui concerne la perte de l'ouïe et la perturbation de la vie marine.

1. Introduction

The Environmental Studies Research Funds (ESRF) program funded an underwater acoustic study to assess ambient noise, anthropogenic noise, and to monitor marine mammal presence along the eastern Canadian coast including the Scotian Shelf, Cabot Strait and Strait of Belle-Isle, Grand Banks and Labrador Shelf. Seismic surveys, vessels, and some marine mammals produce low-frequency sounds that can propagate well in these waters. Low-frequency sound propagation is dependent on the bathymetry, sound speed profile (SSP) in the water column, and the acoustic properties of the subbottom (geoacoustic properties). Bathymetry and the SSP can be easily measured using commonly-available equipment—e.g., sonars and conductivity-temperature-depth (CTD) sensors—but geoacoustic properties are typically difficult and expensive to measure directly, especially over large areas and to subbottom depths sufficient for low-frequency propagation modelling.

Warner and MacGillivray (2018) estimated the geoacoustic bottom properties at 14 of the 20 long-term baseline monitoring sites using an inversion of frequency- and range-dependent measured sound pressure level data from a single seabed-mounted hydrophone and a towed airgun source. The hydrophone measurements were made using Jasco's Autonomous Multichannel Acoustic Recorders (AMARs). The inversion involved a range-dependent Parabolic Equation (PE) acoustic propagation model for simulating transmission loss. The number of sediment layers (between 0 and 4) overlying an acoustic halfspace, the geoacoustic properties, and the airgun source level were all fit by the inversion.

The present document draws from the results of Warner and MacGillivray (2018) to model the underwater noise received at the AMAR depth and location projected by a distant towed airgun array that is representative of a seismic survey source. The modelling results derived using site-specific geoacoustic properties are compared to results produced using generic sandy bottom geoacoustic properties to highlight the importance of local bottom properties on the characterization of the acoustic footprint of seismic surveys. Additionally, historical mean SSP data for representative summer and winter months are used with the site-specific geoacoustic properties to model underwater noise projected in the water column by the same towed airgun array (representative of a seismic survey source).

2. Methods

2.1. Modelling locations

Figure 1 shows the locations of the 20 sites where underwater acoustic noise levels and transmission losses were modelled in this study. Coordinates and depth of each station are shown in Table 1.

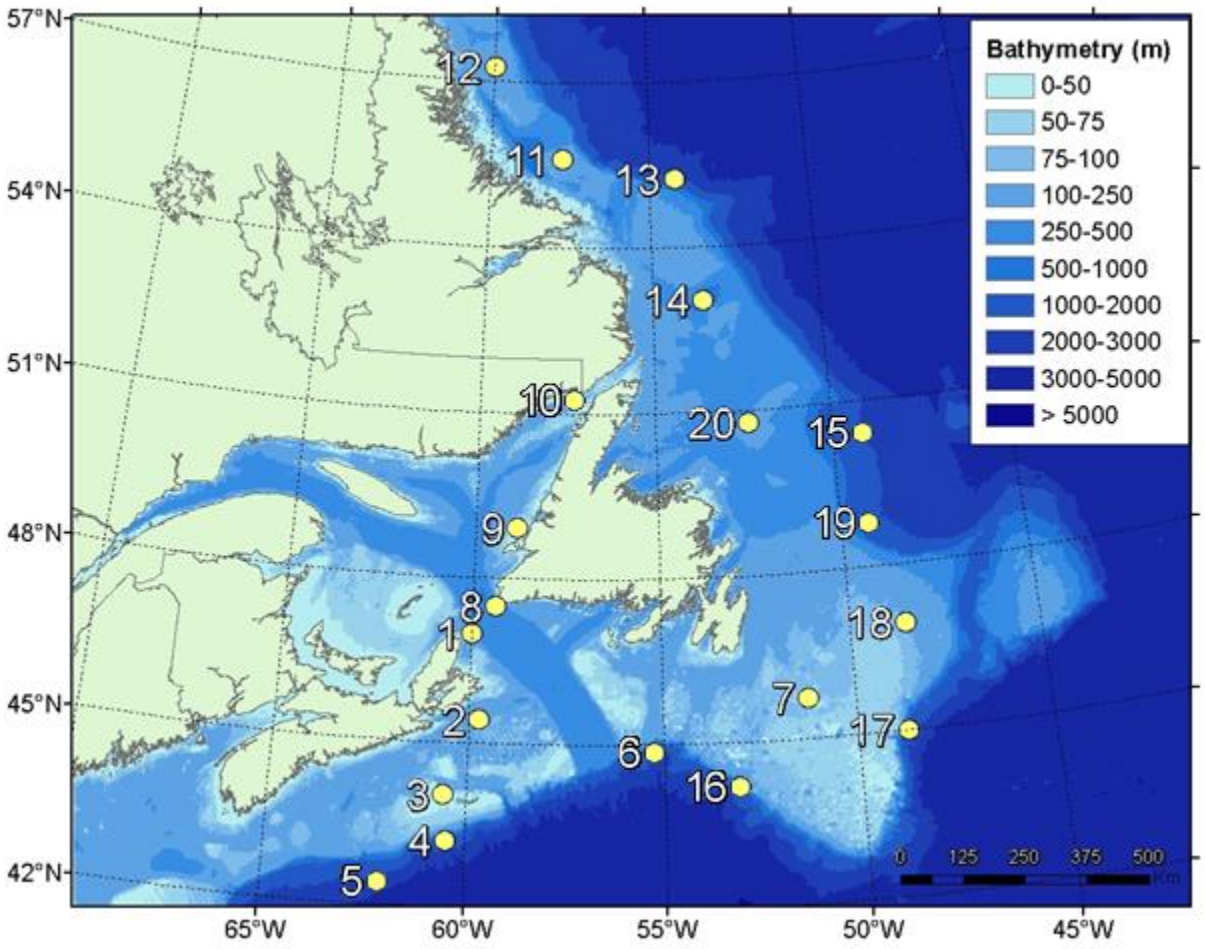

Figure 1. Locations where seismic airgun noise propagation is modelled.

Table 1. Geographic coordinates, water depth, and modelled receiver depth for the transmission loss modelling locations.

Station	Latitude (°N)	Longitude (°W)	UTM easting (m)	UTM northing (m)	UTM zone	Measured water depth (m)	Modelled water depth (m)	Planned mooring offset (m)	Modelled receiver depth (m)
1	46.99134	-60.02403	726279.3	5208500.8	20	186	184.69	-15	171.0
2	45.42599	-59.76398	283777.4	5033990.8	21	122	133.41	-0.5	121.5
3	44.04816	-60.59475	692684.6	4880034.6	20	35	16.73	-0.5	34.5
4	43.21702	-60.49943	703102.6	4787950.8	20	1570	1667.72	-15	1555.0
5	42.5476	-62.17624	567633.9	4710907.2	20	2002	1844.07	-15	1987.0
6	44.85309	-55.27108	636613.1	4968084.7	21	1802	1742.86	-15	1787.0
7	45.70082	-51.23315	481849.5	5060833.8	22	78	77.8	-0.5	77.5
8	47.49307	-59.41325	318230.5	5262782.3	21	420	420.37	-15	405.0
9	48.92733	-58.87786	362452.1	5421076.9	21	44	42.02	-0.5	43.5
10	51.26912	-57.53759	462496.2	5679889.9	21	121	106.47	-0.5	120.5
11	55.603	-57.7504	452721	6162151.4	21	158	150.56	-0.5	157.5
12	57.25273	-60.00175	680866.6	6349500.7	20	138	137.05	-0.5	137.5
13	55.22797	-54.19047	678676	6123759.7	21	1800	1755.66	-15	1785.0
14	53.01567	-53.46022	334967.4	5876844.6	22	582	561.72	-15	567.0
15	50.41327	-49.19638	628144.7	5586136.1	22	1995	1976.44	-15	1980.0
16	44.1923	-53.27441	318239.7	4895746.9	22	1602	1475.6	-15	1587.0
17	44.97141	-48.73373	678705.5	4982272.8	22	1280	1263.07	-15	1265.0
18	46.90877	-48.50418	690064.8	5198050	22	106	104.01	-0.5	105.5
19	48.72873	-49.38087	619066.9	5398565.2	22	1282	1277.45	-15	1267.0
20	50.75232	-52.33602	405755.36	5623133.4	22	249	238.93	-0.5	248.5

2.2. Sound Source for Transmission Loss Modelling

For the purpose of modelling the expected received sound exposure levels from a typical seismic survey source, the acoustic source characteristics were generated for an example airgun array consisting of 24 active elements arranged in three sub-arrays and totalling an airgun capacity volume of 5085 in^3, as shown in Table 2 and Figure 2.

Table 2. Layout of the modelled 5085 in^3 airgun array. Tow depth is 10 m. Firing pressure for all guns is 2000 psi. The tow direction is assumed to be in the positive *x* direction.

Gun	*x* (m)	*y* (m)	Volume (in^3)	Gun	*x* (m)	*y* (m)	Volume (in^3)	Gun	*x* (m)	*y* (m)	Volume (in^3)
1	0	8.5	290	9	0	0.5	290	17	7	-6.65	45
2	0	7.5	290	10	0	-0.5	290	18	7	-7.35	45
3	3	8.5	195	11	3	0.5	195	19	4.2	-6.65	70
4	3	7.5	195	12	3	-0.5	195	20	4.2	-7.35	70
5	6	8	280	13	6	0	280	21	1.4	-6.5	230
6	9	8	195	14	9	0	195	22	1.4	-7.5	230
7	12	8	145	15	12	0	145	23	-1.4	-7.5	230
8	15	8	105	16	15	0	105	24	-7	-7.35	45

The source levels and directivity of the airgun array were predicted with JASCO's Airgun Array Source Model (AASM), which accounts for:

- Array layout
- Volume, tow depth, and firing pressure of each airgun
- Interactions between different airguns in the array

Details of the model are described in Appendix B.5.

The pressure signatures of the individual airguns and the composite 1/3-octave-band point-source equivalent directional levels of the array were modelled over AASM's full frequency range, up to 25 kHz; the horizontal and vertical overpressure signatures, corresponding power spectrum levels, and the horizontal directivity plots are provided to 4 kHz (Figures 3 and 4). Table 3 provides the modelled vertical direction far-field source level (with and without surface ghost effect) and lists the peak pressure (PK) and sound exposure level (SEL) source levels of the arrays in the endfire, broadside, and vertical directions.

Table 3. Airgun array source level specifications in the horizontal and vertical planes for the modelled 5085 in^3 airgun array with a 10 m tow depth.

Direction	PK (dB re 1 µPa·m)	SEL (dB re 1 µPa^2·s·m)	
		10–2000 Hz	2–25 kHz
Broadside	249.7	226.6	189.8
Endfire	249.8	226.4	191.4
Vertical (no ghost)	259.5	232.5	198.4
Vertical (with ghost)	259.5	235.2	201.5

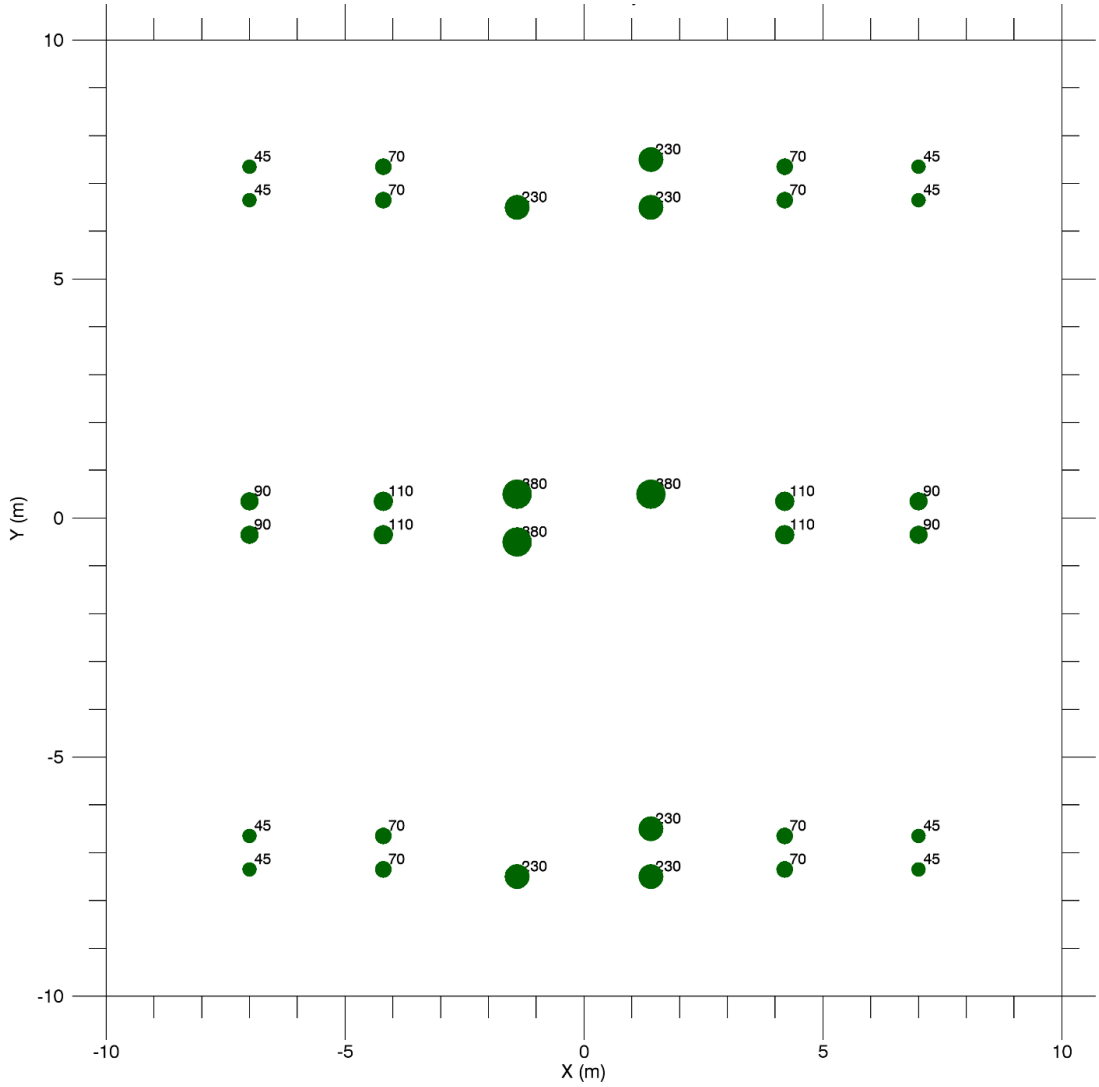

Figure 2. Layout of the modelled 5085 in^3 airgun array, which includes 24 active elements and no inactive elements. Tow depth is 10 m. The labels indicate the firing volume (in cubic inches) for each airgun. The convention is that the array is towed in the positive *x* direction.

Figure 3 shows the broadside (perpendicular to the tow direction), endfire (parallel to the tow direction), and vertical overpressure signatures and corresponding power spectrum levels for the 5085 in^3 airgun array towed at a depth of 10 m. For this array, most of the energy is projected at frequencies below 500 Hz.

Horizontal 1/3-octave-band source levels are shown as a function of band centre frequency and azimuth (Figure 4); directivity in the sound field is most noticeable at mid-frequencies as described in the model details (Appendix B.5).

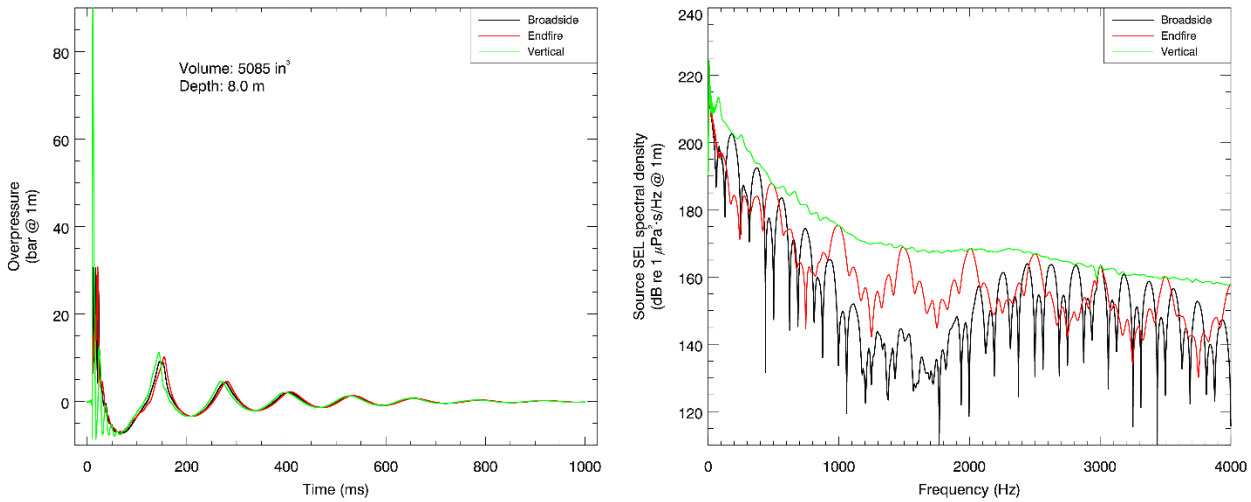

Figure 3. 5085 in^3 airgun array: Predicted source level details. (Left) the overpressure signature and (right) the power spectrum for broadside (perpendicular to tow direction) and endfire (directly aft of the array) directions, and for vertically down.

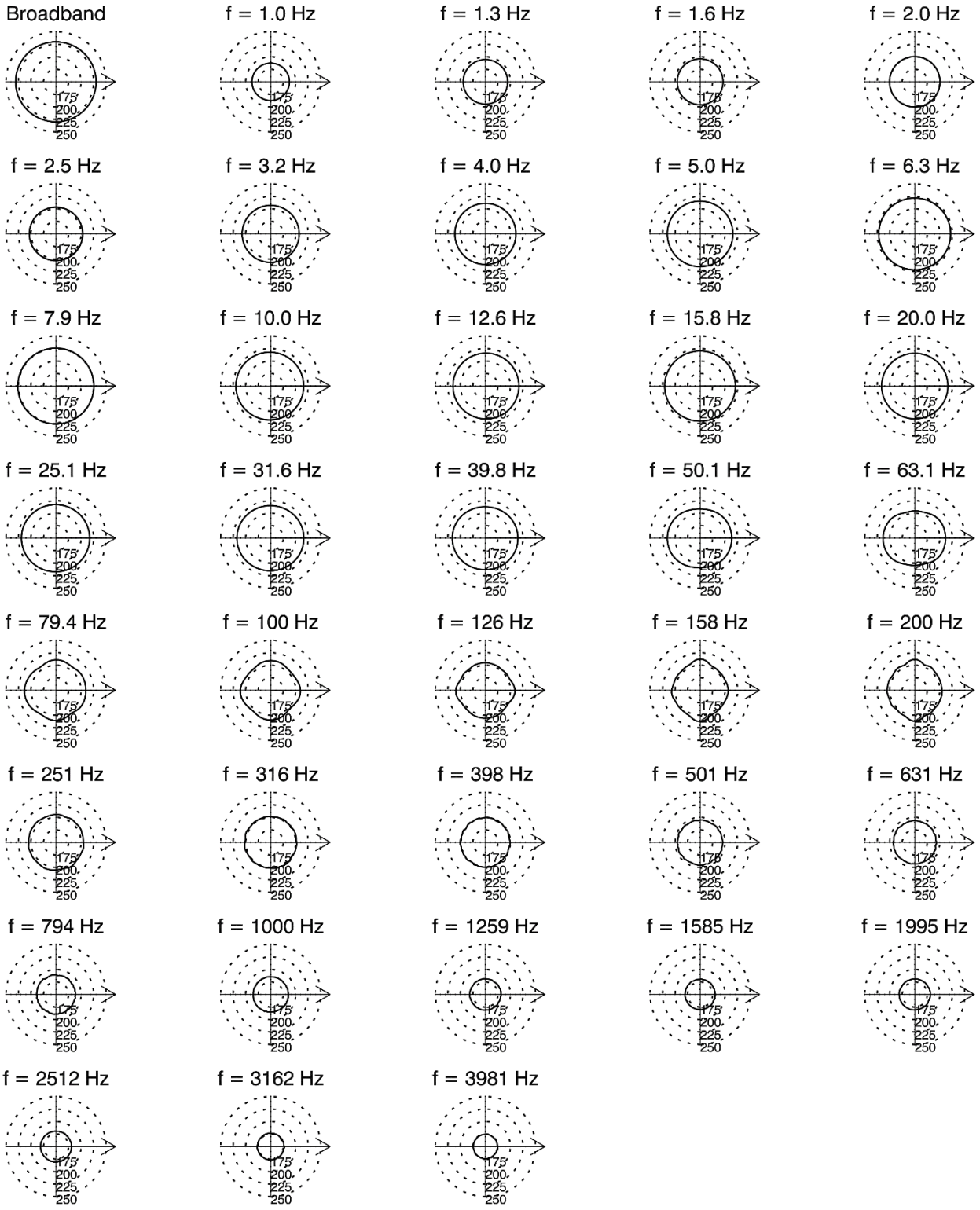

Figure 4. 5085 in^3 airgun array (1–4000 Hz): Directionality of the predicted horizontal source levels. Source levels (in dB re 1 µPa^2·s·m) are shown as a function of azimuth for the centre frequencies of the 1/3-octave-bands modelled; frequencies are shown above the plots. Tow direction is to the right. Tow depth is 10 m (see Figure 2).

2.3. Environmental Parameters

2.3.1. Bathymetry

Water depths throughout the project area were extracted from the SRTM15+ global bathymetry grid (Smith and Sandwell 1997, Becker et al. 2009), a 15 arc-second grid (approximately 350 × 465 m at the studied latitudes) rendered for the entire globe (Rodríguez et al. 2005). The water depth in the modelled sites varies from as little as 35 m in some shallow sites to >4000 m in the deeper abyssal areas east of the continental shelf. The combined effect of water depth and seabed geoacoustics may strongly influence sound propagation. For modelling purposes, the bathymetry was rendered using a uniform horizontal grid resolution of 250 m. Contour lines that illustrate the bathymetry of the modelling areas are shown in the maps of Appendix C.

2.3.2. Water Column Sound Speed Profile

During the AMAR deployment, the conductivity, temperature, depth, and sound speed of the water column were measured with a Minos Plus X CTD (AML Oceanographic) at each deployment location. The SSPs were extended in depth to the maximum water depth measured at each site using the equation of Coppens (1981). According to Warner and Martin (2018), the CTD malfunctioned at sites 7–9 so direct measurements of the SSP were not available. The airgun operators provided a modelled SSP for site 7 based on the location and time of year.

The SSP derived from measured data, as described above, was used in the geoacoustic inversion study. For sites 8 and 9, measured data was not available, so the SSP was derived from temperature and salinity profiles obtained from the U.S. Naval Oceanographic Office's Generalized Digital Environmental Model V 3.0 (GDEM; Teague et al. 1990, Carnes 2009). GDEM provides an ocean climatology of temperature and salinity for the world's oceans on a latitude-longitude grid with 0.25° resolution, with a temporal resolution of one month, based on global historical observations from the U.S. Navy's Master Oceanographic Observational Data Set (MOODS). The climatology profiles include 78 fixed depth points to a maximum depth of 6800 m (where the ocean is that deep). The GDEM temperature-salinity profiles were converted to sound speed profiles according to Coppens (1981).

For the transmission loss modelling described in the present study, GDEM was used to estimate the SSP at all the sites; the GDEM July data was used for the summer modelling, and February for the winter data. Since measured SSP data was not available at all sites even for summer, and at none of the sites for winter, it was deemed more appropriate to use the historical average GDEM profiles for all the transmission loss (TL) modelling, for the sake of consistency and to enable more meaningful comparisons between the TL results for different sites, and between summer and winter results. Appendix B.1 shows all the summer (July) sound speed profiles used for the present transmission loss modelling study, and Appendix B.2 shows the ones used for winter (February).

2.4. Geoacoustic Bottom Parameters

The geoacoustic properties of surficial layers depend on the sediment type. As the porosity decreases, the compressional sound speed, sediment bulk density, and compressional attenuation increase. The MONM transmission loss model (Appendix B.4) assumes a single geoacoustic profile of the seafloor for the entire modelled area. The acoustic properties required by MONM are:

- Sediment bulk density,
- Compressional-wave (or P-wave) sound speed,
- P-wave attenuation in decibels per wavelength,
- Shear-wave (or S-wave) sound speed and S-wave attenuation, in decibels per wavelength.

2.4.1. Generic Sand Geoacoustic Bottom Parameters

A generic geoacoustic profile based on a typical sand bottom (Table 4) is used as a control and a reference point for comparison with transmission loss modelling based on geoacoustic inversion bottom parameters (see Section 2.4.2) and also used to provide geoacoustic parameters for the six sites where the geoacoustic inversion procedure was not possible, or not successful.

Table 4. Geoacoustic parameters derived for a generic sand bottom.

Depth below seafloor (m)	Material	Density (g/cm^3)	P-wave speed (m/s)	P-wave attenuation (dB/λ)	S-wave speed (m/s)	S-wave attenuation (dB/λ)
0–20	Generic sand	2.04–2.10	1670–2050	0.19–1.30	300	0.02
20–350		2.10–2.40	2050–3500	1.30–0.35		
>350		2.60	5500	0.28		

2.4.2. Geoacoustic Inversion Bottom Parameters

Warner and MacGillivray (2018) provide the details of the geoacoustic inversion study that was performed to estimate the geoacoustic bottom properties. The inversions were applied to the received SEL data to estimate subbottom geoacoustic properties along each survey track at 14 sites. The received SEL are dependent on the source levels and the transmission loss (Equation B-1), the latter being dependent on the environment and source/receiver geometry. Source levels were considered unknown parameters and estimated in the inversion. Transmission loss was calculated using JASCO's Marine Operations Noise Model (MONM; see Appendix B.4) using postulated environmental models (i.e., set of site-dependent environmental parameters) and known source and receiver depths and ranges. The results are given in Table 5.

Table 5. Geoacoustic profiles for all sites (S) and tracks (T) where inversion was performed. Compressional wave sound speed (c_p) and attenuation (a_p) as well as density (ρ) are depth-dependent. Shear wave speed (c_s) and attenuation (a_s) are depth-independent (see Warner and Martin 2018).

Depth (mbsf)	c_p (m/s)	ρ (g/cm³)	a_p (dB/λ)	c_s (m/s)	a_s (dB/λ)
S1, T1					
0.0–26.1	1833–2058	1.94–2.22	0.09–0.45	408	3.02
26.1	2493	2.44	0.52		
S2, T1					
0	1753	2.09	0.09	273	3.89
S3, T2					
0.0–168.2	1668–1722	1.74–2.01	0.10–0.02	271	3.56
168.2	1944	2.06	0.2		
S7, T1					
0	1716	1.66	0.18	375	0.13
S8, T2					
0.0–3.5	1457–1576	1.36–1.80	0.09–0.49	627	0.47
3.5	2201	2.19	0.53		
S9, T2					
0.0–257.4	1776–1789	2.22–2.09	0.75–1.00	746	3.88
257.4	1923	2.41	0.02		
S11, T2					
0	1921	2.48	0.46	168	3.00
S12, T2					
0.0–13.2	1578–2065	1.72–2.17	0.07–0.04	287	3.73
13.2	2197	2.47	0.46		
S14, T1					
0.0–45.4	1702–1836	1.96–2.21	0.05–0.23	615	1.84
45.4	2067	2.17	0.6		
S17, T1					
0	1694	2.09	0.12	47	0.83
S18, T1					
0	1916	2.22	0.51	139	1.02
S20, T1					
0	2090	2.21	0.02	74	3.5
S1, T2					
0.0–20.3	1529–1965	1.45–2.30	0.58–0.04	140	3.43
20.3	2330	1.94	0.44		
S2, T2					
0.0–99.1	1762–1867	1.77–2.07	0.05–0.01	406	2.49
99.1	2328	1.97	0.6		
S4, T1					
0.0–143.0	1629–1691	1.58–2.04	0.02–0.02	435	0.24
143	1909	1.94	0.74		
S7, T2					
0.0–91.8	1627–1805	1.99–2.03	0.12–0.06	406	2.58
91.8	2150	2.15	0.69		
S9, T1					
0.0–67.6	1736–1762	1.92–1.77	0.42–0.98	744	3.65
67.6	1802	2.18	0.37		
S11, T1					
0	2014	2.04	0.74	330	1.69
S12, T1					
0.0–20.3	1673–2124	1.81–2.30	0.01–0.47	285	0.88
20.3	2189	2.44	0.99		
S13, T1					
0	1873	2.06	0.03	221	2.71
S14, T2					
0.0–31.2	1525–1554	1.72–1.71	0.09–0.14	473	3.7
31.2	2096	1.49	0.05		
S17, T2					
0.0–115.5	1561–1738	1.68–2.12	0.05–0.49	74	2.25
115.5	1739	1.5	0.14		
S18, T2					
0	2243	1.34	0.95	206	3.6

2.5. Acoustic Effects Criteria

The perceived loudness of sound, especially impulsive noise such as from seismic airguns, is not generally proportional to the instantaneous acoustic pressure. Rather, perceived loudness depends on the time over which the pulse rises, its duration, and its frequency content and, most of all, on the auditory sensitivity of the receiver for the frequencies contained in the sound. Thus, several sound level metrics are commonly used to evaluate noise and its effects on marine life. Table 6 lists the metrics applied in this report: weighted sound exposure level (SEL)—see definition in Appendix A.1. The acoustic metrics in this report reflect the updated ANSI and ISO standards for acoustic terminology, ANSI-ASA S1.1 (R2013) and ISO/DIS 18405.2:2017 (2016).

At what levels acoustic exposure levels might injure or disturb marine mammals is an active research topic. Since the late 1990's, several expert groups have investigated an SEL-based assessment approach for injury (e.g. HESS 1999, Southall et al. 2007; NOAA 2013, 2015; NMFS 2016, 2018). The number of studies that investigate the level of disturbance to marine animals by underwater noise has also increased substantially. Based on the best available science, the following sound level thresholds were assessed:

- Weighted SEL thresholds for injury to marine mammals, based on the 2018 NOAA Technical Guidance (MNFS 2018; see Appendix A.3). SEL is assessed by integrating over the period of the activity or 24 hours, whichever is shorter.
- Behavioural thresholds for impulsive sound sources are generally assessed based on NOAA's MMPA thresholds for behavioural response at an SPL of 160 dB re 1 µPa for impulsive sounds and an SPL of 120 dB re 1 µPa for non-impulsive sounds for all marine mammal species (NOAA 2005). Southall et al. (2007) promoted the use of TTS onset levels as criteria for behavioural disturbance. While this has been recognised by NOAA / NMFS (see Table AE-1 of NMFS 2018), they also take into account that behavioural disruption occurs at levels below onset of TTS. In this study we have reported the TTS levels as a proxy for behavioural threshold, per Southall et al. 2007. Additional details are presented in Appendix A.2.2.

The reported distances to all thresholds are calculated as maximum level over the entire water column. Details on each set of thresholds and the associated frequency-weighting are provided in Appendices A.2–A.3.

Table 6. The marine mammal impacts acoustic thresholds used in this study (based on NMFS 2018).

Hearing group	Impulsive source, PTS-onset	Impulsive source, TTS-onset
	Weighted SEL (24 h)	Weighted SEL (24 h)
Low-frequency cetaceans	183	168
Mid-frequency cetaceans	185	170
High-frequency cetaceans	155	140
Phocid pinnipeds in water	185	170
Otariid pinnipeds in water	203	188

3. Per-Pulse SEL Results

The graphical results of underwater propagation loss modelling of the environmental noise projected in the water column for a towed airgun array that is representative of a seismic survey source are presented in Appendix C in the form of coverage maps. For most of the stations, the modelling for frequencies below 5.5 kHz was performed using the MONM (PE) propagation loss model and above 5.5 kHz the BELLHOP (Gaussian Beam Ray-Theory) model was used; an overview of both models is included in Appendix B.4. For stations 4 and 5, the dividing frequency between the PE and BELLHOP models is 1.65 kHz.

Three rounds of per-pulse sound exposure level (SEL) modelling were performed. In the first round, the SEL received at the planned AMAR location and depth for each of the 20 sites, for a historical average summer (July) SSP, was modelled as a function of the source location (varied in range and azimuth) using geoacoustic parameters for a generic sand bottom. In addition, the same modelling was repeated using the geoacoustic bottom parameters given by Warner and MacGillivray (2018) at the 14 sites where they were available. The modelling results are presented in the form of coloured maps where the colour at any map location represents the predicted received SEL *at the AMAR* for the source located at that spot on the map. In addition to the unweighted SEL results, supplemental maps are presented in each case for five marine mammal received level auditory weightings. See Appendix C.1 to C.6.

In the second round of modelling, also for a historical average summer (July) SSP, the source was held fixed at the planned AMAR location (but at a 10 m tow depth), and the maximum-over-depth per-pulse SEL was calculated for distant receiver locations. These results are similarly displayed in coloured maps of per-pulse SEL, but for the second round modelling the colours on the map represent the maximum-over-depth received level *at that spot on the map*. The modelling used the geoacoustic inversion bottom parameters at the 14 sites where they were available and only used a generic sand bottom at the other six sites. As with the round one modelling, the results are presented in unweighted form and for five marine mammal auditory weightings. See Appendix C.7 to C.12.

The third round of per-pulse SEL modelling was very similar to the second round, the only difference being the substitution of the historical average winter (February) SSP. See Appendix C.13 to C.18.

In most cases, the modelling was limited to a square geographic area of 160 km on each side, centred on the station location. In three cases, the modelling was restricted to a smaller geographic area, no more than 25–30 km from the station location (i.e., the T2-inversion geoacoustic bottom for station 9 and both the T1 and T2-inversion geoacoustic bottoms for station 14). The particulars of the geoacoustic bottom parameters appeared to require more carefully tuned propagation modelling at higher ranges (such as reduced range steps) in these three cases, which was not attempted for this study.

3.1. Tabular Results

A quantitative summary of the second and third round per-pulse SEL results (maximum-over-depth SEL at a distant receiver from a source fixed at the AMAR location and a 10 m tow depth) is provided in Tables 7 through 26.

Table 7. Stun 1: Horizontal distances to modelled maximum-over-depth per-pulse SEL values; maximum (R_{max}, m) and 95% ($R_{95\%}$, m); 5058 in³ airgun array.

SEL (dB re 1 µPa²·s)	Summer		Winter	
	R_{max}	$R_{95\%}$	R_{max}	$R_{95\%}$
210	< 15	< 15	< 15	< 15
205	15	15	15	15
200	23	23	23	23
195	41	39	41	39
190	70	63	72	66
185	309	149	309	159
180	529	379	520	399
175	1,290	950	1,270	963
170	2,980	2,210	2,920	2,310
165	5,120	4,050	5,740	4,210
160	8,390	6,750	10,100	7,080
155	14,000	10,800	20,200	12,200
150	21,200	17,100	53,300	24,700
145	41,700	28,900	79,900	65,200
140	> 80,000	59,200	> 80,000	> 80,000
135		> 80,000		
130				
125				
120				

Table 8. Stn 2: Horizontal distances to modelled maximum-over-depth per-pulse SEL values; maximum (R_{max}, m) and 95% ($R_{95\%}$, m); 5058 in³ airgun array.

SEL (dB re 1 µPa²·s)	Summer		Winter	
	R_{max}	$R_{95\%}$	R_{max}	$R_{95\%}$
210	< 15	< 15	< 15	< 15
205	15	15	15	15
200	23	23	23	23
195	41	39	41	40
190	79	70	80	71
185	219	193	229	202
180	379	341	399	353
175	789	560	849	729
170	2,680	1,940	2,730	2,070
165	4,900	3,960	5,790	4,360
160	9,230	7,410	10,700	8,180
155	18,600	13,400	21,700	15,300
150	26,800	20,700	43,300	27,900
145	42,600	30,900	74,800	46,900
140	52,400	40,400	81,900	73,300
135	69,500	51,000	86,300	77,500
130	> 80,000	66,900	> 113,000	90,500
125		77,500		> 94,600
120		> 80,000		

Table 9. Stn 3: Horizontal distances to modelled maximum-over-depth per-pulse SEL values; maximum (R_{max}, m) and 95% ($R_{95\%}$, m); 5058 in³ airgun array.

SEL (dB re 1 µPa²·s)	Summer		Winter	
	R_{max}	$R_{95\%}$	R_{max}	$R_{95\%}$
210	< 15	< 15	< 15	< 15
205	19	19	19	19
200	29	28	31	31
195	49	42	51	44
190	89	72	99	82
185	189	150	229	189
180	489	399	659	531
175	1,230	1,000	1,380	1,160
170	2,330	1,940	2,730	2,140
165	4,510	3,640	5,180	4,230
160	8,910	6,800	10,100	8,160
155	12,200	9,980	14,600	11,800
150	22,800	17,400	42,000	36,100
145	43,600	37,900	54,200	46,600
140	51,300	45,400	76,500	60,800
135	78,100	64,700	> 80,000	> 80,000
130	> 86,200	83,400		
125		> 86,200		

Table 10. Stn 4: Horizontal distances to modelled maximum-over-depth per-pulse SEL values; maximum (R_{max}, m) and 95% ($R_{95\%}$, m); 5058 in³ airgun array.

SEL (dB re 1 µPa²·s)	Summer		Winter	
	R_{max}	$R_{95\%}$	R_{max}	$R_{95\%}$
210	< 15	< 15	< 15	< 15
205	15	15	15	15
200	23	23	23	23
195	41	39	41	39
190	70	63	70	63
185	129	111	130	113
180	229	198	230	201
175	409	350	410	356
170	729	626	739	633
165	1,330	1,150	1,330	1,150
160	4,830	3,530	5,880	3,710
155	10,200	7,540	17,900	9,100
150	20,800	12,400	43,200	25,700
145	34,900	23,400	> 80,000	71,700
140	74,600	49,000		76,200
135	> 81,600	> 81,600		> 80,000
130				
125				

Table 11. Stn 5: Horizontal distances to modelled maximum-over-depth per-pulse SEL values; maximum (R_{max}, m) and 95% ($R_{95\%}$, m); 5058 in³ airgun array.

SEL (dB re 1 µPa²·s)	Summer		Winter	
	R_{max}	$R_{95\%}$	R_{max}	$R_{95\%}$
210	< 15	< 15	< 15	< 15
205	15	15	15	15
200	23	23	23	23
195	41	40	41	40
190	73	64	73	67
185	130	113	130	114
180	230	198	230	201
175	411	357	420	361
170	760	661	761	667
165	2,700	2,160	2,710	2,160
160	4,270	3,560	5,990	3,960
155	13,200	8,070	20,900	11,200
150	29,100	19,100	52,600	35,400
145	55,100	34,900	> 80,000	71,800
140	> 80,000	69,200		77,400
135		> 80,000		> 80,000
130				
125				

Table 12. Stn 6: Horizontal distances to modelled maximum-over-depth per-pulse SEL values; maximum (R_{max}, m) and 95% ($R_{95\%}$, m); 5058 in³ airgun array.

SEL (dB re 1 µPa²·s)	Summer		Winter	
	R_{max}	$R_{95\%}$	R_{max}	$R_{95\%}$
210	< 15	< 15	< 15	< 15
205	15	15	15	15
200	23	23	23	23
195	41	39	41	39
190	70	63	70	63
185	130	113	130	113
180	239	201	240	205
175	409	353	419	359
170	769	671	779	673
165	2,510	2,080	2,510	2,160
160	13,100	3,530	7,960	3,810
155	16,300	8,560	16,500	11,000
150	30,500	18,600	43,100	26,100
145	57,900	36,100	> 80,000	69,600
140	> 81,600	66,300		77,400
135		> 81,600		> 80,000
130				
125				

Table 13. Stn 7: Horizontal distances to modelled maximum-over-depth per-pulse SEL values; maximum (R_{max}, m) and 95% ($R_{95\%}$, m); 5058 in³ airgun array.

SEL (dB re 1 µPa²·s)	Summer		Winter	
	R_{max}	$R_{95\%}$	R_{max}	$R_{95\%}$
210	< 15	< 15	< 15	< 15
205	15	15	15	15
200	23	23	23	23
195	41	39	41	39
190	90	80	92	82
185	189	164	199	172
180	309	271	329	288
175	739	626	839	689
170	2,230	1,490	2,290	1,780
165	3,640	2,930	4,530	3,350
160	6,610	5,250	8,140	5,960
155	11,100	8,220	16,000	10,000
150	14,200	11,700	23,800	16,700
145	21,100	16,200	39,400	29,600
140	30,700	21,600	61,400	42,300
135	35,200	28,100	> 80,000	69,100
130	39,300	33,700		75,700
125	47,000	40,600		> 80,000
120	59,300	49,900		
115	73,400	60,800		
110	> 80,000	73,900		
105		> 80,000		

Table 14. Stn 8: Horizontal distances to modelled maximum-over-depth per-pulse SEL values; maximum (R_{max}, m) and 95% ($R_{95\%}$, m); 5058 in³ airgun array.

SEL (dB re 1 µPa²·s)	Summer		Winter	
	R_{max}	$R_{95\%}$	R_{max}	$R_{95\%}$
210	< 15	< 15	< 15	< 15
205	15	15	15	15
200	23	23	23	23
195	41	40	41	40
190	70	63	73	67
185	140	117	140	121
180	270	238	270	238
175	650	586	660	598
170	1,340	1,040	1,390	1,110
165	2,500	1,900	3,550	2,080
160	5,040	3,430	7,040	4,160
155	9,190	5,700	17,200	10,700
150	12,200	9,500	40,800	24,300
145	21,400	15,200	> 80,000	66,100
140	50,600	27,900		75,100
135	63,400	53,100		> 80,000
130	> 86,300	> 86,300		
125				

Table 15. Stn 9: Horizontal distances to modelled maximum-over-depth per-pulse SEL values; maximum (R_{max}, m) and 95% ($R_{95\%}$, m); 5058 in³ airgun array.

SEL (dB re 1 µPa²·s)	Summer		Winter	
	R_{max}	$R_{95\%}$	R_{max}	$R_{95\%}$
210	< 15	< 15	< 15	< 15
205	15	15	15	15
200	23	23	23	23
195	40	39	40	39
190	72	66	80	70
185	131	113	139	120
180	210	181	250	201
175	360	302	400	341
170	530	454	690	544
165	770	683	1,130	920
160	1,160	989	2,030	1,550
155	1,550	1,440	3,280	2,570
150	2,220	2,040	5,250	4,000
145	3,380	3,000	6,650	5,480
140	4,660	4,190	8,970	7,090
135	6,430	5,640	13,300	10,400
130	8,600	7,510	17,700	14,300
125	10,800	9,830	38,500	30,800
120	13,600	12,000	> 80,000	73,700
115	16,300	14,300		> 80,000
110	18,500	16,400		
105	20,600	18,900		
100	23,900	20,900		
95	> 25,500	23,200		

Table 16. Stn 10: Horizontal distances to modelled maximum-over-depth per-pulse SEL values; maximum (R_{max}, m) and 95% ($R_{95\%}$, m); 5058 in³ airgun array.

SEL (dB re 1 µPa²·s)	Summer		Winter	
	R_{max}	$R_{95\%}$	R_{max}	$R_{95\%}$
210	< 15	< 15	< 15	< 15
205	15	15	15	15
200	23	23	23	23
195	40	39	40	39
190	82	72	89	80
185	249	211	249	214
180	560	514	569	518
175	1,510	1,090	1,520	1,140
170	2,920	2,330	2,970	2,480
165	6,680	5,040	7,050	5,330
160	9,750	7,930	11,400	8,370
155	19,400	12,300	22,200	14,100
150	23,100	18,300	28,900	20,800
145	33,800	25,800	40,300	30,700
140	49,900	41,100	66,900	51,700
135	66,900	56,200	> 80,000	77,200
130	> 81,600	70,800		> 80,000
125		> 81,600		
120				
115				
110				
105				
100				
95				

Table 17. Stn 11: Horizontal distances to modelled maximum-over-depth per-pulse SEL values; maximum (R_{max}, m) and 95% ($R_{95\%}$, m); 5058 in³ airgun array.

SEL (dB re 1 µPa²·s)	Summer		Winter	
	R_{max}	$R_{95\%}$	R_{max}	$R_{95\%}$
210	< 14	< 14	< 14	< 14
205	14	14	14	14
200	23	23	23	23
195	41	40	41	40
190	80	70	80	70
185	240	206	240	206
180	370	335	370	335
175	1,060	951	1,240	951
170	2,580	1,960	2,570	2,000
165	4,330	3,600	4,330	3,770
160	7,600	6,100	10,400	6,430
155	13,100	9,930	16,500	11,200
150	19,800	14,900	32,000	20,100
145	32,200	23,400	67,500	41,000
140	59,200	41,700	> 80,000	72,400
135	> 80,000	74,100		> 80,000
130		> 80,000		
125				

Table 18. Stn 12: Horizontal distances to modelled maximum-over-depth per-pulse SEL values; maximum (R_{max}, m) and 95% ($R_{95\%}$, m); 5058 in³ airgun array.

SEL (dB re 1 µPa²·s)	Summer		Winter	
	R_{max}	$R_{95\%}$	R_{max}	$R_{95\%}$
210	< 15	< 15	< 15	< 15
205	15	15	15	15
200	23	23	23	23
195	41	39	41	39
190	79	70	79	70
185	270	245	270	243
180	540	411	539	407
175	1,590	1,190	1,590	1,170
170	3,400	2,630	3,940	2,660
165	7,800	5,580	8,230	5,670
160	14,400	9,990	13,400	10,000
155	22,200	16,800	24,100	17,500
150	47,500	27,700	55,500	29,900
145	62,700	44,300	78,400	53,500
140	> 80,000	64,000	> 80,000	75,000
135		> 80,000		> 80,000
130				
125				

Table 19. Stn 13: Horizontal distances to modelled maximum-over-depth per-pulse SEL values; maximum (R_{max}, m) and 95% ($R_{95\%}$, m); 5058 in³ airgun array.

SEL (dB re 1 µPa²·s)	Summer		Winter	
	R_{max}	$R_{95\%}$	R_{max}	$R_{95\%}$
210	< 15	< 15	< 15	< 15
205	15	15	15	15
200	23	23	23	23
195	41	39	41	39
190	79	66	79	66
185	149	121	159	129
180	269	220	279	233
175	479	390	489	399
170	896	734	999	741
165	3,010	2,530	3,020	2,540
160	5,210	3,900	6,130	3,960
155	19,200	9,760	24,000	10,500
150	32,800	21,300	43,000	24,000
145	71,900	51,300	78,600	60,100
140	> 86,300	> 86,300	> 80,000	> 80,000
135				
130				
125				

Table 20. Stn 14: Horizontal distances to modelled maximum-over-depth per-pulse SEL values; maximum (R_{max}, m) and 95% ($R_{95\%}$, m); 5058 in³ airgun array.

SEL (dB re 1 µPa²·s)	Summer		Winter	
	R_{max}	$R_{95\%}$	R_{max}	$R_{95\%}$
210	< 15	< 15	< 15	< 15
205	15	15	15	15
200	23	23	23	23
195	41	39	41	39
190	70	63	70	63
185	130	114	130	114
180	239	205	239	206
175	430	379	430	380
170	1,400	1,130	1,400	1,160
165	> 46,800	> 46,800	25,000	23,300
160			> 27,000	> 27,000
155				
150				
145				
140				
135				
130				
125				

Table 21. Stn 15: Horizontal distances to modelled maximum-over-depth per-pulse SEL values; maximum (R_{max}, m) and 95% ($R_{95\%}$, m); 5058 in³ airgun array.

SEL (dB re 1 µPa²·s)	Summer		Winter	
	R_{max}	$R_{95\%}$	R_{max}	$R_{95\%}$
210	< 15	< 15	< 15	< 15
205	15	15	15	15
200	23	23	23	23
195	41	40	41	40
190	71	64	73	67
185	130	114	130	114
180	230	200	230	202
175	430	378	440	380
170	790	667	800	674
165	2,770	2,250	2,770	2,260
160	4,860	3,740	4,860	3,780
155	16,500	8,410	16,500	8,870
150	36,000	20,100	36,100	21,200
145	64,700	42,600	76,900	47,800
140	> 86,300	73,500	> 80,000	77,000
135		> 86,300		> 80,000
130				
125				

Table 22. Stn 16: Horizontal distances to modelled maximum-over-depth per-pulse SEL values; maximum (R_{max}, m) and 95% ($R_{95\%}$, m); 5058 in³ airgun array.

SEL (dB re 1 µPa²·s)	Summer		Winter	
	R_{max}	$R_{95\%}$	R_{max}	$R_{95\%}$
210	< 15	< 15	< 15	< 15
205	15	15	15	15
200	23	23	23	23
195	41	39	41	39
190	70	63	70	63
185	130	113	131	114
180	229	199	229	200
175	419	357	419	360
170	820	664	824	674
165	2,520	2,180	2,520	2,190
160	9,410	7,100	9,470	7,180
155	16,200	10,100	19,500	12,000
150	25,100	19,300	42,500	23,900
145	51,500	34,500	> 80,000	62,500
140	> 80,000	69,500		77,400
135		> 80,000		> 80,000
130				
125				

Table 23. Stn 17: Horizontal distances to modelled maximum-over-depth per-pulse SEL values; maximum (R_{max}, m) and 95% ($R_{95\%}$, m); 5058 in³ airgun array.

SEL (dB re 1 µPa²·s)	Summer		Winter	
	R_{max}	$R_{95\%}$	R_{max}	$R_{95\%}$
210	< 15	< 15	< 15	< 15
205	15	15	15	15
200	23	23	23	23
195	41	39	41	39
190	70	64	72	66
185	130	116	131	116
180	239	203	239	205
175	440	376	440	379
170	979	724	979	729
165	2,750	2,040	2,750	2,080
160	7,860	3,510	7,860	3,560
155	13,400	8,290	13,400	8,750
150	28,000	17,600	32,600	22,600
145	47,200	37,300	67,400	40,800
140	> 86,200	70,600	> 80,000	75,400
135		> 86,200		> 80,000
130				
125				

Table 24. Stn 18: Horizontal distances to modelled maximum-over-depth per-pulse SEL values; maximum (R_{max}, m) and 95% ($R_{95\%}$, m); 5058 in³ airgun array.

SEL (dB re 1 µPa²·s)	Summer		Winter	
	R_{max}	$R_{95\%}$	R_{max}	$R_{95\%}$
210	< 15	< 15	< 15	< 15
205	15	15	15	15
200	23	23	23	23
195	41	40	41	40
190	92	85	100	86
185	260	206	260	215
180	540	417	560	497
175	1,580	1,200	1,610	1,340
170	3,260	2,520	4,070	2,640
165	7,420	5,530	8,900	6,060
160	14,000	10,400	15,200	11,400
155	22,900	17,100	26,000	19,300
150	36,200	27,000	46,700	32,400
145	53,100	41,100	76,500	52,400
140	78,200	61,700	> 80,000	74,600
135	> 86,300	79,900		> 80,000
130		> 86,300		
125				

Table 25. Stn 19: Horizontal distances to modelled maximum-over-depth per-pulse SEL values; maximum (R_{max}, m) and 95% ($R_{95\%}$, m); 5058 in³ airgun array.

SEL (dB re 1 µPa²·s)	Summer		Winter	
	R_{max}	$R_{95\%}$	R_{max}	$R_{95\%}$
210	< 15	< 15	< 15	< 15
205	15	15	15	15
200	23	23	23	23
195	41	40	41	40
190	71	63	73	67
185	130	114	131	116
180	241	206	250	207
175	430	364	440	369
170	1,610	1,540	1,610	1,540
165	2,530	2,170	2,530	2,190
160	5,380	4,230	5,960	4,510
155	17,700	10,800	17,700	11,500
150	41,300	24,900	44,600	26,900
145	77,000	51,700	79,800	60,800
140	> 86,300	79,100	> 80,000	> 80,000
135		> 86,300		
130				
125				

Table 26. Stn 20: Horizontal distances to modelled maximum-over-depth per-pulse SEL values; maximum (R_{max}, m) and 95% ($R_{95\%}$, m); 5058 in³ airgun array.

SEL (dB re 1 µPa²·s)	Summer		Winter	
	R_{max}	$R_{95\%}$	R_{max}	$R_{95\%}$
210	< 15	< 15	< 15	< 15
205	15	15	15	15
200	23	23	23	23
195	41	40	41	40
190	73	64	73	64
185	210	177	210	177
180	530	410	530	422
175	1,190	946	1,190	970
170	4,140	2,780	4,160	2,890
165	10,700	7,060	11,500	7,670
160	26,000	17,600	27,200	18,200
155	52,400	37,400	51,800	38,300
150	> 86,300	79,200	> 80,000	> 80,000
145		> 86,300		
140				
135				
130				
125				

4. Modelled Survey Cumulative SEL Results

The marine mammal injury (PTS) and temporary threshold shift (TTS) metrics in NMFS (2018) are based on the SEL accumulated over a 24-hour period. The previous section presented SEL coverage distances based on a single pulse from the airgun array. If the airgun were fired *N* times in a 24-hour period, without moving relative to the receiver (i.e., animal) the 24-hour cumulative SEL ($L_{E,24\mathrm{h}}$) could be calculated from the per-pulse SEL ($L_{E,\mathrm{p}}$) using the following formula:

$$L_{E,24\mathrm{h}} = L_{E,\mathrm{P}} + 10\log_{10} N\,. \quad (1)$$

The same $R_{\max}$ or $R_{95\%}$ values shown for the indicated $L_{E,\mathrm{P}}$ value would apply with respect to a 24-hour SEL of $L_{E,24\mathrm{h}}$ if the equivalent $L_{E,\mathrm{p}} = L_{E,24\mathrm{h}} - 10\log_{10} N$ is used as a reference.

This stationary configuration is not generally the situation with actual seismic surveys, however, as the airgun array is typically towed along a survey track, and the distance between the source and the receiver (i.e., animal) shrinks as the source approaches (usually making the noise louder) and then widens as the source passes and recedes (and the sound level drops). For the purpose of modelling a more realistic 24-hour cumulative SEL representative of a seismic survey scenario, the airgun array was simulated to be towed along a single straight survey track, starting 14.8 km due south of the station location, and proceeding on a heading directly north at 4 kts, firing an airgun array pulse every 12 seconds, ending 14.8 km due north of the station. At this speed, the modelled track segment had a duration of 4 hours; 2 hours south of the station and 2 hours north.

A square computational grid of receivers was modelled up to 160 km wide in the north-south and east-west directions, centered on the station, with 10 m grid spacing on an inner 40-km-wide grid, and 30 m grid spacing on the outer part. For every shot fired from the array, the acoustic transmission loss from the location of the array at that time to each point on the grid was used to calculate the SEL received at that grid location from that one pulse, and the SEL received from all the pulses in the survey was accumulated at each grid location. The shortest distance from each grid location to the survey track (i.e., the closest point of approach, or CPA) was then calculated as the minimum distance for $L_{E,24\mathrm{h}}$ not to exceed the SEL value accumulated at that grid location. The SEL value was then tabulated for the maximum of those distances in the grid.

This procedure was applied individually for the set of SEL source level weighting functions listed in Table 6. The safe distance where the threshold value of weighted SEL would be reached was determined from the maximum distances found in the grid for the corresponding $L_{E,24\mathrm{h}}$. These safe distances are reported in Section 4.1 for each station in the study.

4.1. Tabular Results

Tables 27 through 46 provide a quantitative summary of the single pass seismic survey towed airgun array (10 m tow depth) 24-hour cumulative SEL results (maximum-over-depth cumulative SEL at a receiver distant from the source track at the AMAR location). Although the modelling simulated a survey track of 4-hour duration, this was not measurably different from the 24-hour SEL. In the case of a single survey track pass because SEL accumulates rapidly during the approach of a moving source and very little accumulates as the range to the vessel increases (Martin et al. 2017b).

Table 27. Stn 1: Safe distances in metres from a seismic survey track to PTS- and TTS-onset thresholds (NMFS 2018) based on the SEL field for a track, 5058 in³ airgun array.

Marine mammal group	PTS-onset			TTS-onset		
	Weighted SEL (dB re 1 µPa²·s)	Summer safe dist. (m)	Winter safe dist. (m)	Weighted SEL (dB re 1 µPa²·s)	Summer safe dist. (m)	Winter safe dist. (m)
Low-frequency cetaceans	183	1,460	1,520	168	57,100	> 80,000
Mid-frequency cetaceans	185	< 10	< 10	170	< 10	< 10
High-frequency cetaceans	155	10	10	140	450	450
Phocid pinnipeds (underwater)	185	10	10	170	310	340
Otariid pinnipeds (underwater)	203	< 10	< 10	188	< 10	< 10

Table 28. Stn 2: Safe distances in metres from a seismic survey track to PTS- and TTS-onset thresholds (NMFS 2018) based on the SEL field for a track, 5058 in³ airgun array.

Marine mammal group	PTS-onset			TTS-onset		
	Weighted SEL (dB re 1 µPa²·s)	Summer safe dist. (m)	Winter safe dist. (m)	Weighted SEL (dB re 1 µPa²·s)	Summer safe dist. (m)	Winter safe dist. (m)
Low-frequency cetaceans	183	2,050	2,300	168	37,800	> 80,000
Mid-frequency cetaceans	185	< 10	< 10	170	< 10	< 10
High-frequency cetaceans	155	10	10	140	1,480	859
Phocid pinnipeds (underwater)	185	10	10	170	570	430
Otariid pinnipeds (underwater)	203	< 10	< 10	188	< 10	< 10

Table 29. Stn 3: Safe distances in metres from a seismic survey track to PTS- and TTS-onset thresholds (NMFS 2018) based on the SEL field for a track, 5058 in³ airgun array.

Marine mammal group	PTS-onset			TTS-onset		
	Weighted SEL (dB re 1 µPa²·s)	Summer safe dist. (m)	Winter safe dist. (m)	Weighted SEL (dB re 1 µPa²·s)	Summer safe dist. (m)	Winter safe dist. (m)
Low-frequency cetaceans	183	2,870	3,630	168	24,200	30,600
Mid-frequency cetaceans	185	< 10	< 10	170	< 10	< 10
High-frequency cetaceans	155	10	10	140	2,210	2,000
Phocid pinnipeds (underwater)	185	10	10	170	1,620	1,880
Otariid pinnipeds (underwater)	203	< 10	< 10	188	< 10	< 10

Table 30. Stn 4: Safe distances in metres from a seismic survey track to PTS- and TTS-onset thresholds (NMFS 2018) based on the SEL field for a track, 5058 in³ airgun array.

Marine mammal group	PTS-onset			TTS-onset		
	Weighted SEL (dB re 1 µPa²·s)	Summer safe dist. (m)	Winter safe dist. (m)	Weighted SEL (dB re 1 µPa²·s)	Summer safe dist. (m)	Winter safe dist. (m)
Low-frequency cetaceans	183	180	210	168	21,000	> 80,000
Mid-frequency cetaceans	185	< 10	< 10	170	< 10	< 10
High-frequency cetaceans	155	< 10	< 10	140	90	130
Phocid pinnipeds (underwater)	185	10	10	170	80	100
Otariid pinnipeds (underwater)	203	< 10	< 10	188	< 10	< 10

Table 31. Stn 5: Safe distances in metres from a seismic survey track to PTS- and TTS-onset thresholds (NMFS 2018) based on the SEL field for a track, 5058 in³ airgun array.

Marine mammal group	PTS-onset			TTS-onset		
	Weighted SEL (dB re 1 µPa²·s)	Summer safe dist. (m)	Winter safe dist. (m)	Weighted SEL (dB re 1 µPa²·s)	Summer safe dist. (m)	Winter safe dist. (m)
Low-frequency cetaceans	183	190	230	168	34,700	> 80,000
Mid-frequency cetaceans	185	< 10	< 10	170	< 10	< 10
High-frequency cetaceans	155	< 10	< 10	140	90	130
Phocid pinnipeds (underwater)	185	10	10	170	80	110
Otariid pinnipeds (underwater)	203	< 10	< 10	188	< 10	< 10

Table 32. Stn 6: Safe distances in metres from a seismic survey track to PTS- and TTS-onset thresholds (NMFS 2018) based on the SEL field for a track, 5058 in³ airgun array.

Marine mammal group	PTS-onset			TTS-onset		
	Weighted SEL (dB re 1 µPa²·s)	Summer safe dist. (m)	Winter safe dist. (m)	Weighted SEL (dB re 1 µPa²·s)	Summer safe dist. (m)	Winter safe dist. (m)
Low-frequency cetaceans	183	180	210	168	31,200	> 80,000
Mid-frequency cetaceans	185	< 10	< 10	170	< 10	< 10
High-frequency cetaceans	155	10	10	140	130	249
Phocid pinnipeds (underwater)	185	10	10	170	90	100
Otariid pinnipeds (underwater)	203	< 10	< 10	188	< 10	< 10

Table 33. Stn 7: Safe distances in metres from a seismic survey track to PTS- and TTS-onset thresholds (NMFS 2018) based on the SEL field for a track, 5058 in³ airgun array.

Marine mammal group	PTS-onset			TTS-onset		
	Weighted SEL (dB re 1 µPa²·s)	Summer safe dist. (m)	Winter safe dist. (m)	Weighted SEL (dB re 1 µPa²·s)	Summer safe dist. (m)	Winter safe dist. (m)
Low-frequency cetaceans	183	2,190	1,930	168	17,100	40,400
Mid-frequency cetaceans	185	< 10	< 10	170	< 10	< 10
High-frequency cetaceans	155	10	10	140	1,060	710
Phocid pinnipeds (underwater)	185	10	10	170	690	560
Otariid pinnipeds (underwater)	203	< 10	< 10	188	< 10	< 10

Table 34. Stn 8: Safe distances in metres from a seismic survey track to PTS- and TTS-onset thresholds (NMFS 2018) based on the SEL field for a track, 5058 in³ airgun array.

Marine mammal group	PTS-onset			TTS-onset		
	Weighted SEL (dB re 1 µPa²·s)	Summer safe dist. (m)	Winter safe dist. (m)	Weighted SEL (dB re 1 µPa²·s)	Summer safe dist. (m)	Winter safe dist. (m)
Low-frequency cetaceans	183	300	390	168	11,600	> 80,000
Mid-frequency cetaceans	185	< 10	< 10	170	< 10	< 10
High-frequency cetaceans	155	10	10	140	140	230
Phocid pinnipeds (underwater)	185	10	10	170	100	120
Otariid pinnipeds (underwater)	203	< 10	< 10	188	< 10	< 10

Table 35. Stn 9: Safe distances in metres from a seismic survey track to PTS- and TTS-onset thresholds (NMFS 2018) based on the SEL field for a track, 5058 in³ airgun array.

Marine mammal group	PTS-onset			TTS-onset		
	Weighted SEL (dB re 1 µPa²·s)	Summer safe dist. (m)	Winter safe dist. (m)	Weighted SEL (dB re 1 µPa²·s)	Summer safe dist. (m)	Winter safe dist. (m)
Low-frequency cetaceans	183	200	270	168	1,110	5,510
Mid-frequency cetaceans	185	< 10	< 10	170	< 10	< 10
High-frequency cetaceans	155	10	10	140	380	599
Phocid pinnipeds (underwater)	185	10	10	170	100	200
Otariid pinnipeds (underwater)	203	< 10	< 10	188	< 10	< 10

Table 36. Stn 10: Safe distances in metres from a seismic survey track to PTS- and TTS-onset thresholds (NMFS 2018) based on the SEL field for a track, 5058 in³ airgun array.

Marine mammal group	PTS-onset			TTS-onset		
	Weighted SEL (dB re 1 µPa²·s)	Summer safe dist. (m)	Winter safe dist. (m)	Weighted SEL (dB re 1 µPa²·s)	Summer safe dist. (m)	Winter safe dist. (m)
Low-frequency cetaceans	183	2,270	2,220	168	24,400	51,600
Mid-frequency cetaceans	185	< 10	< 10	170	< 10	< 10
High-frequency cetaceans	155	10	10	140	1,330	760
Phocid pinnipeds (underwater)	185	10	10	170	710	619
Otariid pinnipeds (underwater)	203	< 10	< 10	188	< 10	< 10

Table 37. Stn 11: Safe distances in metres from a seismic survey track to PTS- and TTS-onset thresholds (NMFS 2018) based on the SEL field for a track, 5058 in³ airgun array.

Marine mammal group	PTS-onset			TTS-onset		
	Weighted SEL (dB re 1 µPa²·s)	Summer safe dist. (m)	Winter safe dist. (m)	Weighted SEL (dB re 1 µPa²·s)	Summer safe dist. (m)	Winter safe dist. (m)
Low-frequency cetaceans	183	1,620	1,710	168	43,800	> 80,000
Mid-frequency cetaceans	185	< 10	< 10	170	< 10	< 10
High-frequency cetaceans	155	10	10	140	850	680
Phocid pinnipeds (underwater)	185	10	10	170	390	410
Otariid pinnipeds (underwater)	203	< 10	< 10	188	< 10	< 10

Table 38. Stn 12: Safe distances in metres from a seismic survey track to PTS- and TTS-onset thresholds (NMFS 2018) based on the SEL field for a track, 5058 in³ airgun array.

Marine mammal group	PTS-onset			TTS-onset		
	Weighted SEL (dB re 1 µPa²·s)	Summer	Winter	Weighted SEL (dB re 1 µPa²·s)	Summer	Winter
Low-frequency cetaceans	183	3,350	3,590	168	> 80,000	> 80,000
Mid-frequency cetaceans	185	< 10	< 10	170	< 10	< 10
High-frequency cetaceans	155	10	10	140	740	629
Phocid pinnipeds (underwater)	185	10	10	170	830	760
Otariid pinnipeds (underwater)	203	< 10	< 10	188	< 10	< 10

Table 39. Stn 13: Safe distances in metres from a seismic survey track to PTS- and TTS-onset thresholds (NMFS 2018) based on the SEL field for a track, 5058 in³ airgun array.

Marine mammal group	PTS-onset			TTS-onset		
	Weighted SEL (dB re 1 µPa²·s)	Summer safe dist. (m)	Winter safe dist. (m)	Weighted SEL (dB re 1 µPa²·s)	Summer safe dist. (m)	Winter safe dist. (m)
Low-frequency cetaceans	183	200	210	168	52,300	> 80,000
Mid-frequency cetaceans	185	< 10	< 10	170	< 10	< 10
High-frequency cetaceans	155	10	10	140	150	230
Phocid pinnipeds (underwater)	185	10	10	170	90	100
Otariid pinnipeds (underwater)	203	< 10	< 10	188	< 10	< 10

Table 40. Stn 14: Safe distances in metres from a seismic survey track to PTS- and TTS-onset thresholds (NMFS 2018) based on the SEL field for a track, 5058 in³ airgun array.

Marine mammal group	PTS-onset			TTS-onset		
	Weighted SEL (dB re 1 µPa²·s)	Summer safe dist. (m)	Winter safe dist. (m)	Weighted SEL (dB re 1 µPa²·s)	Summer safe dist. (m)	Winter safe dist. (m)
Low-frequency cetaceans	183	340	360	168	> 35,000	> 50,000
Mid-frequency cetaceans	185	< 10	< 10	170	< 10	< 10
High-frequency cetaceans	155	10	10	140	160	200
Phocid pinnipeds (underwater)	185	10	10	170	100	110
Otariid pinnipeds (underwater)	203	< 10	< 10	188	< 10	< 10

Table 41. Stn 15: Safe distances in metres from a seismic survey track to PTS- and TTS-onset thresholds (NMFS 2018) based on the SEL field for a track, 5058 in³ airgun array.

Marine mammal group	PTS-onset			TTS-onset		
	Weighted SEL (dB re 1 µPa²·s)	Summer safe dist. (m)	Winter safe dist. (m)	Weighted SEL (dB re 1 µPa²·s)	Summer safe dist. (m)	Winter safe dist. (m)
Low-frequency cetaceans	183	190	190	168	47,200	> 80,000
Mid-frequency cetaceans	185	< 10	< 10	170	< 10	< 10
High-frequency cetaceans	155	10	10	140	140	190
Phocid pinnipeds (underwater)	185	10	10	170	80	100
Otariid pinnipeds (underwater)	203	< 10	< 10	188	< 10	< 10

Table 42. Stn 16: Safe distances in metres from a seismic survey track to PTS- and TTS-onset thresholds (NMFS 2018) based on the SEL field for a track, 5058 in³ airgun array.

Marine mammal group	PTS-onset			TTS-onset		
	Weighted SEL (dB re 1 µPa²·s)	Summer safe dist. (m)	Winter safe dist. (m)	Weighted SEL (dB re 1 µPa²·s)	Summer safe dist. (m)	Winter safe dist. (m)
Low-frequency cetaceans	183	210	230	168	28,700	> 80,000
Mid-frequency cetaceans	185	< 10	< 10	170	< 10	< 10
High-frequency cetaceans	155	10	10	140	140	300
Phocid pinnipeds (underwater)	185	10	10	170	90	110
Otariid pinnipeds (underwater)	203	< 10	< 10	188	< 10	< 10

Table 43. Stn 17: Safe distances in metres from a seismic survey track to PTS- and TTS-onset thresholds (NMFS 2018) based on the SEL field for a track, 5058 in³ airgun array.

Marine mammal group	PTS-onset			TTS-onset		
	Weighted SEL (dB re 1 µPa²·s)	Summer safe dist. (m)	Winter safe dist. (m)	Weighted SEL (dB re 1 µPa²·s)	Summer safe dist. (m)	Winter safe dist. (m)
Low-frequency cetaceans	183	210	210	168	39,200	> 80,000
Mid-frequency cetaceans	185	< 10	< 10	170	< 10	< 10
High-frequency cetaceans	155	10	10	140	150	190
Phocid pinnipeds (underwater)	185	10	10	170	90	100
Otariid pinnipeds (underwater)	203	< 10	< 10	188	< 10	< 10

Table 44. Stn 18: Safe distances in metres from a seismic survey track to PTS- and TTS-onset thresholds (NMFS 2018) based on the SEL field for a track, 5058 in³ airgun array.

Marine mammal group	PTS-onset			TTS-onset		
	Weighted SEL (dB re 1 µPa²·s)	Summer safe dist. (m)	Winter safe dist. (m)	Weighted SEL (dB re 1 µPa²·s)	Summer safe dist. (m)	Winter safe dist. (m)
Low-frequency cetaceans	183	3,850	3,890	168	50,800	> 80,000
Mid-frequency cetaceans	185	< 10	< 10	170	< 10	< 10
High-frequency cetaceans	155	10	10	140	1,570	1,150
Phocid pinnipeds (underwater)	185	10	10	170	1,280	1,230
Otariid pinnipeds (underwater)	203	< 10	< 10	188	< 10	< 10

Table 45. Stn 19: Safe distances in metres from a seismic survey track to PTS- and TTS-onset thresholds (NMFS 2018) based on the SEL field for a track, 5058 in³ airgun array.

Marine mammal group	PTS-onset			TTS-onset		
	Weighted SEL (dB re 1 µPa²·s)	Summer safe dist. (m)	Winter safe dist. (m)	Weighted SEL (dB re 1 µPa²·s)	Summer safe dist. (m)	Winter safe dist. (m)
Low-frequency cetaceans	183	210	230	168	43,600	> 80,000
Mid-frequency cetaceans	185	< 10	< 10	170	< 10	< 10
High-frequency cetaceans	155	10	10	140	150	210
Phocid pinnipeds (underwater)	185	10	10	170	90	100
Otariid pinnipeds (underwater)	203	< 10	< 10	188	< 10	< 10

Table 46. Stn 20: Safe distances in metres from a seismic survey track to PTS- and TTS-onset thresholds (NMFS 2018) based on the SEL field for a track, 5058 in³ airgun array.

Marine mammal group	PTS-onset			TTS-onset		
	Weighted SEL (dB re 1 µPa²·s)	Summer safe dist. (m)	Winter safe dist. (m)	Weighted SEL (dB re 1 µPa²·s)	Summer safe dist. (m)	Winter safe dist. (m)
Low-frequency cetaceans	183	3,980	4,140	168	> 80,000	> 80,000
Mid-frequency cetaceans	185	< 10	< 10	170	< 10	< 10
High-frequency cetaceans	155	10	10	140	620	570
Phocid pinnipeds (underwater)	185	10	10	170	540	510
Otariid pinnipeds (underwater)	203	< 10	< 10	188	< 10	< 10

5. Discussion and Conclusion

The results show that low-frequency cetaceans, which are the large baleen whales, are the most likely to be injured by seismic airgun arrays. The effects were most pronounced in shallow water areas where the sound is effectively trapped in a smaller volume of water. Measurements of received levels close to seismic arrays suggest that high-frequency mammals, such as porpoise, may also be exposed to injurious sound levels (Martin et al. 2017a, Martin et al. 2017b). Further work validating the predicted high-frequency sound levels from airgun arrays is likely required.

Some of the Temporary Threshold Shift (TTS) radii for low-frequency mammals extended beyond 80 km in winter propagation conditions. These long ranges were caused by trapping of sound near the sea surface from the upward refracting sound speed profile. The acoustic propagation model employed did not include a rough surface that would scatter the sound, reducing the amplitude at long ranges. Therefore, these long ranges should be used with caution.

The differences between the modelling results obtained with a generic sand bottom and with the geoacoustic inversion bottom parameters, as can be seen in Appendices C.1 to C.6, show that an improved understanding of the in-situ geoacoustic bottom parameters can be important for accurately assessing the impacts of seismic survey environmental noise on the marine mammals in the areas studied.

These differences were more pronounced, of course, in cases where the propagating sound energy significantly interacted with the sea bottom. This was usually the case in shallow water (under 300 m depth) and often the case in medium depth zones (300 to 1000 m) where the SSP is downward refracting. The isothermal and pressure gradient characteristics of deep ocean waters generally result in minimal bottom interaction for sound propagating from a source near the surface.

An example of the differences in sound propagation in shallow water for a generic sand bottom versus a geoacoustic bottom derived from acoustic inversion computations can be seen in Appendix C, Figure C-7 and C-8. The first of these, for the generic sand bottom, shows per-pulse SEL at levels of 180 dB re 1 $\mu Pa^2 \cdot s$ or higher extending in an oval round the source up to 1.2 km wide, whereas in the second figure, pertaining to a geoacoustic bottom derived from the inversion computations, the equivalent oval was only half as wide.

The differences were more complex at longer ranges, where bottom interactions were further compounded. The 125dB re 1 $\mu Pa^2 \cdot s$ SEL level, for example, extended out to 60–70 km in the generally northward sectors in both figures, as this is the direction of deeper water, with reduced bottom interaction impacts; however, for the southern sector, the water remains very shallow, and the 125 dB re 1 $\mu Pa^2 \cdot s$ SEL level extended only about 10 km in the generic sand figure, but to about 30 km in the inversion geoacoustics figure. This is the reverse of the pattern that was observed for the 180 dB re 1 $\mu Pa^2 \cdot s$ contour (at shorter ranges), and this illustrates the complexity of the bottom interaction impacts on the acoustic propagation and the importance of accurate geoacoustic bottom estimation.

The modelling results compiled in Section 3 and Appendix C, provide a useful reference for a summary understanding of propagation conditions and typical received levels that pertain to noise from seismic surveys in the areas covered by this study. The marine mammal impact safe distances compiled in Section 4, although for a particular airgun array and a single north-south survey pass, provide a set of representative examples that can be used for initial stages of survey planning, prior to specific modelling, and also to compare the relative differences in impacts due to different oceanographic conditions.

Glossary

attenuation
The gradual loss of acoustic energy from absorption and scattering as sound propagates through a medium.

background noise
Total of all sources of interference in a system used for the production, detection, measurement, or recording of a signal, independent of the presence of the signal (ANSI S1.1-1994 R2004). Ambient noise detected, measured, or recorded with a signal is part of the background noise.

bandwidth
The range of frequencies over which a sound occurs. Broadband refers to a source that produces sound over a broad range of frequencies whereas narrowband sources produce sounds over a narrow frequency range (e.g., sonar) (ANSI/ASA S1.13-2005 R2010).

broadband sound level
The total sound pressure level measured over a specified frequency range. If the frequency range is unspecified, it refers to the entire measured frequency range.

compressional wave
A mechanical vibration wave in which the direction of particle motion is parallel to the direction of propagation. Also called primary wave or P-wave.

decibel (dB)
One-tenth of a bel. Unit of level when the base of the logarithm is the tenth root of ten, and the quantities concerned are proportional to power (ANSI S1.1-1994 R2004).

frequency
The rate of oscillation of a periodic function measured in cycles-per-unit-time. The reciprocal of the period. Unit: hertz (Hz). Symbol: *f*. 1 Hz is equal to 1 cycle per second.

geoacoustic
Relating to the acoustic properties of the seabed.

hertz (Hz)
A unit of frequency defined as one cycle per second.

hydrophone
An underwater sound pressure transducer. A passive electronic device for recording or listening to underwater sound.

impulsive sound
Sound that is typically brief and intermittent with rapid (within a few seconds) rise time and decay back to ambient levels (NOAA 2013, ANSI S12.7-1986 R2006). For example, seismic airguns and impact pile driving.

octave
The interval between a sound and another sound with double or half the frequency. For example, one octave above 200 Hz is 400 Hz, and one octave below 200 Hz is 100 Hz.

parabolic equation (PE) method
A computationally-efficient solution to the acoustic wave equation that is used to model transmission loss. The parabolic equation approximation omits effects of back-scattered sound, simplifying the computation of transmission loss. The effect of back-scattered sound is negligible for most ocean-acoustic propagation problems.

peak pressure level (peak)
The maximum instantaneous sound pressure level, in a stated frequency band, within a stated period. Also called zero-to-peak pressure level. Unit: decibel (dB).

point source
A source that radiates sound as if from a single point (ANSI S1.1-1994 R2004).

pressure, acoustic
The deviation from the ambient hydrostatic pressure caused by a sound wave. Also called overpressure. Unit: pascal (Pa). Symbol: *p*.

shear wave
A mechanical vibration wave in which the direction of particle motion is perpendicular to the direction of propagation. Also called secondary wave or S-wave. Shear waves propagate only in solid media, such as sediments or rock. Shear waves in the seabed can be converted to compressional waves in water at the water-seabed interface.

signature
Pressure signal generated by a source.

sound
A time-varying pressure disturbance generated by mechanical vibration waves travelling through a fluid medium such as air or water.

sound exposure
Time integral of squared, instantaneous frequency-weighted sound pressure over a stated time interval or event. Unit: pascal-squared second ($Pa^2 \cdot s$) (ANSI S1.1-1994 R2004).

sound exposure level (SEL)
A cumulative measure related to the sound energy in one or more pulses. Unit: dB re 1 $\mu Pa^2 \cdot s$. SEL is expressed over the summation period (e.g., per-pulse SEL [for airguns], single-strike SEL [for pile drivers], 24-hour SEL).

sound pressure level (SPL)
The decibel ratio of the time-mean-square sound pressure, in a stated frequency band, to the square of the reference sound pressure (ANSI S1.1-1994 R2004).

For sound in water, the reference sound pressure is one micropascal (p_0 = 1 µPa) and the unit for SPL is dB re 1 µPa:

$$\mathrm{SPL} = 10\log_{10}\left(p^2 / p_0^2\right) = 20\log_{10}\left(p / p_0\right)$$

Unless otherwise stated, SPL refers to the root-mean-square sound pressure level. See also 90% sound pressure level and fast-average sound pressure level.

sound speed profile
The speed of sound in the water column as a function of depth below the water surface.

source level (SL)
The sound level measured in the far-field and scaled back to a standard reference distance of 1 metre from the acoustic centre of the source. Unit: dB re 1 µPa·m (sound pressure level) or dB re 1 µPa²·s·m (sound exposure level).

spectrum
An acoustic signal represented in terms of its power (or energy) distribution compared with frequency.

transmission loss (TL)
The decibel reduction in sound level between two stated points that results from sound spreading away from an acoustic source subject to the influence of the surrounding environment. Also called propagation loss.

wavelength
Distance over which a wave completes one oscillation cycle. Unit: meter (m). Symbol: λ.

Literature Cited

[HESS] High Energy Seismic Survey. 1999. *High Energy Seismic Survey Review Process and Interim Operational Guidelines for Marine Surveys Offshore Southern California*. Prepared for the California State Lands Commission and the United States Minerals Management Service Pacific Outer Continental Shelf Region by the High Energy Seismic Survey Team, Camarillo, California. 98 pp.

[ISO] International Organization for Standardization. 2016. *ISO/DIS 18405.2:2017. Underwater acoustics—Terminology*. Geneva. https://www.iso.org/standard/62406.html.

[NMFS] National Marine Fisheries Service. 1998. *Acoustic Criteria Workshop*. Dr. Roger Gentry and Dr. Jeanette Thomas Co-Chairs.

[NMFS] National Marine Fisheries Service. 2013. *Marine Mammals: Interim Sound Threshold Guidance* (webpage). National Marine Fisheries Service, National Oceanic and Atmospheric Administration, U.S. Department of Commerce. http://www.westcoast.fisheries.noaa.gov/protected_species/marine_mammals/threshold_guidance.html.

[NMFS] National Marine Fisheries Service. 2016. *Technical Guidance for Assessing the Effects of Anthropogenic Sound on Marine Mammal Hearing: Underwater Acoustic Thresholds for Onset of Permanent and Temporary Threshold Shifts.* U.S. Department of Commerce, NOAA. NOAA Technical Memorandum NMFS-OPR-55. 178 pp. http://www.nmfs.noaa.gov/pr/acoustics/Acoustic%20Guidance%20Files/opr-55_acoustic_guidance_tech_memo.pdf.

[NMFS] National Marine Fisheries Service. 2018. *2018 Revision to: Technical Guidance for Assessing the Effects of Anthropogenic Sound on Marine Mammal Hearing (Version 2.0): Underwater Thresholds for Onset of Permanent and Temporary Threshold Shifts*. U.S. Department of Commerce, NOAA. NOAA Technical Memorandum NMFS-OPR-59. 167 pp. https://www.fisheries.noaa.gov/webdam/download/75962998.

[NOAA] National Oceanic and Atmospheric Administration. 2005. *The Federal Register*.

[NOAA] National Oceanic and Atmospheric Administration. 2013. *Draft guidance for assessing the effects of anthropogenic sound on marine mammals: Acoustic threshold levels for onset of permanent and temporary threshold shifts*, December 2013, Silver Spring, MD: NMFS Office of Protected Resources, p. 76. http://www.nmfs.noaa.gov/pr/acoustics/draft_acoustic_guidance_2013.pdf.

[NOAA] National Oceanic and Atmospheric Administration. 2015. *Draft guidance for assessing the effects of anthropogenic sound on marine mammal hearing: Underwater acoustic threshold levels for onset of permanent and temporary threshold shifts*, July 2015, 180 pp. Silver Spring, Maryland: NMFS Office of Protected Resources. http://www.nmfs.noaa.gov/pr/acoustics/draft%20acoustic%20guidance%20July%202015.pdf.

[NOAA] National Oceanic and Atmospheric Administration. 2016. *Document Containing Proposed Changes to the NOAA Draft Guidance for Assessing the Effects of Anthropogenic Sound on Marine Mammal Hearing: Underwater Acoustic Threshold Levels for Onset of Permanent and Temporary Threshold Shifts*, p. 24. http://www.nmfs.noaa.gov/pr/acoustics/draft_guidance_march_2016_.pdf.

[ONR] Office of Naval Research. 1998. *ONR Workshop on the Effect of Anthropogenic Noise in the Marine Environment*. Dr. R. Gisiner Chair.

Aerts, L., M. Blees, S. Blackwell, C. Greene, K. Kim, D. Hannay, and M. Austin. 2008. *Marine mammal monitoring and mitigation during BP Liberty OBC seismic survey in Foggy Island Bay, Beaufort Sea, July–August 2008: 90-day report*. Document Number LGL Report P1011-1. Report by LGL Alaska Research Associates Inc., LGL Ltd., Greeneridge Sciences Inc. and JASCO Applied Sciences for BP Exploration Alaska. 199 pp. http://www.nmfs.noaa.gov/pr/pdfs/permits/bp_liberty_monitoring.pdf.

ANSI S12.7-1986. R2006. *American National Standard Methods for Measurements of Impulsive Noise*. American National Standards Institute, New York.

ANSI S1.1-1994. R2004. *American National Standard Acoustical Terminology*. American National Standards Institute, New York.

ANSI S1.1-2013. R2013. *American National Standard Acoustical Terminology*. American National Standards Institute, New York.

ANSI/ASA S1.13-2005. R2010. *American National Standard Measurement of Sound Pressure Levels in Air*. American National Standards Institute and Acoustical Society of America, New York.

Babushina, Y.S., G.L. Zaslavskii, and L.I. Yurkevich. 1991. Air and underwater hearing characteristics of the northern fur seal: Audiograms, frequency and differential thresholds. *Biophysics* 39: 900-913.

Becker, J.J., D.T. Sandwell, W.H.F. Smith, J. Braud, B. Binder, J. Depner, D. Fabre, J. Factor, S. Ingalls, et al. 2009. Global Bathymetry and Elevation Data at 30 Arc Seconds Resolution: SRTM30_PLUS. *Marine Geodesy* 32(4): 355-371.

Carnes, M.R. 2009. *Description and Evaluation of GDEM-V 3.0*. NRL Memorandum Report 7330-09-9165. U.S. Naval Research Laboratory, Stennis Space Center, MS. 21 p.

Collins, M.D. 1993. A split-step Padé solution for the parabolic equation method. *Journal of the Acoustical Society of America* 93(4): 1736–1742.

Collins, M.D., R.J. Cederberg, D.B. King, and S. Chin-Bing. 1996. Comparison of algorithms for solving parabolic wave equations. *Journal of the Acoustical Society of America* 100(1): 178–182.

Coppens, A.B. 1981. Simple equations for the speed of sound in Neptunian waters. *Journal of the Acoustical Society of America* 69:862–863.

Delarue, J., K.A. Kowarski, E.E. Maxner, J.T. MacDonnell, and S.B. Martin. 2018. *Acoustic Monitoring Along Canada's East Coast: August 2015 to July 2017*. Document Number 01279, Environmental Studies Research Funds Report Number 215, Version 1.0. Technical report by JASCO Applied Sciences for Environmental Studies Research Fund, Dartmouth, NS, Canada. 120 pp + appendices.

Dragoset, W.H. 1984. A comprehensive method for evaluating the design of airguns and airgun arrays. *16th Annual Proc. Offshore Tech. Conf*. Volume 3. pp 75–84.

Ellison, W.T. and P.J. Stein. 1999. *SURTASS LFA High Frequency Marine Mammal Monitoring (HF/M3) Sonar: Sustem Description and Test & Evaluation*. Under U.S. Navy Contract N66604-98-D-5725.

Finneran, J.J. 2015. *Auditory weighting functions and TTS/PTS exposure functions for cetaceans and marine carnivores*. San Diego: SSC Pacific.

Finneran, J.J. 2016. *Auditory weighting functions and TTS/PTS exposure functions for marine mammals exposed to underwater noise*. Technical Report for Space and Naval Warfare Systems Center Pacific, San Diego, CA. 49 pp. http://www.dtic.mil/dtic/tr/fulltext/u2/1026445.pdf.

Finneran, J.J. and A.K. Jenkins. 2012. *Criteria and thresholds for U.S. Navy acoustic and explosive effects analysis*. SPAWAR Systems Center Pacific, San Diego, CA. 64 pp.

Finneran, J.J. and C.E. Schlundt. 2010. Frequency-dependent and longitudinal changes in noise-induced hearing loss in a bottlenose dolphin (*Tursiops truncatus*). *Journal of the Acoustical Society of America* 128(2): 567-570. https://doi.org/10.1121/1.3458814.

Fisher, F.H. and V.P. Simmons. 1977. Sound absorption in sea water. *Journal of the Acoustical Society of America* 62(3): 558-564. https://doi.org/10.1121/1.381574.

Funk, D., D. Hannay, D. Ireland, R. Rodrigues, and W. Koski (eds.). 2008. *Marine mammal monitoring and mitigation during open water seismic exploration by Shell Offshore Inc. in the Chukchi and Beaufort Seas, July–November 2007: 90-day report*. LGL Report P969-1. Prepared by LGL Alaska Research Associates Inc., LGL Ltd., and JASCO Research Ltd. for Shell Offshore Inc., National Marine Fisheries Service (US), and US Fish and Wildlife Service. 218 pp.

Hannay, D. and R. Racca. 2005. *Acoustic Model Validation*. Document Number 0000-S-90-04-T-7006-00-E, Revision 02. Technical report for Sakhalin Energy Investment Company Ltd. by JASCO Research Ltd. 34 pp.

Henderson, D., and Hamernik, R.P. 1986. Impulse noise: Critical review. *Journal of the Acoustical Society of America*, 80: 569-584.

Ireland, D.S., R. Rodrigues, D. Funk, W. Koski, and D. Hannay. 2009. *Marine mammal monitoring and mitigation during open water seismic exploration by Shell Offshore Inc. in the Chukchi and Beaufort Seas, July–October 2008: 90-Day Report*. Document Number LGL Report P1049-1. 277 pp.

Ireland, D.S., R. Rodrigues, D. Funk, W.R. Koski, and D.E. Hannay. 2009. *Marine mammal monitoring and mitigation during open water seismic exploration by Shell Offshore Inc. in the Chukchi and Beaufort Seas, July–October 2008: 90-Day Report*. Document Number LGL Report P1049-1. 277 pp.

Kastak, D. and R.J. Schusterman. 1998. Low-frequency amphibious hearing in pinnipeds: Methods, measurements, noise, and ecology. *Journal of the Acoustical Society of America* 103(4): 2216-2228. https://doi.org/10.1121/1.421367.

Kastelein, R.A., R. van Schie, W.C. Verboom, and D. de Haan. 2005. Underwater hearing sensitivity of a male and a female Steller sea lion (*Eumetopias jubatus*). *Journal of the Acoustical Society of America* 118(3): 1820-1829. http://dx.doi.org/10.1121/1.1992650.

Landro, M. 1992. Modeling of GI gun signatures. *Geophysical Prospecting* 40: 721–747. https://doi.org/10.1111/j.1365-2478.1992.tb00549.x

Laws, M., L. Hatton, and M. Haartsen. 1990. Computer modeling of clustered airguns. *First Break* 8: 331–338.

Lucke, K., U. Siebert, P. Lepper, A., and M.-A. Blanchet. 2009. Temporary shift in masked hearing thresholds in a harbor porpoise (*Phocoena phocoena*) after exposure to seismic airgun stimuli. *Journal of the Acoustical Society of America* 125(6): 4060-4070. https://asa.scitation.org/doi/10.1121/1.3117443.

Lurton, X. 2002. *An Introduction to Underwater Acoustics: Principles and Applications*. Springer, Chichester, U.K.

Malme, C.I., P.R. Miles, C.W. Clark, P. Tyack, and J.E. Bird. 1984. *Investigations of the potential effects of underwater noise from petroleum industry activities on migrating gray whale behavior. Phase II: January 1984 migration*. Report Number BBN Report 5586. Bolt Beranek and Newman Inc. 357 pp.

Malme, C.I., P.R. Miles, C.W. Clark, P. Tyak, and J.E. Bird. 1983. *Investigations of the Potential Effects of Underwater Noise from Petroleum Industry Activities on Migrating Gray Whale Behavior*. Report Number 5366. http://www.boem.gov/BOEM-Newsroom/Library/Publications/1983/rpt5366.aspx.

Martin, B., K. Broker, M.-N.R. Matthews, J. MacDonnell, and L. Bailey. 2015. *Comparison of measured and modeled air-gun array sound levels in Baffin Bay, West Greenland. OceanNoise 2015*, 11–15 May, Barcelona, Spain.

Martin, B.S., E. Maxner, M. Wood, L. Horwich, and K. Kowarski. 2017a. *Soundscape Characterization and Marine Mammal Presence on the Eastern Grand Banks, NF: September to October 2017*. Document Number 01305. Version 1.0. Technical report by JASCO Applied Sciences for DFO Newfoundland.

Martin, S.B., M.-N.R. Matthews, J.T. MacDonnell, and K. Bröker. 2017b. Characteristics of seismic survey pulses and the ambient soundscape in Baffin Bay and Melville Bay, West Greenland. *Journal of the Acoustical Society of America* 142(6): 3331-3346. https://doi.org/10.1121/1.5014049.

Mattsson, A. and M. Jenkerson. 2008. *Single Airgun and Cluster Measurement Project. Joint Industry Programme (JIP) on Exploration and Production Sound and Marine Life Proramme Review*, October 28-30. International Association of Oil and Gas Producers, Houston, TX.

Moore, P.W.B. and R.J. Schusterman. 1987. Audiometric assessment of northern fur seals, *Callorhinus ursinus*. *Marine Mammal Science* 3: 31-53.

Mulsow, J. and C. Reichmuth. 2007. Electrophysiological assessment of temporal resolution in pinnipeds. *Aquatic Mammals* 33: 122-131.

Mulsow, J., C. Reichmuth, F.M.D. Gulland, D.A.S. Rosen, and J.J. Finneran. 2011b. Aerial audiograms of several California sea lions (*Zalophus californianus*) and Steller sea lions (*Eumetopias jubatus*) measured using single and multiple simultaneous auditory steady-state response methods. *Journal of Experimental Biology* 214: 1138-1147. http://jeb.biologists.org/content/jexbio/214/7/1138.full.pdf.

Mulsow, J., J.J. Finneran, and D.S. Houser. 2011a. California sea lion (*Zalophus californianus*) aerial hearing sensitivity measured using auditory steady-state response and psychophysical methods. *Journal of the Acoustical Society of America* 129: 2298-2306. https://asa.scitation.org/doi/10.1121/1.3552882.

Nedwell, J.R. and A.W. Turnpenny. 1998. The use of a generic frequency weighting scale in estimating environmental effect. *Workshop on Seismics and Marine Mammals*. 23–25th June 1998, London, U.K.

Nedwell, J.R., A.W.H. Turnpenny, J. Lovell, S.J. Parvin, R. Workman, and J.A.L. Spinks. 2007. *A validation of the dB_{ht} as a measure of the behavioural and auditory effects of underwater noise*. Report No. 534R1231 prepared by Subacoustech Ltd. for the UK Department of Business, Enterprise and Regulatory Reform under Project No. RDCZ/011/0004. www.subacoustech.com/information/downloads/reports/534R1231.pdf.

O'Neill, C., D. Leary, and A. McCrodan. 2010. Sound Source Verification. (Chapter 3) *In* Blees, M.K., K.G. Hartin, D.S. Ireland, and D. Hannay (eds.). *Marine mammal monitoring and mitigation during open water seismic exploration by Statoil USA E&P Inc. in the Chukchi Sea, August–October 2010: 90-day report*. LGL Report P1119. Prepared by LGL Alaska Research Associates Inc., LGL Ltd., and JASCO Applied Sciences Ltd. for Statoil USA E&P Inc., National Marine Fisheries Service (US), and US Fish and Wildlife Service. 1–34.

Payne, R. and D. Webb. 1971. Orientation by means of long range acoustic signaling in baleen whales. *Annals of the New York Academy of Sciences* 188: 110-142. https://doi.org/10.1111/j.1749-6632.1971.tb13093.x.

Porter, M.B. and Y.-C. Liu. 1994. Finite-element ray tracing. *In*: Lee, D. and M.H. Schultz (eds.). *Proceedings of the International Conference on Theoretical and Computational Acoustics*. Volume 2. World Scientific Publishing Co. 947-956 pp.

Racca, R., A. Rutenko, K. Bröker, and G. Gailey. 2012b. *Model based sound level estimation and in-field adjustment for real-time mitigation of behavioural impacts from a seismic survey and post-event evaluation of sound exposure for individual whales*. *Acoustics 2012 Fremantle: Acoustics, Development and the Environment*, Fremantle, Australia. http://www.acoustics.asn.au/conference_proceedings/AAS2012/papers/p92.pdf.

Racca, R., A. Rutenko, K. Bröker, and M. Austin. 2012a. A line in the water – design and enactment of a closed loop, model based sound level boundary estimation strategy for mitigation of behavioural impacts from a seismic survey. *11th European Conference on Underwater Acoustics 2012*. Volume 34(3), Edinburgh, United Kingdom.

Richardson, W.J., B. Würsig, and C.R. Greene, Jr. 1986. Reactions of bowhead whales, *Balaena mysticetus*, to seismic exploration in the Canadian Beaufort Sea. *Journal of the Acoustical Society of America* 79(4): 1117-1128. https://doi.org/10.1121/1.393384.

Richardson, W.J., B. Würsig, and C.R. Greene, Jr. 1990. Reactions of bowhead whales, *Balaena mysticetus*, to drilling and dredging noise in the Canadian Beaufort Sea. *Marine Environmental Research* 29(2): 135-160. https://doi.org/10.1016/0141-1136(90)90032-J.

Richardson, W.J., C.R. Greene, Jr., C.I. Malme, and D.H. Thomson. 1995. *Marine Mammals and Noise*. Academic Press, San Diego, California. 576.

Rodríguez, E., C.S. Morris, Y.J.E. Belz, E.C. Chapin, J.M. Martin, W. Daffer, and S. Hensley. 2005. *An Assessment of the SRTM Topographic Products.* Document Number JPL D-31639. Jet Propulsion Laboratory, Pasadena, CA.

Schusterman, R.J., R.F. Balliet, and J. Nixon. 1972. Underwater audiogram of the California sea lion by the conditioned vocalization technique. *Journal of the Experimental Analysis of Behavior* 17: 339-350. https://www.ncbi.nlm.nih.gov/pmc/articles/PMC1333909/pdf/jeabehav00130-0042.pdf.

Smith, W.H. and D.T. Sandwell. 1997. Global sea floor topography from satellite altimetry and ship depth soundings. *Science* 277(5334): 1956-1962.

Southall, B.L., A.E. Bowles, W.T. Ellison, J.J. Finneran, R.L. Gentry, C.R. Greene, Jr., D. Kastak, D.R. Ketten, J.H. Miller, et al. 2007. Marine Mammal Noise Exposure Criteria: Initial Scientific Recommendations. *Aquatic Mammals* 33(4): 411-521. https://doi.org/10.1080/09524622.2008.9753846.

Teague, W.J., M.J. Carron, and P.J. Hogan. 1990. A comparison between the Generalized Digital Environmental Model and Levitus climatologies. *Journal of Geophysical Research* 95(C5):7167–7183.

Warner, G.A. and A.O. MacGillivray. 2018. *Analysis of Acoustic Particle Motion Data from the Svein Vaage Airgun Study: Final Report*. Document Number 01656, Environmental Studies Research Funds Report Number 216, Version 1.0. Technical report by JASCO Applied Sciences for Environmental Studies Research Fund, Dartmouth, NS, Canada. 56 pp + appendices.

Warner, G. and Martin, B. 2018. *ESRF Received Level Study: Estimation of subbottom geoacoustic properties from offshore airgun surveys in Atlantic Canada*. Document 01616, Version 1.0. Technical report by JASCO Applied Sciences for Environmental Studies Research Fund.

Warner, G., C. Erbe, and D. Hannay. 2010. Underwater Sound Measurements. (Chapter 3) *In* Reiser, C.M., D.W. Funk, R. Rodrigues, and D. Hannay (eds.). *Marine Mammal Monitoring and Mitigation during Open Water Shallow Hazards and Site Clearance Surveys by Shell Offshore Inc. in the Alaskan Chukchi Sea, July–October 2009: 90-Day Report*. LGL Report P1112-1. Report by LGL Alaska Research Associates Inc. and JASCO Applied Sciences for Shell Offshore Inc., National Marine Fisheries Service (US), and US Fish and Wildlife Service. 1–54.

Wood, J., B.L. Southall, and D.J. Tollit. 2012. *PG&E offshore 3-D Seismic Survey Project Environmental Impact Report–Marine Mammal Technical Draft Report*. SMRU Ltd. 121 pp. https://www.coastal.ca.gov/energy/seismic/mm-technical-report-EIR.pdf.

Zhang, Z.Y. and C.T. Tindle. 1995. Improved equivalent fluid approximations for a low shear speed ocean bottom. *Journal of the Acoustical Society of America* 98(6): 3391-3396. https://doi.org/10.1121/1.413789.

Ziolkowski, A. 1970. A method for calculating the output pressure waveform from an air gun. *Geophysical Journal of the Royal Astronomical Society* 21(2): 137-161.

Appendix A. Underwater Acoustics

This section provides a detailed description of the acoustic metrics relevant to the modelling study and the modelling methodology.

A.1. Acoustic Metrics

Underwater sound pressure amplitude is measured in decibels (dB) relative to a fixed reference pressure of p_0 = 1 µPa. Several sound level metrics are commonly used to quantify noise. We provide specific definitions of relevant metrics used in the accompanying report. Where possible we follow the ANSI and ISO standard definitions and symbols for sound metrics, but these standards are not always consistent.

The zero-to-peak sound pressure level, or peak sound pressure level (PK; dB re 1 µPa), is the maximum instantaneous sound pressure level in a stated frequency band attained by an acoustic pressure signal, $p(t)$:

$$L_{p,pk} = 20 \log_{10} \left[\frac{\max\left(\left| p(t) \right|\right)}{p_0} \right]. \tag{A-1}$$

Acoustic recorders saturate or clip when the peak level exceeds the maximum or minimum level the acoustic recorder can quantify. Recorder saturation precludes quantitative analysis of acoustic data.

The sound exposure level (SEL, dB re 1 µPa²·s) is a measure related to the acoustic energy contained in one or more acoustic events. The SEL for a single event is computed from the time-integral of the squared pressure over the full event duration (T):

$$L_E = 10 \log_{10} \left(\int_T p^2(t) dt \Big/ T_0 p_0^2 \right) \tag{A-2}$$

where T_0 is a reference time interval of 1 s. The SEL continues to increase with time when non-zero pressure signals are present.

The distribution of a sound's energy with frequency is described by the sound's spectrum. The sound spectrum can be split into a series of adjacent frequency bands. Splitting a spectrum into 1 Hz wide bands, called passbands, yields the energy spectral density (ESD) of the sound. The ESD is calculated as the squared value of the Fourier transform of the signal $p(t)$:

$$\Psi(f) \equiv ESD(f) = \left(\int p(t) e^{-2\pi i f t} dt \right)^2. \tag{A-3}$$

Harrison and Harrison (1995) showed a relationship between frequency and range averaging for broadband sounds. Gaussian frequency averaging can be easily applied to ESD data measured at discrete ranges and corresponding Gaussian range averaging can be easily applied to modelled ESD data at discrete frequencies. Exploiting this relationship provides robust ESD data over a fractional bandwidth and a computationally efficient method for modelling those data at a single frequency. Gaussian frequency averaging is calculated using

$$I_f = \frac{\int \Psi(f, r_0) \exp(-(f - f_0)^2 / (\kappa f_0)^2) df}{\int \exp(-(f - f_0)^2 / (\kappa f_0)^2) df}, \tag{A-4}$$

where f_0 is the centre frequency, r_0 is the measurement range, and κ is the fractional bandwidth (unitless). The corresponding range average is

$$I_r = \frac{\int \Psi(f_0, r) \exp(-(r - r_0)^2 / (\kappa r_0)^2) dr}{\int \exp(-(r - r_0)^2 / (\kappa r_0)^2) dr}, \quad \text{(A-5)}$$

where κ is the same value as in Equation A-4.

ESD levels are calculated by taking 10 times the logarithm of the ESD (which can be frequency-averaged or not):

$$L_\Psi = 10 \log_{10}\left(\Psi / \Psi_0\right) \quad \text{(A-6)}$$

where Ψ_0 is 1 µPa^2·s/Hz. The sum of (non-frequency averaged) ESD levels over frequency is equivalent to the SEL.

A.1.1. 1/3-Octave-Band Analysis

The distribution of a sound's power with frequency is described by the sound's spectrum. The sound spectrum can be split into a series of adjacent frequency bands. Splitting a spectrum into 1 Hz wide bands, called passbands, yields the power spectral density of the sound. This splitting of the spectrum into passbands of a constant width of 1 Hz, however, does not represent how animals perceive sound.

Because animals perceive exponential increases in frequency rather than linear increases, analyzing a sound spectrum with passbands that increase exponentially in size better approximates real-world scenarios. In underwater acoustics, a spectrum is commonly split into 1/3-octave-bands, which are one-third of an octave wide; each octave represents a doubling in sound frequency. The centre frequency of the ith 1/3-octave-band, $f_c(i)$, is defined as:

$$f_c(i) = 10^{i/10}, \quad \text{(A-7)}$$

and the low (f_{lo}) and high (f_{hi}) frequency limits of the ith 1/3-octave-band are defined as:

$$f_{lo} = 10^{-1/20} f_c(i) \quad \text{and} \quad f_{hi} = 10^{1/20} f_c(i) \; . \quad \text{(A-8)}$$

The 1/3-octave-bands become wider with increasing frequency, and on a logarithmic scale the bands appear equally spaced (Figure A-1). The acoustic modelling spans from band 10 ($f_c(10)$ = 10 Hz) to band 44 ($f_c(44)$ = 25 kHz).

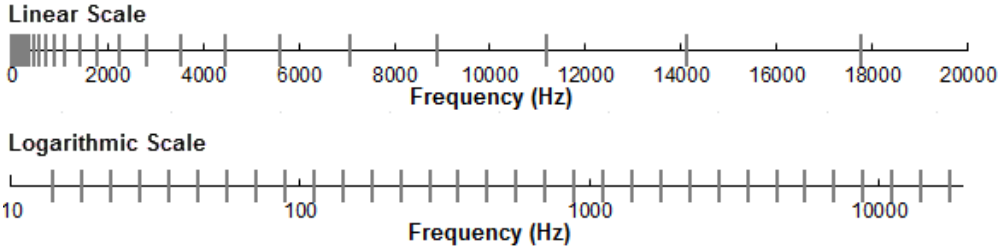

Figure A-1. One-third-octave-bands shown on a linear frequency scale and on a logarithmic scale.

The sound pressure level in the *i*th 1/3-octave-band $(L_b^{(i)})$ is computed from the power spectrum $S(f)$ between f_{lo} and f_{hi}:

$$L_{\mathrm{b}}^{(i)} = 10\log_{10}\left(\int_{f_{lo}}^{f_{hi}} S(f)\,df\right), \tag{A-9}$$

Summing the sound pressure level of all the 1/3-octave-bands yields the broadband sound pressure level:

$$\text{Broadband SPL} = 10\log_{10}\sum_i 10^{L_{\mathrm{b}}^{(i)}/10}, \tag{A-10}$$

Figure A-2 shows an example of how the 1/3-octave-band sound pressure levels compare to the power spectrum of an ambient noise signal. Because the 1/3-octave-bands are wider with increasing frequency, the 1/3-octave-band SPL is higher than the power spectrum, especially at higher frequencies. Acoustic modelling of 1/3-octave-bands require less computation time than 1 Hz bands and still resolves the frequency-dependence of the sound source and the propagation environment.

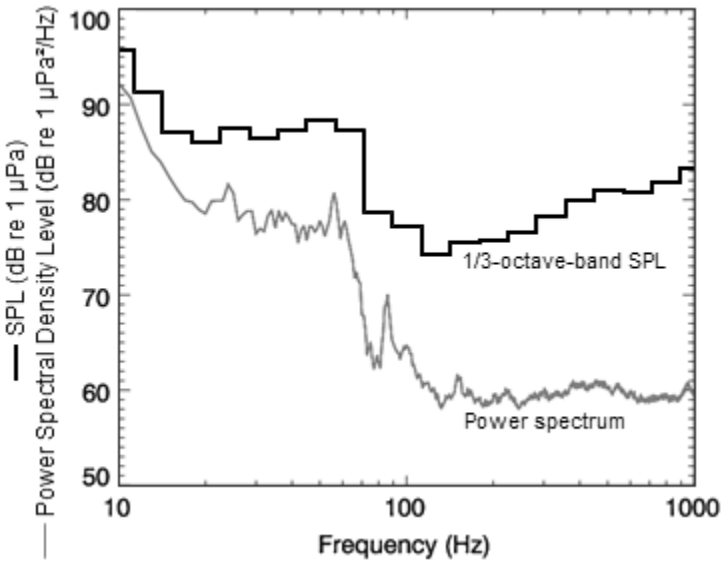

Figure A-2. A power spectrum and the corresponding 1/3-octave-band sound pressure levels of example ambient noise shown on a logarithmic frequency scale.

A.2. Marine Mammal Impact Criteria

It has been long recognized that marine mammals can be adversely affected by underwater anthropogenic noise. For example, Payne and Webb (1971) suggest that communication distances of fin whales are reduced by shipping sounds. Subsequently, similar concerns arose regarding effects of other underwater noise sources and the possibility that impulsive sources—primarily airguns used in seismic surveys—could cause auditory injury. This led to a series of workshops held in the late 1990s, conducted to address acoustic mitigation requirements for seismic surveys and other underwater noise sources (NMFS 1998, ONR 1998, Nedwell and Turnpenny 1998, HESS 1999, Ellison and Stein 1999). In the years since these early workshops, a variety of thresholds have been proposed for both injury (Appendix A.2.1) and disturbance (Appendix A.2.2). The following sections summarize the development of the current thresholds relevant to this study; this remains an active research topic, however.

A.2.1. Injury

The NMFS SPL criteria for injury to marine mammals from acoustic exposure were set according to recommendations for cautionary estimates of sound levels leading to onset of permanent hearing threshold shift (PTS). The U.S. National Marine Fisheries Service (NMFS) has set a threshold for underwater noise exposure at an SPL of 180 dB re 1 µPa for mysticetes (baleen whales), sperm whales (*Physeter macrocephalus*), and *Kogia spp*. and an SPL of 190 dB re 1 µPa for pinnipeds and most odontocetes (toothed whales), for all types of sound sources except tactical sonar and explosives (NMFS 2018). These injury thresholds are applied to individual noise pulses or instantaneous sound levels and do not consider the overall duration of the noise or its acoustic frequency distribution.

Criteria that do not account for exposure duration or noise spectra are generally insufficient on their own for assessing hearing injury. Human workplace noise assessment metrics consider the SPL, as well as the duration of exposure and sound spectral characteristics. For example, the International Institute of Noise Control Engineering (I-INCE) and the Occupational Safety and Health Administration (OSHA) suggest thresholds in C-weighted peak pressure level and A-weighted time-average sound level (dB(A)[1] L_{eq}). They also suggest exchange rates that increase the allowable thresholds for each halving or doubling of exposure time. This approach assumes that hearing damage depends on the relative loudness perceived by the human ear and that the ear might partially recover from past exposures, particularly if there are periods of quiet nested within the overall exposure.

In recognition of shortcomings of the SPL-only based injury criteria, in 2005 NMFS sponsored the Noise Criteria Group to review literature on marine mammal hearing to propose new noise exposure criteria. Members of this expert group published a landmark paper (Southall et al. 2007) that suggested assessment methods similar to those applied for humans. The resulting recommendations introduced dual acoustic injury criteria for impulsive sounds that included peak pressure level thresholds and SEL_{24h} thresholds, where the subscripted 24h refers to the accumulation period for calculating SEL. The peak pressure level criterion is not frequency weighted whereas the SEL_{24h} is frequency weighted according to one of four marine mammal species hearing groups: Low-, Mid- and High-Frequency Cetaceans (LF, MF, and HF respectively) and Pinnipeds in Water (PINN). These weighting functions are referred to as M-weighting filters (analogous to the C-weighting filter for humans; Appendix A.3). The SEL_{24h} Permanent Threshold Shift (PTS) values were obtained by applying a growth function of 2.3 dB to the Temporary Threshold Shift (TTS) value for each dB increase in noise, which was derived from experiments in terrestrial mammals (specifically chinchillas, Henderson and Hamernik 1986). This function translates to a PTS criterion (for impulses) of 15 dB above the onset level for TTS in marine mammals (defined above as 6 dB TTS). The Southall et al. (2007) recommendations do not specify an exchange rate, which suggests that the thresholds are the same regardless of the duration of exposure (i.e., it infers a 3 dB exchange rate).

[1] The “A” and “C” refer to specific frequency-dependent filters shaped according to a human equal loudness contour.

Wood et al. (2012) refined Southall et al.'s (2007) thresholds, suggesting lower injury values for LF and HF cetaceans, while retaining the filter shapes (Appendix A.3). Their revised thresholds were based on TTS-onset levels in harbour porpoises from Lucke et al. (2009), which led to a revised impulsive sound PTS threshold for HF cetaceans of 179 dB re 1 µPa^2·s. Because there were no data available for baleen whales, Wood et al. (2012) based their recommendations for LF cetaceans on results obtained from MF cetacean studies. In particular they referenced Finneran and Schlundt (2010) research, which found MF cetaceans are more sensitive to non-impulsive sound exposure than Southall et al. (2007) assumed. Wood et al. (2012) thus, recommended a more conservative TTS-onset level for LFC of 192 dB re 1 µPa^2·s.

Also in 2012, the US Navy recommended a different set of criteria for assessing Navy operations (Finneran and Jenkins 2012). Their analysis incorporated new dolphin equal-loudness contours[2] to update weighting functions and injury thresholds for LF, MF, and HF cetaceans. They recommended separating the pinniped group into otariids (eared seals) and phocids (earless seals) and assigning adjusted frequency thresholds to the former based on several sensitivity studies (Schusterman et al. 1972, Moore and Schusterman 1987, Babushina et al. 1991, Kastak and Schusterman 1998, Kastelein et al. 2005, Mulsow and Reichmuth 2007, Mulsow et al. 2011a, Mulsow et al. 2011b).

Although a definitive approach is not yet apparent, there is consensus in the research community that an SEL-based method is preferable either separately or in addition to an SPL-based approach to assess the potential for injuries. In August 2016, after substantial public and expert input into three draft versions and based largely on the above-mentioned literature (NOAA 2013, 2015, 2016), NMFS finalized and promulgated technical guidance for assessing the effect of anthropogenic sound on marine mammal hearing (NMFS 2018). The guidance describes injury criteria with new thresholds and frequency weighting functions for the five hearing groups described by Finneran and Jenkins (2012). Table A-1 provide the recommended thresholds.

Table A-1. Marine mammal injury (PTS onset) thresholds based on NMFS (2018).

Hearing group	Impulsive source		Non-impulsive source
	PK	Weighted SEL (24 h)	Weighted SEL (24 h)
Low-frequency cetaceans	219	183	199
Mid-frequency cetaceans	230	185	198
High-frequency cetaceans	202	155	173
Phocid pinnipeds in water	218	185	201
Otariid pinnipeds in water	232	203	219

A.2.2. Disturbance

The NOAA/NMFS currently uses SPL thresholds for behavioural response of 160 dB re 1 µPa for impulsive sounds and 120 dB re 1 µPa for non-impulsive sounds for all marine mammal species (NOAA 2005), based on observations of mysticetes (Malme et al. 1983, Malme et al. 1984, Richardson et al. 1986, Richardson et al. 1990). These disturbance thresholds are under review and a new set of behavioural criteria will be implemented in due course. NOAA/NMFS makes exceptions on a species-specific and sub-population specific basis where warranted. Southall et al. (2007) promoted the use of TTS onset levels as criteria for behavioural disturbance. While this has been recognised by NOAA/NMFS, they also take into account that behavioural disruption occurs at levels below onset of TTS. In their 2013-Draft Guidance (NOAA 2013), it is stated: "NOAA currently is in the process of developing 24 new

[2] An equal-loudness contour is the measured sound pressure level (dB re 1 µPa for underwater sounds) over frequency, for which a listener perceives a constant loudness when exposed to pure tones.

thresholds for onset of behavioral effects. When that process is completed, TTS will be addressed for purposes of take quantification. In the meantime, the TTS thresholds presented [*in the Draft Guidance*] represent the best available science and will be used in the comprehensive effects analyses under the MMPA and the ESA and may inform the development of mitigation and monitoring."

A.3. Marine Mammal Frequency Weighting

The potential for noise to affect animals depends on how well the animals can hear it. Noises are less likely to disturb or injure an animal if they are at frequencies that the animal cannot hear well. An exception occurs when the sound pressure is so high that it can physically injure an animal by non-auditory means (i.e., barotrauma). For sound levels below such extremes, the importance of sound components at particular frequencies can be scaled by frequency weighting relevant to an animal's sensitivity to those frequencies (Nedwell and Turnpenny 1998, Nedwell et al. 2007).

A.3.1. Marine Mammal Frequency Weighting Functions

In 2015, a U.S. Navy technical report by Finneran (2015) recommended new auditory weighting functions. The overall shape of the auditory weighting functions is similar to human A-weighting functions, which follows the sensitivity of the human ear at low sound levels. The new frequency-weighting function is expressed as:

$$G(f) = K + 10\log_{10}\left[\left(\frac{(f/f_{lo})^{2a}}{\left[1+(f/f_{lo})^{2}\right]^{a}\left[1+(f/f_{hi})^{2}\right]^{b}}\right)\right], \qquad \text{(A-11)}$$

Finneran (2015) proposed five functional hearing groups for marine mammals in water: low-, mid-, and high-frequency cetaceans, phocid pinnipeds, and otariid pinnipeds. The parameters for these frequency-weighting functions were further modified the following year (Finneran 2016) and were adopted in NOAA's technical guidance that assesses noise impacts on marine mammals (NMFS 2018). Table A-2 lists the frequency-weighting parameters for each hearing group; Figure A-3 shows the resulting frequency-weighting curves.

Table A-2. Parameters for the auditory weighting functions recommended by NMFS (2018).

Hearing group	*a*	*b*	f_{lo} (Hz)	f_{hi} (Hz)	*K* (dB)
Low-frequency cetaceans	1.0	2	200	19,000	0.13
Mid-frequency cetaceans	1.6	2	8,800	110,000	1.20
High-frequency cetaceans	1.8	2	12,000	140,000	1.36
Phocid pinnipeds in water	1.0	2	1,900	30,000	0.75
Otariid pinnipeds in water	2.0	2	940	25,000	0.64

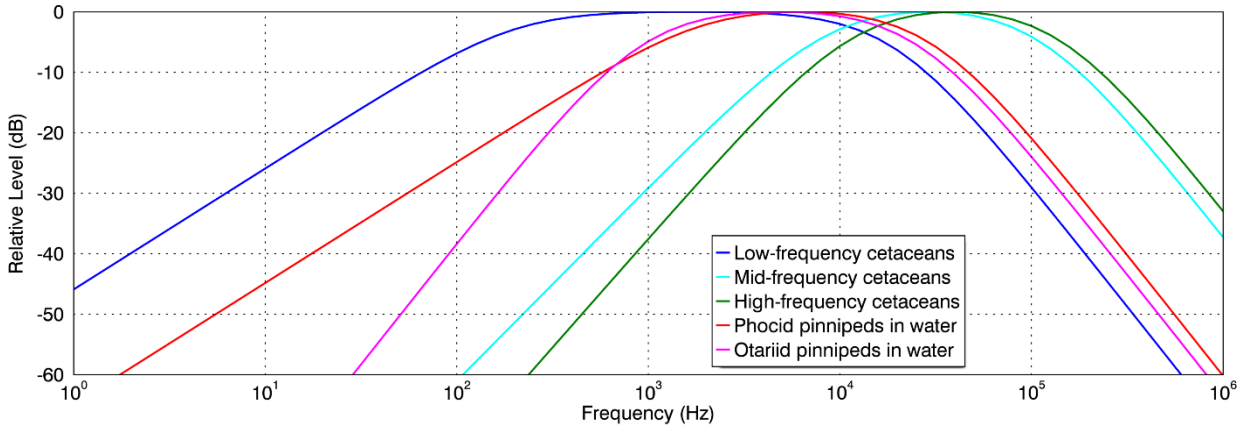

Figure A-3. Auditory weighting functions for functional marine mammal hearing groups as recommended by NMFS (2018).

Appendix B. Sound Propagation Modelling

B.1. Summer Sound Speed Profiles

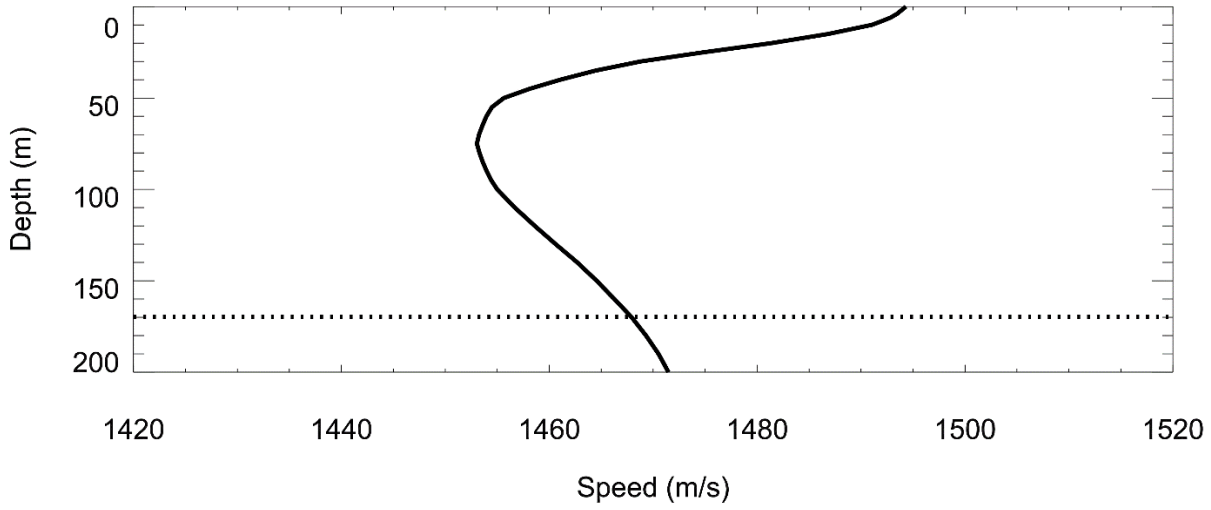

Figure B-1. Site 1: Historical average (GDEM) sound speed profile for July. The dashed line indicates the AMAR deployment depth.

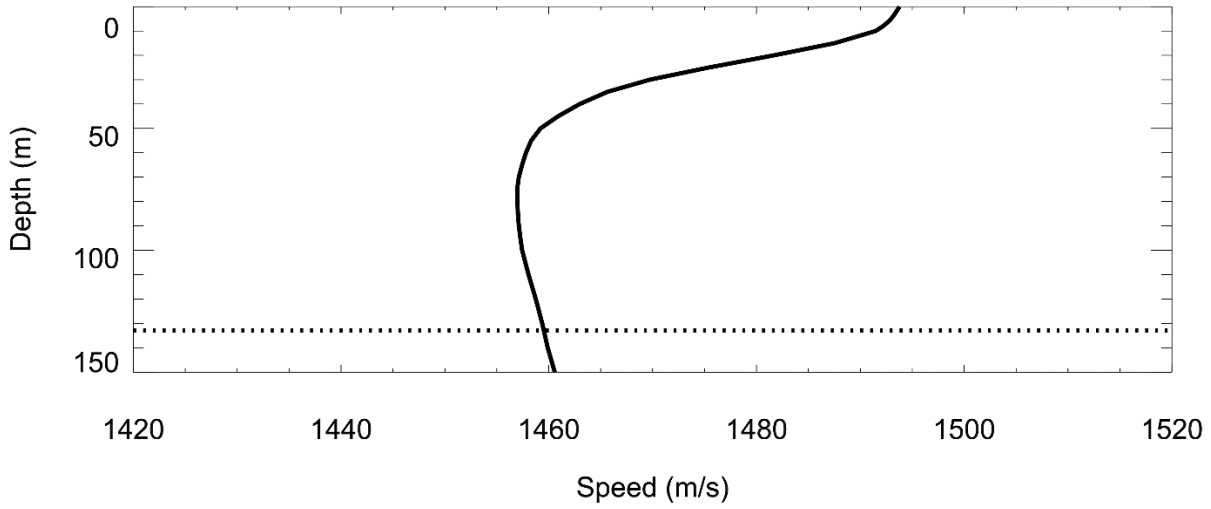

Figure B-2. Site 2: Historical average (GDEM) sound speed profile for July. The dashed line indicates the AMAR deployment depth.

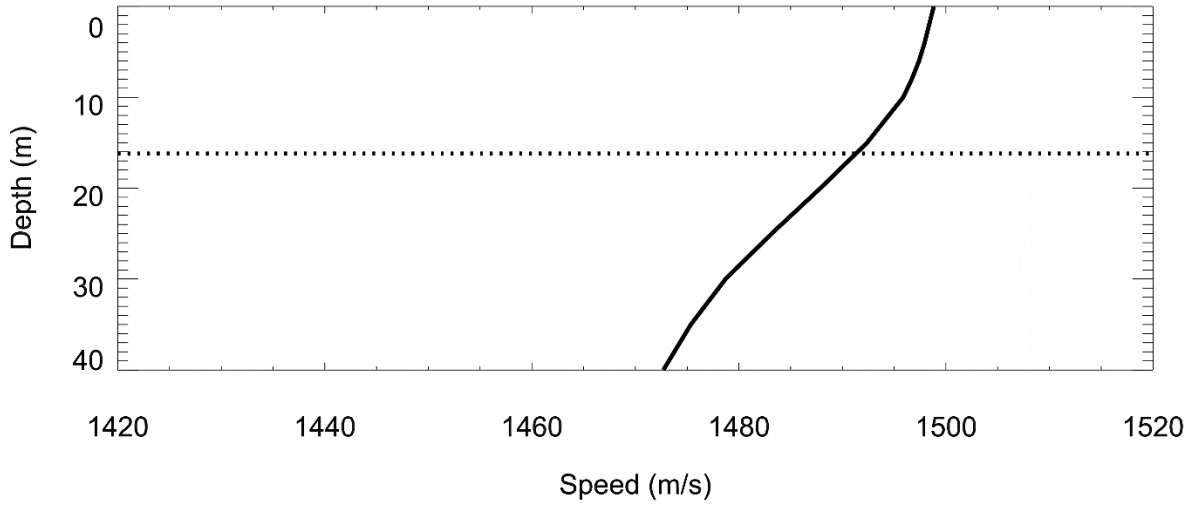

Figure B-3. Site 3: Historical average (GDEM) sound speed profile for July. The dashed line indicates the AMAR deployment depth.

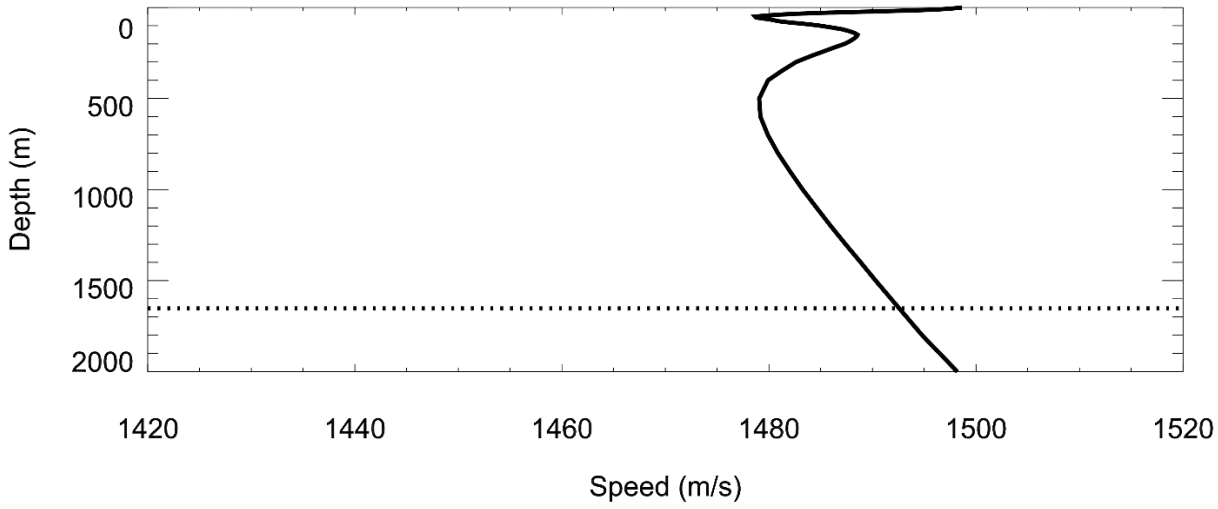

Figure B-4. Site 4: Historical average (GDEM) sound speed profile for July. The dashed line indicates the AMAR deployment depth.

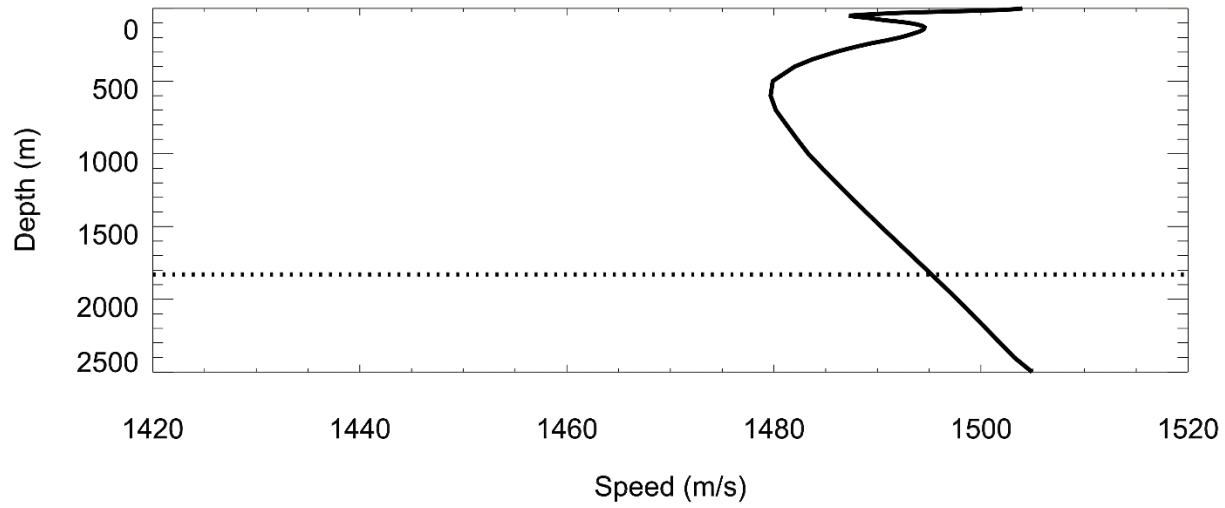

Figure B-5. Site 5: Historical average (GDEM) sound speed profile for July. The dashed line indicates the AMAR deployment depth.

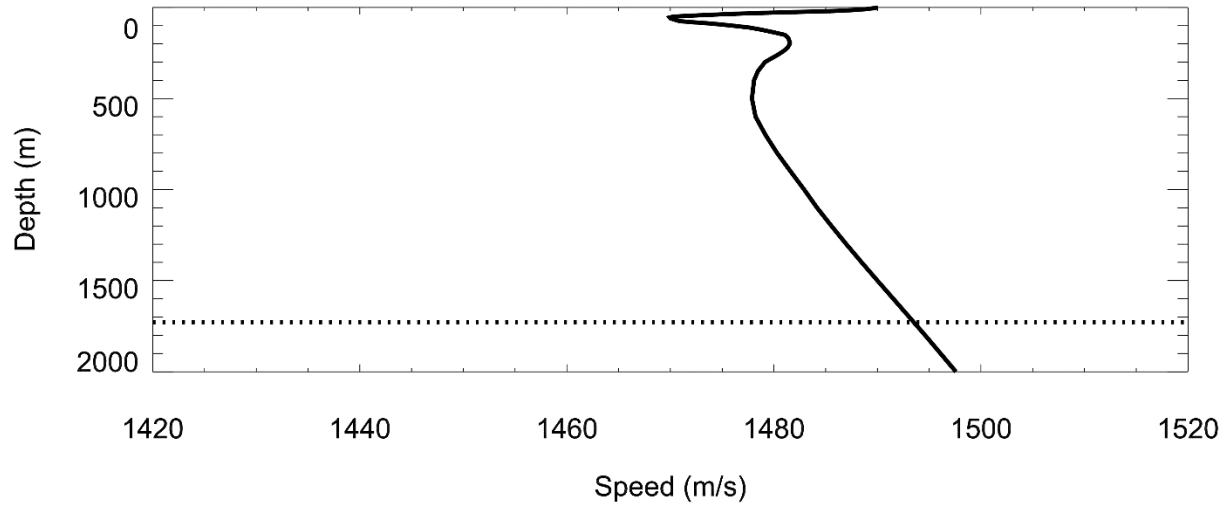

Figure B-6. Site 6: Historical average (GDEM) sound speed profile for July. The dashed line indicates the AMAR deployment depth.

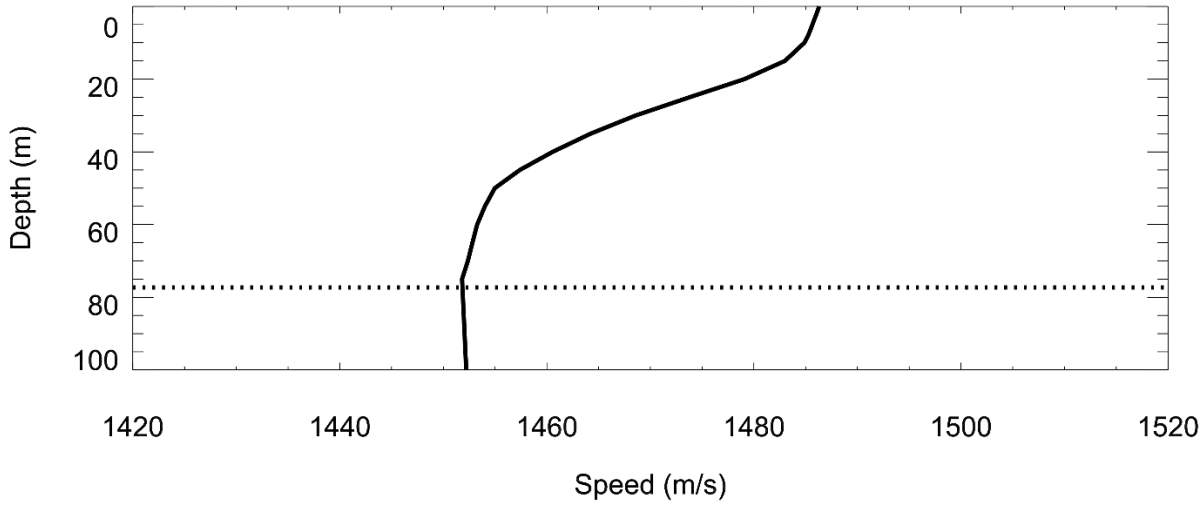

Figure B-7. Site 7: Historical average (GDEM) sound speed profile for July. The dashed line indicates the AMAR deployment depth.

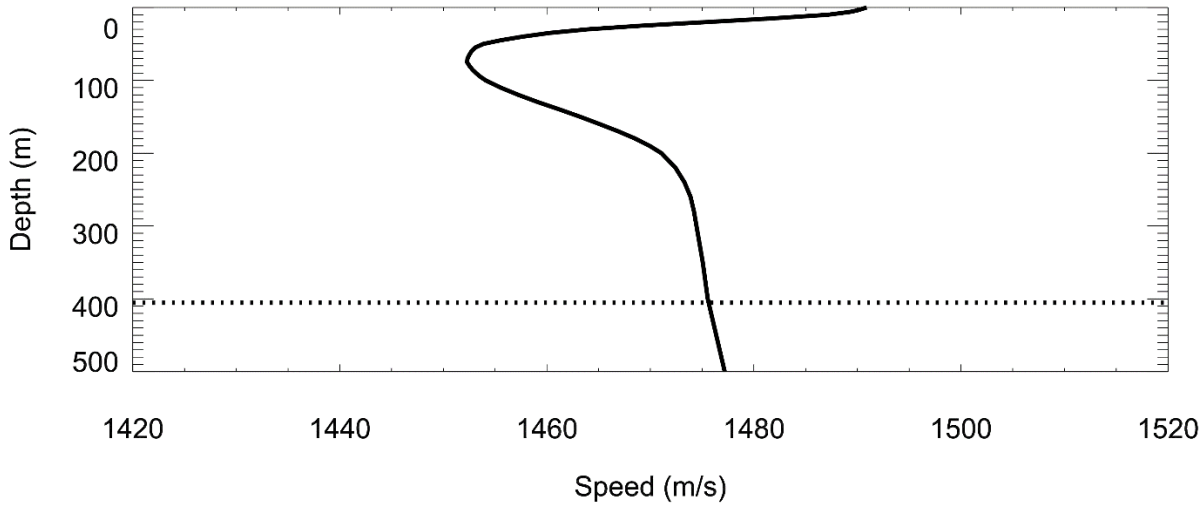

Figure B-8. Site 8: Historical average (GDEM) sound speed profile for July. The dashed line indicates the AMAR deployment depth.

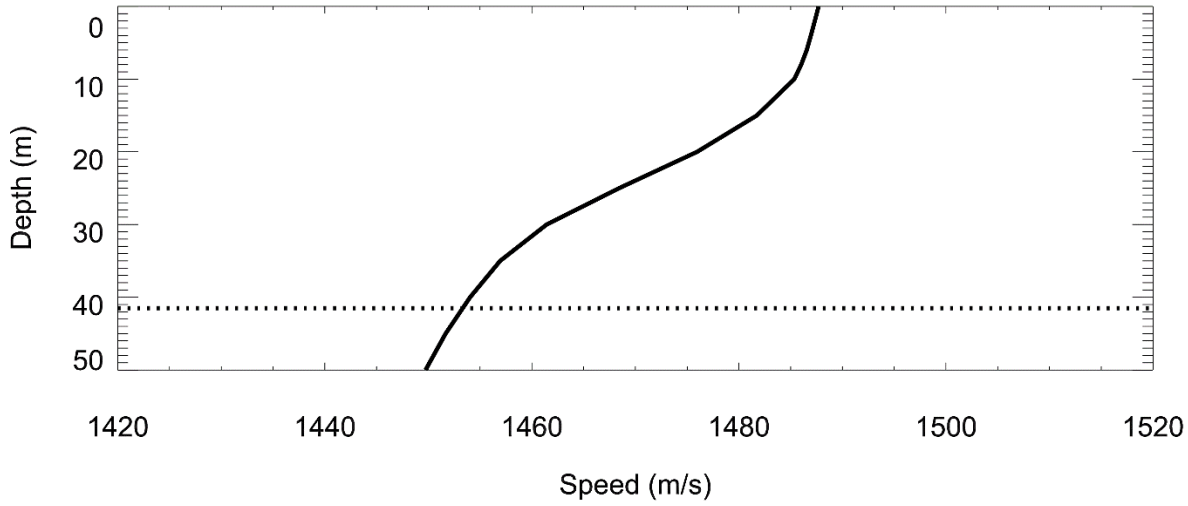

Figure B-9. Site 9: Historical average (GDEM) sound speed profile for July. The dashed line indicates the AMAR deployment depth.

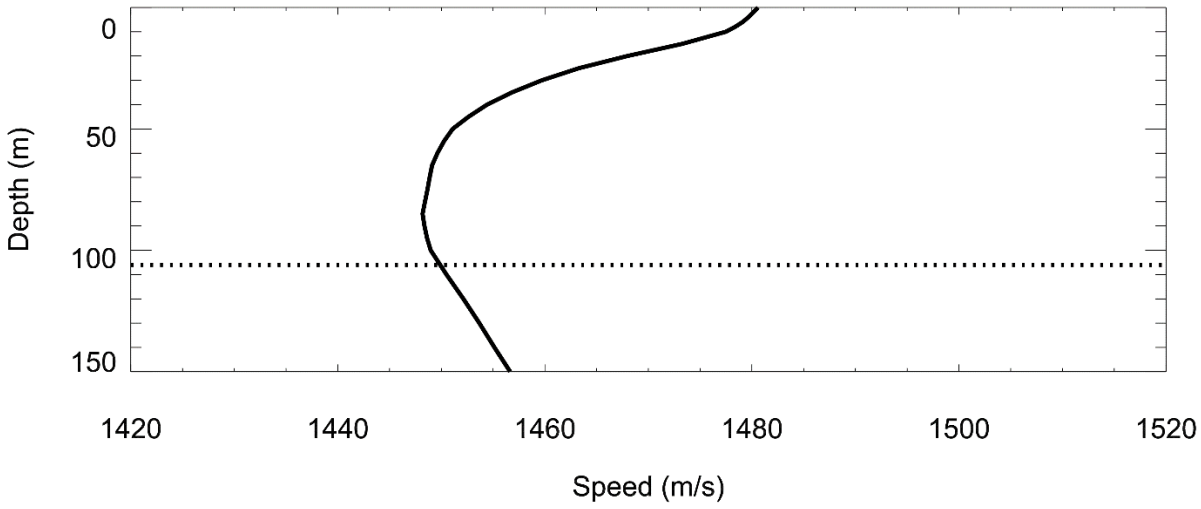

Figure B-10. Site 10: Historical average (GDEM) sound speed profile for July. The dashed line indicates the AMAR deployment depth.

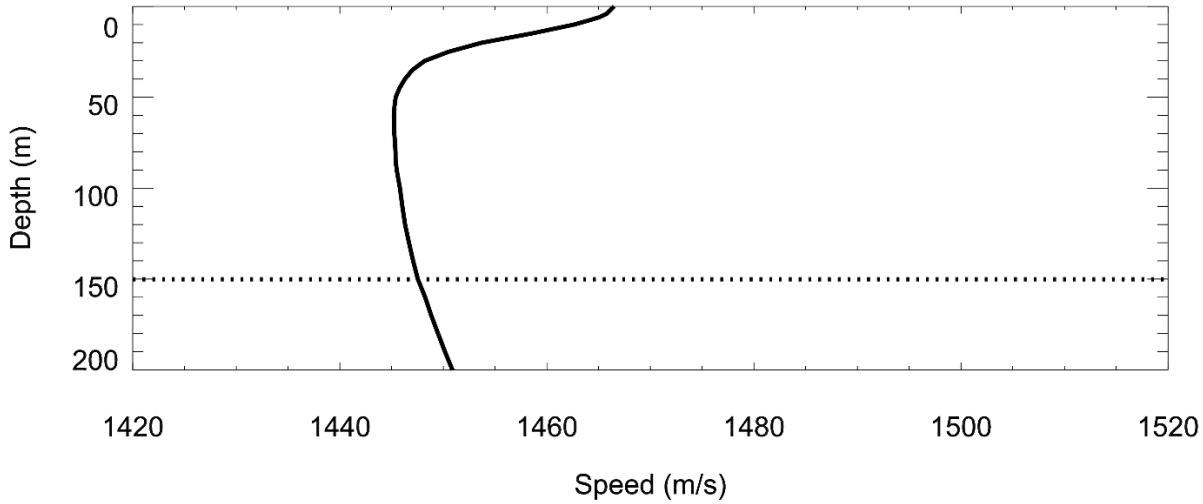

Figure B-11. Site 11: Historical average (GDEM) sound speed profile for July. The dashed line indicates the AMAR deployment depth.

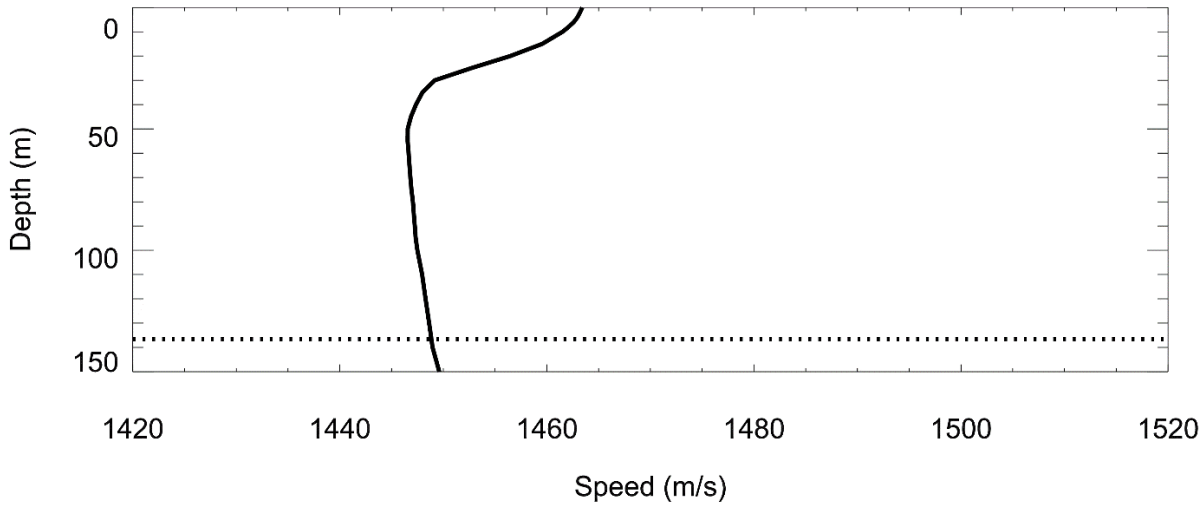

Figure B-12. Site 12: Historical average (GDEM) sound speed profile for July. The dashed line indicates the AMAR deployment depth.

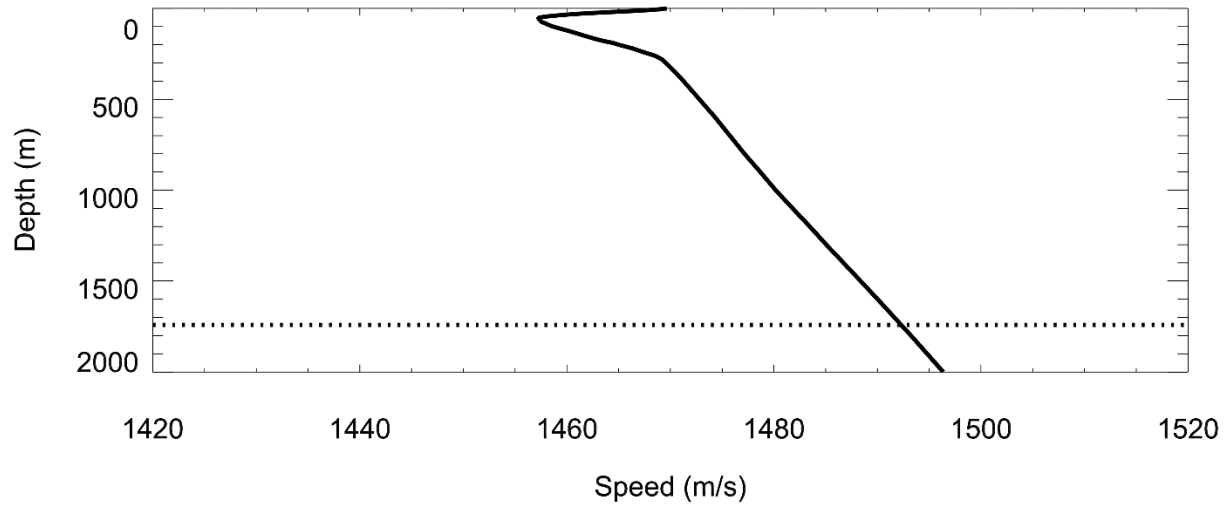

Figure B-13. Site 13: Historical average (GDEM) sound speed profile for July. The dashed line indicates the AMAR deployment depth.

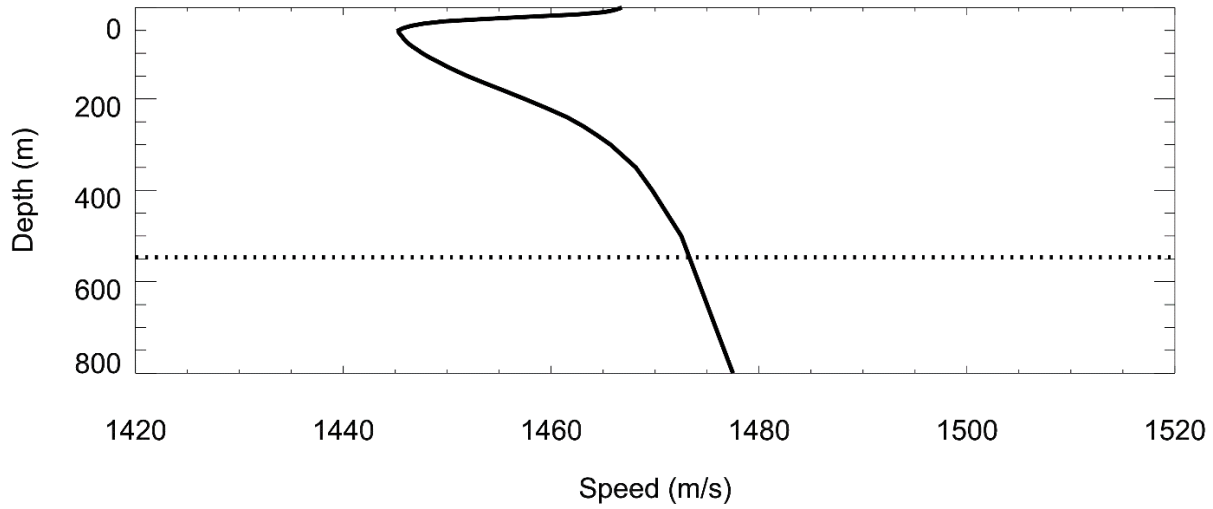

Figure B-14. Site 14: Historical average (GDEM) sound speed profile for July. The dashed line indicates the AMAR deployment depth.

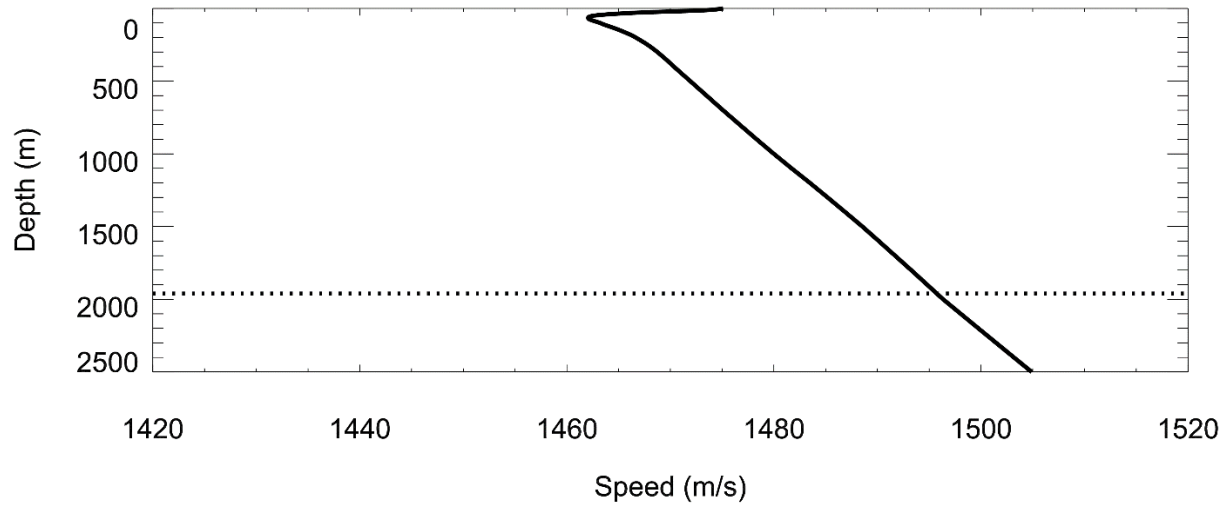

Figure B-15. Site 15: Historical average (GDEM) sound speed profile for July. The dashed line indicates the AMAR deployment depth.

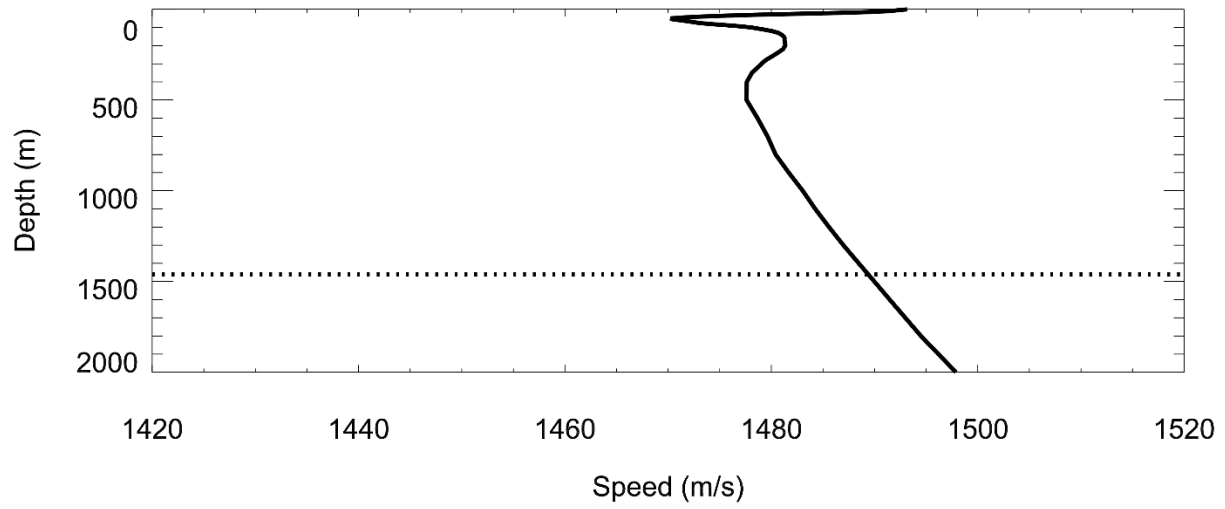

Figure B-16. Site 16: Historical average (GDEM) sound speed profile for July. The dashed line indicates the AMAR deployment depth.

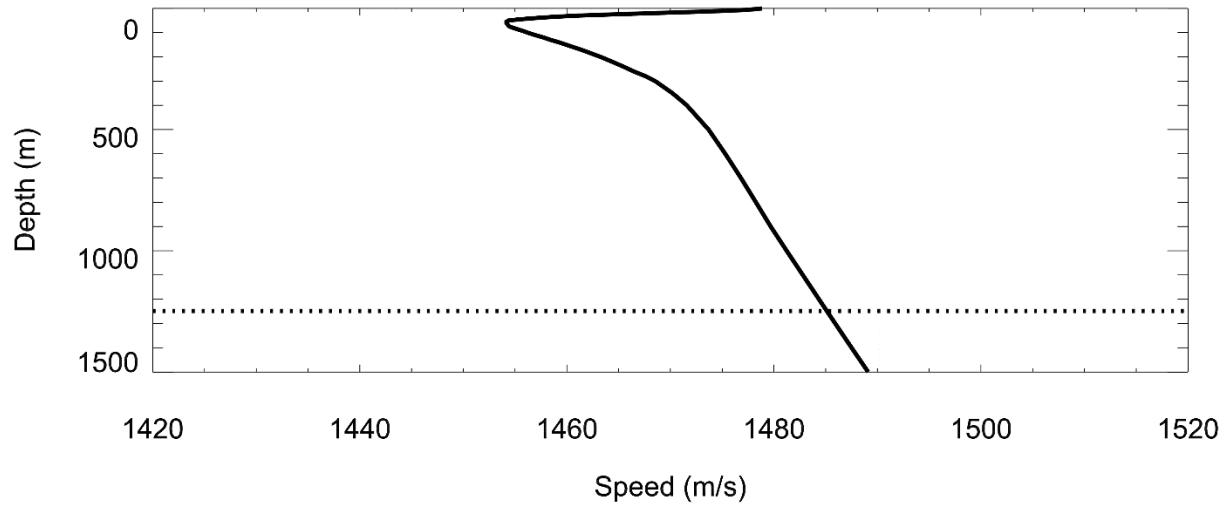

Figure B-17. Site 17: Historical average (GDEM) sound speed profile for July. The dashed line indicates the AMAR deployment depth.

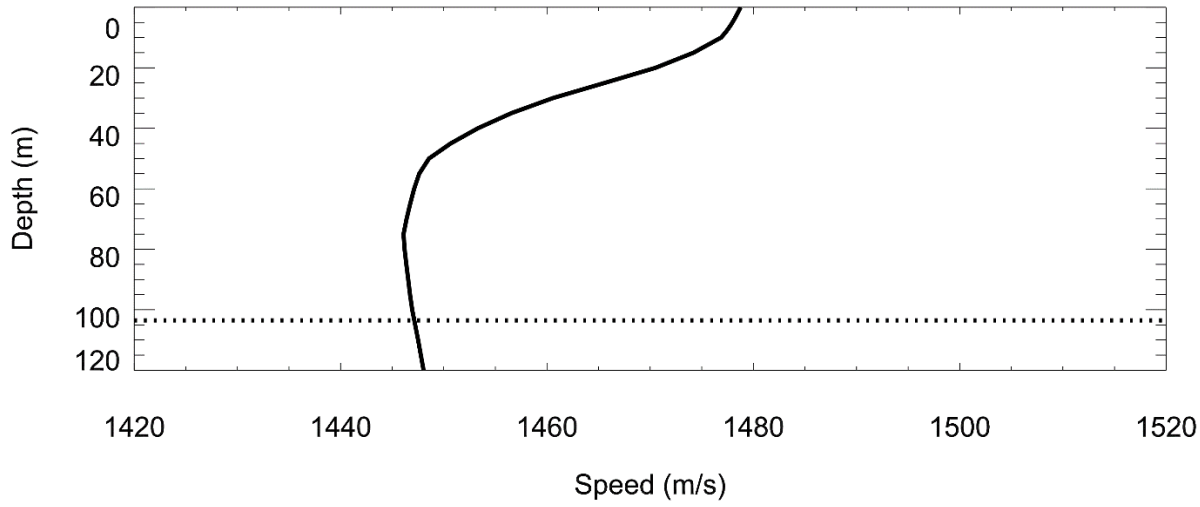

Figure B-18. Site 18: Historical average (GDEM) sound speed profile for July. The dashed line indicates the AMAR deployment depth.

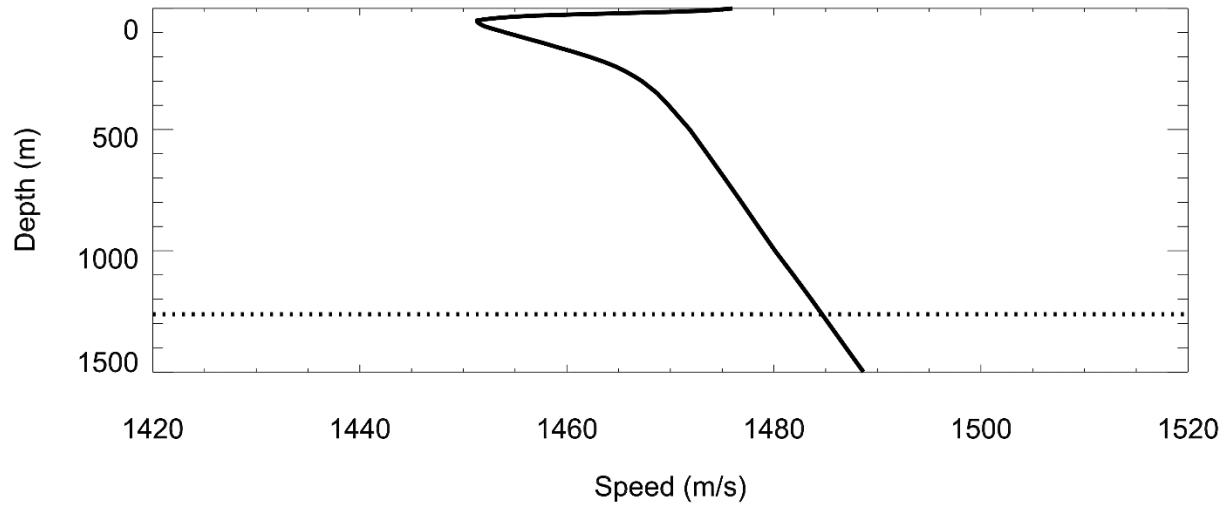

Figure B-19. Site 19: Historical average (GDEM) sound speed profile for July. The dashed line indicates the AMAR deployment depth.

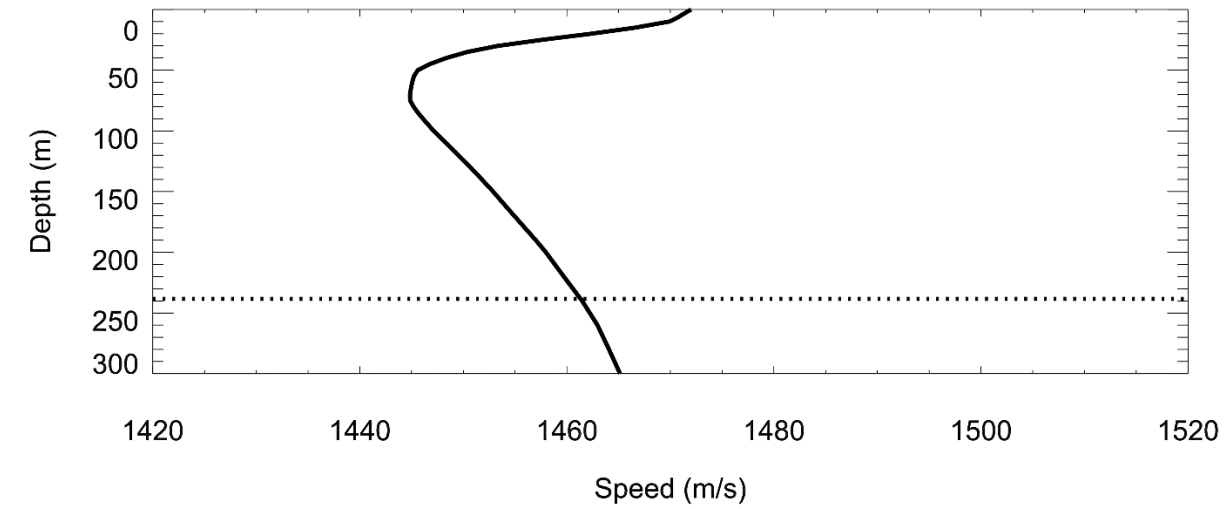

Figure B-20. Site 20: Historical average (GDEM) sound speed profile for July. The dashed line indicates the AMAR deployment depth.

B.2. Winter Sound Speed Profiles

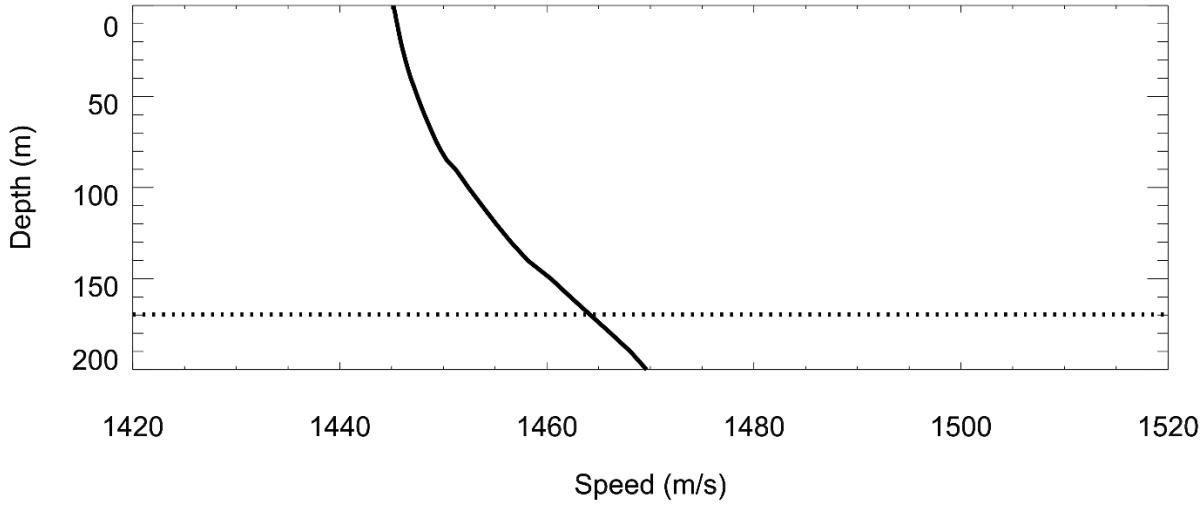

Figure B-21. Site 1: Historical average (GDEM) sound speed profile for February. The dashed line indicates the AMAR deployment depth.

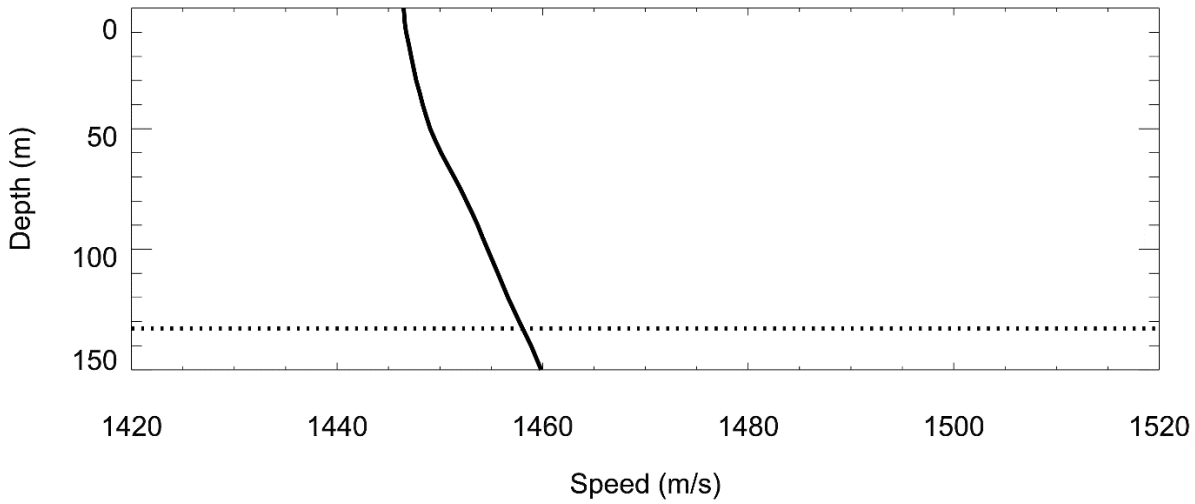

Figure B-22. Site 2: Historical average (GDEM) sound speed profile for February. The dashed line indicates the AMAR deployment depth.

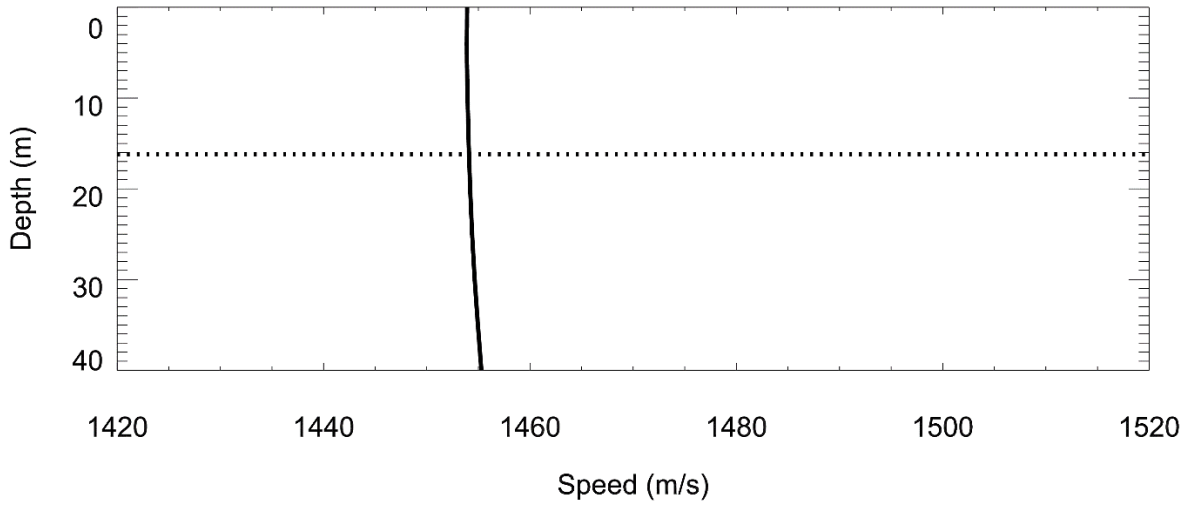

Figure B-23. Site 3: Historical average (GDEM) sound speed profile for February. The dashed line indicates the AMAR deployment depth.

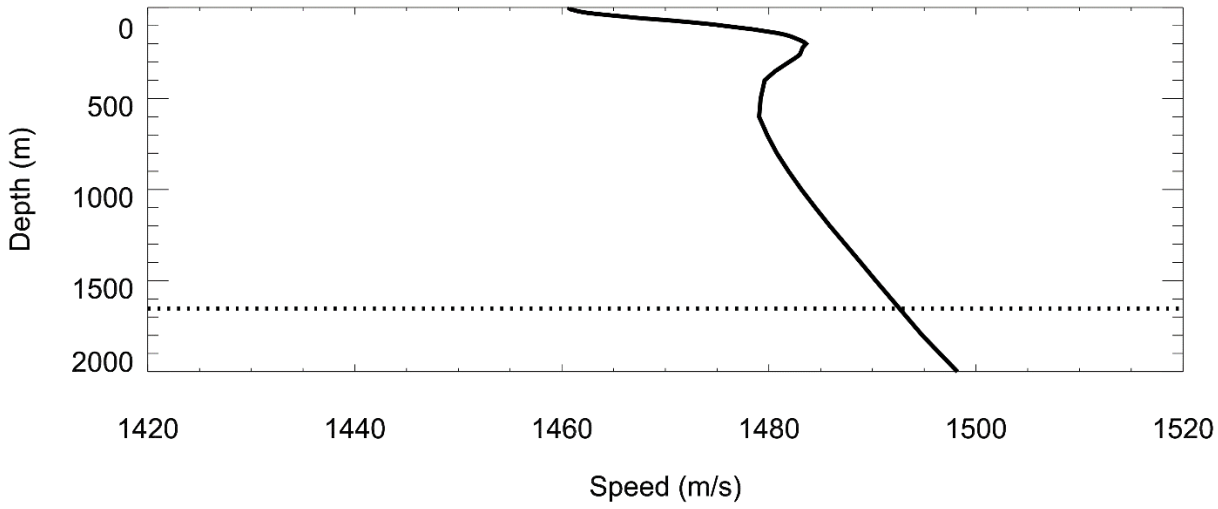

Figure B-24. Site 4: Historical average (GDEM) sound speed profile for February. The dashed line indicates the AMAR deployment depth.

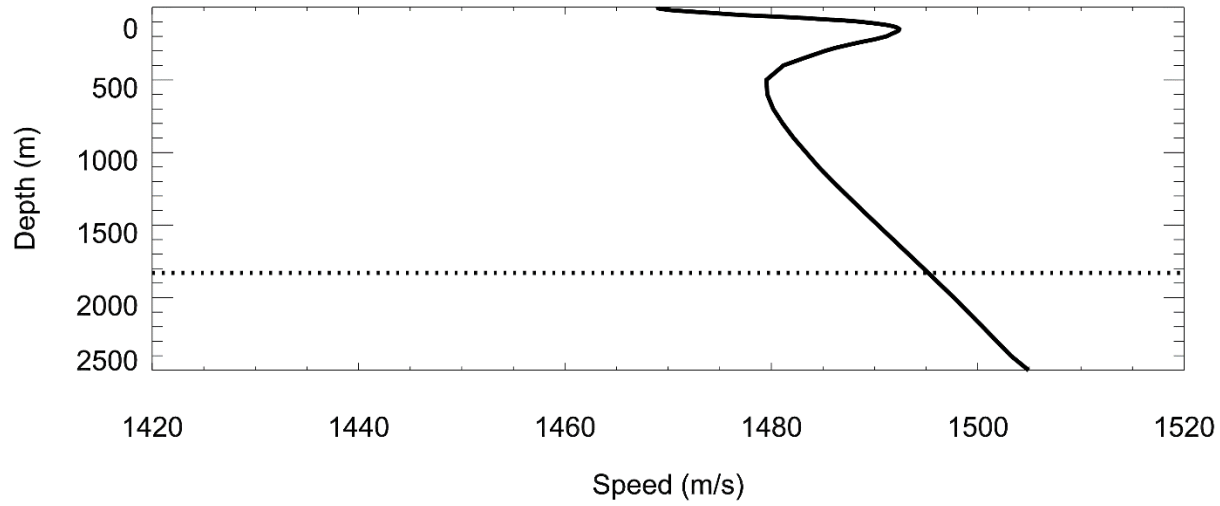

Figure B-25. Site 5: Historical average (GDEM) sound speed profile for February. The dashed line indicates the AMAR deployment depth.

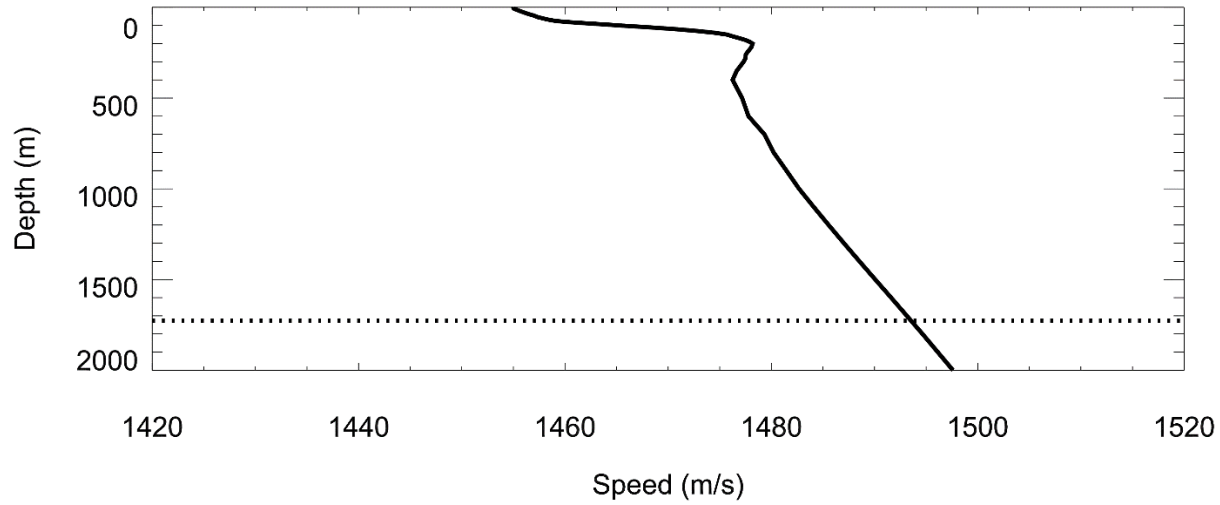

Figure B-26. Site 6: Historical average (GDEM) sound speed profile for February. The dashed line indicates the AMAR deployment depth.

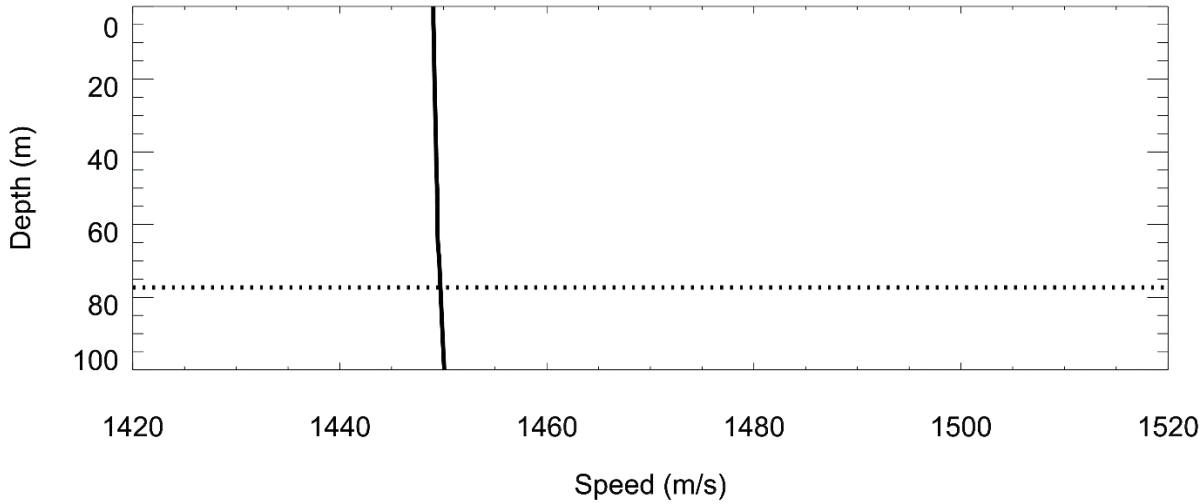

Figure B-27. Site 7: Historical average (GDEM) sound speed profile for February. The dashed line indicates the AMAR deployment depth.

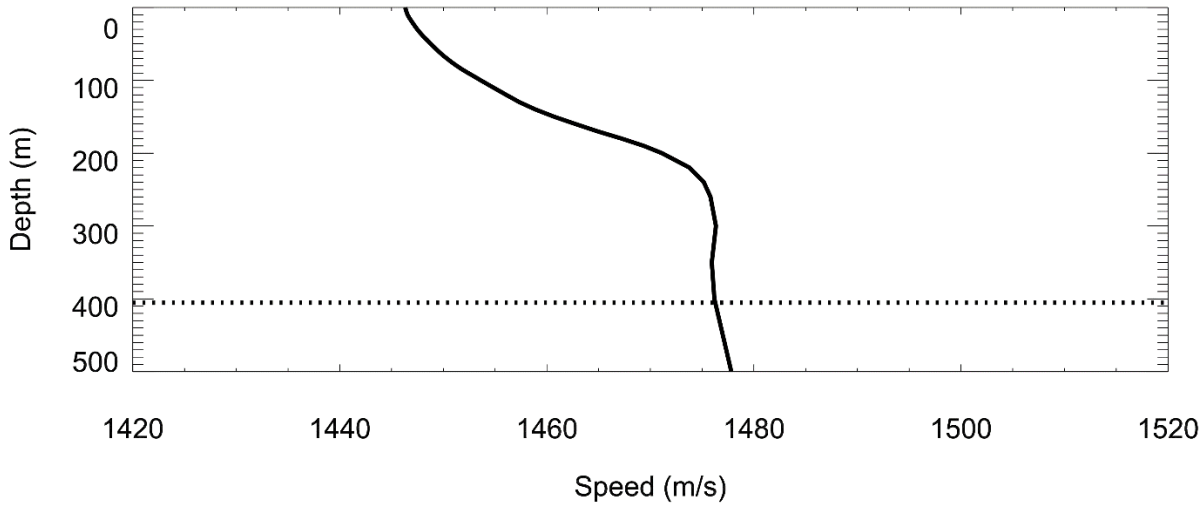

Figure B-28. Site 8: Historical average (GDEM) sound speed profile for February. The dashed line indicates the AMAR deployment depth.

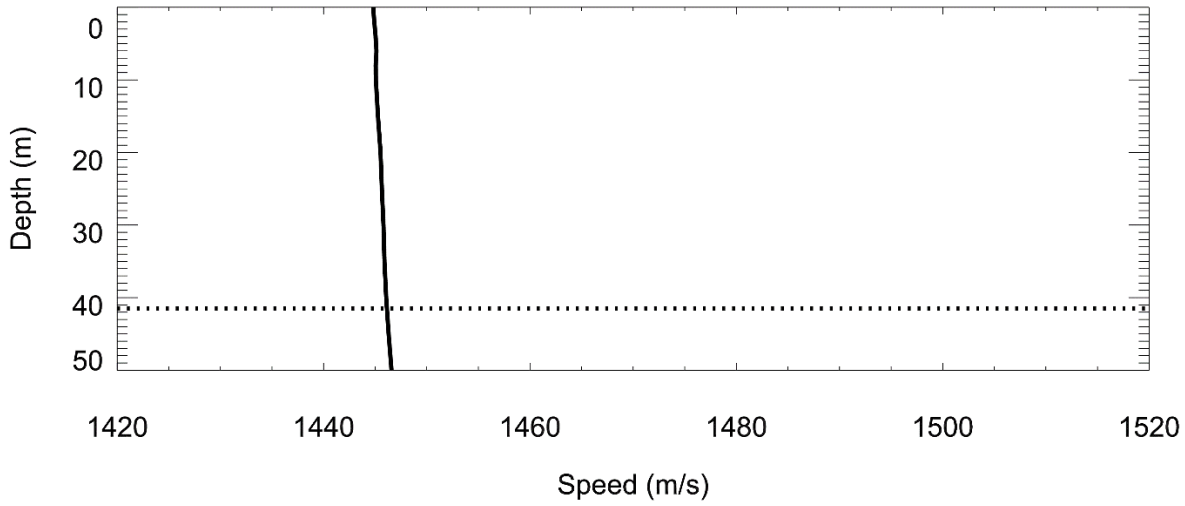

Figure B-29. Site 9: Historical average (GDEM) sound speed profile for February. The dashed line indicates the AMAR deployment depth.

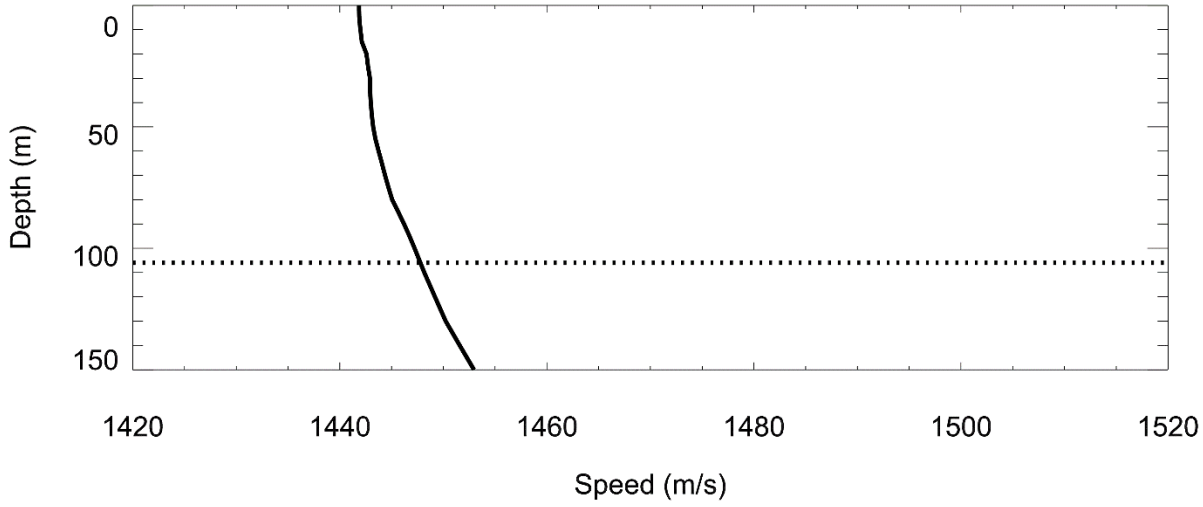

Figure B-30. Site 10: Historical average (GDEM) sound speed profile for February. The dashed line indicates the AMAR deployment depth.

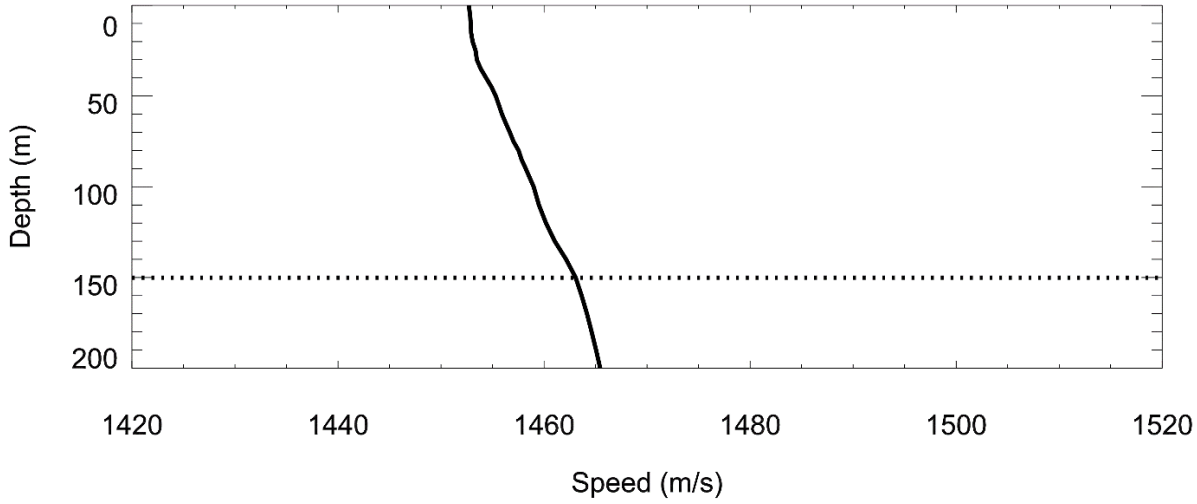

Figure B-31. Site 11: Historical average (GDEM) sound speed profile for February. The dashed line indicates the AMAR deployment depth.

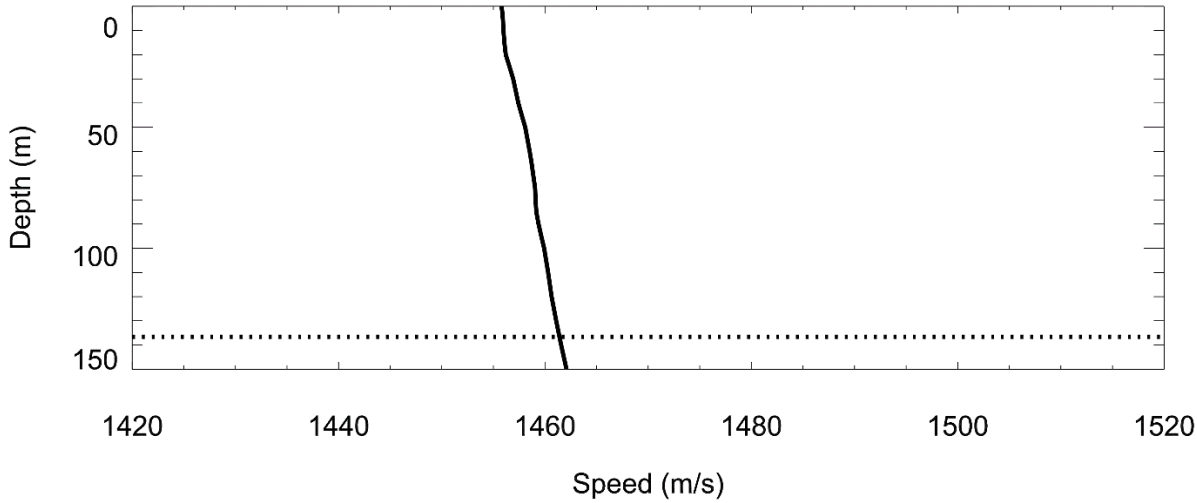

Figure B-32. Site 12: Historical average (GDEM) sound speed profile for February. The dashed line indicates the AMAR deployment depth.

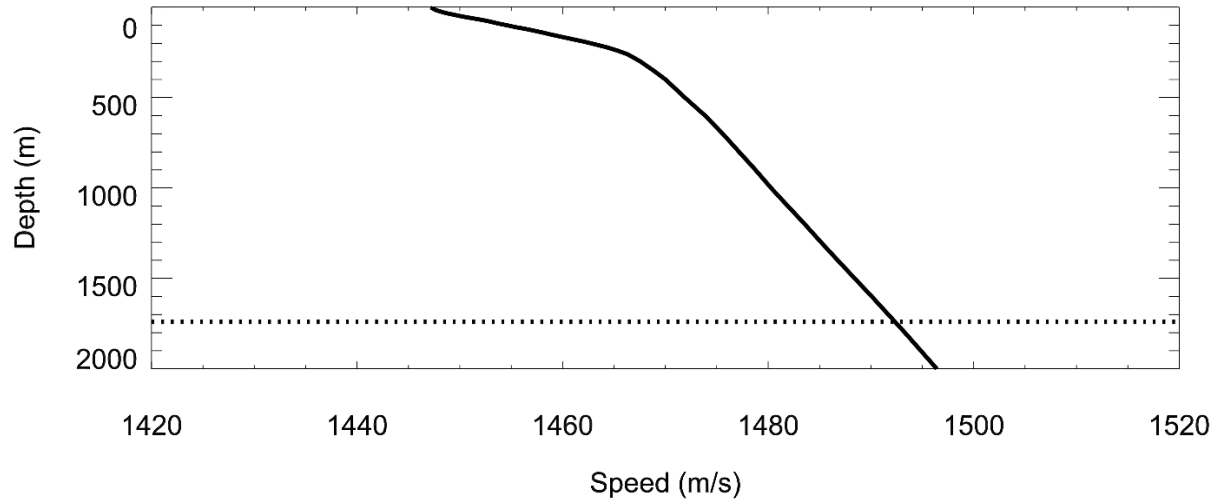

Figure B-33. Site 13: Historical average (GDEM) sound speed profile for February. The dashed line indicates the AMAR deployment depth.

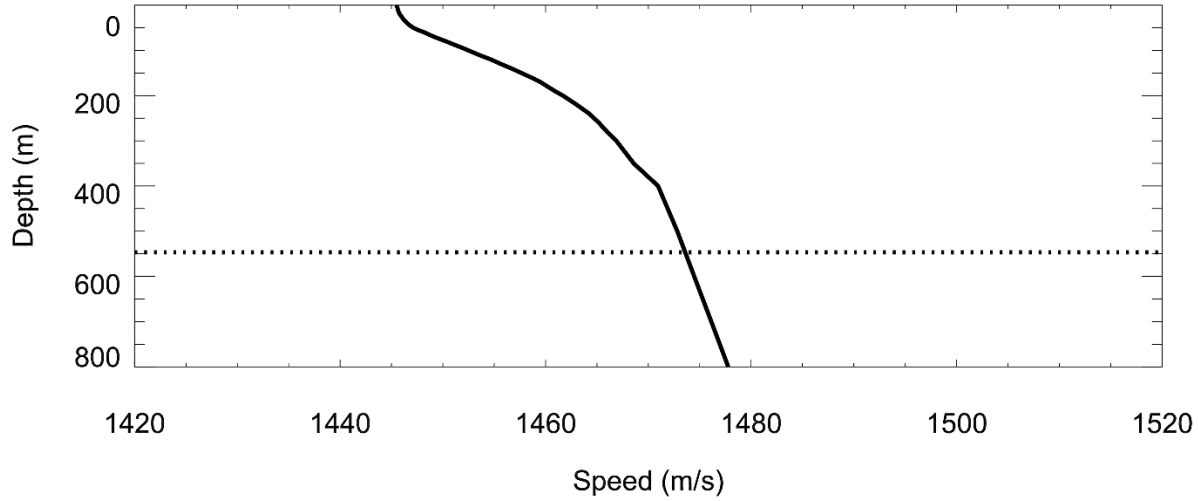

Figure B-34. Site 14: Historical average (GDEM) sound speed profile for February. The dashed line indicates the AMAR deployment depth.

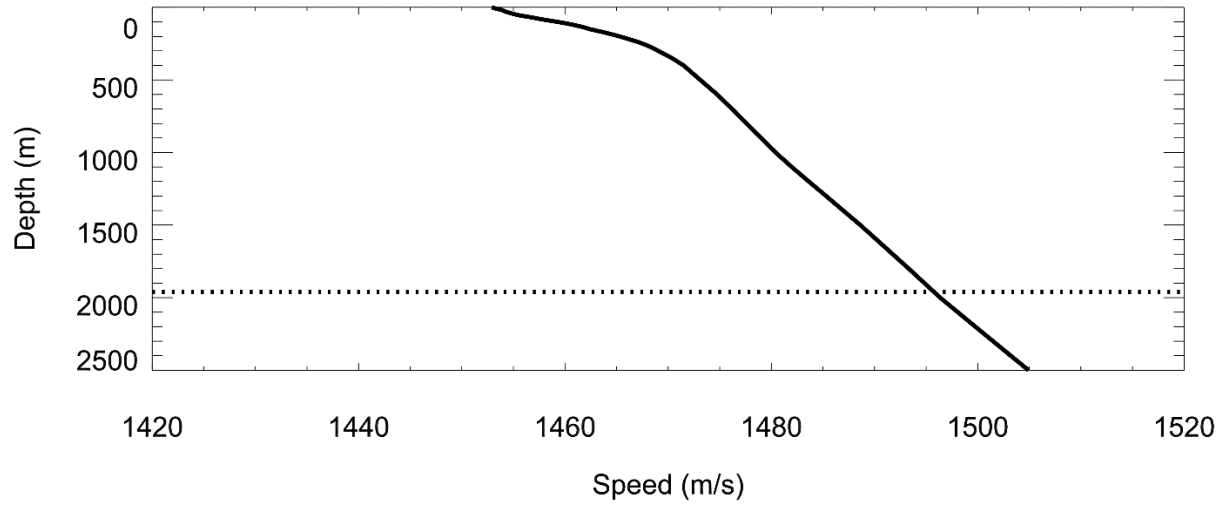

Figure B-35. Site 15: Historical average (GDEM) sound speed profile for February. The dashed line indicates the AMAR deployment depth.

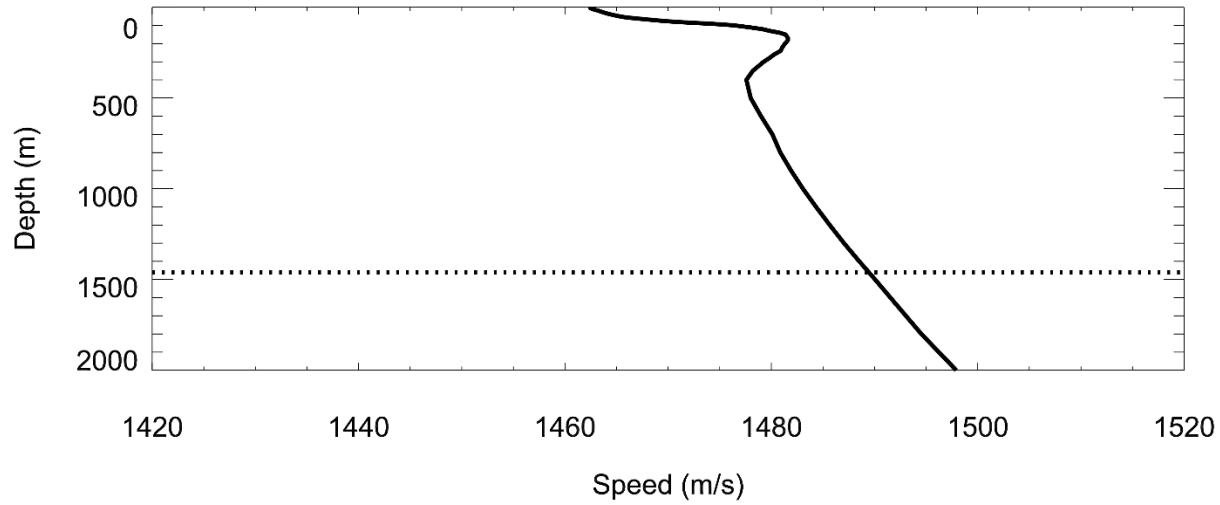

Figure B-36. Site 16: Historical average (GDEM) sound speed profile for February. The dashed line indicates the AMAR deployment depth.

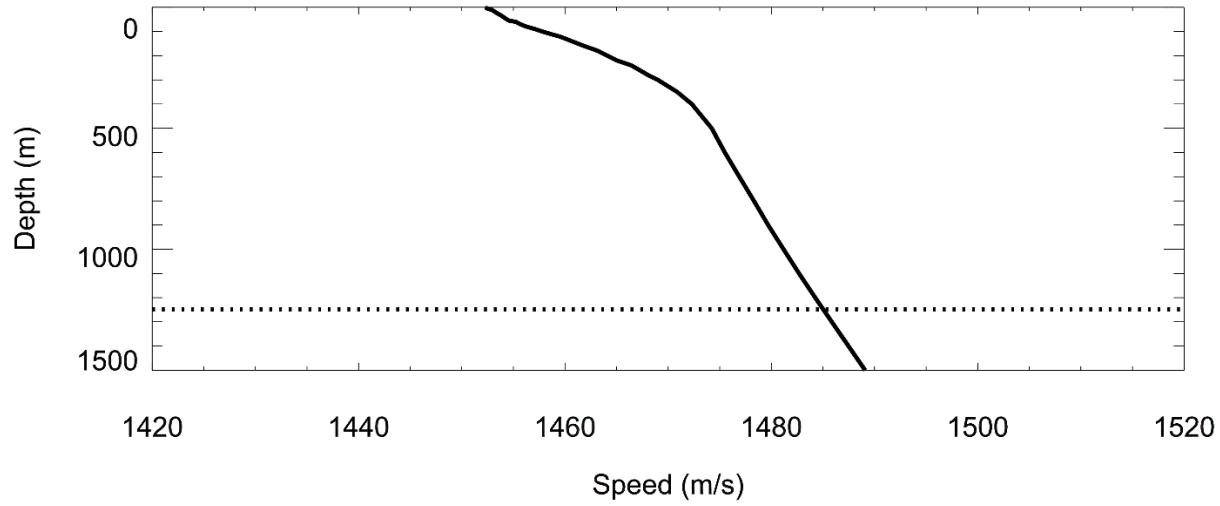

Figure B-37. Site 17: Historical average (GDEM) sound speed profile for February. The dashed line indicates the AMAR deployment depth.

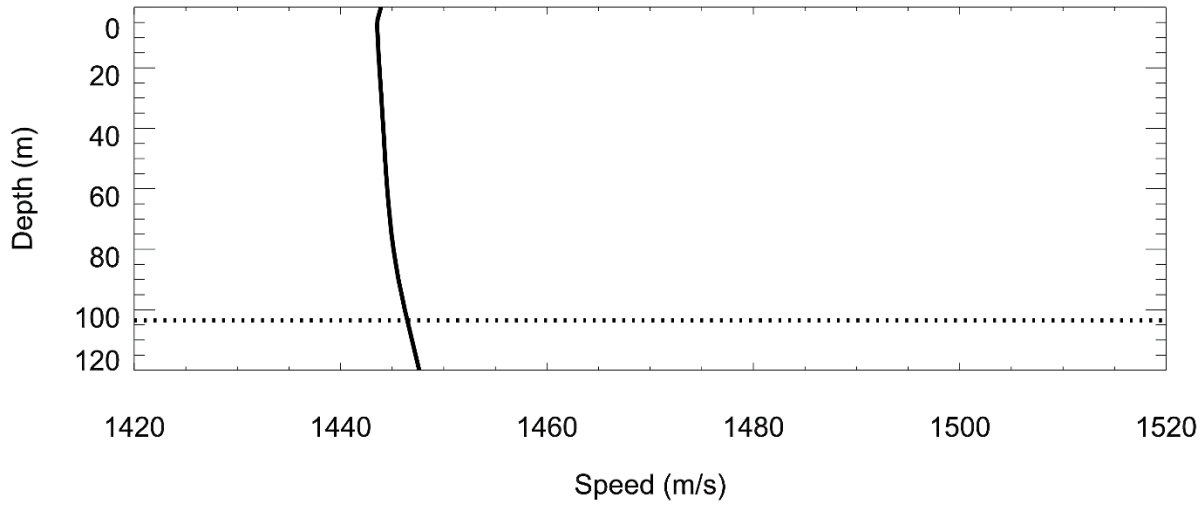

Figure B-38. Site 18: Historical average (GDEM) sound speed profile for February. The dashed line indicates the AMAR deployment depth.

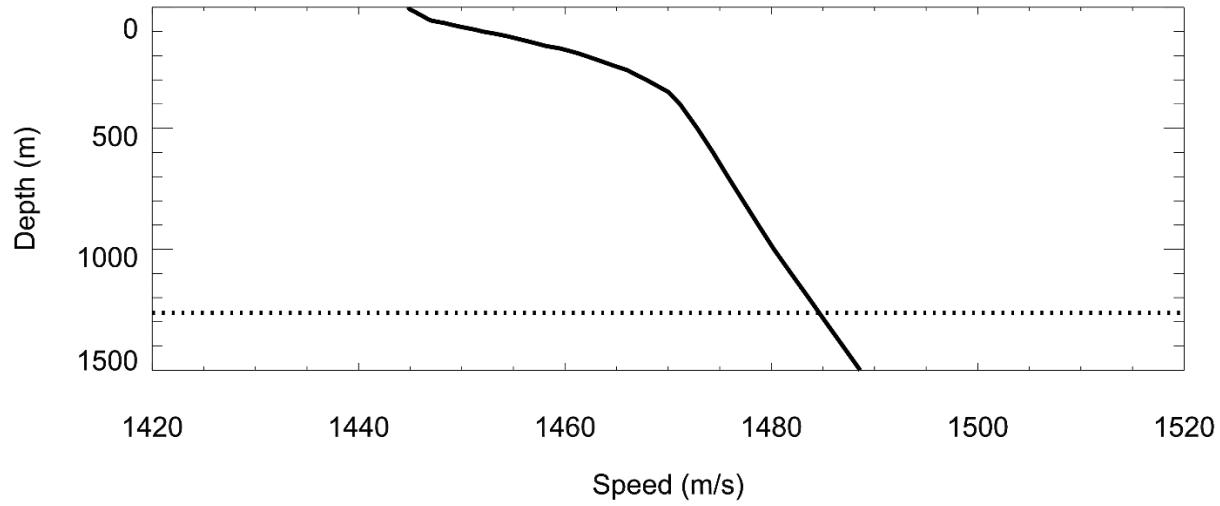

Figure B-39. Site 19: Historical average (GDEM) sound speed profile for February. The dashed line indicates the AMAR deployment depth.

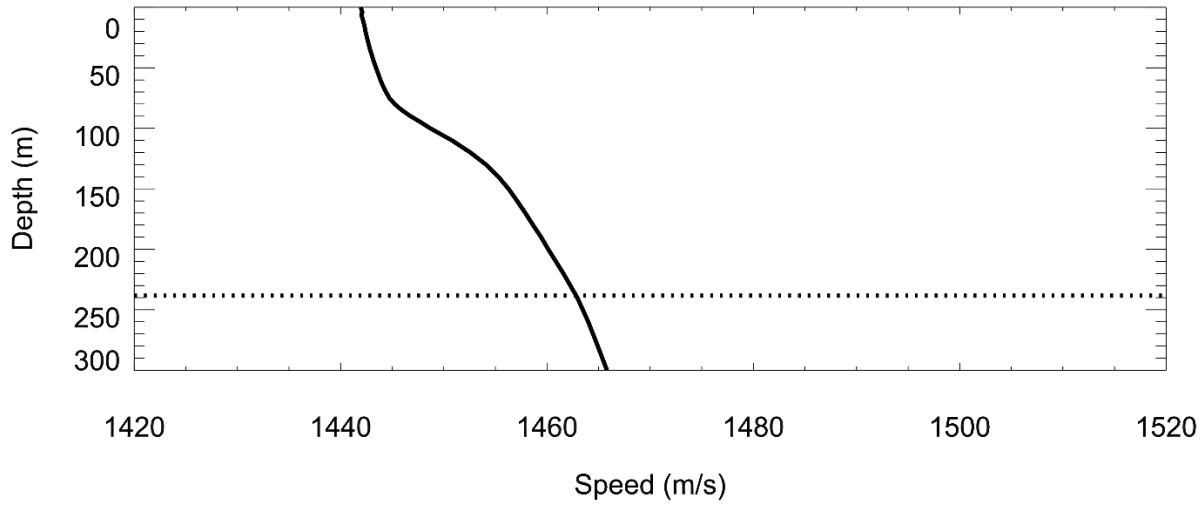

Figure B-40. Site 20: Historical average (GDEM) sound speed profile for February. The dashed line indicates the AMAR deployment depth.

B.3. Transmission Loss

The propagation of sound through the environment is modelled by predicting the acoustic transmission loss—a measure, in decibels, of the decrease in sound level between a source and a receiver some distance away. Transmission loss occurs through geometrical spreading and when sound is absorbed and scattered by seawater, and absorbed, scattered, and reflected at the water surface and within the subbottom. Transmission loss depends on the frequency of sound and the acoustic properties of the ocean and subbottom.

If the acoustic source level (SL), expressed in dB re 1 $\mu Pa^2 \cdot s/Hz \cdot m$, and transmission loss (TL), in units of dB re 1 m, at a given frequency are known, then the received level (RL) at a receiver location can be calculated in dB re 1 $\mu Pa^2 \cdot s/Hz$ by:

$$RL = SL - TL \, . \qquad \text{(B-1)}$$

B.4. Noise Propagation with MONM and BELLHOP

Underwater sound propagation (i.e., transmission loss) at frequencies of 10 Hz to 25 kHz was predicted with JASCO's Marine Operations Noise Model (MONM) and BELLHOP. The models compute received per-pulse SEL for directional impulsive sources, and SEL over 1 s for non-impulsive sources, at a specified source depth.

MONM computes acoustic propagation at low frequency (below 1 kHz for the present study) via a wide-angle parabolic equation solution to the acoustic wave equation (Collins 1993) based on a version of the U.S. Naval Research Laboratory's Range-dependent Acoustic Model (RAM), which has been modified to account for a solid seabed (Zhang and Tindle 1995). The parabolic equation method has been extensively benchmarked and is widely employed in the underwater acoustics community (Collins et al. 1996). MONM computes acoustic propagation at high frequency (below 2–25 kHz) via the BELLHOP Gaussian beam acoustic ray-trace model (Porter and Liu 1994). This version of MONM accounts for sound attenuation due to energy absorption through ion relaxation and viscosity of water in addition to acoustic attenuation due to reflection at the medium boundaries and internal layers (Fisher and Simmons 1977). The former type of sound attenuation is significant for frequencies higher than 5 kHz and cannot be neglected without noticeably affecting the model results. MONM's predictions have been validated against experimental data from several underwater acoustic measurement programs conducted by JASCO (Hannay and Racca 2005, Aerts et al. 2008, Funk et al. 2008, Ireland et al. 2009, O'Neill et al. 2010, Warner et al. 2010, Racca et al. 2012a, Racca et al. 2012b, Martin et al. 2015).

MONM accounts for the additional reflection loss at the seabed, which results from partial conversion of incident compressional waves to shear waves at the seabed and sub-bottom interfaces, and it includes wave attenuations in all layers. MONM incorporates the following site-specific environmental properties: a bathymetric grid of the modelled area, underwater sound speed as a function of depth, and a geoacoustic profile based on the overall stratified composition of the seafloor.

MONM computes acoustic fields in three dimensions by modelling transmission loss within two-dimensional (2-D) vertical planes aligned along radials covering a 360° swath from the source, an approach commonly referred to as N×2-D. These vertical radial planes are separated by an angular step size of $\Delta\theta$, yielding $N = 360°/\Delta\theta$ number of planes (Figure B-41).

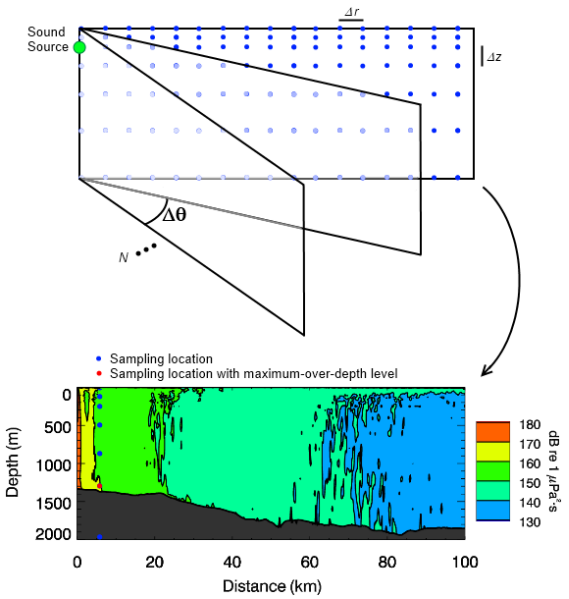

Figure B-41. The N×2-D and maximum-over-depth modelling approach used by MONM.

MONM treats frequency dependence by computing acoustic transmission loss at the centre frequencies of 1/3-octave-bands. Sufficiently many 1/3-octave-bands, starting at 10 Hz, are modelled to include the majority of acoustic energy emitted by the source. At each centre frequency, the transmission loss is modelled within each of the N vertical planes as a function of depth and range from the source. The 1/3-octave-band received per-pulse SELs are computed by subtracting the band transmission loss values from the directional source level in that frequency band. Composite broadband received SELs are then computed by summing the received 1/3-octave-band levels.

The received per-pulse SEL sound field within each vertical radial plane is sampled at various ranges from the source, generally with a fixed radial step size. At each sampling range along the surface, the sound field is sampled at various depths, with the step size between samples increasing with depth below the surface. The step sizes are chosen to provide increased coverage near the depth of the source and at depths of interest in terms of the sound speed profile. For areas with deep water, sampling is not performed at depths beyond those reachable by marine mammals. The received per-pulse SEL at a surface sampling location is taken as the maximum value that occurs over all samples within the water column, i.e., the maximum-over-depth received per-pulse SEL. These maximum-over-depth per-pulse SELs are presented as colour contours around the source (Figure B-42).

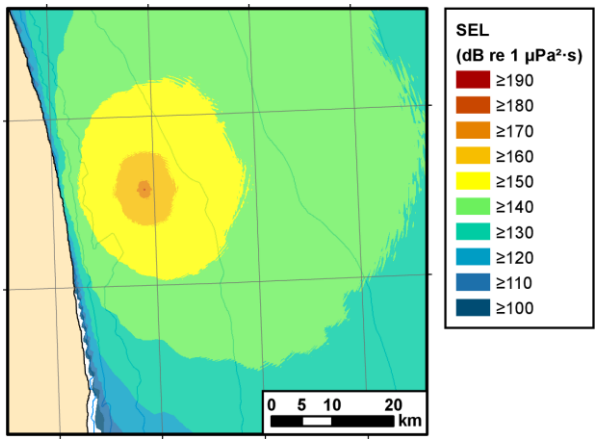

Figure B-42. Example of a maximum-over-depth SEL colour contour map for an unspecified source.

B.5. Acoustic Source Model

The source levels and directivity of the airgun array were predicted with JASCO's Airgun Array Source Model (AASM). AASM includes low- and high-frequency modules for predicting different components of the airgun array spectrum. The low-frequency module is based on the physics of oscillation and radiation of airgun bubbles, as originally described by Ziolkowski (1970), that solves the set of parallel differential equations that govern bubble oscillations. Physical effects accounted for in the simulation include pressure interactions between airguns, port throttling, bubble damping, and generator-injector (GI) gun behaviour discussed by Dragoset (1984), Laws et al. (1990), and Landro (1992). A global optimization algorithm tunes free parameters in the model to a large library of airgun source signatures.

While airgun signatures are highly repeatable at the low frequencies, which are used for seismic imaging, their sound emissions have a large random component at higher frequencies that cannot be predicted deterministically. Therefore, the high-frequency module of AASM uses a stochastic simulation to predict the sound emissions of individual airguns above 800 Hz, using a multivariate statistical model. The current version of AASM has been tuned to fit a large library of high quality seismic source signature data obtained from the Joint Industry Program (JIP) on Sound and Marine Life (Mattsson and Jenkerson 2008). The stochastic model uses a Monte-Carlo simulation of the random component of the high-frequency spectrum of each airgun in an array. The mean high-frequency spectra from the stochastic model augment the low-frequency signatures from the physical model, allowing AASM to predict airgun source levels at frequencies up to 25,000 Hz.

AASM produces a set of "notional" signatures for each array element based on:

- Array layout
- Volume, tow depth, and firing pressure of each airgun
- Interactions between different airguns in the array

These notional signatures are the pressure waveforms of the individual airguns at a standard reference distance of 1 m; they account for the interactions with the other airguns in the array. The signatures are summed with the appropriate phase delays to obtain the far-field source signature of the entire array in all directions. This far-field array signature is filtered into 1/3-octave-bands to compute the source levels of the array as a function of frequency band and azimuthal angle in the horizontal plane (at the source depth), after which it is considered to be a directional point source in the far field.

A seismic array consists of many sources and the point-source assumption is invalid in the near field where the array elements add incoherently. The maximum extent of the near field of an array (R_{nf}) is:

$$R_{\mathrm{nf}} < \frac{l^2}{4\lambda} \tag{B-2}$$

where λ is the sound wavelength and l is the longest dimension of the array (Lurton 2002, §5.2.4). For example, an airgun array length of $l = 21$ m yields a near-field range of 147 m at 2 kHz and 7 m at 100 Hz. Beyond this R_{nf} range, the array is assumed to radiate like a directional point source and is treated as such for propagation modelling.

The interactions between individual elements of the array create directionality in the overall acoustic emission. Generally, this directionality is prominent mainly at frequencies in the mid-range between tens of hertz to several hundred hertz. At lower frequencies, with acoustic wavelengths much larger than the inter-airgun separation distances, the directionality is small. At higher frequencies, the pattern of lobes is too finely spaced to be resolved and the effective directivity is less.

Appendix C. Transmission Loss Modelling Results

C.1. Modelling Unweighted Received Level at the AMAR Location

This section presents the results of modelling the per-pulse sound exposure level (SEL) received at the AMAR location and depth as a function of the source location (varied in range and azimuth) for each of the 20 sites using a generic sand bottom; in addition, the modelling is repeated using the geoacoustic inversion bottom parameters at the 14 sites where they are available. The modelling results are presented in the form of coloured maps where the colour at any map location represents the predicted received level at the AMAR for the source located at that spot on the map. This section includes only the unweighted per-pulse SEL results; additional maps for marine mammal received level auditory weightings are presented in adjoining sections.

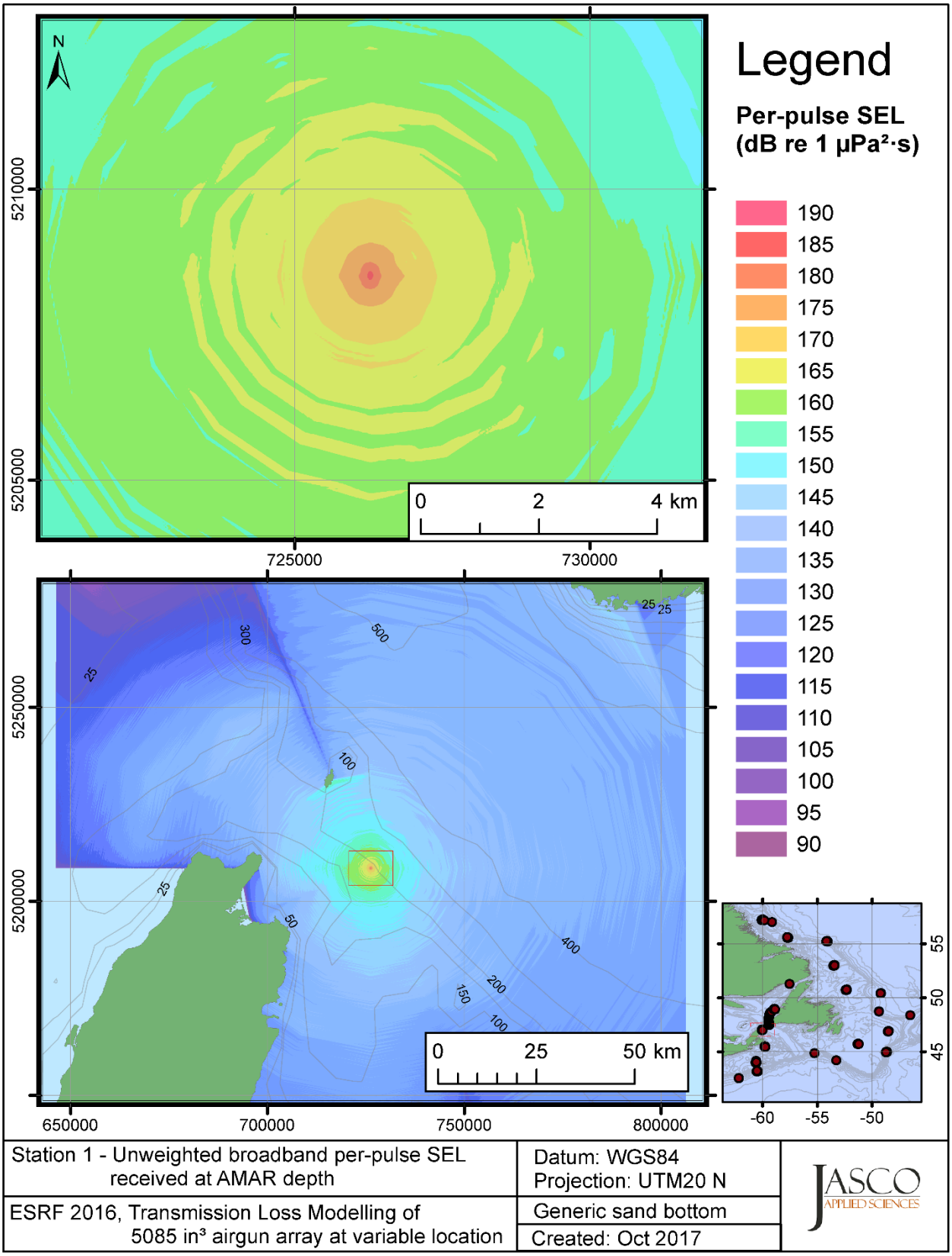

Figure C-1. Stn 1, unweighted SEL received at the AMAR location and depth, modelled using a generic sand bottom, with in-situ July SSP and the airgun array located at any point on the map.

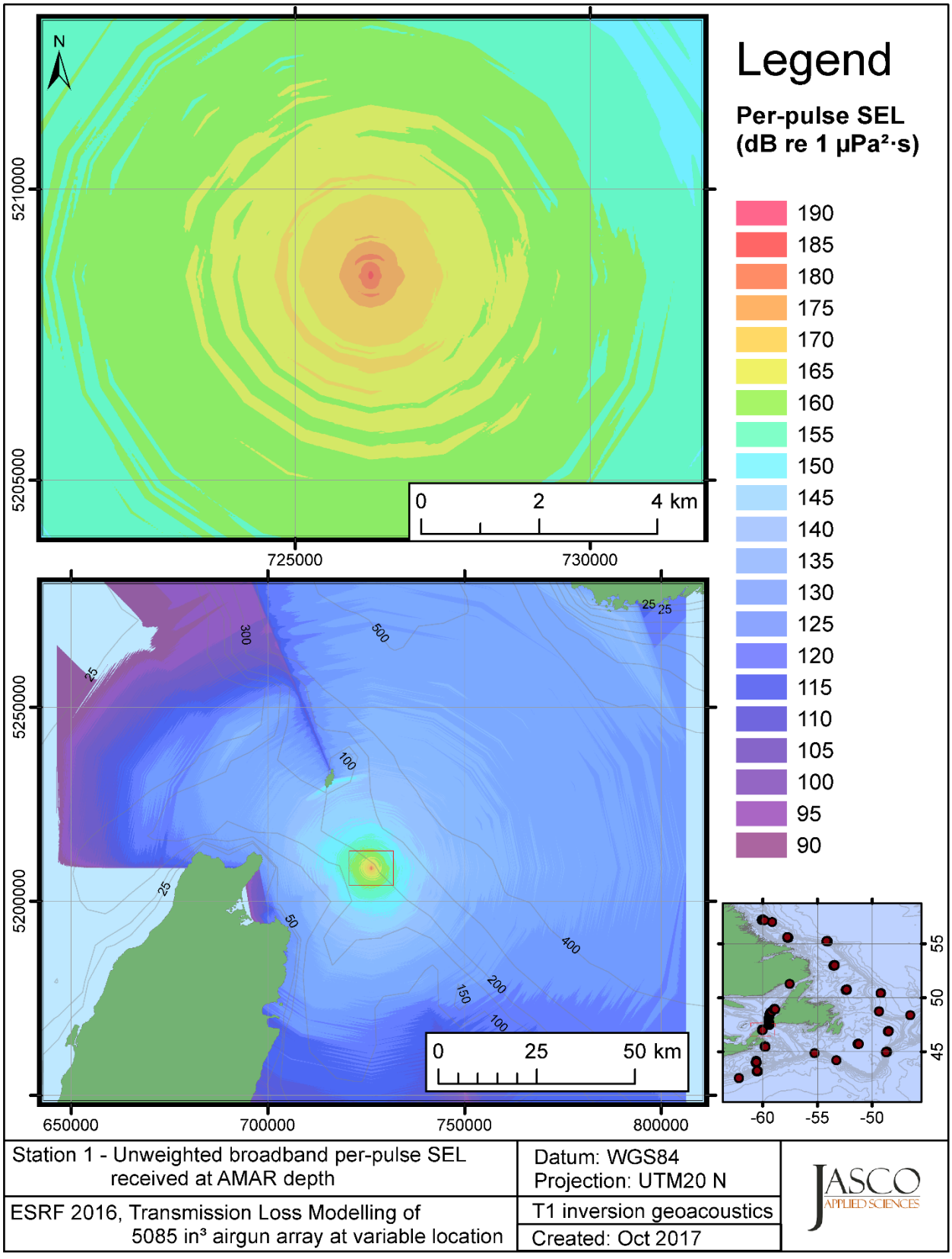

Figure C-2. Stn 1, unweighted SEL received at the AMAR location and depth, modelled using the track 1 inversion geoacoustic bottom, with in-situ July SSP and the airgun array located at any point on the map.

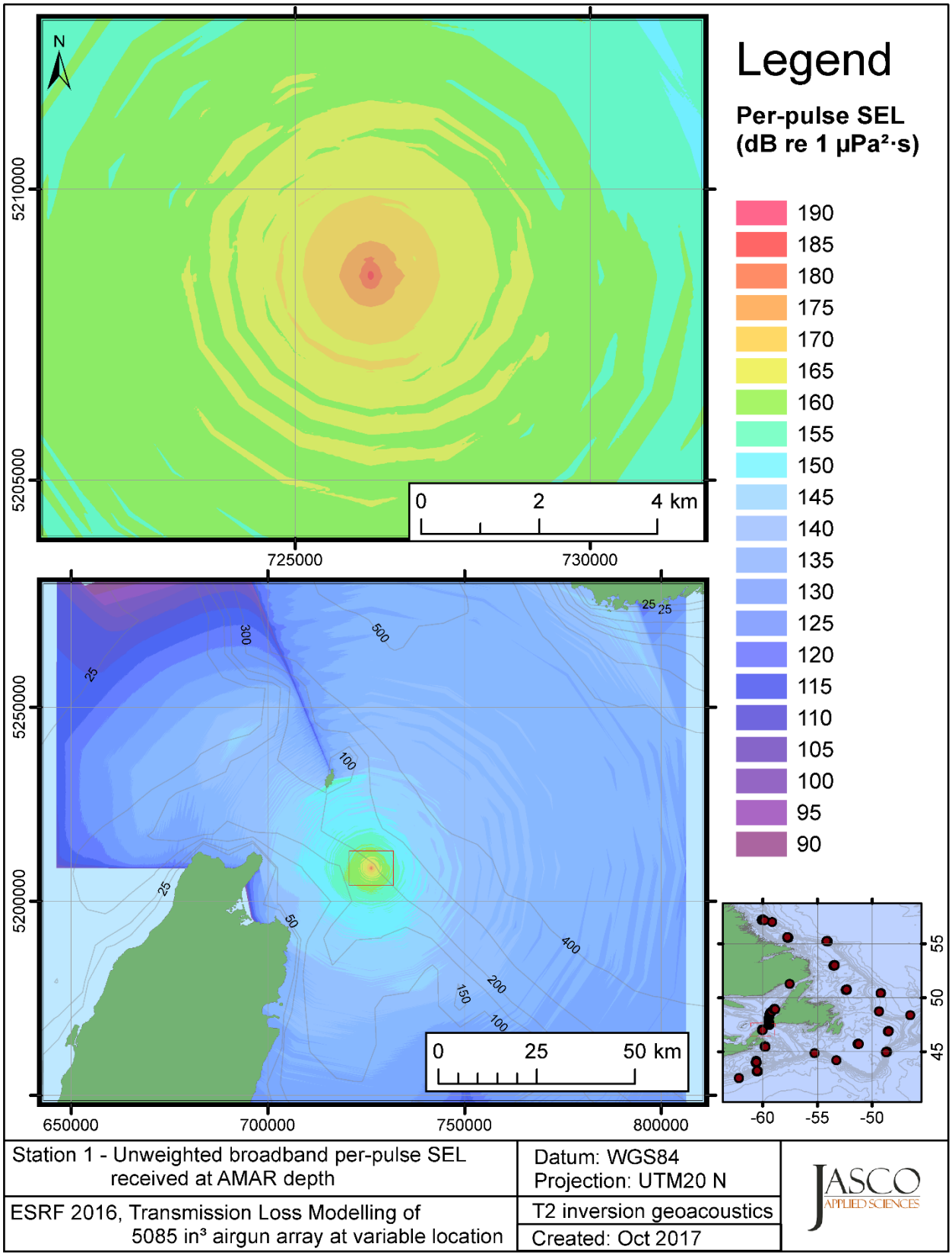

Figure C-3. Stn 1, unweighted SEL received at the AMAR location and depth, modelled using the track 2 inversion geoacoustic bottom, with in-situ July SSP and the airgun array located at any point on the map.

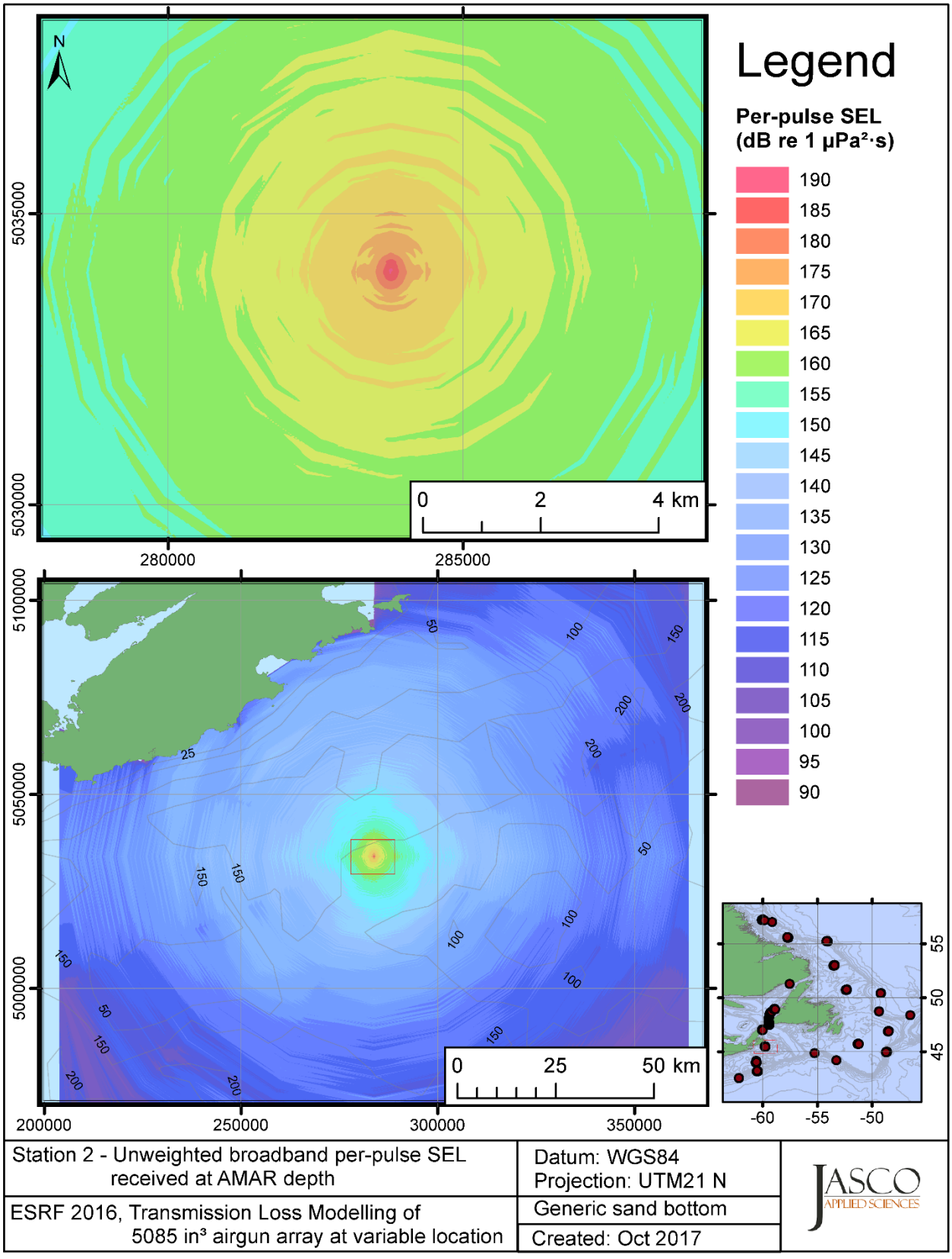

Figure C-4. Stn 2, unweighted SEL received at the AMAR location and depth, modelled using a generic sand bottom, with in-situ July SSP and the airgun array located at any point on the map.

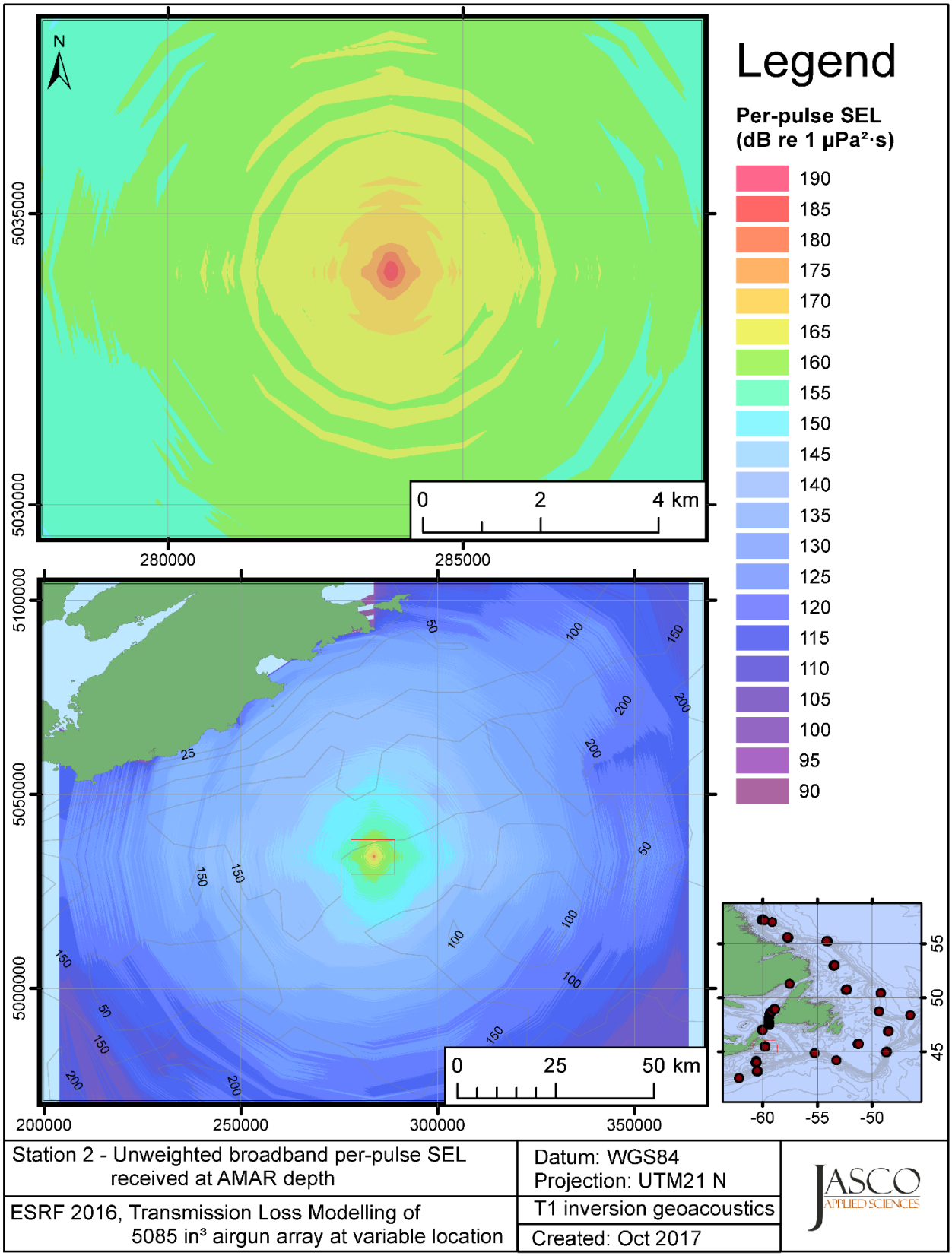

Figure C-5. Stn 2, unweighted SEL received at the AMAR location and depth, modelled using the track 1 inversion geoacoustic bottom, with in-situ July SSP and the airgun array located at any point on the map.

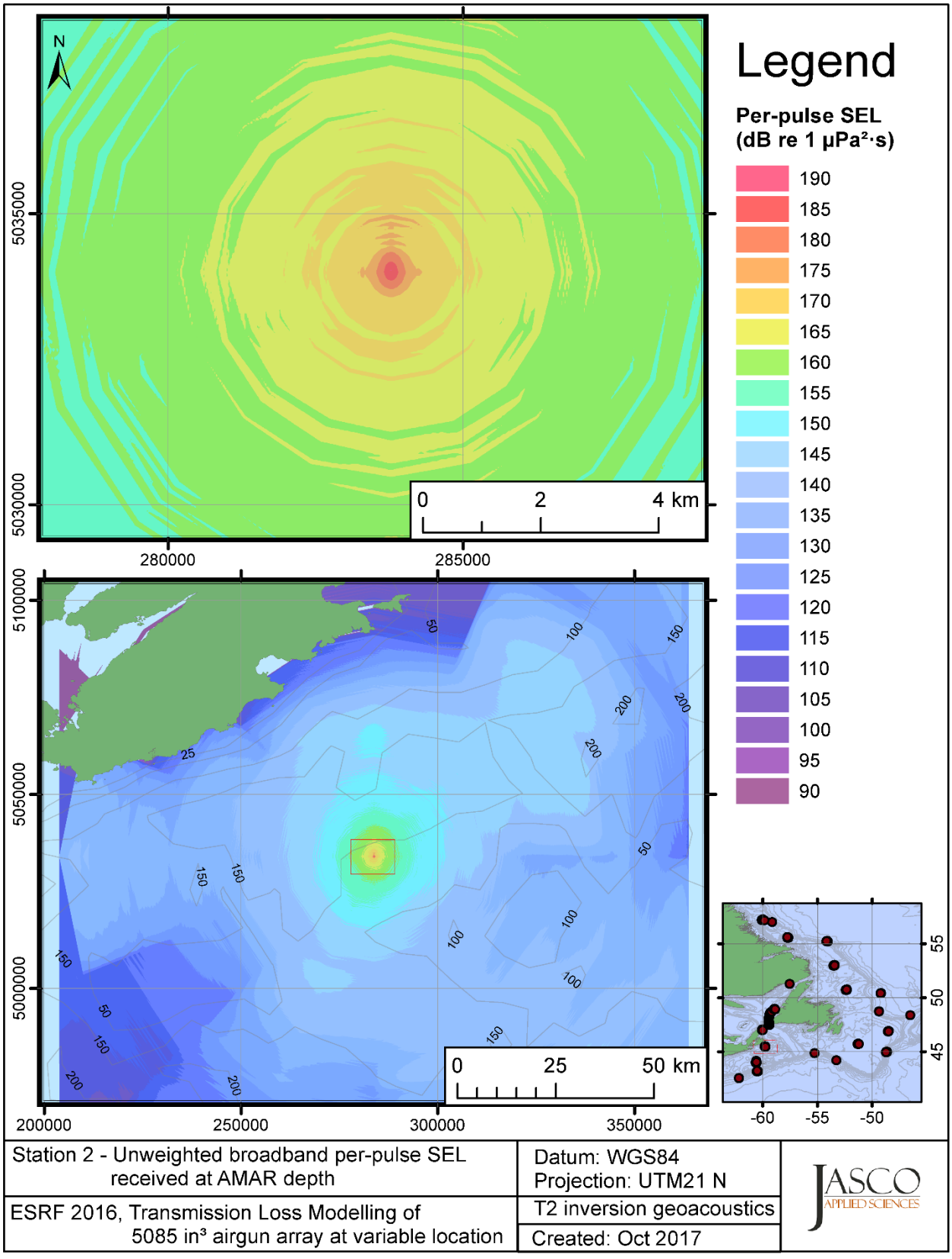

Figure C-6. Stn 2, unweighted SEL received at the AMAR location and depth, modelled using the track 2 inversion geoacoustic bottom, with in-situ July SSP and the airgun array located at any point on the map.

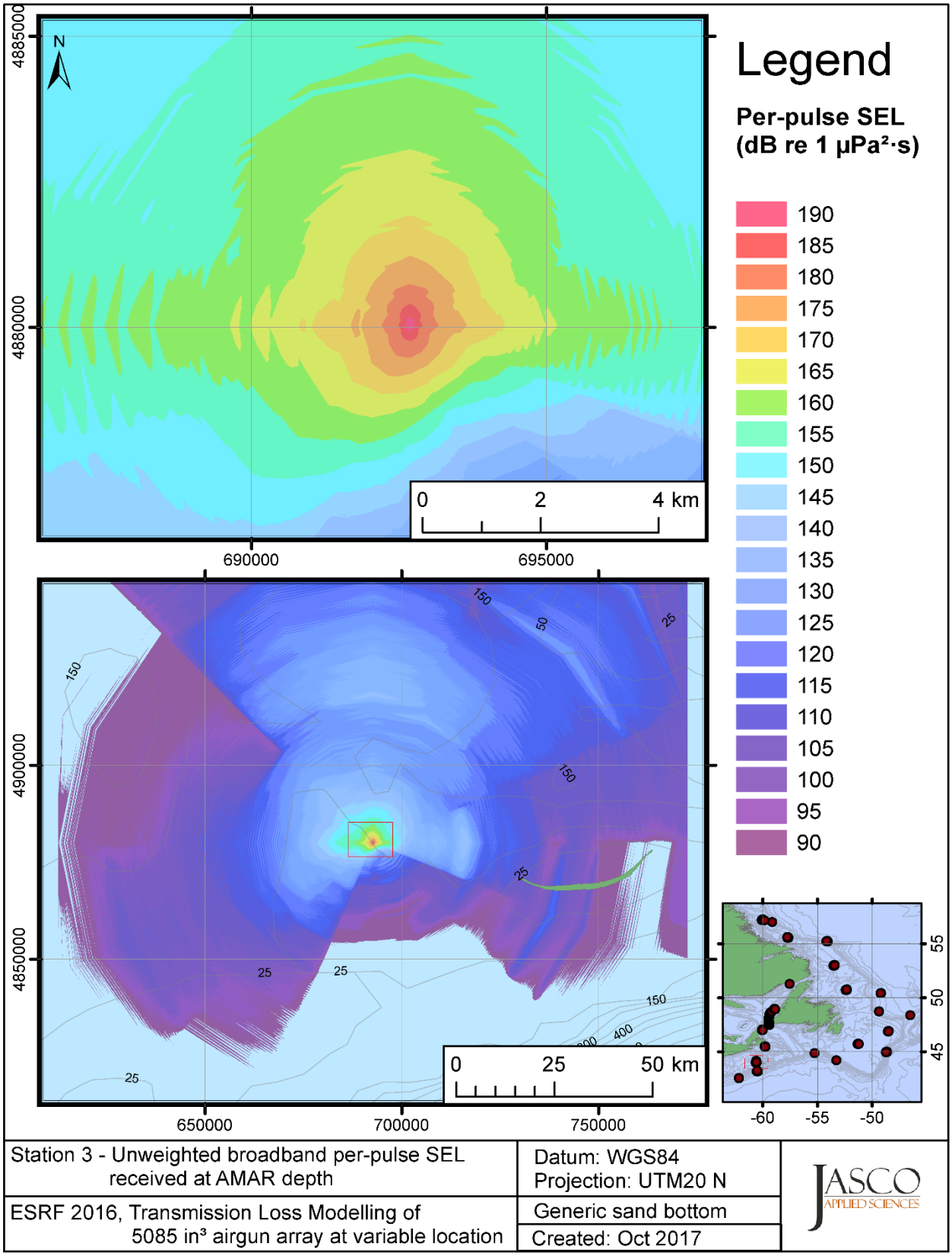

Figure C-7. Stn 3, unweighted SEL received at the AMAR location and depth, modelled using a generic sand bottom, with in-situ July SSP and the airgun array located at any point on the map.

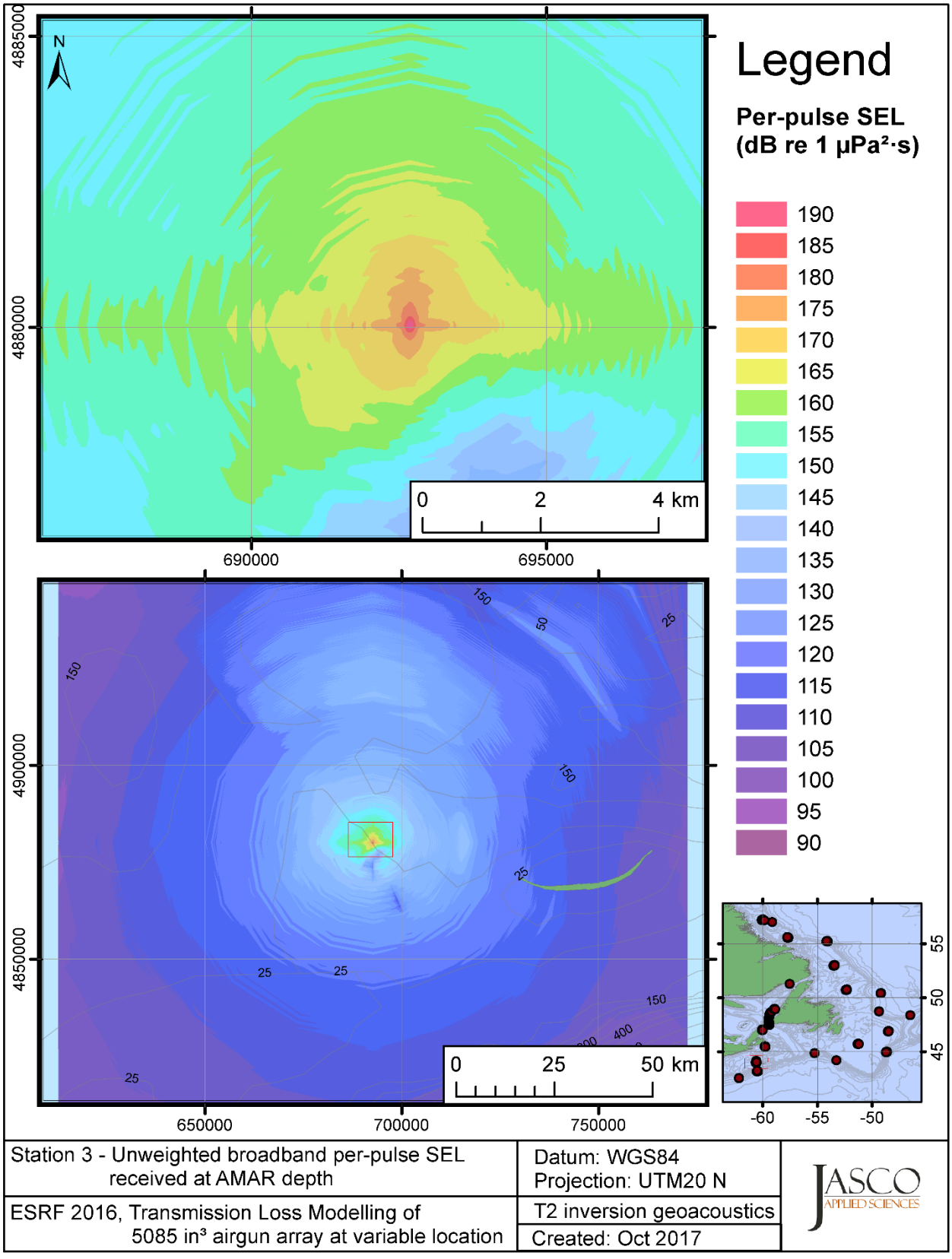

Figure C-8. Stn 3, unweighted SEL received at the AMAR location and depth, modelled using the track 2 inversion geoacoustic bottom, with in-situ July SSP and the airgun array located at any point on the map.

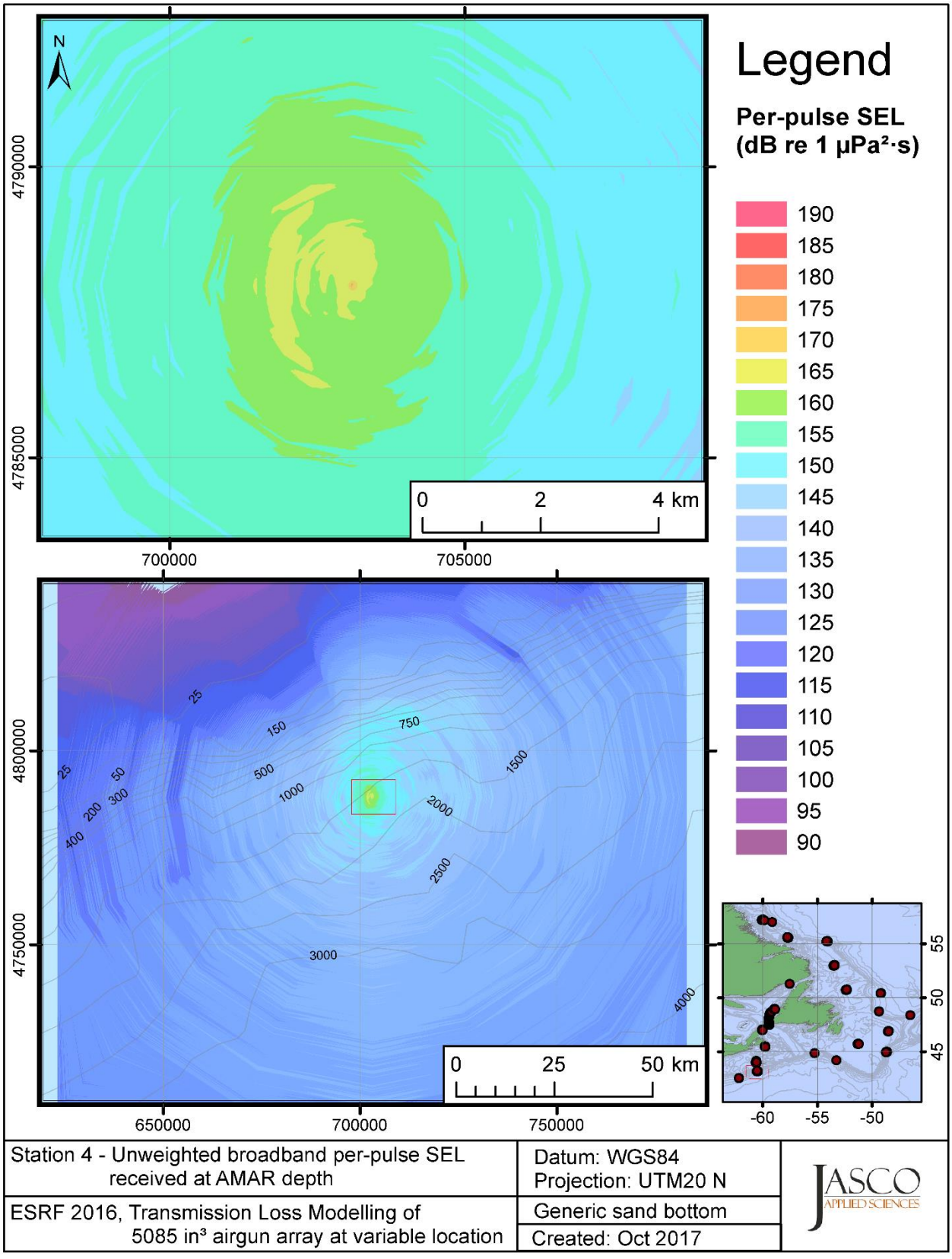

Figure C-9. Stn 4, unweighted SEL received at the AMAR location and depth, modelled using a generic sand bottom, with in-situ July SSP and the airgun array located at any point on the map.

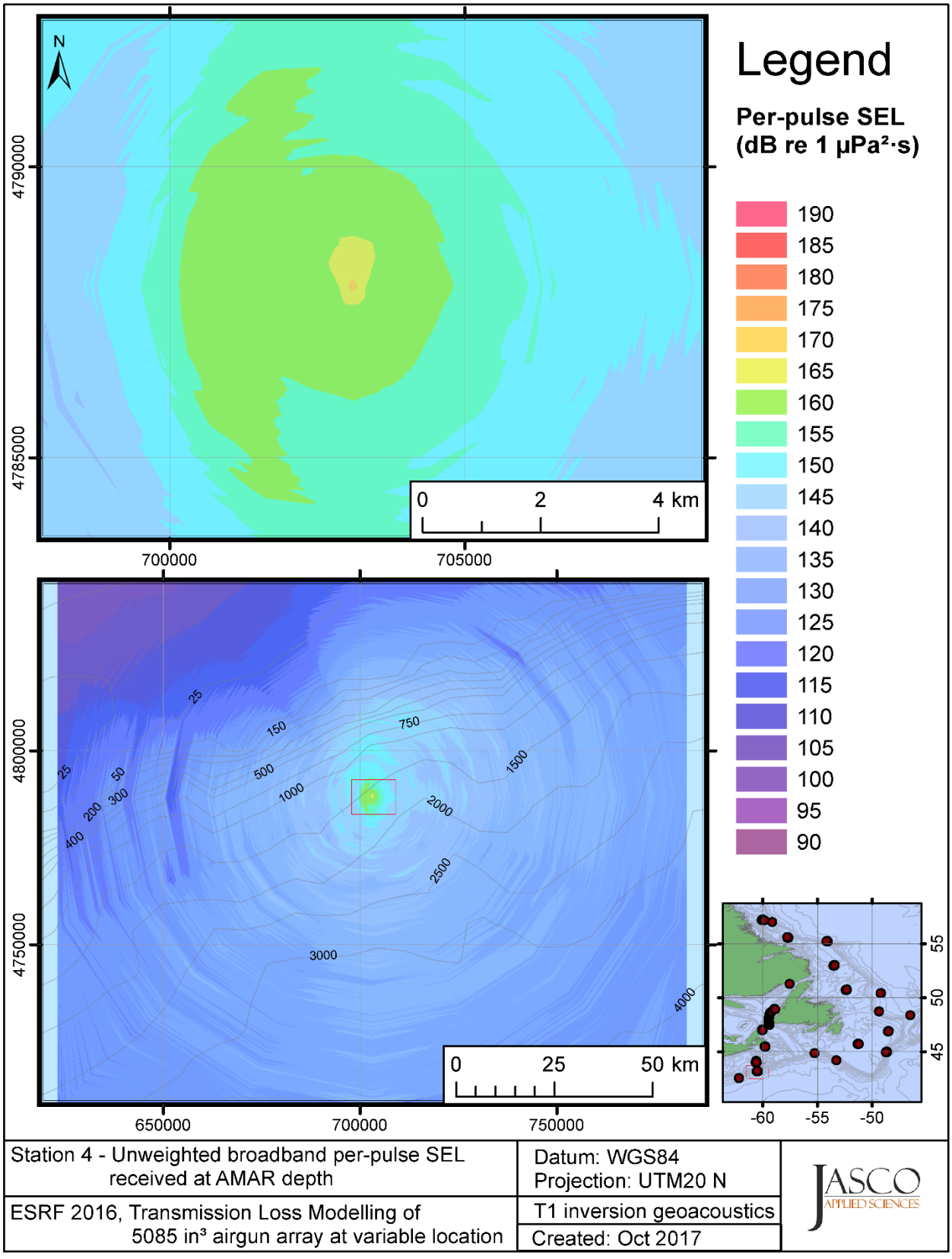

Figure C-10. Stn 4, unweighted SEL received at the AMAR location and depth, modelled using the track 1 inversion geoacoustic bottom, with in-situ July SSP and the airgun array located at any point on the map.

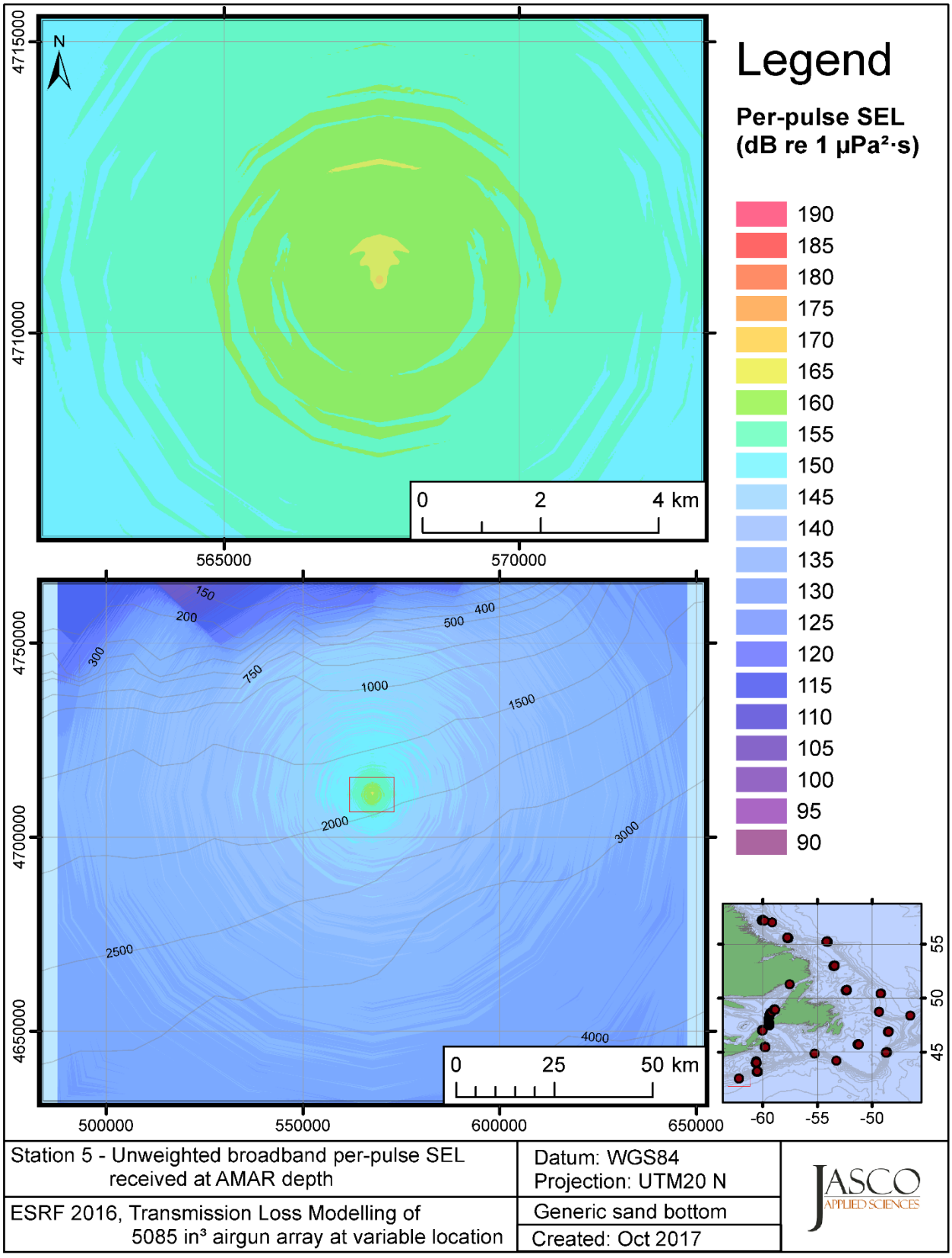

Figure C-11. Stn 5, unweighted SEL received at the AMAR location and depth, modelled using a generic sand bottom, with in-situ July SSP and the airgun array located at any point on the map.

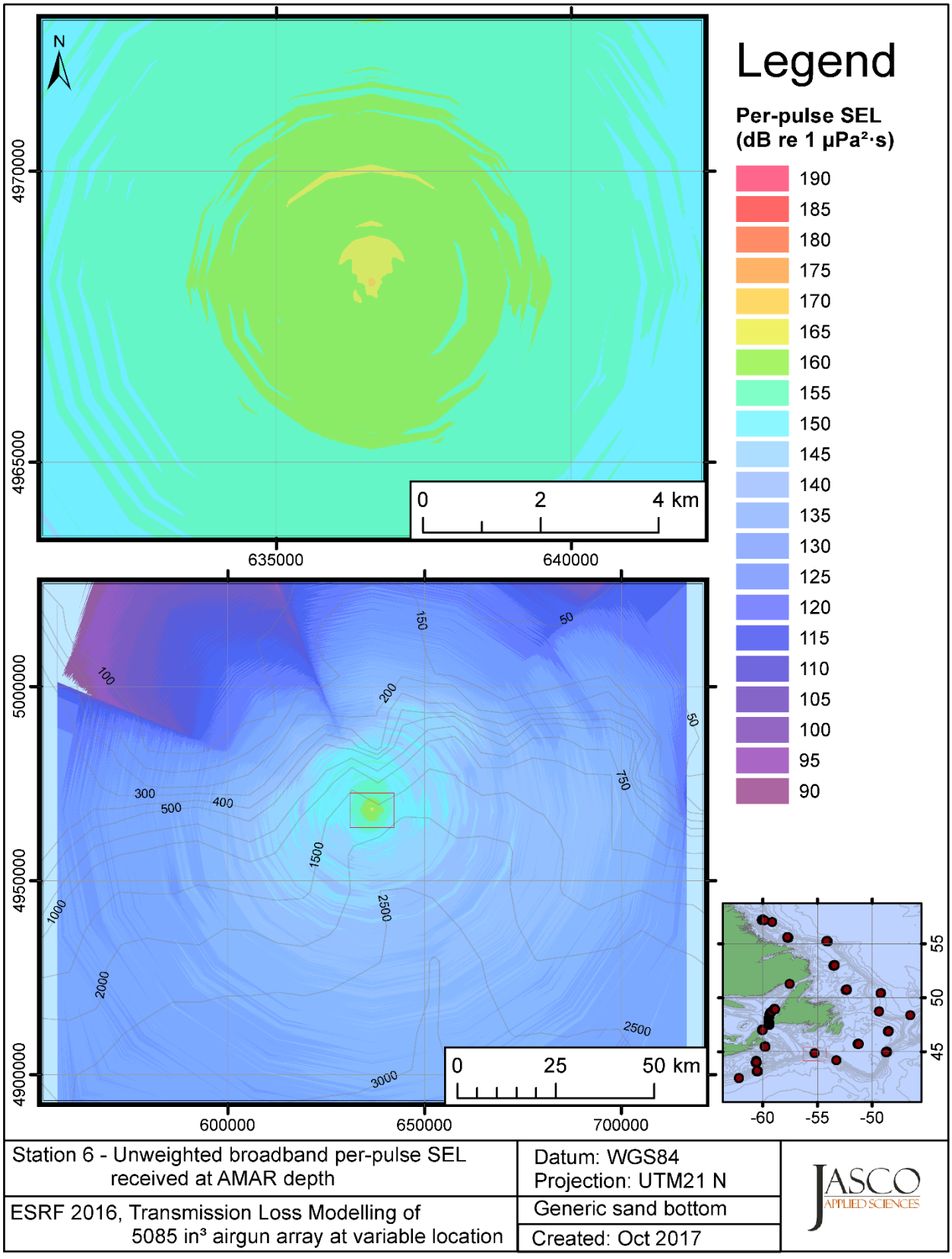

Figure C-12. Stn 6, unweighted SEL received at the AMAR location and depth, modelled using a generic sand bottom, with in-situ July SSP and the airgun array located at any point on the map.

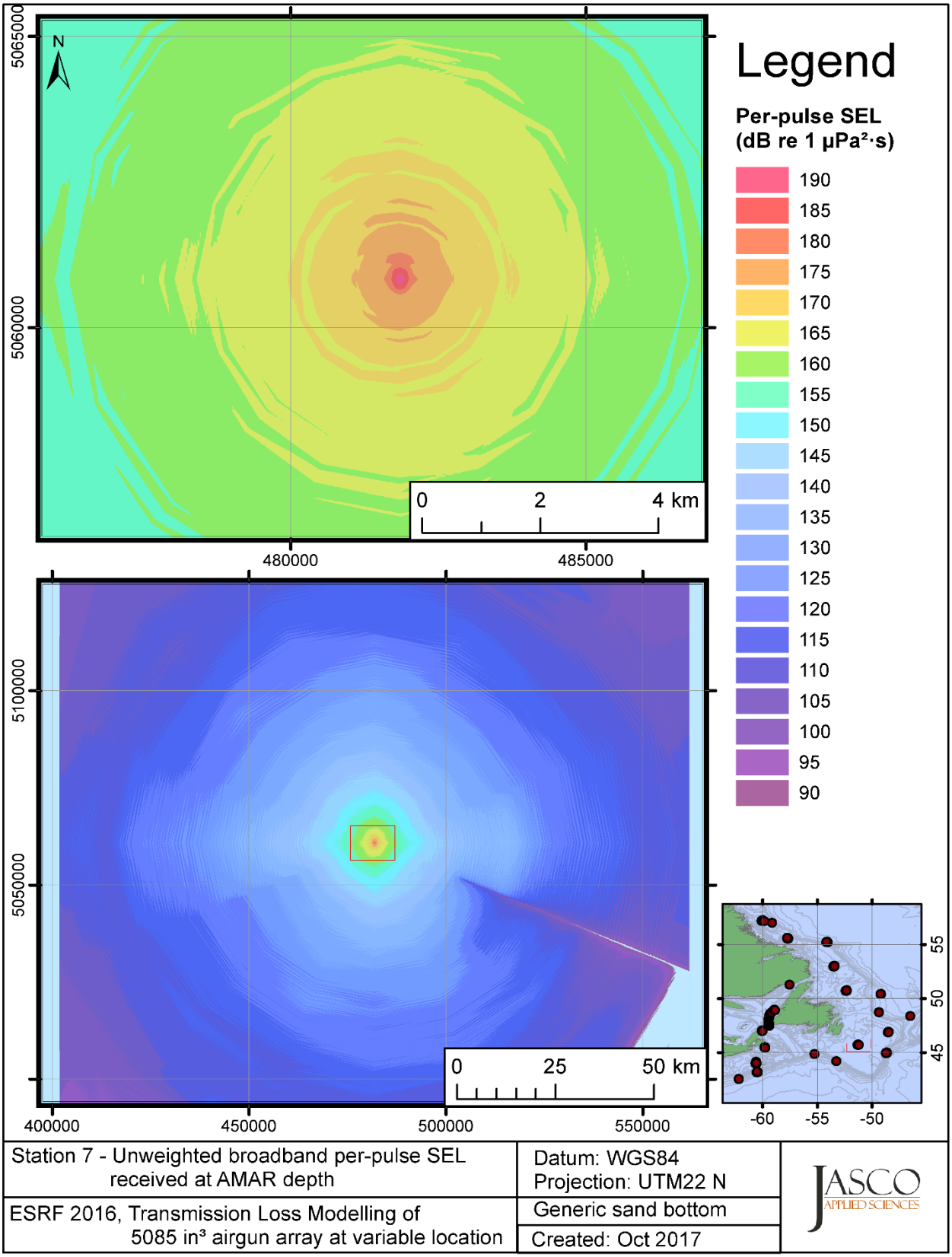

Figure C-13. Stn 7, unweighted SEL received at the AMAR location and depth, modelled using a generic sand bottom, with in-situ July SSP and the airgun array located at any point on the map.

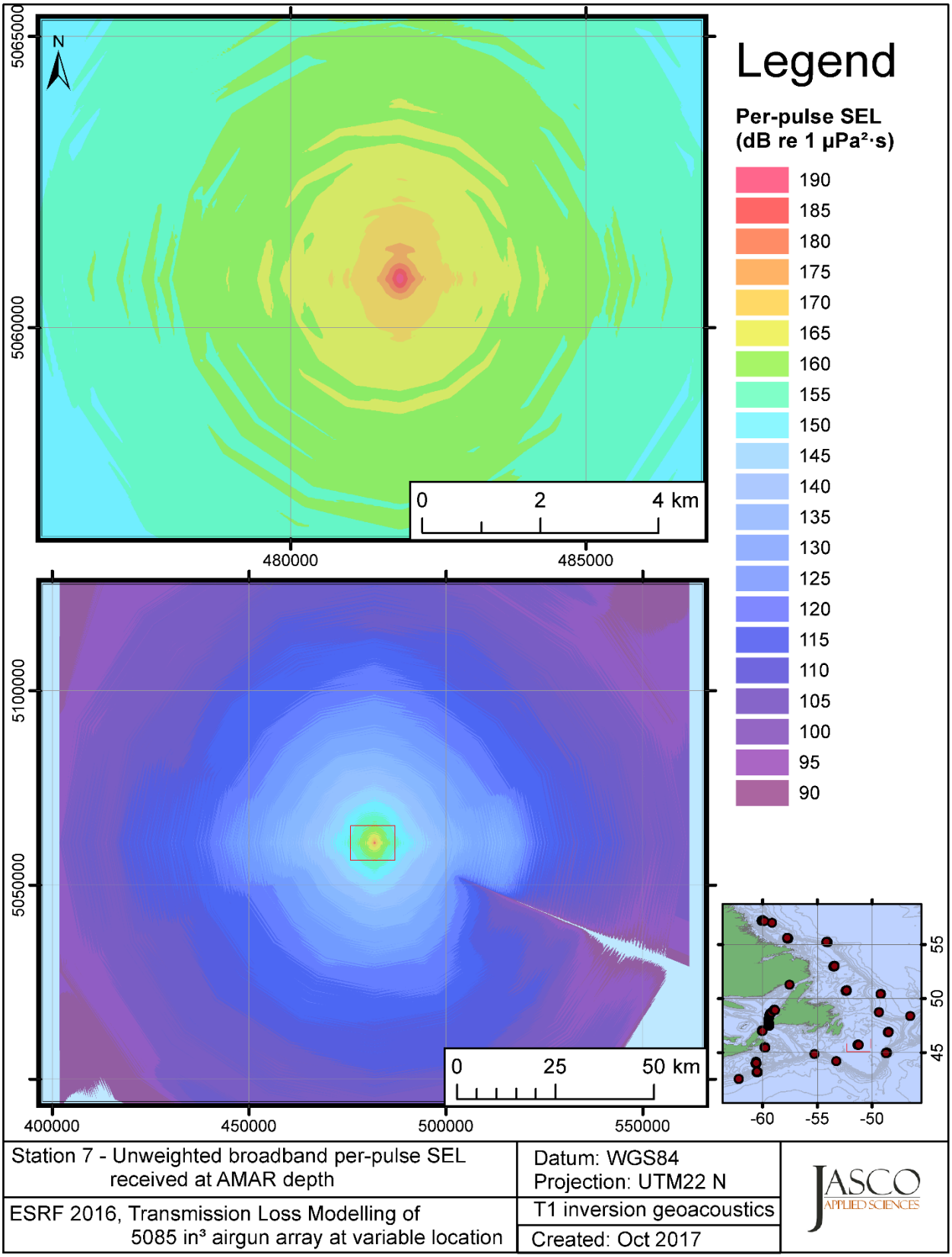

Figure C-14. Stn 7, unweighted SEL received at the AMAR location and depth, modelled using the track 1 inversion geoacoustic bottom, with in-situ July SSP and the airgun array located at any point on the map.

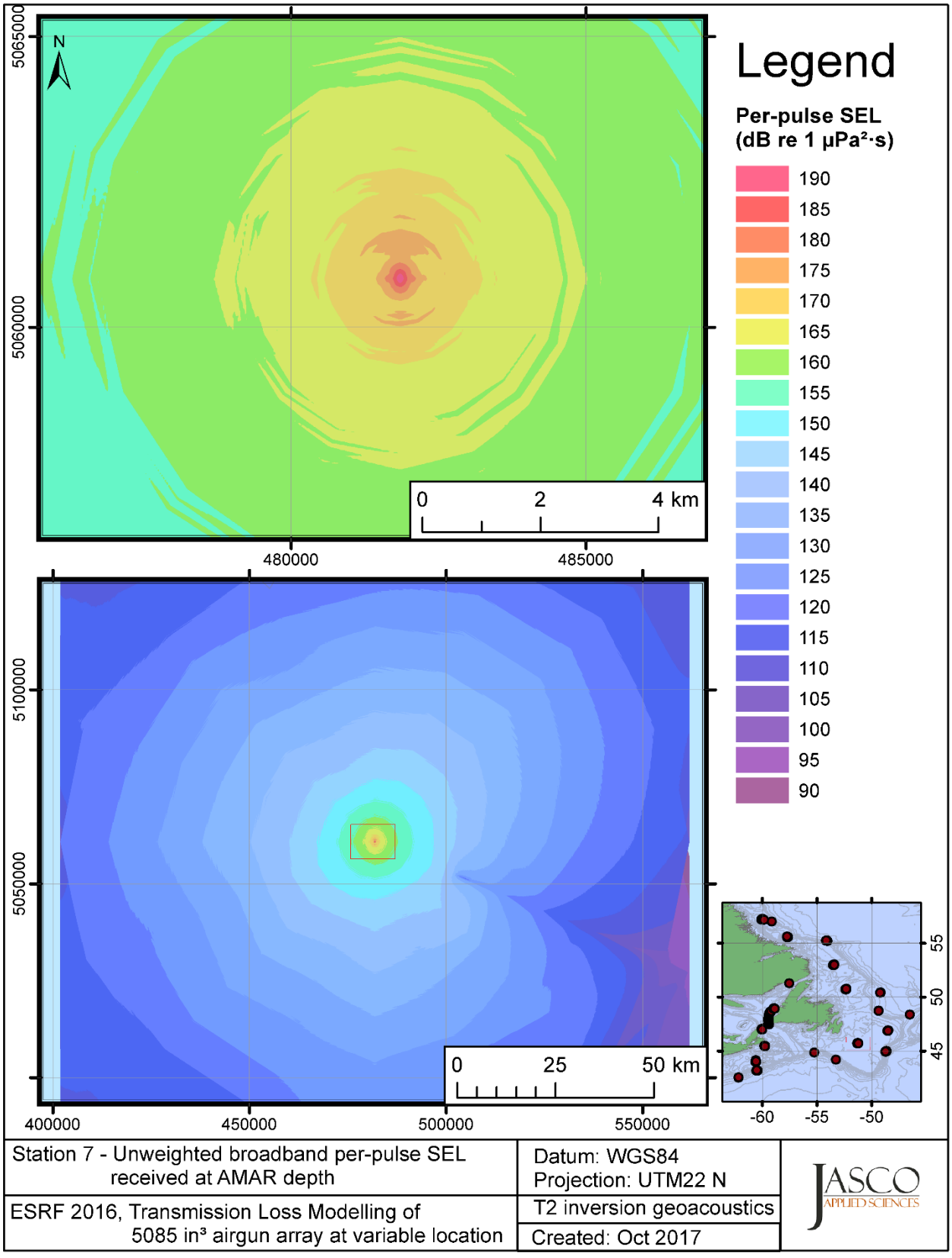

Figure C-15. Stn 7, unweighted SEL received at the AMAR location and depth, modelled using the track 2 inversion geoacoustic bottom, with in-situ July SSP and the airgun array located at any point on the map.

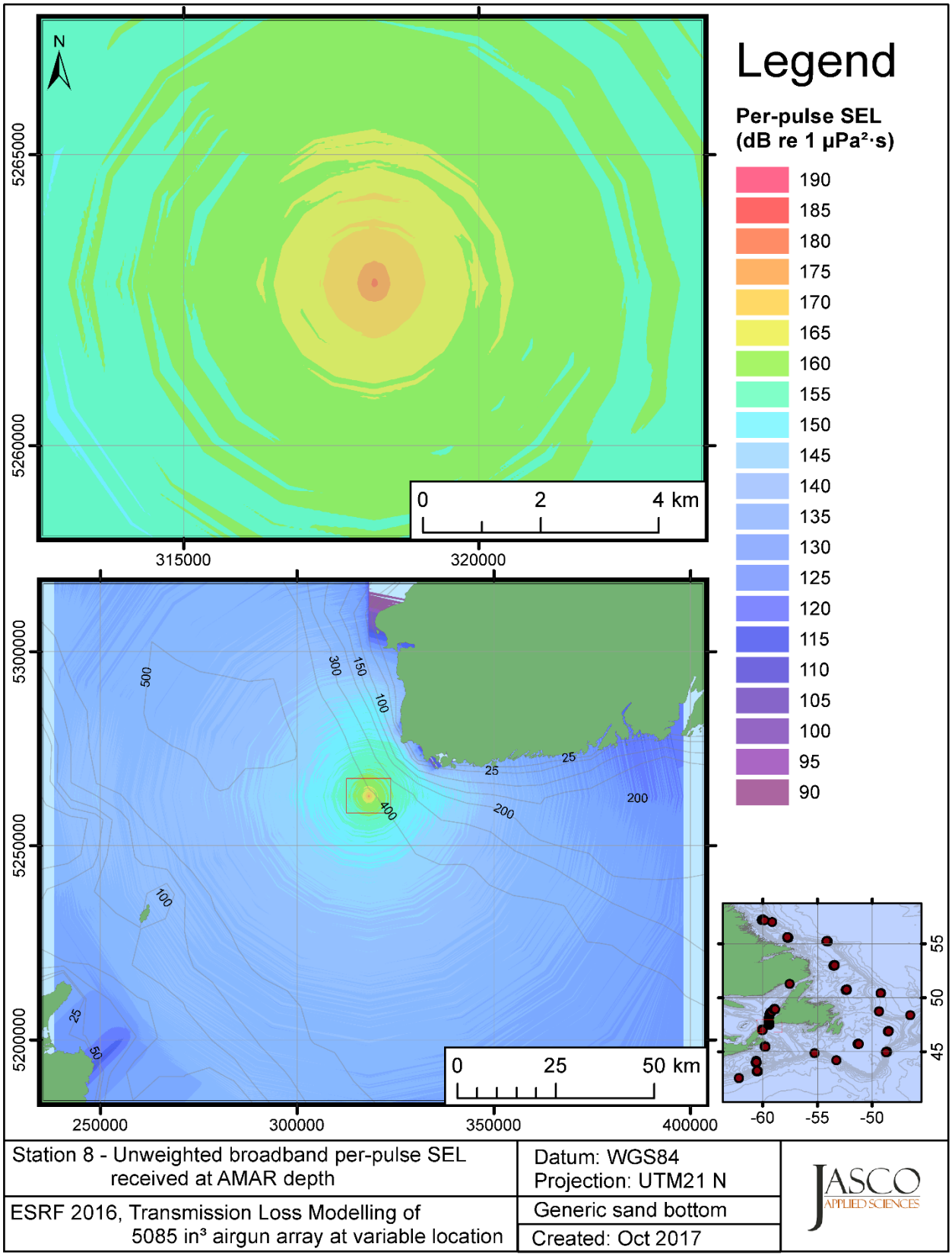

Figure C-16. Stn 8, unweighted SEL received at the AMAR location and depth, modelled using a generic sand bottom, with GDEM July SSP and the airgun array located at any point on the map.

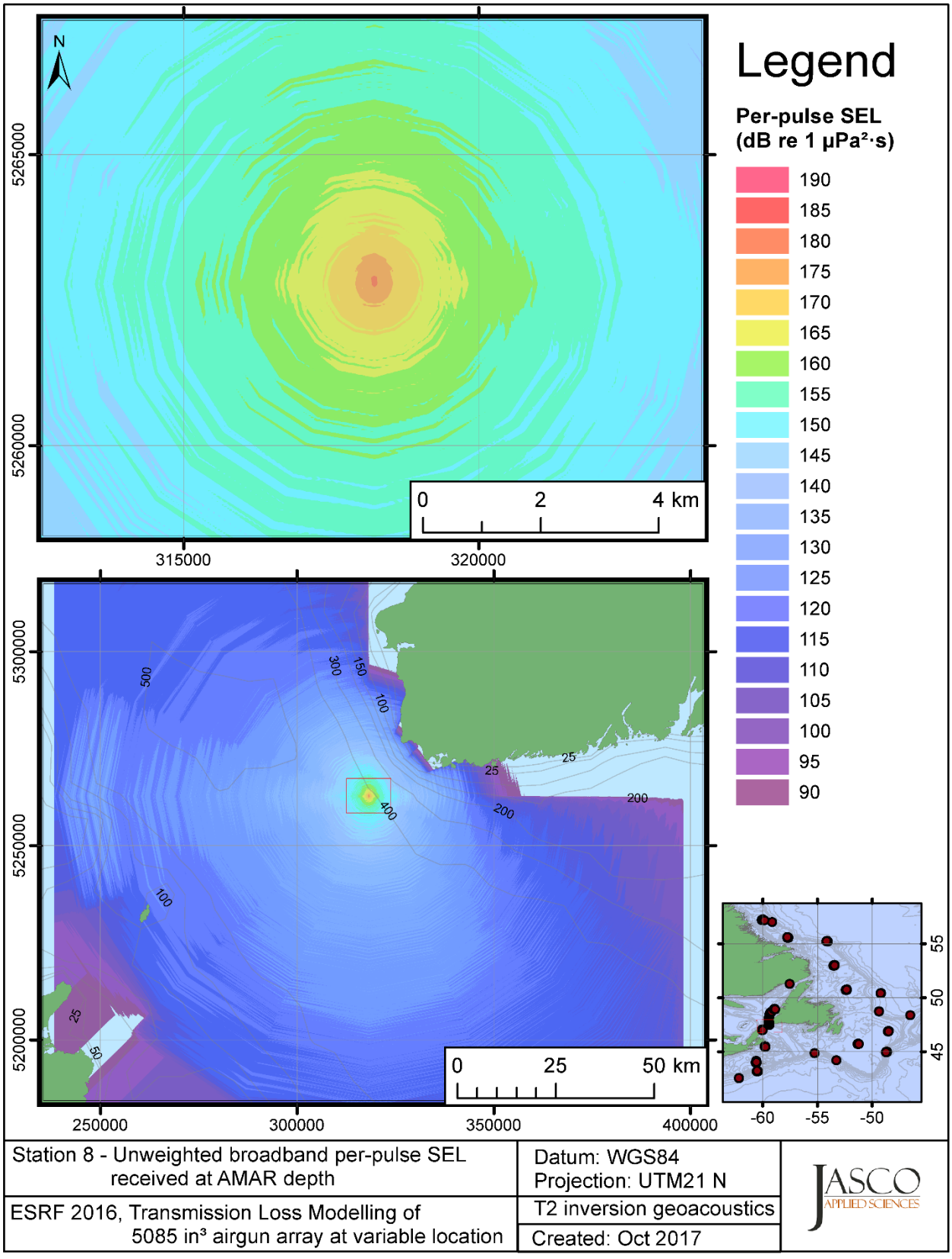

Figure C-17. Stn 8, unweighted SEL received at the AMAR location and depth, modelled using the track 2 inversion geoacoustic bottom, with GDEM July SSP and the airgun array located at any point on the map.

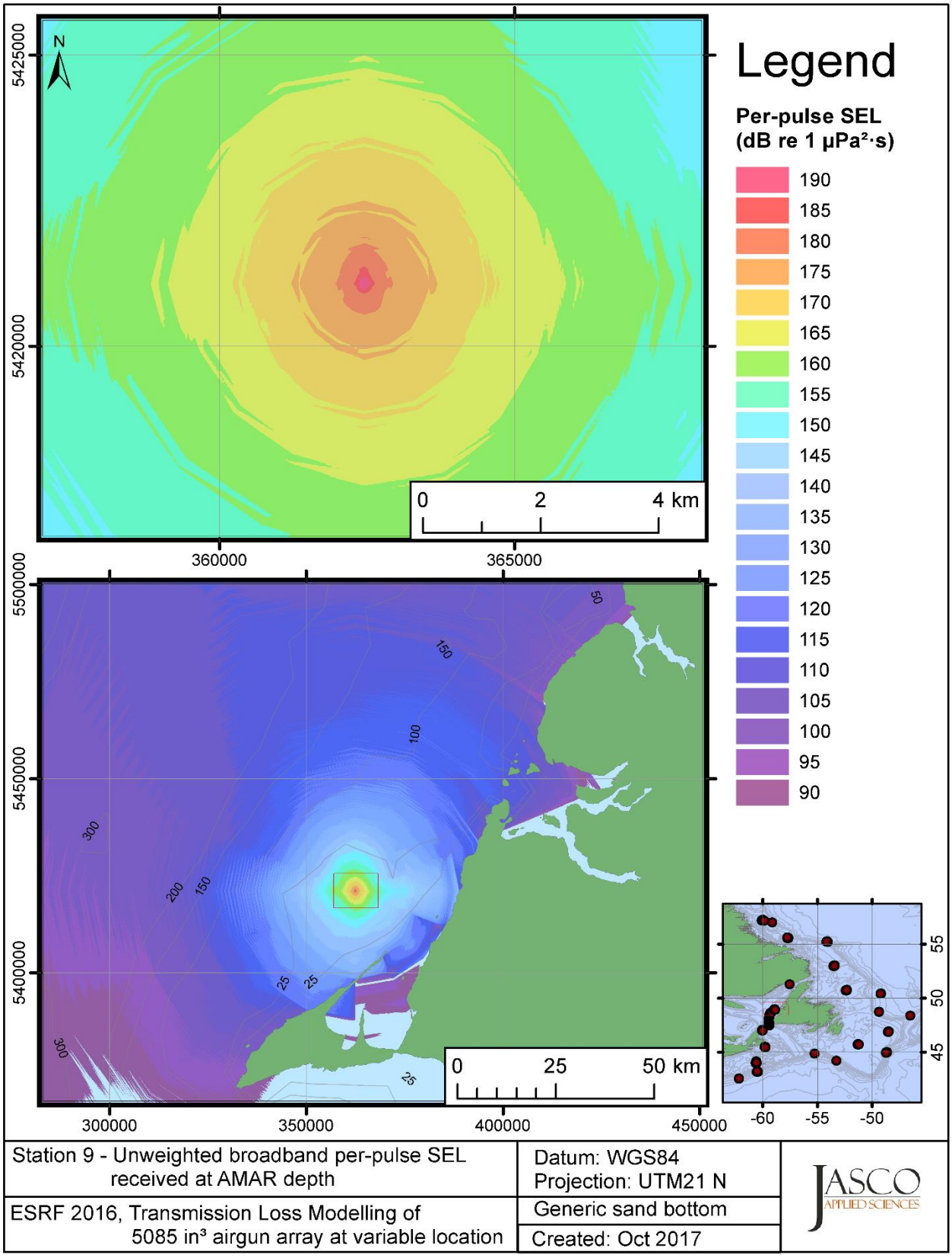

Figure C-18. Stn 9, unweighted SEL received at the AMAR location and depth, modelled using a generic sand bottom, with GDEM July SSP and the airgun array located at any point on the map.

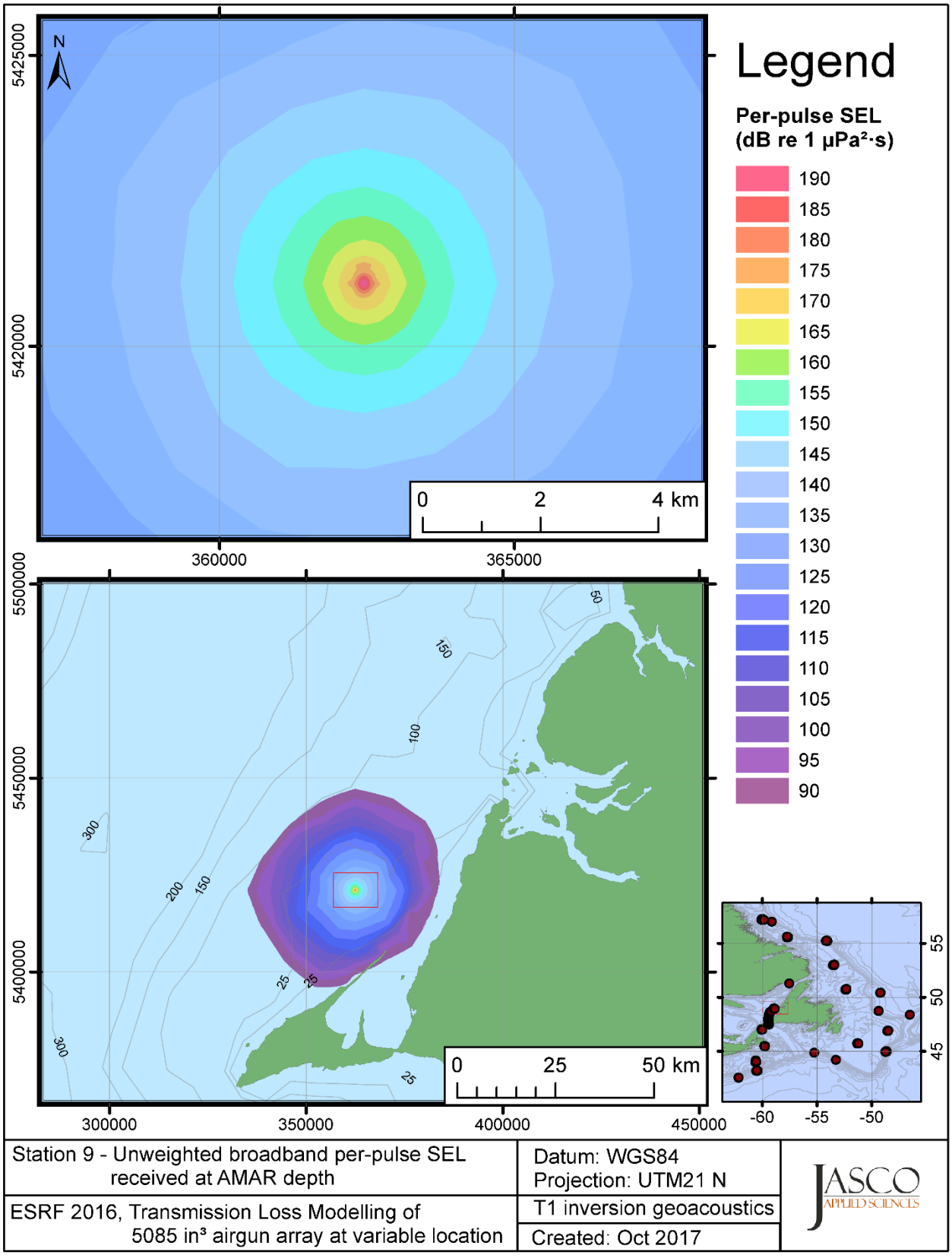

Figure C-19. Stn 9, unweighted SEL received at the AMAR location and depth, modelled using the track 1 inversion geoacoustic bottom, with GDEM July SSP and the airgun array located at any point on the map.

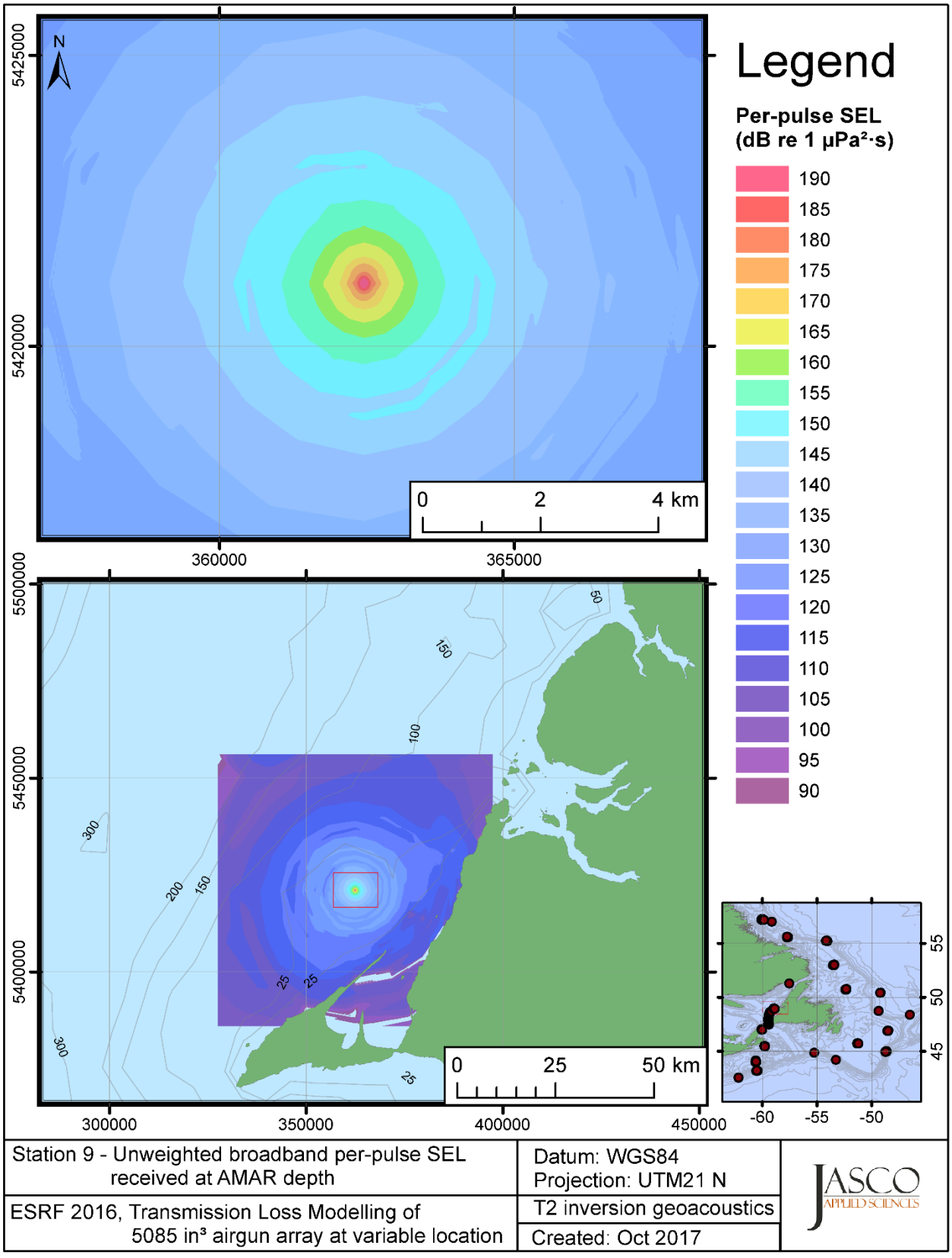

Figure C-20. Stn 9, unweighted SEL received at the AMAR location and depth, modelled using the track 2 inversion geoacoustic bottom, with GDEM July SSP and the airgun array located at any point on the map.

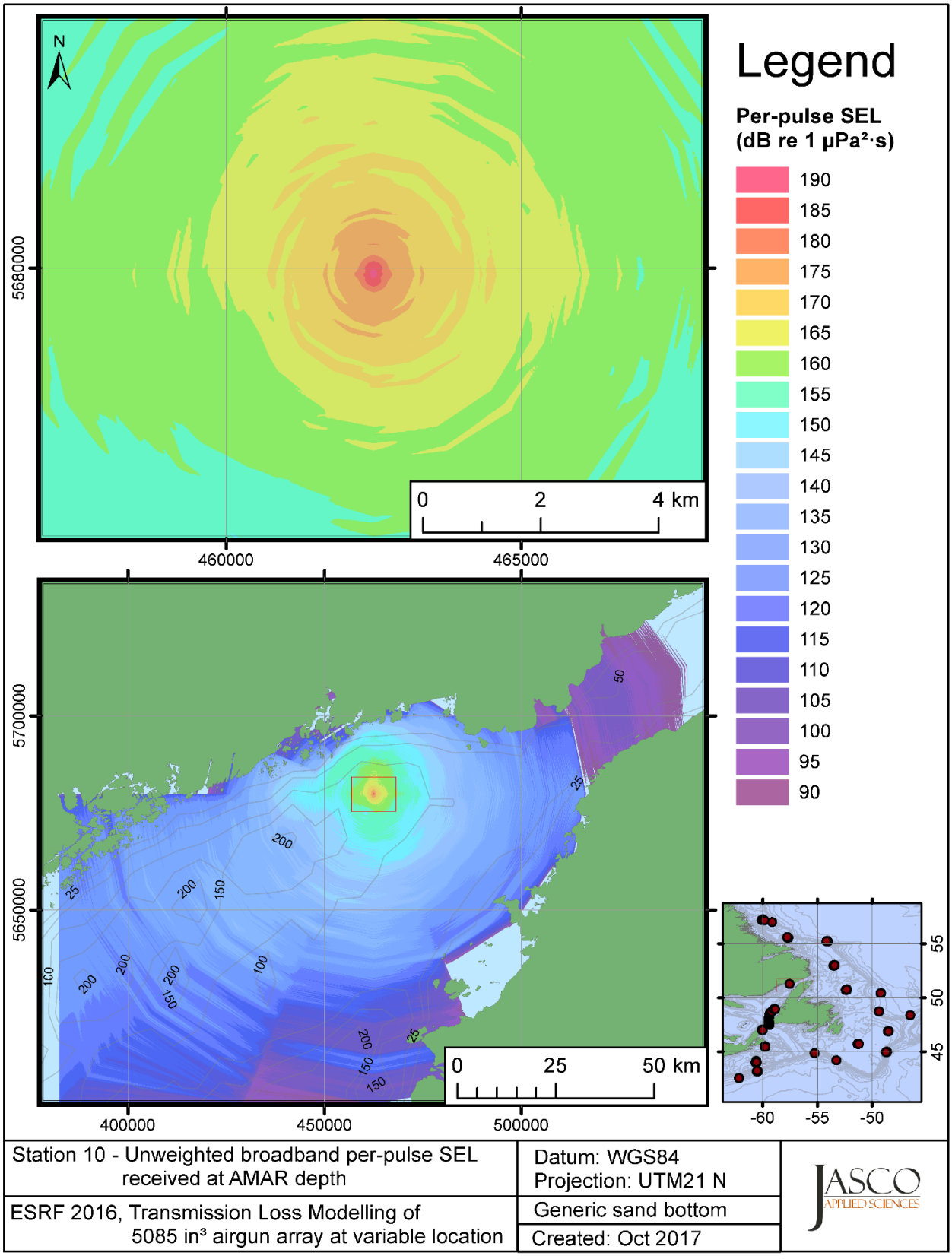

Figure C-21. Stn 10, unweighted SEL received at the AMAR location and depth, modelled using a generic sand bottom, with in-situ July SSP and the airgun array located at any point on the map.

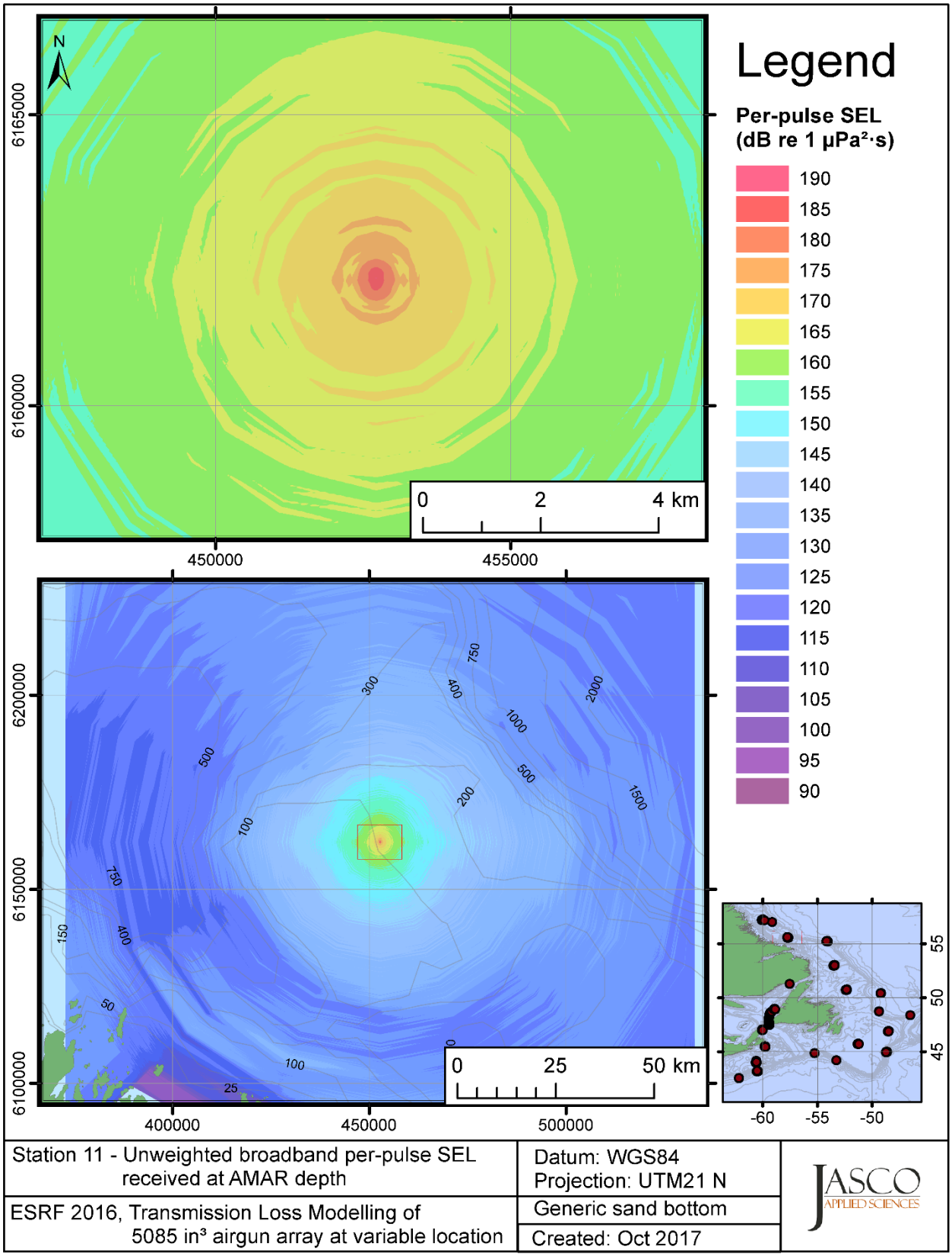

Figure C-22. Stn 11, unweighted SEL received at the AMAR location and depth, modelled using a generic sand bottom, with in-situ July SSP and the airgun array located at any point on the map.

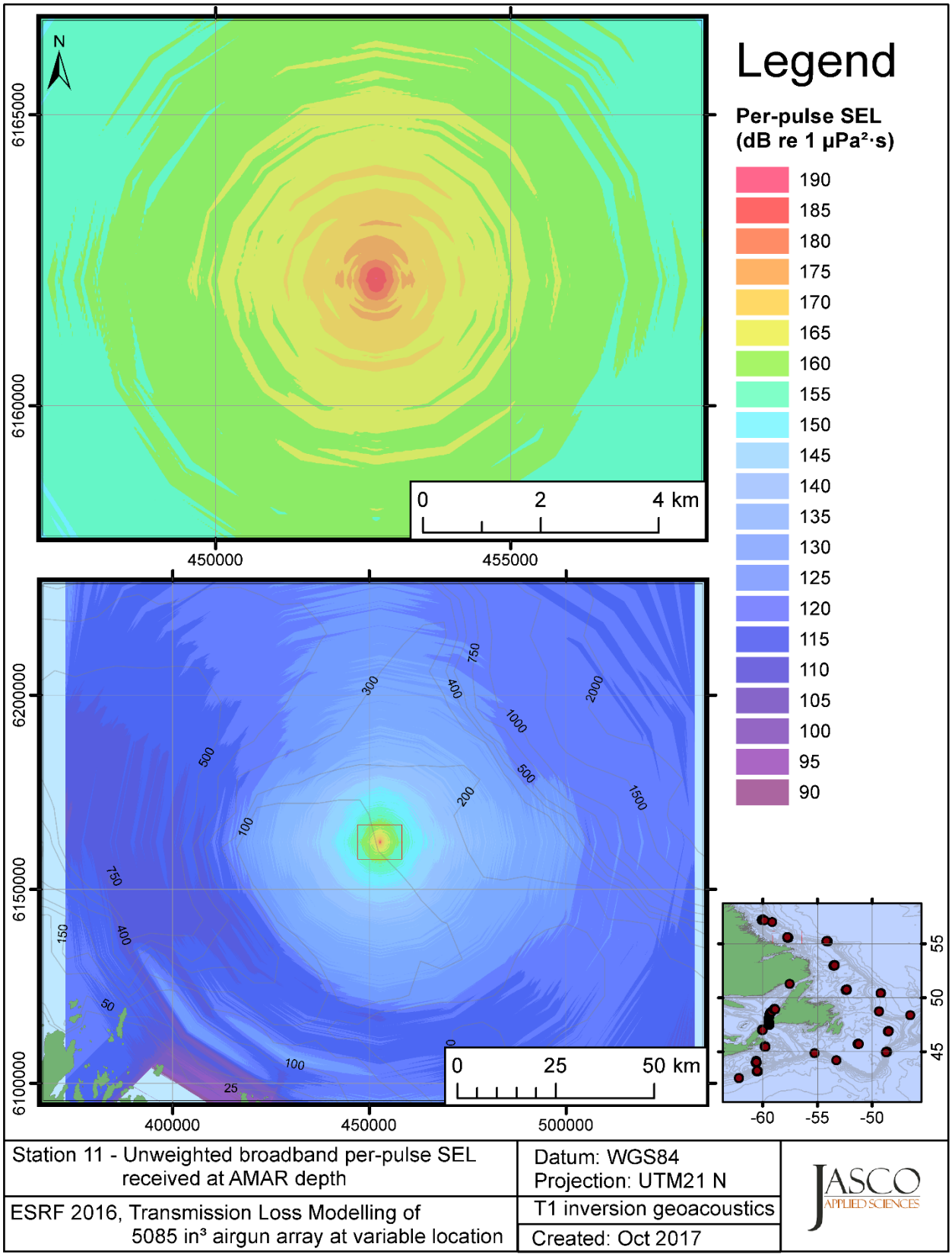

Figure C-23. Stn 11, unweighted SEL received at the AMAR location and depth, modelled using the track 1 inversion geoacoustic bottom, with in-situ July SSP and the airgun array located at any point on the map.

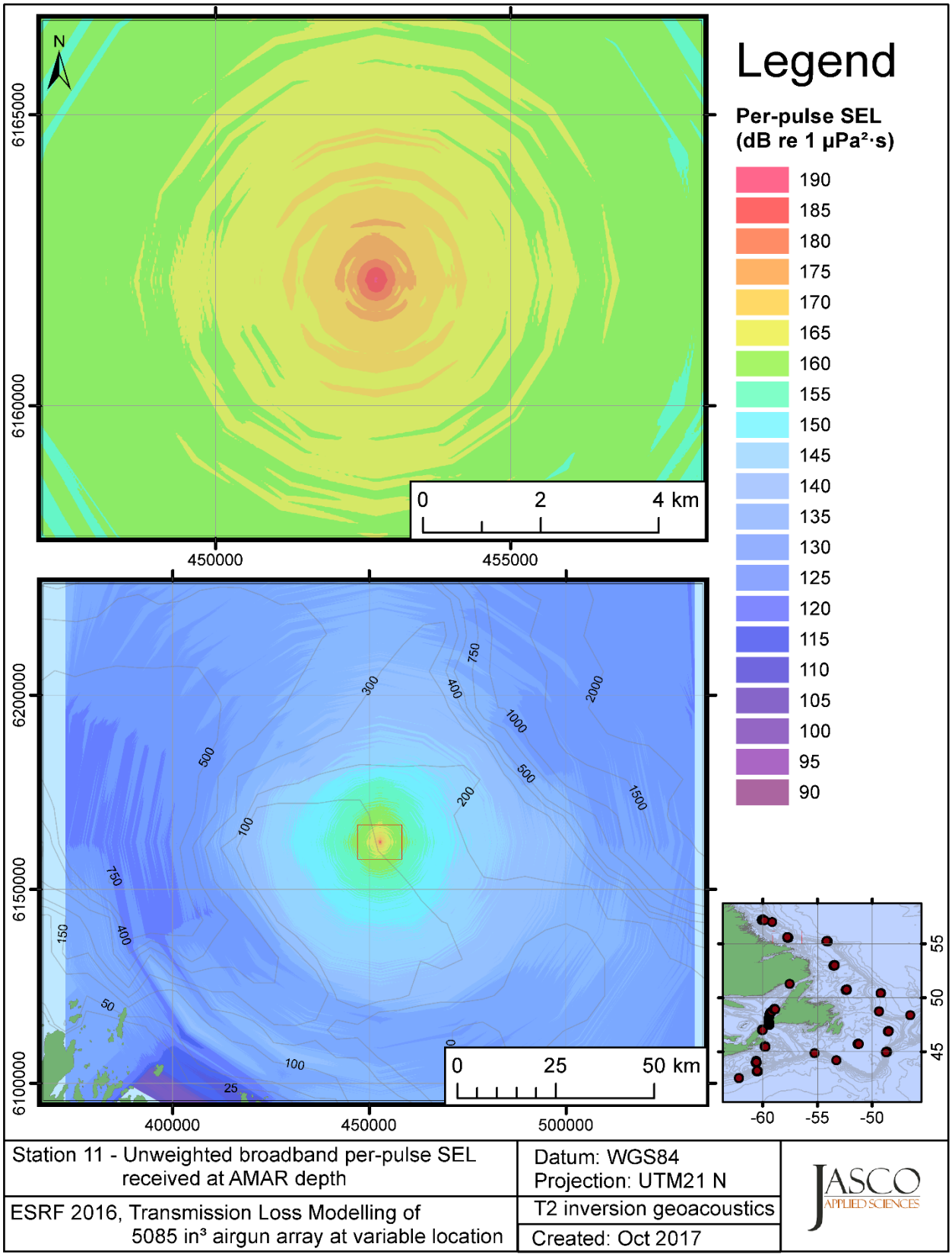

Figure C-24. Stn 11, unweighted SEL received at the AMAR location and depth, modelled using the track 2 inversion geoacoustic bottom, with in-situ July SSP and the airgun array located at any point on the map.

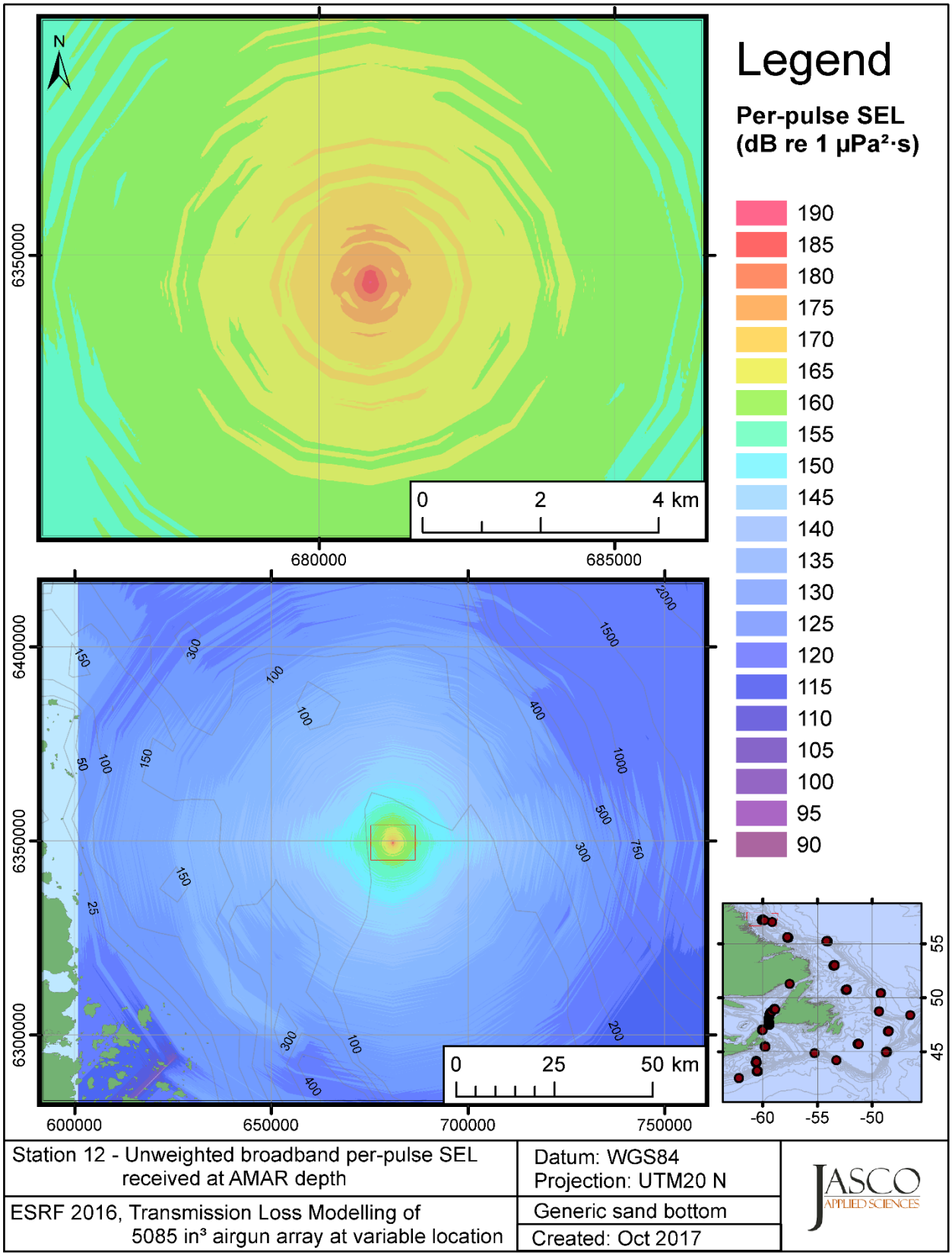

Figure C-25. Stn 12, unweighted SEL received at the AMAR location and depth, modelled using a generic sand bottom, with in-situ July SSP and the airgun array located at any point on the map.

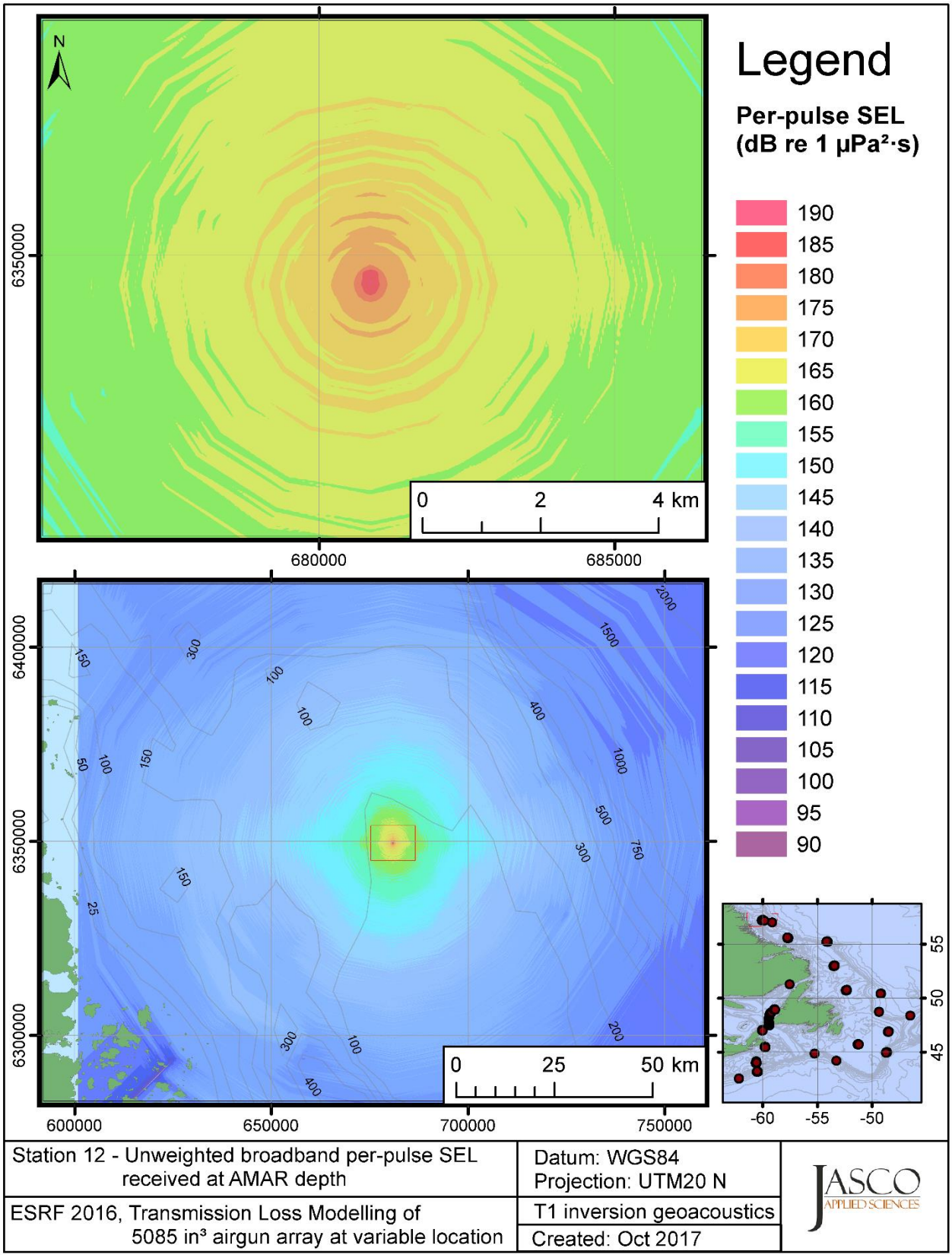

Figure C-26. Stn 12, unweighted SEL received at the AMAR location and depth, modelled using the track 1 inversion geoacoustic bottom, with in-situ July SSP and the airgun array located at any point on the map.

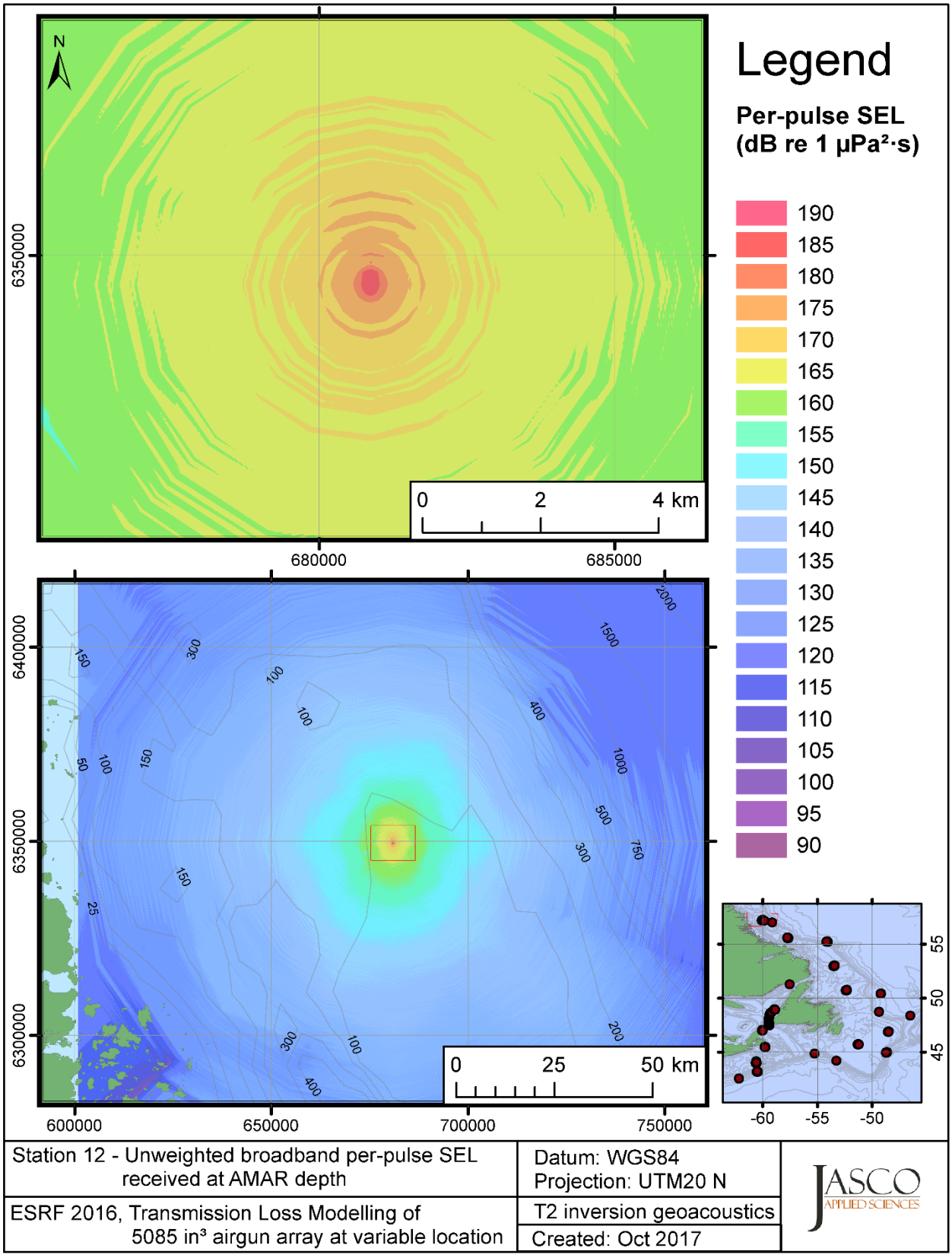

Figure C-27. Stn 12, unweighted SEL received at the AMAR location and depth, modelled using the track 2 inversion geoacoustic bottom, with in-situ July SSP and the airgun array located at any point on the map.

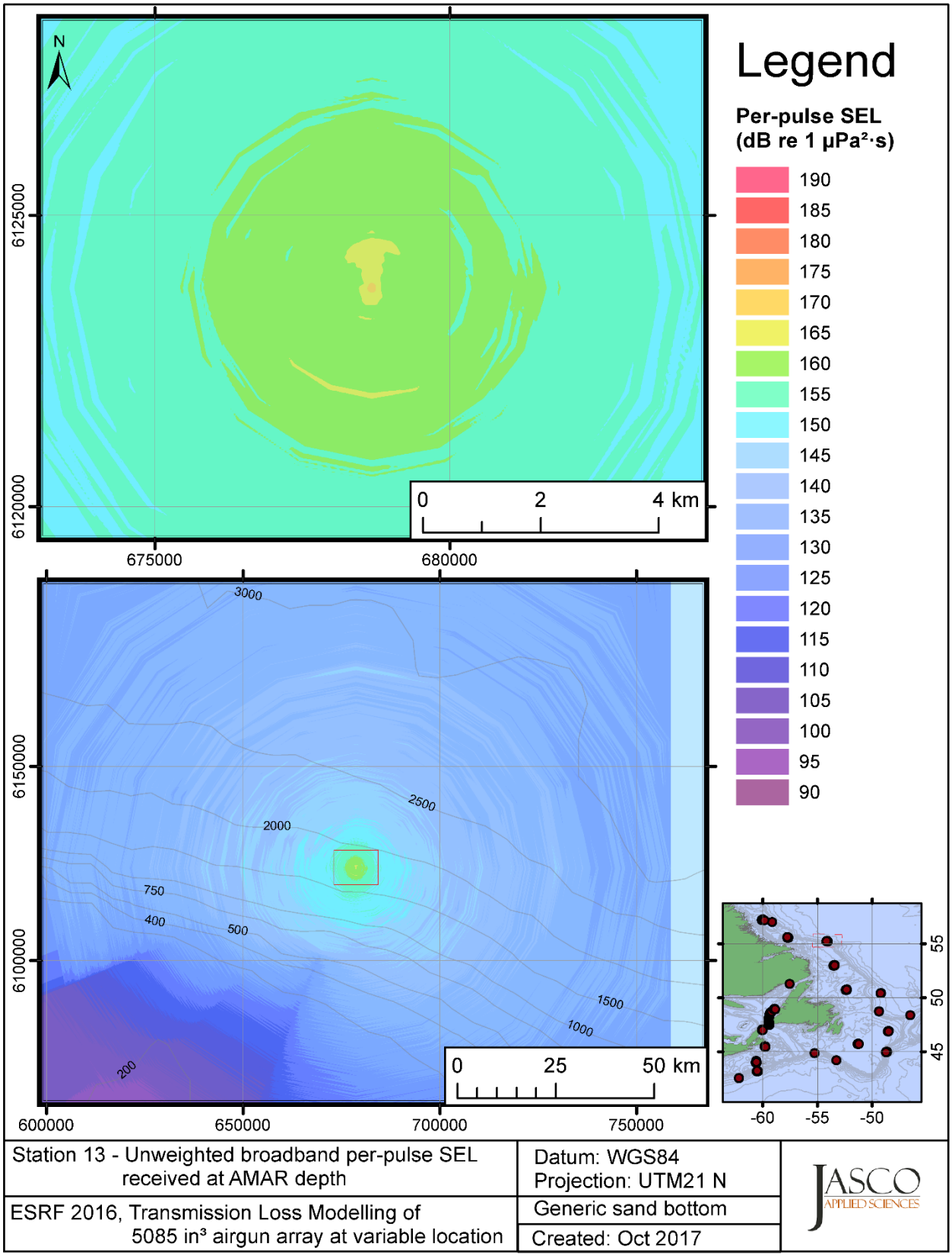

Figure C-28. Stn 13, unweighted SEL received at the AMAR location and depth, modelled using a generic sand bottom, with in-situ July SSP and the airgun array located at any point on the map.

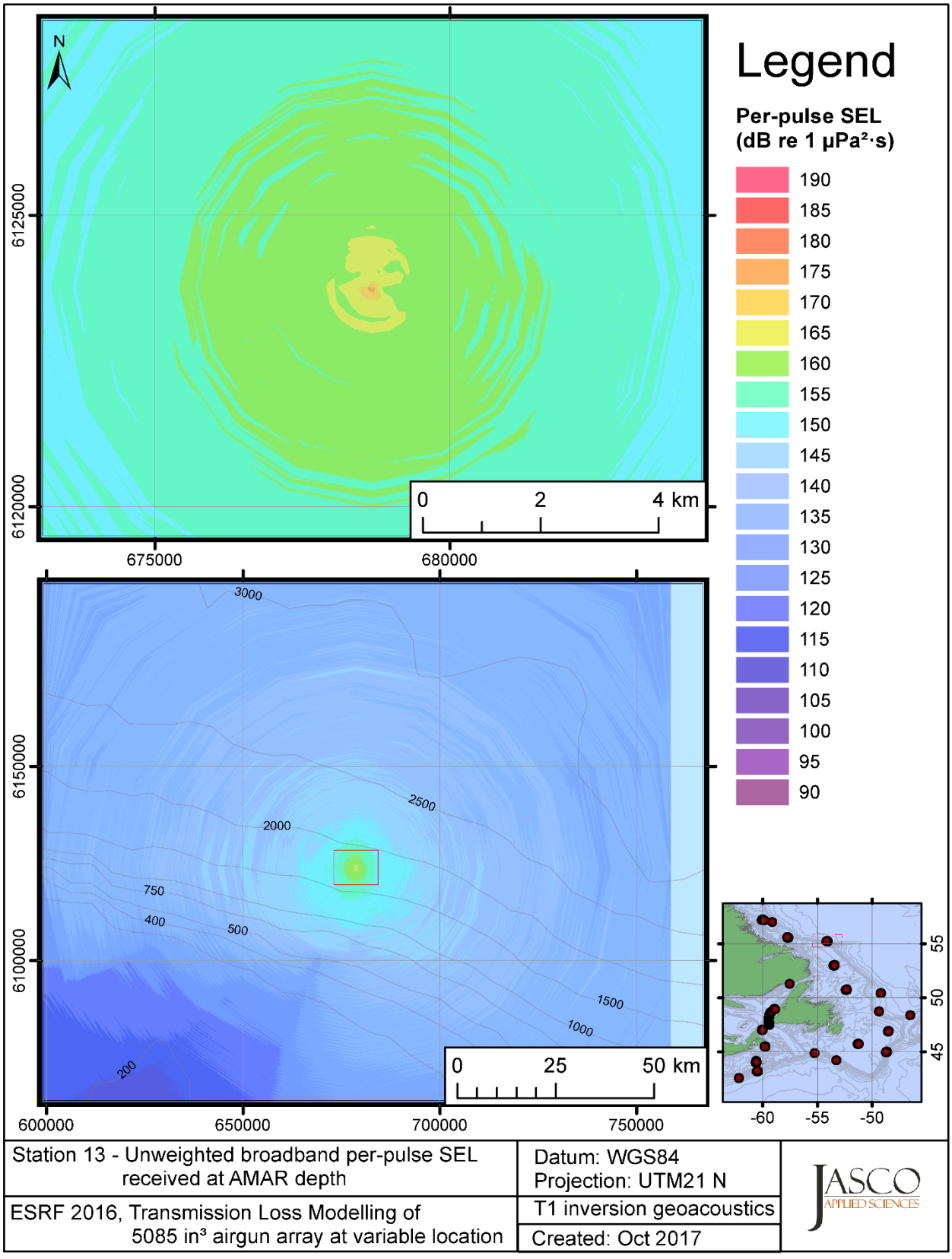

Figure C-29. Stn 13, unweighted SEL received at the AMAR location and depth, modelled using the track 1 inversion geoacoustic bottom, with in-situ July SSP and the airgun array located at any point on the map.

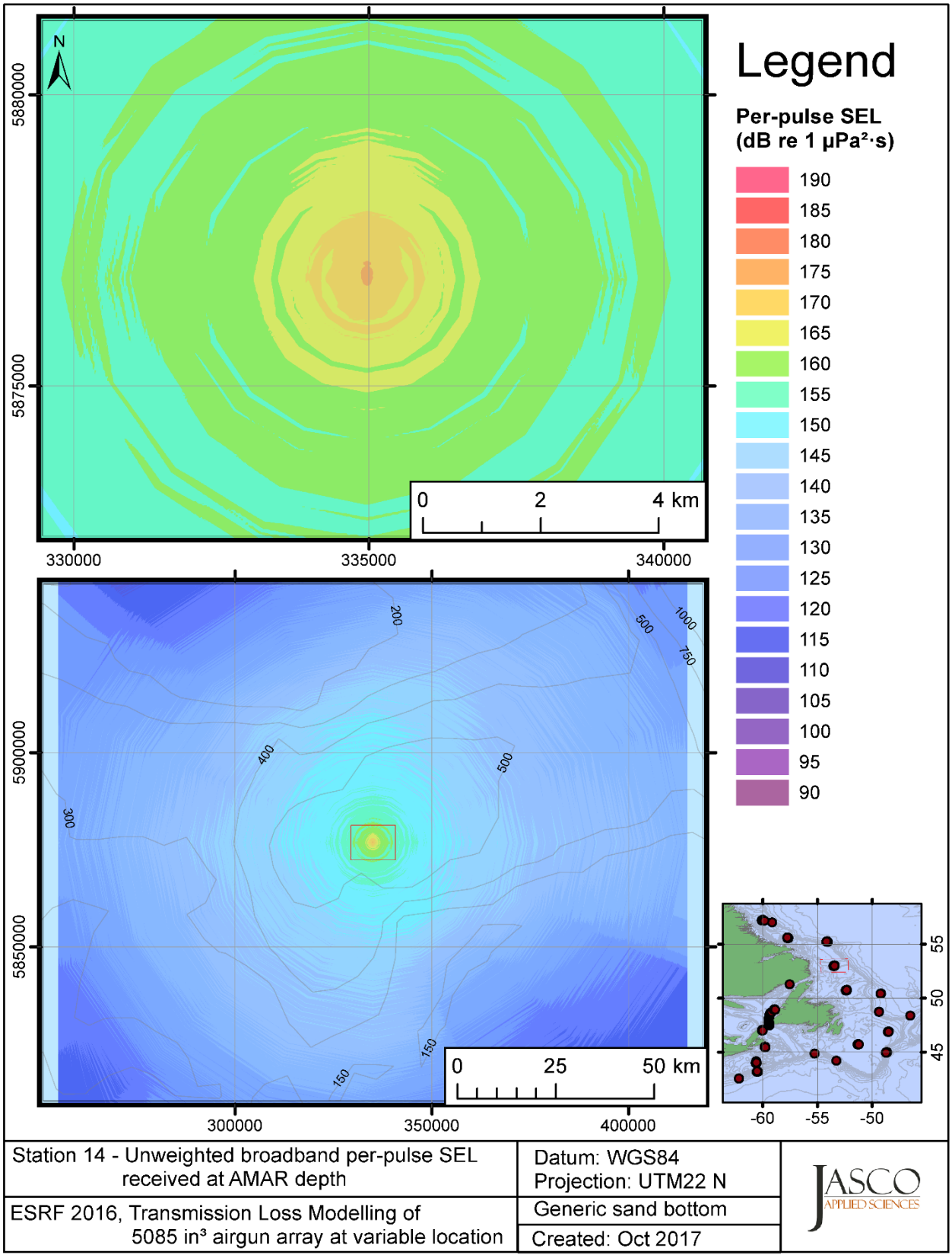

Figure C-30. Stn 14, unweighted SEL received at the AMAR location and depth, modelled using a generic sand bottom, with in-situ July SSP and the airgun array located at any point on the map.

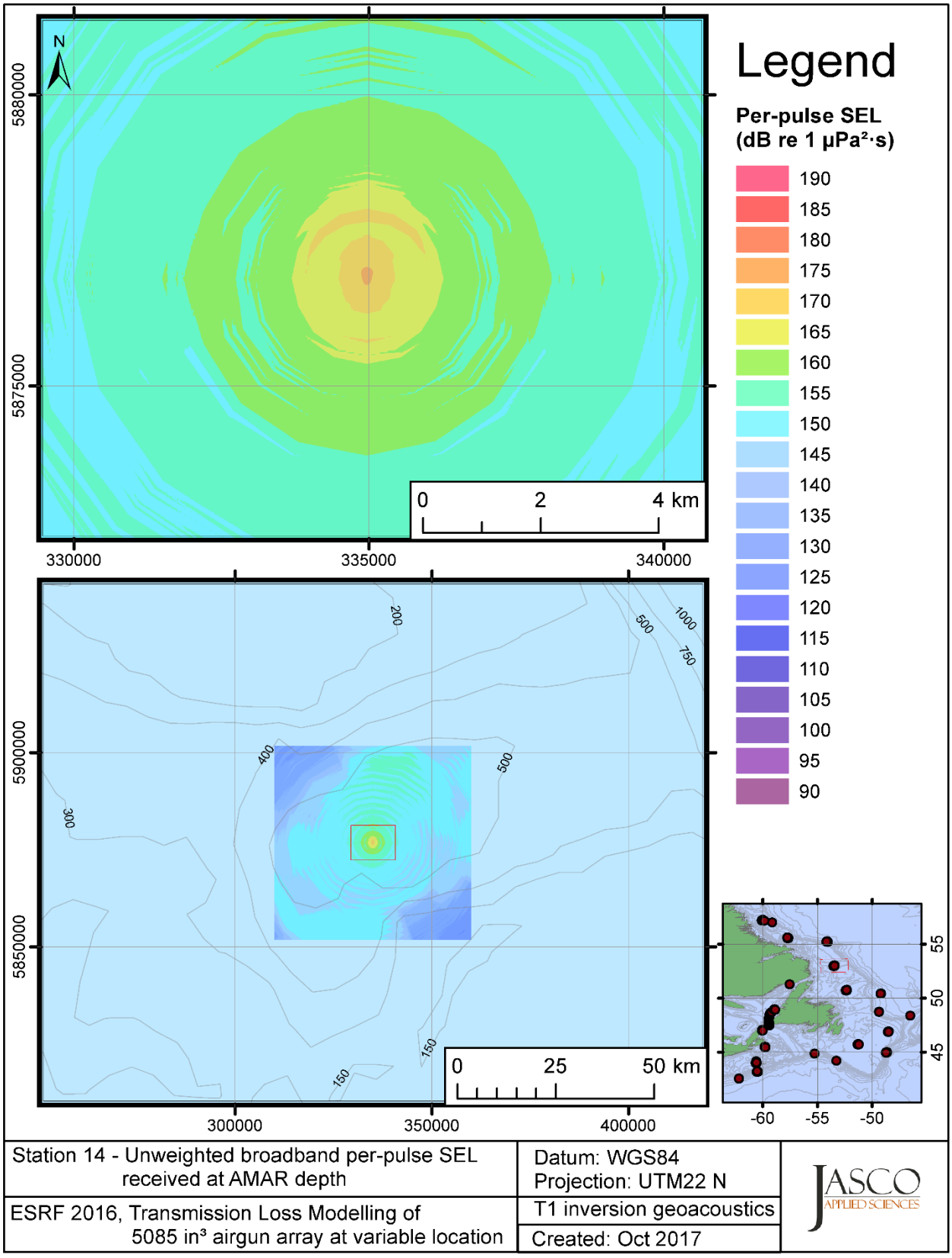

Figure C-31. Stn 14, unweighted SEL received at the AMAR location and depth, modelled using the track 1 inversion geoacoustic bottom, with in-situ July SSP and the airgun array located at any point on the map.

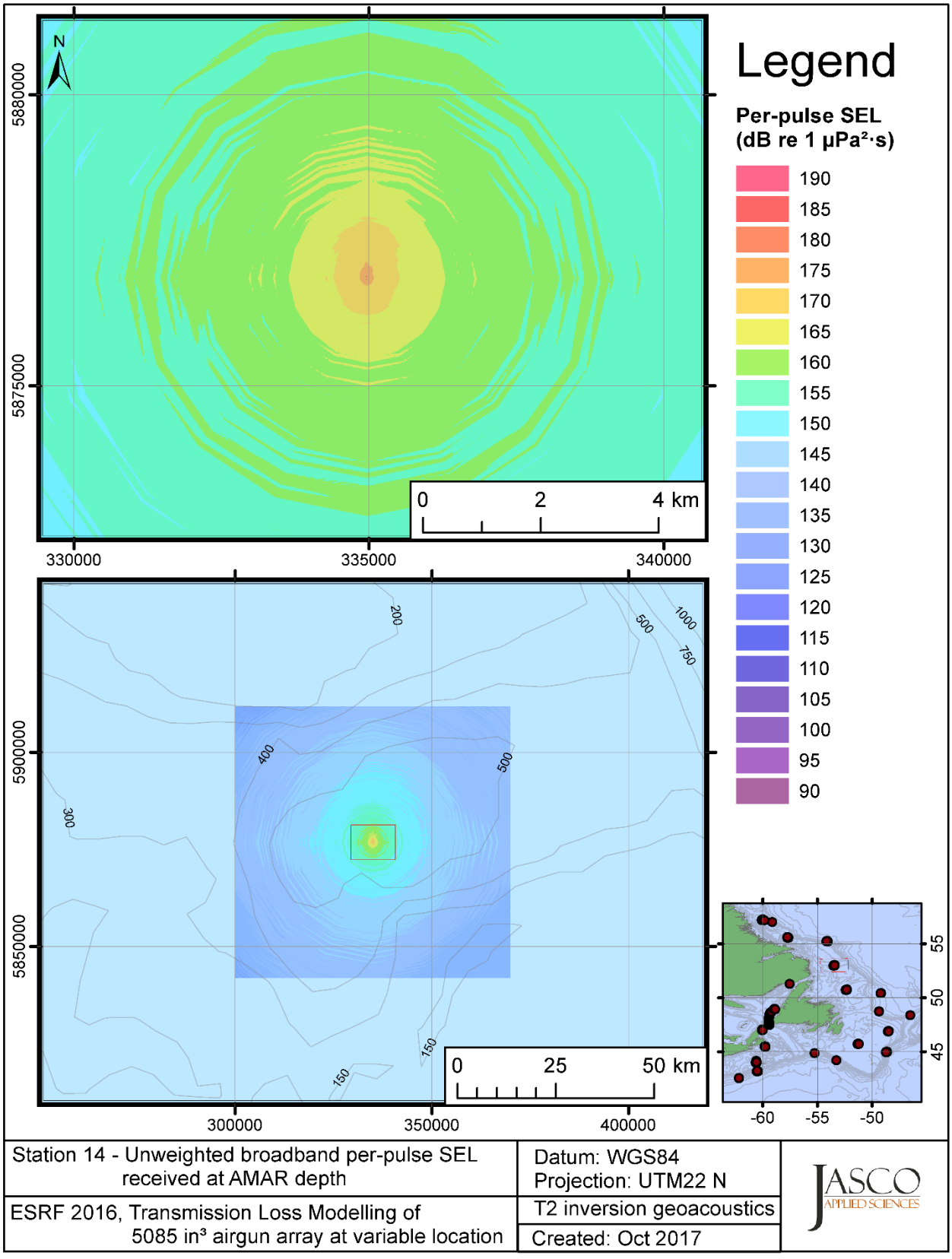

Figure C-32. Stn 14, unweighted SEL received at the AMAR location and depth, modelled using the track 2 inversion geoacoustic bottom, with in-situ July SSP and the airgun array located at any point on the map.

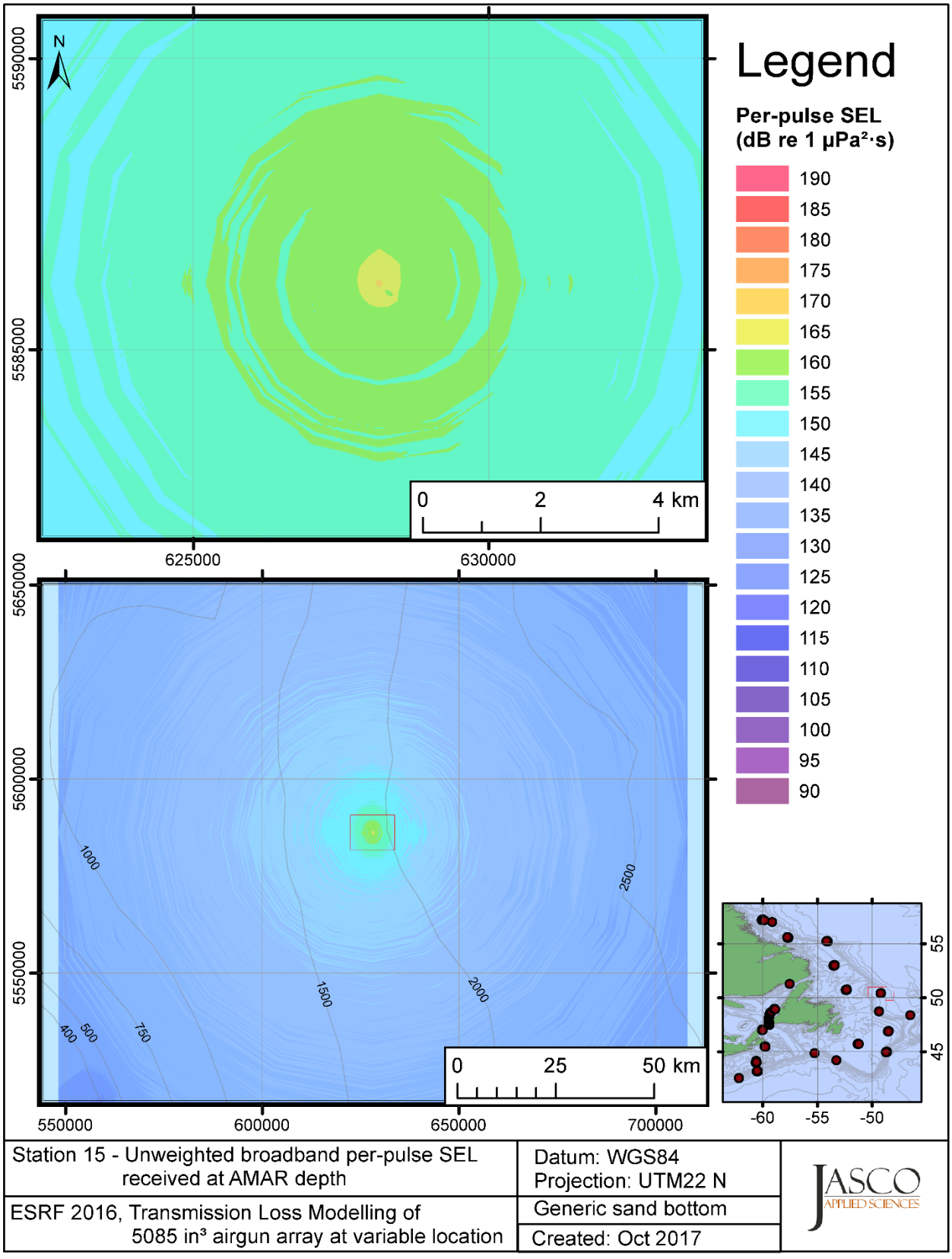

Figure C-33. Stn 15, unweighted SEL received at the AMAR location and depth, modelled using a generic sand bottom, with in-situ July SSP and the airgun array located at any point on the map.

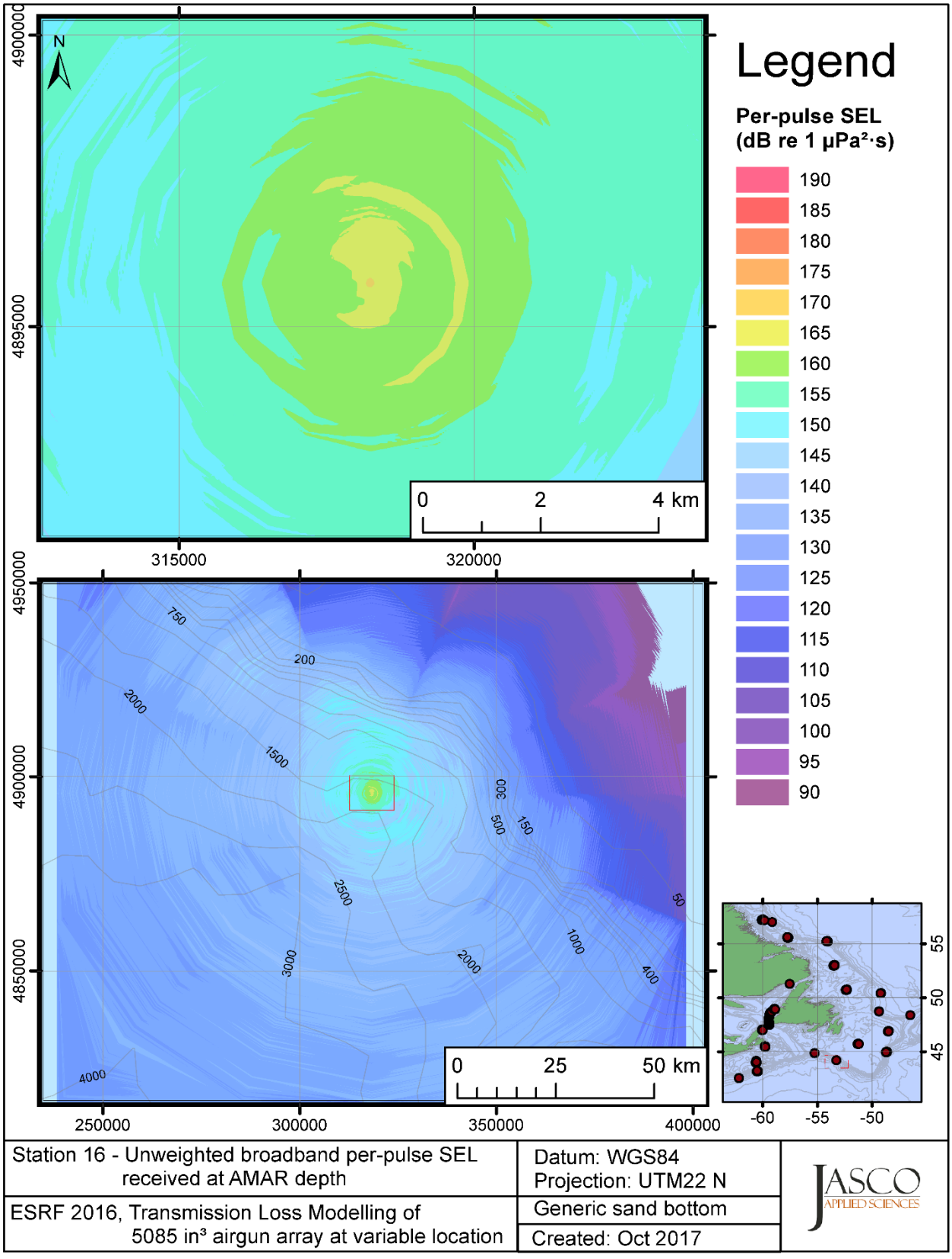

Figure C-34. Stn 16, unweighted SEL received at the AMAR location and depth, modelled using a generic sand bottom, with in-situ July SSP and the airgun array located at any point on the map.

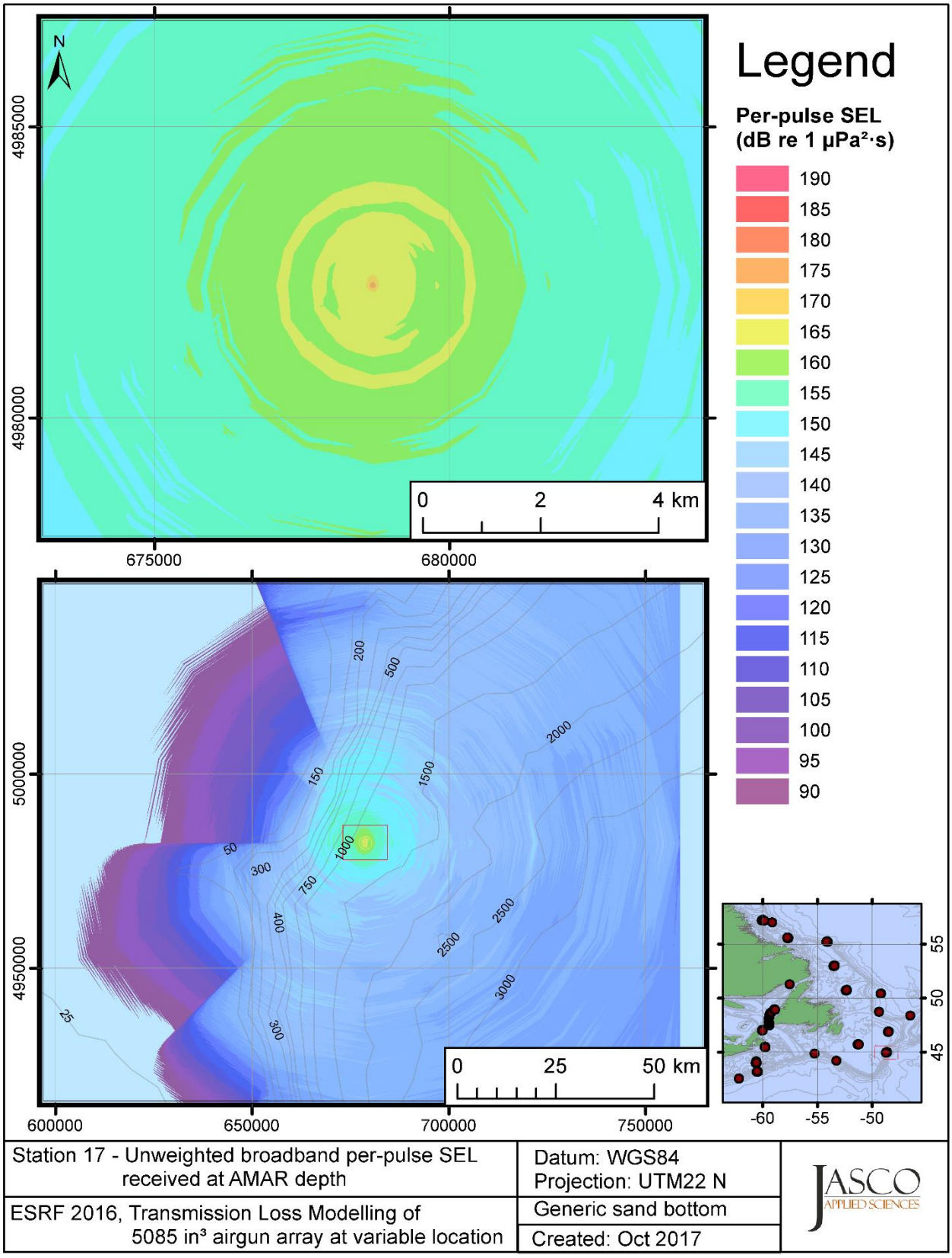

Figure C-35. Stn 17, unweighted SEL received at the AMAR location and depth, modelled using a generic sand bottom, with in-situ July SSP and the airgun array located at any point on the map.

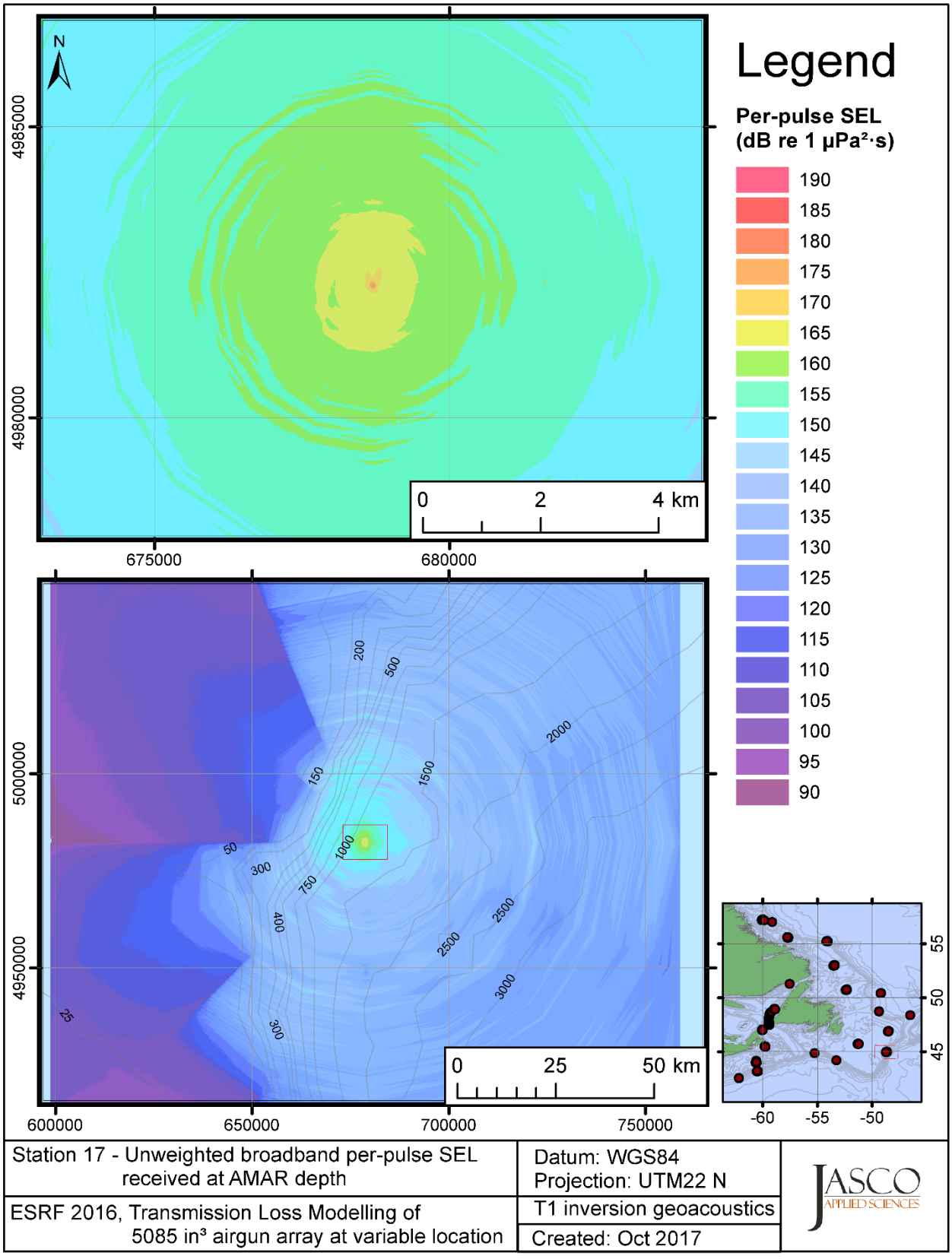

Figure C-36. Stn 17, unweighted SEL received at the AMAR location and depth, modelled using the track 1 inversion geoacoustic bottom, with in-situ July SSP and the airgun array located at any point on the map.

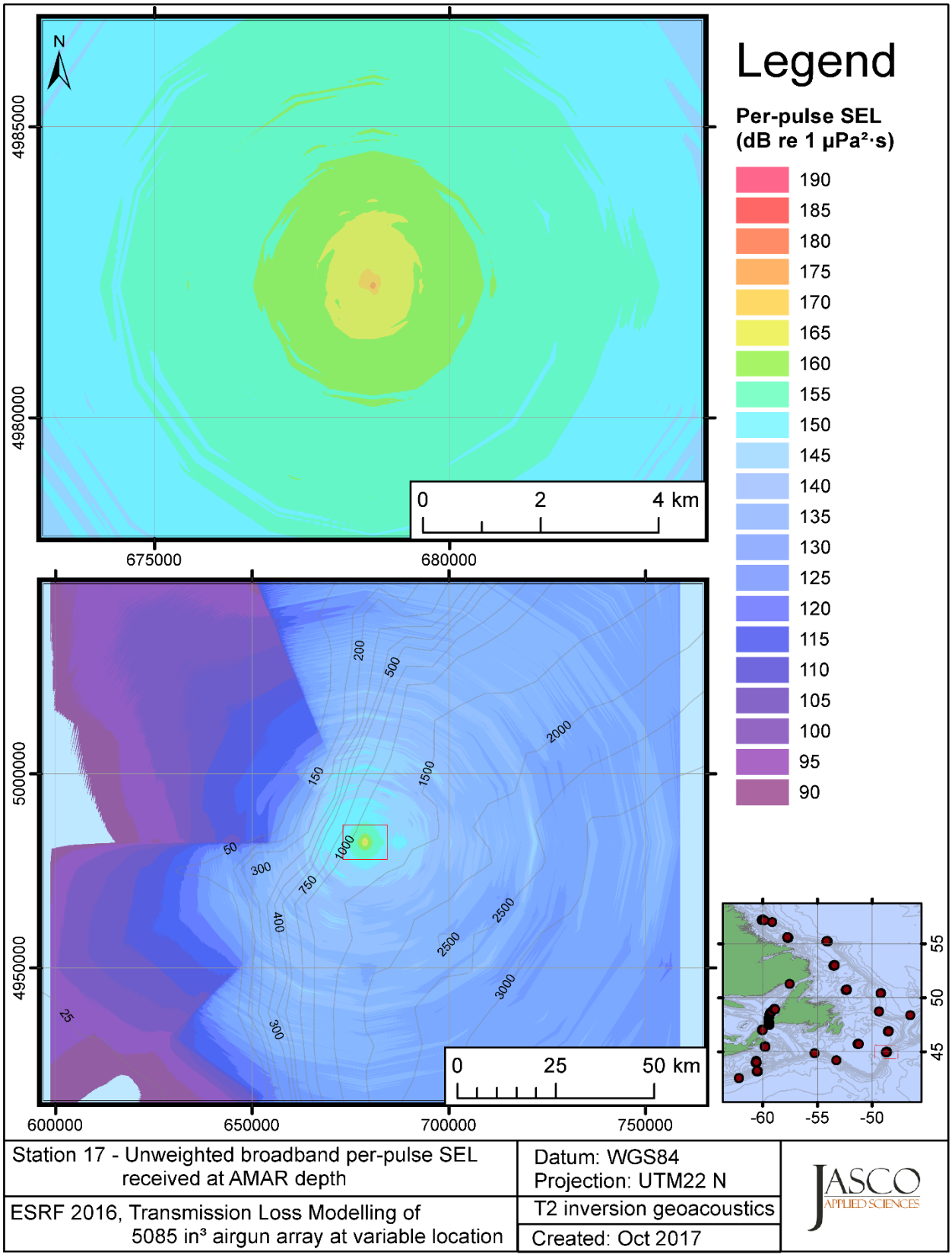

Figure C-37. Stn 17, unweighted SEL received at the AMAR location and depth, modelled using the track 2 inversion geoacoustic bottom, with in-situ July SSP and the airgun array located at any point on the map.

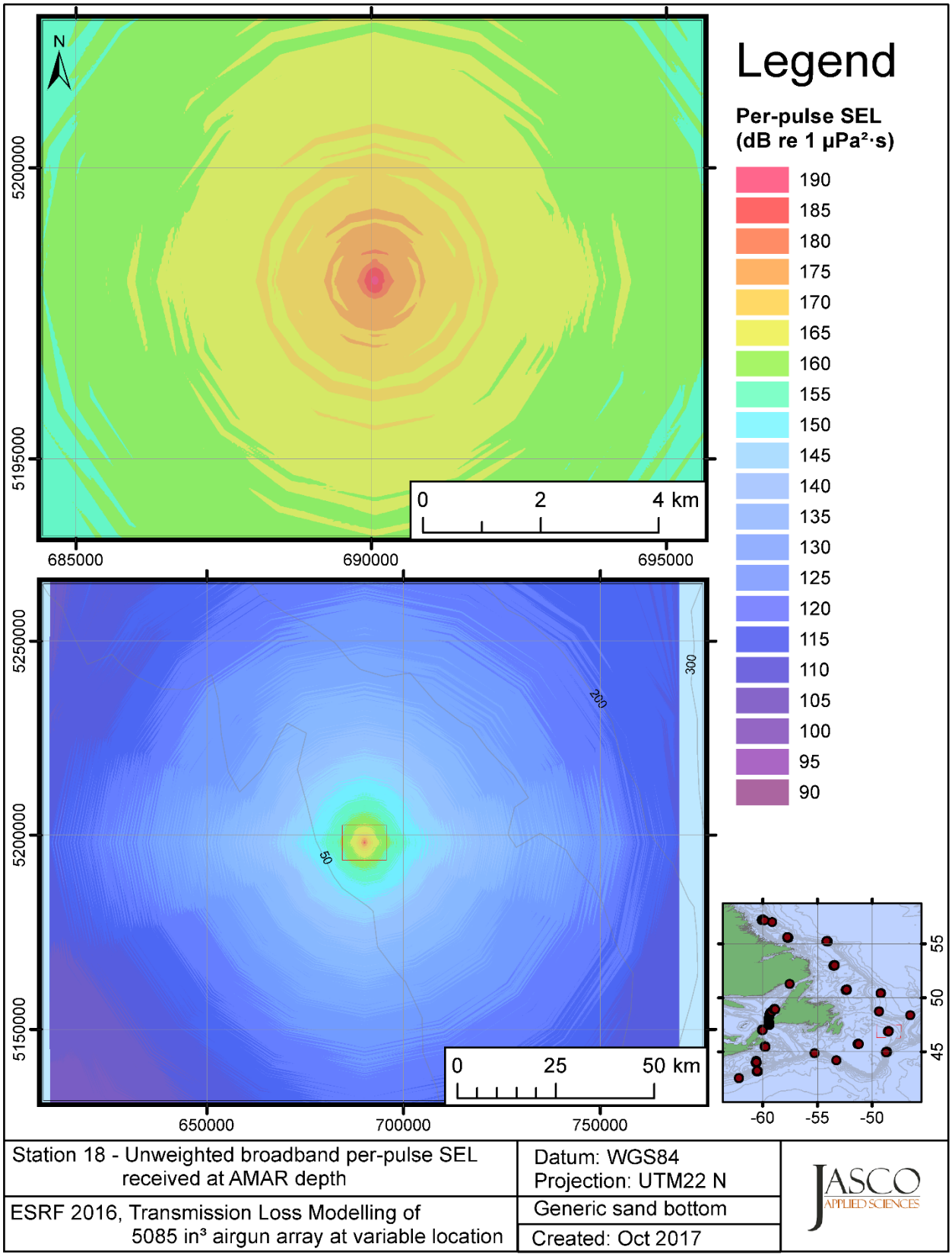

Figure C-38. Stn 18, unweighted SEL received at the AMAR location and depth, modelled using a generic sand bottom, with in-situ July SSP and the airgun array located at any point on the map.

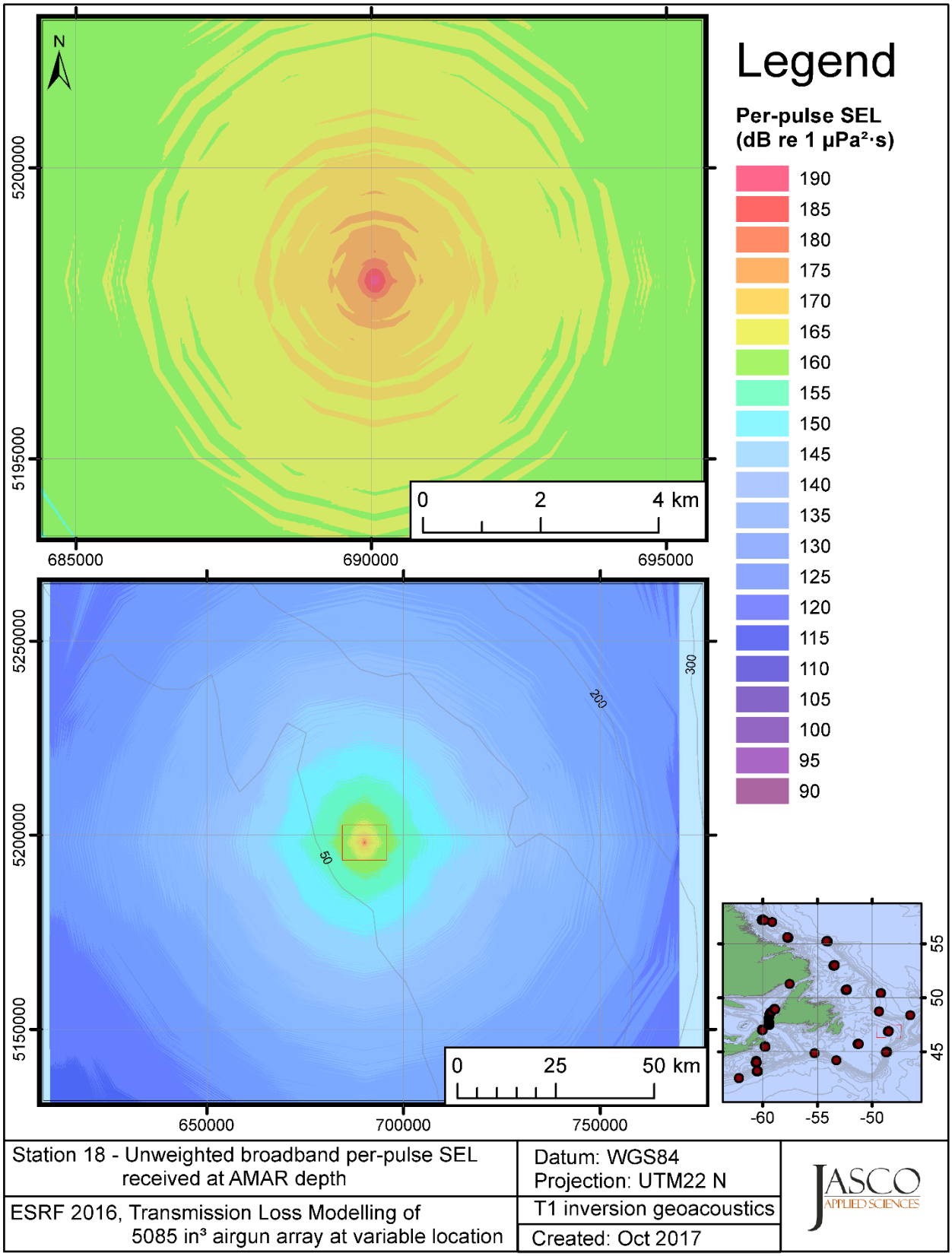

Figure C-39. Stn 18, unweighted SEL received at the AMAR location and depth, modelled using the track 1 inversion geoacoustic bottom, with in-situ July SSP and the airgun array located at any point on the map.

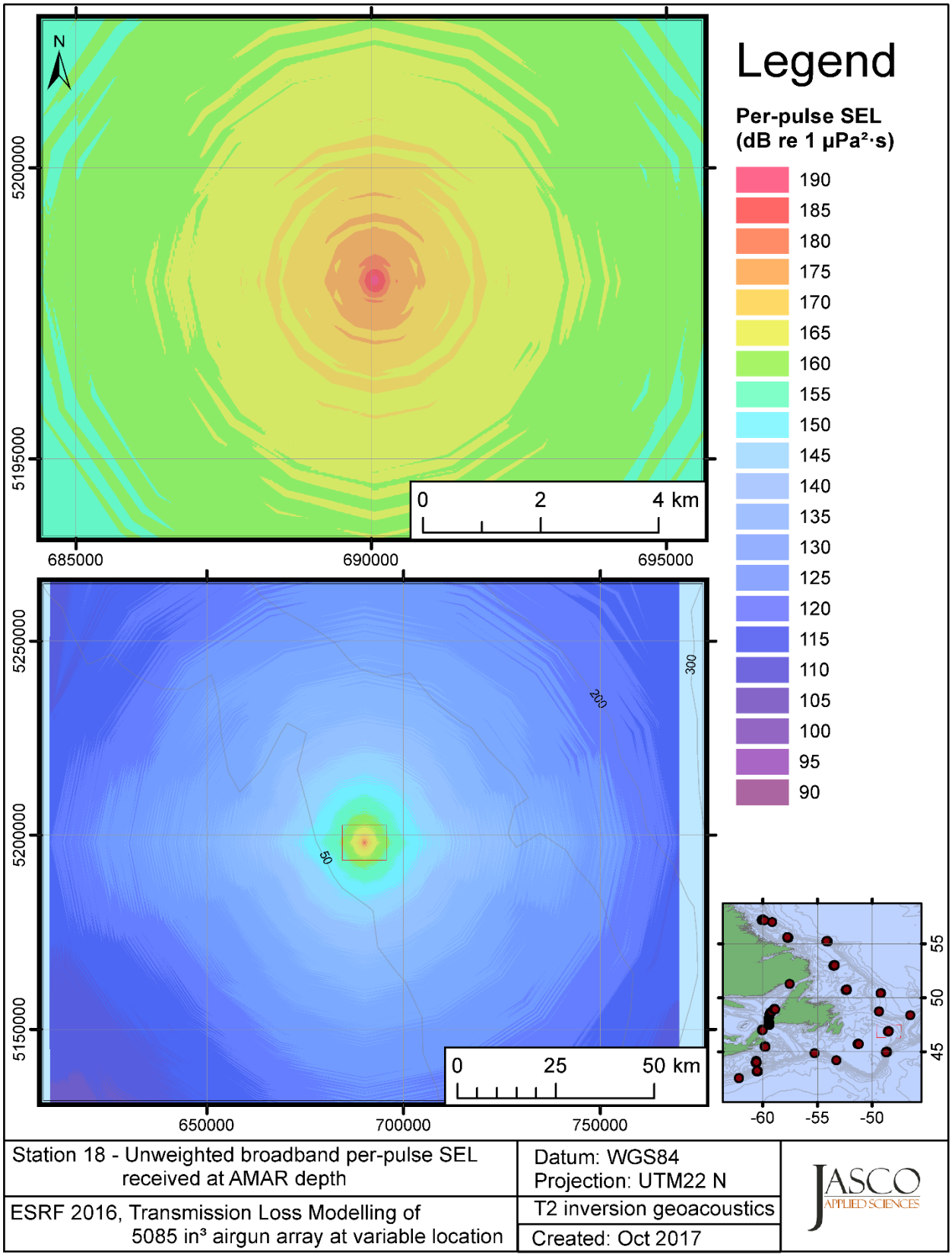

Figure C-40. Stn 18, unweighted SEL received at the AMAR location and depth, modelled using the track 2 inversion geoacoustic bottom, with in-situ July SSP and the airgun array located at any point on the map.

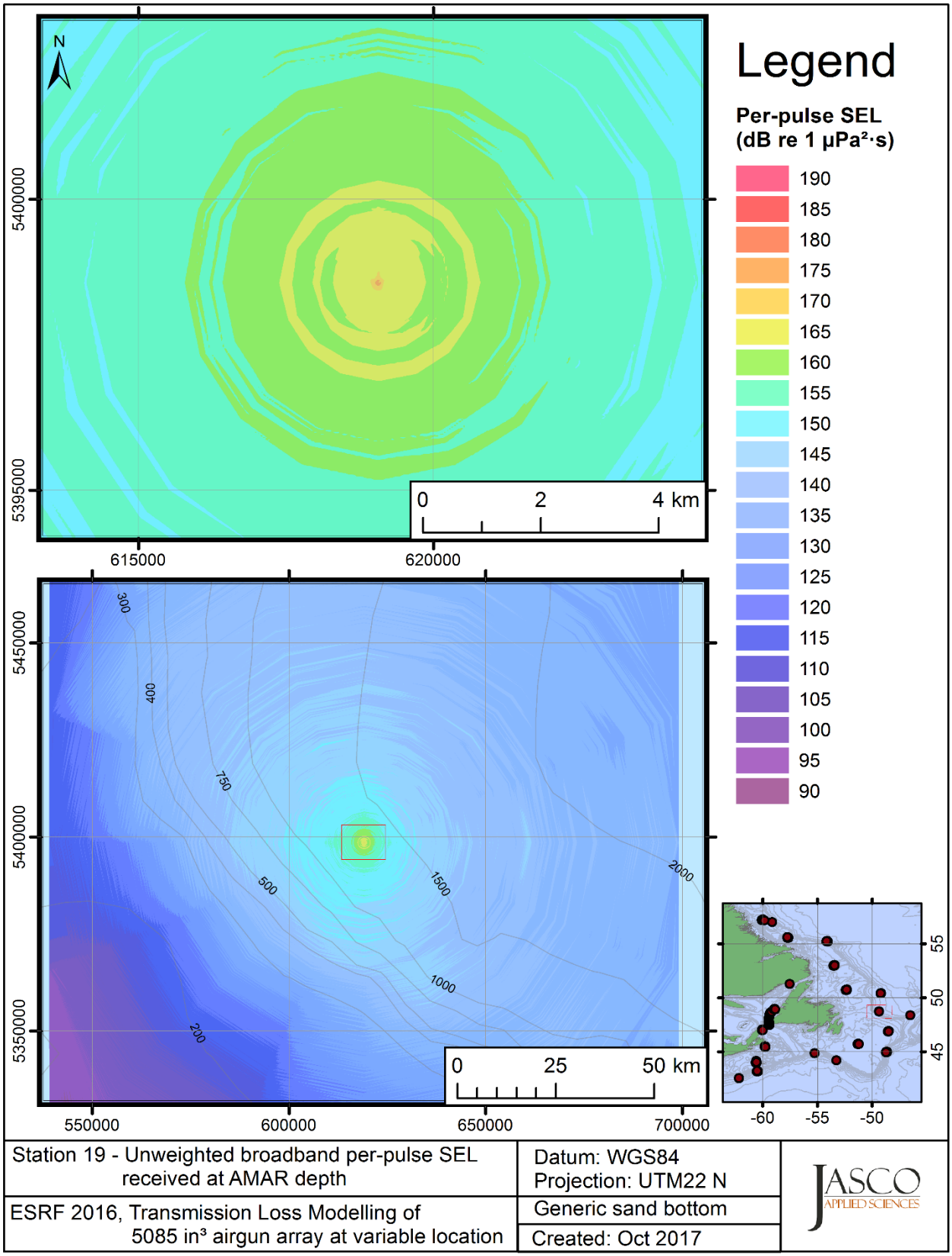

Figure C-41. Stn 19, unweighted SEL received at the AMAR location and depth, modelled using a generic sand bottom, with in-situ July SSP and the airgun array located at any point on the map.

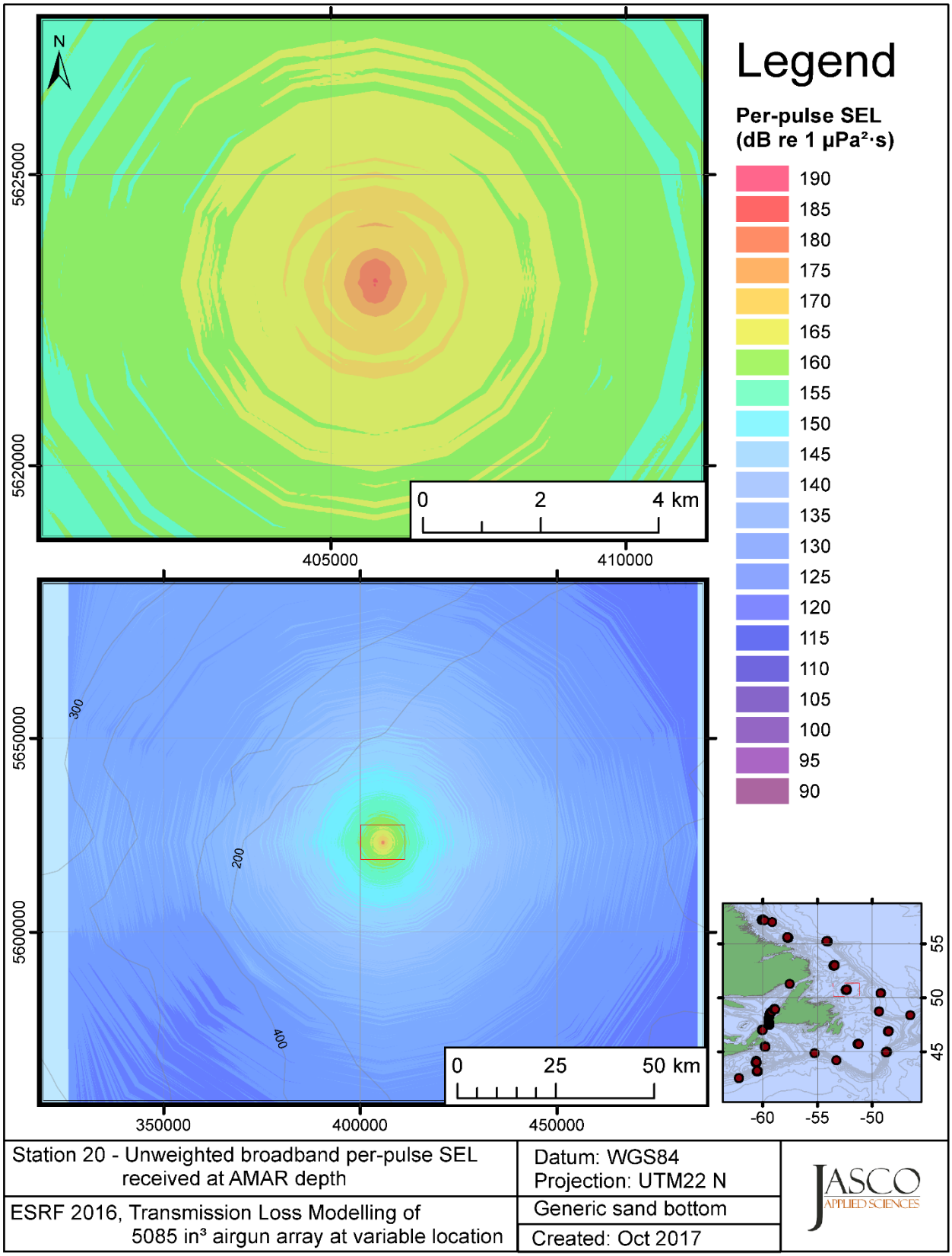

Figure C-42. Stn 20, unweighted SEL received at the AMAR location and depth, modelled using a generic sand bottom, with in-situ July SSP and the airgun array located at any point on the map.

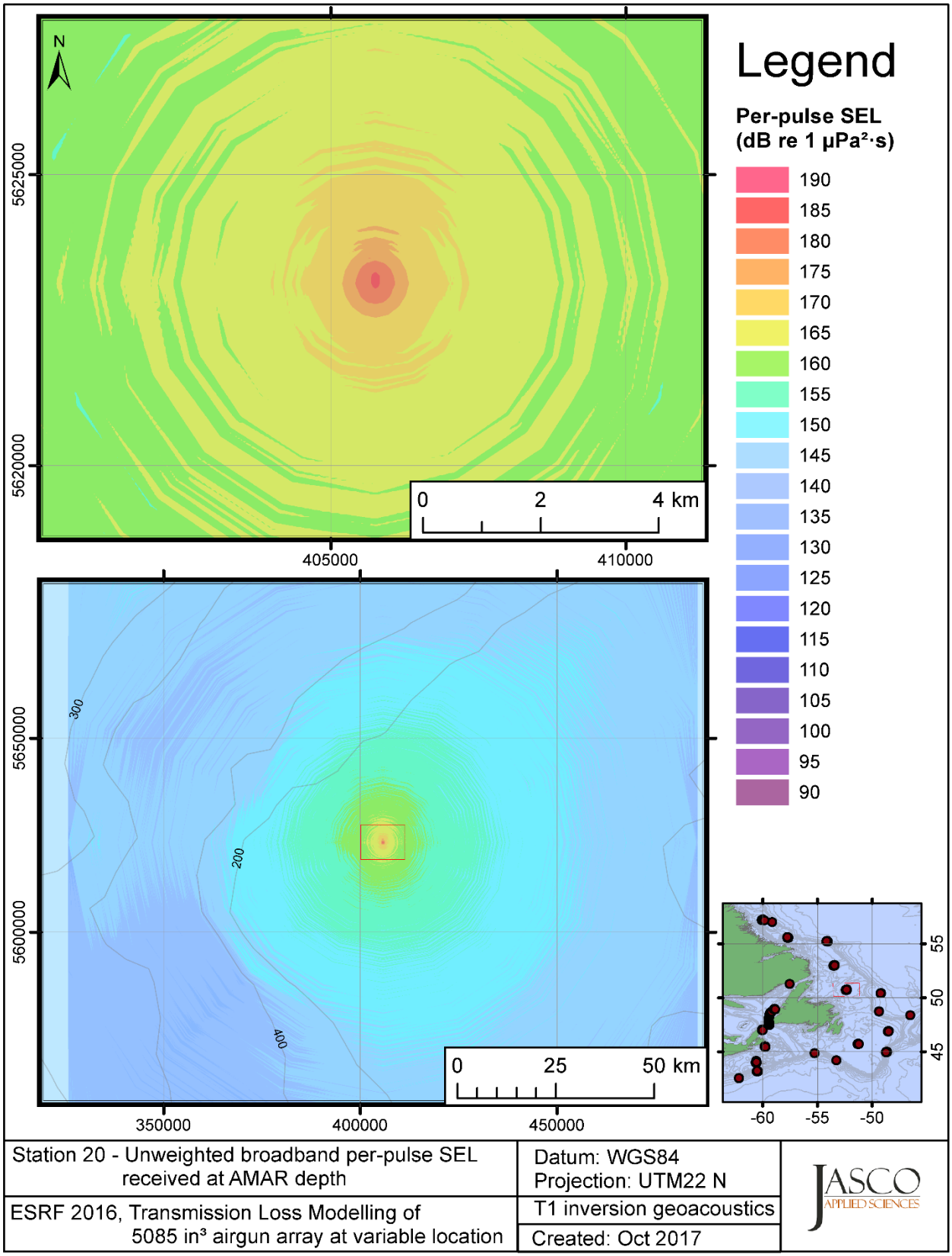

Figure C-43. Stn 20, unweighted SEL received at the AMAR location and depth, modelled using the track 1 inversion geoacoustic bottom, with in-situ July SSP and the airgun array located at any point on the map.

C.2. Modelling LF M-weighted Received Level at the AMAR Location

This section presents the results of modelling the per-pulse sound exposure level (SEL) received at the AMAR location and depth as a function of the source location (varied in range and azimuth) for each of the 20 sites using a generic sand bottom; in addition, the modelling is repeated using the geoacoustic inversion bottom parameters at the 14 sites where they are available. The modelling results are presented in the form of coloured maps where the colour at any map location represents the predicted received level at the AMAR for the source located at that spot on the map. This section includes only the low-frequency cetaceans (LF) marine-mammal-weighted per-pulse SEL results; additional maps for other marine mammal received level auditory weighting functions are presented in adjoining sections.

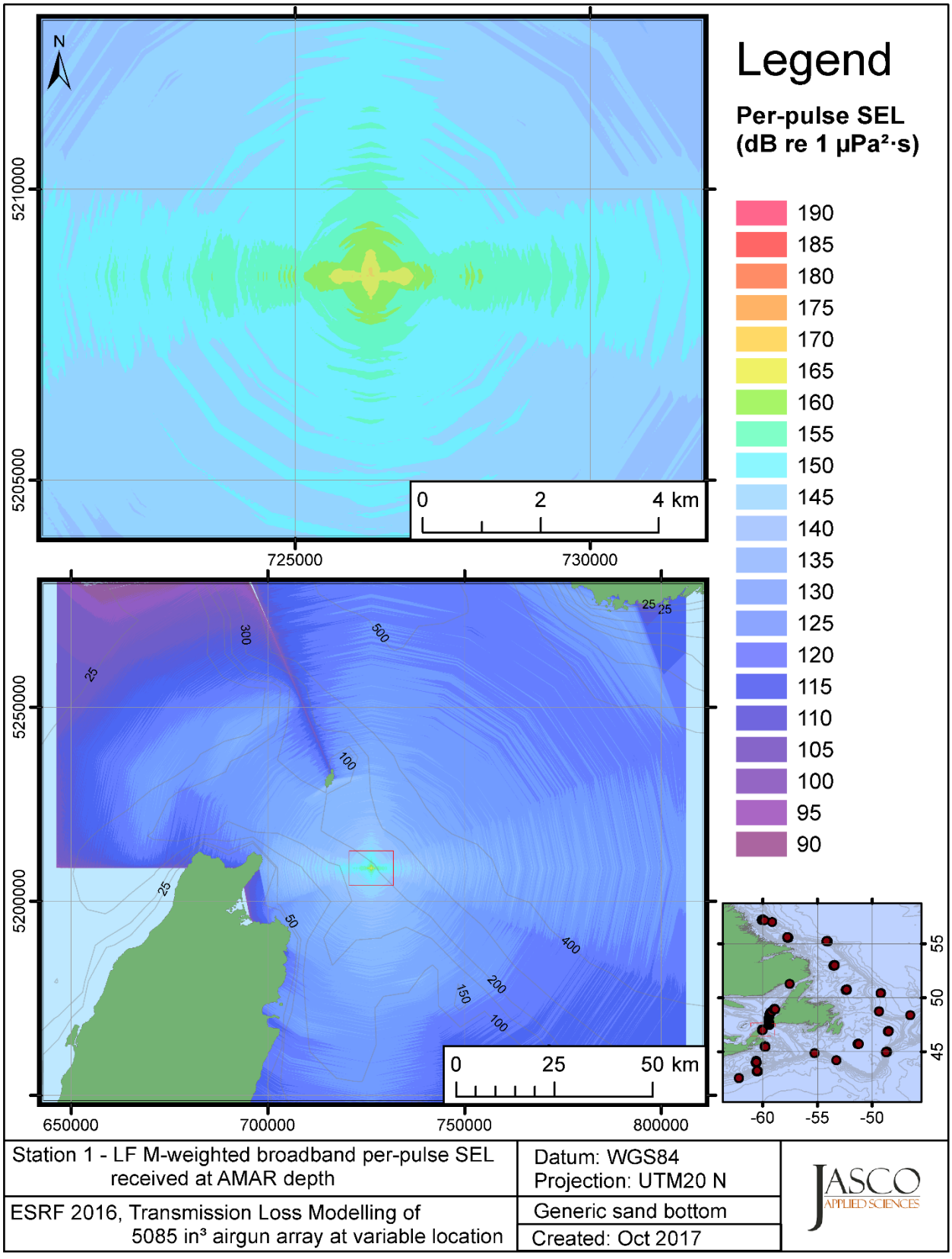

Figure C-44. Stn 1, LF M-weighted SEL received at the AMAR location and depth, modelled using a generic sand bottom, with in-situ July SSP and the airgun array located at any point on the map.

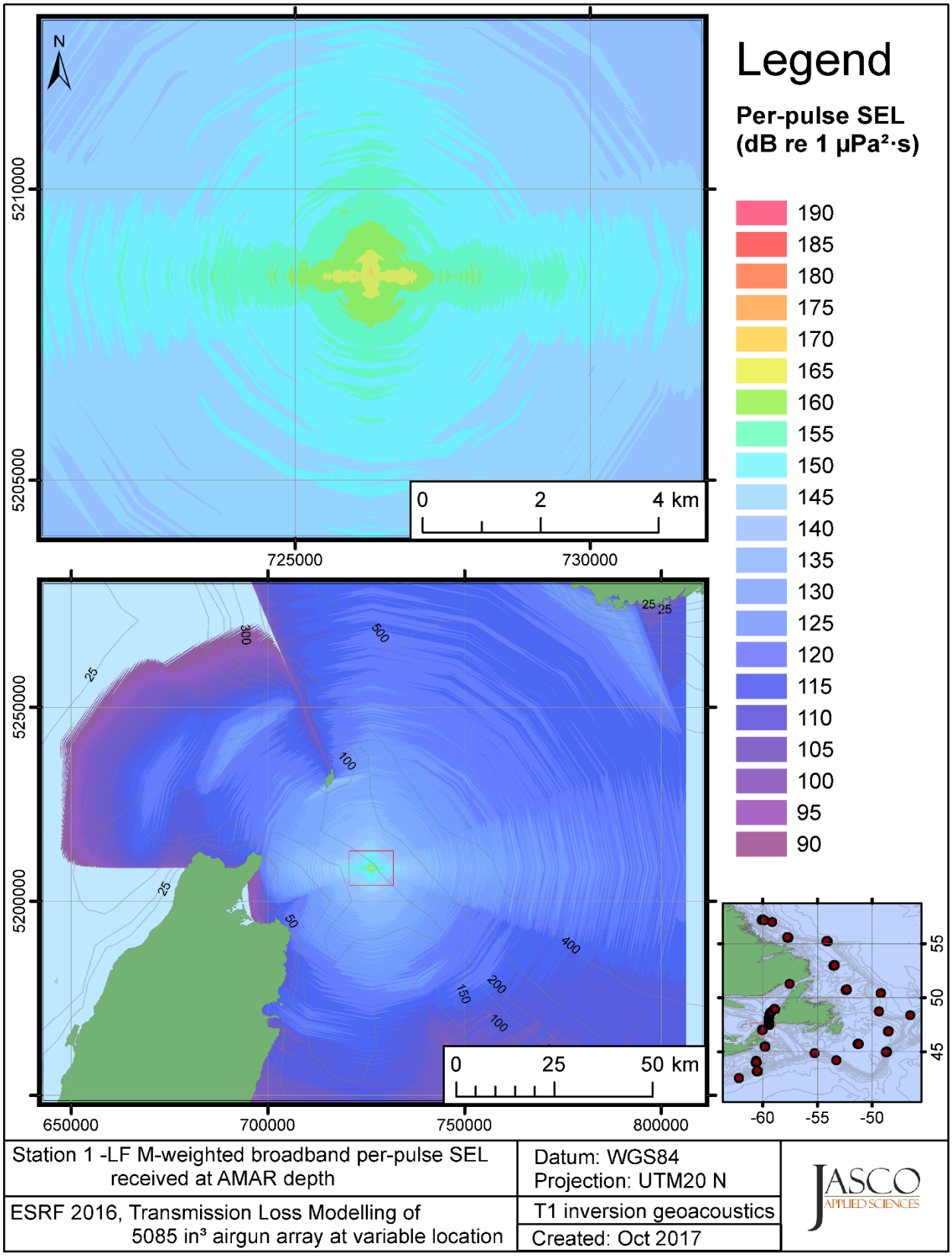

Figure C-45. Stn 1, LF M-weighted SEL received at the AMAR location and depth, modelled using the track 1 inversion geoacoustic bottom, with in-situ July SSP and the airgun array located at any point on the map.

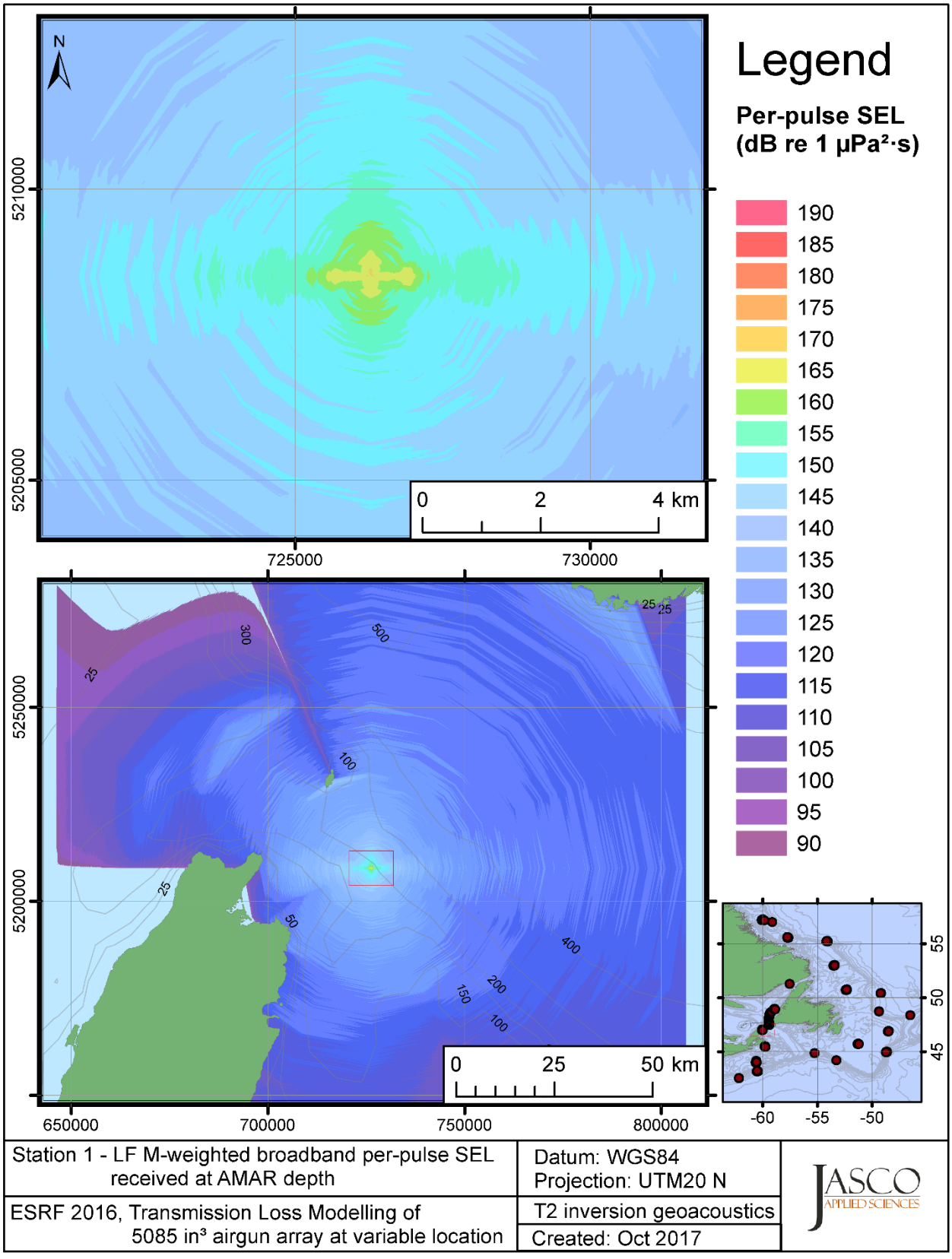

Figure C-46. Stn 1, LF M-weighted SEL received at the AMAR location and depth, modelled using the track 2 inversion geoacoustic bottom, with in-situ July SSP and the airgun array located at any point on the map.

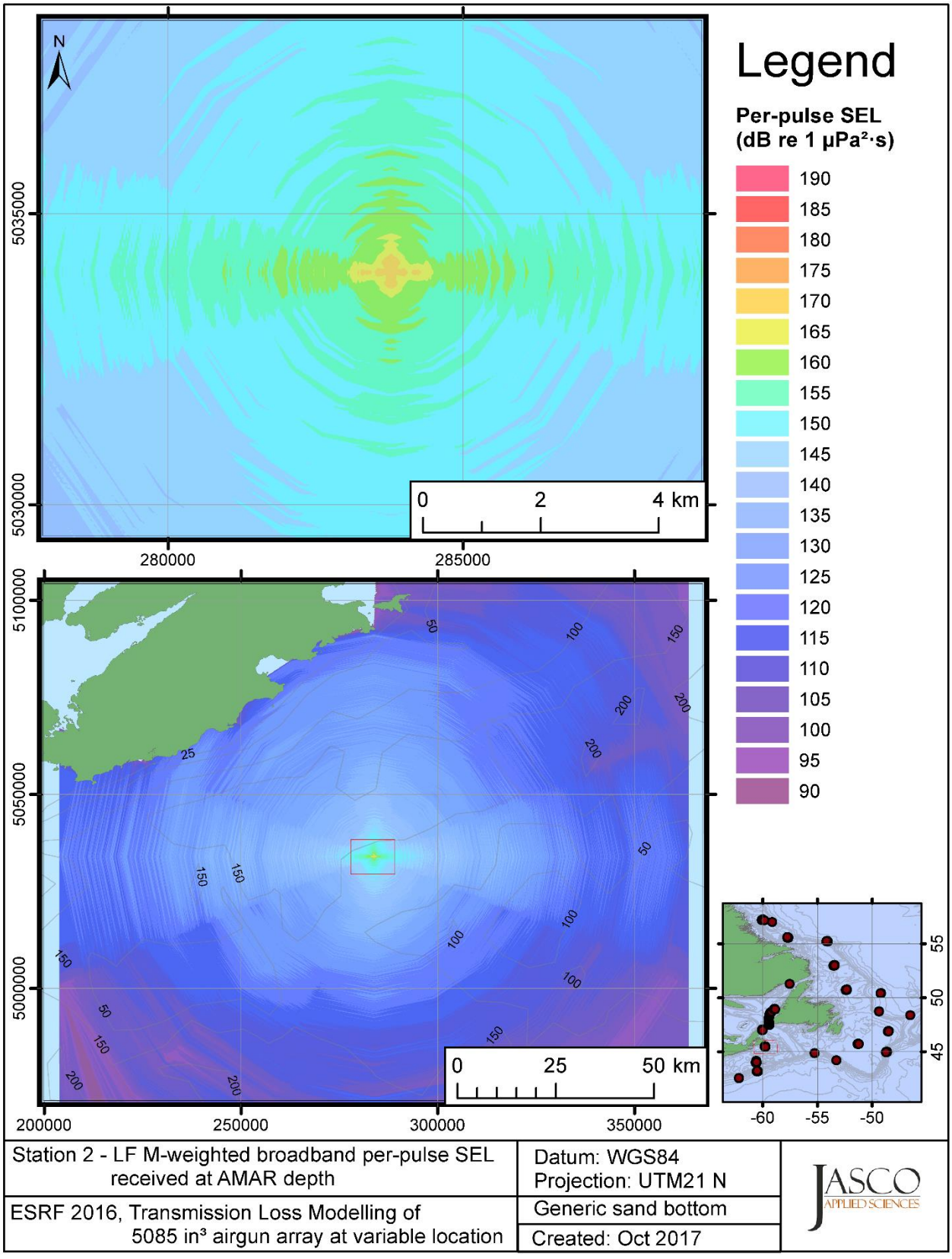

Figure C-47. Stn 2, LF M-weighted SEL received at the AMAR location and depth, modelled using a generic sand bottom, with in-situ July SSP and the airgun array located at any point on the map.

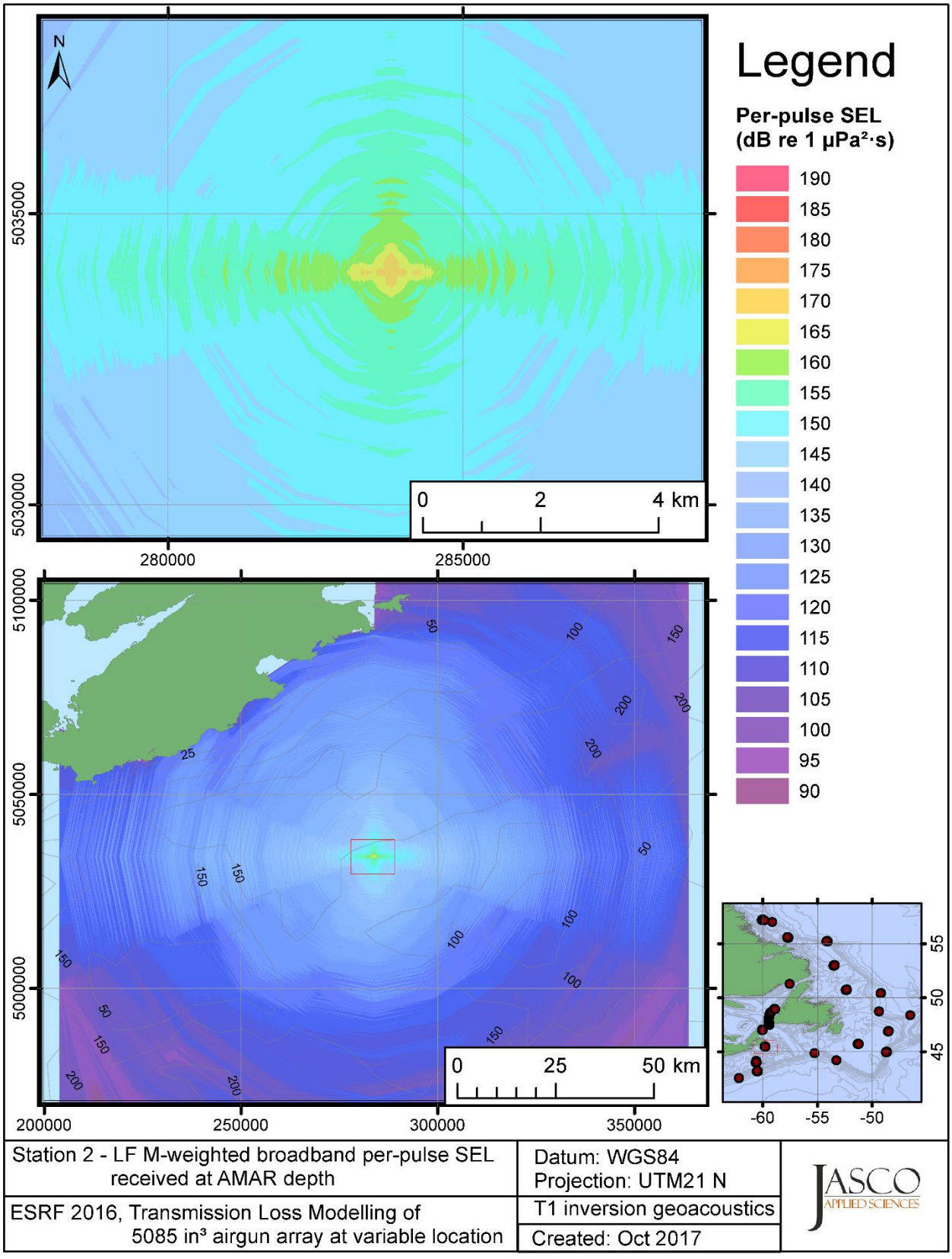

Figure C-48. Stn 2, LF M-weighted SEL received at the AMAR location and depth, modelled using the track 1 inversion geoacoustic bottom, with in-situ July SSP and the airgun array located at any point on the map.

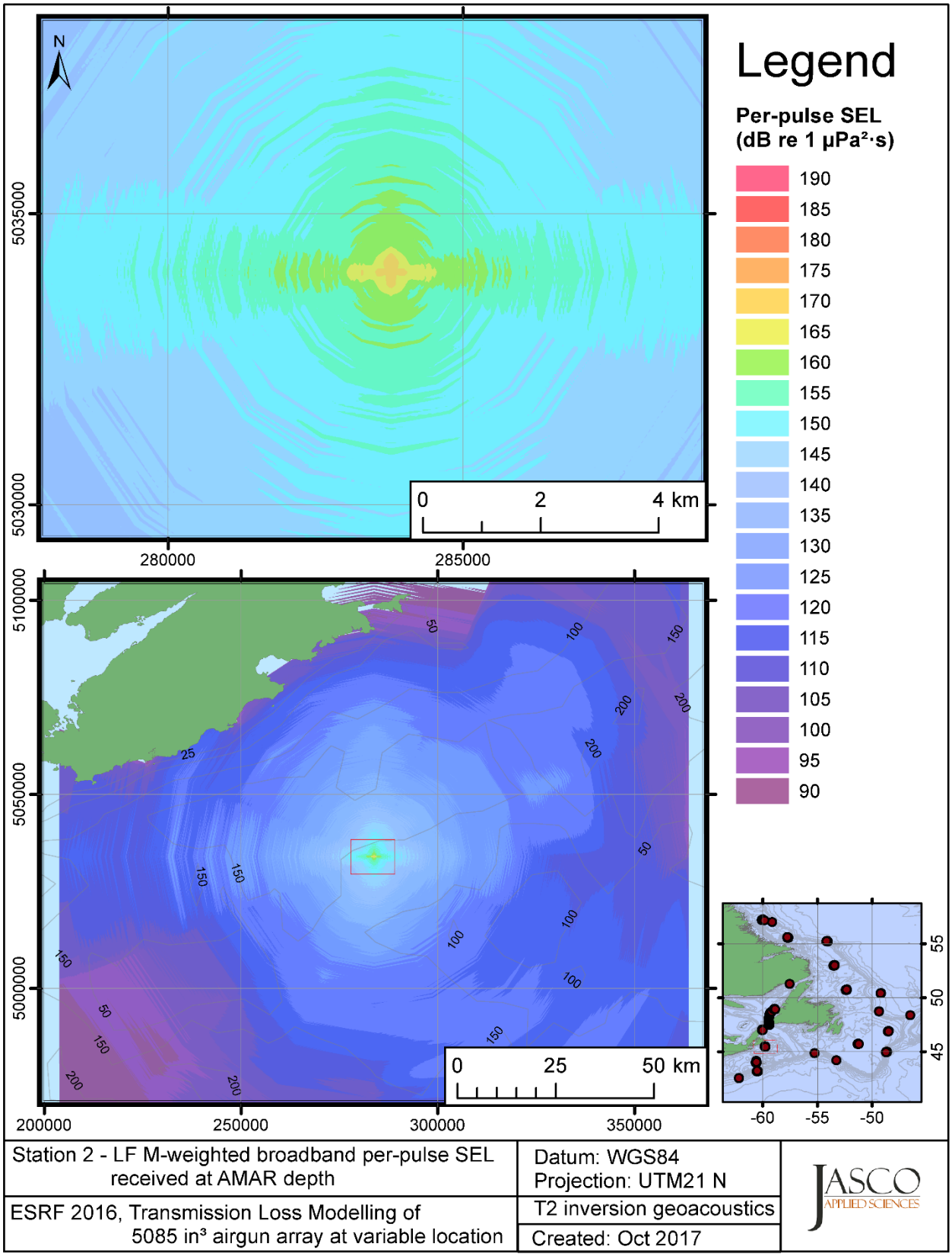

Figure C-49. Stn 2, LF M-weighted SEL received at the AMAR location and depth, modelled using the track 2 inversion geoacoustic bottom, with in-situ July SSP and the airgun array located at any point on the map.

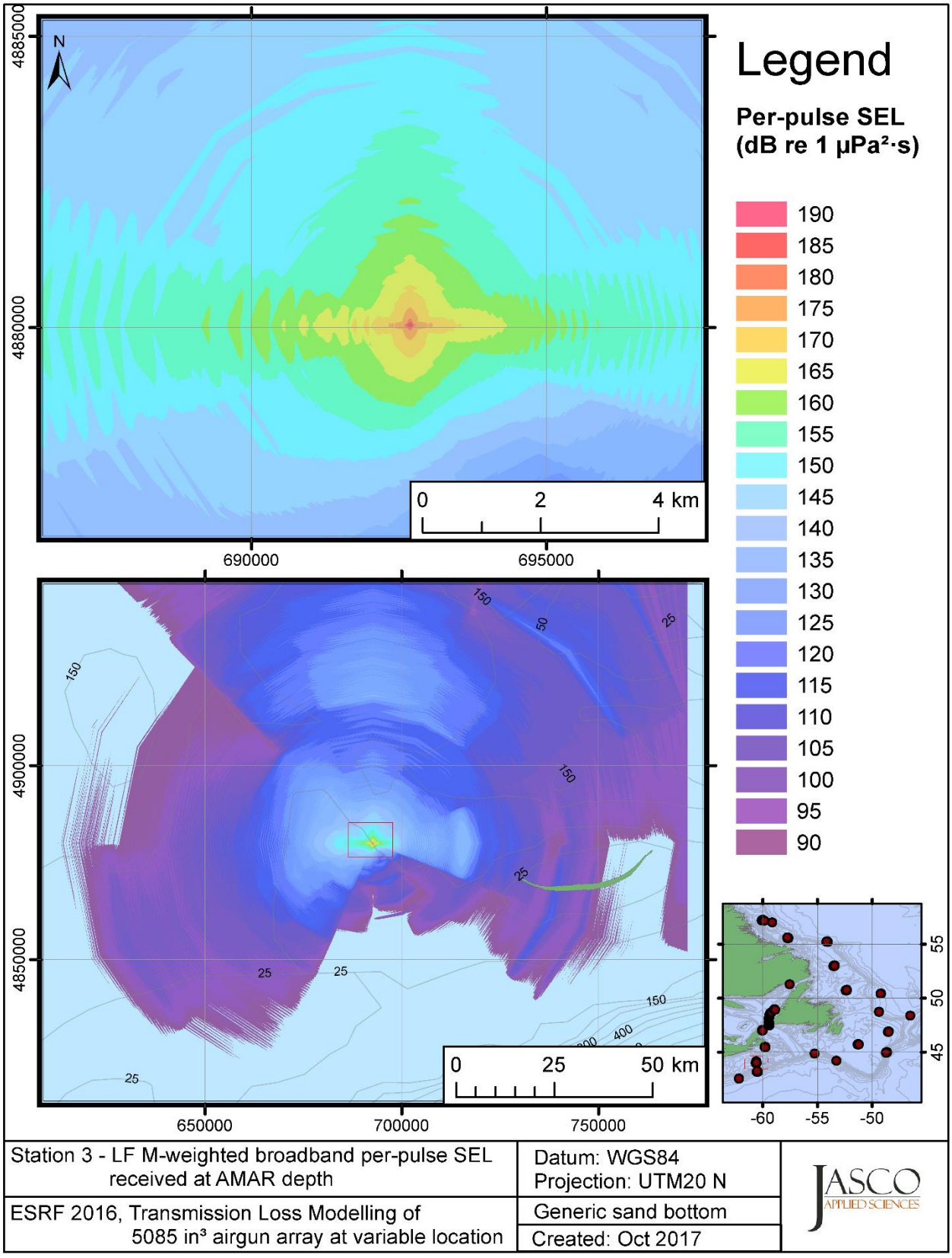

Figure C-50. Stn 3, LF M-weighted SEL received at the AMAR location and depth, modelled using a generic sand bottom, with in-situ July SSP and the airgun array located at any point on the map.

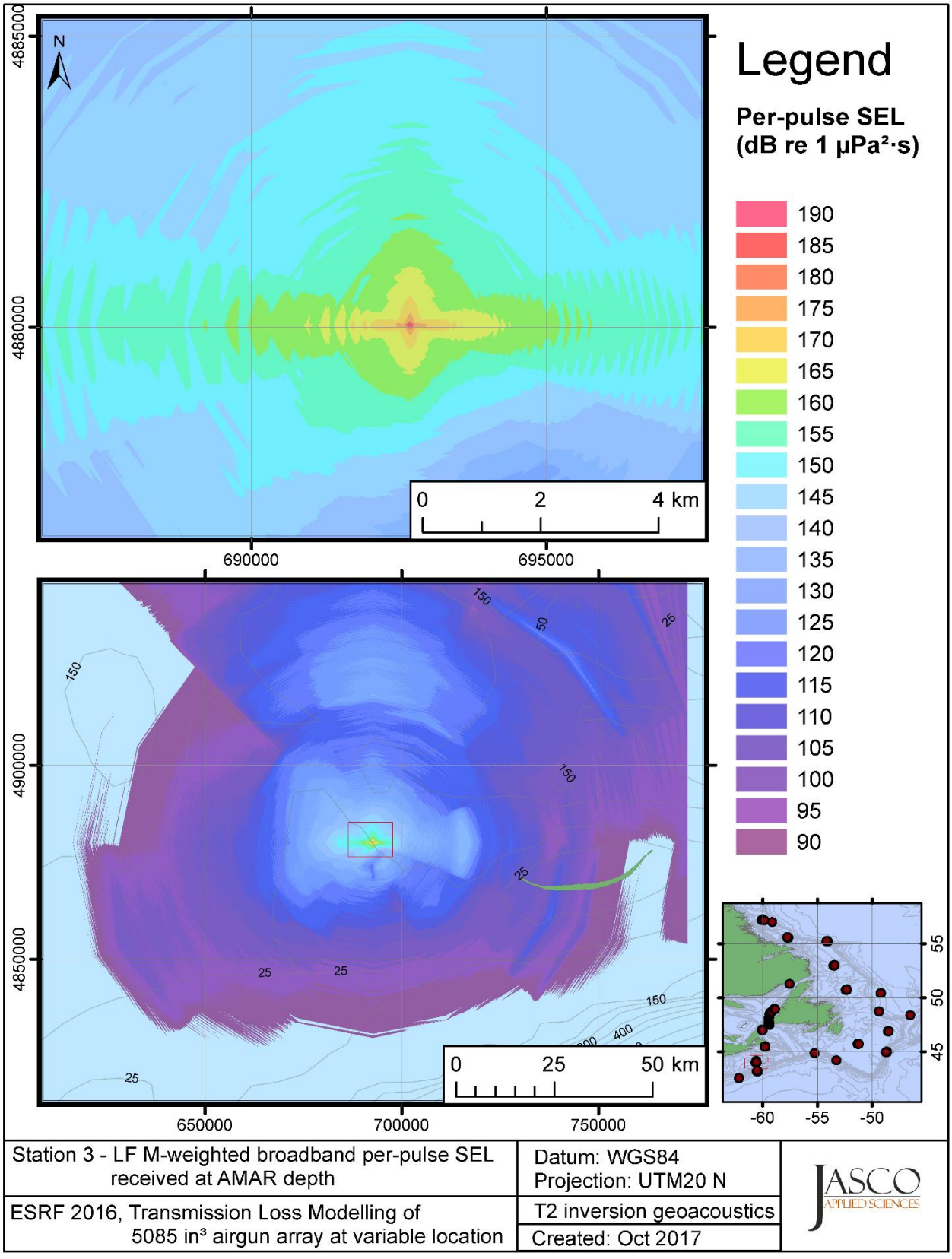

Figure C-51. Stn 3, LF M-weighted SEL received at the AMAR location and depth, modelled using the track 2 inversion geoacoustic bottom, with in-situ July SSP and the airgun array located at any point on the map.

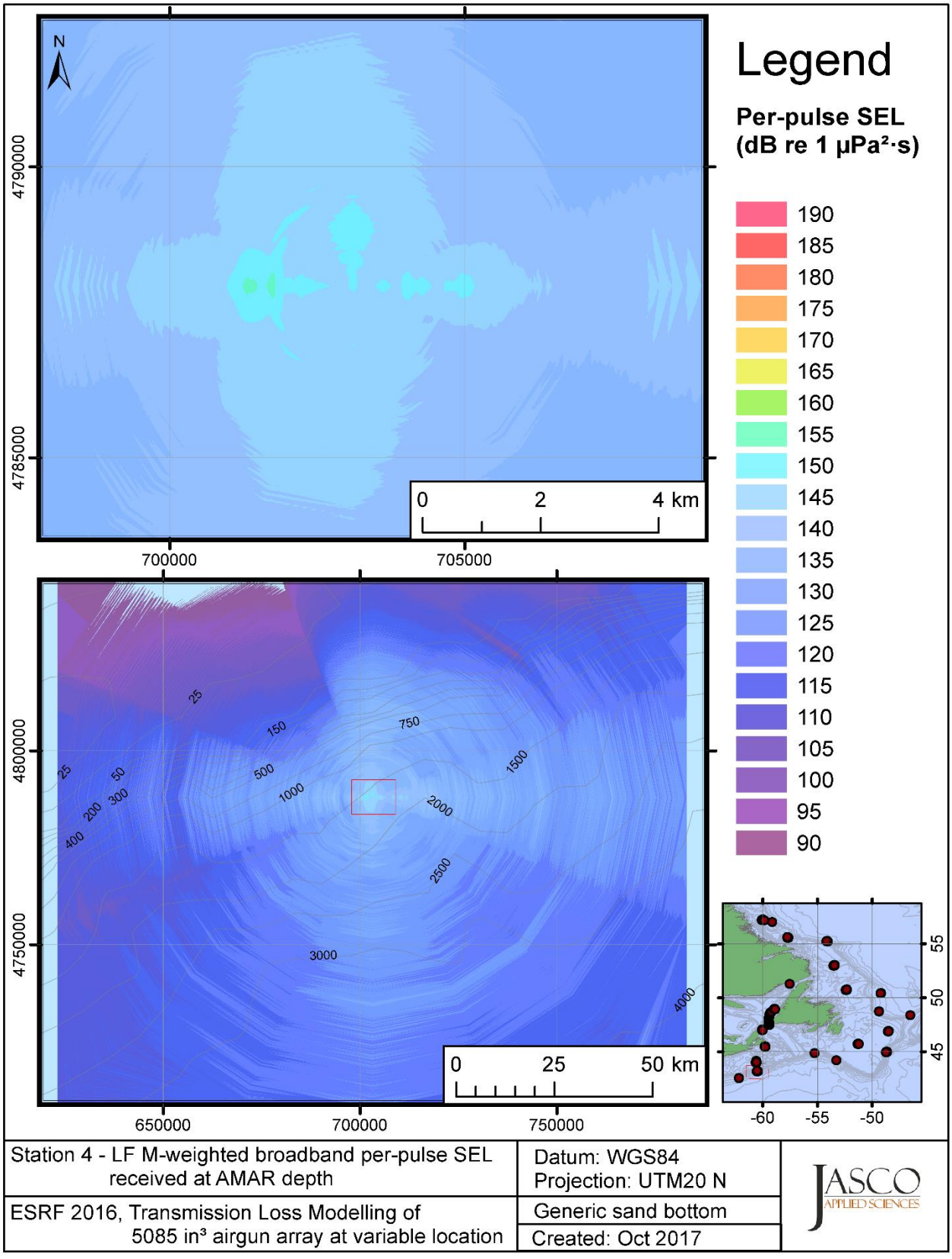

Figure C-52. Stn 4, LF M-weighted SEL received at the AMAR location and depth, modelled using a generic sand bottom, with in-situ July SSP and the airgun array located at any point on the map.

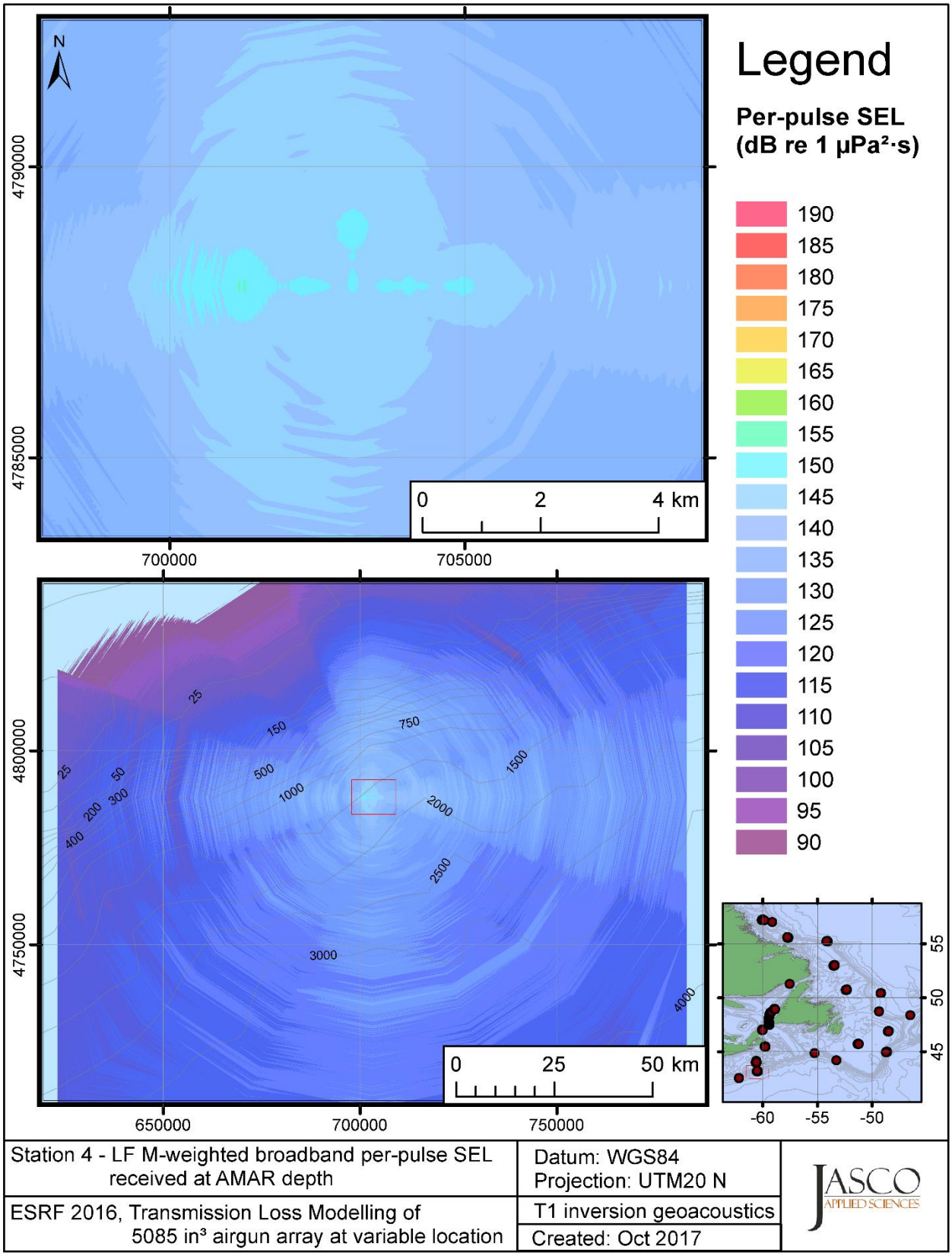

Figure C-53. Stn 4, LF M-weighted SEL received at the AMAR location and depth, modelled using the track 1 inversion geoacoustic bottom, with in-situ July SSP and the airgun array located at any point on the map.

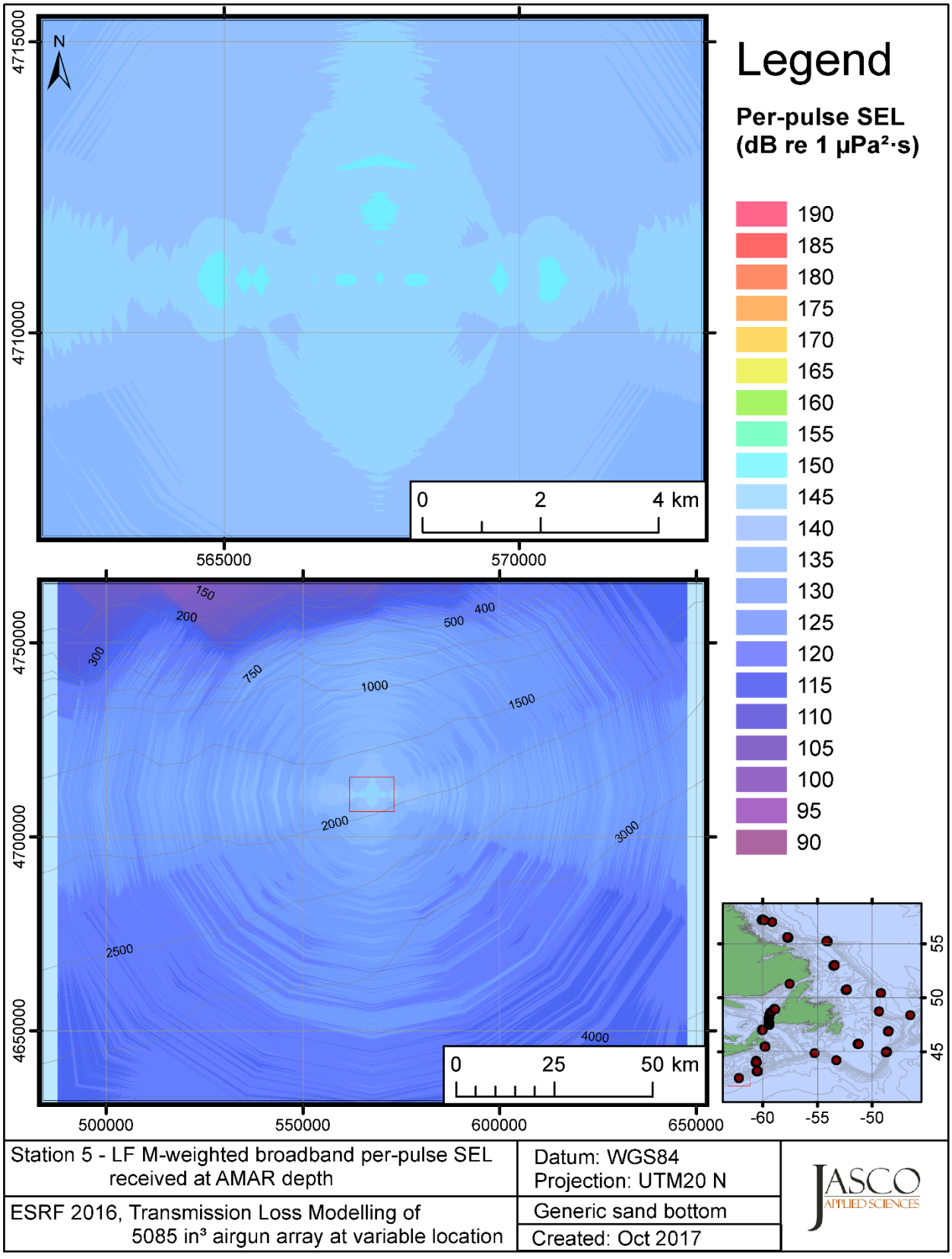

Figure C-54. Stn 5, LF M-weighted SEL received at the AMAR location and depth, modelled using a generic sand bottom, with in-situ July SSP and the airgun array located at any point on the map.

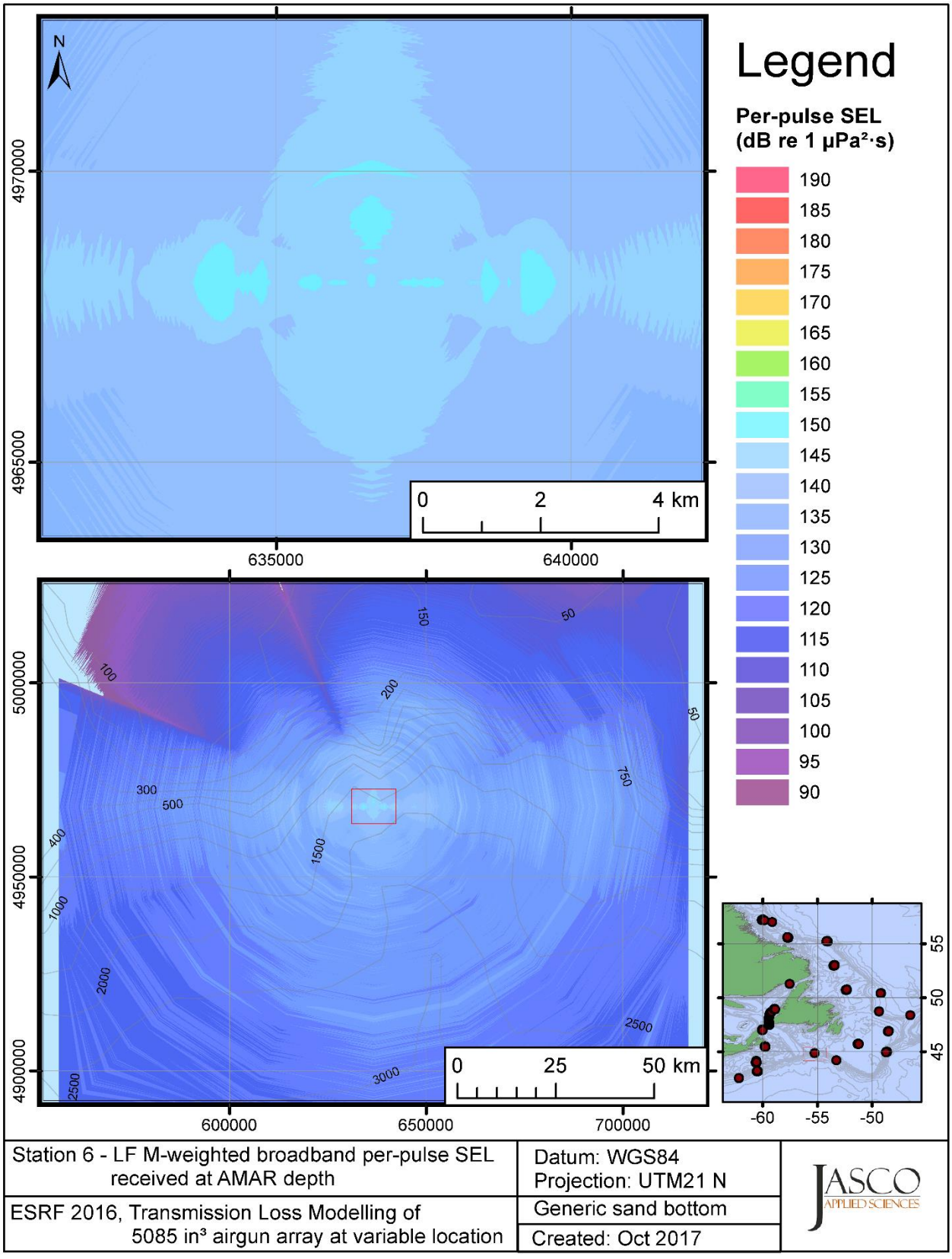

Figure C-55. Stn 6, LF M-weighted SEL received at the AMAR location and depth, modelled using a generic sand bottom, with in-situ July SSP and the airgun array located at any point on the map.

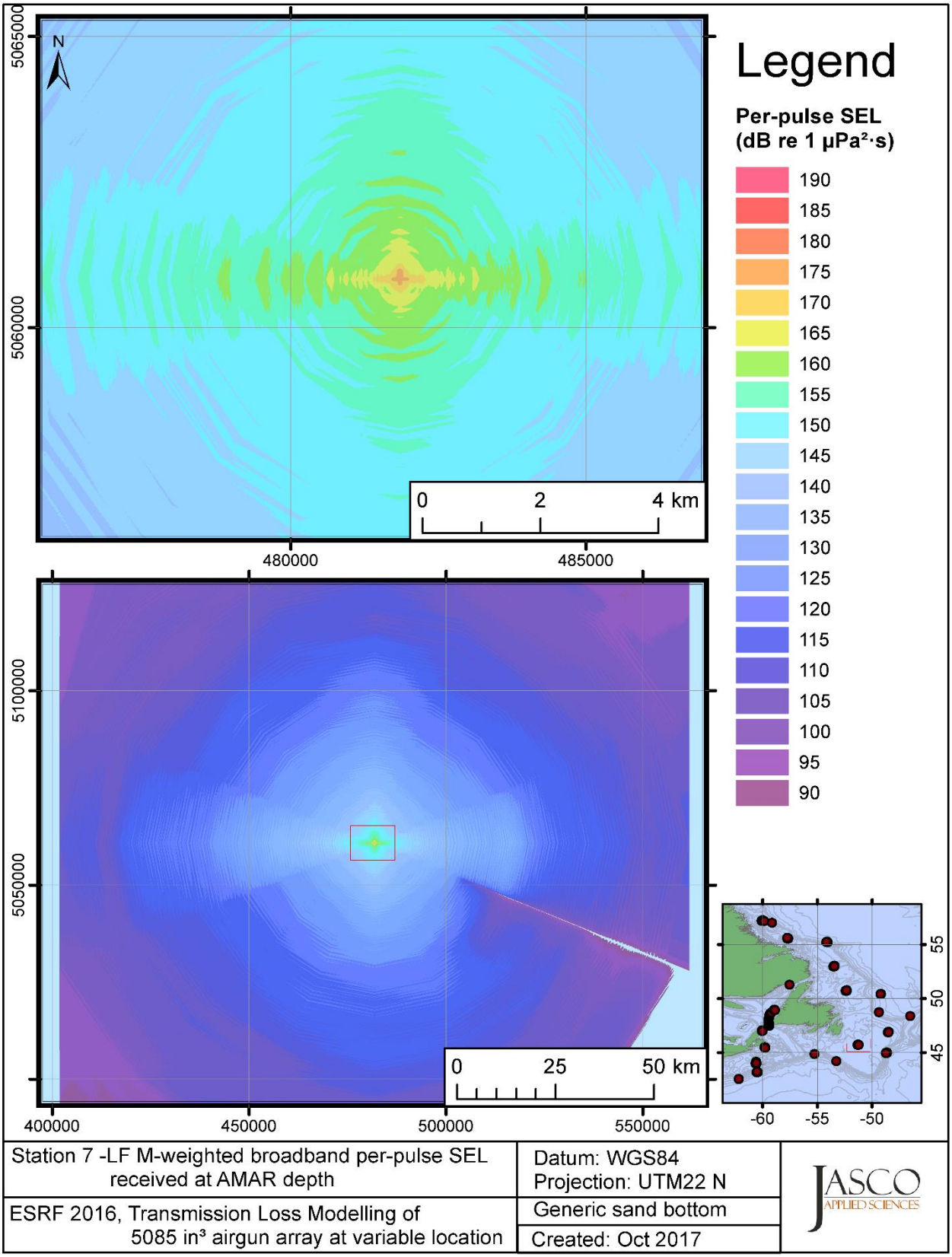

Figure C-56. Stn 7, LF M-weighted SEL received at the AMAR location and depth, modelled using a generic sand bottom, with in-situ July SSP and the airgun array located at any point on the map.

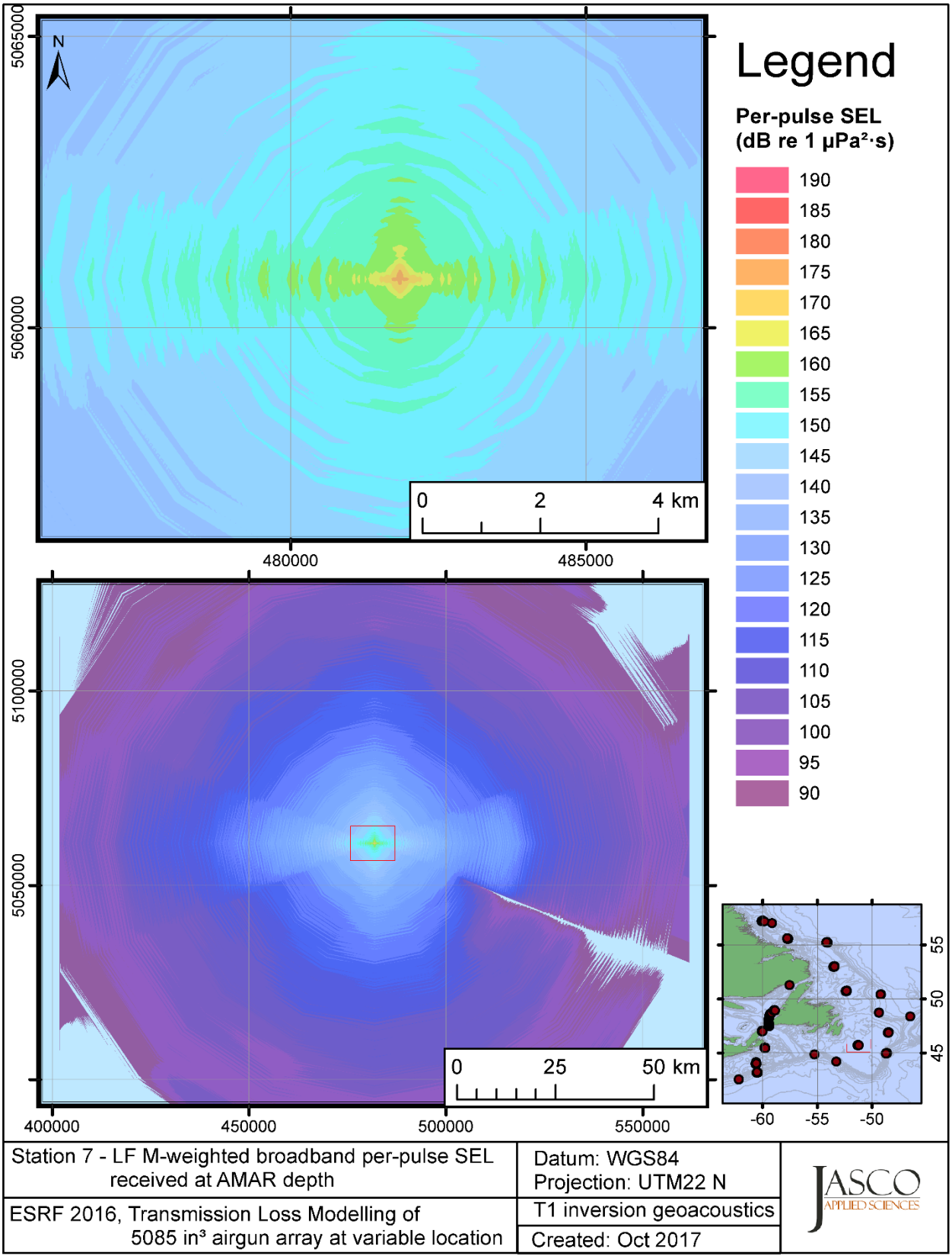

Figure C-57. Stn 7, LF M-weighted SEL received at the AMAR location and depth, modelled using the track 1 inversion geoacoustic bottom, with in-situ July SSP and the airgun array located at any point on the map.

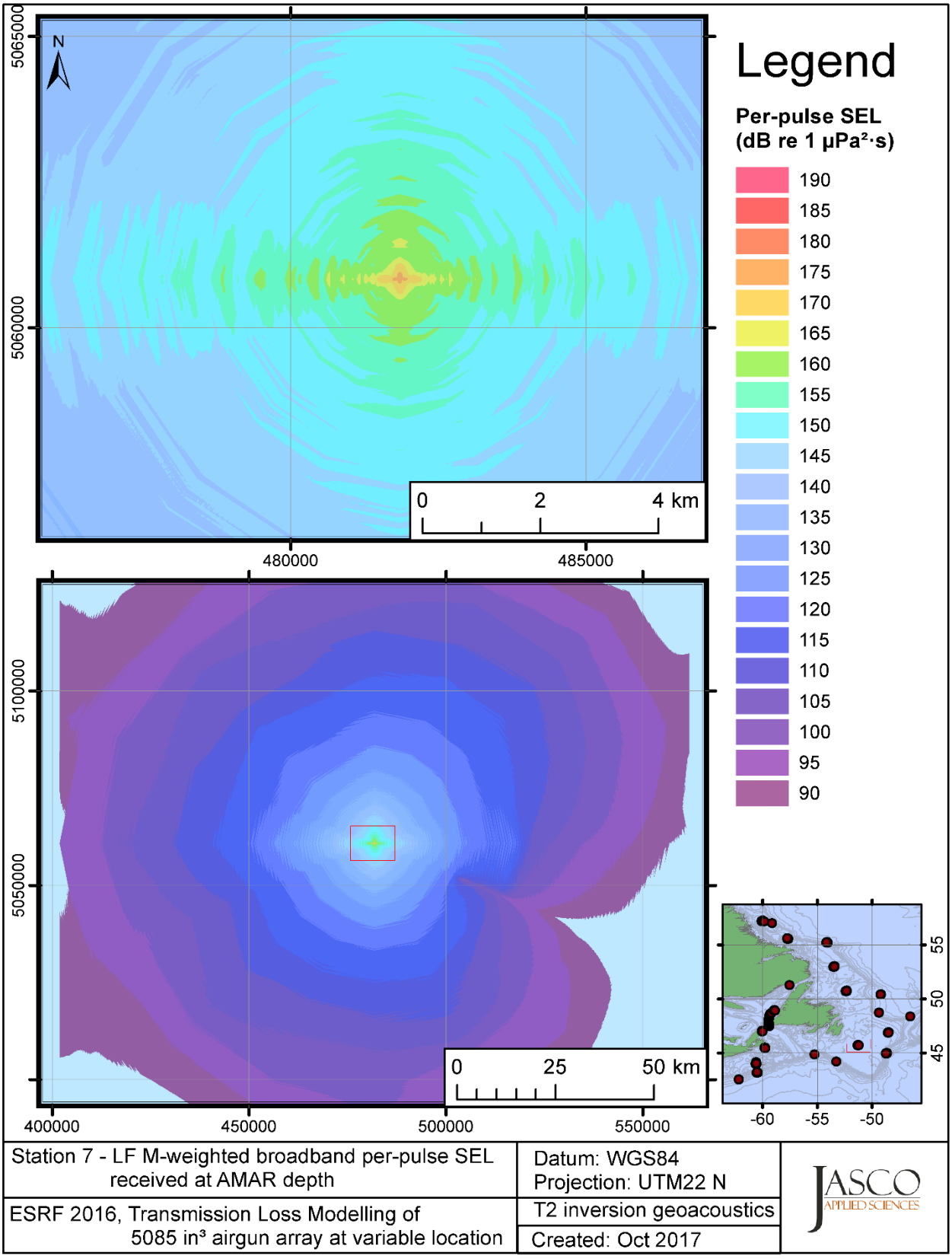

Figure C-58. Stn 7, LF M-weighted SEL received at the AMAR location and depth, modelled using the track 2 inversion geoacoustic bottom, with in-situ July SSP and the airgun array located at any point on the map.

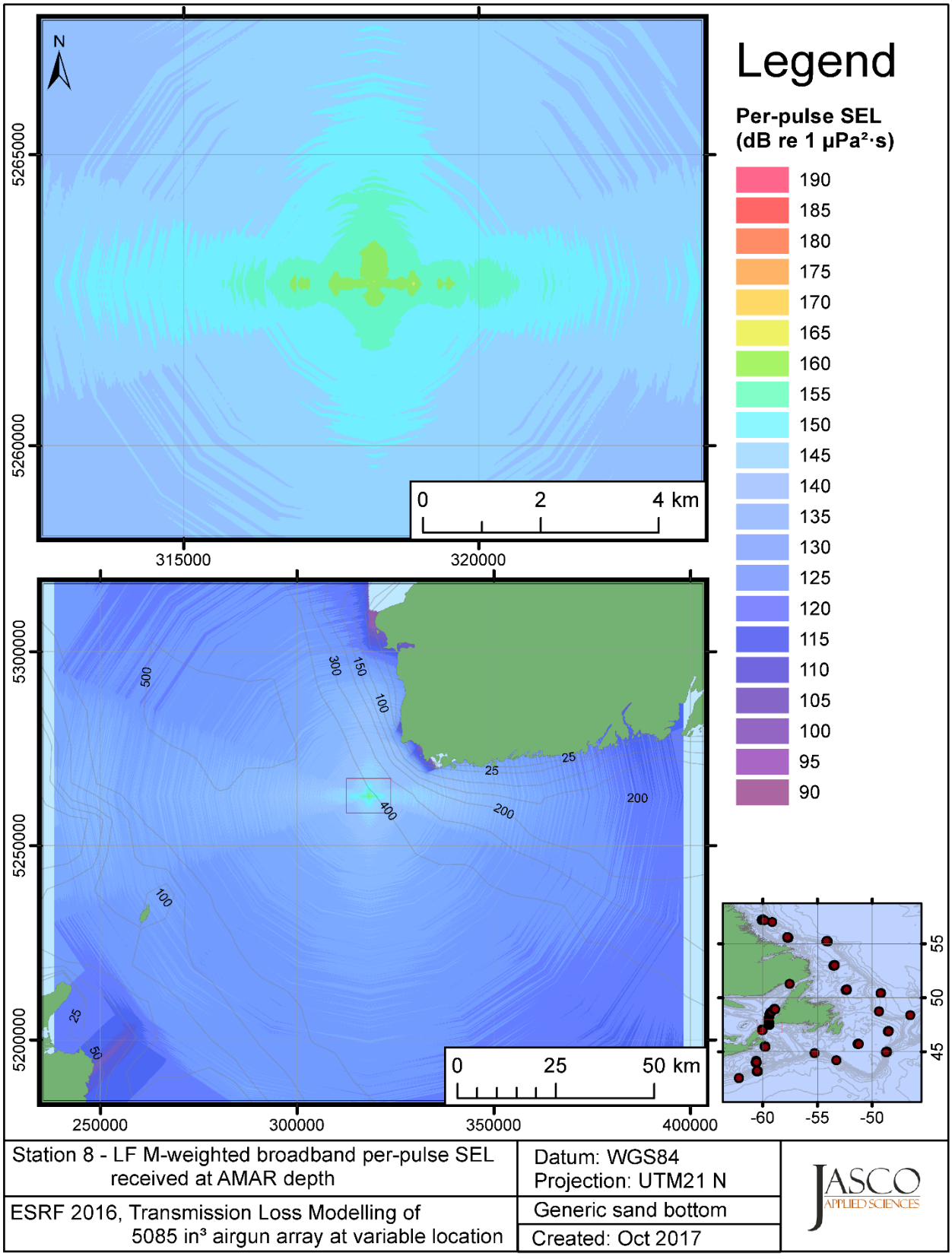

Figure C-59. Stn 8, LF M-weighted SEL received at the AMAR location and depth, modelled using a generic sand bottom, with GDEM July SSP and the airgun array located at any point on the map.

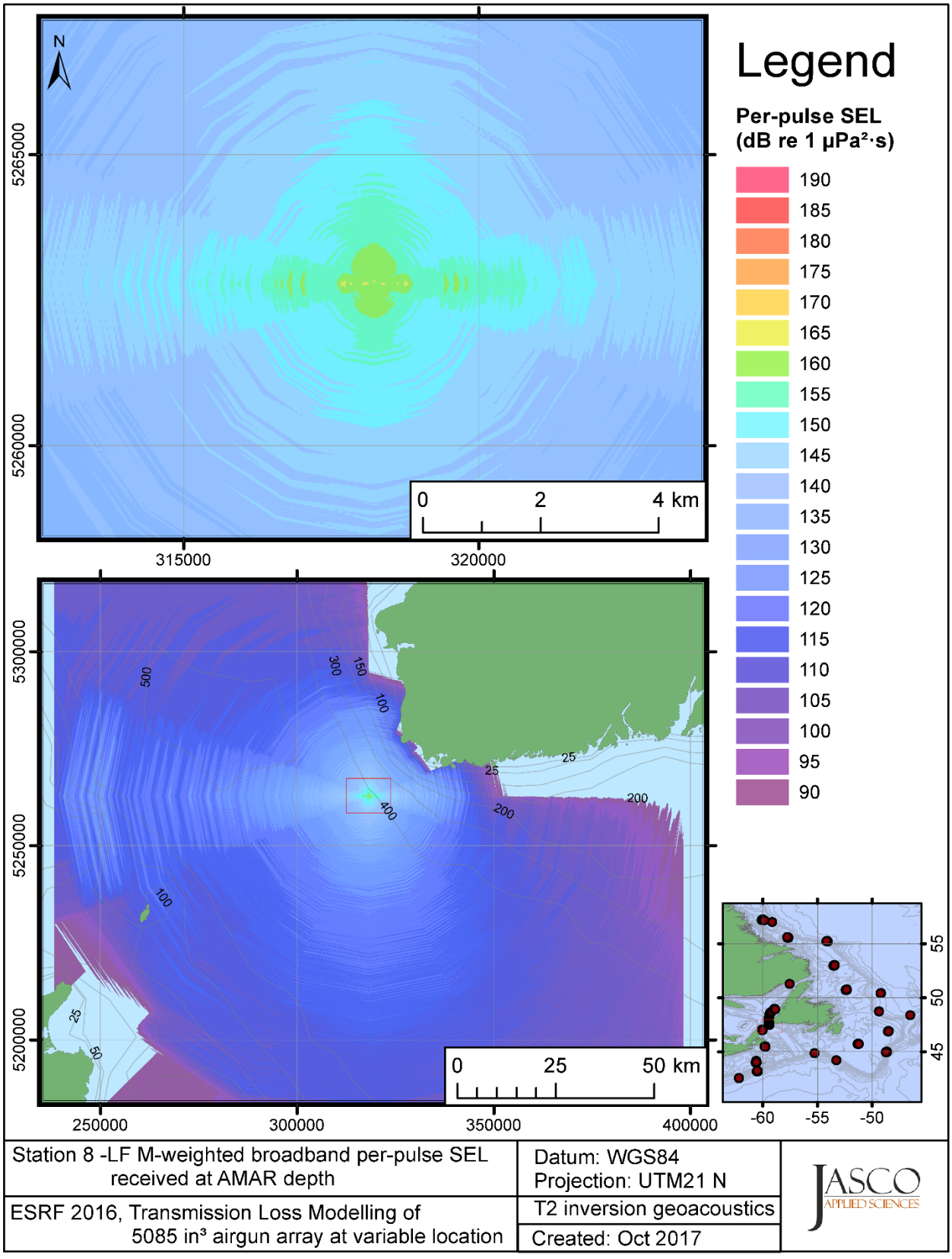

Figure C-60. Stn 8, LF M-weighted SEL received at the AMAR location and depth, modelled using the track 2 inversion geoacoustic bottom, with GDEM July SSP and the airgun array located at any point on the map.

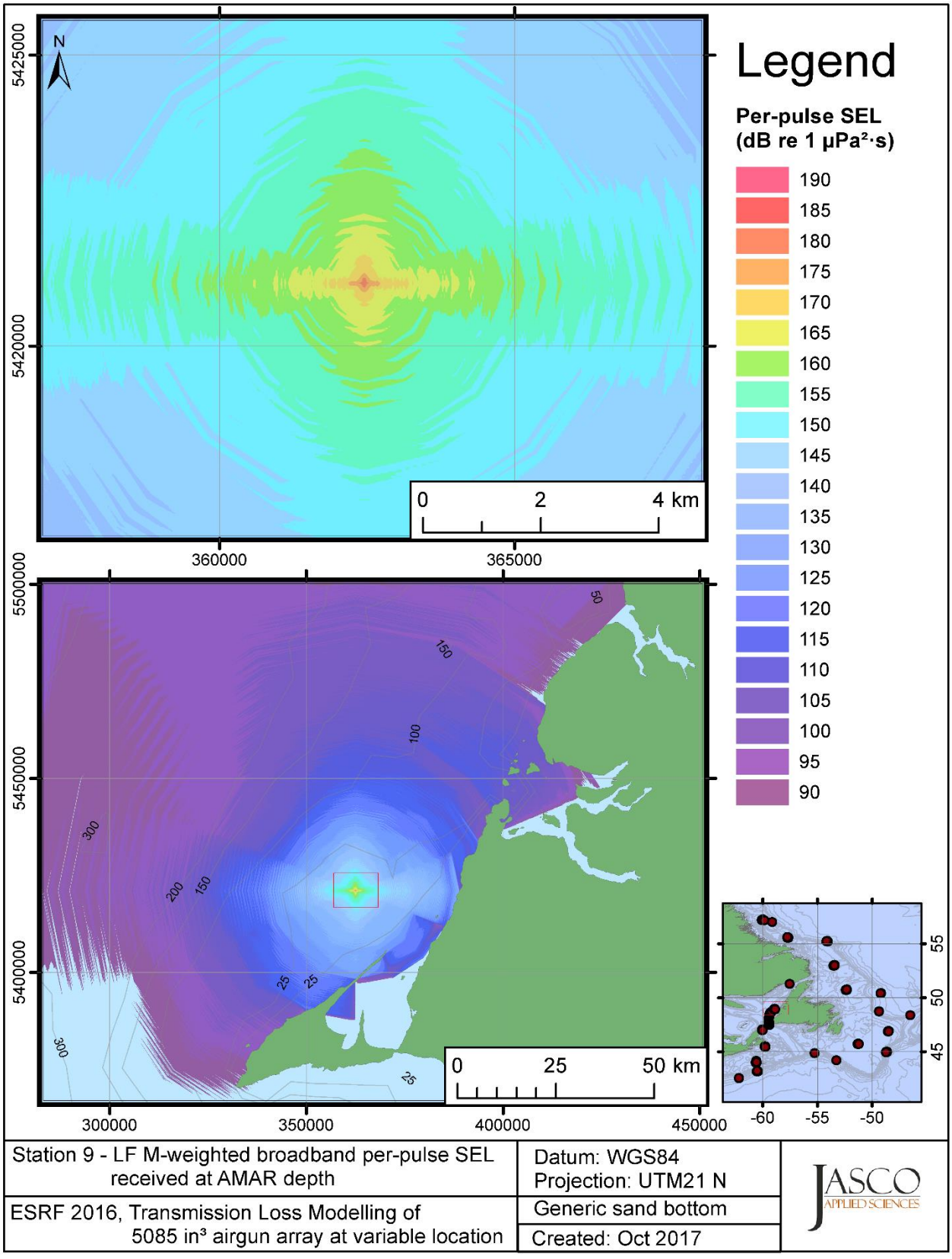

Figure C-61. Stn 9, LF M-weighted SEL received at the AMAR location and depth, modelled using a generic sand bottom, with GDEM July SSP and the airgun array located at any point on the map.

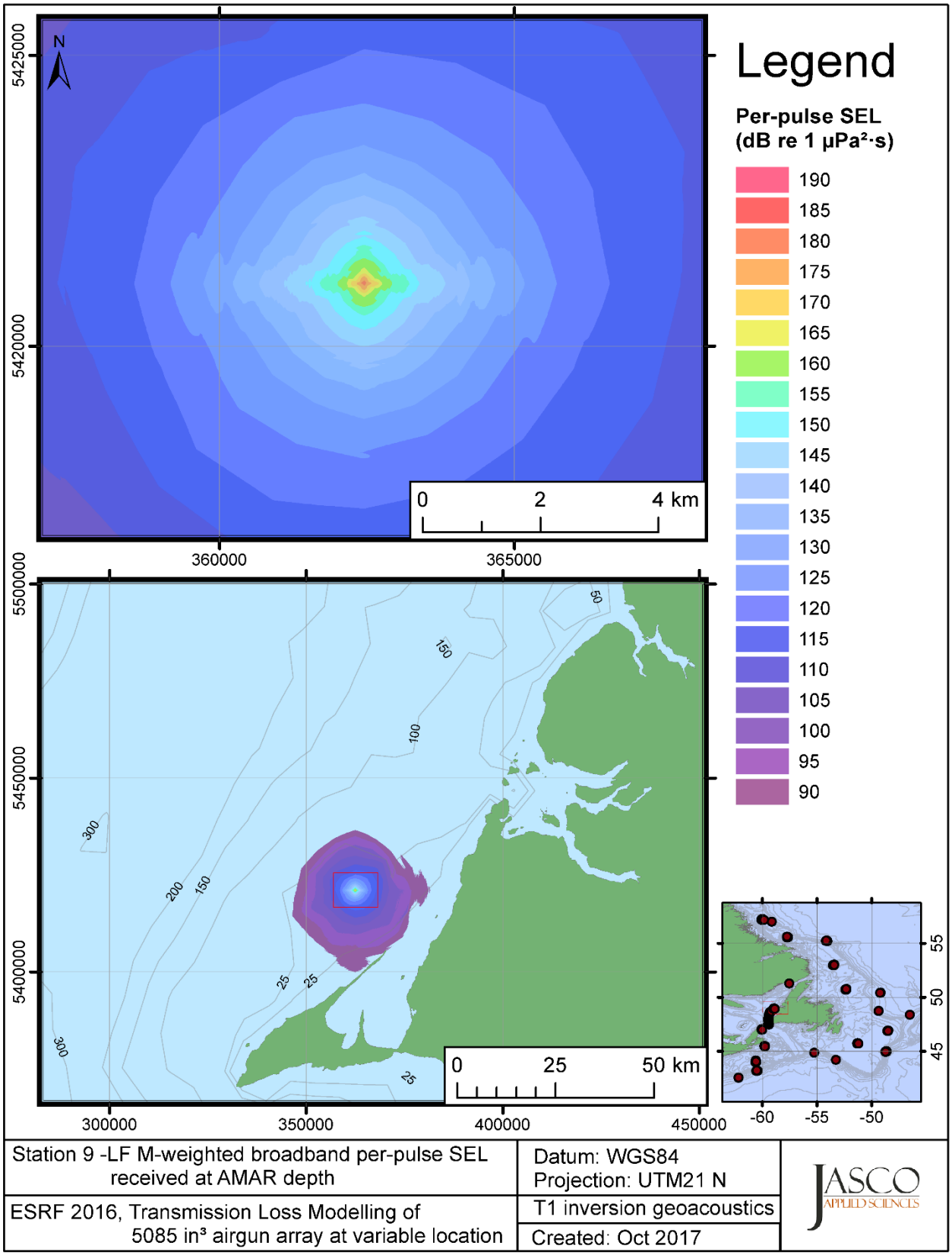

Figure C-62. Stn 9, LF M-weighted SEL received at the AMAR location and depth, modelled using the track 1 inversion geoacoustic bottom, with GDEM July SSP and the airgun array located at any point on the map.

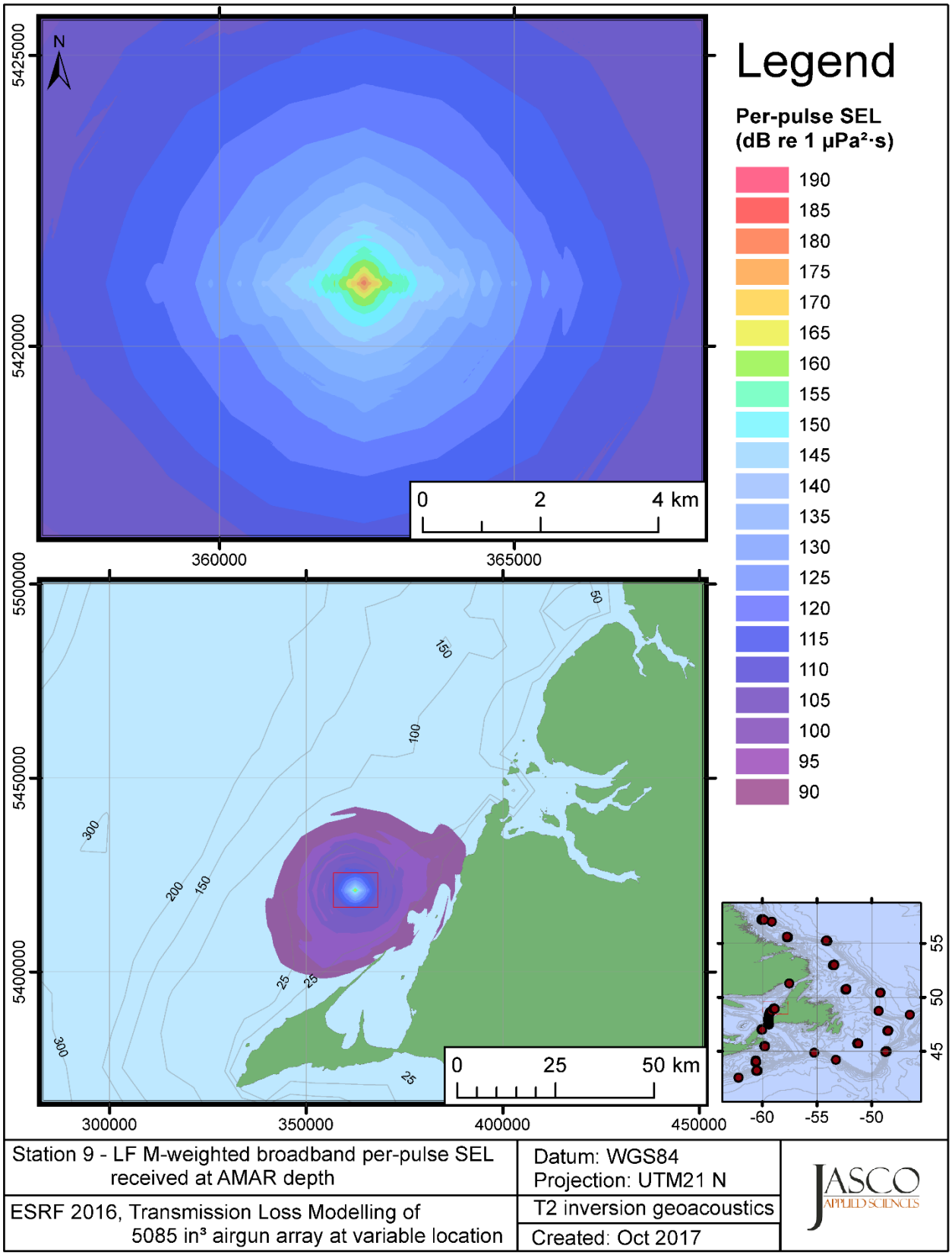

Figure C-63. Stn 9, LF M-weighted SEL received at the AMAR location and depth, modelled using the track 2 inversion geoacoustic bottom, with GDEM July SSP and the airgun array located at any point on the map.

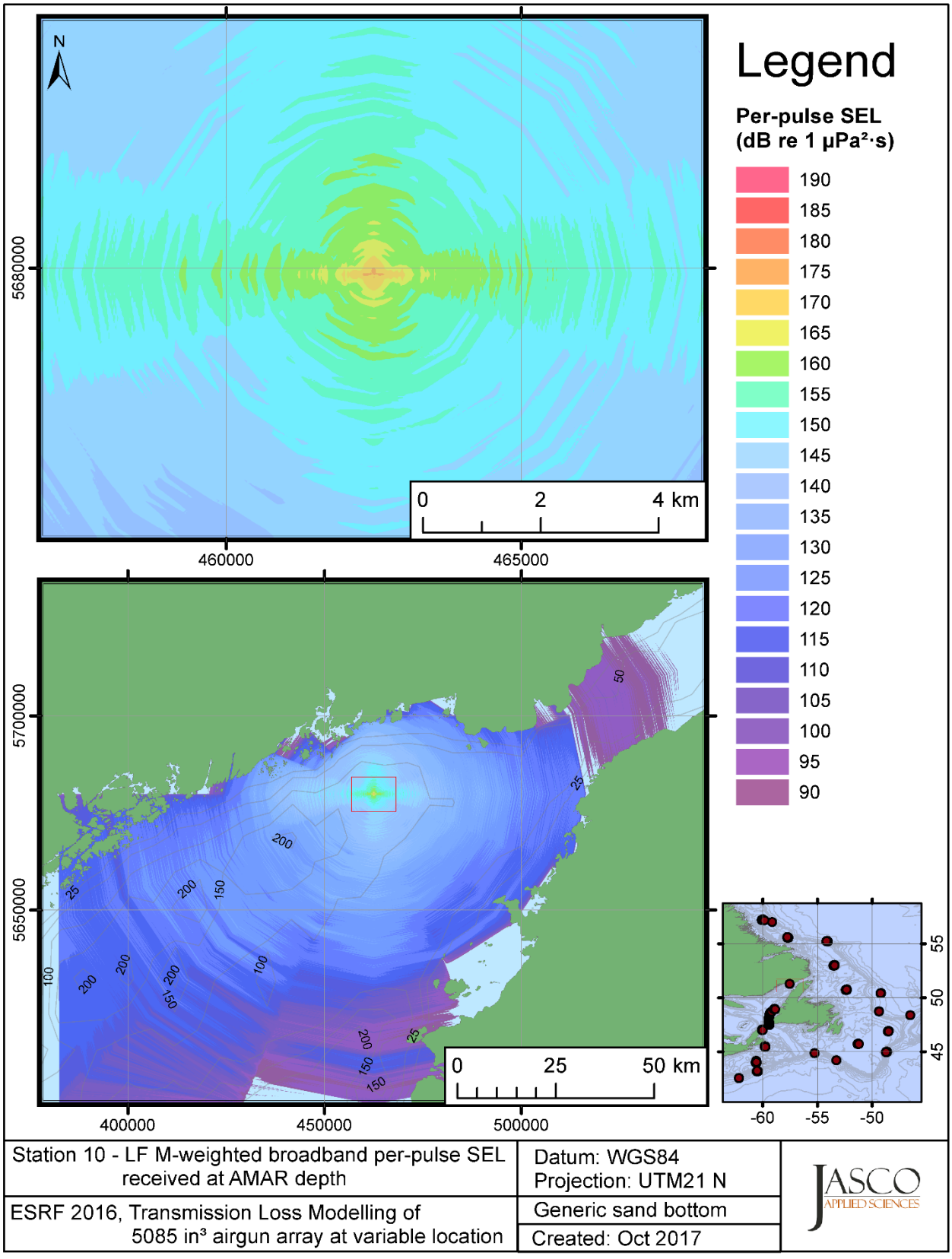

Figure C-64. Stn 10, LF M-weighted SEL received at the AMAR location and depth, modelled using a generic sand bottom, with in-situ July SSP and the airgun array located at any point on the map.

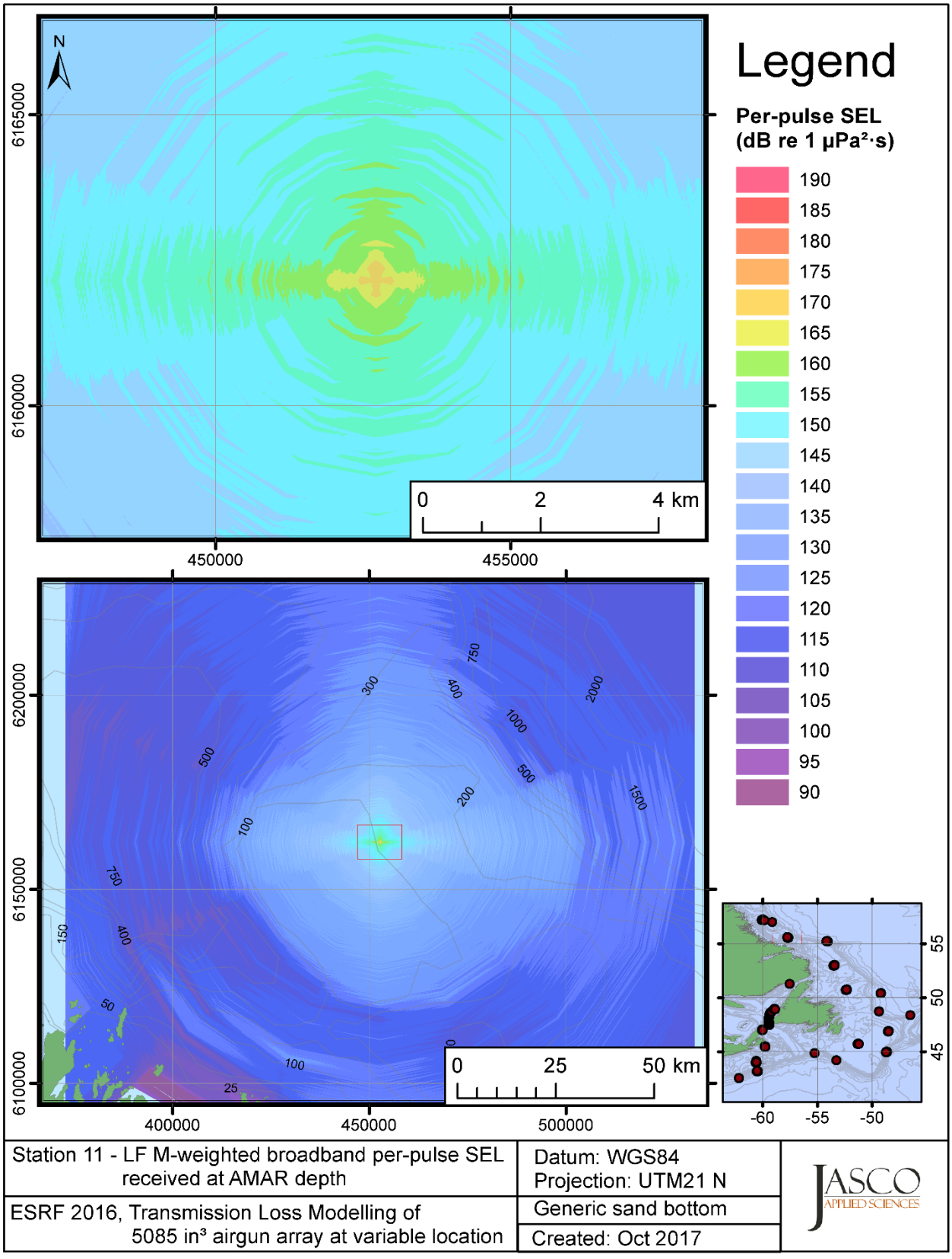

Figure C-65. Stn 11, LF M-weighted SEL received at the AMAR location and depth, modelled using a generic sand bottom, with in-situ July SSP and the airgun array located at any point on the map.

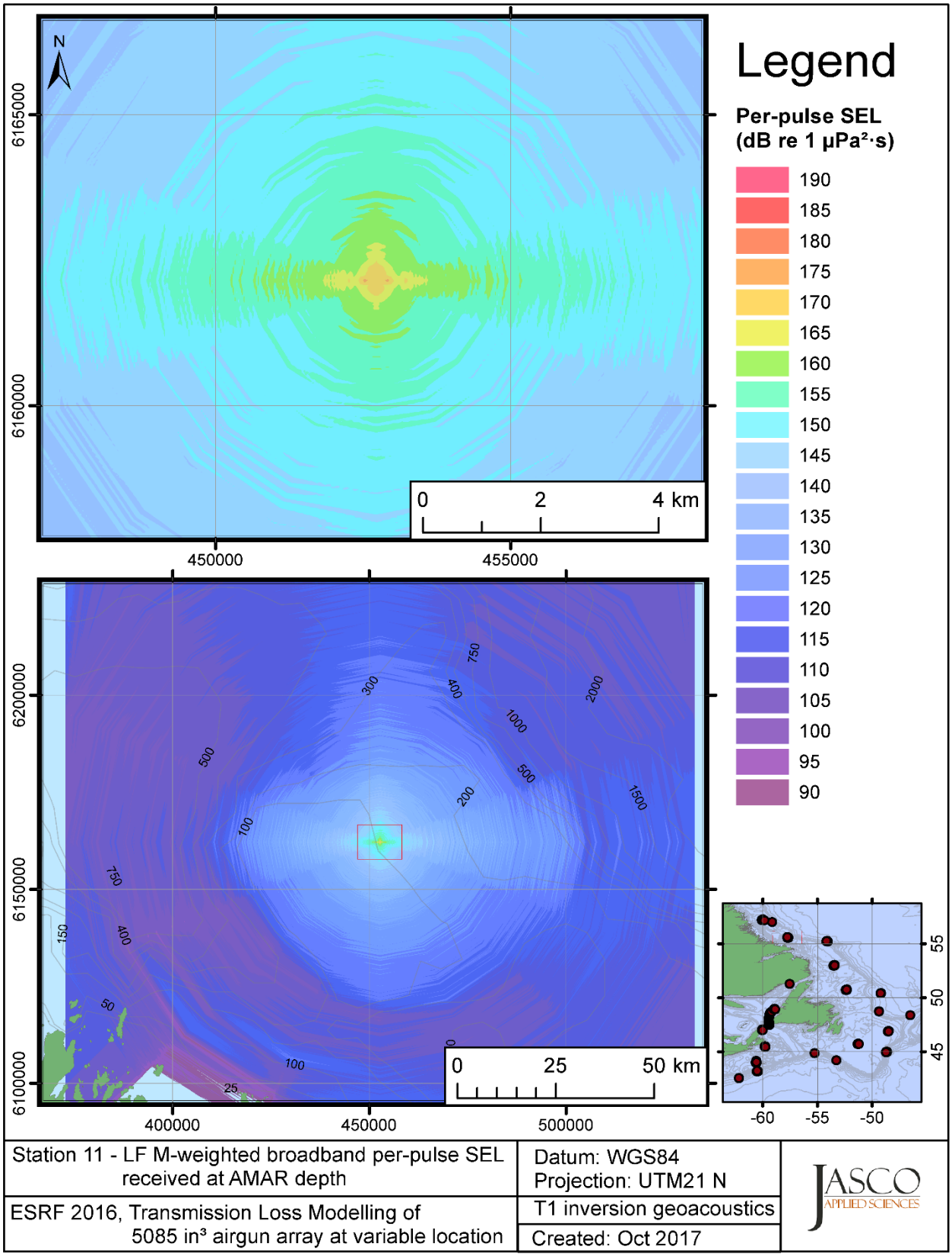

Figure C-66. Stn 11, LF M-weighted SEL received at the AMAR location and depth, modelled using the track 1 inversion geoacoustic bottom, with in-situ July SSP and the airgun array located at any point on the map.

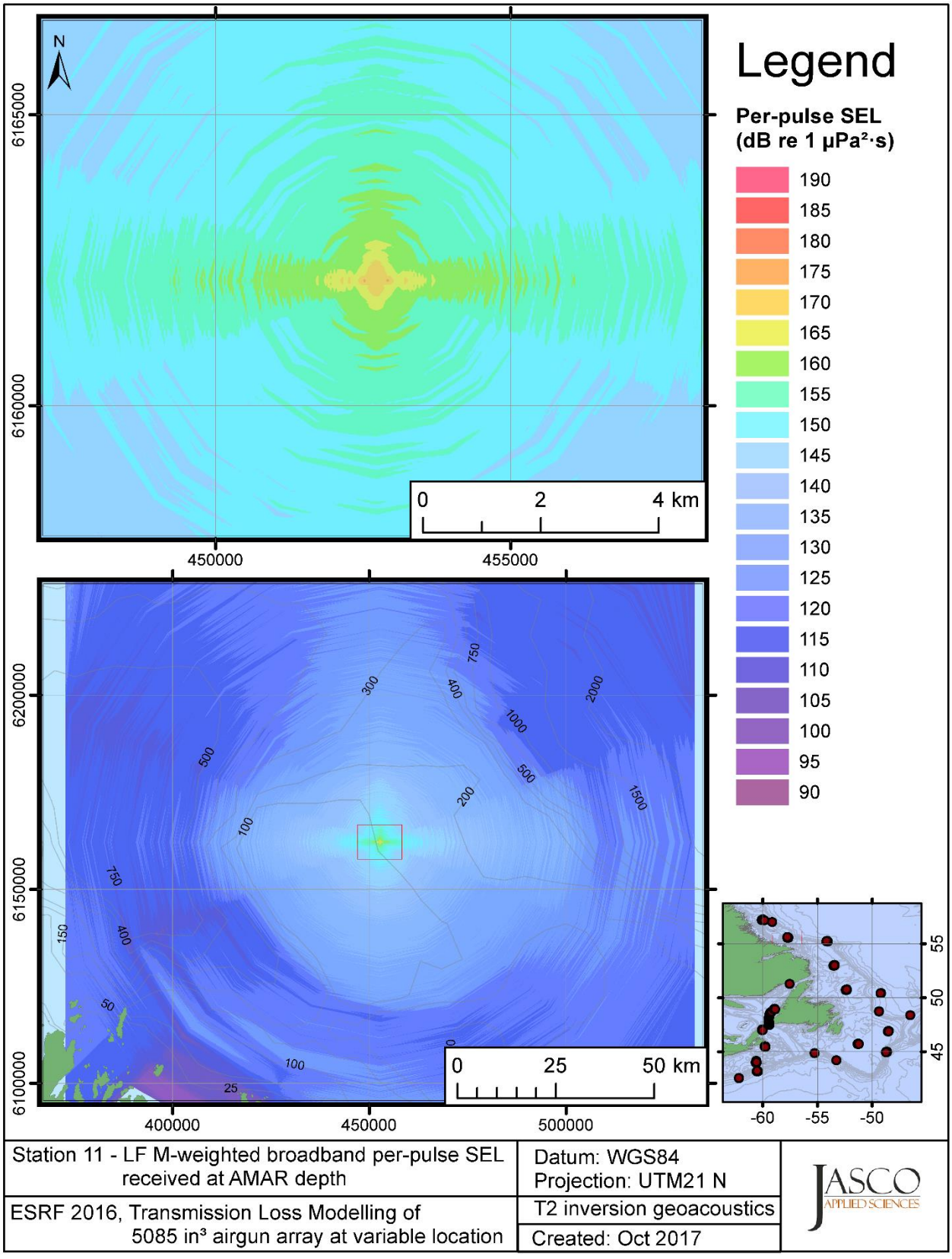

Figure C-67. Stn 11, LF M-weighted SEL received at the AMAR location and depth, modelled using the track 2 inversion geoacoustic bottom, with in-situ July SSP and the airgun array located at any point on the map.

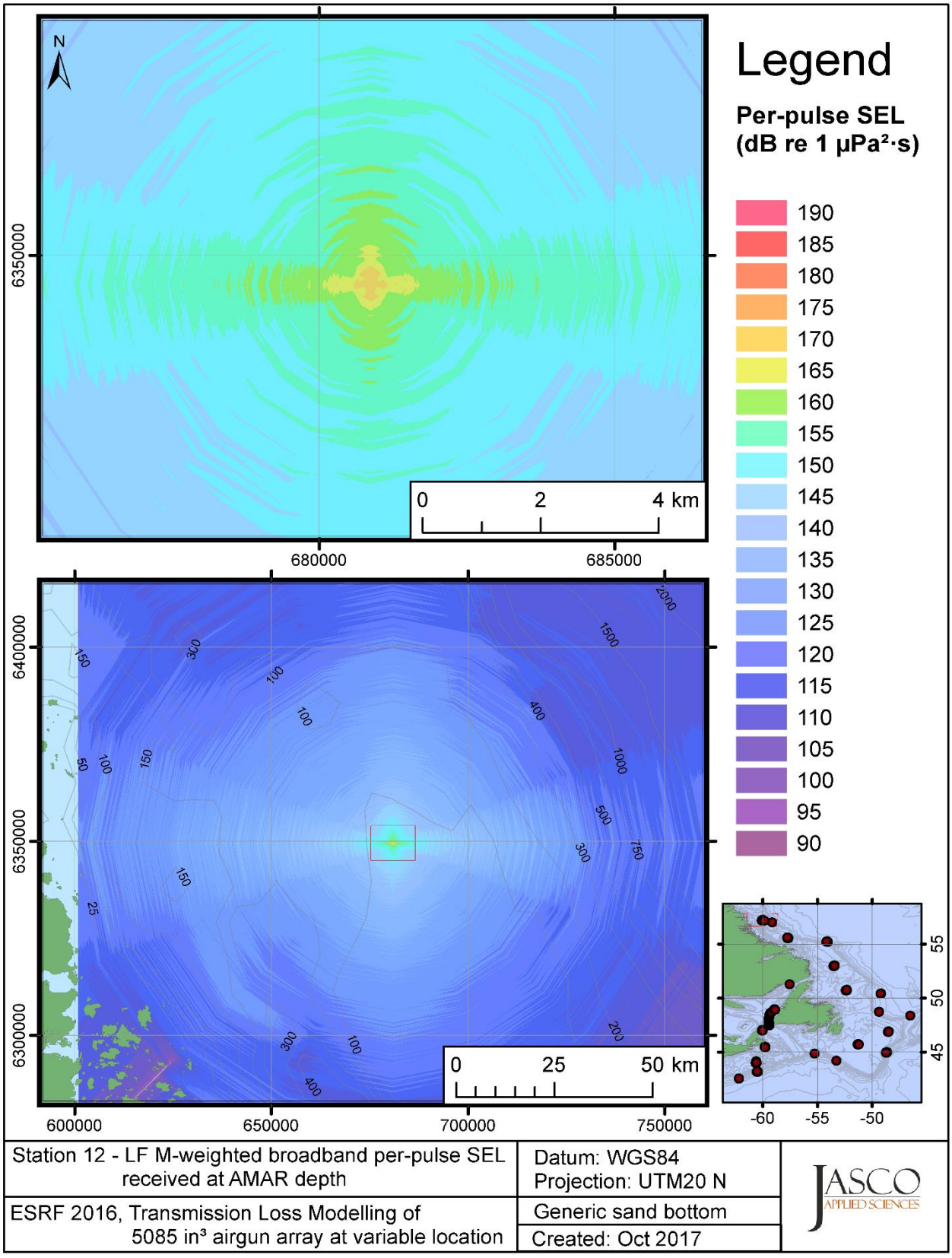

Figure C-68. Stn 12, LF M-weighted SEL received at the AMAR location and depth, modelled using a generic sand bottom, with in-situ July SSP and the airgun array located at any point on the map.

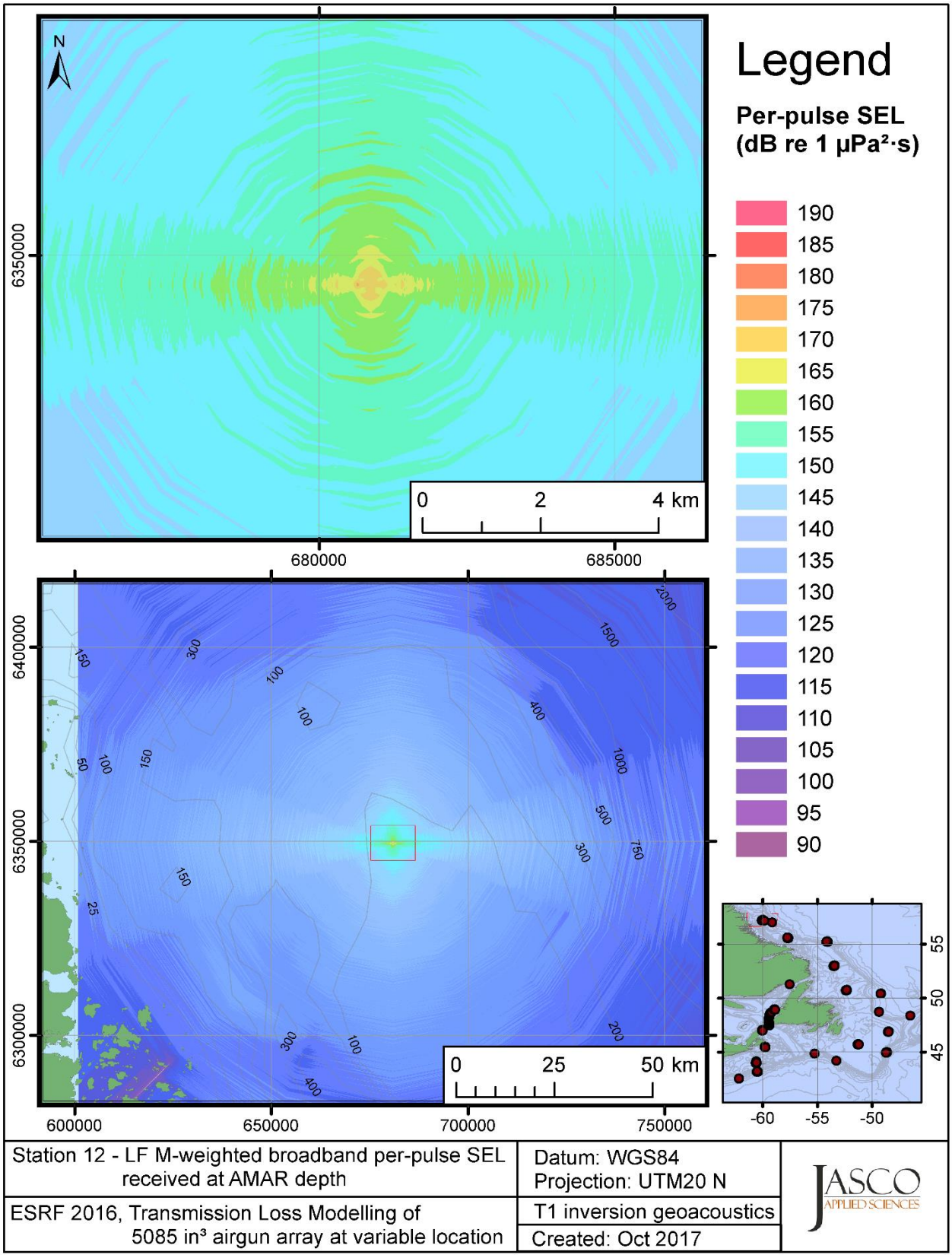

Figure C-69. Stn 12, LF M-weighted SEL received at the AMAR location and depth, modelled using the track 1 inversion geoacoustic bottom, with in-situ July SSP and the airgun array located at any point on the map.

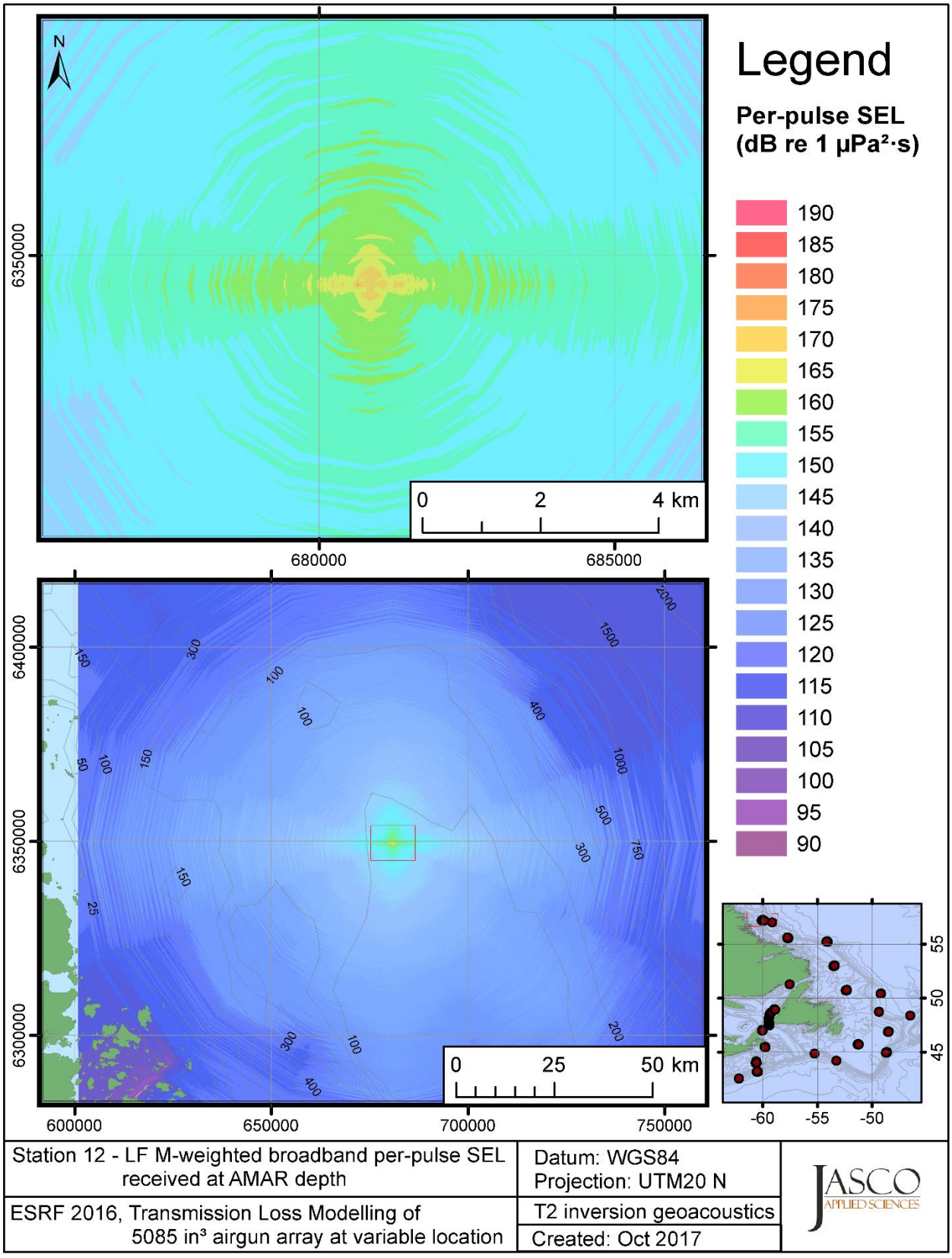

Figure C-70. Stn 12, LF M-weighted SEL received at the AMAR location and depth, modelled using the track 2 inversion geoacoustic bottom, with in-situ July SSP and the airgun array located at any point on the map.

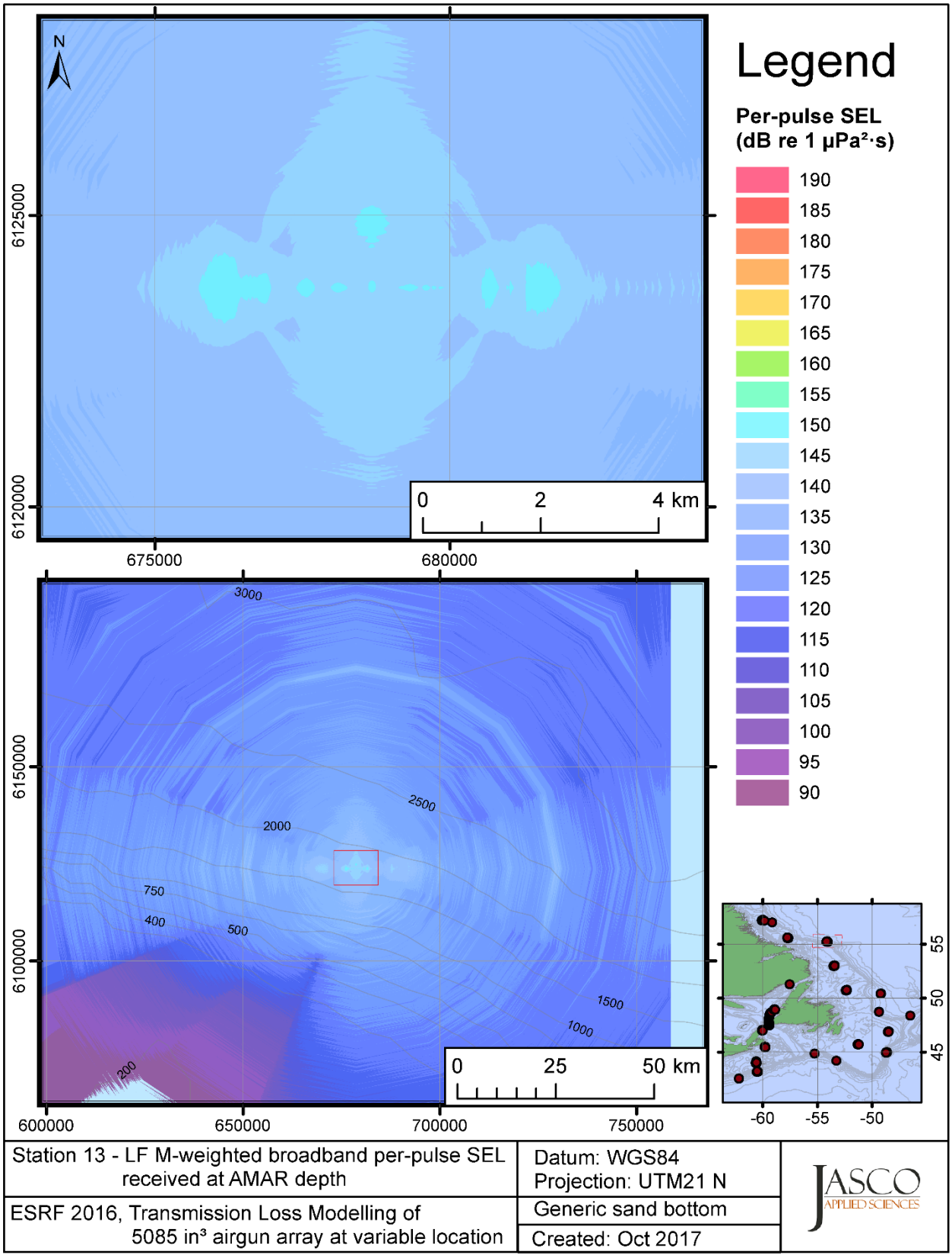

Figure C-71. Stn 13, LF M-weighted SEL received at the AMAR location and depth, modelled using a generic sand bottom, with in-situ July SSP and the airgun array located at any point on the map.

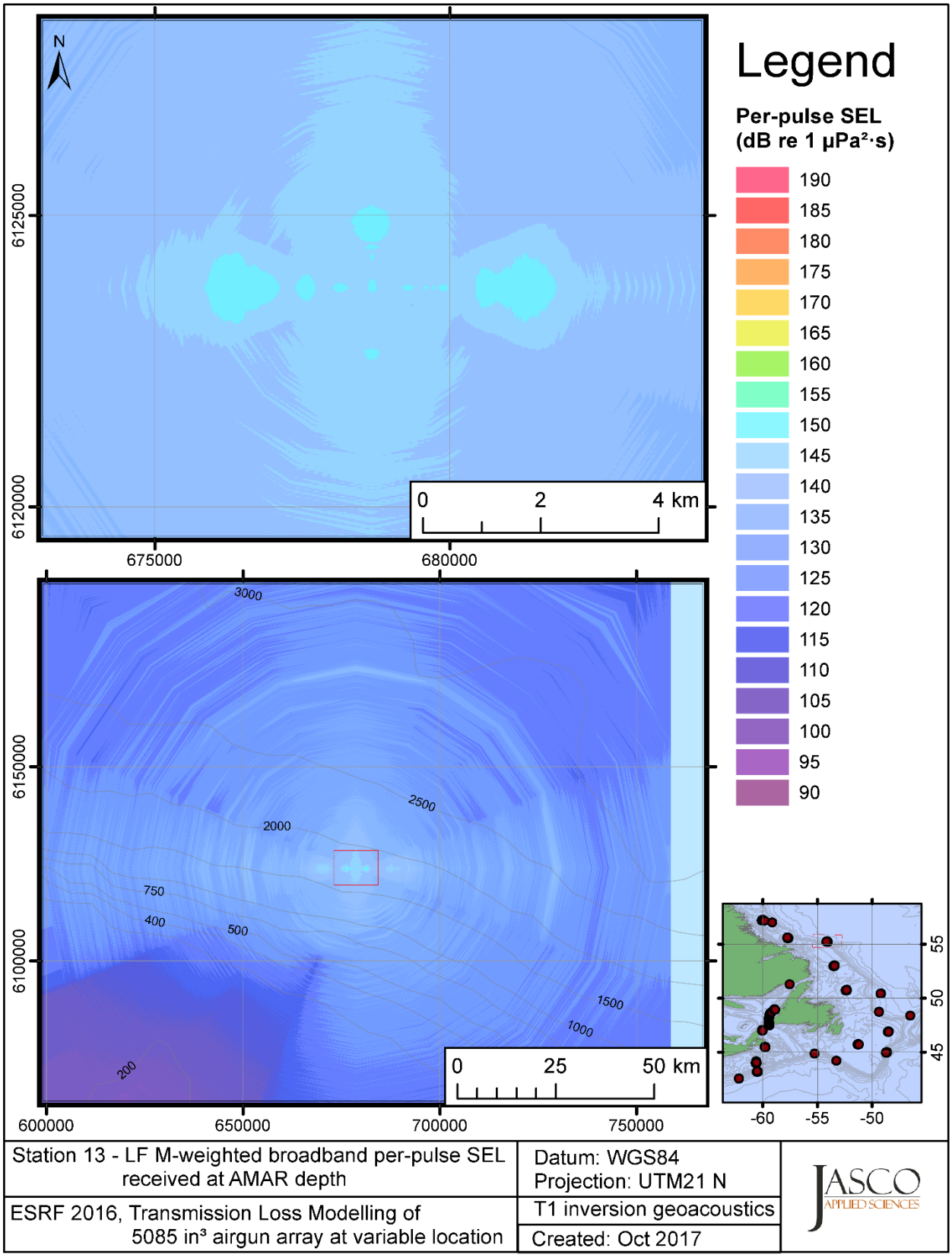

Figure C-72. Stn 13, LF M-weighted SEL received at the AMAR location and depth, modelled using the track 1 inversion geoacoustic bottom, with in-situ July SSP and the airgun array located at any point on the map.

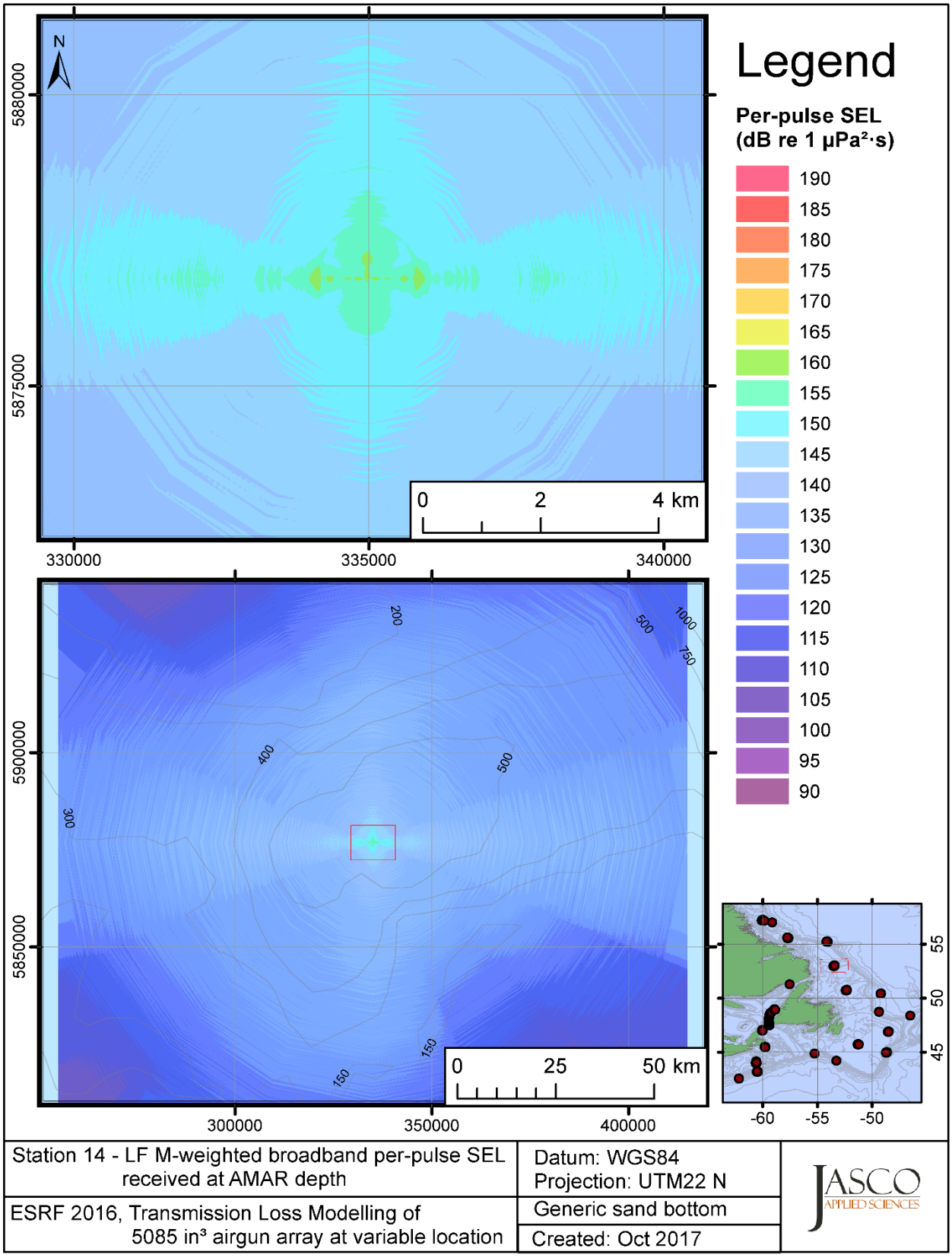

Figure C-73. Stn 14, LF M-weighted SEL received at the AMAR location and depth, modelled using a generic sand bottom, with in-situ July SSP and the airgun array located at any point on the map.

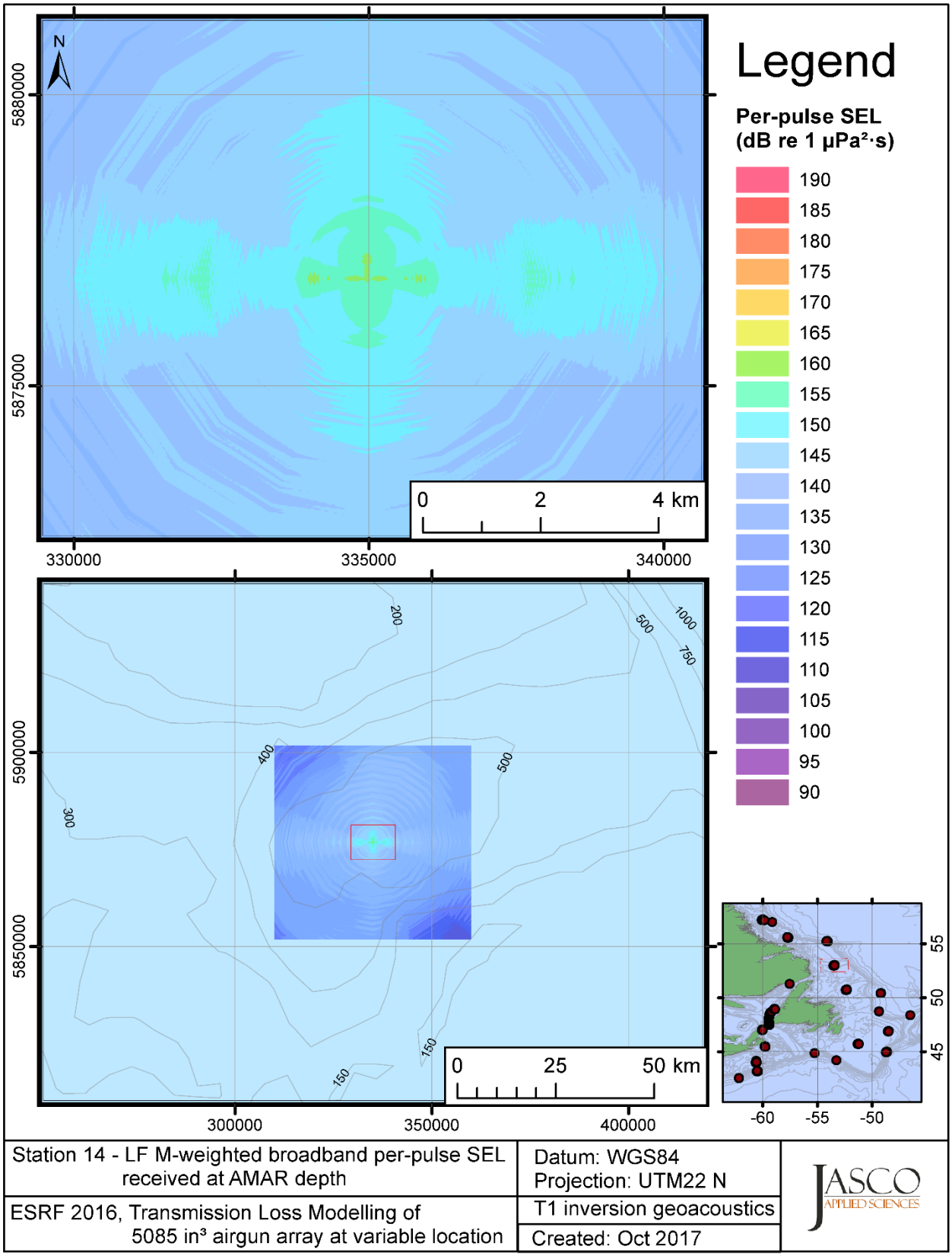

Figure C-74. Stn 14, LF M-weighted SEL received at the AMAR location and depth, modelled using the track 1 inversion geoacoustic bottom, with in-situ July SSP and the airgun array located at any point on the map.

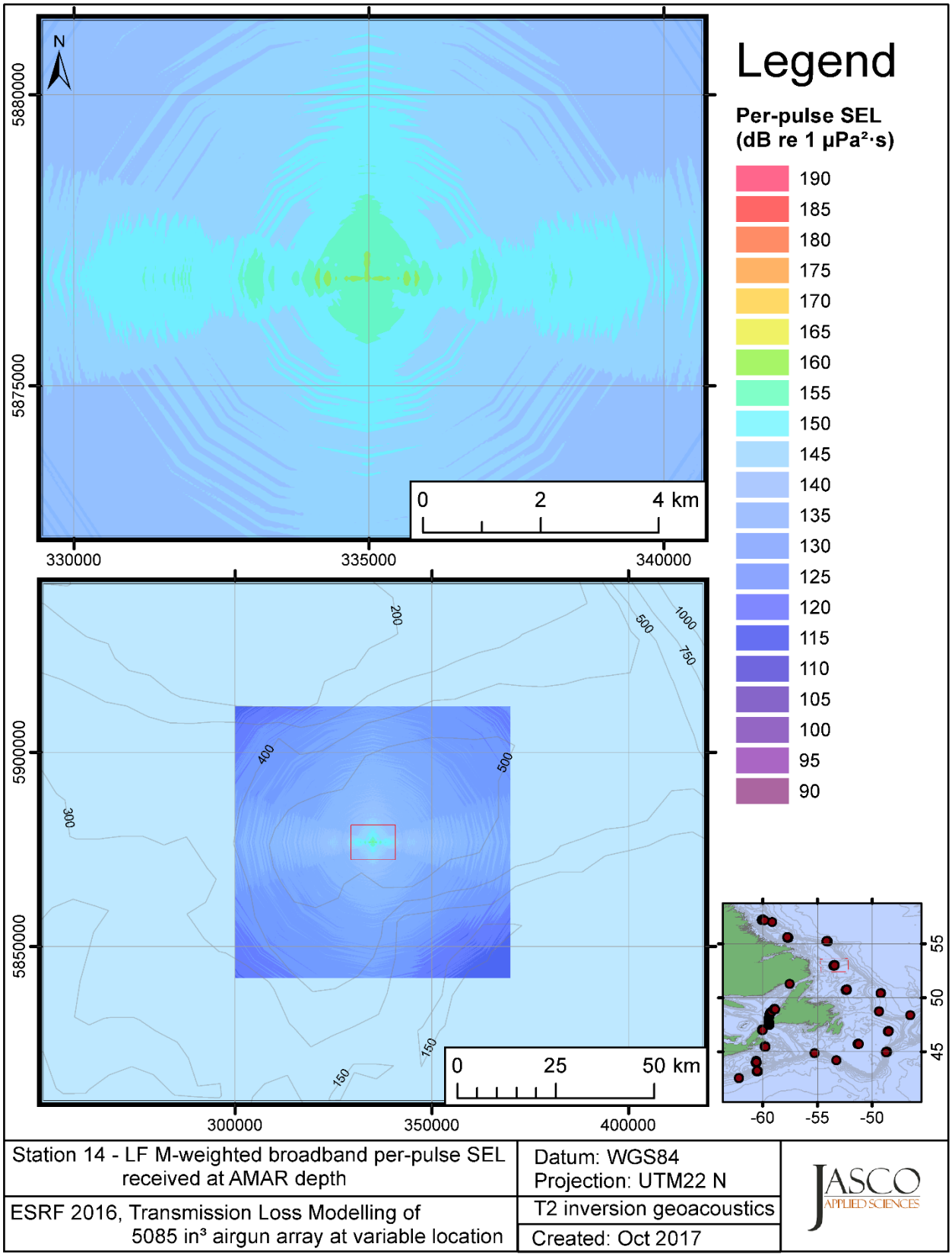

Figure C-75. Stn 14, LF M-weighted SEL received at the AMAR location and depth, modelled using the track 2 inversion geoacoustic bottom, with in-situ July SSP and the airgun array located at any point on the map.

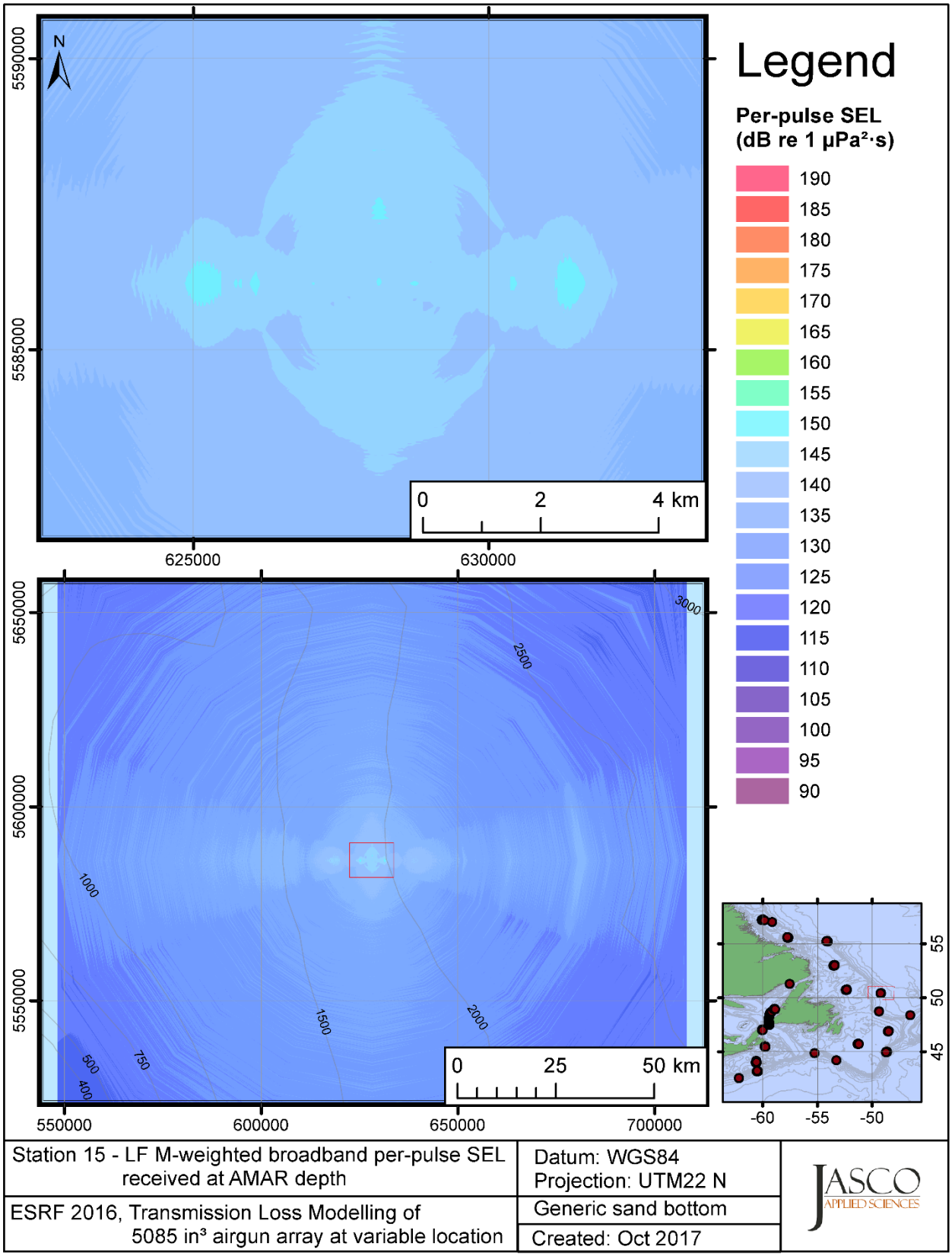

Figure C-76. Stn 15, LF M-weighted SEL received at the AMAR location and depth, modelled using a generic sand bottom, with in-situ July SSP and the airgun array located at any point on the map.

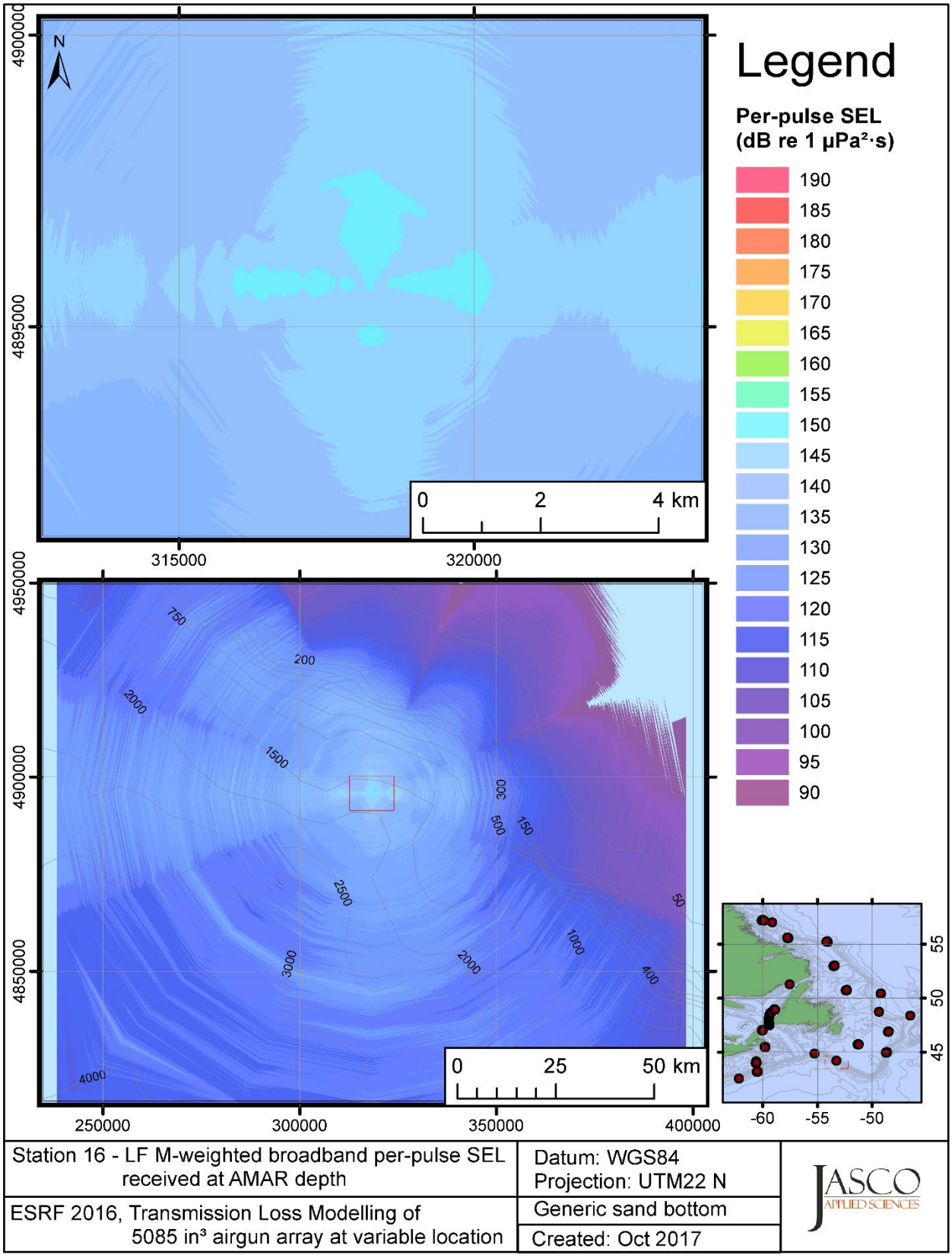

Figure C-77. Stn 16, LF M-weighted SEL received at the AMAR location and depth, modelled using a generic sand bottom, with in-situ July SSP and the airgun array located at any point on the map.

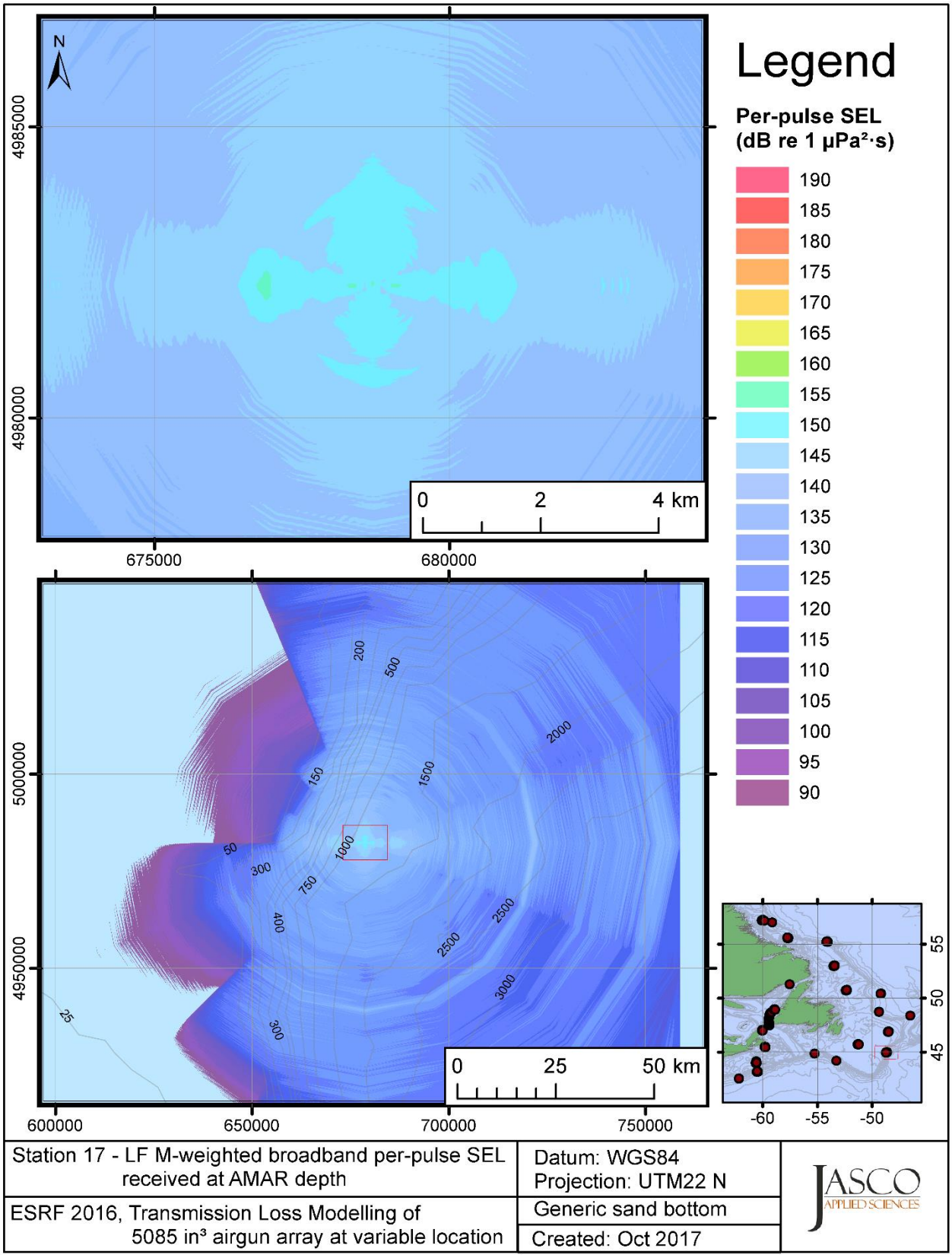

Figure C-78. Stn 17, LF M-weighted SEL received at the AMAR location and depth, modelled using a generic sand bottom, with in-situ July SSP and the airgun array located at any point on the map.

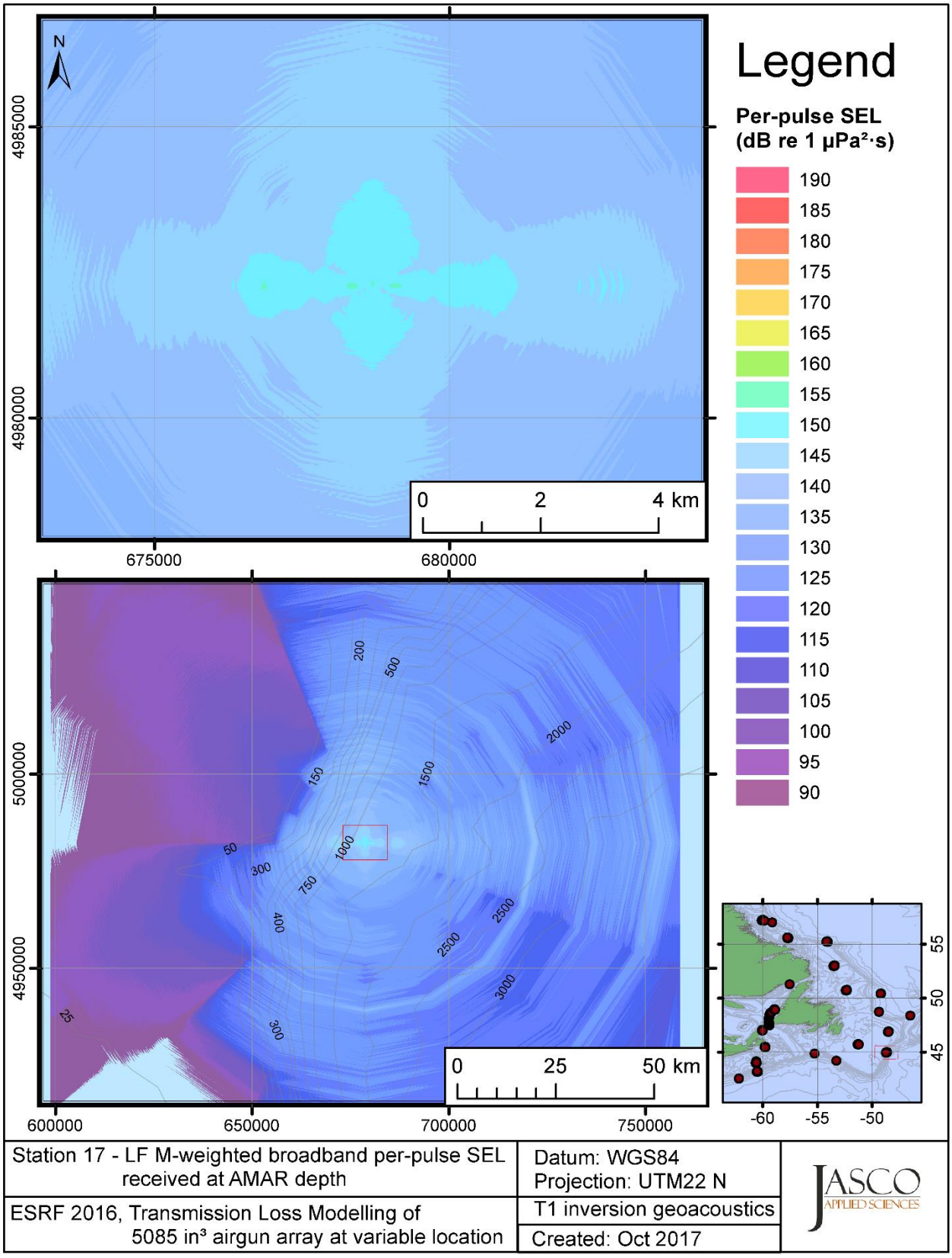

Figure C-79. Stn 17, LF M-weighted SEL received at the AMAR location and depth, modelled using the track 1 inversion geoacoustic bottom, with in-situ July SSP and the airgun array located at any point on the map.

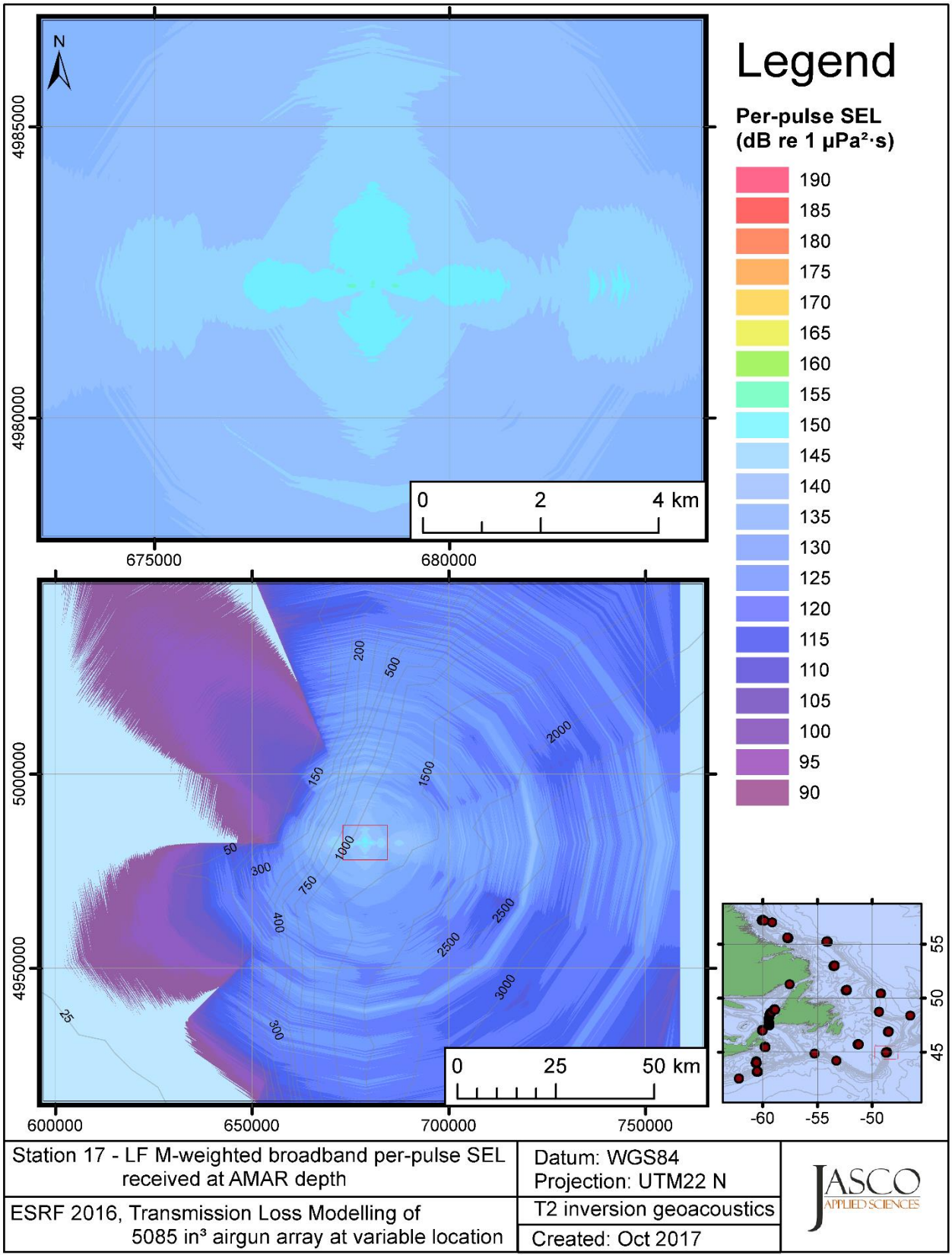

Figure C-80. Stn 17, LF M-weighted SEL received at the AMAR location and depth, modelled using the track 2 inversion geoacoustic bottom, with in-situ July SSP and the airgun array located at any point on the map.

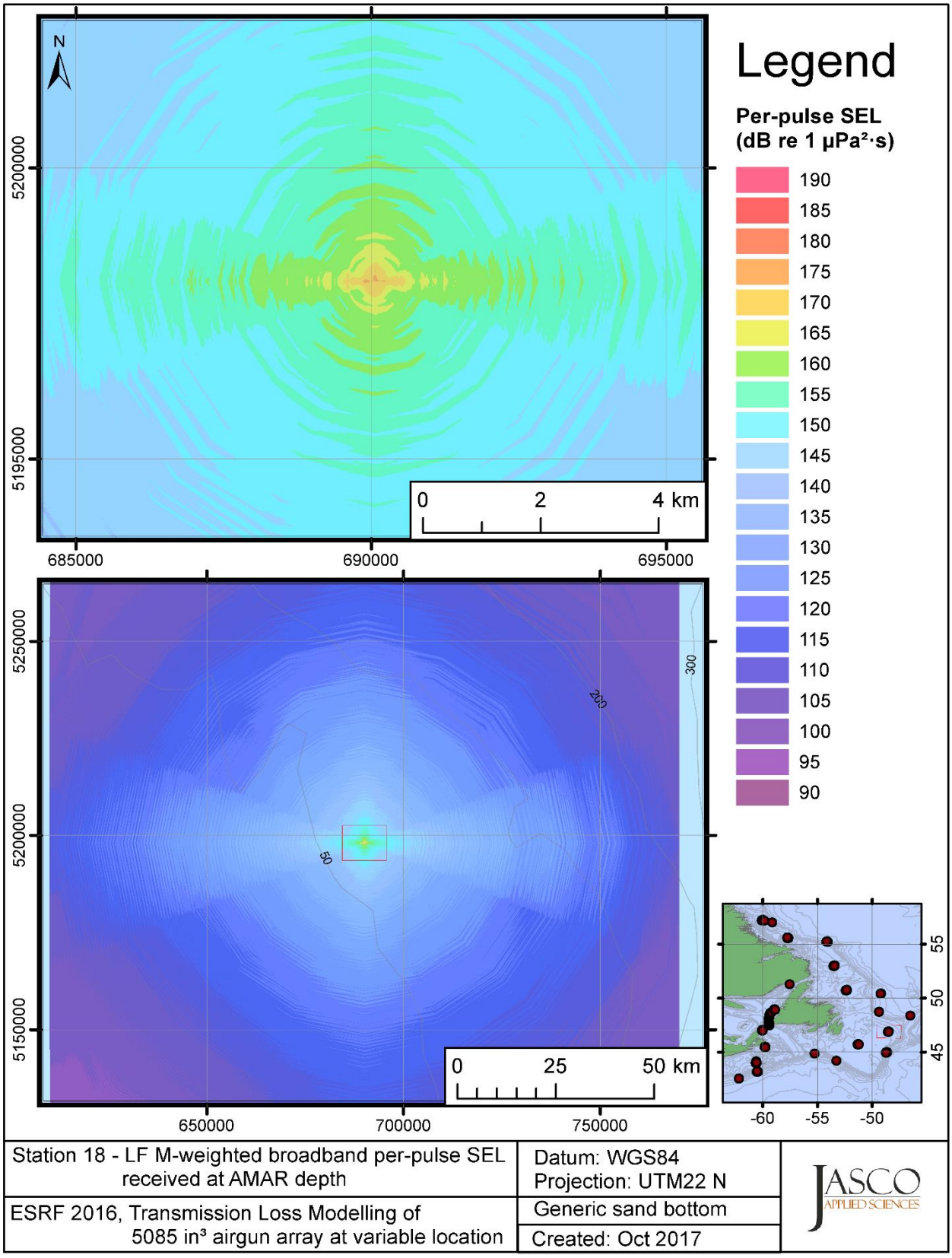

Figure C-81. Stn 18, LF M-weighted SEL received at the AMAR location and depth, modelled using a generic sand bottom, with in-situ July SSP and the airgun array located at any point on the map.

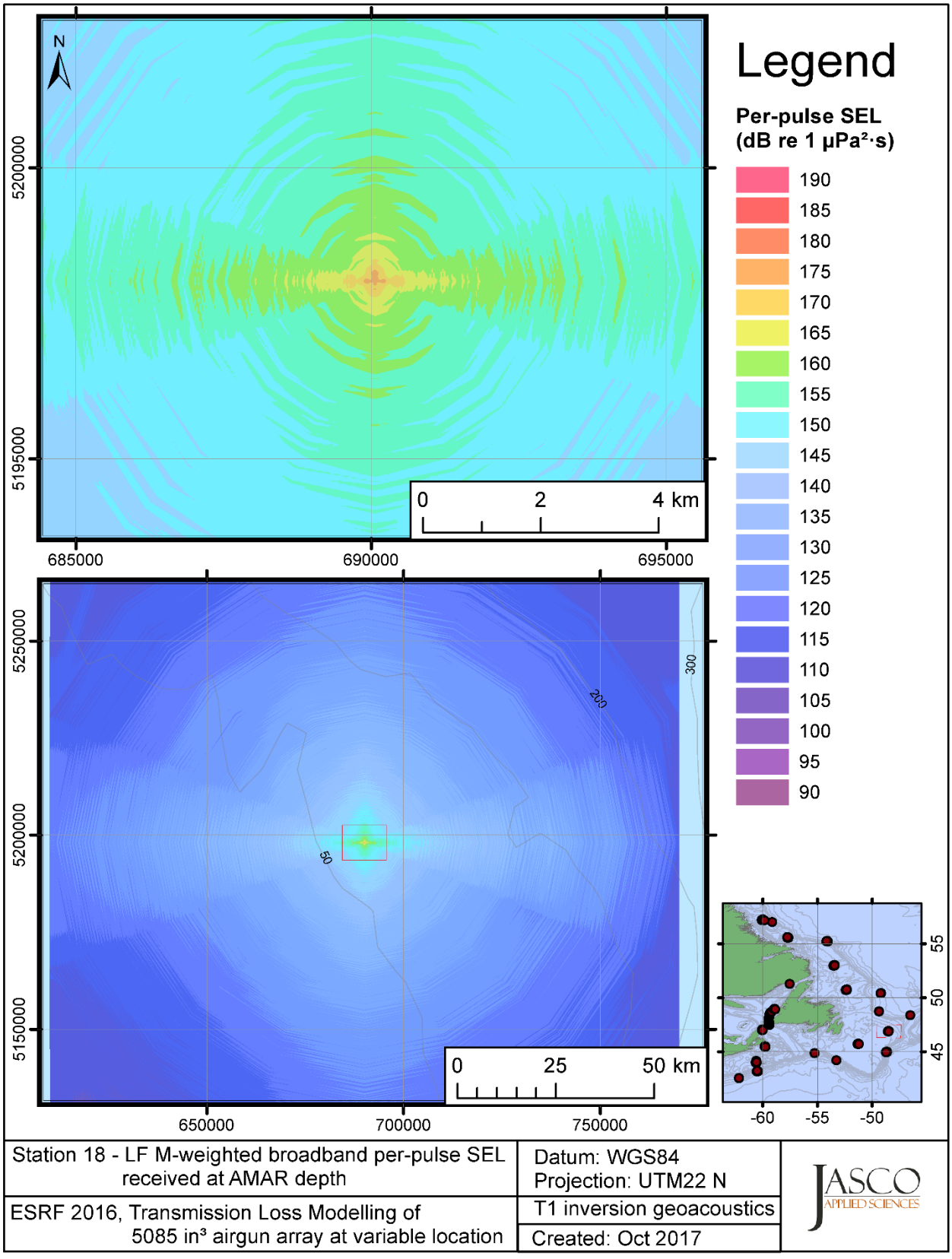

Figure C-82. Stn 18, LF M-weighted SEL received at the AMAR location and depth, modelled using the track 1 inversion geoacoustic bottom, with in-situ July SSP and the airgun array located at any point on the map.

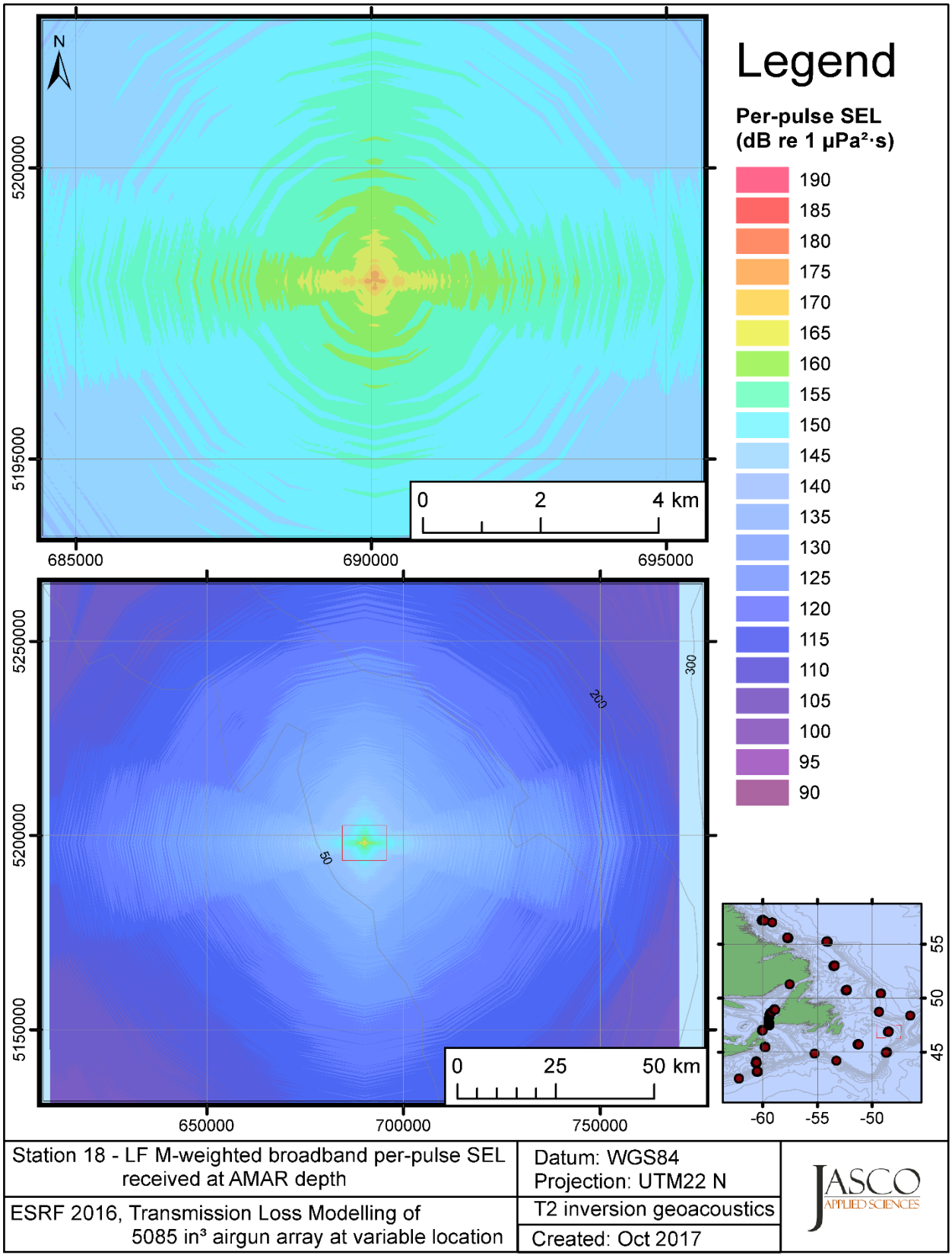

Figure C-83. Stn 18, LF M-weighted SEL received at the AMAR location and depth, modelled using the track 2 inversion geoacoustic bottom, with in-situ July SSP and the airgun array located at any point on the map.

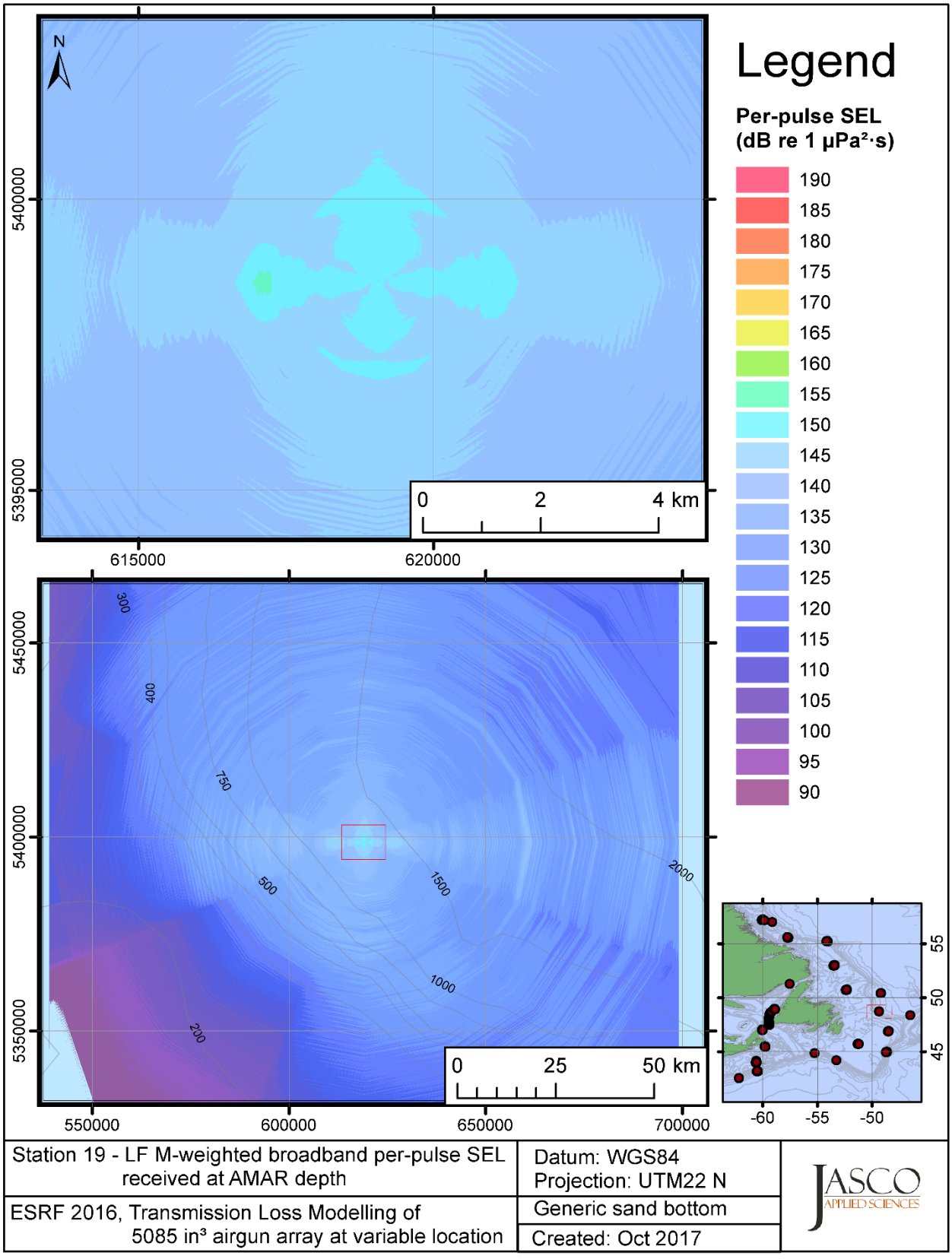

Figure C-84. Stn 19, LF M-weighted SEL received at the AMAR location and depth, modelled using a generic sand bottom, with in-situ July SSP and the airgun array located at any point on the map.

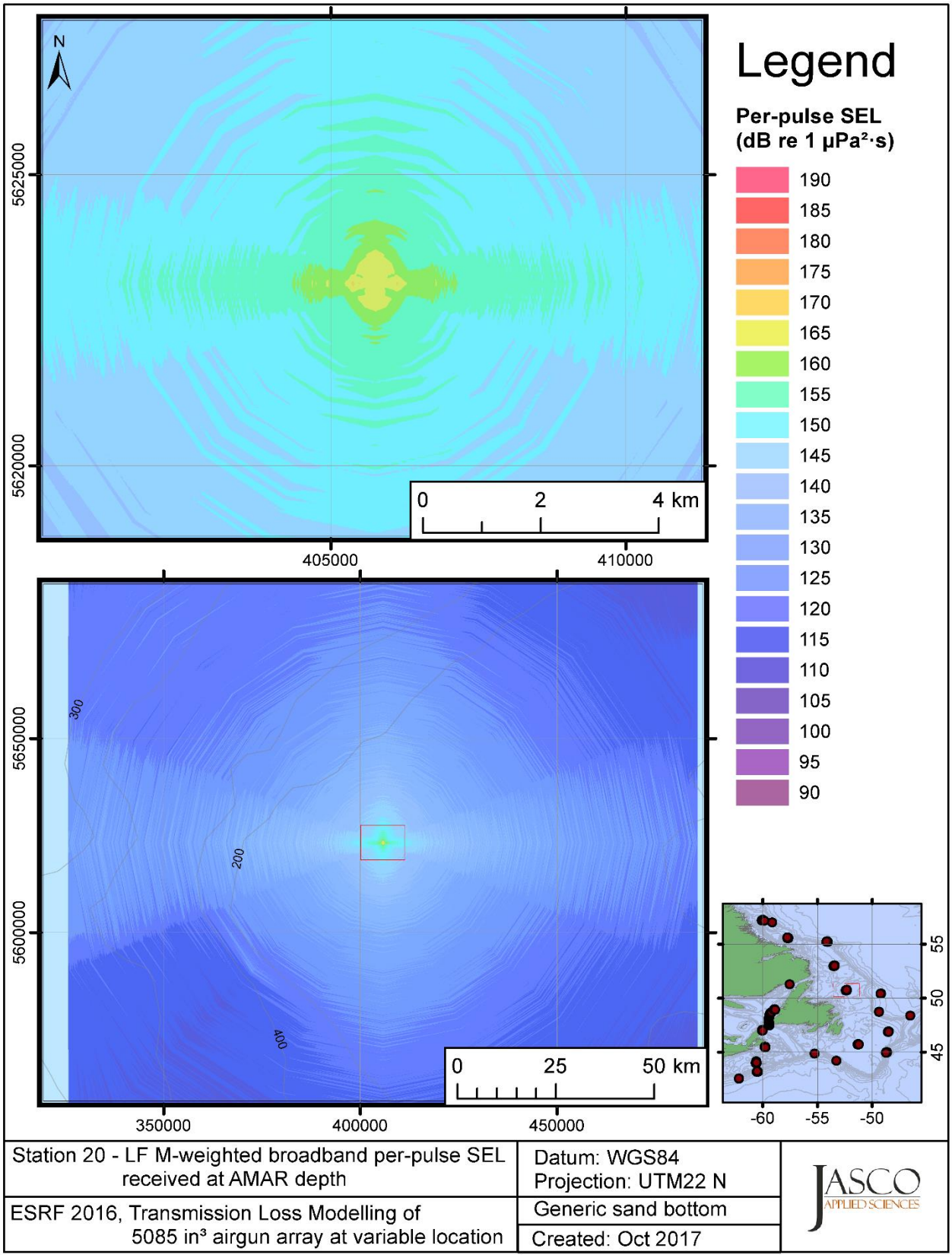

Figure C-85. Stn 20, LF M-weighted SEL received at the AMAR location and depth, modelled using a generic sand bottom, with in-situ July SSP and the airgun array located at any point on the map.

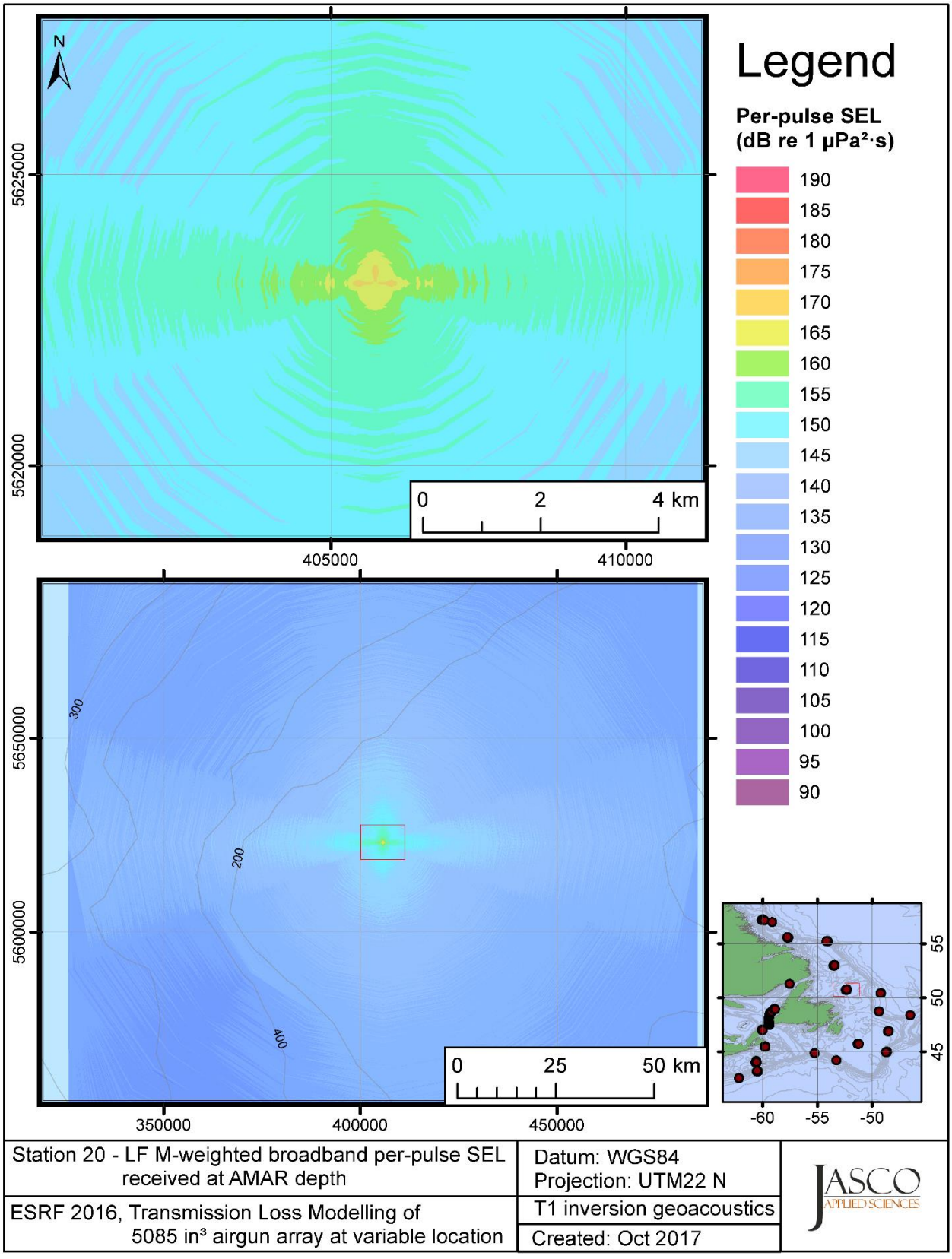

Figure C-86. Stn 20, LF M-weighted SEL received at the AMAR location and depth, modelled using the track 1 inversion geoacoustic bottom, with in-situ July SSP and the airgun array located at any point on the map.

C.3. Modelling MF M-weighted Received Level at the AMAR Location

This section presents the results of modelling the per-pulse sound exposure level (SEL) received at the AMAR location and depth as a function of the source location (varied in range and azimuth) for each of the 20 sites using a generic sand bottom; in addition, the modelling is repeated using the geoacoustic inversion bottom parameters at the 14 sites where they are available. The modelling results are presented in the form of coloured maps where the colour at any map location represents the predicted received level at the AMAR for the source located at that spot on the map. This section includes only the medium-frequency cetaceans (MF) marine-mammal-weighted per-pulse SEL results; additional maps for other marine mammal received level auditory weighting functions are presented in adjoining sections.

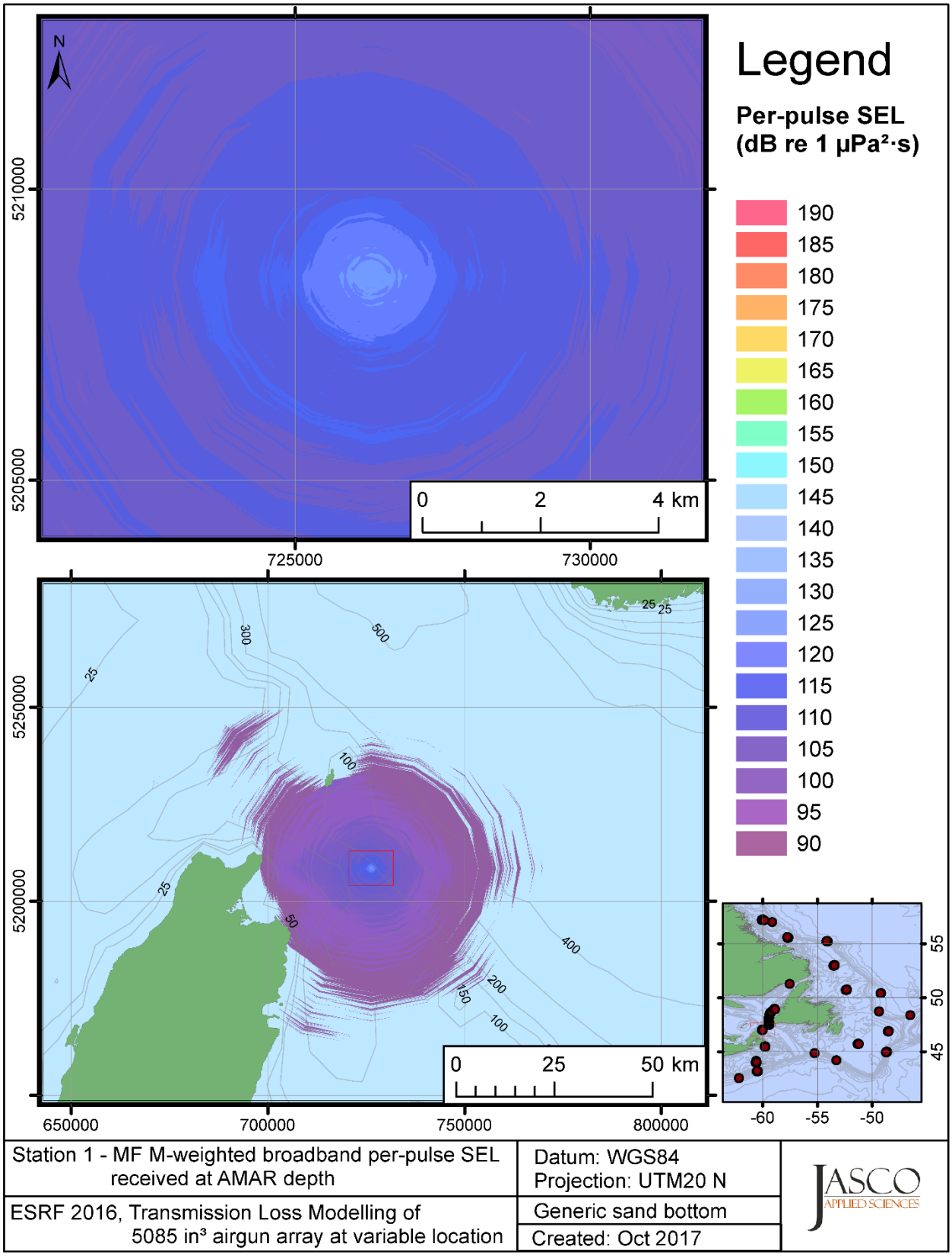

Figure C-87. Stn 1, MF M-weighted SEL received at the AMAR location and depth, modelled using a generic sand bottom, with in-situ July SSP and the airgun array located at any point on the map.

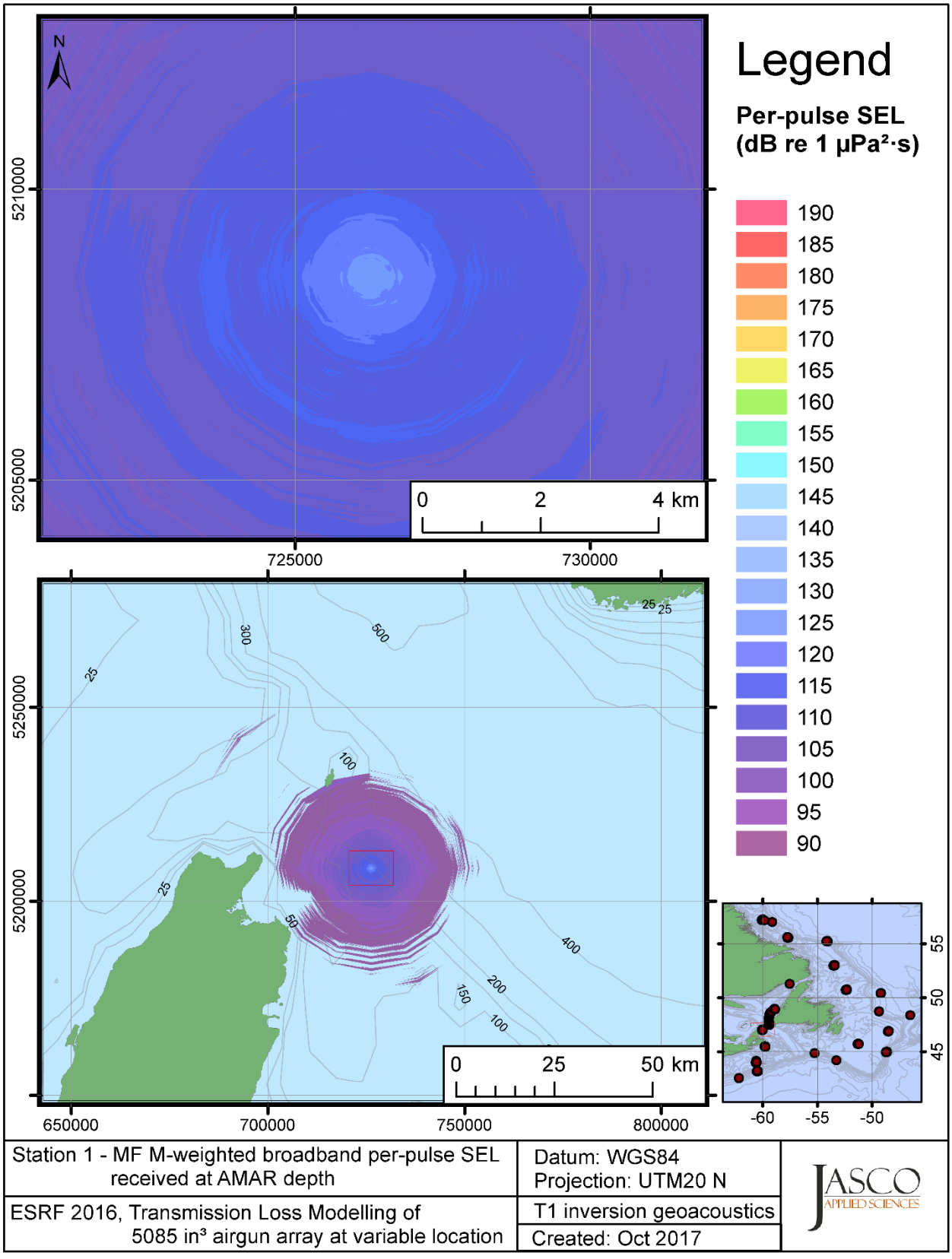

Figure C-88. Stn 1, MF M-weighted SEL received at the AMAR location and depth, modelled using the track 1 inversion geoacoustic bottom, with in-situ July SSP and the airgun array located at any point on the map.

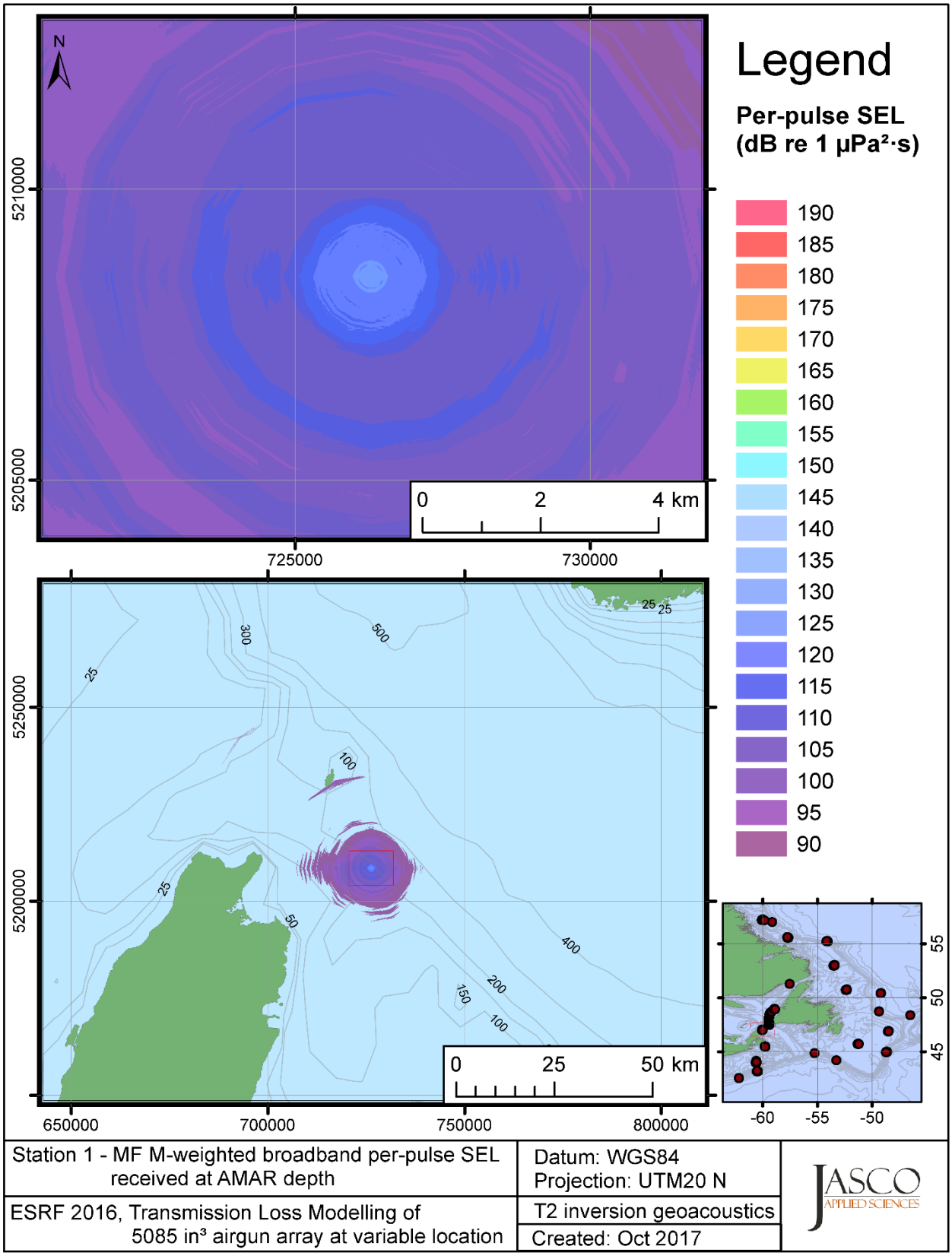

Figure C-89. Stn 1, MF M-weighted SEL received at the AMAR location and depth, modelled using the track 2 inversion geoacoustic bottom, with in-situ July SSP and the airgun array located at any point on the map.

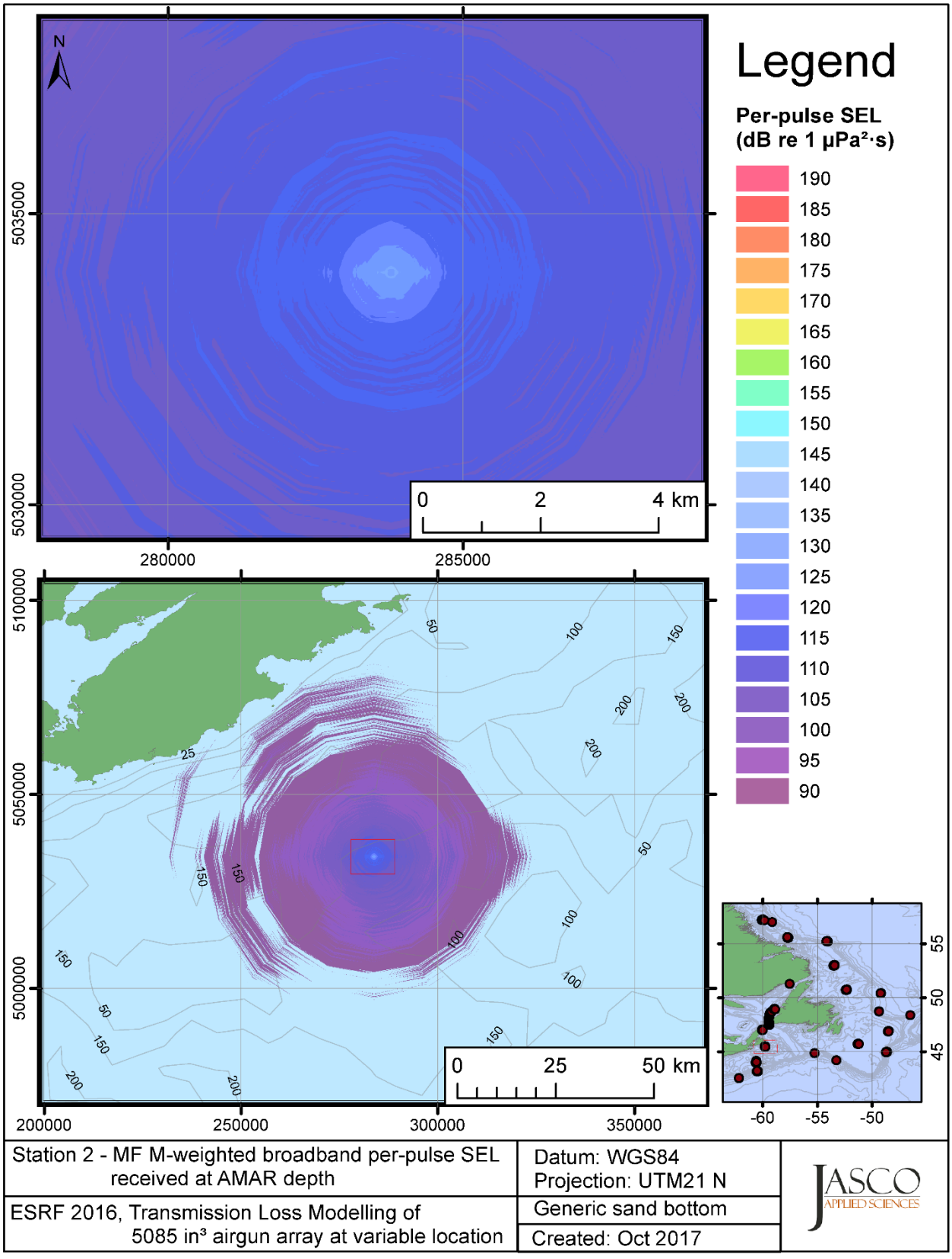

Figure C-90. Stn 2, MF M-weighted SEL received at the AMAR location and depth, modelled using a generic sand bottom, with in-situ July SSP and the airgun array located at any point on the map.

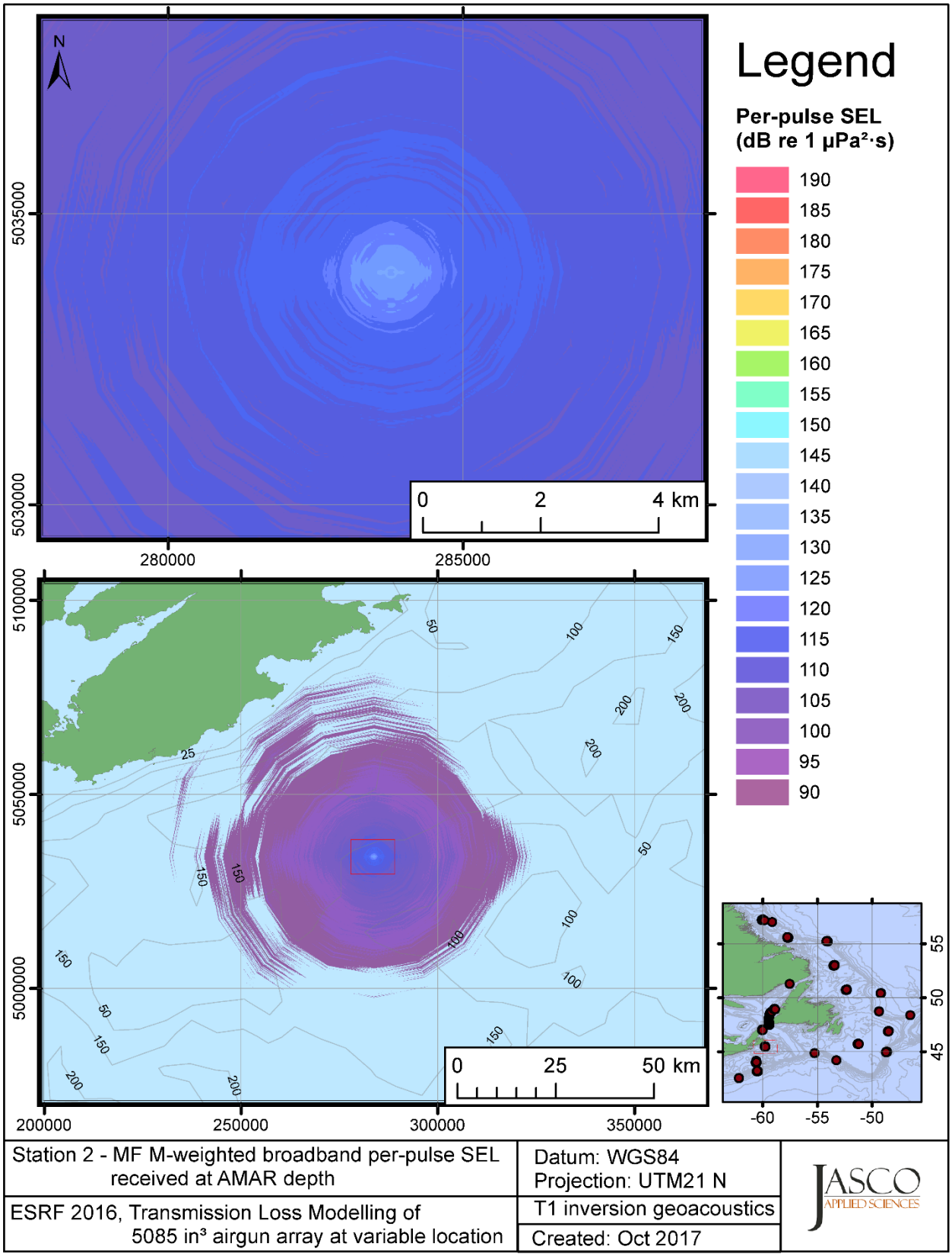

Figure C-91. Stn 2, MF M-weighted SEL received at the AMAR location and depth, modelled using the track 1 inversion geoacoustic bottom, with in-situ July SSP and the airgun array located at any point on the map.

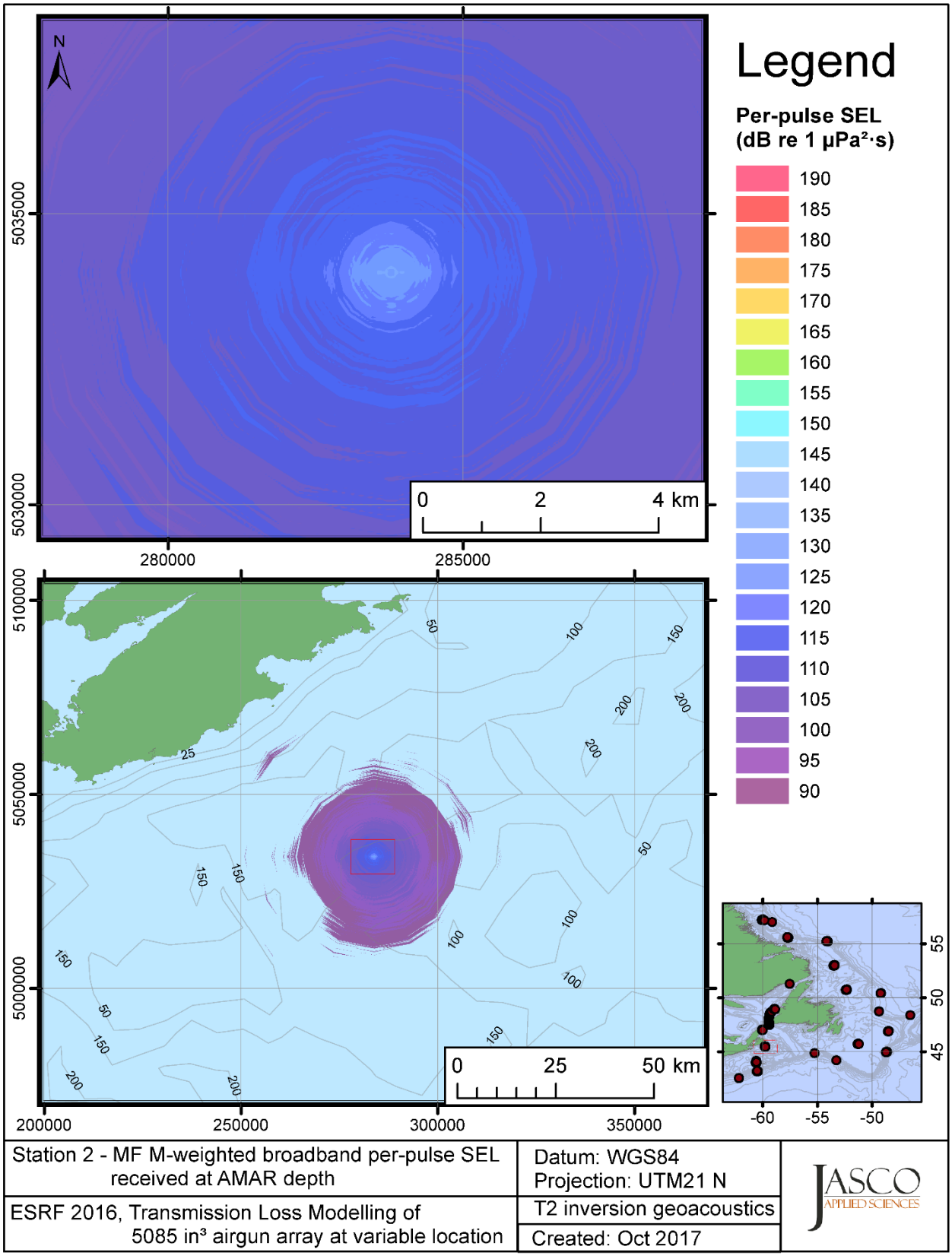

Figure C-92. Stn 2, MF M-weighted SEL received at the AMAR location and depth, modelled using the track 2 inversion geoacoustic bottom, with in-situ July SSP and the airgun array located at any point on the map.

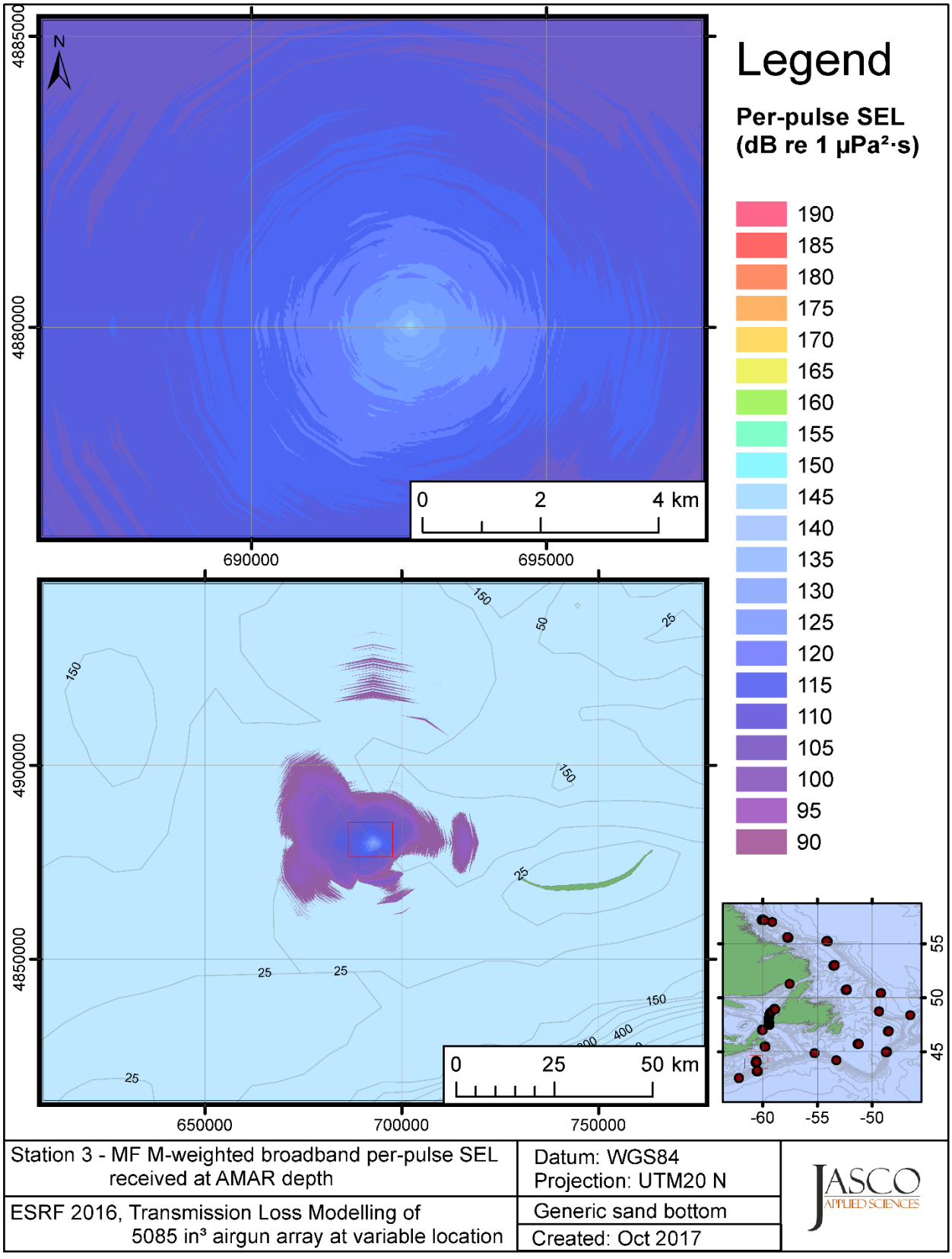

Figure C-93. Stn 3, MF M-weighted SEL received at the AMAR location and depth, modelled using a generic sand bottom, with in-situ July SSP and the airgun array located at any point on the map.

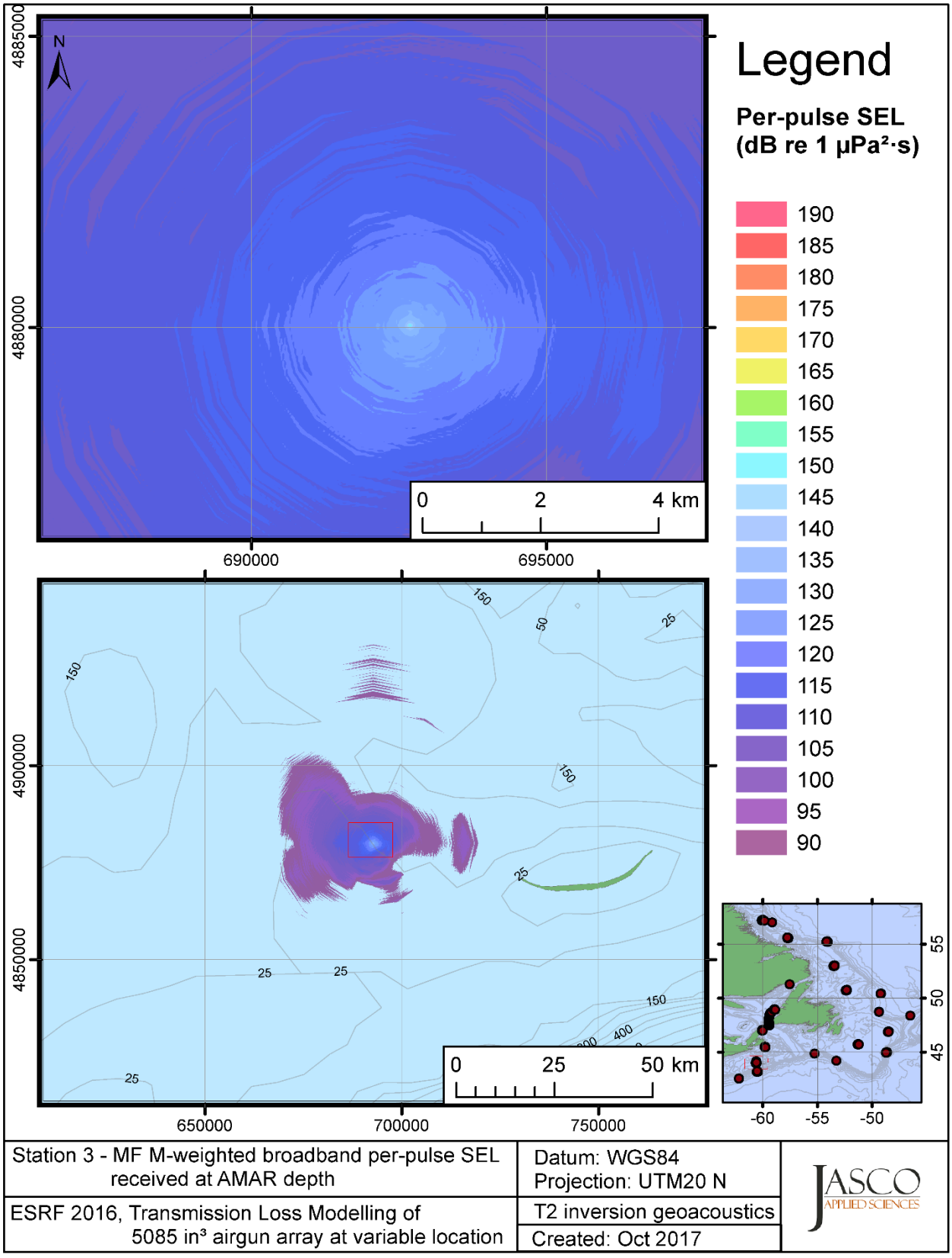

Figure C-94. Stn 3, MF M-weighted SEL received at the AMAR location and depth, modelled using the track 2 inversion geoacoustic bottom, with in-situ July SSP and the airgun array located at any point on the map.

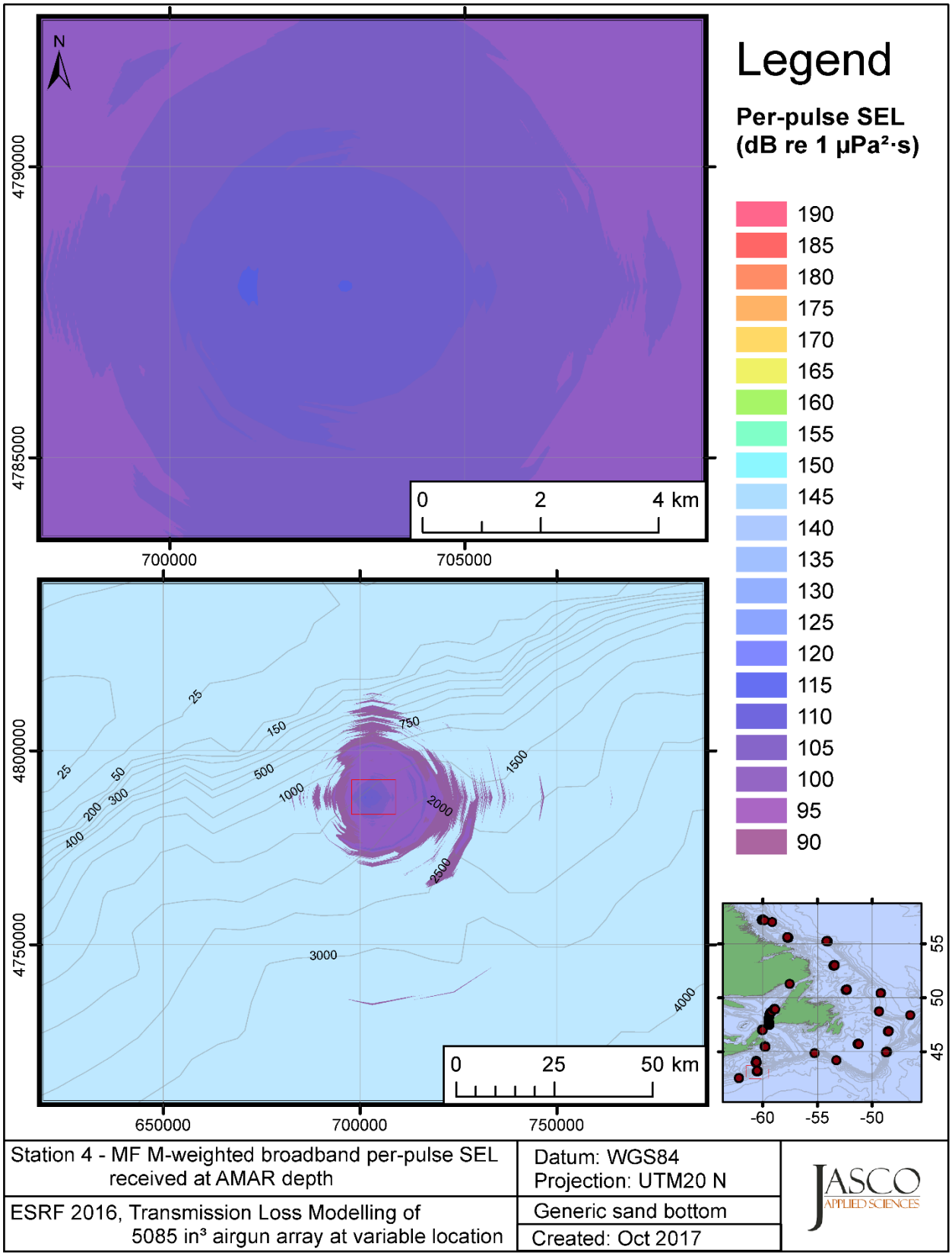

Figure C-95. Stn 4, MF M-weighted SEL received at the AMAR location and depth, modelled using a generic sand bottom, with in-situ July SSP and the airgun array located at any point on the map.

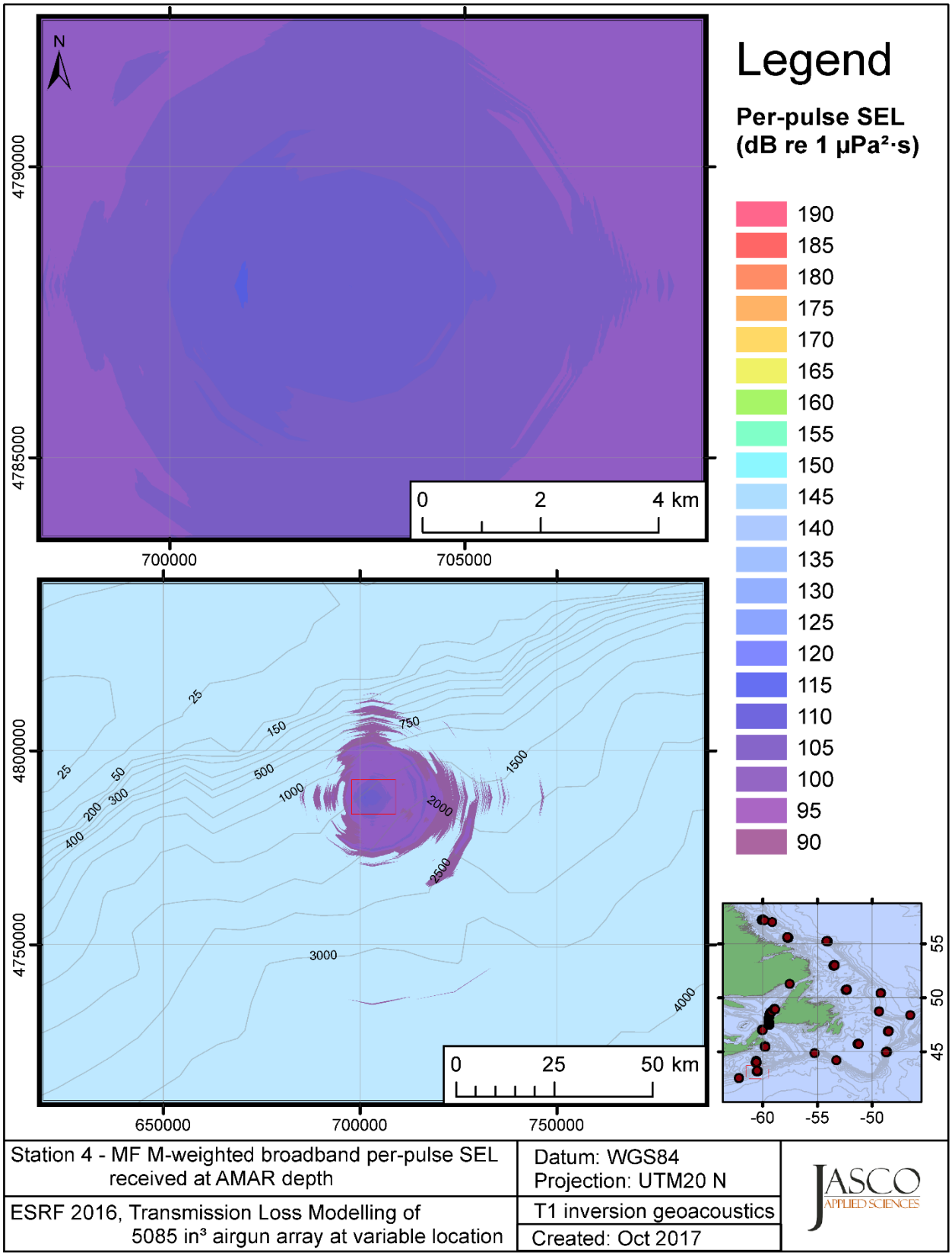

Figure C-96. Stn 4, MF M-weighted SEL received at the AMAR location and depth, modelled using the track 1 inversion geoacoustic bottom, with in-situ July SSP and the airgun array located at any point on the map.

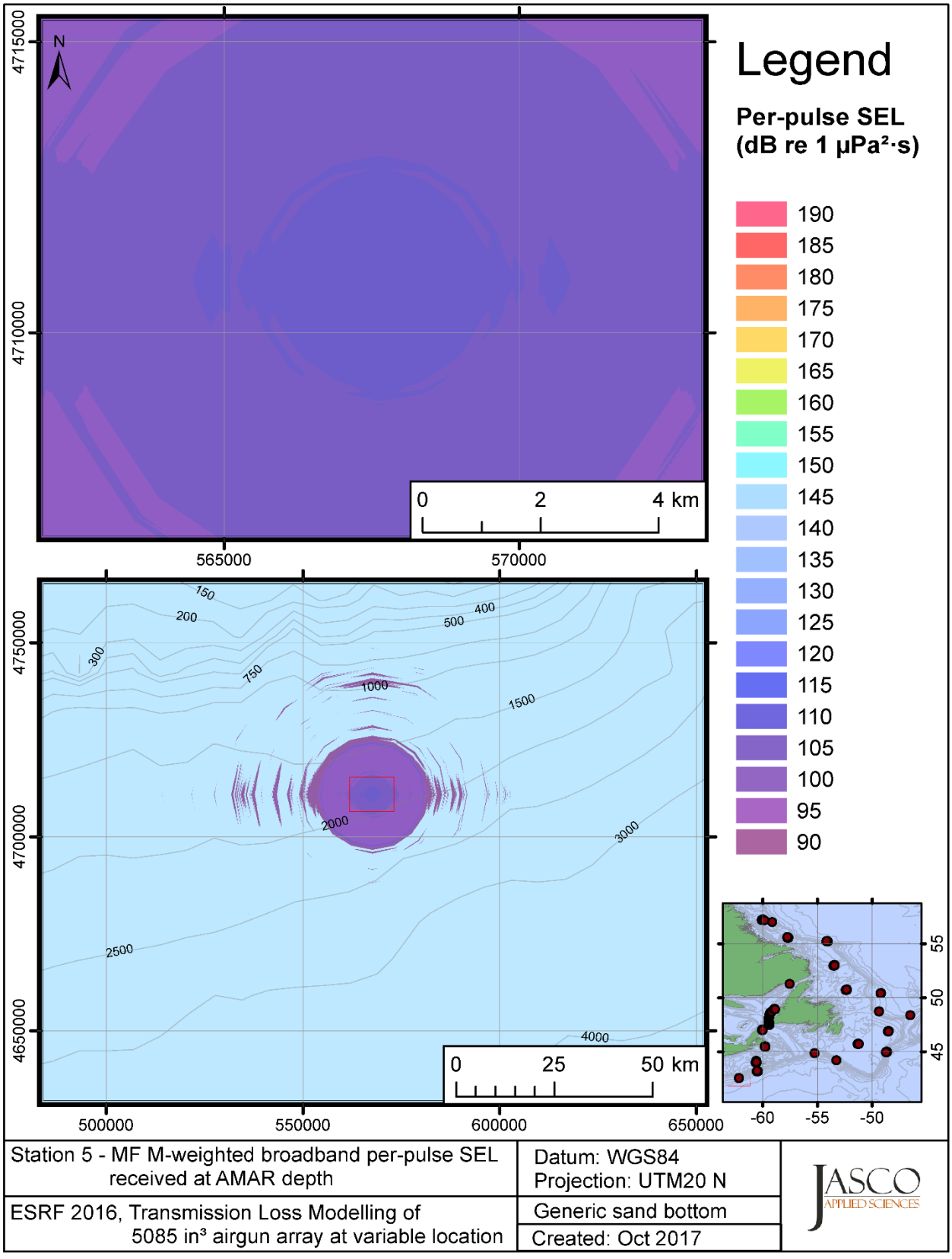

Figure C-97. Stn 5, MF M-weighted SEL received at the AMAR location and depth, modelled using a generic sand bottom, with in-situ July SSP and the airgun array located at any point on the map.

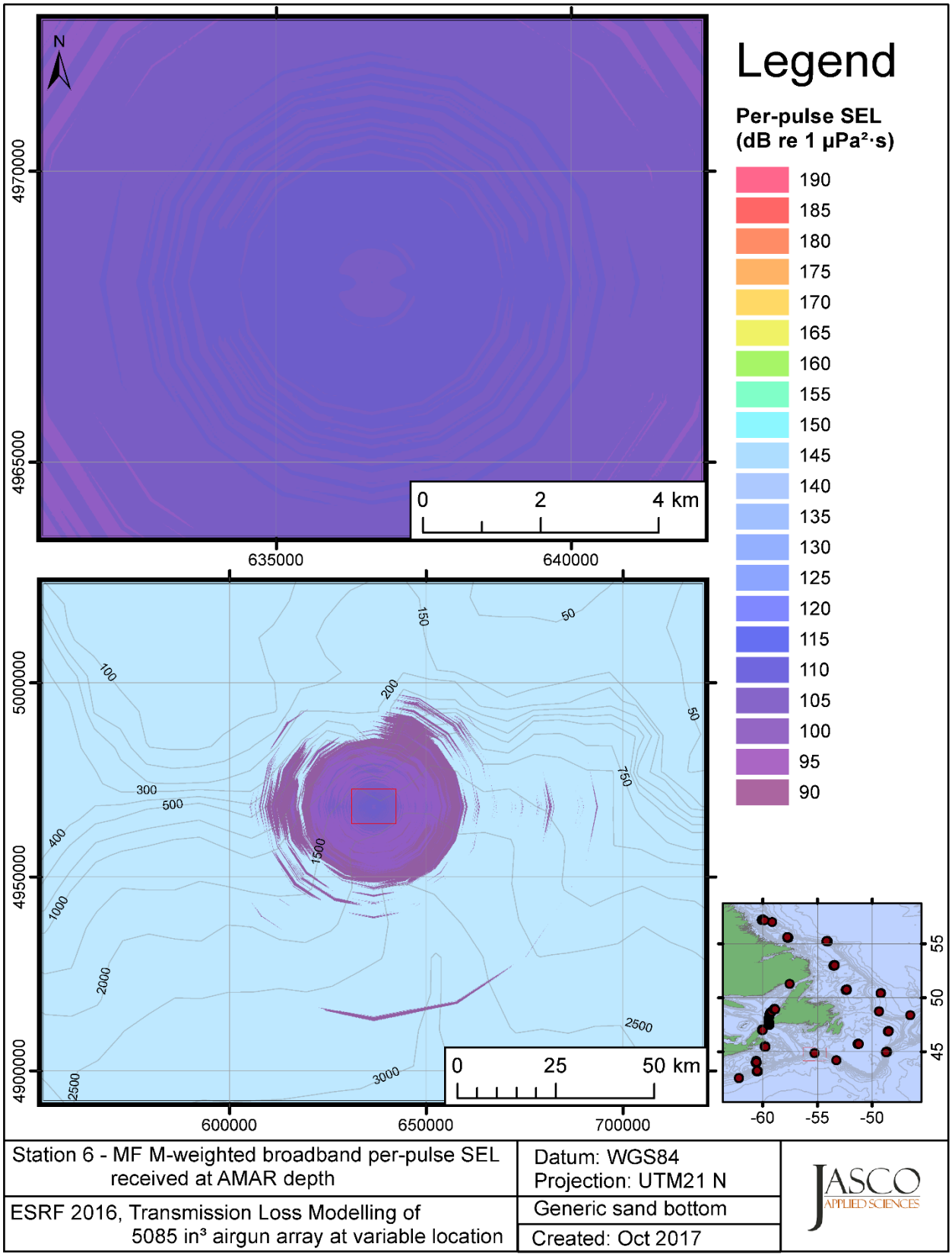

Figure C-98. Stn 6, MF M-weighted SEL received at the AMAR location and depth, modelled using a generic sand bottom, with in-situ July SSP and the airgun array located at any point on the map.

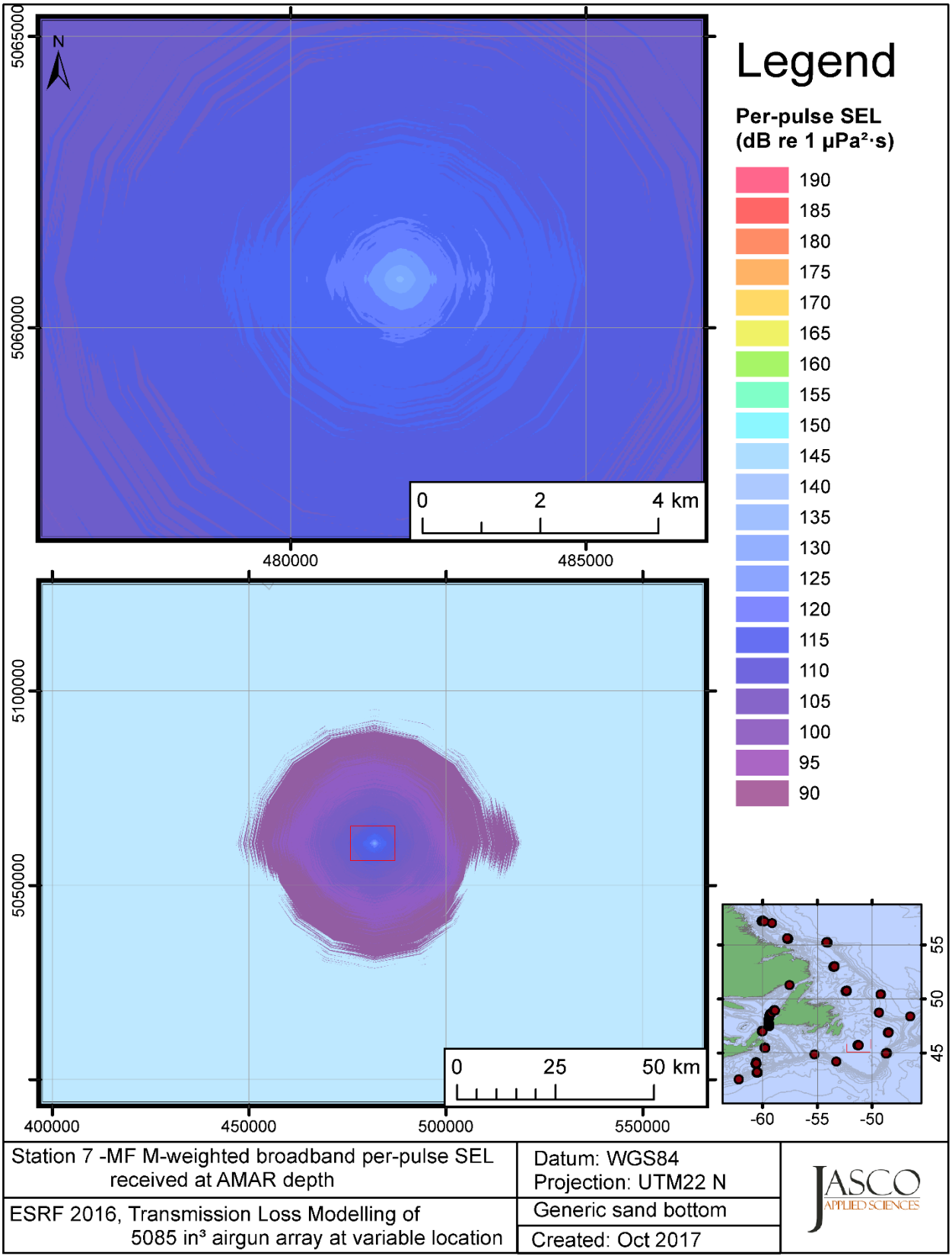

Figure C-99. Stn 7, MF M-weighted SEL received at the AMAR location and depth, modelled using a generic sand bottom, with in-situ July SSP and the airgun array located at any point on the map.

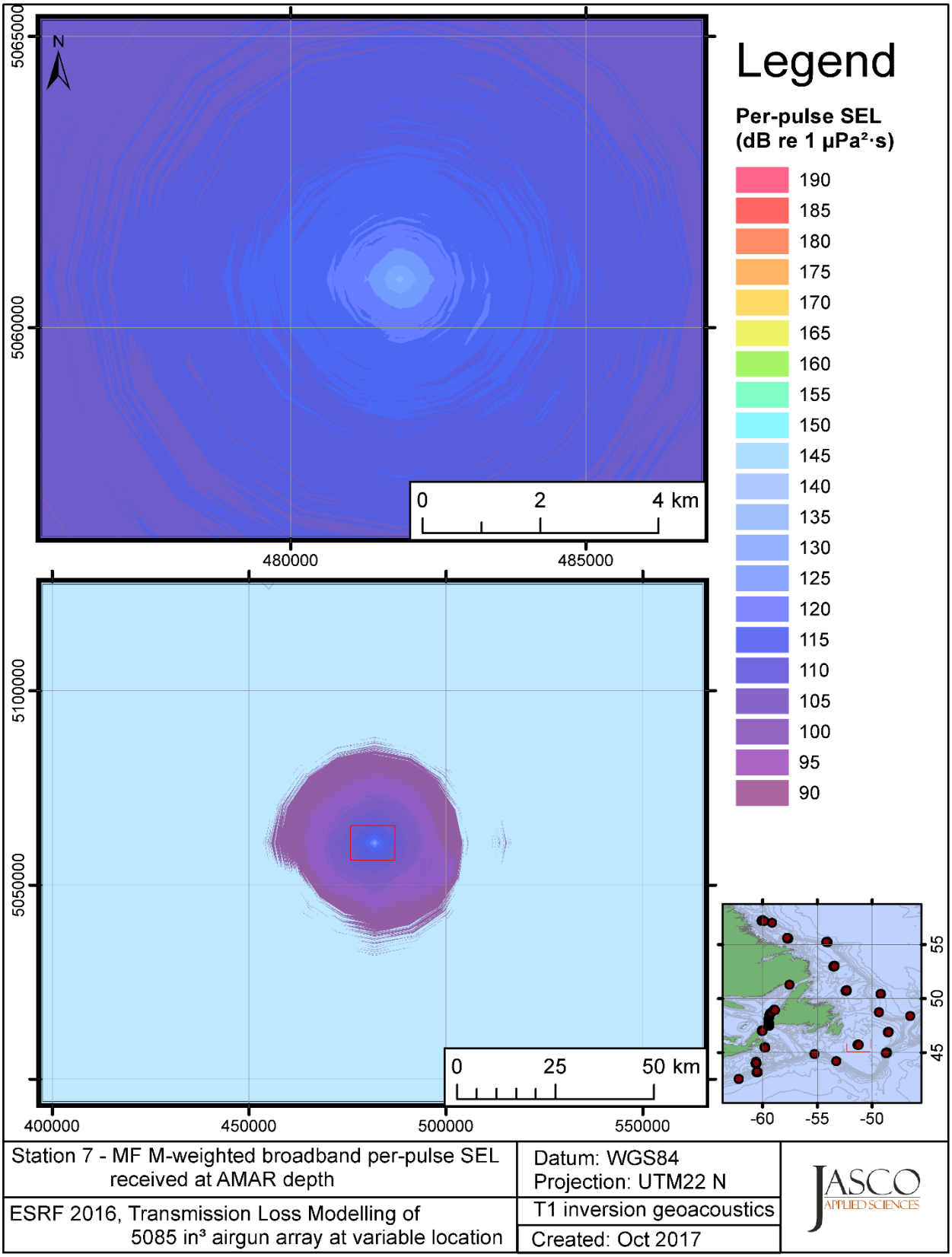

Figure C-100. Stn 7, MF M-weighted SEL received at the AMAR location and depth, modelled using the track 1 inversion geoacoustic bottom, with in-situ July SSP and the airgun array located at any point on the map.

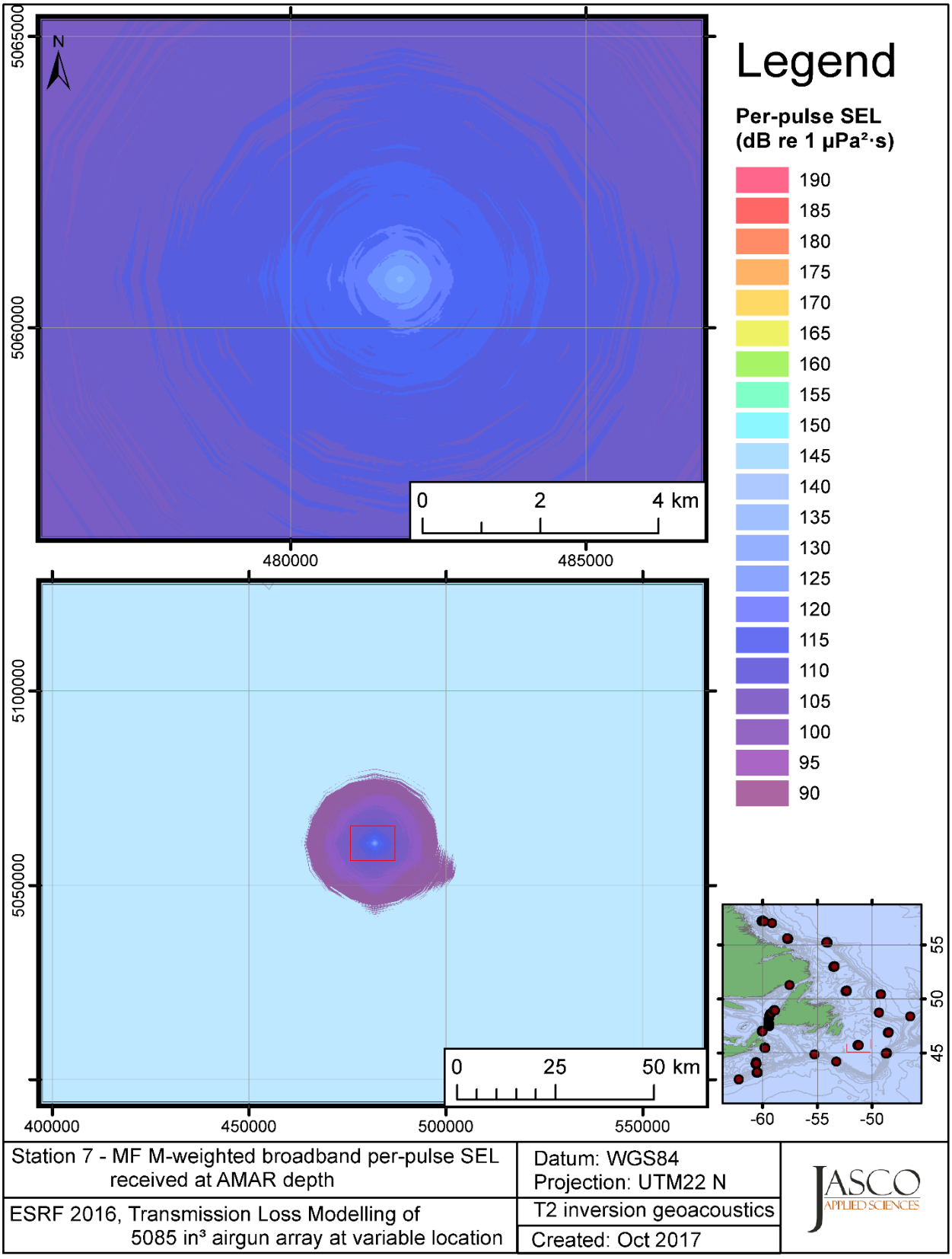

Figure C-101. Stn 7, MF M-weighted SEL received at the AMAR location and depth, modelled using the track 2 inversion geoacoustic bottom, with in-situ July SSP and the airgun array located at any point on the map.

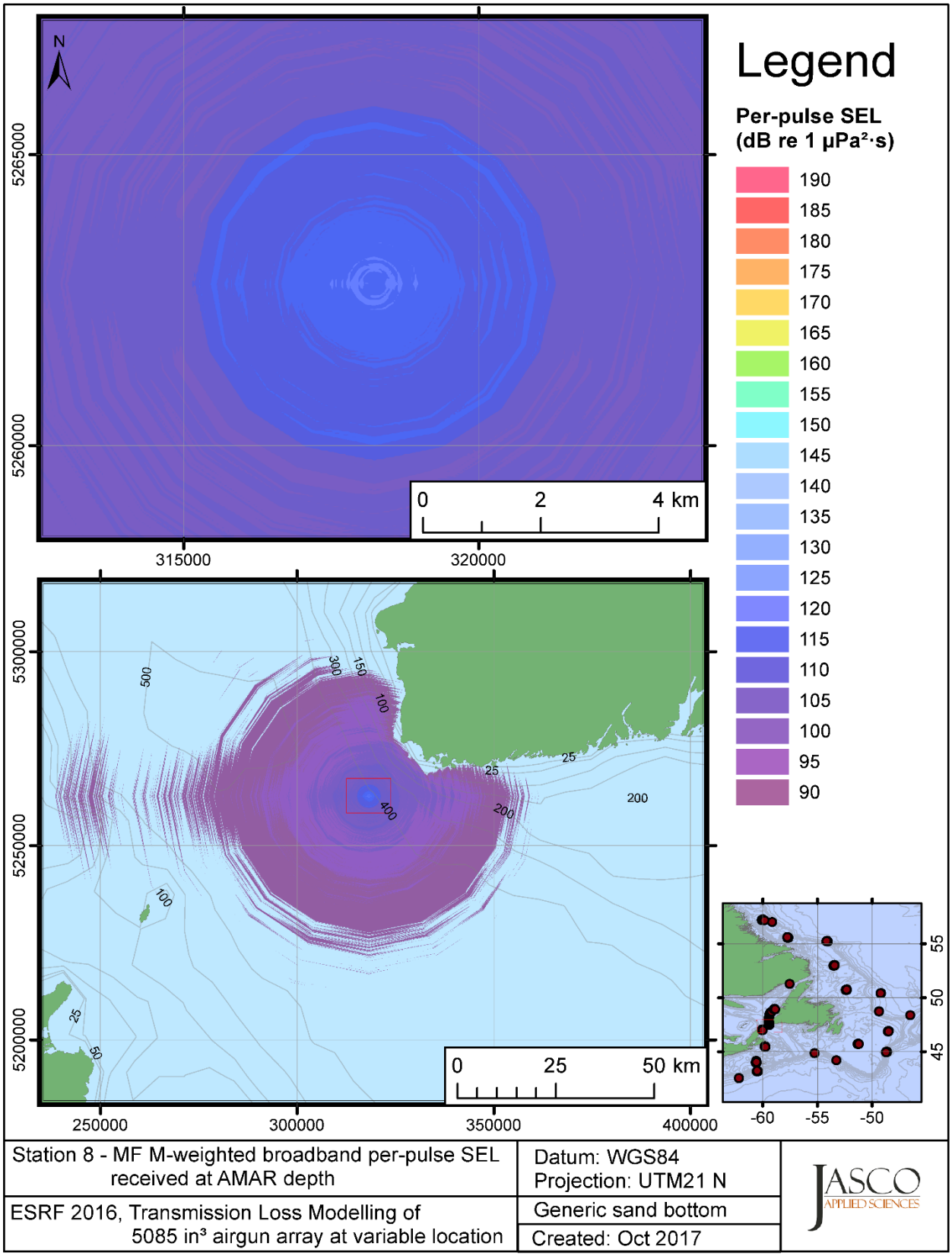

Figure C-102. Stn 8, MF M-weighted SEL received at the AMAR location and depth, modelled using a generic sand bottom, with GDEM July SSP and the airgun array located at any point on the map.

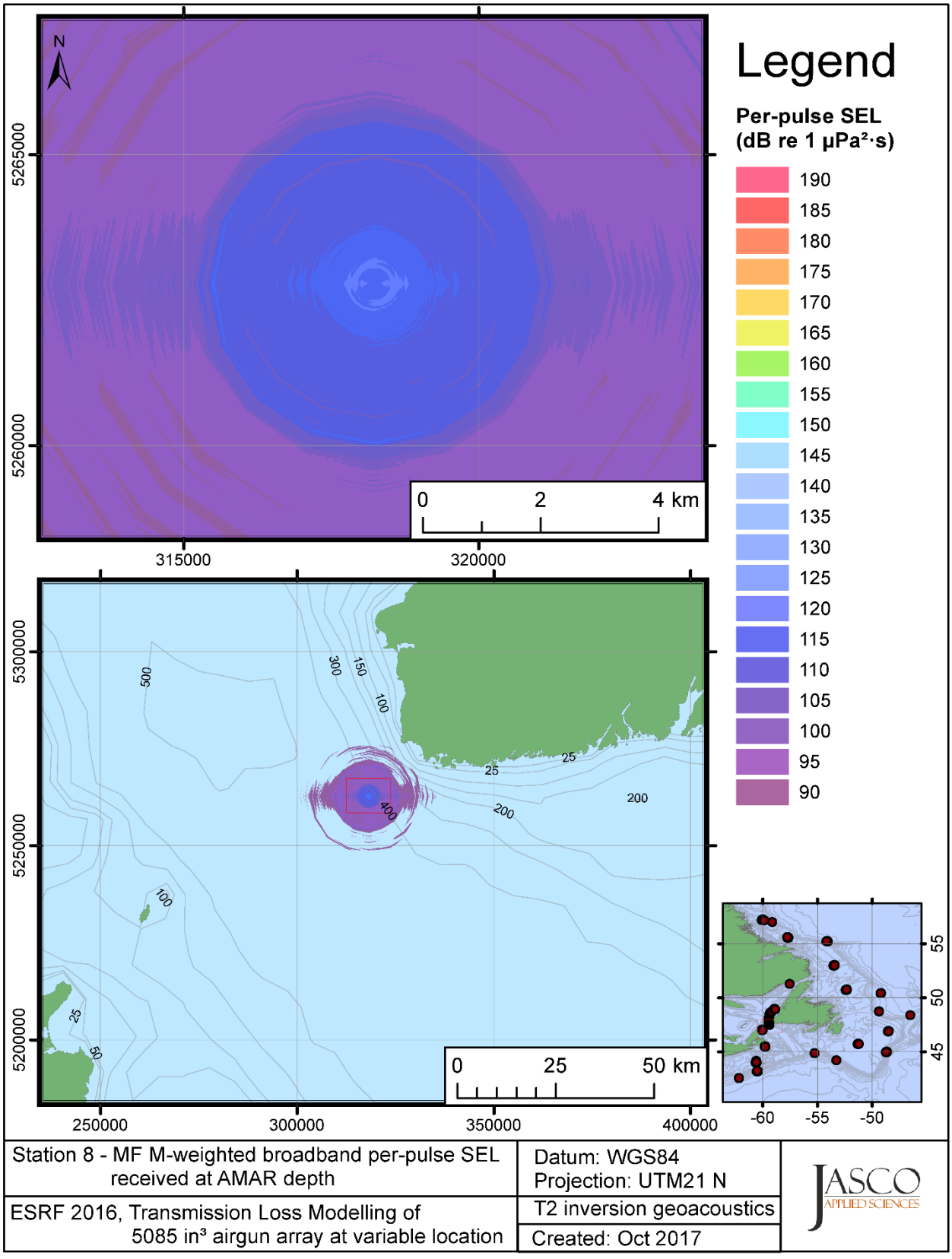

Figure C-103. Stn 8, MF M-weighted SEL received at the AMAR location and depth, modelled using the track 2 inversion geoacoustic bottom, with GDEM July SSP and the airgun array located at any point on the map.

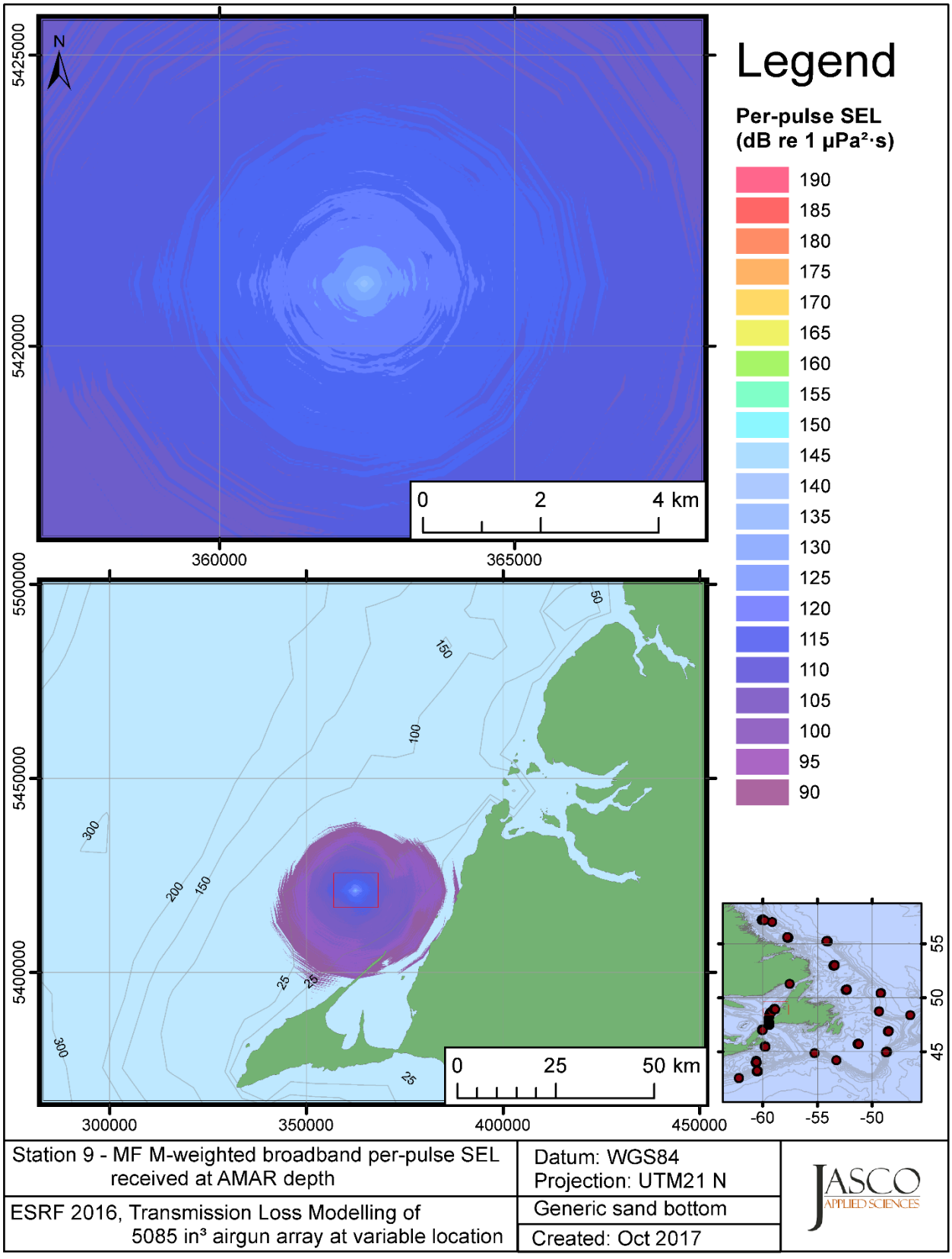

Figure C-104. Stn 9, MF M-weighted SEL received at the AMAR location and depth, modelled using a generic sand bottom, with GDEM July SSP and the airgun array located at any point on the map.

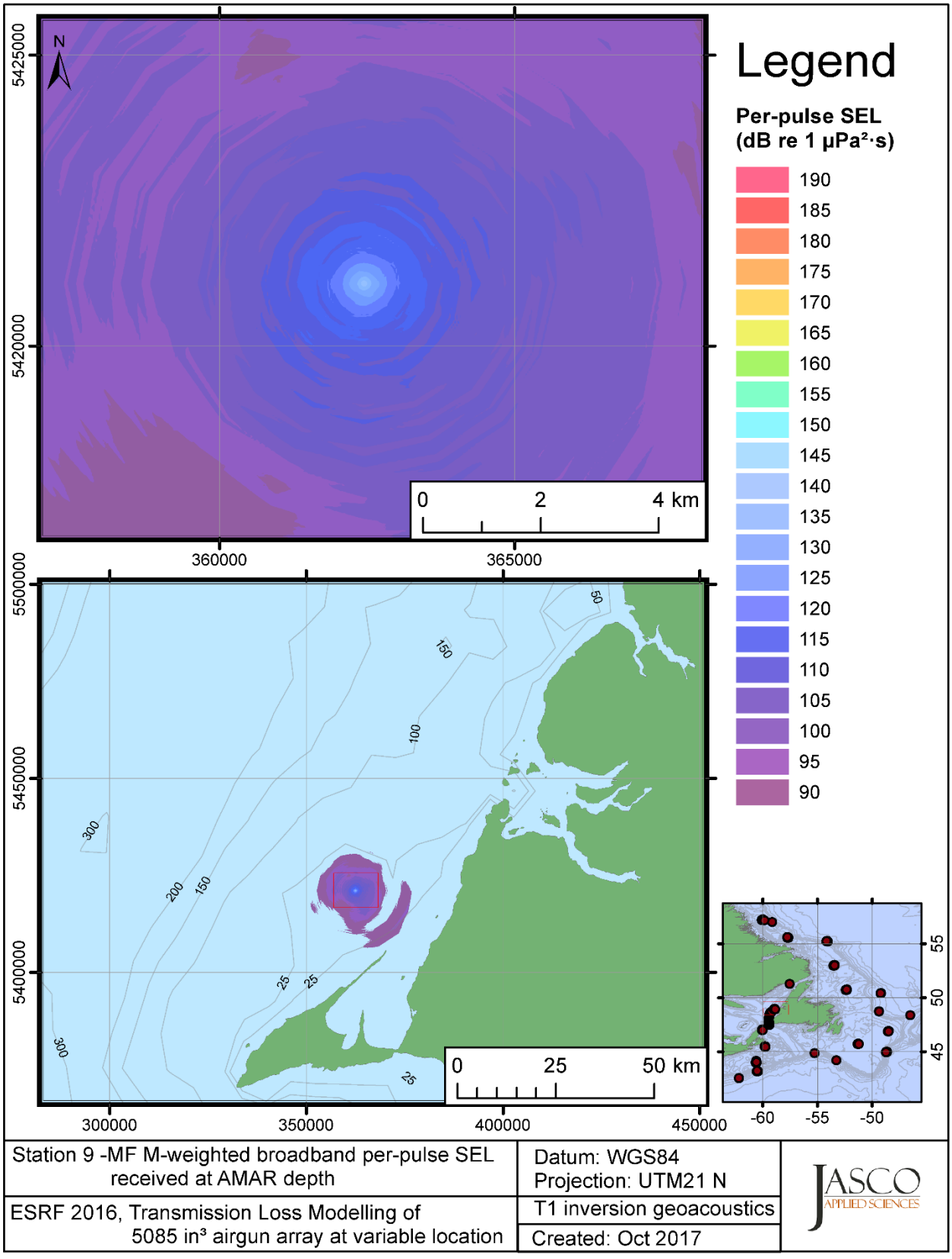

Figure C-105. Stn 9, MF M-weighted SEL received at the AMAR location and depth, modelled using the track 1 inversion geoacoustic bottom, with GDEM July SSP and the airgun array located at any point on the map.

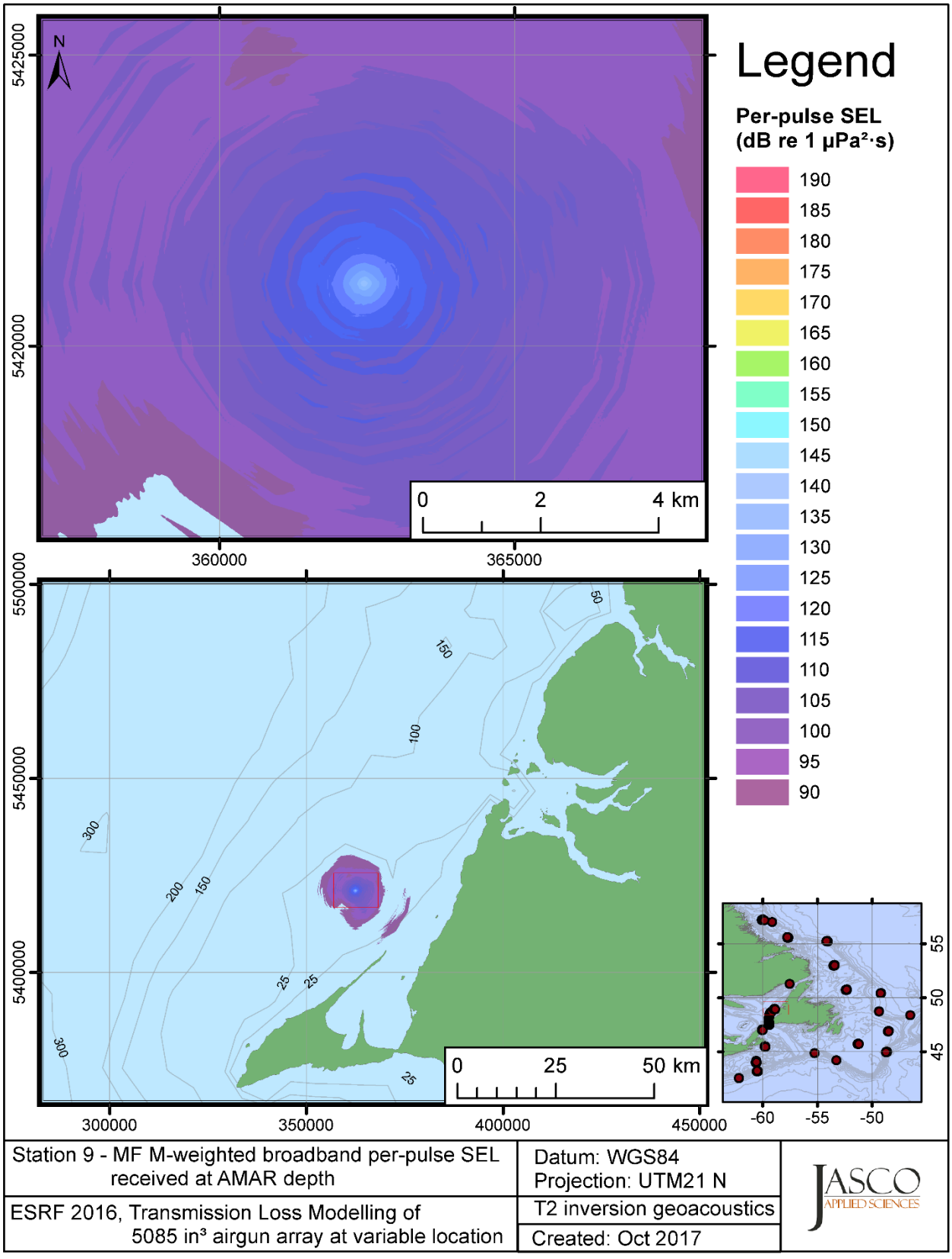

Figure C-106. Stn 9, MF M-weighted SEL received at the AMAR location and depth, modelled using the track 2 inversion geoacoustic bottom, with GDEM July SSP and the airgun array located at any point on the map.

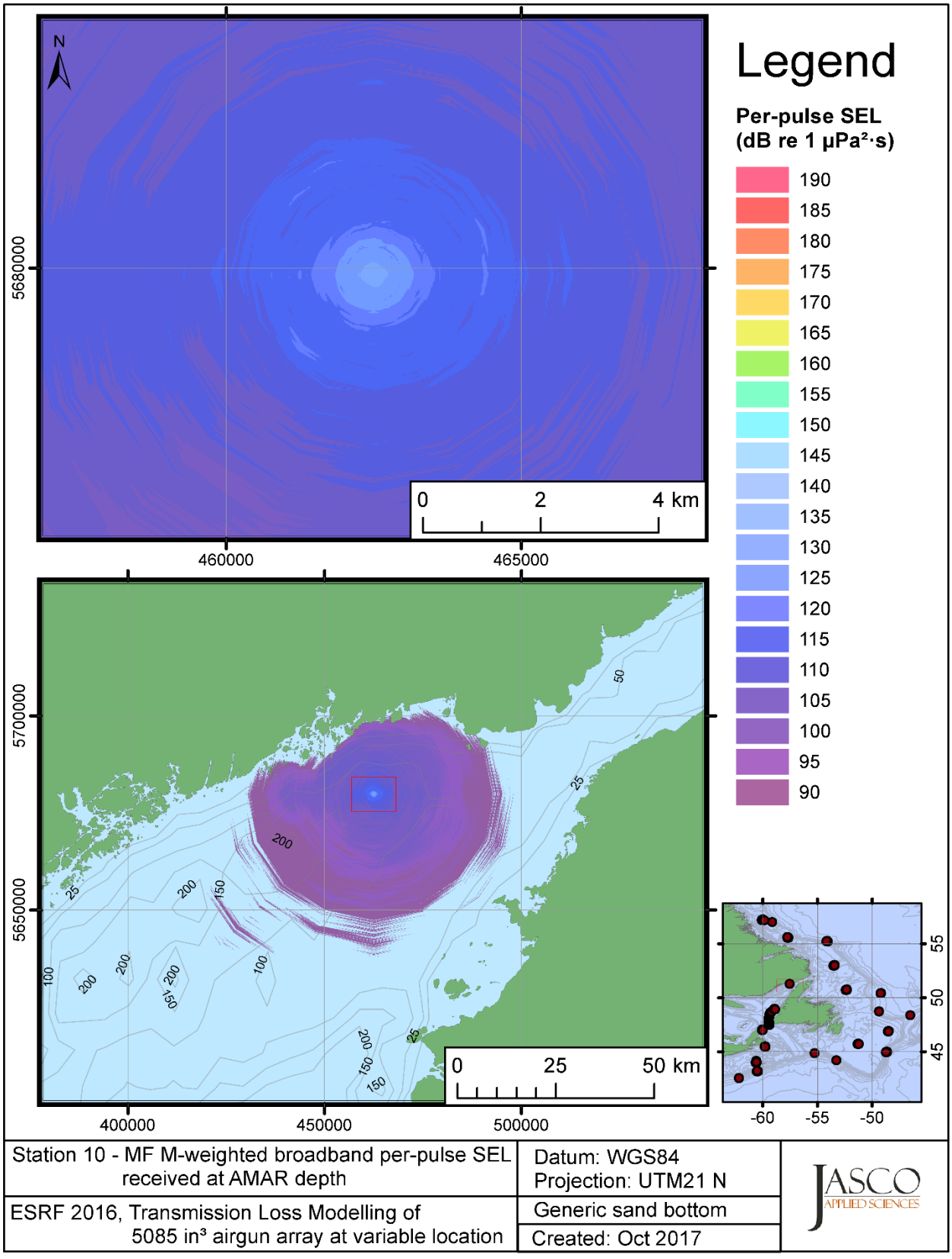

Figure C-107. Stn 10, MF M-weighted SEL received at the AMAR location and depth, modelled using a generic sand bottom, with in-situ July SSP and the airgun array located at any point on the map.

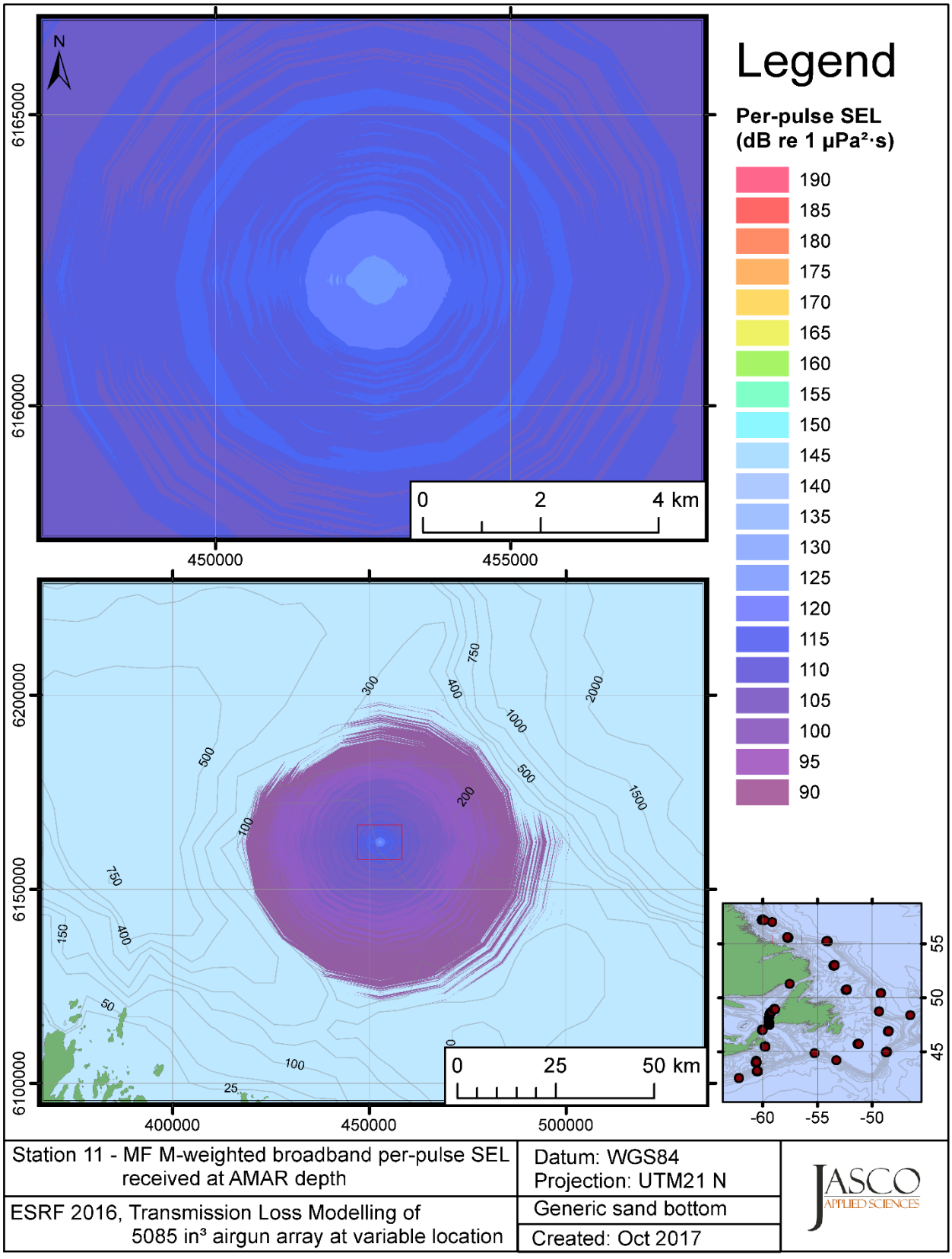

Figure C-108. Stn 11, MF M-weighted SEL received at the AMAR location and depth, modelled using a generic sand bottom, with in-situ July SSP and the airgun array located at any point on the map.

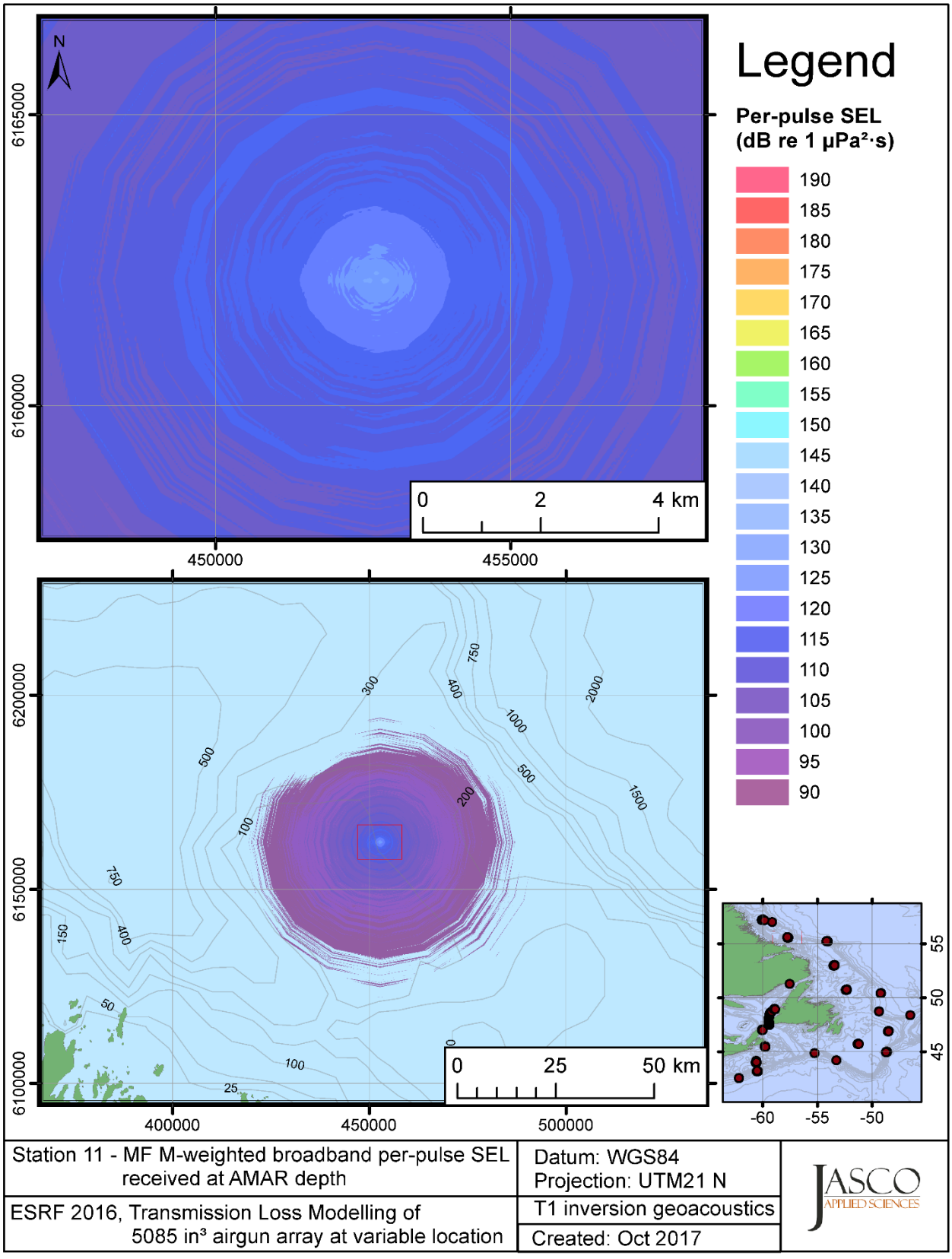

Figure C-109. Stn 11, MF M-weighted SEL received at the AMAR location and depth, modelled using the track 1 inversion geoacoustic bottom, with in-situ July SSP and the airgun array located at any point on the map.

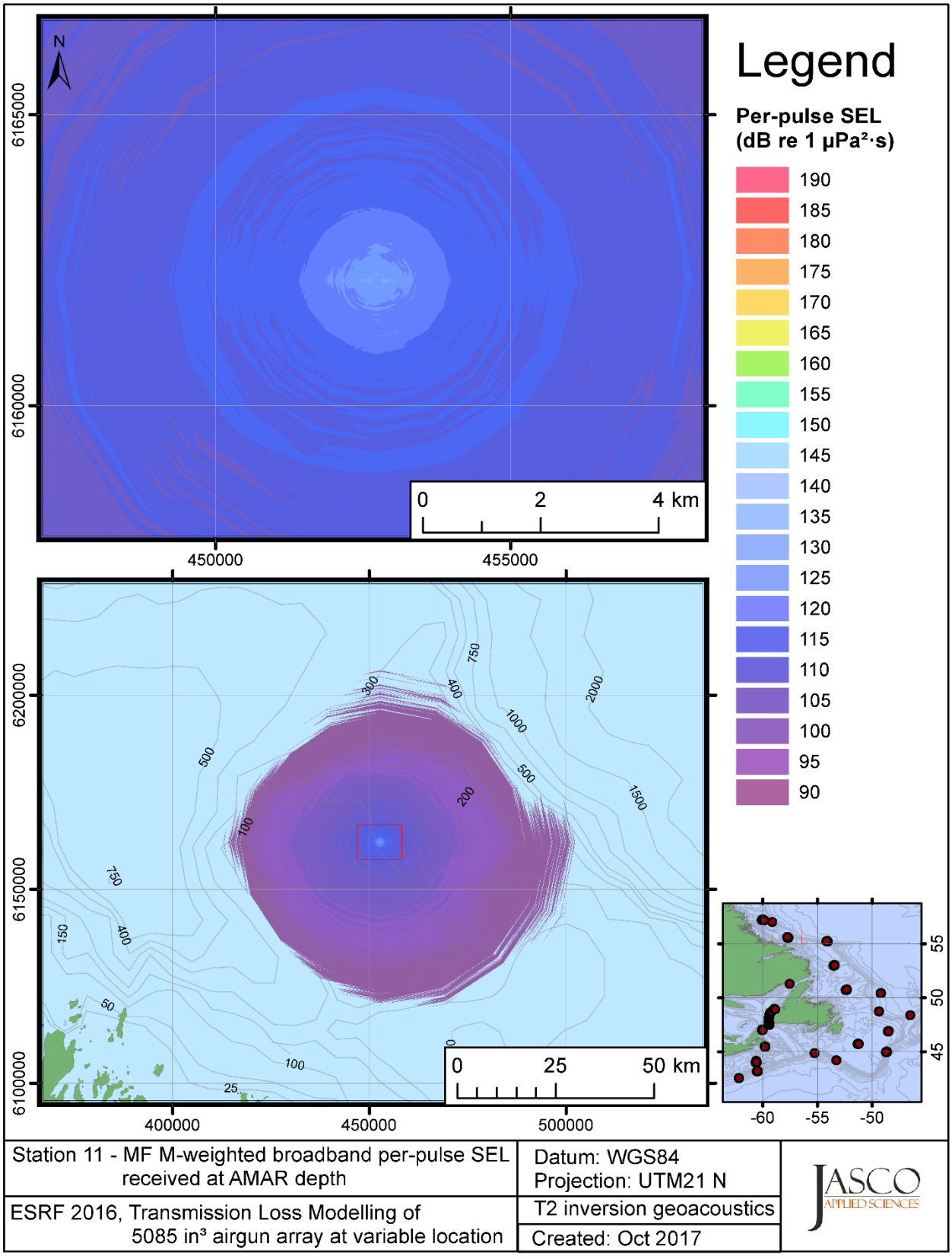

Figure C-110. Stn 11, MF M-weighted SEL received at the AMAR location and depth, modelled using the track 2 inversion geoacoustic bottom, with in-situ July SSP and the airgun array located at any point on the map.

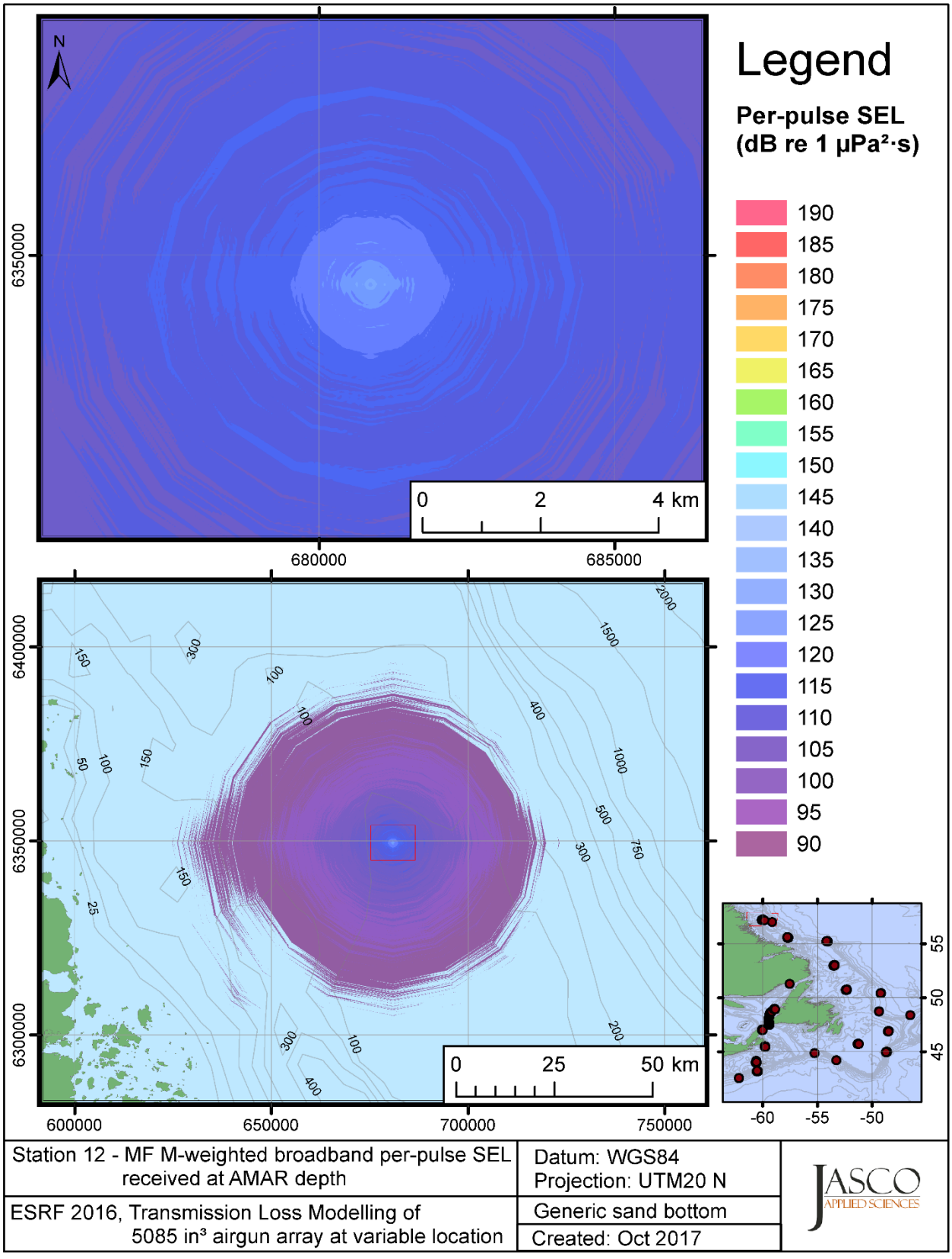

Figure C-111. Stn 12, MF M-weighted SEL received at the AMAR location and depth, modelled using a generic sand bottom, with in-situ July SSP and the airgun array located at any point on the map.

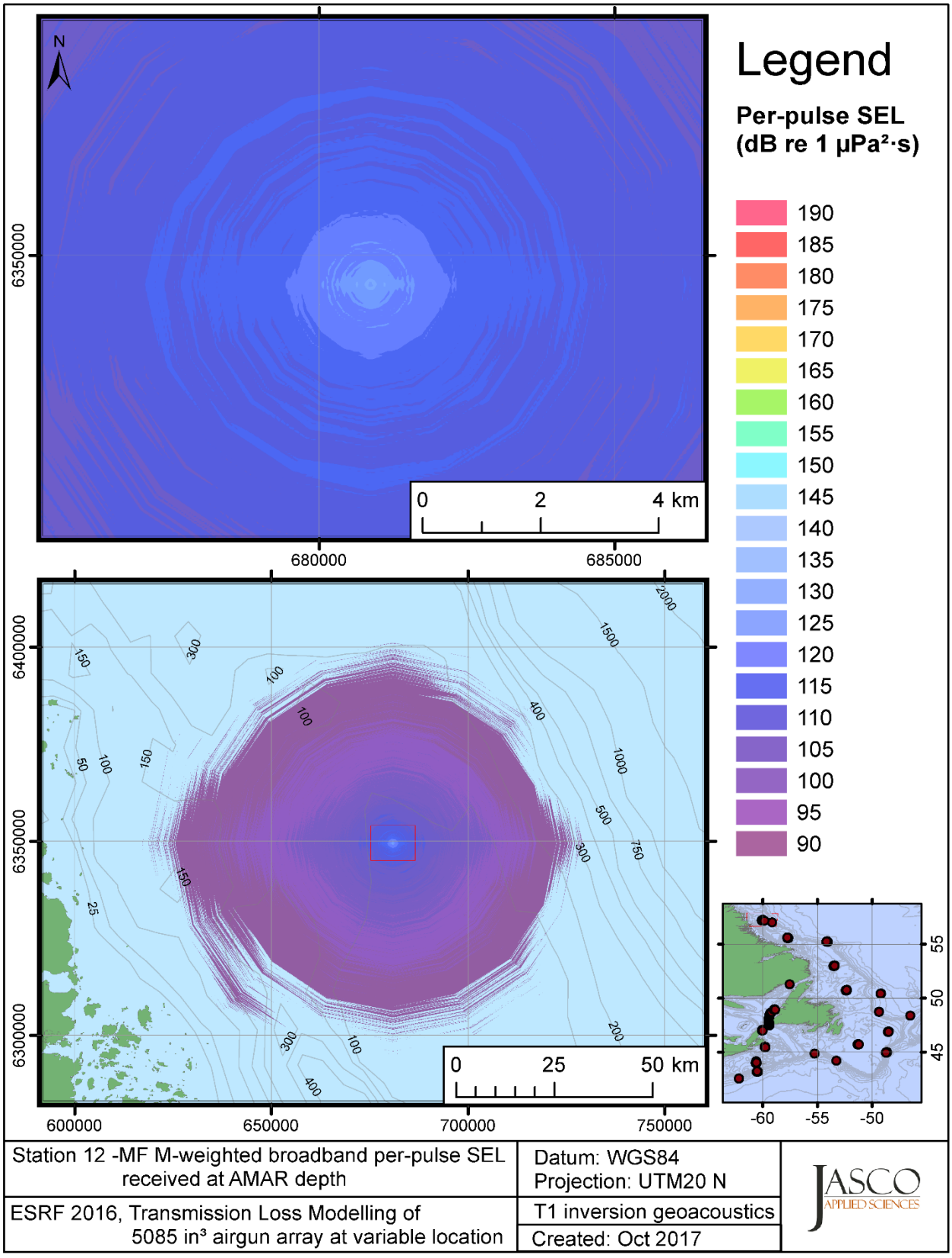

Figure C-112. Stn 12, MF M-weighted SEL received at the AMAR location and depth, modelled using the track 1 inversion geoacoustic bottom, with in-situ July SSP and the airgun array located at any point on the map.

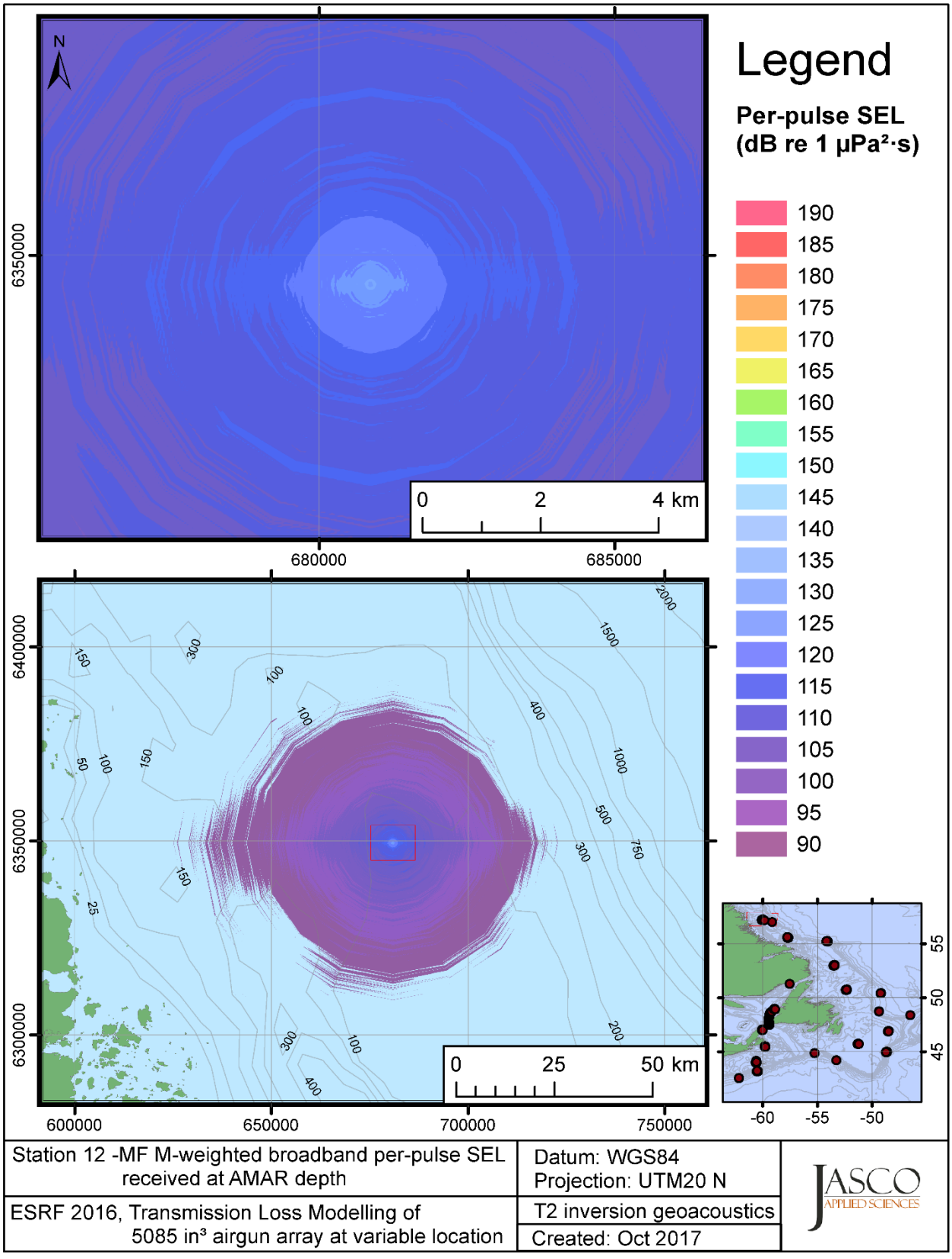

Figure C-113. Stn 12, MF M-weighted SEL received at the AMAR location and depth, modelled using the track 2 inversion geoacoustic bottom, with in-situ July SSP and the airgun array located at any point on the map.

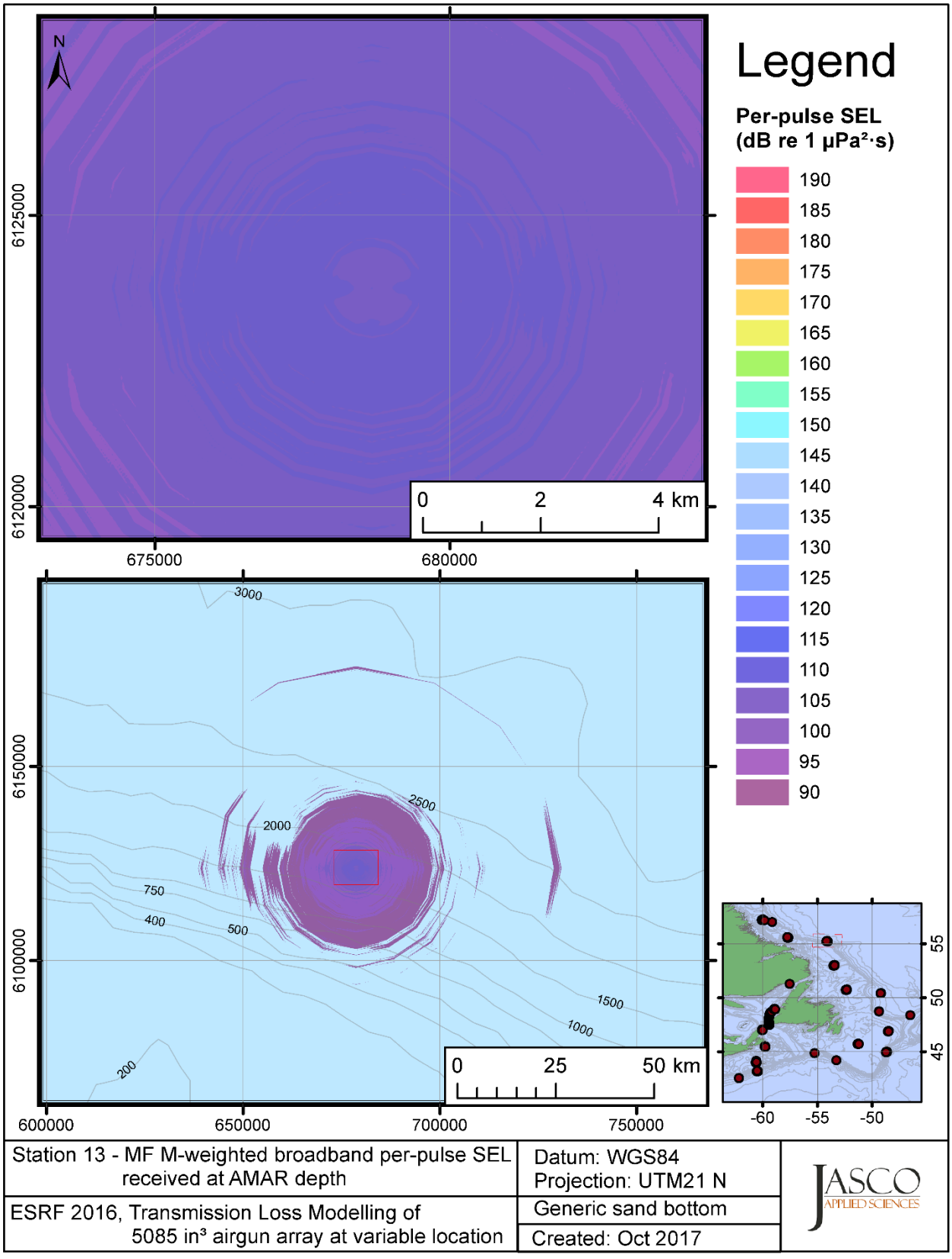

Figure C-114. Stn 13, MF M-weighted SEL received at the AMAR location and depth, modelled using a generic sand bottom, with in-situ July SSP and the airgun array located at any point on the map.

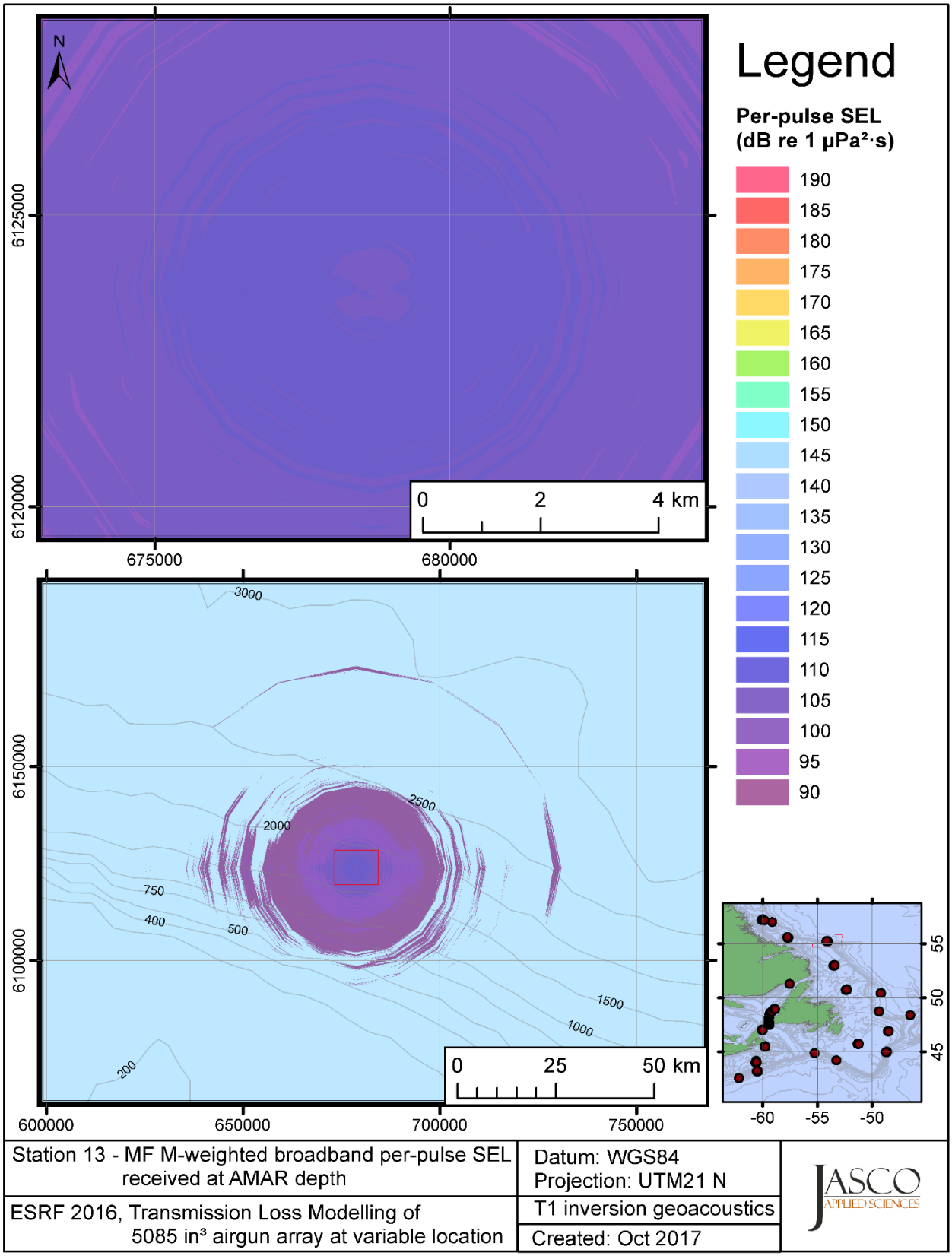

Figure C-115. Stn 13, MF M-weighted SEL received at the AMAR location and depth, modelled using the track 1 inversion geoacoustic bottom, with in-situ July SSP and the airgun array located at any point on the map.

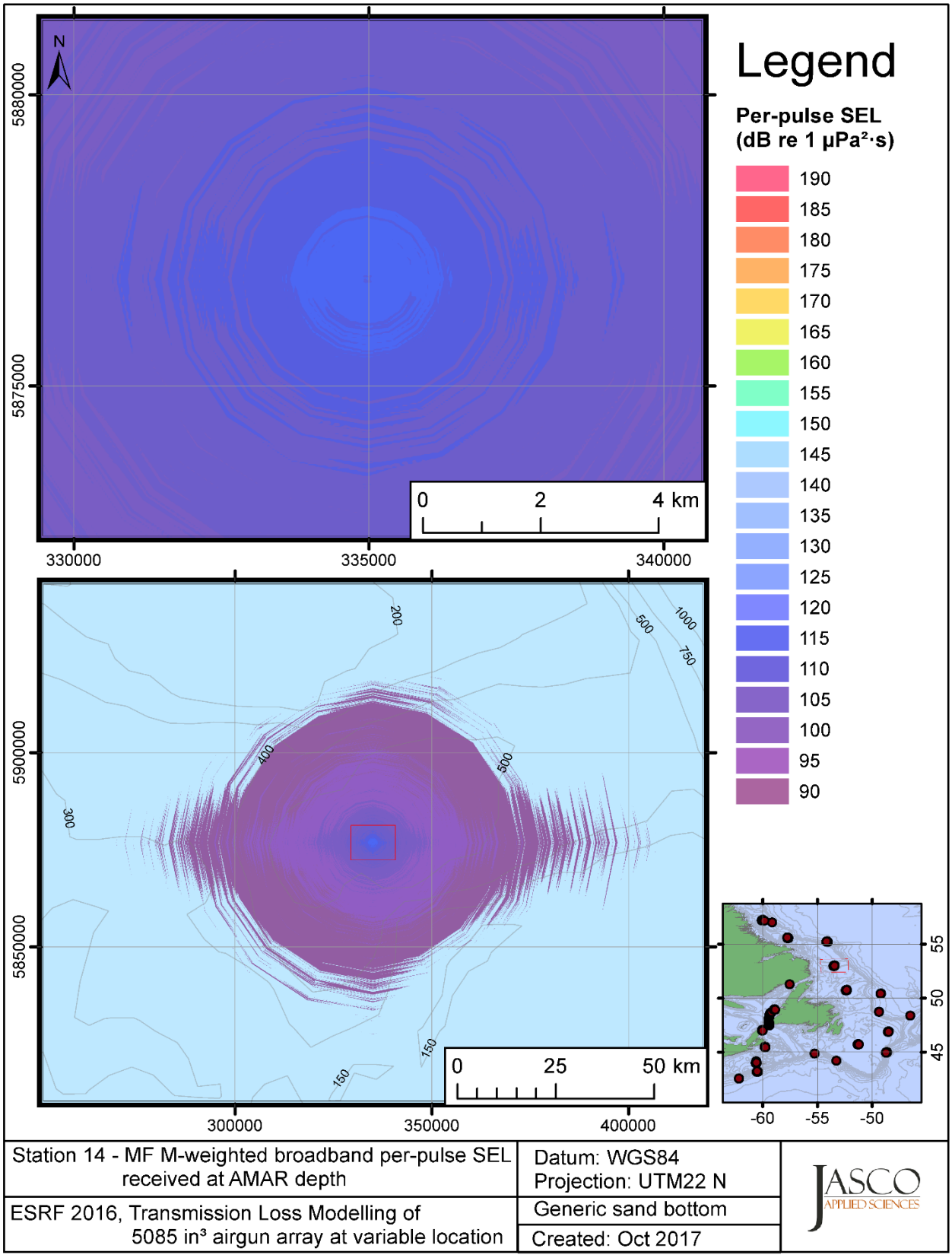

Figure C-116. Stn 14, MF M-weighted SEL received at the AMAR location and depth, modelled using a generic sand bottom, with in-situ July SSP and the airgun array located at any point on the map.

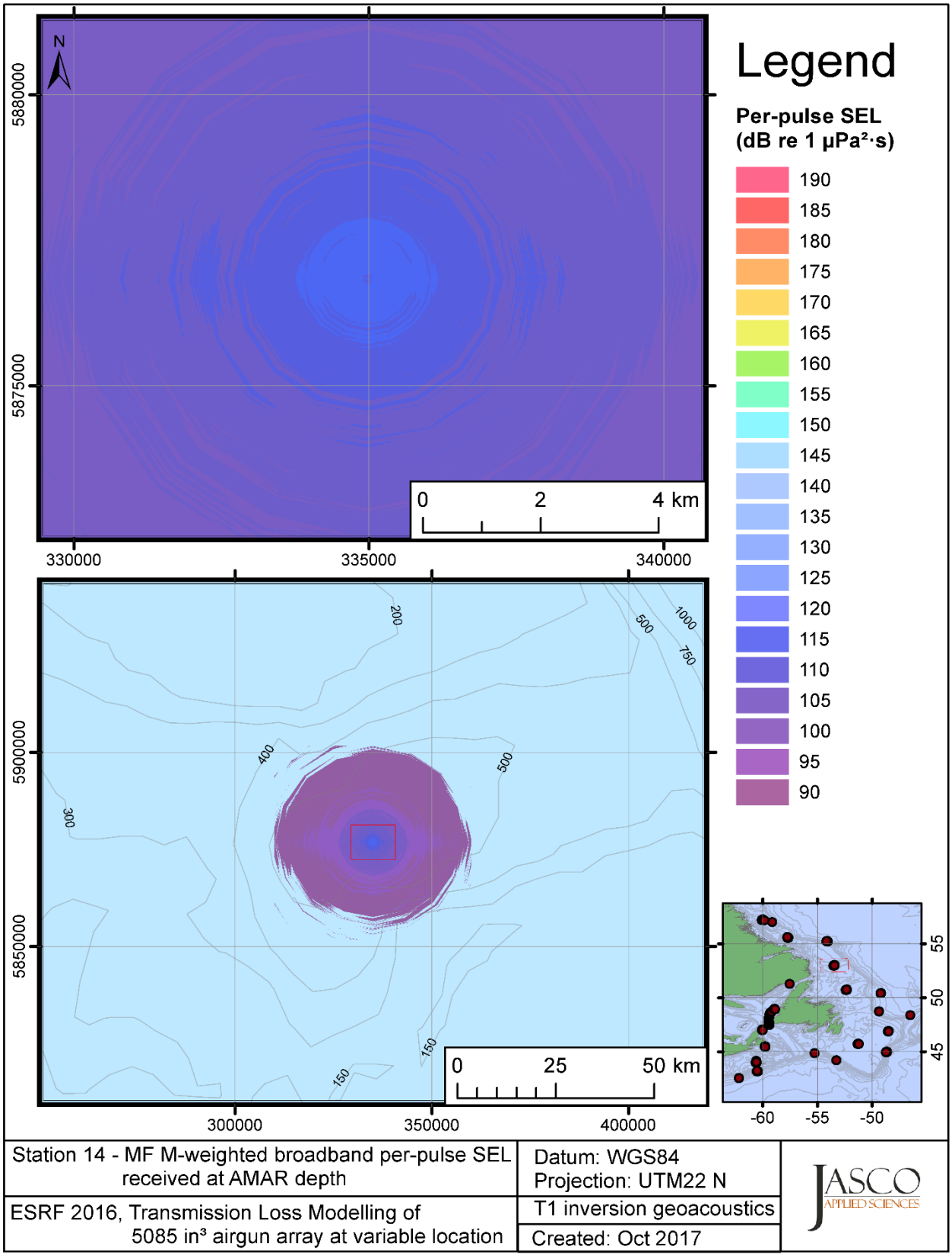

Figure C-117. Stn 14, MF M-weighted SEL received at the AMAR location and depth, modelled using the track 1 inversion geoacoustic bottom, with in-situ July SSP and the airgun array located at any point on the map.

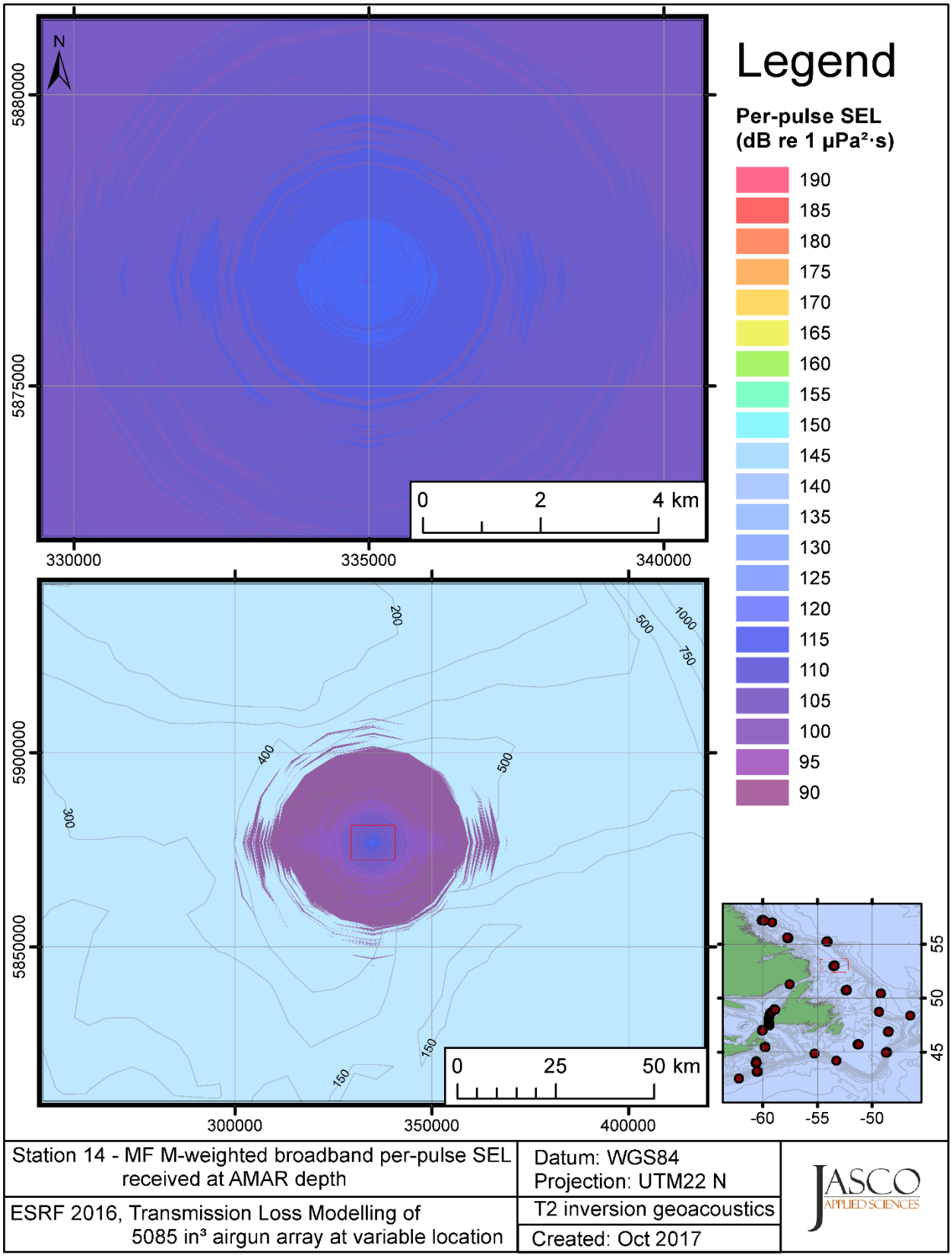

Figure C-118. Stn 14, MF M-weighted SEL received at the AMAR location and depth, modelled using the track 2 inversion geoacoustic bottom, with in-situ July SSP and the airgun array located at any point on the map.

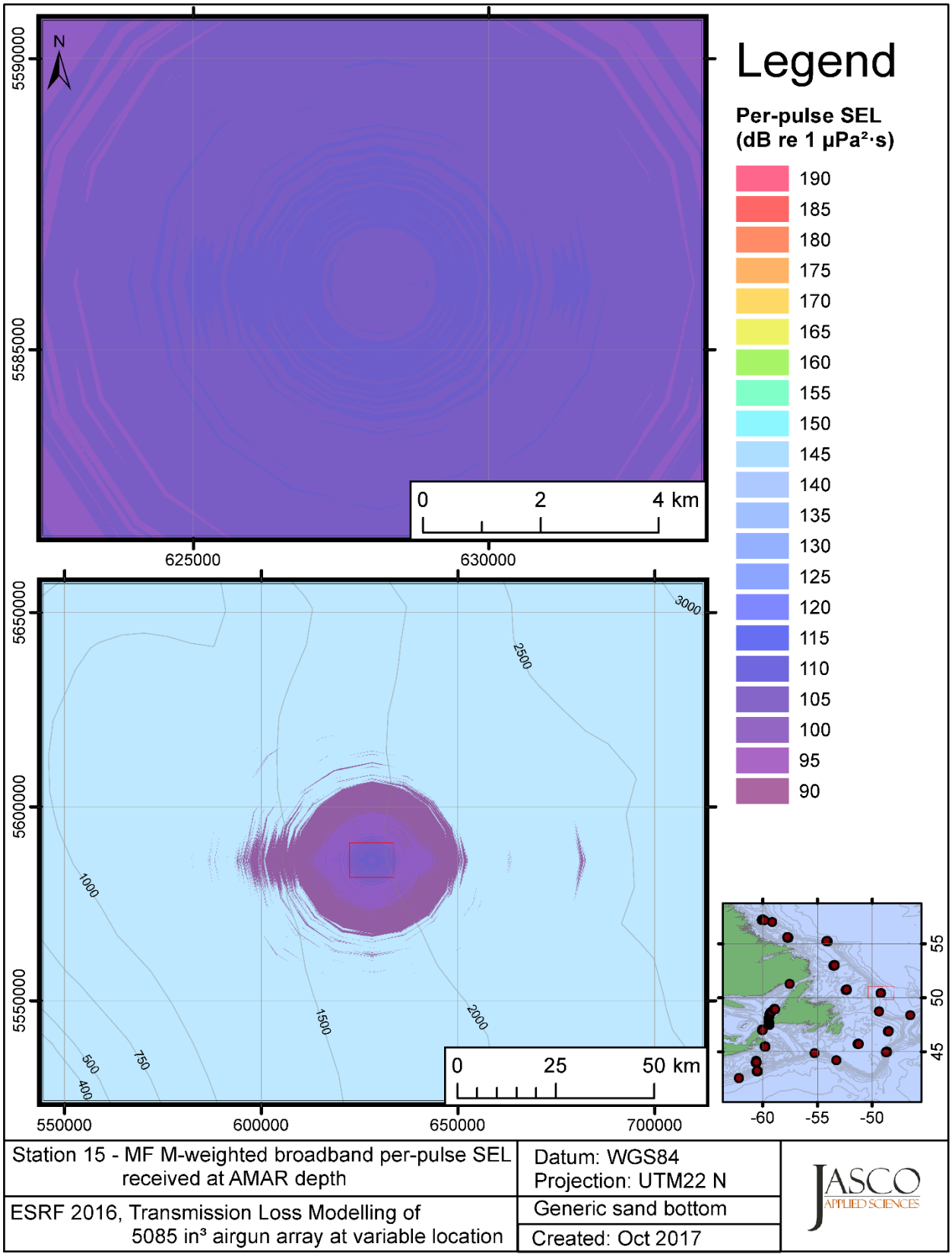

Figure C-119. Stn 15, MF M-weighted SEL received at the AMAR location and depth, modelled using a generic sand bottom, with in-situ July SSP and the airgun array located at any point on the map.

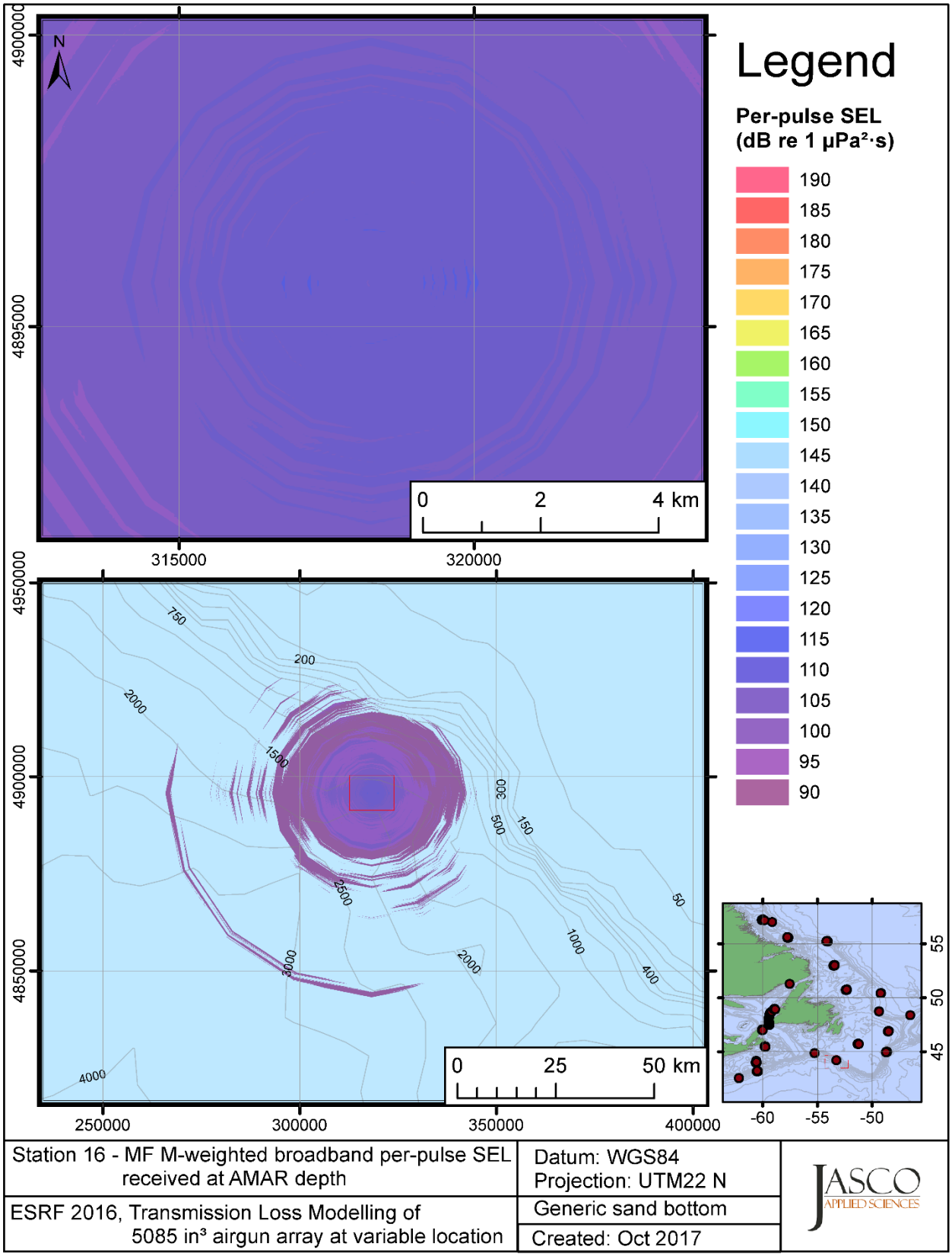

Figure C-120. Stn 16, MF M-weighted SEL received at the AMAR location and depth, modelled using a generic sand bottom, with in-situ July SSP and the airgun array located at any point on the map.

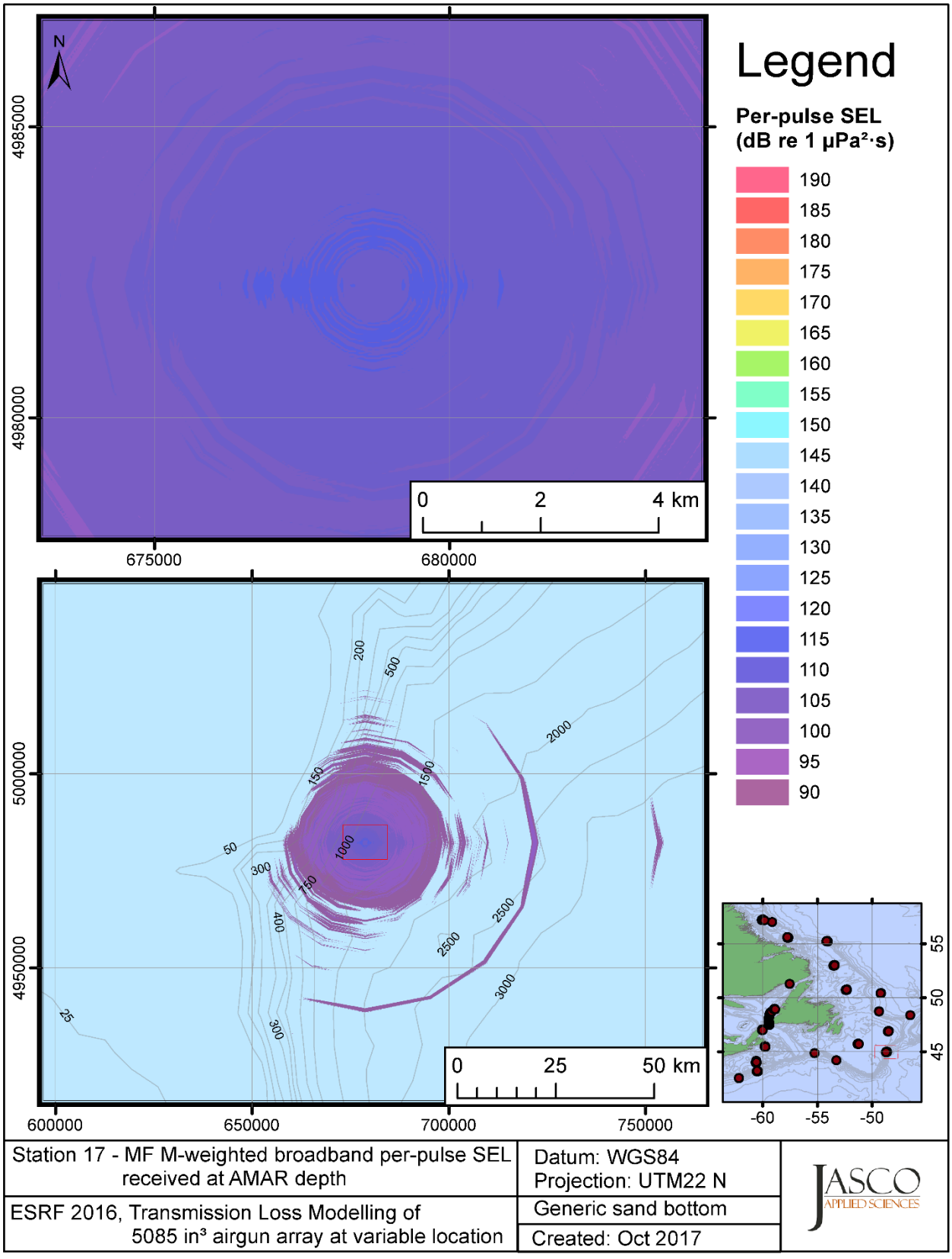

Figure C-121. Stn 17, MF M-weighted SEL received at the AMAR location and depth, modelled using a generic sand bottom, with in-situ July SSP and the airgun array located at any point on the map.

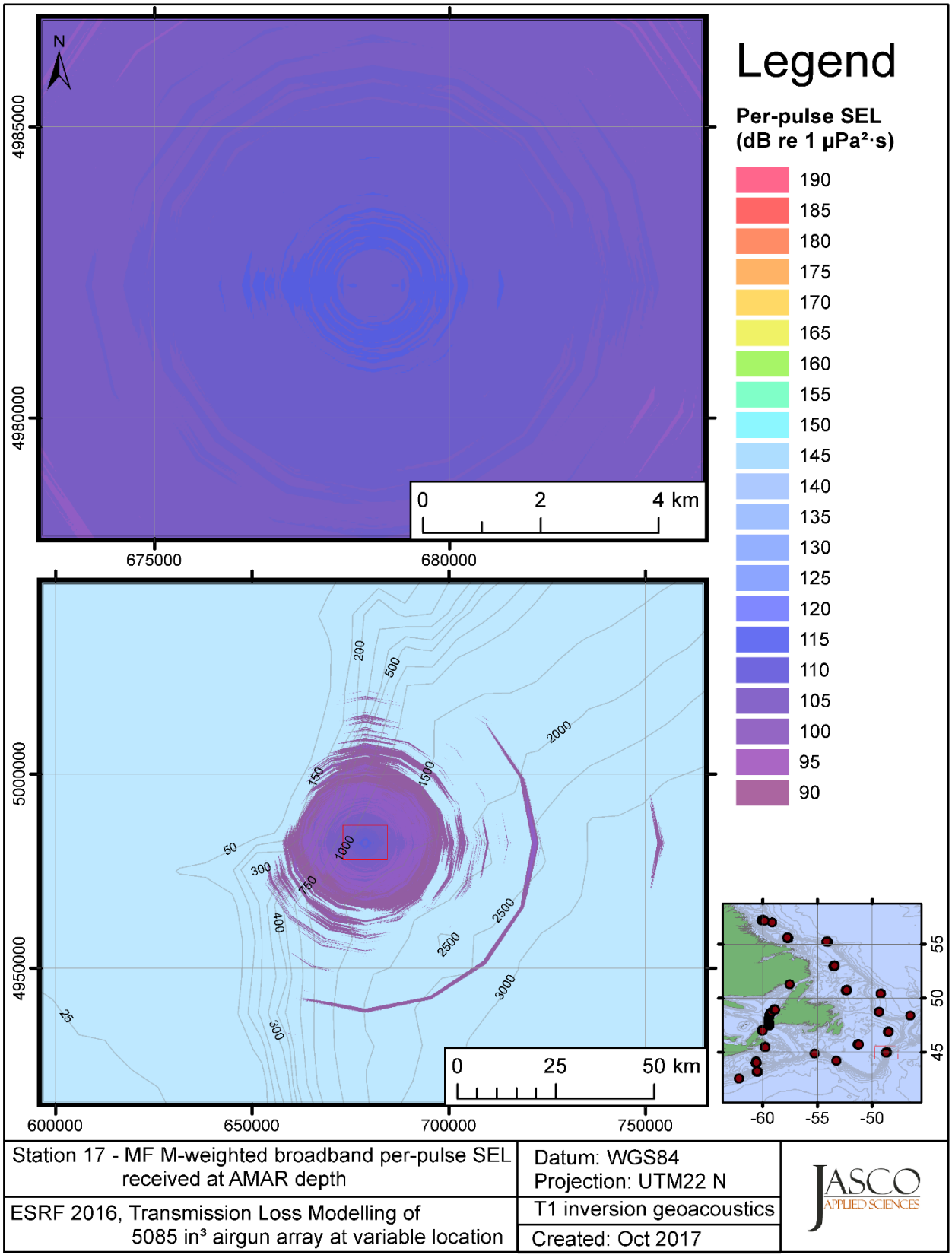

Figure C-122. Stn 17, MF M-weighted SEL received at the AMAR location and depth, modelled using the track 1 inversion geoacoustic bottom, with in-situ July SSP and the airgun array located at any point on the map.

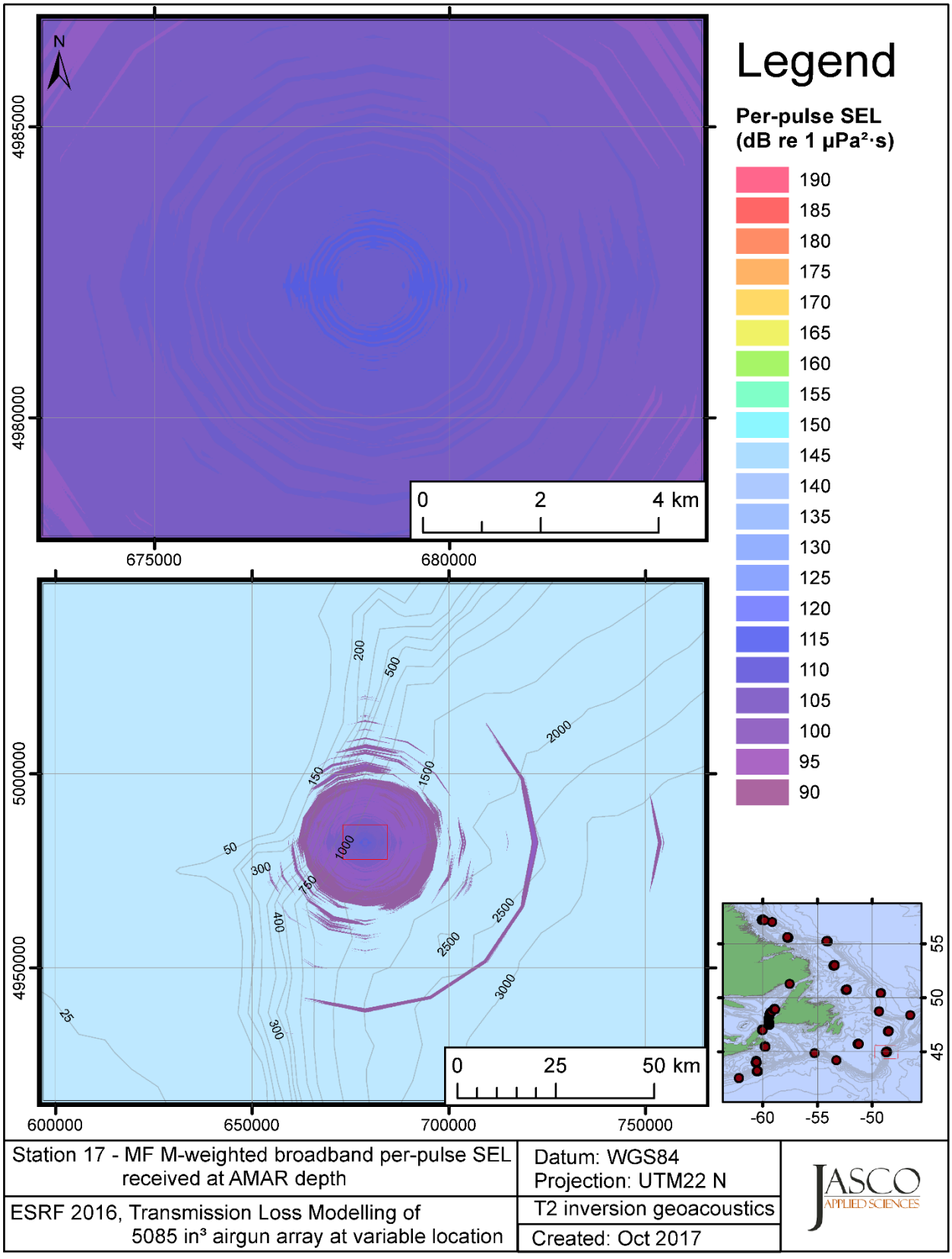

Figure C-123. Stn 17, MF M-weighted SEL received at the AMAR location and depth, modelled using the track 2 inversion geoacoustic bottom, with in-situ July SSP and the airgun array located at any point on the map.

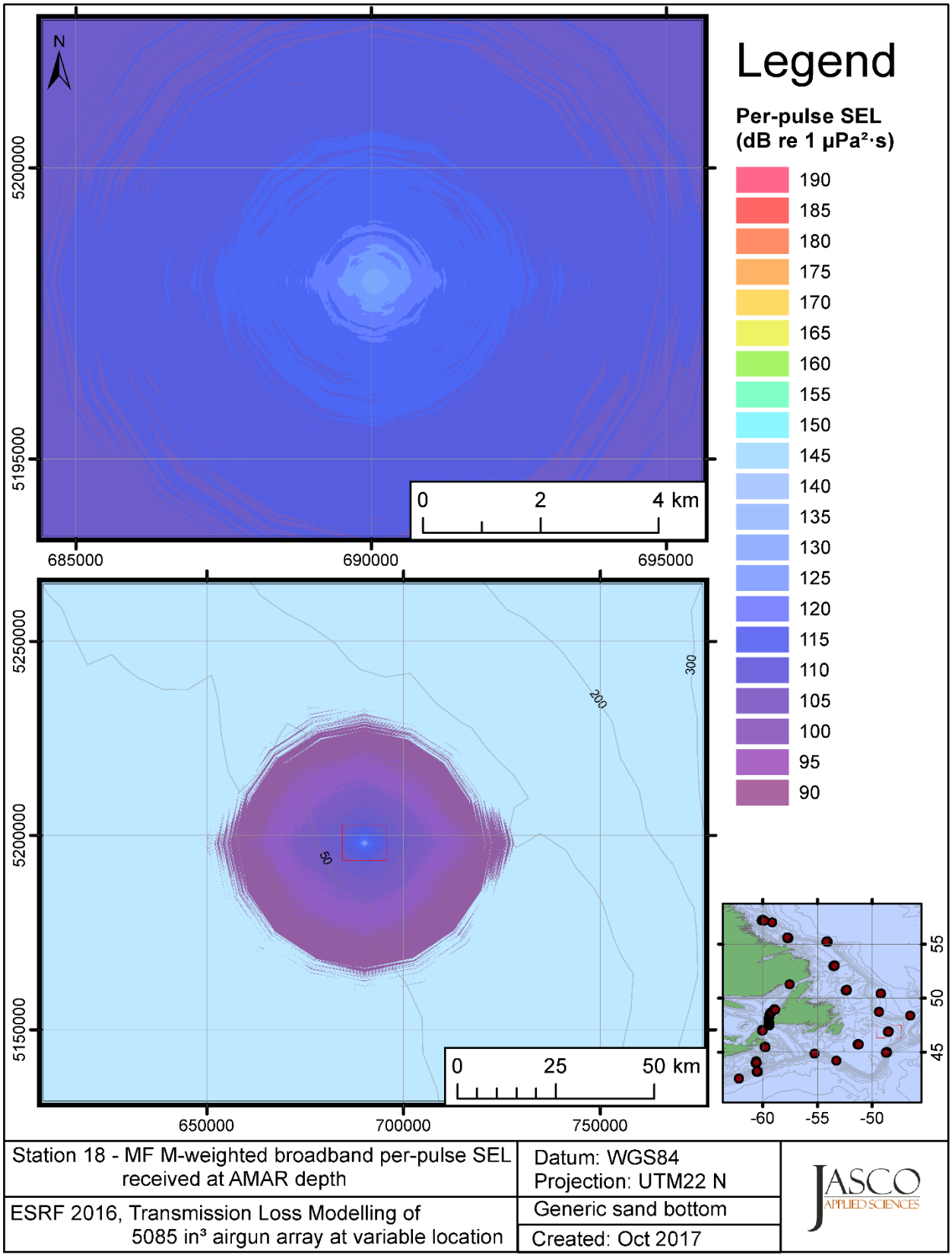

Figure C-124. Stn 18, MF M-weighted SEL received at the AMAR location and depth, modelled using a generic sand bottom, with in-situ July SSP and the airgun array located at any point on the map.

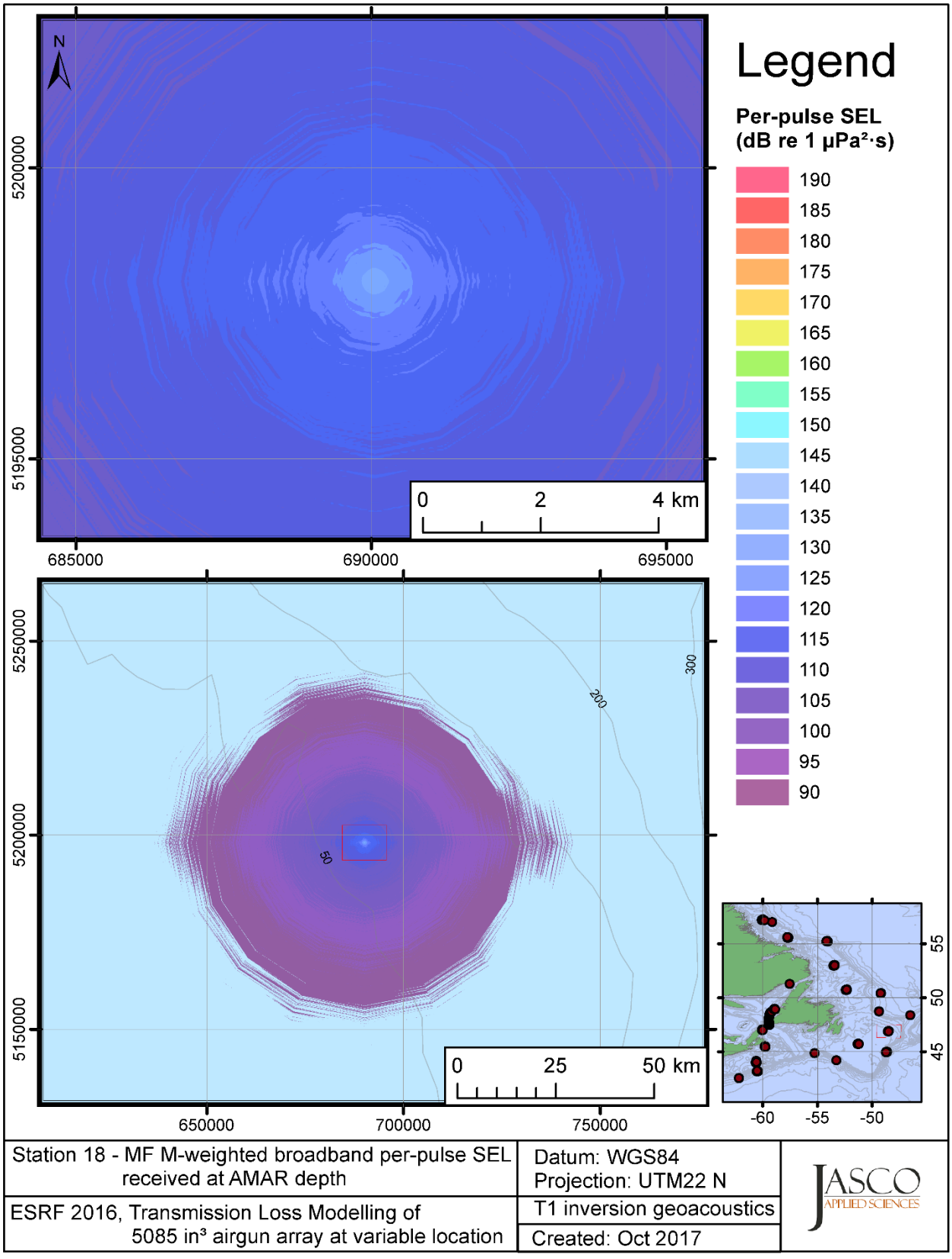

Figure C-125. Stn 18, MF M-weighted SEL received at the AMAR location and depth, modelled using the track 1 inversion geoacoustic bottom, with in-situ July SSP and the airgun array located at any point on the map.

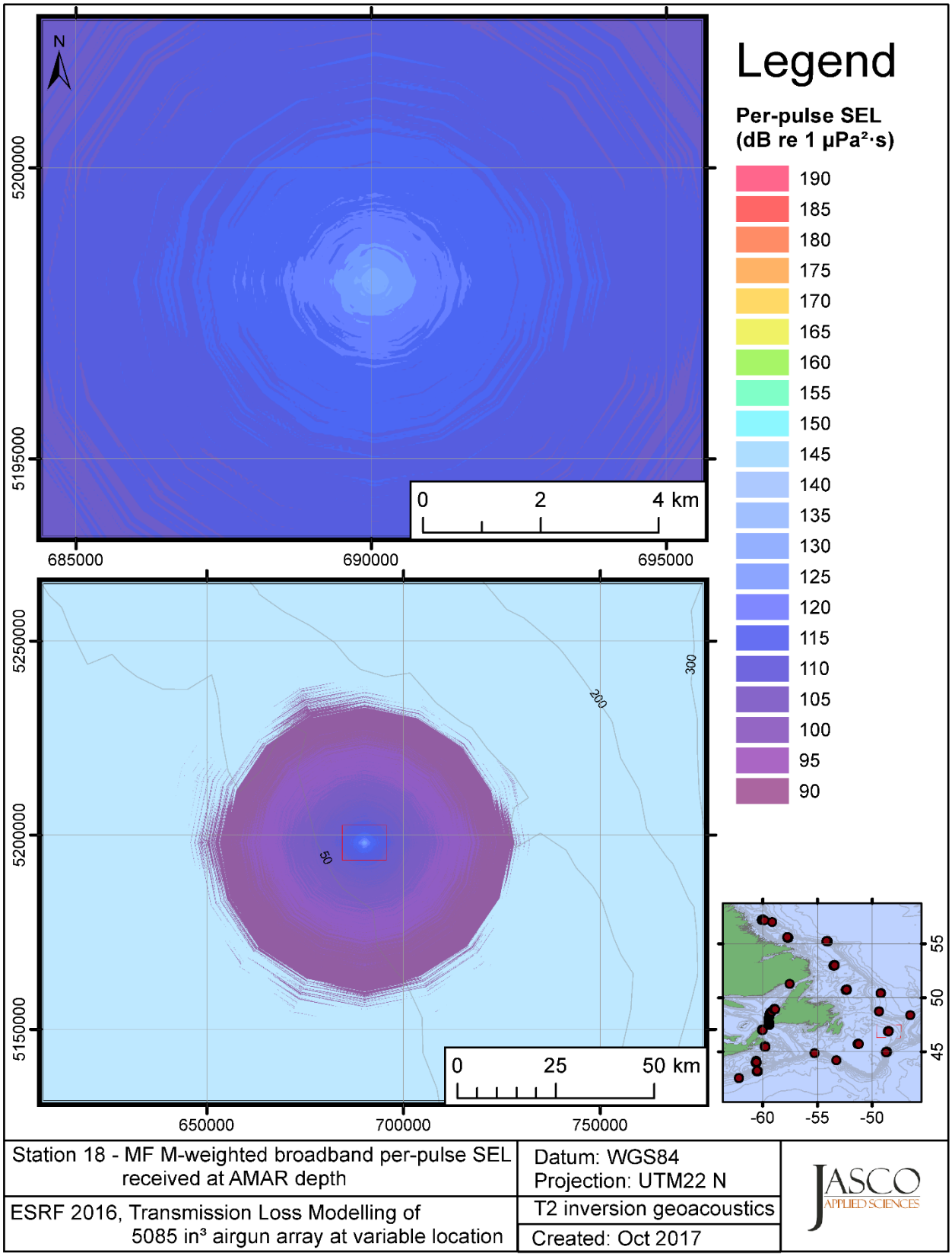

Figure C-126. Stn 18, MF M-weighted SEL received at the AMAR location and depth, modelled using the track 2 inversion geoacoustic bottom, with in-situ July SSP and the airgun array located at any point on the map.

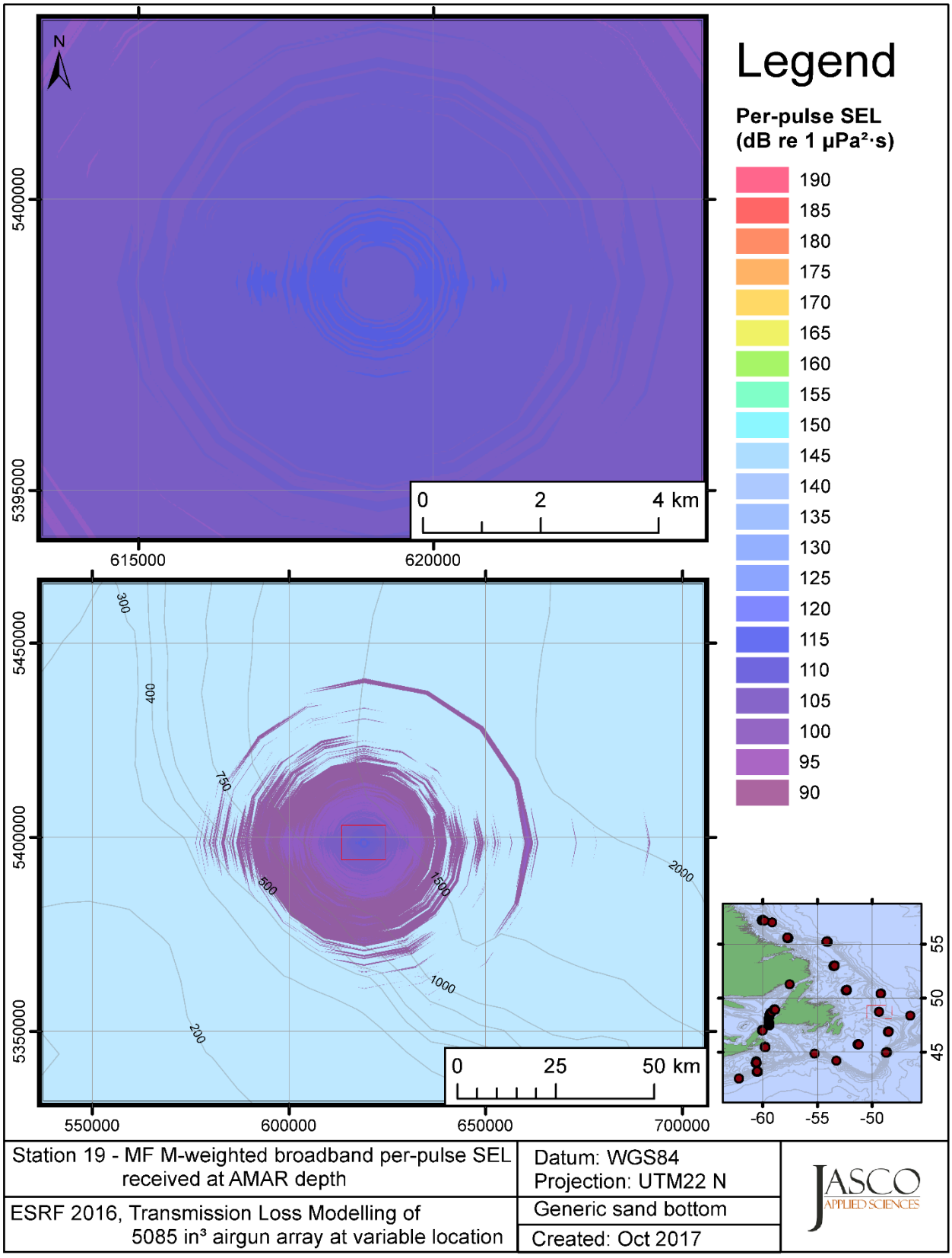

Figure C-127. Stn 19, MF M-weighted SEL received at the AMAR location and depth, modelled using a generic sand bottom, with in-situ July SSP and the airgun array located at any point on the map.

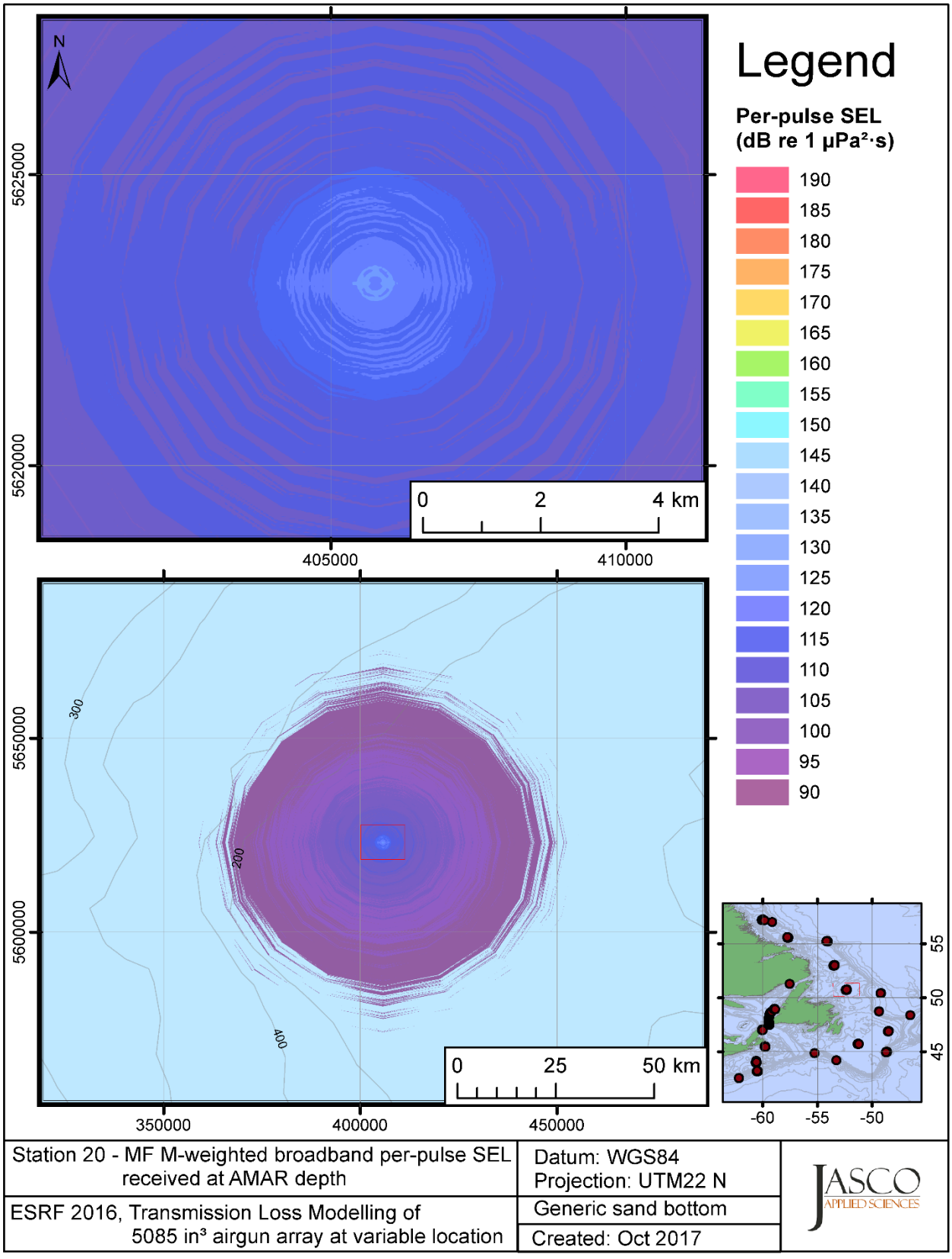

Figure C-128. Stn 20, MF M-weighted SEL received at the AMAR location and depth, modelled using a generic sand bottom, with in-situ July SSP and the airgun array located at any point on the map.

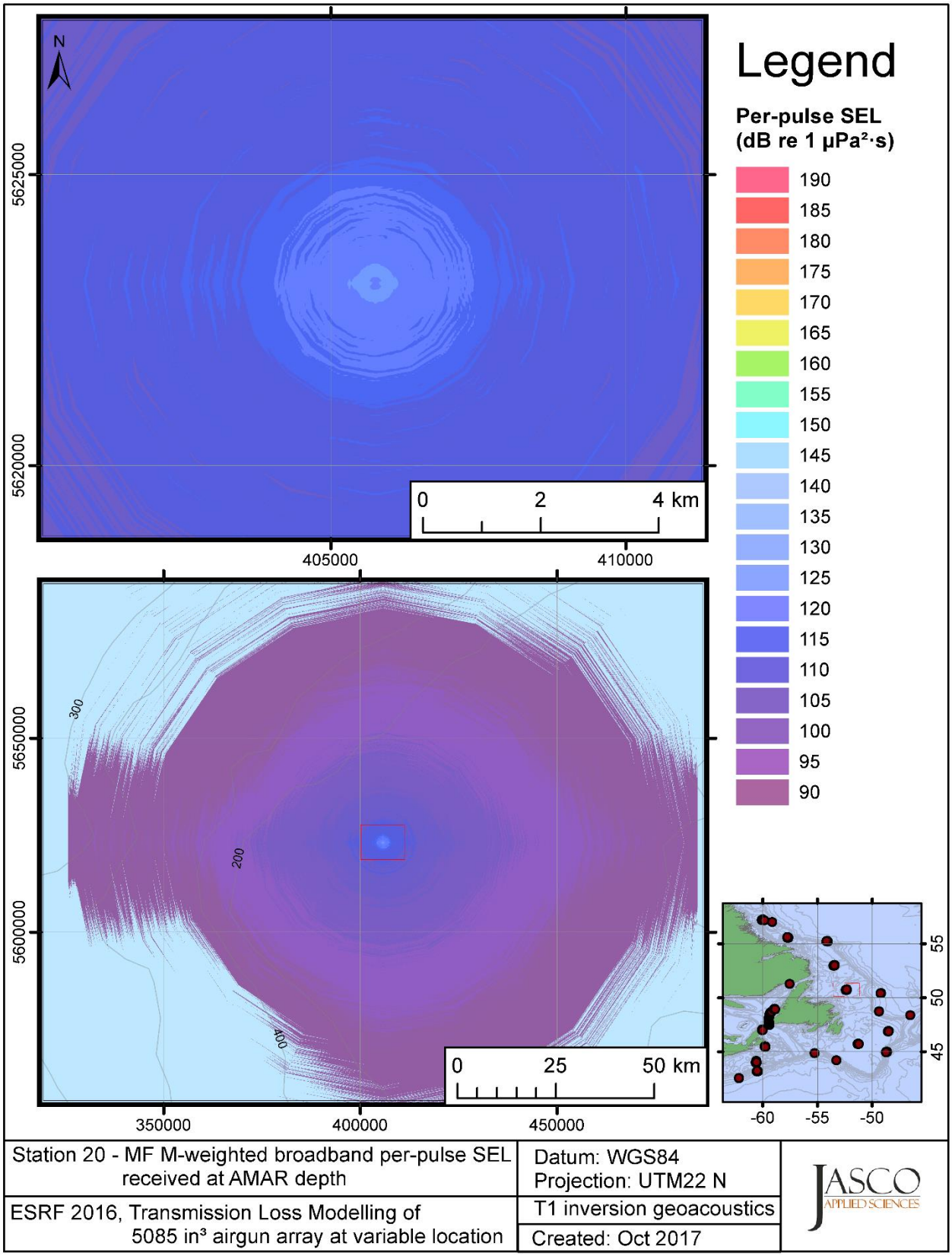

Figure C-129. Stn 20, MF M-weighted SEL received at the AMAR location and depth, modelled using the track 1 inversion geoacoustic bottom, with in-situ July SSP and the airgun array located at any point on the map.

C.4. Modelling HF M-weighted Received Level at the AMAR Location

This section presents the results of modelling the per-pulse sound exposure level (SEL) received at the AMAR location and depth as a function of the source location (varied in range and azimuth) for each of the 20 sites using a generic sand bottom; in addition, the modelling is repeated using the geoacoustic inversion bottom parameters at the 14 sites where they are available. The modelling results are presented in the form of coloured maps where the colour at any map location represents the predicted received level at the AMAR for the source located at that spot on the map. This section includes only the high-frequency cetaceans (HF) marine-mammal-weighted per-pulse SEL results; additional maps for other marine mammal received level auditory weighting functions are presented in adjoining sections.

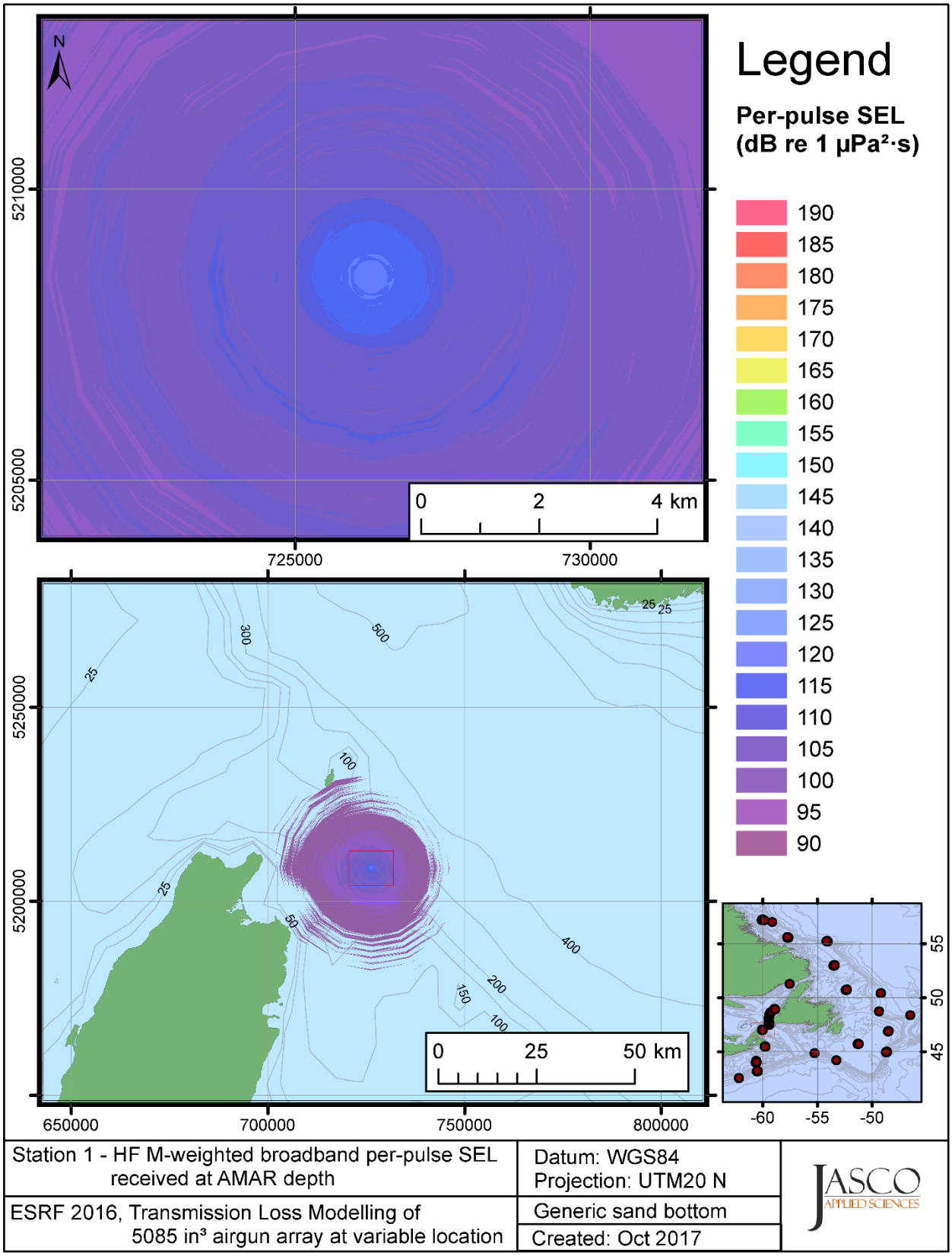

Figure C-130. Stn 1, HF M-weighted SEL received at the AMAR location and depth, modelled using a generic sand bottom, with in-situ July SSP and the airgun array located at any point on the map.

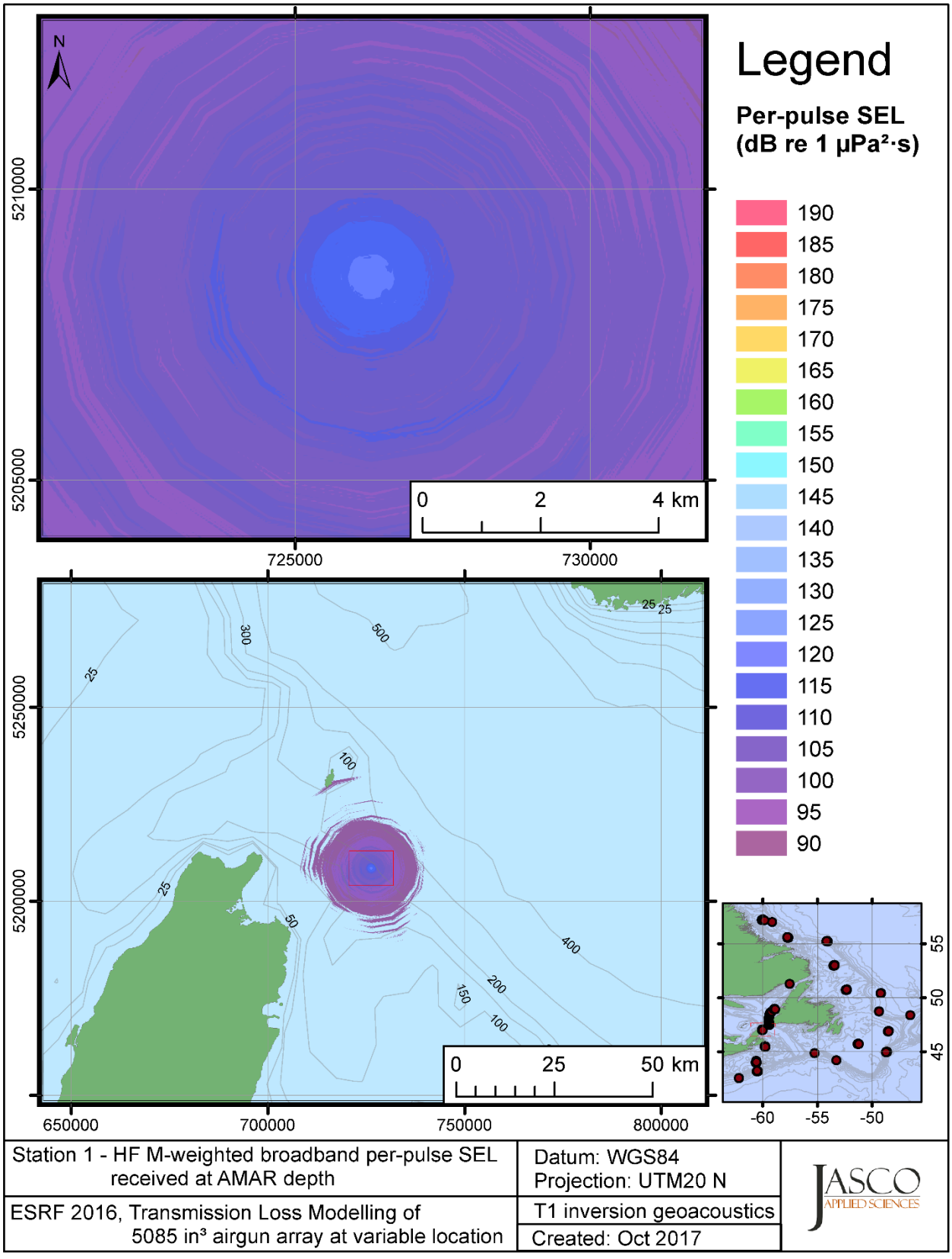

Figure C-131. Stn 1, HF M-weighted SEL received at the AMAR location and depth, modelled using the track 1 inversion geoacoustic bottom, with in-situ July SSP and the airgun array located at any point on the map.

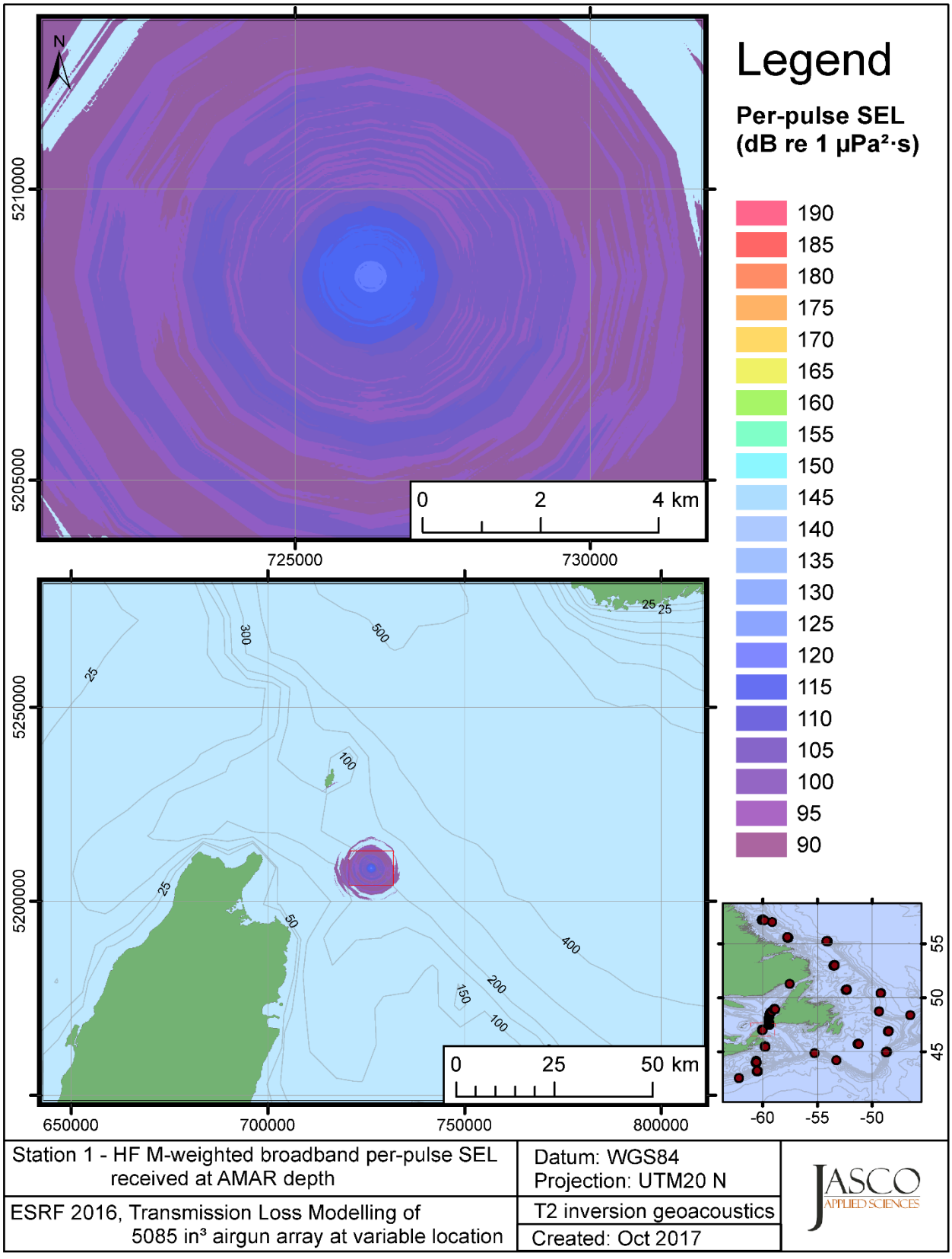

Figure C-132. Stn 1, HF M-weighted SEL received at the AMAR location and depth, modelled using the track 2 inversion geoacoustic bottom, with in-situ July SSP and the airgun array located at any point on the map.

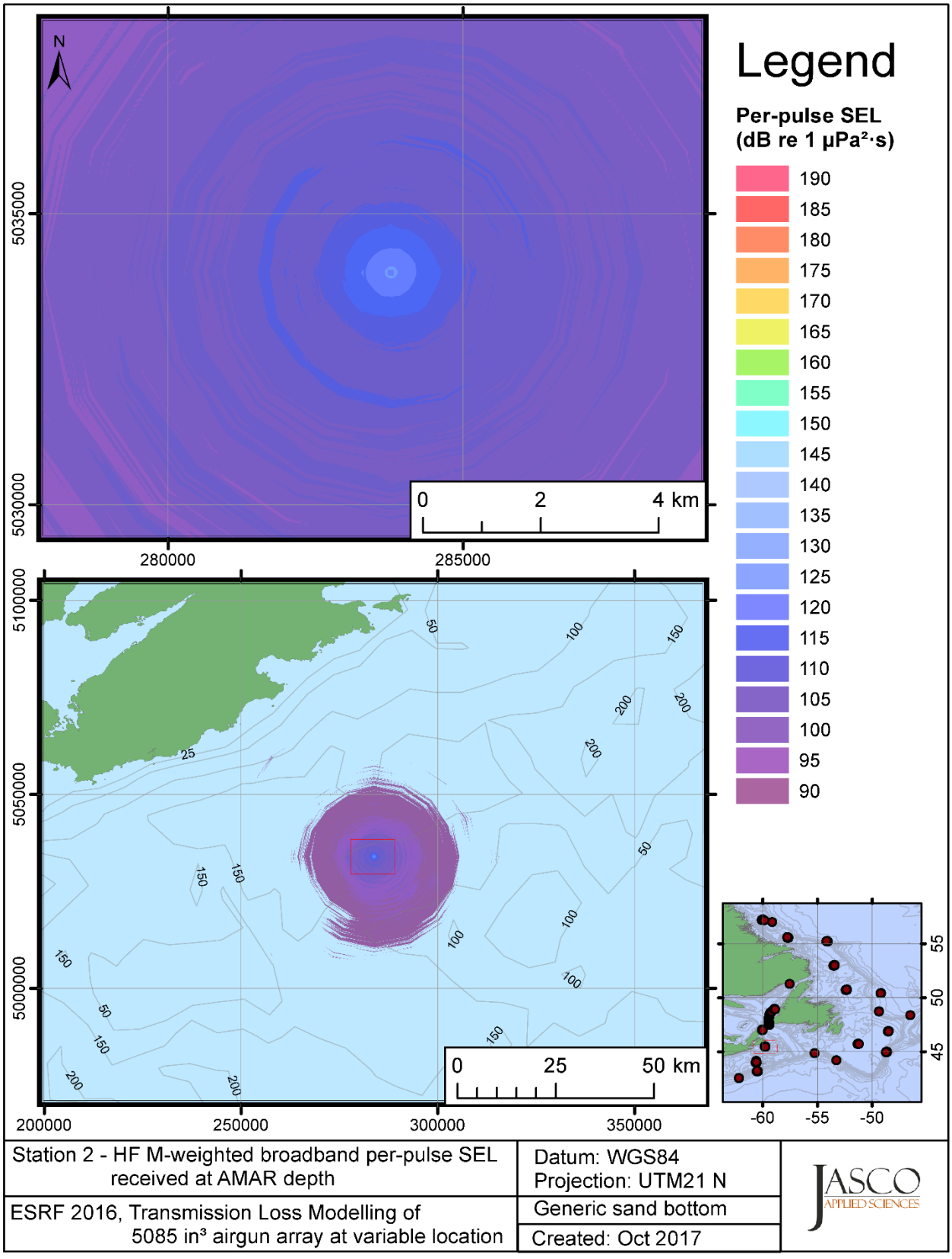

Figure C-133. Stn 2, HF M-weighted SEL received at the AMAR location and depth, modelled using a generic sand bottom, with in-situ July SSP and the airgun array located at any point on the map.

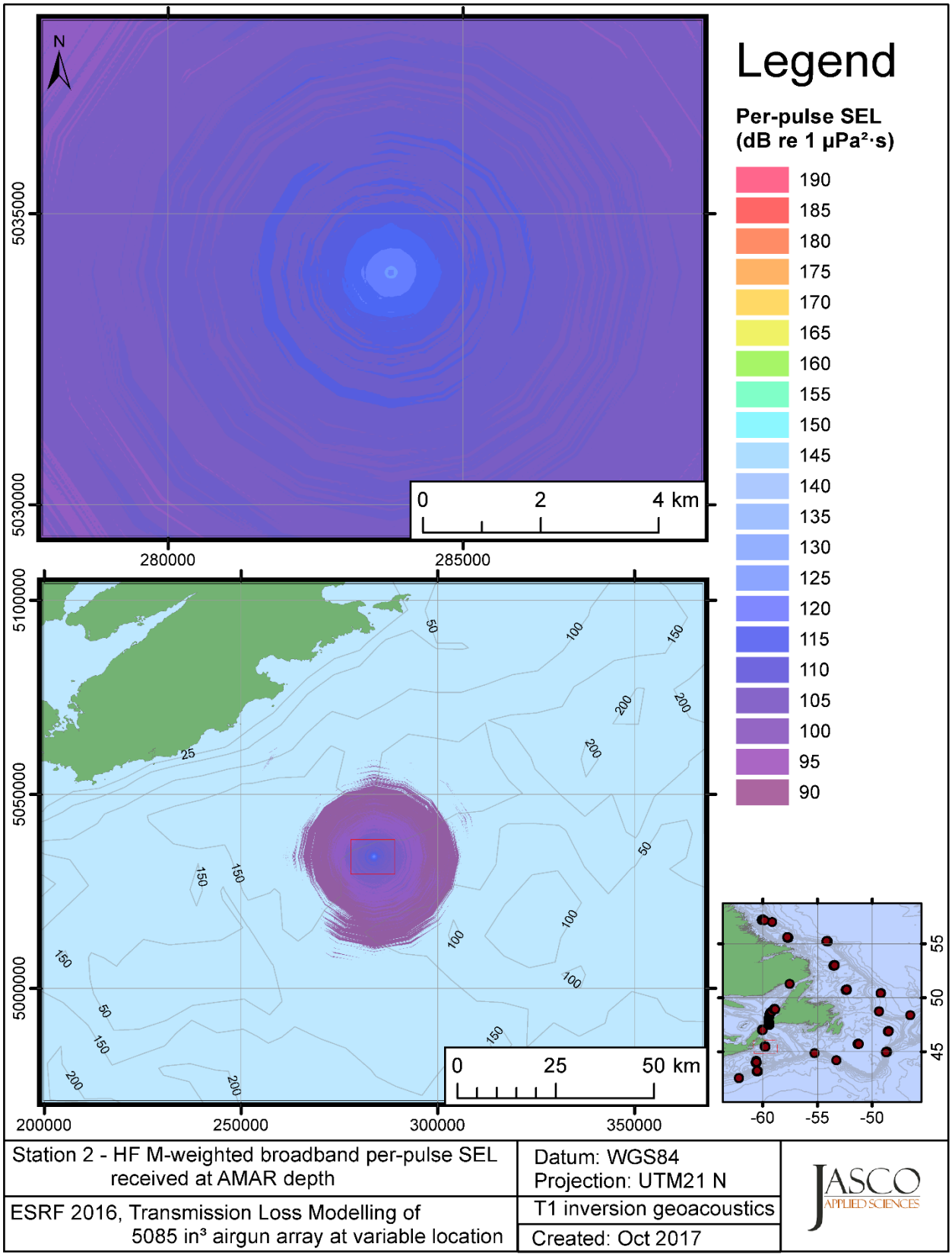

Figure C-134. Stn 2, HF M-weighted SEL received at the AMAR location and depth, modelled using the track 1 inversion geoacoustic bottom, with in-situ July SSP and the airgun array located at any point on the map.

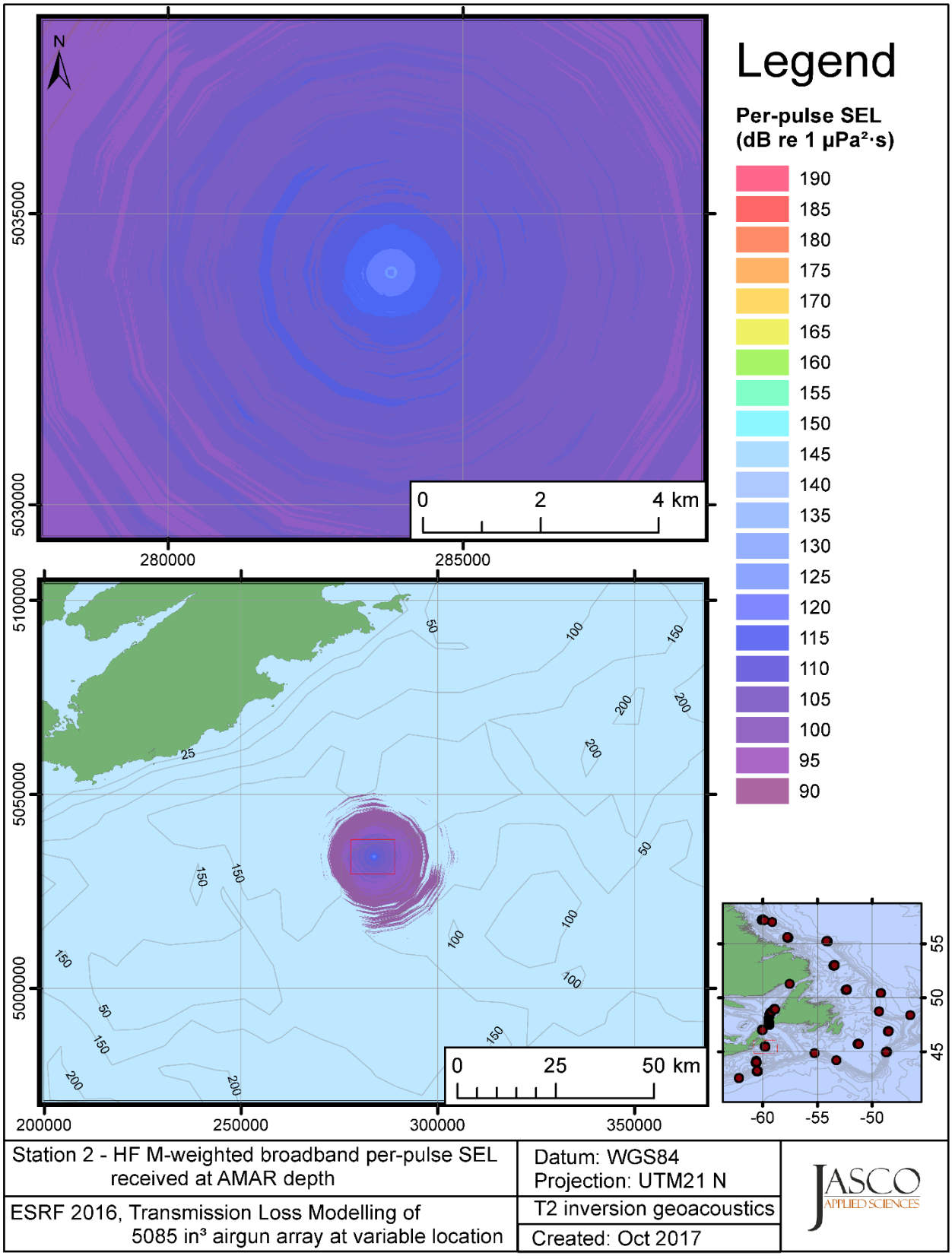

Figure C-135. Stn 2, HF M-weighted SEL received at the AMAR location and depth, modelled using the track 2 inversion geoacoustic bottom, with in-situ July SSP and the airgun array located at any point on the map.

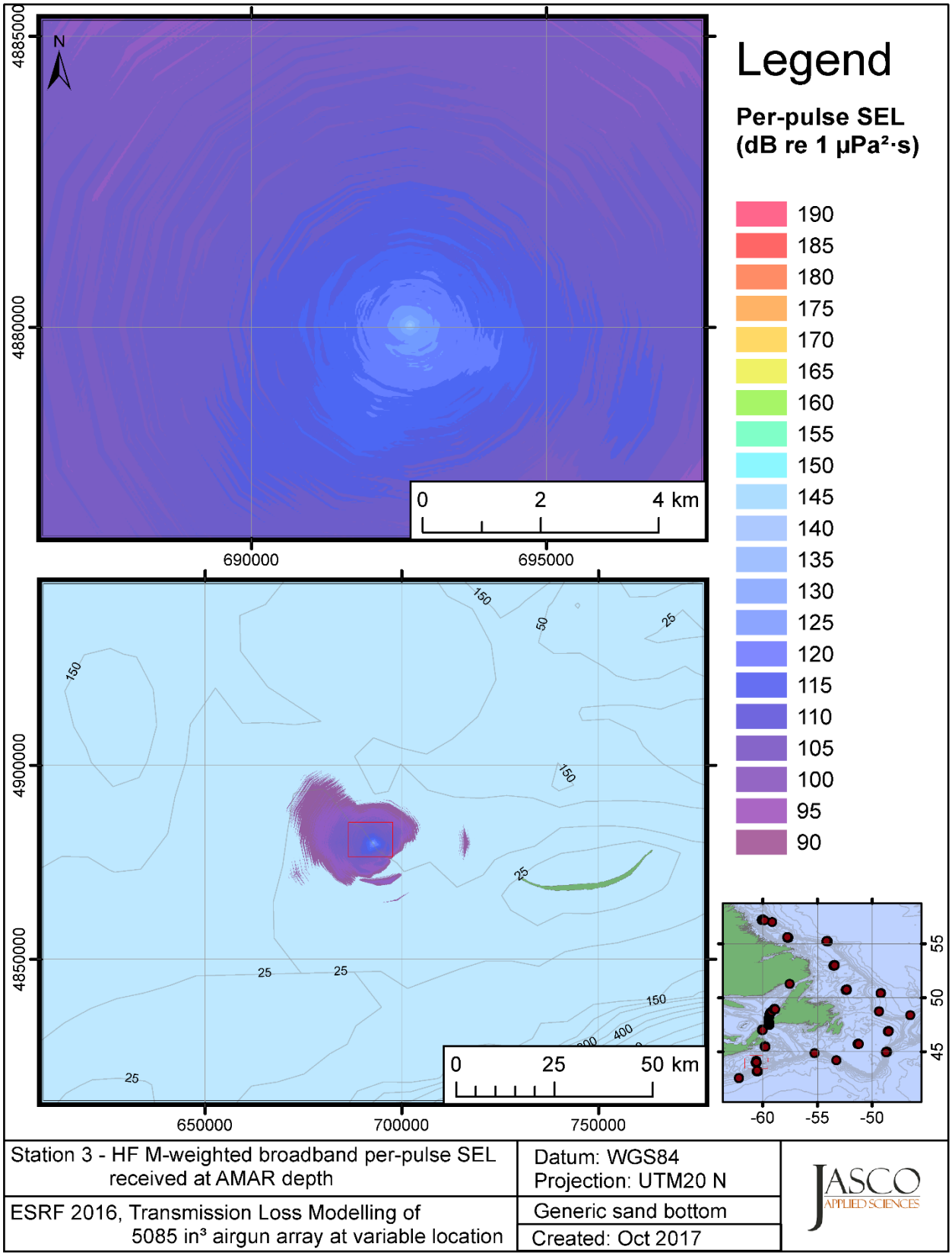

Figure C-136. Stn 3, HF M-weighted SEL received at the AMAR location and depth, modelled using a generic sand bottom, with in-situ July SSP and the airgun array located at any point on the map.

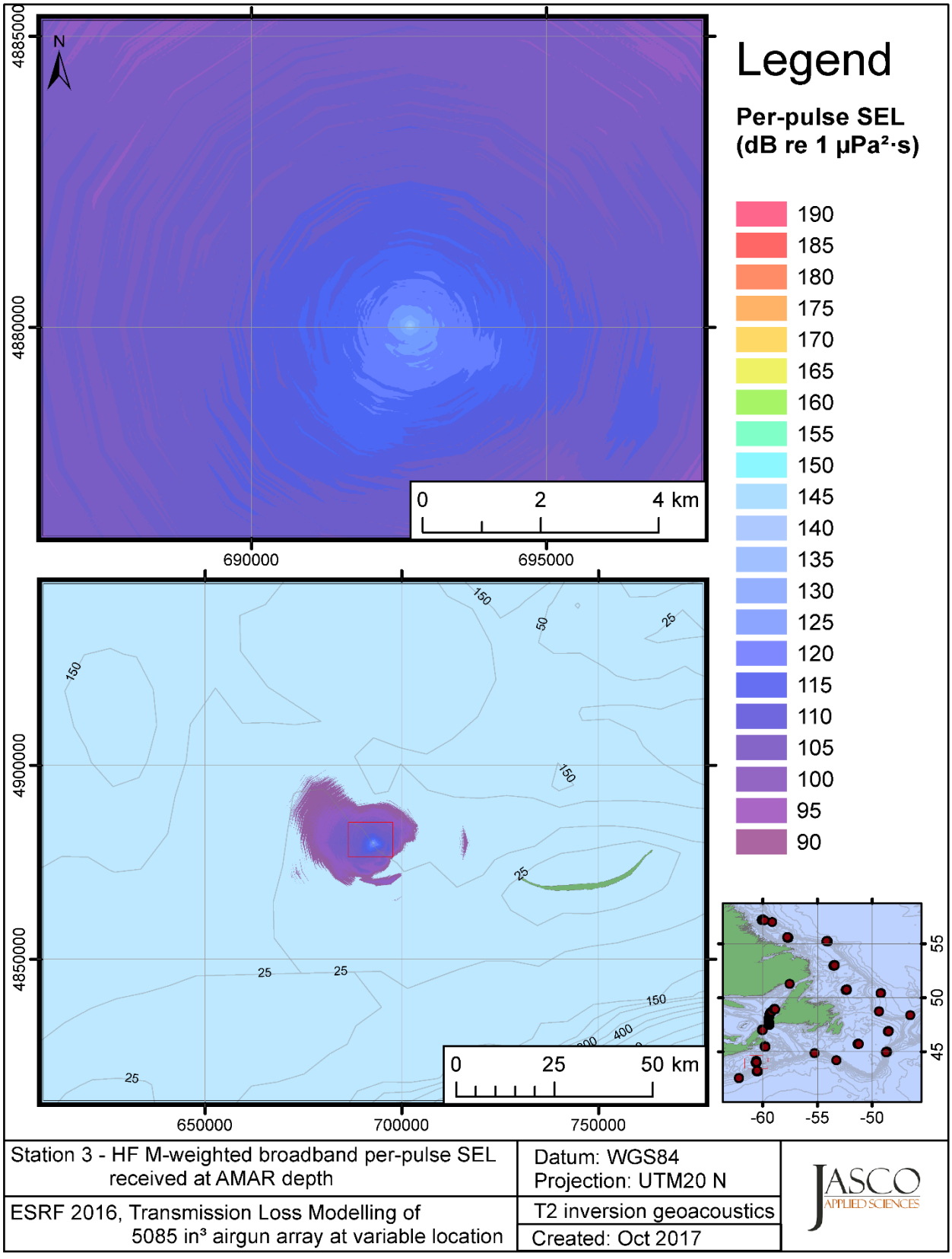

Figure C-137. Stn 3, HF M-weighted SEL received at the AMAR location and depth, modelled using the track 2 inversion geoacoustic bottom, with in-situ July SSP and the airgun array located at any point on the map.

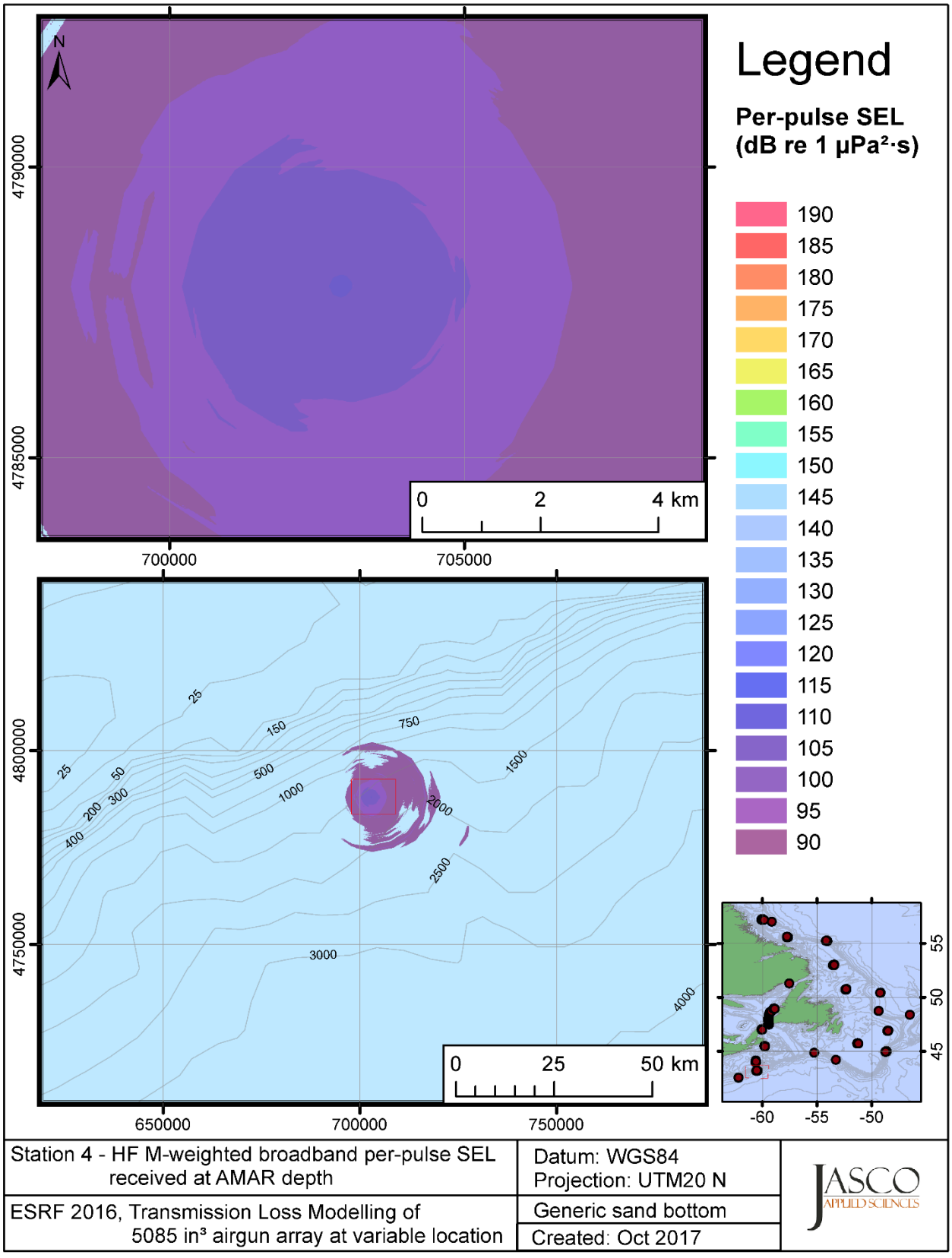

Figure C-138. Stn 4, HF M-weighted SEL received at the AMAR location and depth, modelled using a generic sand bottom, with in-situ July SSP and the airgun array located at any point on the map.

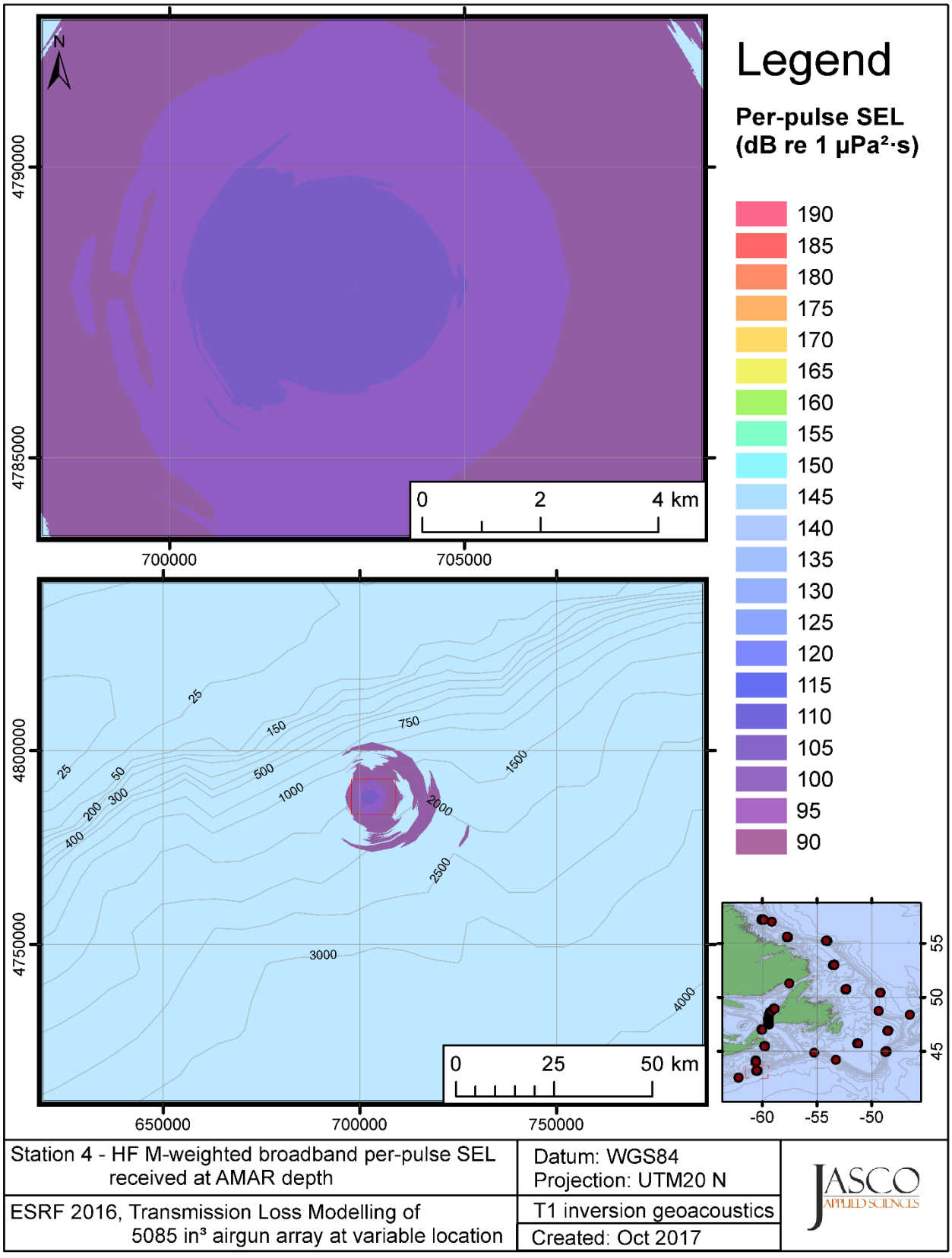

Figure C-139. Stn 4, HF M-weighted SEL received at the AMAR location and depth, modelled using the track 1 inversion geoacoustic bottom, with in-situ July SSP and the airgun array located at any point on the map.

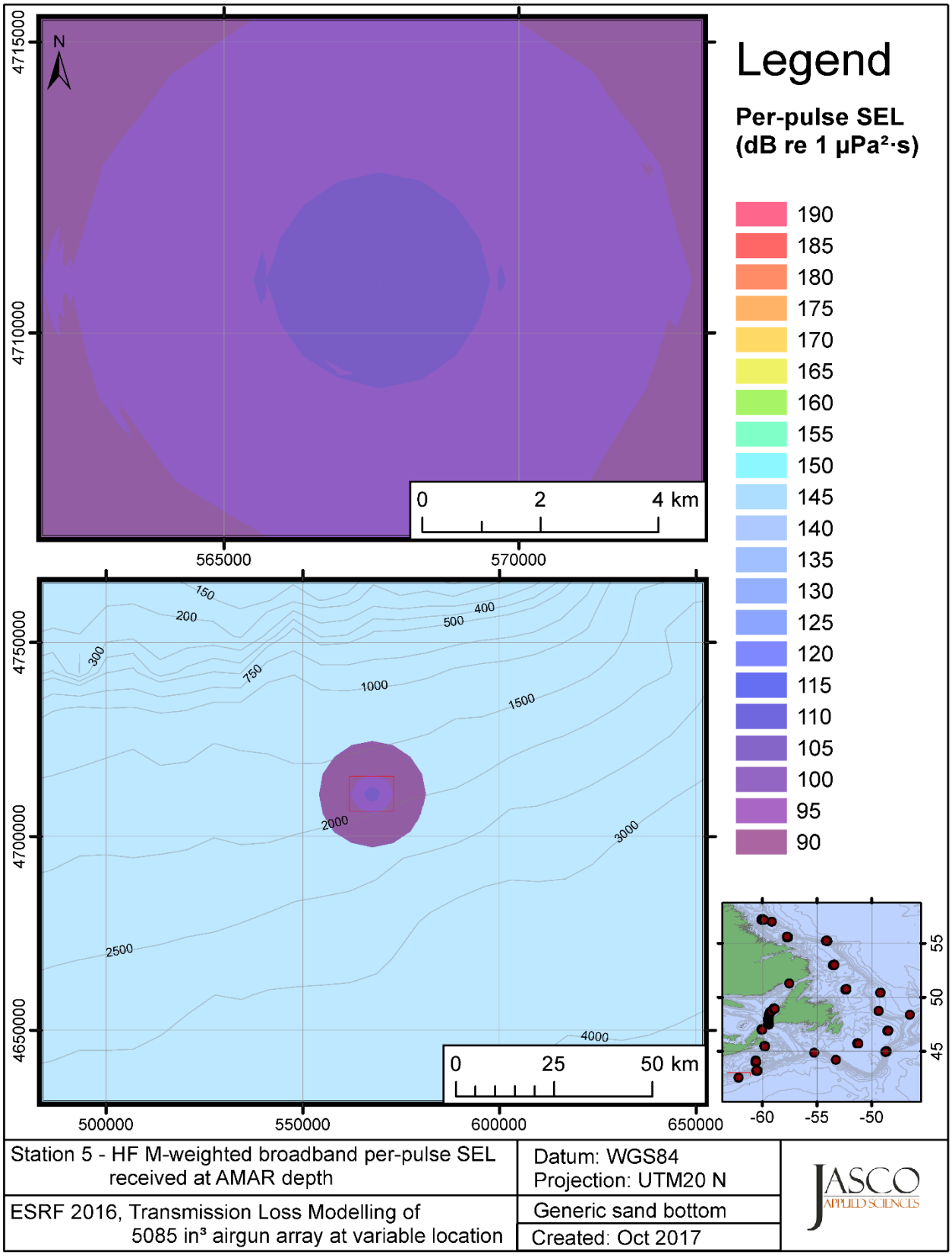

Figure C-140. Stn 5, HF M-weighted SEL received at the AMAR location and depth, modelled using a generic sand bottom, with in-situ July SSP and the airgun array located at any point on the map.

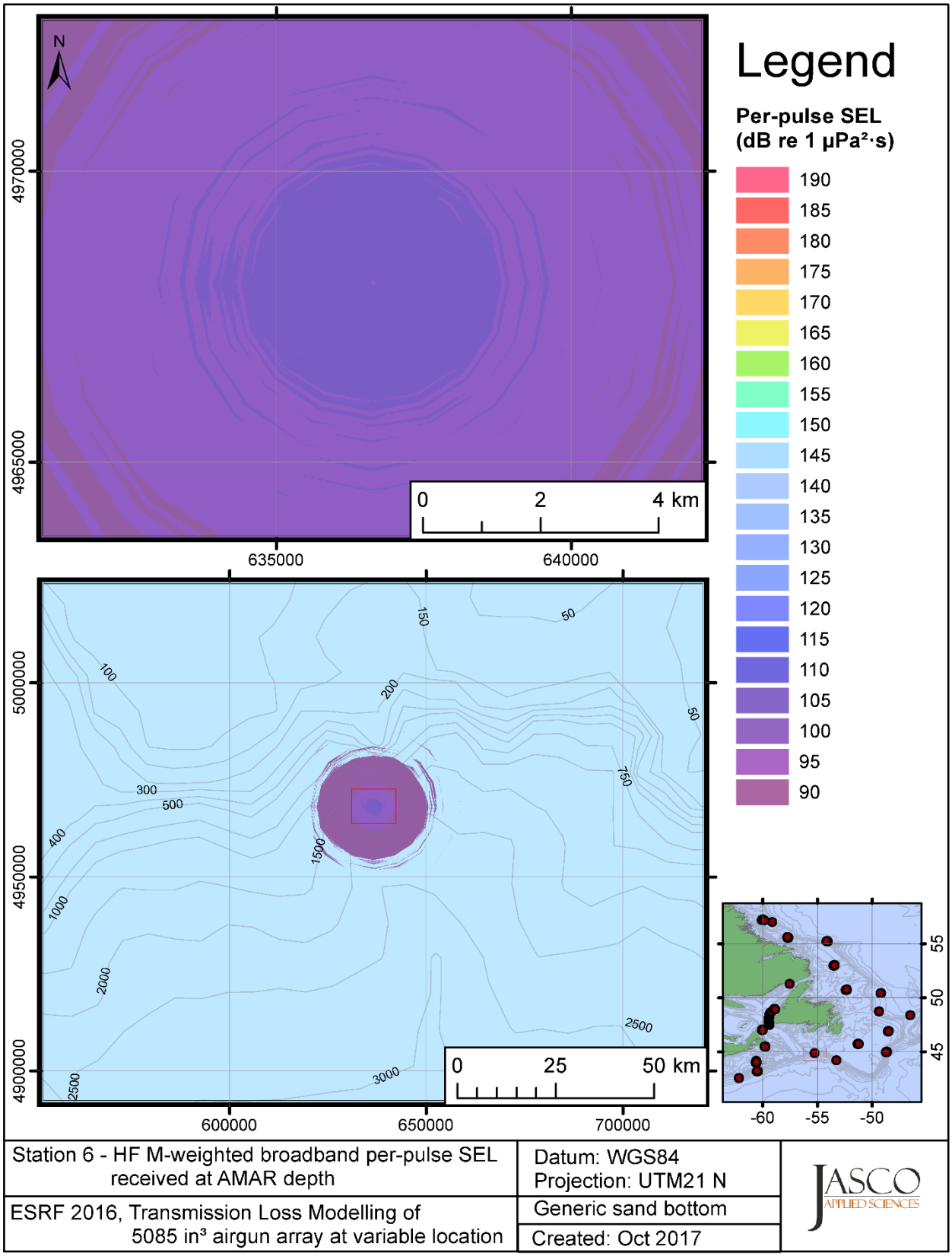

Figure C-141. Stn 6, HF M-weighted SEL received at the AMAR location and depth, modelled using a generic sand bottom, with in-situ July SSP and the airgun array located at any point on the map.

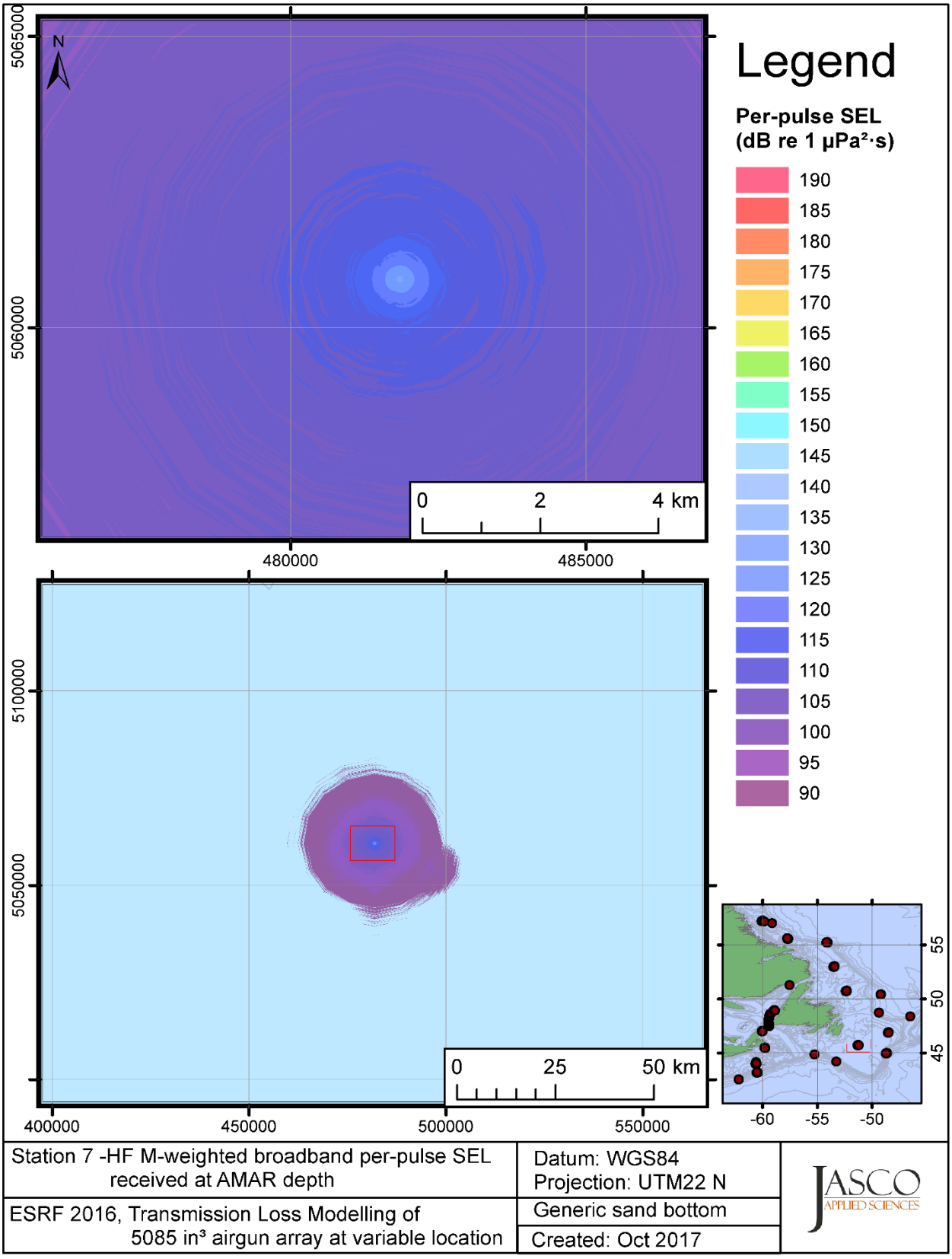

Figure C-142. Stn 7, HF M-weighted SEL received at the AMAR location and depth, modelled using a generic sand bottom, with in-situ July SSP and the airgun array located at any point on the map.

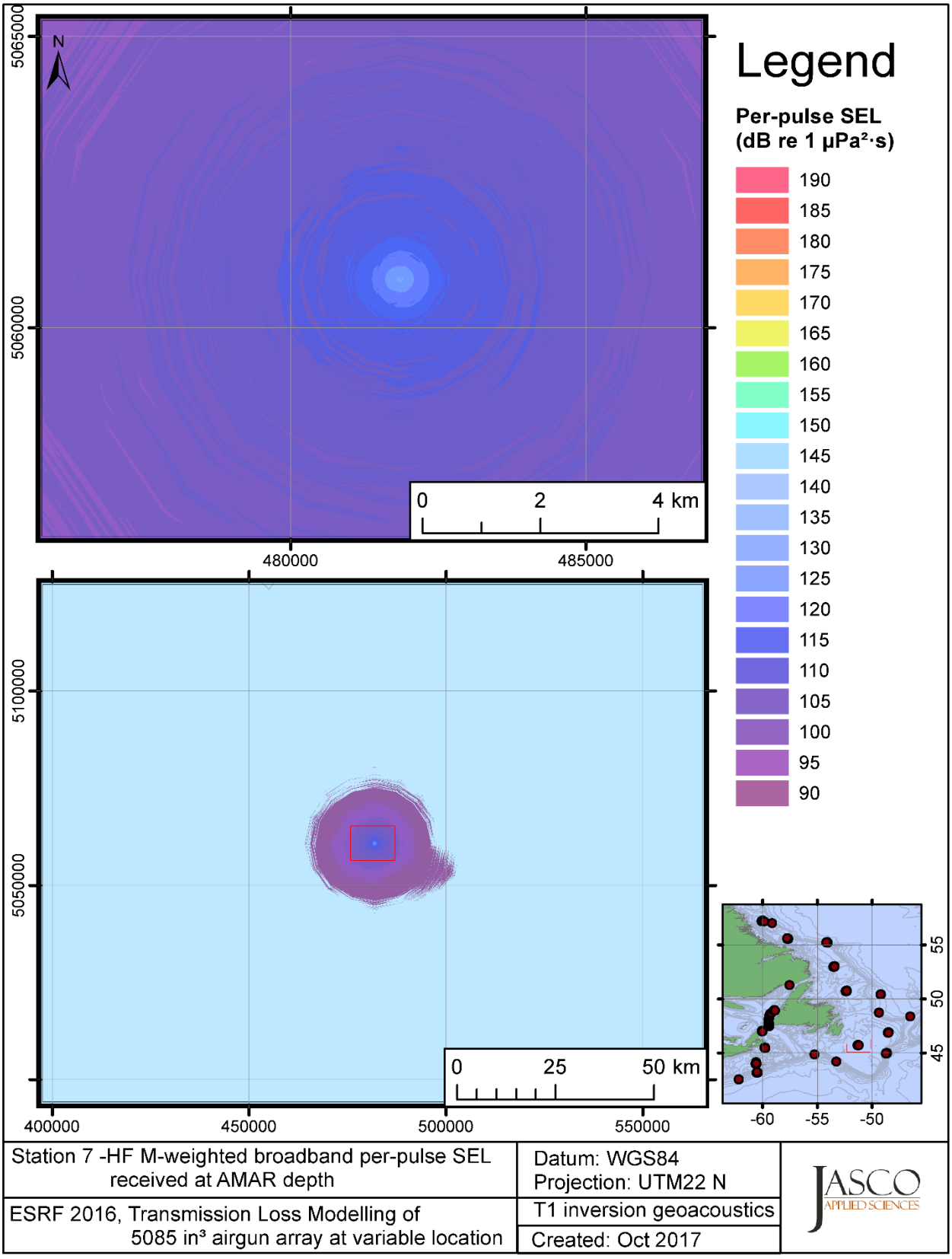

Figure C-143. Stn 7, HF M-weighted SEL received at the AMAR location and depth, modelled using the track 1 inversion geoacoustic bottom, with in-situ July SSP and the airgun array located at any point on the map.

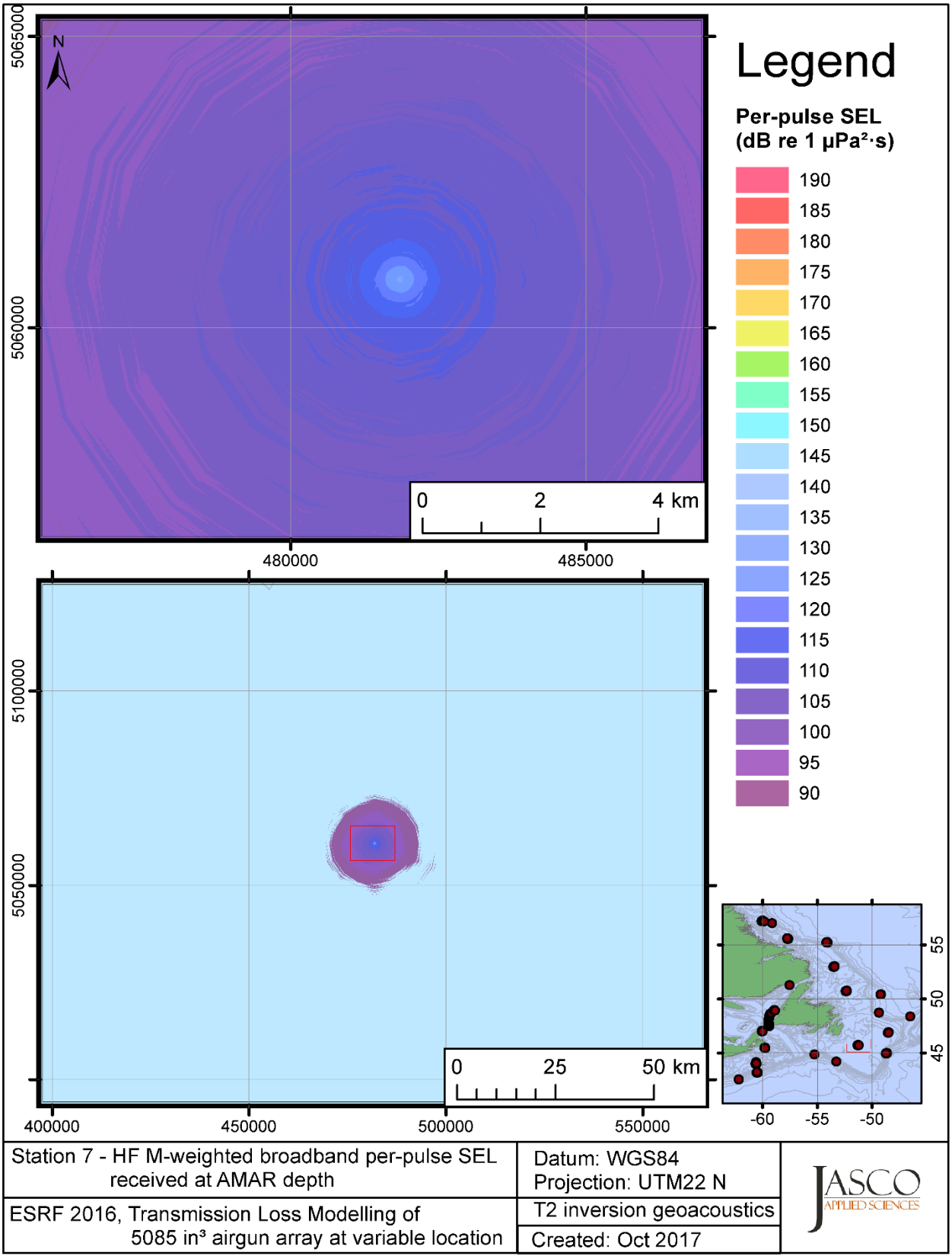

Figure C-144. Stn 7, HF M-weighted SEL received at the AMAR location and depth, modelled using the track 2 inversion geoacoustic bottom, with in-situ July SSP and the airgun array located at any point on the map.

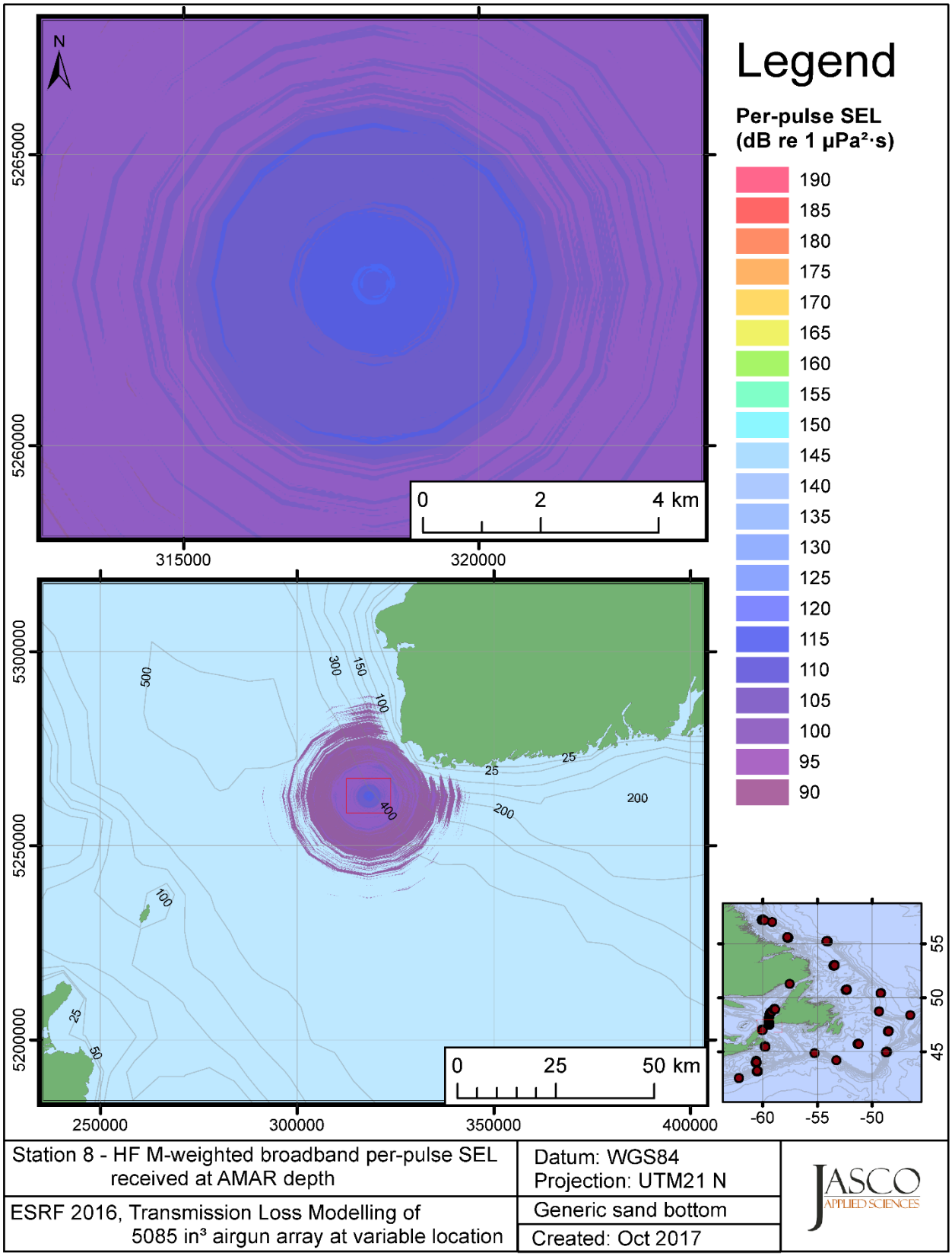

Figure C-145. Stn 8, HF M-weighted SEL received at the AMAR location and depth, modelled using a generic sand bottom, with GDEM July SSP and the airgun array located at any point on the map.

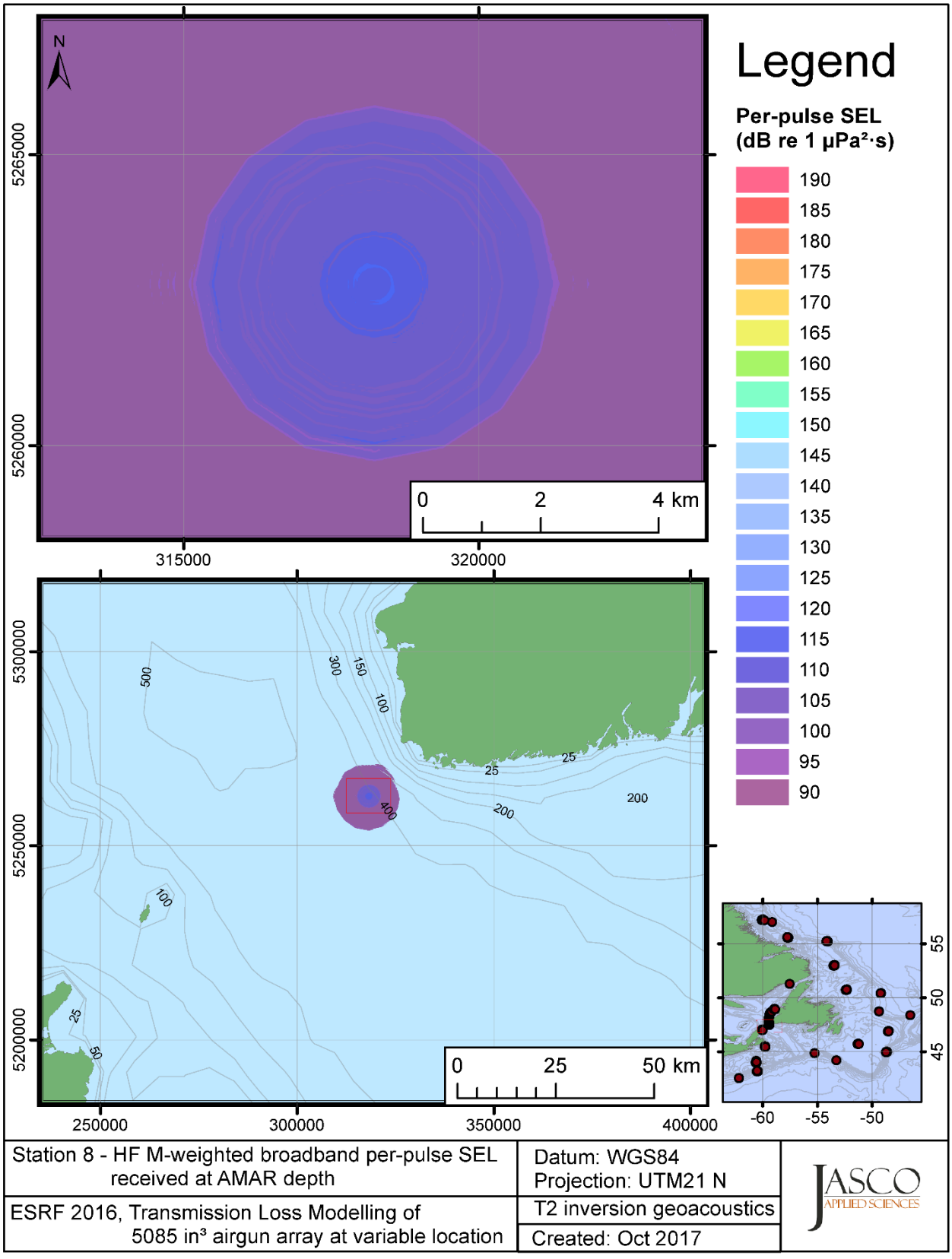

Figure C-146. Stn 8, HF M-weighted SEL received at the AMAR location and depth, modelled using the track 2 inversion geoacoustic bottom, with GDEM July SSP and the airgun array located at any point on the map.

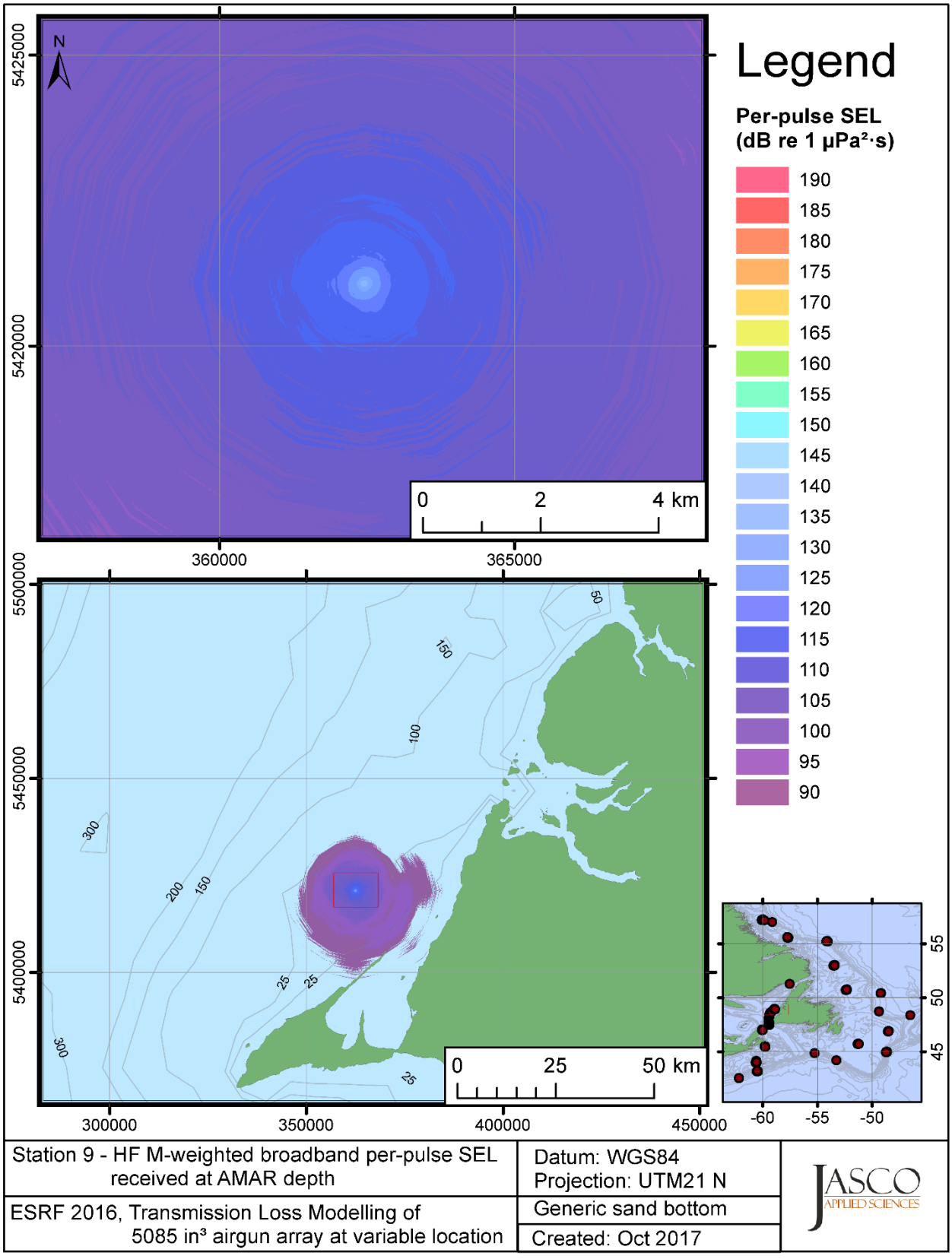

Figure C-147. Stn 9, HF M-weighted SEL received at the AMAR location and depth, modelled using a generic sand bottom, with GDEM July SSP and the airgun array located at any point on the map.

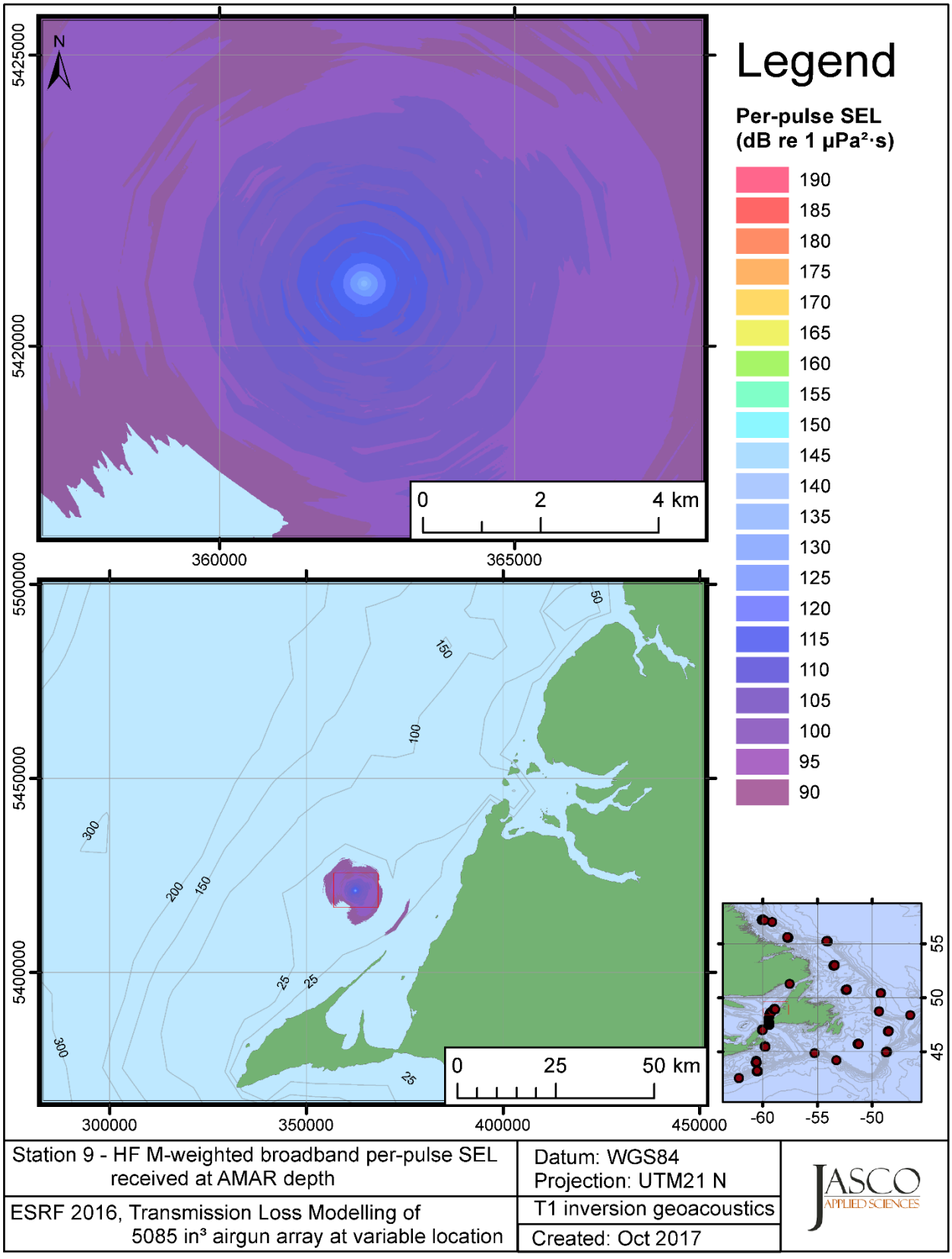

Figure C-148. Stn 9, HF M-weighted SEL received at the AMAR location and depth, modelled using the track 1 inversion geoacoustic bottom, with GDEM July SSP and the airgun array located at any point on the map.

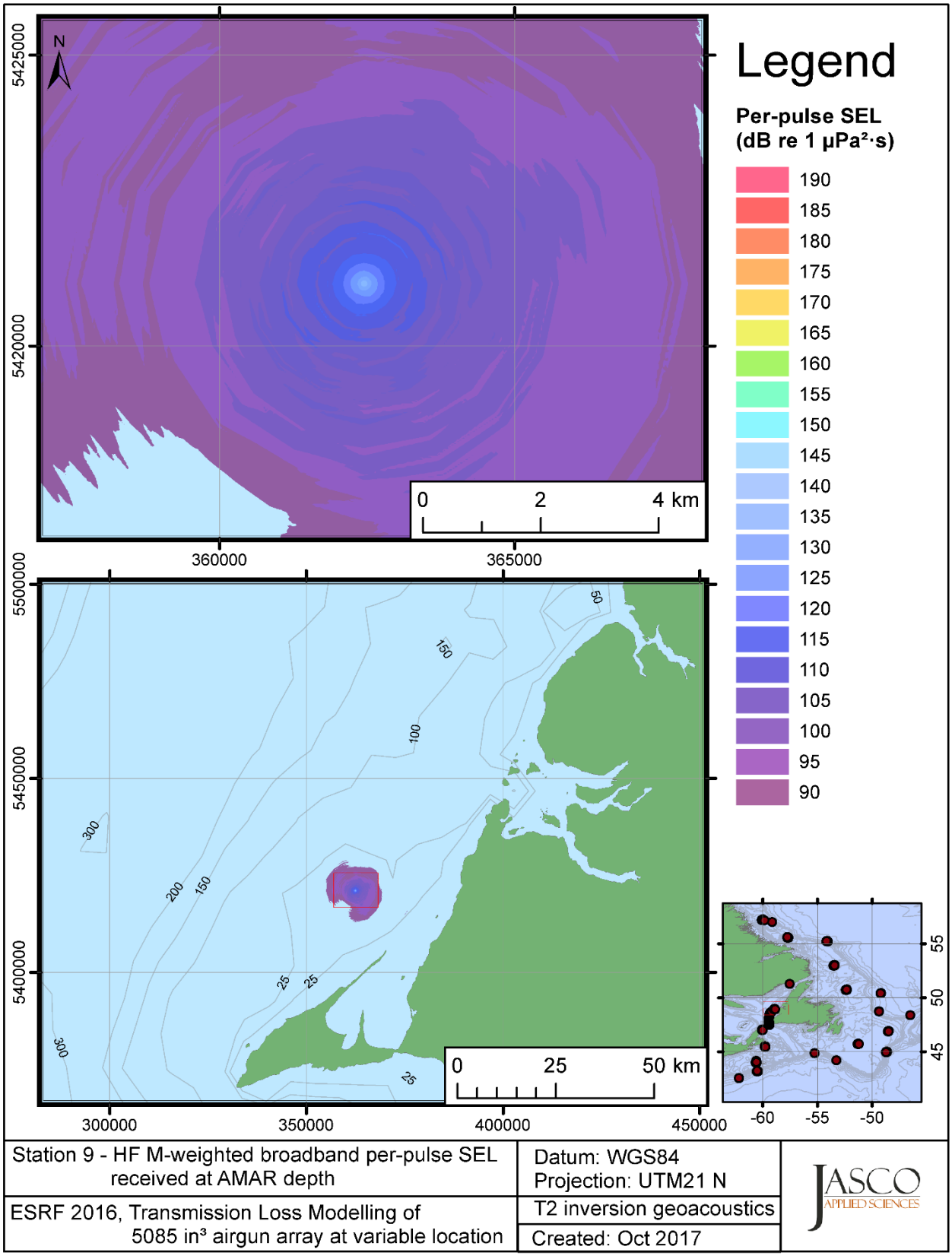

Figure C-149. Stn 9, HF M-weighted SEL received at the AMAR location and depth, modelled using the track 2 inversion geoacoustic bottom, with GDEM July SSP and the airgun array located at any point on the map.

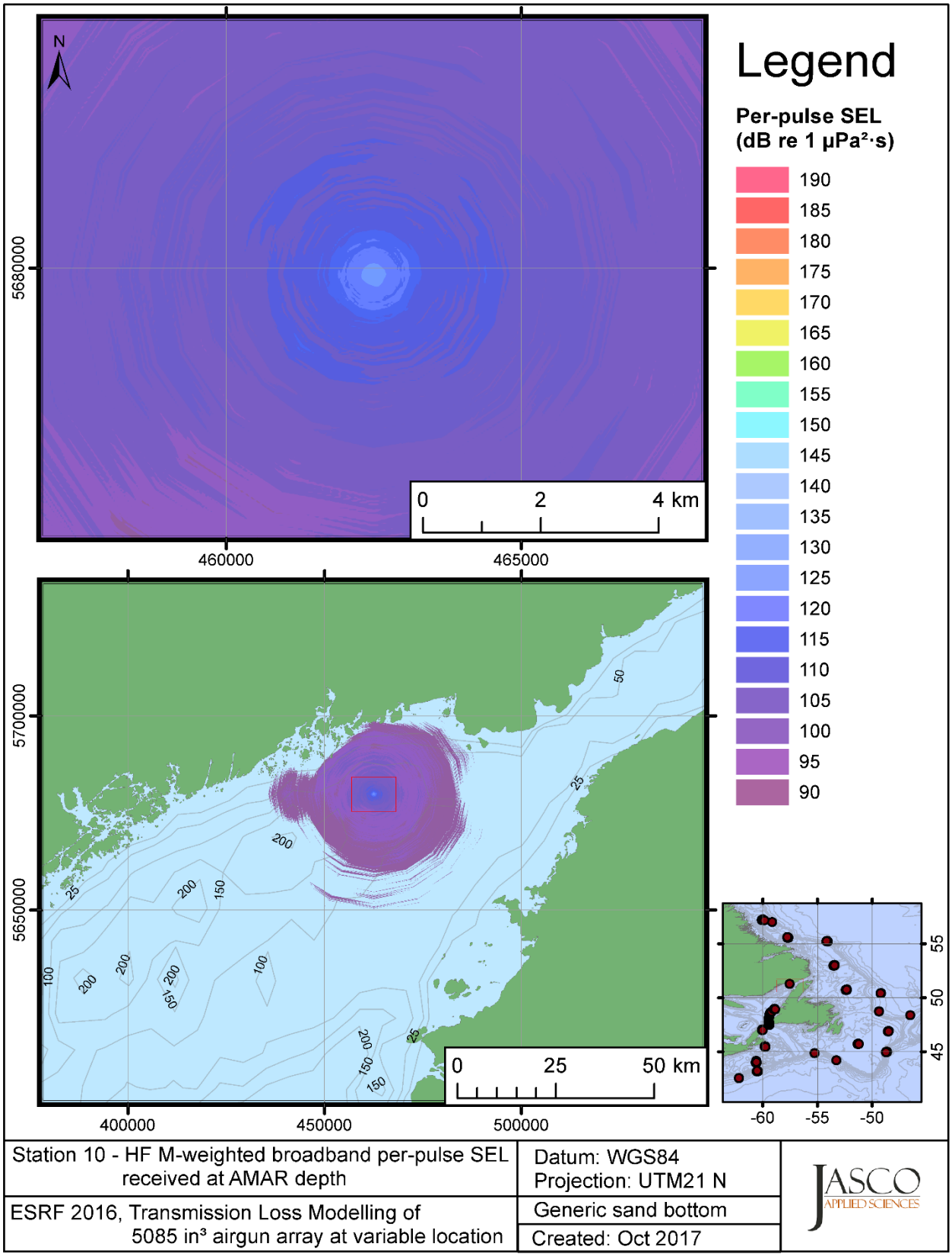

Figure C-150. Stn 10, HF M-weighted SEL received at the AMAR location and depth, modelled using a generic sand bottom, with in-situ July SSP and the airgun array located at any point on the map.

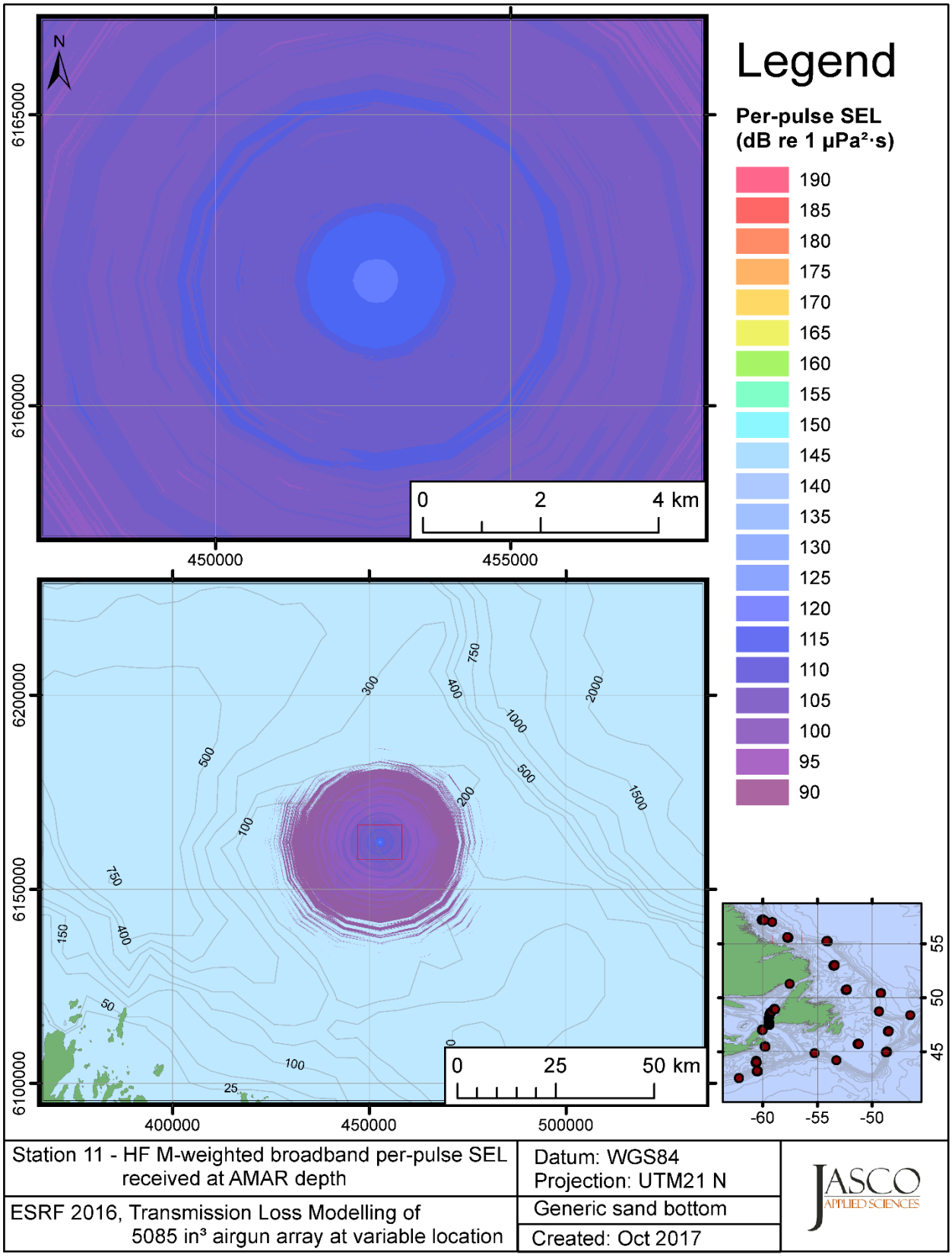

Figure C-151. Stn 11, HF M-weighted SEL received at the AMAR location and depth, modelled using a generic sand bottom, with in-situ July SSP and the airgun array located at any point on the map.

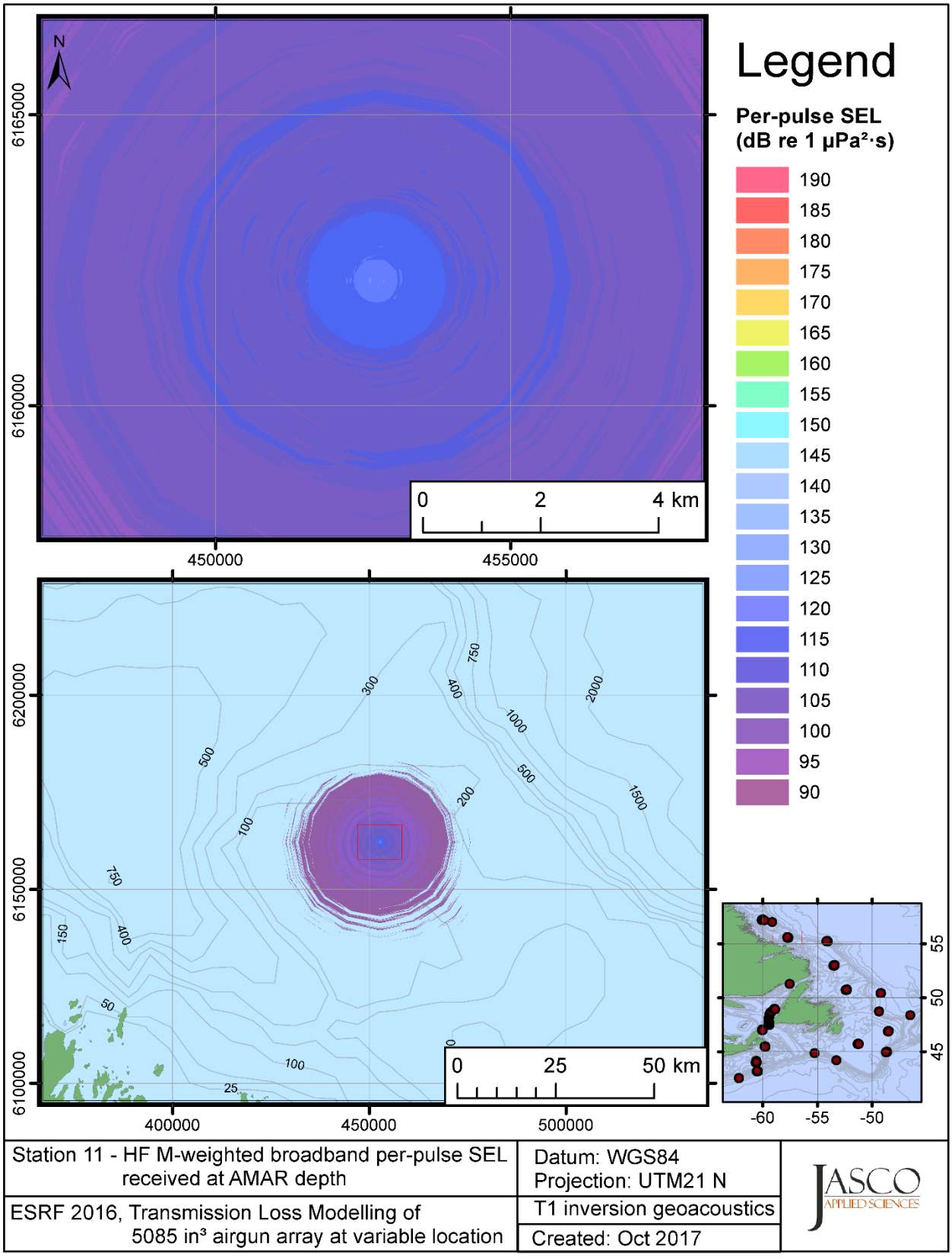

Figure C-152. Stn 11, HF M-weighted SEL received at the AMAR location and depth, modelled using the track 1 inversion geoacoustic bottom, with in-situ July SSP and the airgun array located at any point on the map.

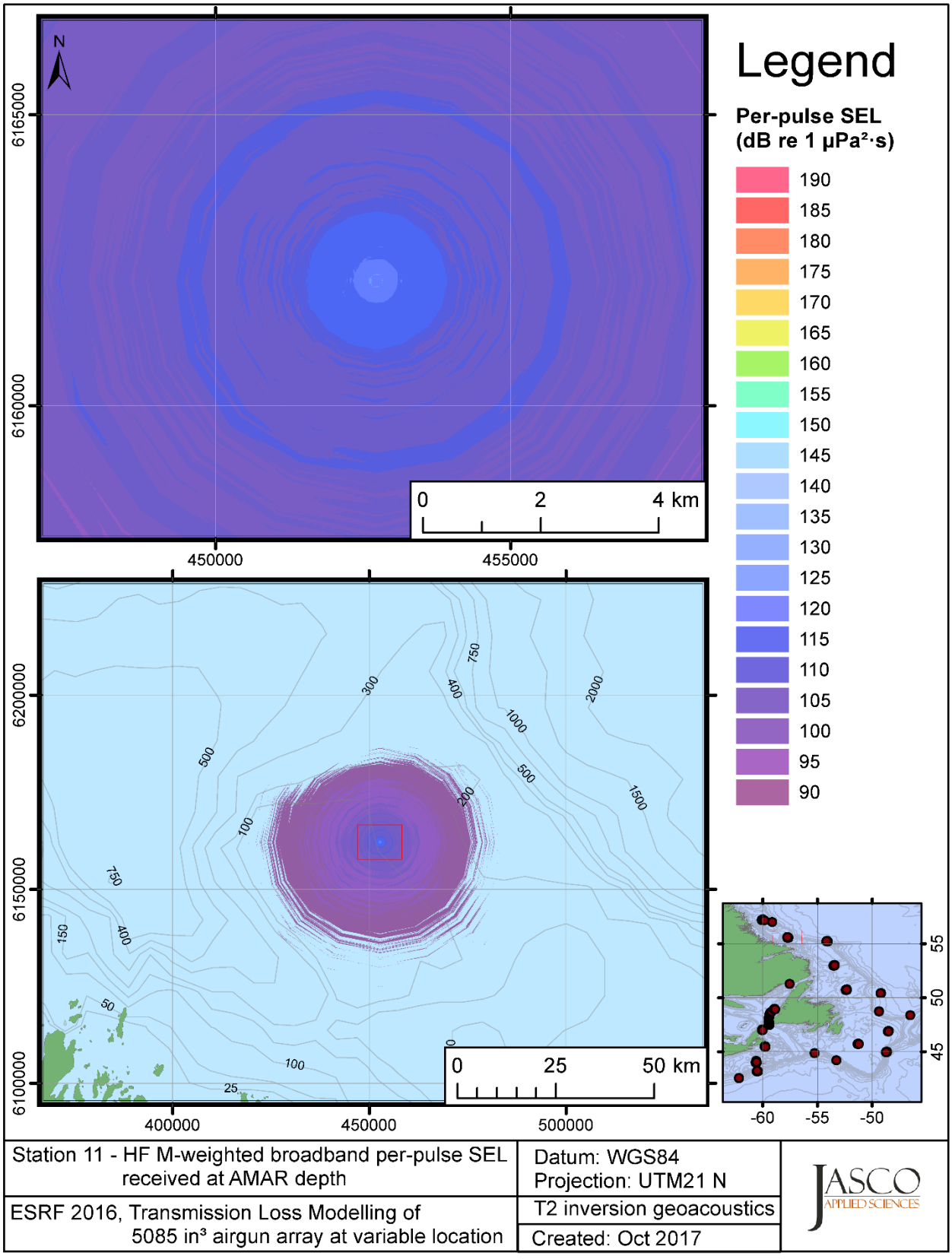

Figure C-153. Stn 11, HF M-weighted SEL received at the AMAR location and depth, modelled using the track 2 inversion geoacoustic bottom, with in-situ July SSP and the airgun array located at any point on the map.

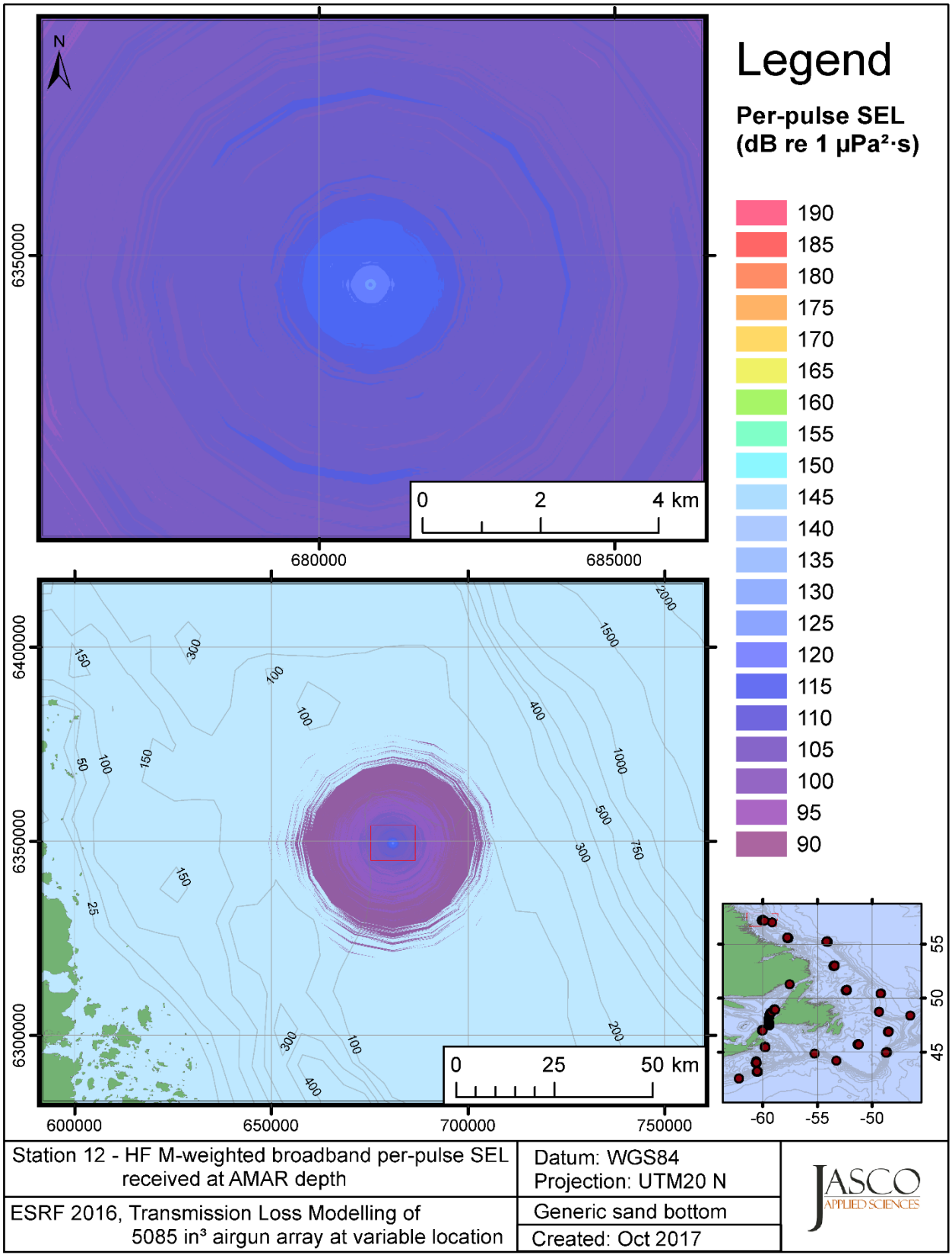

Figure C-154. Stn 12, HF M-weighted SEL received at the AMAR location and depth, modelled using a generic sand bottom, with in-situ July SSP and the airgun array located at any point on the map.

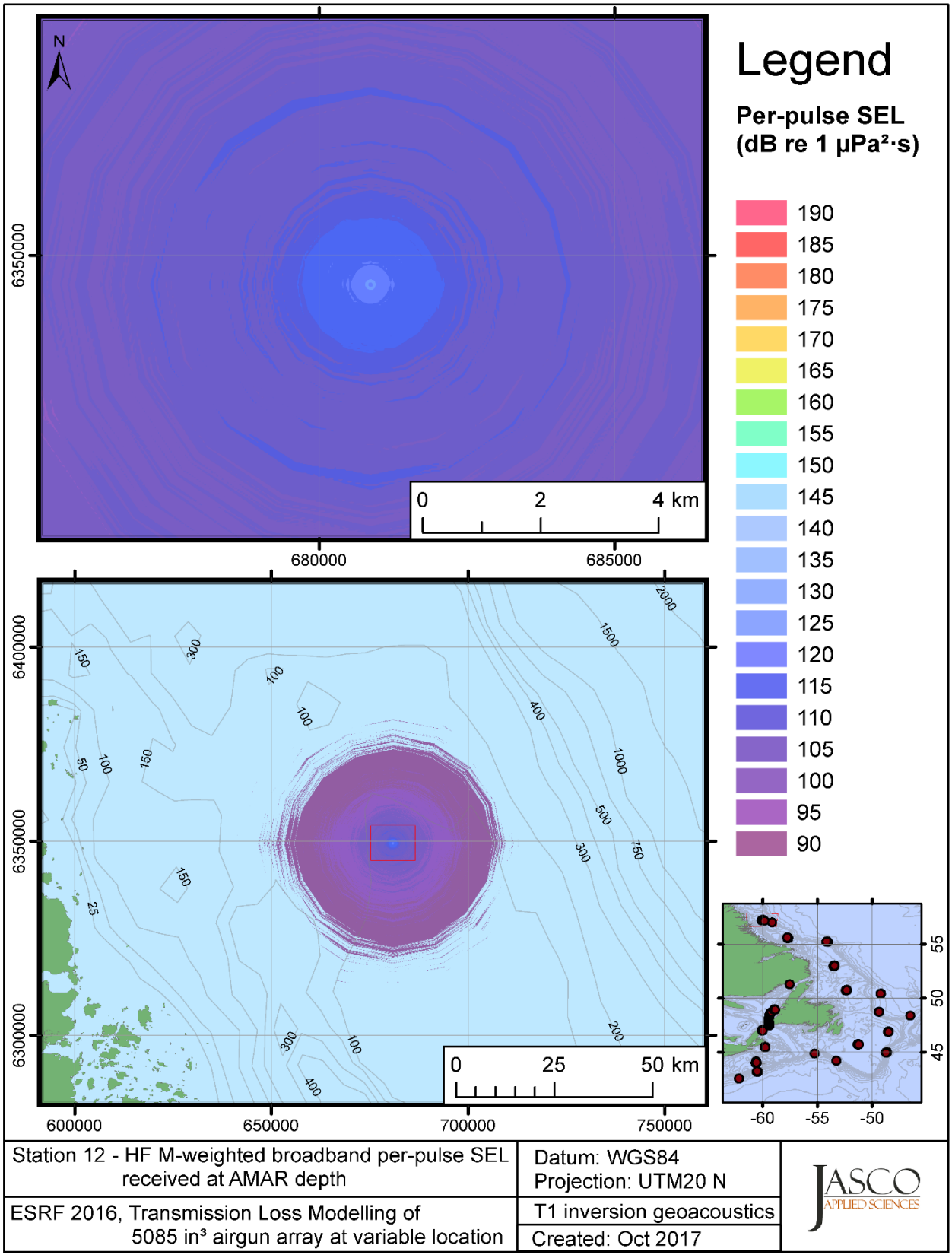

Figure C-155. Stn 12, HF M-weighted SEL received at the AMAR location and depth, modelled using the track 1 inversion geoacoustic bottom, with in-situ July SSP and the airgun array located at any point on the map.

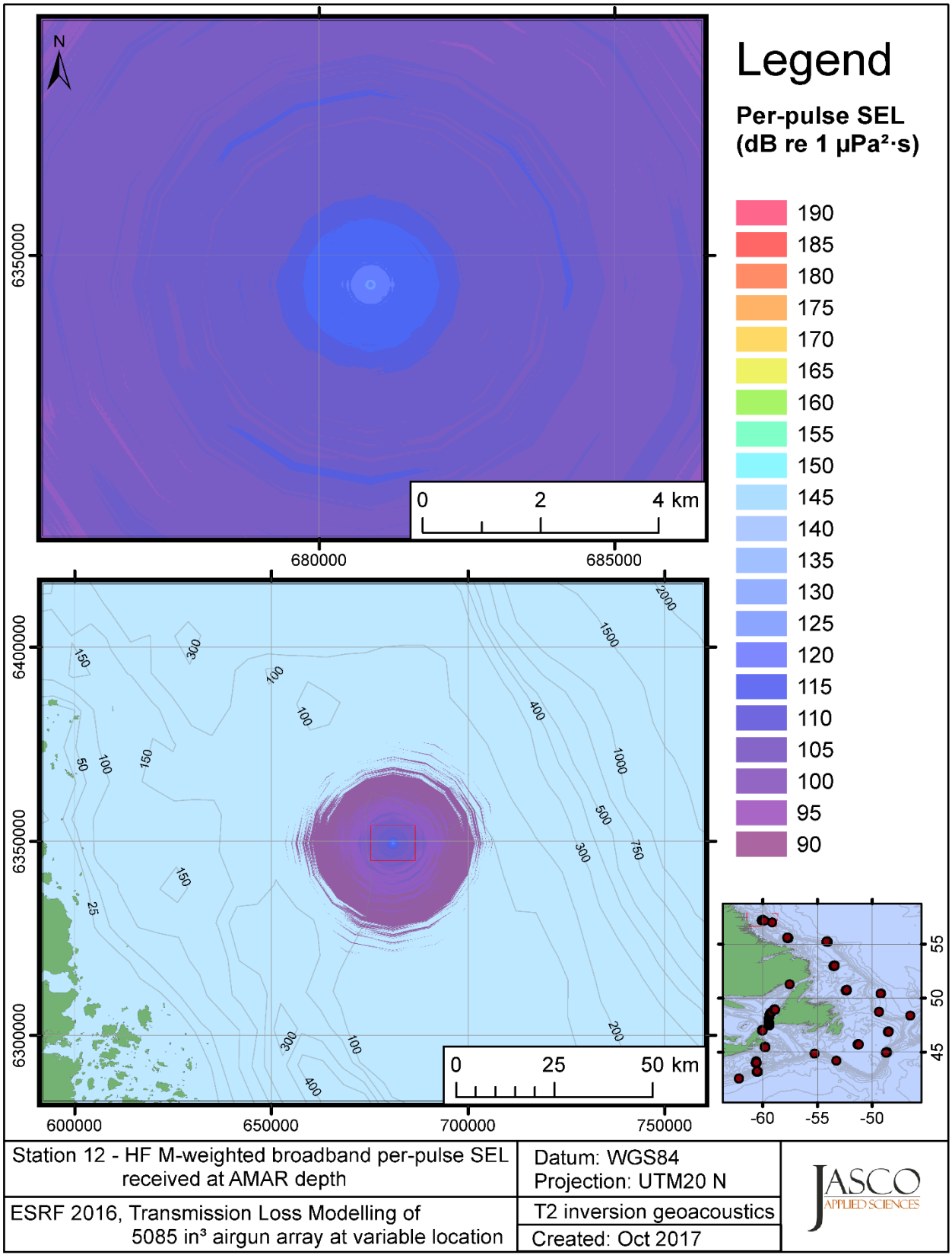

Figure C-156. Stn 12, HF M-weighted SEL received at the AMAR location and depth, modelled using the track 2 inversion geoacoustic bottom, with in-situ July SSP and the airgun array located at any point on the map.

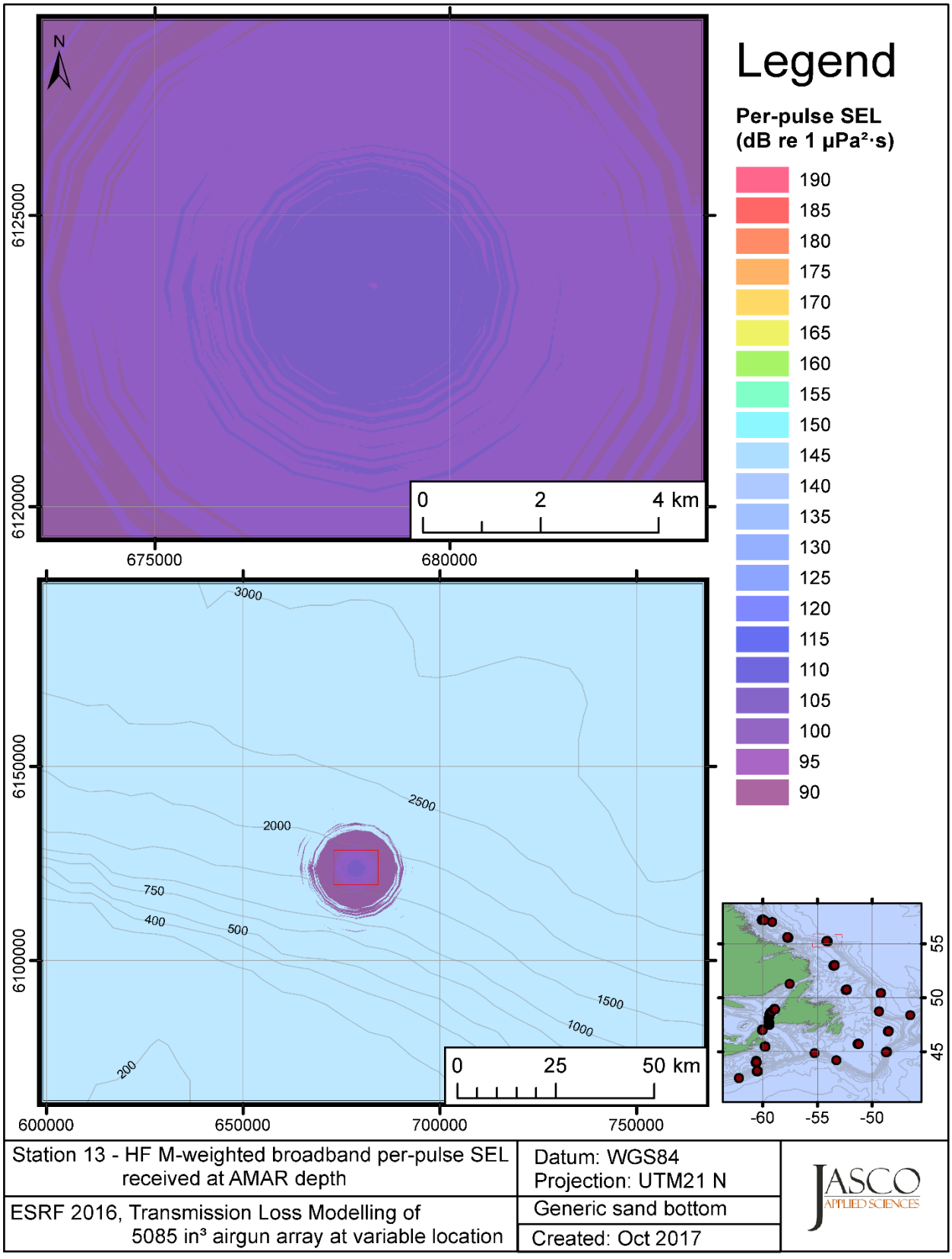

Figure C-157. Stn 13, HF M-weighted SEL received at the AMAR location and depth, modelled using a generic sand bottom, with in-situ July SSP and the airgun array located at any point on the map.

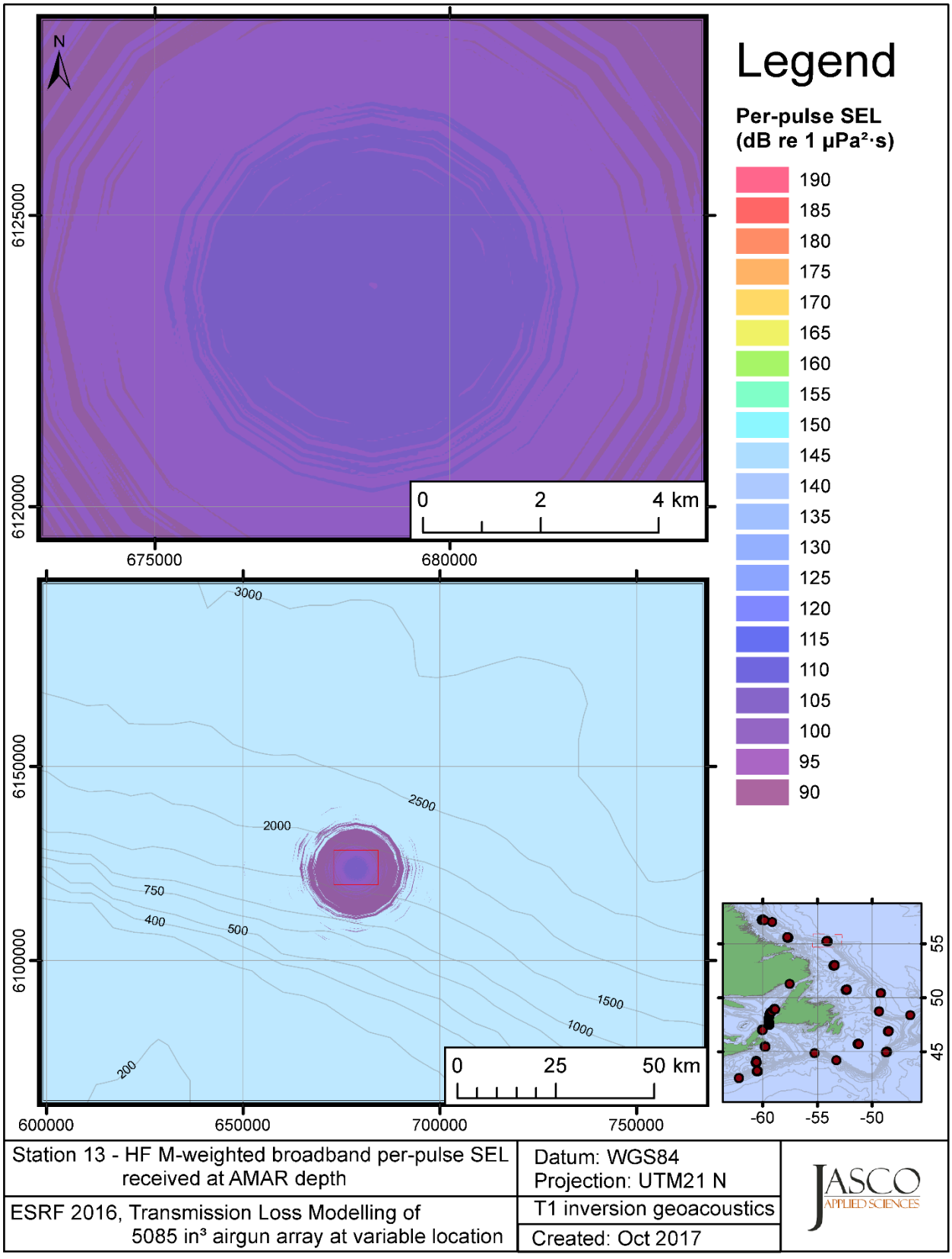

Figure C-158. Stn 13, HF M-weighted SEL received at the AMAR location and depth, modelled using the track 1 inversion geoacoustic bottom, with in-situ July SSP and the airgun array located at any point on the map.

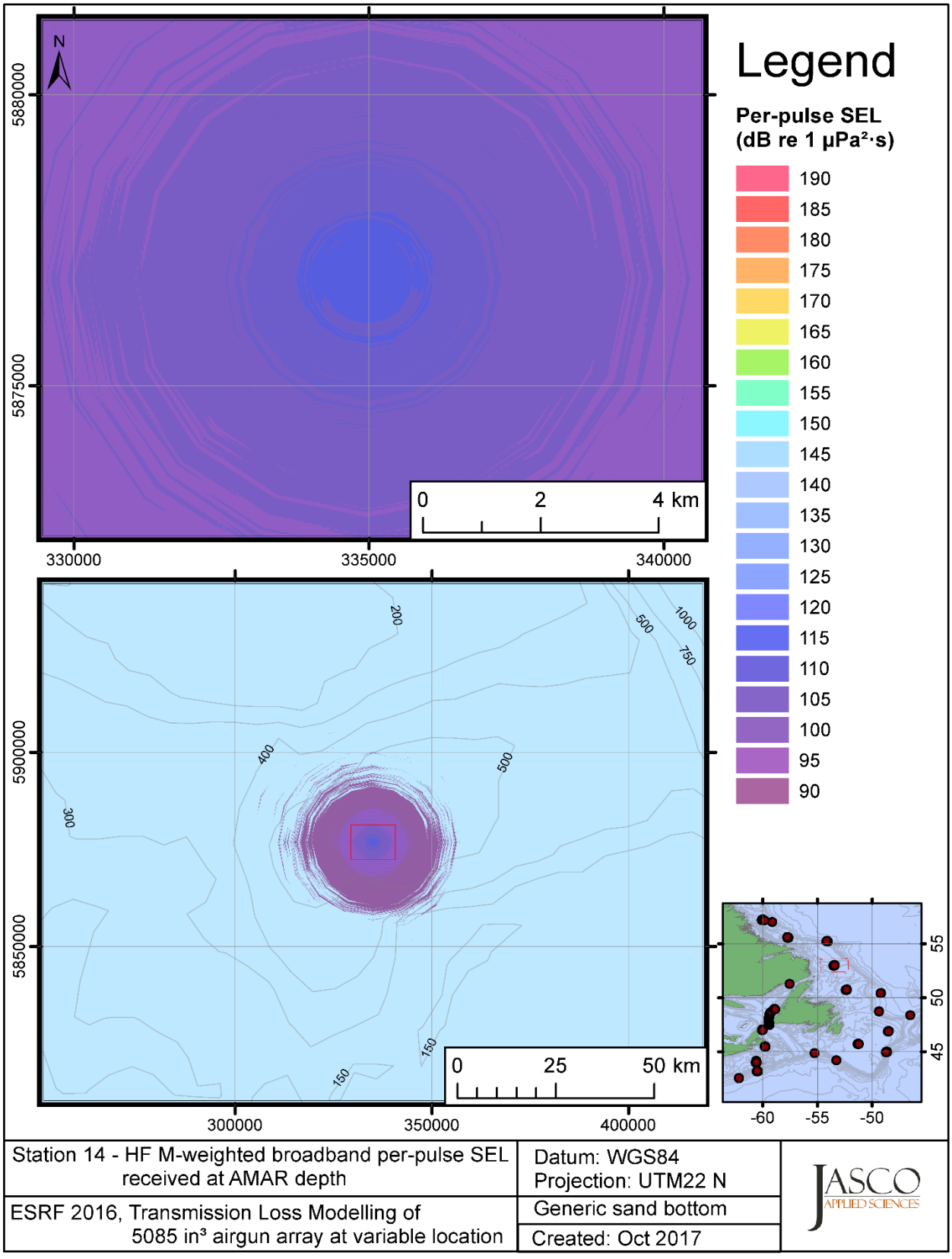

Figure C-159. Stn 14, HF M-weighted SEL received at the AMAR location and depth, modelled using a generic sand bottom, with in-situ July SSP and the airgun array located at any point on the map.

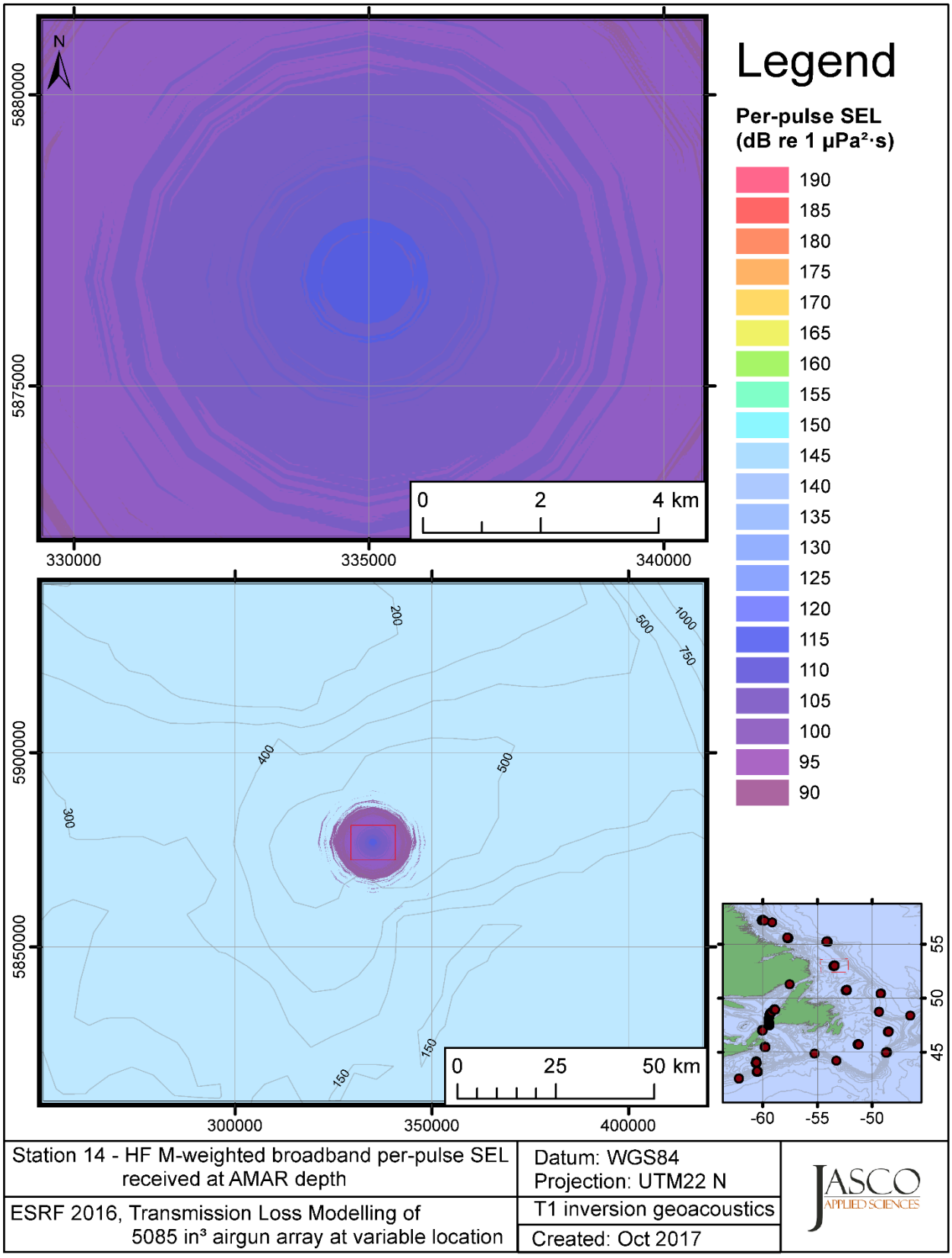

Figure C-160. Stn 14, HF M-weighted SEL received at the AMAR location and depth, modelled using the track 1 inversion geoacoustic bottom, with in-situ July SSP and the airgun array located at any point on the map.

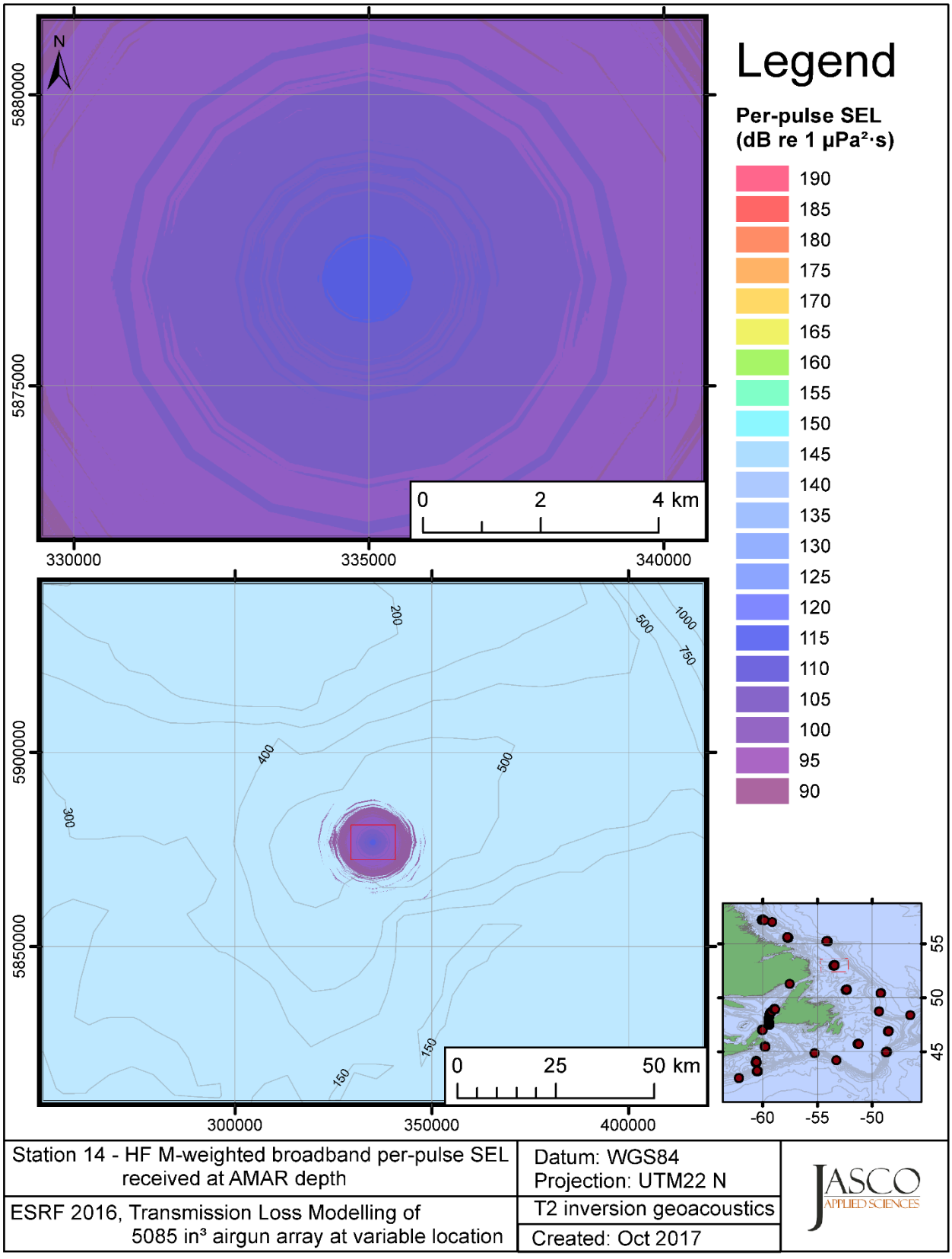

Figure C-161. Stn 14, HF M-weighted SEL received at the AMAR location and depth, modelled using the track 2 inversion geoacoustic bottom, with in-situ July SSP and the airgun array located at any point on the map.

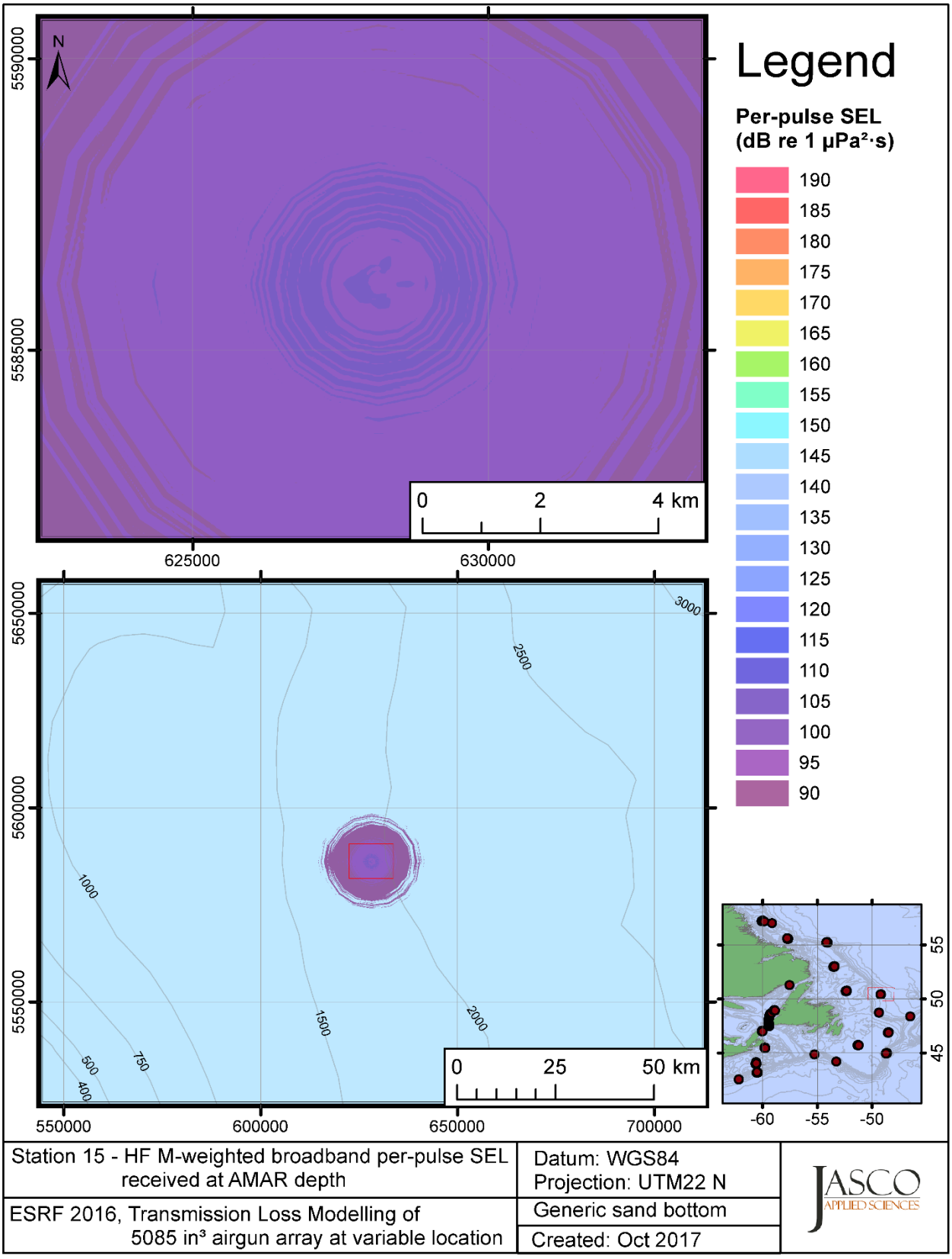

Figure C-162. Stn 15, HF M-weighted SEL received at the AMAR location and depth, modelled using a generic sand bottom, with in-situ July SSP and the airgun array located at any point on the map.

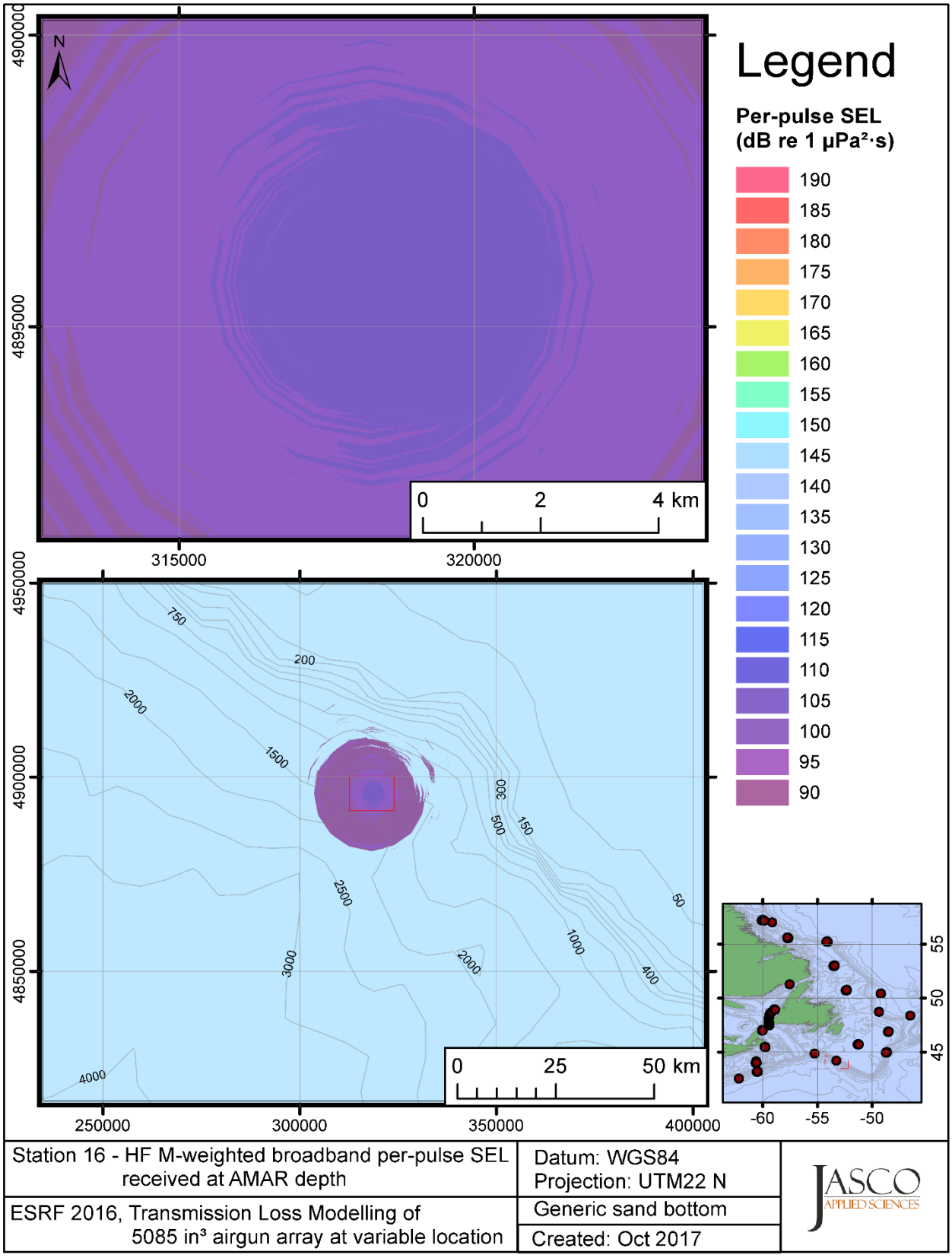

Figure C-163. Stn 16, HF M-weighted SEL received at the AMAR location and depth, modelled using a generic sand bottom, with in-situ July SSP and the airgun array located at any point on the map.

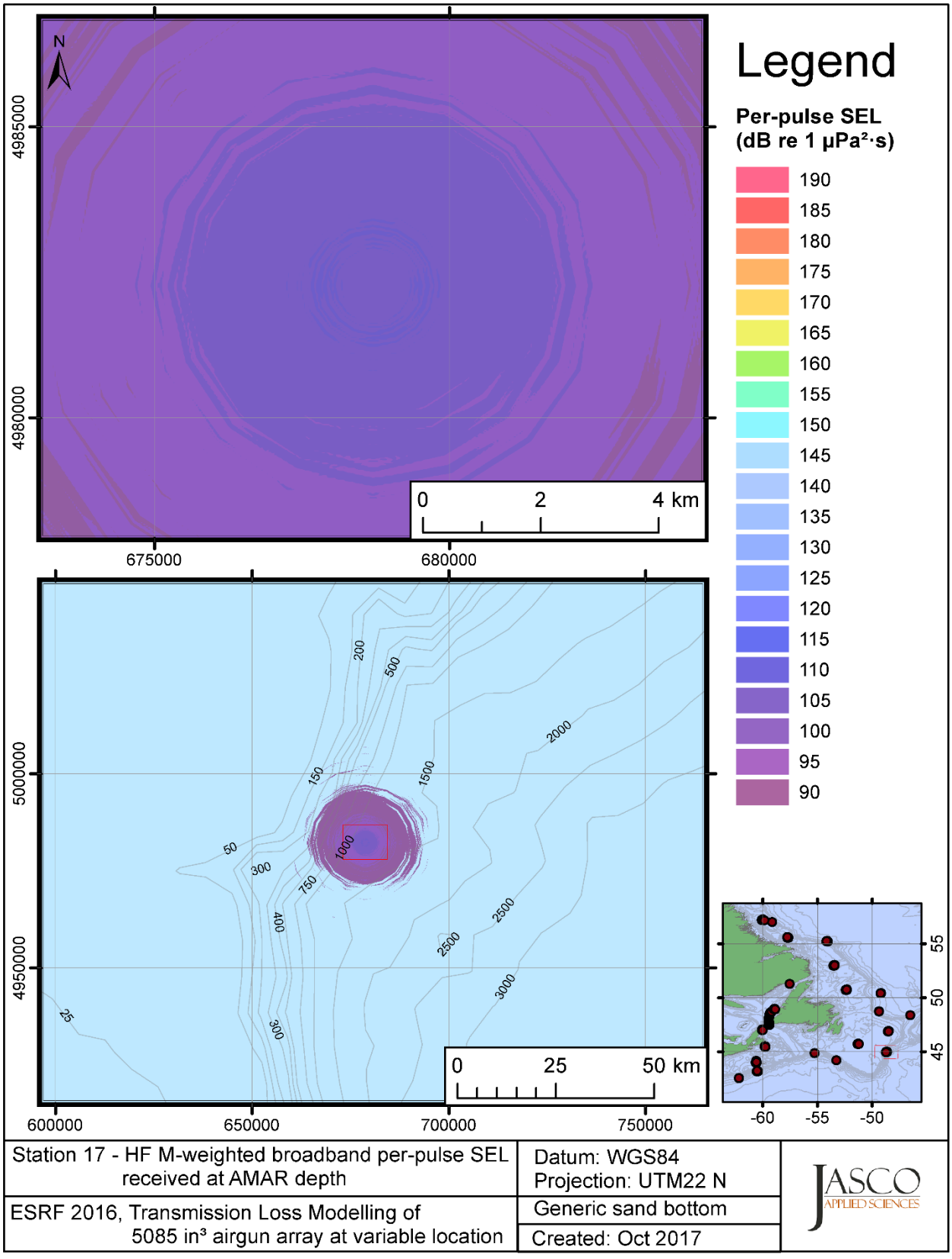

Figure C-164. Stn 17, HF M-weighted SEL received at the AMAR location and depth, modelled using a generic sand bottom, with in-situ July SSP and the airgun array located at any point on the map.

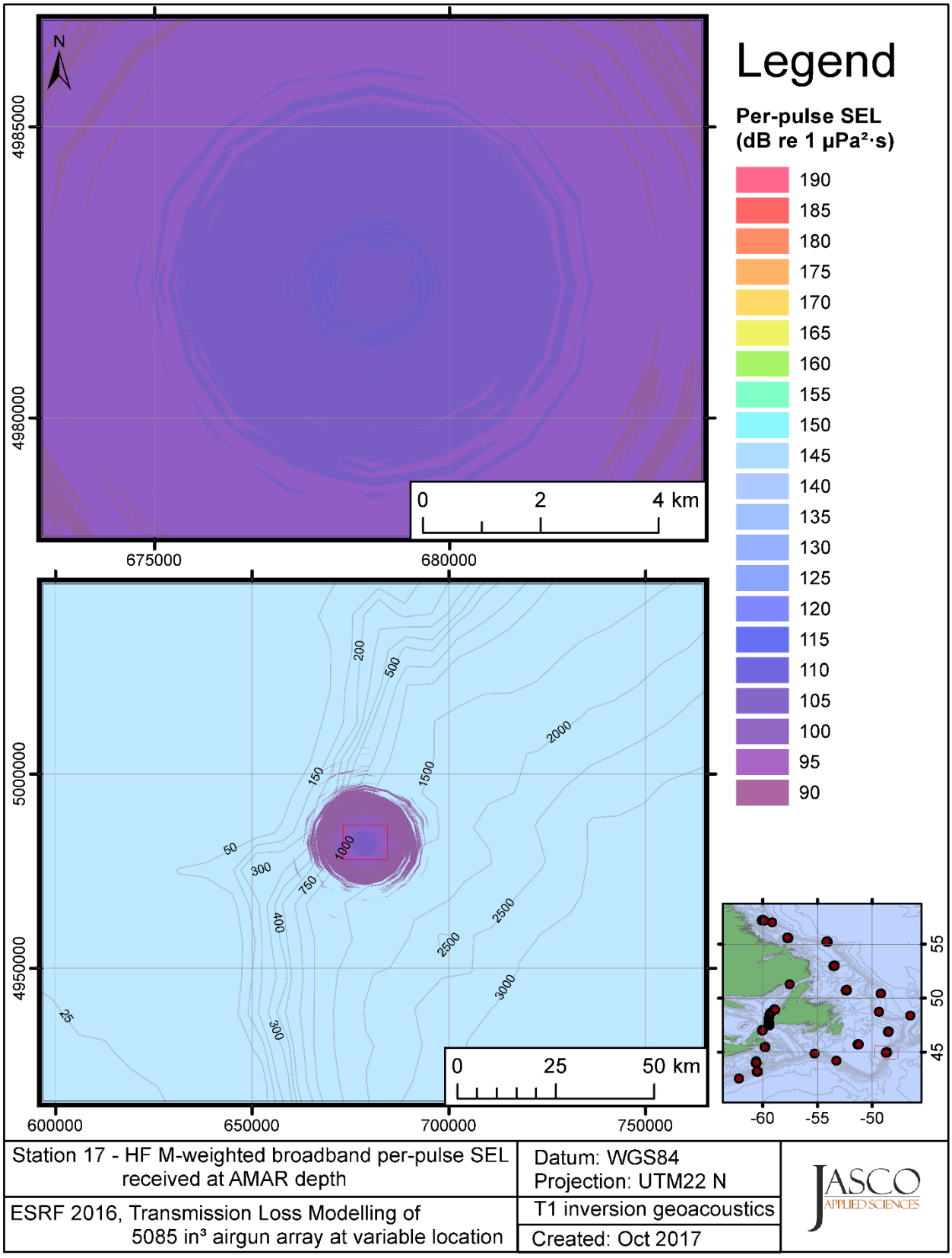

Figure C-165. Stn 17, HF M-weighted SEL received at the AMAR location and depth, modelled using the track 1 inversion geoacoustic bottom, with in-situ July SSP and the airgun array located at any point on the map.

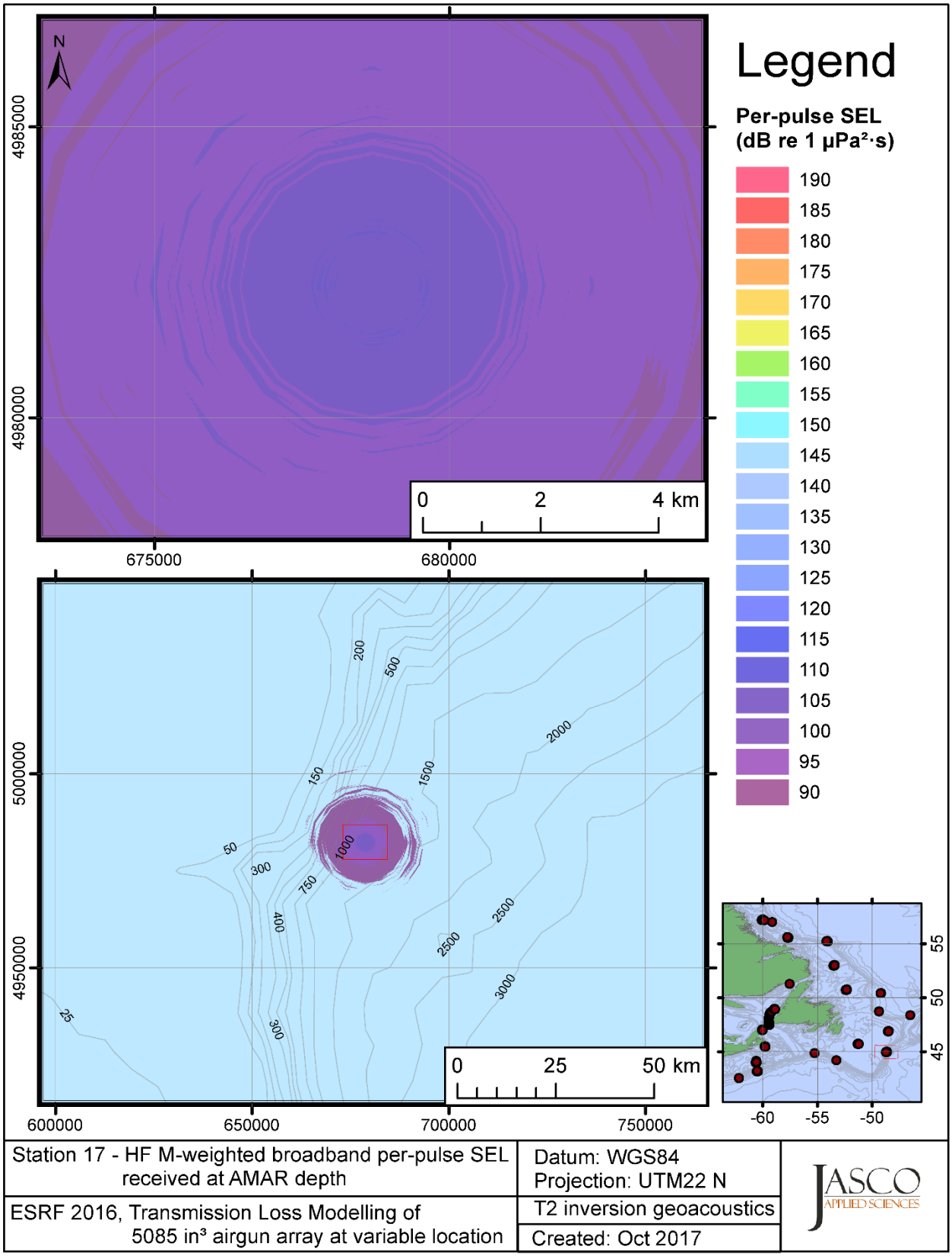

Figure C-166. Stn 17, HF M-weighted SEL received at the AMAR location and depth, modelled using the track 2 inversion geoacoustic bottom, with in-situ July SSP and the airgun array located at any point on the map.

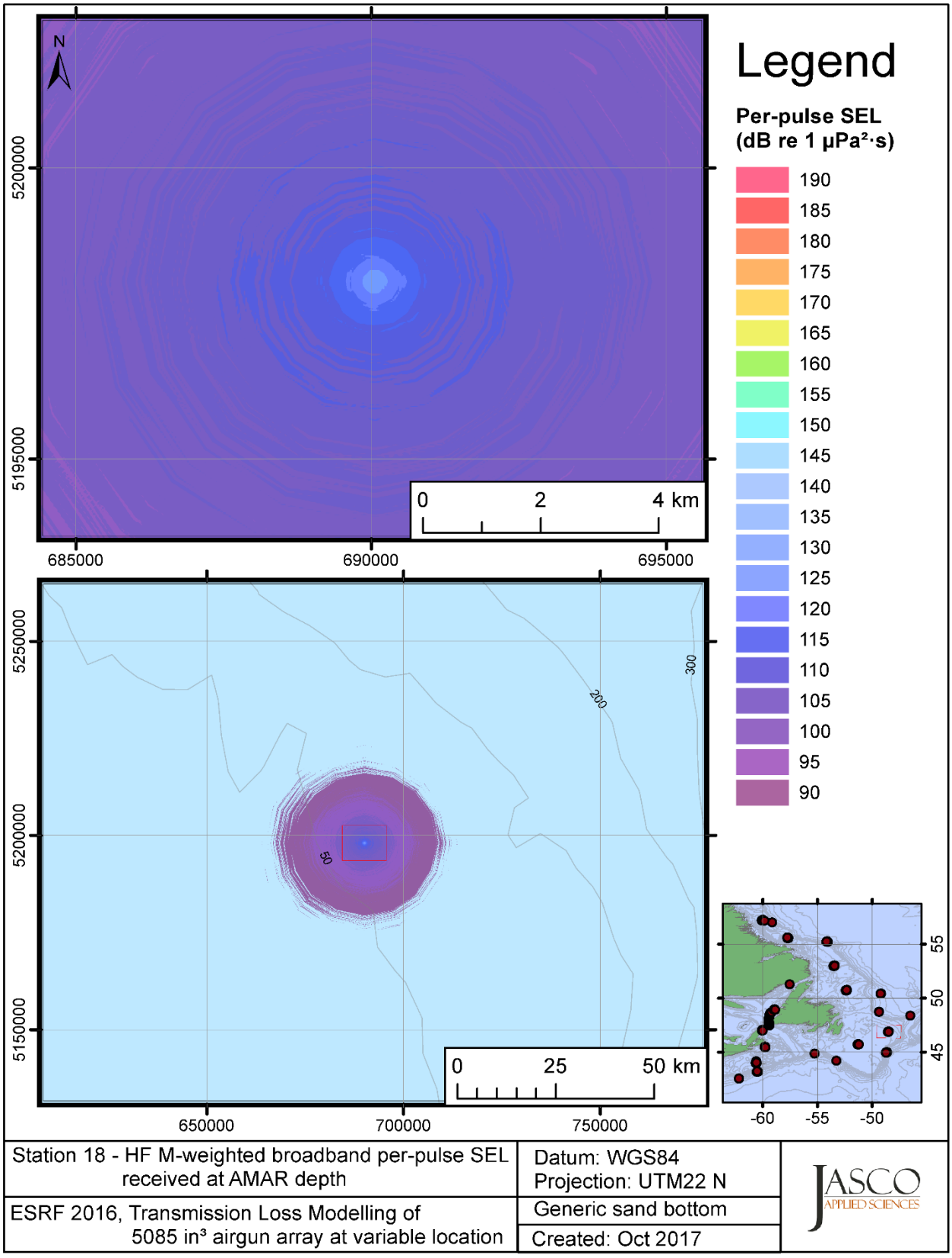

Figure C-167. Stn 18, HF M-weighted SEL received at the AMAR location and depth, modelled using a generic sand bottom, with in-situ July SSP and the airgun array located at any point on the map.

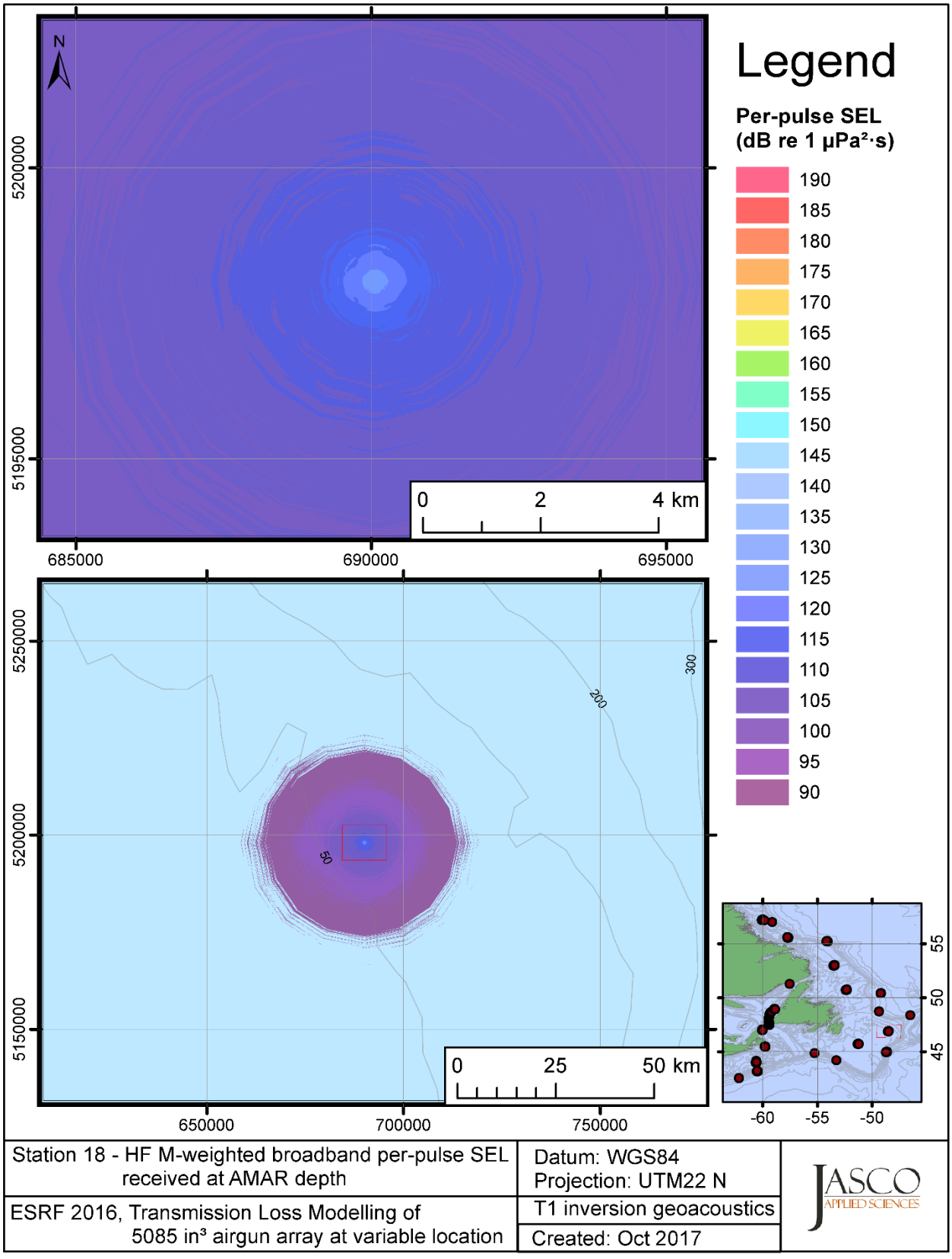

Figure C-168. Stn 18, HF M-weighted SEL received at the AMAR location and depth, modelled using the track 1 inversion geoacoustic bottom, with in-situ July SSP and the airgun array located at any point on the map.

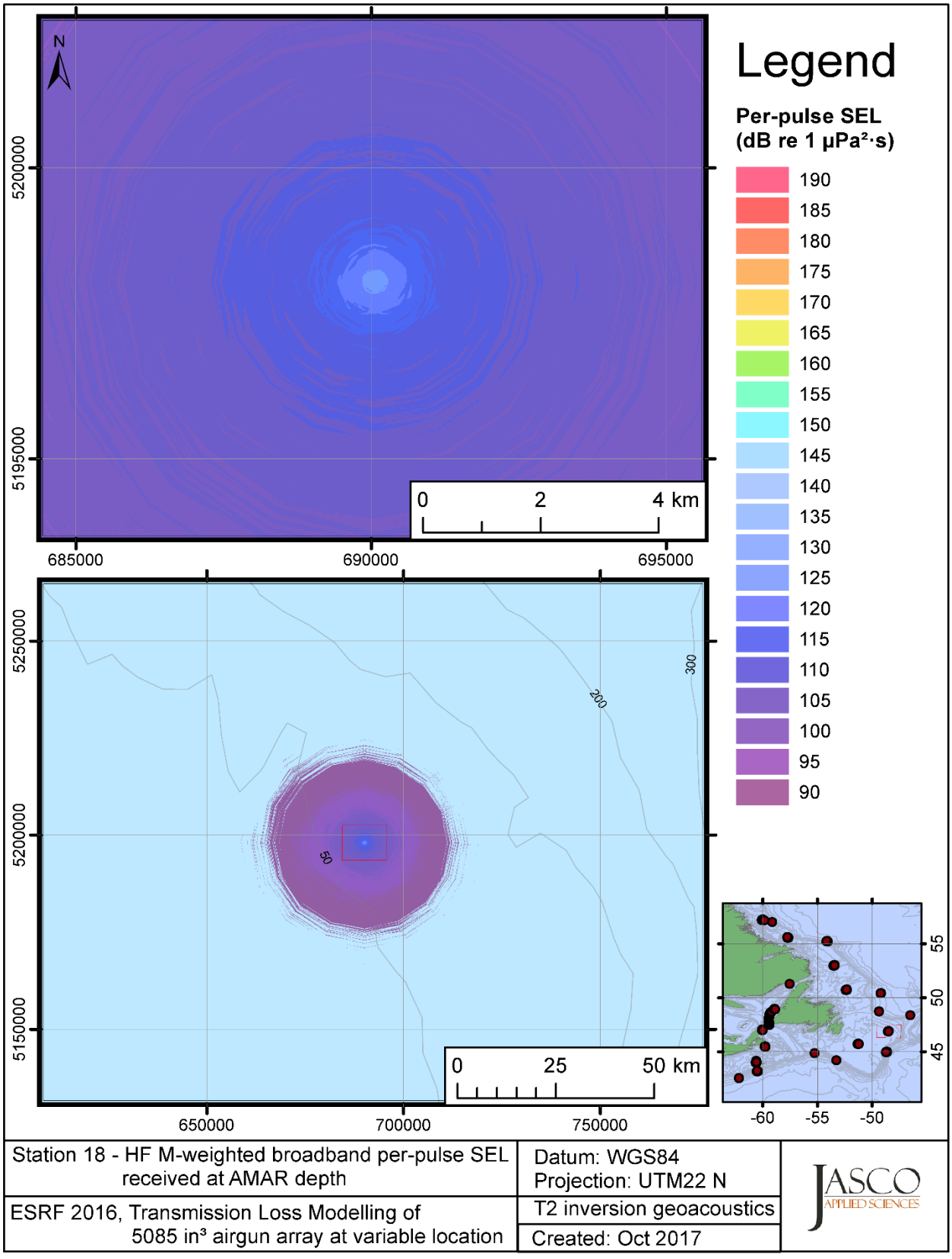

Figure C-169. Stn 18, HF M-weighted SEL received at the AMAR location and depth, modelled using the track 2 inversion geoacoustic bottom, with in-situ July SSP and the airgun array located at any point on the map.

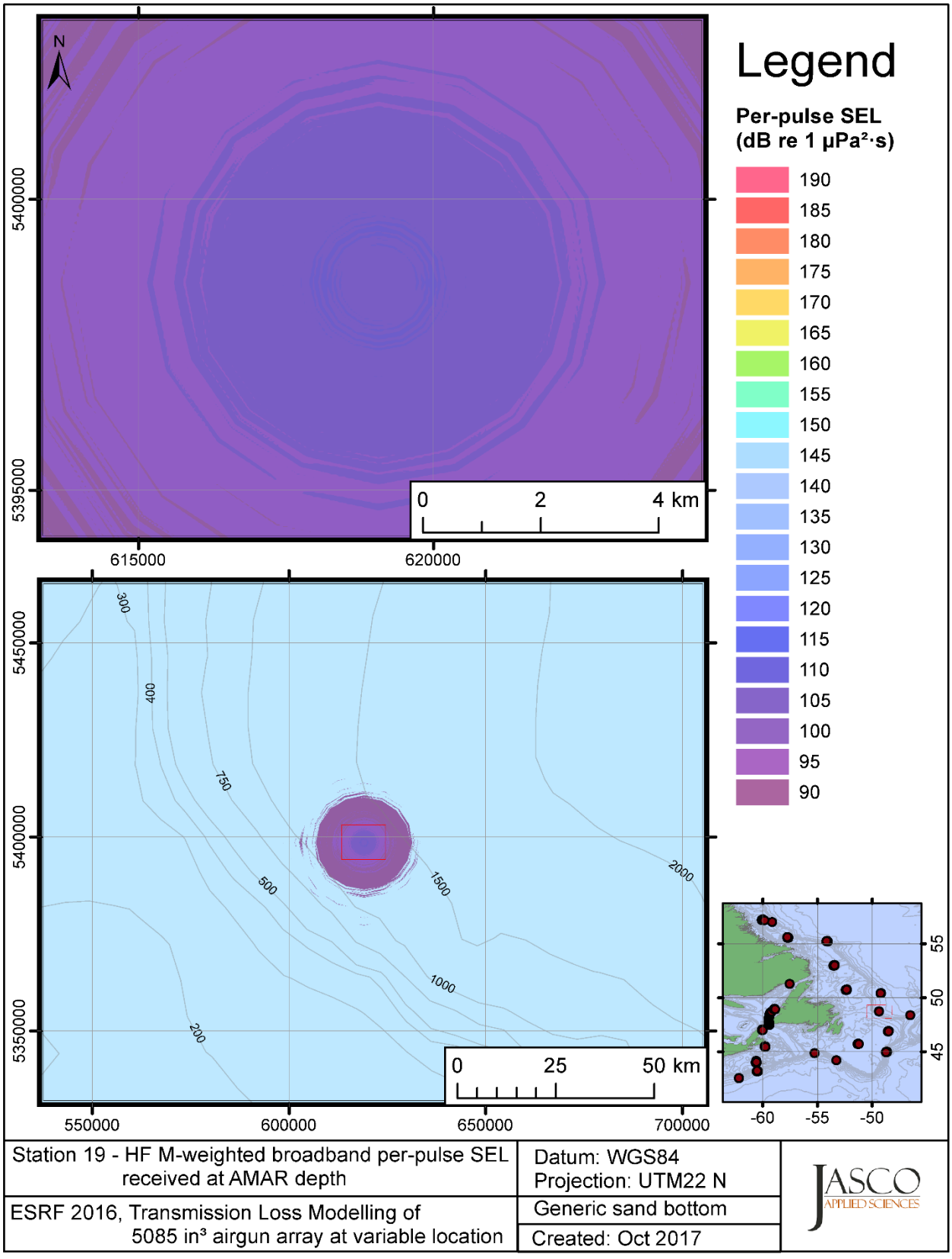

Figure C-170. Stn 19, HF M-weighted SEL received at the AMAR location and depth, modelled using a generic sand bottom, with in-situ July SSP and the airgun array located at any point on the map.

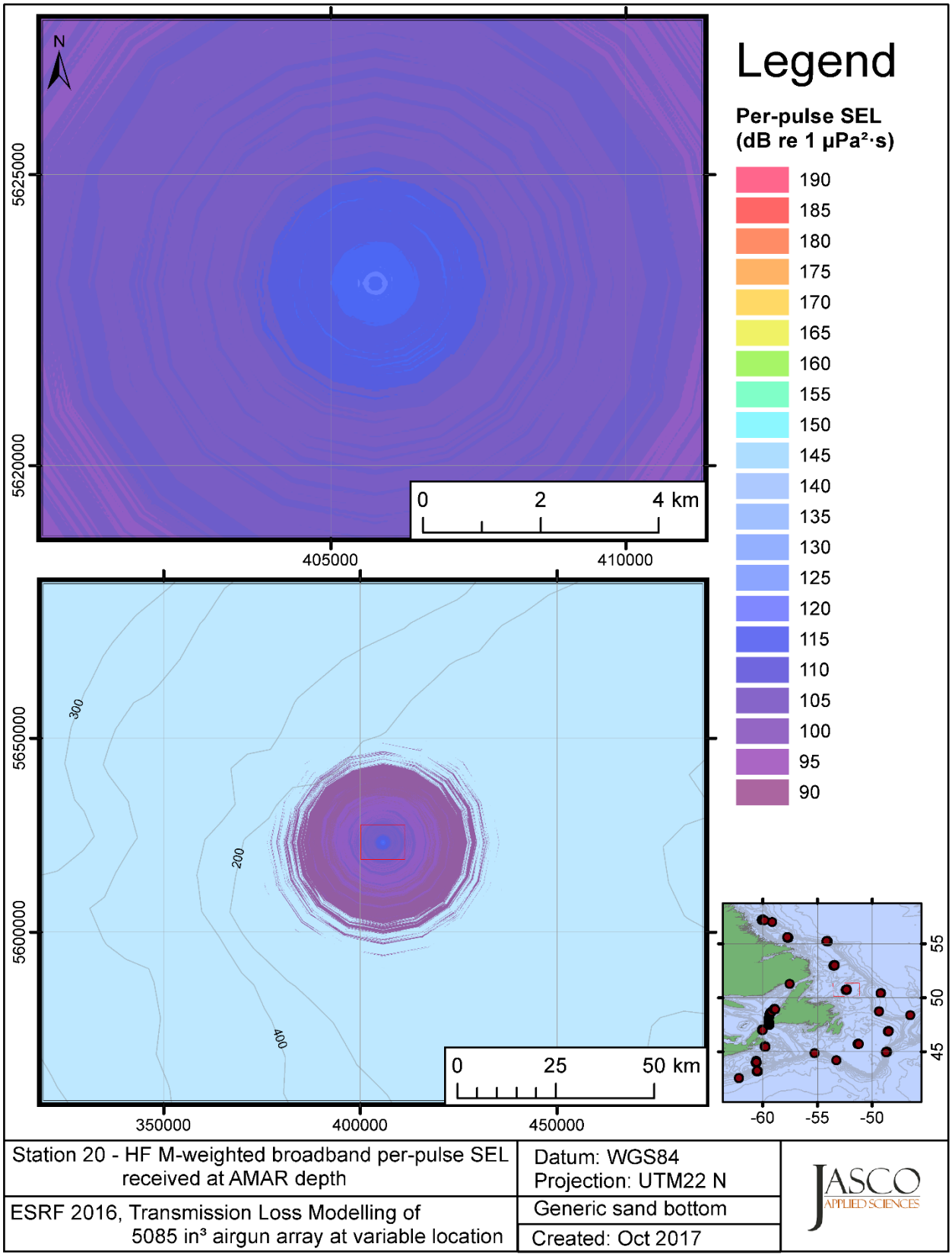

Figure C-171. Stn 20, HF M-weighted SEL received at the AMAR location and depth, modelled using a generic sand bottom, with in-situ July SSP and the airgun array located at any point on the map.

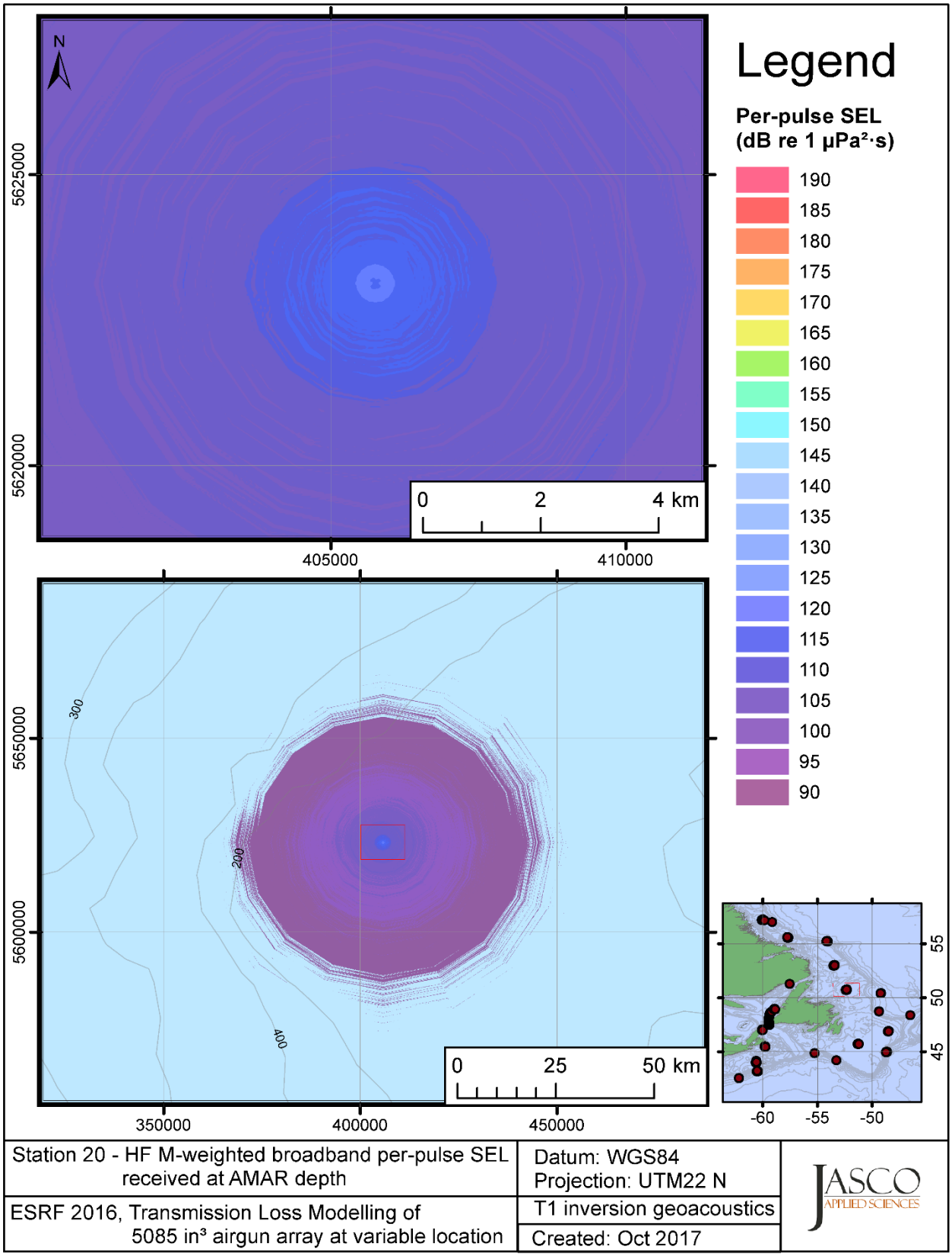

Figure C-172. Stn 20, HF M-weighted SEL received at the AMAR location and depth, modelled using the track 1 inversion geoacoustic bottom, with in-situ July SSP and the airgun array located at any point on the map.

C.5. Modelling OP M-weighted Received Level at the AMAR Location

This section presents the results of modelling the per-pulse sound exposure level (SEL) received at the AMAR location and depth as a function of the source location (varied in range and azimuth) for each of the 20 sites using a generic sand bottom; in addition, the modelling is repeated using the geoacoustic inversion bottom parameters at the 14 sites where they are available. The modelling results are presented in the form of coloured maps where the colour at any map location represents the predicted received level at the AMAR for the source located at that spot on the map. This section includes only the otariid pinnipeds in water (OP) marine-mammal-weighted per-pulse SEL results; additional maps for other marine mammal received level auditory weighting functions are presented in adjoining sections.

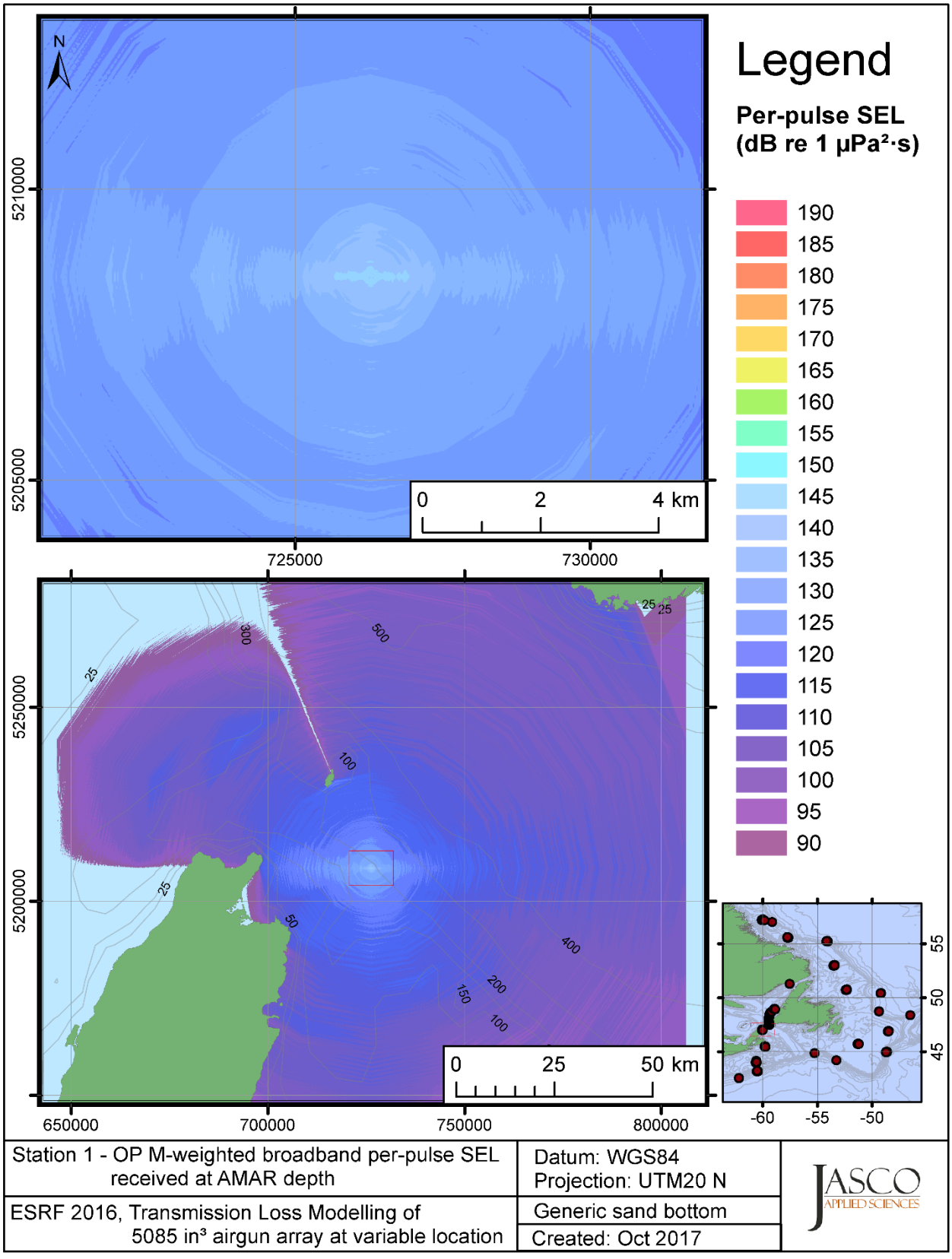

Figure C-173. Stn 1, OP M-weighted SEL received at the AMAR location and depth, modelled using a generic sand bottom, with in-situ July SSP and the airgun array located at any point on the map.

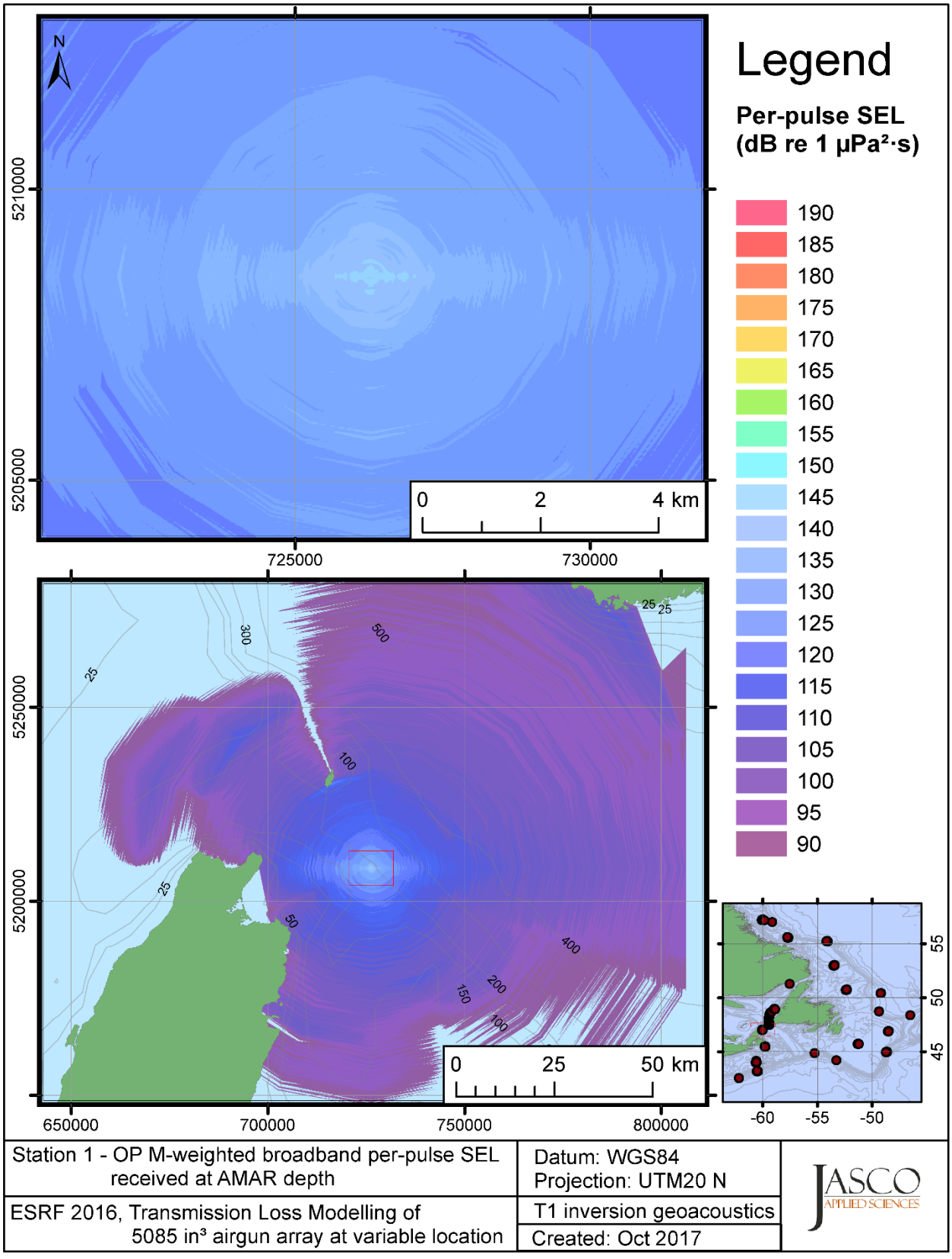

Figure C-174. Stn 1, OP M-weighted SEL received at the AMAR location and depth, modelled using the track 1 inversion geoacoustic bottom, with in-situ July SSP and the airgun array located at any point on the map.

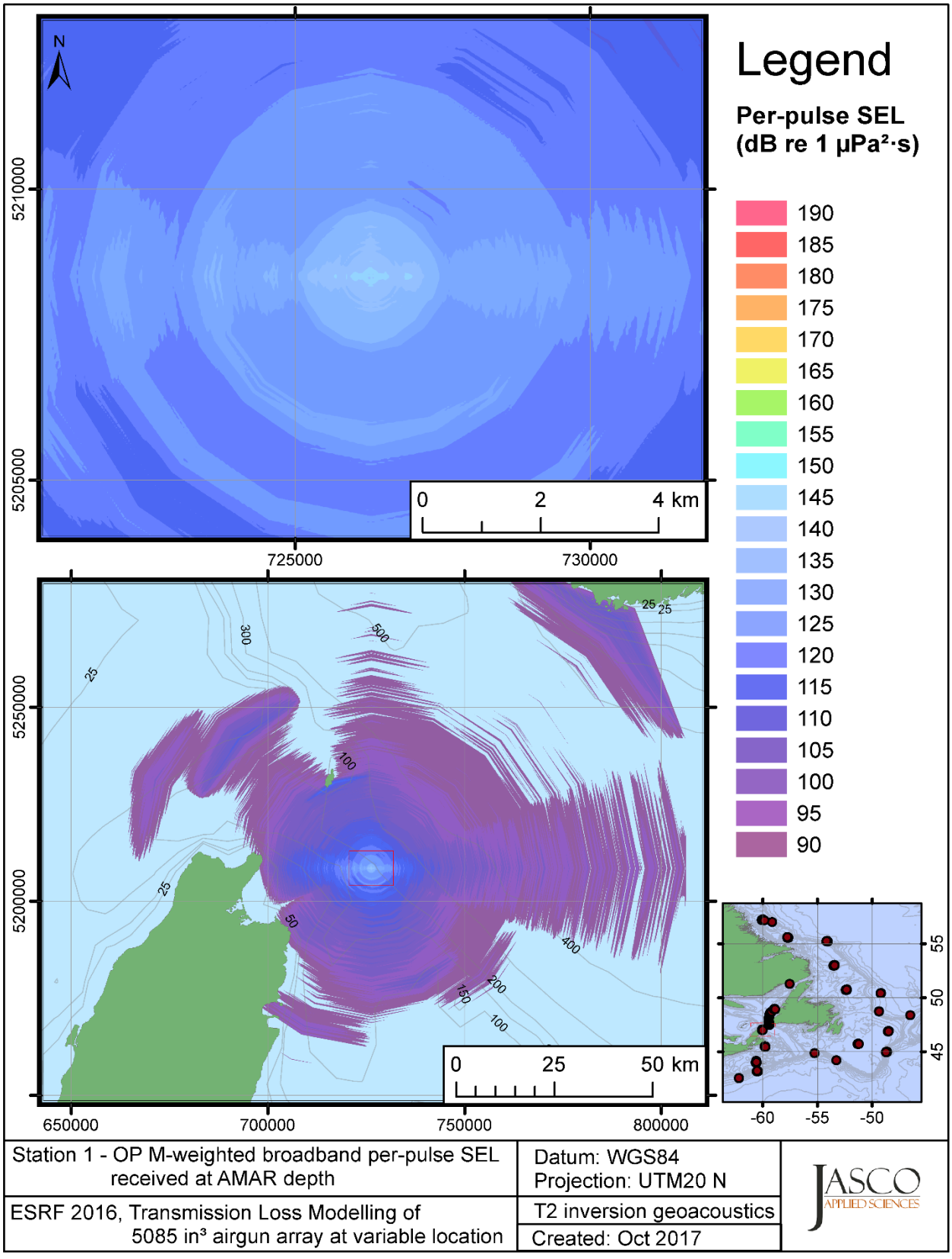

Figure C-175. Stn 1, OP M-weighted SEL received at the AMAR location and depth, modelled using the track 2 inversion geoacoustic bottom, with in-situ July SSP and the airgun array located at any point on the map.

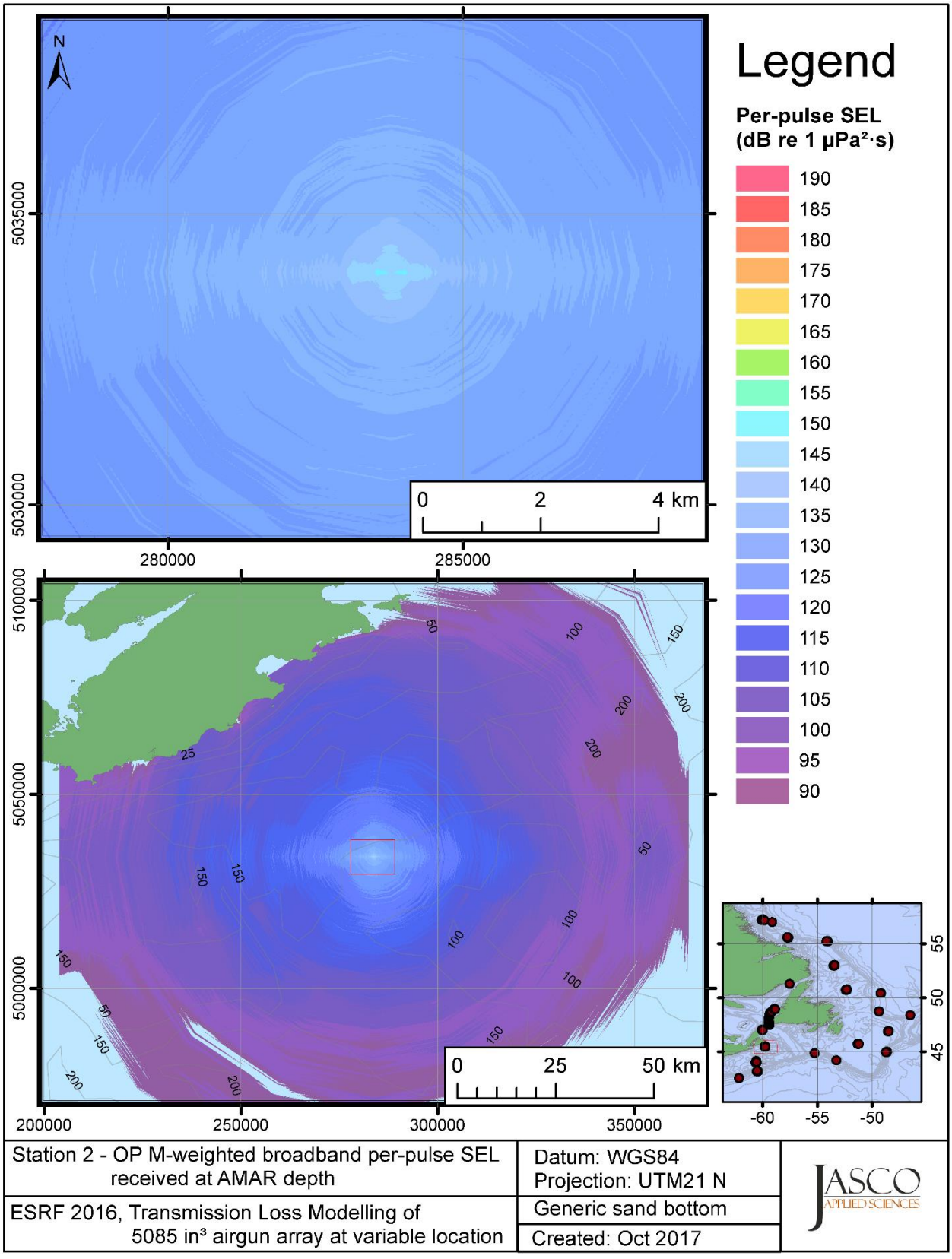

Figure C-176. Stn 2, OP M-weighted SEL received at the AMAR location and depth, modelled using a generic sand bottom, with in-situ July SSP and the airgun array located at any point on the map.

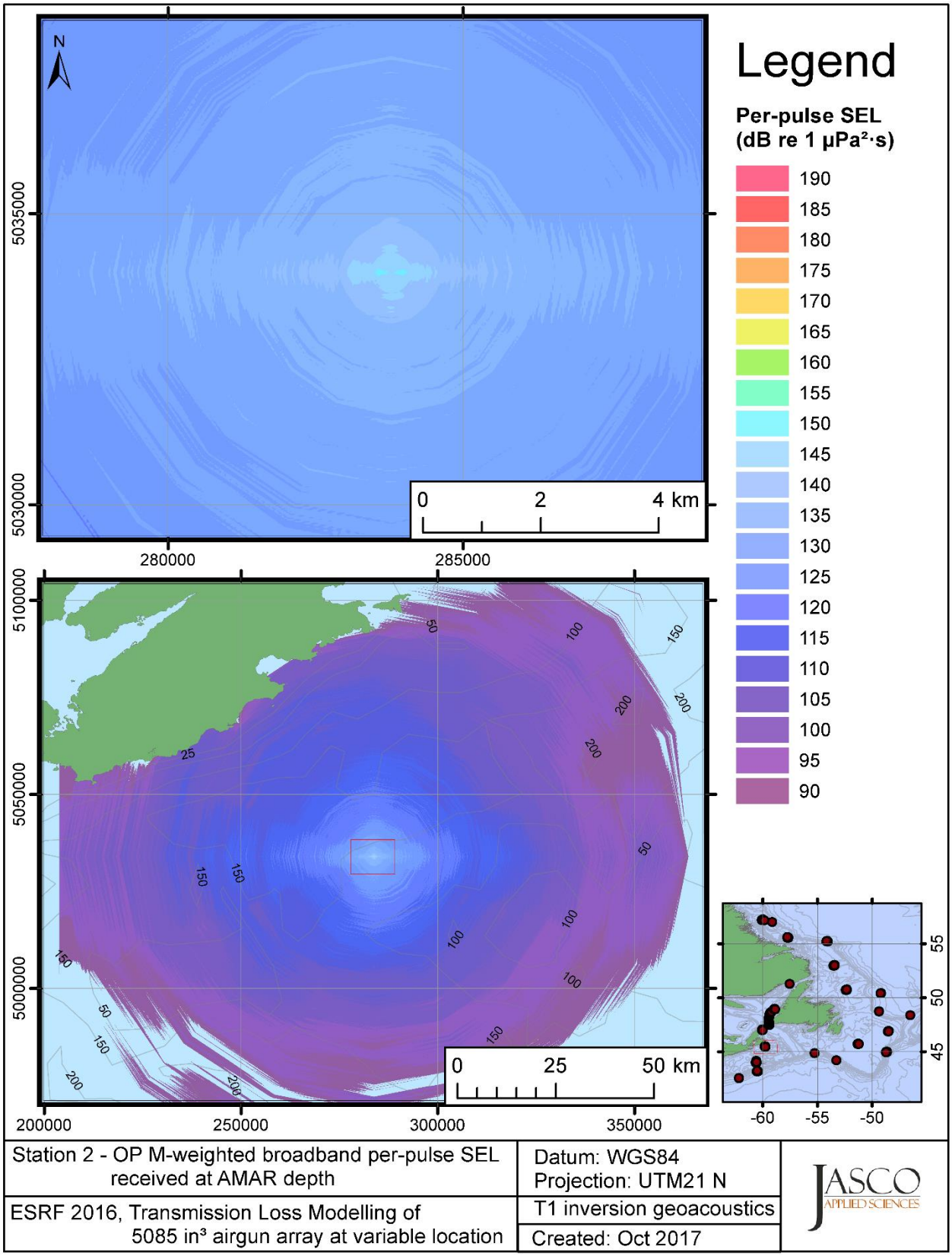

Figure C-177. Stn 2, OP M-weighted SEL received at the AMAR location and depth, modelled using the track 1 inversion geoacoustic bottom, with in-situ July SSP and the airgun array located at any point on the map.

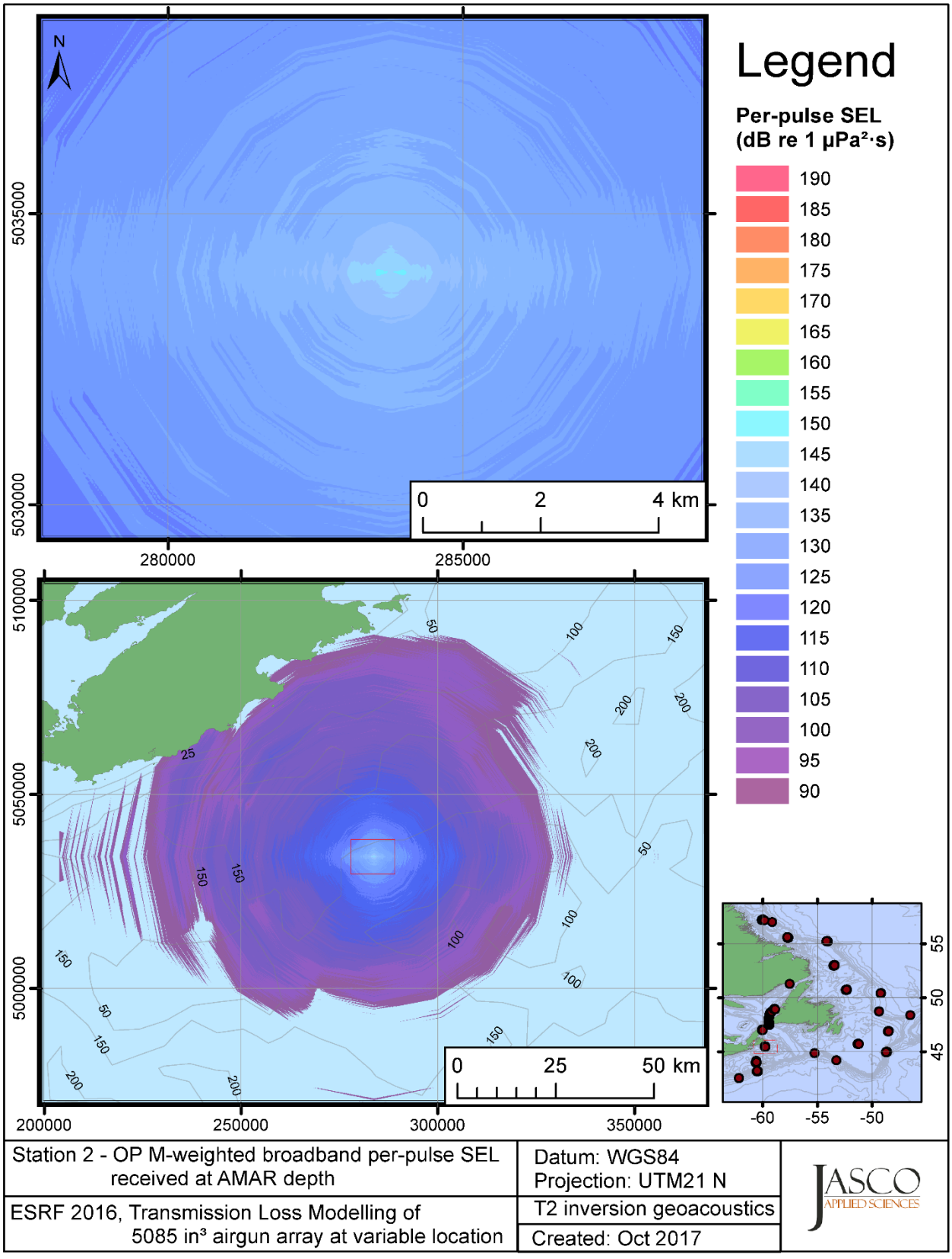

Figure C-178. Stn 2, OP M-weighted SEL received at the AMAR location and depth, modelled using the track 2 inversion geoacoustic bottom, with in-situ July SSP and the airgun array located at any point on the map.

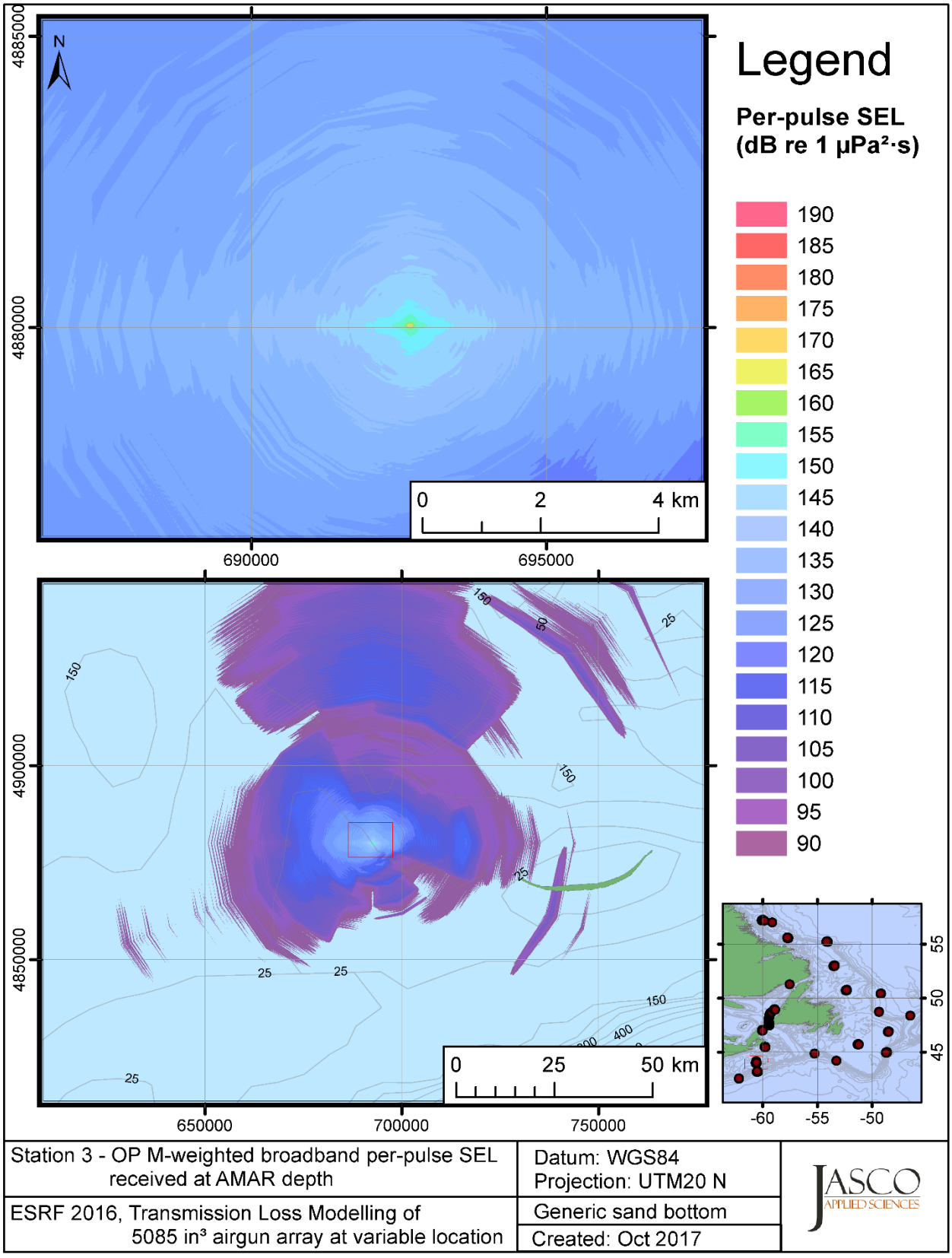

Figure C-179. Stn 3, OP M-weighted SEL received at the AMAR location and depth, modelled using a generic sand bottom, with in-situ July SSP and the airgun array located at any point on the map.

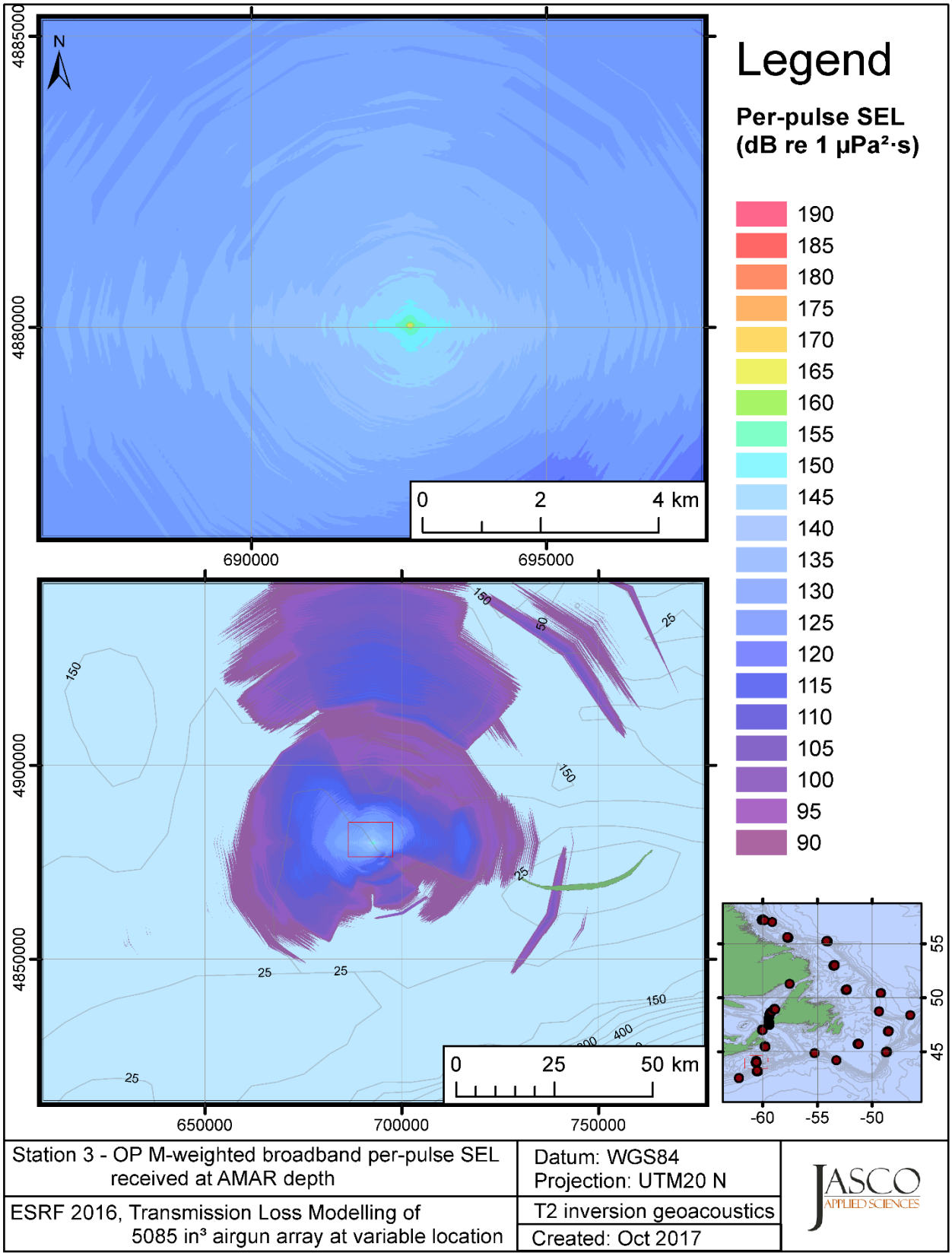

Figure C-180. Stn 3, OP M-weighted SEL received at the AMAR location and depth, modelled using the track 2 inversion geoacoustic bottom, with in-situ July SSP and the airgun array located at any point on the map.

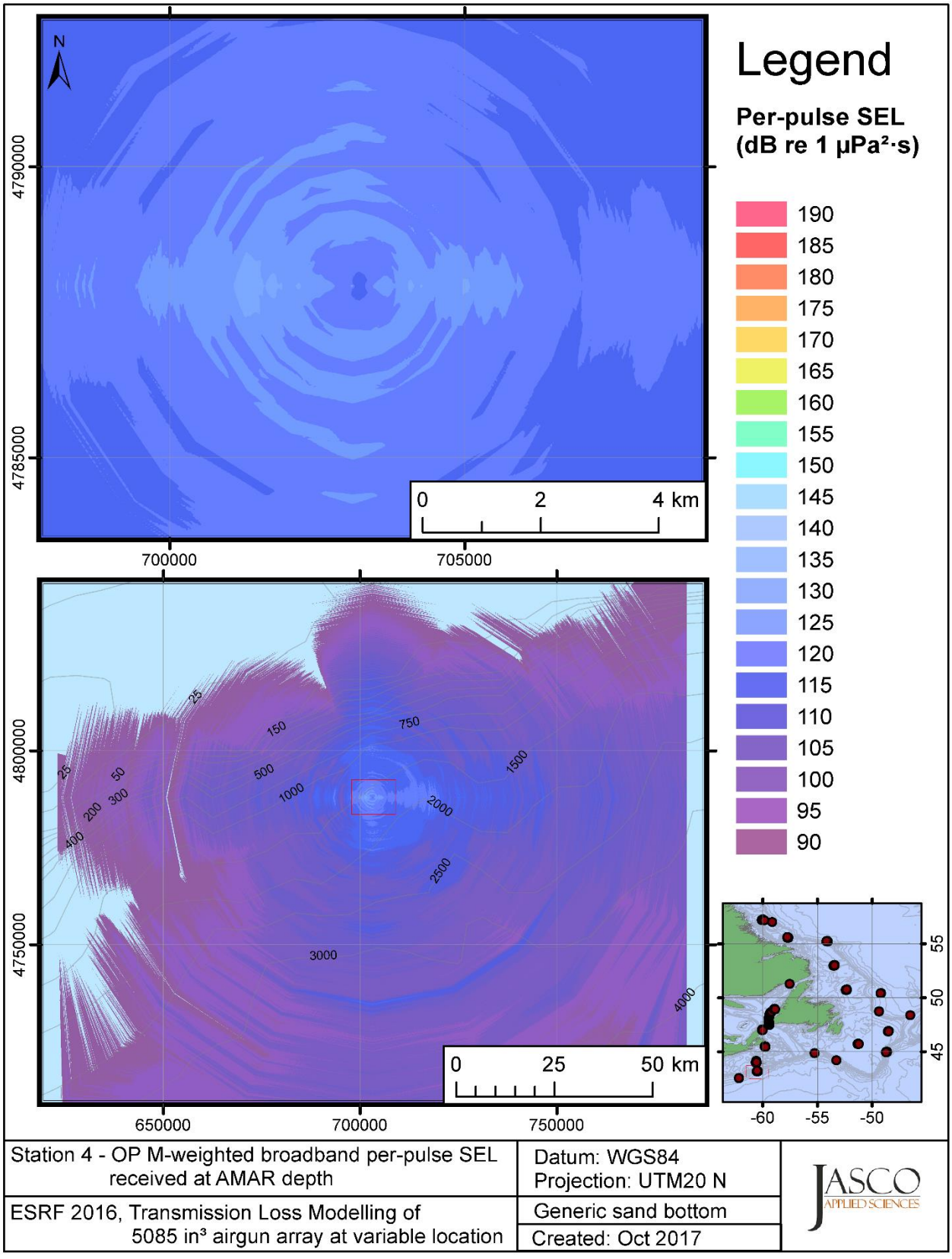

Figure C-181. Stn 4, OP M-weighted SEL received at the AMAR location and depth, modelled using a generic sand bottom, with in-situ July SSP and the airgun array located at any point on the map.

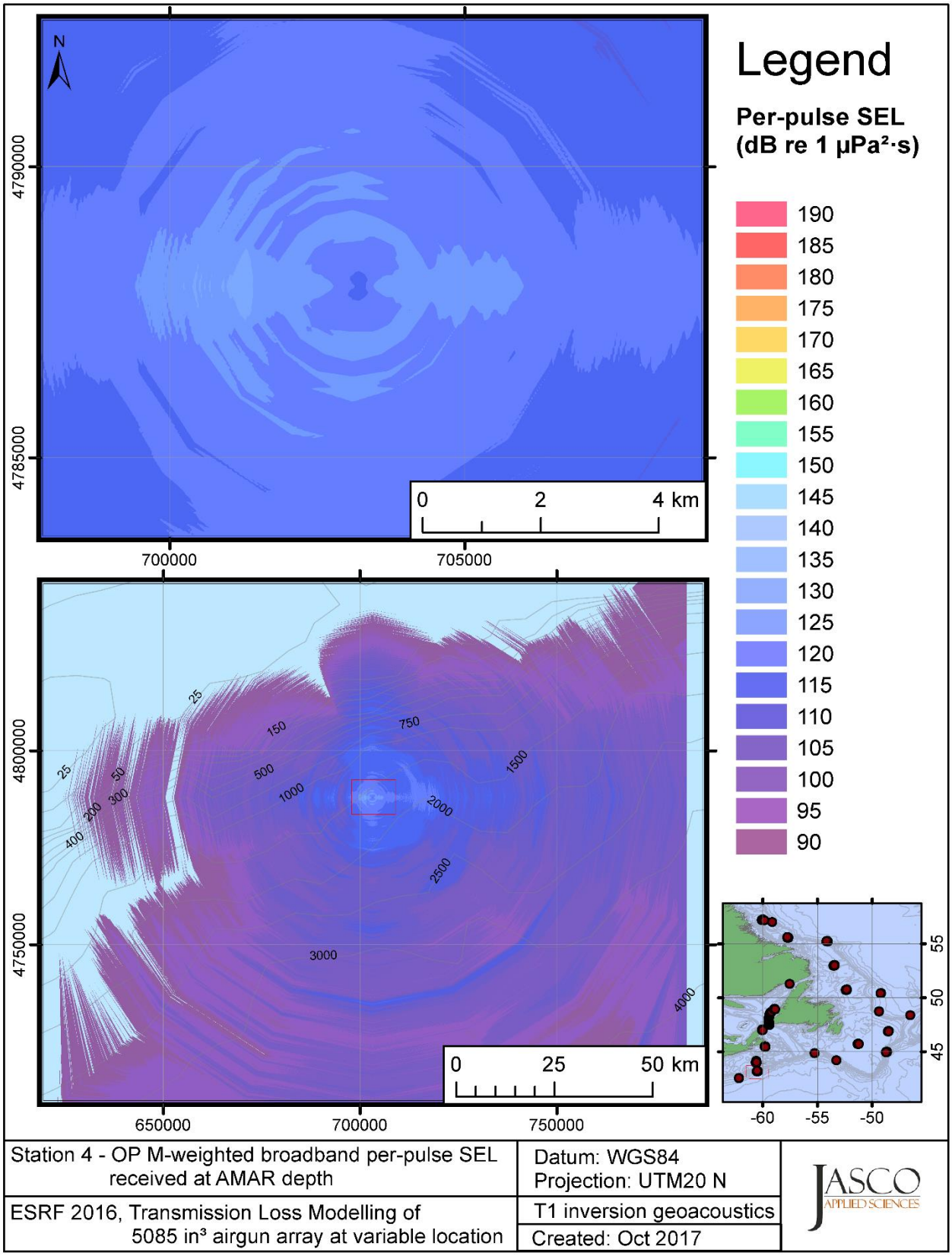

Figure C-182. Stn 4, OP M-weighted SEL received at the AMAR location and depth, modelled using the track 1 inversion geoacoustic bottom, with in-situ July SSP and the airgun array located at any point on the map.

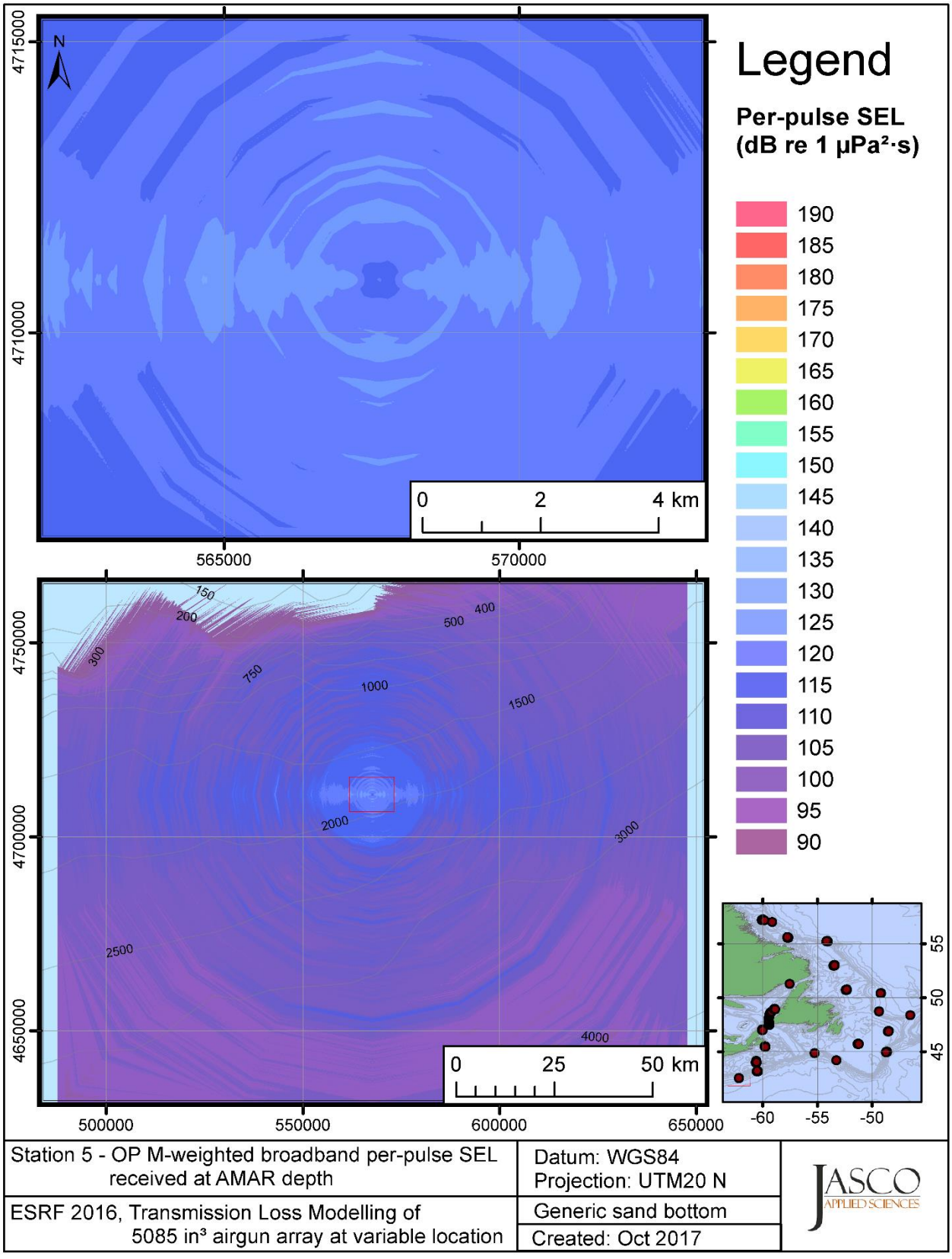

Figure C-183. Stn 5, OP M-weighted SEL received at the AMAR location and depth, modelled using a generic sand bottom, with in-situ July SSP and the airgun array located at any point on the map.

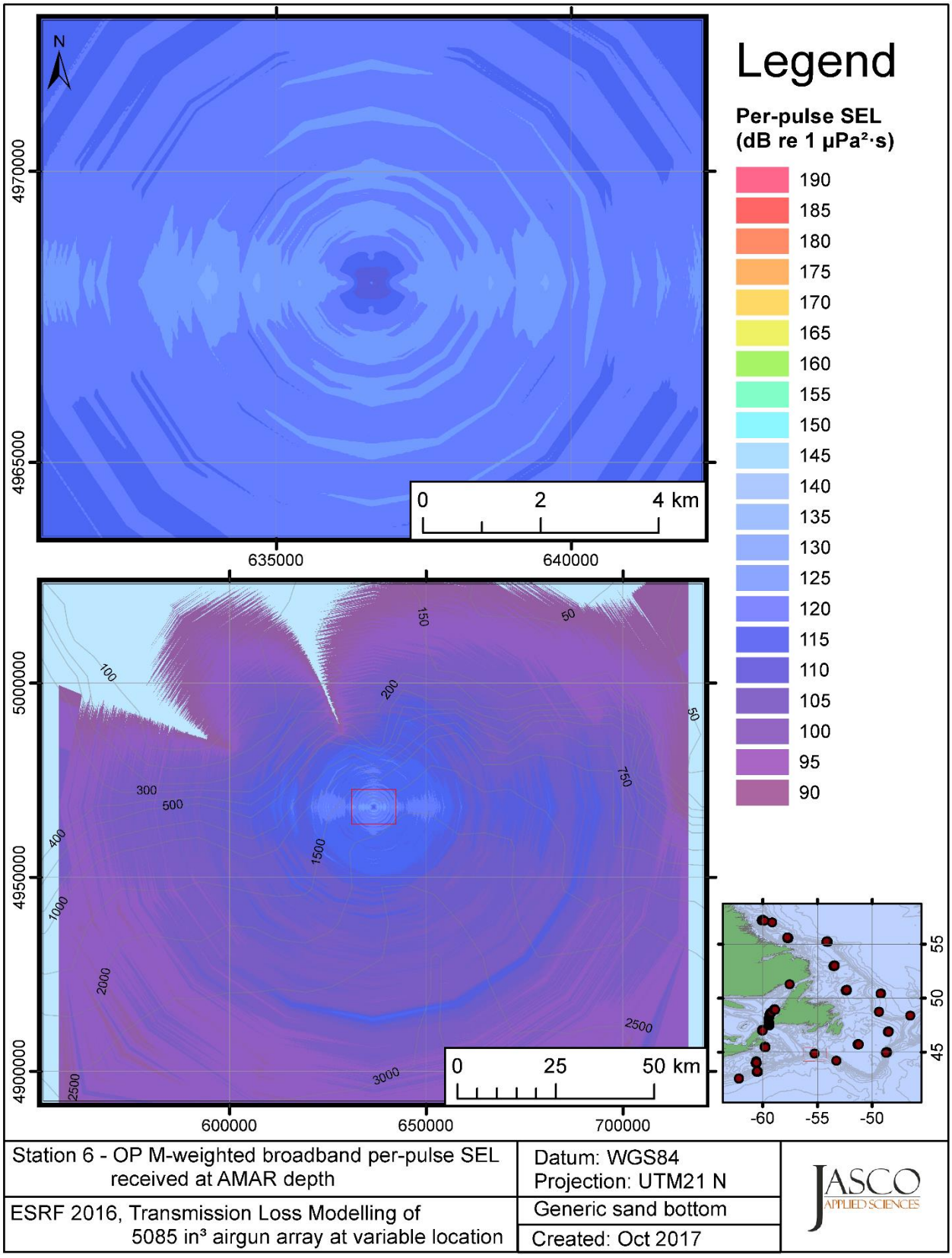

Figure C-184. Stn 6, OP M-weighted SEL received at the AMAR location and depth, modelled using a generic sand bottom, with in-situ July SSP and the airgun array located at any point on the map.

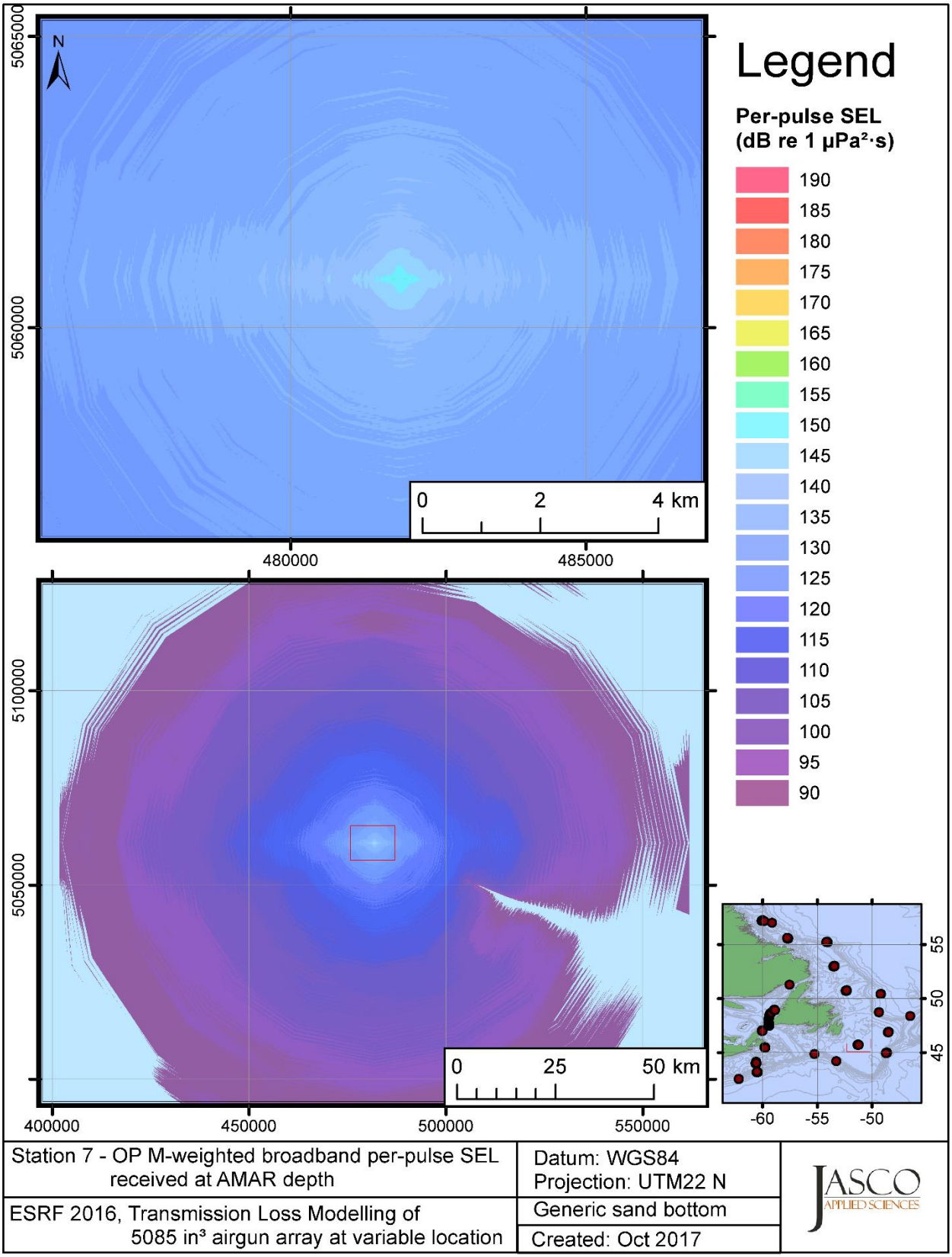

Figure C-185. Stn 7, OP M-weighted SEL received at the AMAR location and depth, modelled using a generic sand bottom, with in-situ July SSP and the airgun array located at any point on the map.

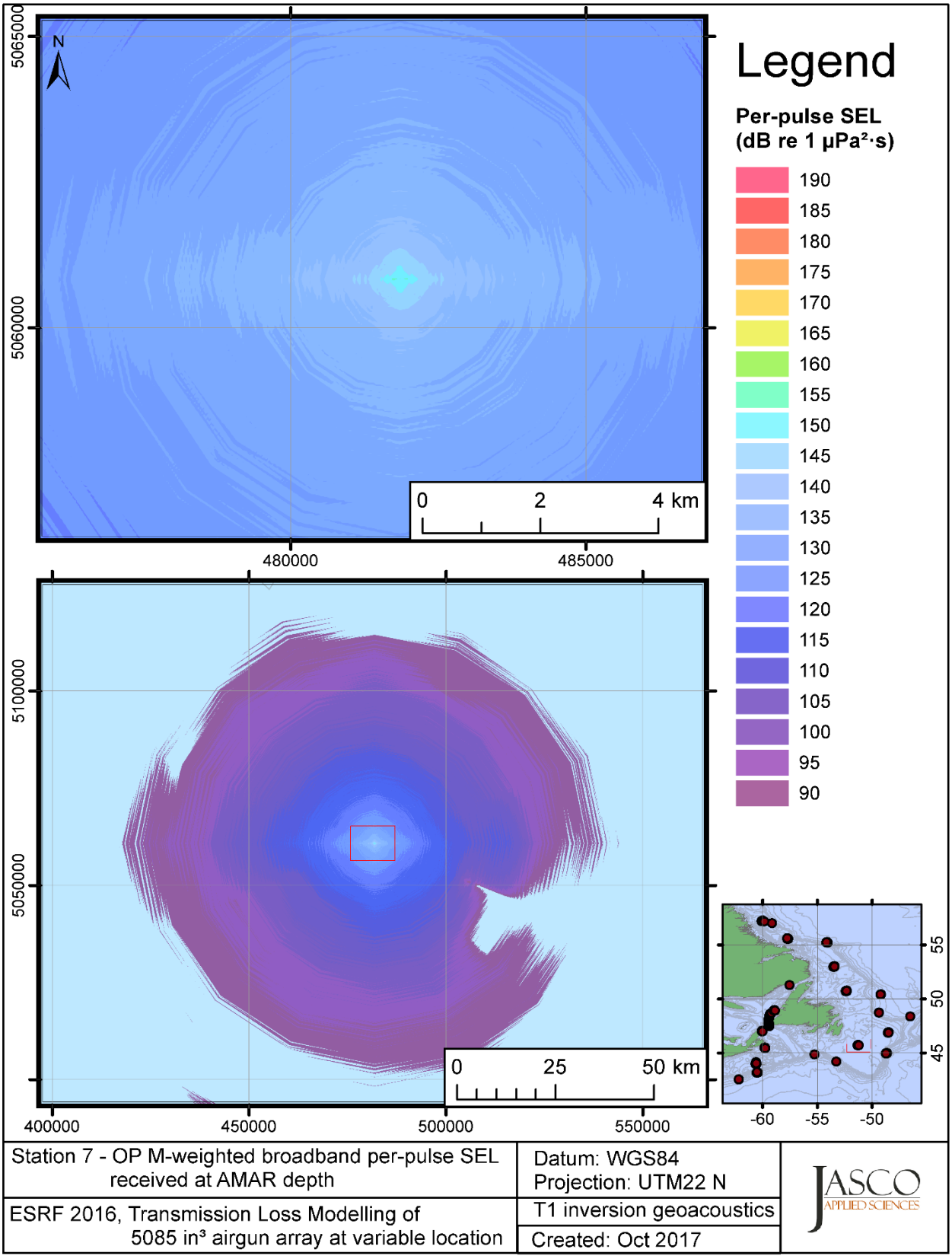

Figure C-186. Stn 7, OP M-weighted SEL received at the AMAR location and depth, modelled using the track 1 inversion geoacoustic bottom, with in-situ July SSP and the airgun array located at any point on the map.

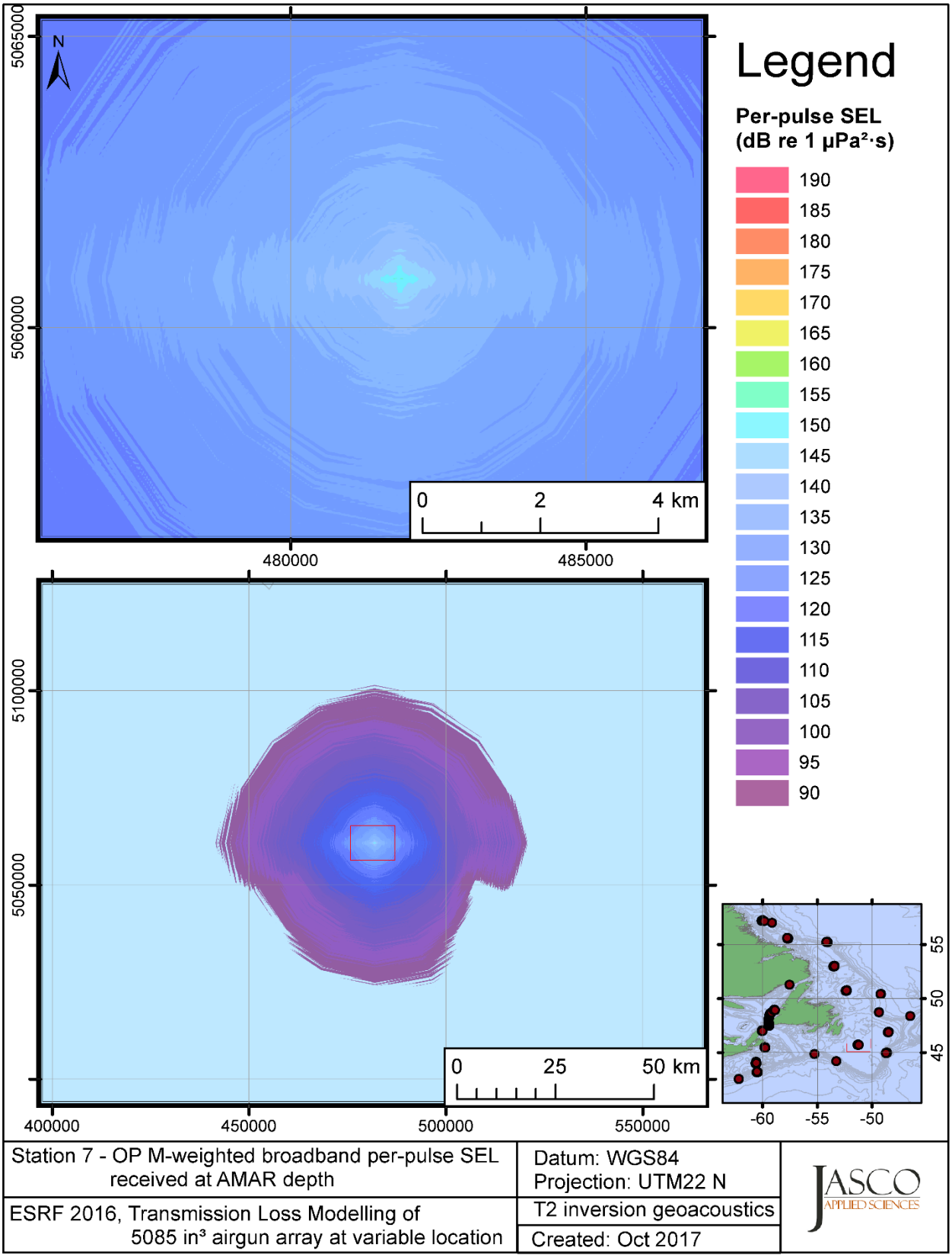

Figure C-187. Stn 7, OP M-weighted SEL received at the AMAR location and depth, modelled using the track 2 inversion geoacoustic bottom, with in-situ July SSP and the airgun array located at any point on the map.

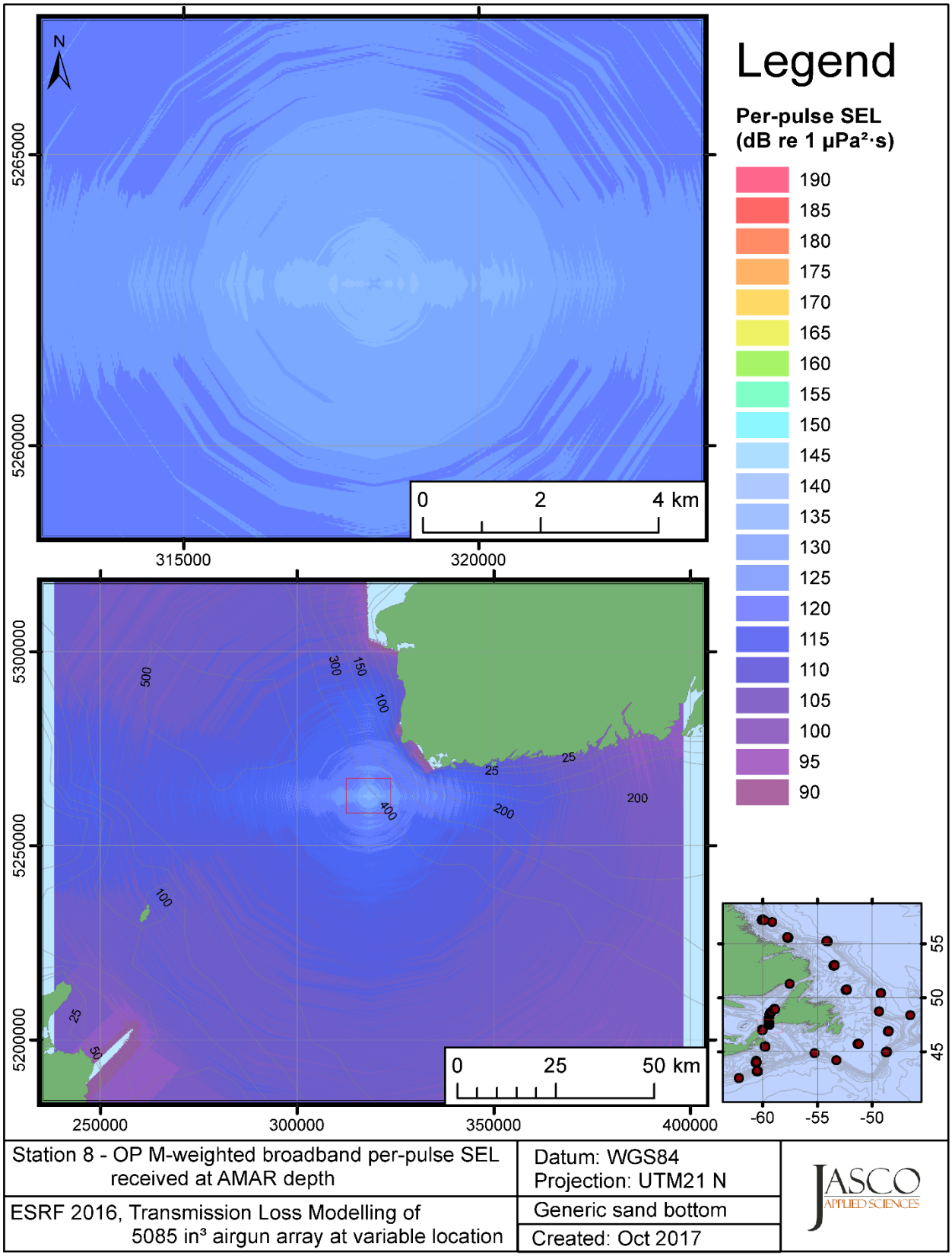

Figure C-188. Stn 8, OP M-weighted SEL received at the AMAR location and depth, modelled using a generic sand bottom, with GDEM July SSP and the airgun array located at any point on the map.

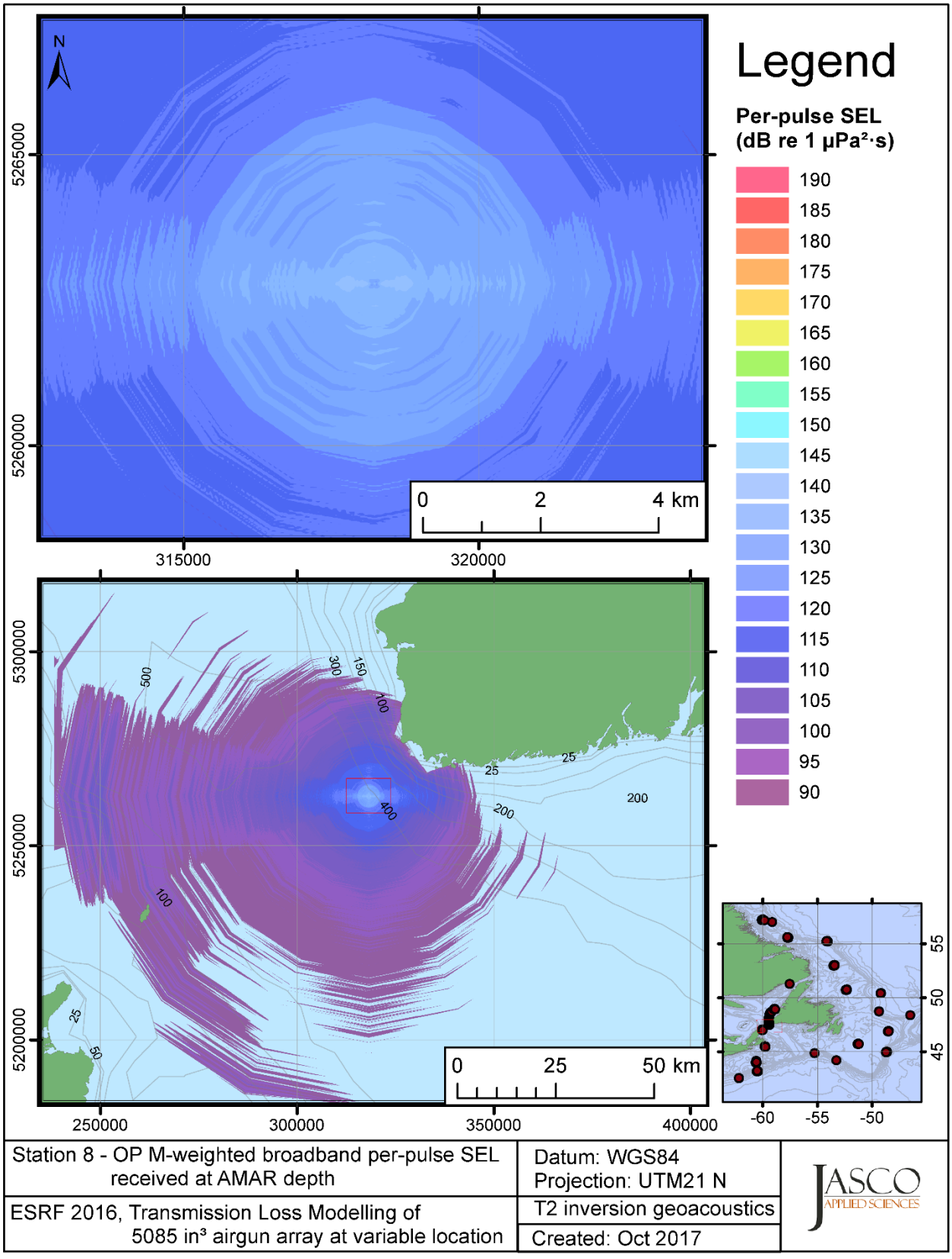

Figure C-189. Stn 8, OP M-weighted SEL received at the AMAR location and depth, modelled using the track 2 inversion geoacoustic bottom, with GDEM July SSP and the airgun array located at any point on the map.

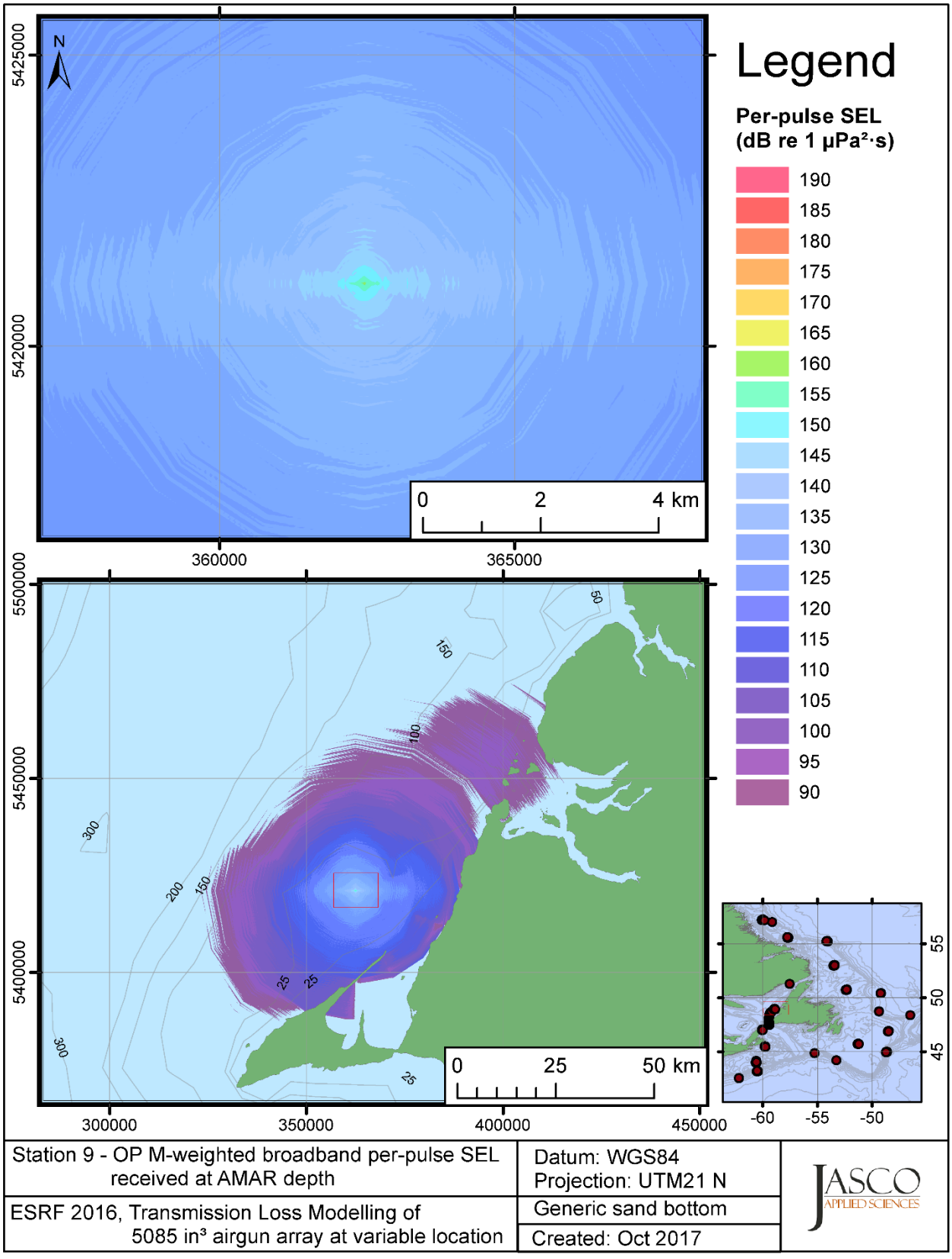

Figure C-190. Stn 9, OP M-weighted SEL received at the AMAR location and depth, modelled using a generic sand bottom, with GDEM July SSP and the airgun array located at any point on the map.

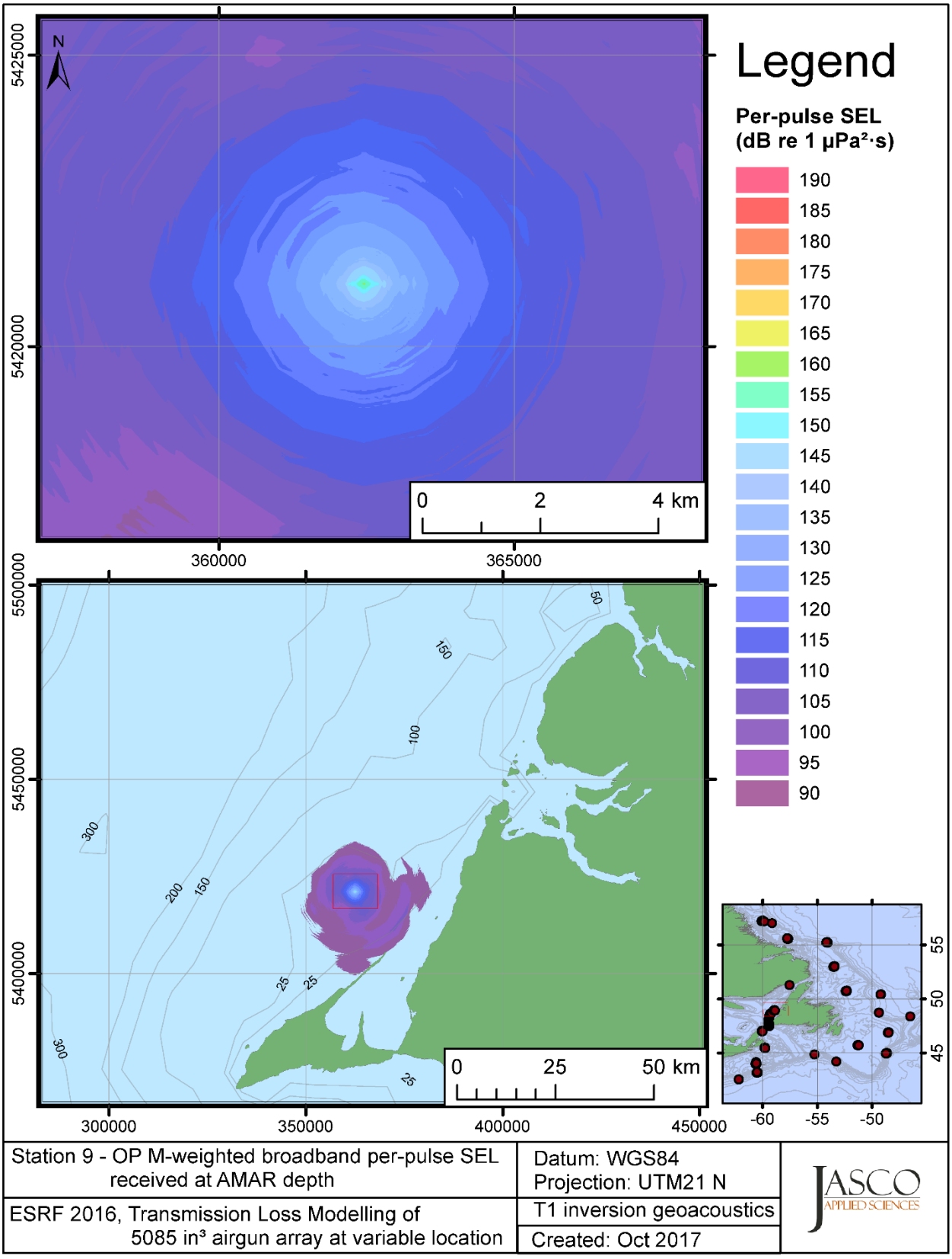

Figure C-191. Stn 9, OP M-weighted SEL received at the AMAR location and depth, modelled using the track 1 inversion geoacoustic bottom, with GDEM July SSP and the airgun array located at any point on the map.

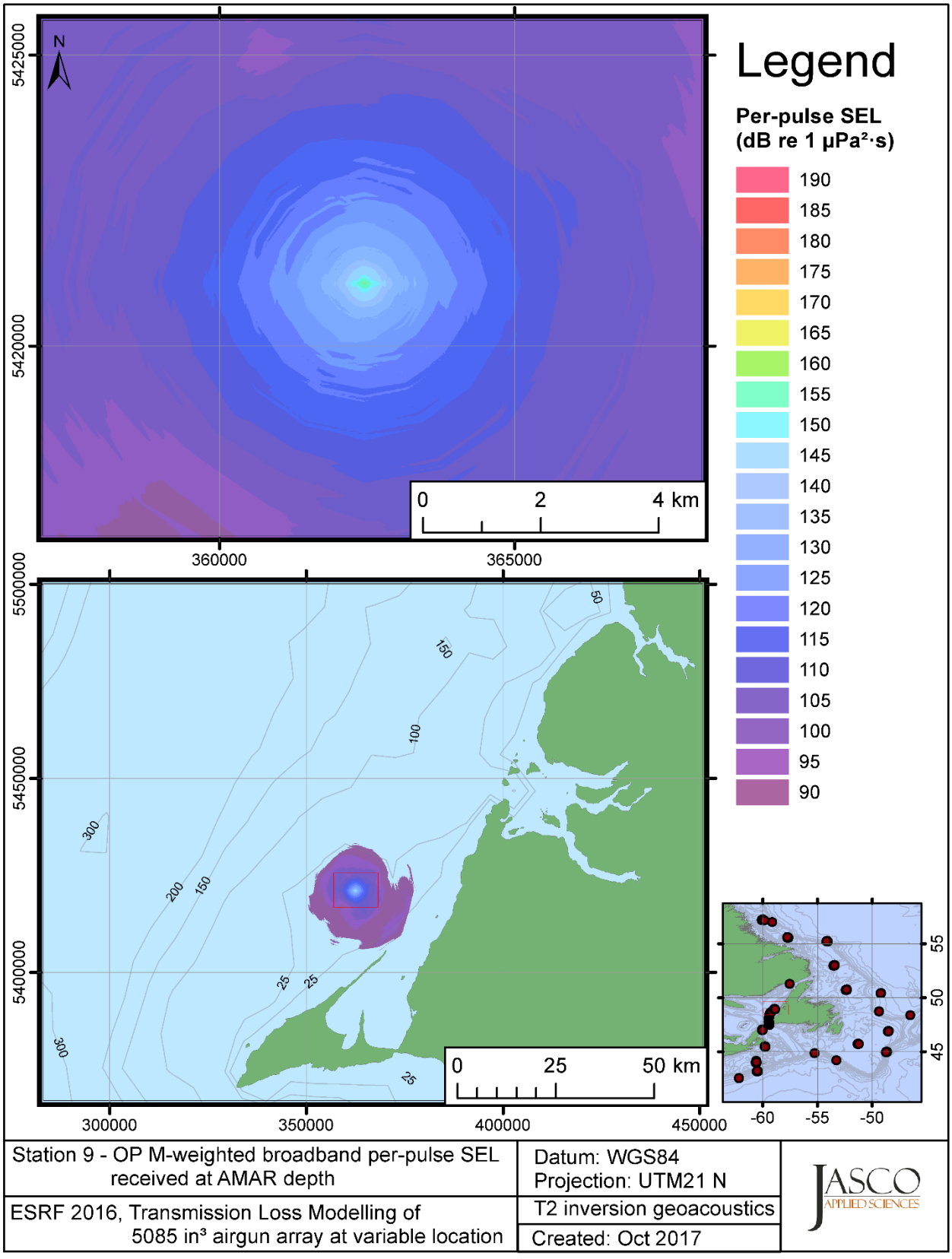

Figure C-192. Stn 9, OP M-weighted SEL received at the AMAR location and depth, modelled using the track 2 inversion geoacoustic bottom, with GDEM July SSP and the airgun array located at any point on the map.

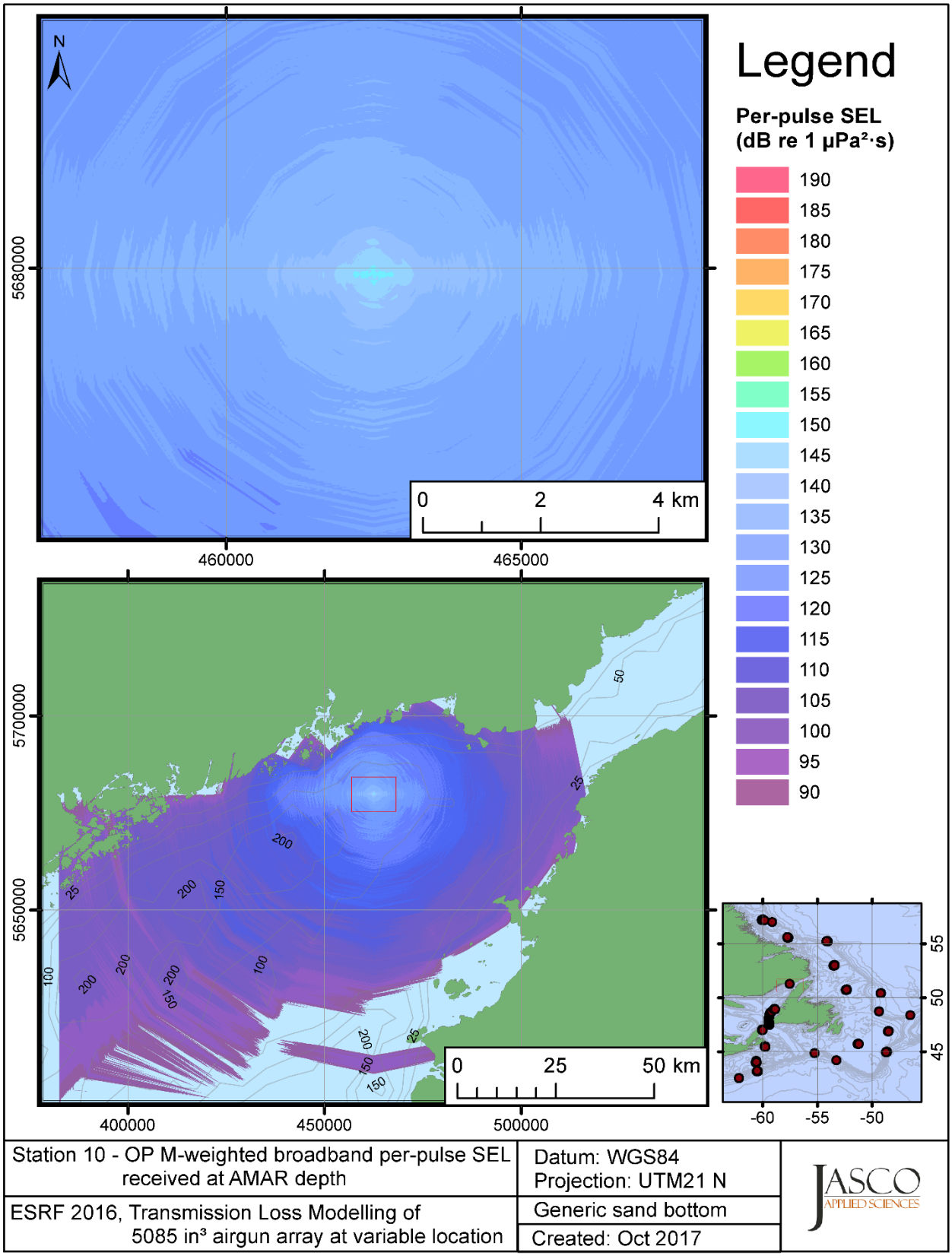

Figure C-193. Stn 10, OP M-weighted SEL received at the AMAR location and depth, modelled using a generic sand bottom, with in-situ July SSP and the airgun array located at any point on the map.

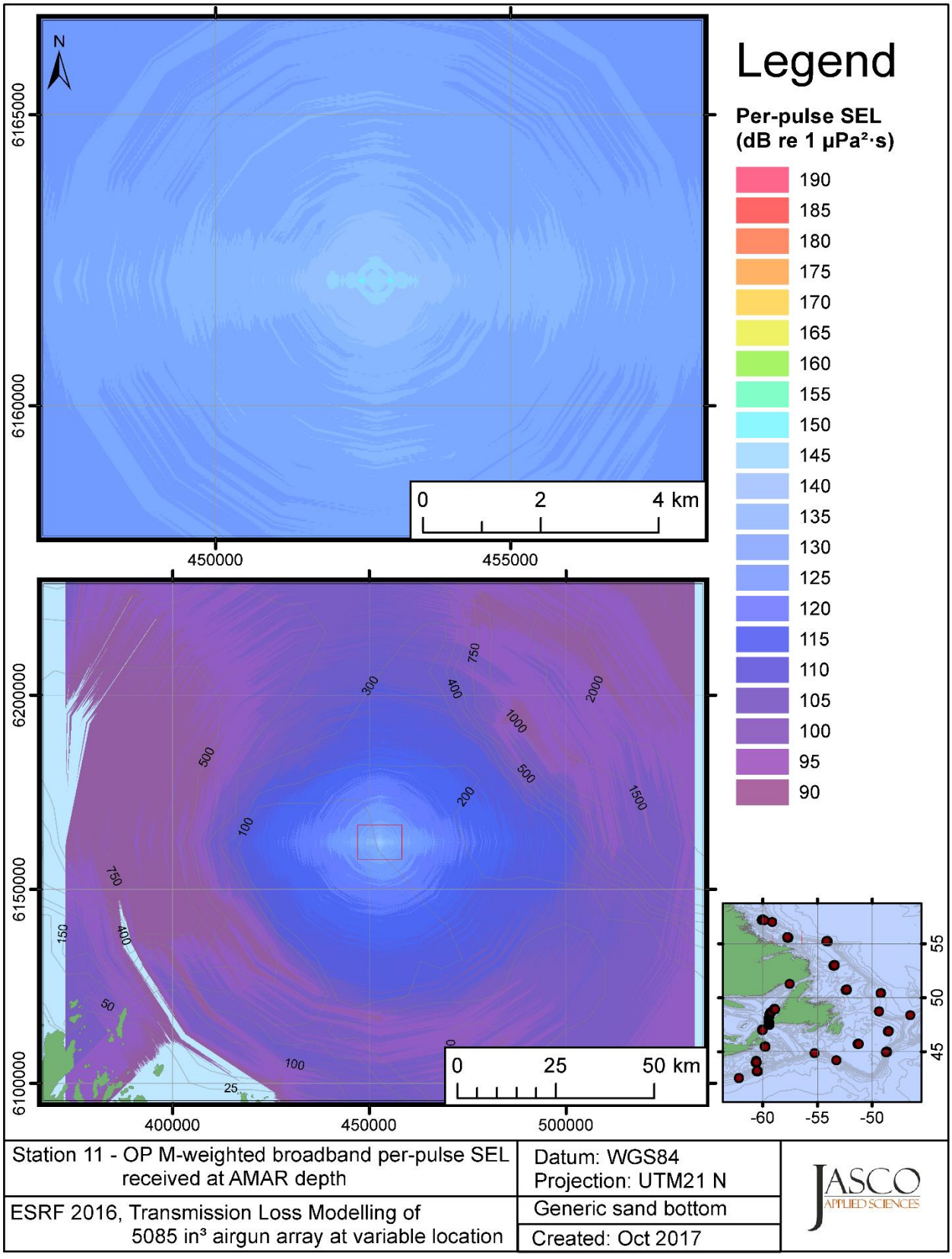

Figure C-194. Stn 11, OP M-weighted SEL received at the AMAR location and depth, modelled using a generic sand bottom, with in-situ July SSP and the airgun array located at any point on the map.

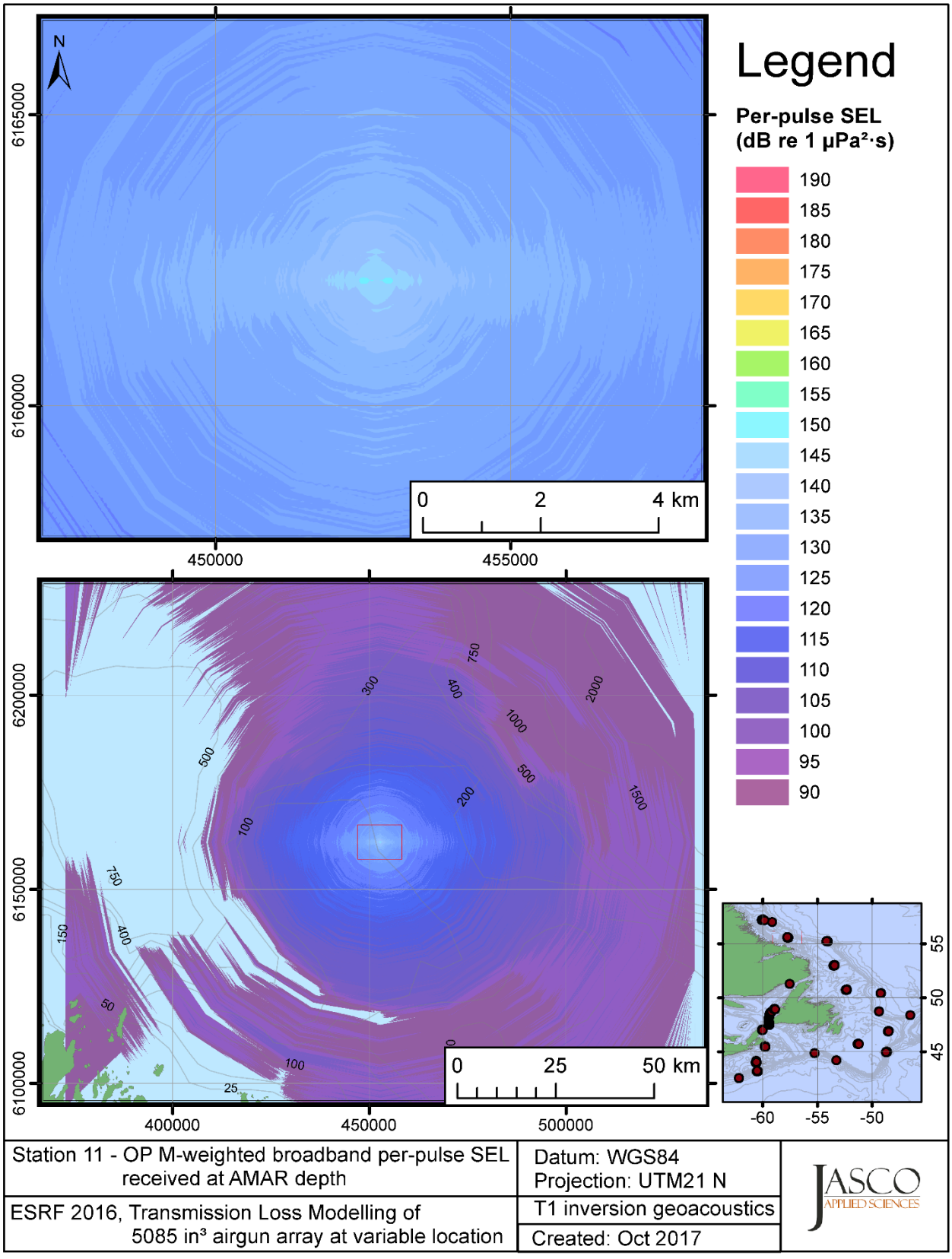

Figure C-195. Stn 11, OP M-weighted SEL received at the AMAR location and depth, modelled using the track 1 inversion geoacoustic bottom, with in-situ July SSP and the airgun array located at any point on the map.

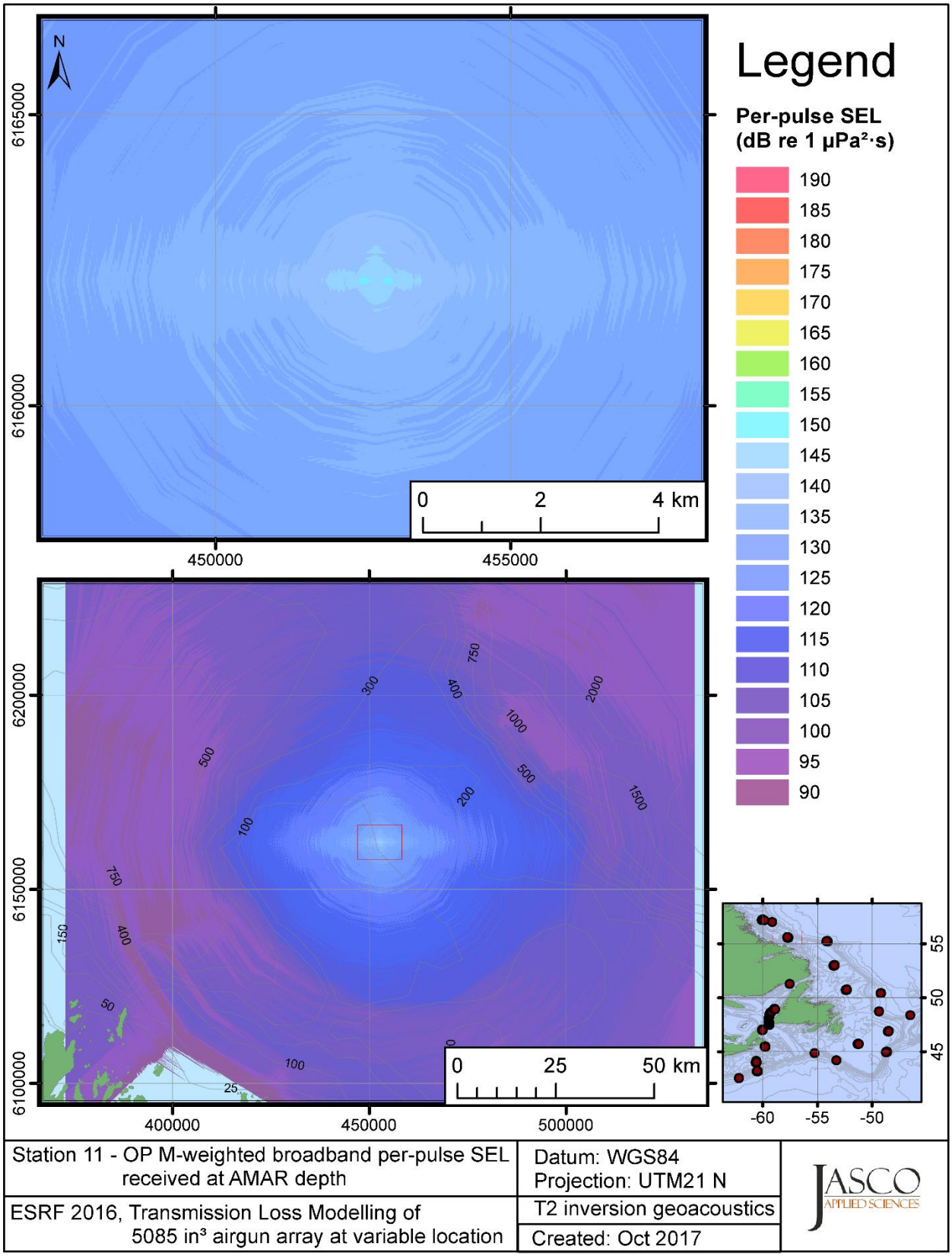

Figure C-196. Stn 11, OP M-weighted SEL received at the AMAR location and depth, modelled using the track 2 inversion geoacoustic bottom, with in-situ July SSP and the airgun array located at any point on the map.

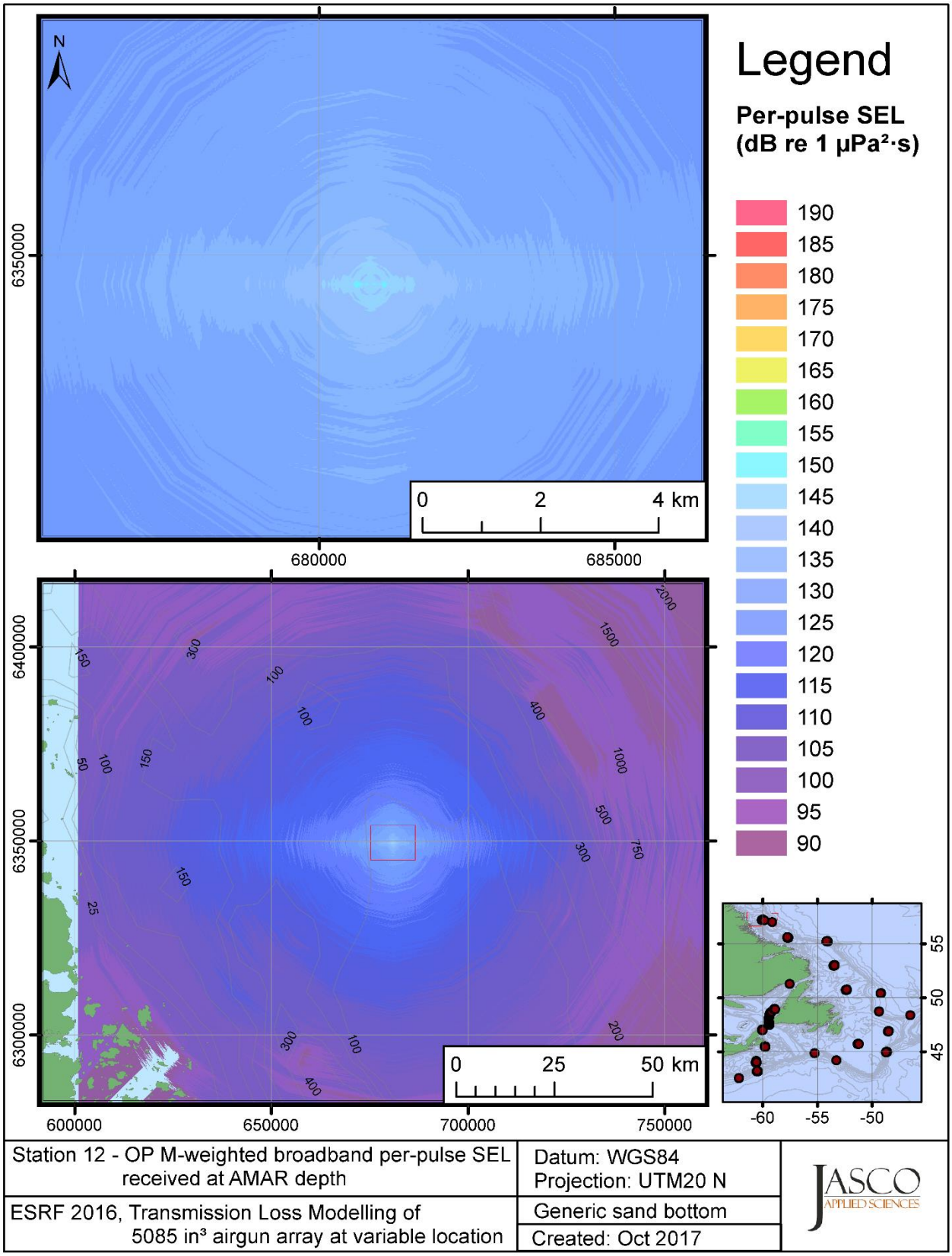

Figure C-197. Stn 12, OP M-weighted SEL received at the AMAR location and depth, modelled using a generic sand bottom, with in-situ July SSP and the airgun array located at any point on the map.

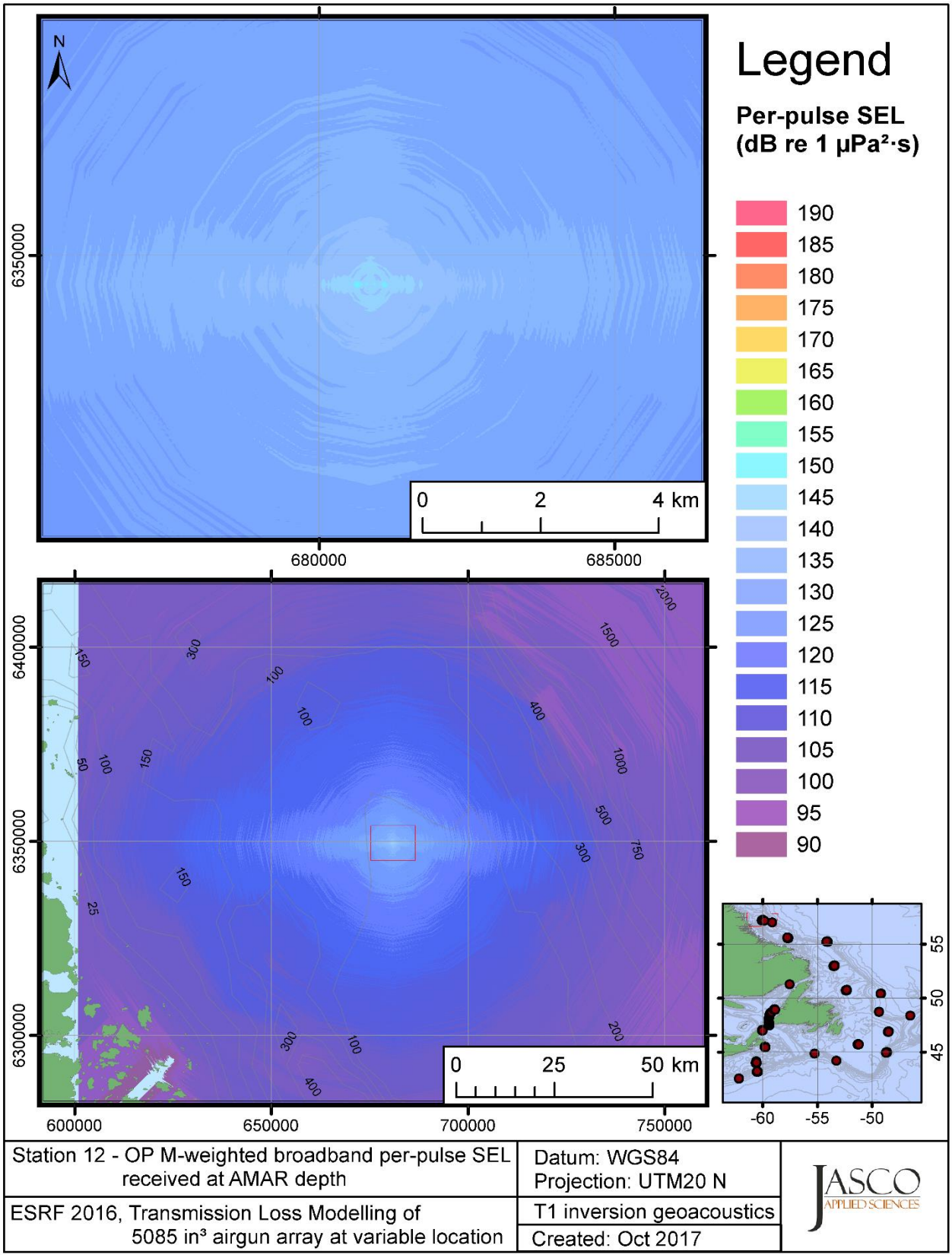

Figure C-198. Stn 12, OP M-weighted SEL received at the AMAR location and depth, modelled using the track 1 inversion geoacoustic bottom, with in-situ July SSP and the airgun array located at any point on the map.

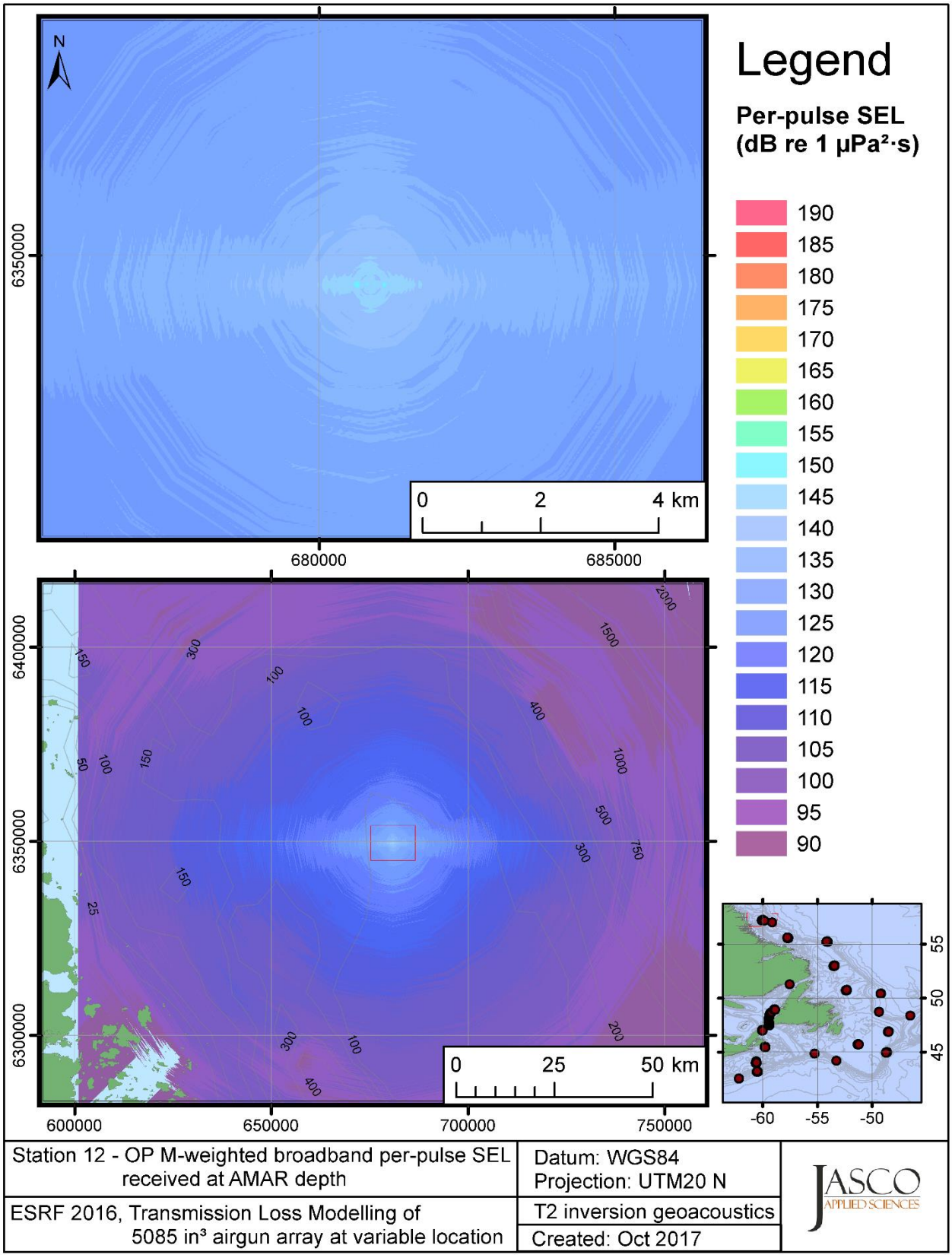

Figure C-199. Stn 12, OP M-weighted SEL received at the AMAR location and depth, modelled using the track 2 inversion geoacoustic bottom, with in-situ July SSP and the airgun array located at any point on the map.

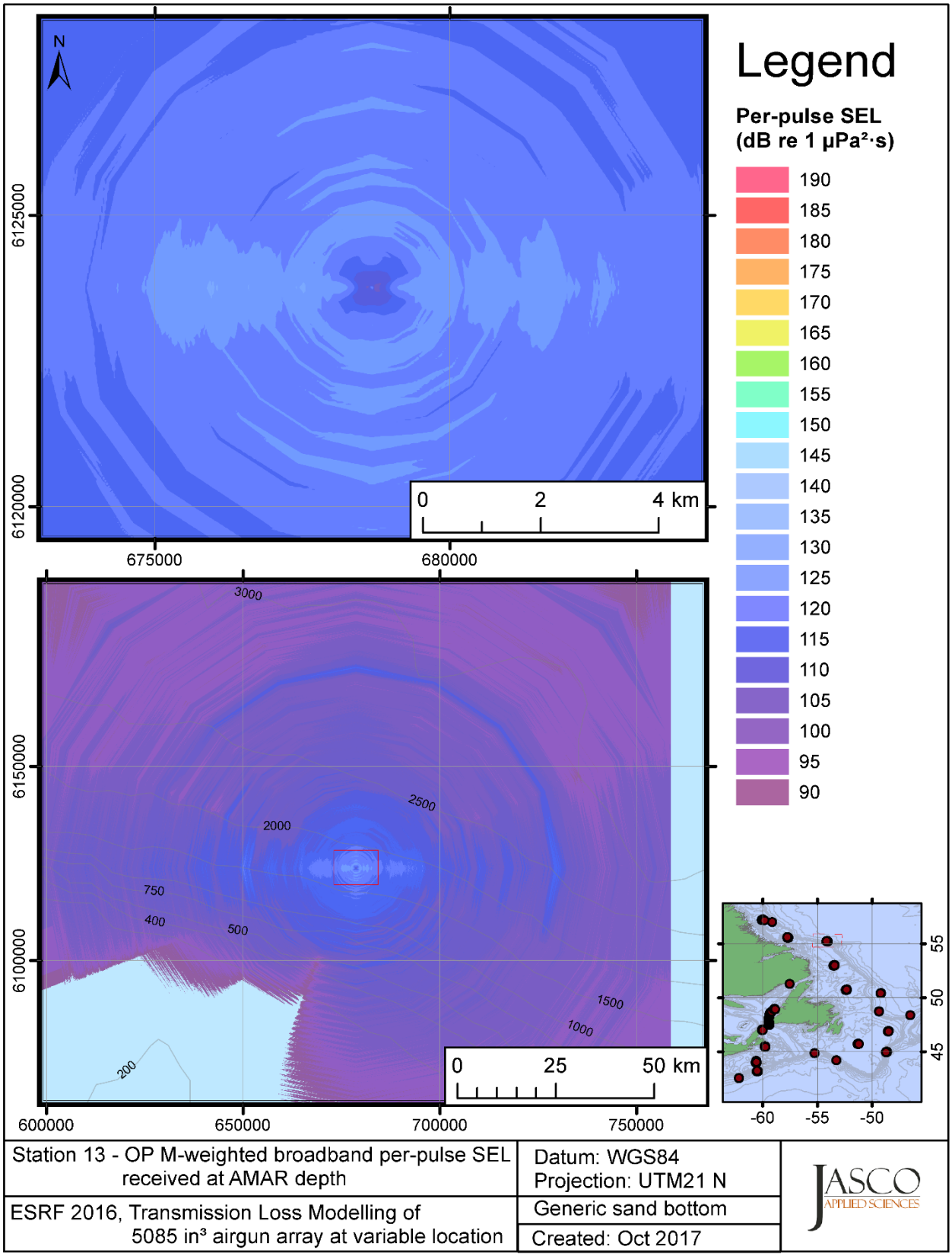

Figure C-200. Stn 13, OP M-weighted SEL received at the AMAR location and depth, modelled using a generic sand bottom, with in-situ July SSP and the airgun array located at any point on the map.

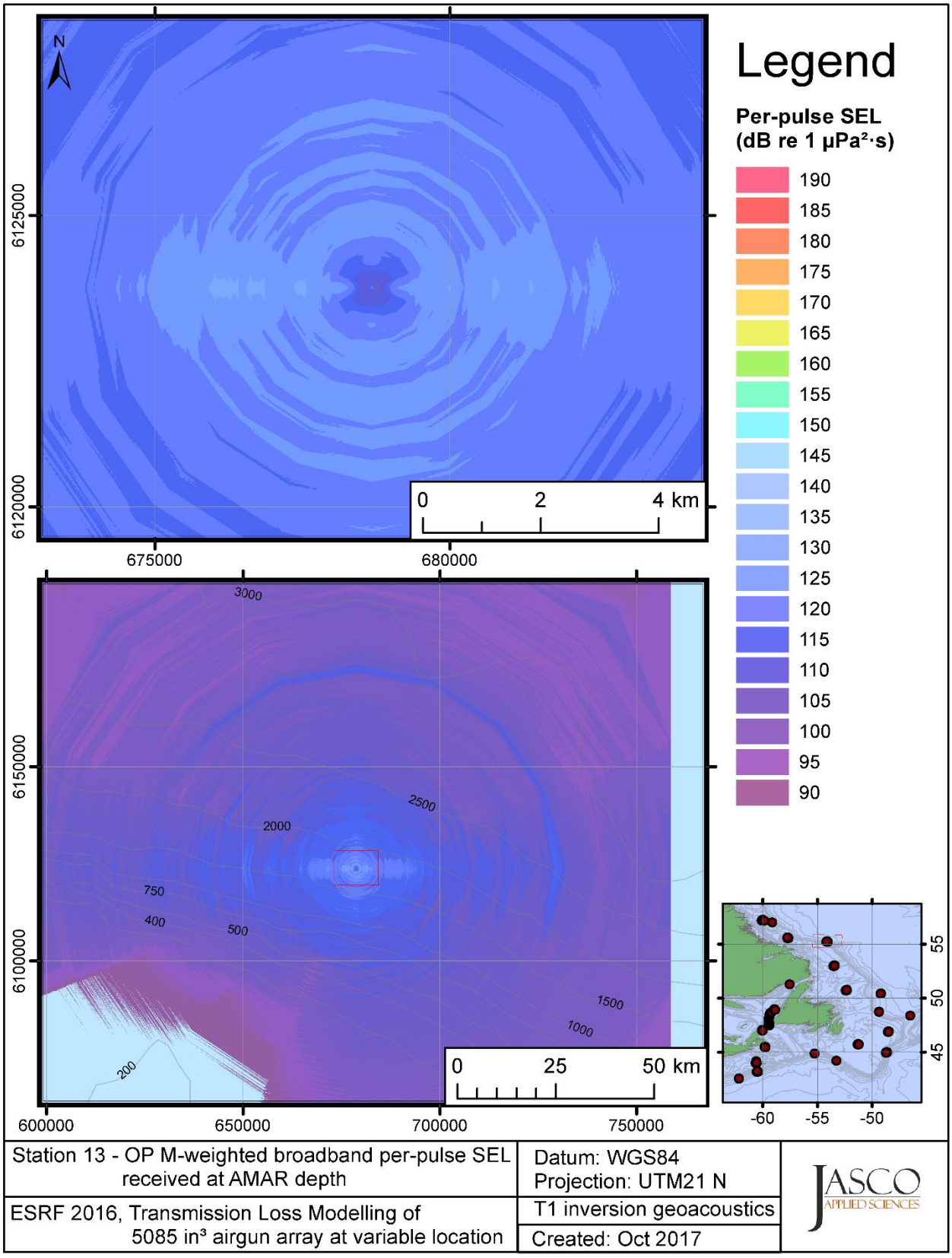

Figure C-201. Stn 13, OP M-weighted SEL received at the AMAR location and depth, modelled using the track 1 inversion geoacoustic bottom, with in-situ July SSP and the airgun array located at any point on the map.

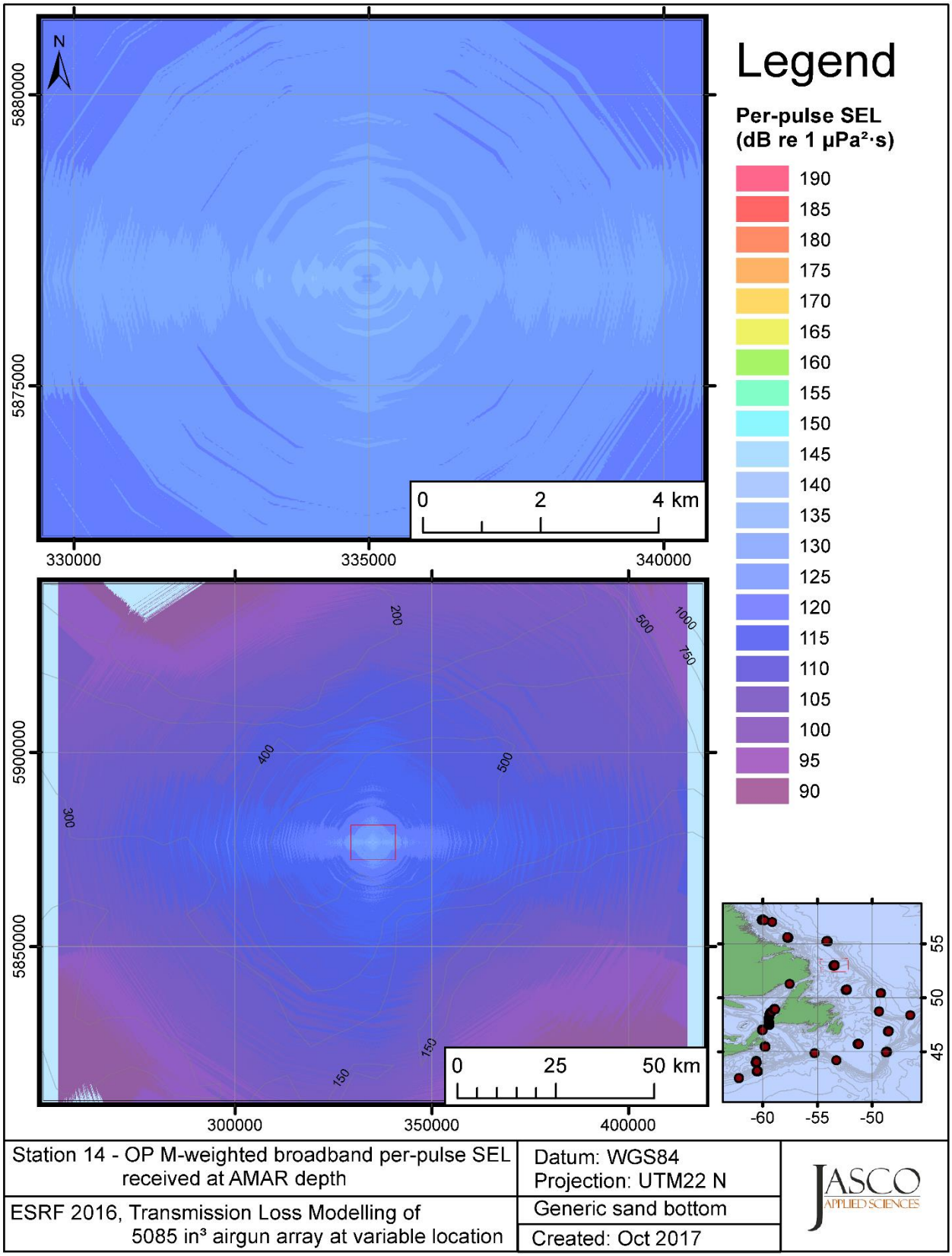

Figure C-202. Stn 14, OP M-weighted SEL received at the AMAR location and depth, modelled using a generic sand bottom, with in-situ July SSP and the airgun array located at any point on the map.

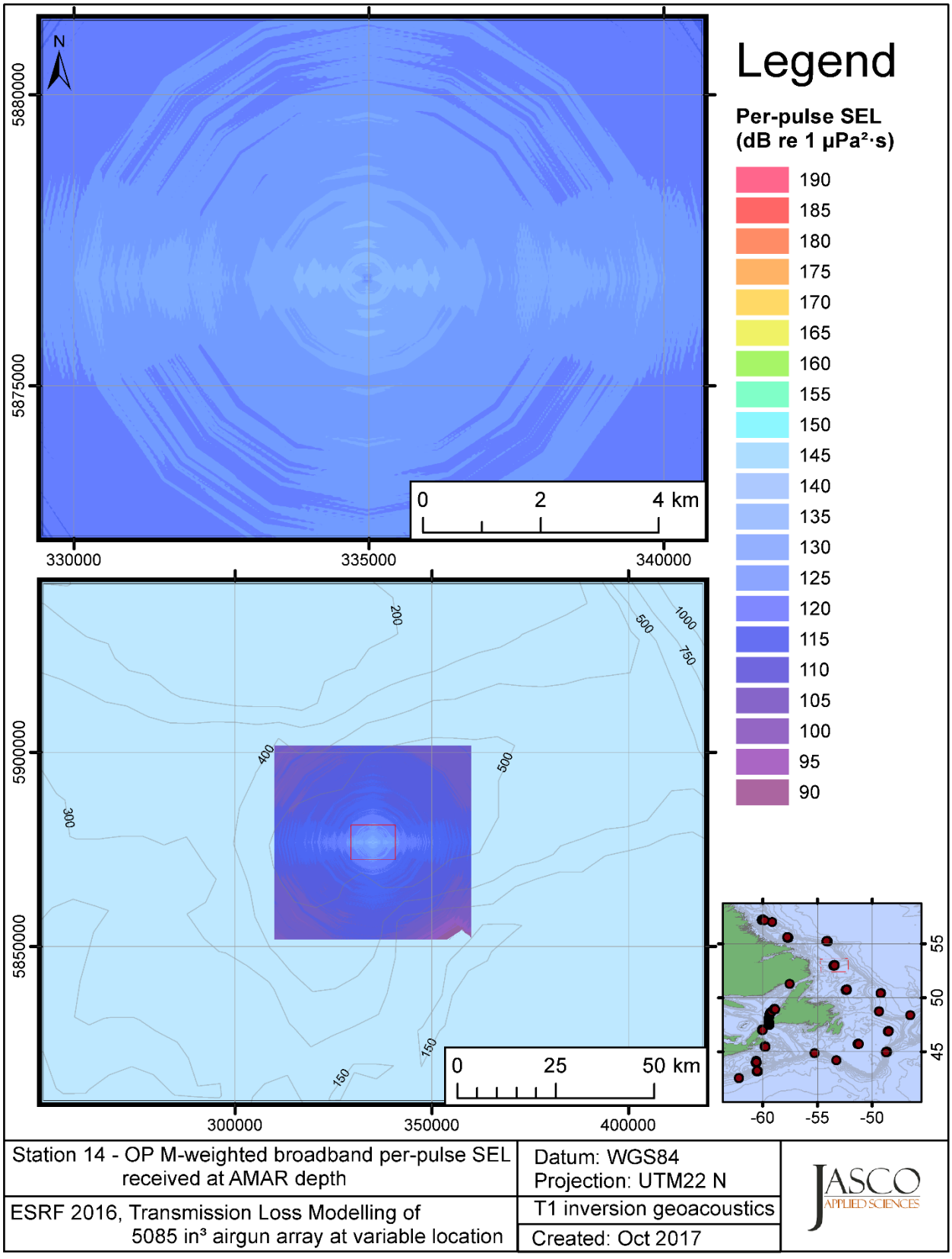

Figure C-203. Stn 14, OP M-weighted SEL received at the AMAR location and depth, modelled using the track 1 inversion geoacoustic bottom, with in-situ July SSP and the airgun array located at any point on the map.

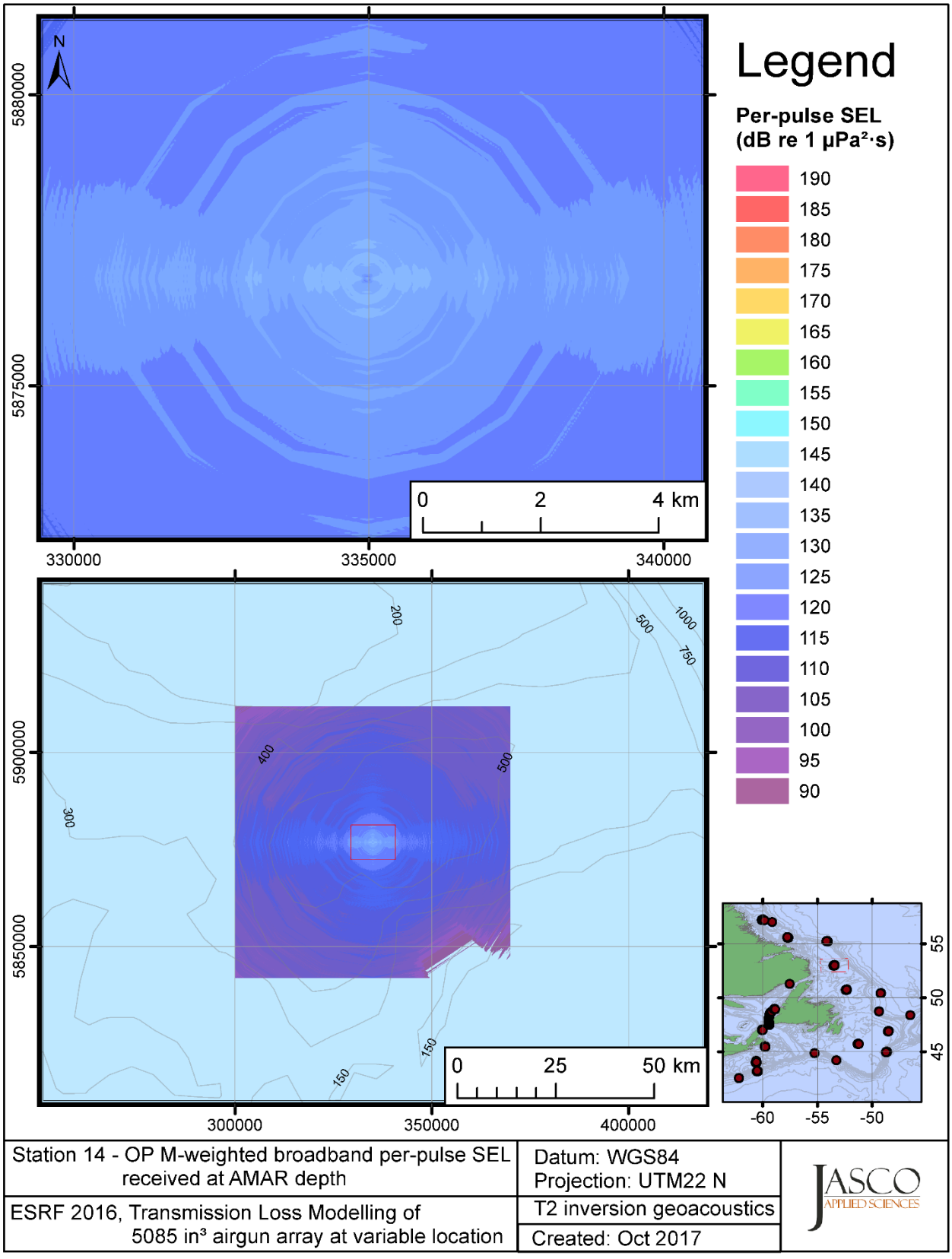

Figure C-204. Stn 14, OP M-weighted SEL received at the AMAR location and depth, modelled using the track 2 inversion geoacoustic bottom, with in-situ July SSP and the airgun array located at any point on the map.

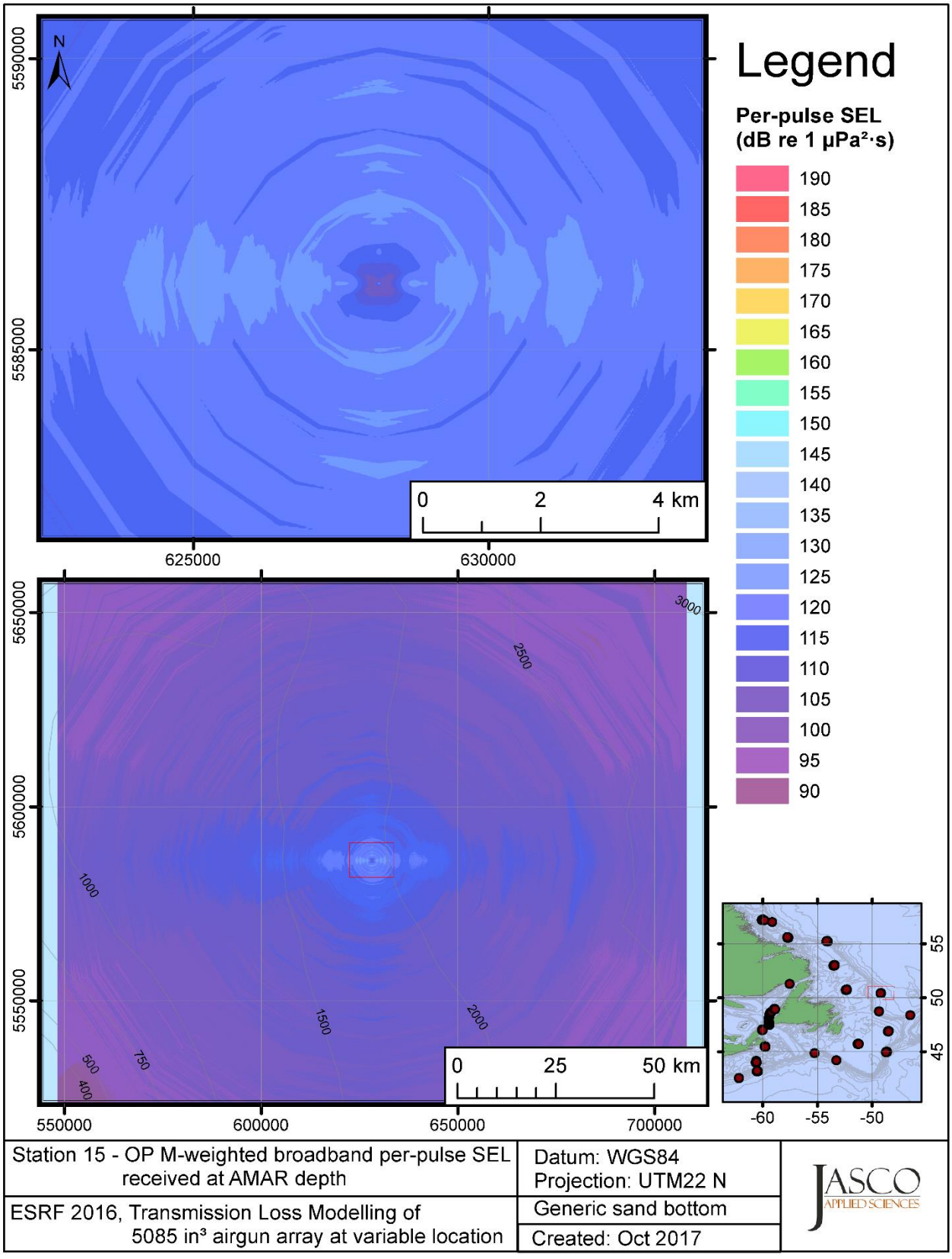

Figure C-205. Stn 15, OP M-weighted SEL received at the AMAR location and depth, modelled using a generic sand bottom, with in-situ July SSP and the airgun array located at any point on the map.

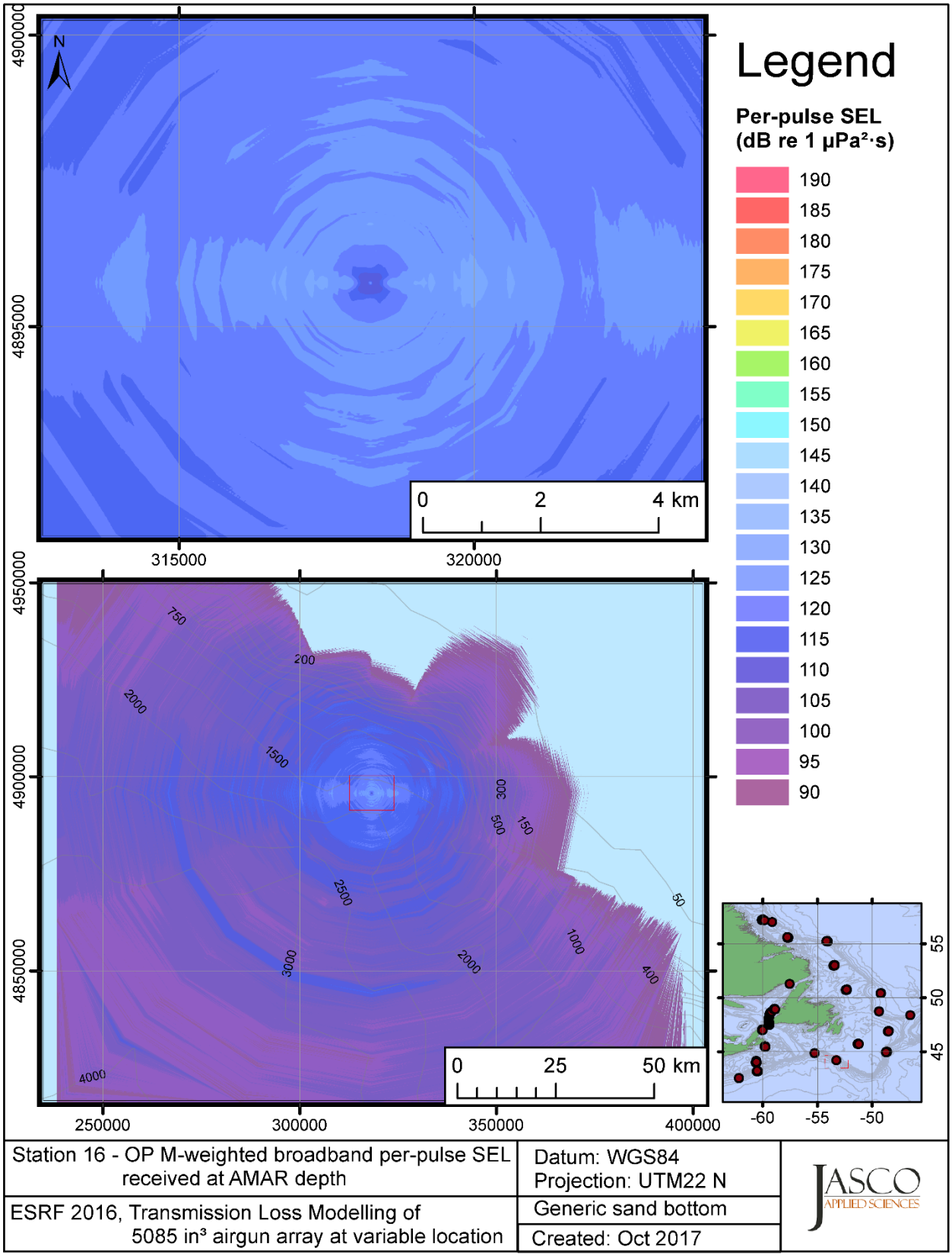

Figure C-206. Stn 16, OP M-weighted SEL received at the AMAR location and depth, modelled using a generic sand bottom, with in-situ July SSP and the airgun array located at any point on the map.

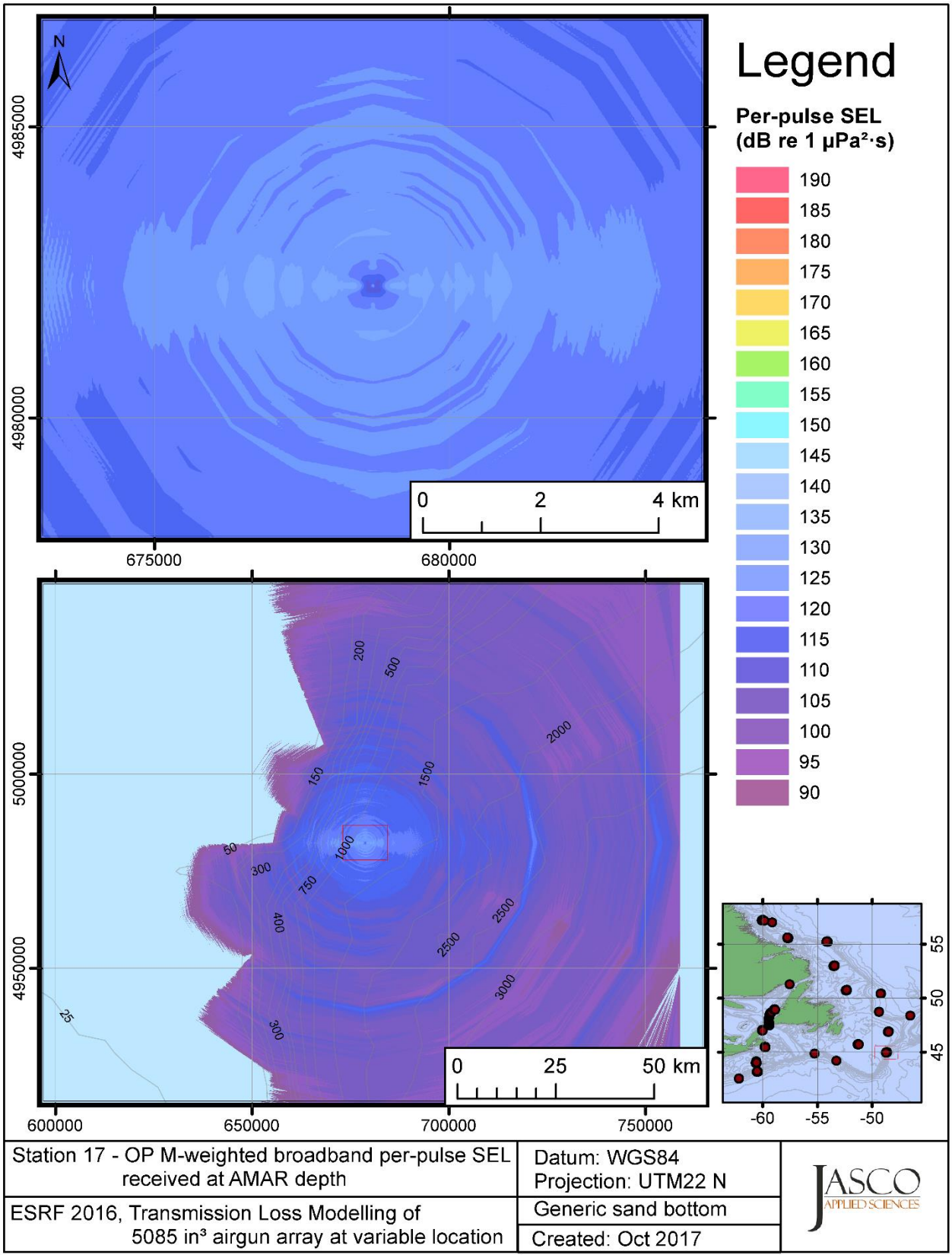

Figure C-207. Stn 17, OP M-weighted SEL received at the AMAR location and depth, modelled using a generic sand bottom, with in-situ July SSP and the airgun array located at any point on the map.

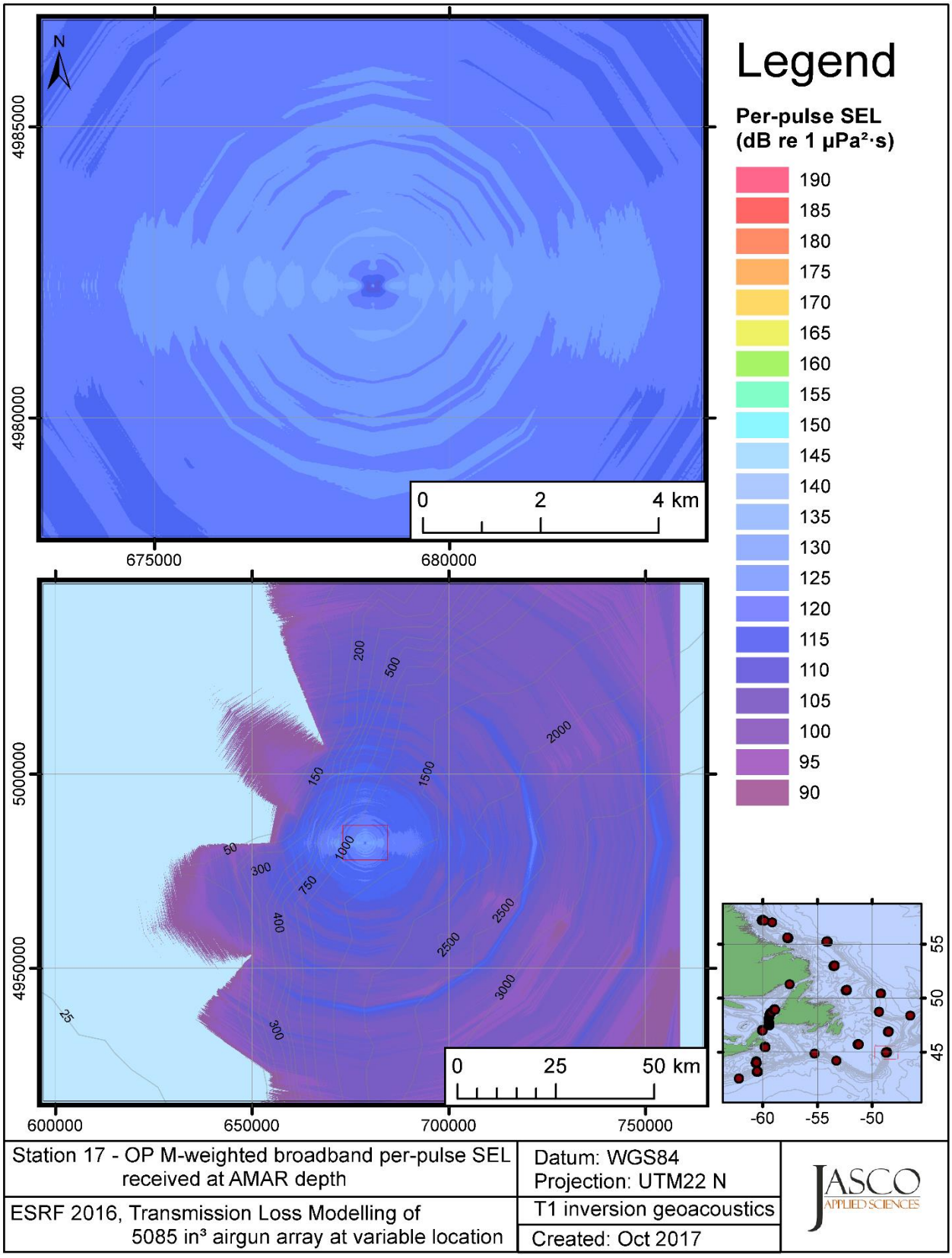

Figure C-208. Stn 17, OP M-weighted SEL received at the AMAR location and depth, modelled using the track 1 inversion geoacoustic bottom, with in-situ July SSP and the airgun array located at any point on the map.

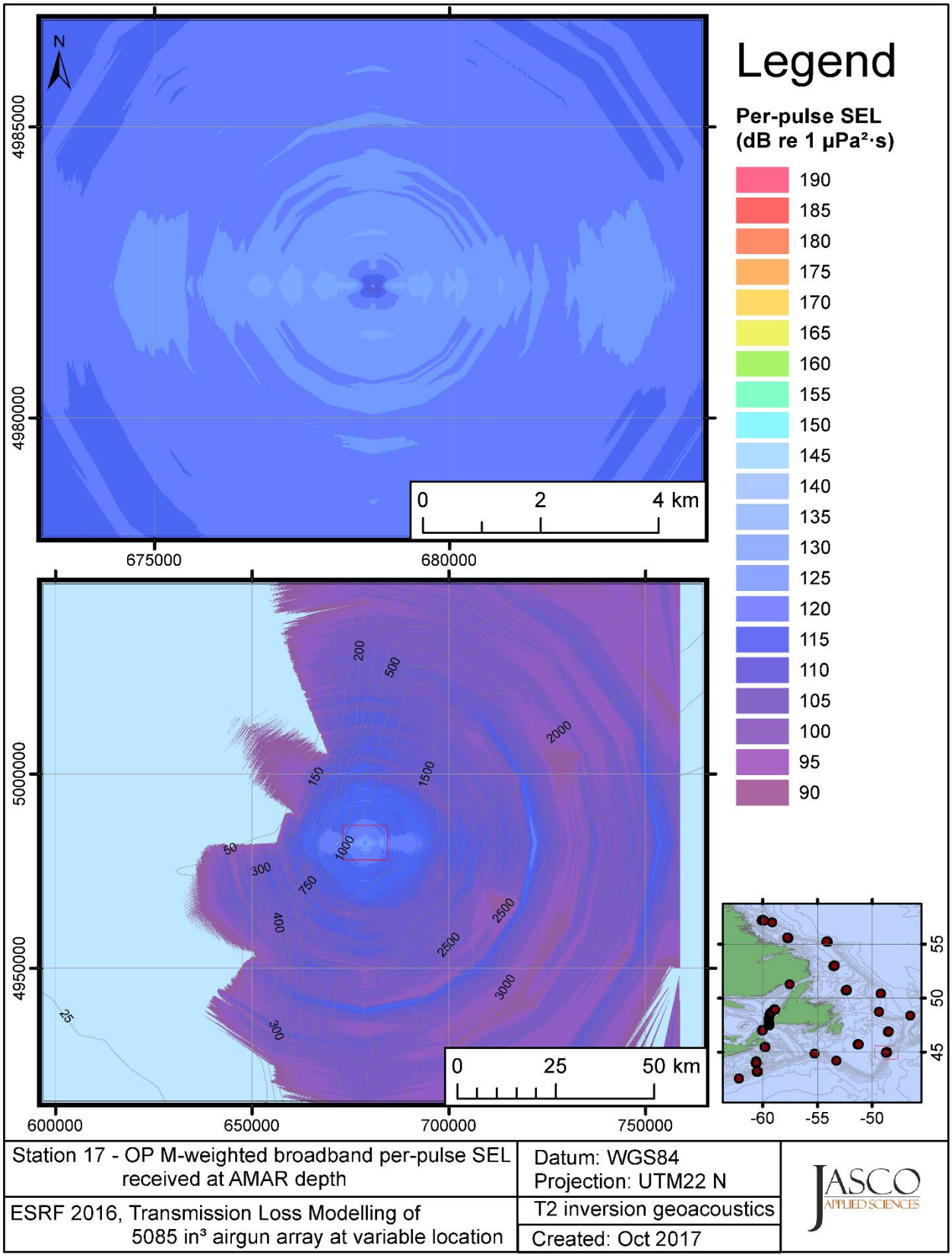

Figure C-209. Stn 17, OP M-weighted SEL received at the AMAR location and depth, modelled using the track 2 inversion geoacoustic bottom, with in-situ July SSP and the airgun array located at any point on the map.

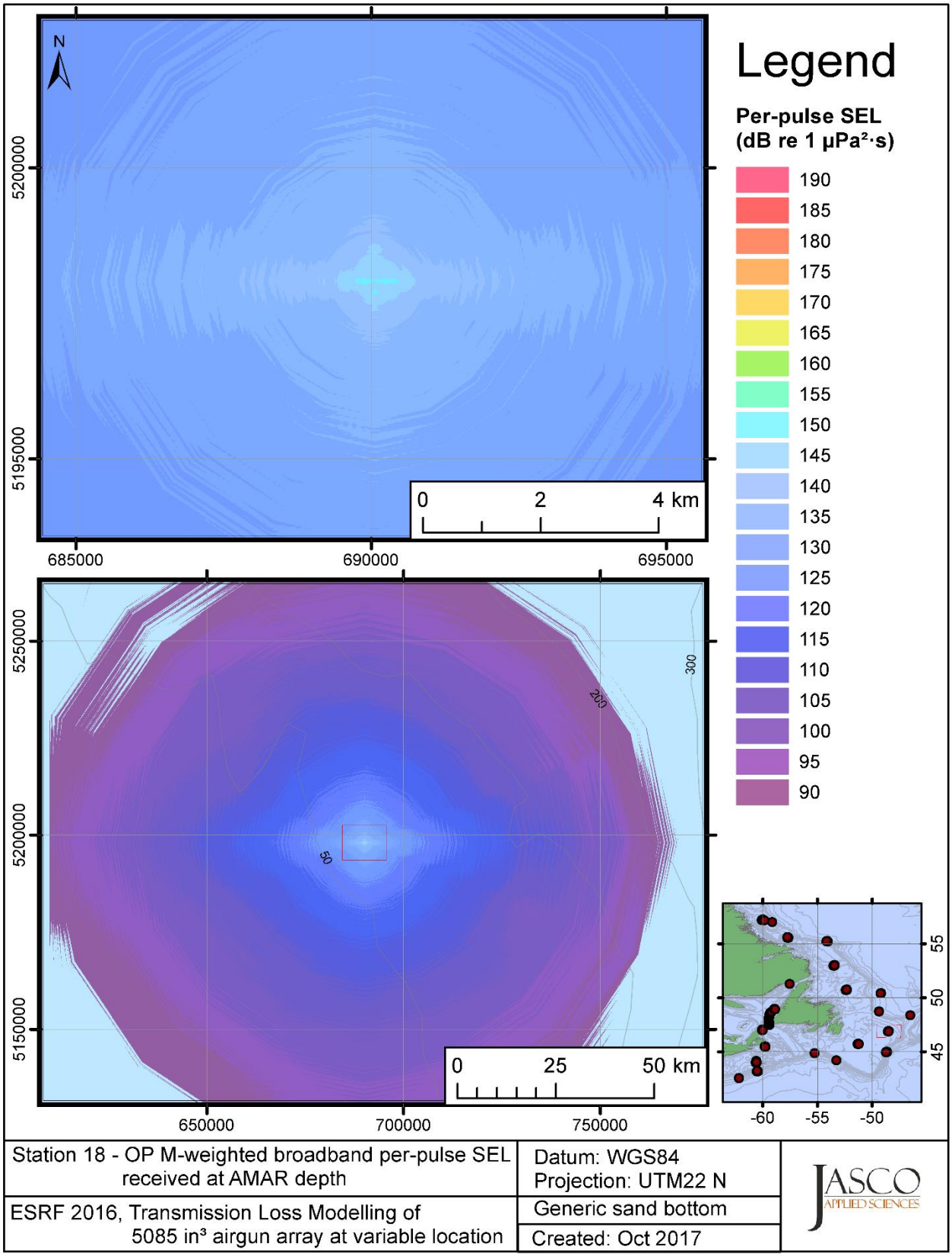

Figure C-210. Stn 18, OP M-weighted SEL received at the AMAR location and depth, modelled using a generic sand bottom, with in-situ July SSP and the airgun array located at any point on the map.

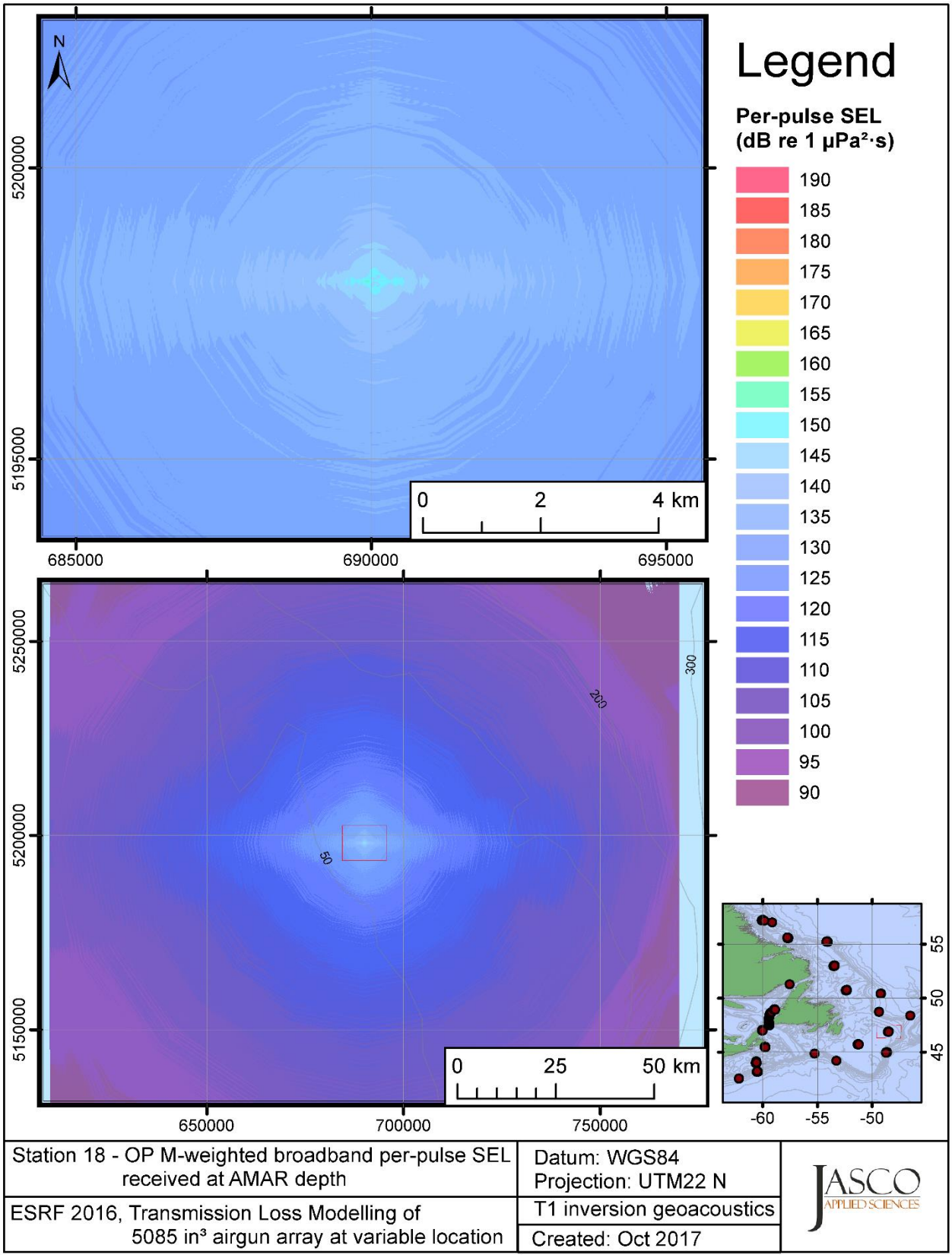

Figure C-211. Stn 18, OP M-weighted SEL received at the AMAR location and depth, modelled using the track 1 inversion geoacoustic bottom, with in-situ July SSP and the airgun array located at any point on the map.

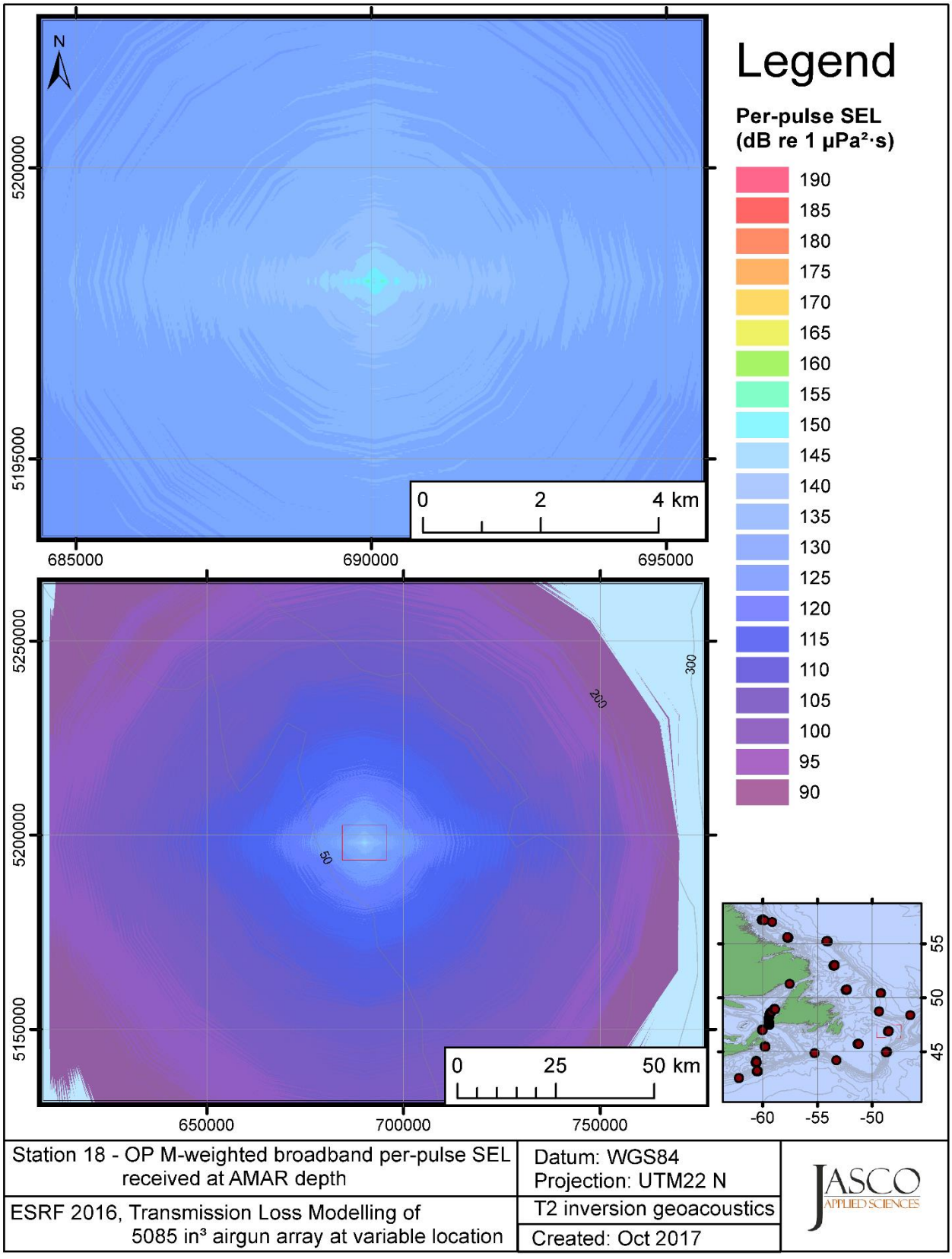

Figure C-212. Stn 18, OP M-weighted SEL received at the AMAR location and depth, modelled using the track 2 inversion geoacoustic bottom, with in-situ July SSP and the airgun array located at any point on the map.

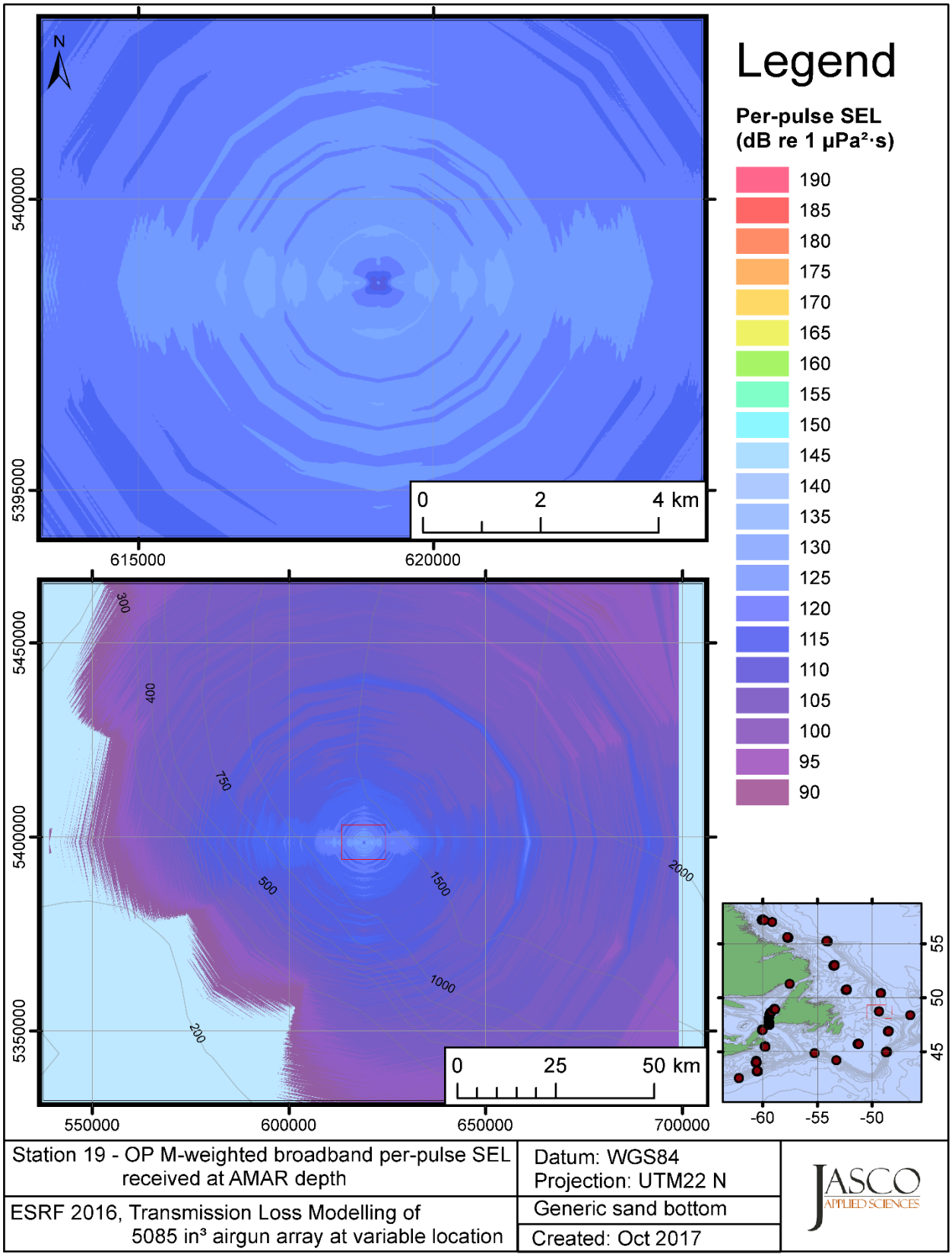

Figure C-213. Stn 19, OP M-weighted SEL received at the AMAR location and depth, modelled using a generic sand bottom, with in-situ July SSP and the airgun array located at any point on the map.

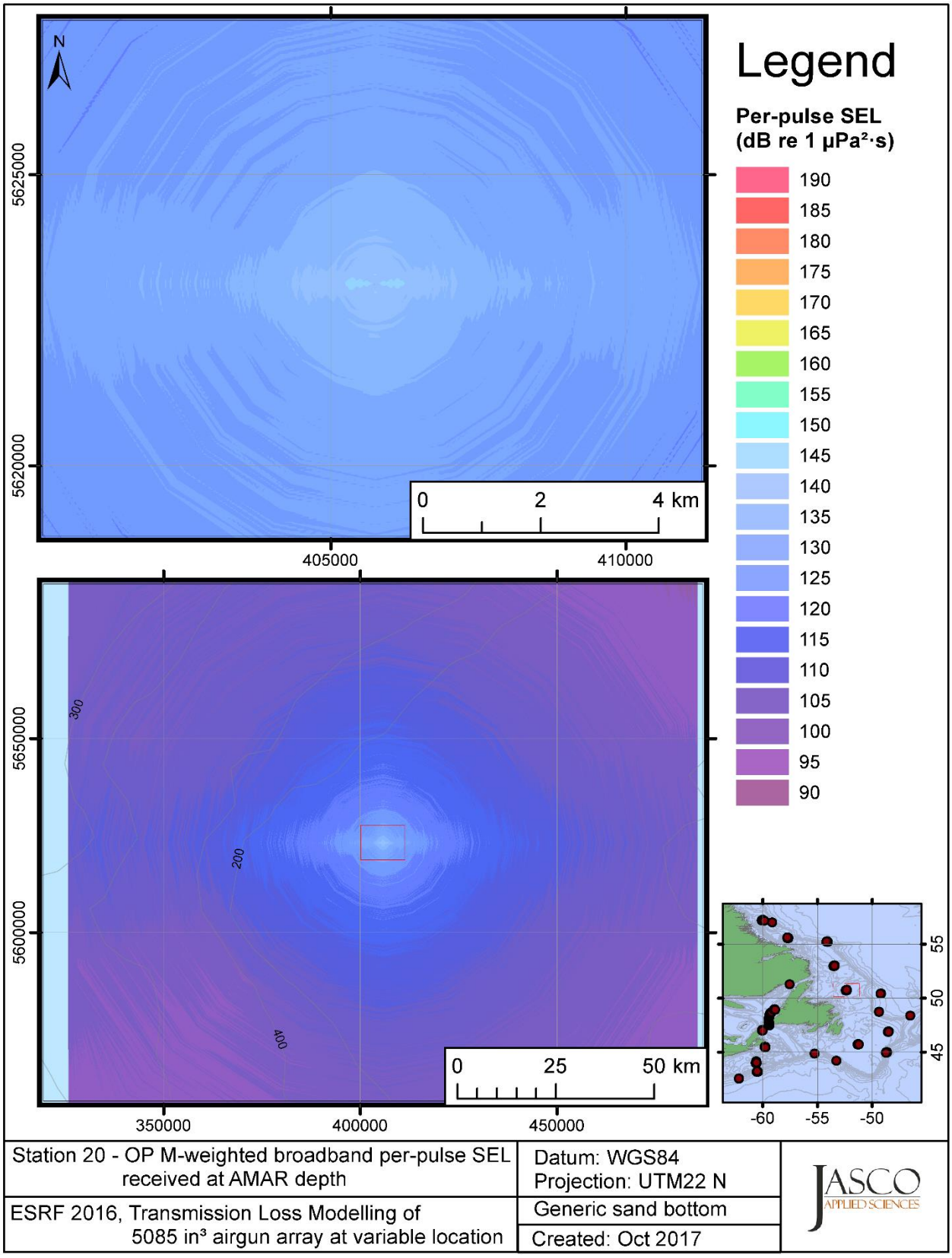

Figure C-214. Stn 20, OP M-weighted SEL received at the AMAR location and depth, modelled using a generic sand bottom, with in-situ July SSP and the airgun array located at any point on the map.

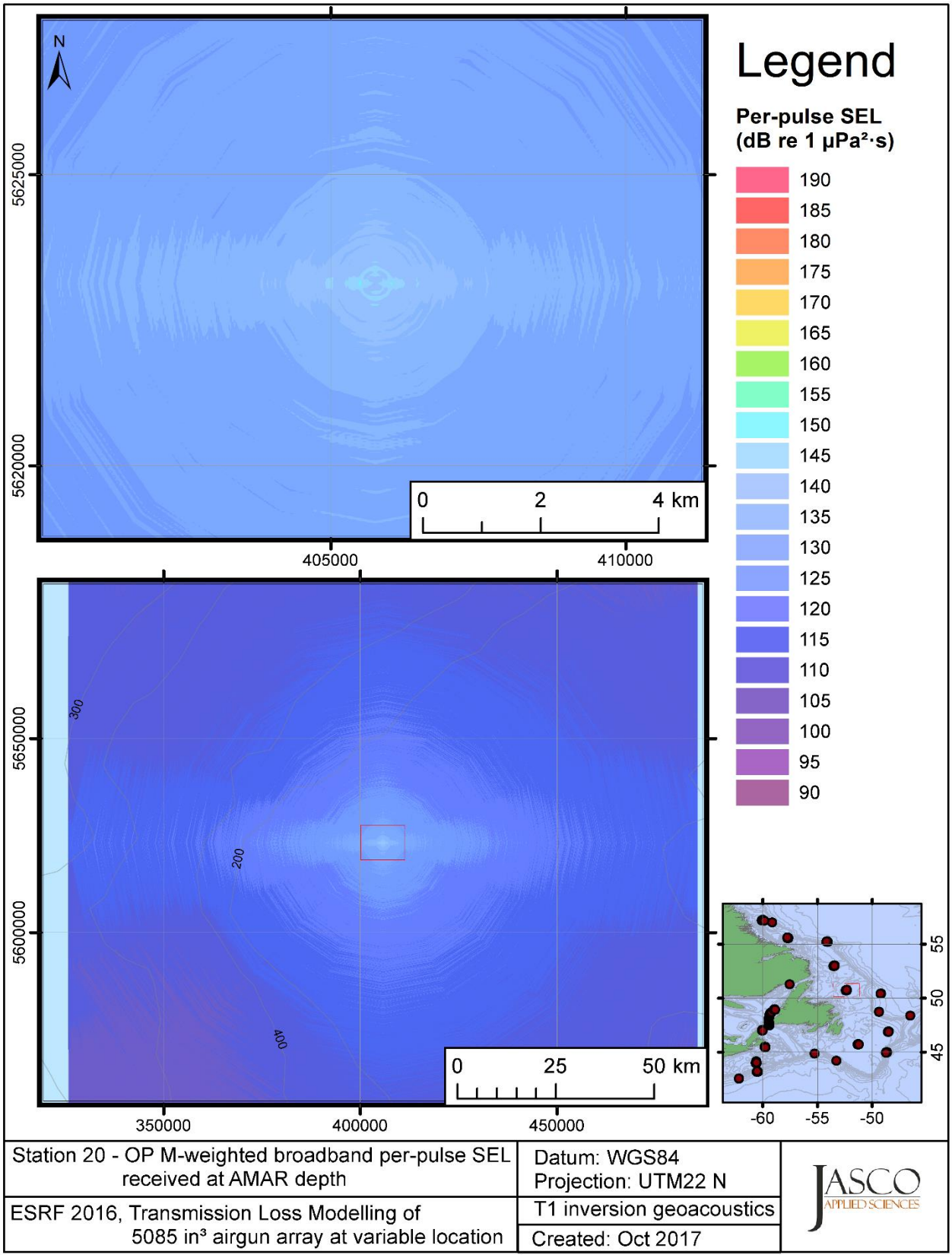

Figure C-215. Stn 20, OP M-weighted SEL received at the AMAR location and depth, modelled using the track 1 inversion geoacoustic bottom, with in-situ July SSP and the airgun array located at any point on the map.

C.6. Modelling PP M-weighted Received Level at the AMAR Location

This section presents the results of modelling the per-pulse sound exposure level (SEL) received at the AMAR location and depth as a function of the source location (varied in range and azimuth) for each of the 20 sites using a generic sand bottom; in addition, the modelling is repeated using the geoacoustic inversion bottom parameters at the 14 sites where they are available. The modelling results are presented in the form of coloured maps where the colour at any map location represents the predicted received level at the AMAR for the source located at that spot on the map. This section includes only the phocid pinnipeds in water (PP) marine-mammal-weighted per-pulse SEL results; additional maps for other marine mammal received level auditory weighting functions are presented in adjoining sections.

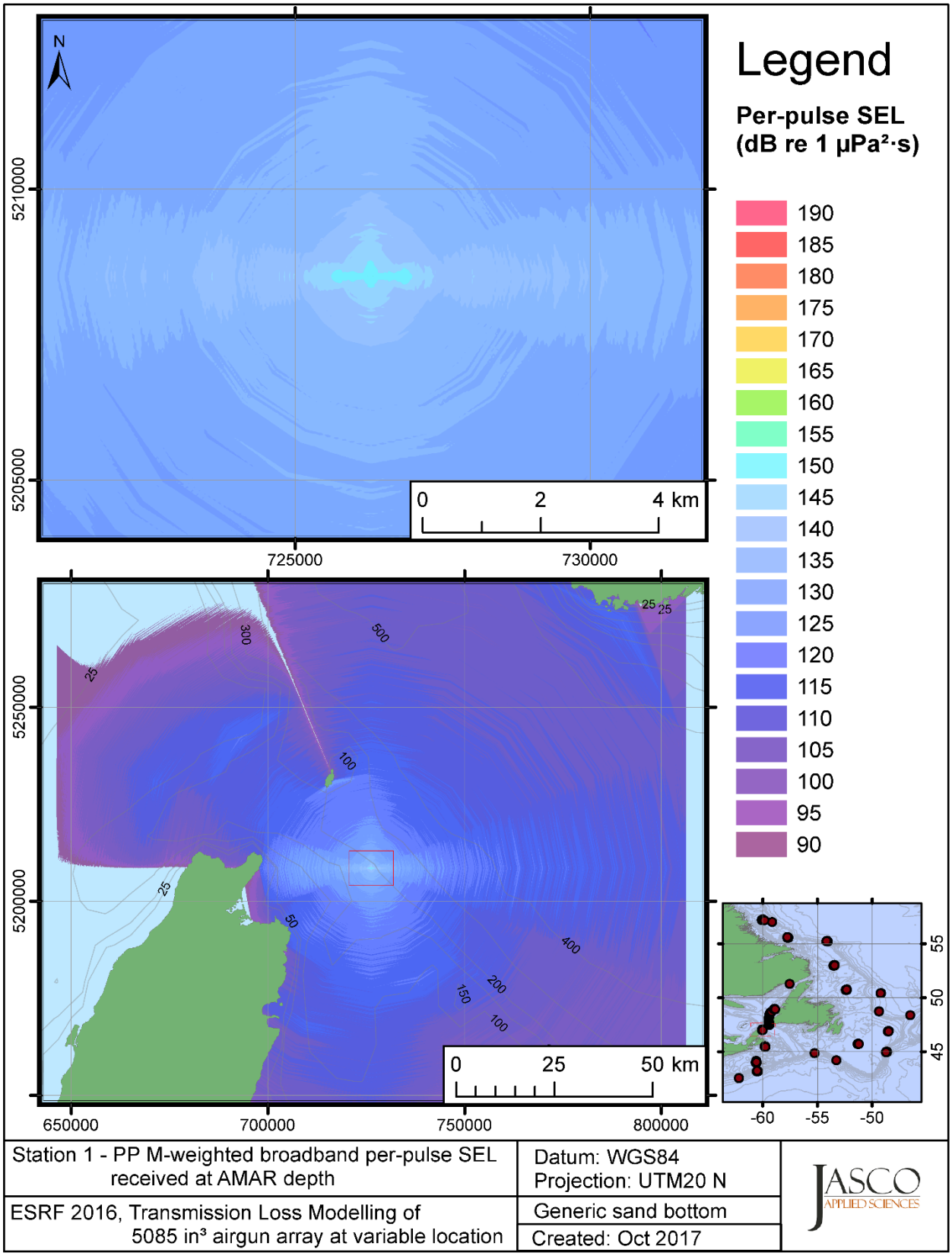

Figure C-216. Stn 1, PP M-weighted SEL received at the AMAR location and depth, modelled using a generic sand bottom, with in-situ July SSP and the airgun array located at any point on the map.

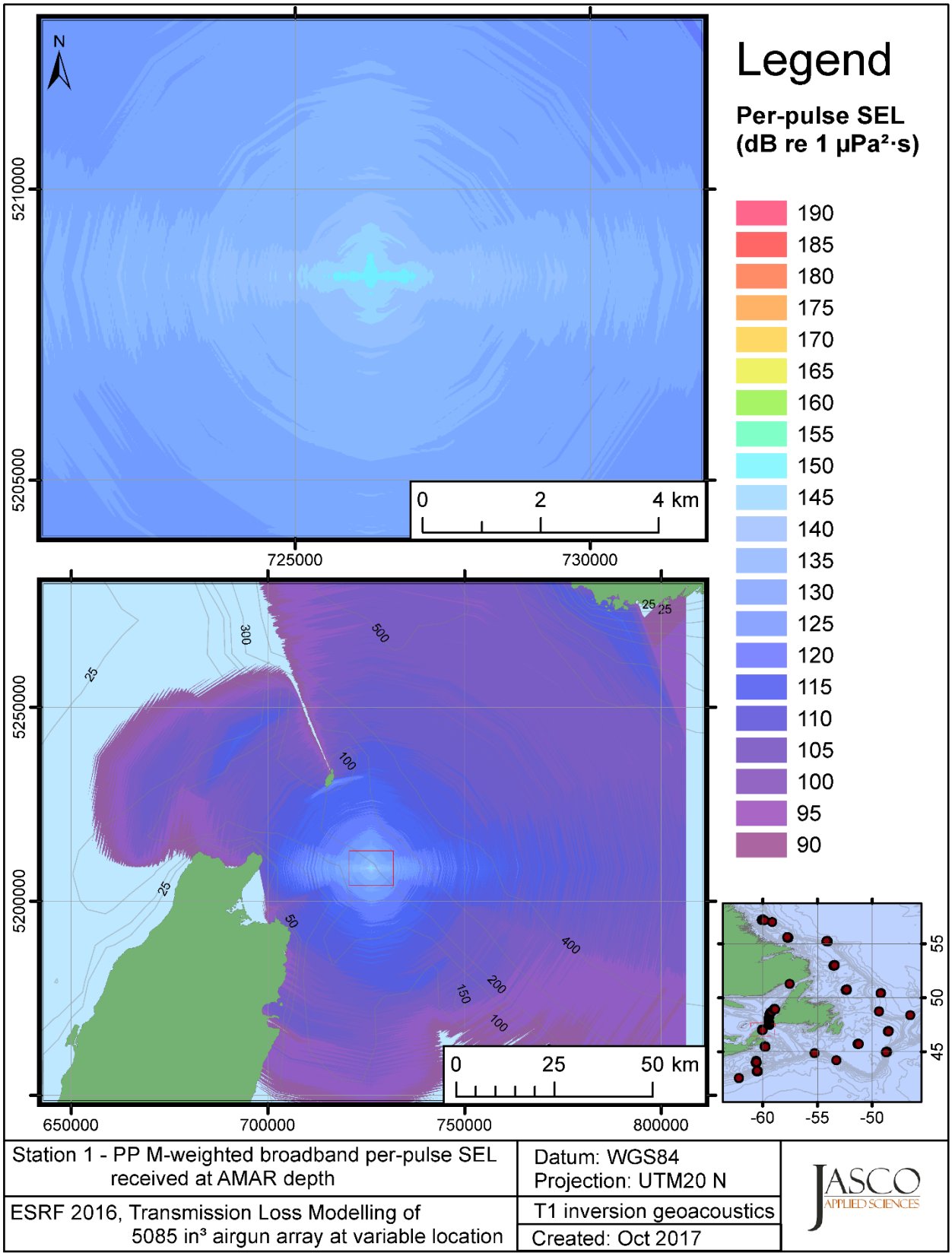

Figure C-217. Stn 1, PP M-weighted SEL received at the AMAR location and depth, modelled using the track 1 inversion geoacoustic bottom, with in-situ July SSP and the airgun array located at any point on the map.

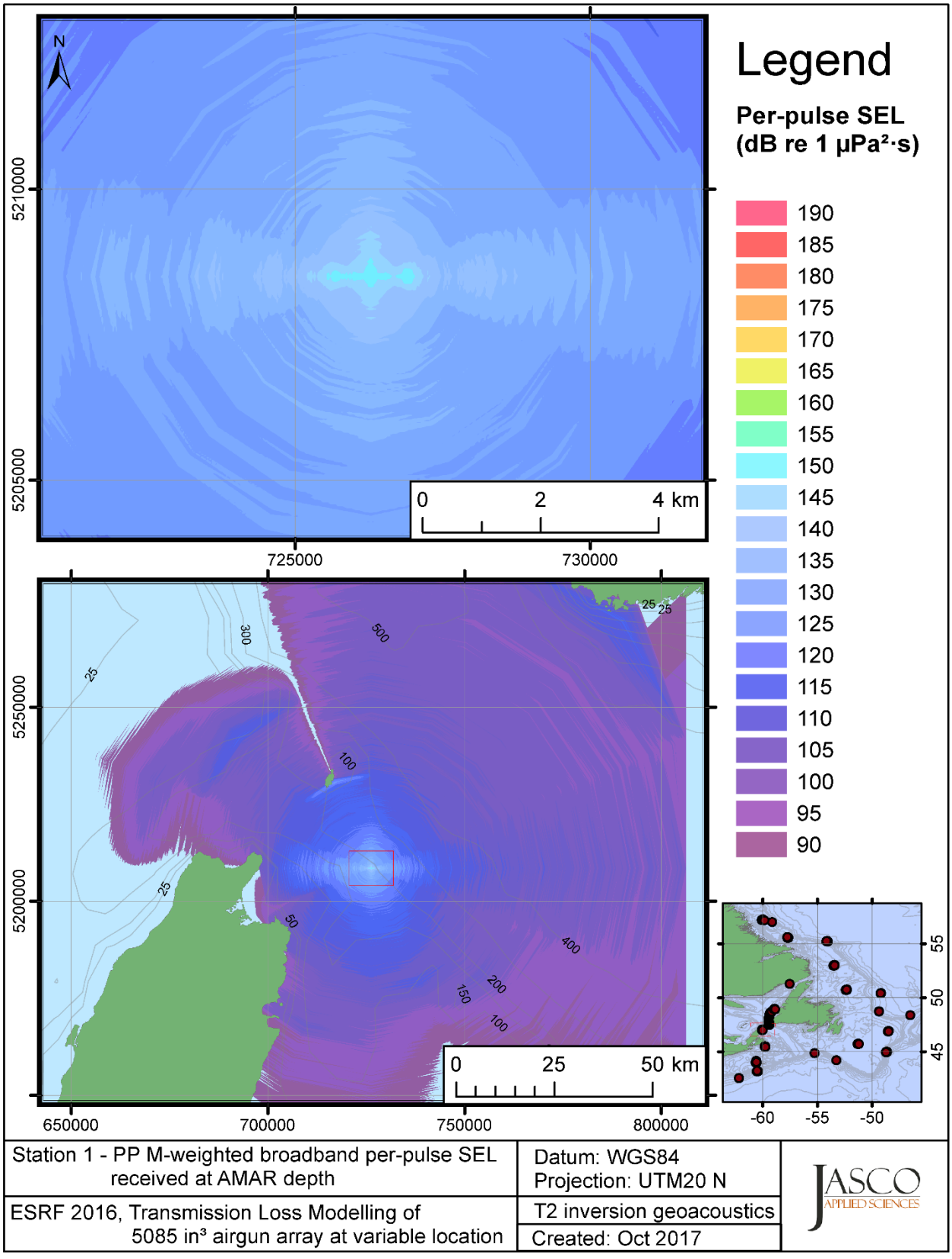

Figure C-218. Stn 1, PP M-weighted SEL received at the AMAR location and depth, modelled using the track 2 inversion geoacoustic bottom, with in-situ July SSP and the airgun array located at any point on the map.

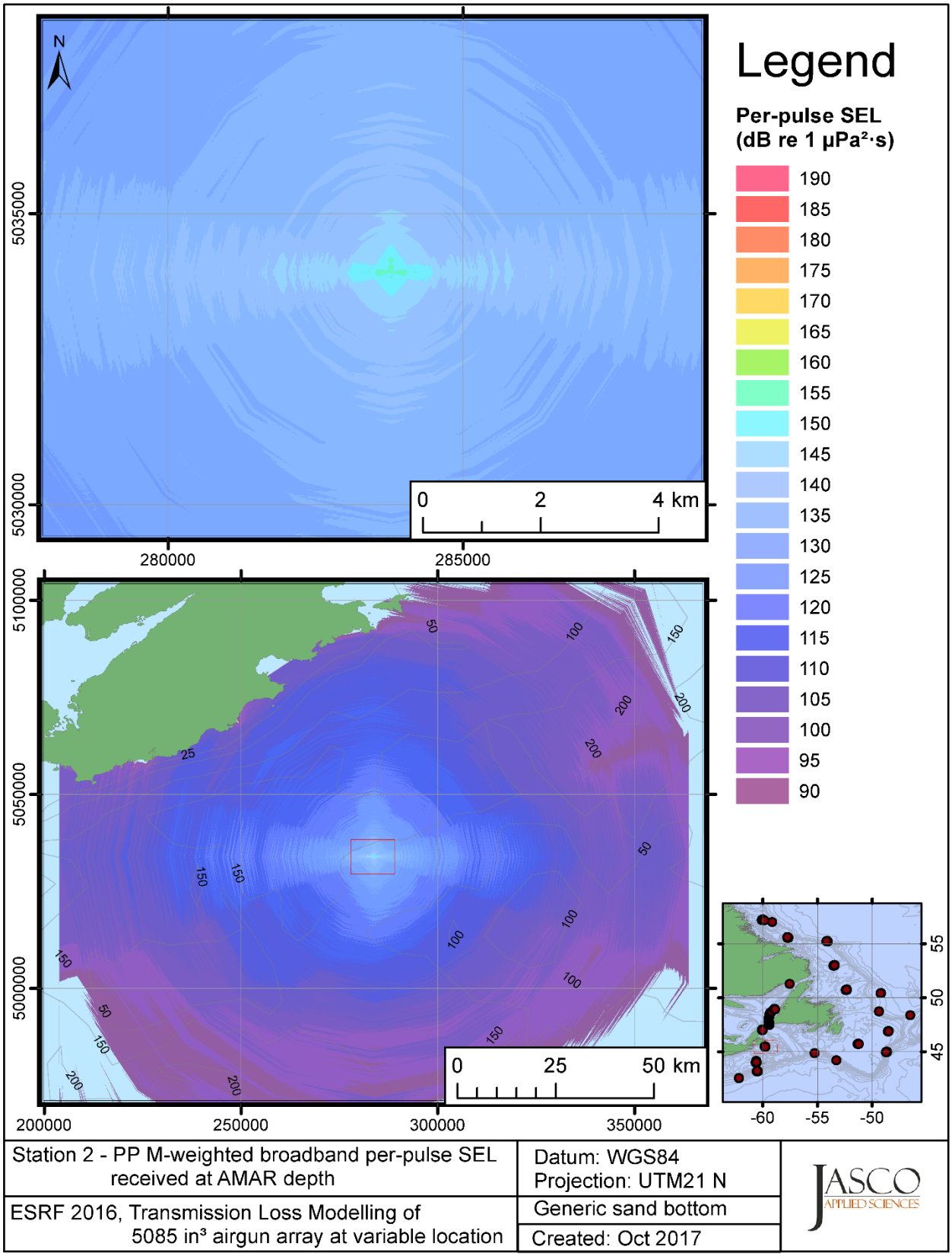

Figure C-219. Stn 2, PP M-weighted SEL received at the AMAR location and depth, modelled using a generic sand bottom, with in-situ July SSP and the airgun array located at any point on the map.

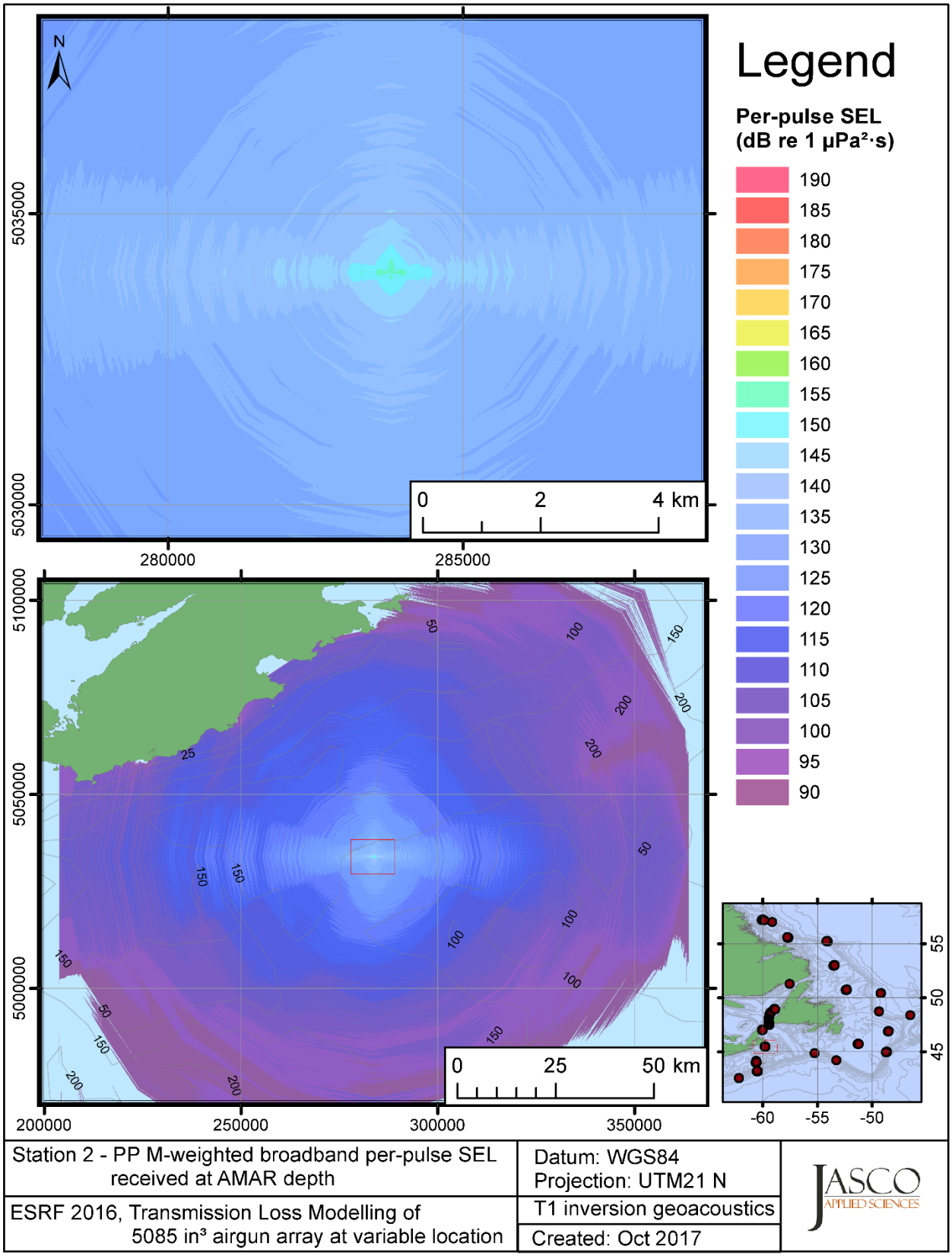

Figure C-220. Stn 2, PP M-weighted SEL received at the AMAR location and depth, modelled using the track 1 inversion geoacoustic bottom, with in-situ July SSP and the airgun array located at any point on the map.

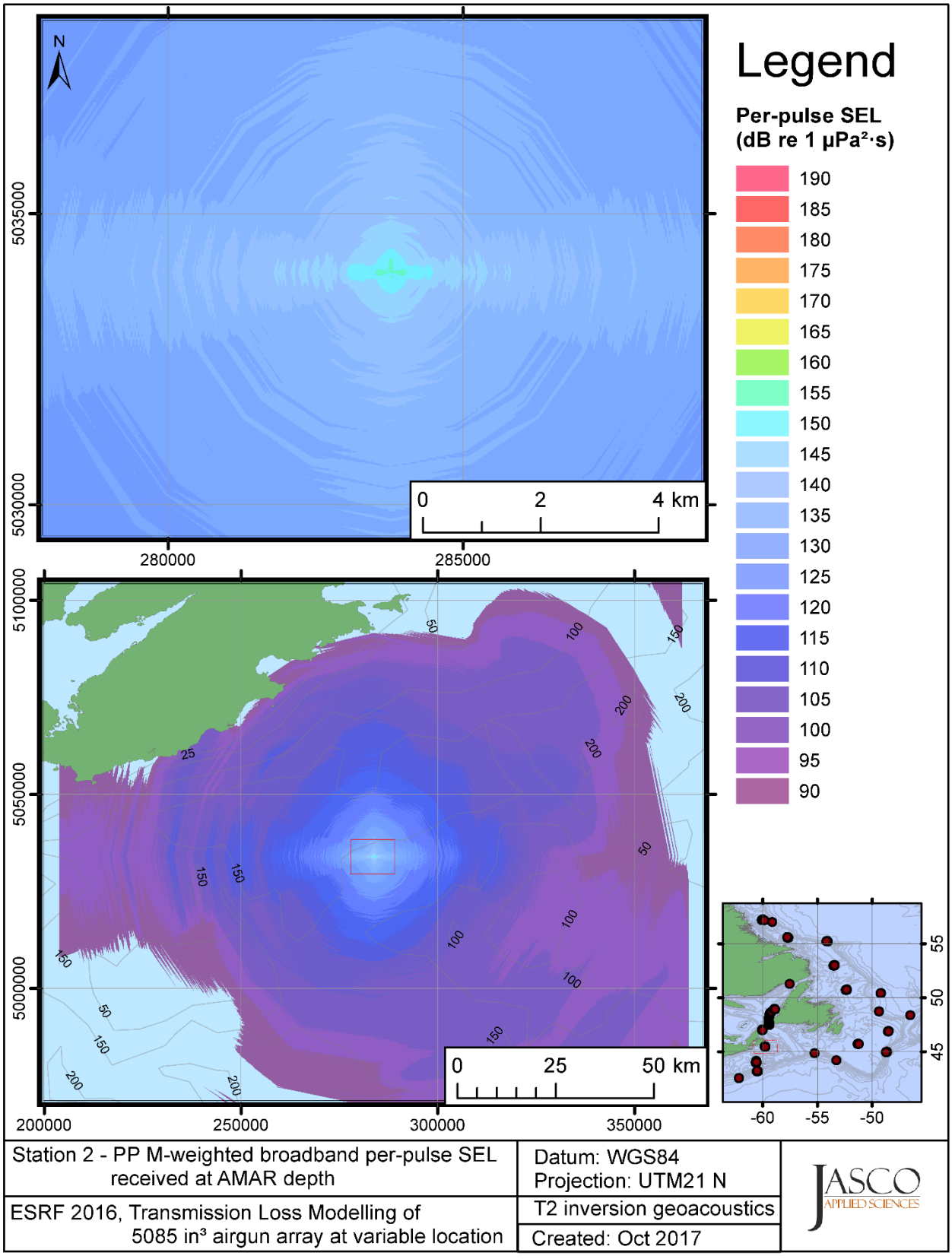

Figure C-221. Stn 2, PP M-weighted SEL received at the AMAR location and depth, modelled using the track 2 inversion geoacoustic bottom, with in-situ July SSP and the airgun array located at any point on the map.

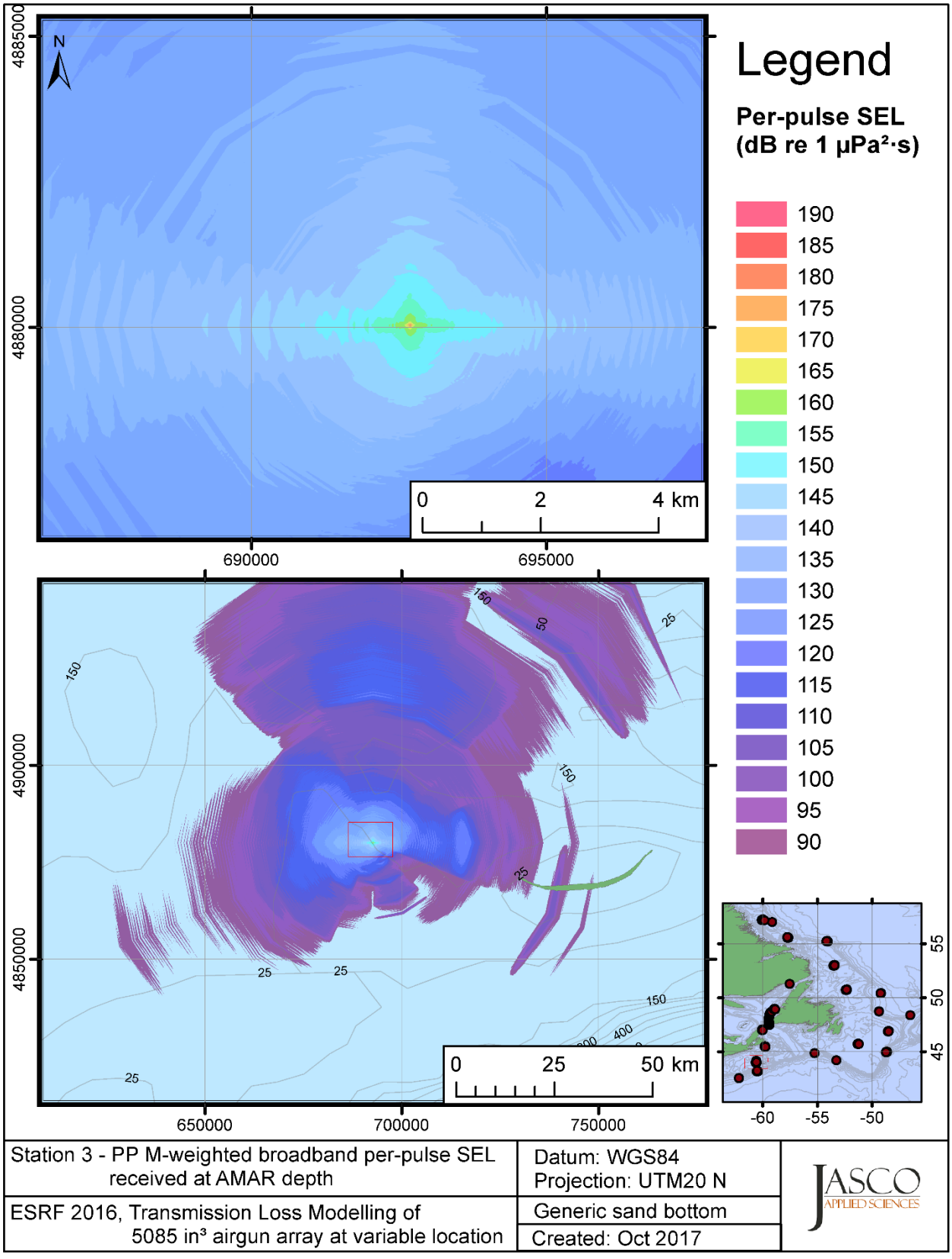

Figure C-222. Stn 3, PP M-weighted SEL received at the AMAR location and depth, modelled using a generic sand bottom, with in-situ July SSP and the airgun array located at any point on the map.

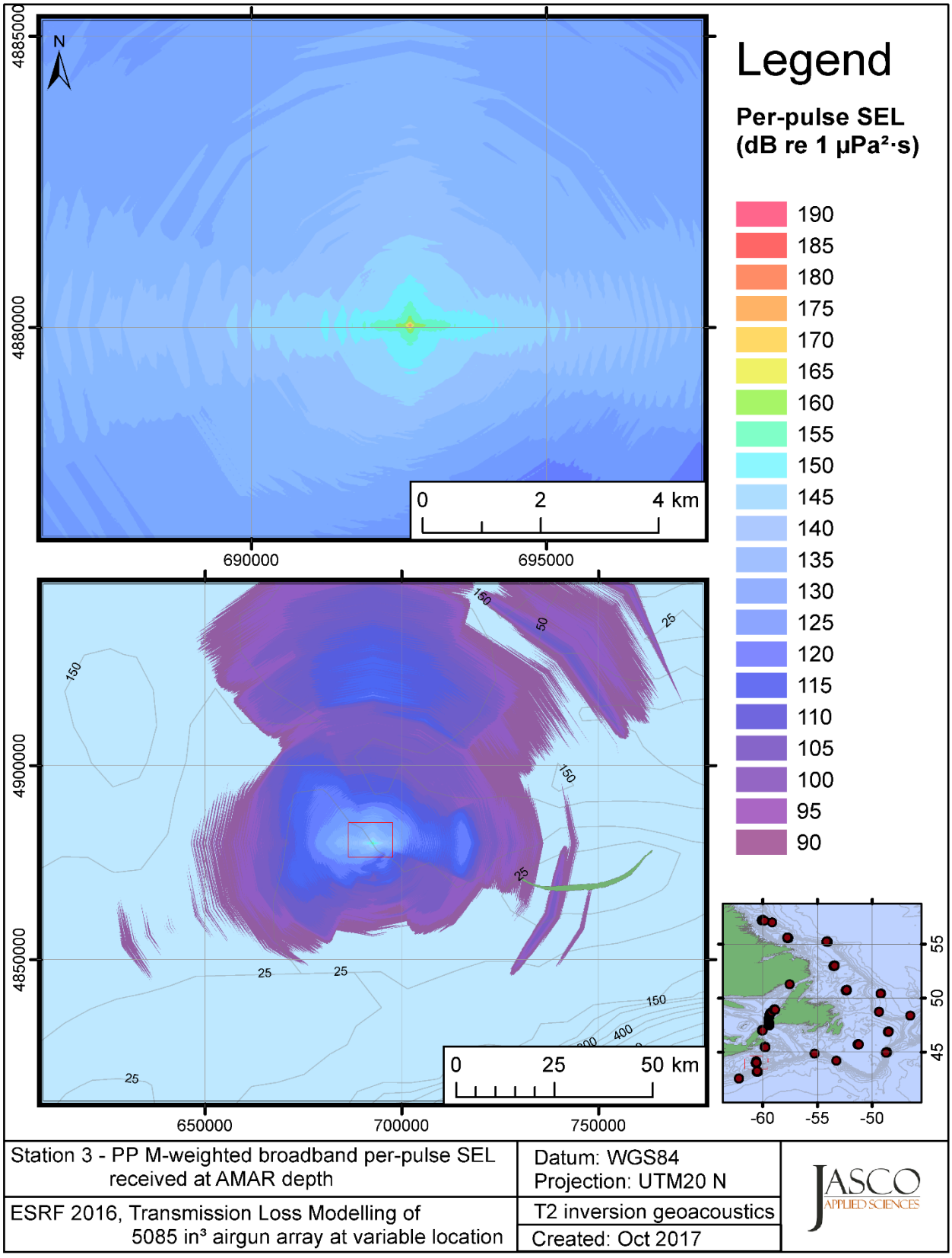

Figure C-223. Stn 3, PP M-weighted SEL received at the AMAR location and depth, modelled using the track 2 inversion geoacoustic bottom, with in-situ July SSP and the airgun array located at any point on the map.

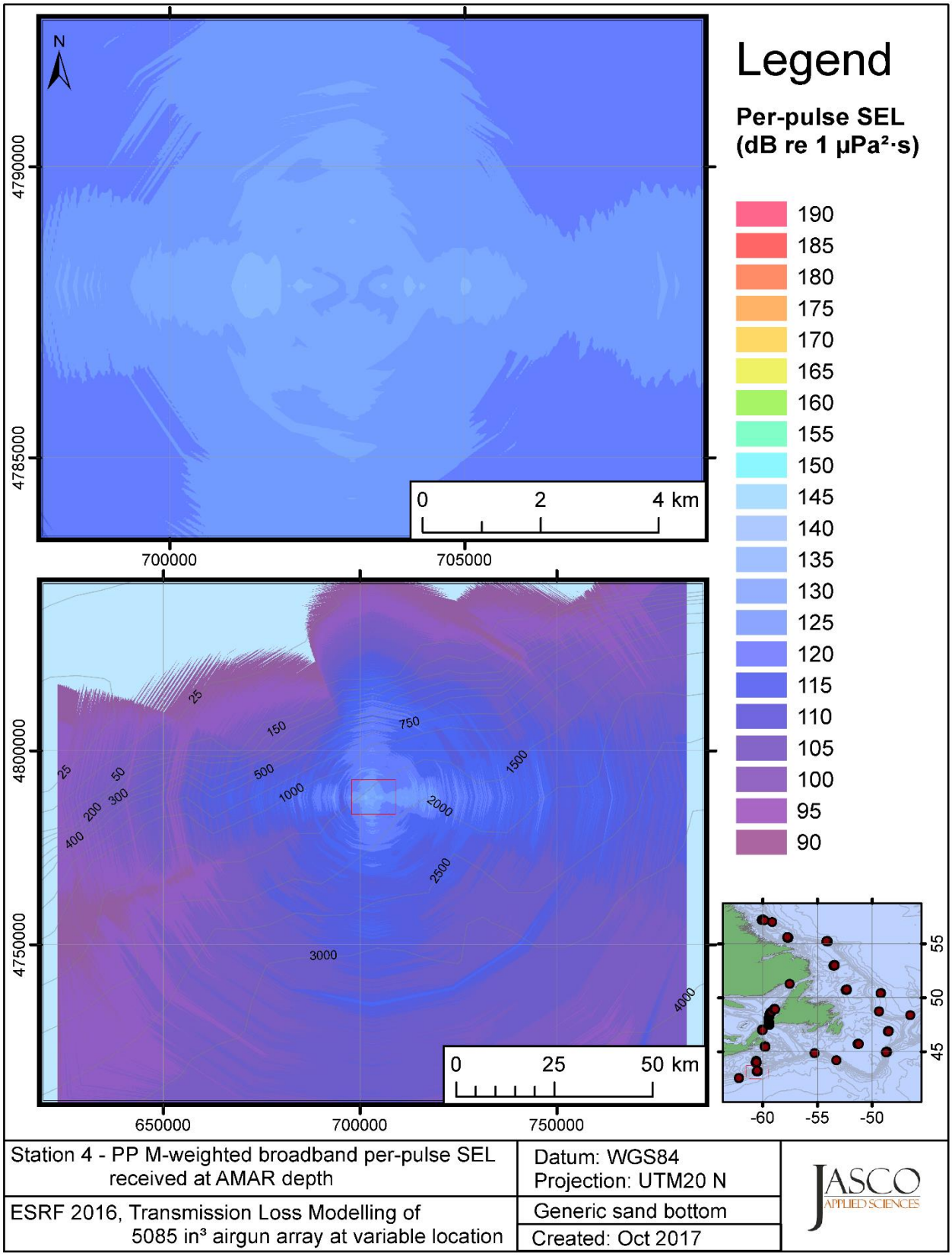

Figure C-224. Stn 4, PP M-weighted SEL received at the AMAR location and depth, modelled using a generic sand bottom, with in-situ July SSP and the airgun array located at any point on the map.

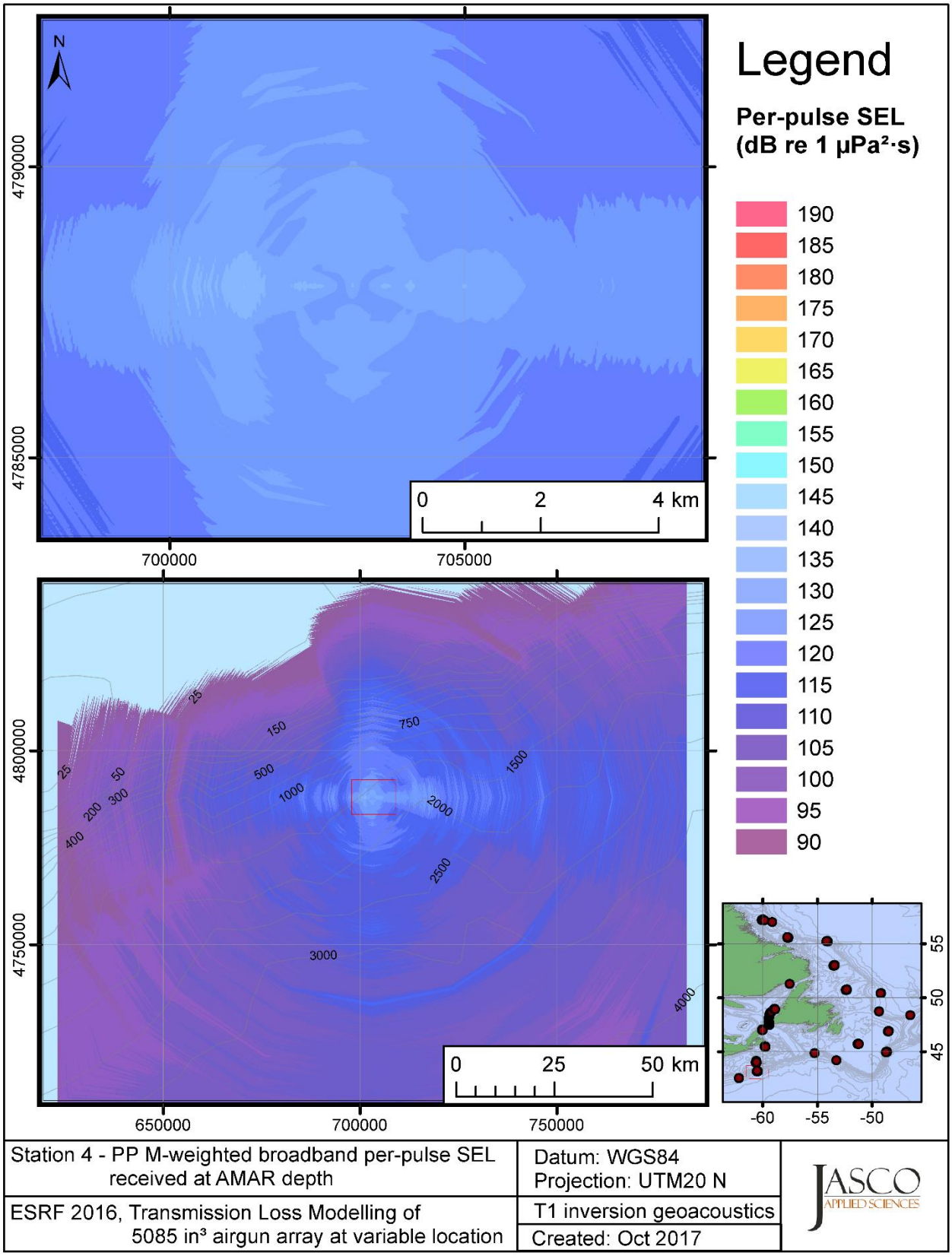

Figure C-225. Stn 4, PP M-weighted SEL received at the AMAR location and depth, modelled using the track 1 inversion geoacoustic bottom, with in-situ July SSP and the airgun array located at any point on the map.

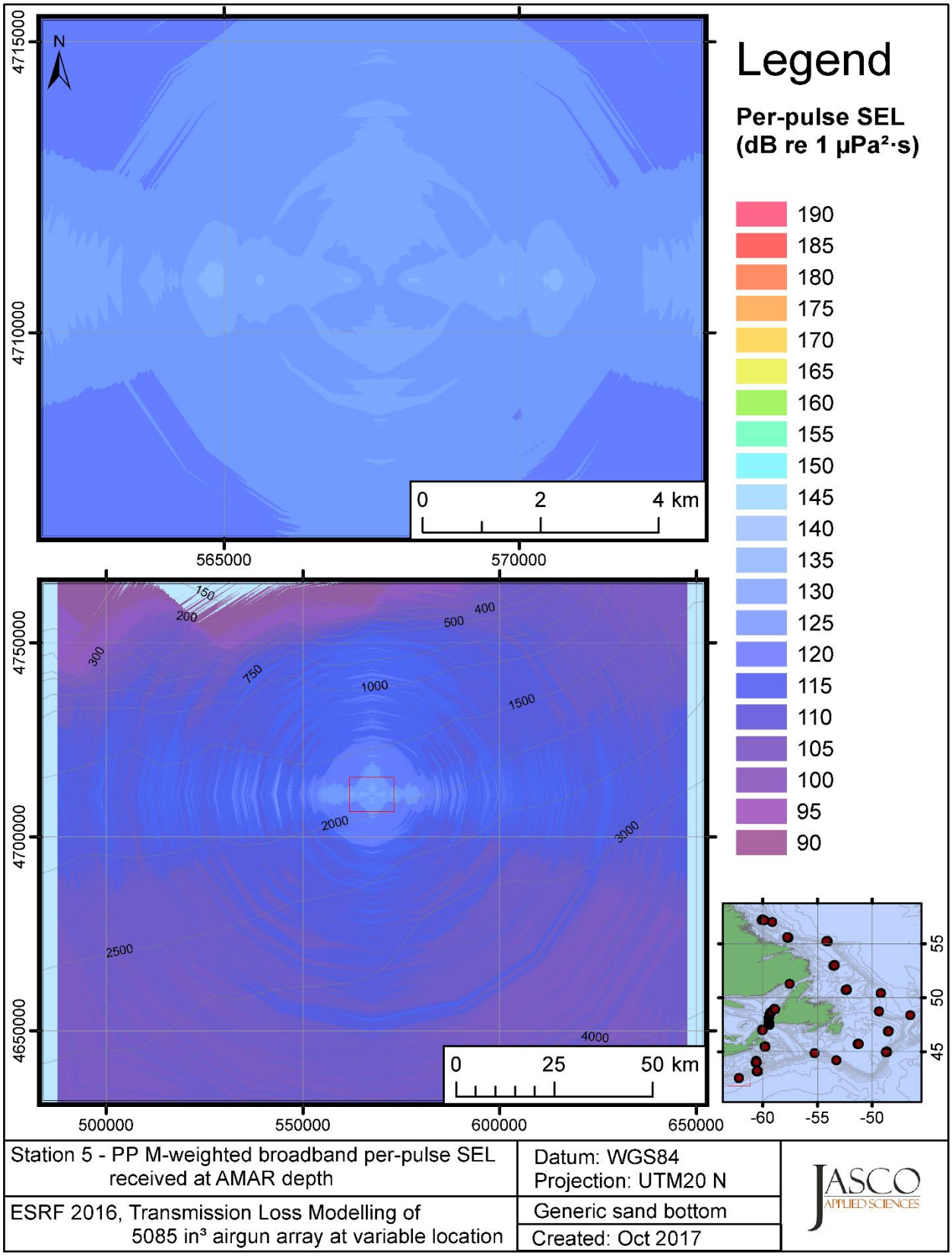

Figure C-226. Stn 5, PP M-weighted SEL received at the AMAR location and depth, modelled using a generic sand bottom, with in-situ July SSP and the airgun array located at any point on the map.

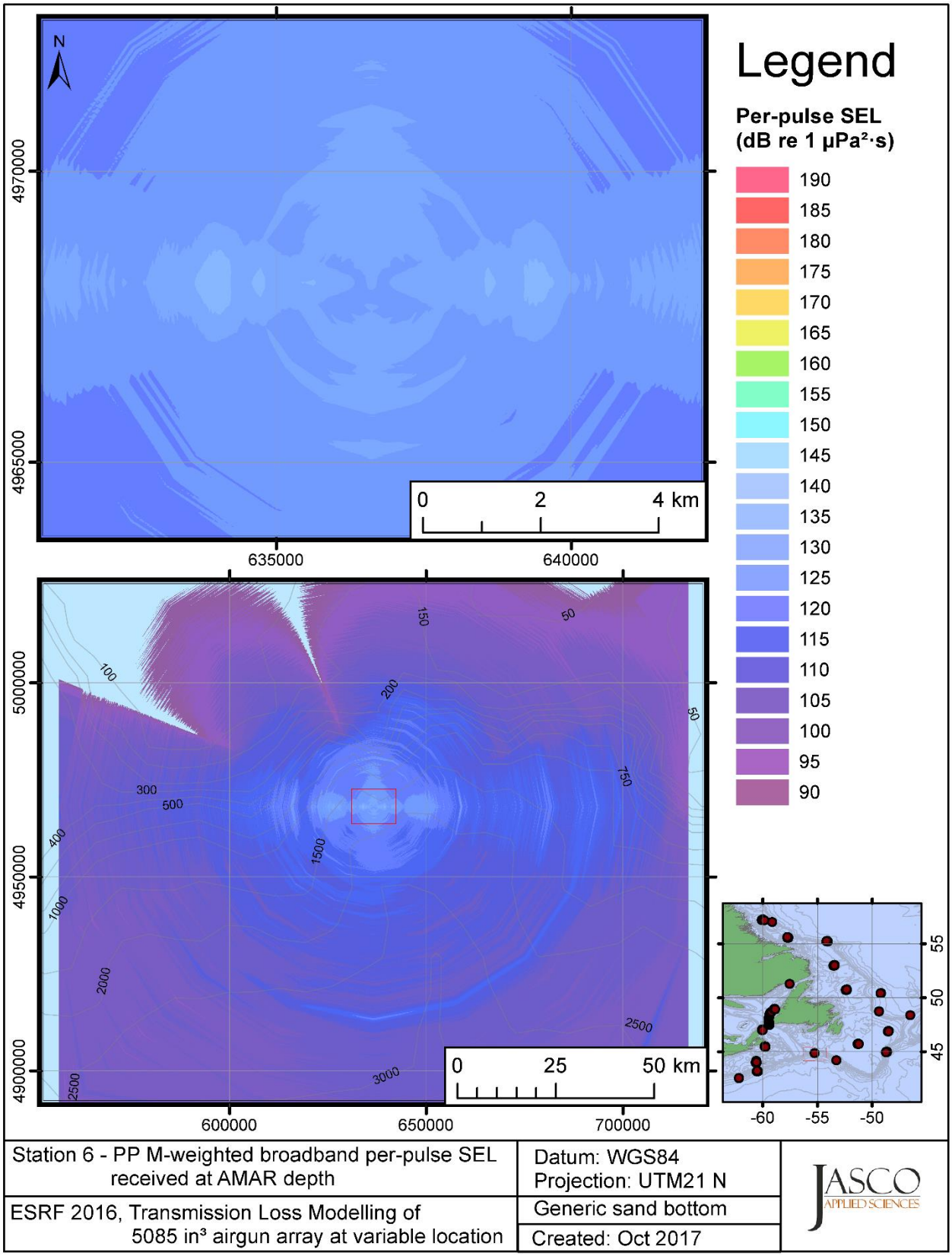

Figure C-227. Stn 6, PP M-weighted SEL received at the AMAR location and depth, modelled using a generic sand bottom, with in-situ July SSP and the airgun array located at any point on the map.

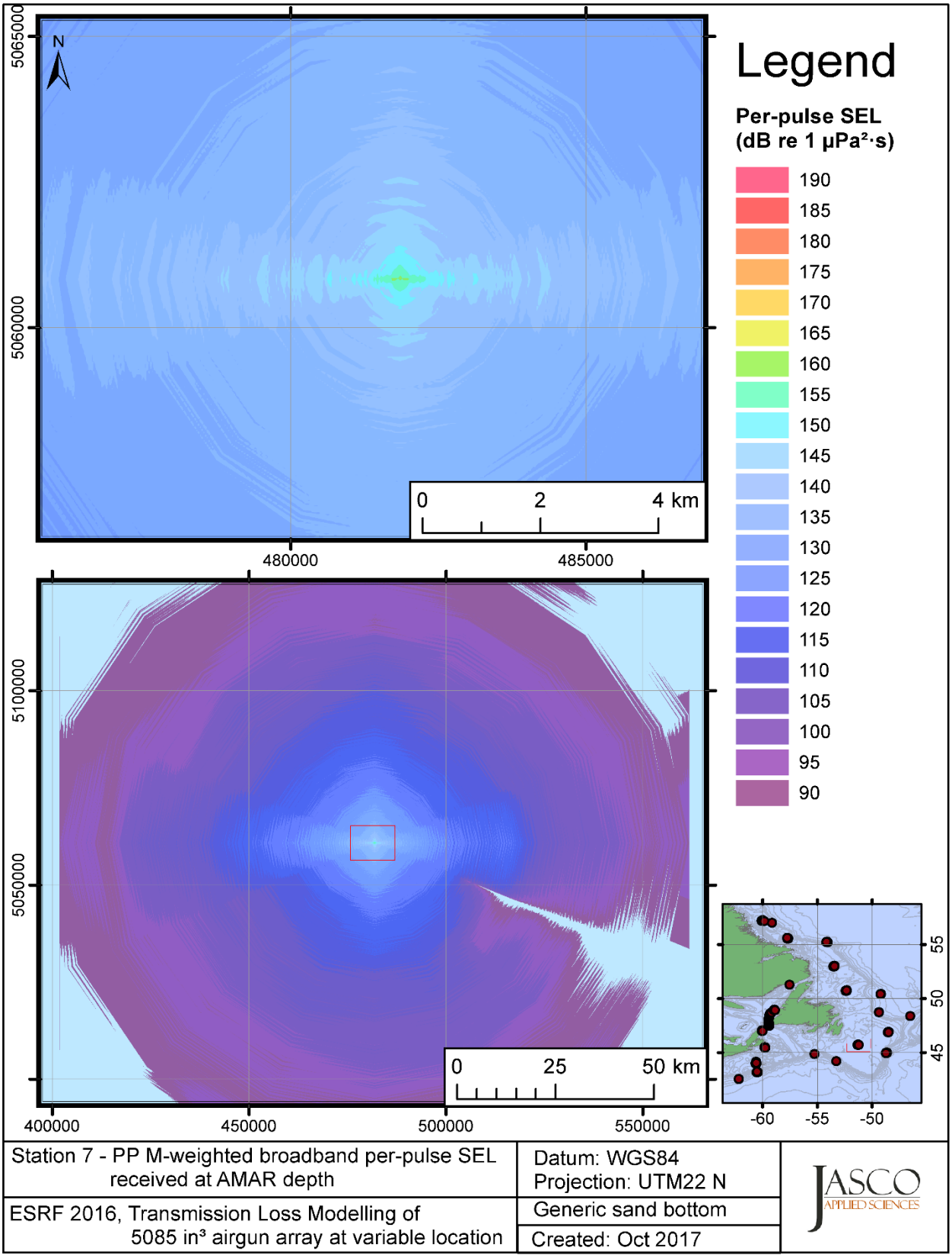

Figure C-228. Stn 7, PP M-weighted SEL received at the AMAR location and depth, modelled using a generic sand bottom, with in-situ July SSP and the airgun array located at any point on the map.

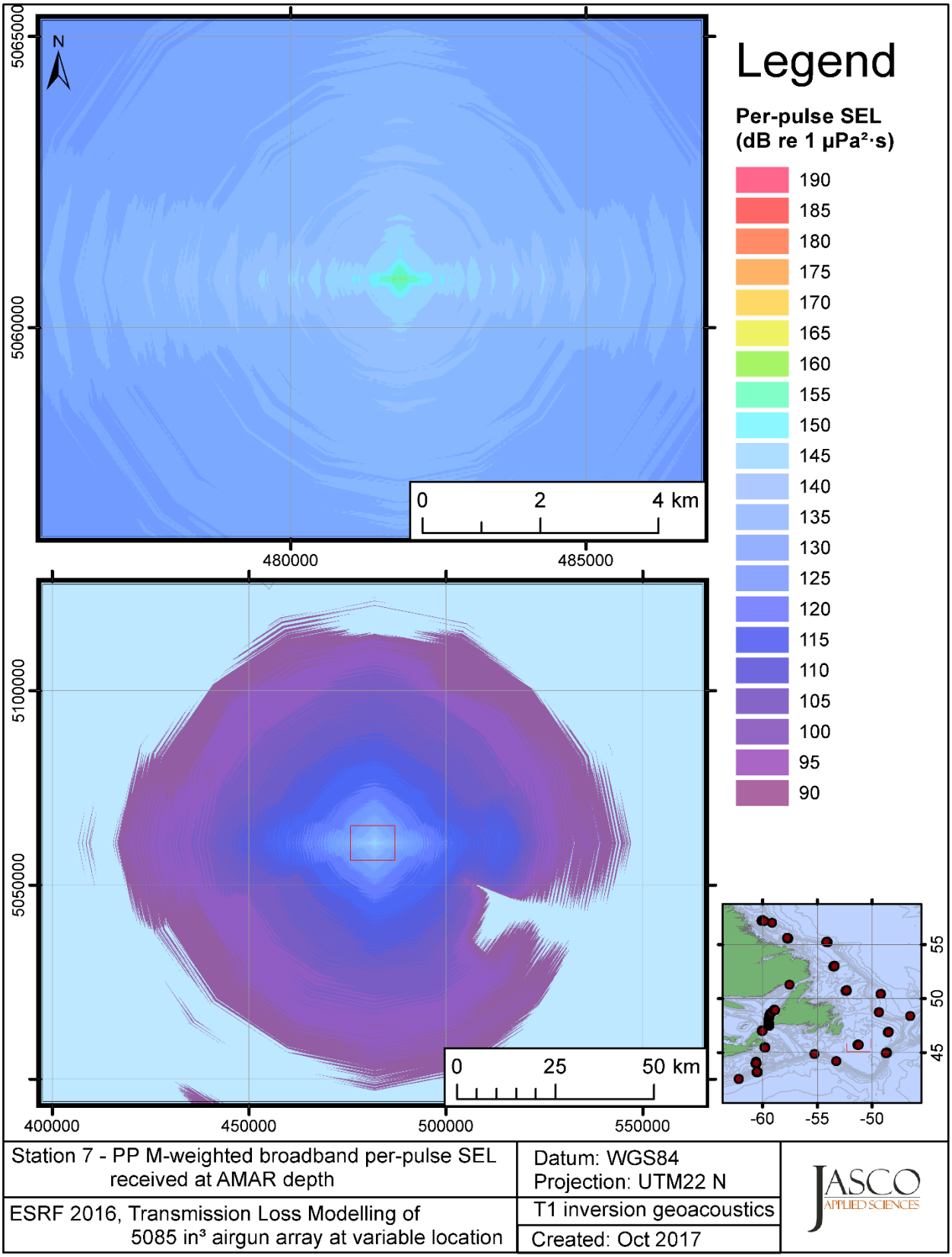

Figure C-229. Stn 7, PP M-weighted SEL received at the AMAR location and depth, modelled using the track 1 inversion geoacoustic bottom, with in-situ July SSP and the airgun array located at any point on the map.

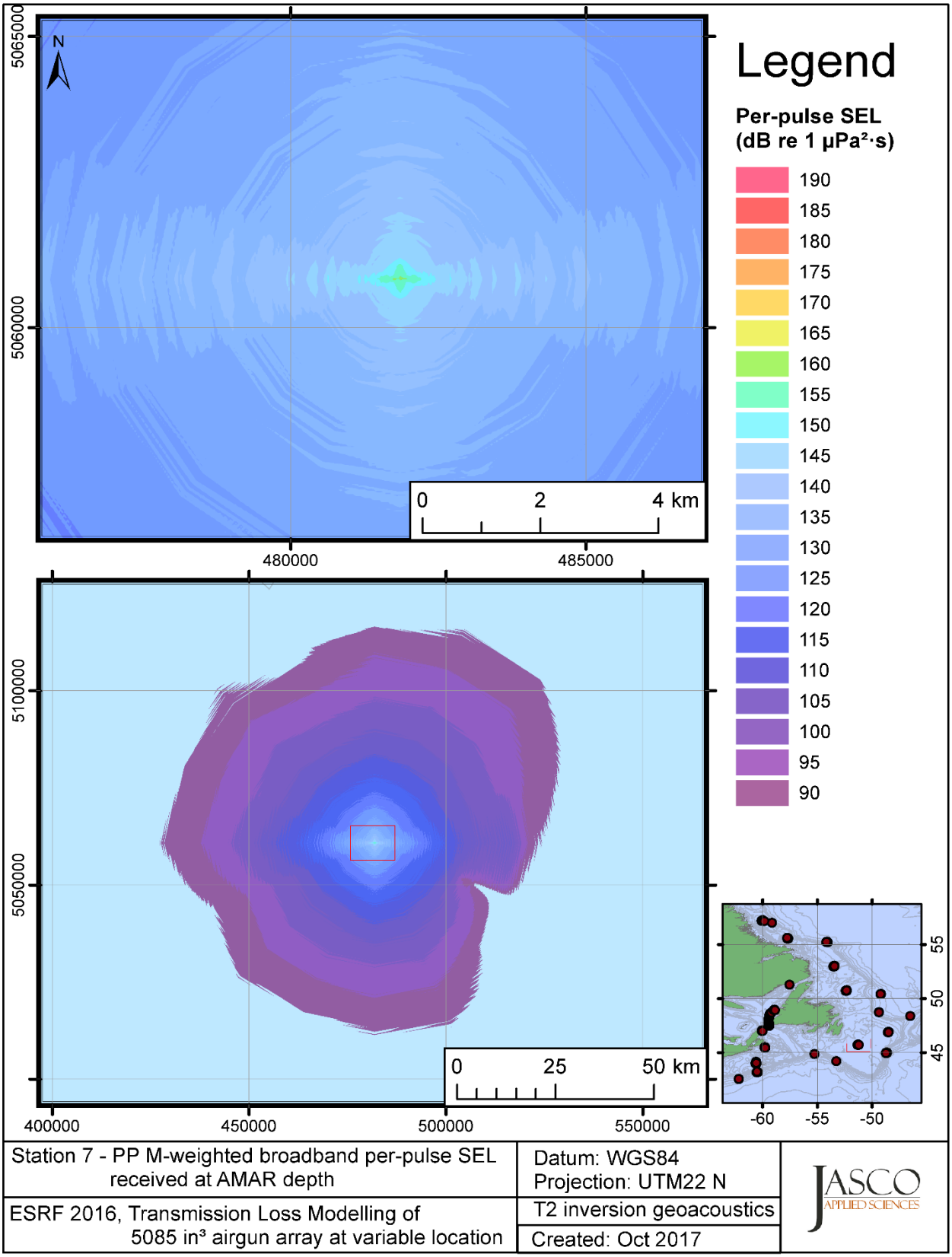

Figure C-230. Stn 7, PP M-weighted SEL received at the AMAR location and depth, modelled using the track 2 inversion geoacoustic bottom, with in-situ July SSP and the airgun array located at any point on the map.

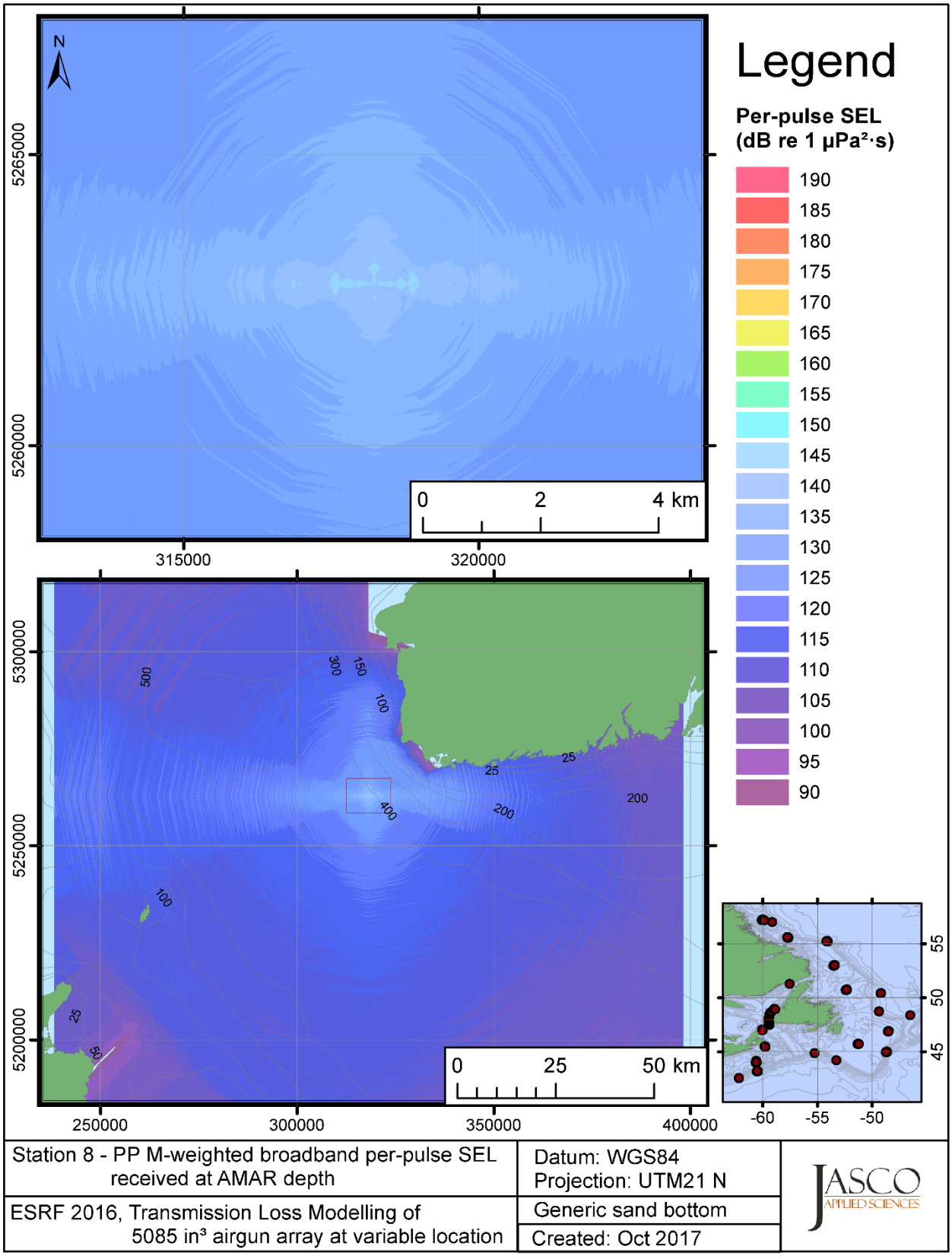

Figure C-231. Stn 8, PP M-weighted SEL received at the AMAR location and depth, modelled using a generic sand bottom, with GDEM July SSP and the airgun array located at any point on the map.

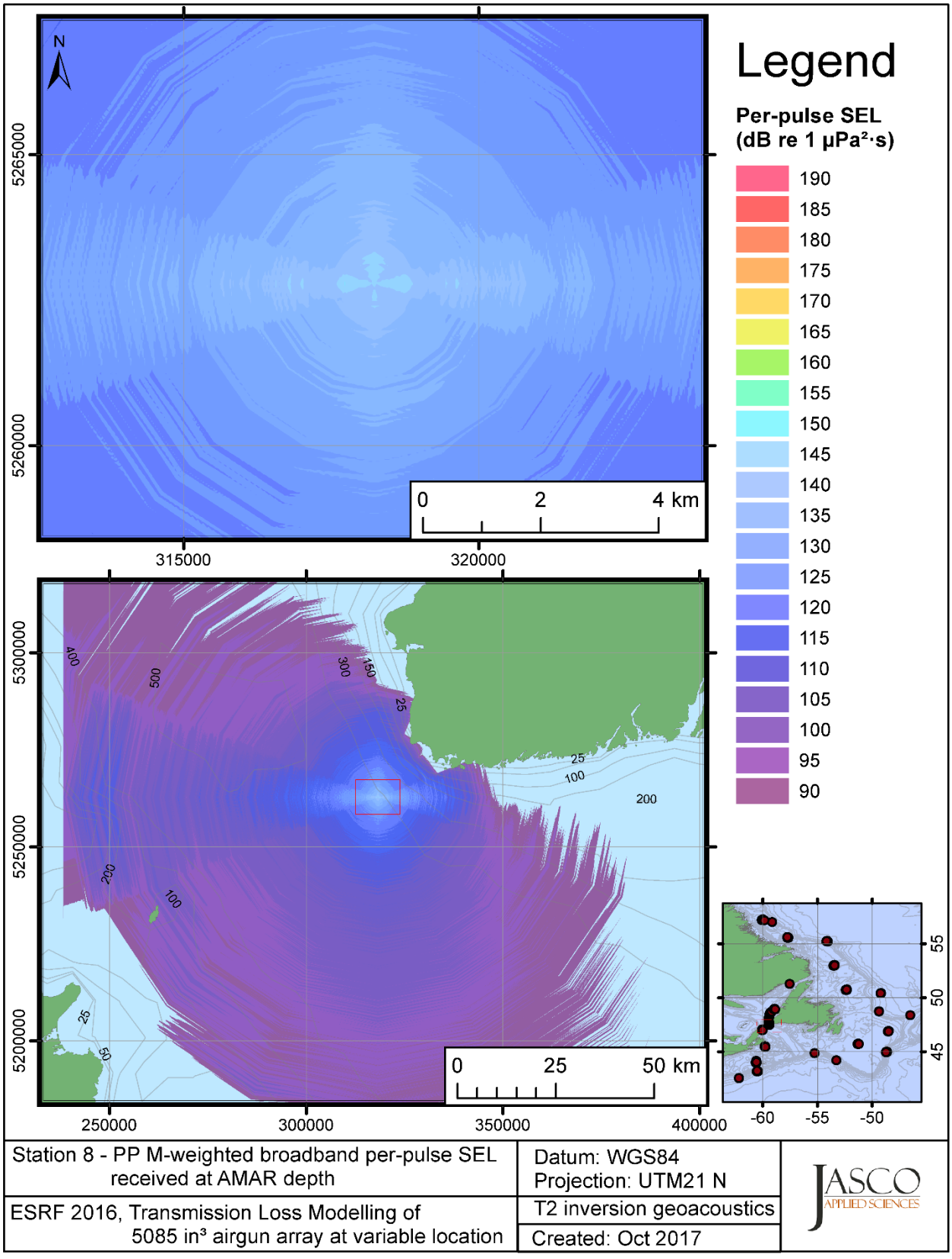

Figure C-232. Stn 8, PP M-weighted SEL received at the AMAR location and depth, modelled using the track 2 inversion geoacoustic bottom, with GDEM July SSP and the airgun array located at any point on the map.

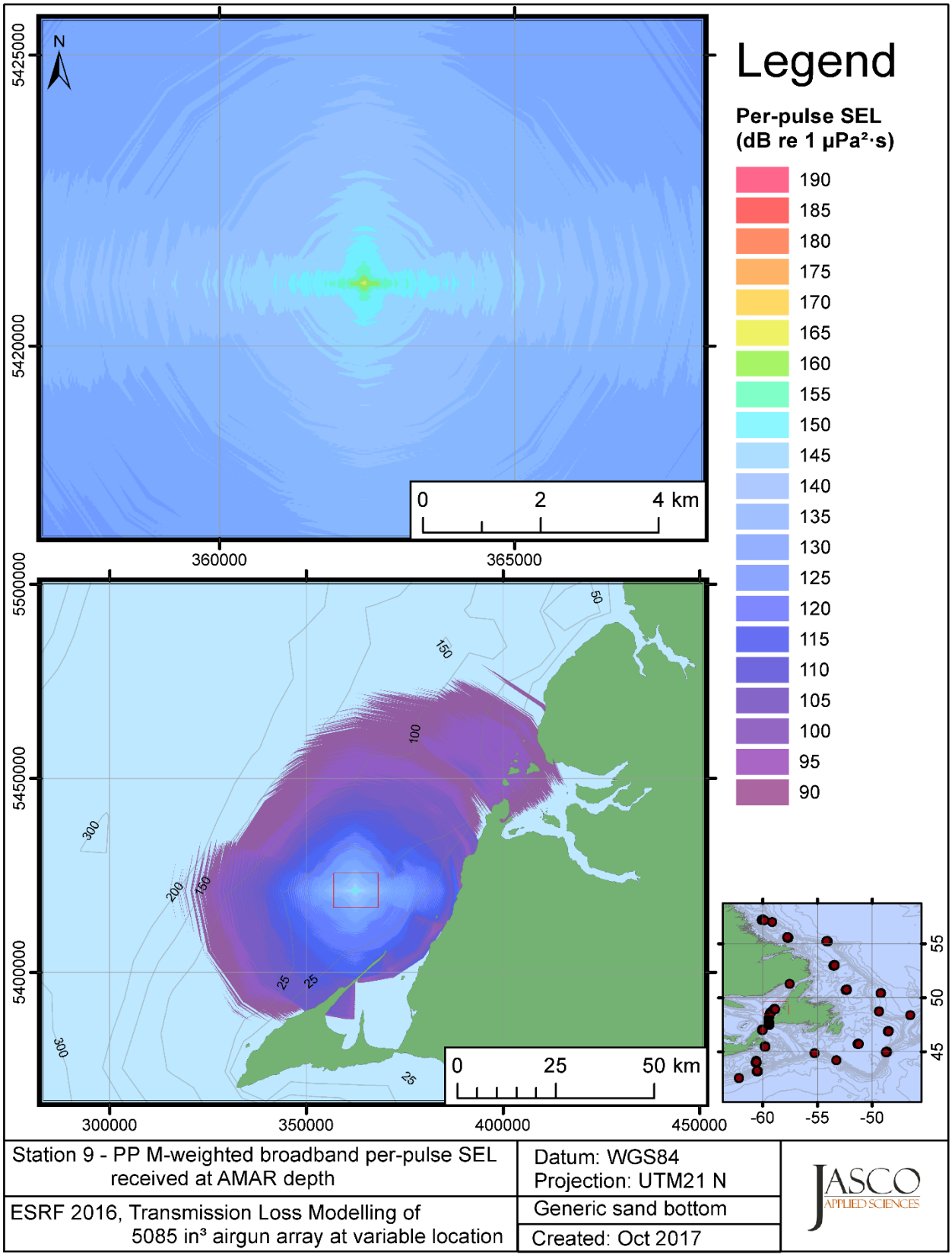

Figure C-233. Stn 9, PP M-weighted SEL received at the AMAR location and depth, modelled using a generic sand bottom, with GDEM July SSP and the airgun array located at any point on the map.

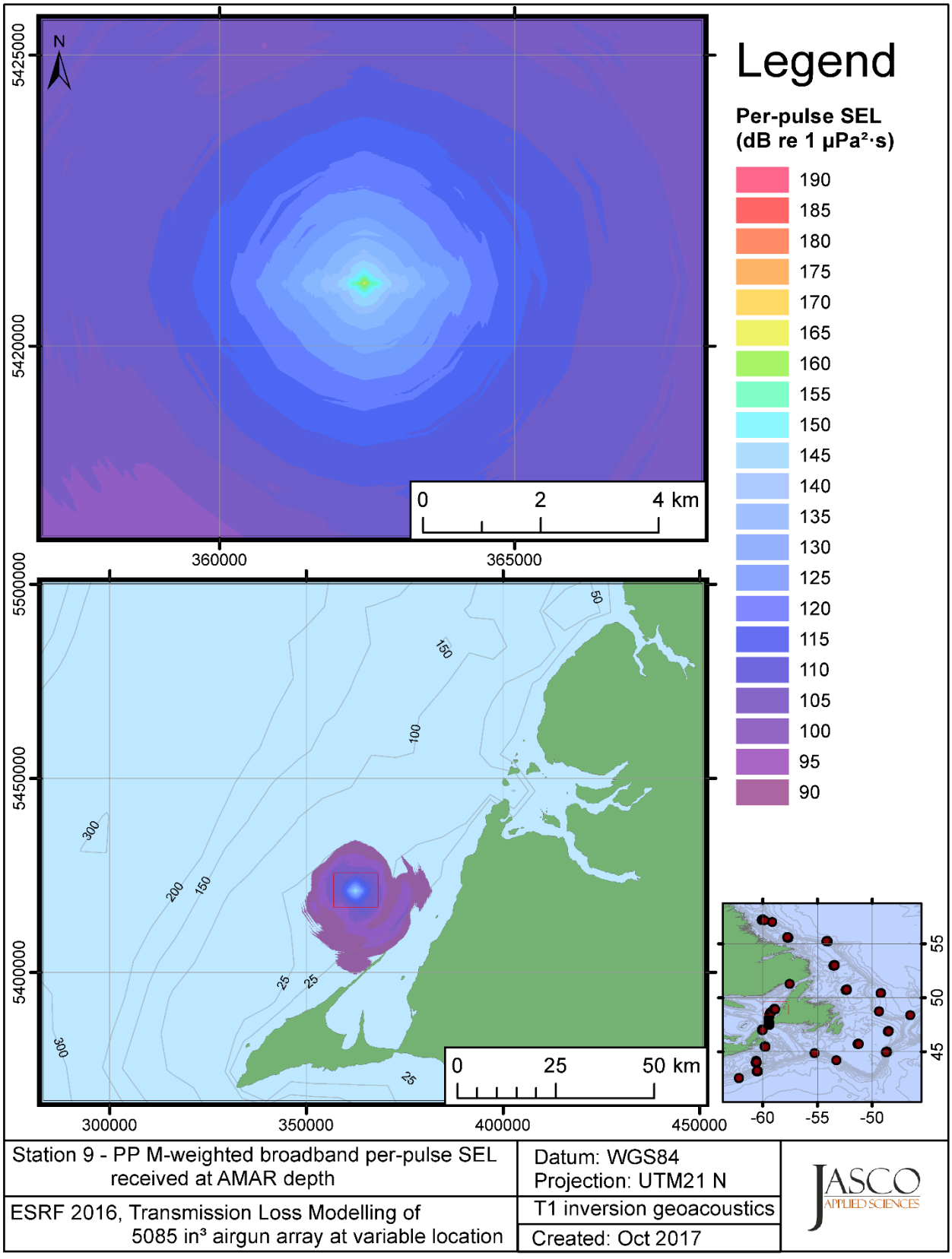

Figure C-234. Stn 9, PP M-weighted SEL received at the AMAR location and depth, modelled using the track 1 inversion geoacoustic bottom, with GDEM July SSP and the airgun array located at any point on the map.

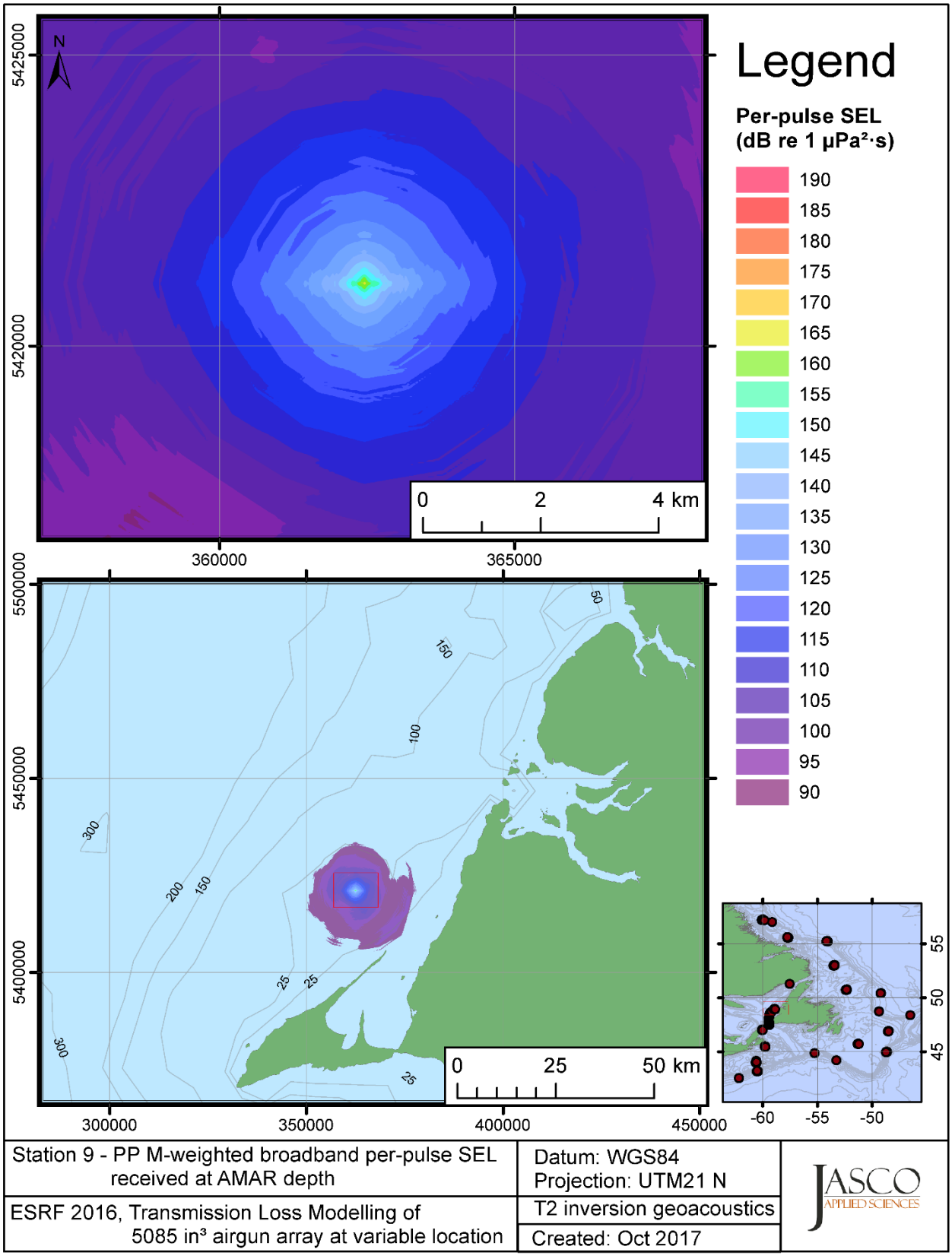

Figure C-235. Stn 9, PP M-weighted SEL received at the AMAR location and depth, modelled using the track 2 inversion geoacoustic bottom, with GDEM July SSP and the airgun array located at any point on the map.

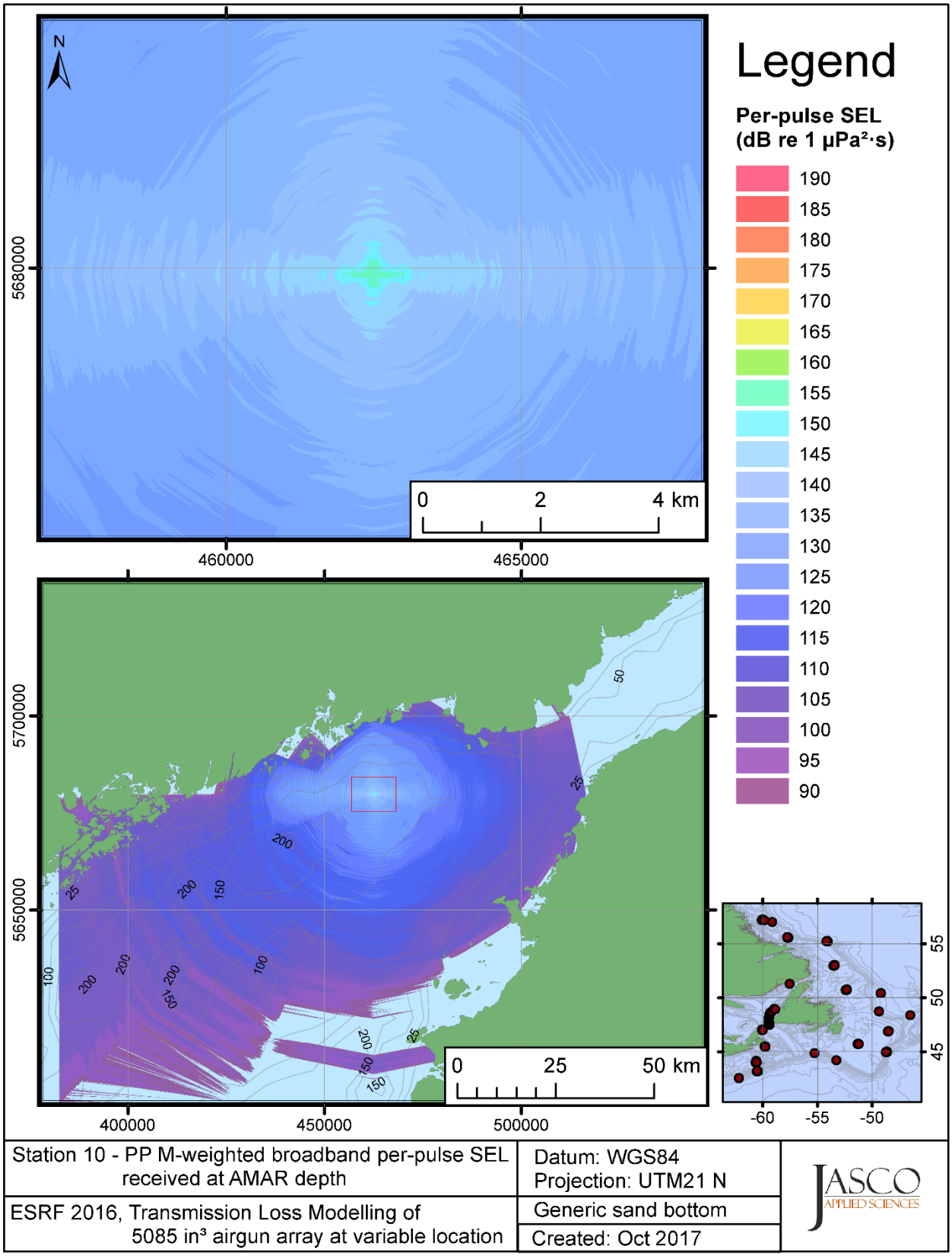

Figure C-236. Stn 10, PP M-weighted SEL received at the AMAR location and depth, modelled using a generic sand bottom, with in-situ July SSP and the airgun array located at any point on the map.

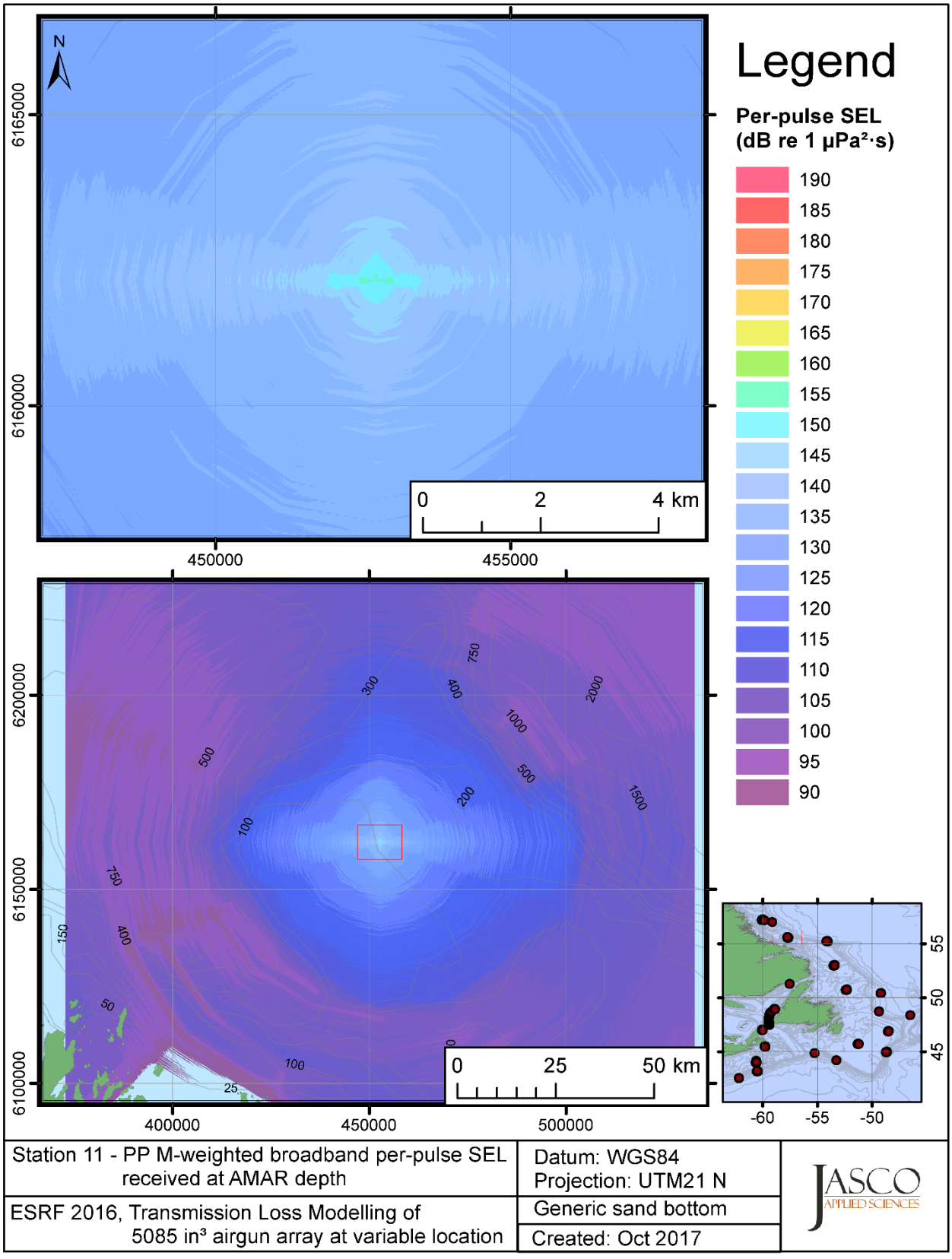

Figure C-237. Stn 11, PP M-weighted SEL received at the AMAR location and depth, modelled using a generic sand bottom, with in-situ July SSP and the airgun array located at any point on the map.

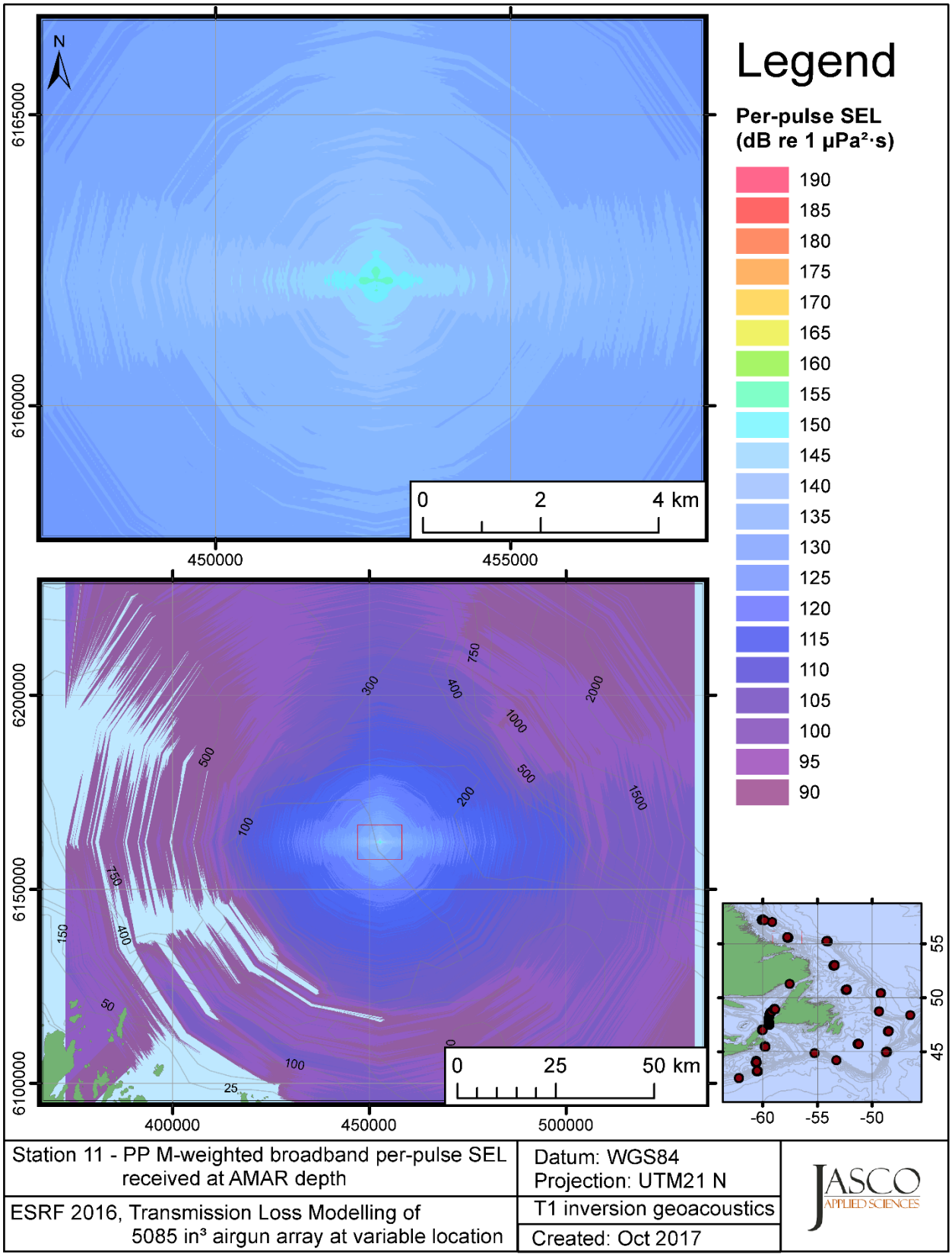

Figure C-238. Stn 11, PP M-weighted SEL received at the AMAR location and depth, modelled using the track 1 inversion geoacoustic bottom, with in-situ July SSP and the airgun array located at any point on the map.

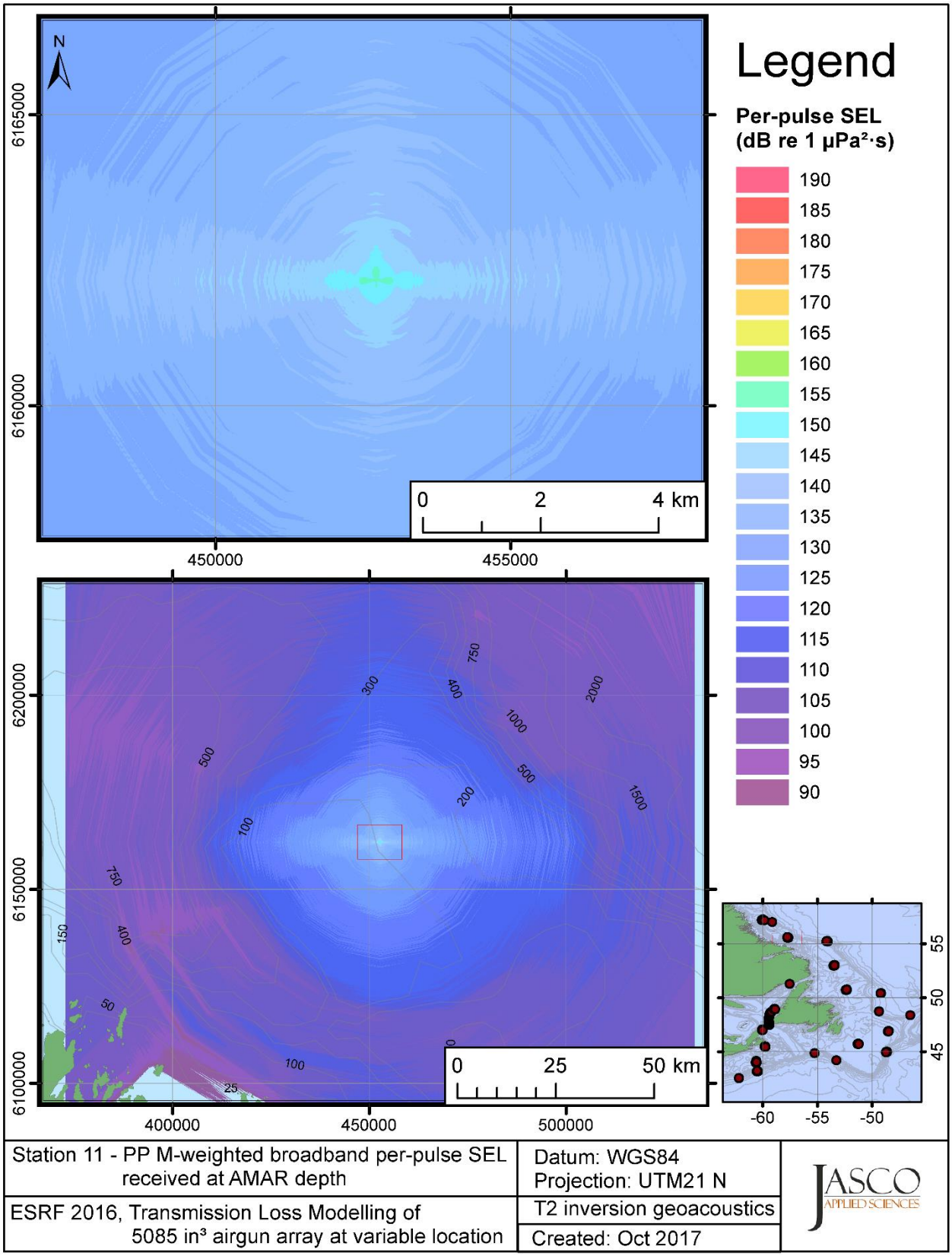

Figure C-239. Stn 11, PP M-weighted SEL received at the AMAR location and depth, modelled using the track 2 inversion geoacoustic bottom, with in-situ July SSP and the airgun array located at any point on the map.

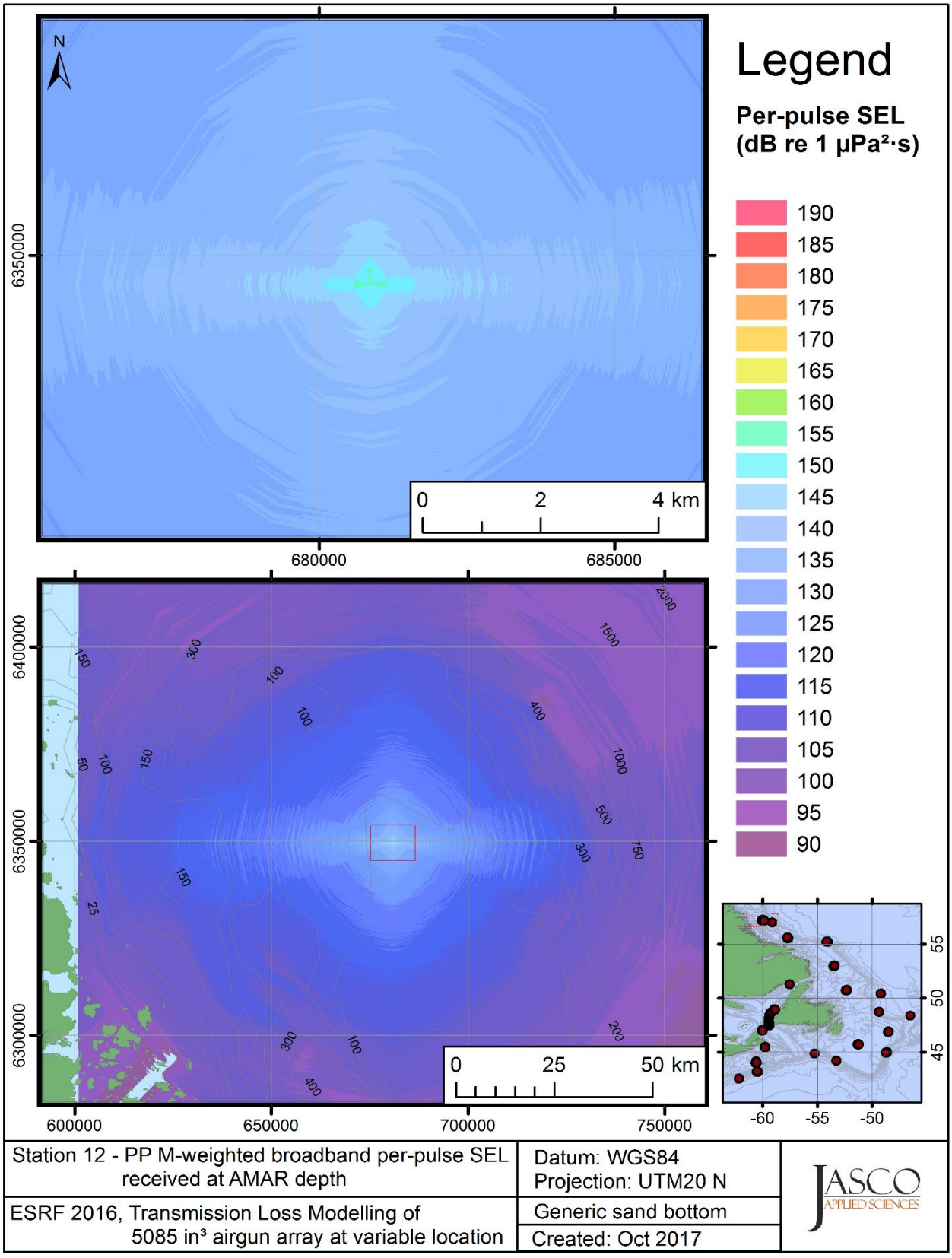

Figure C-240. Stn 12, PP M-weighted SEL received at the AMAR location and depth, modelled using a generic sand bottom, with in-situ July SSP and the airgun array located at any point on the map.

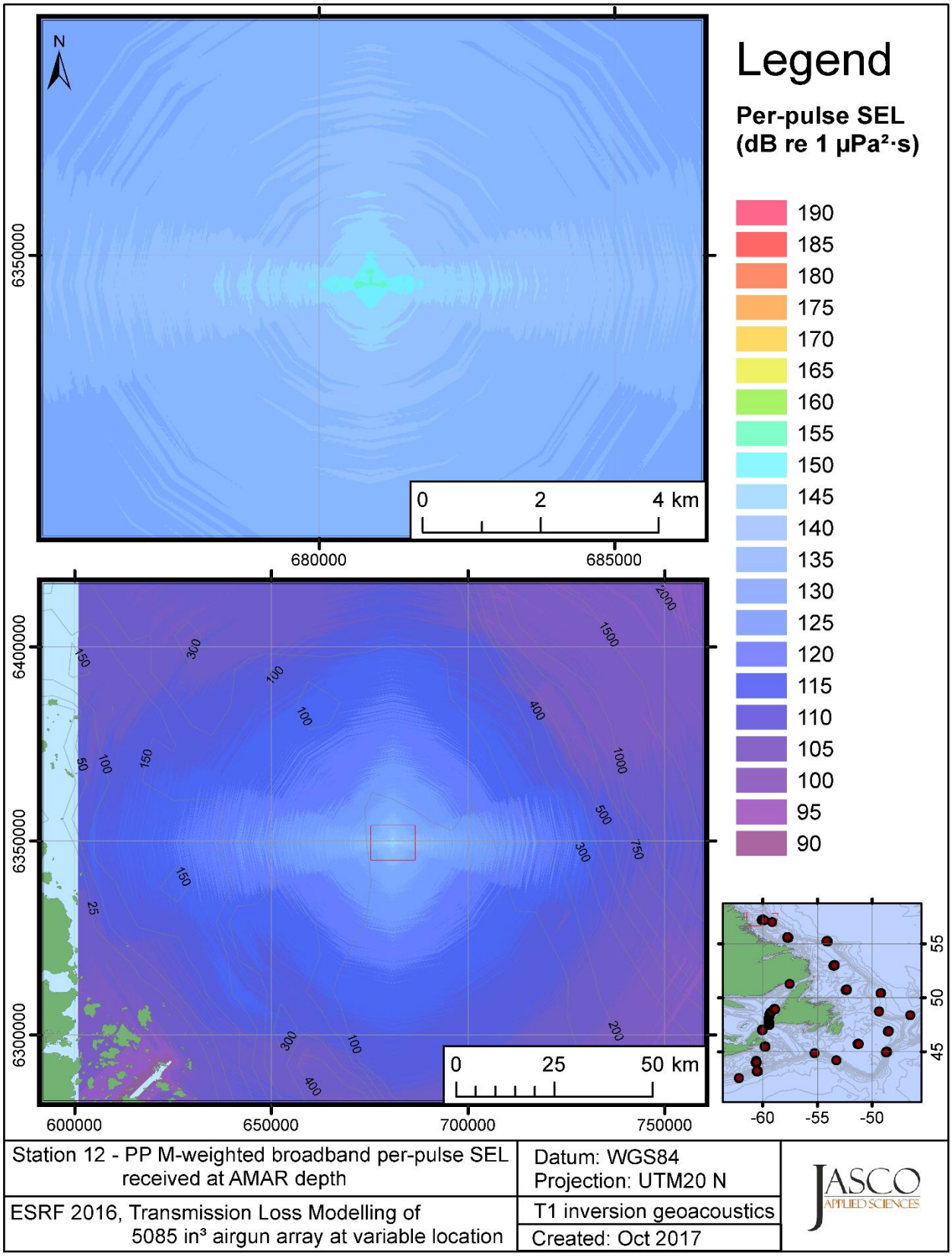

Figure C-241. Stn 12, PP M-weighted SEL received at the AMAR location and depth, modelled using the track 1 inversion geoacoustic bottom, with in-situ July SSP and the airgun array located at any point on the map.

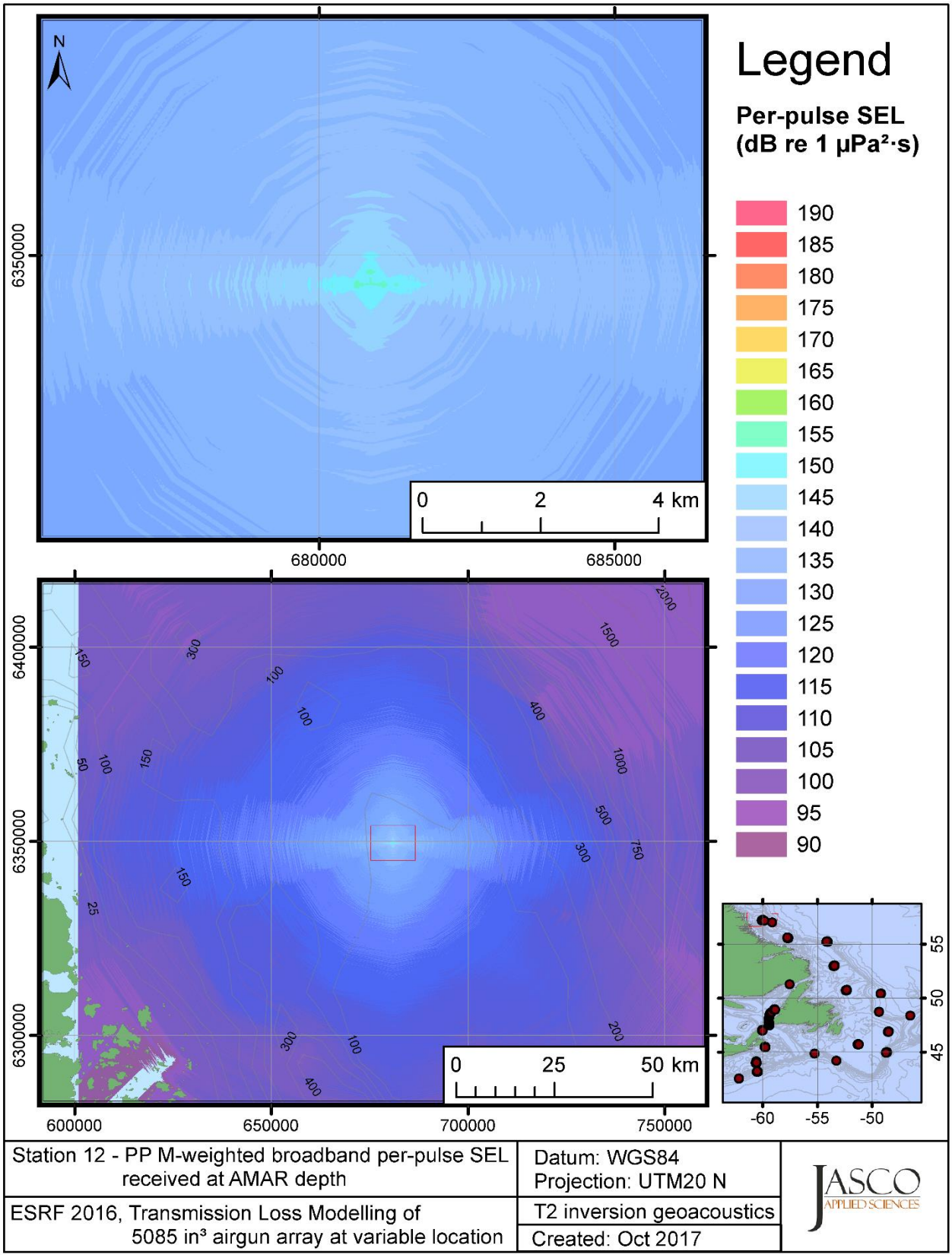

Figure C-242. Stn 12, PP M-weighted SEL received at the AMAR location and depth, modelled using the track 2 inversion geoacoustic bottom, with in-situ July SSP and the airgun array located at any point on the map.

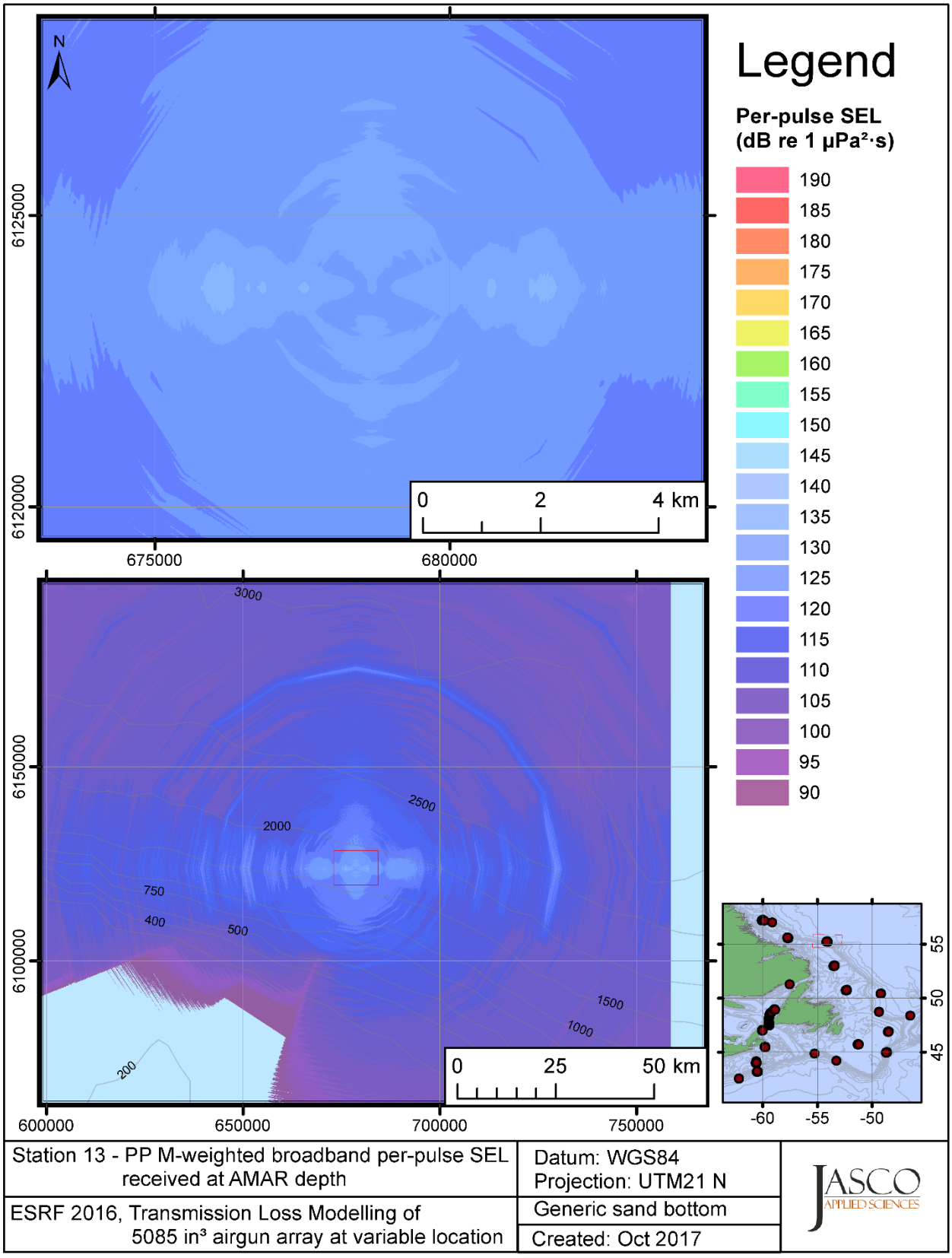

Figure C-243. Stn 13, PP M-weighted SEL received at the AMAR location and depth, modelled using a generic sand bottom, with in-situ July SSP and the airgun array located at any point on the map.

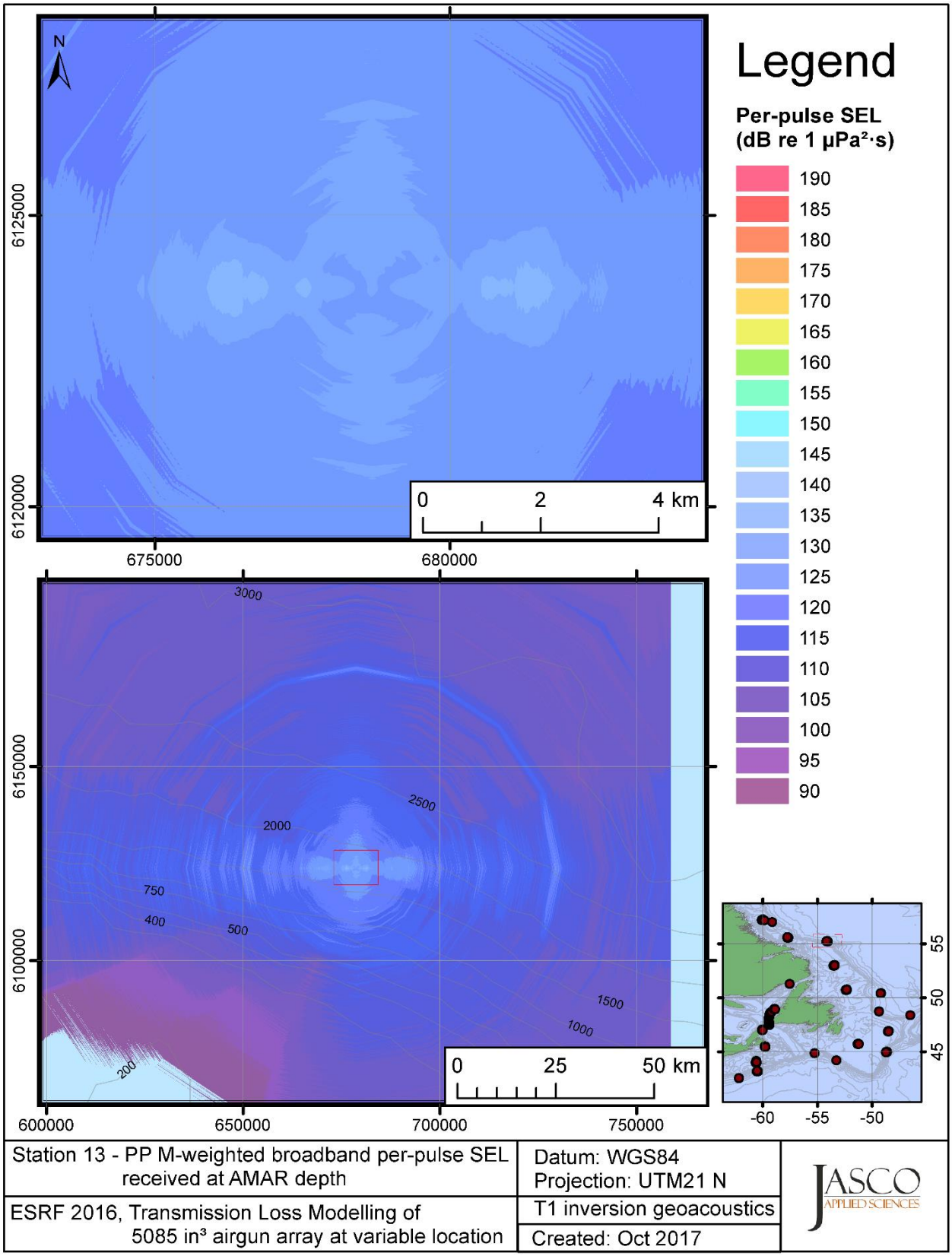

Figure C-244. Stn 13, PP M-weighted SEL received at the AMAR location and depth, modelled using the track 1 inversion geoacoustic bottom, with in-situ July SSP and the airgun array located at any point on the map.

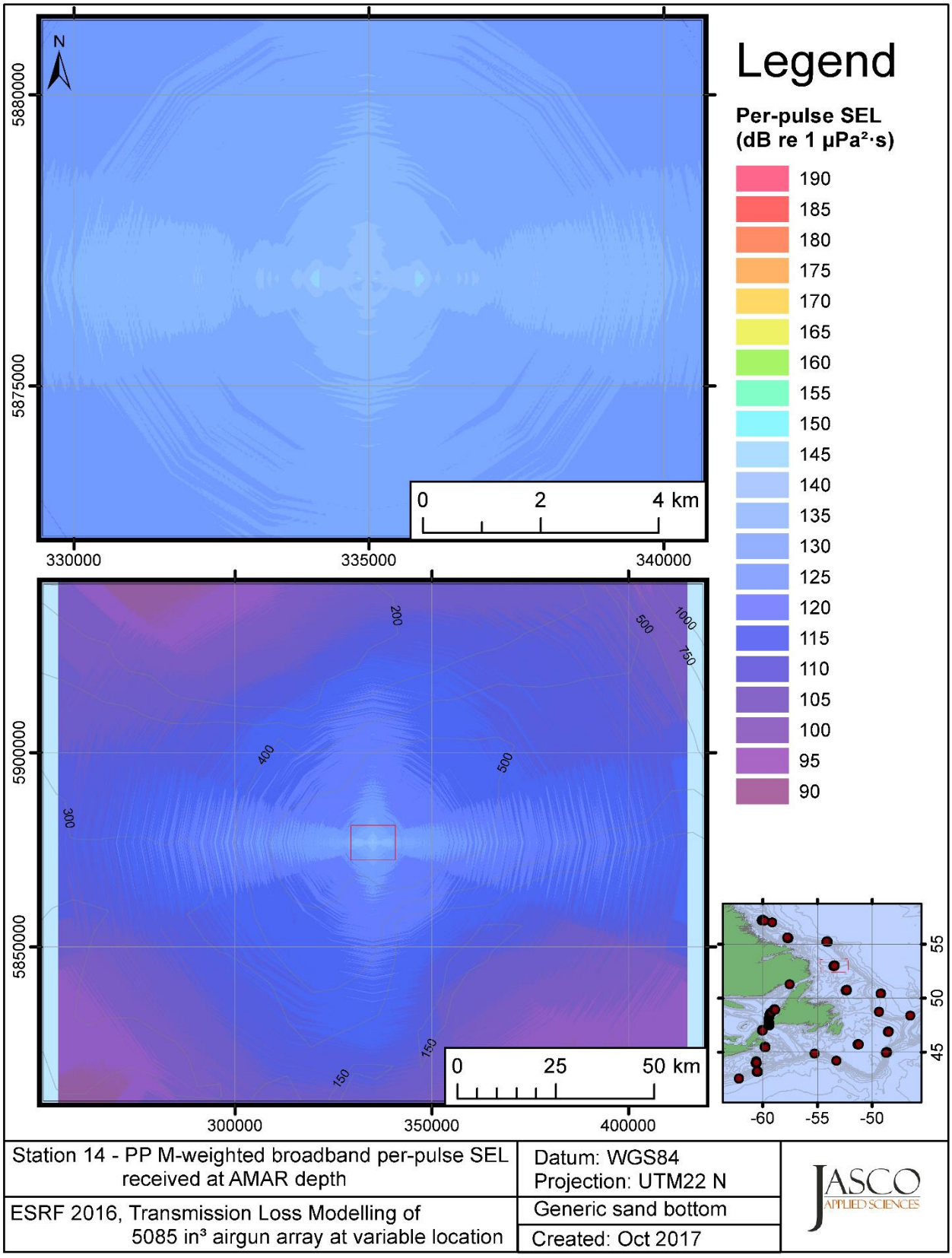

Figure C-245. Stn 14, PP M-weighted SEL received at the AMAR location and depth, modelled using a generic sand bottom, with in-situ July SSP and the airgun array located at any point on the map.

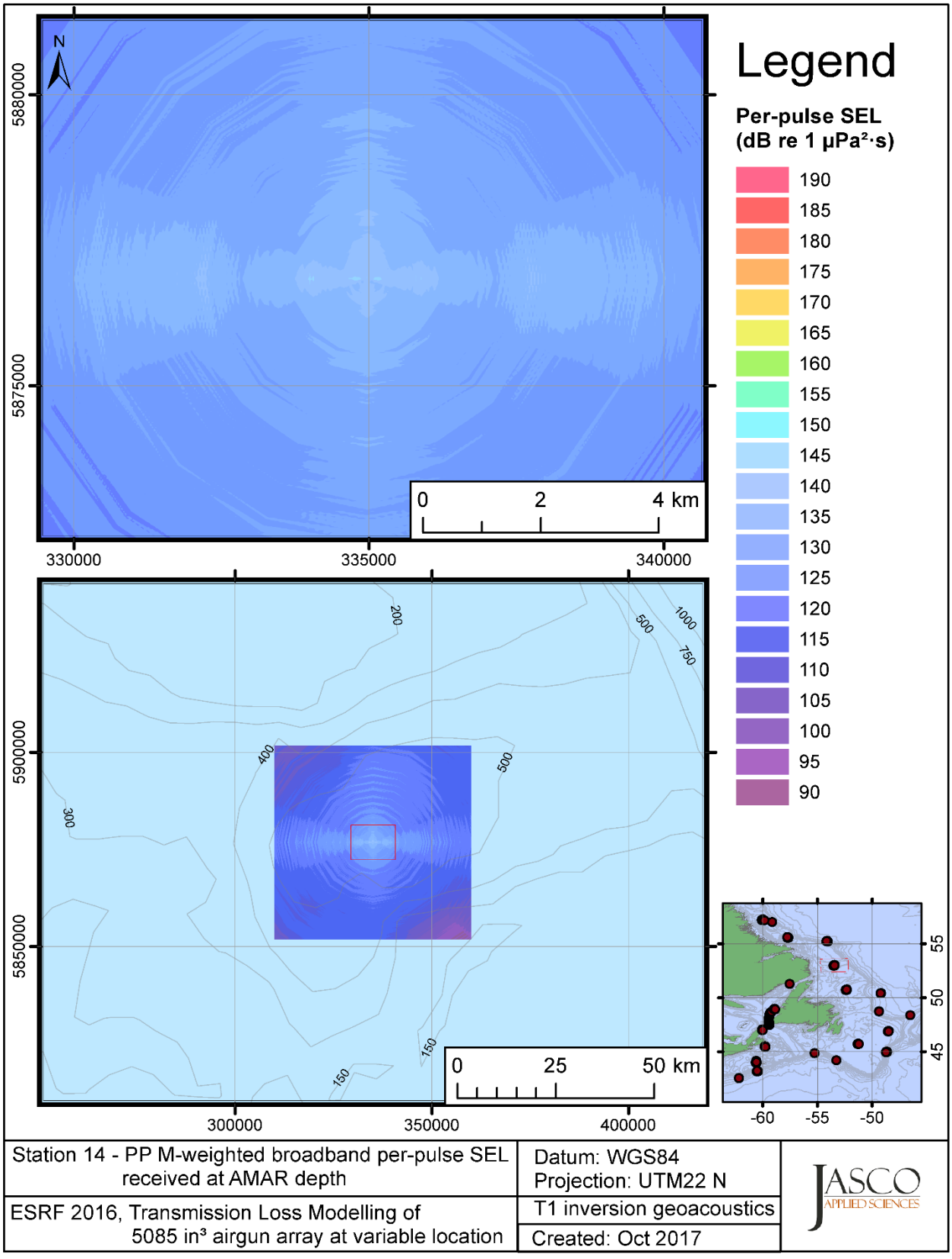

Figure C-246. Stn 14, PP M-weighted SEL received at the AMAR location and depth, modelled using the track 1 inversion geoacoustic bottom, with in-situ July SSP and the airgun array located at any point on the map.

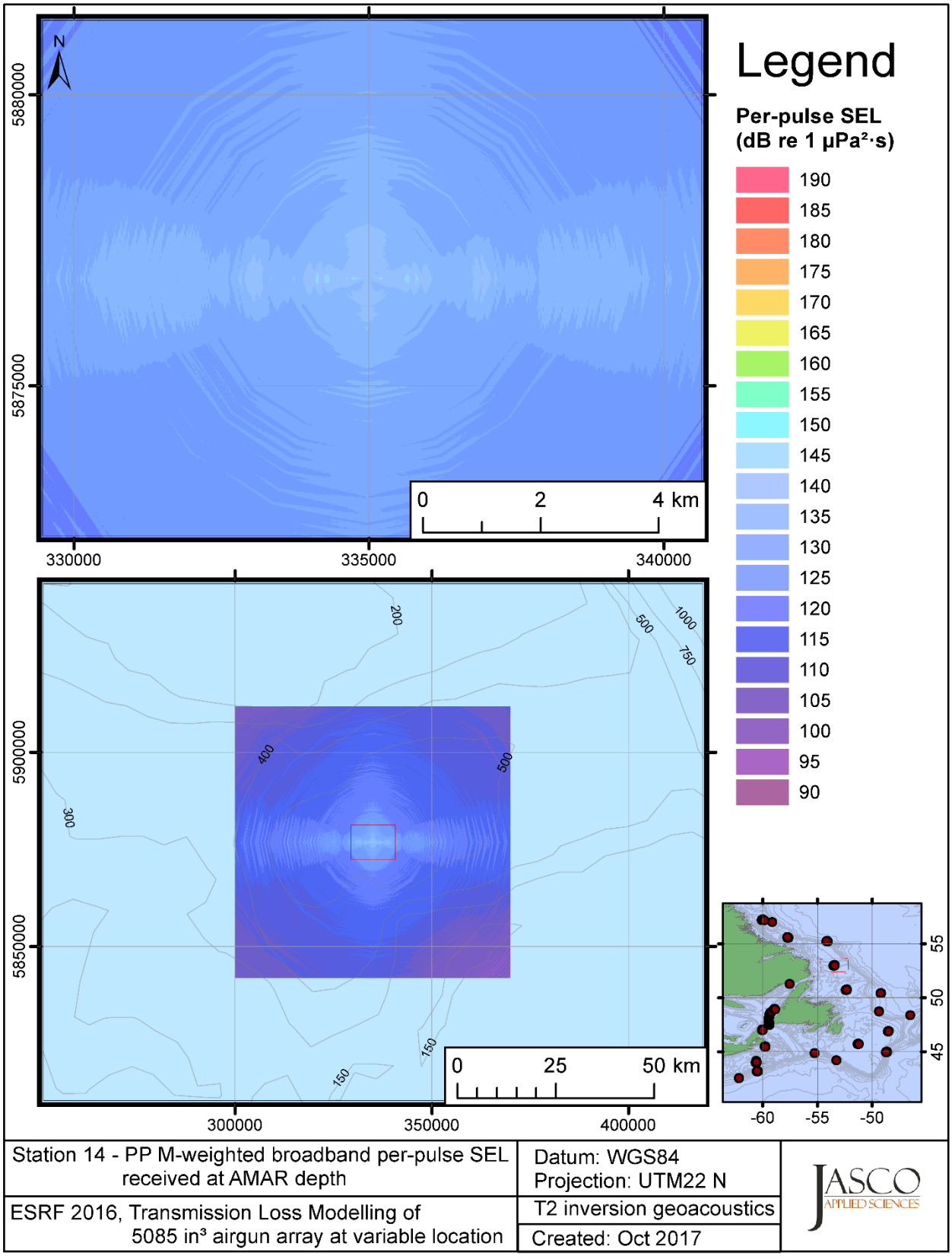

Figure C-247. Stn 14, PP M-weighted SEL received at the AMAR location and depth, modelled using the track 2 inversion geoacoustic bottom, with in-situ July SSP and the airgun array located at any point on the map.

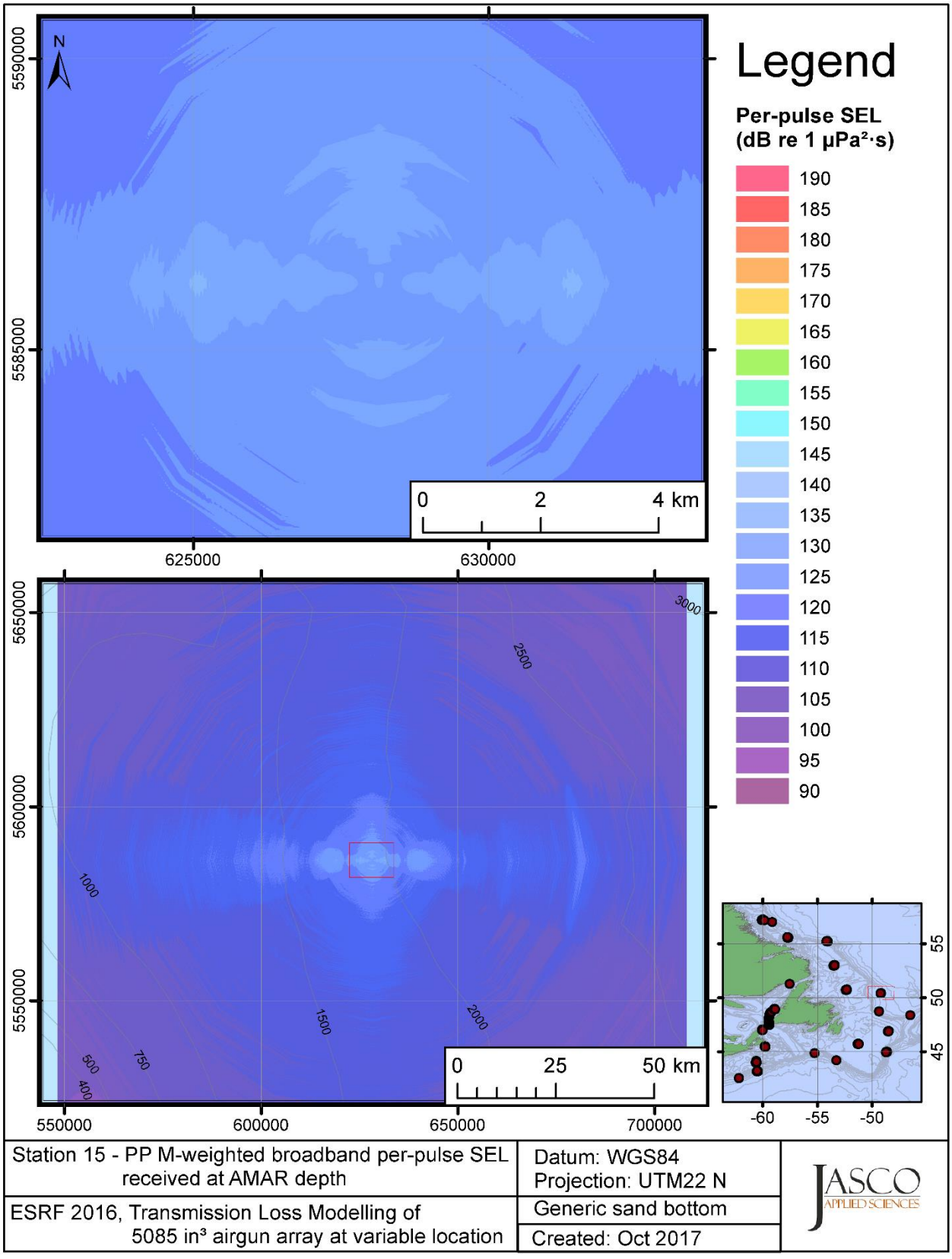

Figure C-248. Stn 15, PP M-weighted SEL received at the AMAR location and depth, modelled using a generic sand bottom, with in-situ July SSP and the airgun array located at any point on the map.

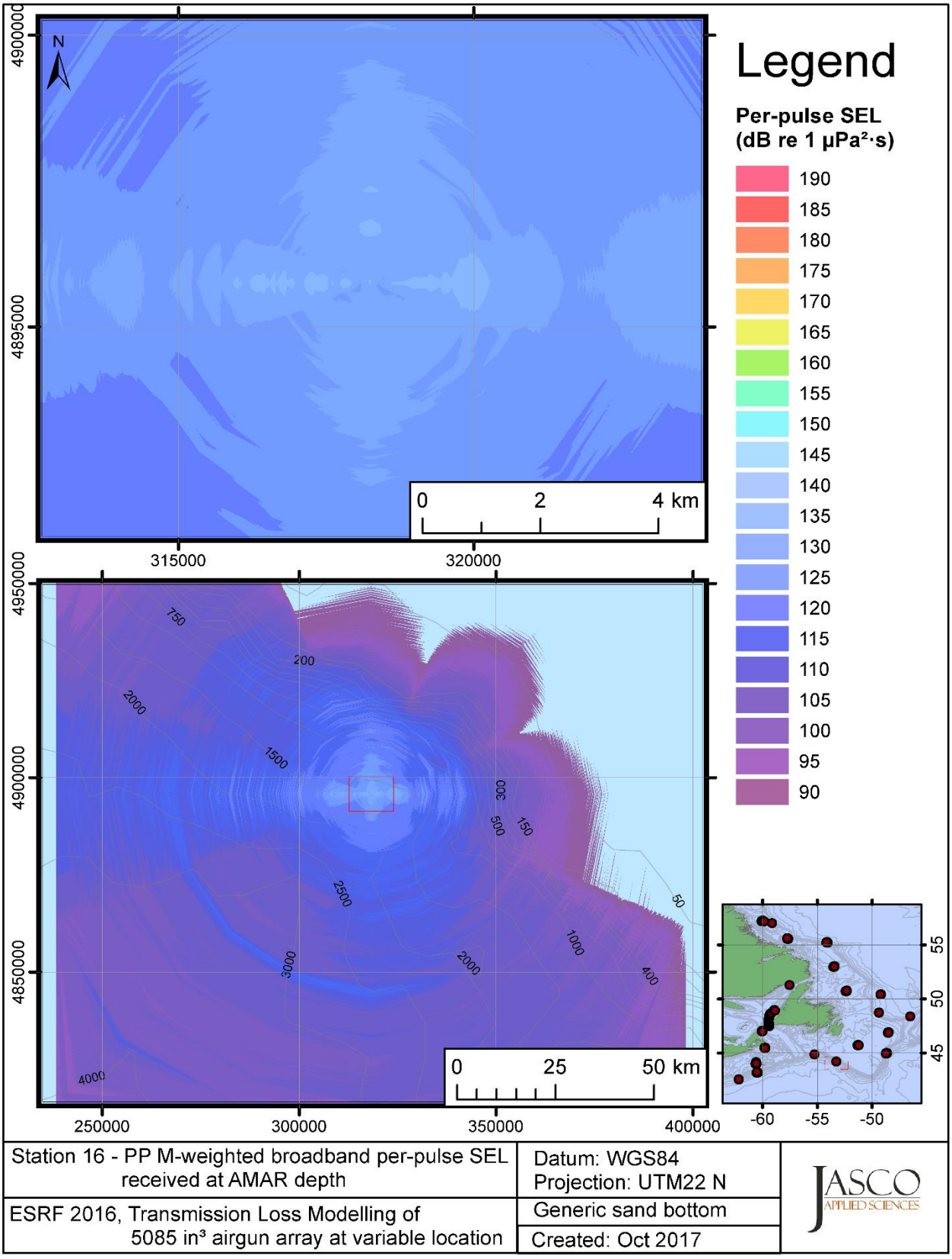

Figure C-249. Stn 16, PP M-weighted SEL received at the AMAR location and depth, modelled using a generic sand bottom, with in-situ July SSP and the airgun array located at any point on the map.

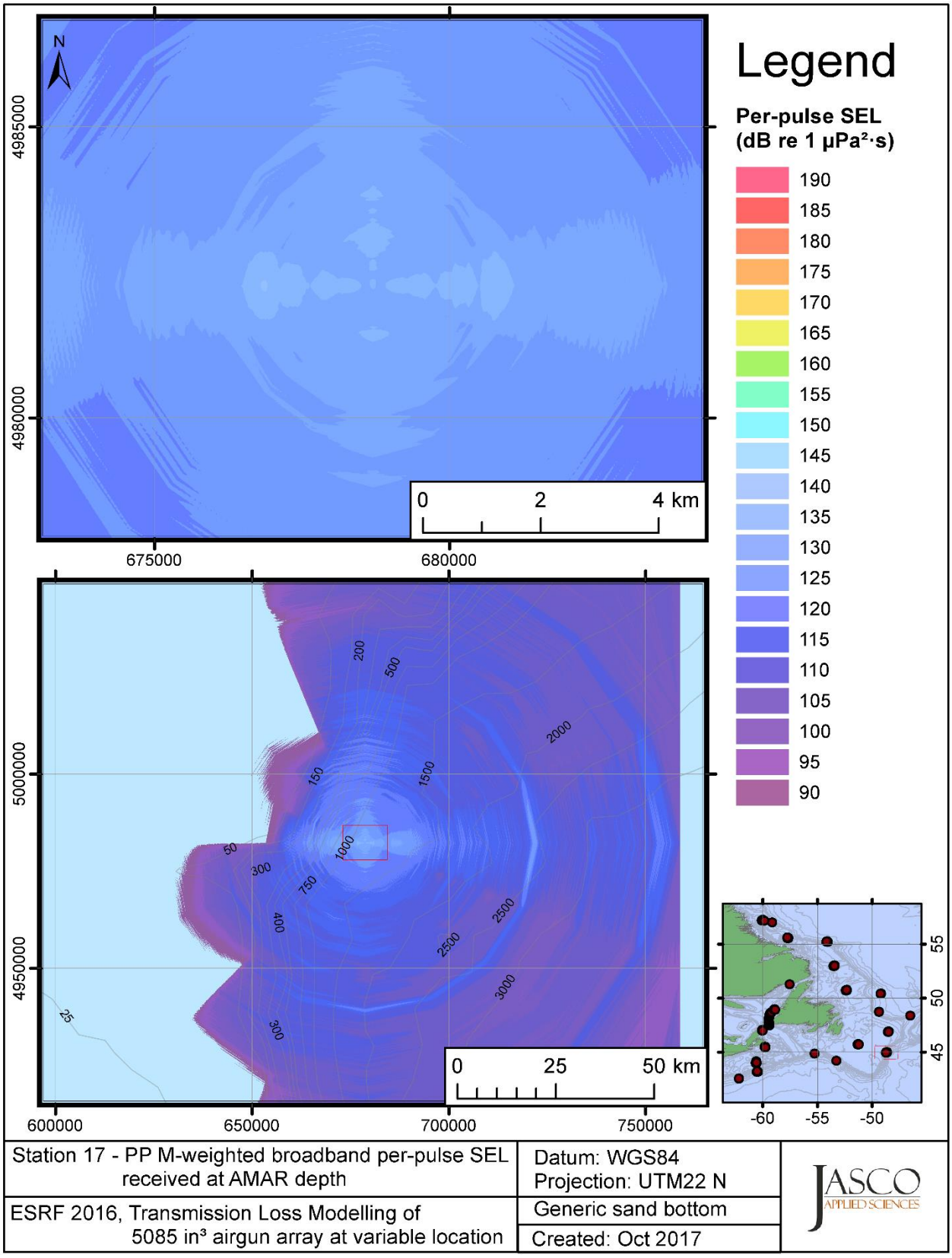

Figure C-250. Stn 17, PP M-weighted SEL received at the AMAR location and depth, modelled using a generic sand bottom, with in-situ July SSP and the airgun array located at any point on the map.

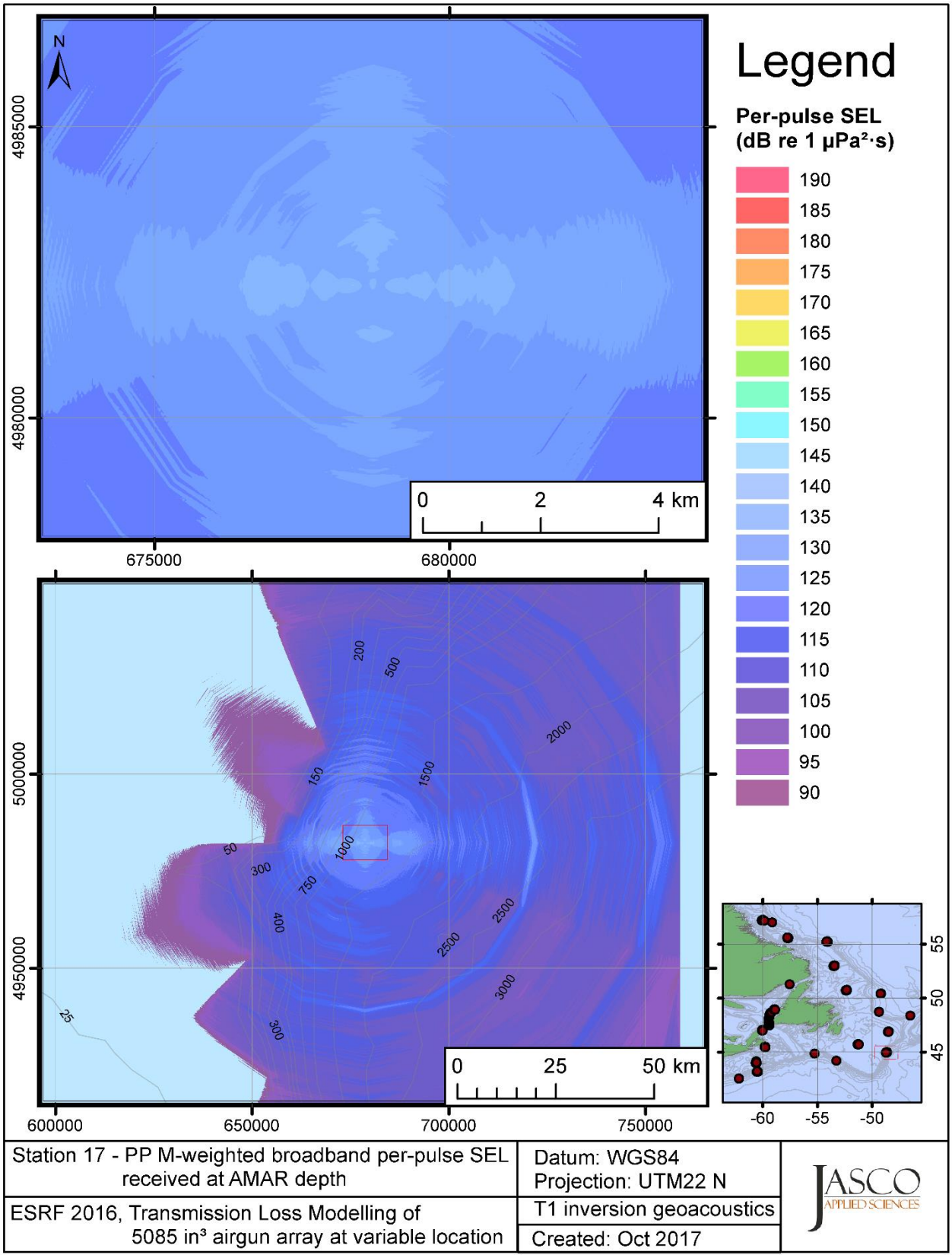

Figure C-251. Stn 17, PP M-weighted SEL received at the AMAR location and depth, modelled using the track 1 inversion geoacoustic bottom, with in-situ July SSP and the airgun array located at any point on the map.

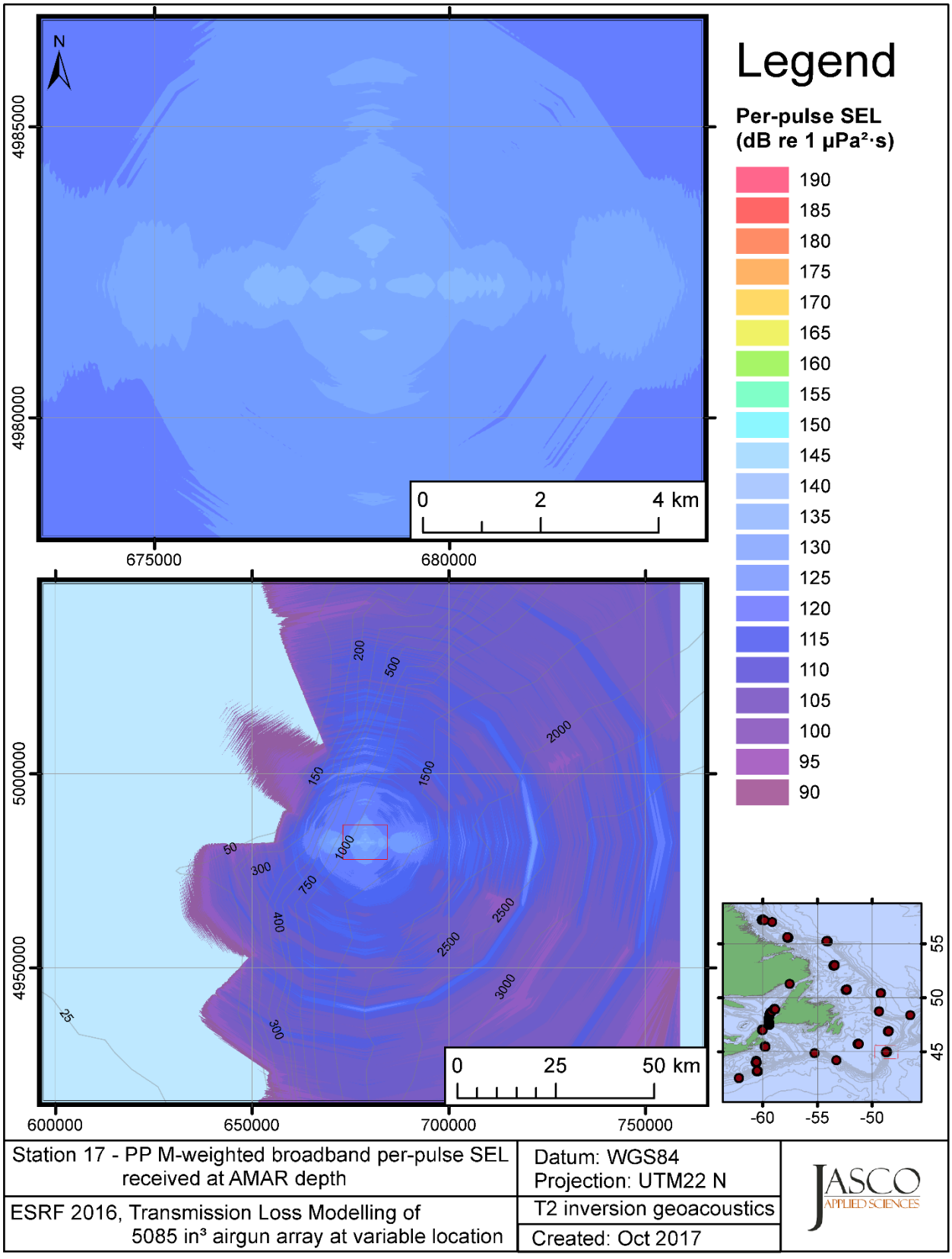

Figure C-252. Stn 17, PP M-weighted SEL received at the AMAR location and depth, modelled using the track 2 inversion geoacoustic bottom, with in-situ July SSP and the airgun array located at any point on the map.

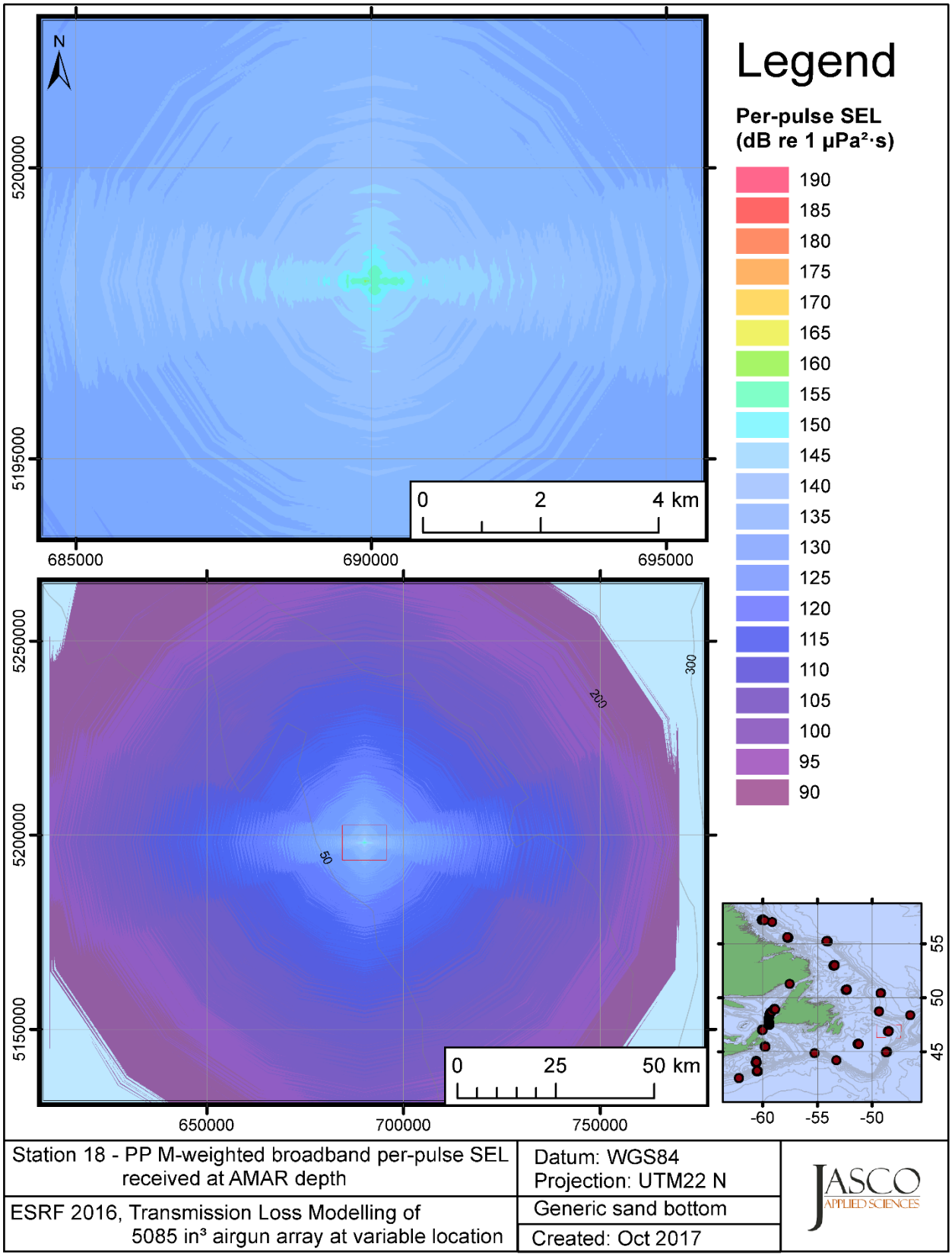

Figure C-253. Stn 18, PP M-weighted SEL received at the AMAR location and depth, modelled using a generic sand bottom, with in-situ July SSP and the airgun array located at any point on the map.

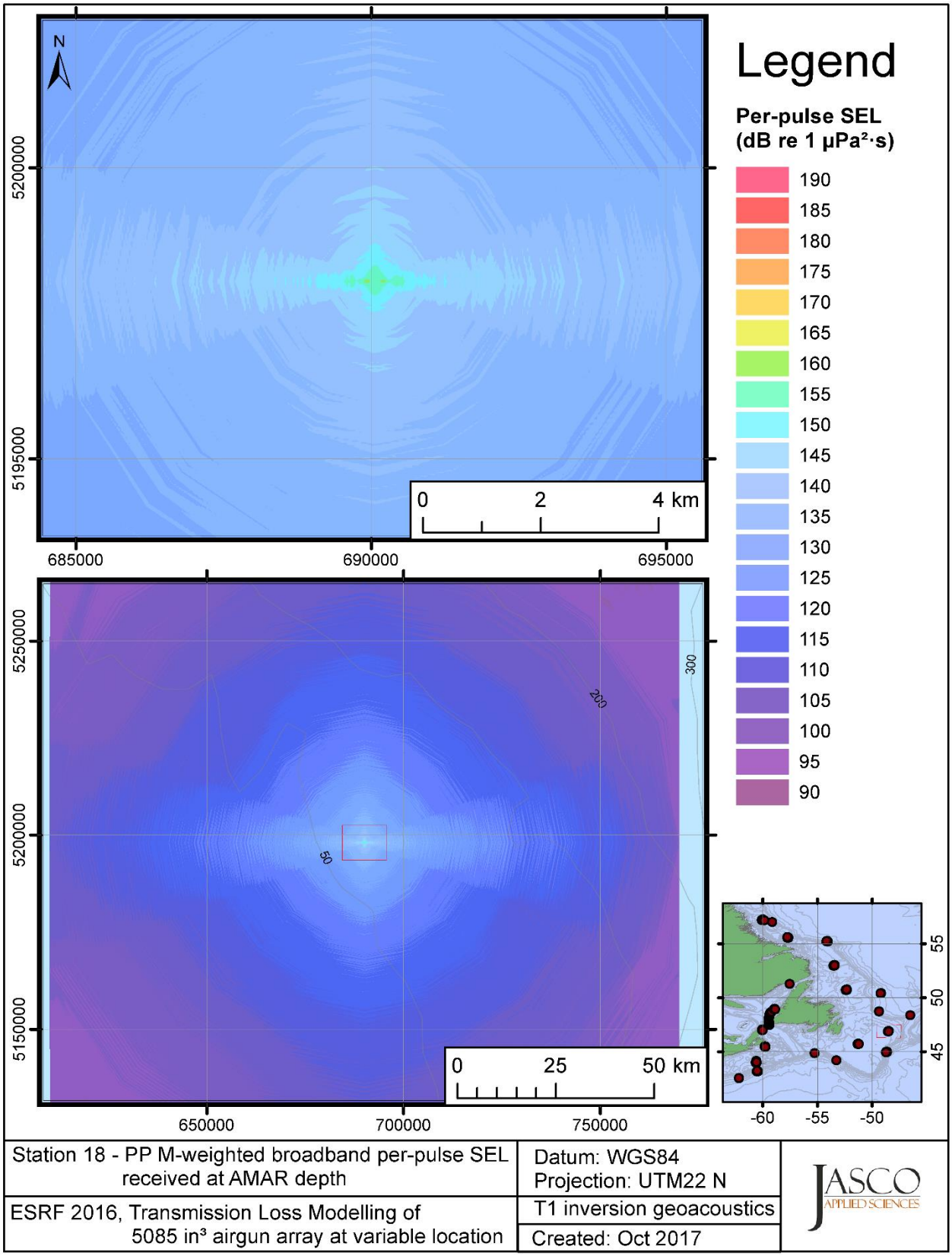

Figure C-254. Stn 18, PP M-weighted SEL received at the AMAR location and depth, modelled using the track 1 inversion geoacoustic bottom, with in-situ July SSP and the airgun array located at any point on the map.

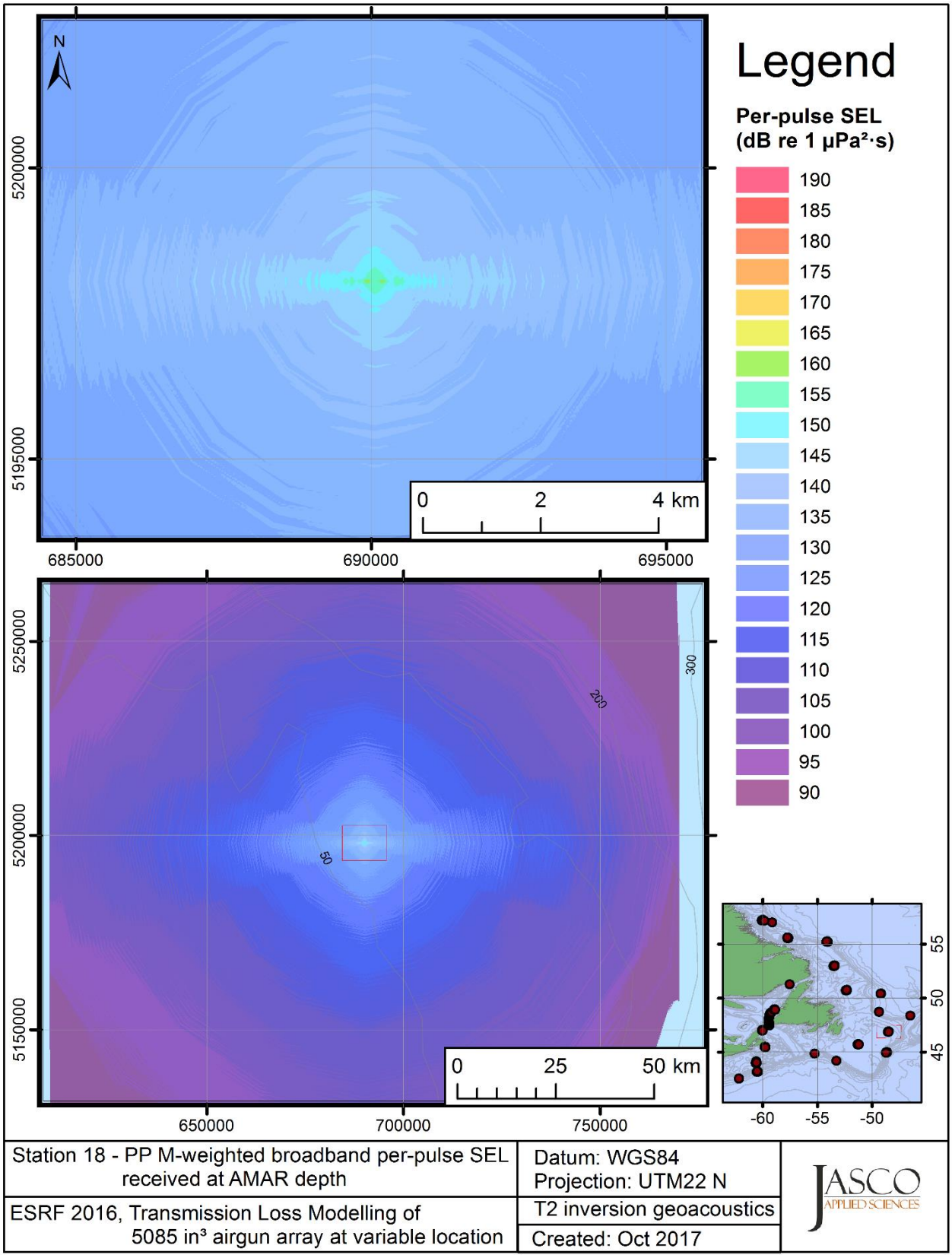

Figure C-255. Stn 18, PP M-weighted SEL received at the AMAR location and depth, modelled using the track 2 inversion geoacoustic bottom, with in-situ July SSP and the airgun array located at any point on the map.

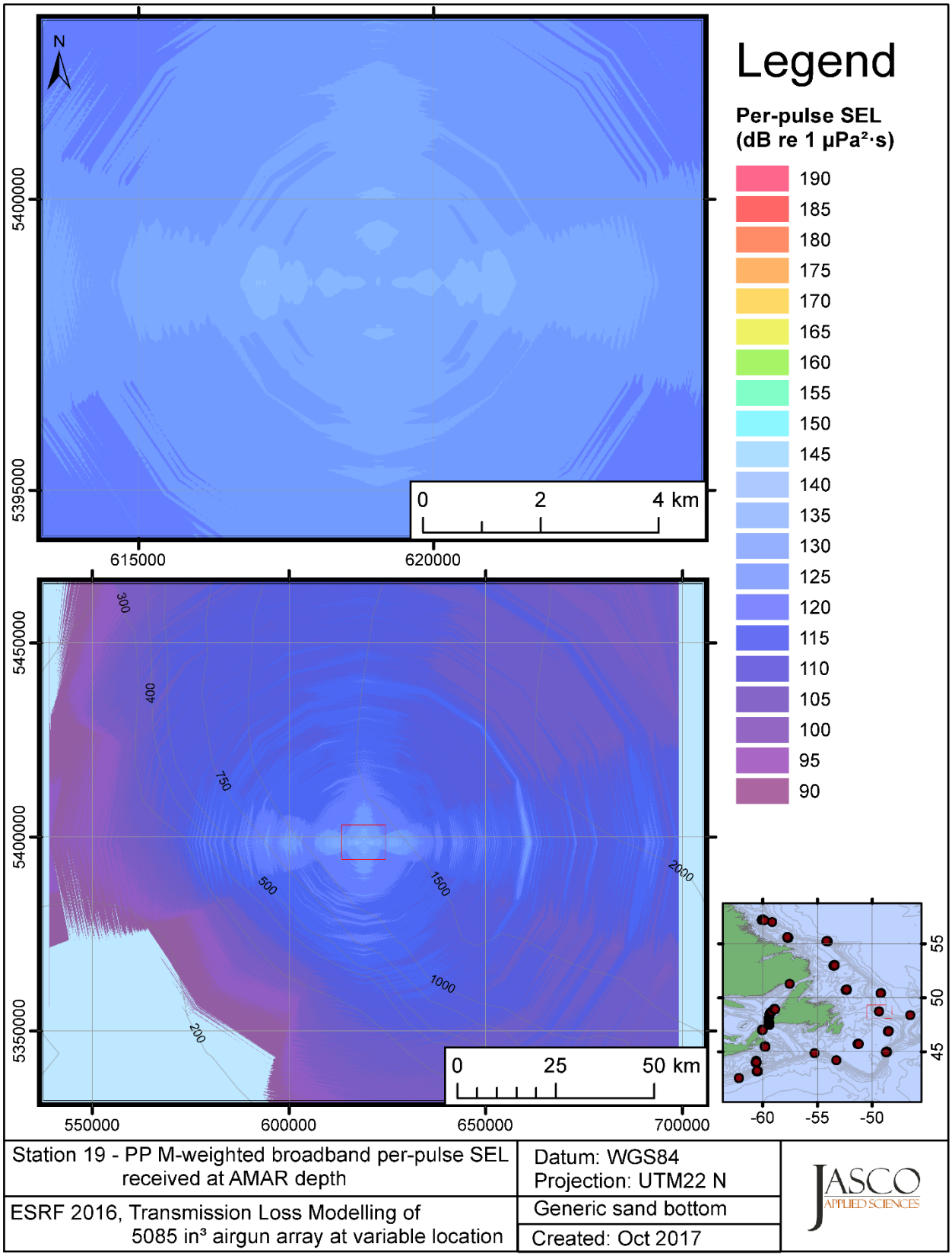

Figure C-256. Stn 19, PP M-weighted SEL received at the AMAR location and depth, modelled using a generic sand bottom, with in-situ July SSP and the airgun array located at any point on the map.

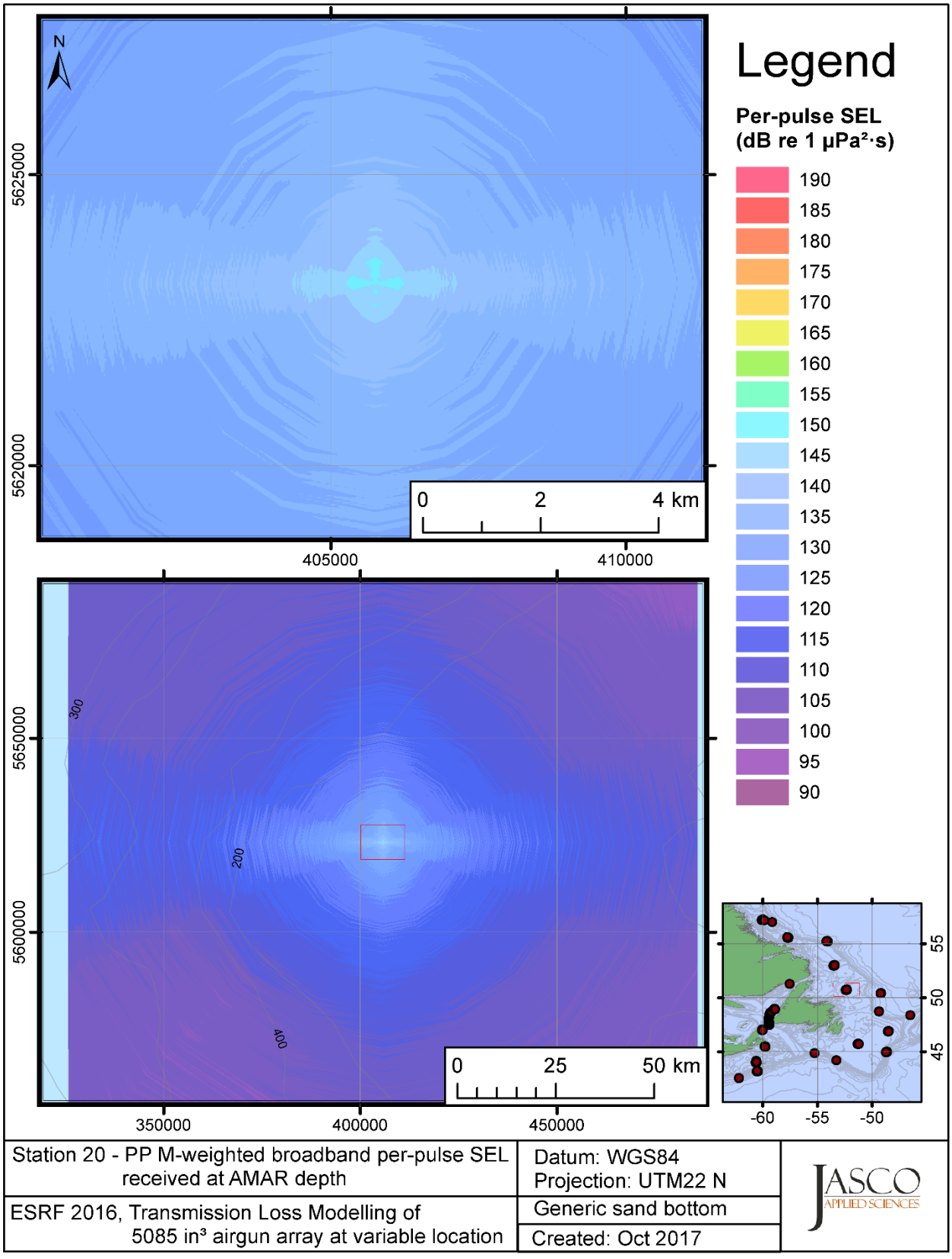

Figure C-257. Stn 20, PP M-weighted SEL received at the AMAR location and depth, modelled using a generic sand bottom, with in-situ July SSP and the airgun array located at any point on the map.

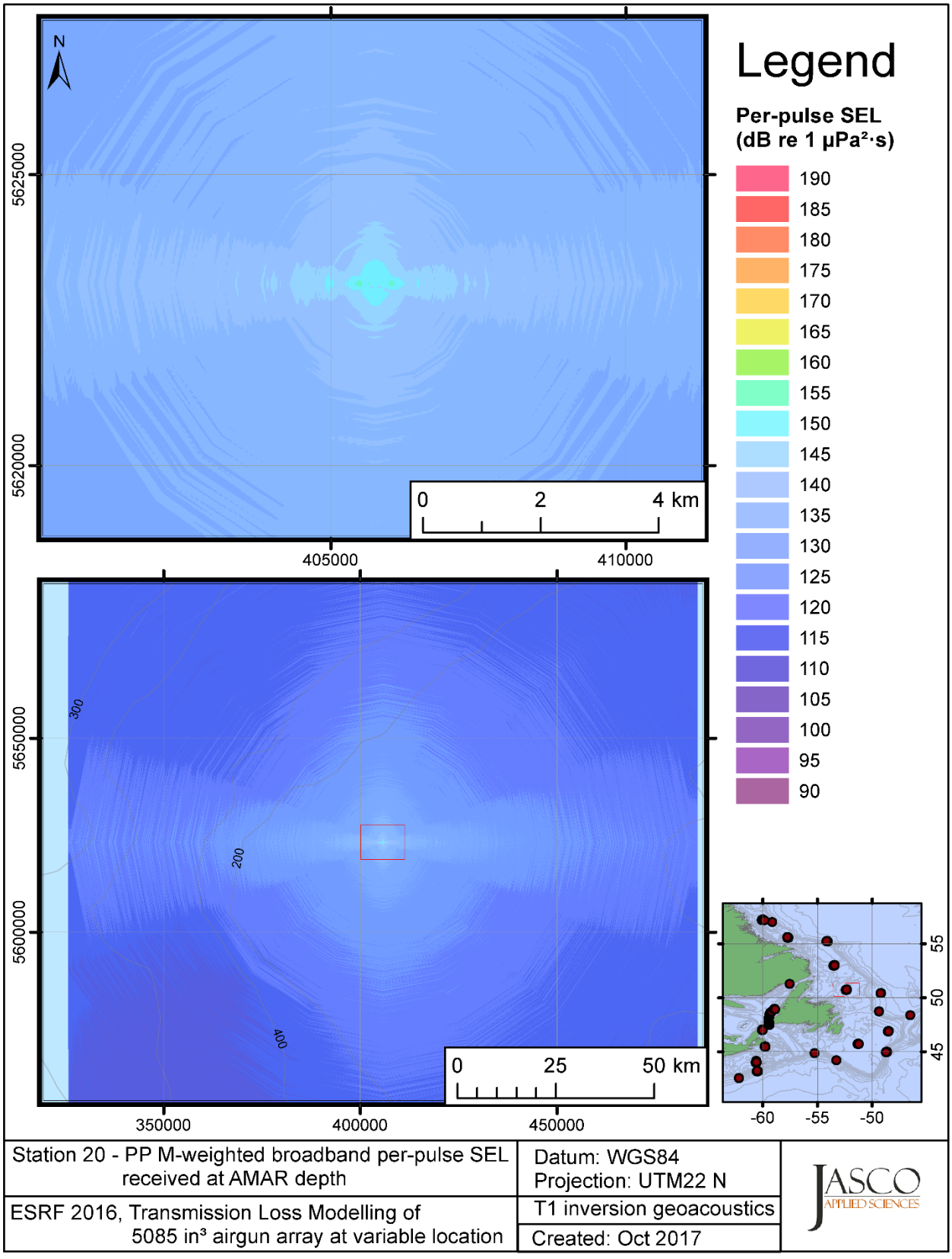

Figure C-258. Stn 20, PP M-weighted SEL received at the AMAR location and depth, modelled using the track 1 inversion geoacoustic bottom, with in-situ July SSP and the airgun array located at any point on the map.

C.7. Modelling Unweighted Max-over-depth Received Level at Distant Locations - Summer

This section presents the results of modelling the maximum-over-depth per-pulse sound exposure level (SEL) received at distant receiver locations (varied in range and azimuth) for the source held fixed at the AMAR location. The modelling uses the geoacoustic inversion bottom parameters at the 14 sites where they are available and only uses a generic sand bottom at the other six sites. The modelling results are presented in the form of coloured maps where the colour at any map location represents the predicted maximum-over-depth received level at that spot on the map. This section includes only the unweighted per-pulse SEL results; additional maps for marine mammal received level auditory weightings are presented in adjoining sections. The sound speed profiles (SSP) used are detailed in Appendix B.1.

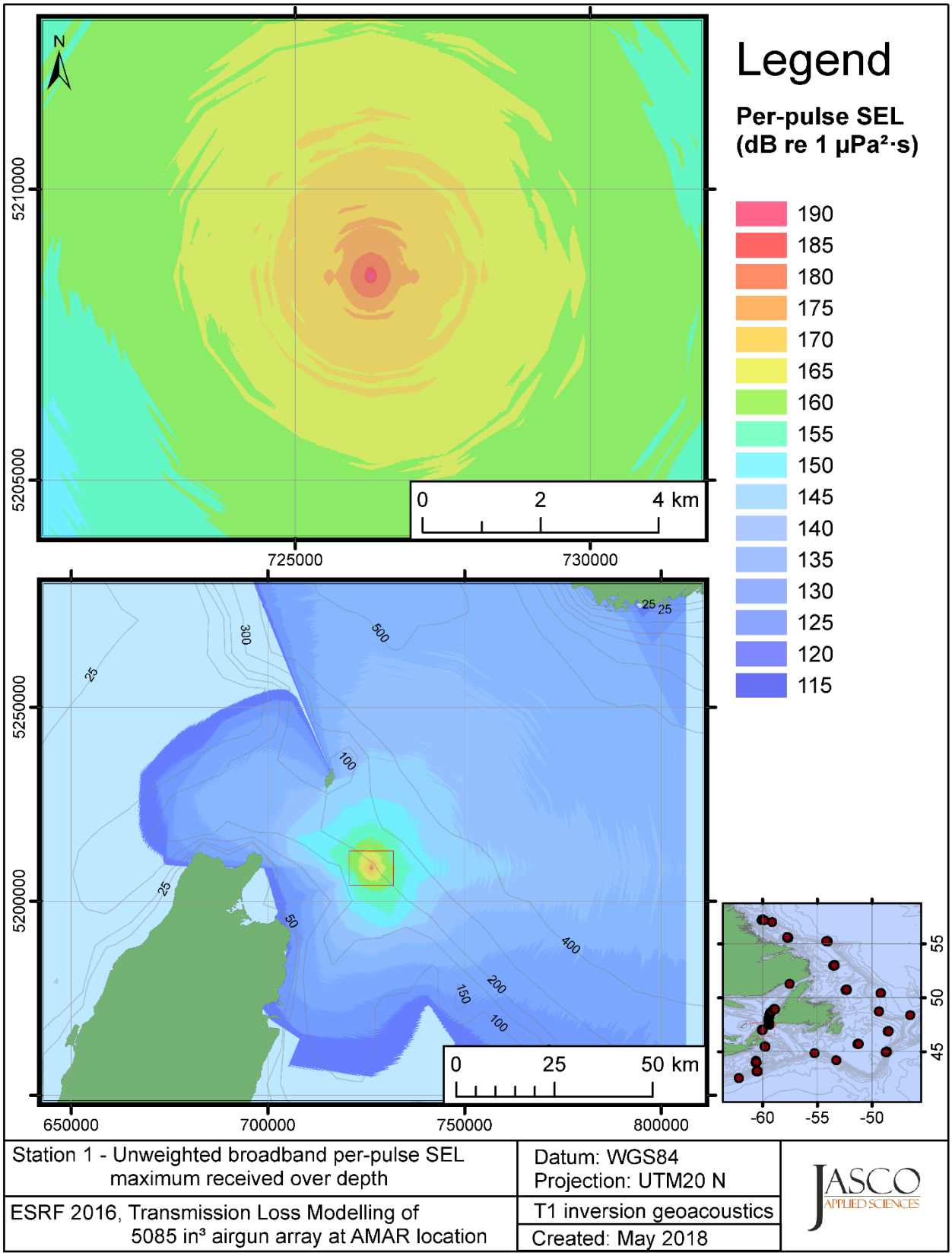

Figure C-259. Stn 1, unweighted maximum-over-depth SEL received at any location on the map, modelled using the track 1 inversion geoacoustic bottom, with the airgun array at the AMAR location and in-situ July SSP.

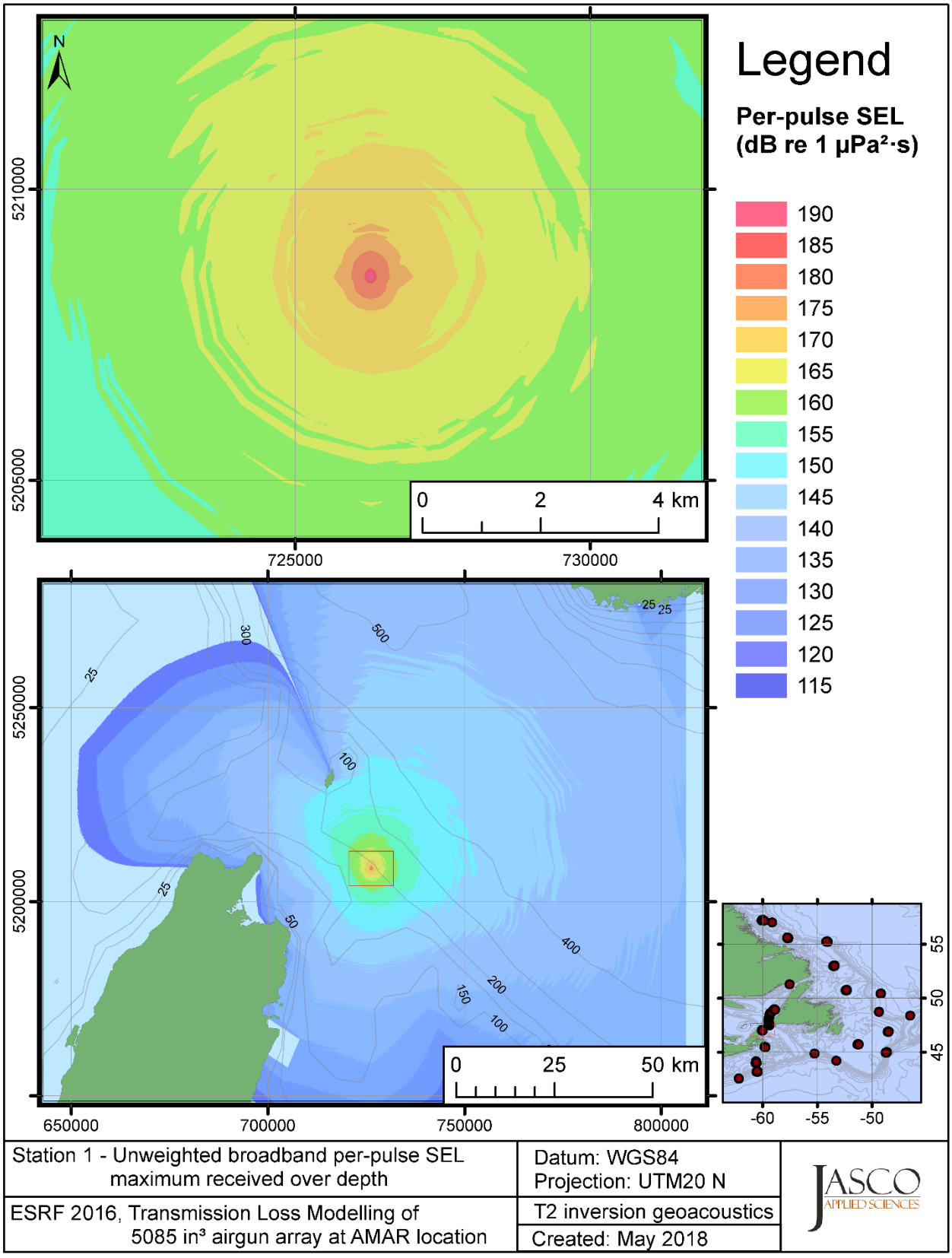

Figure C-260. Stn 1, unweighted maximum-over-depth SEL received at any location on the map, modelled using the track 2 inversion geoacoustic bottom, with the airgun array at the AMAR location and in-situ July SSP.

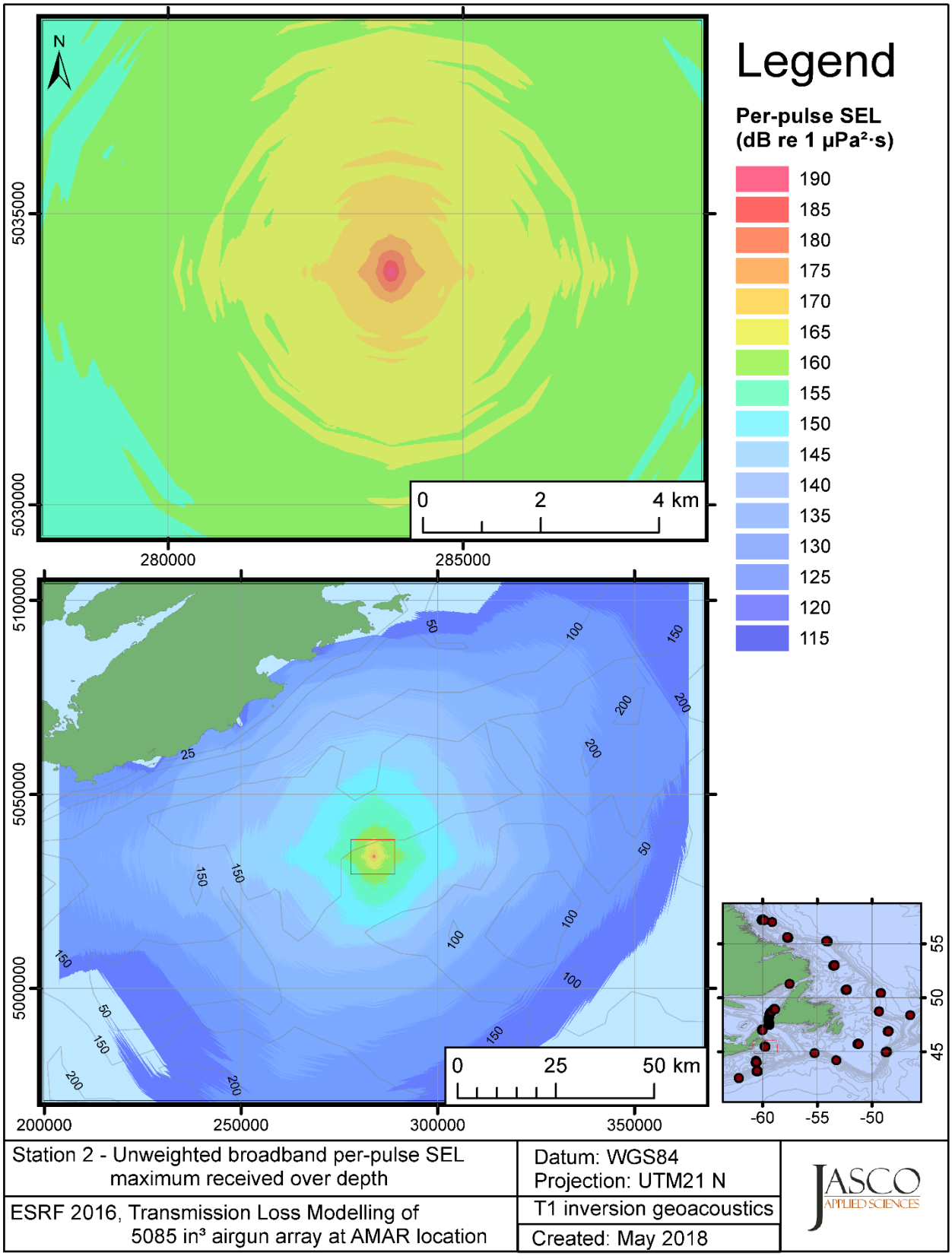

Figure C-261. Stn 2, unweighted maximum-over-depth SEL received at any location on the map, modelled using the track 1 inversion geoacoustic bottom, with the airgun array at the AMAR location and in-situ July SSP.

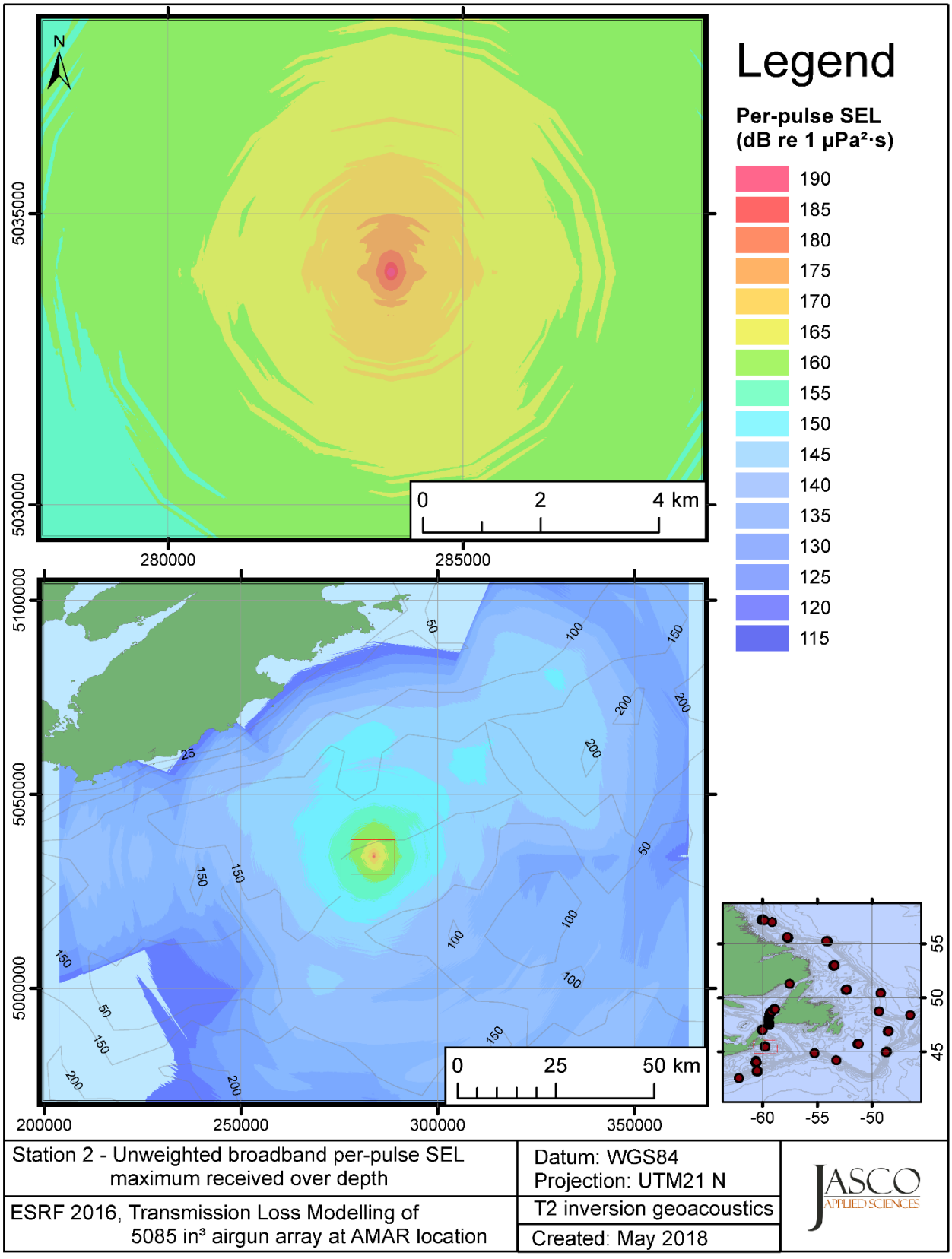

Figure C-262. Stn 2, unweighted maximum-over-depth SEL received at any location on the map, modelled using the track 2 inversion geoacoustic bottom, with the airgun array at the AMAR location and in-situ July SSP.

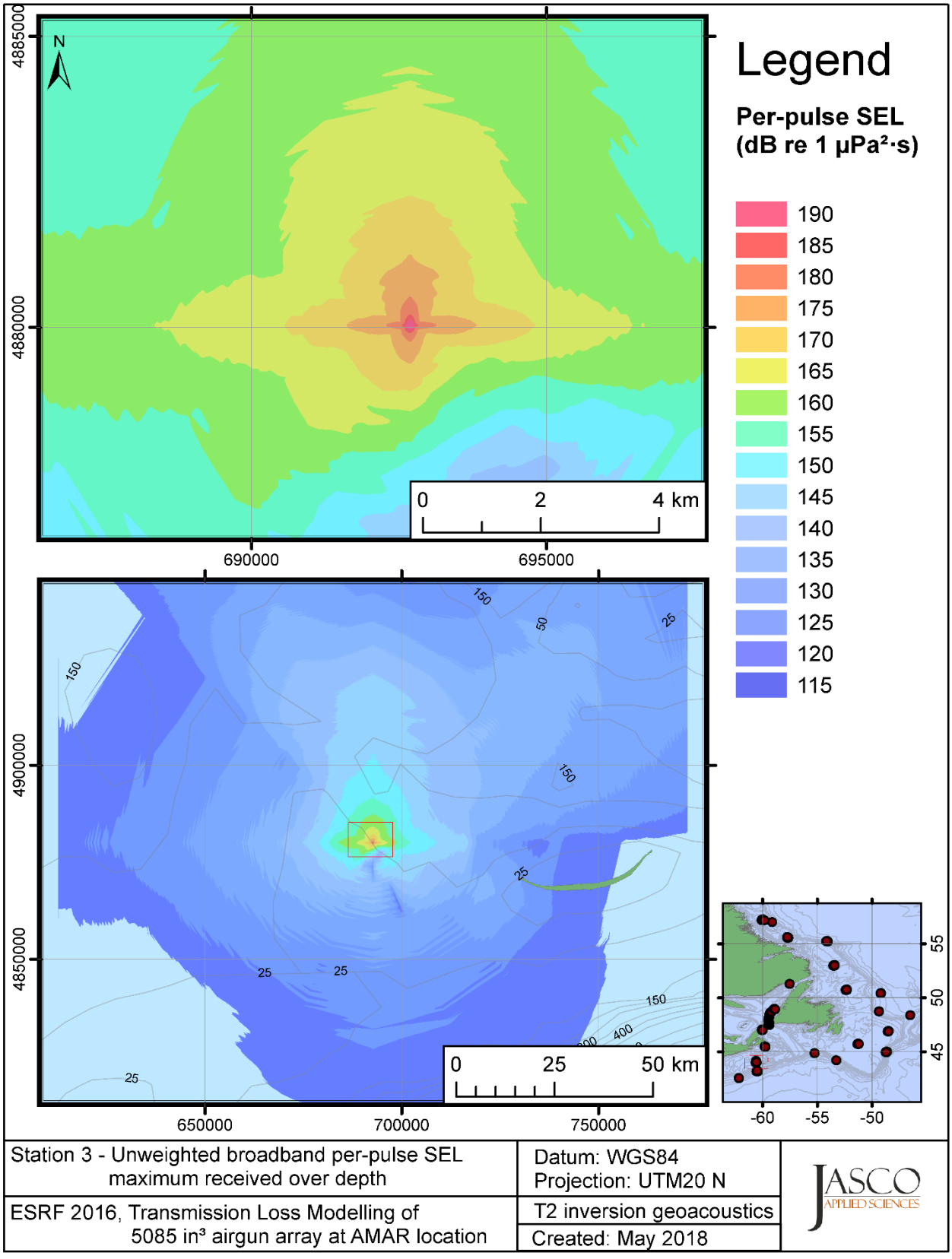

Figure C-263. Stn 3, unweighted maximum-over-depth SEL received at any location on the map, modelled using the track 2 inversion geoacoustic bottom, with the airgun array at the AMAR location and in-situ July SSP.

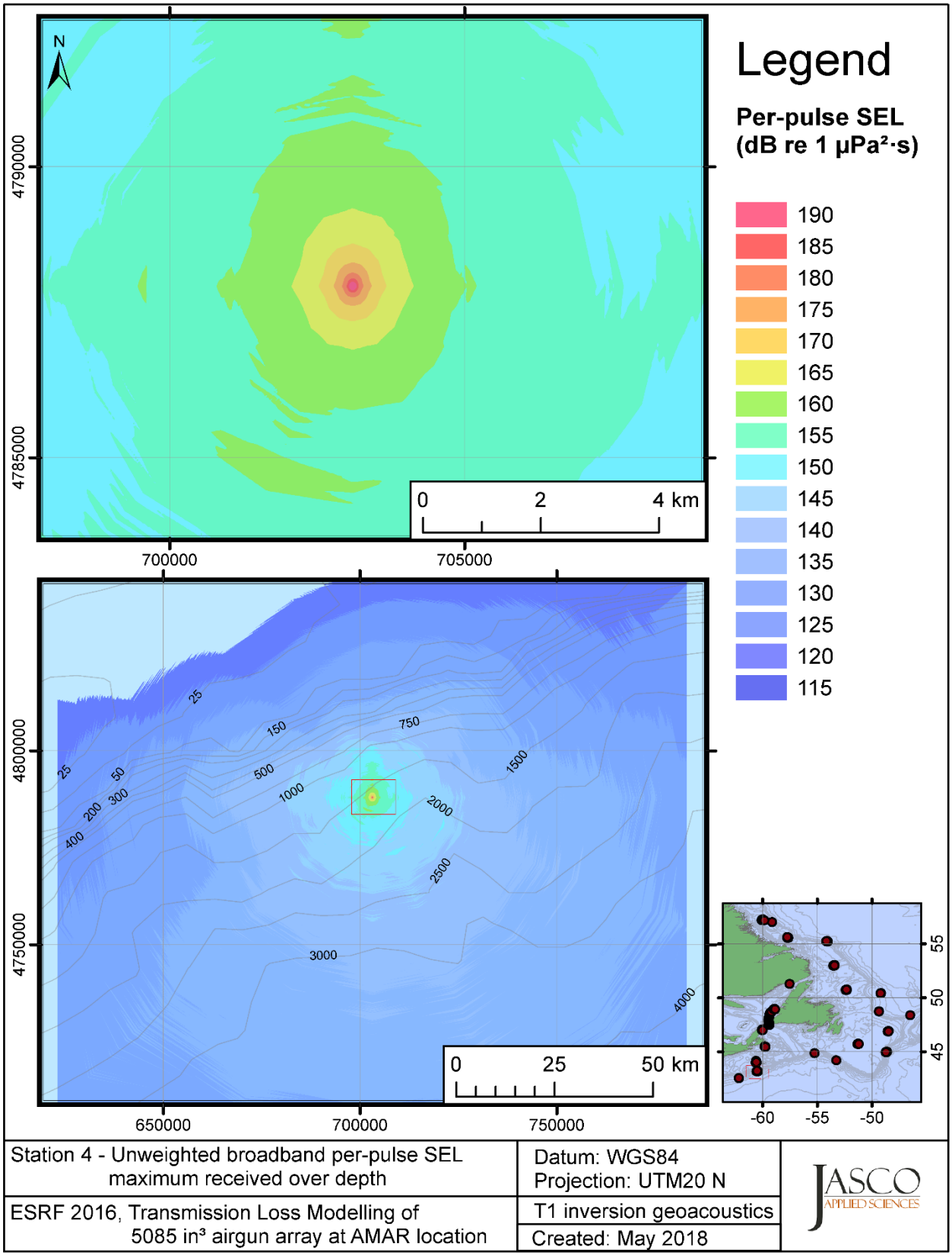

Figure C-264. Stn 4, unweighted maximum-over-depth SEL received at any location on the map, modelled using the track 1 inversion geoacoustic bottom, with the airgun array at the AMAR location and in-situ July SSP.

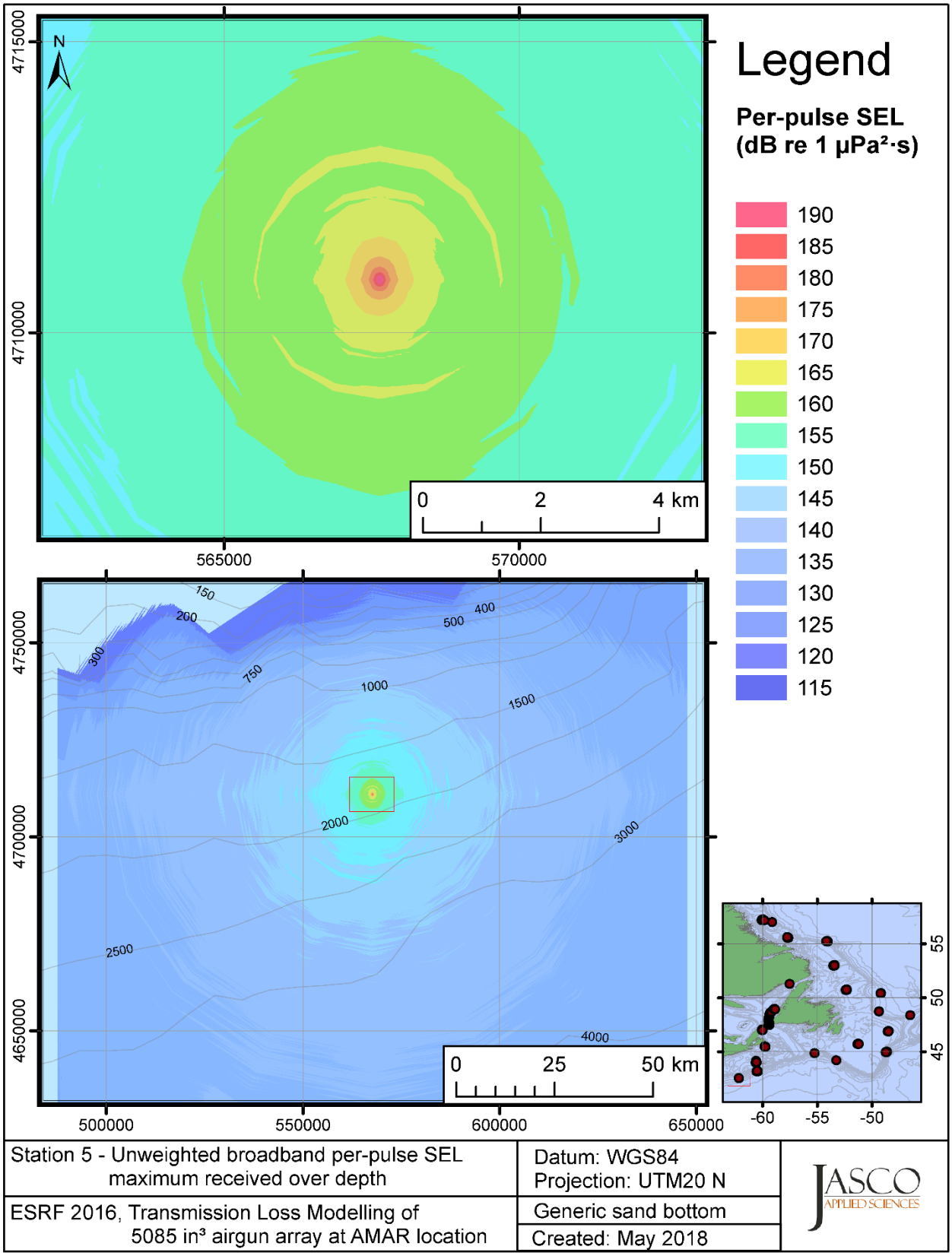

Figure C-265. Stn 5, unweighted maximum-over-depth SEL received at any location on the map, modelled using a generic sand bottom, with the airgun array at the AMAR location and in-situ July SSP.

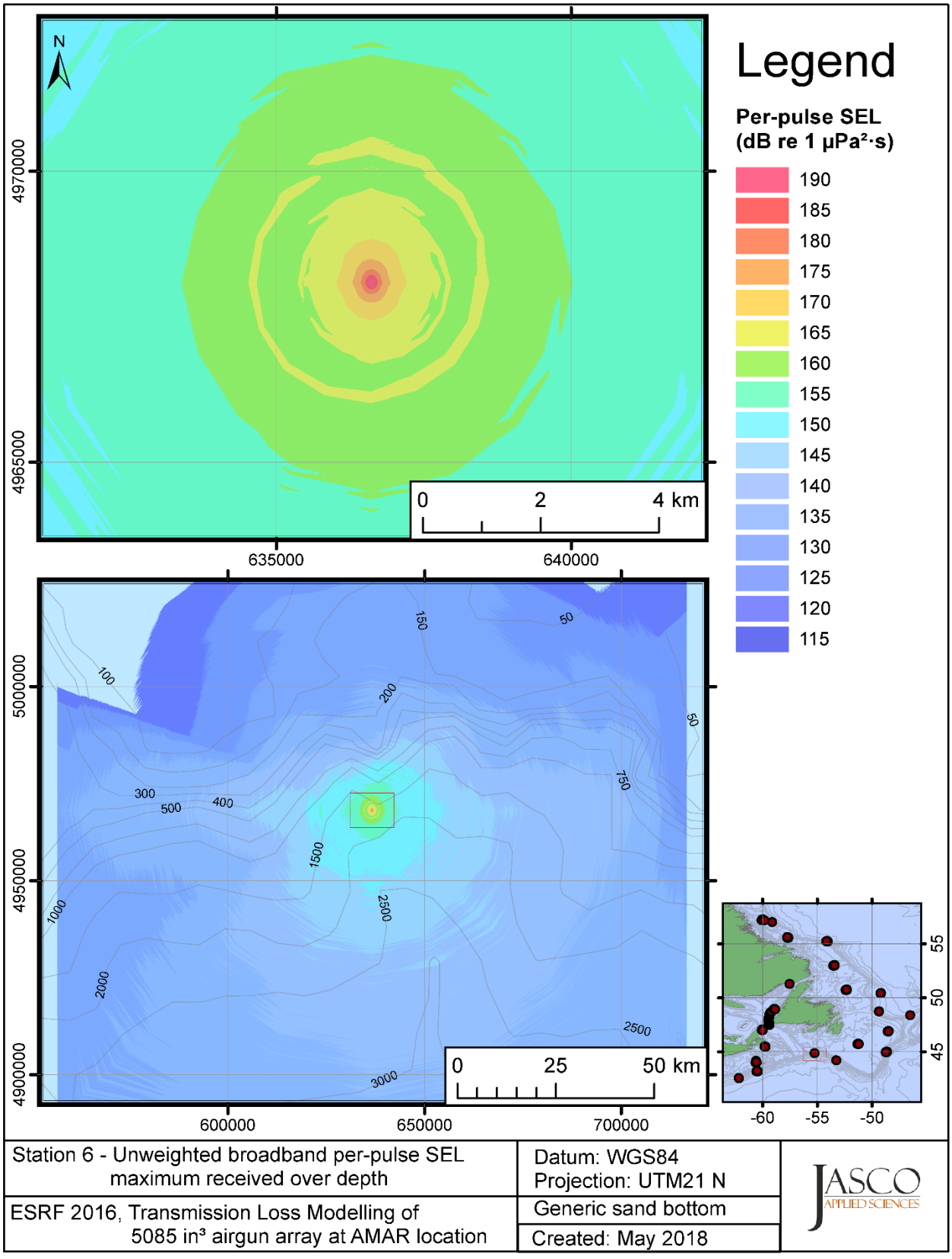

Figure C-266. Stn 6, unweighted maximum-over-depth SEL received at any location on the map, modelled using a generic sand bottom, with the airgun array at the AMAR location and in-situ July SSP.

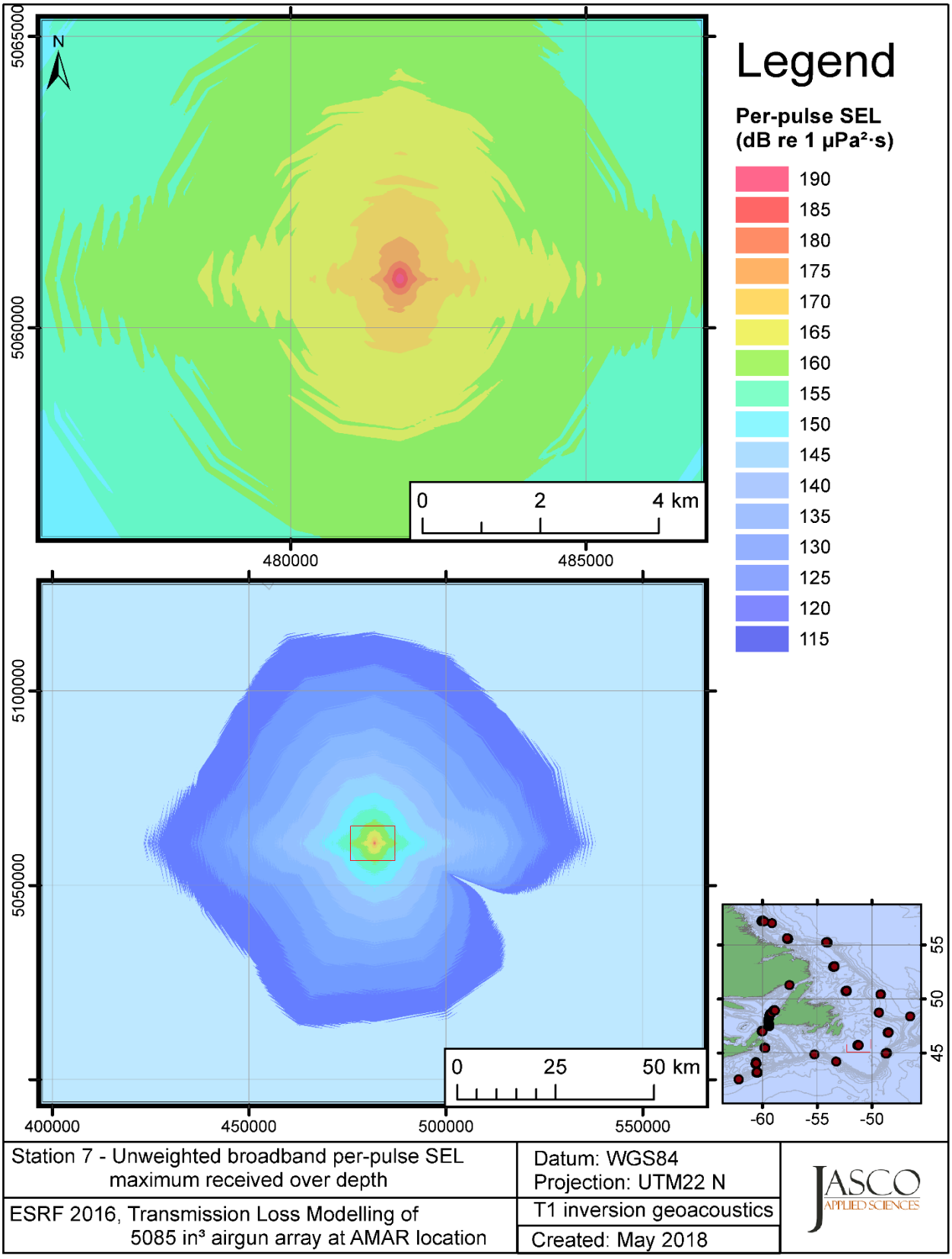

Figure C-267. Stn 7, unweighted maximum-over-depth SEL received at any location on the map, modelled using the track 1 inversion geoacoustic bottom, with the airgun array at the AMAR location and in-situ July SSP.

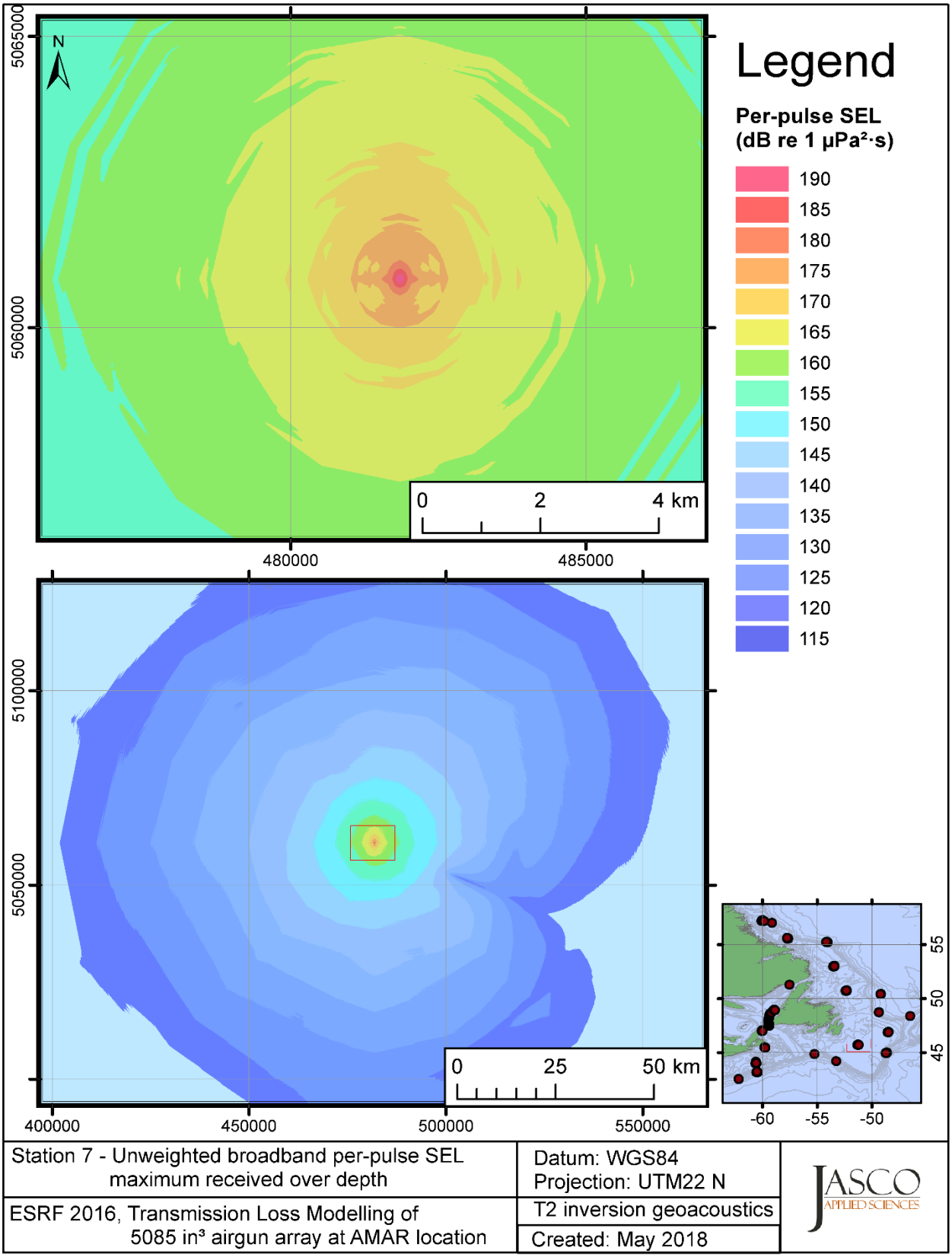

Figure C-268. Stn 7, unweighted maximum-over-depth SEL received at any location on the map, modelled using the track 2 inversion geoacoustic bottom, with the airgun array at the AMAR location and in-situ July SSP.

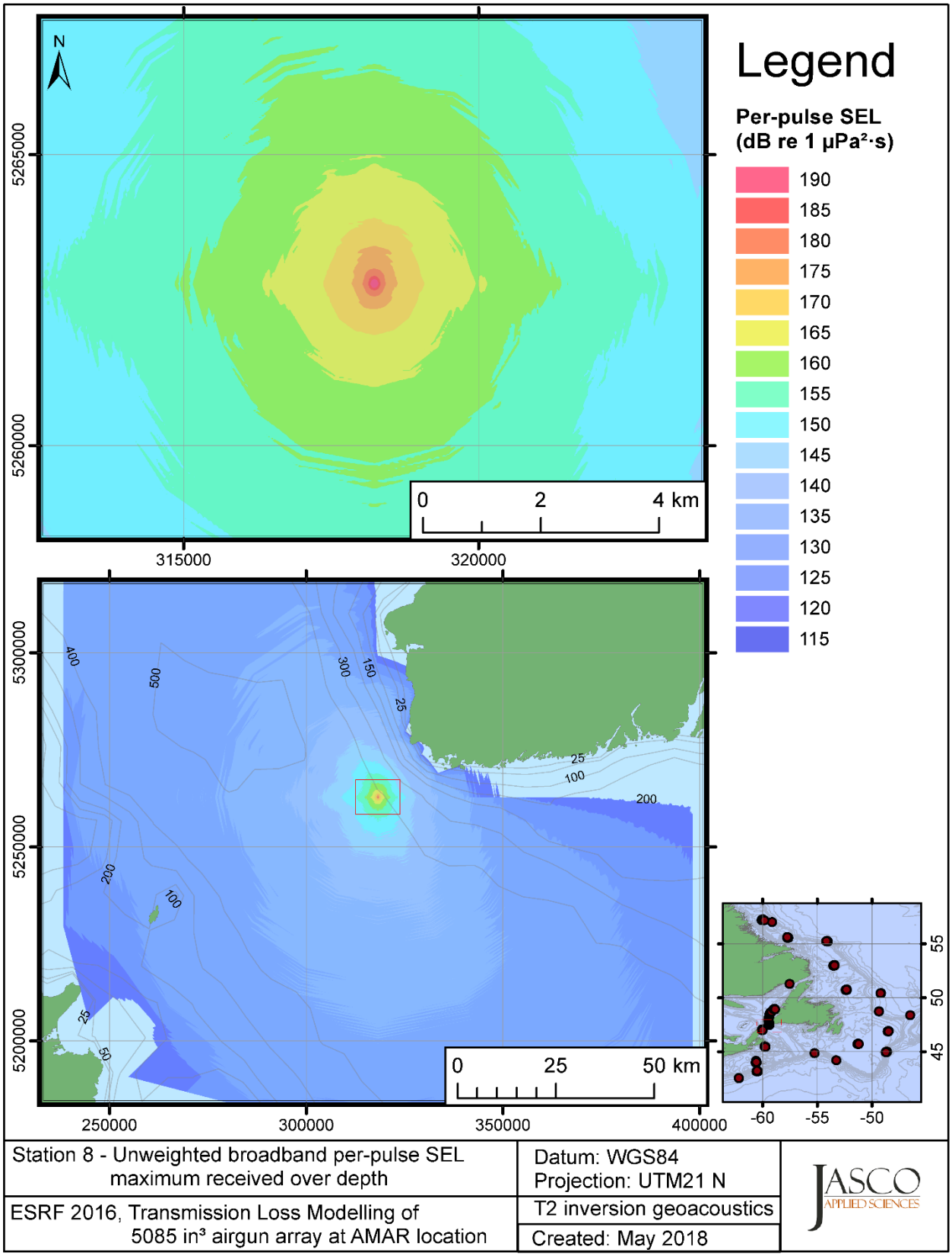

Figure C-269. Stn 8, unweighted maximum-over-depth SEL received at any location on the map, modelled using the track 2 inversion geoacoustic bottom, with the airgun array at the AMAR location and GDEM July SSP.

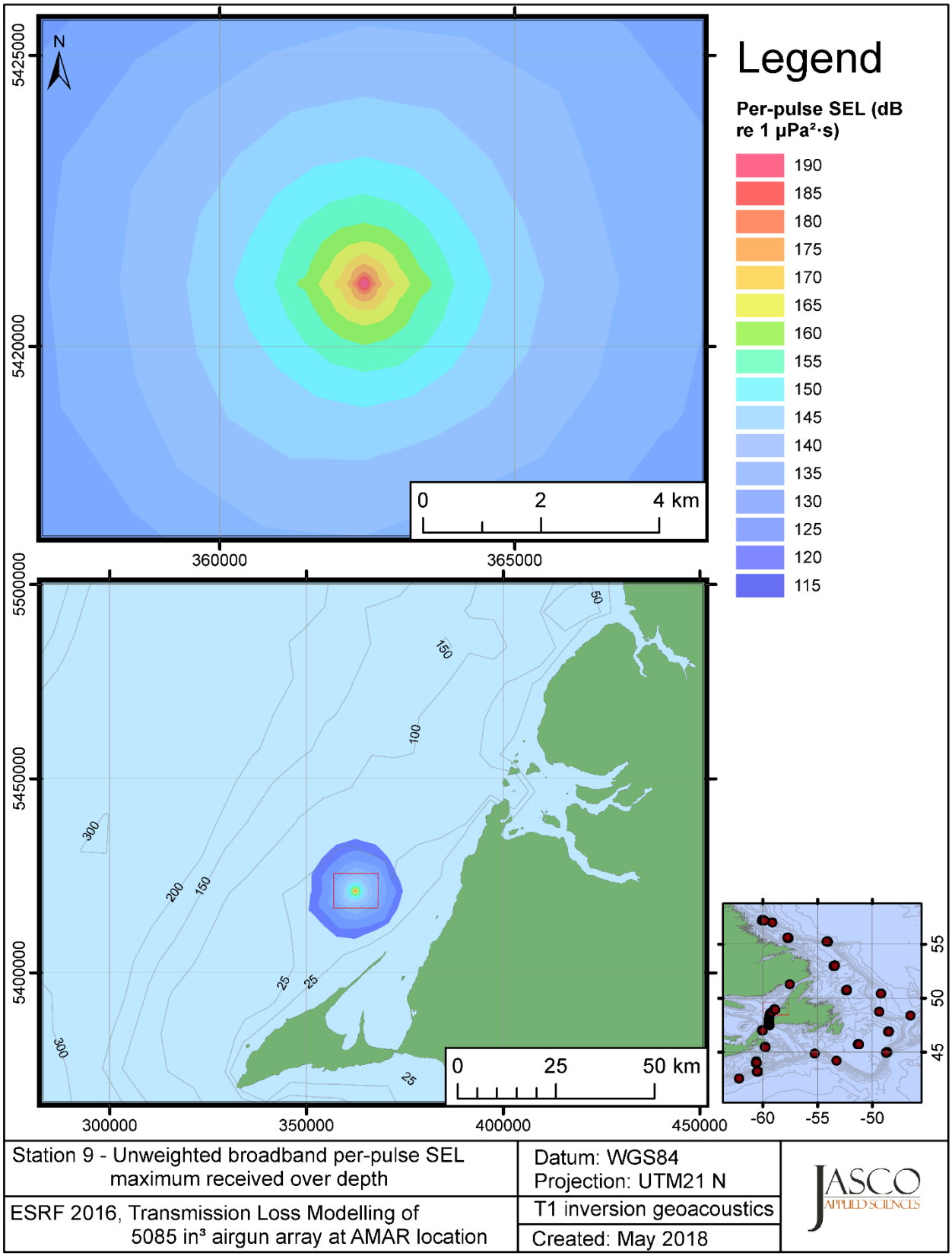

Figure C-270. Stn 9, unweighted maximum-over-depth SEL received at any location on the map, modelled using the track 1 inversion geoacoustic bottom, with the airgun array at the AMAR location and GDEM July SSP.

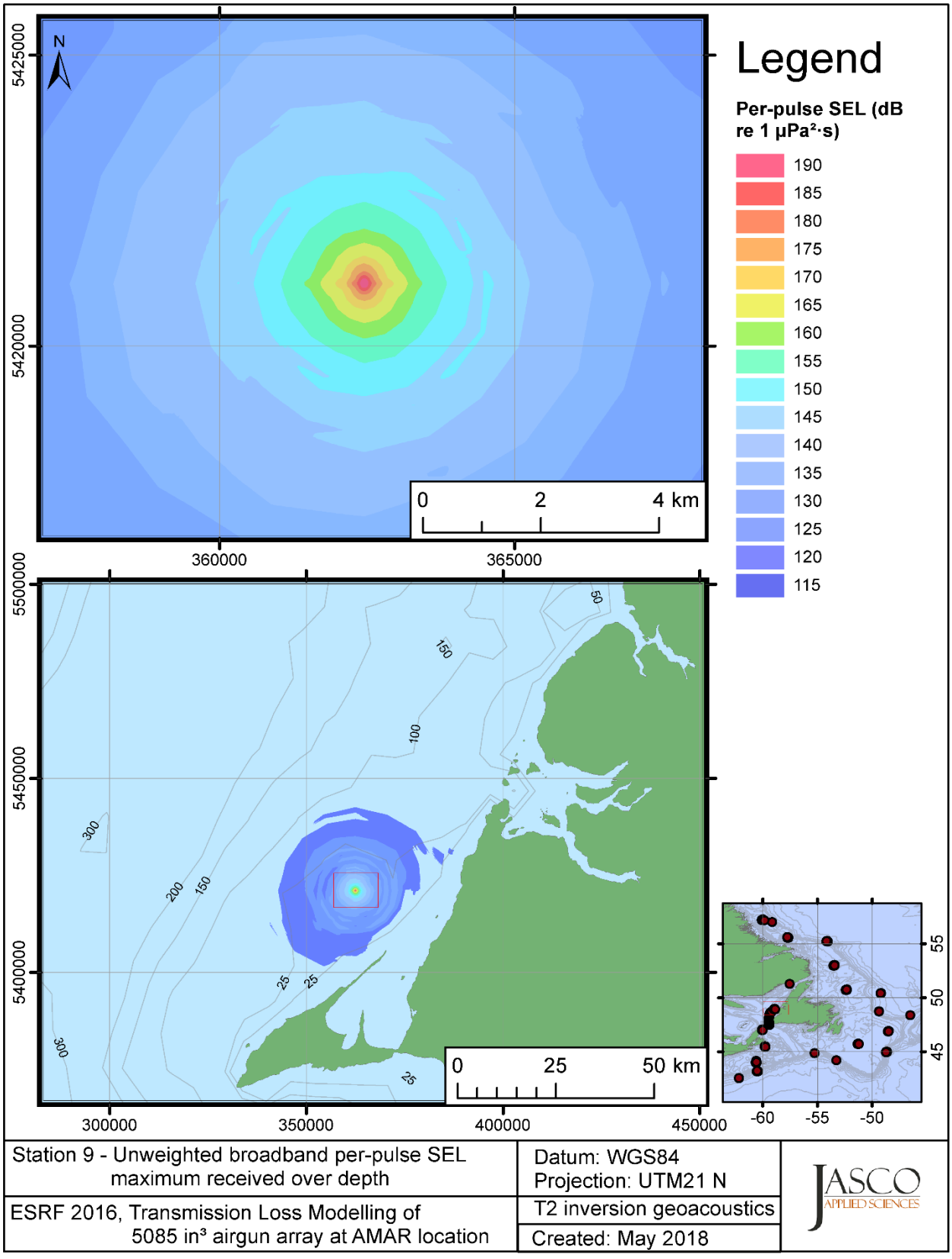

Figure C-271. Stn 9, unweighted maximum-over-depth SEL received at any location on the map, modelled using the track 2 inversion geoacoustic bottom, with the airgun array at the AMAR location and GDEM July SSP.

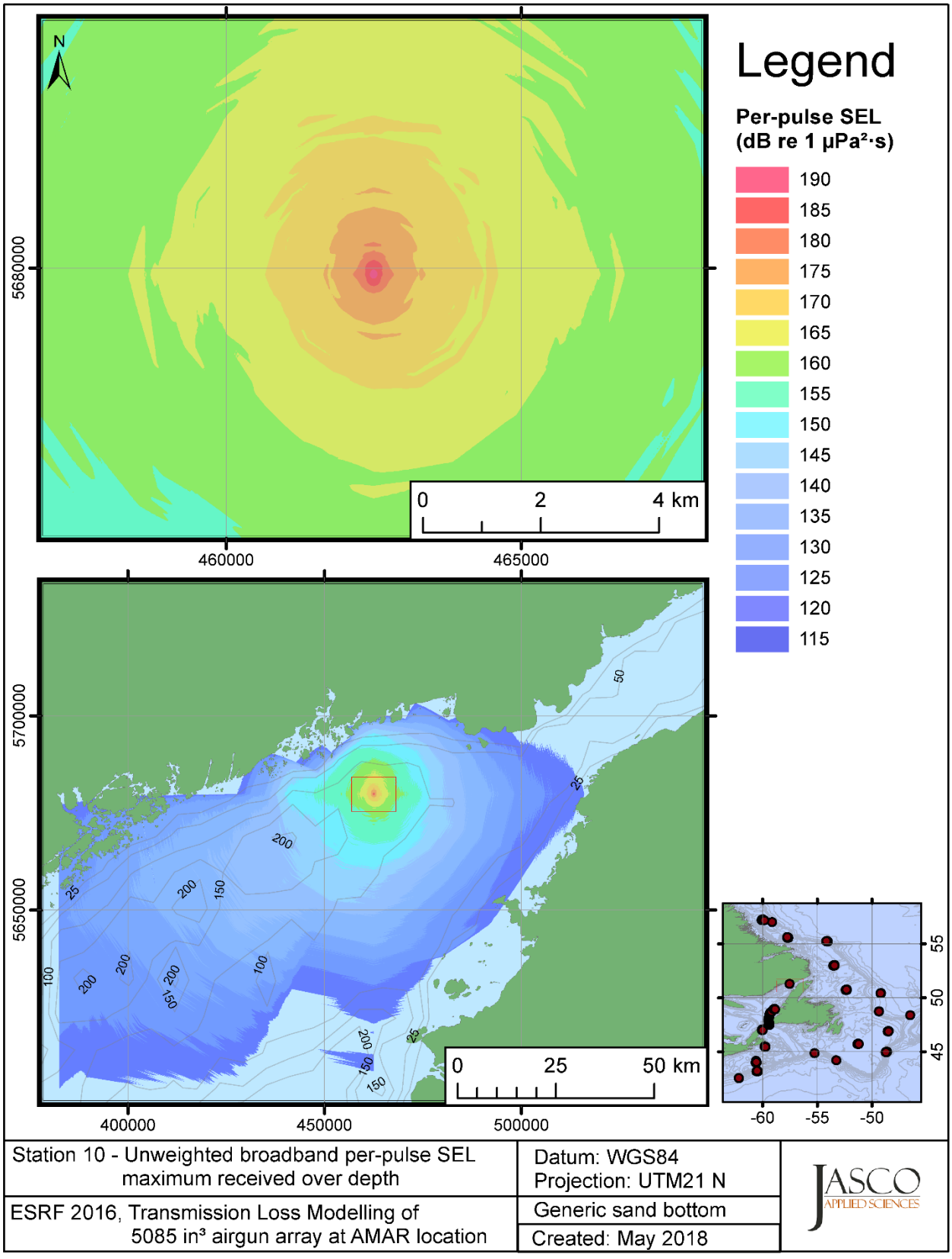

Figure C-272. Stn 10, unweighted maximum-over-depth SEL received at any location on the map, modelled using a generic sand bottom, with the airgun array at the AMAR location and in-situ July SSP.

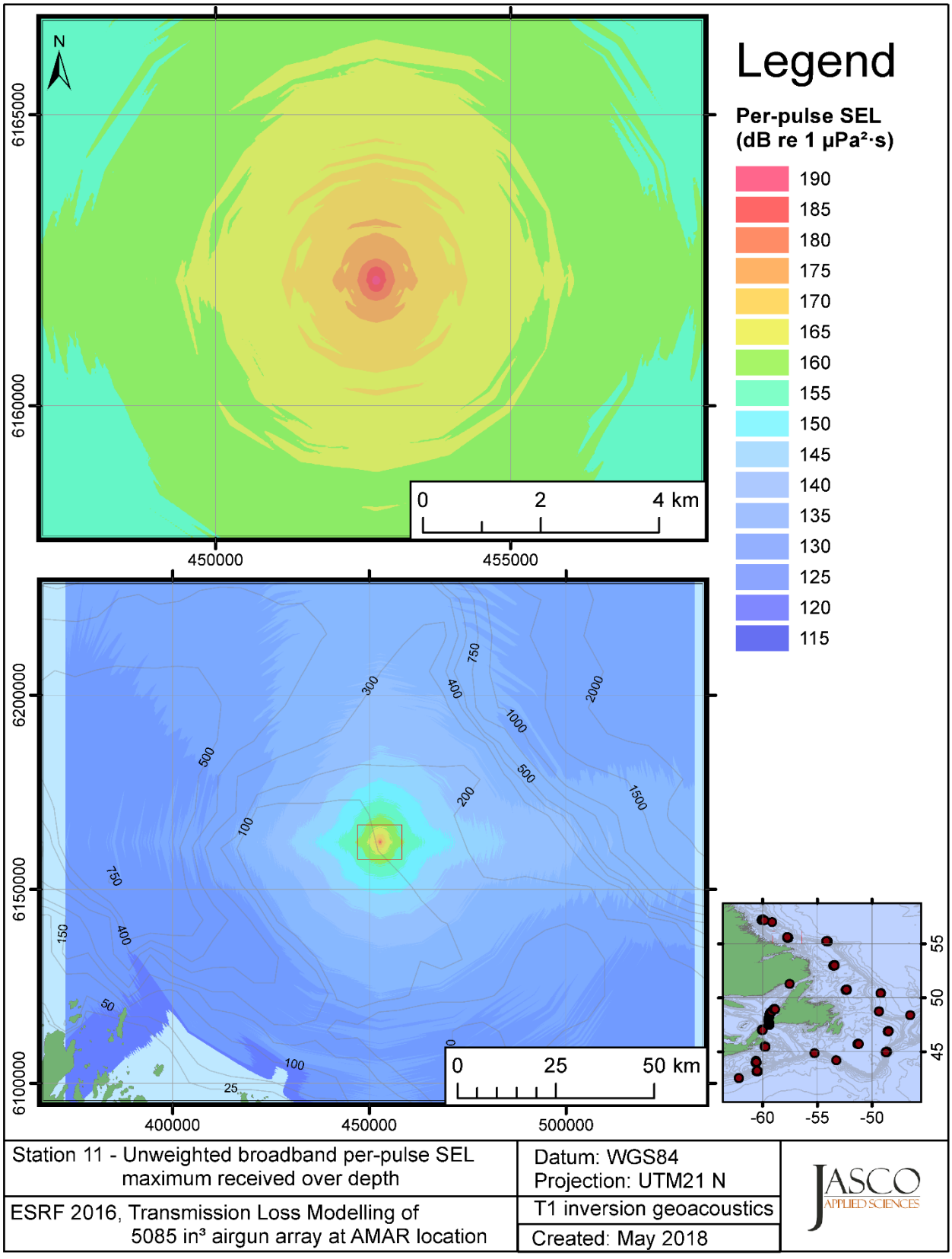

Figure C-273. Stn 11, unweighted maximum-over-depth SEL received at any location on the map, modelled using the track 1 inversion geoacoustic bottom, with the airgun array at the AMAR location and in-situ July SSP.

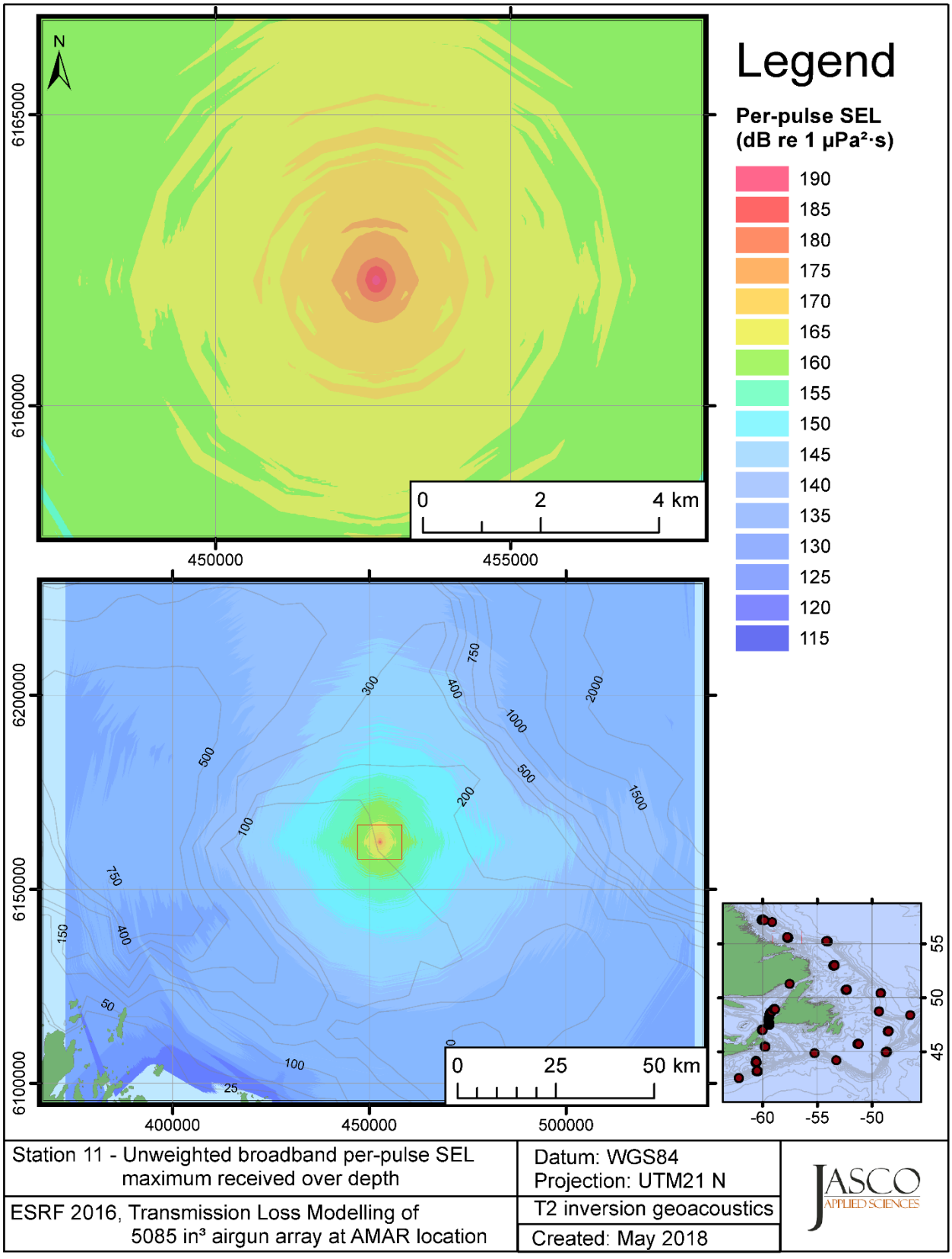

Figure C-274. Stn 11, unweighted maximum-over-depth SEL received at any location on the map, modelled using the track 2 inversion geoacoustic bottom, with the airgun array at the AMAR location and in-situ July SSP.

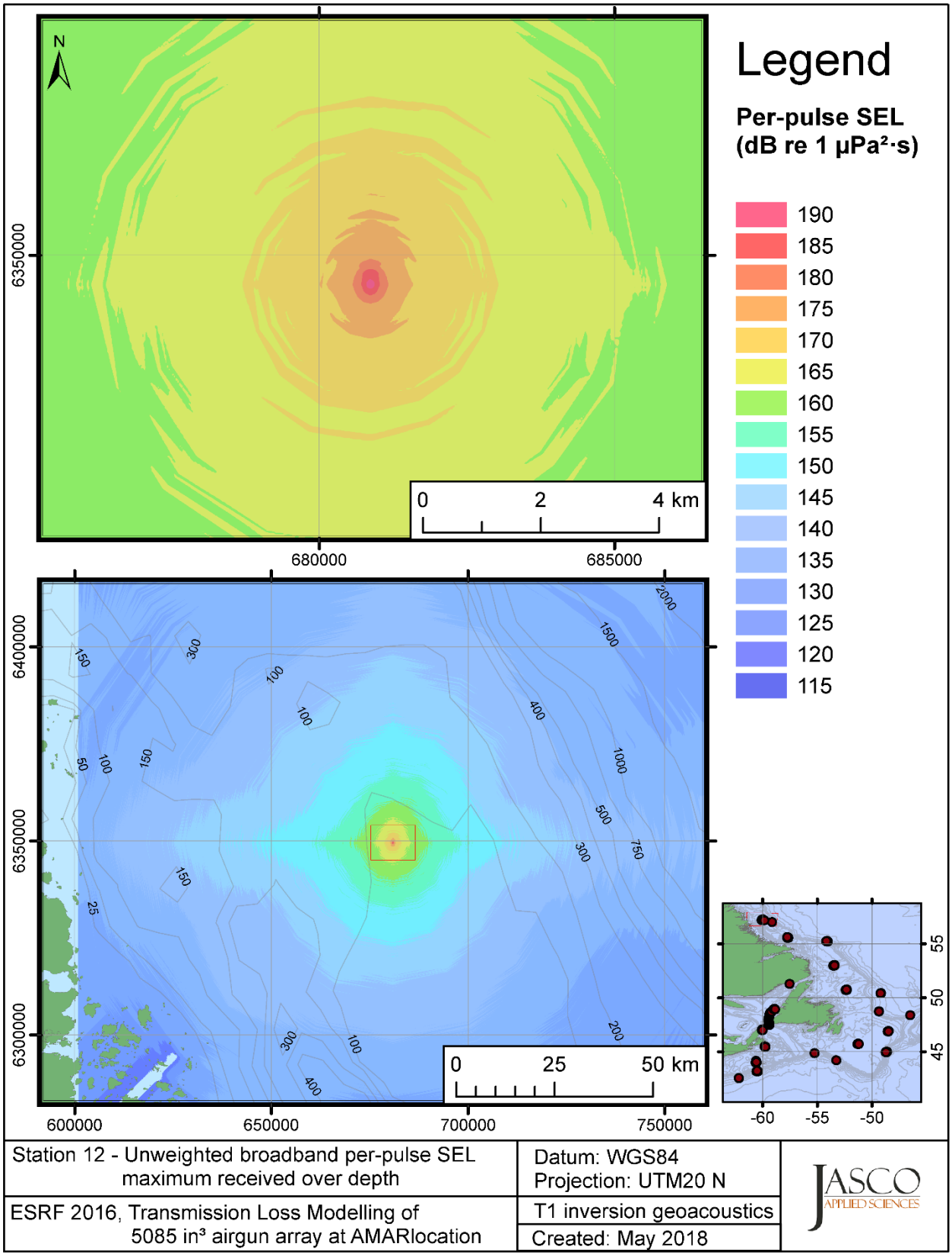

Figure C-275. Stn 12, unweighted maximum-over-depth SEL received at any location on the map, modelled using the track 1 inversion geoacoustic bottom, with the airgun array at the AMAR location and in-situ July SSP.

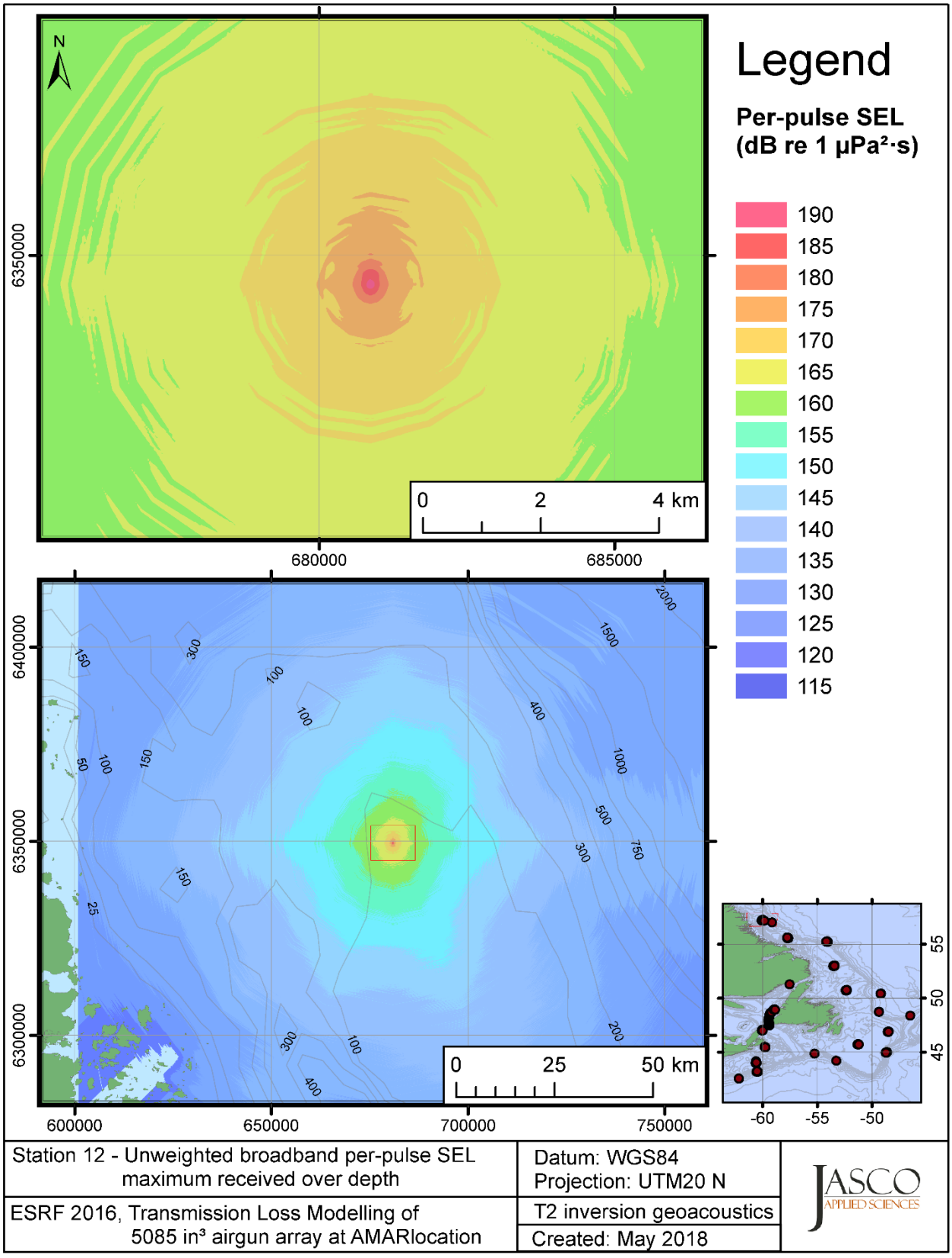

Figure C-276. Stn 12, unweighted maximum-over-depth SEL received at any location on the map, modelled using the track 2 inversion geoacoustic bottom, with the airgun array at the AMAR location and in-situ July SSP.

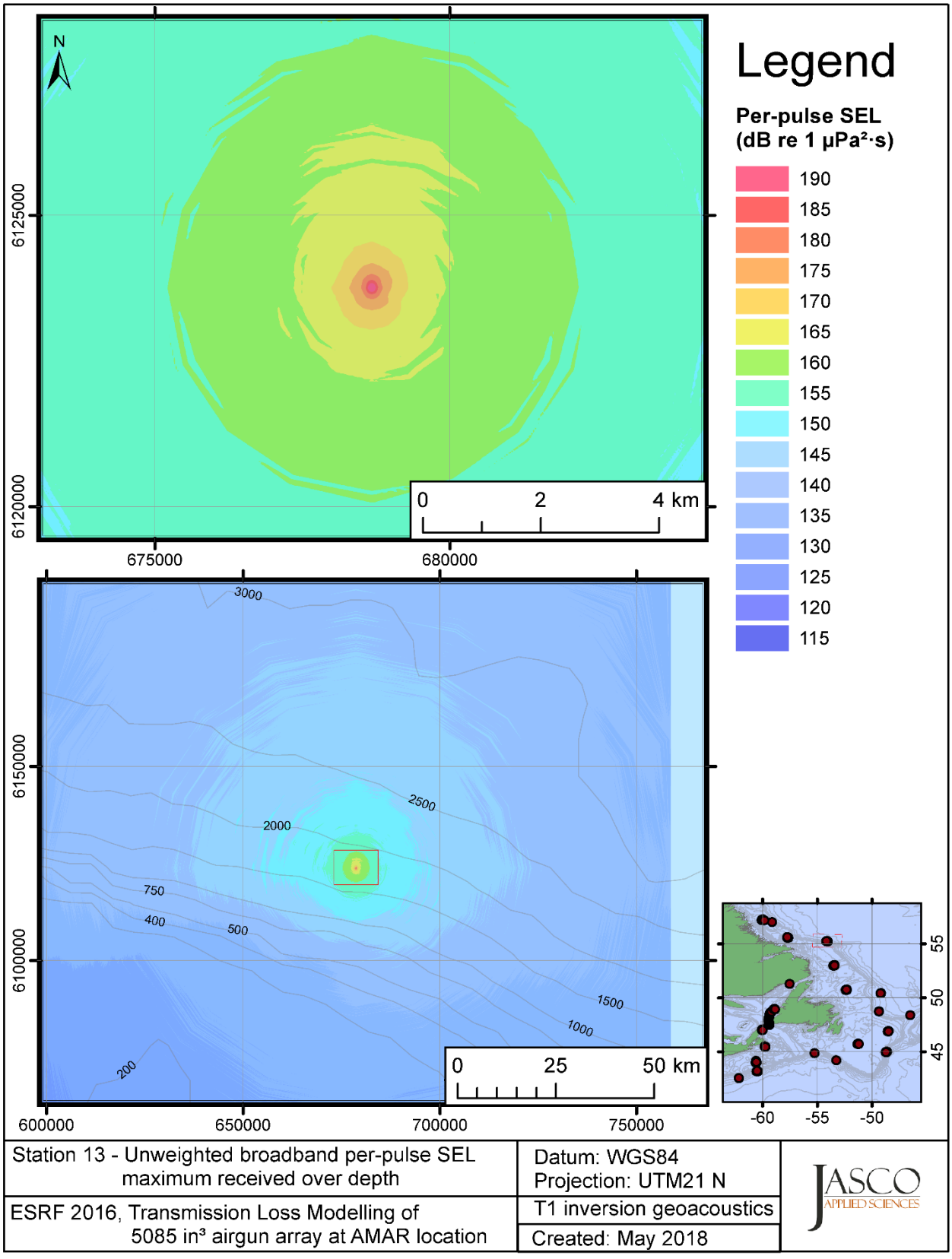

Figure C-277. Stn 13, unweighted maximum-over-depth SEL received at any location on the map, modelled using the track 1 inversion geoacoustic bottom, with the airgun array at the AMAR location and in-situ July SSP.

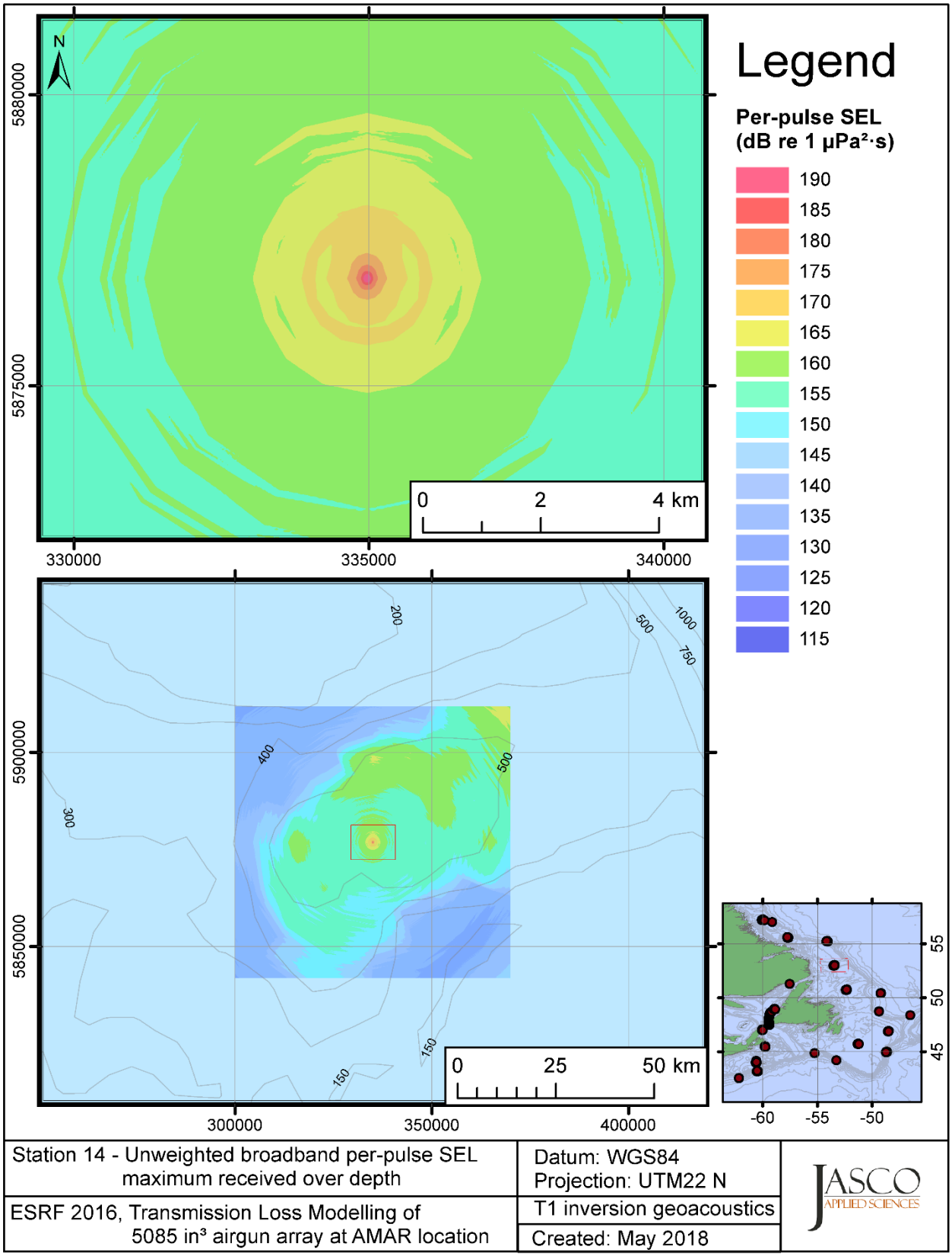

Figure C-278. Stn 14, unweighted maximum-over-depth SEL received at any location on the map, modelled using the track 1 inversion geoacoustic bottom, with the airgun array at the AMAR location and in-situ July SSP.

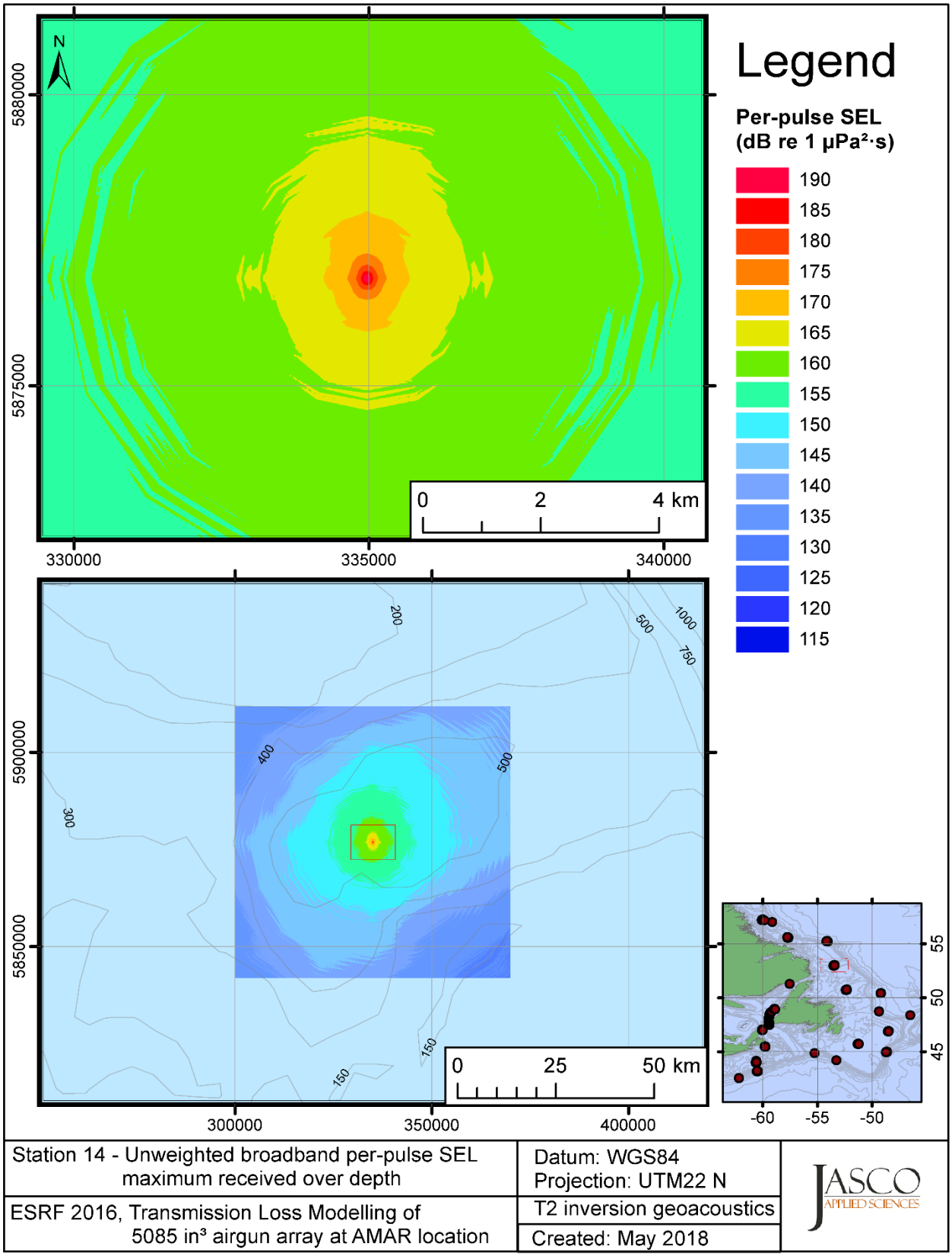

Figure C-279. Stn 14, unweighted maximum-over-depth SEL received at any location on the map, modelled using the track 2 inversion geoacoustic bottom, with the airgun array at the AMAR location and in-situ July SSP.

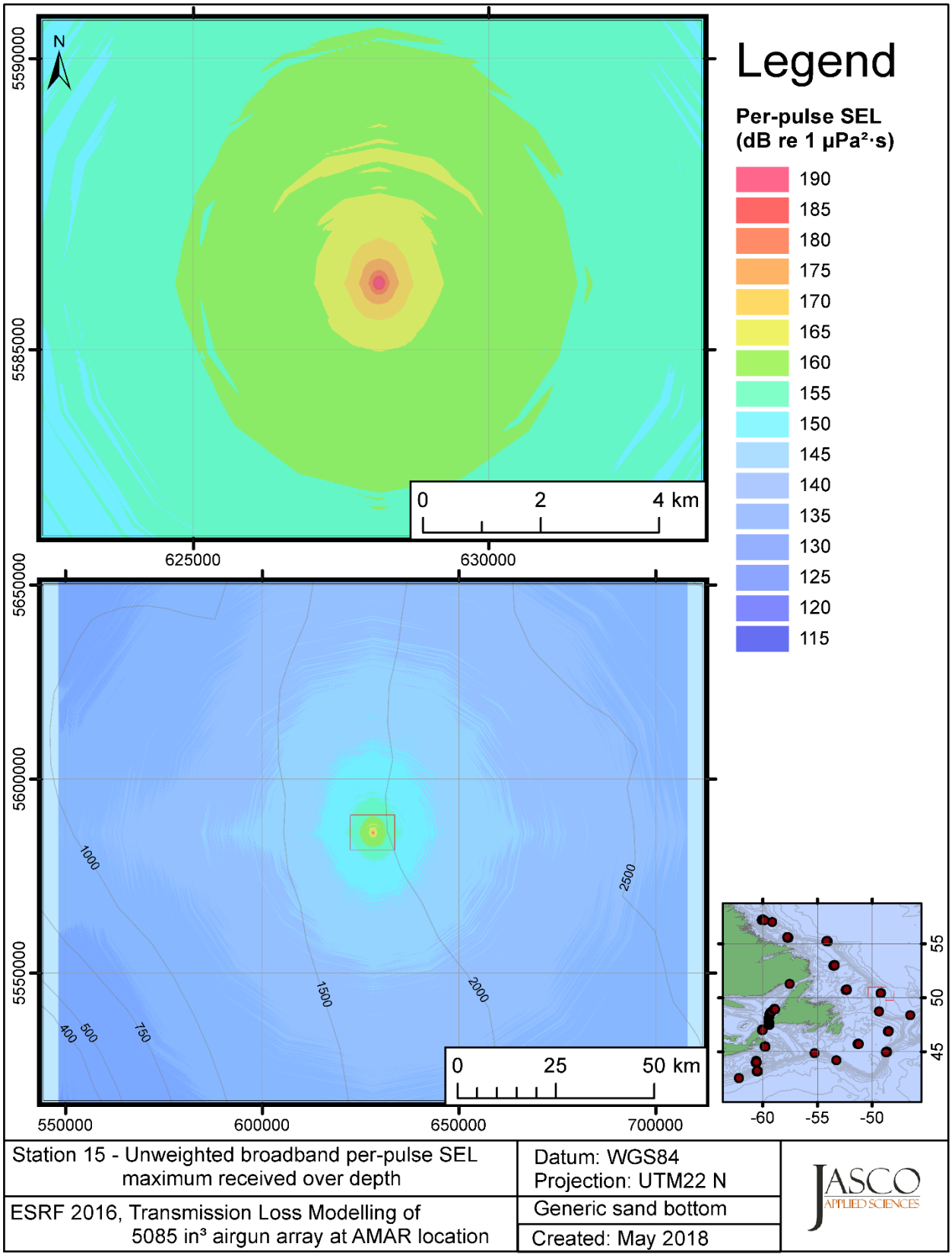

Figure C-280. Stn 15, unweighted maximum-over-depth SEL received at any location on the map, modelled using a generic sand bottom, with the airgun array at the AMAR location and in-situ July SSP.

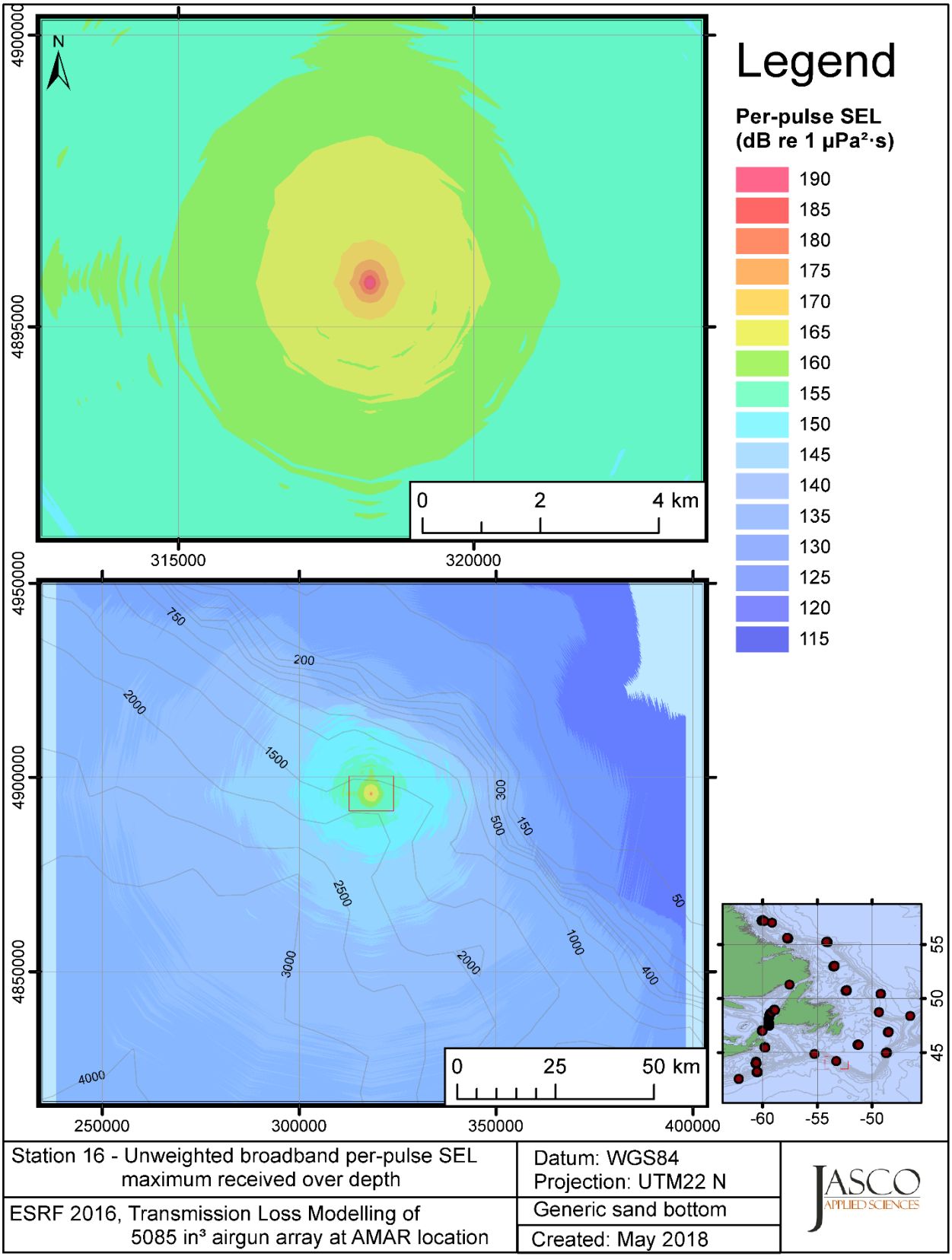

Figure C-281. Stn 16, unweighted maximum-over-depth SEL received at any location on the map, modelled using a generic sand bottom, with the airgun array at the AMAR location and in-situ July SSP.

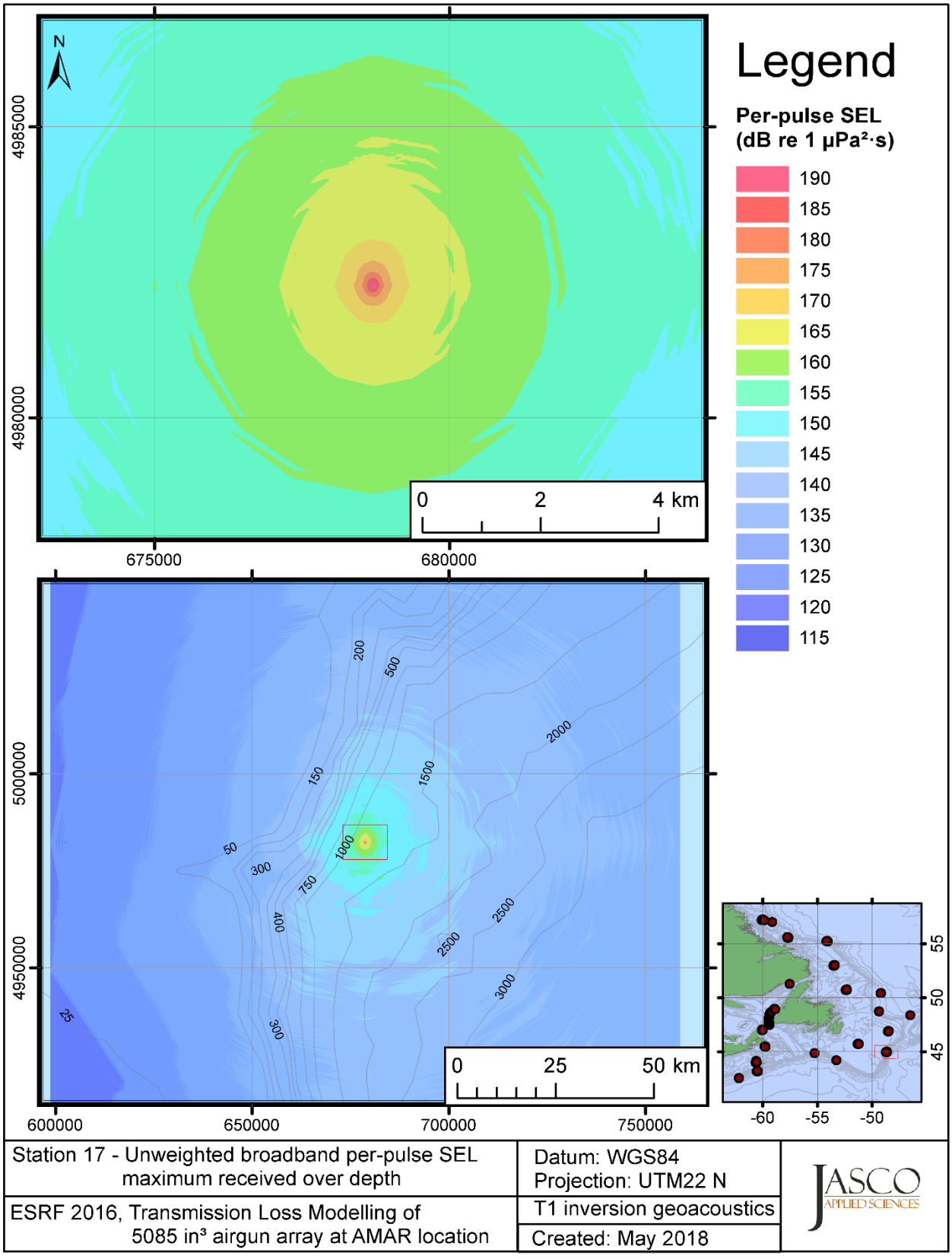

Figure C-282. Stn 17, unweighted maximum-over-depth SEL received at any location on the map, modelled using the track 1 inversion geoacoustic bottom, with the airgun array at the AMAR location and in-situ July SSP.

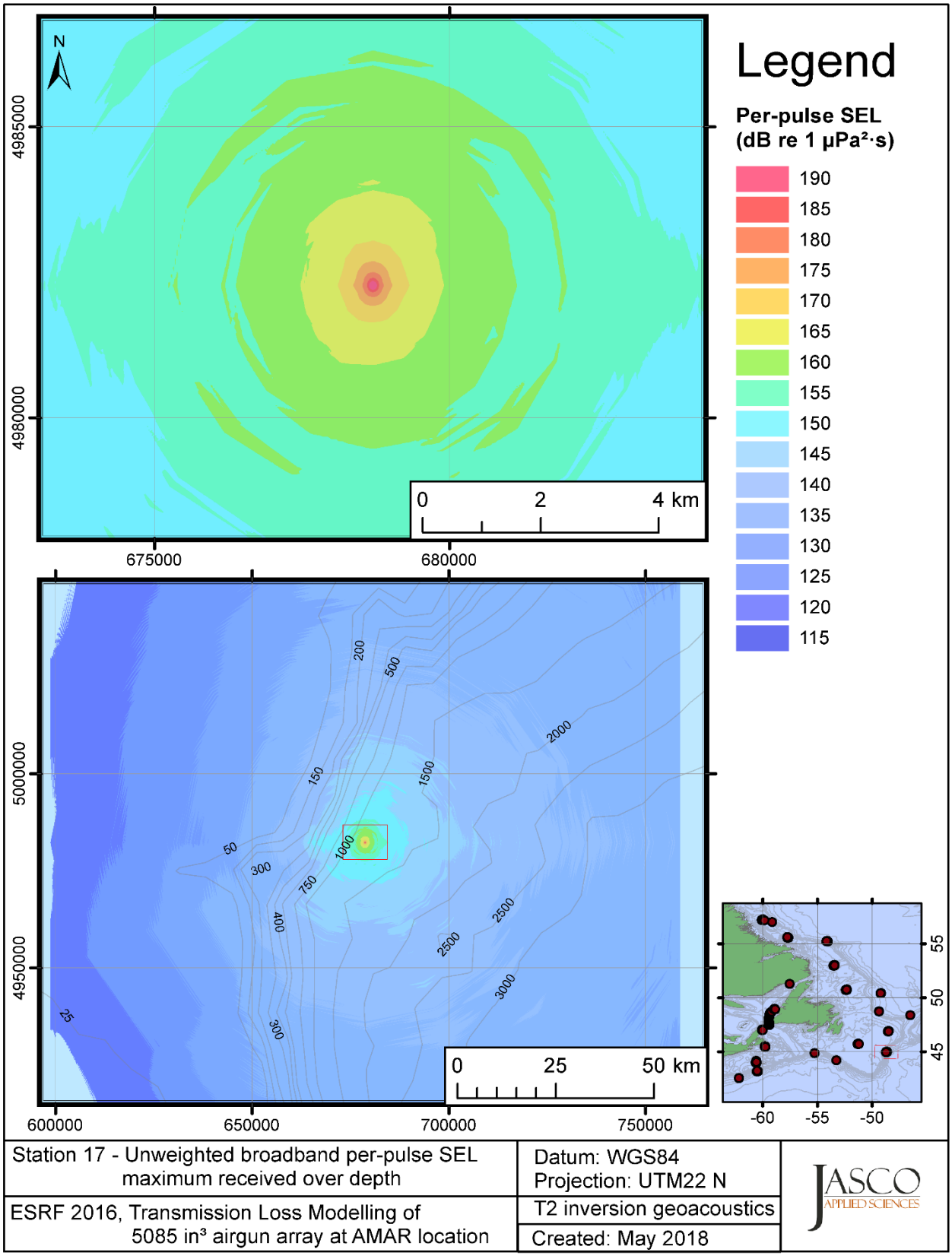

Figure C-283. Stn 17, unweighted maximum-over-depth SEL received at any location on the map, modelled using the track 2 inversion geoacoustic bottom, with the airgun array at the AMAR location and in-situ July SSP.

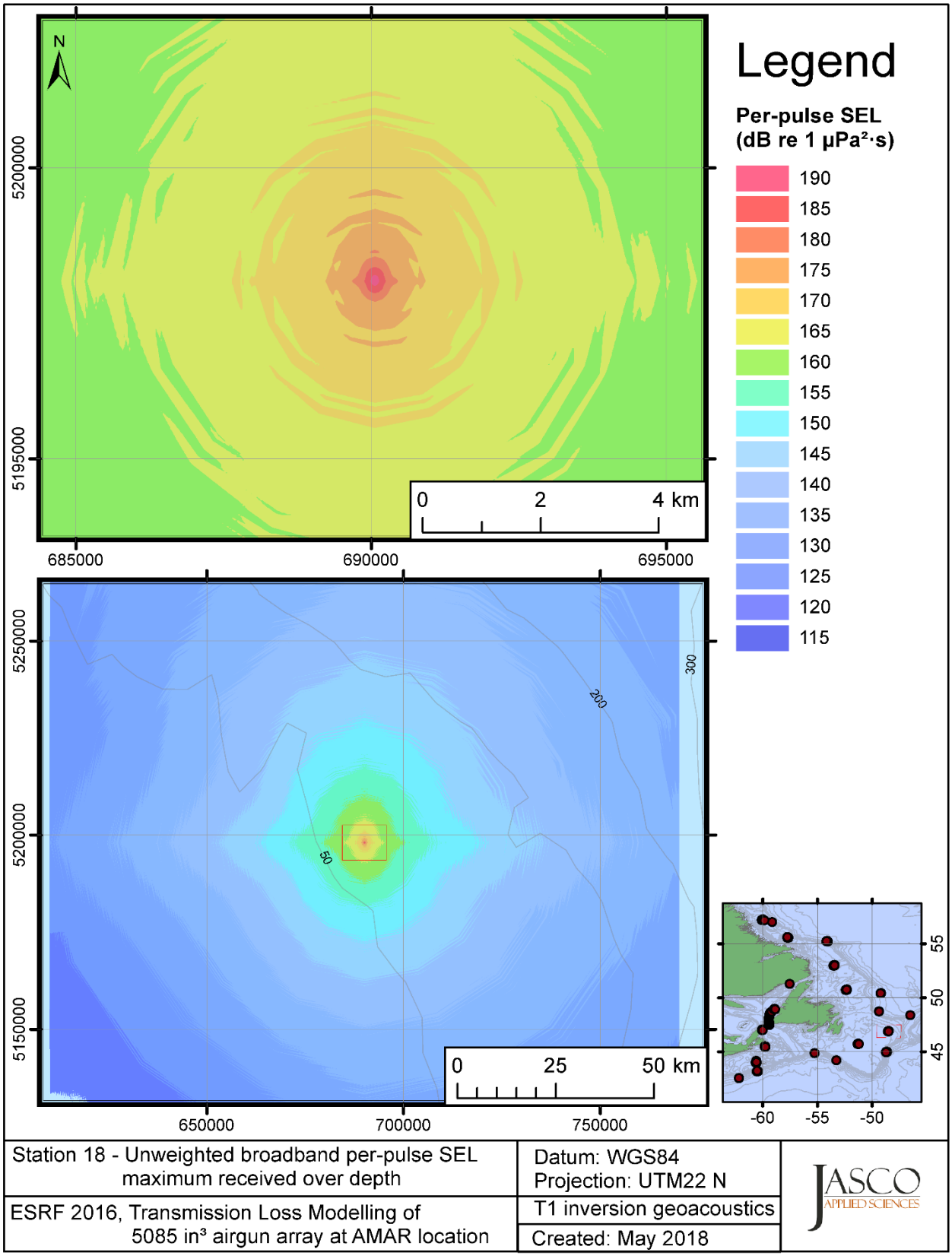

Figure C-284. Stn 18, unweighted maximum-over-depth SEL received at any location on the map, modelled using the track 1 inversion geoacoustic bottom, with the airgun array at the AMAR location and in-situ July SSP.

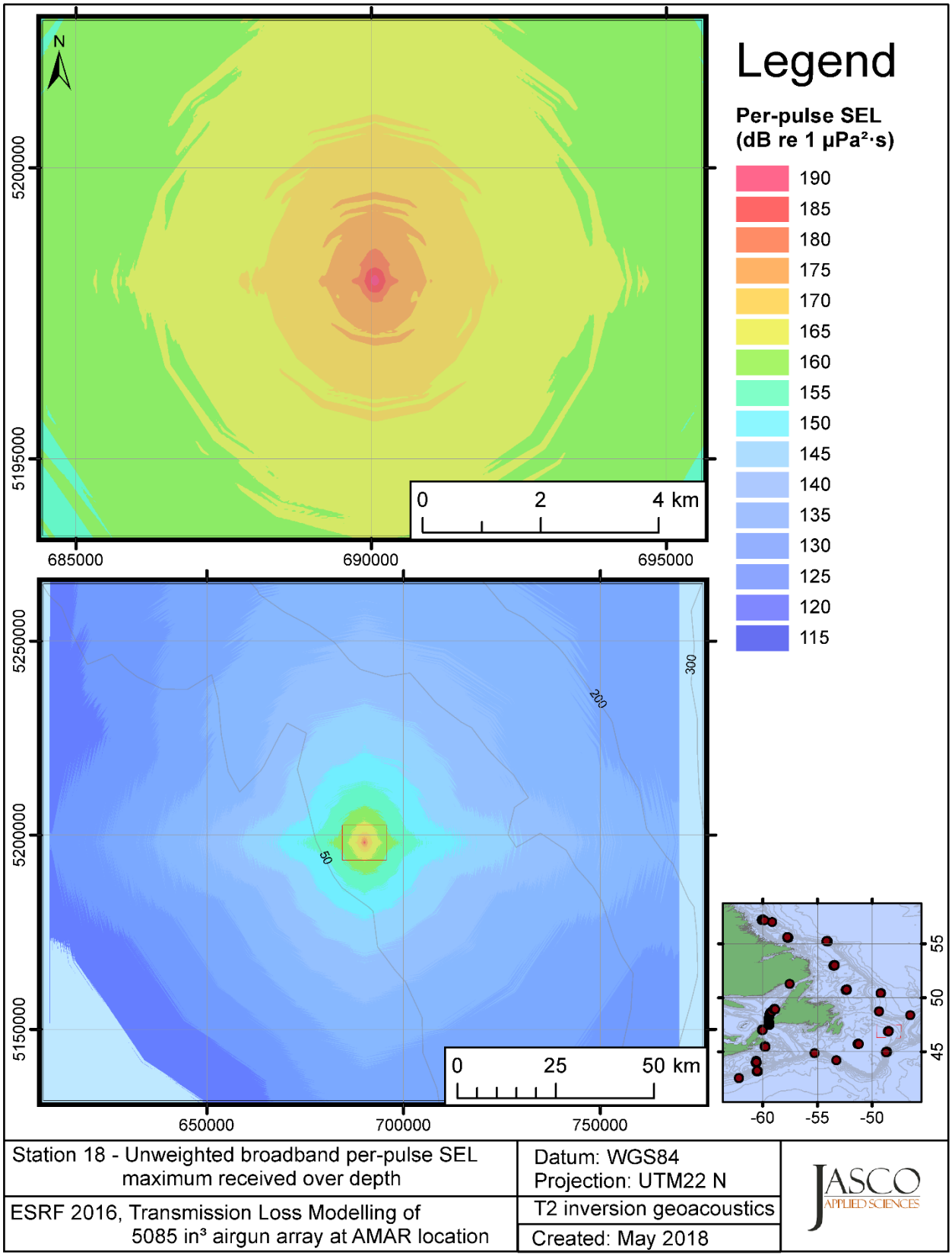

Figure C-285. Stn 18, unweighted maximum-over-depth SEL received at any location on the map, modelled using the track 2 inversion geoacoustic bottom, with the airgun array at the AMAR location and in-situ July SSP.

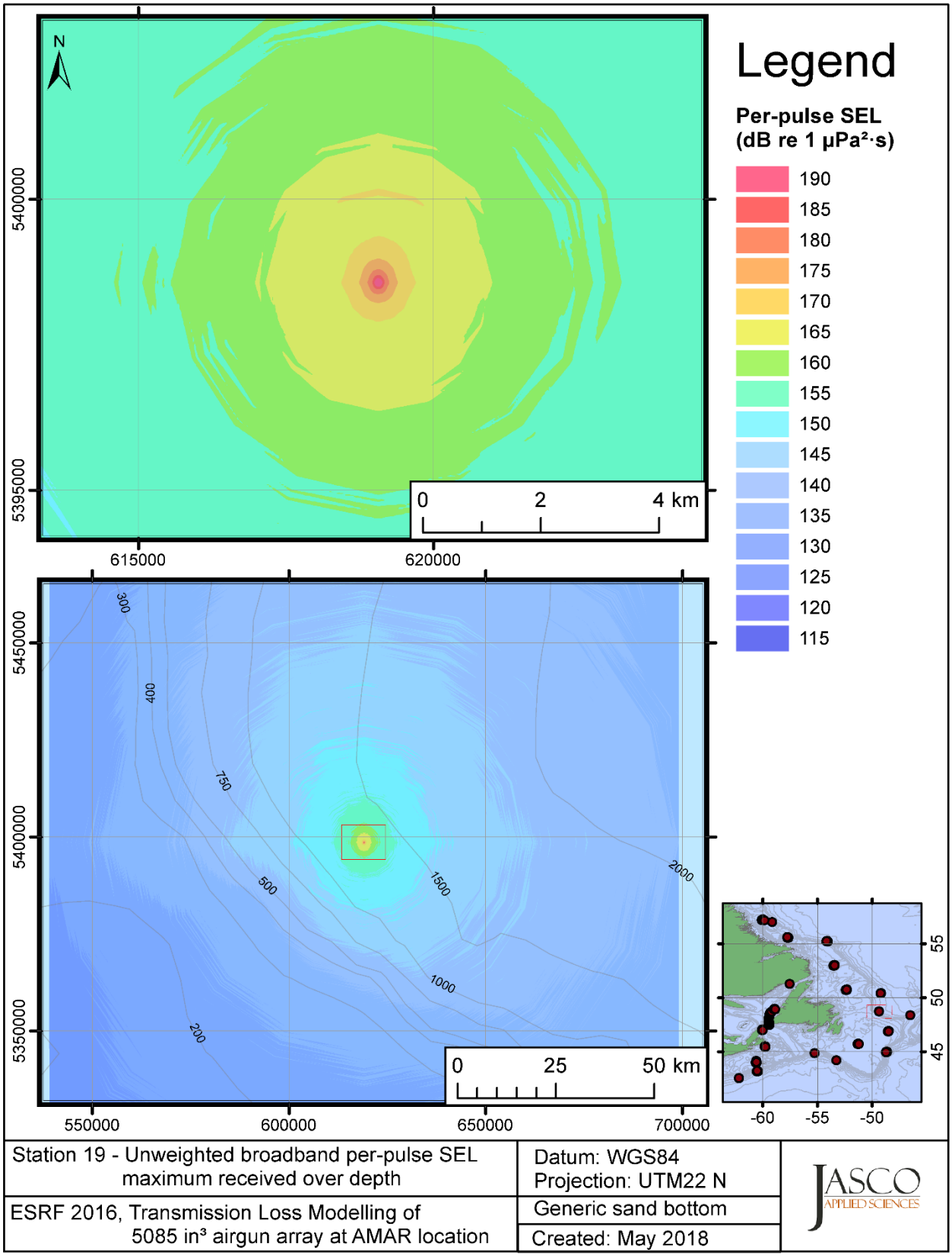

Figure C-286. Stn 19, unweighted maximum-over-depth SEL received at any location on the map, modelled using a generic sand bottom, with the airgun array at the AMAR location and in-situ July SSP.

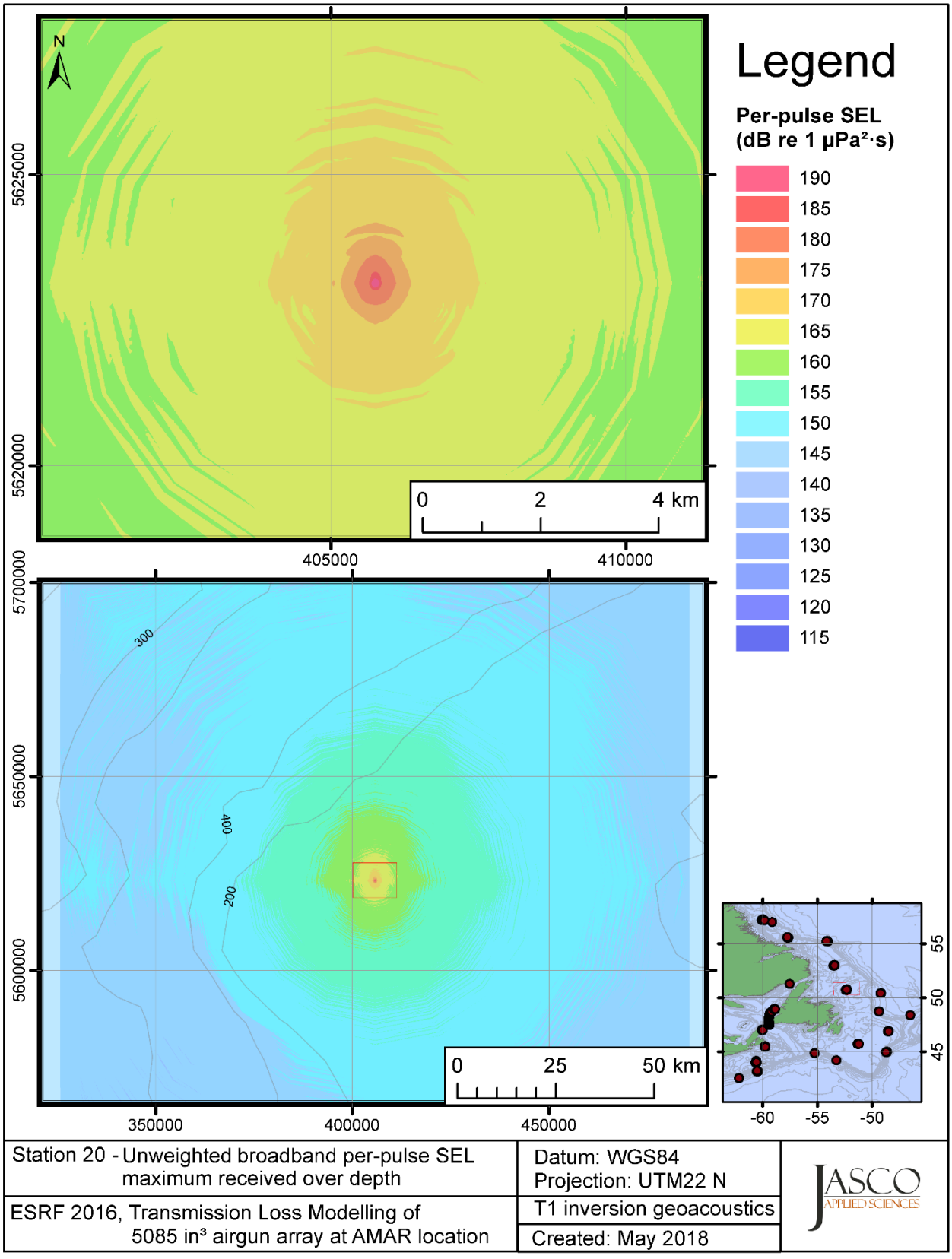

Figure C-287. Stn 20, unweighted maximum-over-depth SEL received at any location on the map, modelled using the track 1 inversion geoacoustic bottom, with the airgun array at the AMAR location and in-situ July SSP.

C.8. Modelling LF M-weighted Max-over-depth Received Level at Distant Locations - Summer

This section presents the results of modelling the maximum-over-depth per-pulse sound exposure level (SEL) received at distant receiver locations (varied in range and azimuth) for the source held fixed at the AMAR location. The modelling uses the geoacoustic inversion bottom parameters at the 14 sites where they are available and only uses a generic sand bottom at the other six sites. The modelling results are presented in the form of coloured maps where the colour at any map location represents the predicted maximum-over-depth received level at that spot on the map. This section includes only the low-frequency cetaceans (LF) marine-mammal-weighted per-pulse SEL results; additional maps for other marine mammal received level auditory weightings are presented in adjoining sections. The sound speed profiles (SSP) used are detailed in Appendix B.1.

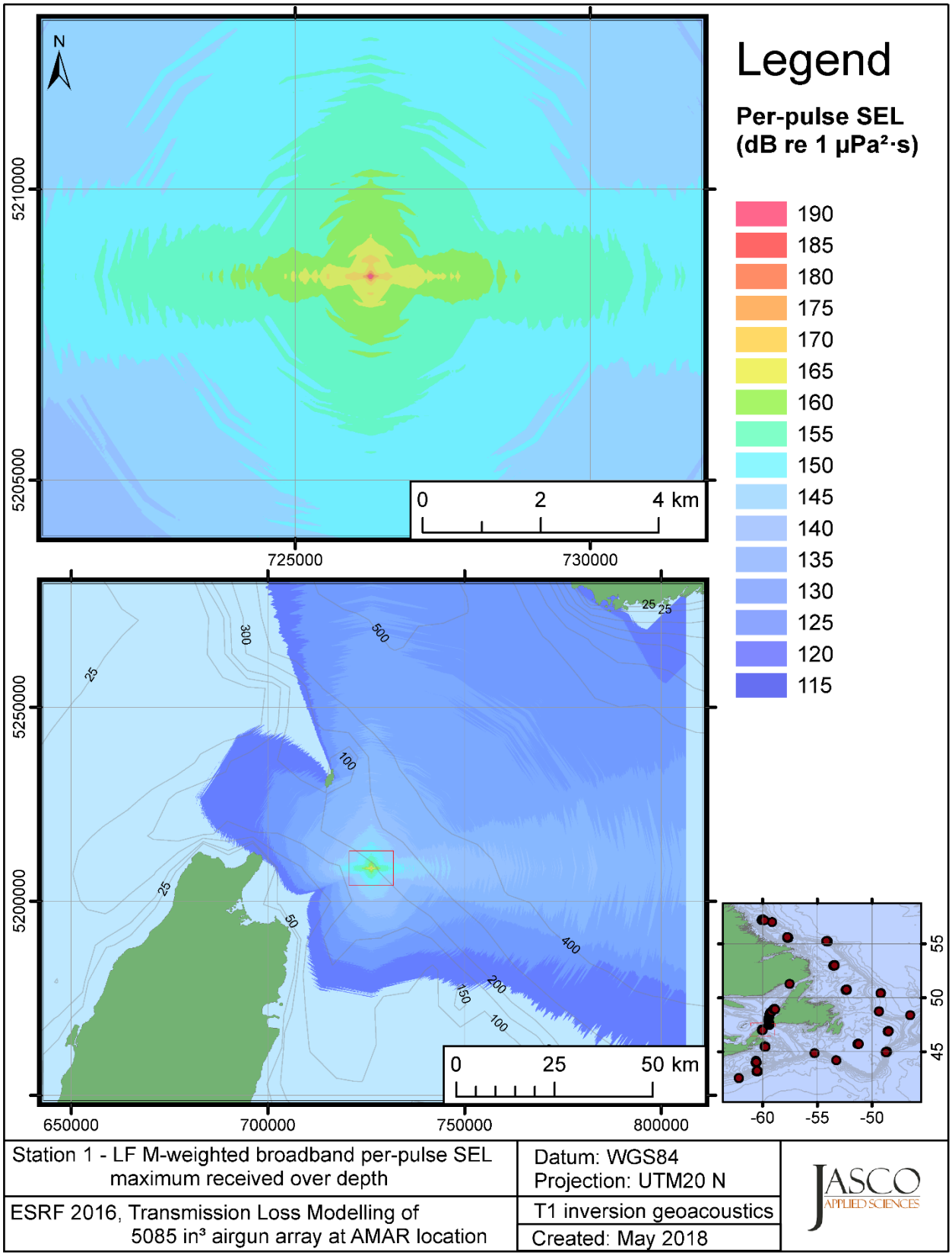

Figure C-288. Stn 1, LF M-weighted maximum-over-depth SEL received at any location on the map, modelled using the track 1 inversion geoacoustic bottom, with the airgun array at the AMAR location and in-situ July SSP.

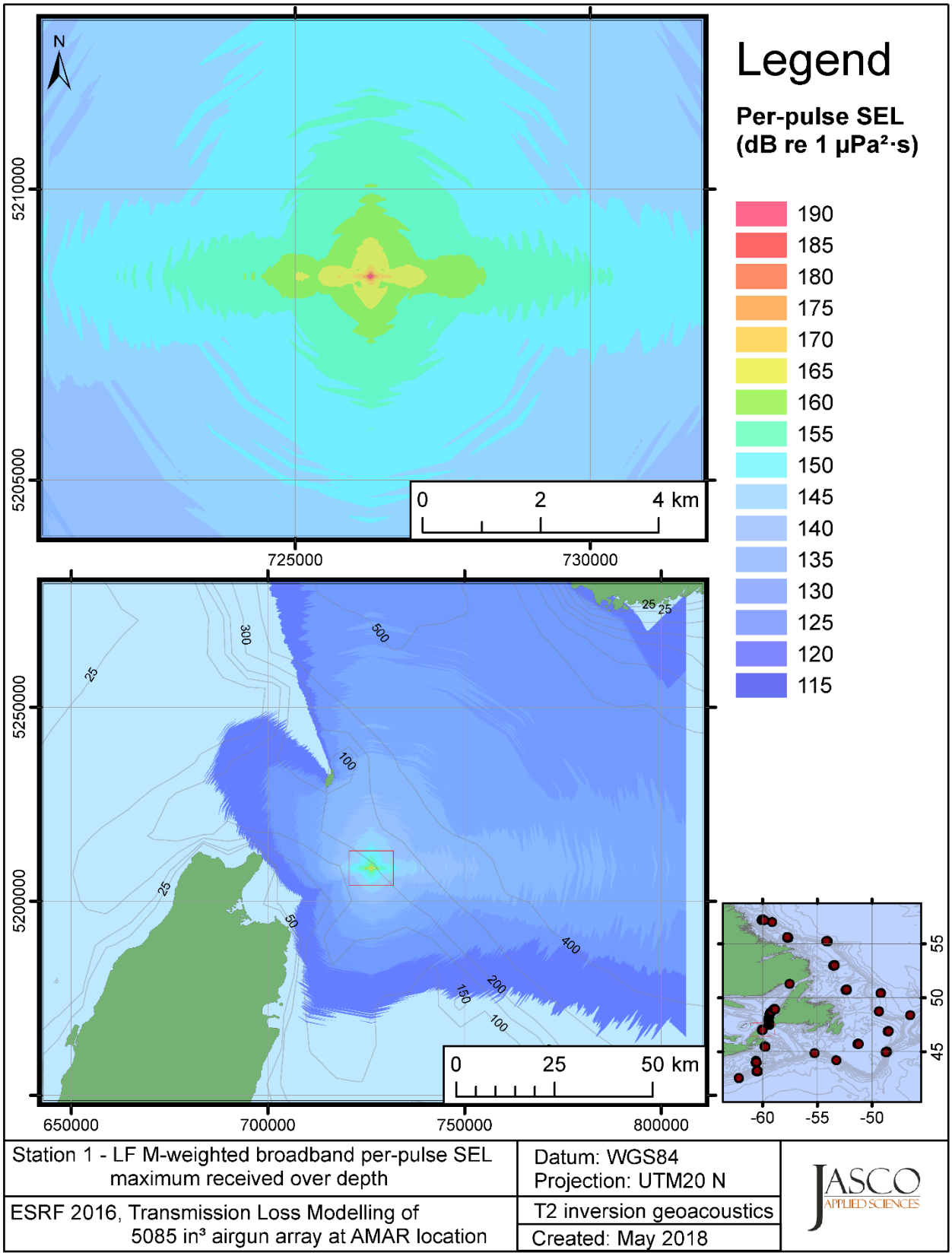

Figure C-289. Stn 1, LF M-weighted maximum-over-depth SEL received at any location on the map, modelled using the track 2 inversion geoacoustic bottom, with the airgun array at the AMAR location and in-situ July SSP.

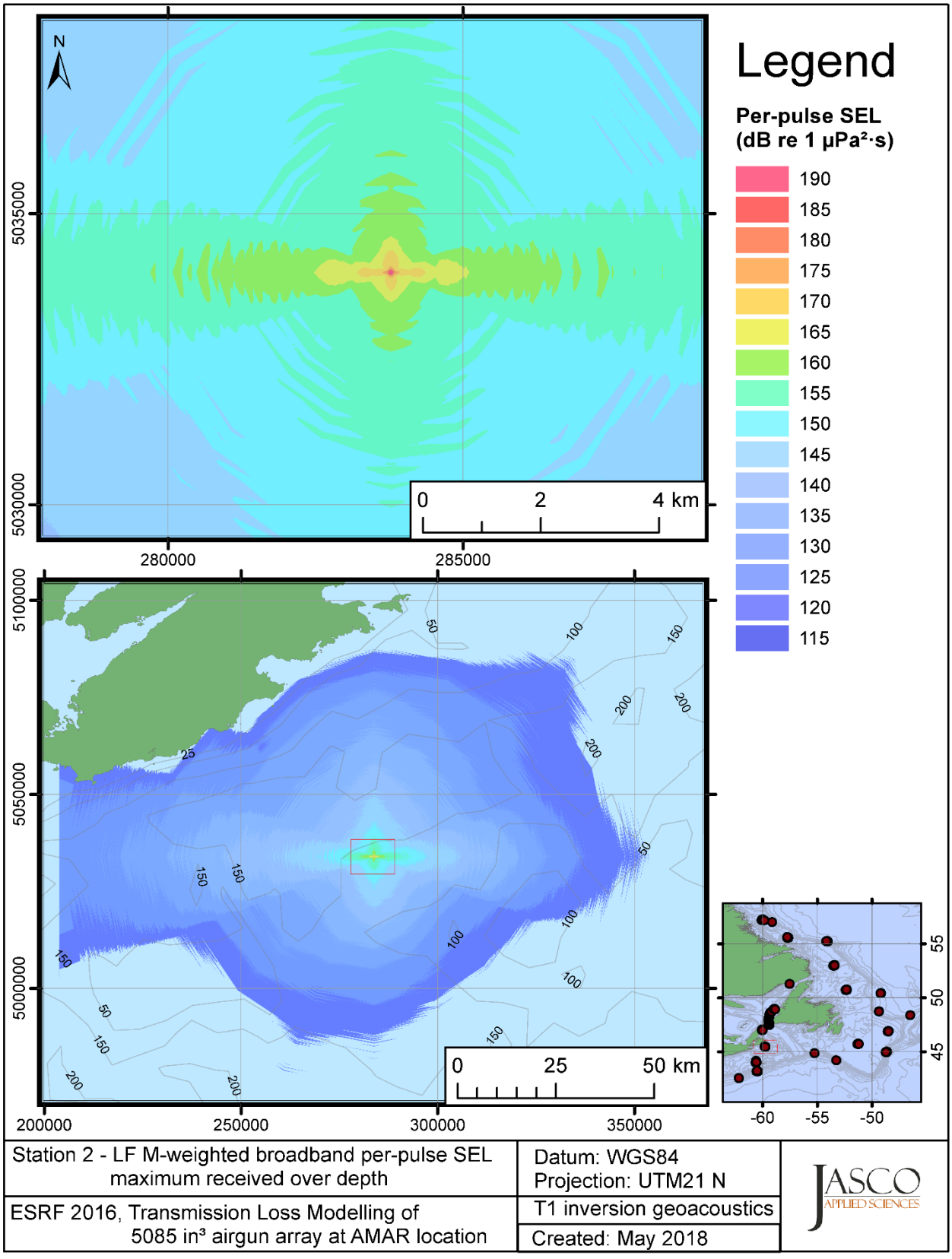

Figure C-290. Stn 2, LF M-weighted maximum-over-depth SEL received at any location on the map, modelled using the track 1 inversion geoacoustic bottom, with the airgun array at the AMAR location and in-situ July SSP.

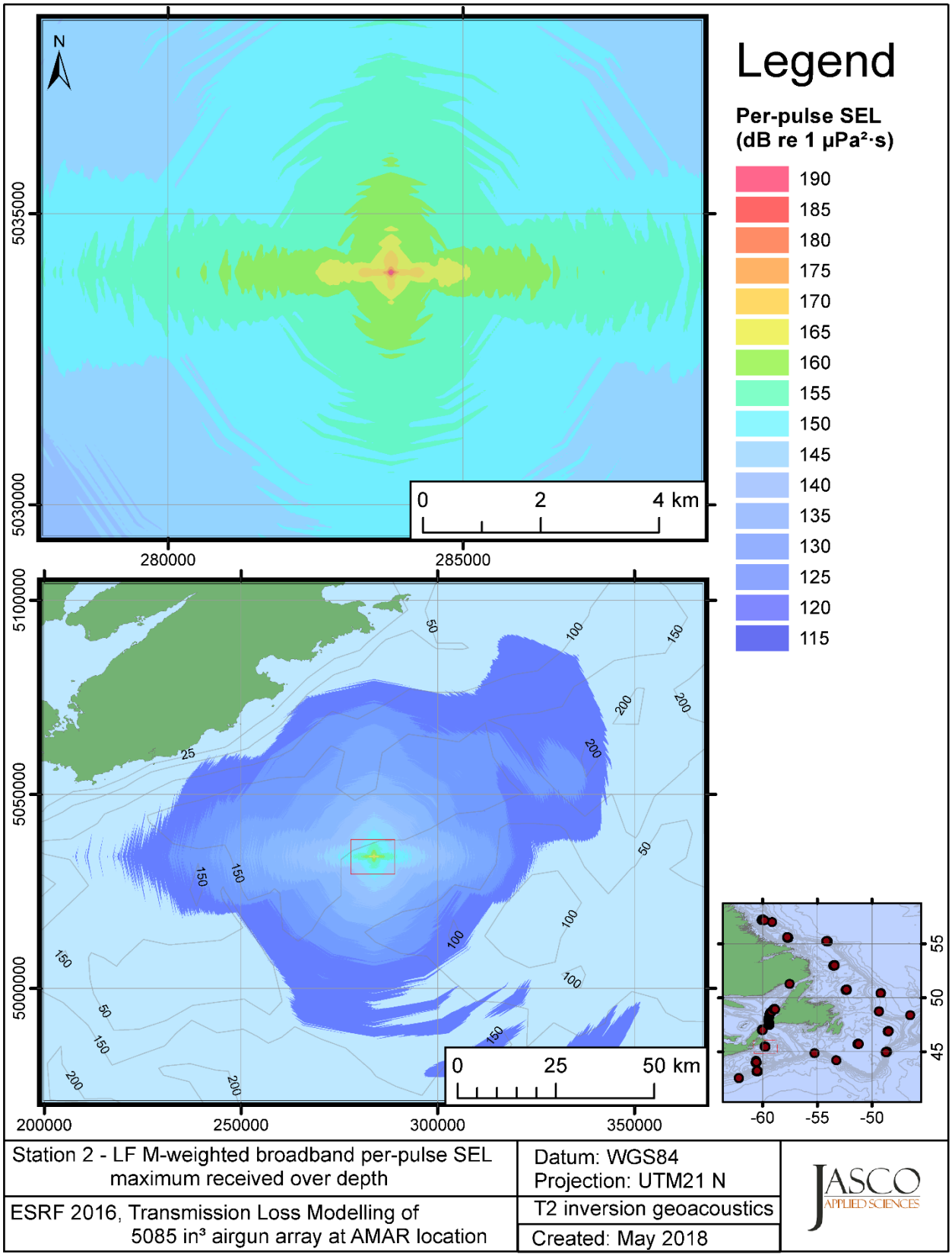

Figure C-291. Stn 2, LF M-weighted maximum-over-depth SEL received at any location on the map, modelled using the track 2 inversion geoacoustic bottom, with the airgun array at the AMAR location and in-situ July SSP.

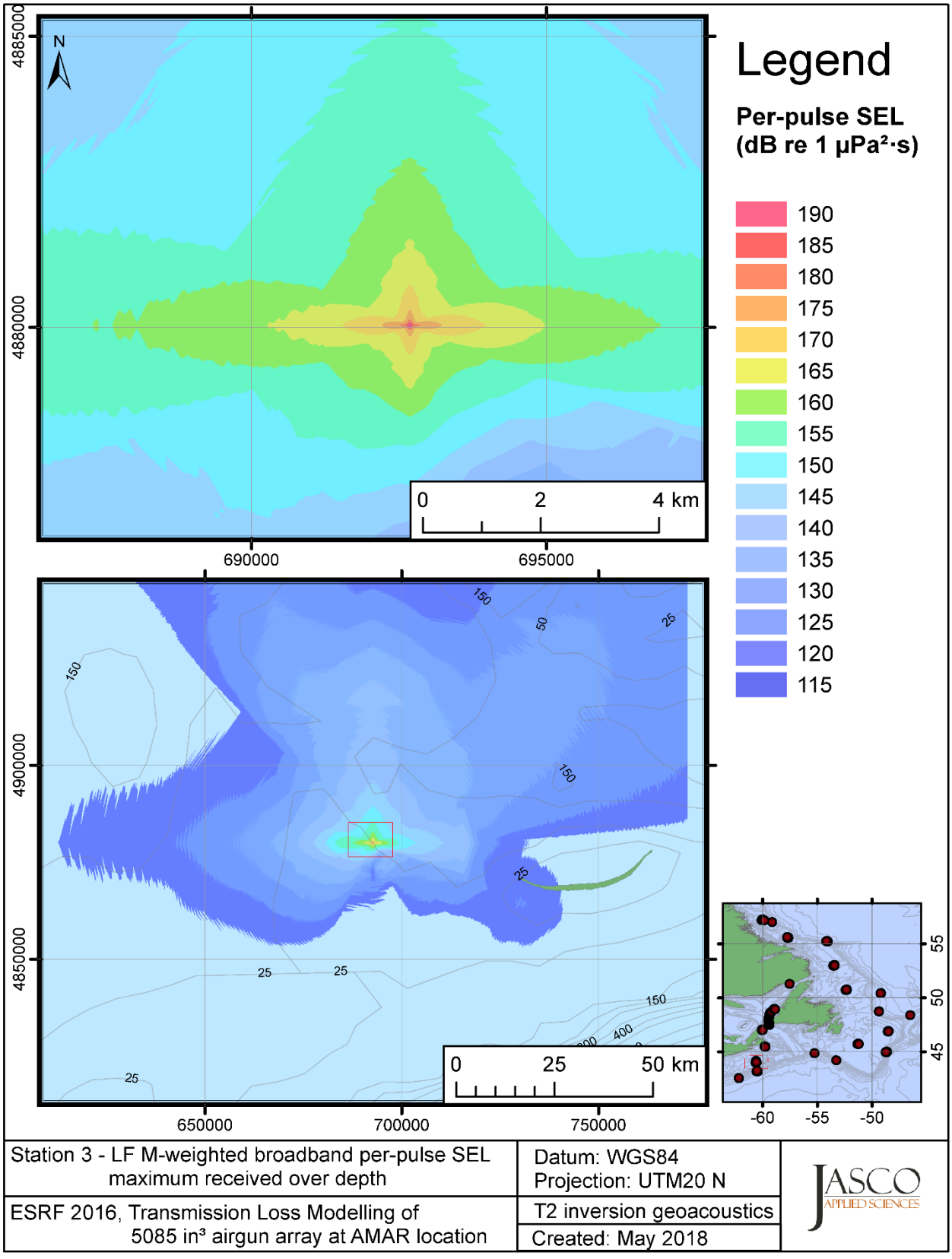

Figure C-292. Stn 3, LF M-weighted maximum-over-depth SEL received at any location on the map, modelled using the track 2 inversion geoacoustic bottom, with the airgun array at the AMAR location and in-situ July SSP.

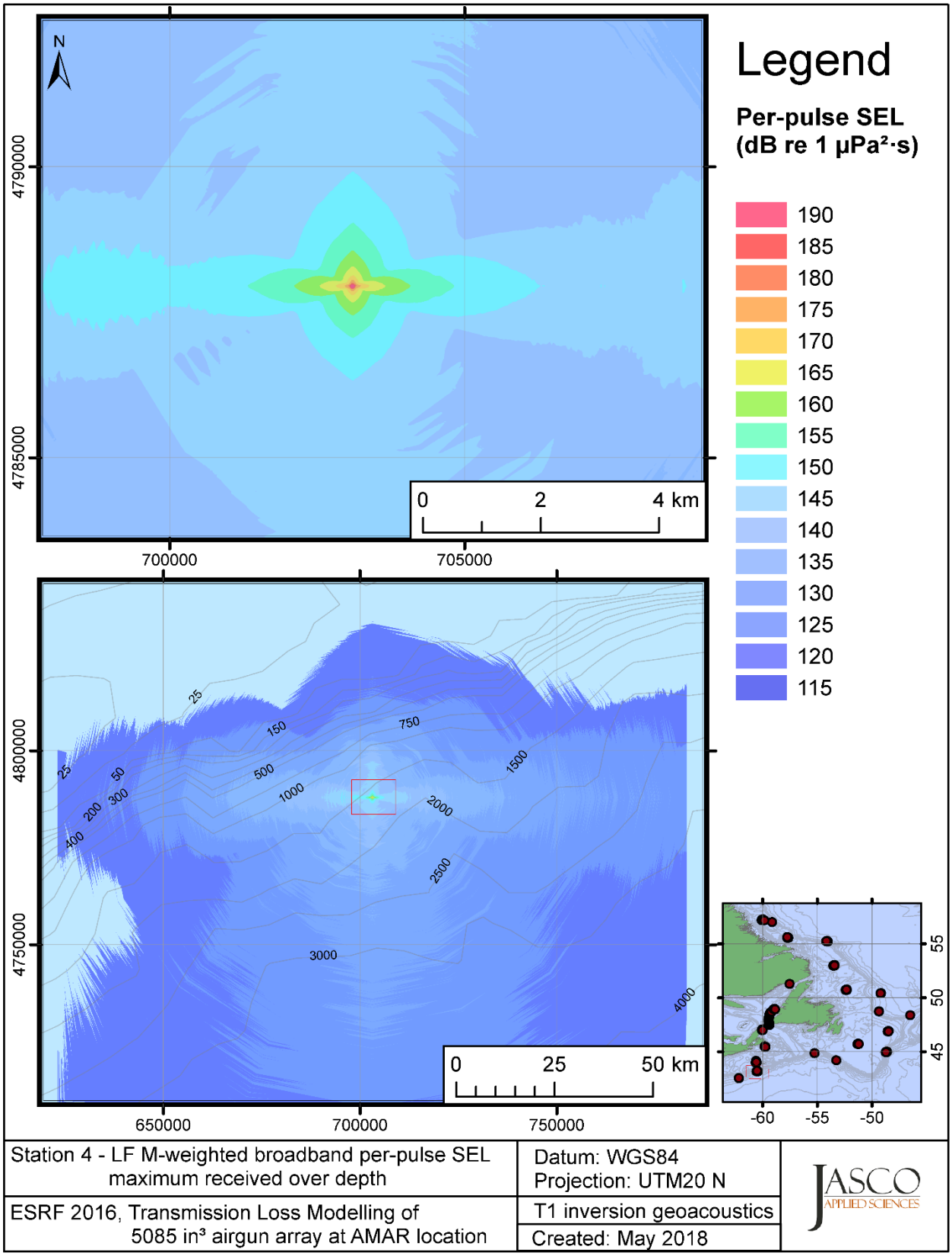

Figure C-293. Stn 4, LF M-weighted maximum-over-depth SEL received at any location on the map, modelled using the track 1 inversion geoacoustic bottom, with the airgun array at the AMAR location and in-situ July SSP.

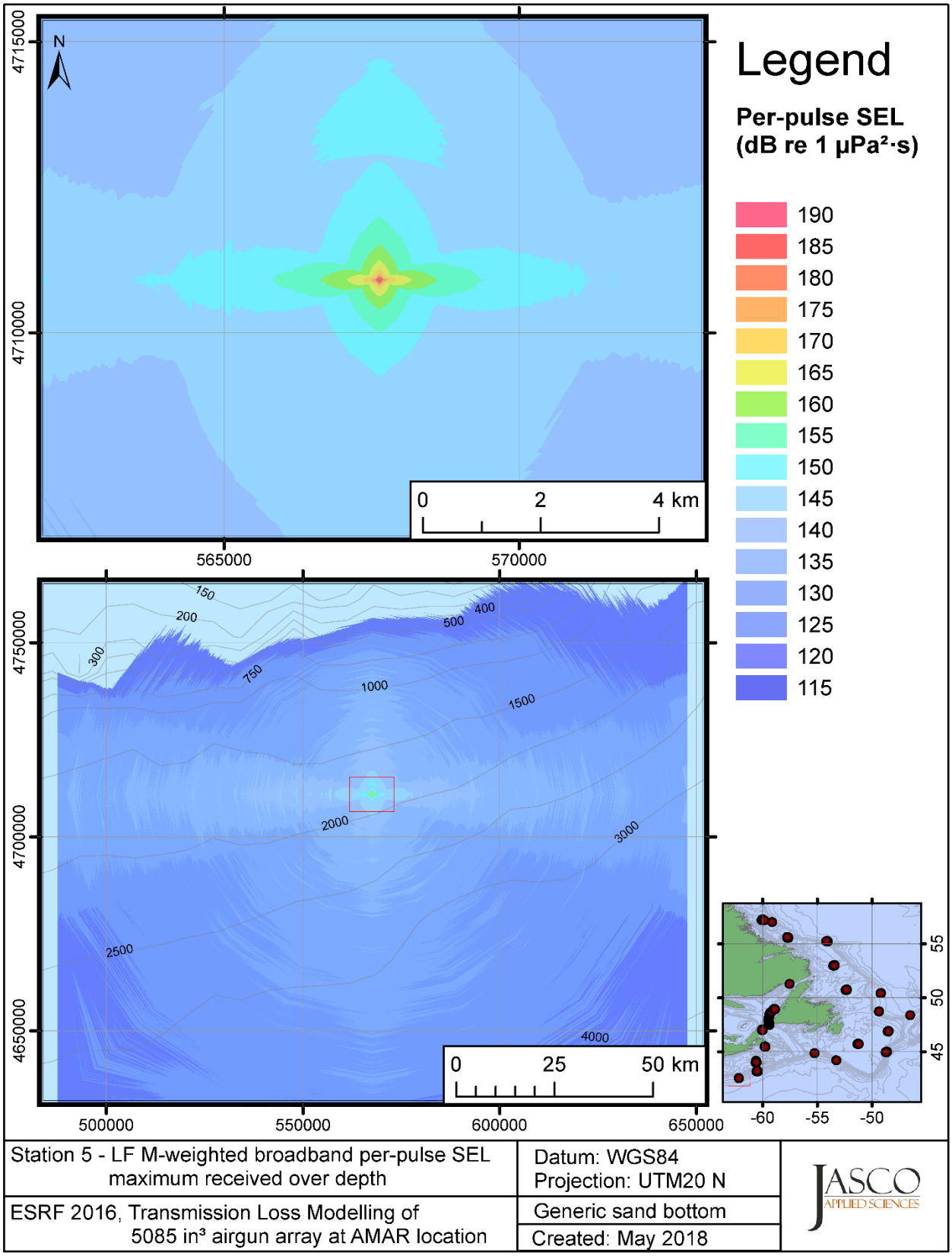

Figure C-294. Stn 5, LF M-weighted maximum-over-depth SEL received at any location on the map, modelled using a generic sand bottom, with the airgun array at the AMAR location and in-situ July SSP.

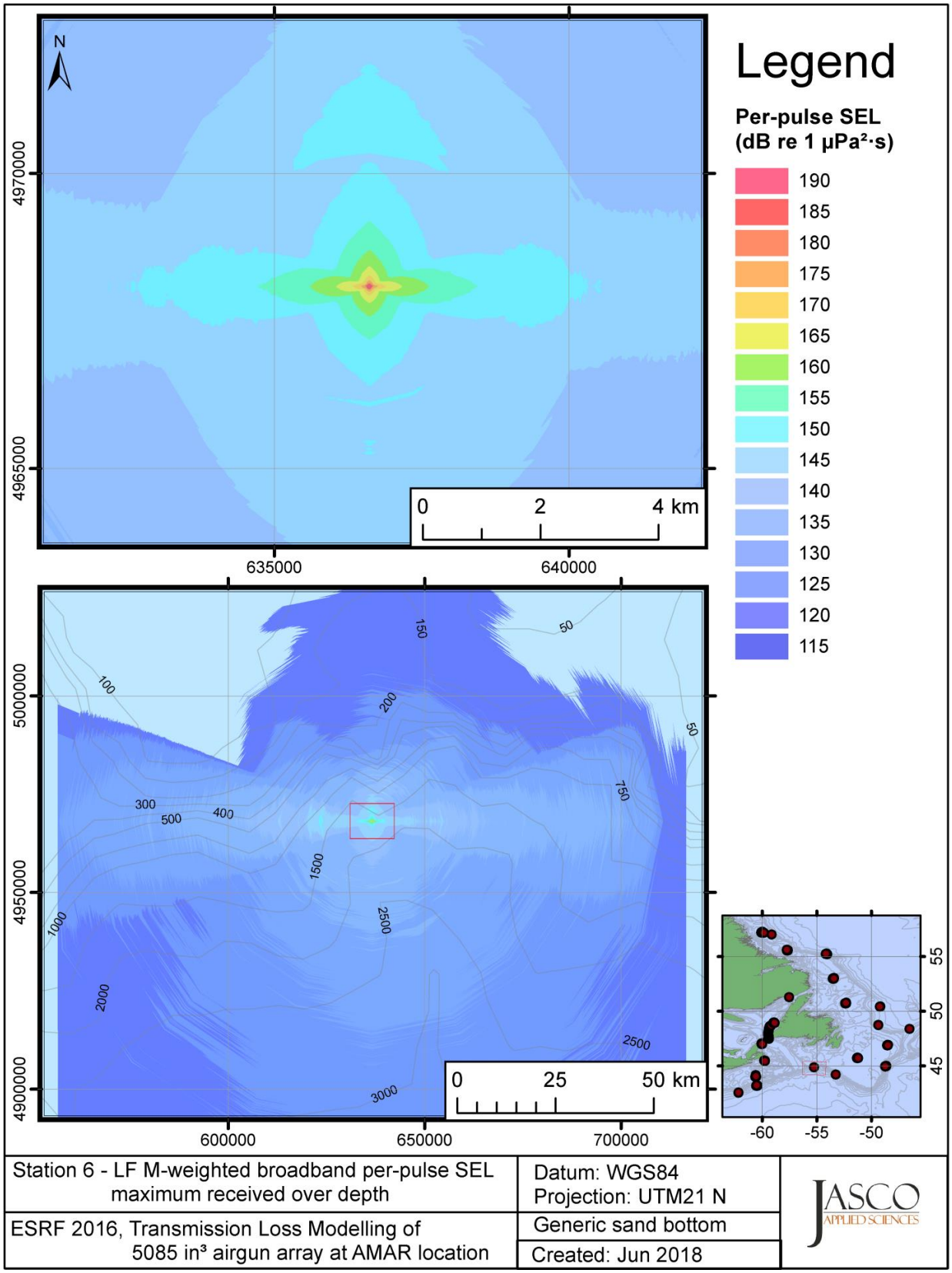

Figure C-295. Stn 6, LF M-weighted maximum-over-depth SEL received at any location on the map, modelled using a generic sand bottom, with the airgun array at the AMAR location and in-situ July SSP.

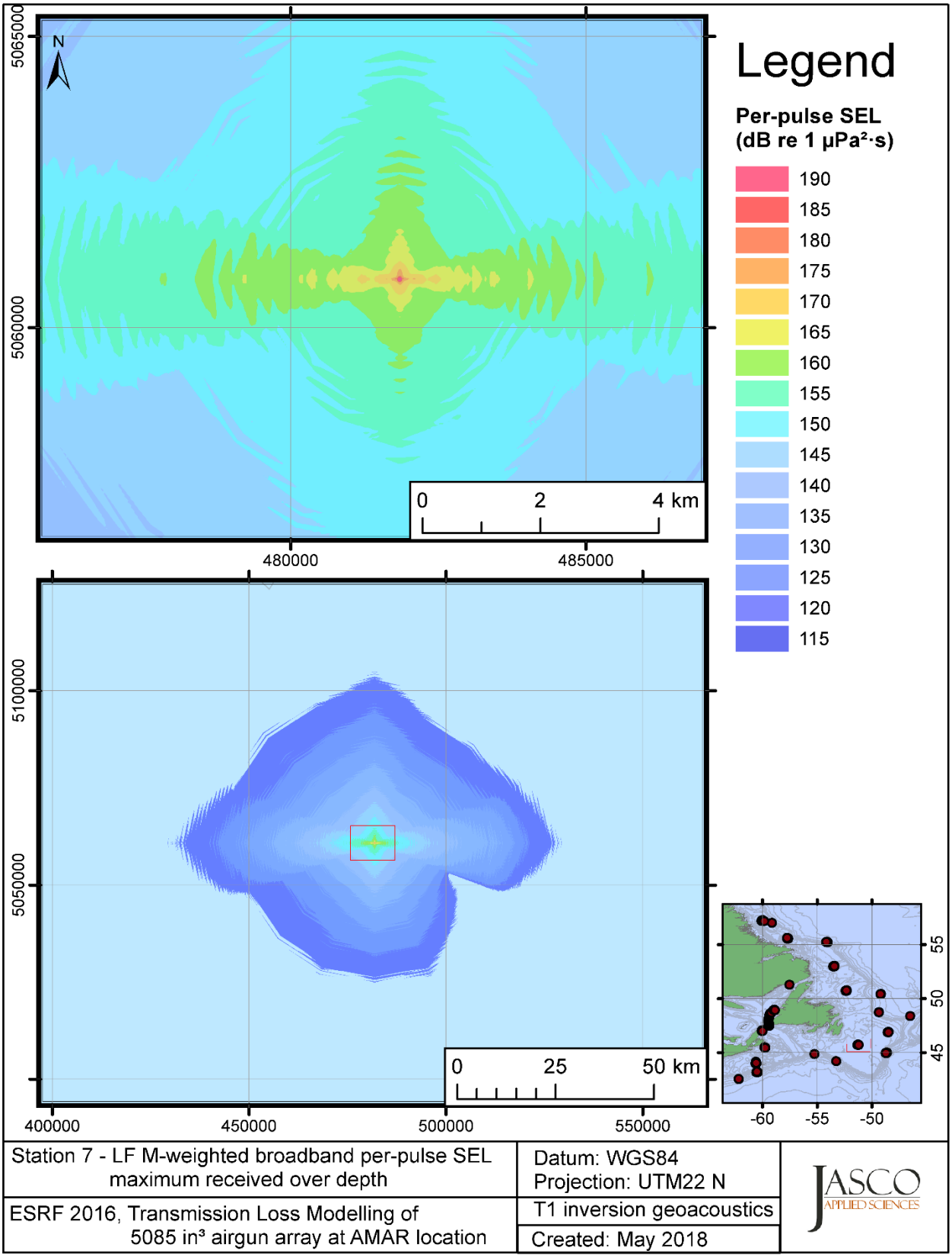

Figure C-296. Stn 7, LF M-weighted maximum-over-depth SEL received at any location on the map, modelled using the track 1 inversion geoacoustic bottom, with the airgun array at the AMAR location and in-situ July SSP.

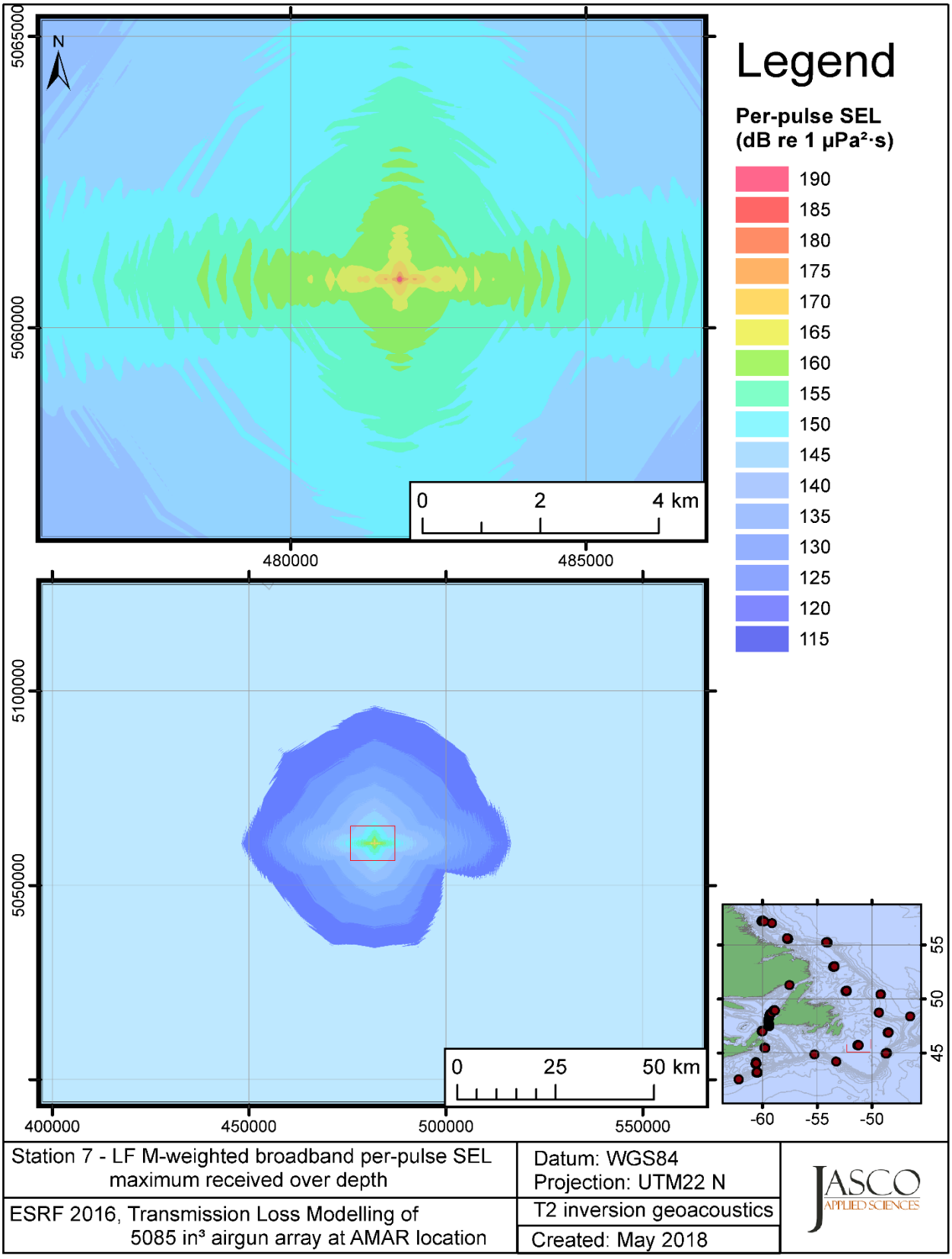

Figure C-297. Stn 7, LF M-weighted maximum-over-depth SEL received at any location on the map, modelled using the track 2 inversion geoacoustic bottom, with the airgun array at the AMAR location and in-situ July SSP.

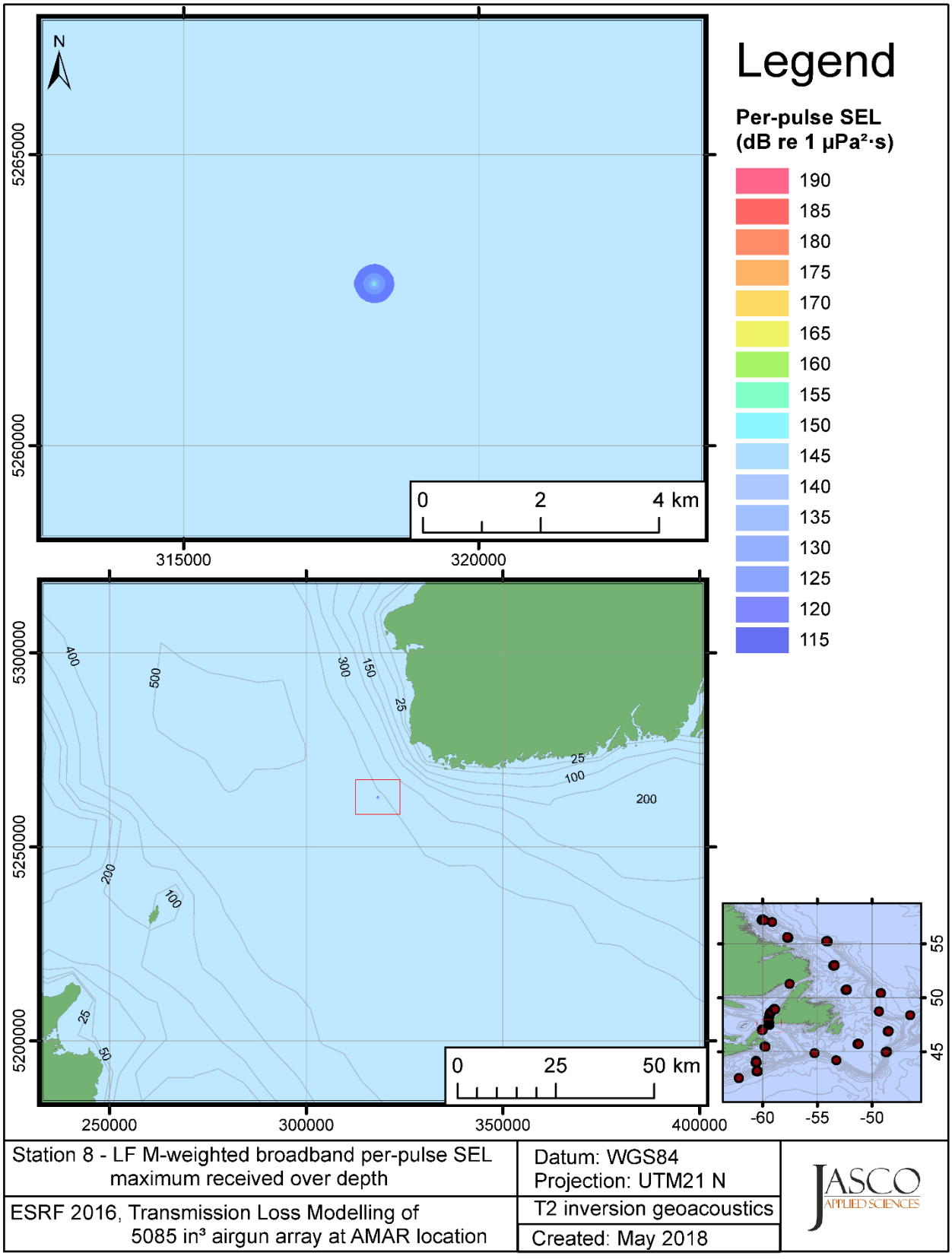

Figure C-298. Stn 8, LF M-weighted maximum-over-depth SEL received at any location on the map, modelled using the track 2 inversion geoacoustic bottom, with the airgun array at the AMAR location and GDEM July SSP.

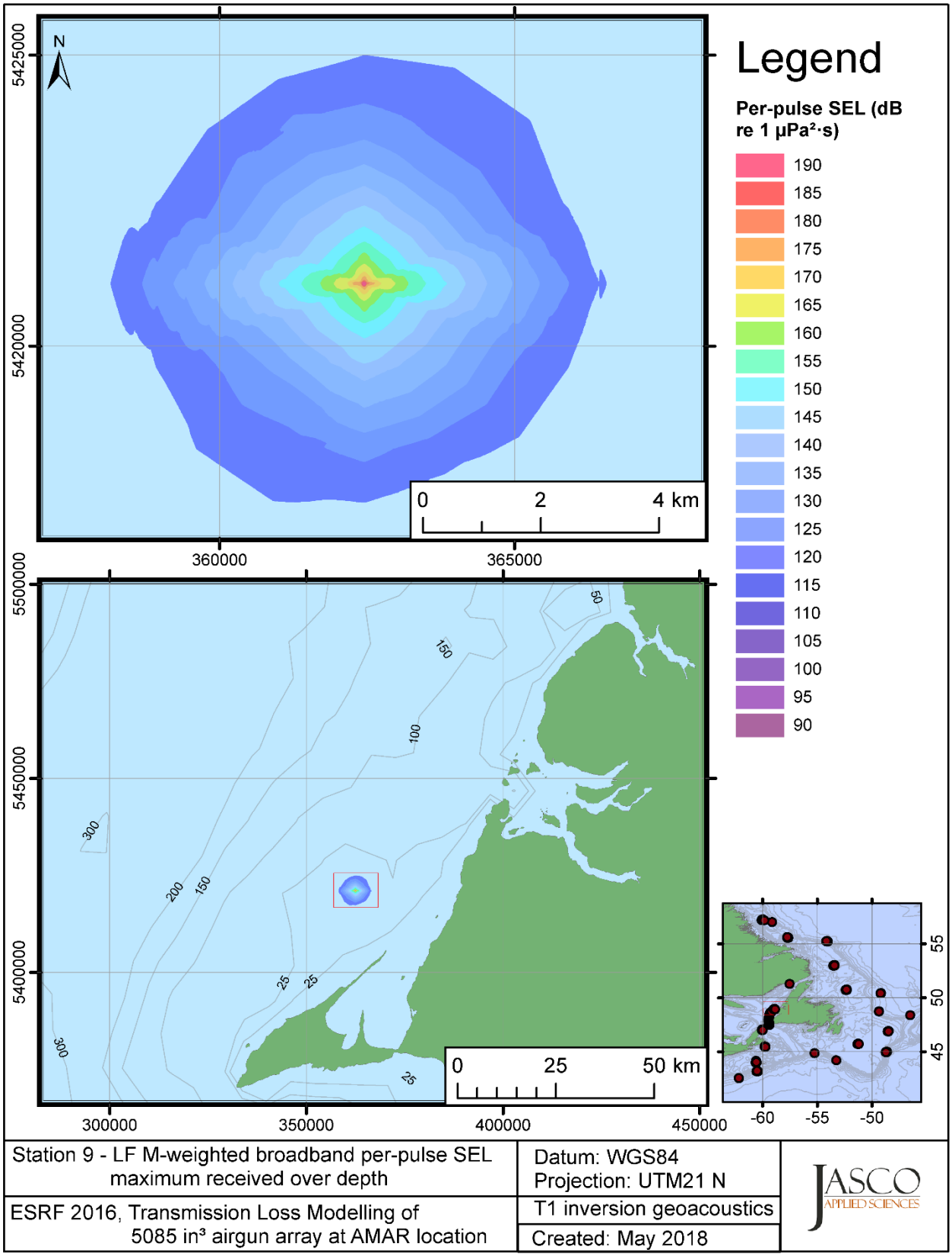

Figure C-299. Stn 9, LF M-weighted maximum-over-depth SEL received at any location on the map, modelled using the track 1 inversion geoacoustic bottom, with the airgun array at the AMAR location and GDEM July SSP.

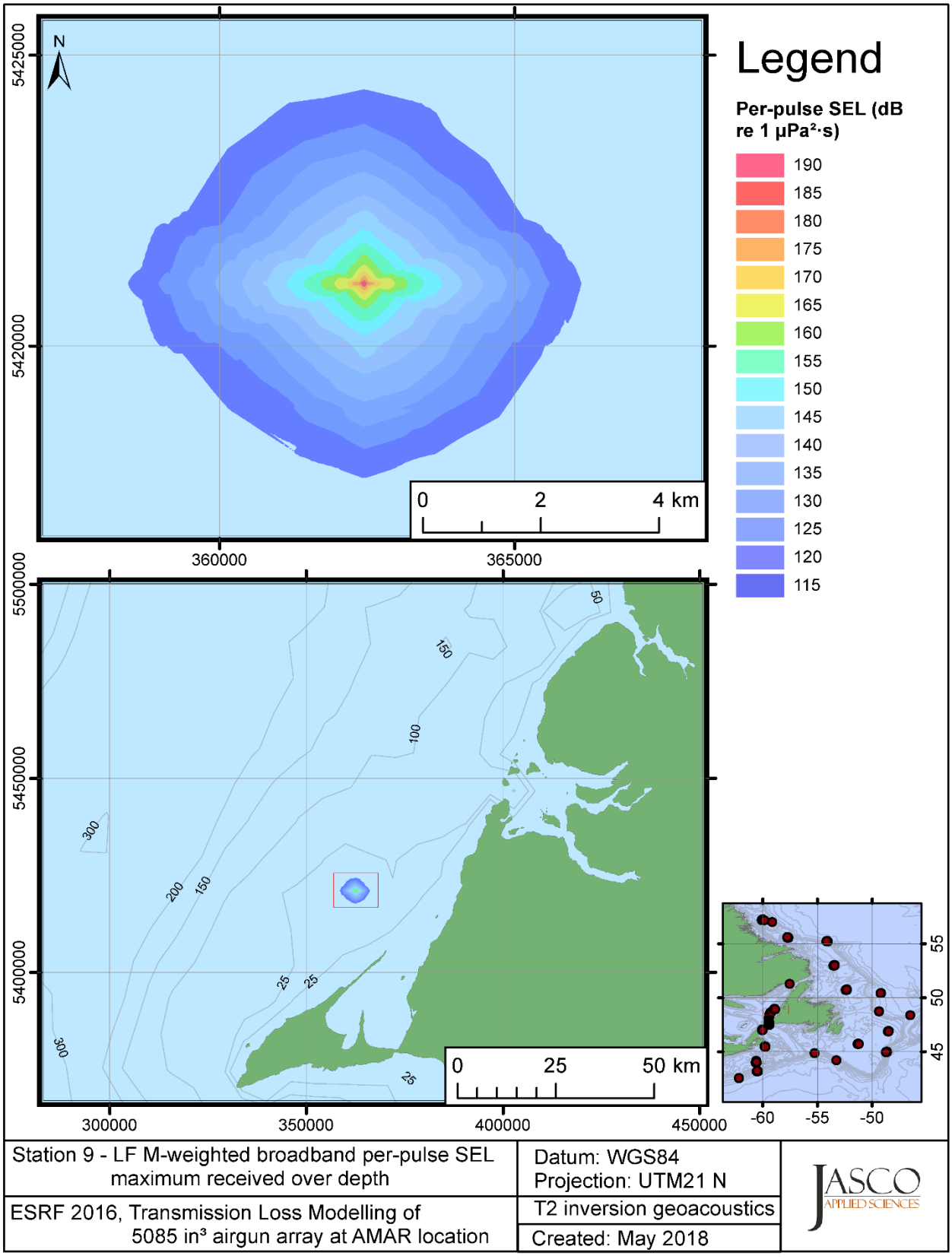

Figure C-300. Stn 9, LF M-weighted maximum-over-depth SEL received at any location on the map, modelled using the track 2 inversion geoacoustic bottom, with the airgun array at the AMAR location and GDEM July SSP.

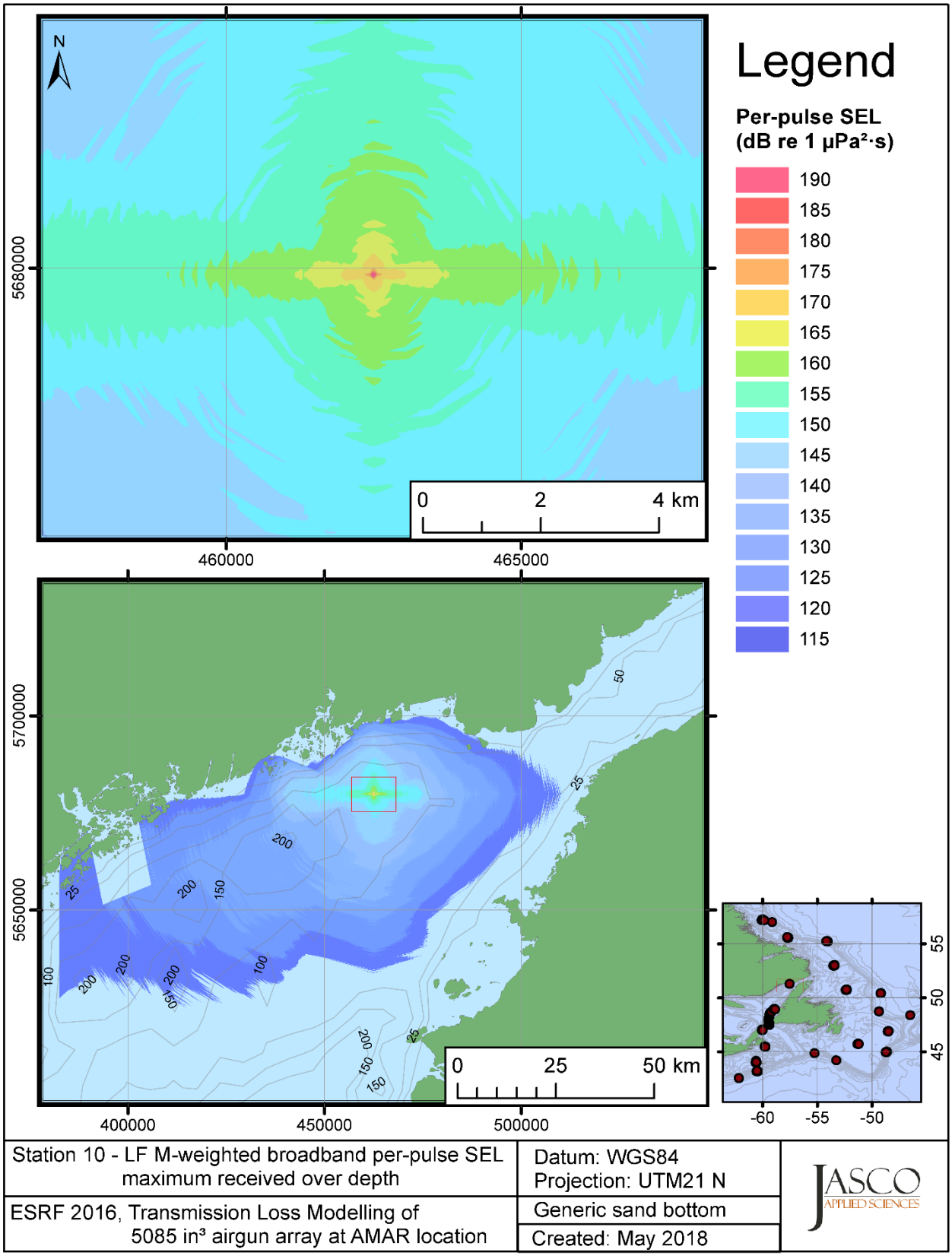

Figure C-301. Stn 10, LF M-weighted maximum-over-depth SEL received at any location on the map, modelled using a generic sand bottom, with the airgun array at the AMAR location and in-situ July SSP.

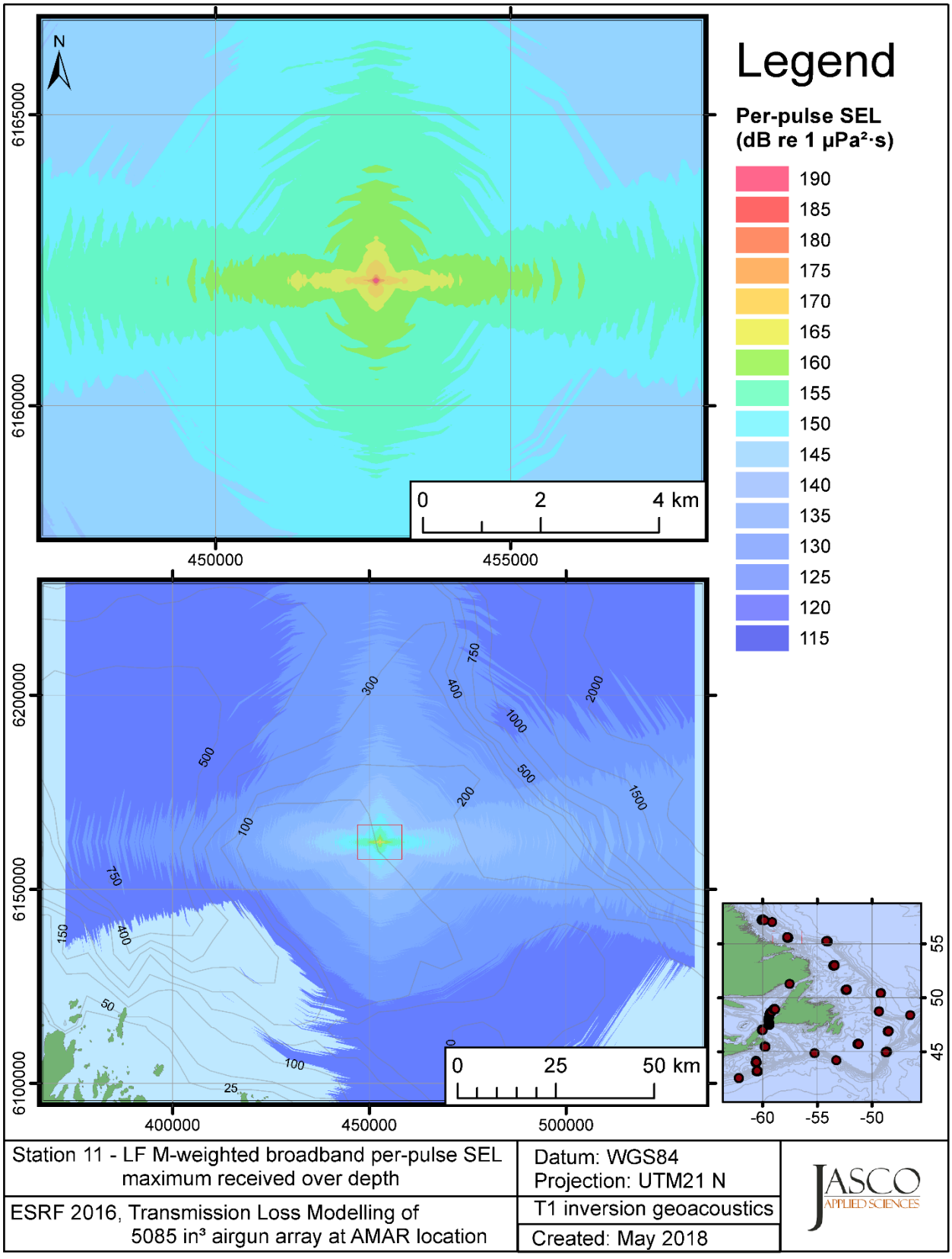

Figure C-302. Stn 11, LF M-weighted maximum-over-depth SEL received at any location on the map, modelled using the track 1 inversion geoacoustic bottom, with the airgun array at the AMAR location and in-situ July SSP.

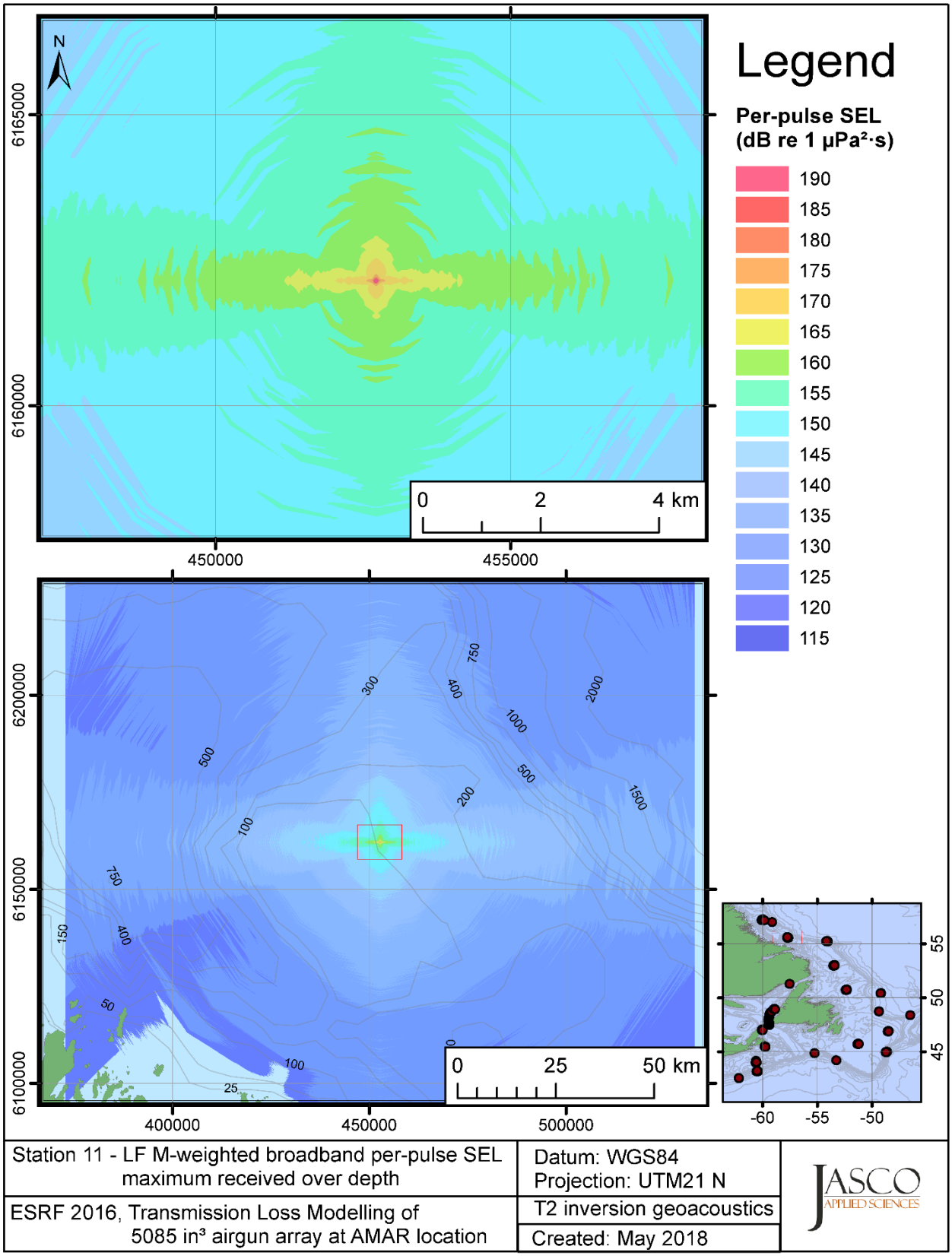

Figure C-303. Stn 11, LF M-weighted maximum-over-depth SEL received at any location on the map, modelled using the track 2 inversion geoacoustic bottom, with the airgun array at the AMAR location and in-situ July SSP.

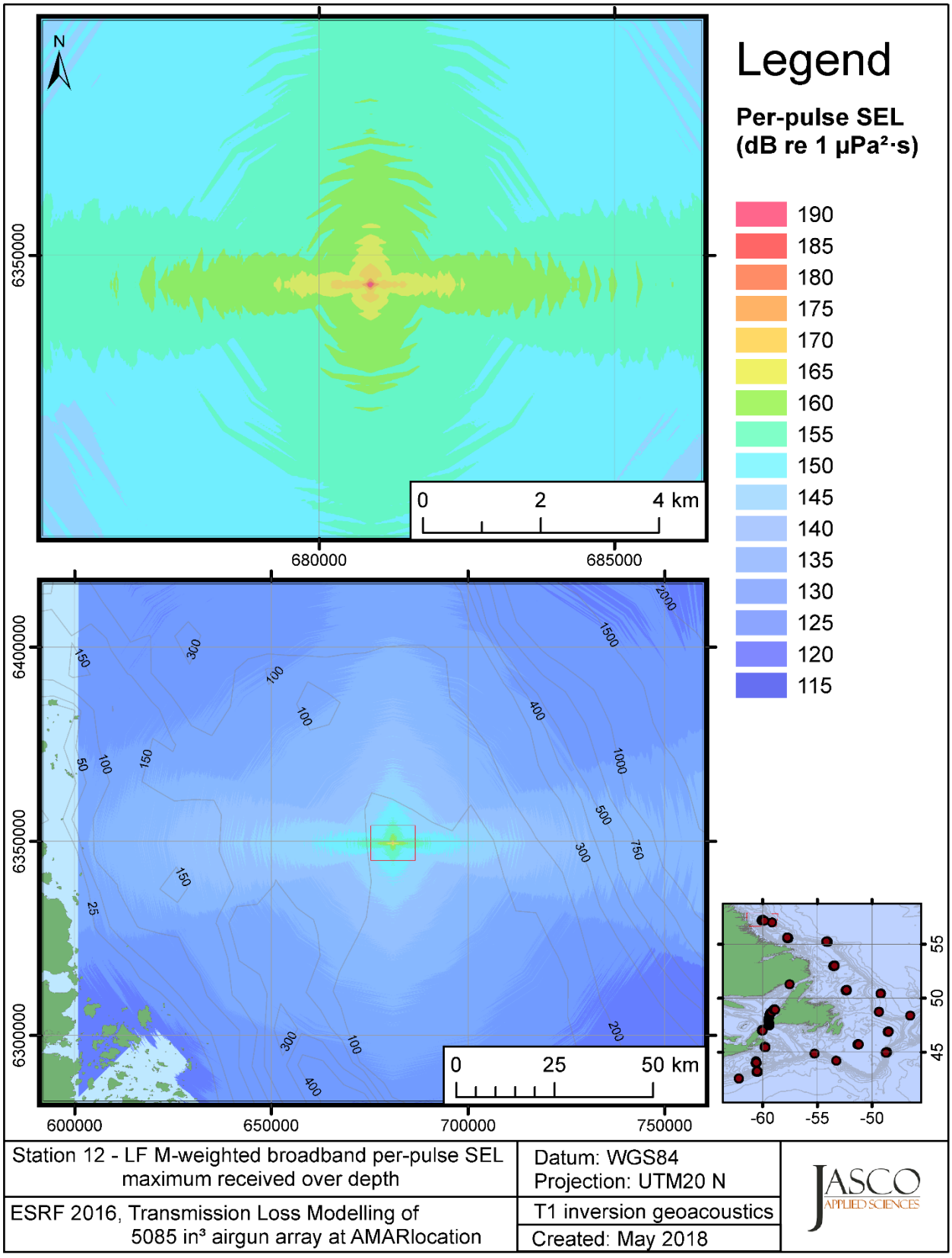

Figure C-304. Stn 12, LF M-weighted maximum-over-depth SEL received at any location on the map, modelled using the track 1 inversion geoacoustic bottom, with the airgun array at the AMAR location and in-situ July SSP.

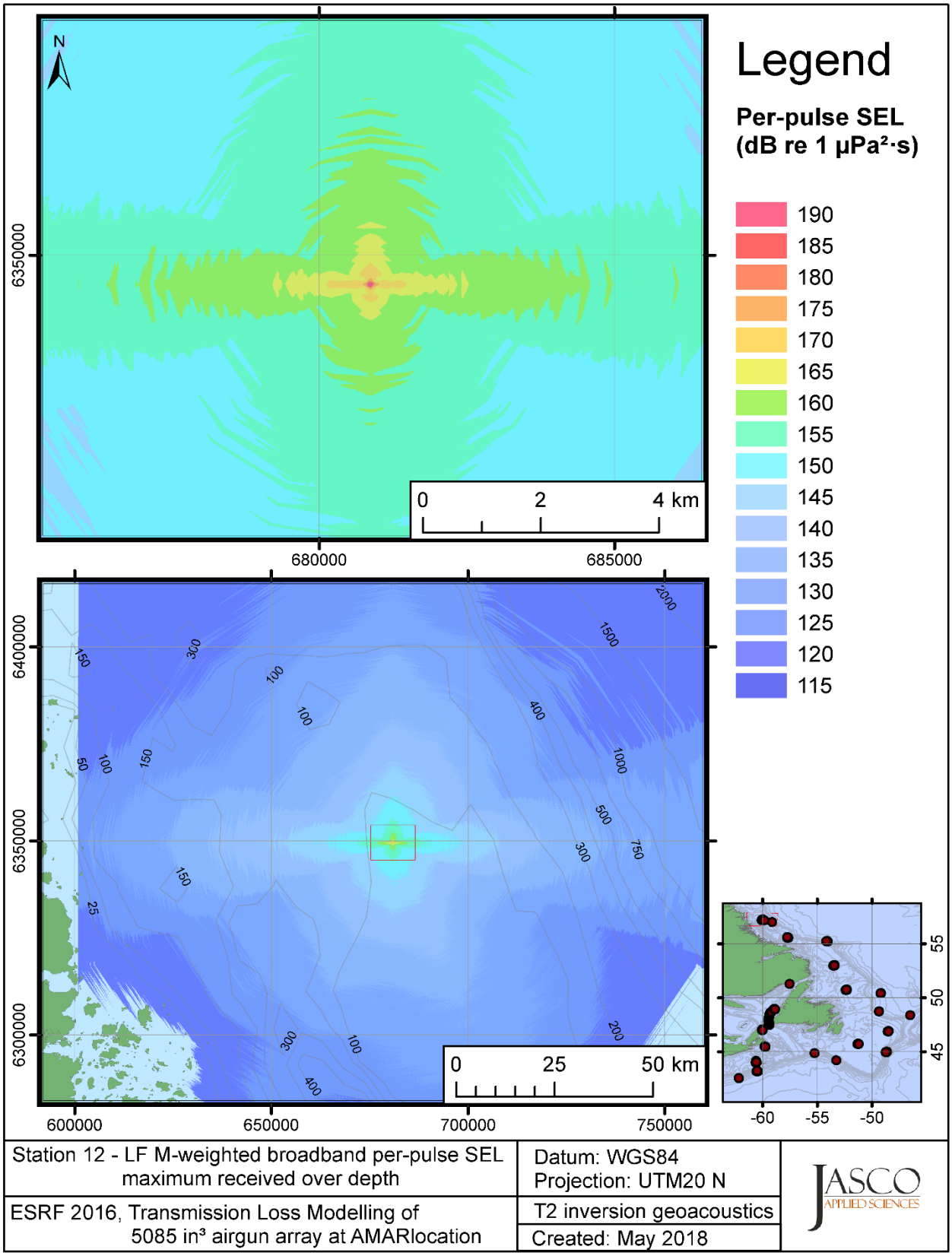

Figure C-305. Stn 12, LF M-weighted maximum-over-depth SEL received at any location on the map, modelled using the track 2 inversion geoacoustic bottom, with the airgun array at the AMAR location and in-situ July SSP.

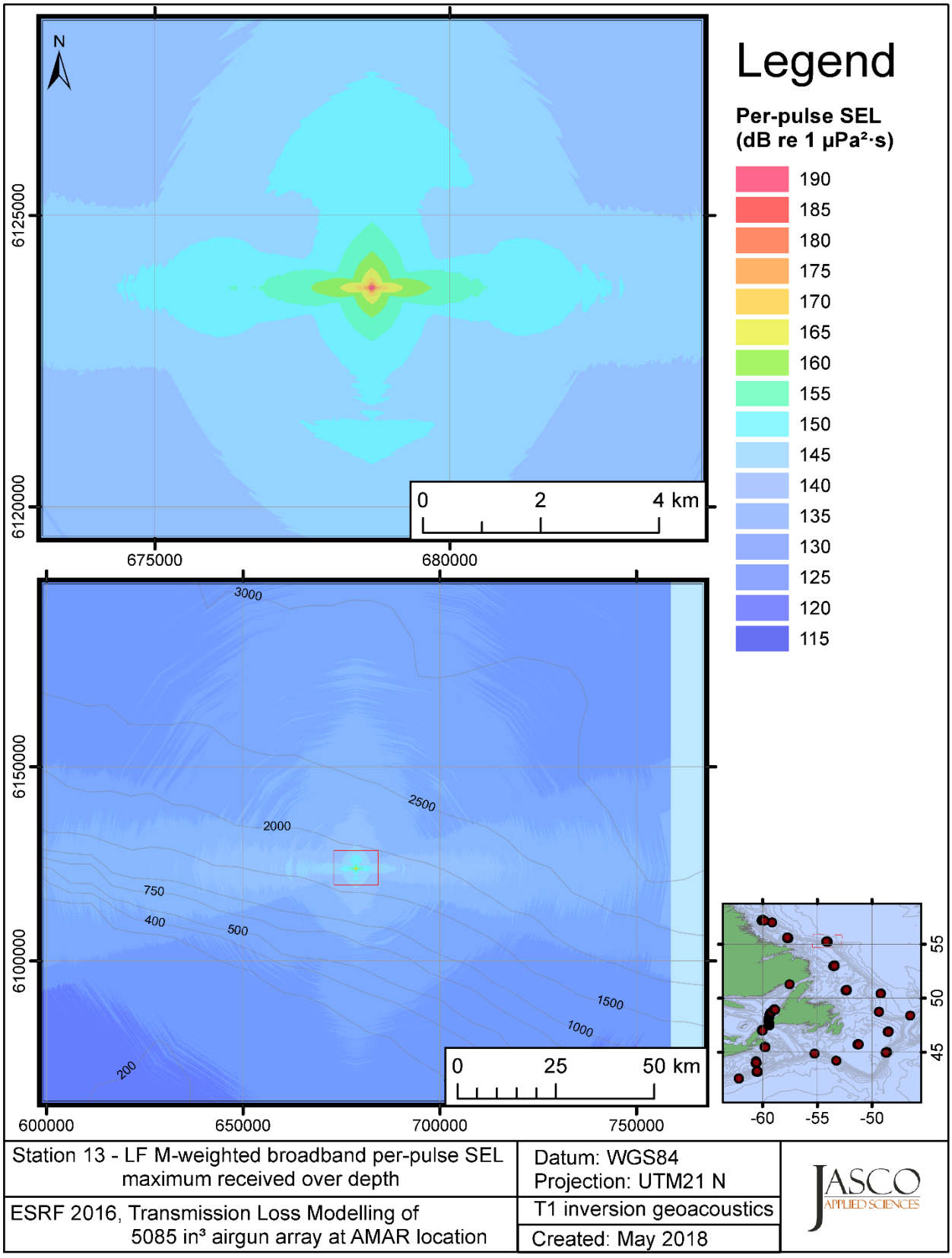

Figure C-306. Stn 13, LF M-weighted maximum-over-depth SEL received at any location on the map, modelled using the track 1 inversion geoacoustic bottom, with the airgun array at the AMAR location and in-situ July SSP.

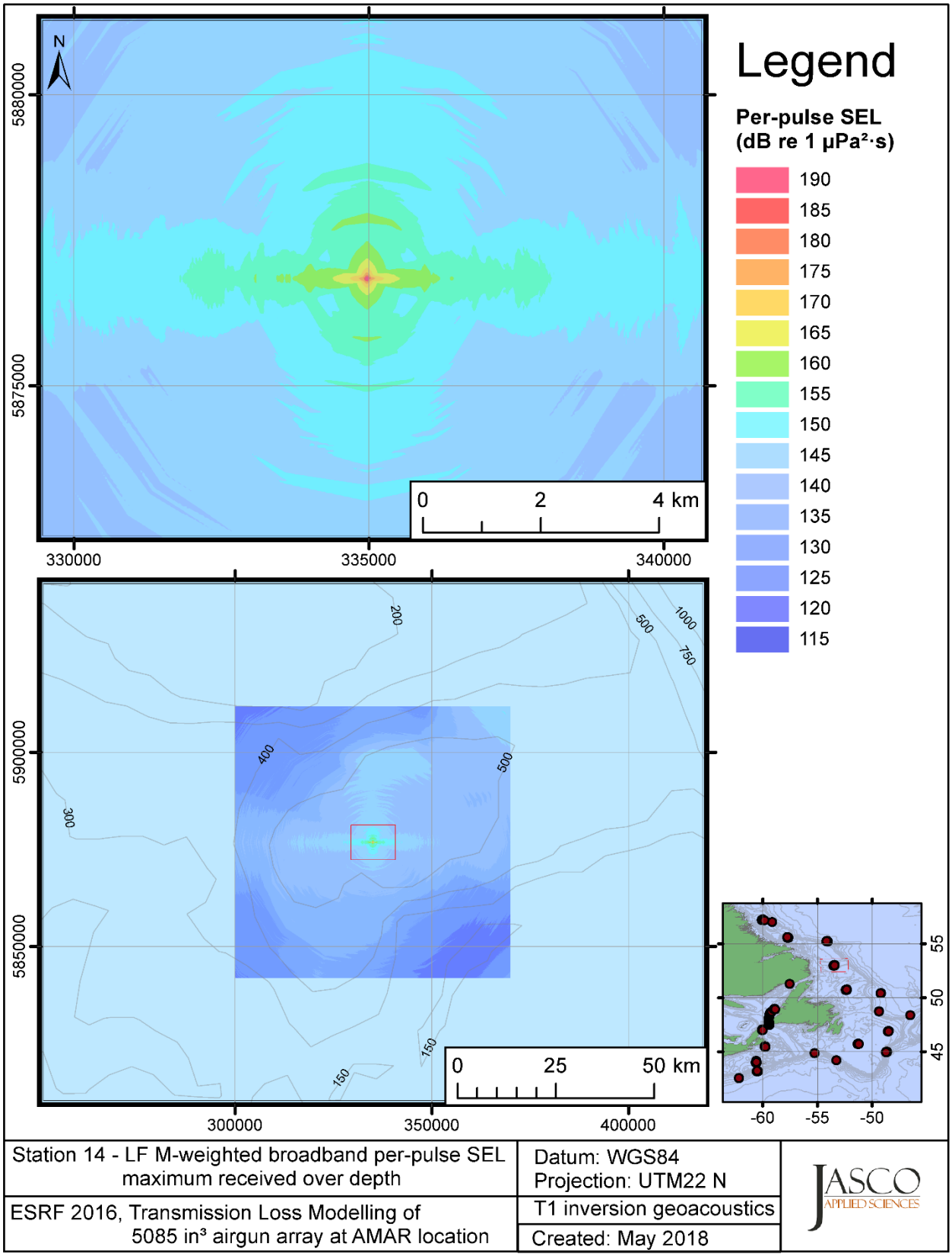

Figure C-307. Stn 14, LF M-weighted maximum-over-depth SEL received at any location on the map, modelled using the track 1 inversion geoacoustic bottom, with the airgun array at the AMAR location and in-situ July SSP.

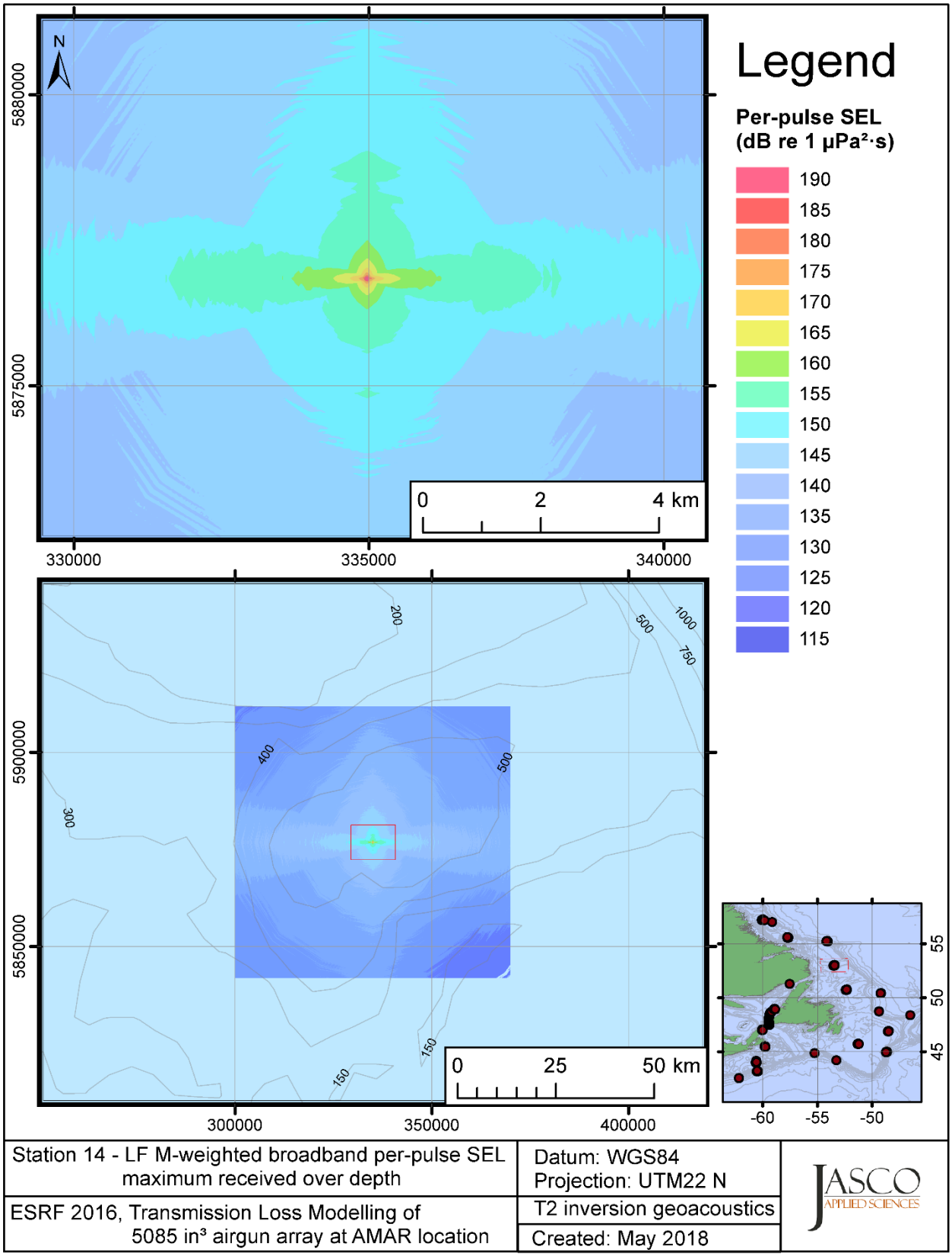

Figure C-308. Stn 14, LF M-weighted maximum-over-depth SEL received at any location on the map, modelled using the track 2 inversion geoacoustic bottom, with the airgun array at the AMAR location and in-situ July SSP.

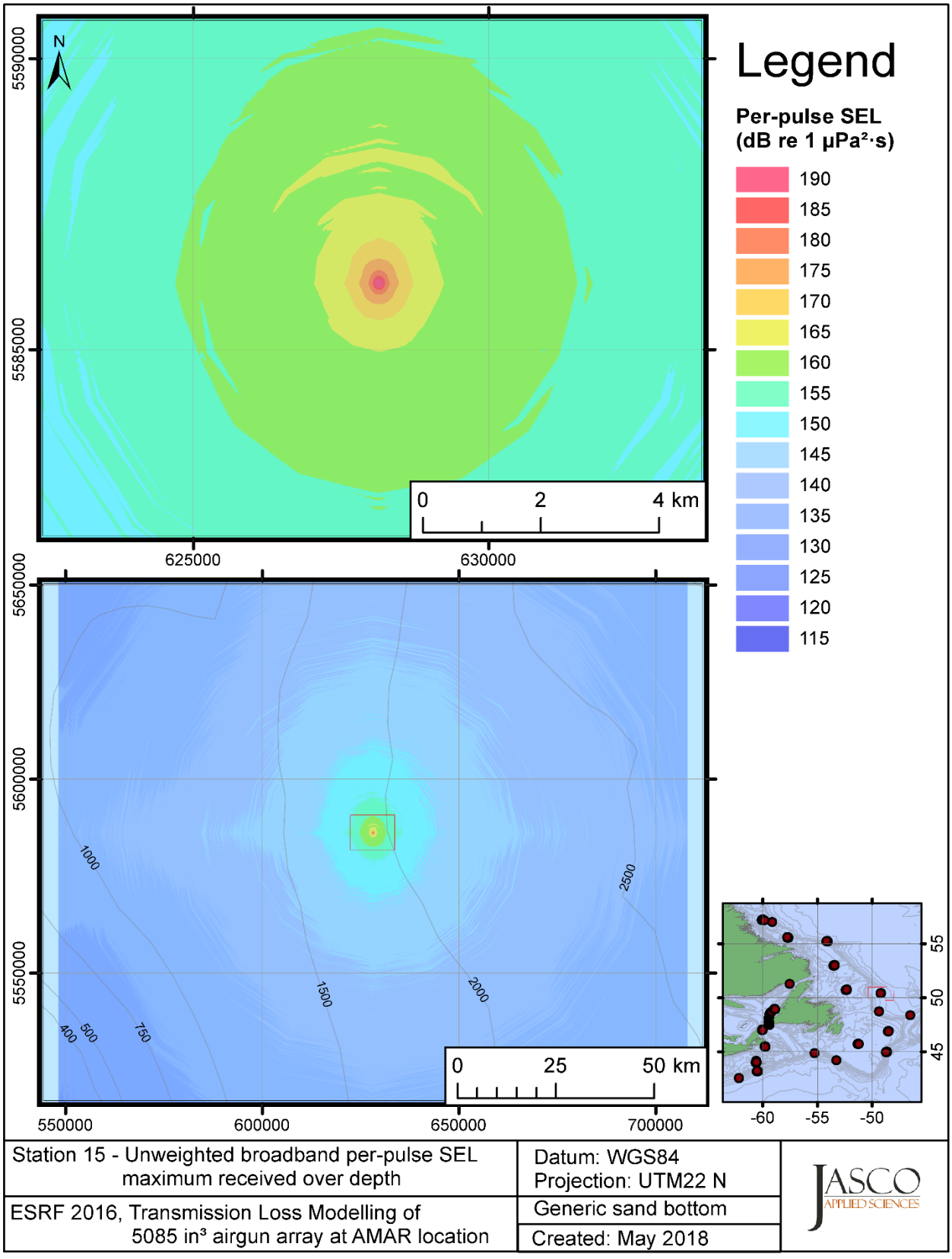

Figure C-309. Stn 15, LF M-weighted maximum-over-depth SEL received at any location on the map, modelled using a generic sand bottom, with the airgun array at the AMAR location and in-situ July SSP.

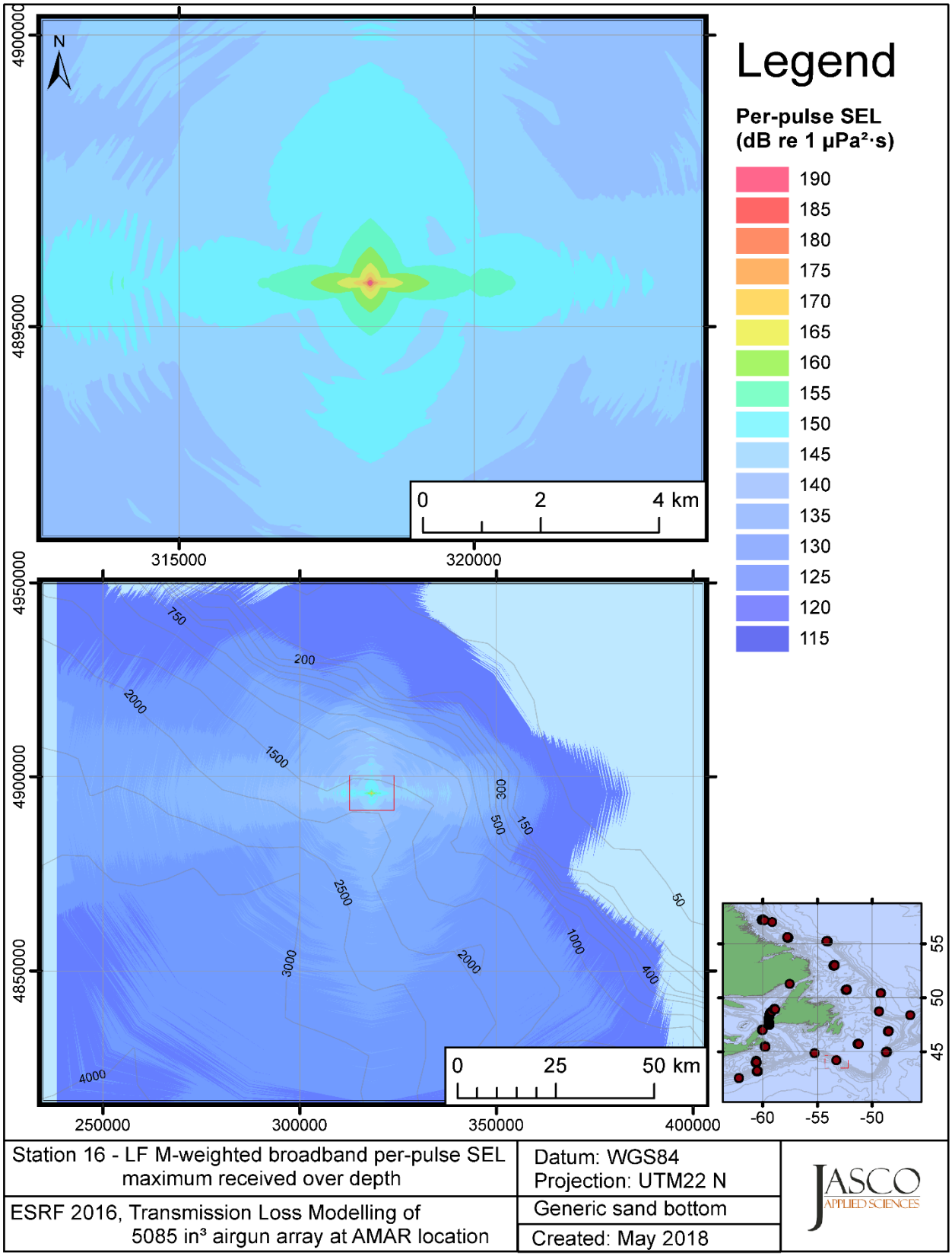

Figure C-310. Stn 16, LF M-weighted maximum-over-depth SEL received at any location on the map, modelled using a generic sand bottom, with the airgun array at the AMAR location and in-situ July SSP.

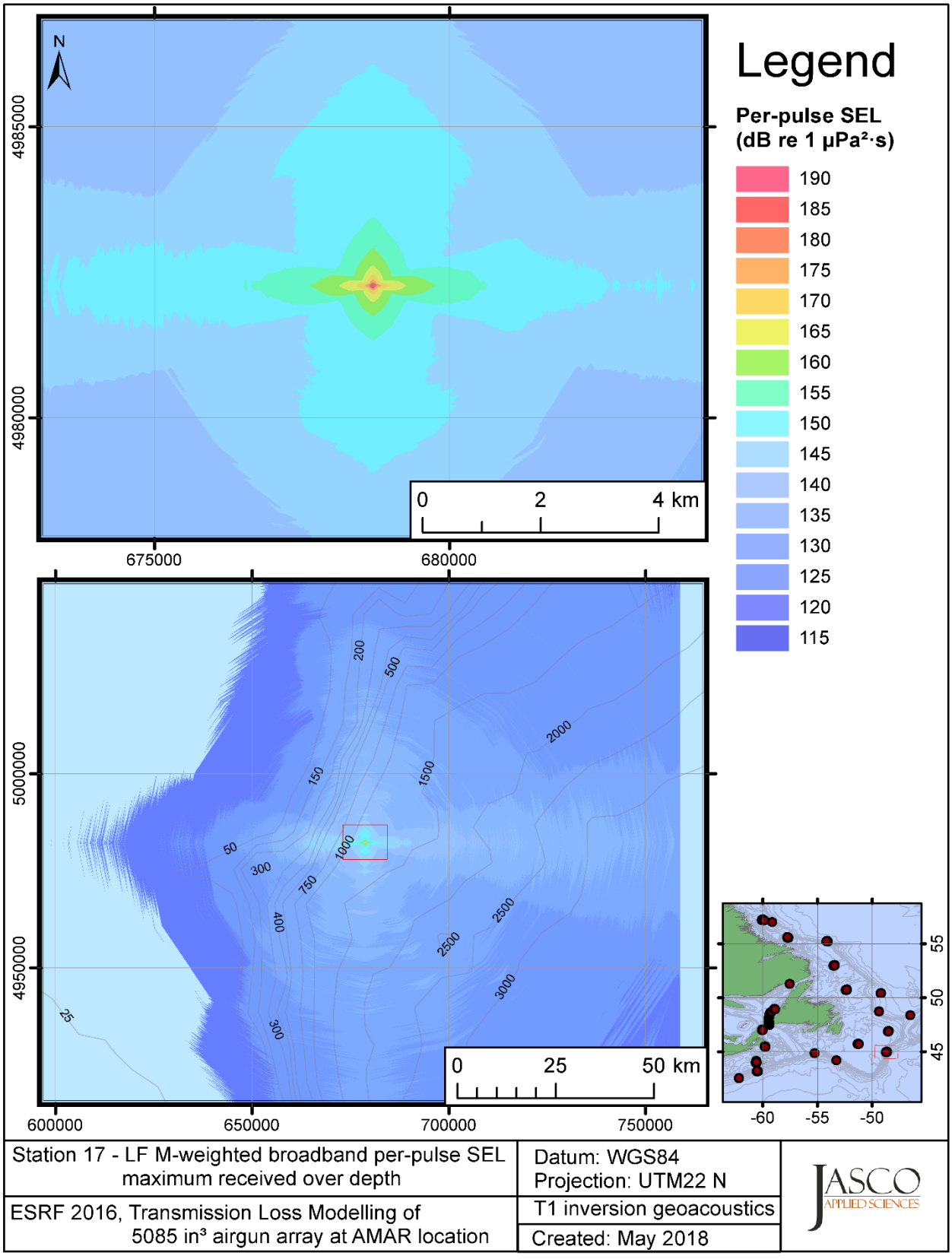

Figure C-311. Stn 17, LF M-weighted maximum-over-depth SEL received at any location on the map, modelled using the track 1 inversion geoacoustic bottom, with the airgun array at the AMAR location and in-situ July SSP.

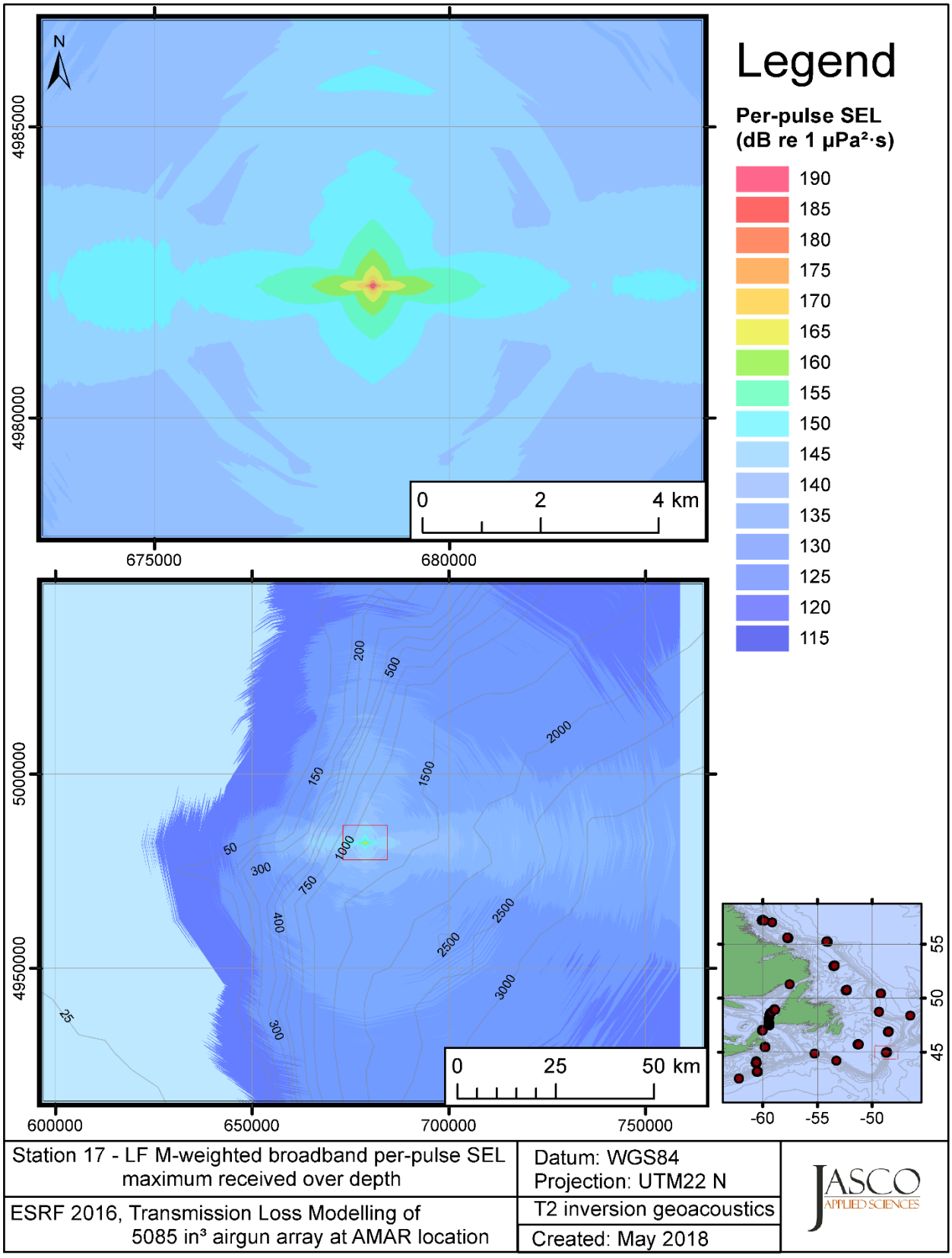

Figure C-312. Stn 17, LF M-weighted maximum-over-depth SEL received at any location on the map, modelled using the track 2 inversion geoacoustic bottom, with the airgun array at the AMAR location and in-situ July SSP.

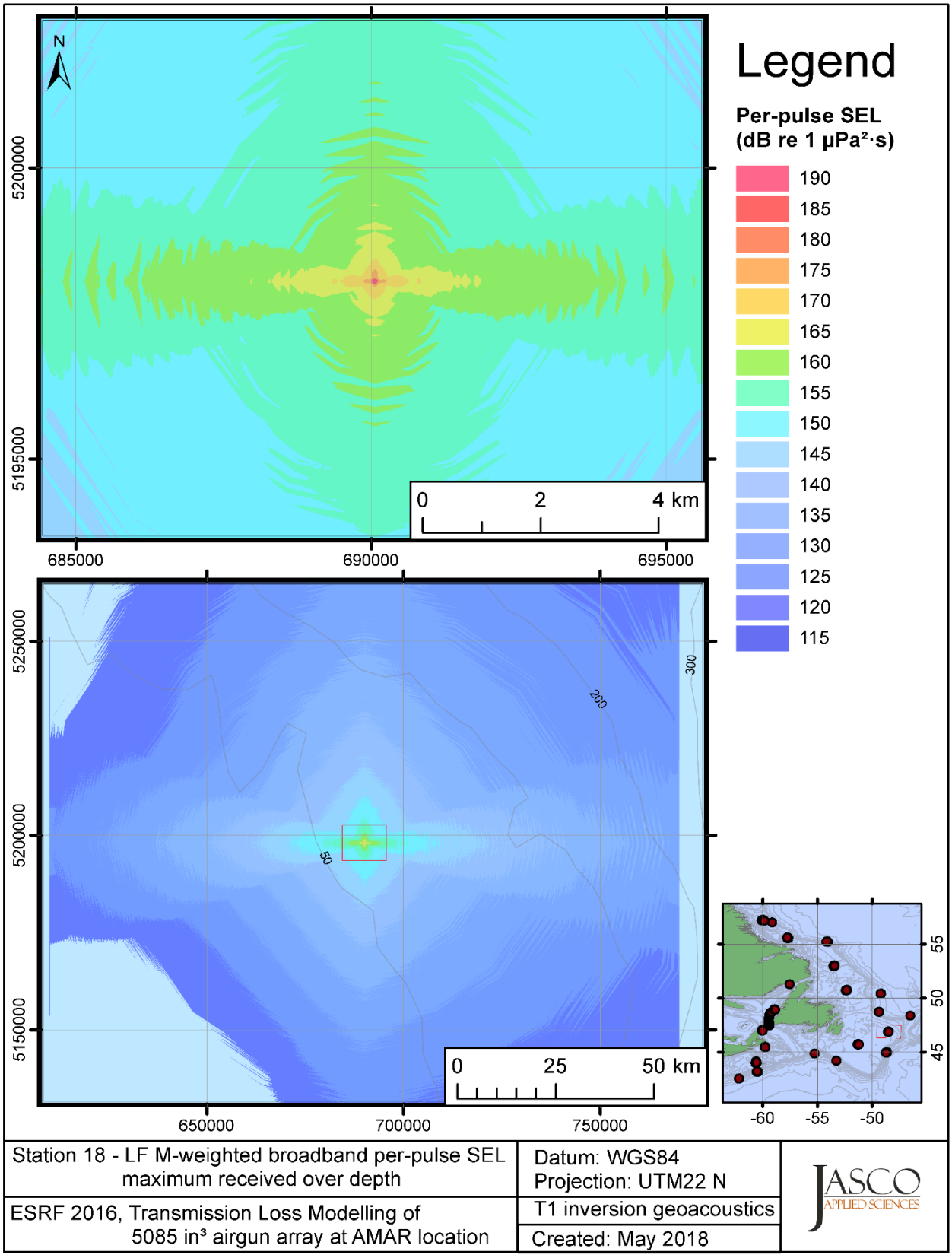

Figure C-313. Stn 18, LF M-weighted maximum-over-depth SEL received at any location on the map, modelled using the track 1 inversion geoacoustic bottom, with the airgun array at the AMAR location and in-situ July SSP.

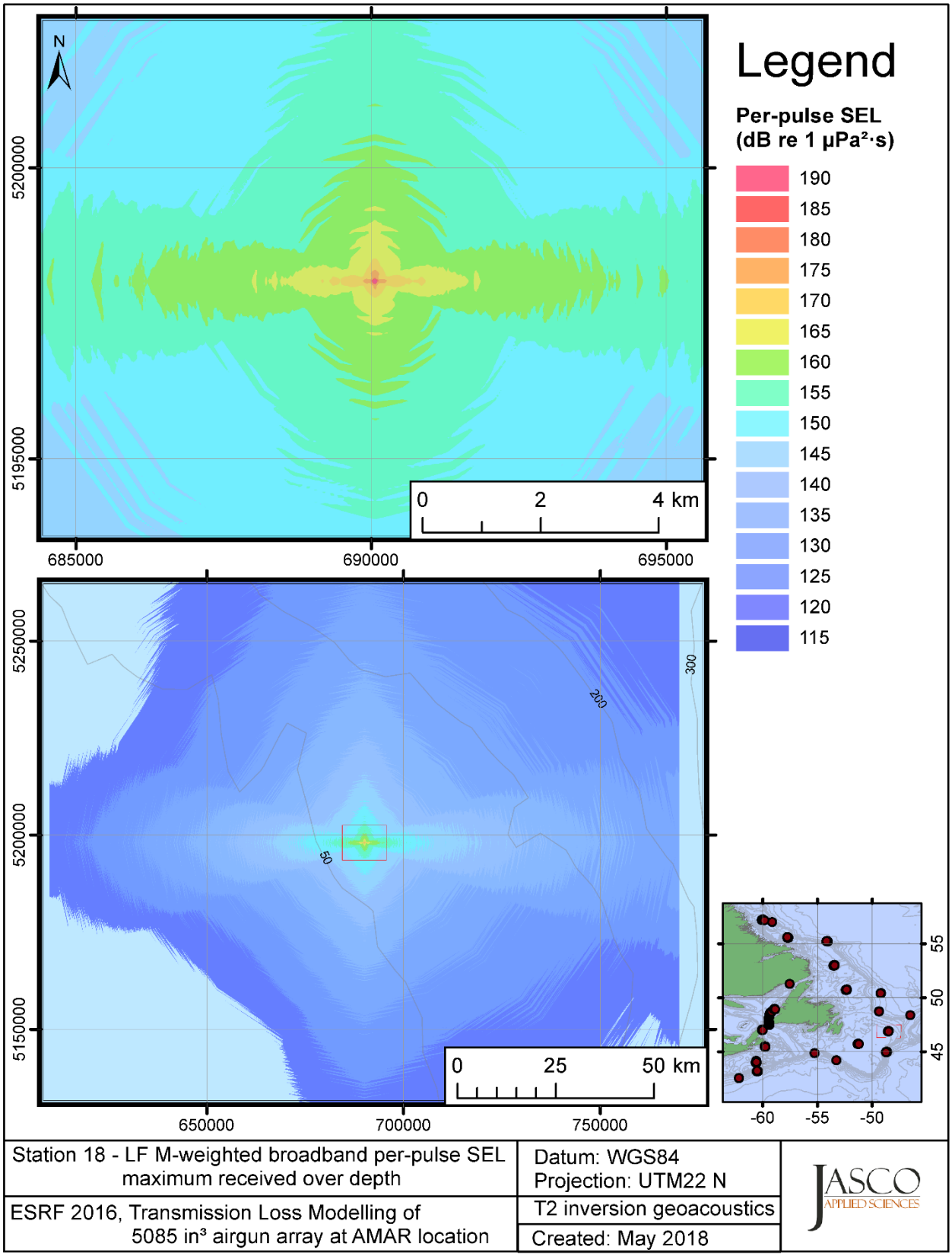

Figure C-314. Stn 18, LF M-weighted maximum-over-depth SEL received at any location on the map, modelled using the track 2 inversion geoacoustic bottom, with the airgun array at the AMAR location and in-situ July SSP.

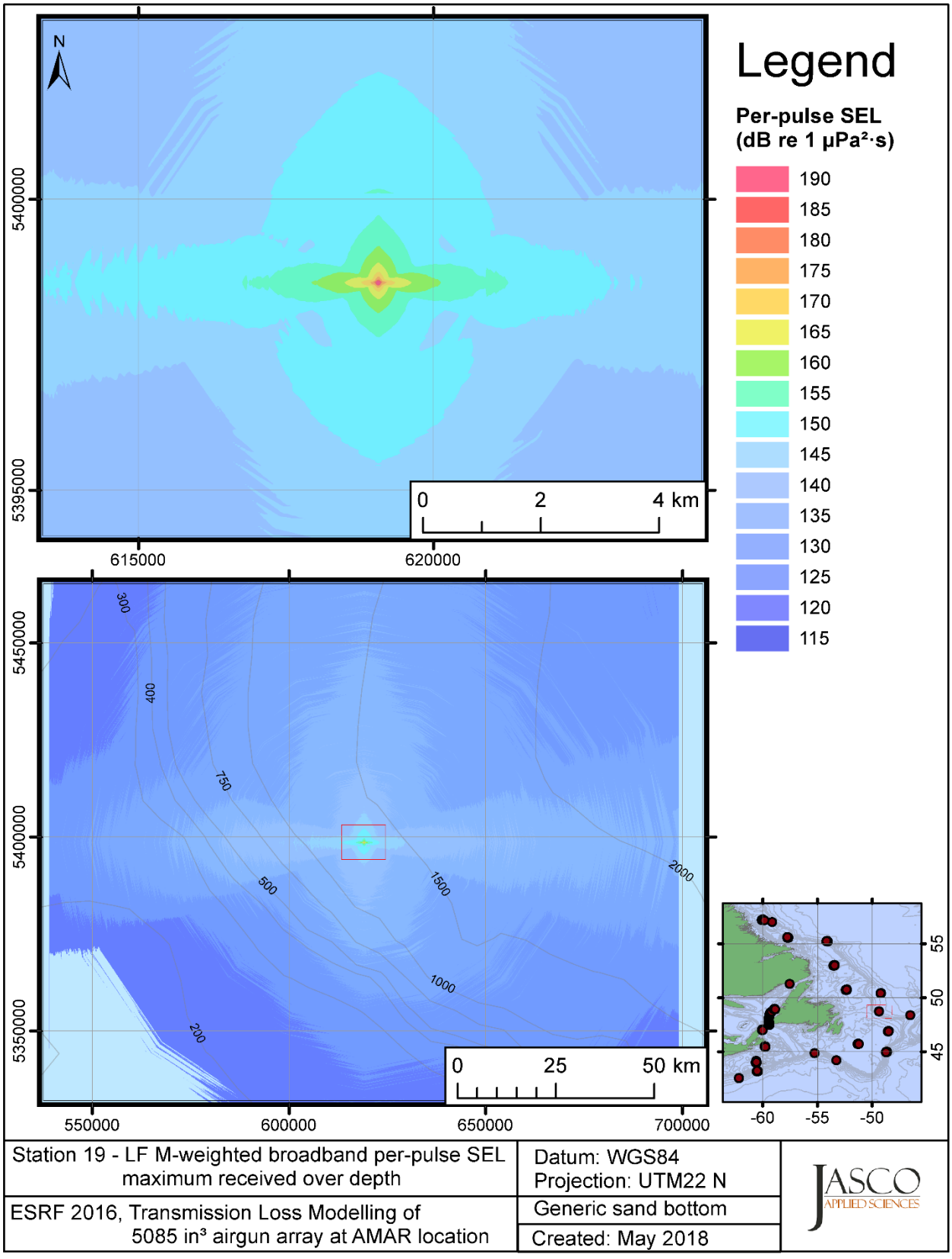

Figure C-315. Stn 19, LF M-weighted maximum-over-depth SEL received at any location on the map, modelled using a generic sand bottom, with the airgun array at the AMAR location and in-situ July SSP.

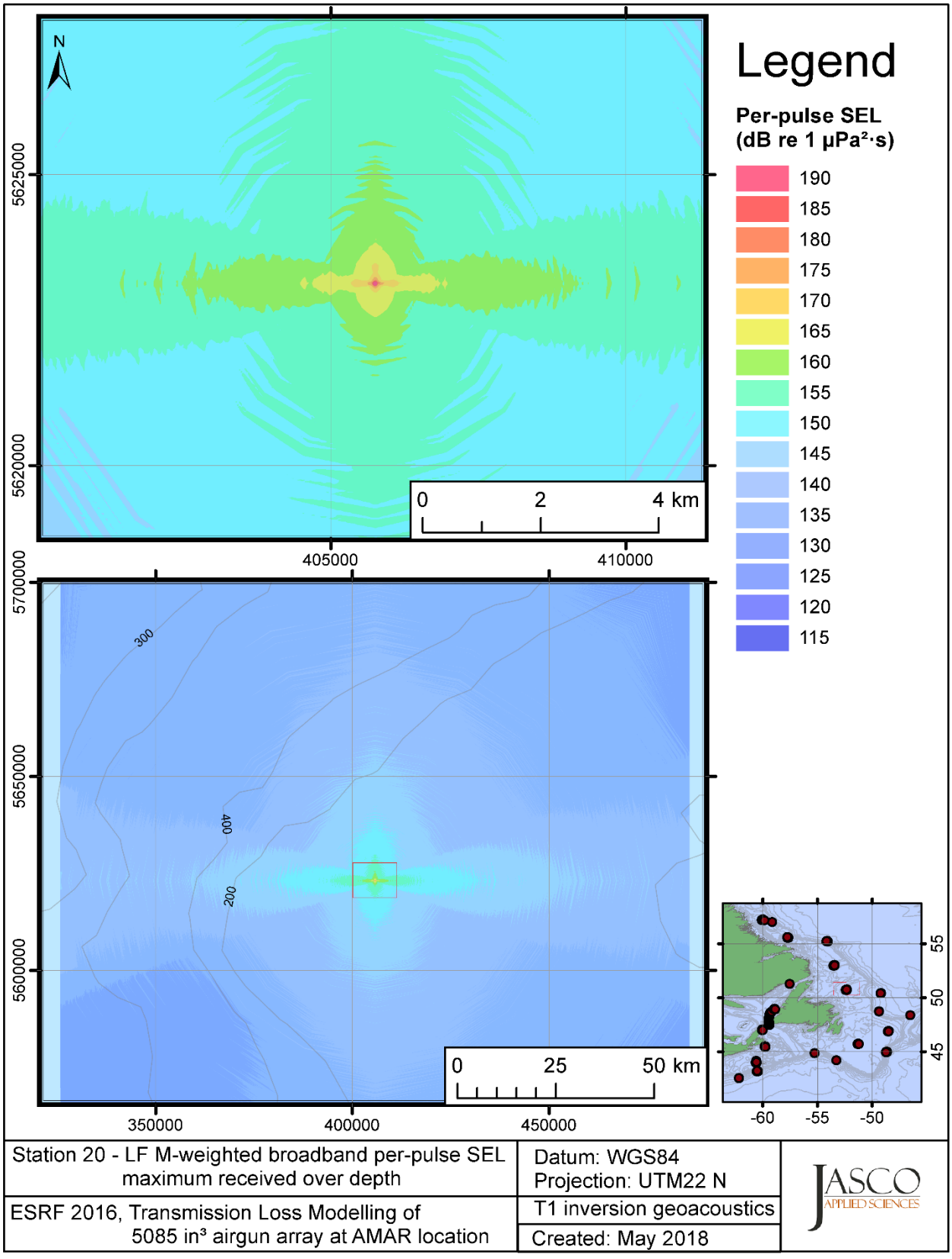

Figure C-316. Stn 20, LF M-weighted maximum-over-depth SEL received at any location on the map, modelled using the track 1 inversion geoacoustic bottom, with the airgun array at the AMAR location and in-situ July SSP.

C.9. Modelling MF M-weighted Max-over-depth Received Level at Distant Locations - Summer

This section presents the results of modelling the maximum-over-depth per-pulse sound exposure level (SEL) received at distant receiver locations (varied in range and azimuth) for the source held fixed at the AMAR location. The modelling uses the geoacoustic inversion bottom parameters at the 14 sites where they are available and only uses a generic sand bottom at the other six sites. The modelling results are presented in the form of coloured maps where the colour at any map location represents the predicted maximum-over-depth received level at that spot on the map. This section includes only the medium-frequency cetaceans (MF) marine-mammal-weighted per-pulse SEL results; additional maps for other marine mammal received level auditory weightings are presented in adjoining sections. The sound speed profiles (SSP) used are detailed in Appendix B.1.

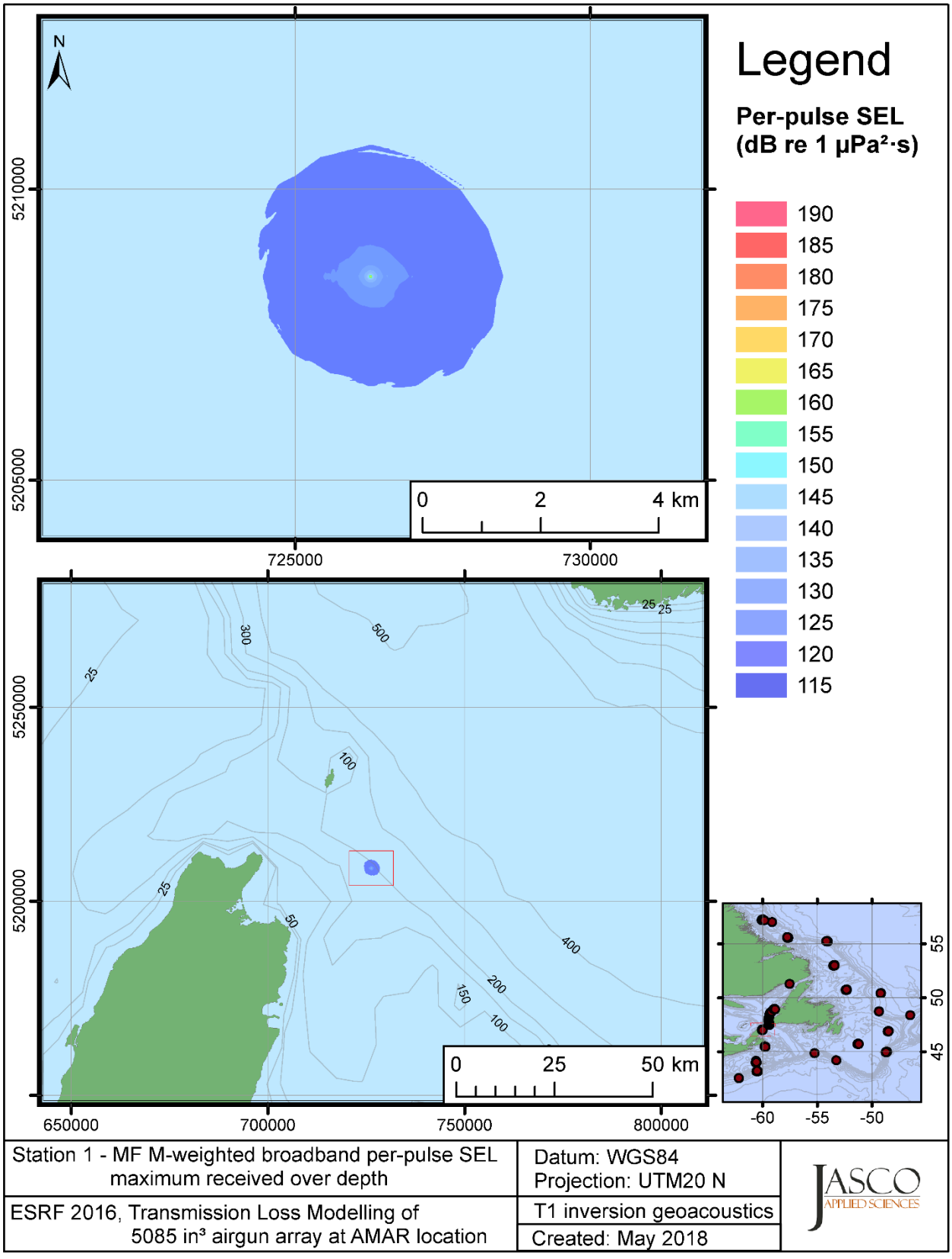

Figure C-317. Stn 1, MF M-weighted maximum-over-depth SEL received at any location on the map, modelled using the track 1 inversion geoacoustic bottom, with the airgun array at the AMAR location and in-situ July SSP.

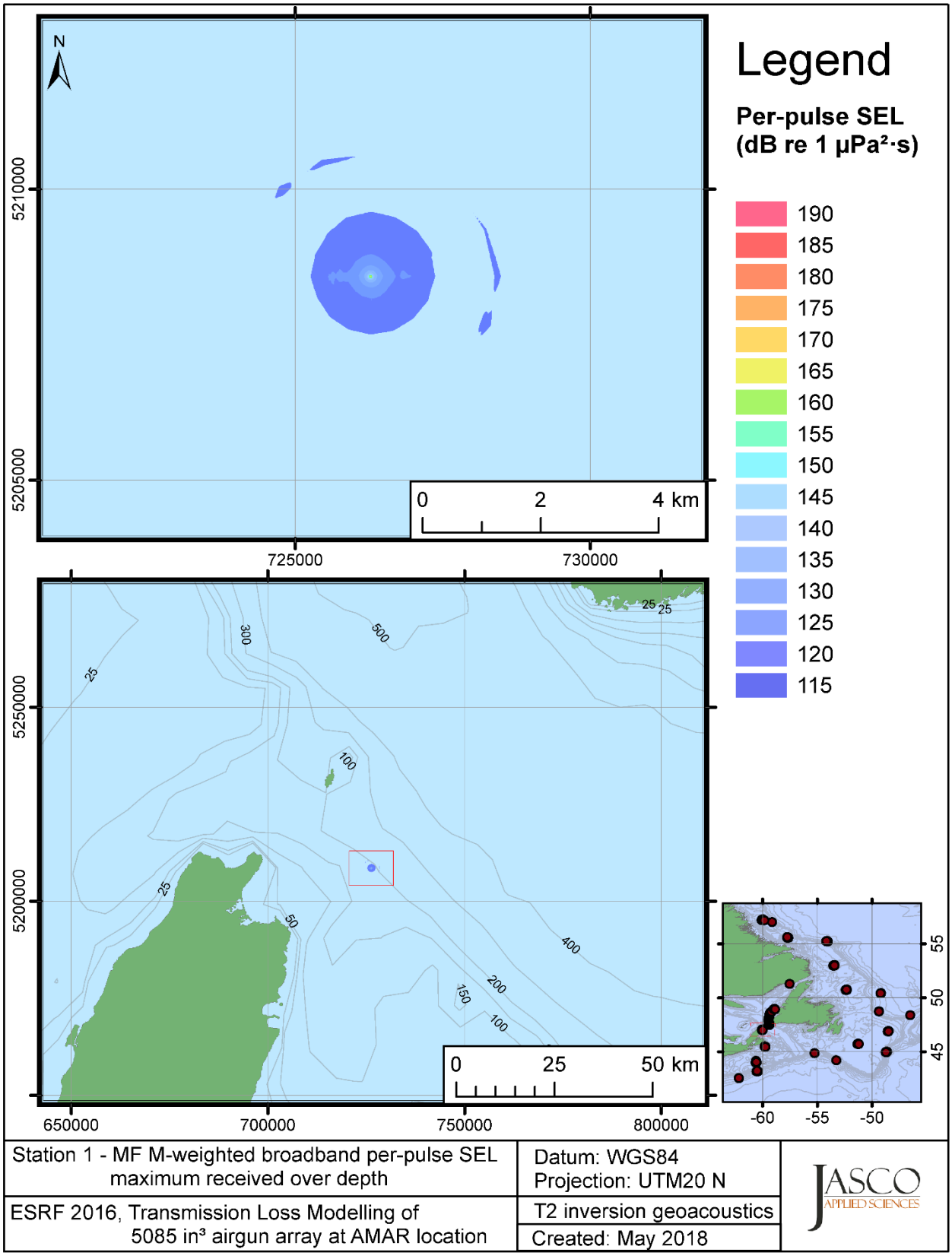

Figure C-318. Stn 1, MF M-weighted maximum-over-depth SEL received at any location on the map, modelled using the track 2 inversion geoacoustic bottom, with the airgun array at the AMAR location and in-situ July SSP.

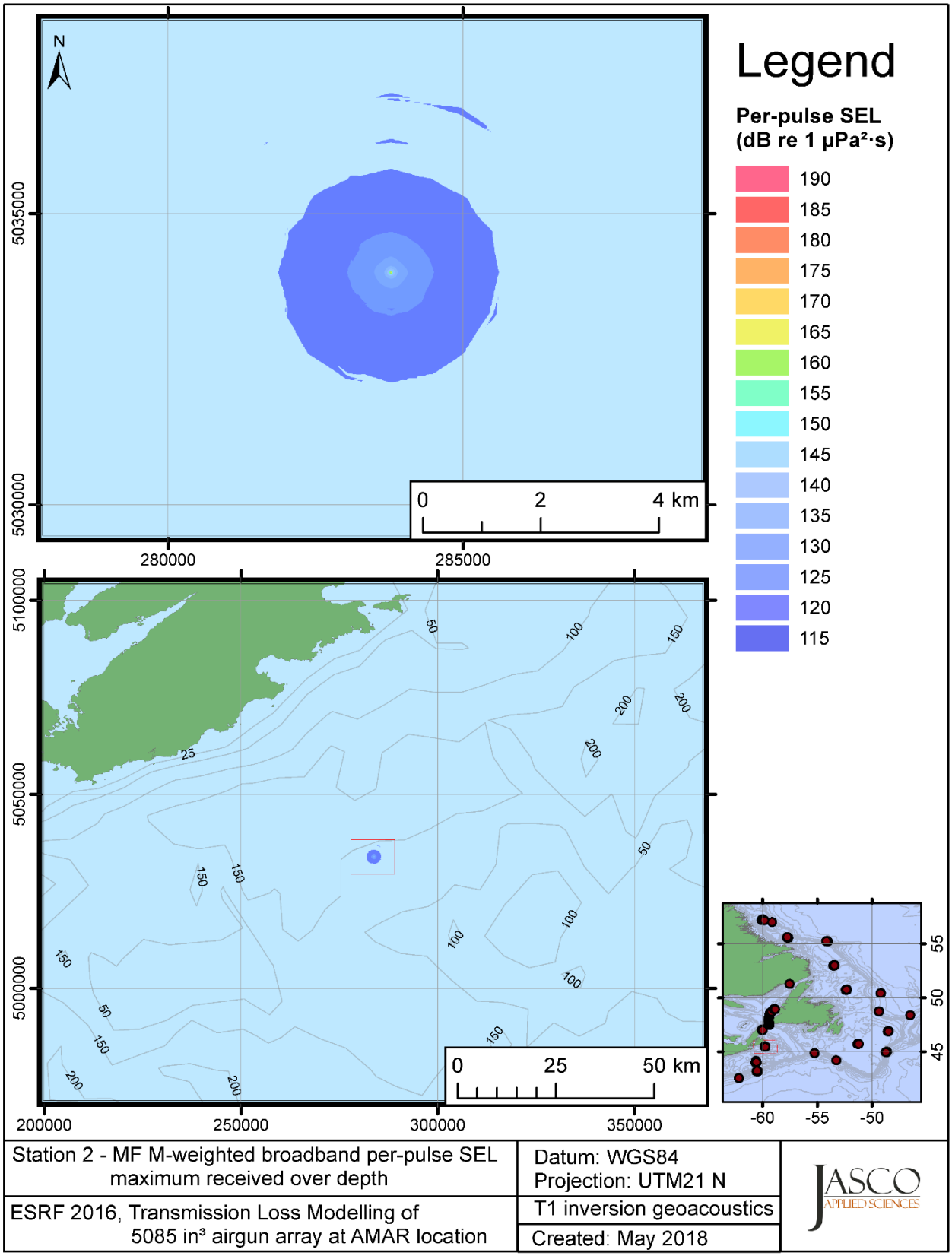

Figure C-319. Stn 2, MF M-weighted maximum-over-depth SEL received at any location on the map, modelled using the track 1 inversion geoacoustic bottom, with the airgun array at the AMAR location and in-situ July SSP.

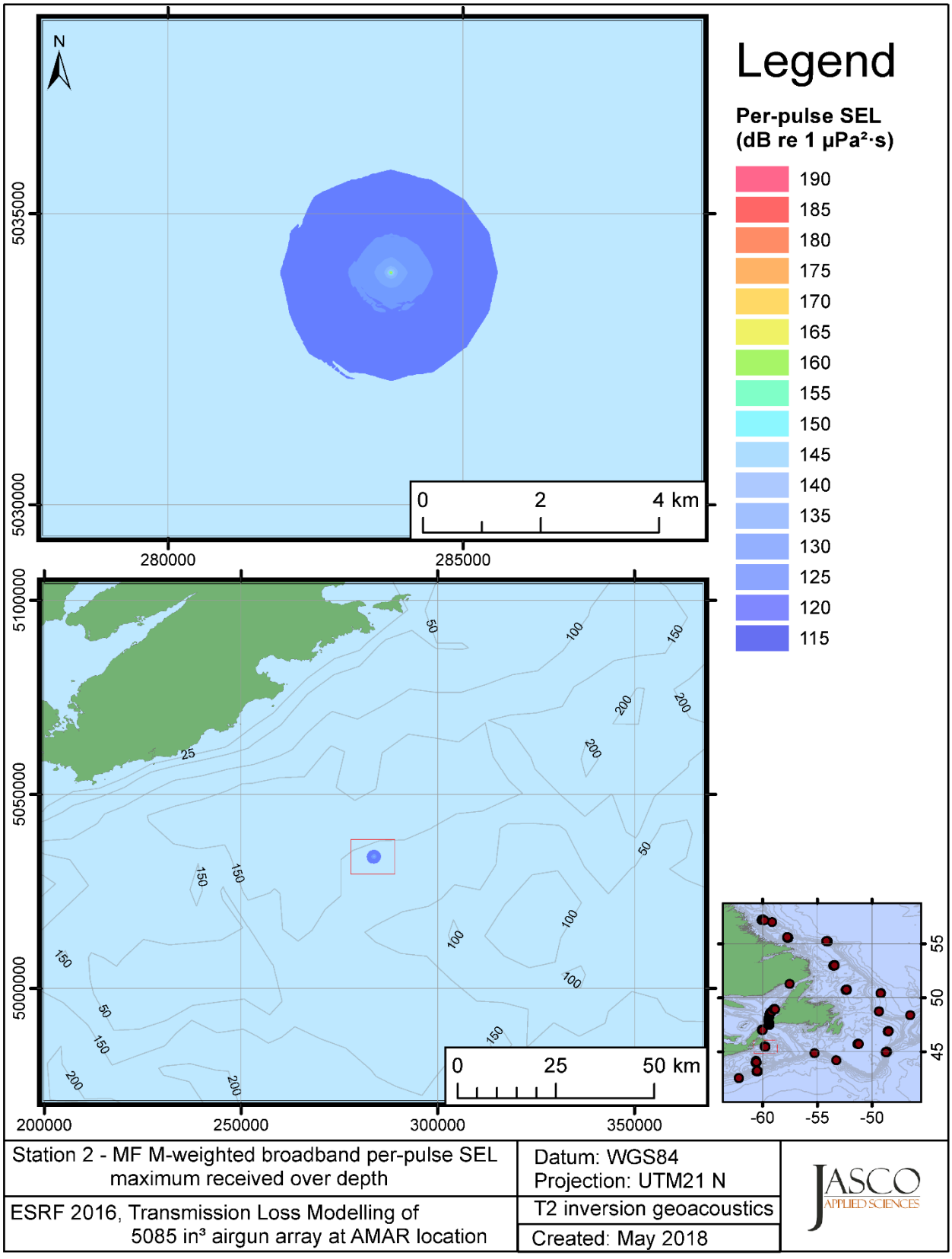

Figure C-320. Stn 2, MF M-weighted maximum-over-depth SEL received at any location on the map, modelled using the track 2 inversion geoacoustic bottom, with the airgun array at the AMAR location and in-situ July SSP.

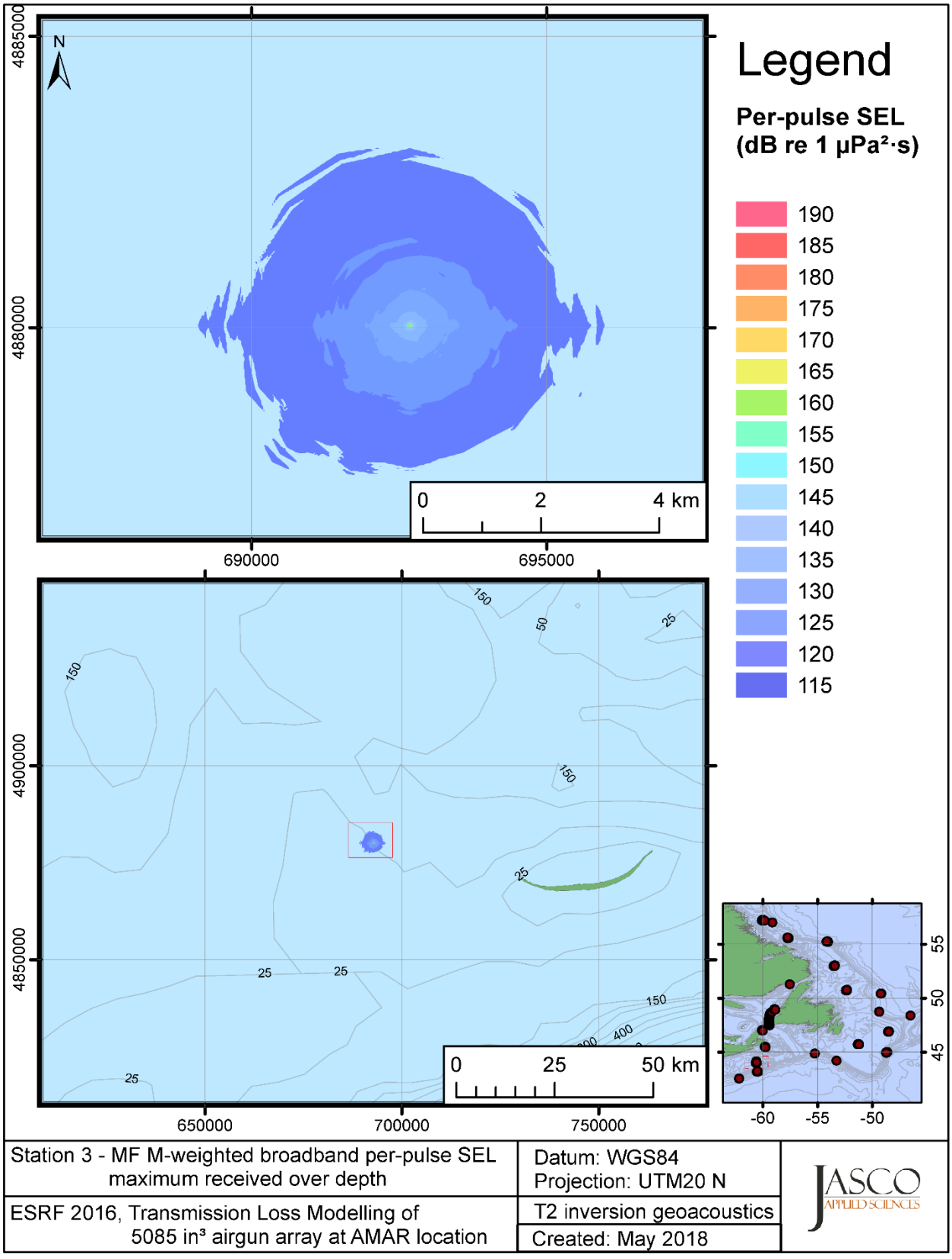

Figure C-321. Stn 3, MF M-weighted maximum-over-depth SEL received at any location on the map, modelled using the track 2 inversion geoacoustic bottom, with the airgun array at the AMAR location and in-situ July SSP.

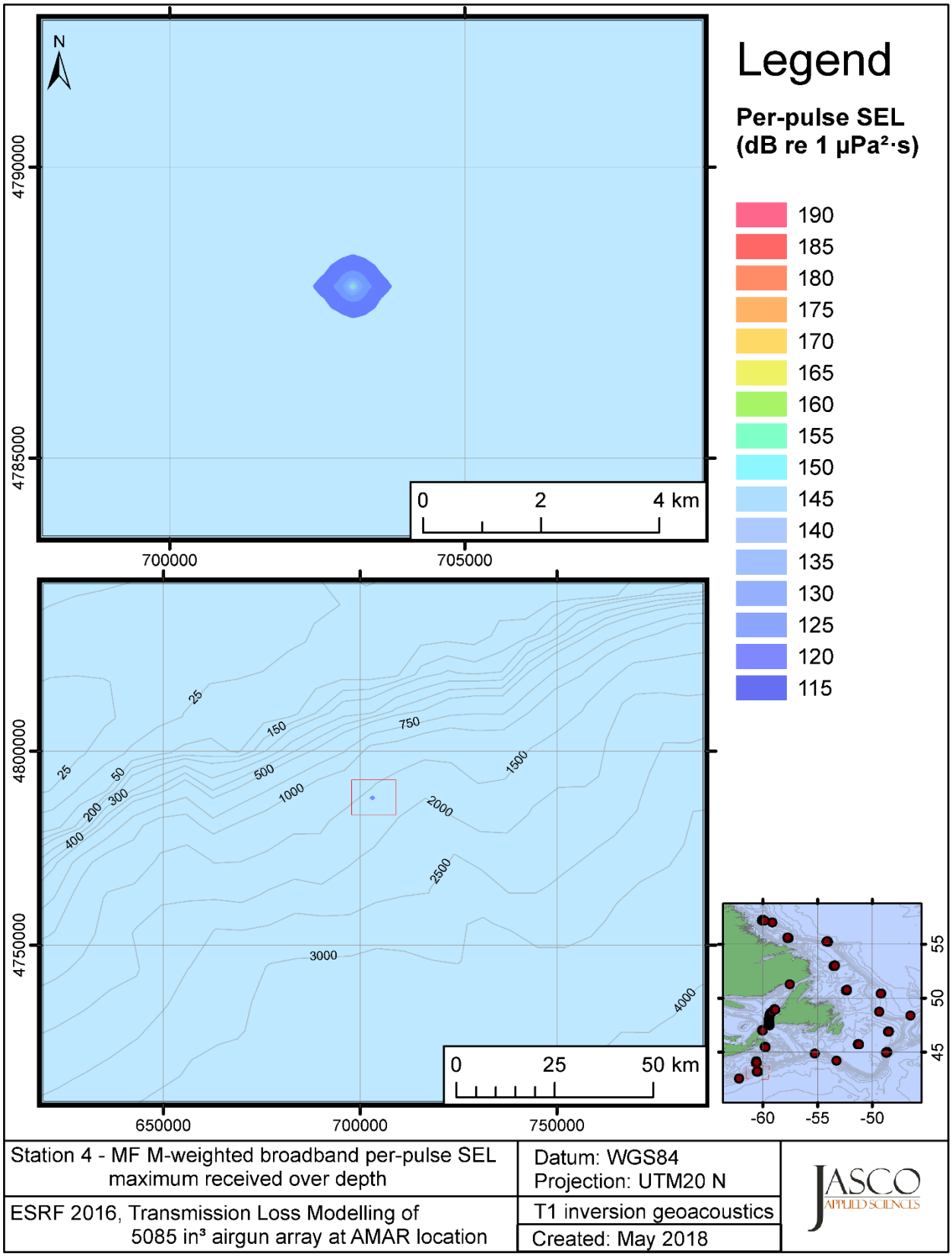

Figure C-322. Stn 4, MF M-weighted maximum-over-depth SEL received at any location on the map, modelled using the track 1 inversion geoacoustic bottom, with the airgun array at the AMAR location and in-situ July SSP.

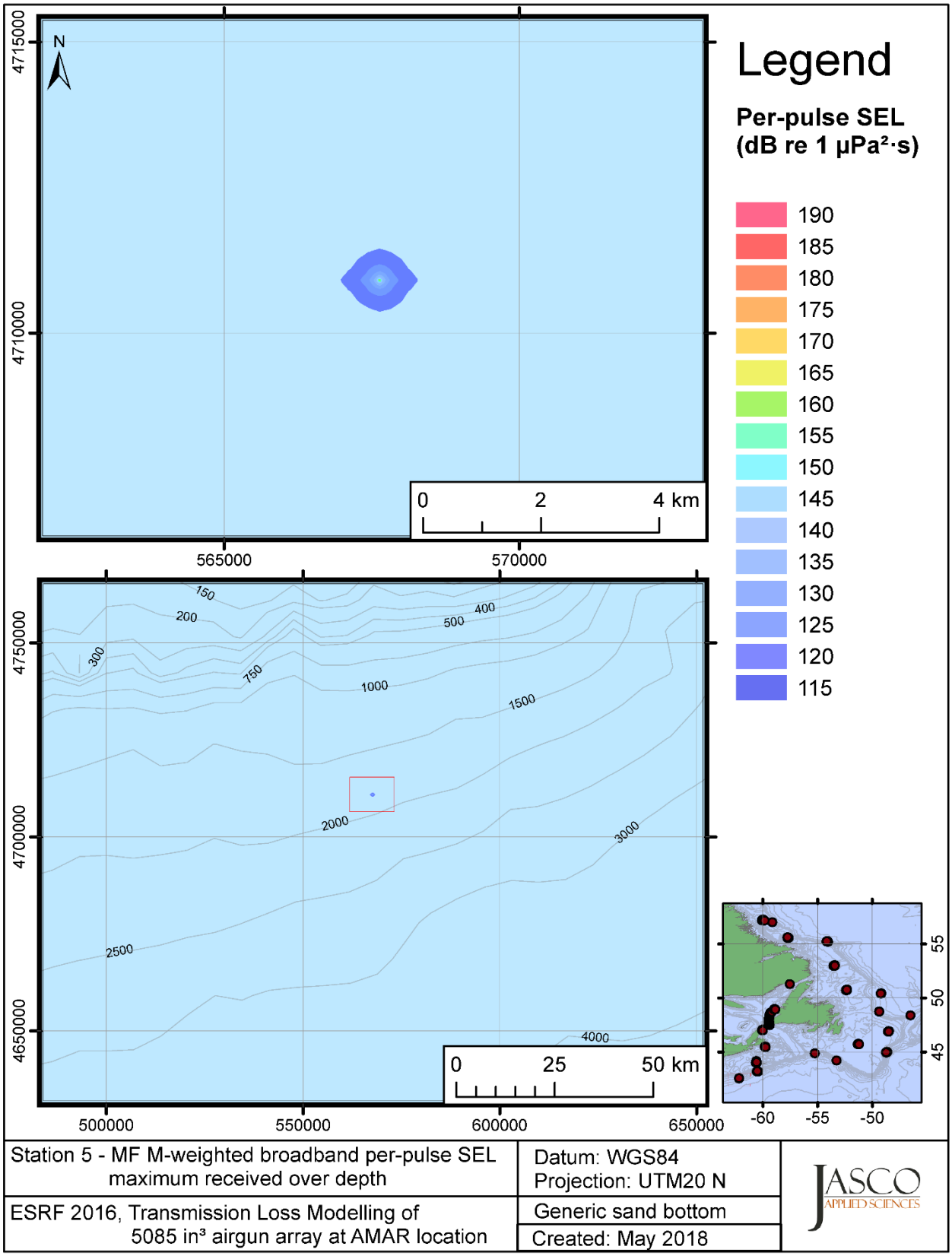

Figure C-323. Stn 5, MF M-weighted maximum-over-depth SEL received at any location on the map, modelled using a generic sand bottom, with the airgun array at the AMAR location and in-situ July SSP.

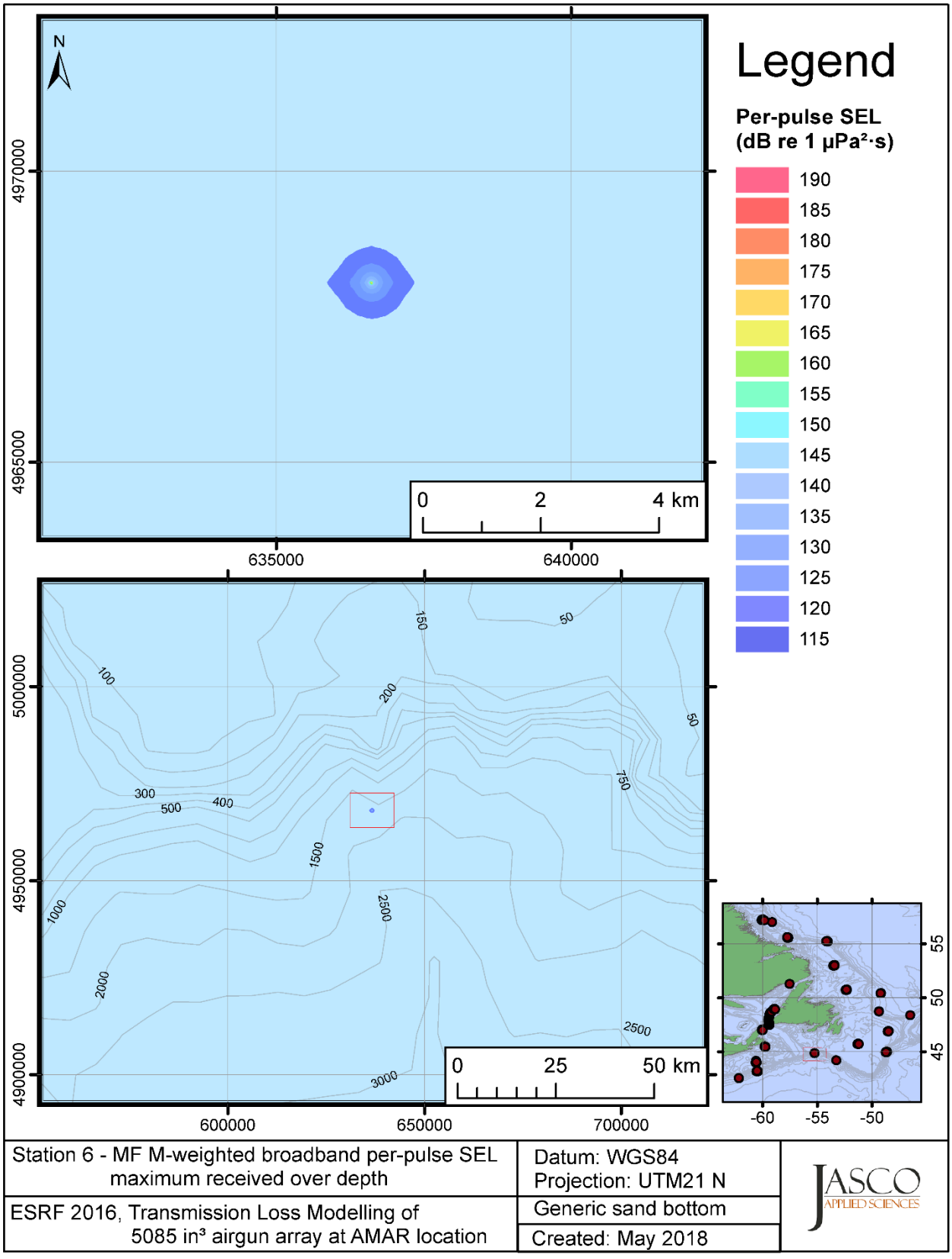

Figure C-324. Stn 6, MF M-weighted maximum-over-depth SEL received at any location on the map, modelled using a generic sand bottom, with the airgun array at the AMAR location and in-situ July SSP.

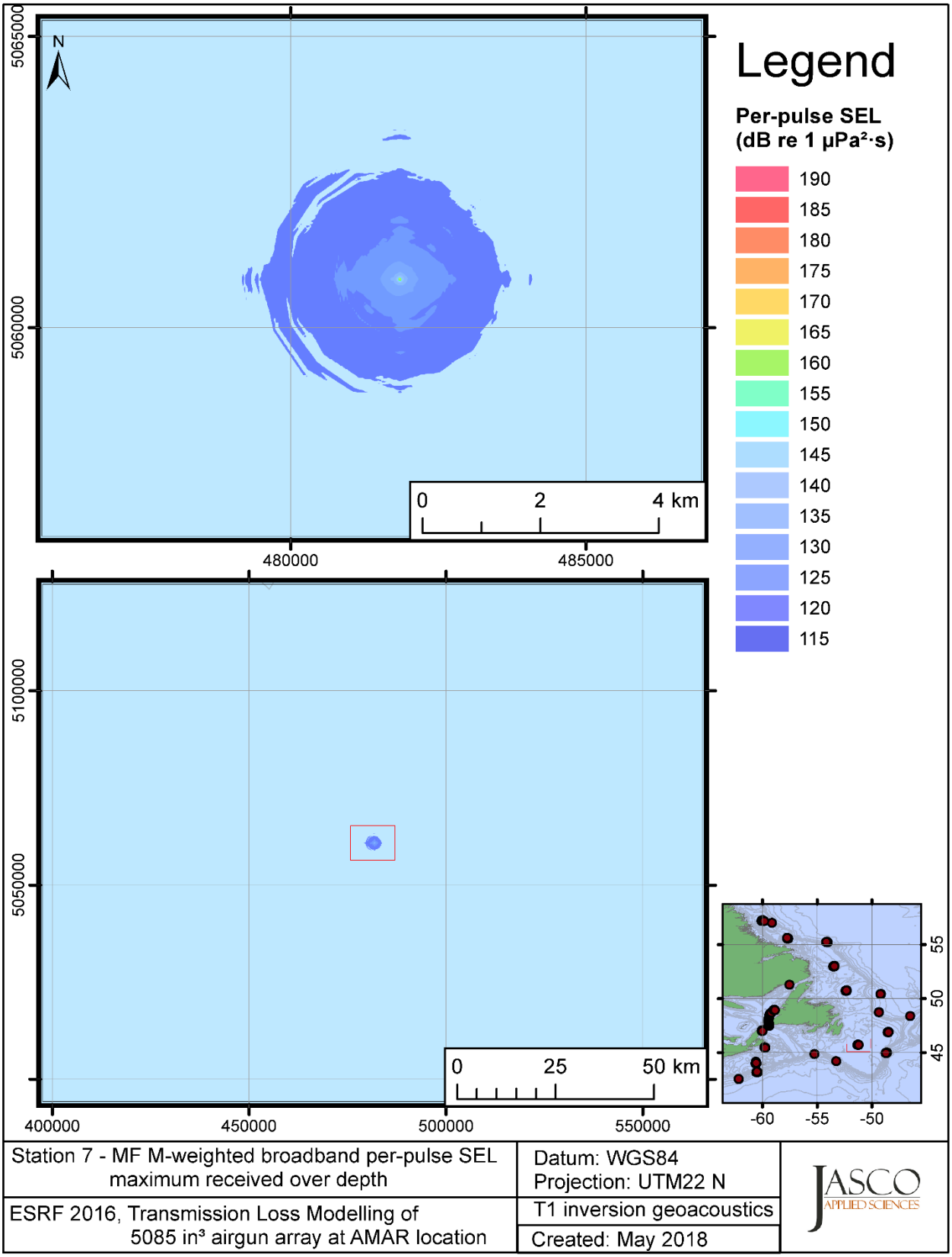

Figure C-325. Stn 7, MF M-weighted maximum-over-depth SEL received at any location on the map, modelled using the track 1 inversion geoacoustic bottom, with the airgun array at the AMAR location and in-situ July SSP.

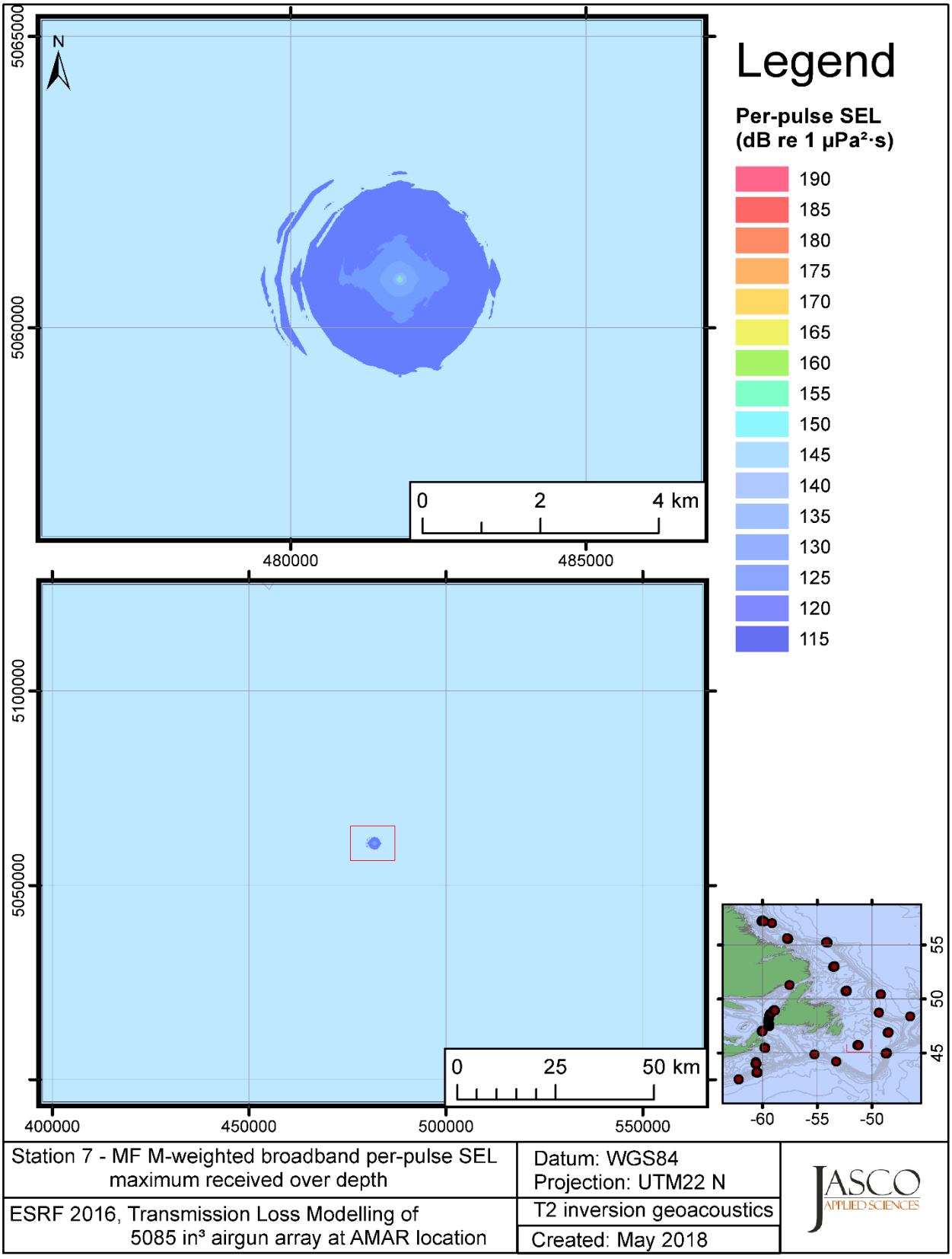

Figure C-326. Stn 7, MF M-weighted maximum-over-depth SEL received at any location on the map, modelled using the track 2 inversion geoacoustic bottom, with the airgun array at the AMAR location and in-situ July SSP.

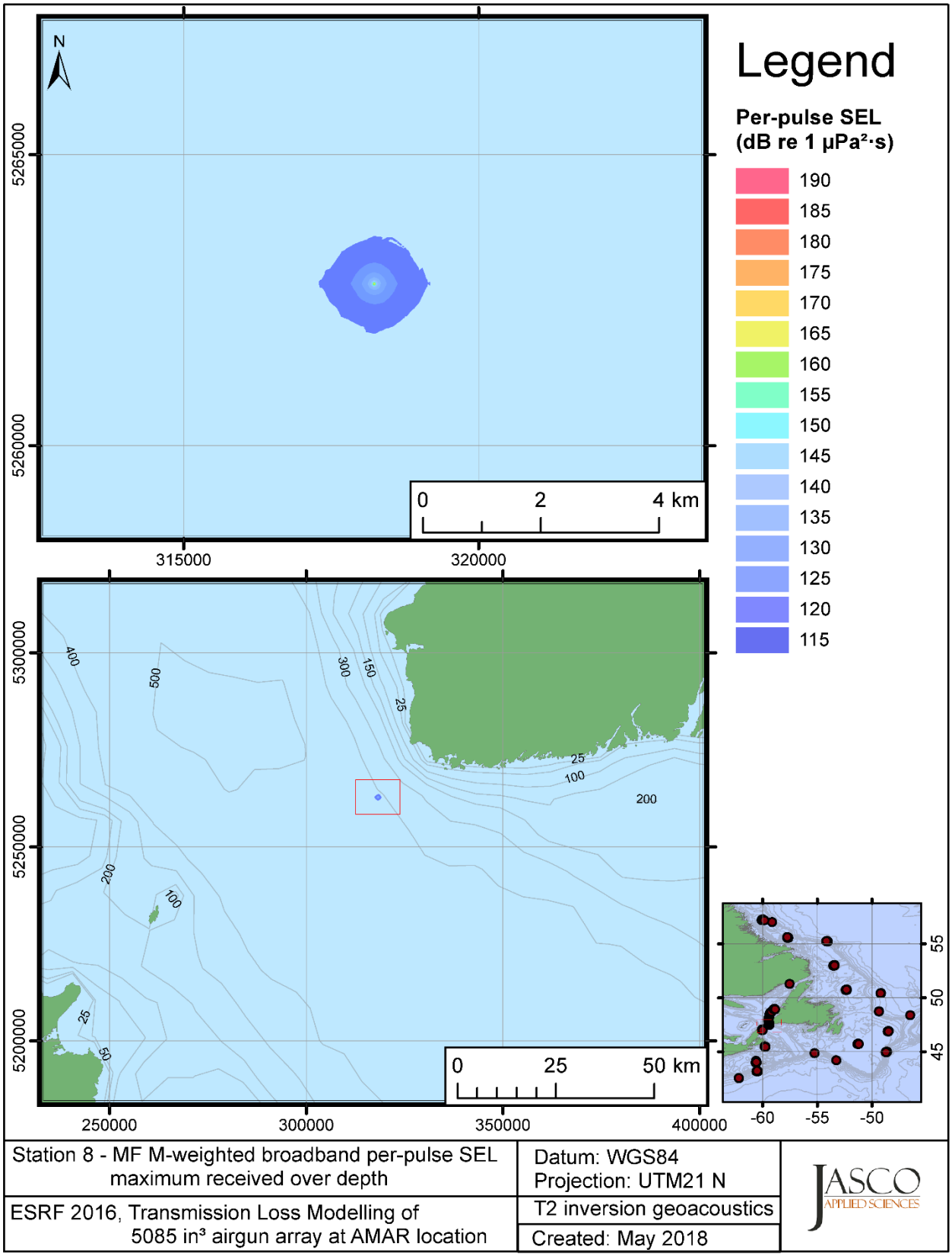

Figure C-327. Stn 8, MF M-weighted maximum-over-depth SEL received at any location on the map, modelled using the track 2 inversion geoacoustic bottom, with the airgun array at the AMAR location and GDEM July SSP.

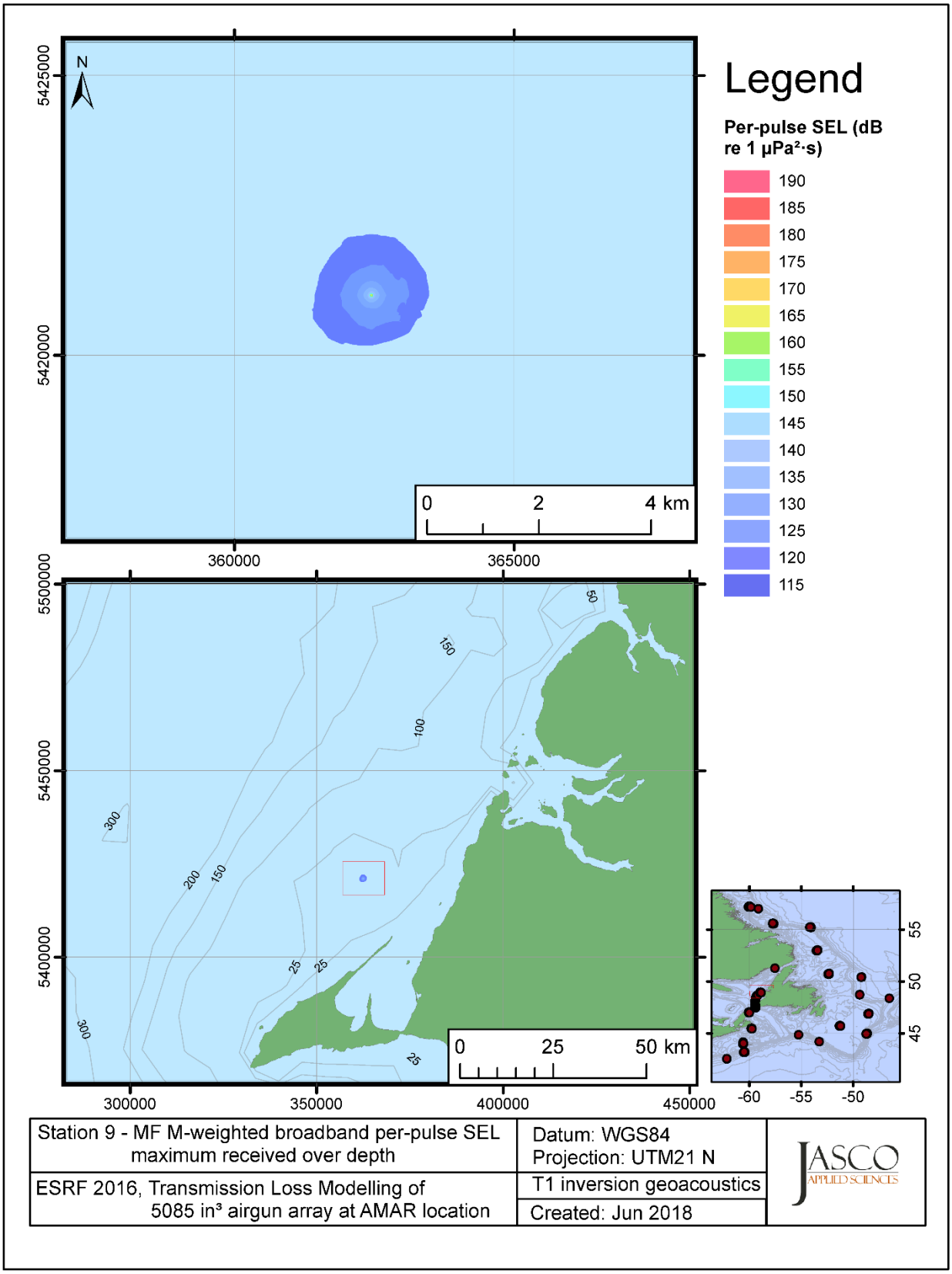

Figure C-328. Stn 9, MF M-weighted maximum-over-depth SEL received at any location on the map, modelled using the track 1 inversion geoacoustic bottom, with the airgun array at the AMAR location and GDEM July SSP.

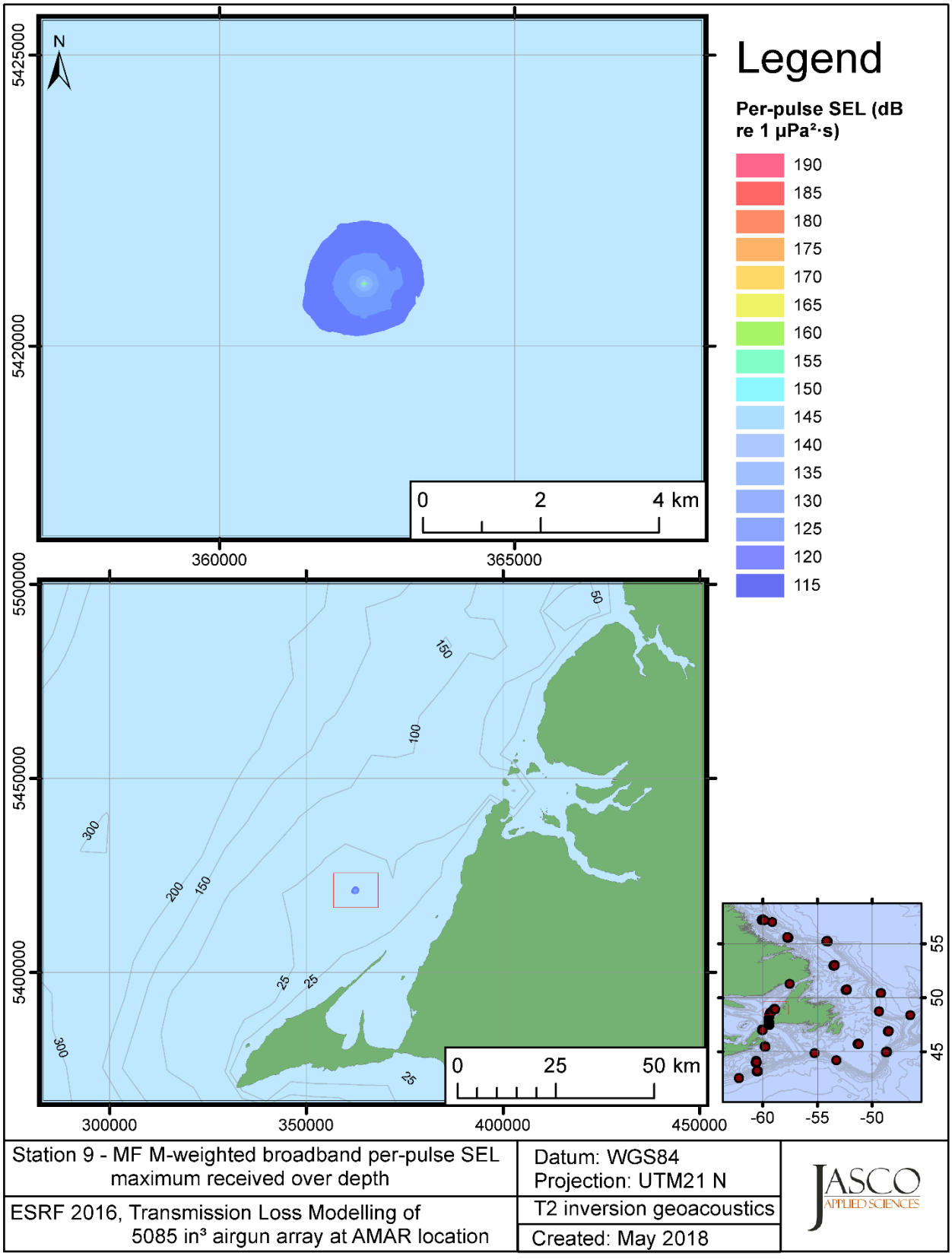

Figure C-329. Stn 9, MF M-weighted maximum-over-depth SEL received at any location on the map, modelled using the track 2 inversion geoacoustic bottom, with the airgun array at the AMAR location and GDEM July SSP.

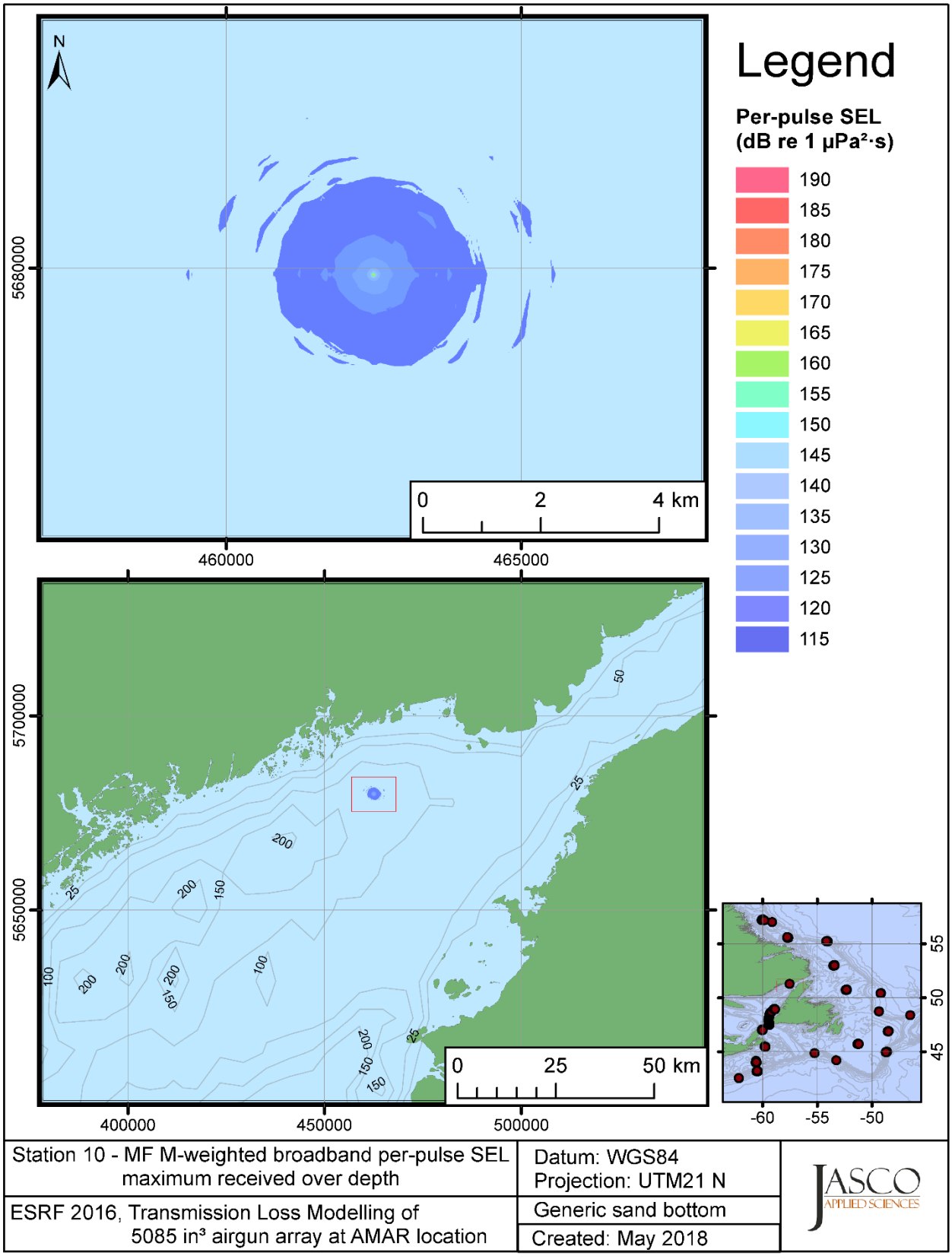

Figure C-330. Stn 10, MF M-weighted maximum-over-depth SEL received at any location on the map, modelled using a generic sand bottom, with the airgun array at the AMAR location and in-situ July SSP.

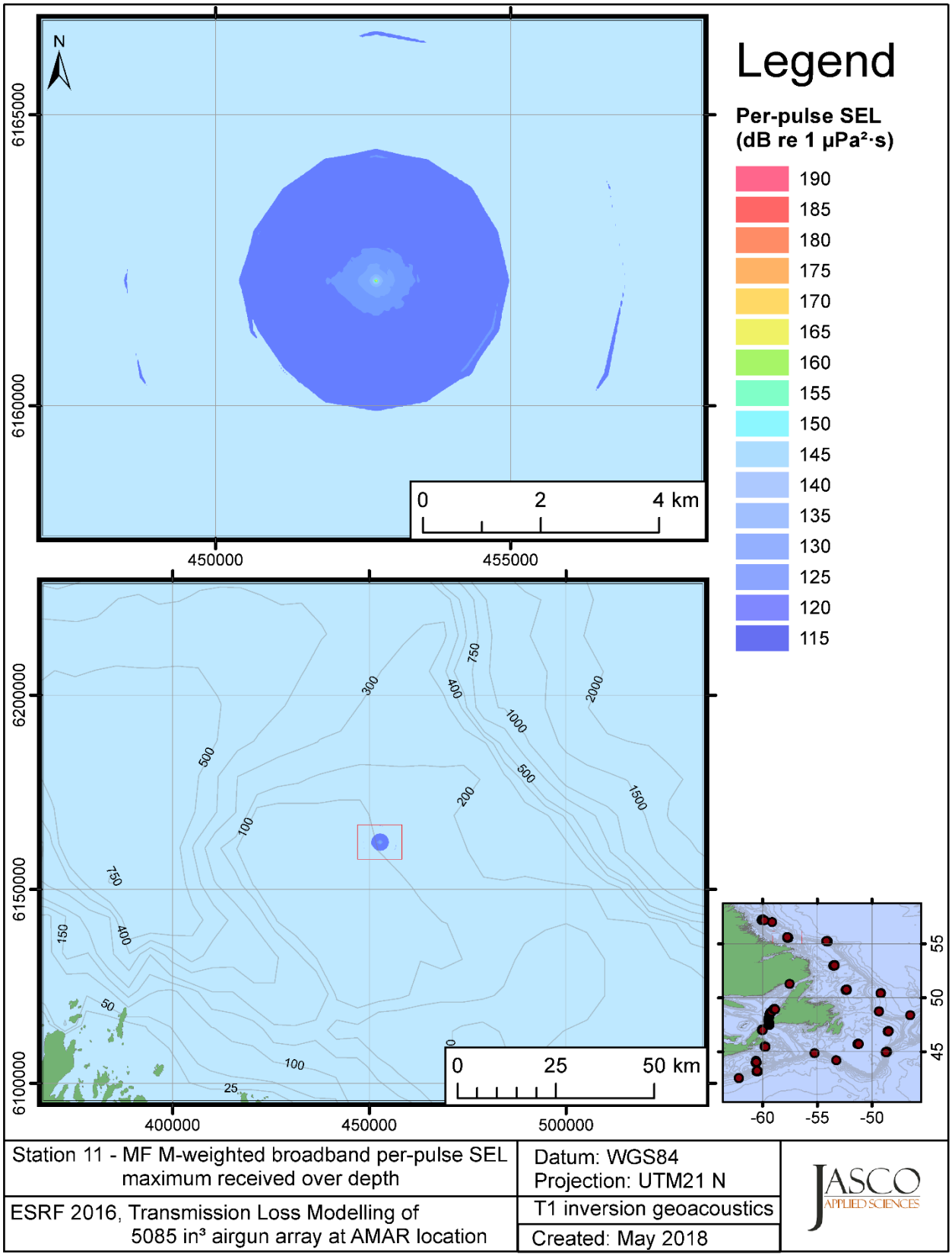

Figure C-331. Stn 11, MF M-weighted maximum-over-depth SEL received at any location on the map, modelled using the track 1 inversion geoacoustic bottom, with the airgun array at the AMAR location and in-situ July SSP.

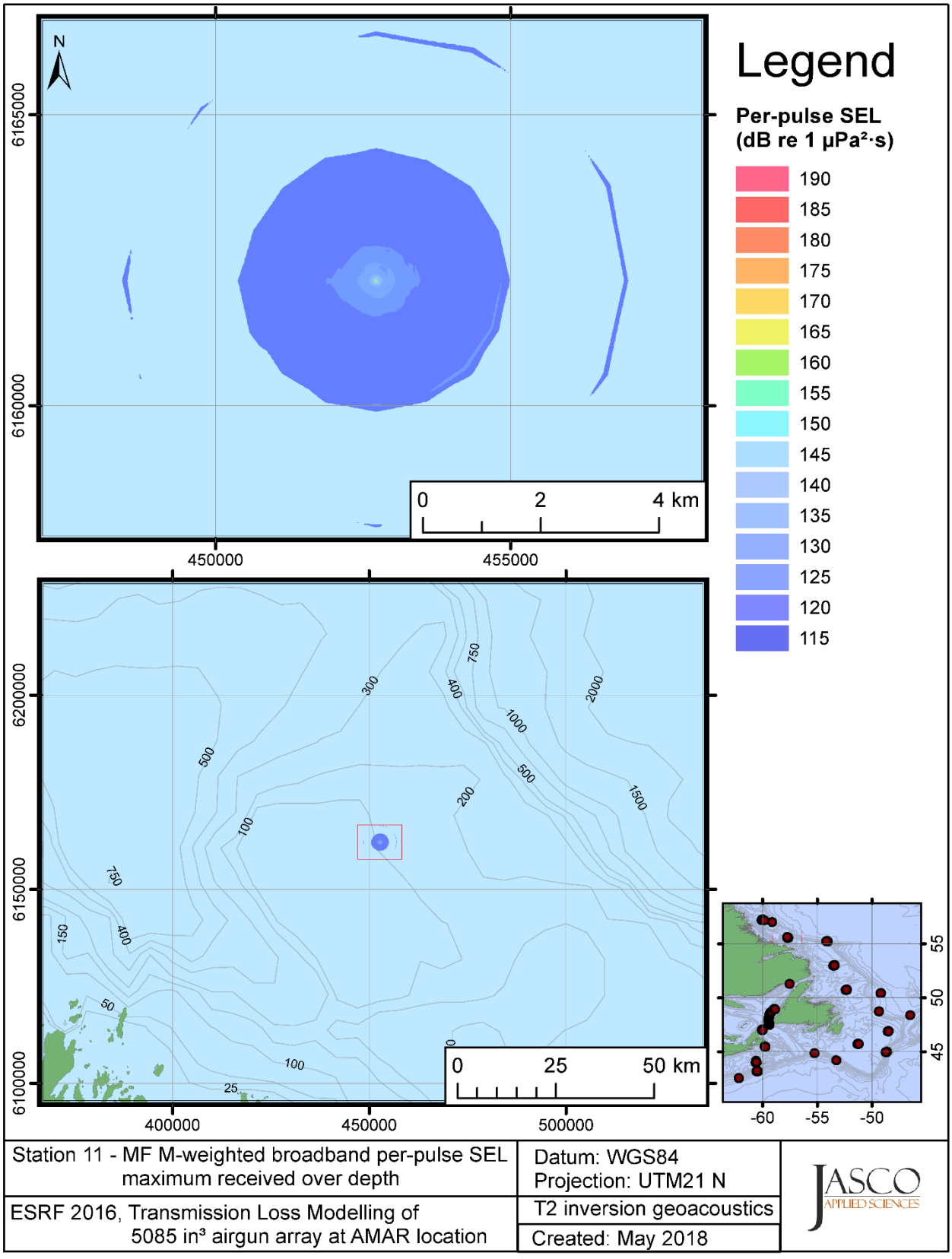

Figure C-332. Stn 11, MF M-weighted maximum-over-depth SEL received at any location on the map, modelled using the track 2 inversion geoacoustic bottom, with the airgun array at the AMAR location and in-situ July SSP.

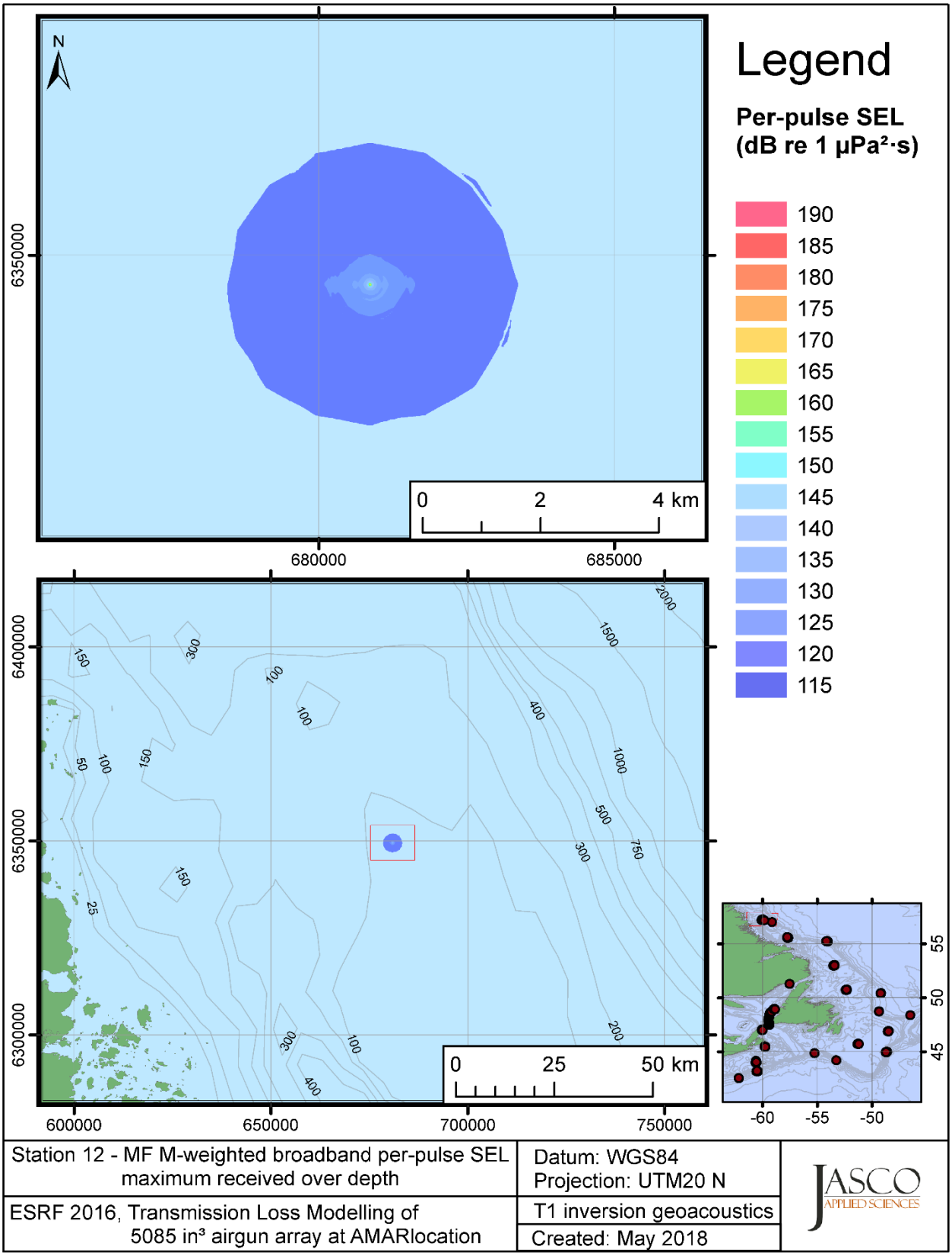

Figure C-333. Stn 12, MF M-weighted maximum-over-depth SEL received at any location on the map, modelled using the track 1 inversion geoacoustic bottom, with the airgun array at the AMAR location and in-situ July SSP.

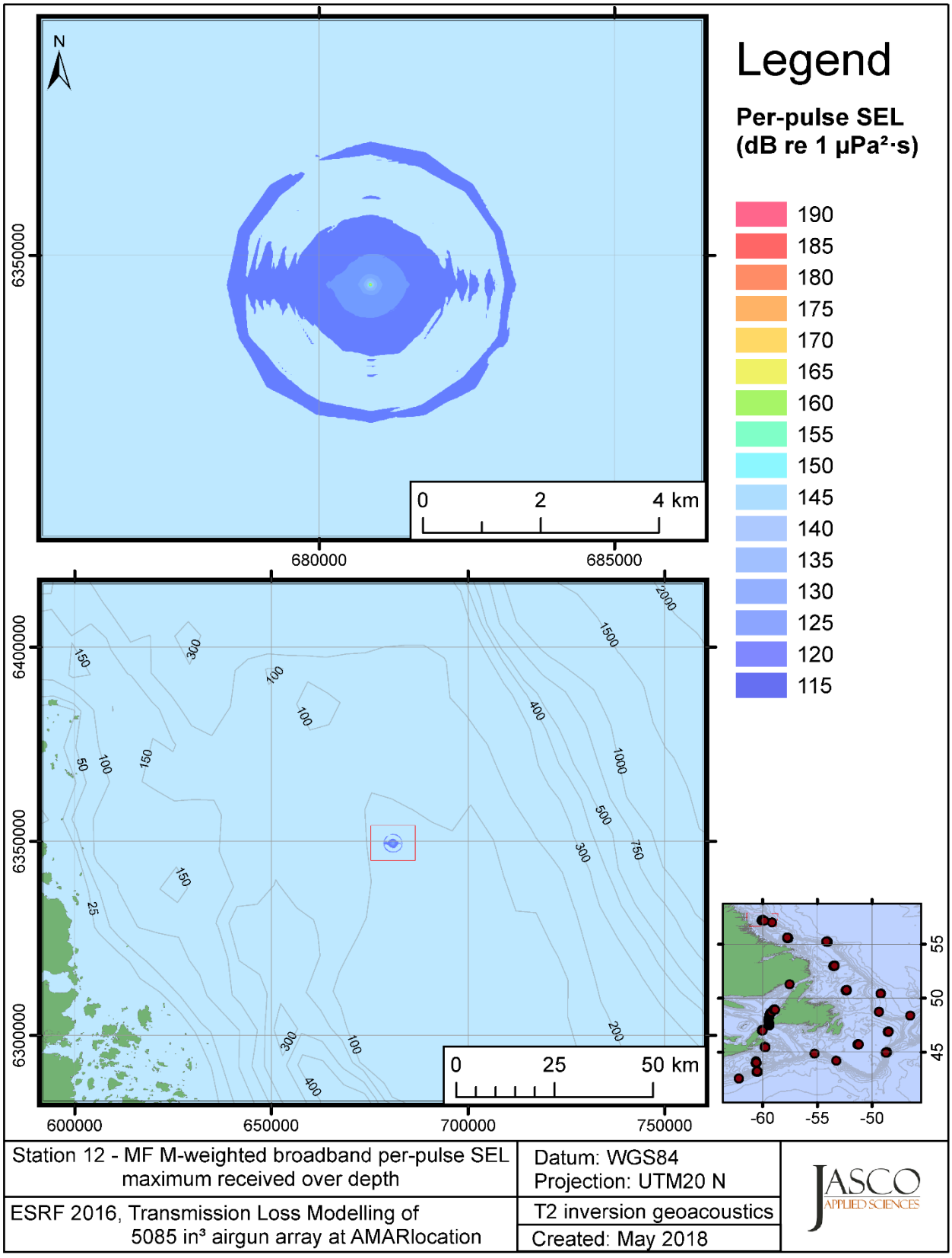

Figure C-334. Stn 12, MF M-weighted maximum-over-depth SEL received at any location on the map, modelled using the track 2 inversion geoacoustic bottom, with the airgun array at the AMAR location and in-situ July SSP.

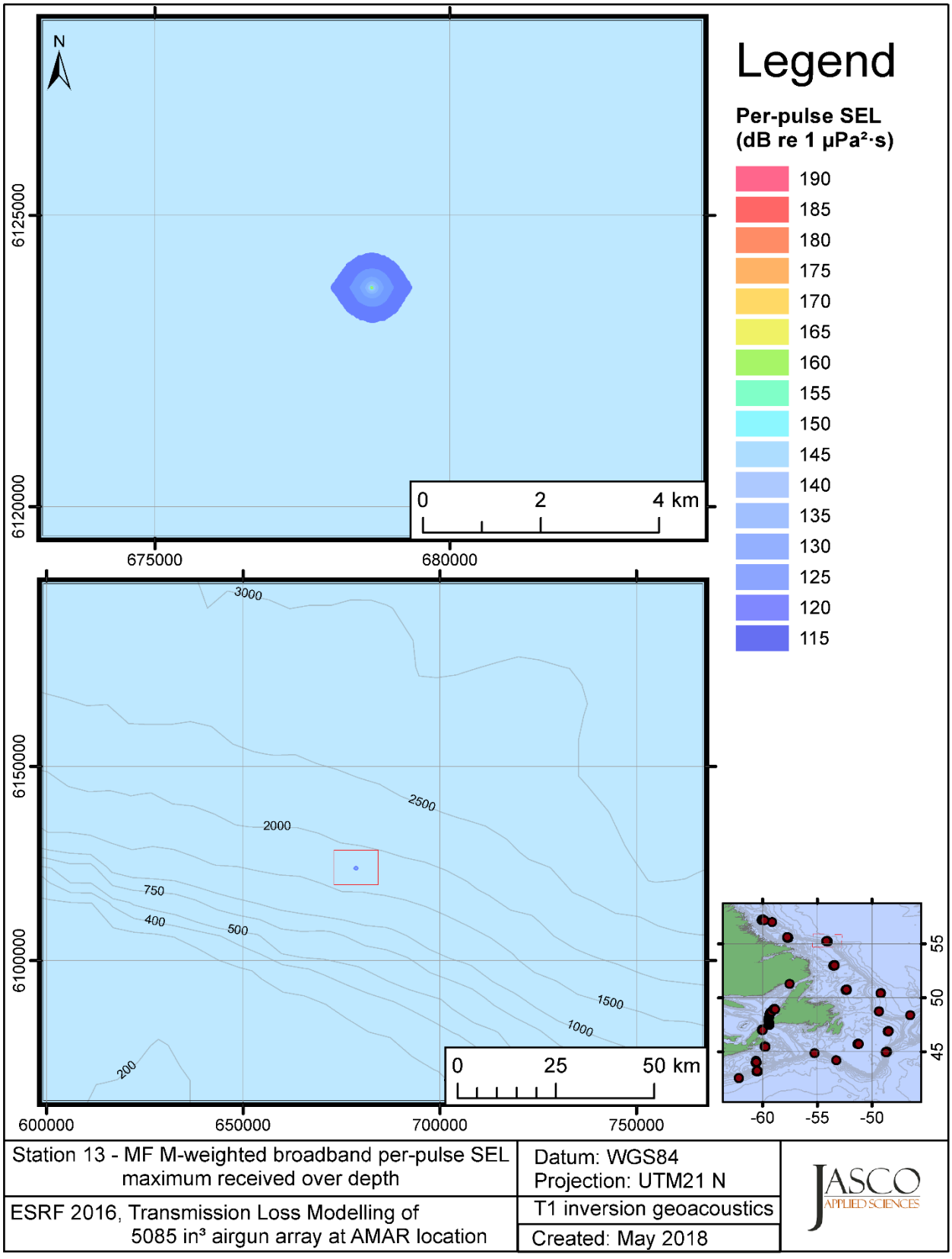

Figure C-335. Stn 13, MF M-weighted maximum-over-depth SEL received at any location on the map, modelled using the track 1 inversion geoacoustic bottom, with the airgun array at the AMAR location and in-situ July SSP.

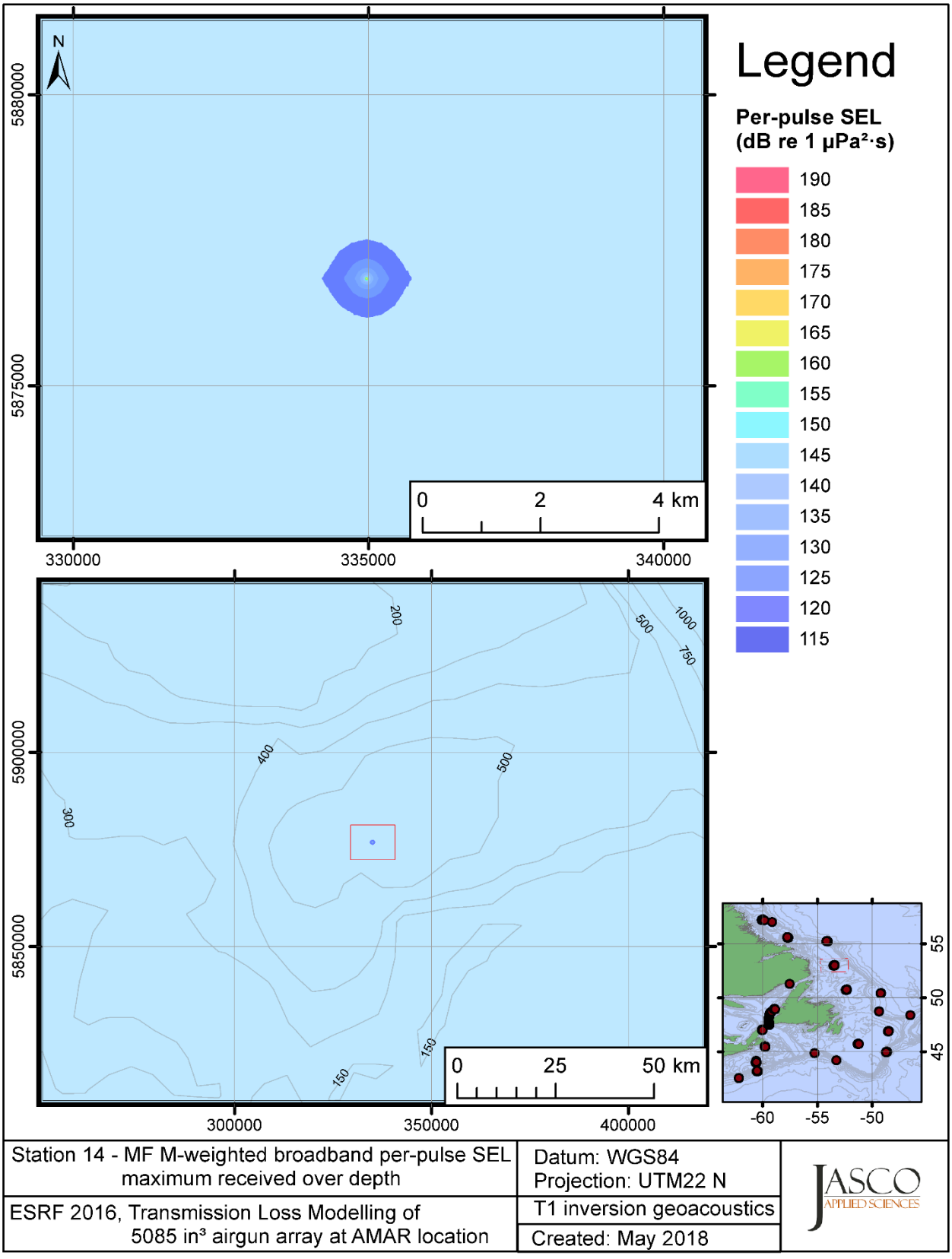

Figure C-336. Stn 14, MF M-weighted maximum-over-depth SEL received at any location on the map, modelled using the track 1 inversion geoacoustic bottom, with the airgun array at the AMAR location and in-situ July SSP.

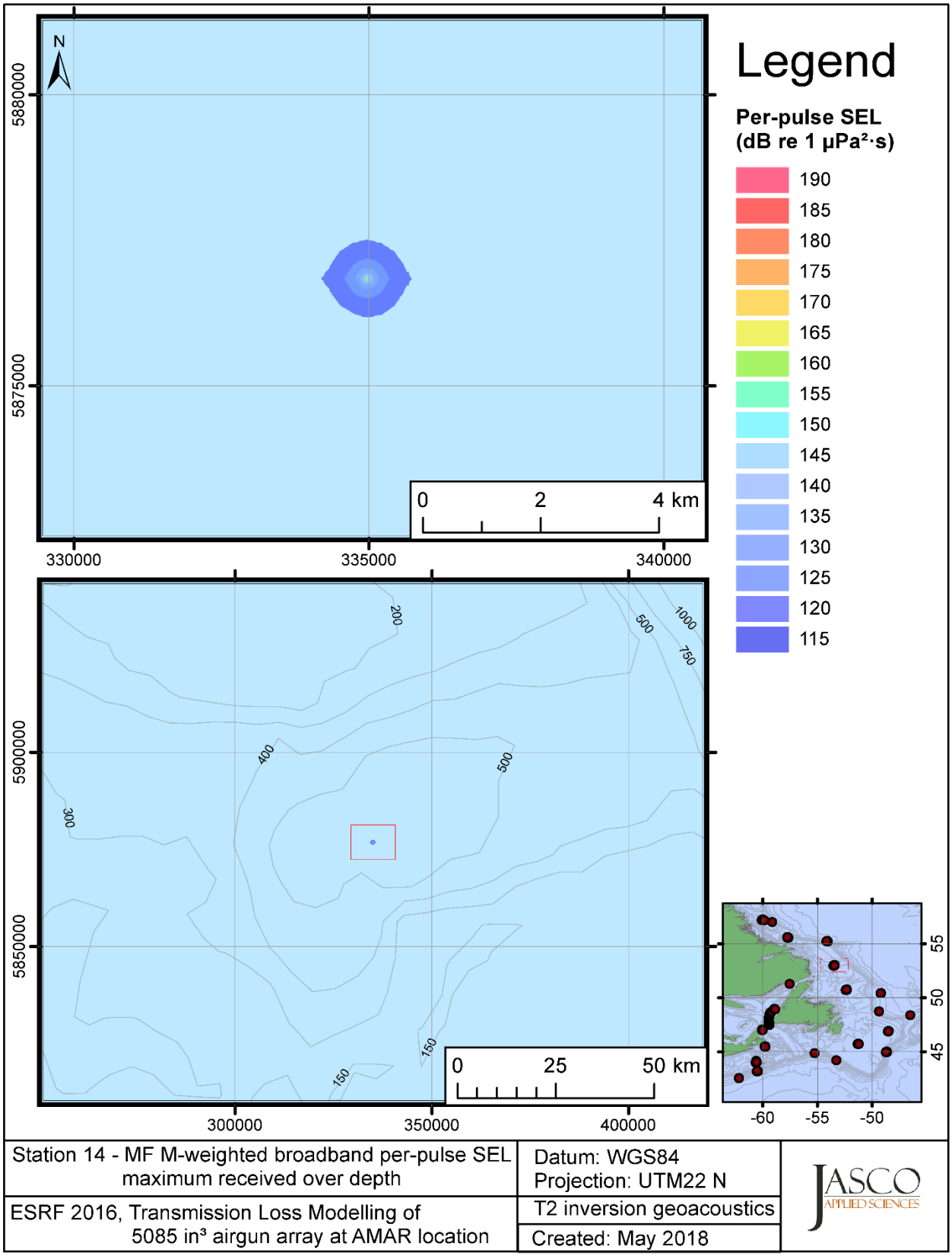

Figure C-337. Stn 14, MF M-weighted maximum-over-depth SEL received at any location on the map, modelled using the track 2 inversion geoacoustic bottom, with the airgun array at the AMAR location and in-situ July SSP.

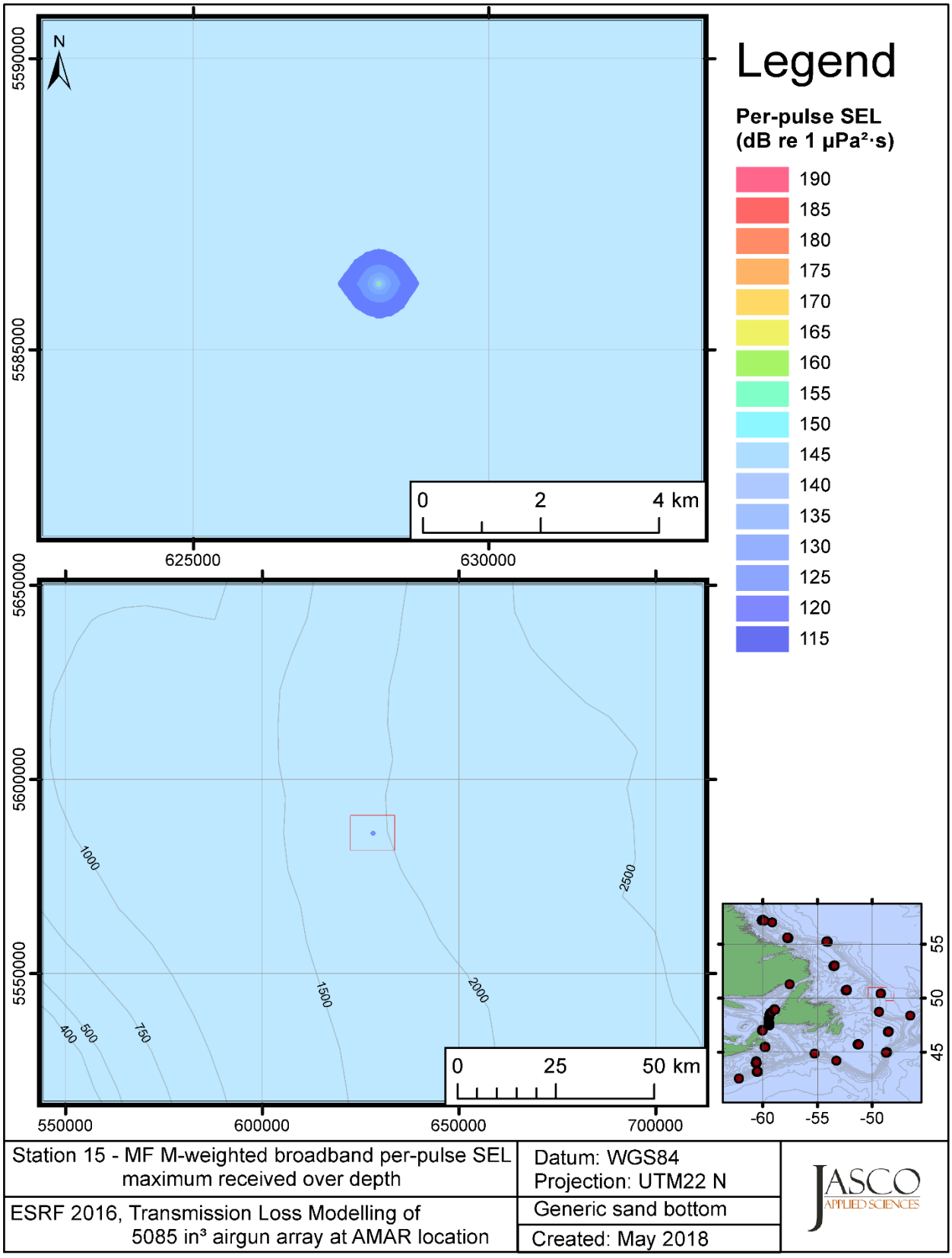

Figure C-338. Stn 15, MF M-weighted maximum-over-depth SEL received at any location on the map, modelled using a generic sand bottom, with the airgun array at the AMAR location and in-situ July SSP.

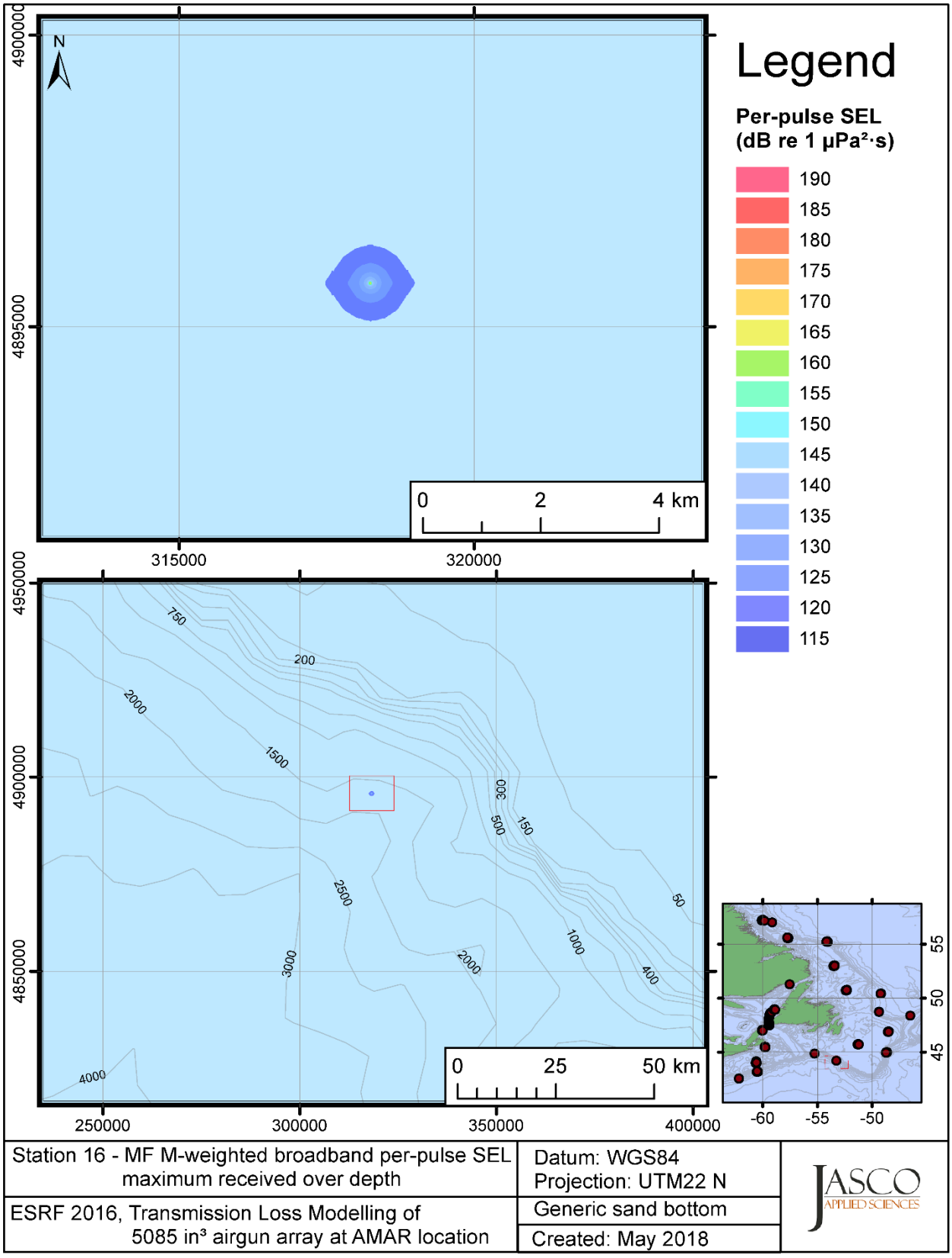

Figure C-339. Stn 16, MF M-weighted maximum-over-depth SEL received at any location on the map, modelled using a generic sand bottom, with the airgun array at the AMAR location and in-situ July SSP.

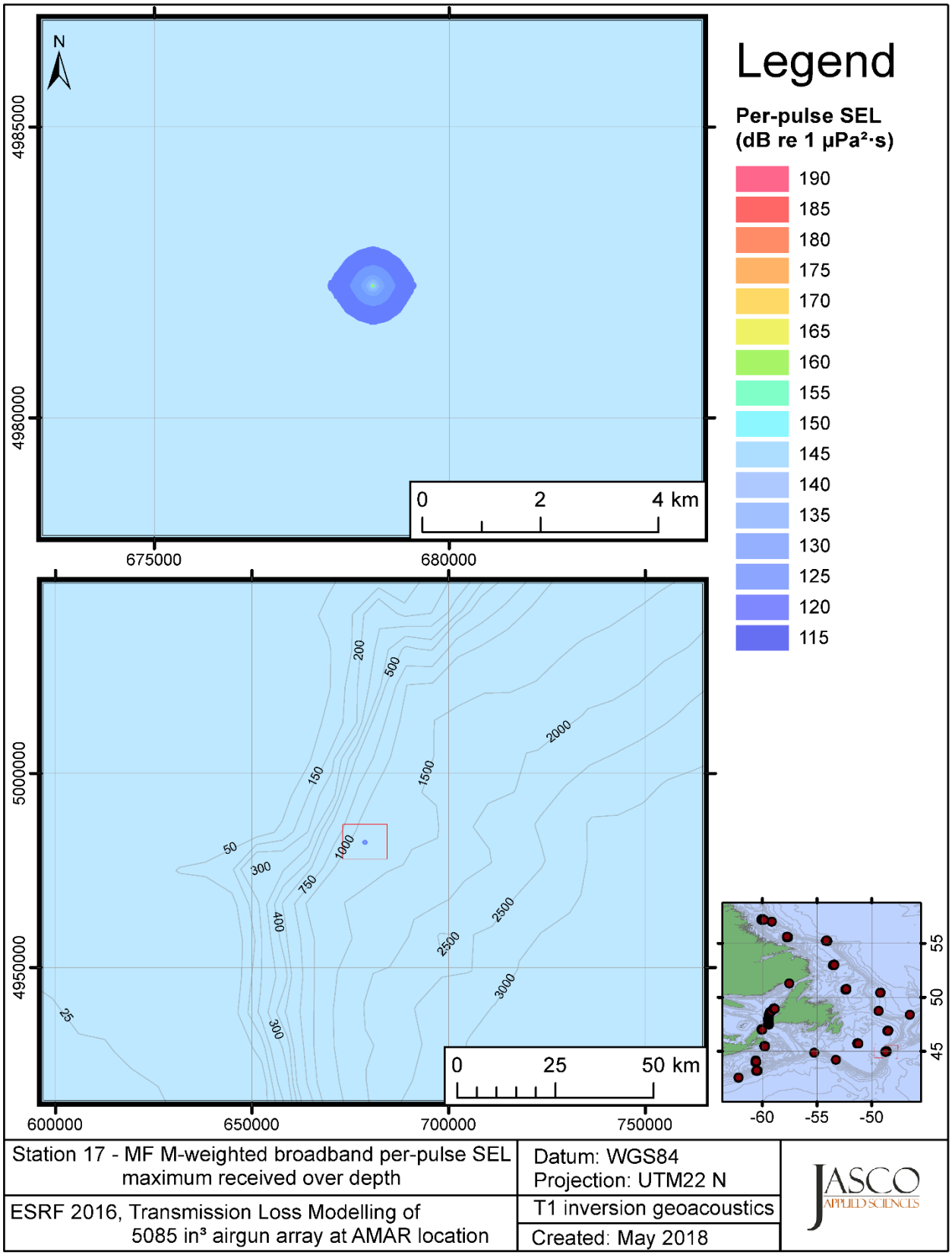

Figure C-340. Stn 17, MF M-weighted maximum-over-depth SEL received at any location on the map, modelled using the track 1 inversion geoacoustic bottom, with the airgun array at the AMAR location and in-situ July SSP.

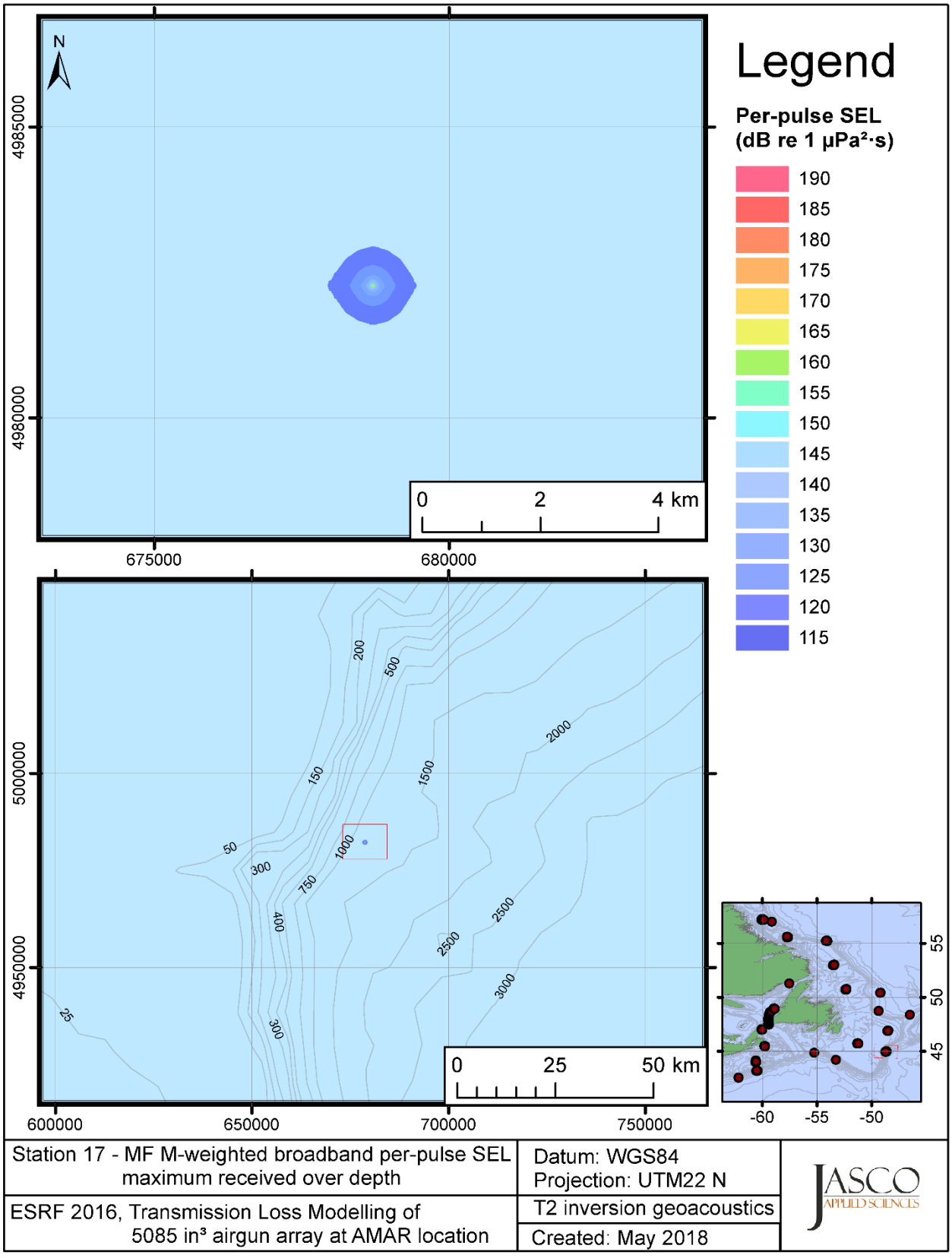

Figure C-341. Stn 17, MF M-weighted maximum-over-depth SEL received at any location on the map, modelled using the track 2 inversion geoacoustic bottom, with the airgun array at the AMAR location and in-situ July SSP.

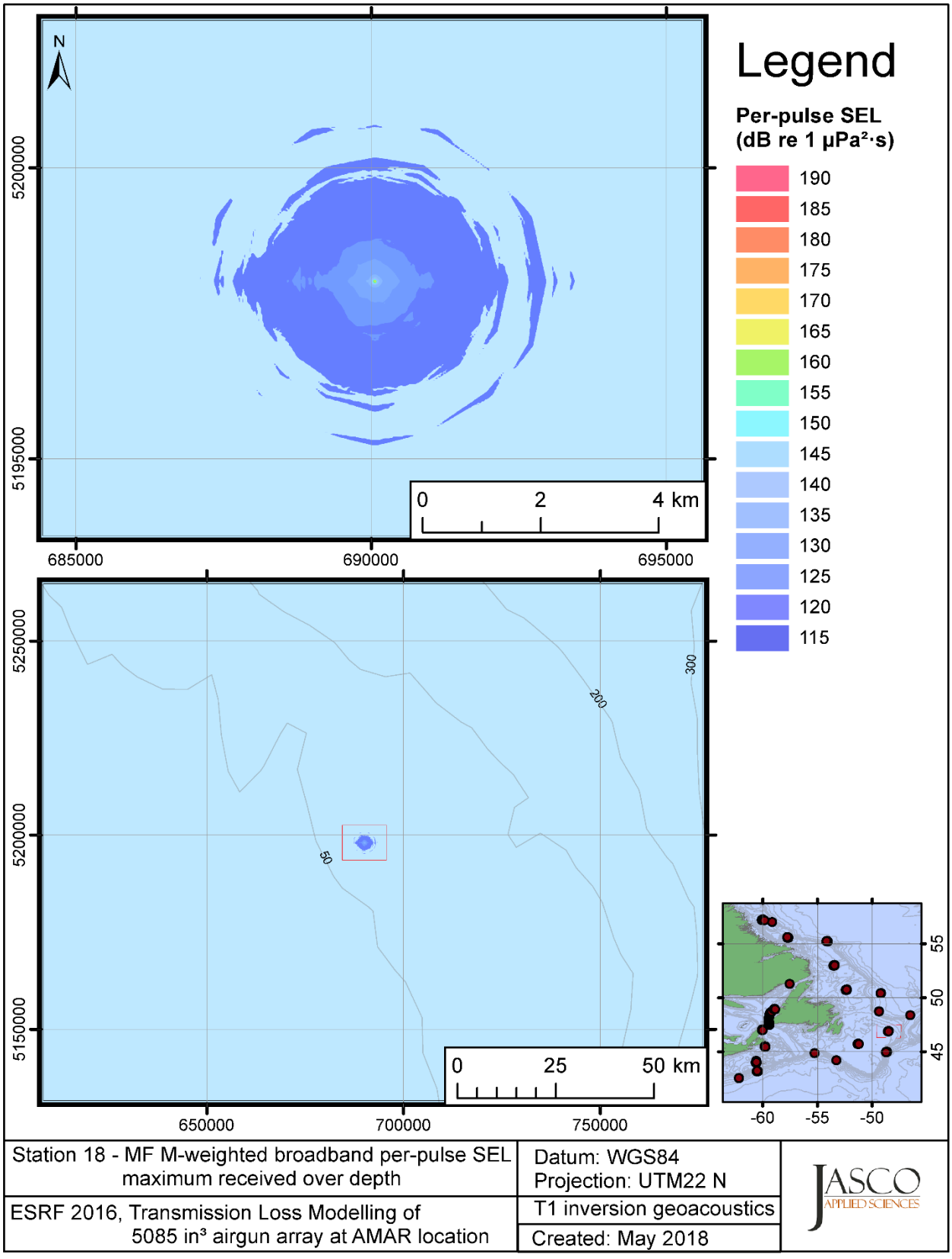

Figure C-342. Stn 18, MF M-weighted maximum-over-depth SEL received at any location on the map, modelled using the track 1 inversion geoacoustic bottom, with the airgun array at the AMAR location and in-situ July SSP.

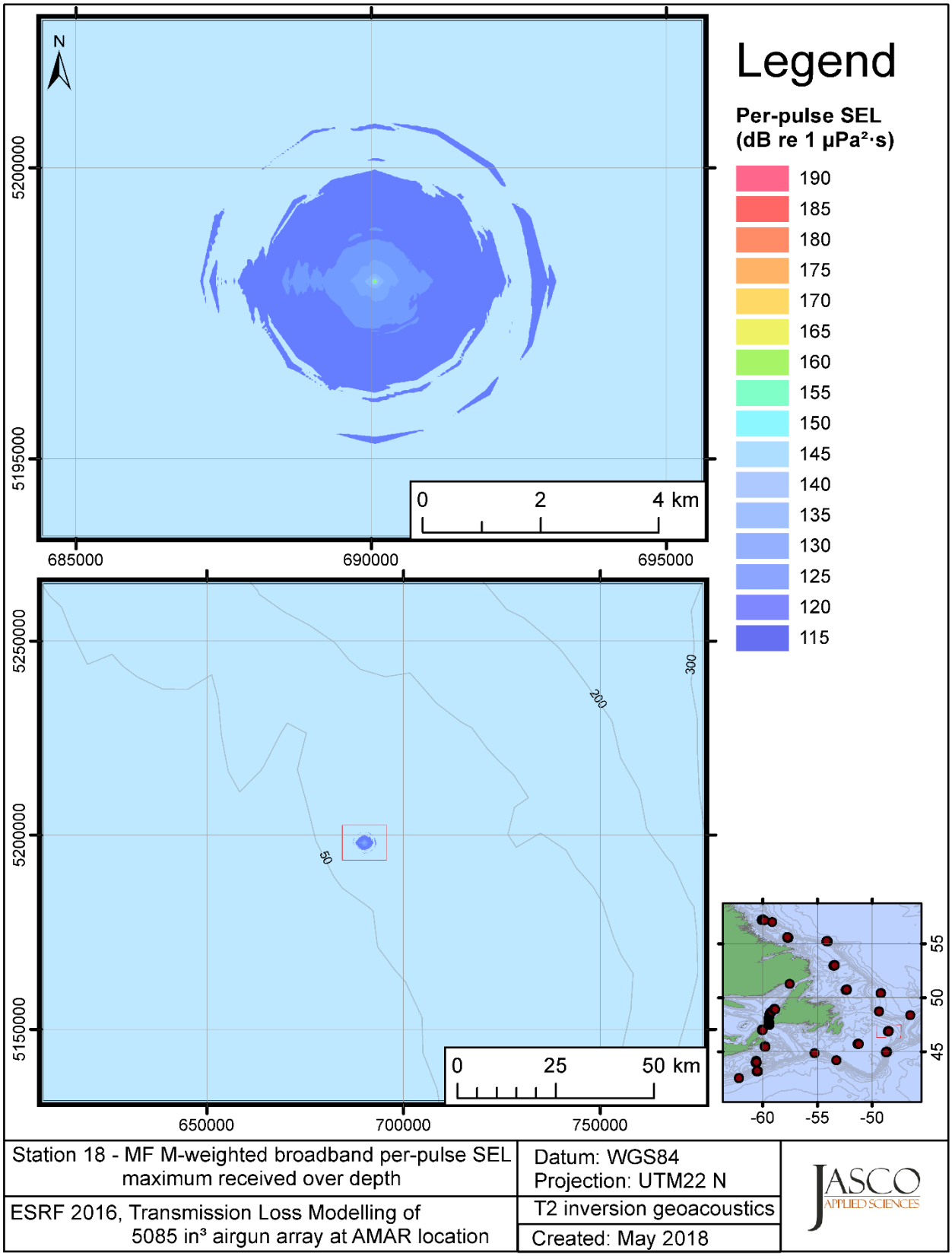

Figure C-343. Stn 18, MF M-weighted maximum-over-depth SEL received at any location on the map, modelled using the track 2 inversion geoacoustic bottom, with the airgun array at the AMAR location and in-situ July SSP.

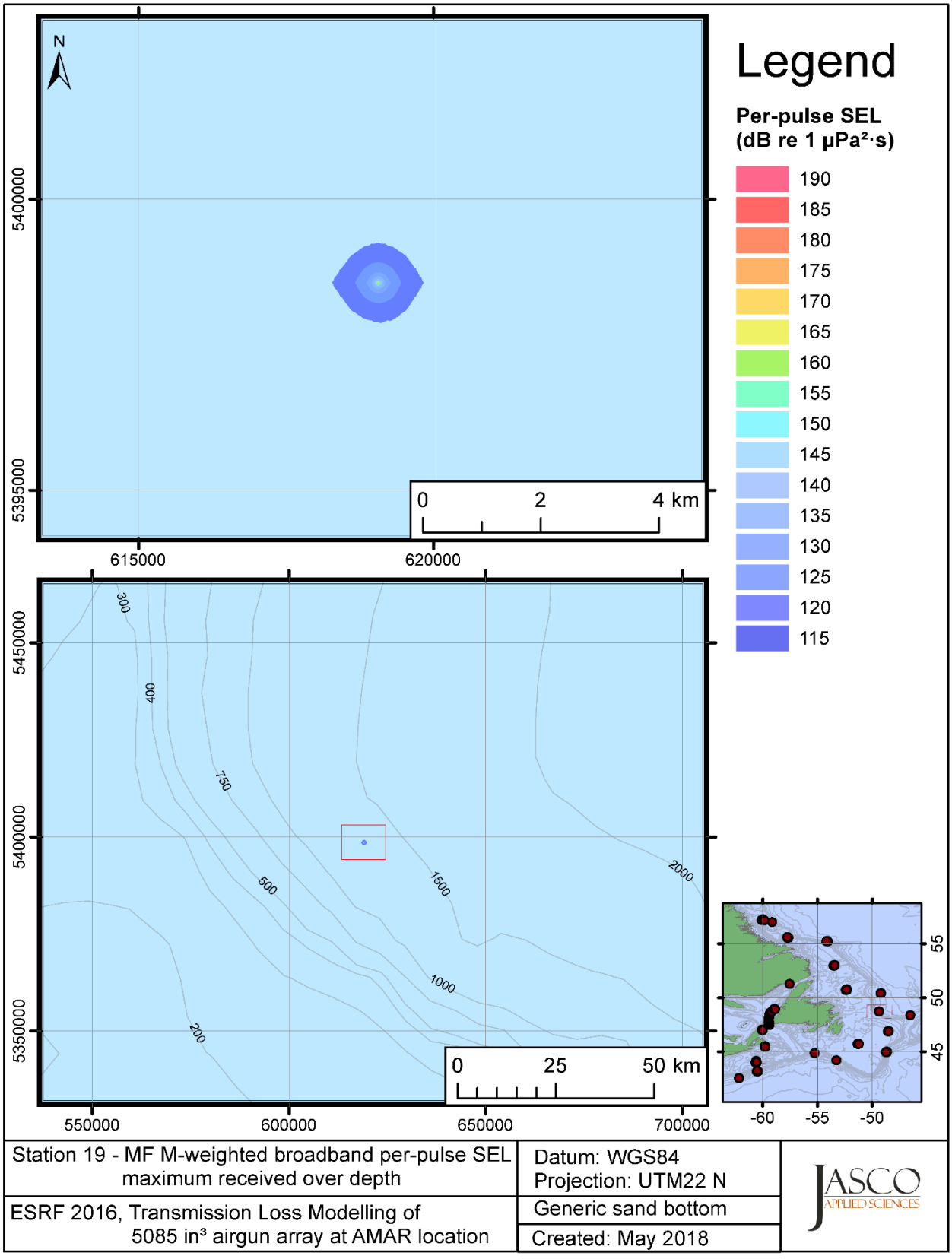

Figure C-344. Stn 19, MF M-weighted maximum-over-depth SEL received at any location on the map, modelled using a generic sand bottom, with the airgun array at the AMAR location and in-situ July SSP.

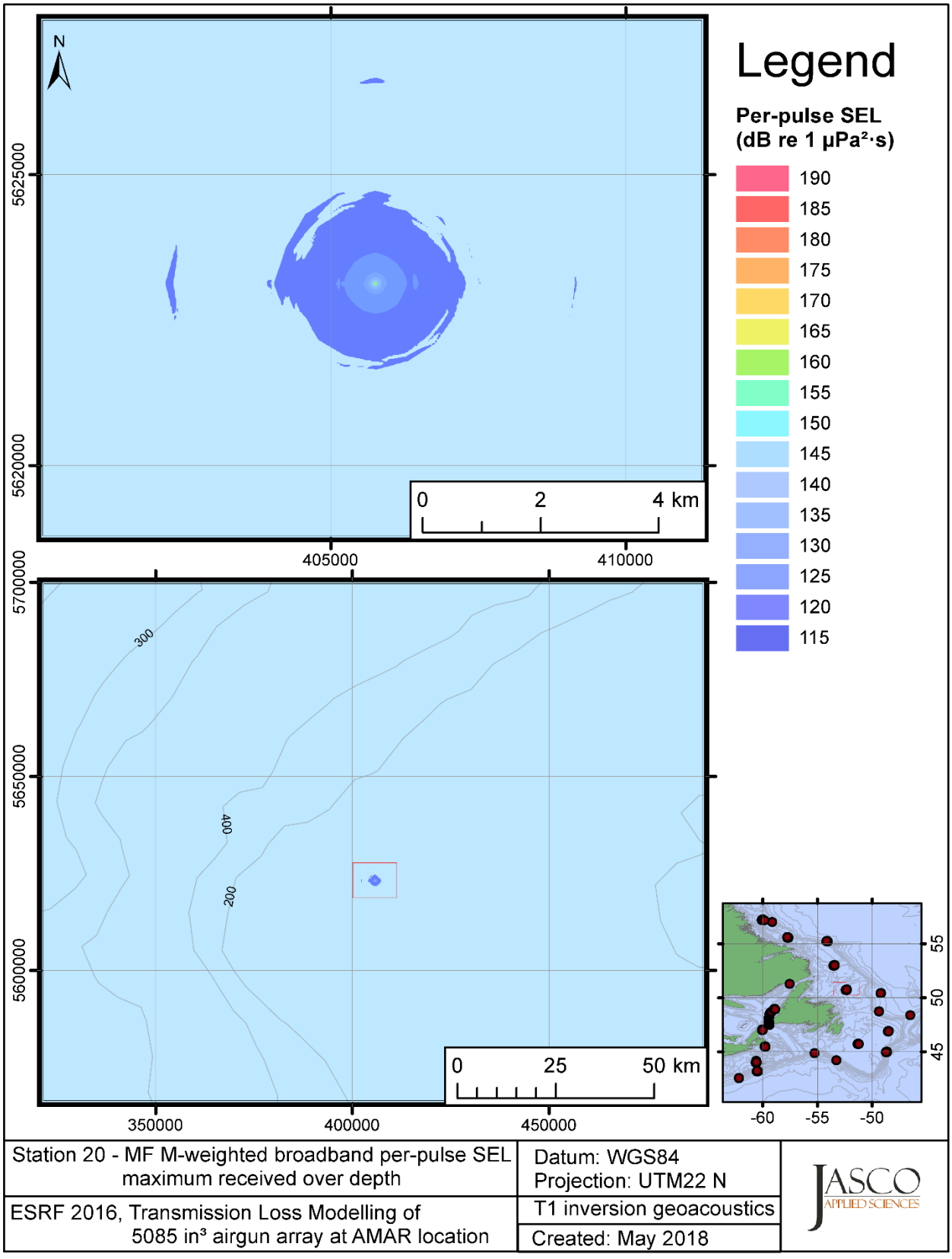

Figure C-345. Stn 20, MF M-weighted maximum-over-depth SEL received at any location on the map, modelled using the track 1 inversion geoacoustic bottom, with the airgun array at the AMAR location and in-situ July SSP.

C.10. Modelling HF M-weighted Max-over-depth Received Level at Distant Locations - Summer

This section presents the results of modelling the maximum-over-depth per-pulse sound exposure level (SEL) received at distant receiver locations (varied in range and azimuth) for the source held fixed at the AMAR location. The modelling uses the geoacoustic inversion bottom parameters at the 14 sites where they are available and only uses a generic sand bottom at the other six sites. The modelling results are presented in the form of coloured maps where the colour at any map location represents the predicted maximum-over-depth received level at that spot on the map. This section includes only the high-frequency cetaceans (HF) marine-mammal-weighted per-pulse SEL results; additional maps for other marine mammal received level auditory weightings are presented in adjoining sections. The sound speed profiles (SSP) used are detailed in Appendix B.1.

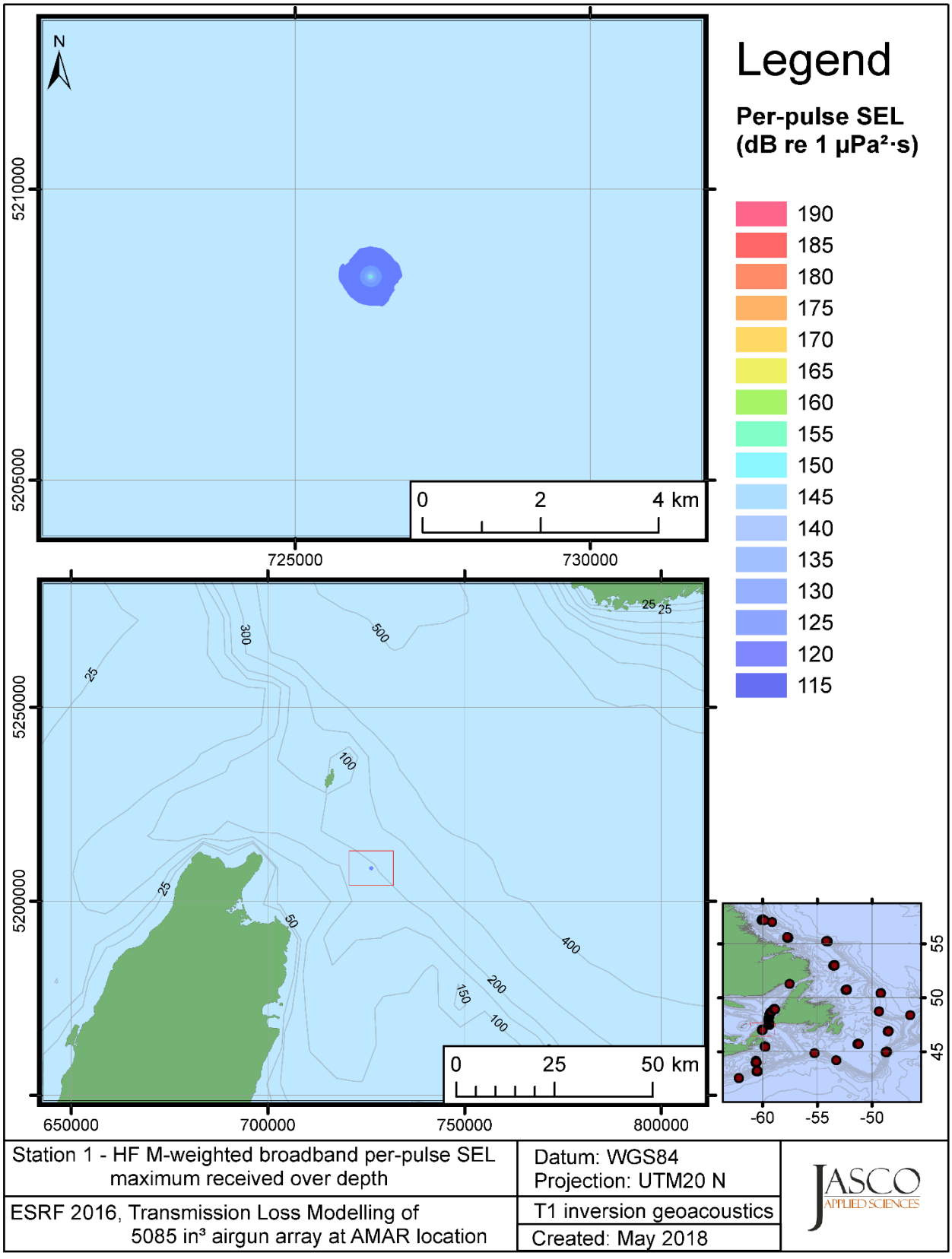

Figure C-346. Stn 1, HF M-weighted maximum-over-depth SEL received at any location on the map, modelled using the track 1 inversion geoacoustic bottom, with the airgun array at the AMAR location and in-situ July SSP.

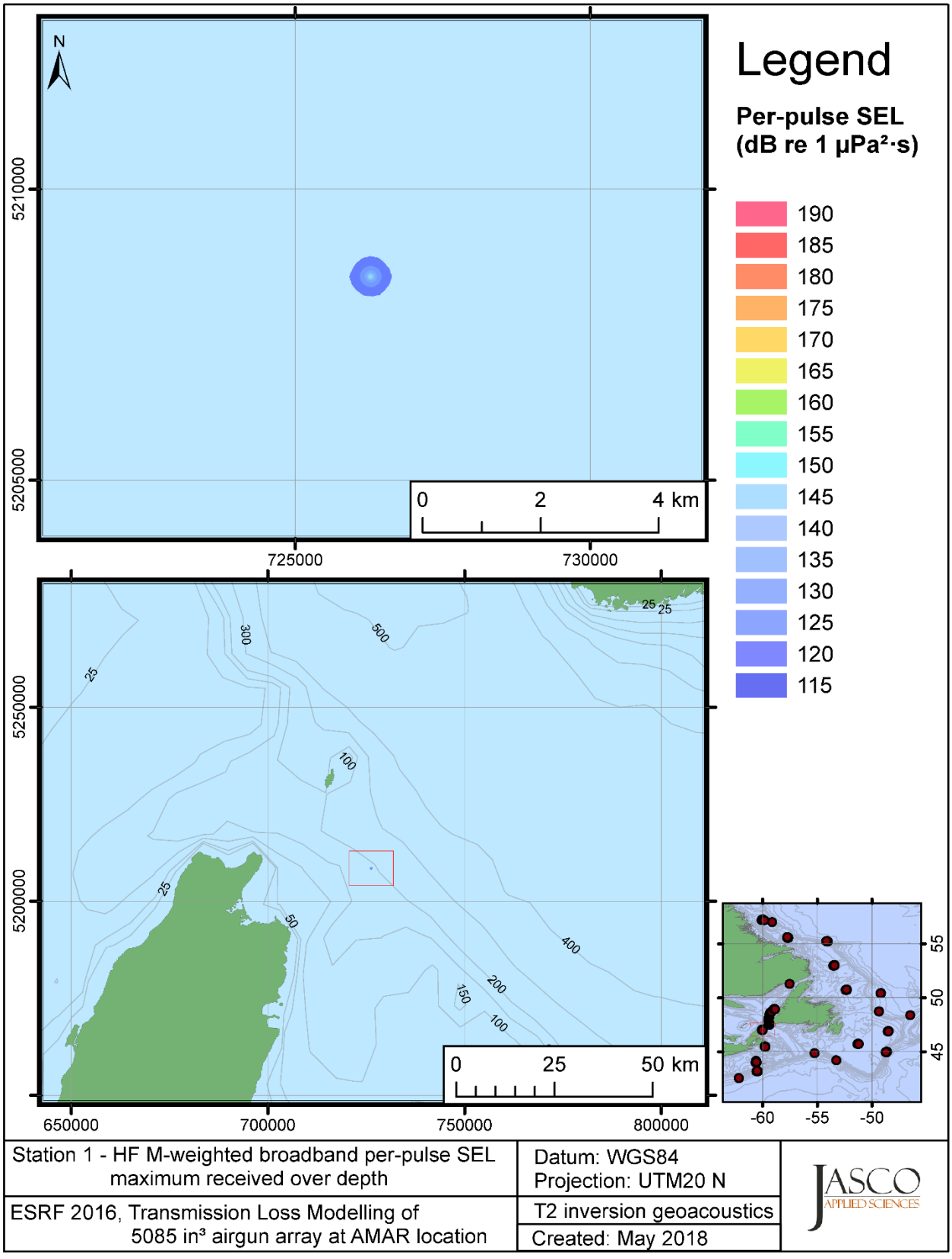

Figure C-347. Stn 1, HF M-weighted maximum-over-depth SEL received at any location on the map, modelled using the track 2 inversion geoacoustic bottom, with the airgun array at the AMAR location and in-situ July SSP.

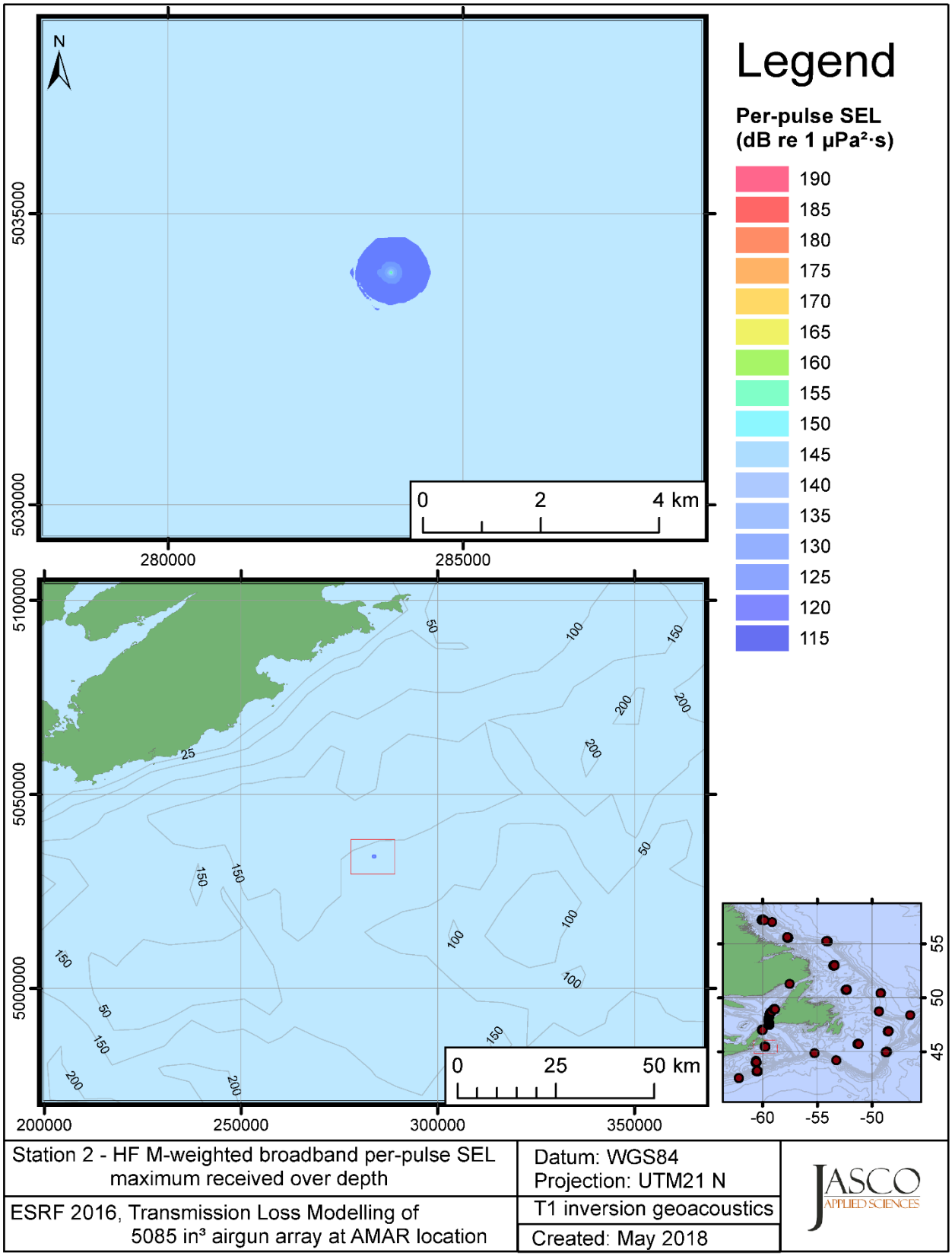

Figure C-348. Stn 2, HF M-weighted maximum-over-depth SEL received at any location on the map, modelled using the track 1 inversion geoacoustic bottom, with the airgun array at the AMAR location and in-situ July SSP.

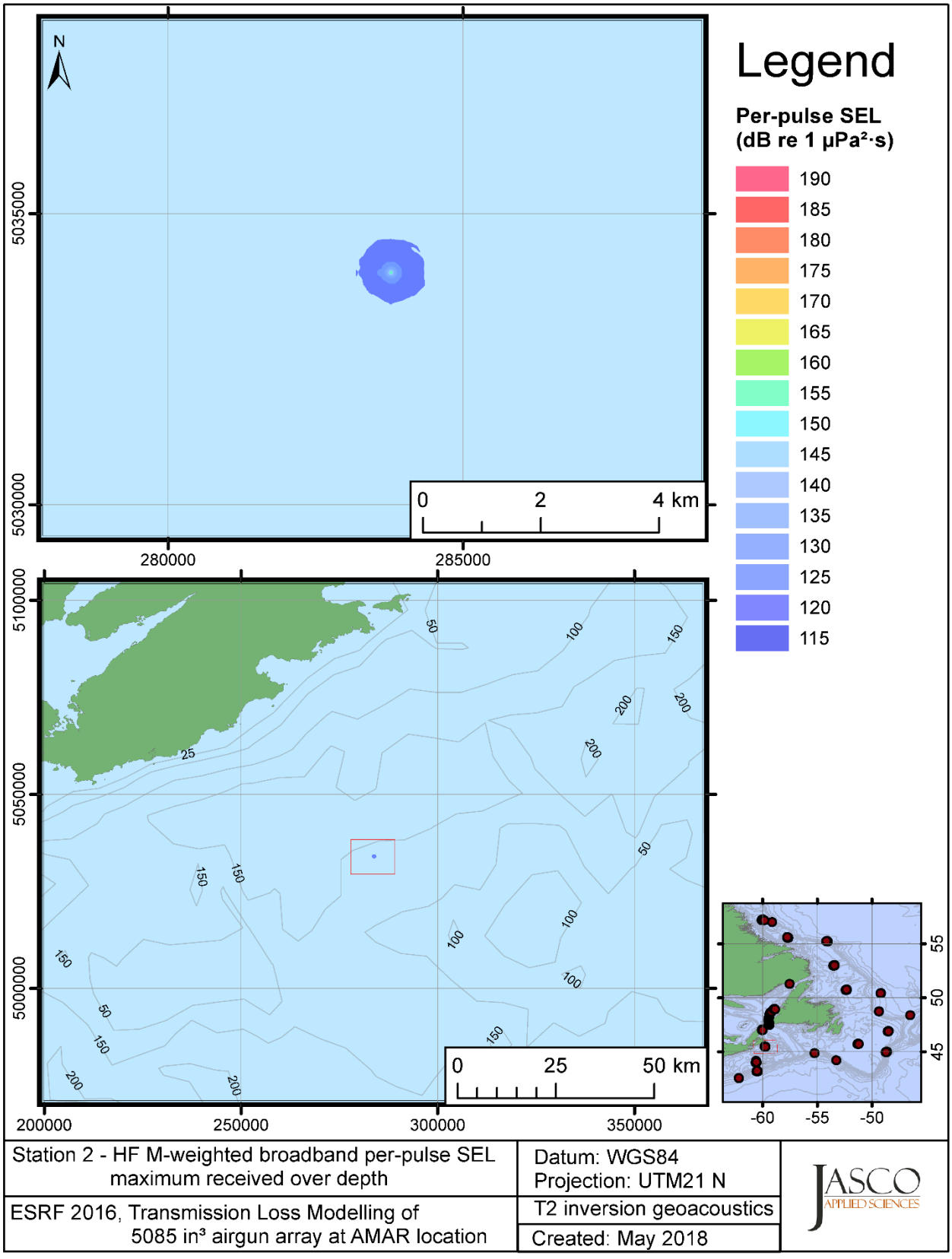

Figure C-349. Stn 2, HF M-weighted maximum-over-depth SEL received at any location on the map, modelled using the track 2 inversion geoacoustic bottom, with the airgun array at the AMAR location and in-situ July SSP.

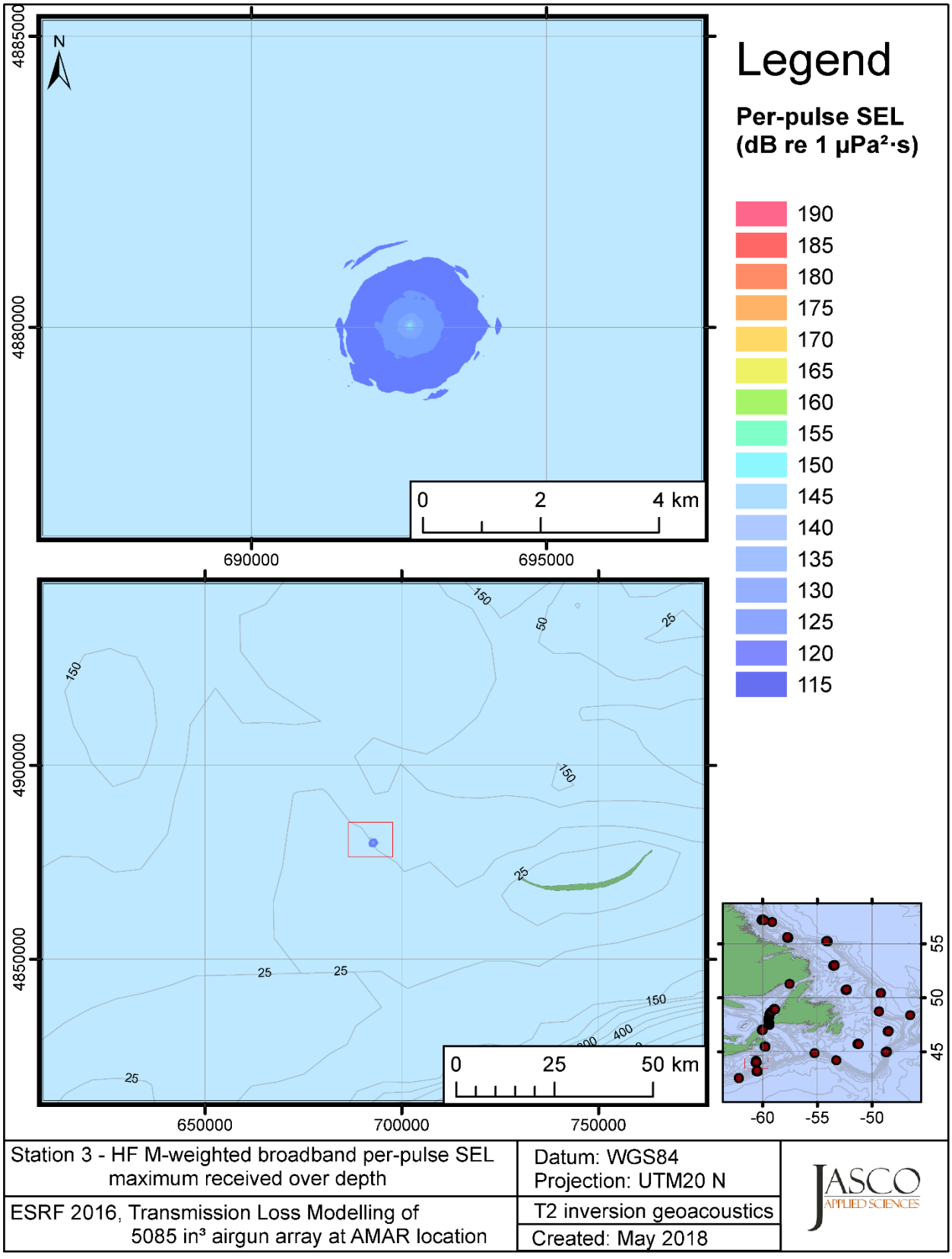

Figure C-350. Stn 3, HF M-weighted maximum-over-depth SEL received at any location on the map, modelled using the track 2 inversion geoacoustic bottom, with the airgun array at the AMAR location and in-situ July SSP.

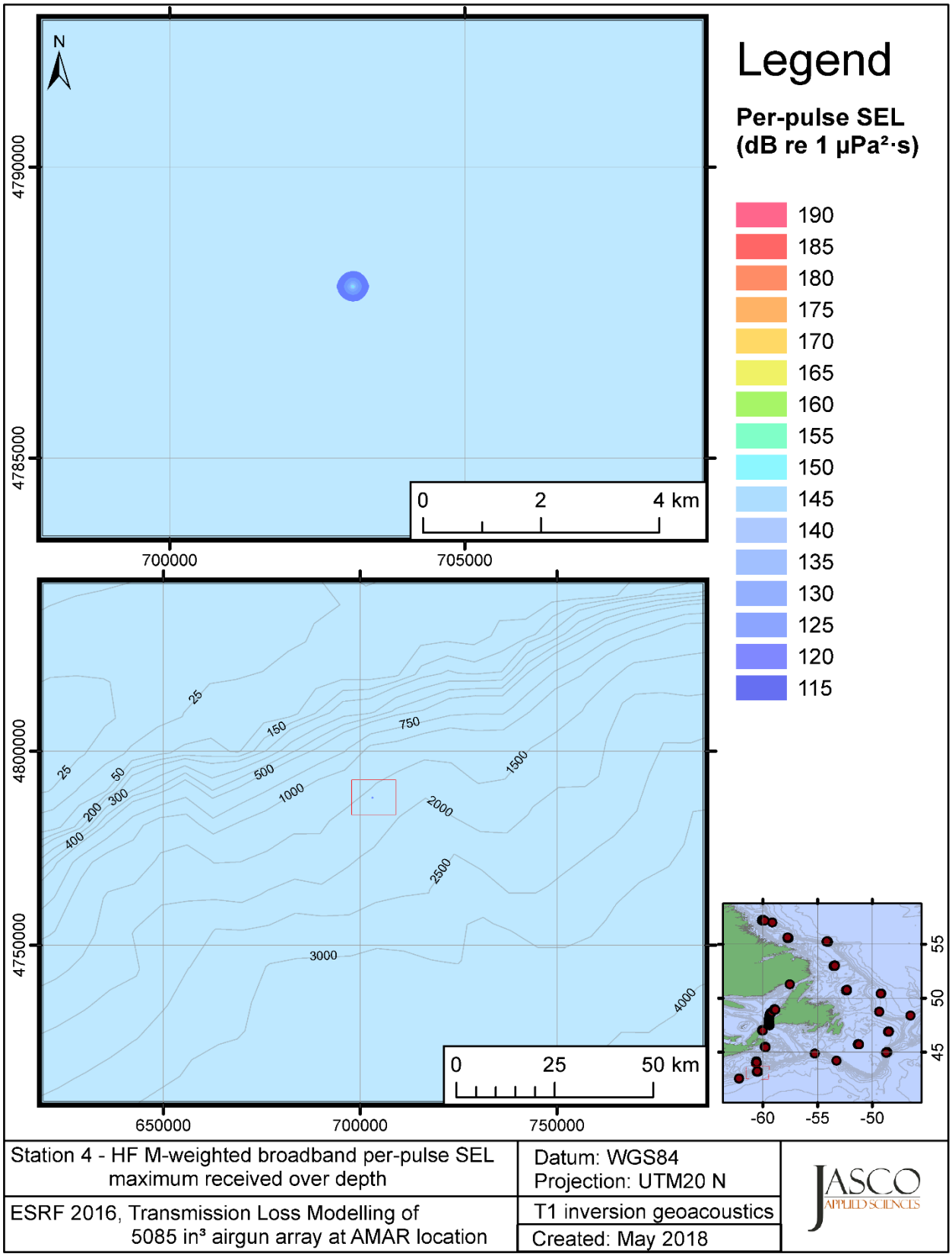

Figure C-351. Stn 4, HF M-weighted maximum-over-depth SEL received at any location on the map, modelled using the track 1 inversion geoacoustic bottom, with the airgun array at the AMAR location and in-situ July SSP.

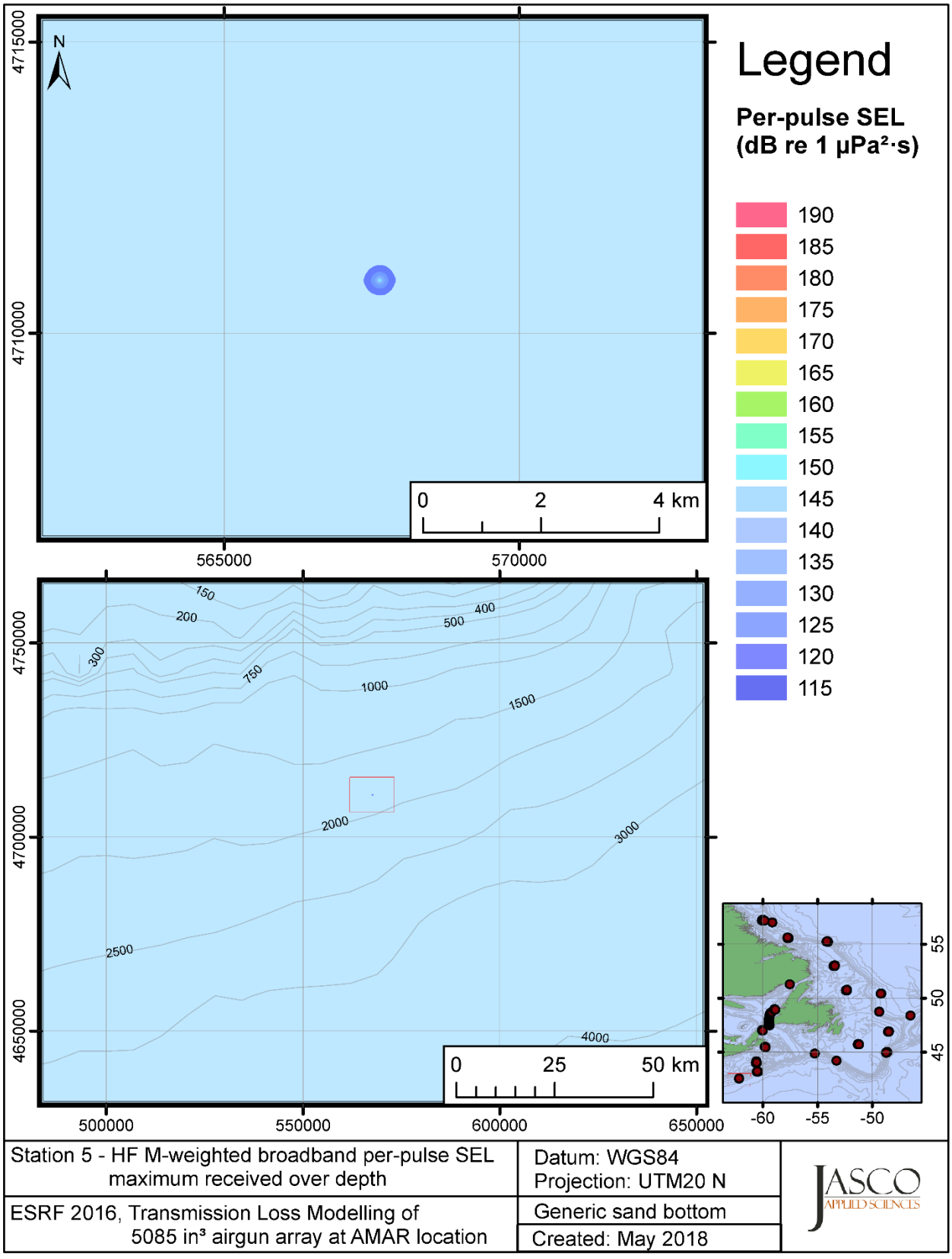

Figure C-352. Stn 5, HF M-weighted maximum-over-depth SEL received at any location on the map, modelled using a generic sand bottom, with the airgun array at the AMAR location and in-situ July SSP.

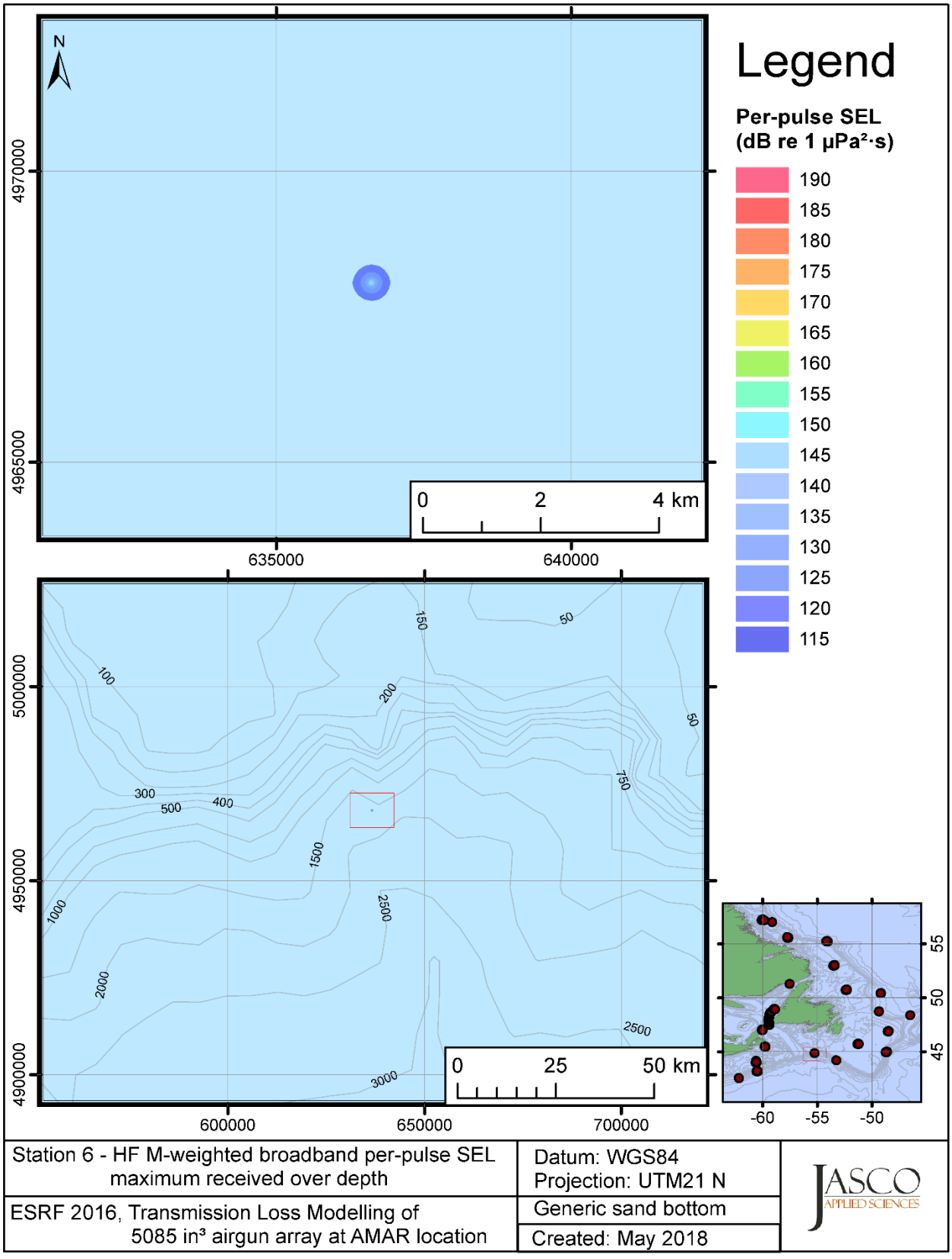

Figure C-353. Stn 6, HF M-weighted maximum-over-depth SEL received at any location on the map, modelled using a generic sand bottom, with the airgun array at the AMAR location and in-situ July SSP.

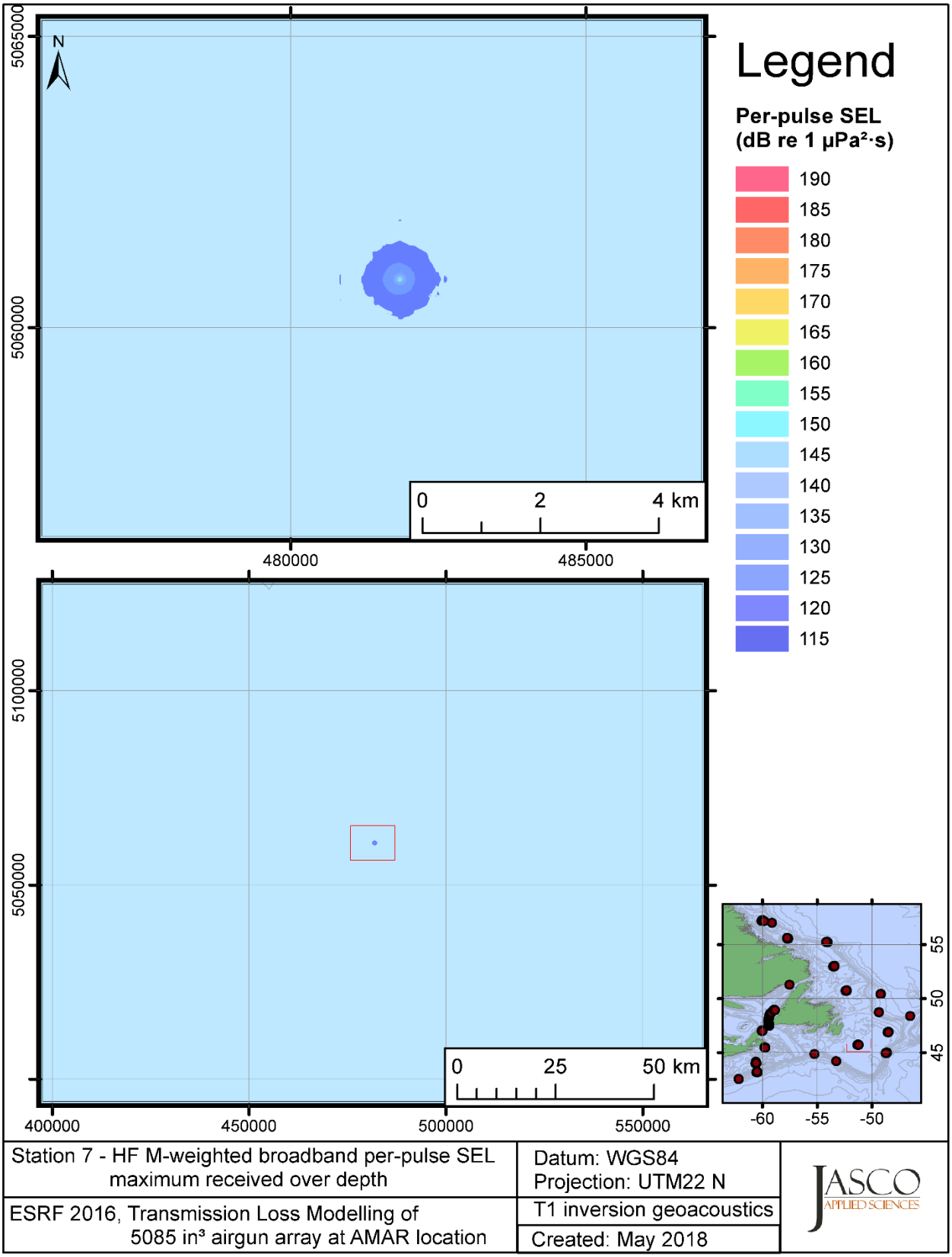

Figure C-354. Stn 7, HF M-weighted maximum-over-depth SEL received at any location on the map, modelled using the track 1 inversion geoacoustic bottom, with the airgun array at the AMAR location and in-situ July SSP.

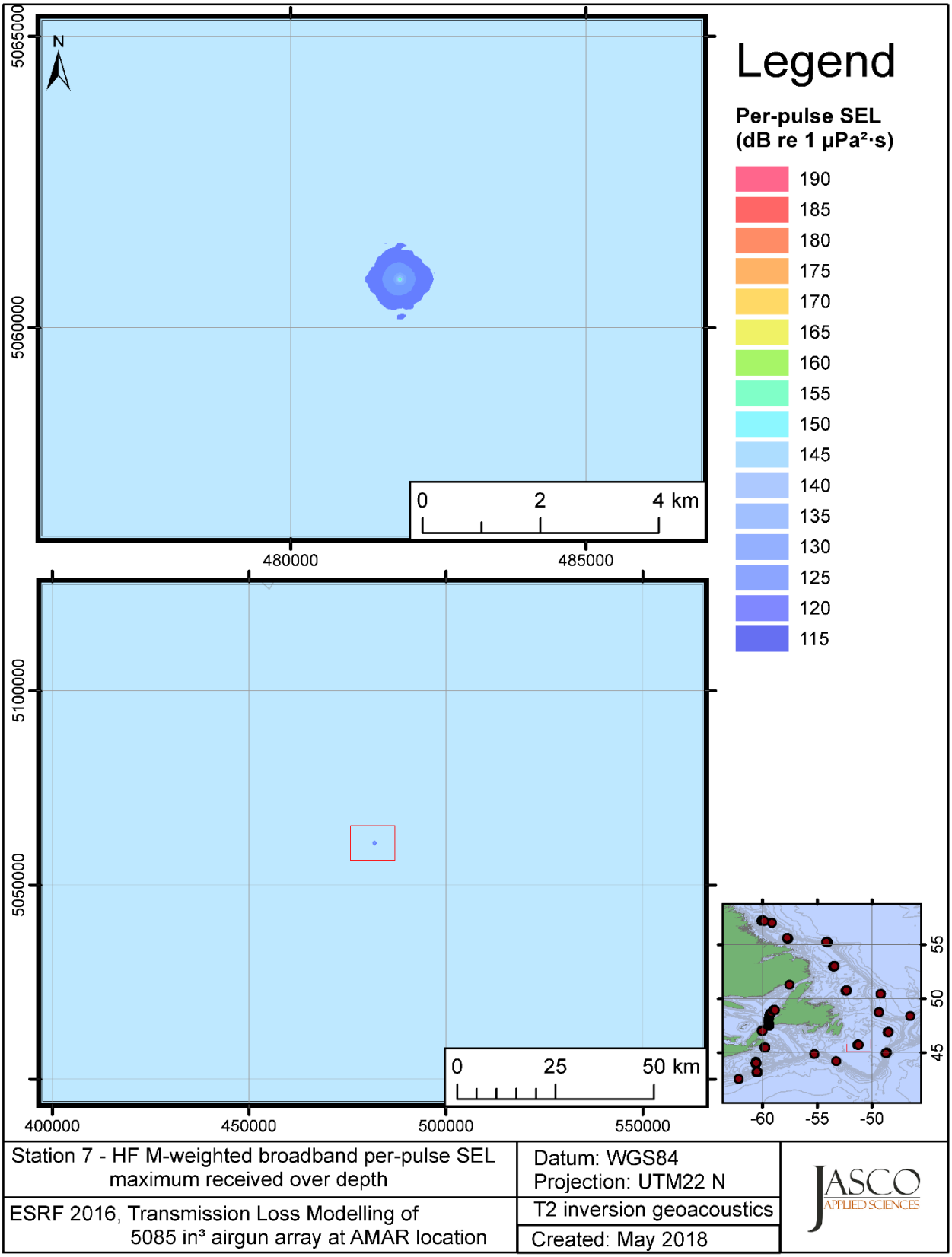

Figure C-355. Stn 7, HF M-weighted maximum-over-depth SEL received at any location on the map, modelled using the track 2 inversion geoacoustic bottom, with the airgun array at the AMAR location and in-situ July SSP.

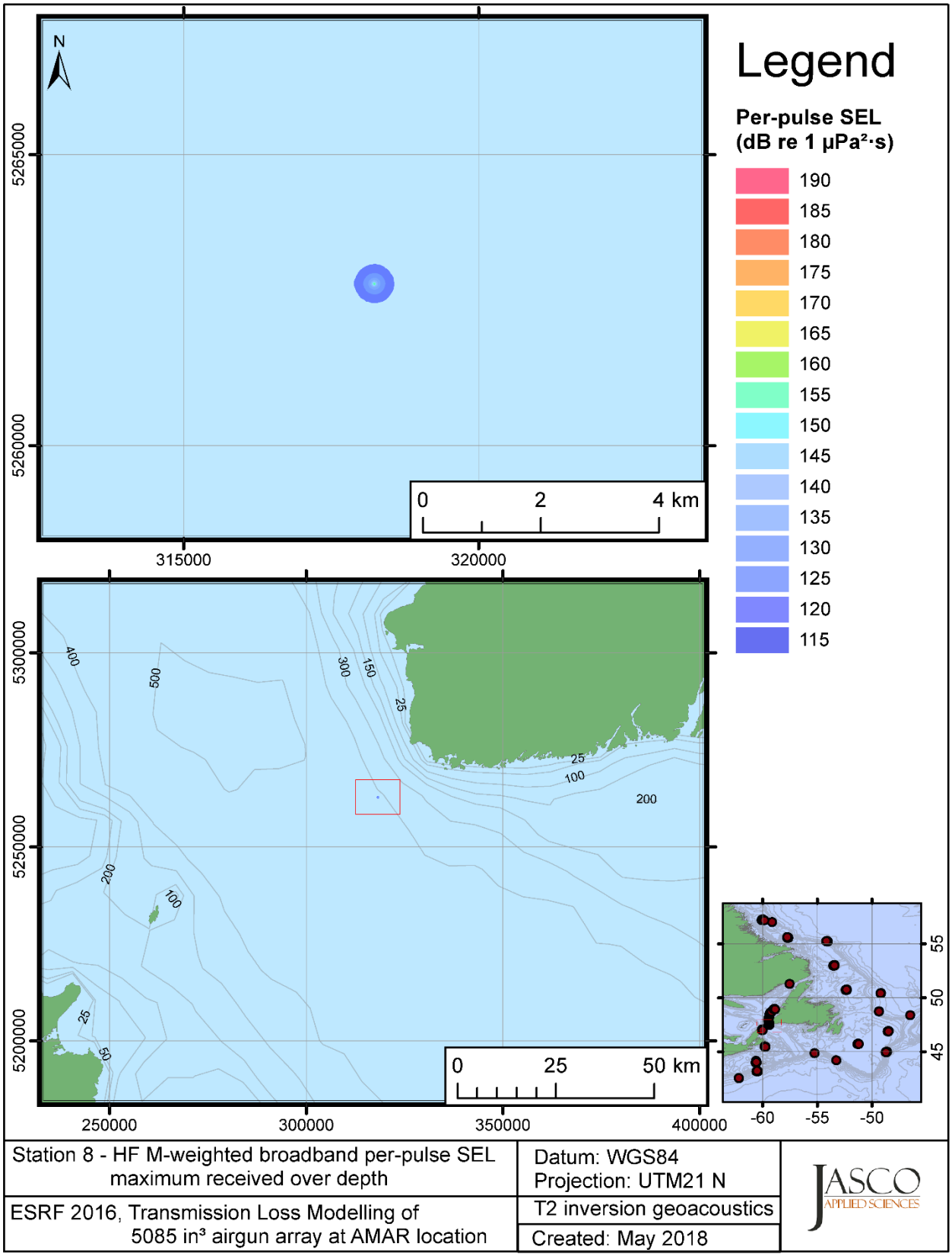

Figure C-356. Stn 8, HF M-weighted maximum-over-depth SEL received at any location on the map, modelled using the track 2 inversion geoacoustic bottom, with the airgun array at the AMAR location and GDEM July SSP.

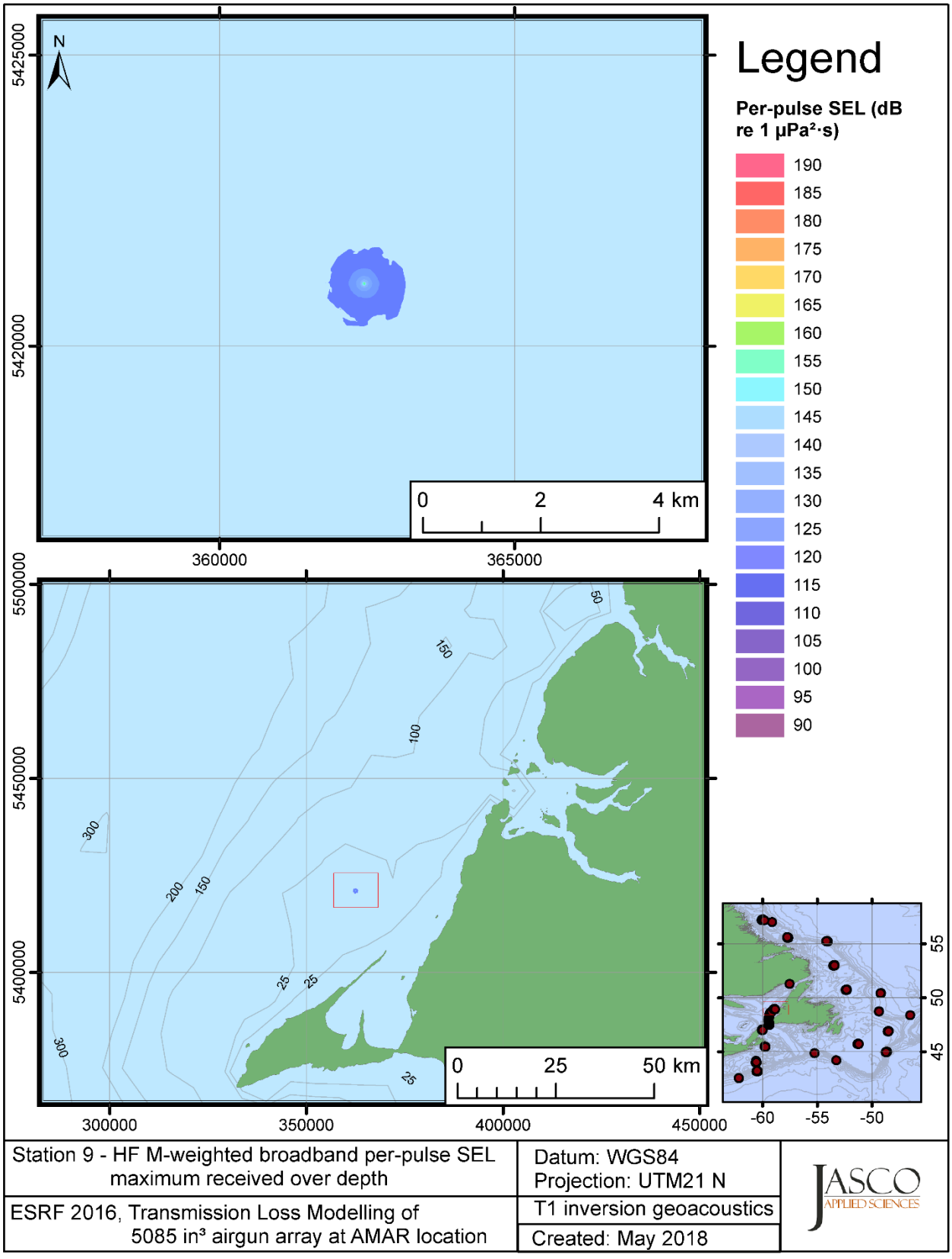

Figure C-357. Stn 9, HF M-weighted maximum-over-depth SEL received at any location on the map, modelled using the track 1 inversion geoacoustic bottom, with the airgun array at the AMAR location and GDEM July SSP.

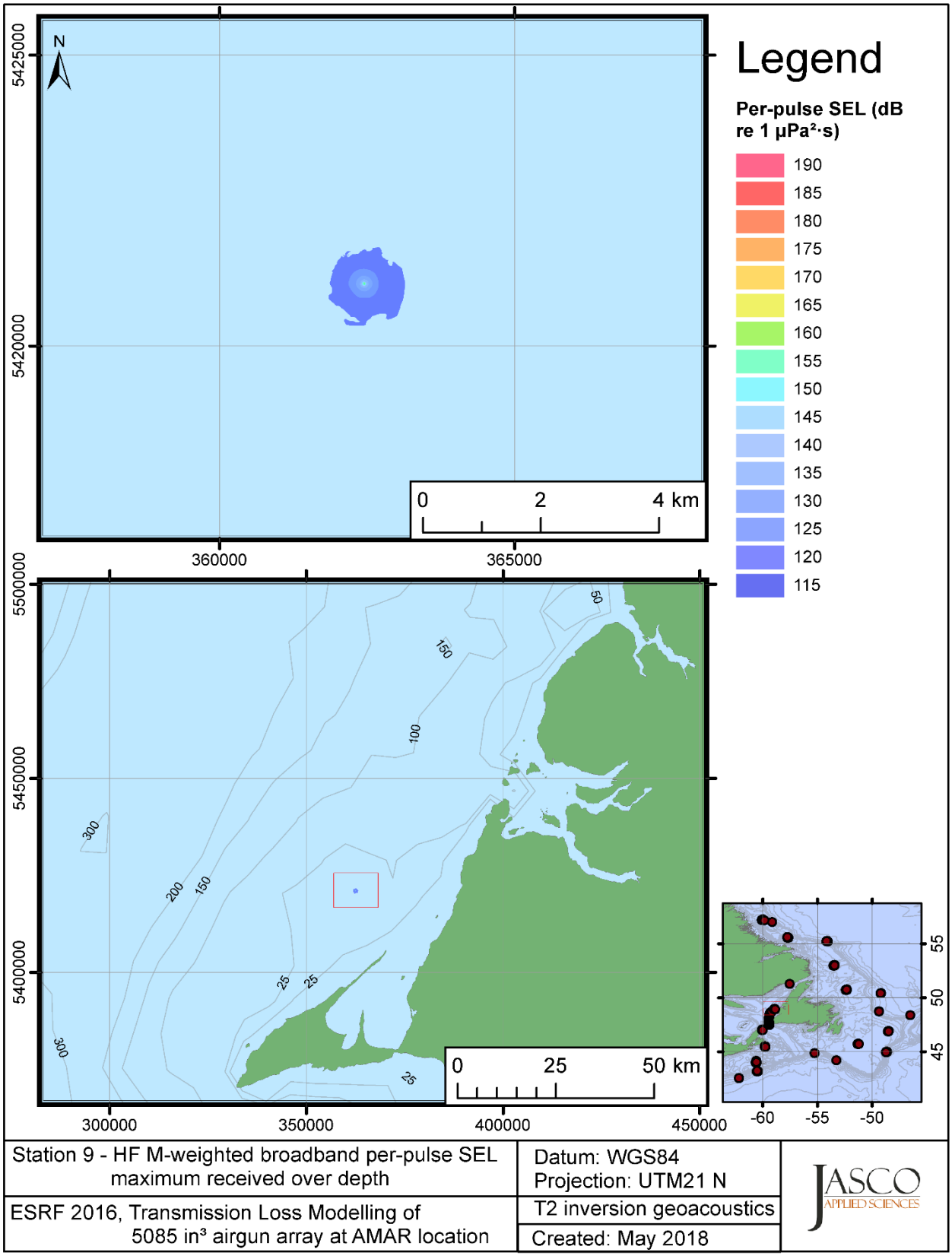

Figure C-358. Stn 9, HF M-weighted maximum-over-depth SEL received at any location on the map, modelled using the track 2 inversion geoacoustic bottom, with the airgun array at the AMAR location and GDEM July SSP.

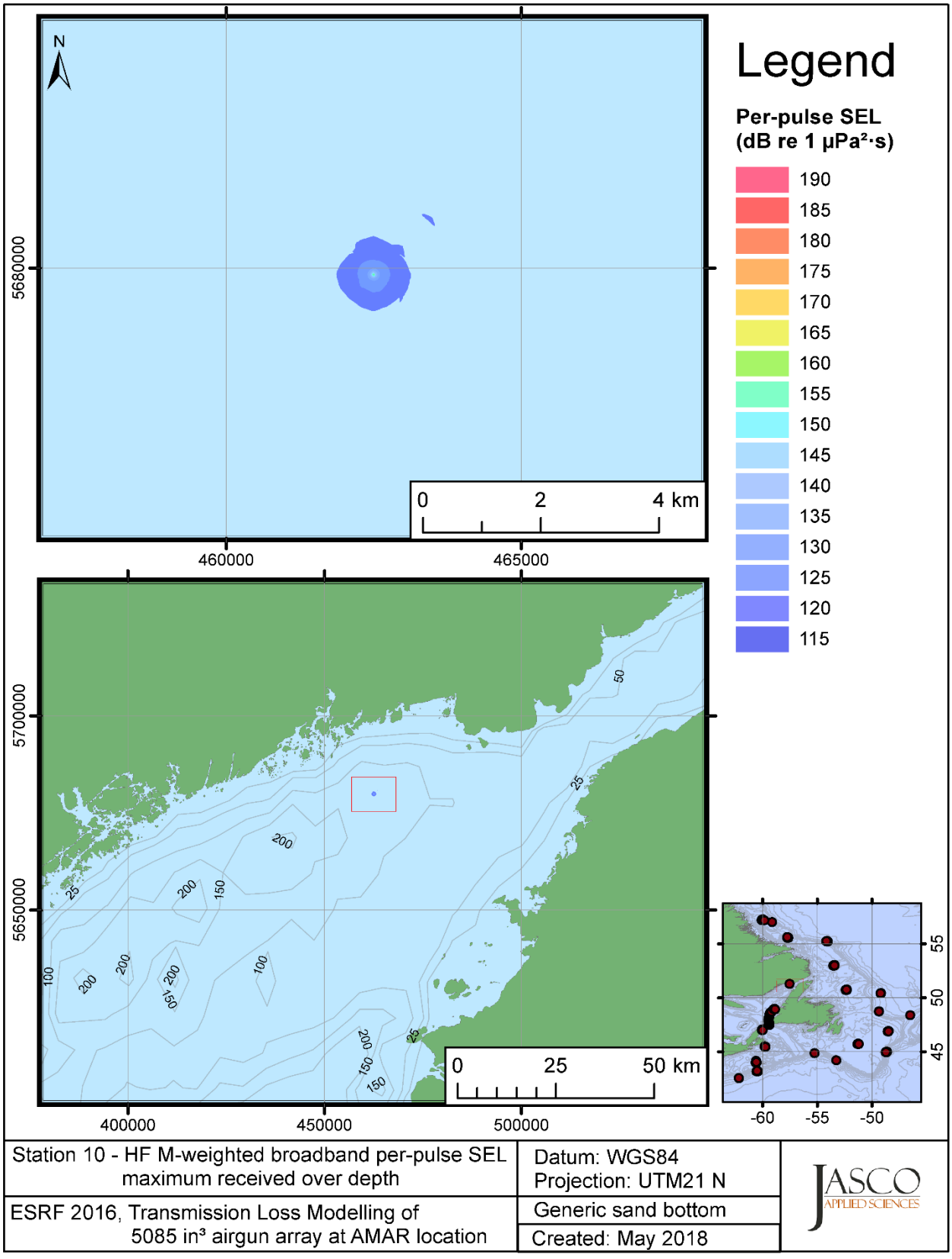

Figure C-359. Stn 10, HF M-weighted maximum-over-depth SEL received at any location on the map, modelled using a generic sand bottom, with the airgun array at the AMAR location and in-situ July SSP.

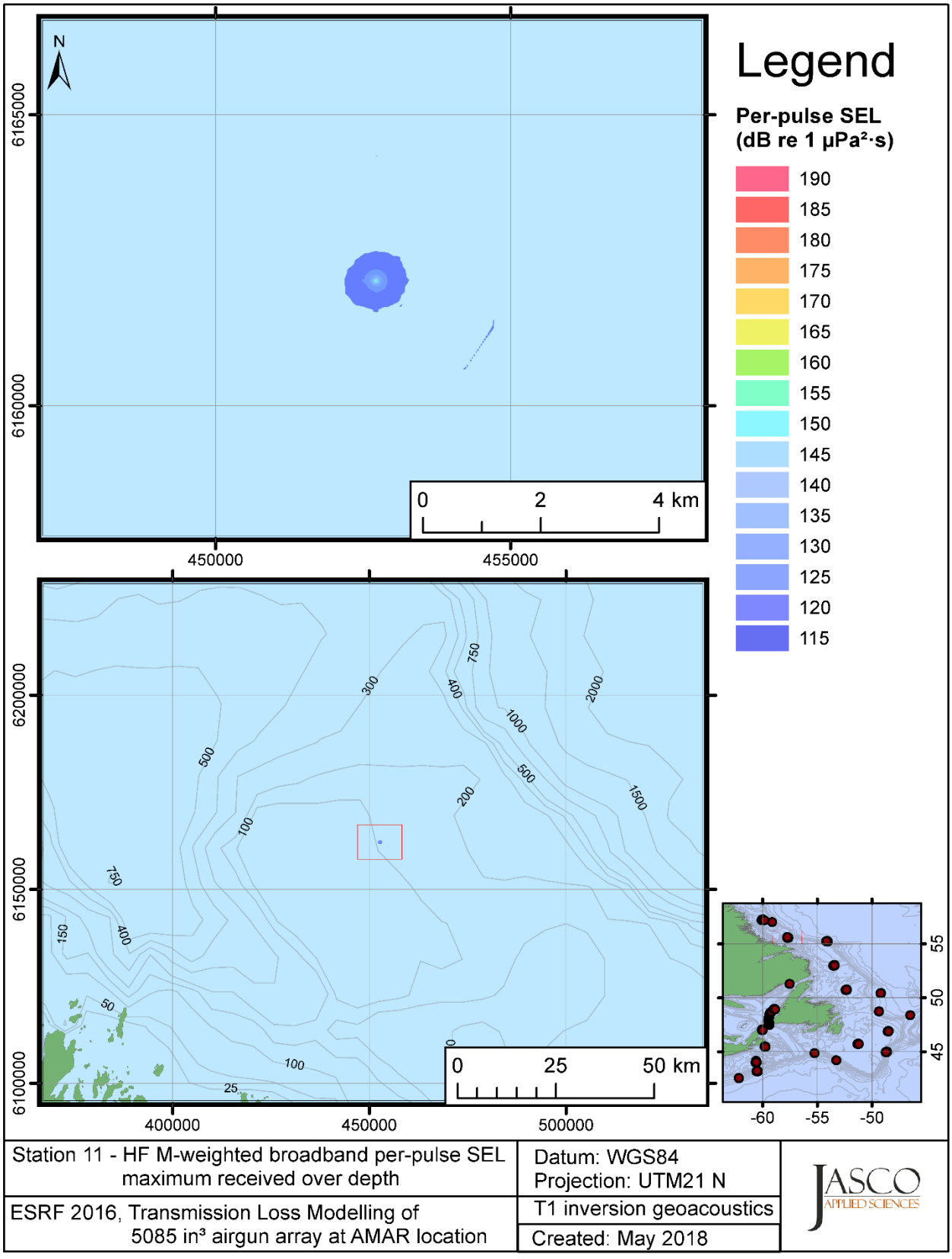

Figure C-360. Stn 11, HF M-weighted maximum-over-depth SEL received at any location on the map, modelled using the track 1 inversion geoacoustic bottom, with the airgun array at the AMAR location and in-situ July SSP.

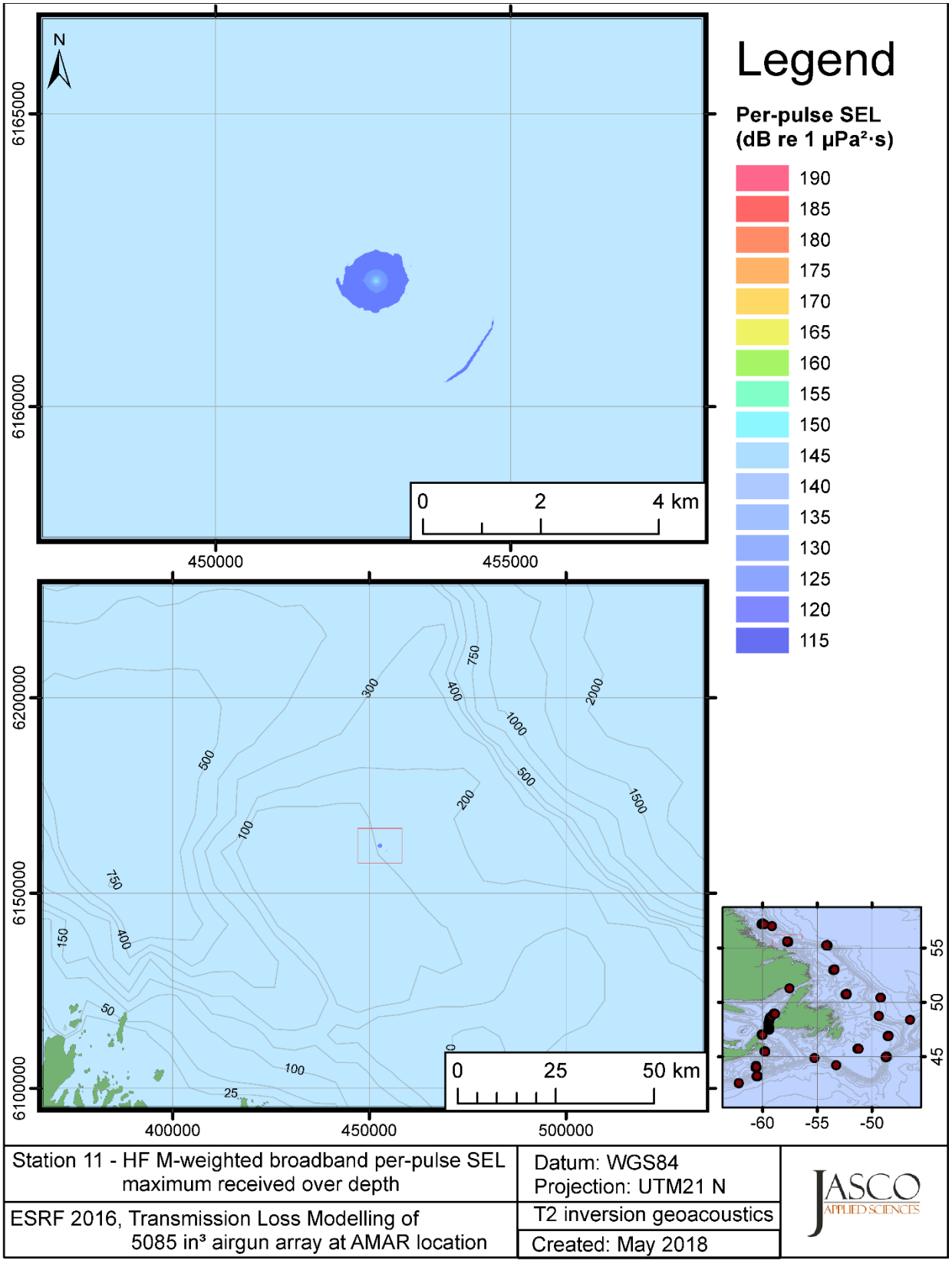

Figure C-361. Stn 11, HF M-weighted maximum-over-depth SEL received at any location on the map, modelled using the track 2 inversion geoacoustic bottom, with the airgun array at the AMAR location and in-situ July SSP.

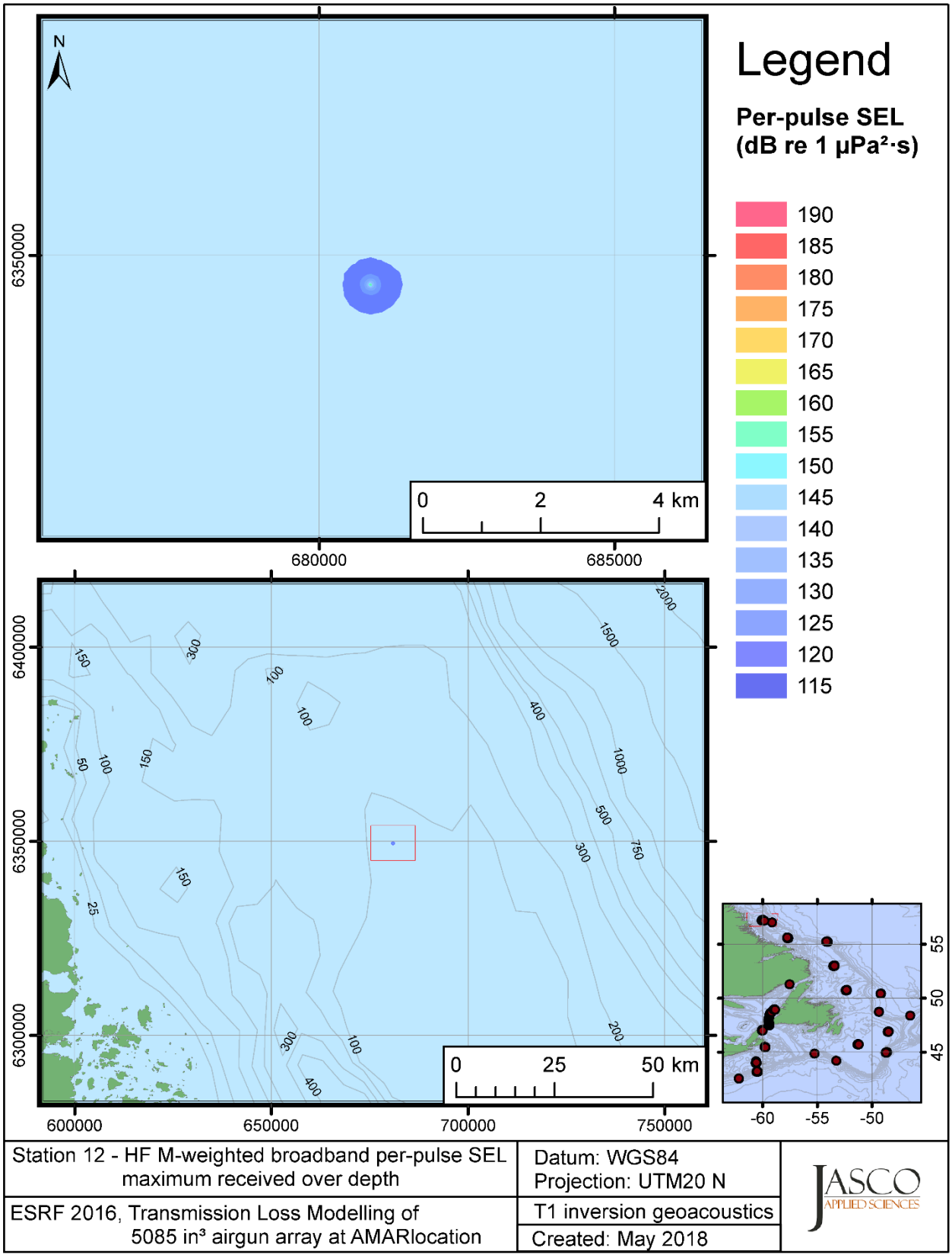

Figure C-362. Stn 12, HF M-weighted maximum-over-depth SEL received at any location on the map, modelled using the track 1 inversion geoacoustic bottom, with the airgun array at the AMAR location and in-situ July SSP.

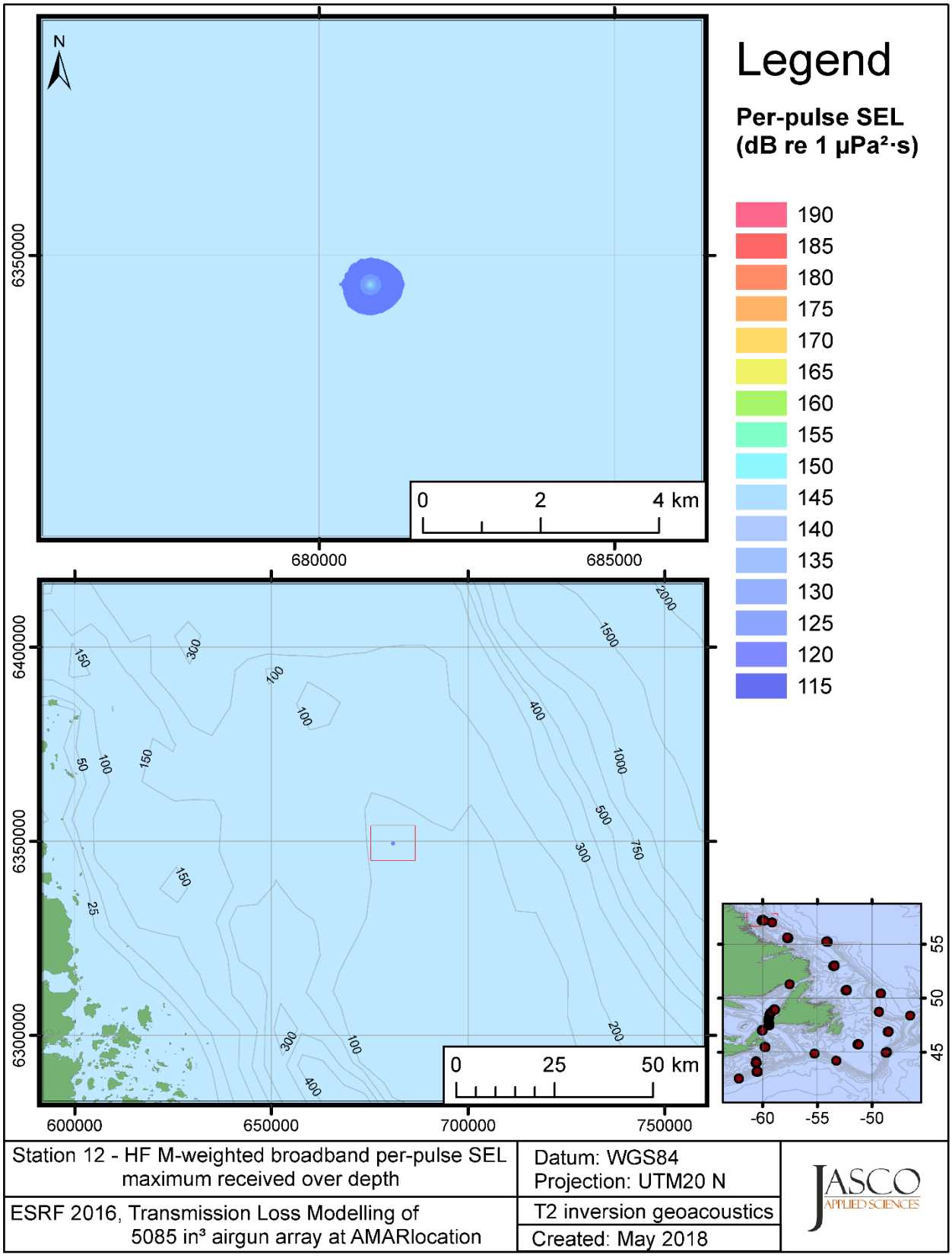

Figure C-363. Stn 12, HF M-weighted maximum-over-depth SEL received at any location on the map, modelled using the track 2 inversion geoacoustic bottom, with the airgun array at the AMAR location and in-situ July SSP.

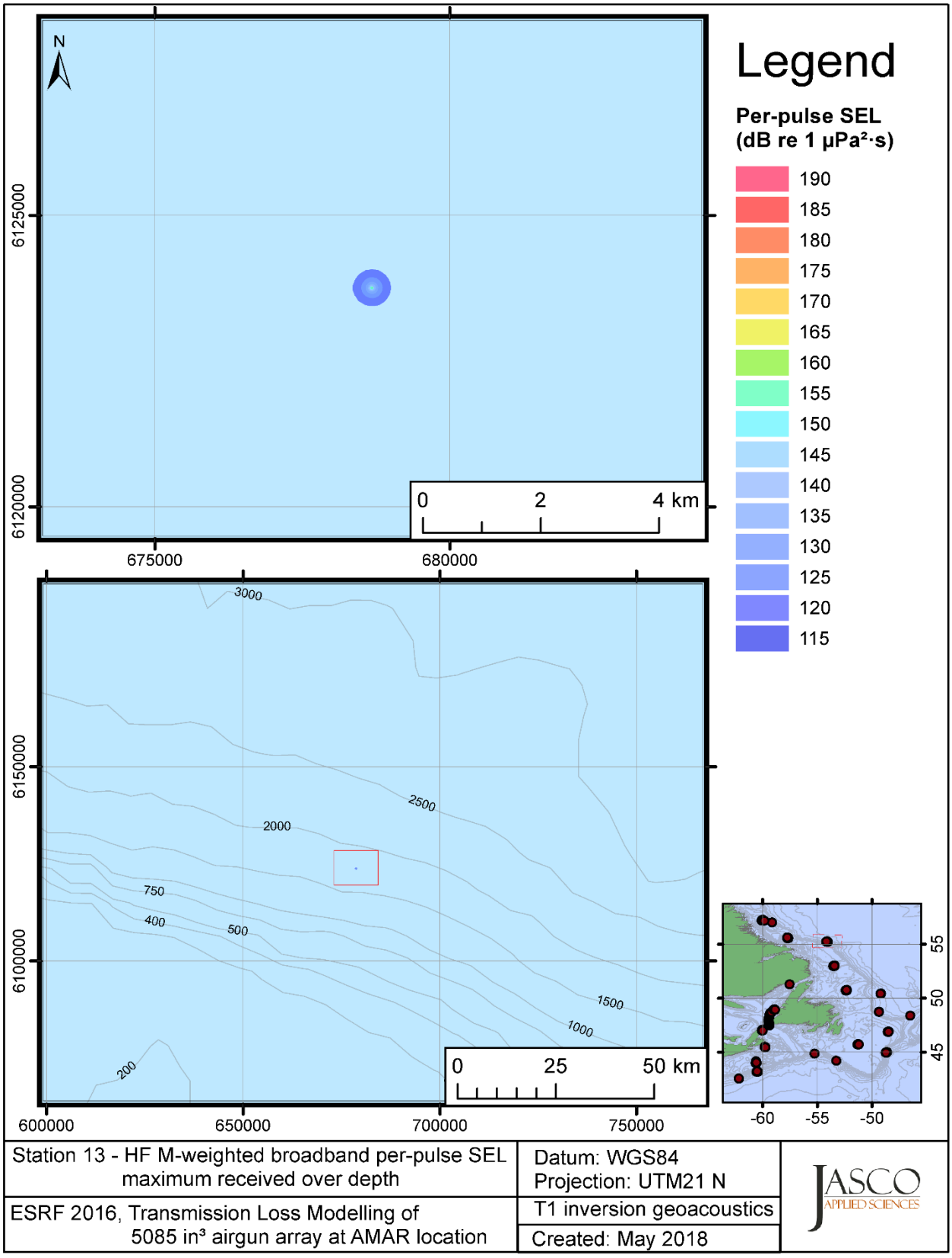

Figure C-364. Stn 13, HF M-weighted maximum-over-depth SEL received at any location on the map, modelled using the track 1 inversion geoacoustic bottom, with the airgun array at the AMAR location and in-situ July SSP.

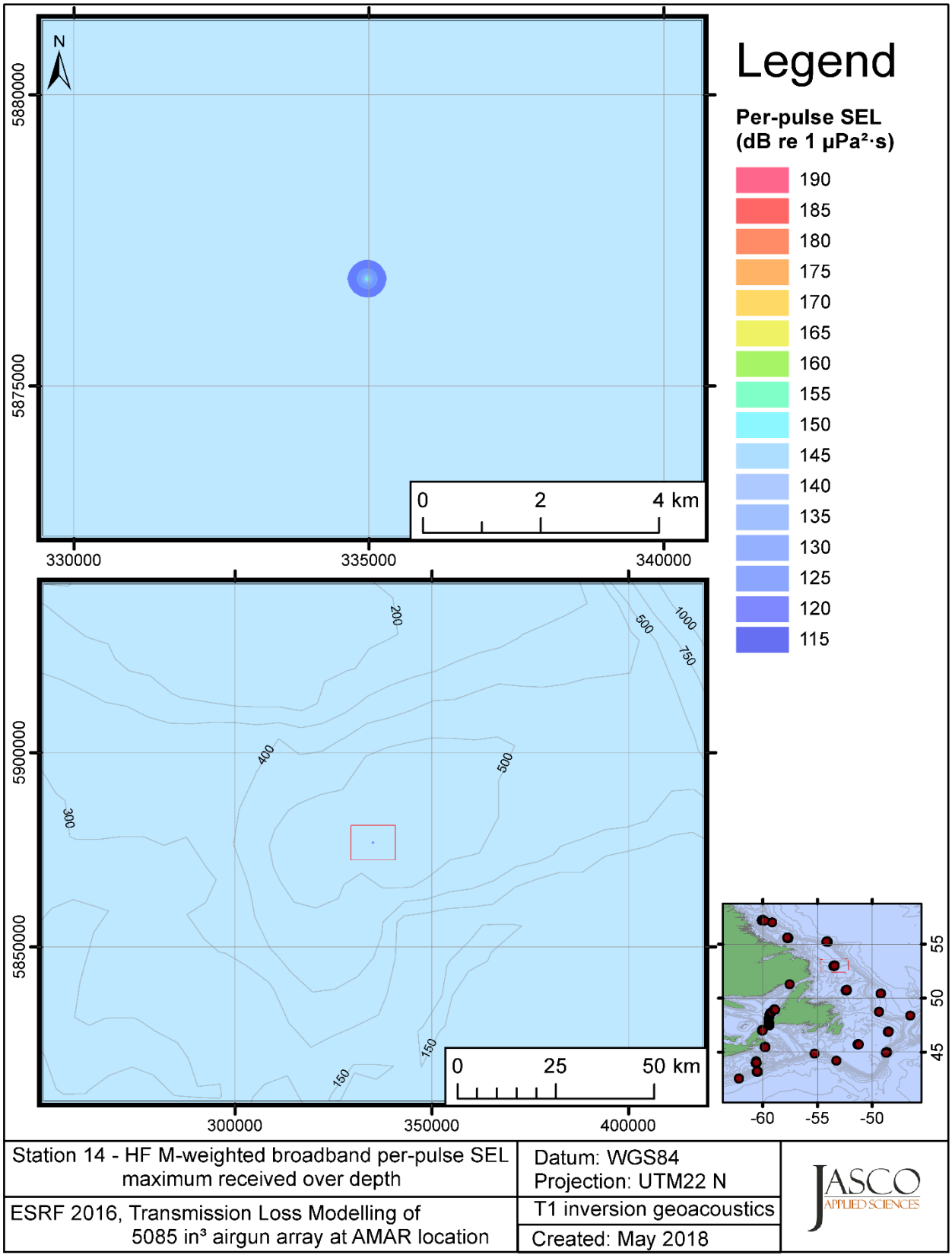

Figure C-365. Stn 14, HF M-weighted maximum-over-depth SEL received at any location on the map, modelled using the track 1 inversion geoacoustic bottom, with the airgun array at the AMAR location and in-situ July SSP.

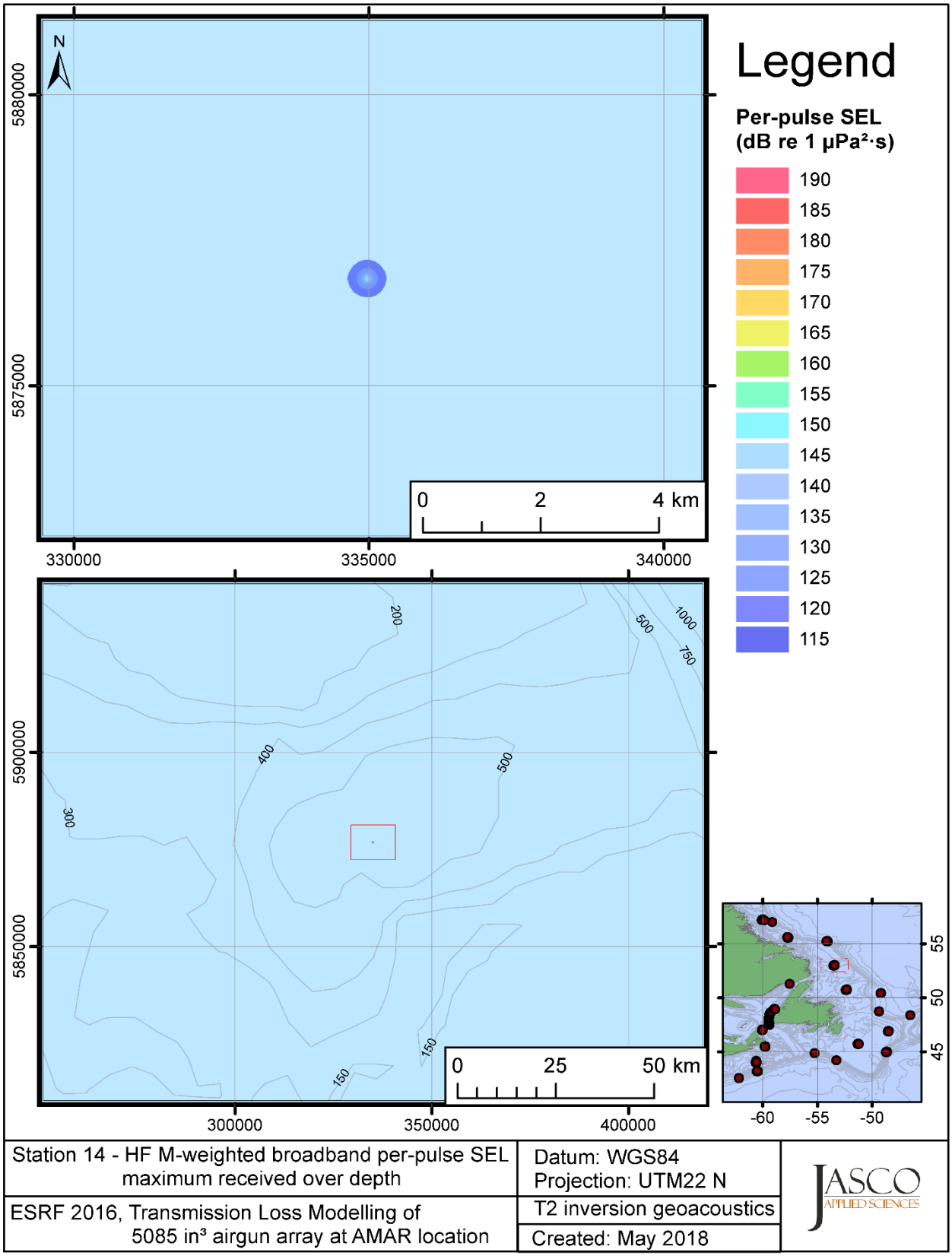

Figure C-366. Stn 14, HF M-weighted maximum-over-depth SEL received at any location on the map, modelled using the track 2 inversion geoacoustic bottom, with the airgun array at the AMAR location and in-situ July SSP.

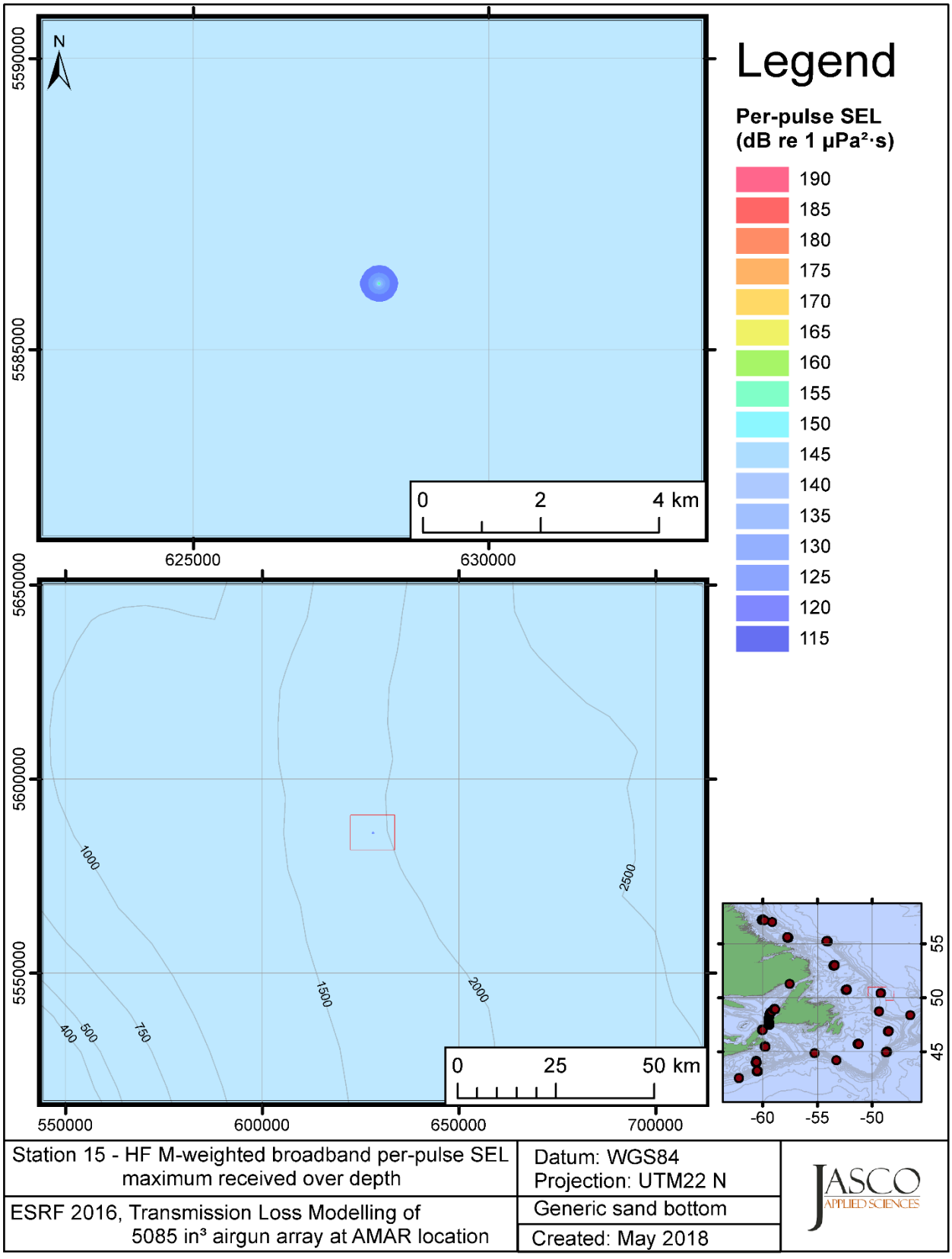

Figure C-367. Stn 15, HF M-weighted maximum-over-depth SEL received at any location on the map, modelled using a generic sand bottom, with the airgun array at the AMAR location and in-situ July SSP.

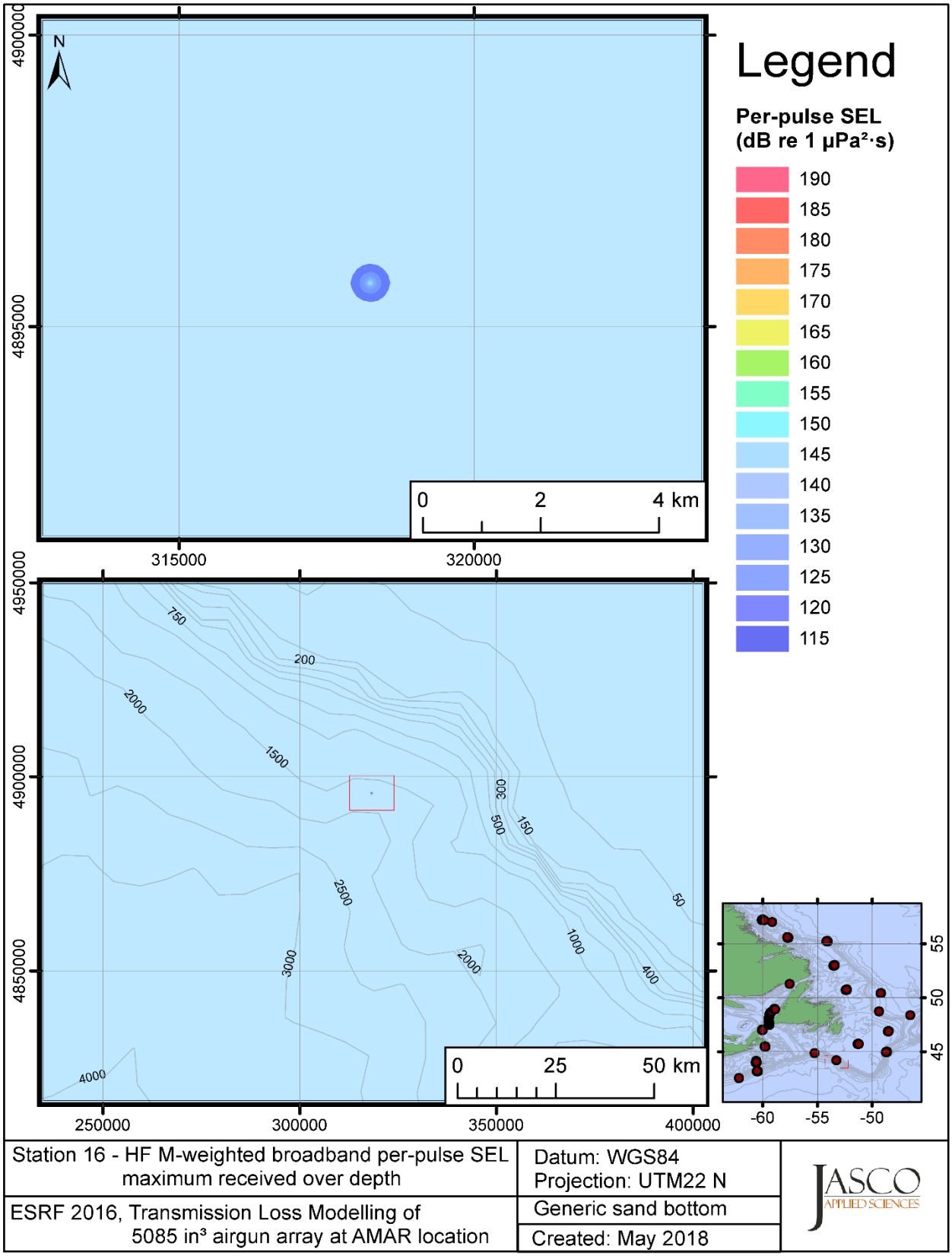

Figure C-368. Stn 16, HF M-weighted maximum-over-depth SEL received at any location on the map, modelled using a generic sand bottom, with the airgun array at the AMAR location and in-situ July SSP.

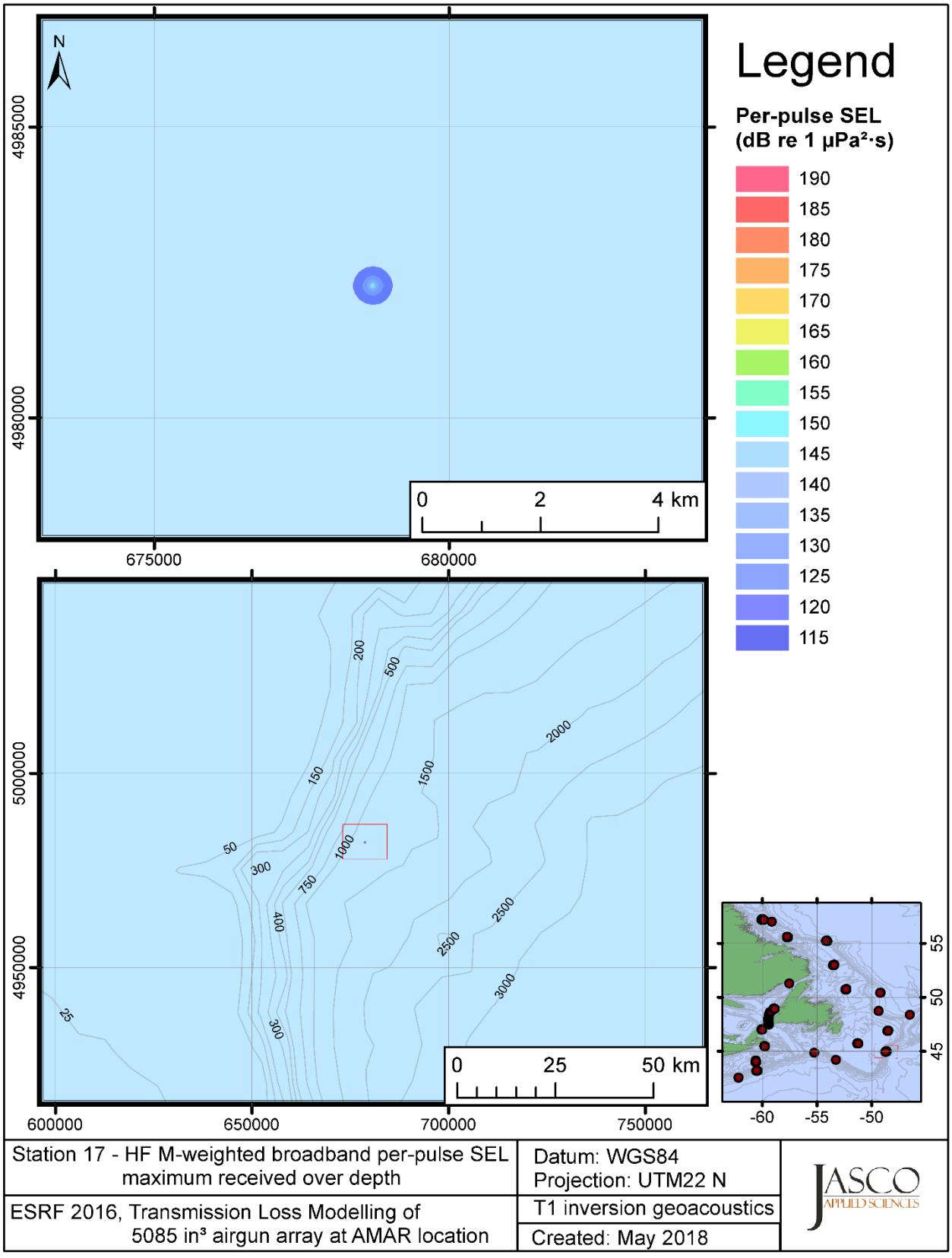

Figure C-369. Stn 17, HF M-weighted maximum-over-depth SEL received at any location on the map, modelled using the track 1 inversion geoacoustic bottom, with the airgun array at the AMAR location and in-situ July SSP.

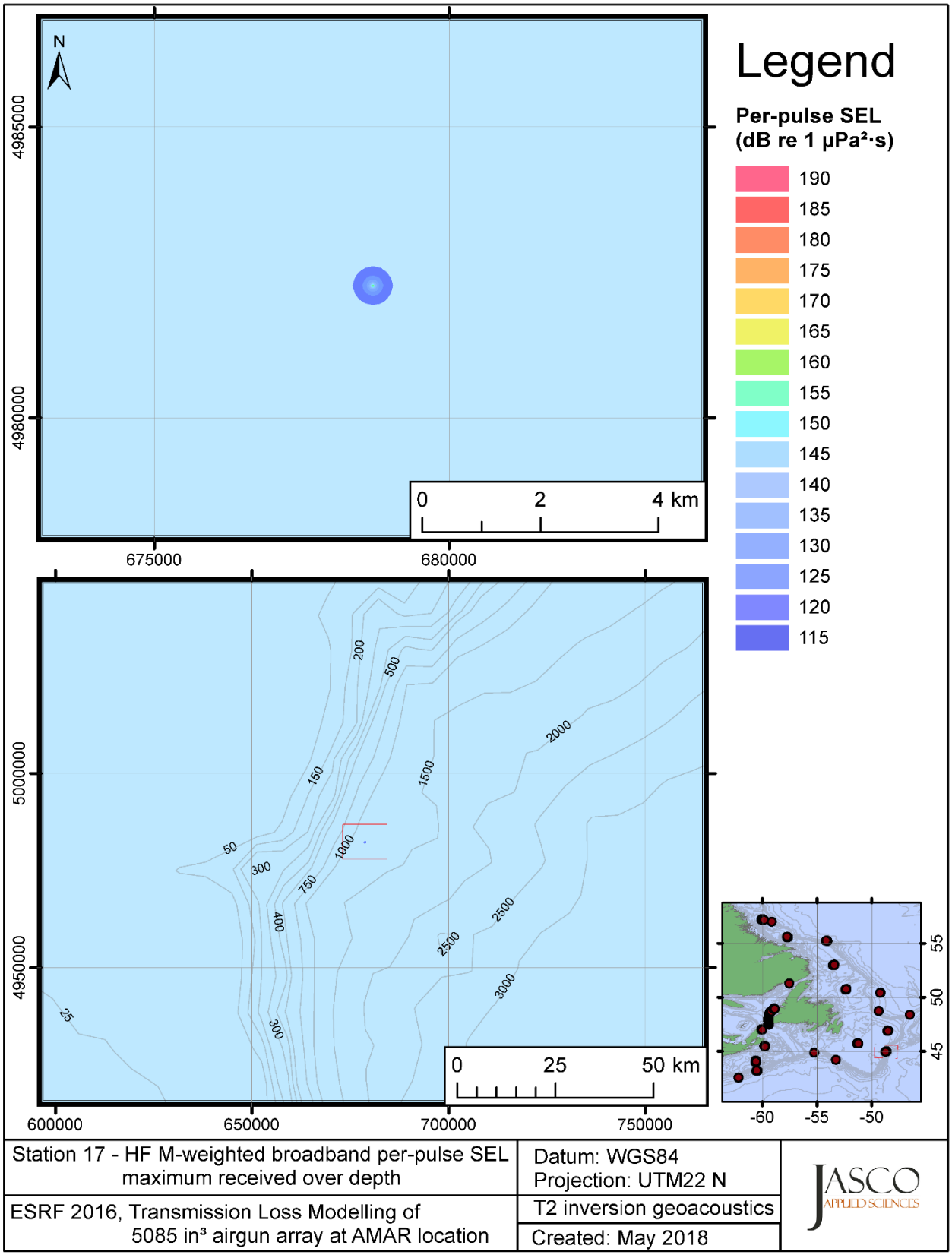

Figure C-370. Stn 17, HF M-weighted maximum-over-depth SEL received at any location on the map, modelled using the track 2 inversion geoacoustic bottom, with the airgun array at the AMAR location and in-situ July SSP.

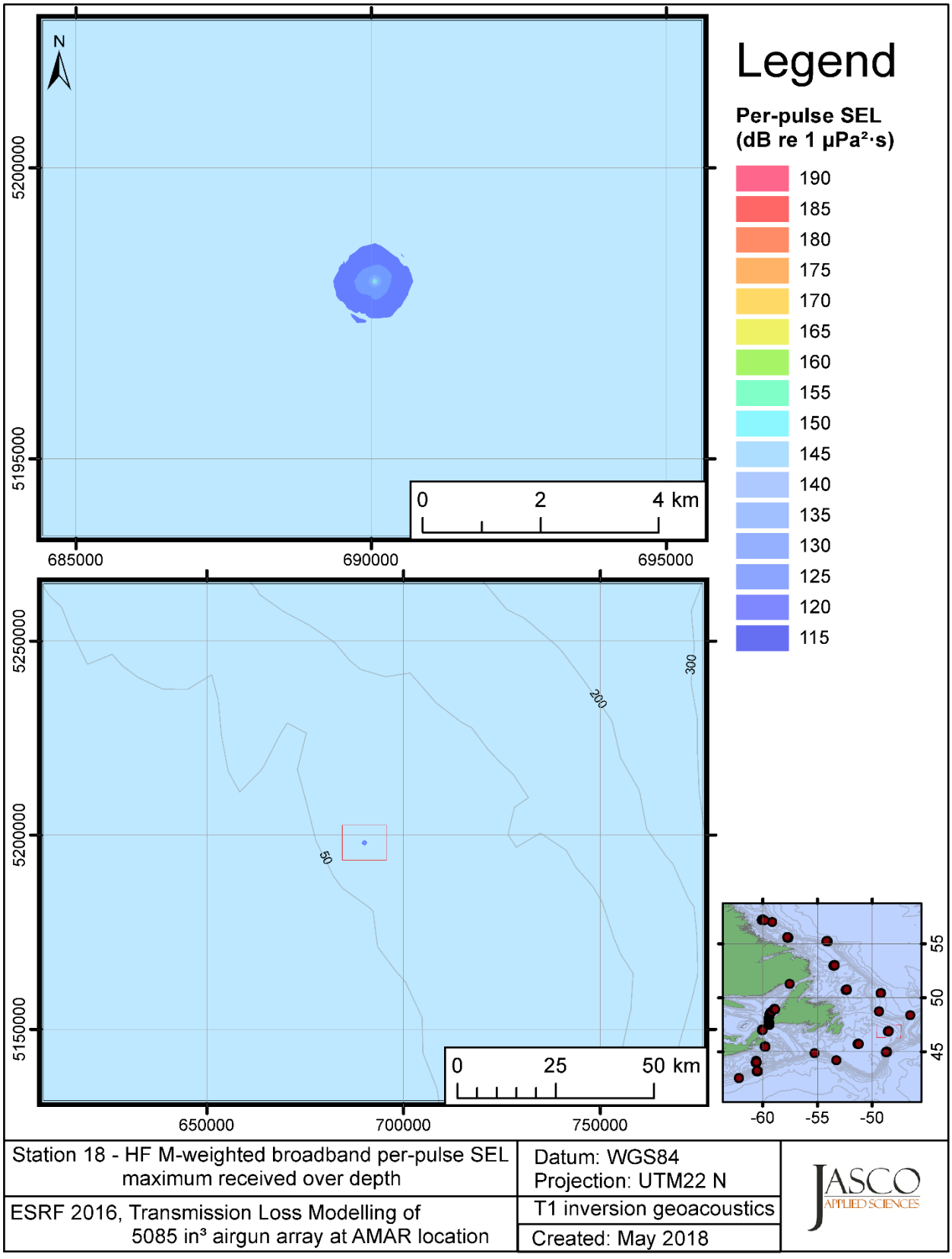

Figure C-371. Stn 18, HF M-weighted maximum-over-depth SEL received at any location on the map, modelled using the track 1 inversion geoacoustic bottom, with the airgun array at the AMAR location and in-situ July SSP.

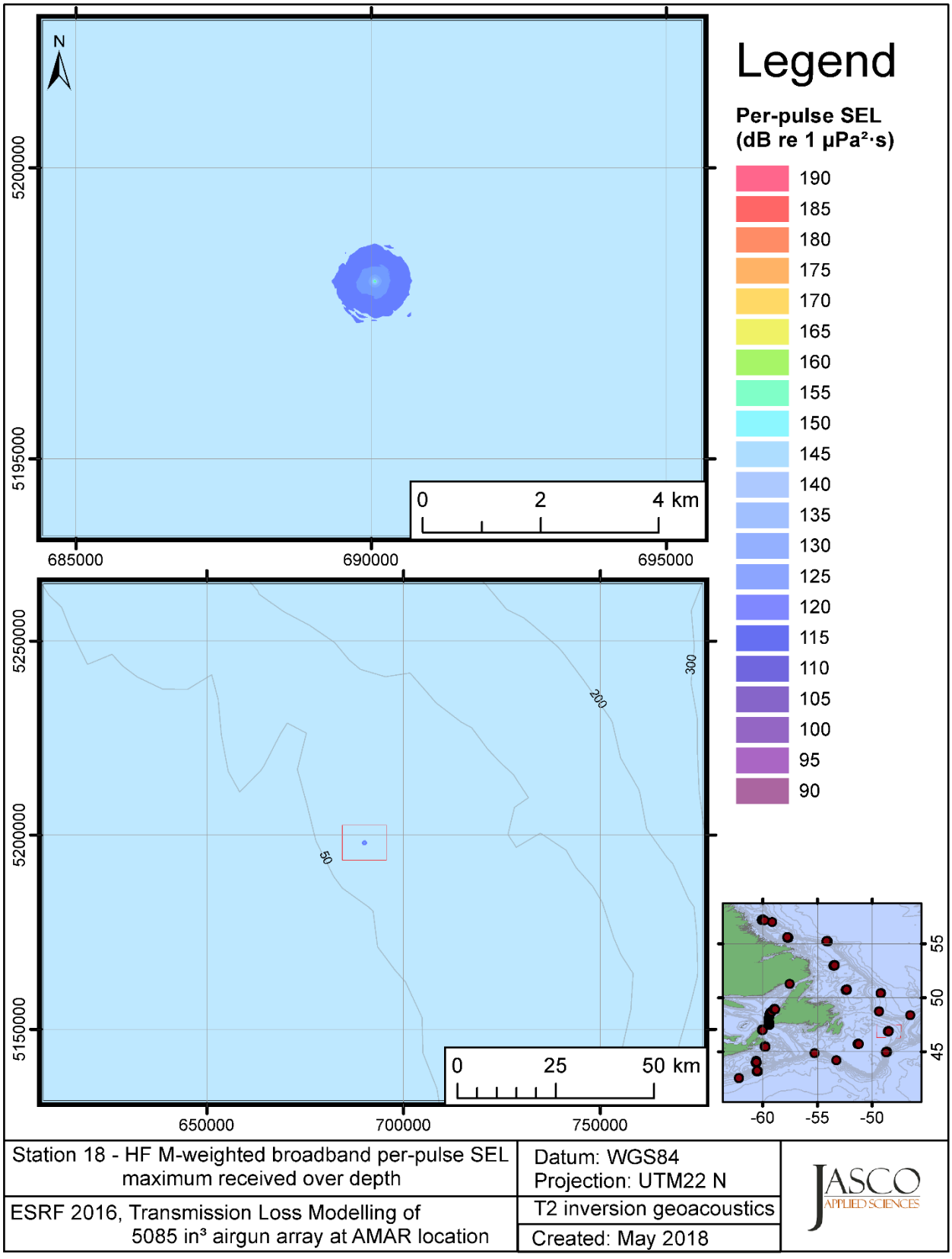

Figure C-372. Stn 18, HF M-weighted maximum-over-depth SEL received at any location on the map, modelled using the track 2 inversion geoacoustic bottom, with the airgun array at the AMAR location and in-situ July SSP.

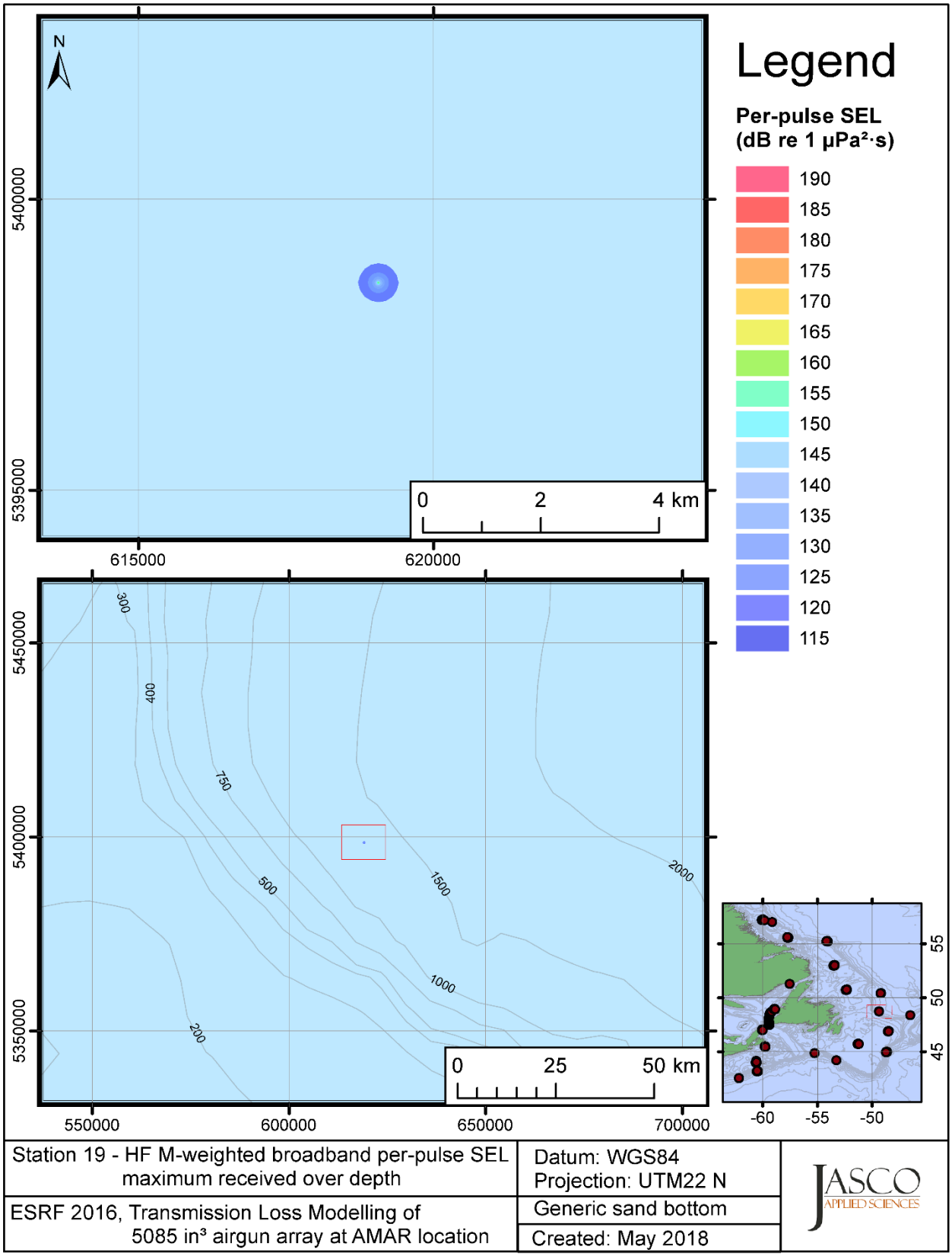

Figure C-373. Stn 19, HF M-weighted maximum-over-depth SEL received at any location on the map, modelled using a generic sand bottom, with the airgun array at the AMAR location and in-situ July SSP.

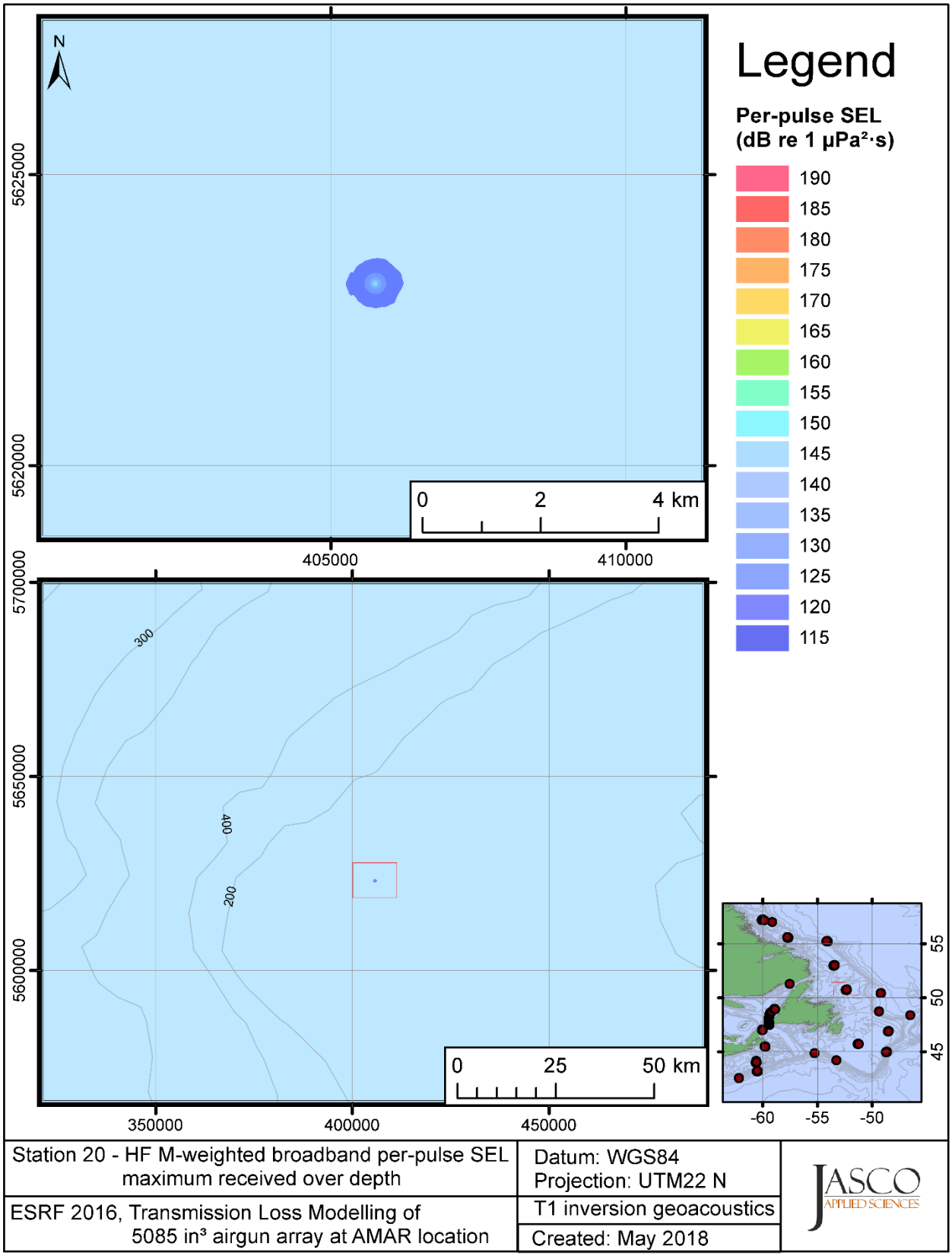

Figure C-374. Stn 20, HF M-weighted maximum-over-depth SEL received at any location on the map, modelled using the track 1 inversion geoacoustic bottom, with the airgun array at the AMAR location and in-situ July SSP.

C.11. Modelling OP M-weighted Max-over-depth Received Level at Distant Locations - Summer

This section presents the results of modelling the maximum-over-depth per-pulse sound exposure level (SEL) received at distant receiver locations (varied in range and azimuth) for the source held fixed at the AMAR location. The modelling uses the geoacoustic inversion bottom parameters at the 14 sites where they are available and only uses a generic sand bottom at the other six sites. The modelling results are presented in the form of coloured maps where the colour at any map location represents the predicted maximum-over-depth received level at that spot on the map. This section includes only the otariid pinnipeds in water (OP) marine-mammal-weighted per-pulse SEL results; additional maps for other marine mammal received level auditory weightings are presented in adjoining sections. The sound speed profiles (SSP) used are detailed in Appendix B.1.

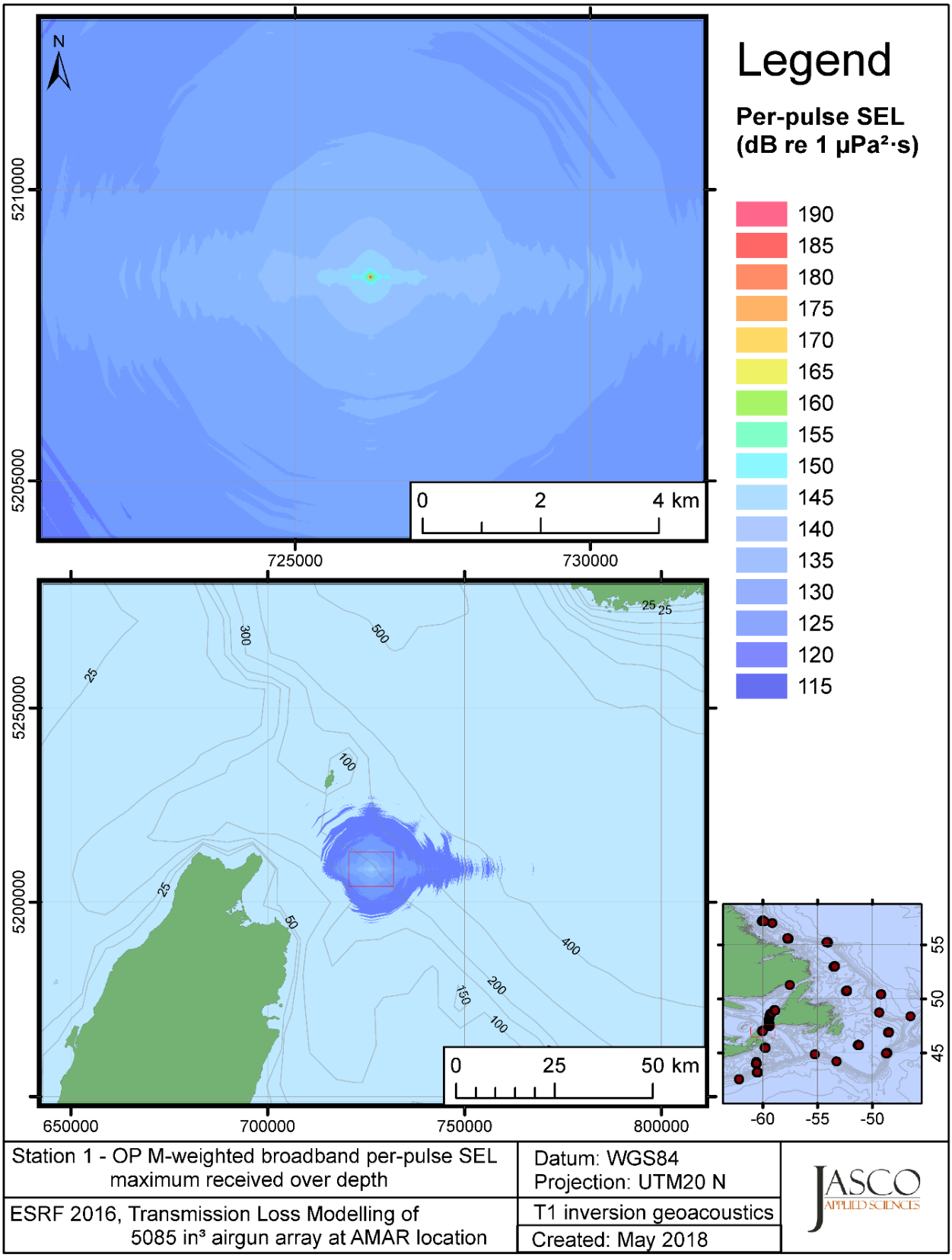

Figure C-375. Stn 1, OP M-weighted maximum-over-depth SEL received at any location on the map, modelled using the track 1 inversion geoacoustic bottom, with the airgun array at the AMAR location and in-situ July SSP.

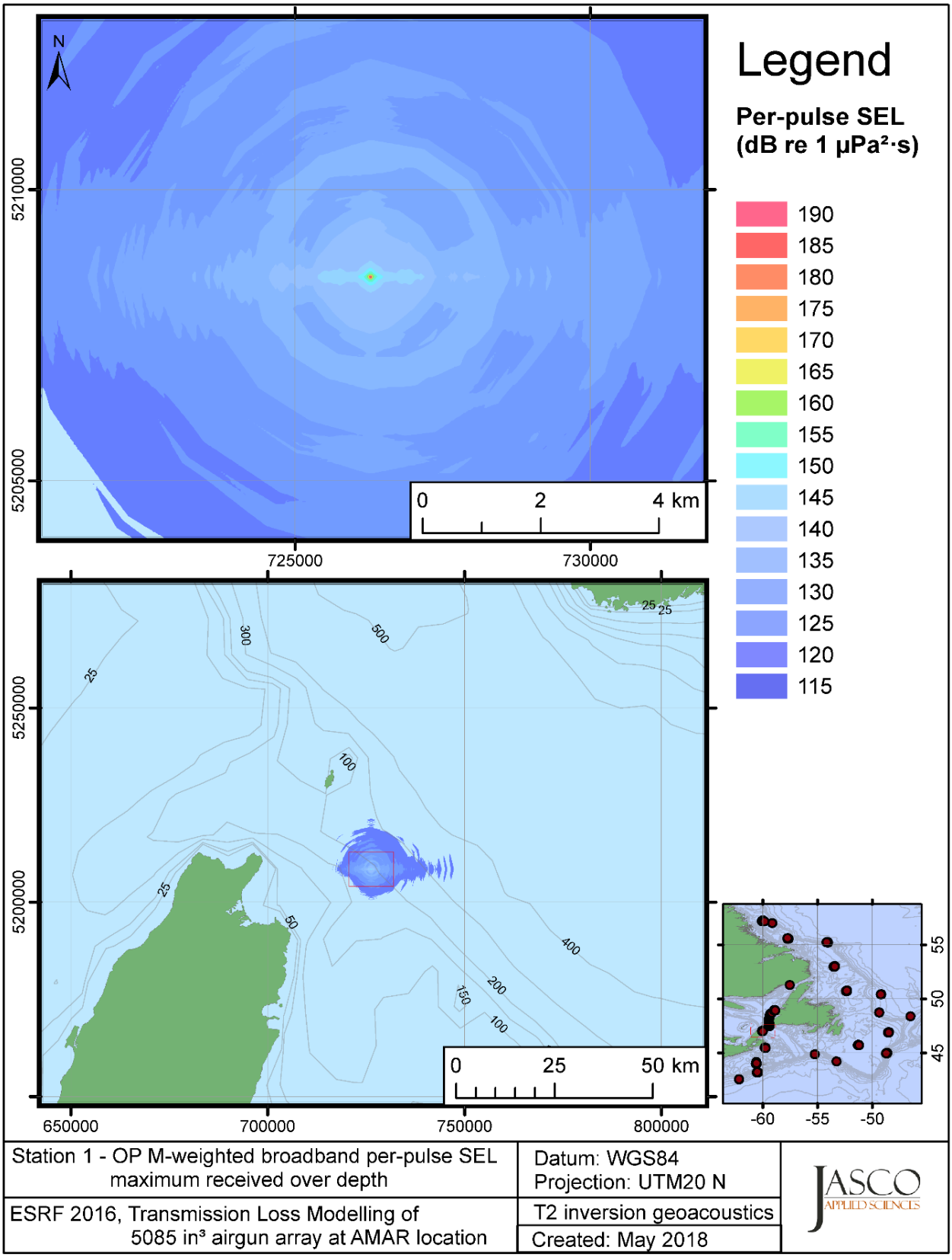

Figure C-376. Stn 1, OP M-weighted maximum-over-depth SEL received at any location on the map, modelled using the track 2 inversion geoacoustic bottom, with the airgun array at the AMAR location and in-situ July SSP.

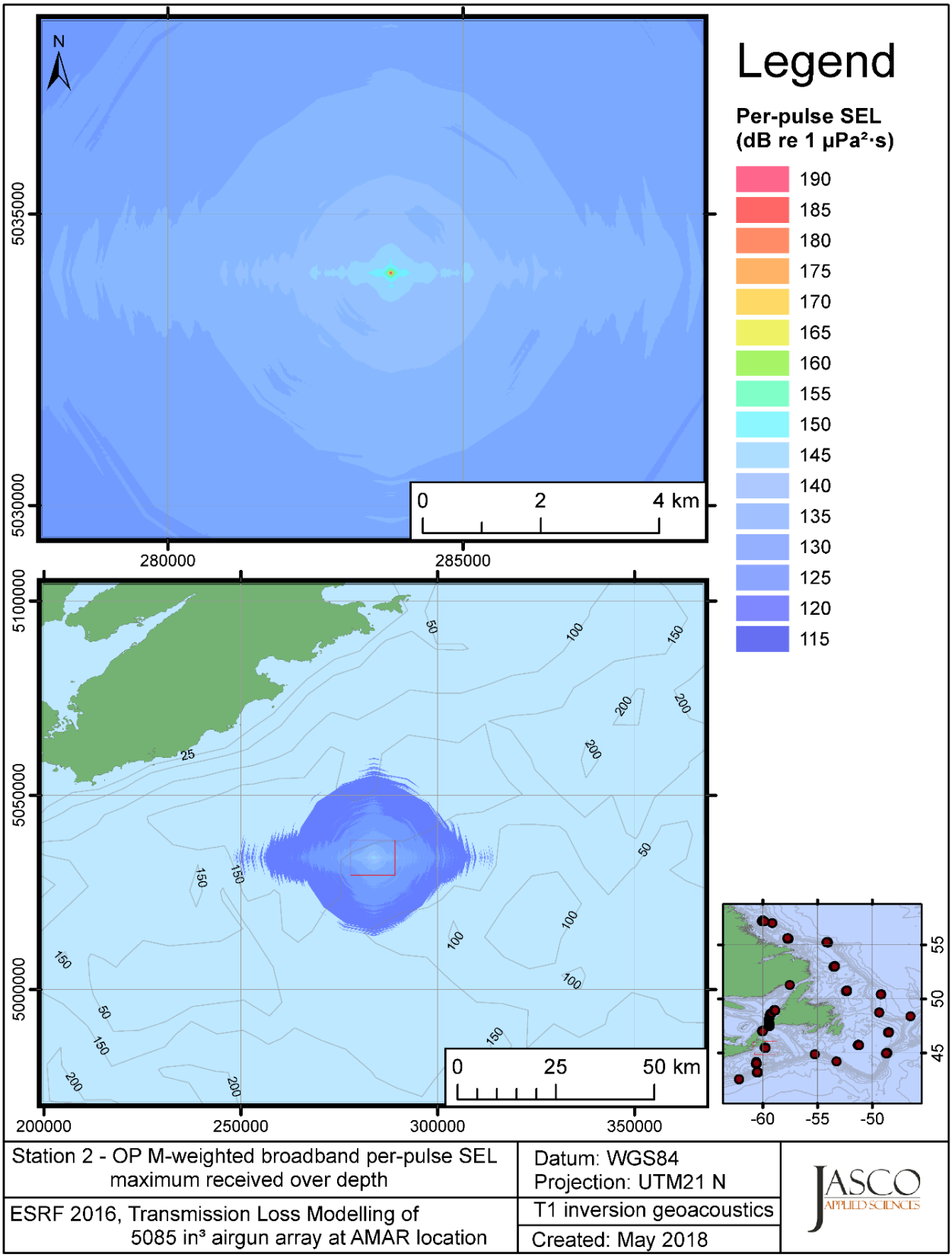

Figure C-377. Stn 2, OP M-weighted maximum-over-depth SEL received at any location on the map, modelled using the track 1 inversion geoacoustic bottom, with the airgun array at the AMAR location and in-situ July SSP.

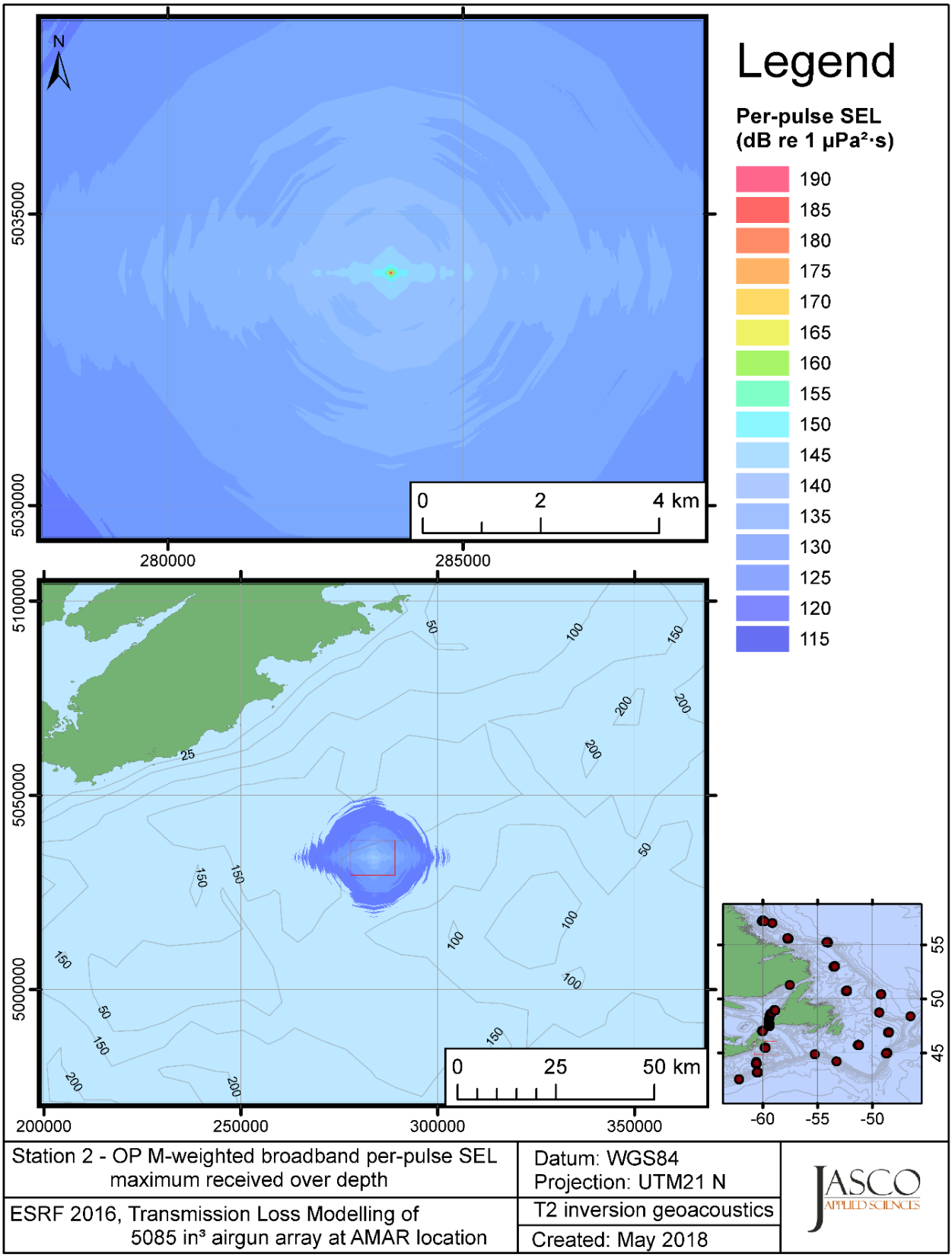

Figure C-378. Stn 2, OP M-weighted maximum-over-depth SEL received at any location on the map, modelled using the track 2 inversion geoacoustic bottom, with the airgun array at the AMAR location and in-situ July SSP.

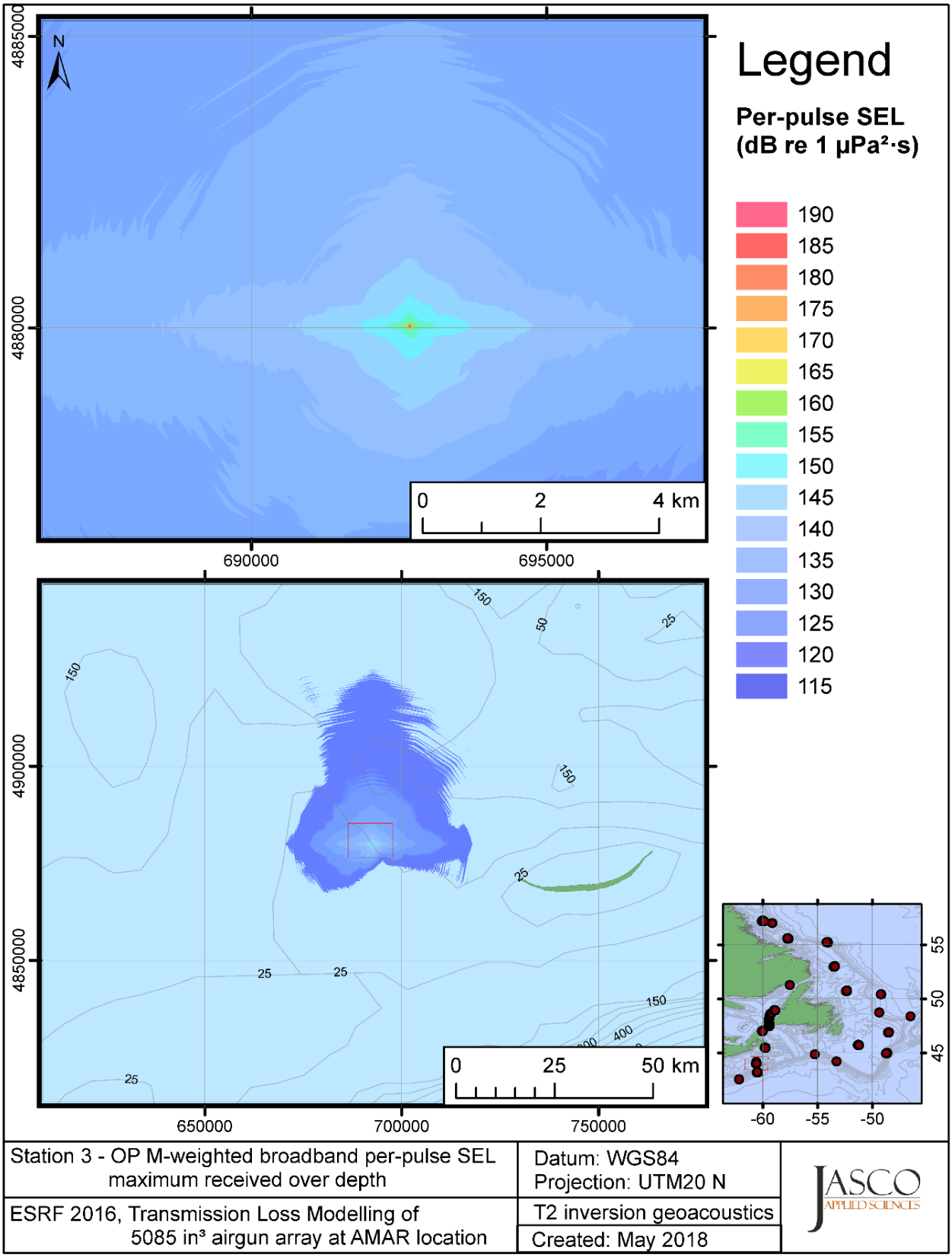

Figure C-379. Stn 3, OP M-weighted maximum-over-depth SEL received at any location on the map, modelled using the track 2 inversion geoacoustic bottom, with the airgun array at the AMAR location and in-situ July SSP.

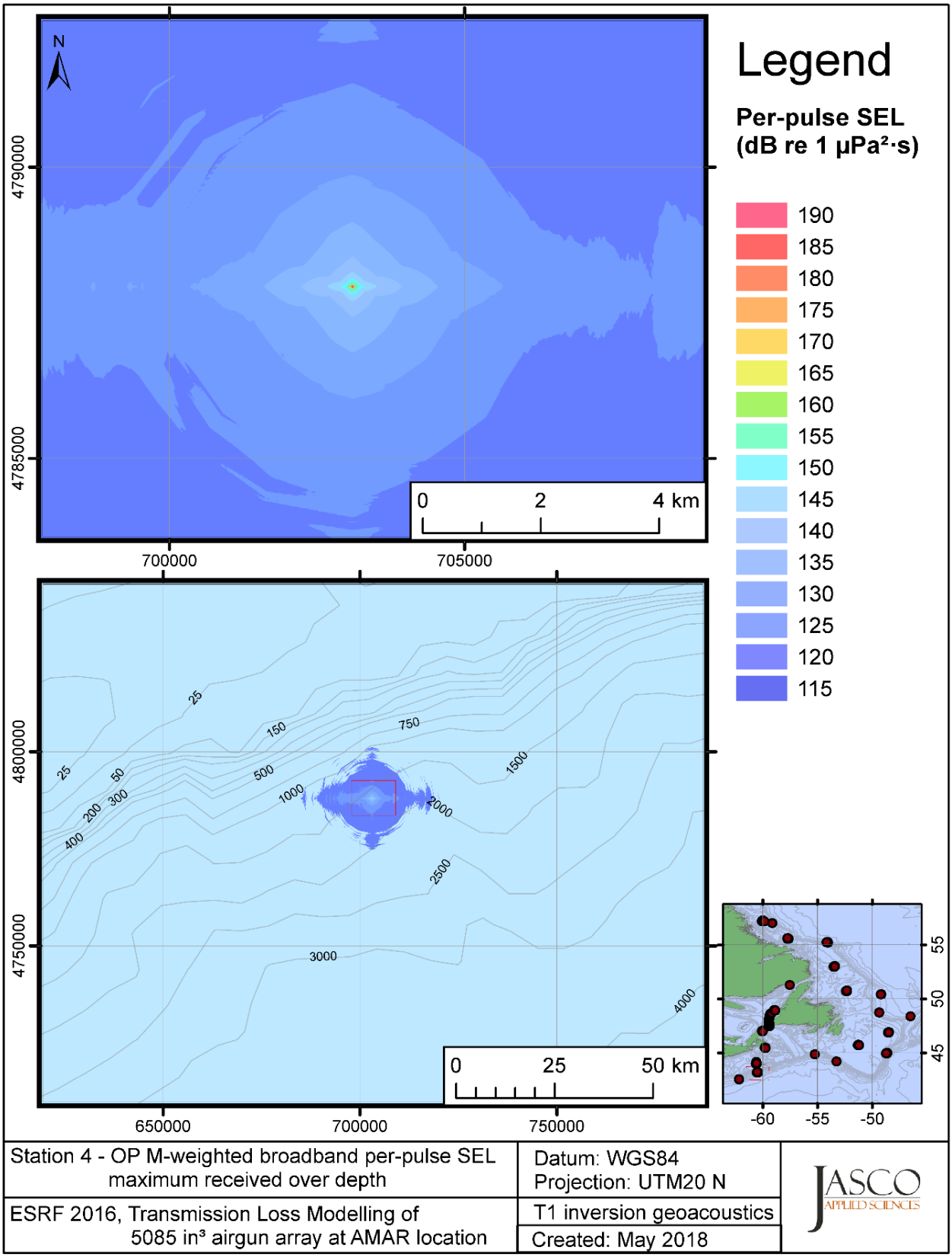

Figure C-380. Stn 4, OP M-weighted maximum-over-depth SEL received at any location on the map, modelled using the track 1 inversion geoacoustic bottom, with the airgun array at the AMAR location and in-situ July SSP.

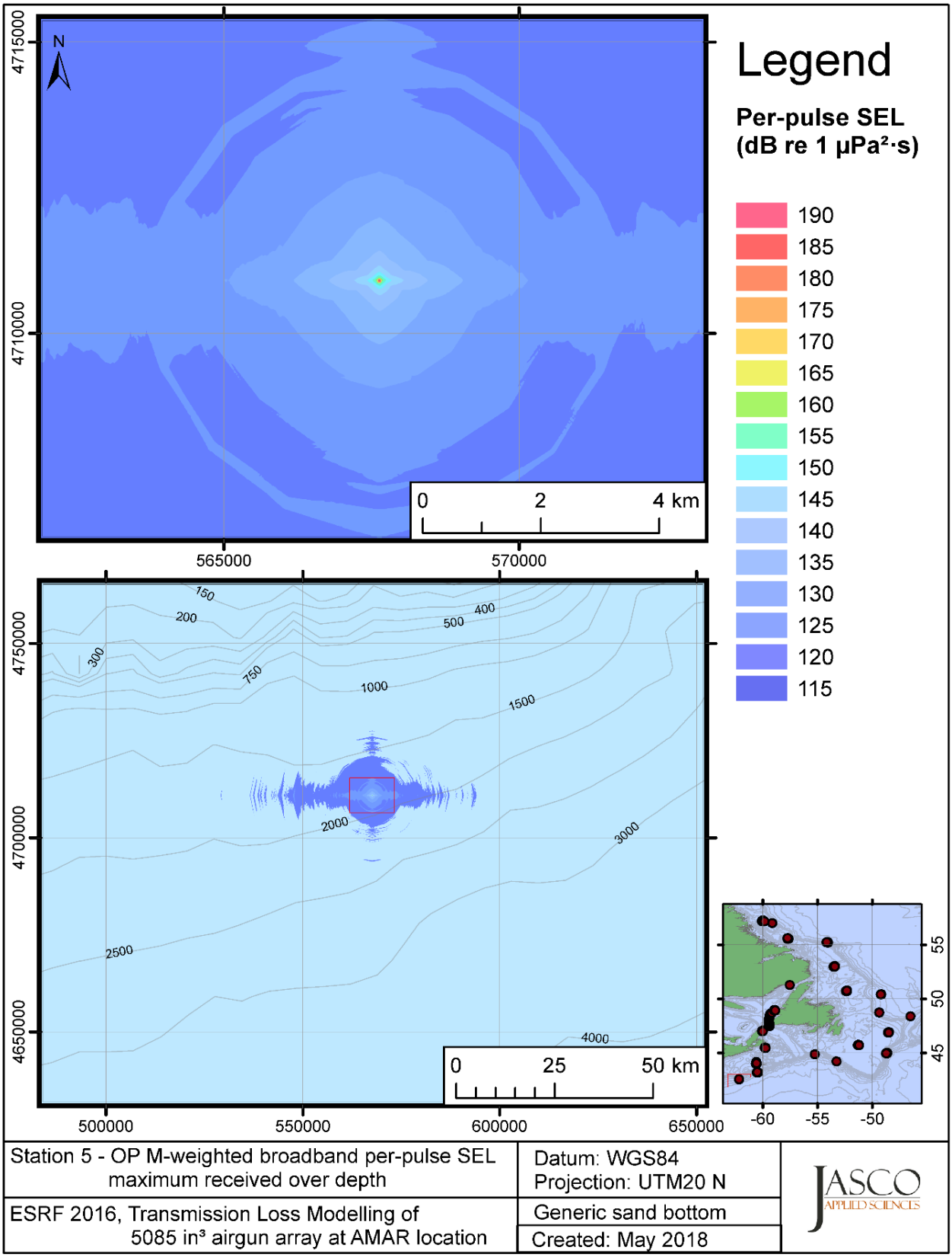

Figure C-381. Stn 5, OP M-weighted maximum-over-depth SEL received at any location on the map, modelled using a generic sand bottom, with the airgun array at the AMAR location and in-situ July SSP.

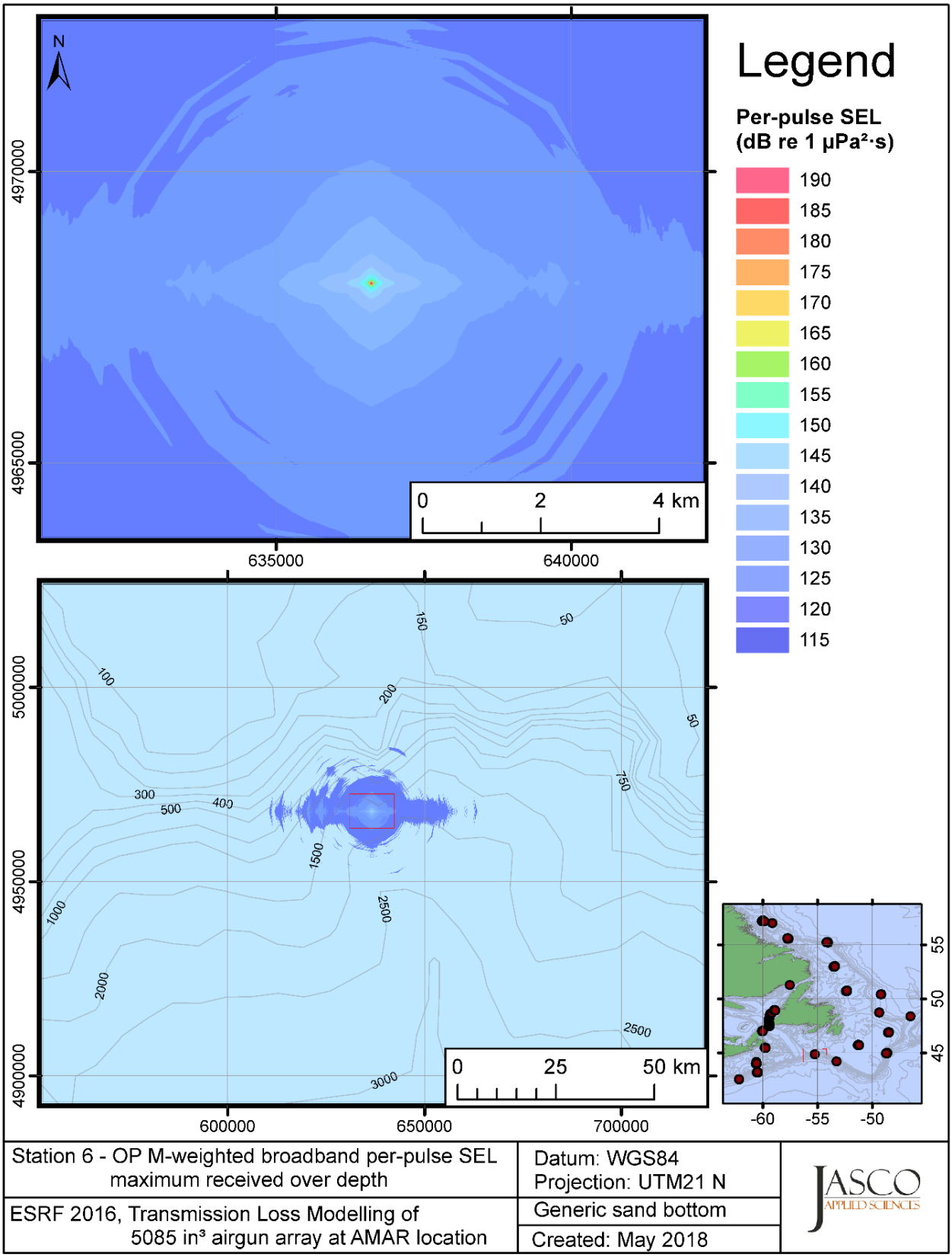

Figure C-382. Stn 6, OP M-weighted maximum-over-depth SEL received at any location on the map, modelled using a generic sand bottom, with the airgun array at the AMAR location and in-situ July SSP.

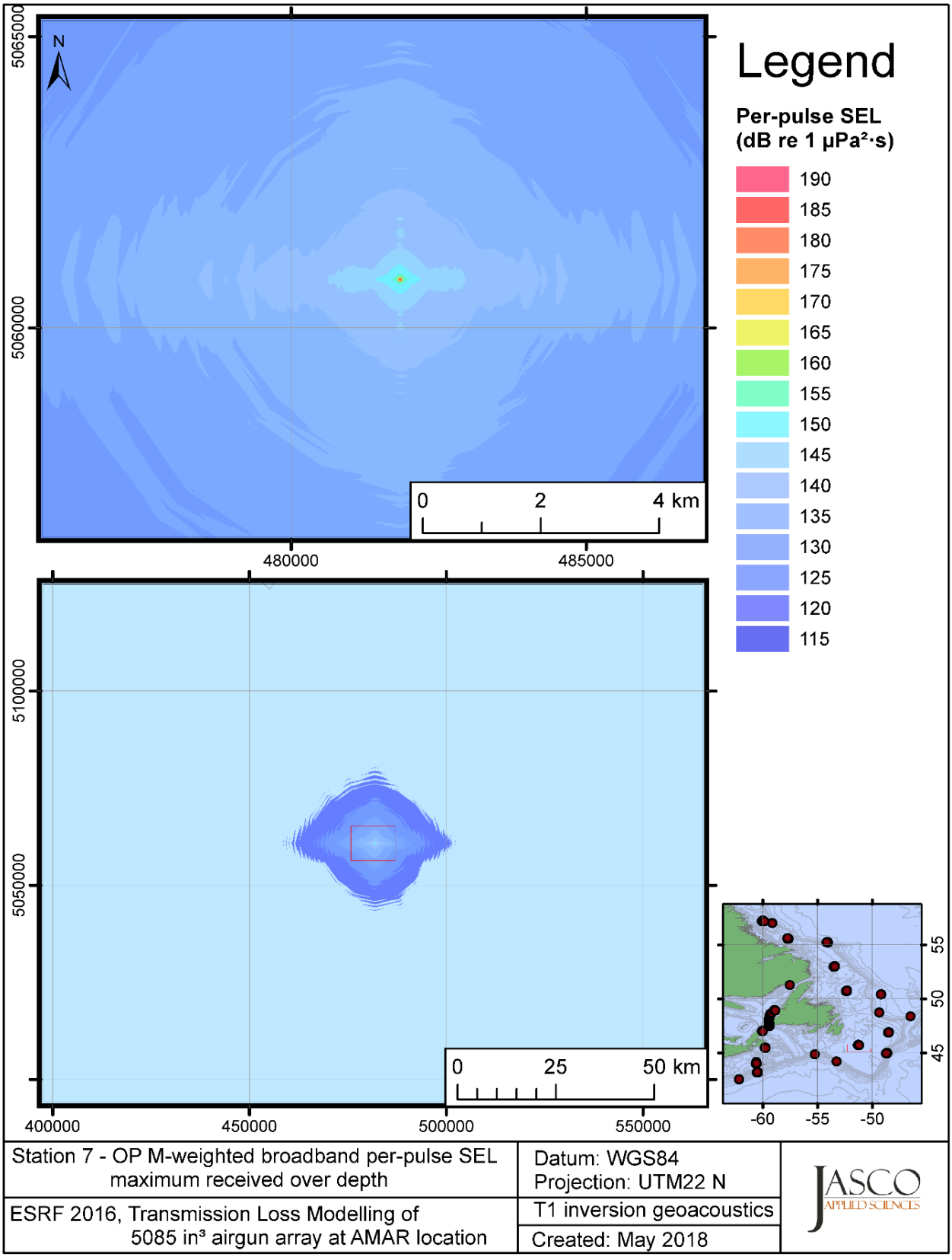

Figure C-383. Stn 7, OP M-weighted maximum-over-depth SEL received at any location on the map, modelled using the track 1 inversion geoacoustic bottom, with the airgun array at the AMAR location and in-situ July SSP.

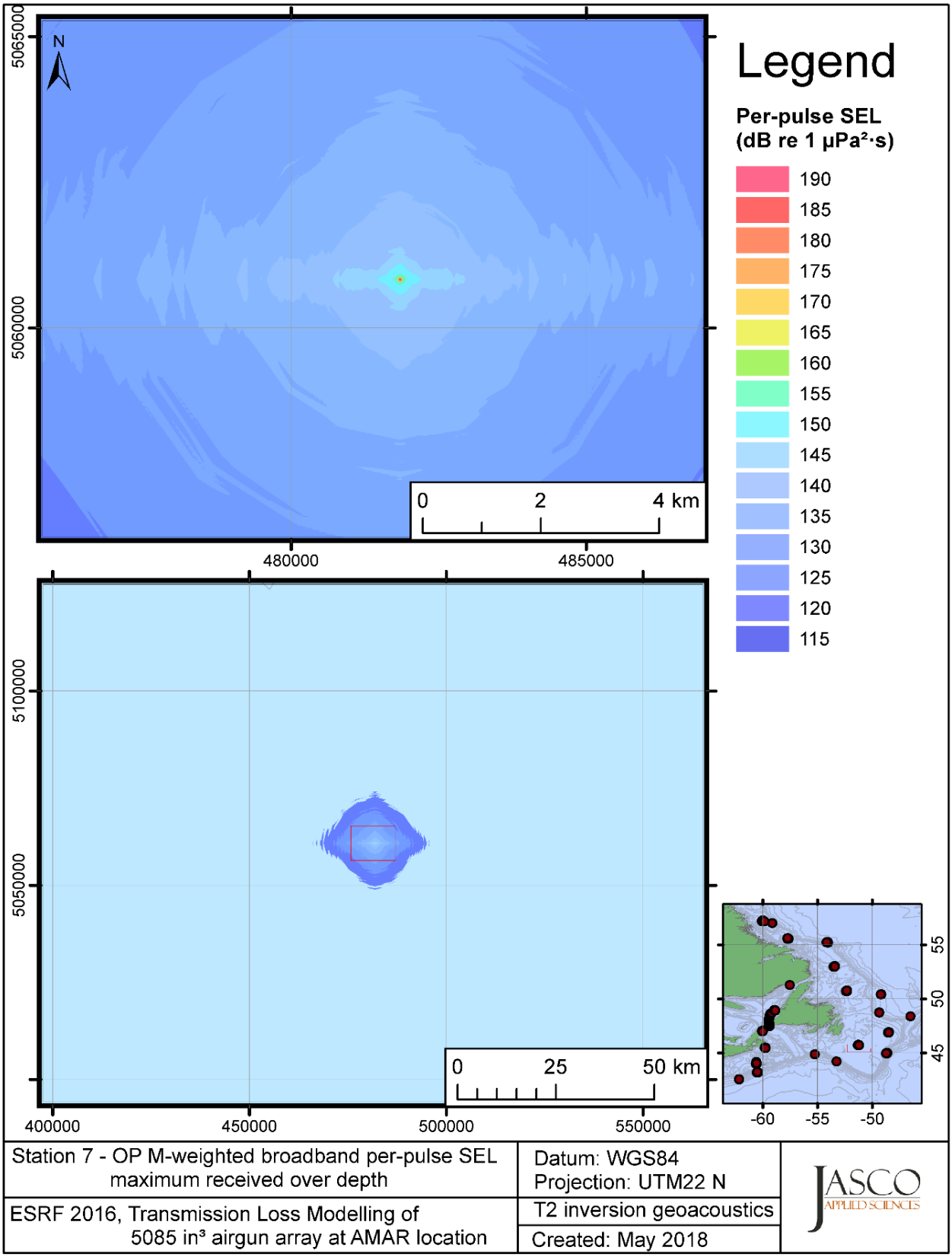

Figure C-384. Stn 7, OP M-weighted maximum-over-depth SEL received at any location on the map, modelled using the track 2 inversion geoacoustic bottom, with the airgun array at the AMAR location and in-situ July SSP.

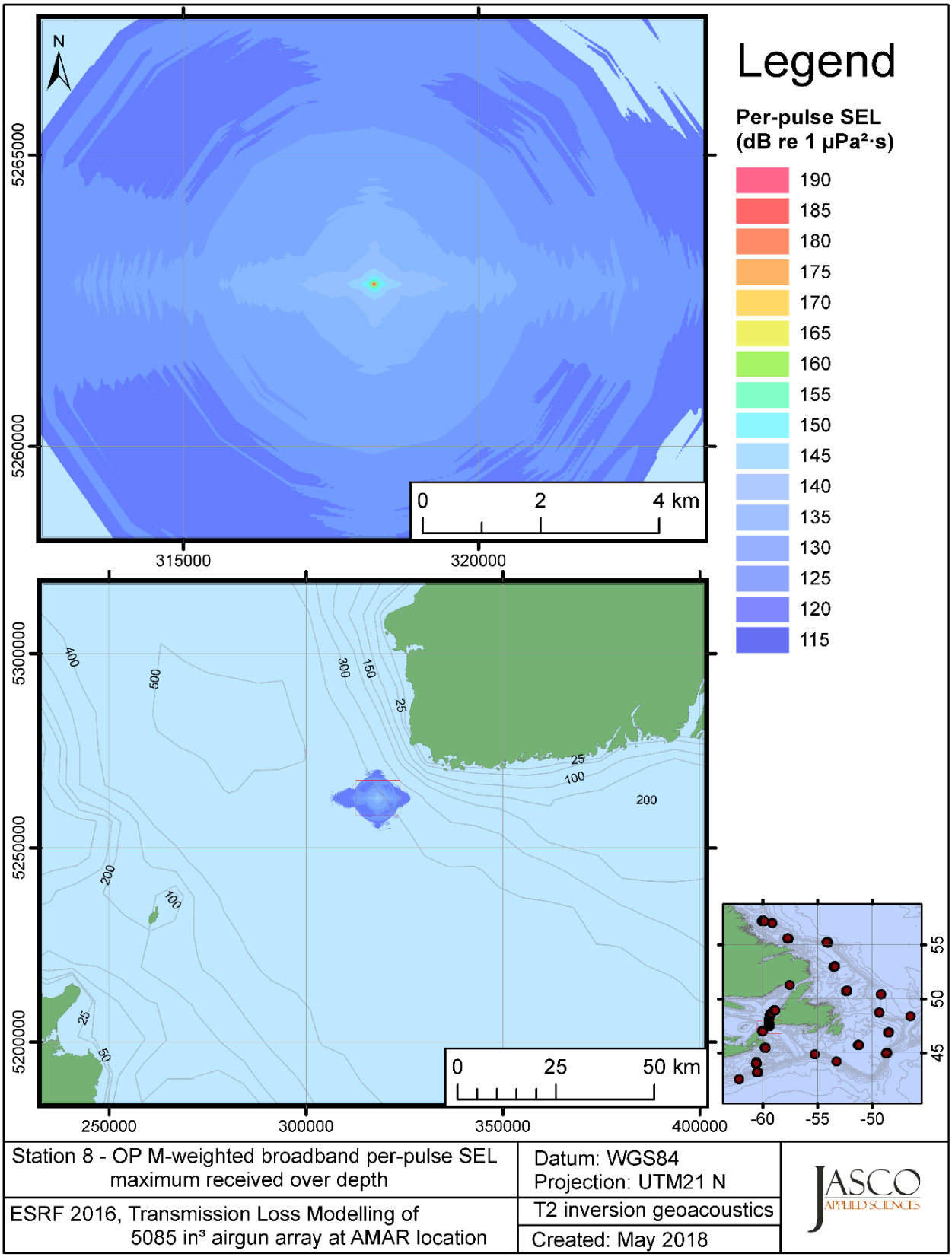

Figure C-385. Stn 8, OP M-weighted maximum-over-depth SEL received at any location on the map, modelled using the track 2 inversion geoacoustic bottom, with the airgun array at the AMAR location and GDEM July SSP.

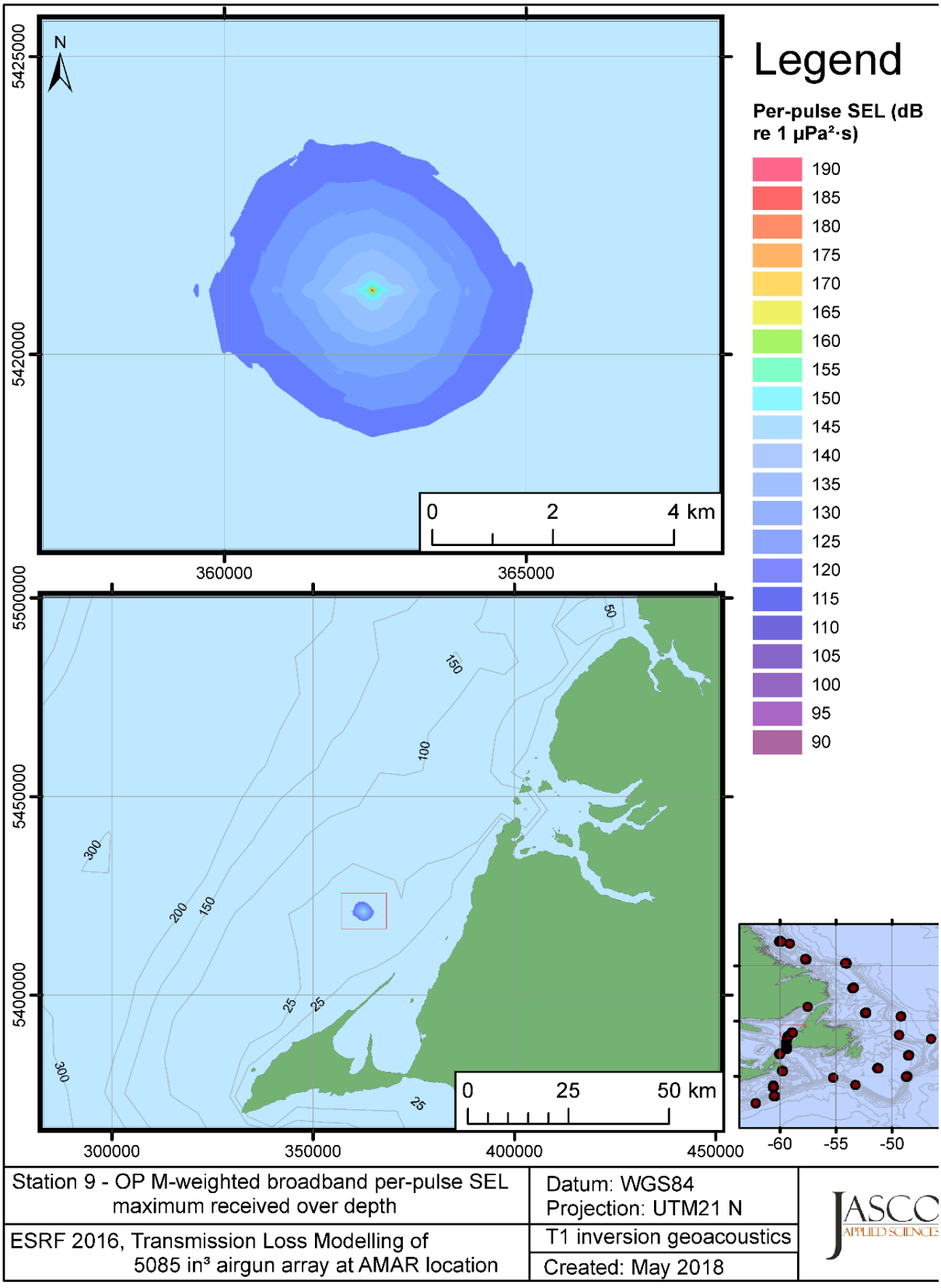

Figure C-386. Stn 9, OP M-weighted maximum-over-depth SEL received at any location on the map, modelled using the track 1 inversion geoacoustic bottom, with the airgun array at the AMAR location and GDEM July SSP.

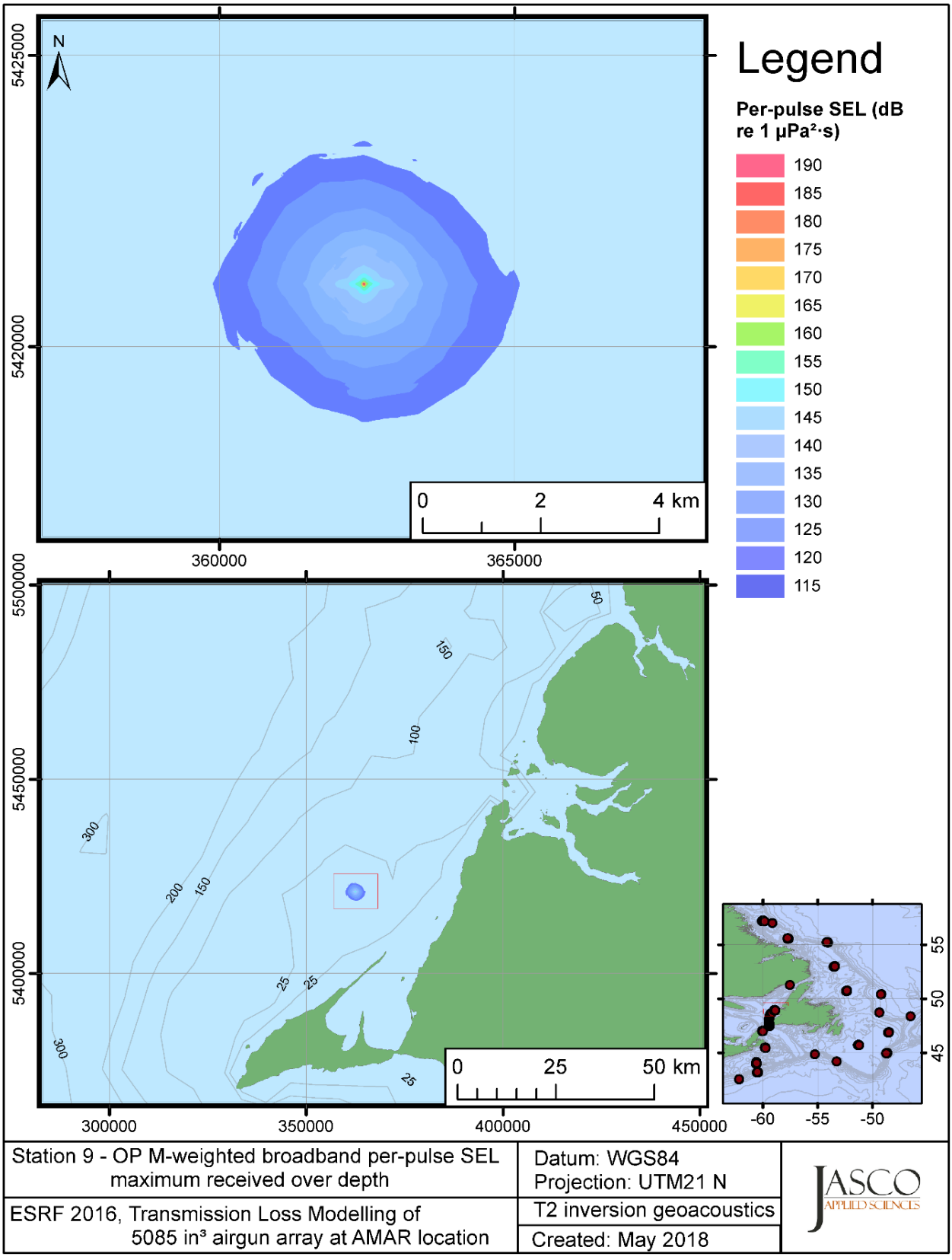

Figure C-387. Stn 9, OP M-weighted maximum-over-depth SEL received at any location on the map, modelled using the track 2 inversion geoacoustic bottom, with the airgun array at the AMAR location and GDEM July SSP.

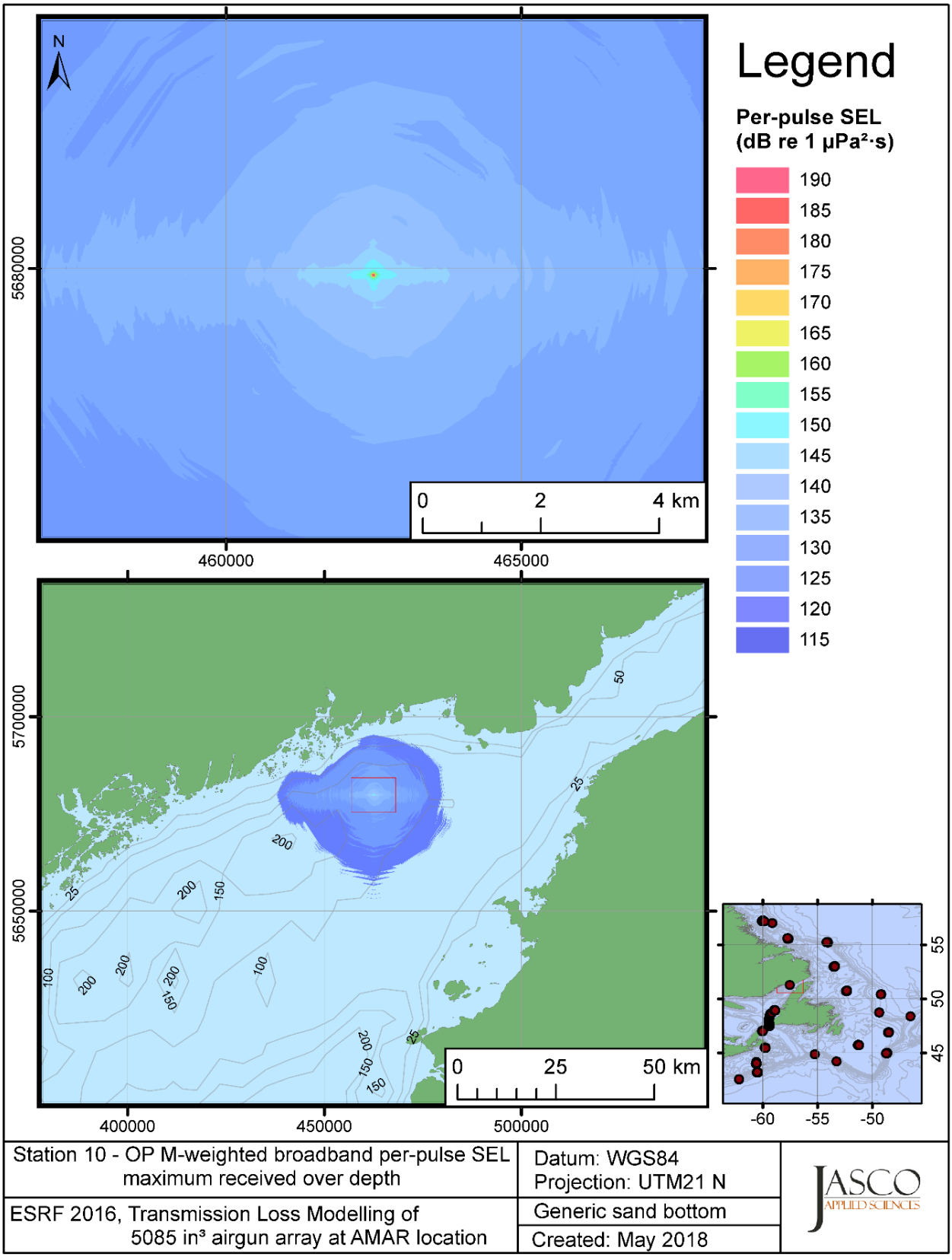

Figure C-388. Stn 10, OP M-weighted maximum-over-depth SEL received at any location on the map, modelled using a generic sand bottom, with the airgun array at the AMAR location and in-situ July SSP.

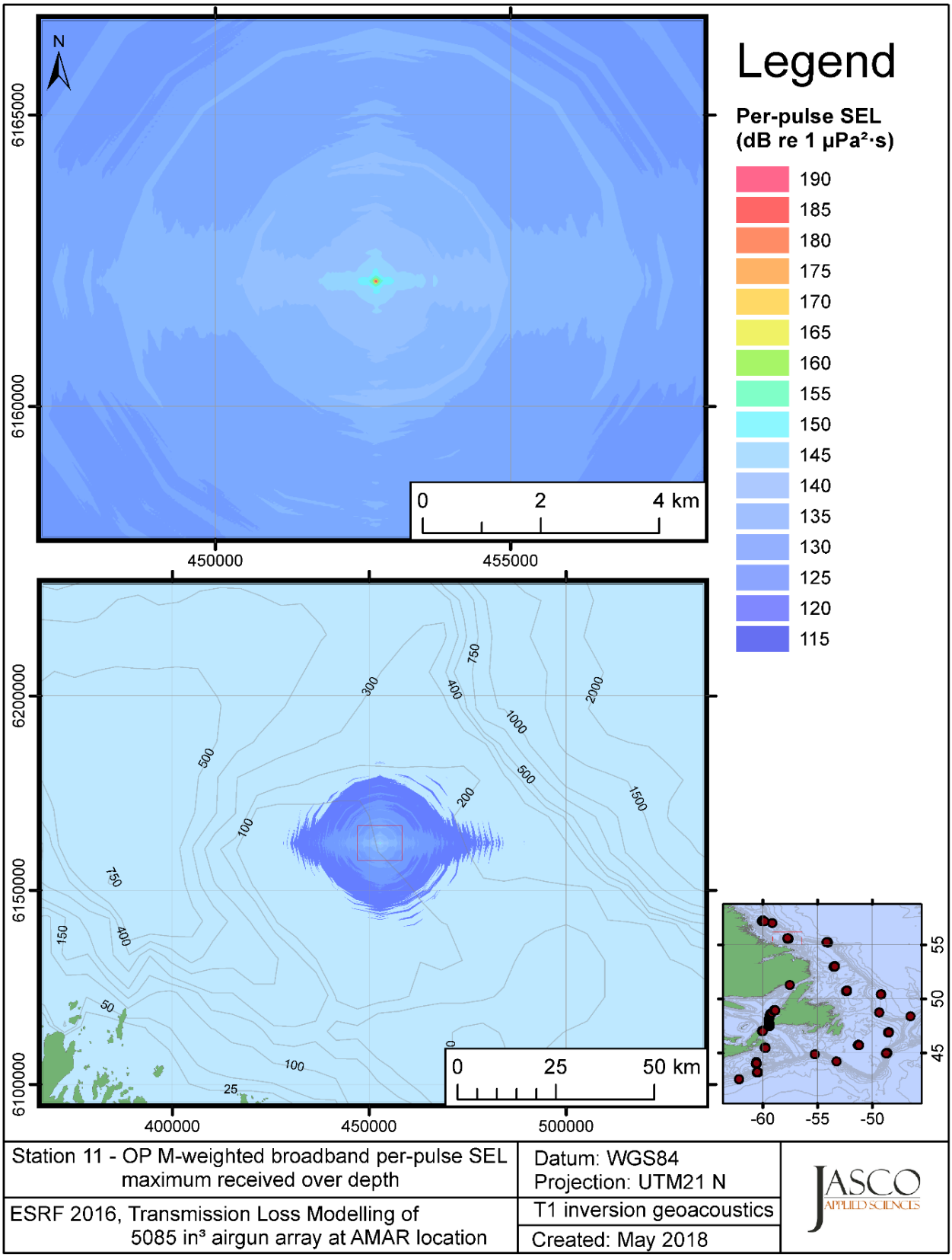

Figure C-389. Stn 11, OP M-weighted maximum-over-depth SEL received at any location on the map, modelled using the track 1 inversion geoacoustic bottom, with the airgun array at the AMAR location and in-situ July SSP.

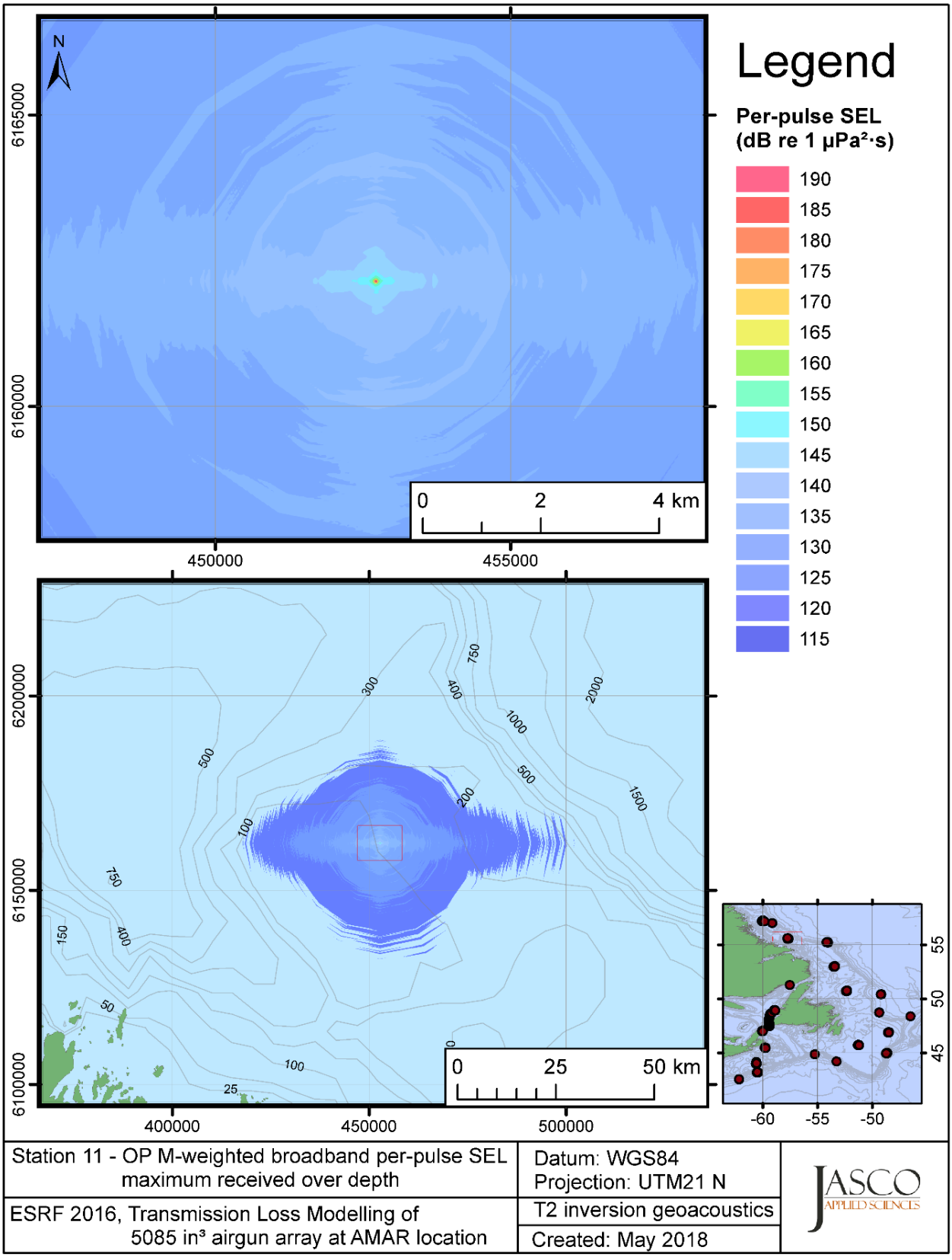

Figure C-390. Stn 11, OP M-weighted maximum-over-depth SEL received at any location on the map, modelled using the track 2 inversion geoacoustic bottom, with the airgun array at the AMAR location and in-situ July SSP.

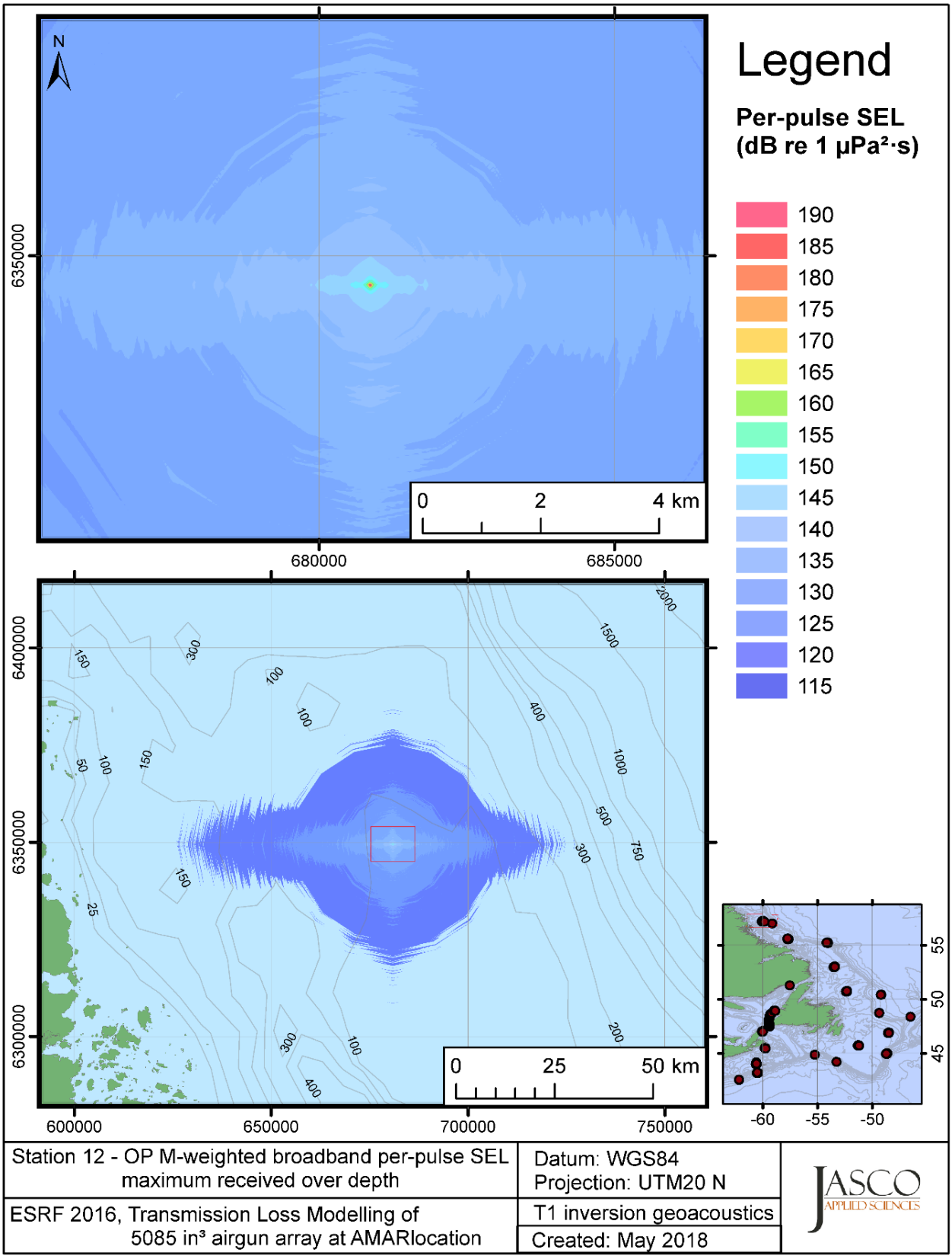

Figure C-391. Stn 12, OP M-weighted maximum-over-depth SEL received at any location on the map, modelled using the track 1 inversion geoacoustic bottom, with the airgun array at the AMAR location and in-situ July SSP.

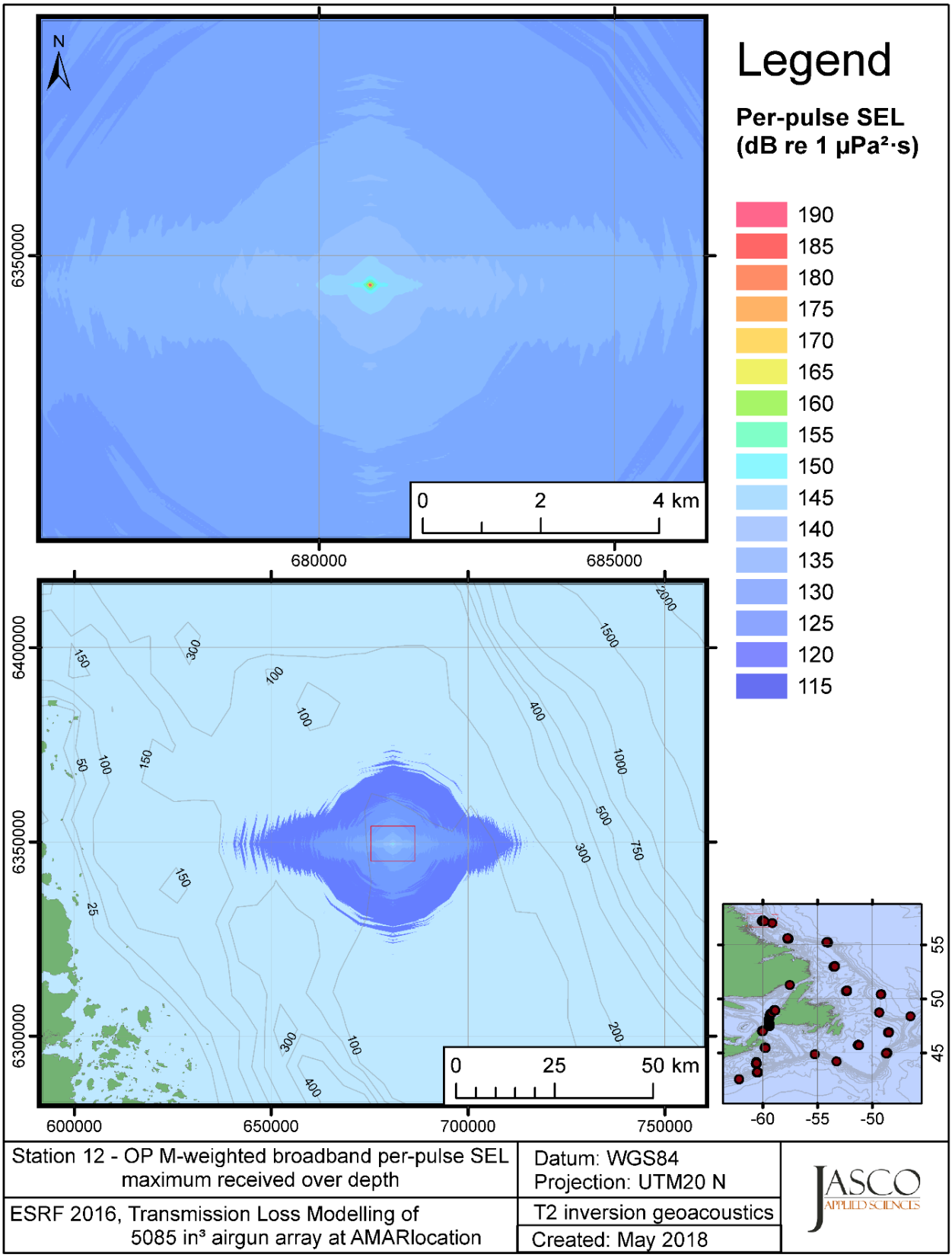

Figure C-392. Stn 12, OP M-weighted maximum-over-depth SEL received at any location on the map, modelled using the track 2 inversion geoacoustic bottom, with the airgun array at the AMAR location and in-situ July SSP.

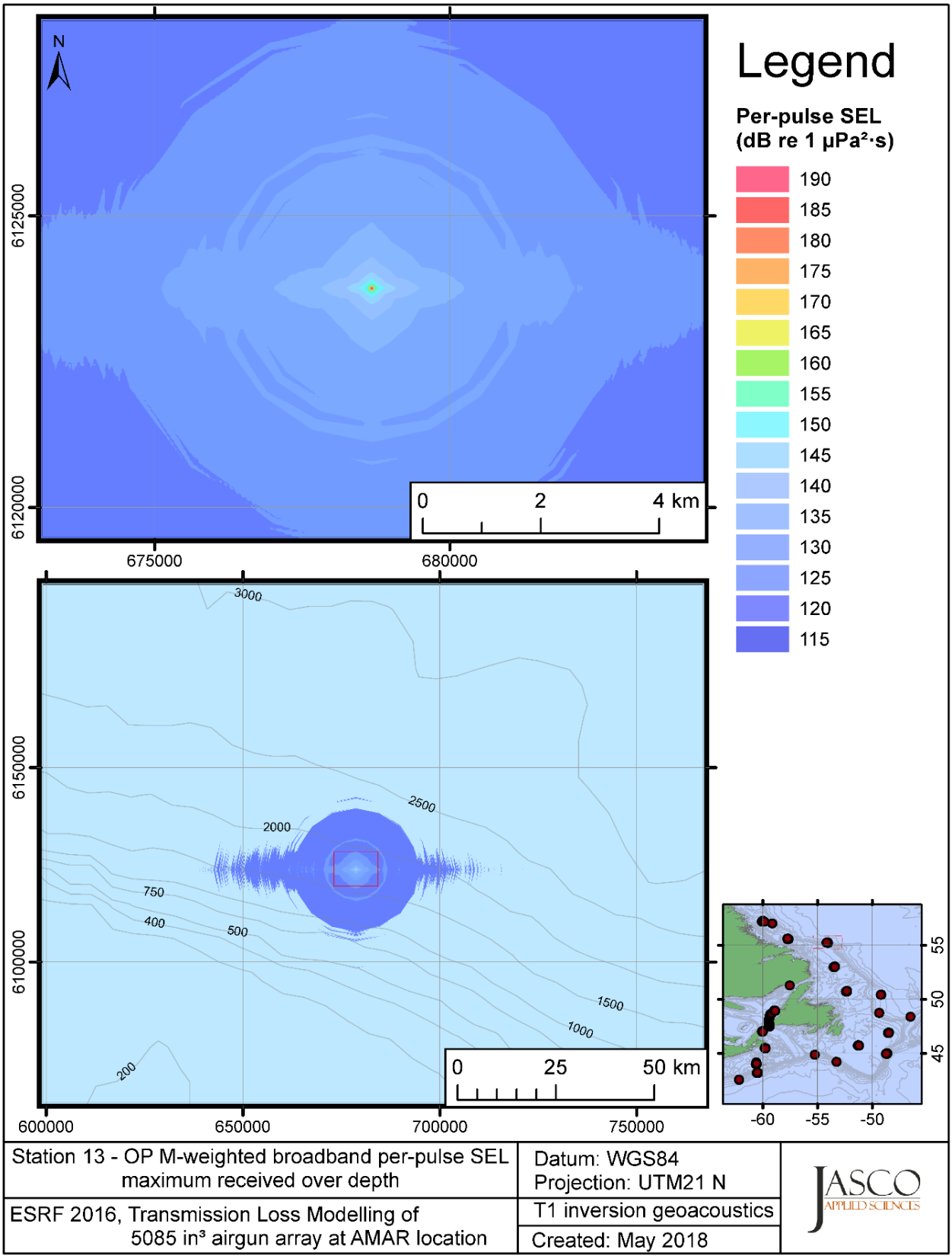

Figure C-393. Stn 13, OP M-weighted maximum-over-depth SEL received at any location on the map, modelled using the track 1 inversion geoacoustic bottom, with the airgun array at the AMAR location and in-situ July SSP.

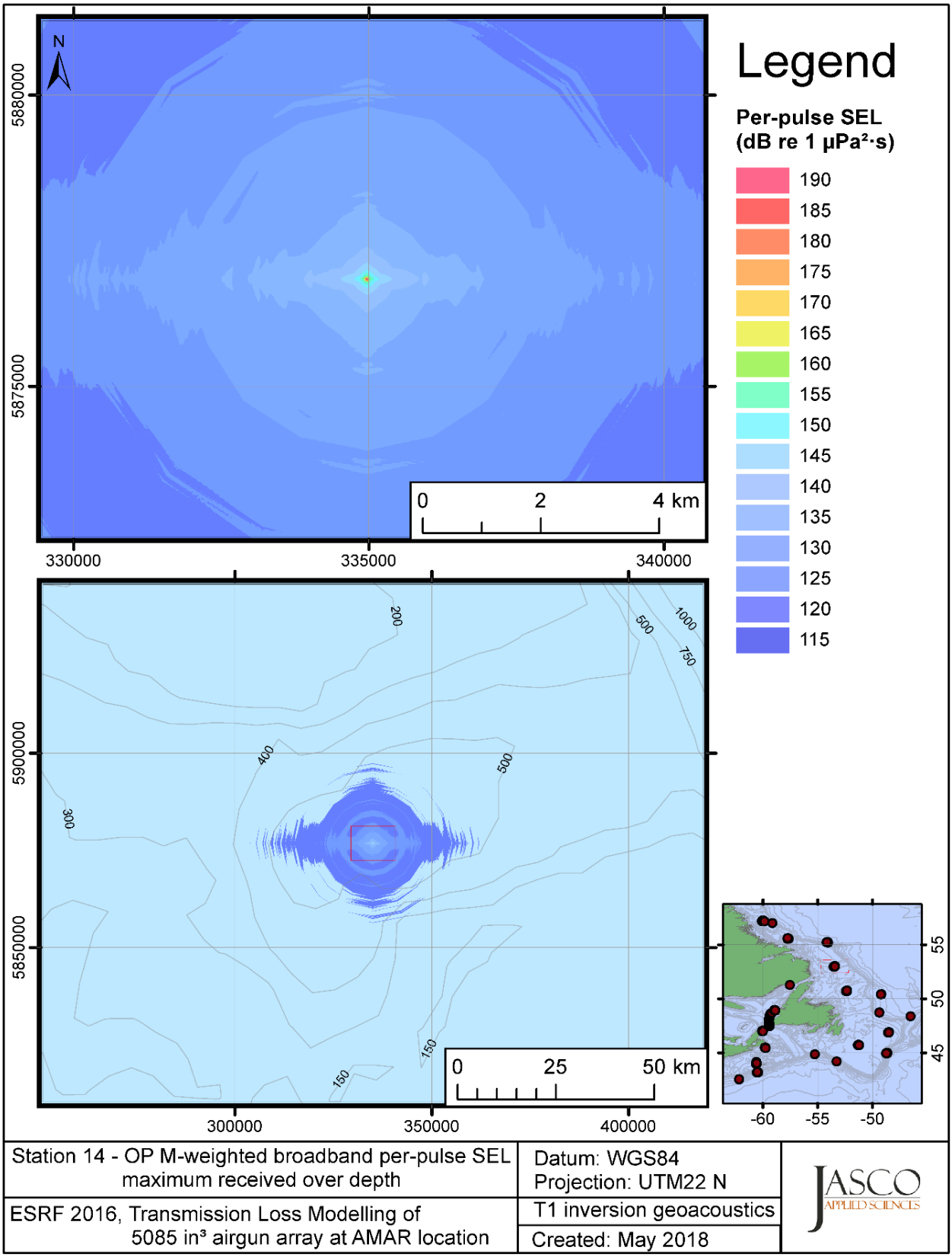

Figure C-394. Stn 14, OP M-weighted maximum-over-depth SEL received at any location on the map, modelled using the track 1 inversion geoacoustic bottom, with the airgun array at the AMAR location and in-situ July SSP.

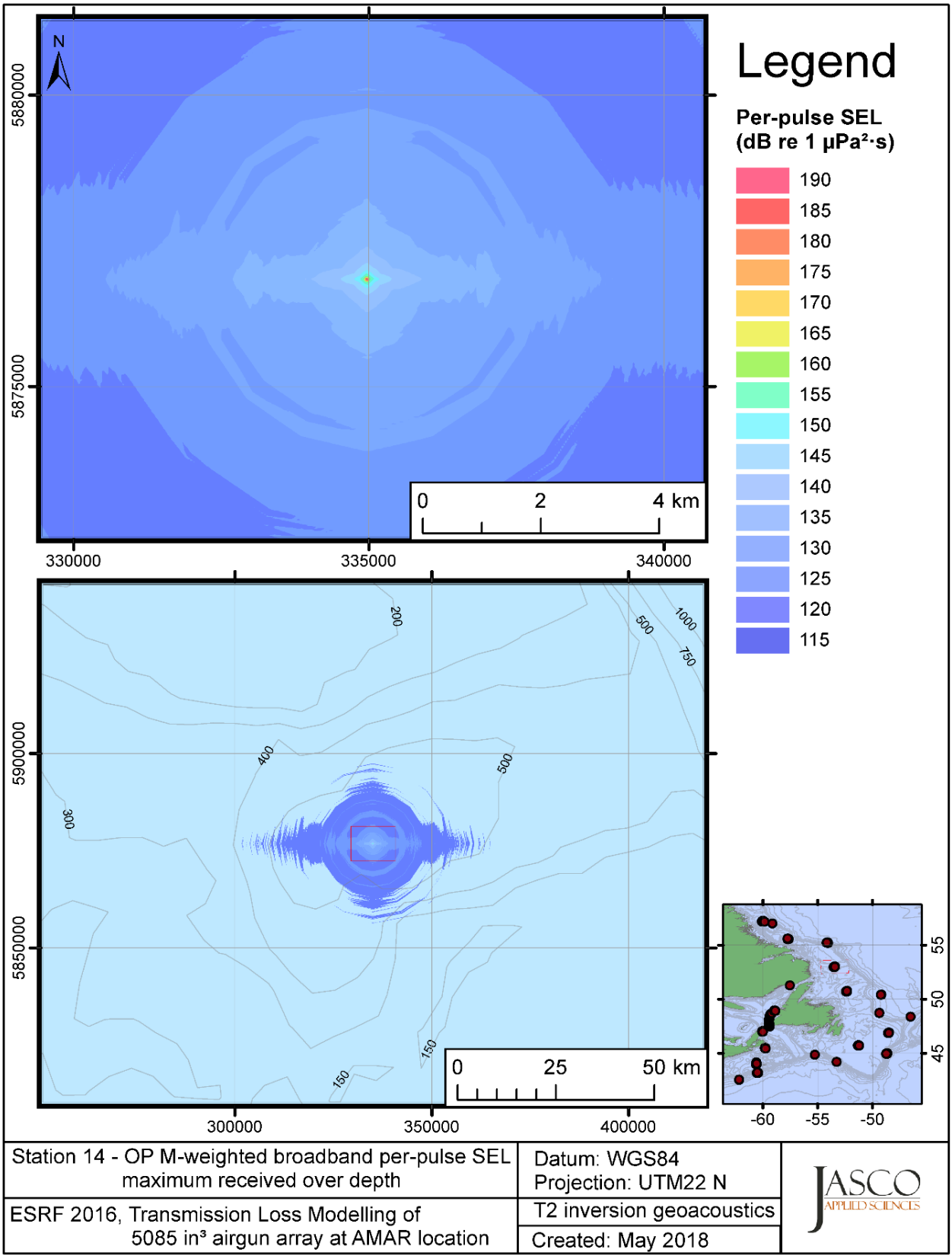

Figure C-395. Stn 14, OP M-weighted maximum-over-depth SEL received at any location on the map, modelled using the track 2 inversion geoacoustic bottom, with the airgun array at the AMAR location and in-situ July SSP.

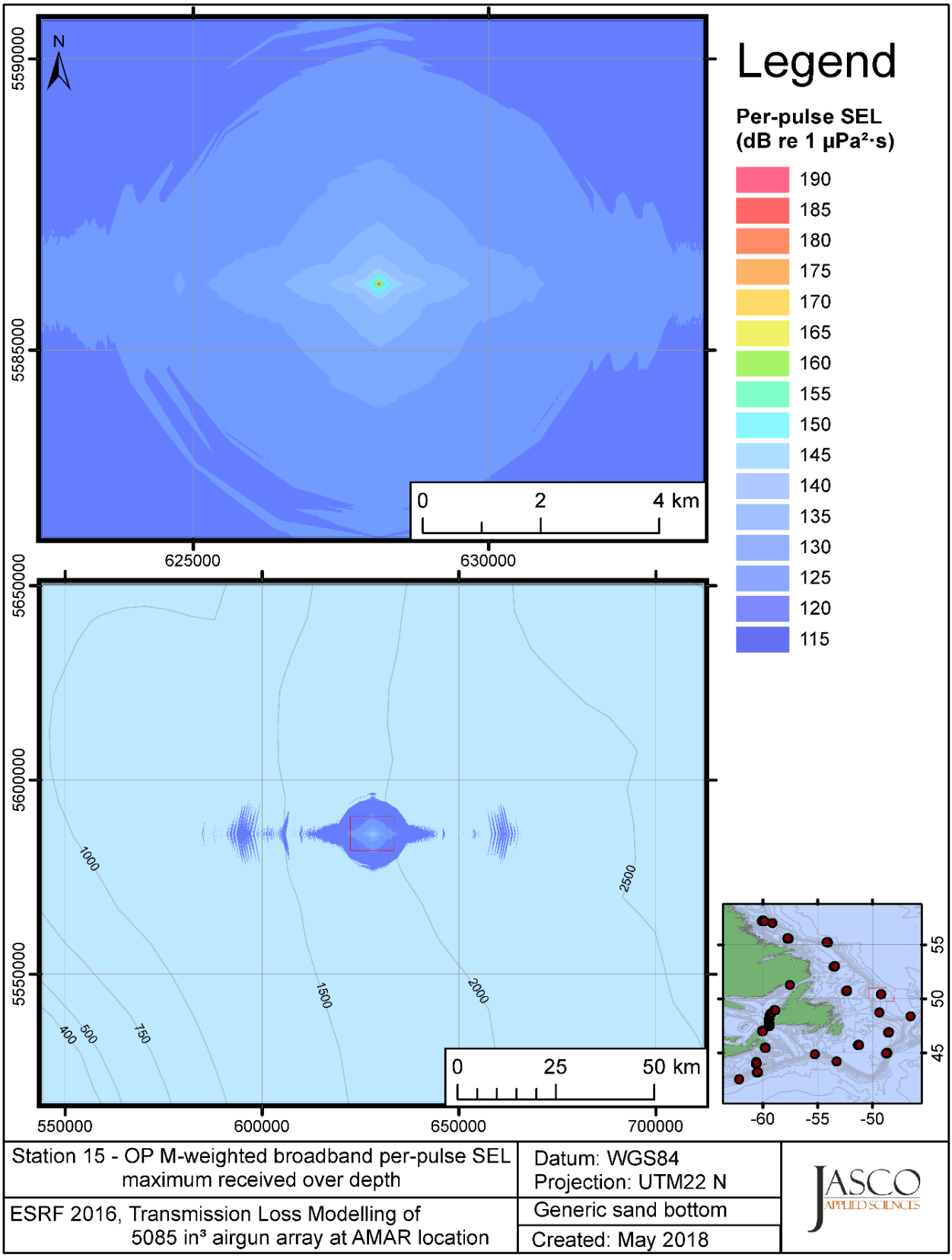

Figure C-396. Stn 15, OP M-weighted maximum-over-depth SEL received at any location on the map, modelled using a generic sand bottom, with the airgun array at the AMAR location and in-situ July SSP.

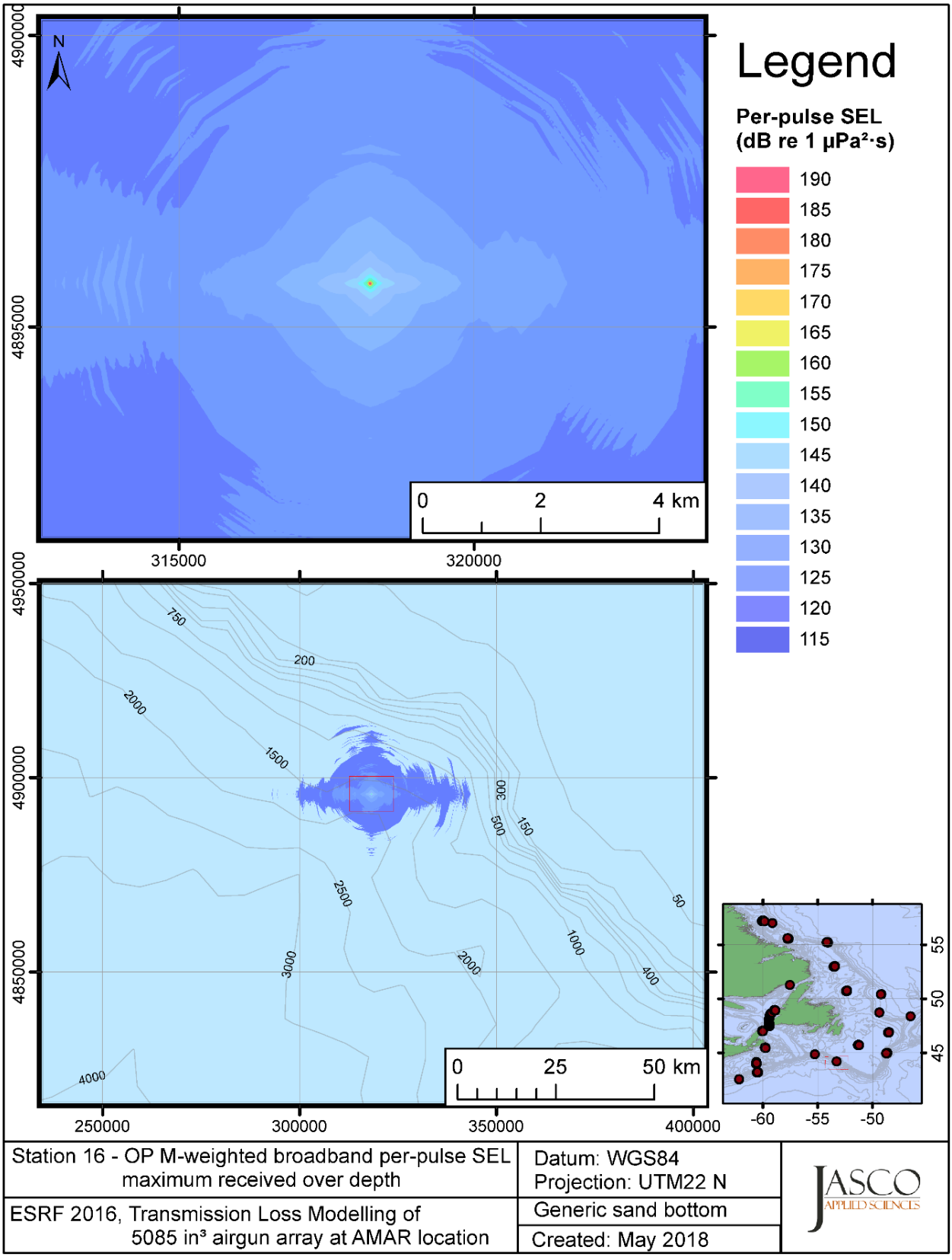

Figure C-397. Stn 16, OP M-weighted maximum-over-depth SEL received at any location on the map, modelled using a generic sand bottom, with the airgun array at the AMAR location and in-situ July SSP.

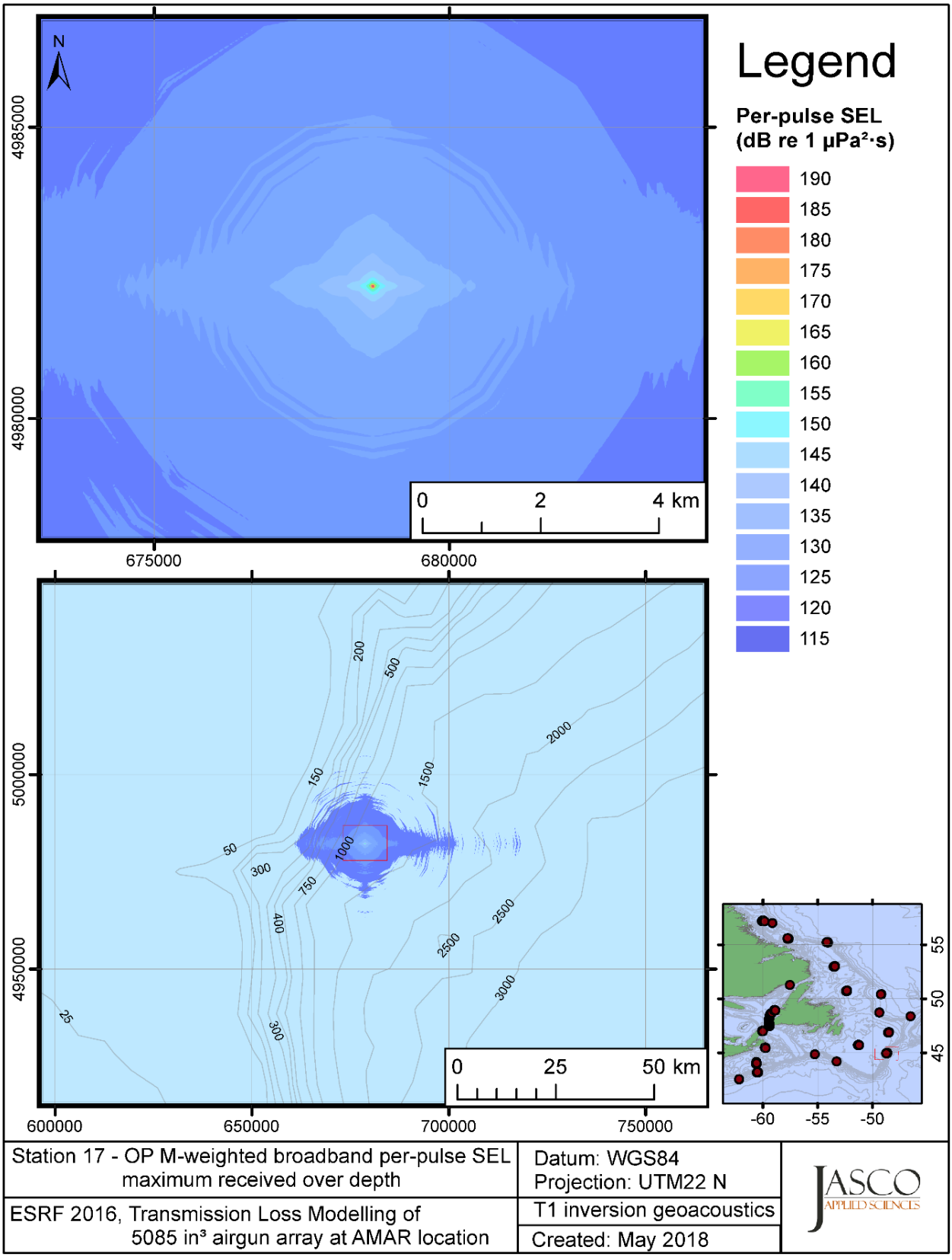

Figure C-398. Stn 17, OP M-weighted maximum-over-depth SEL received at any location on the map, modelled using the track 1 inversion geoacoustic bottom, with the airgun array at the AMAR location and in-situ July SSP.

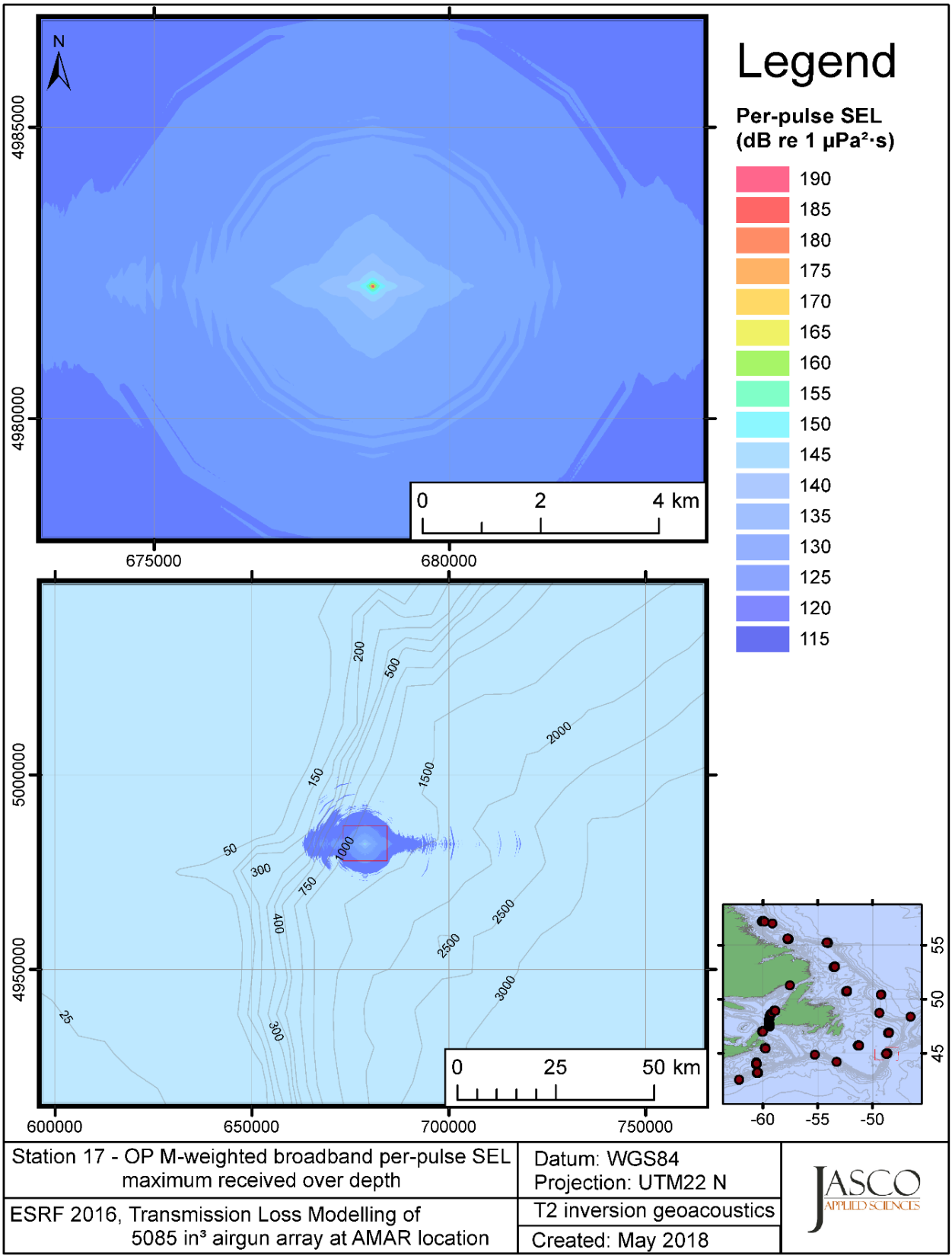

Figure C-399. Stn 17, OP M-weighted maximum-over-depth SEL received at any location on the map, modelled using the track 2 inversion geoacoustic bottom, with the airgun array at the AMAR location and in-situ July SSP.

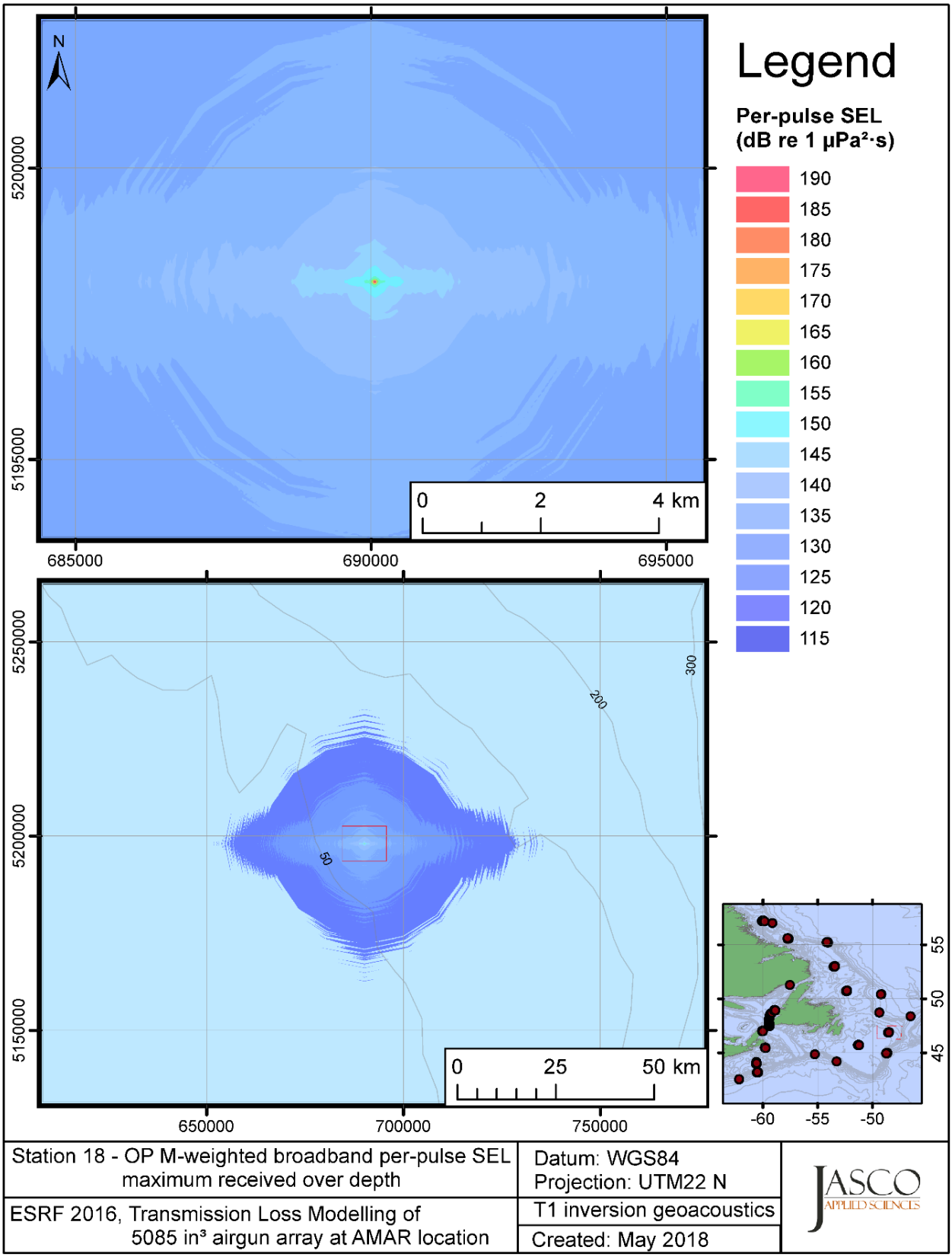

Figure C-400. Stn 18, OP M-weighted maximum-over-depth SEL received at any location on the map, modelled using the track 1 inversion geoacoustic bottom, with the airgun array at the AMAR location and in-situ July SSP.

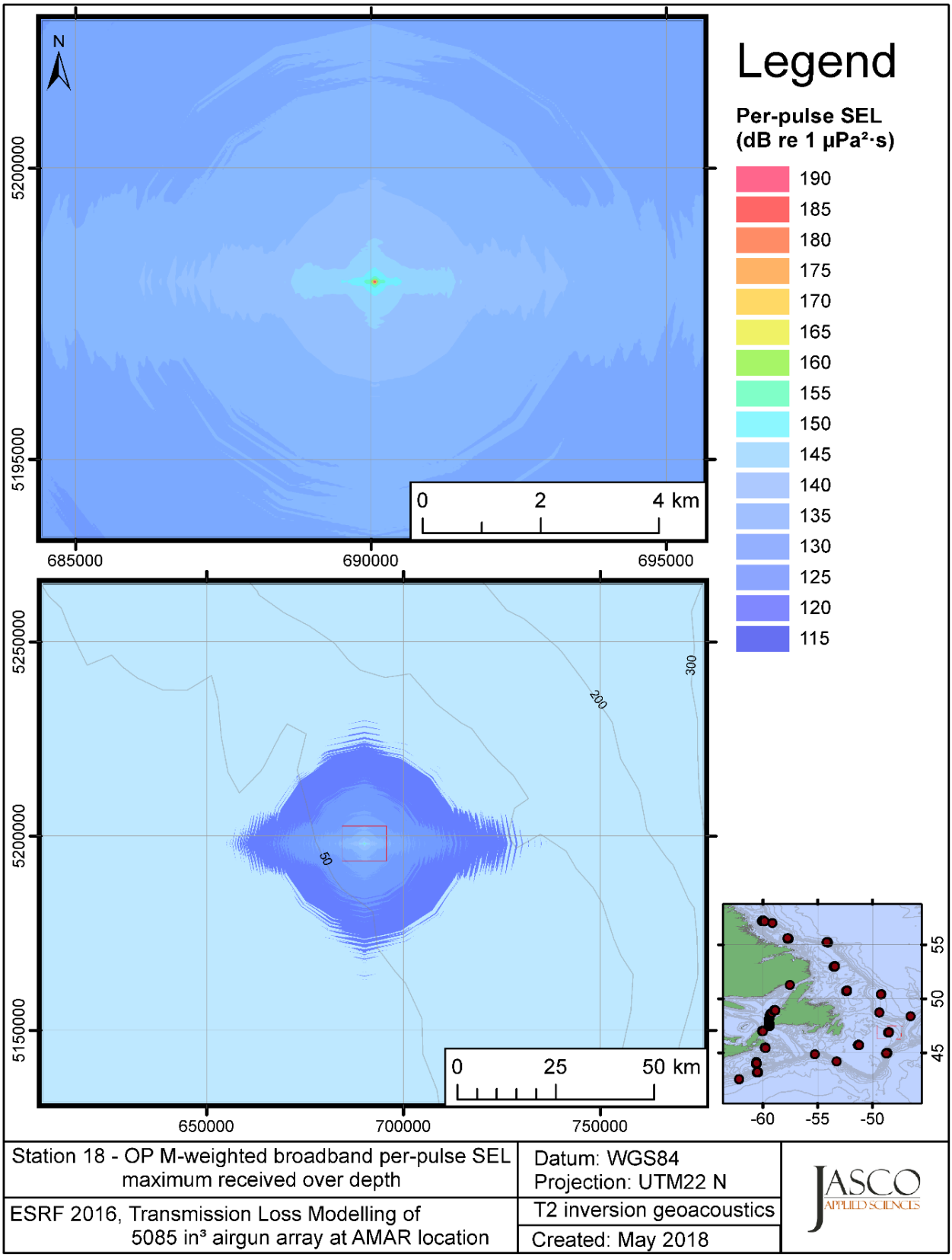

Figure C-401. Stn 18, OP M-weighted maximum-over-depth SEL received at any location on the map, modelled using the track 2 inversion geoacoustic bottom, with the airgun array at the AMAR location and in-situ July SSP.

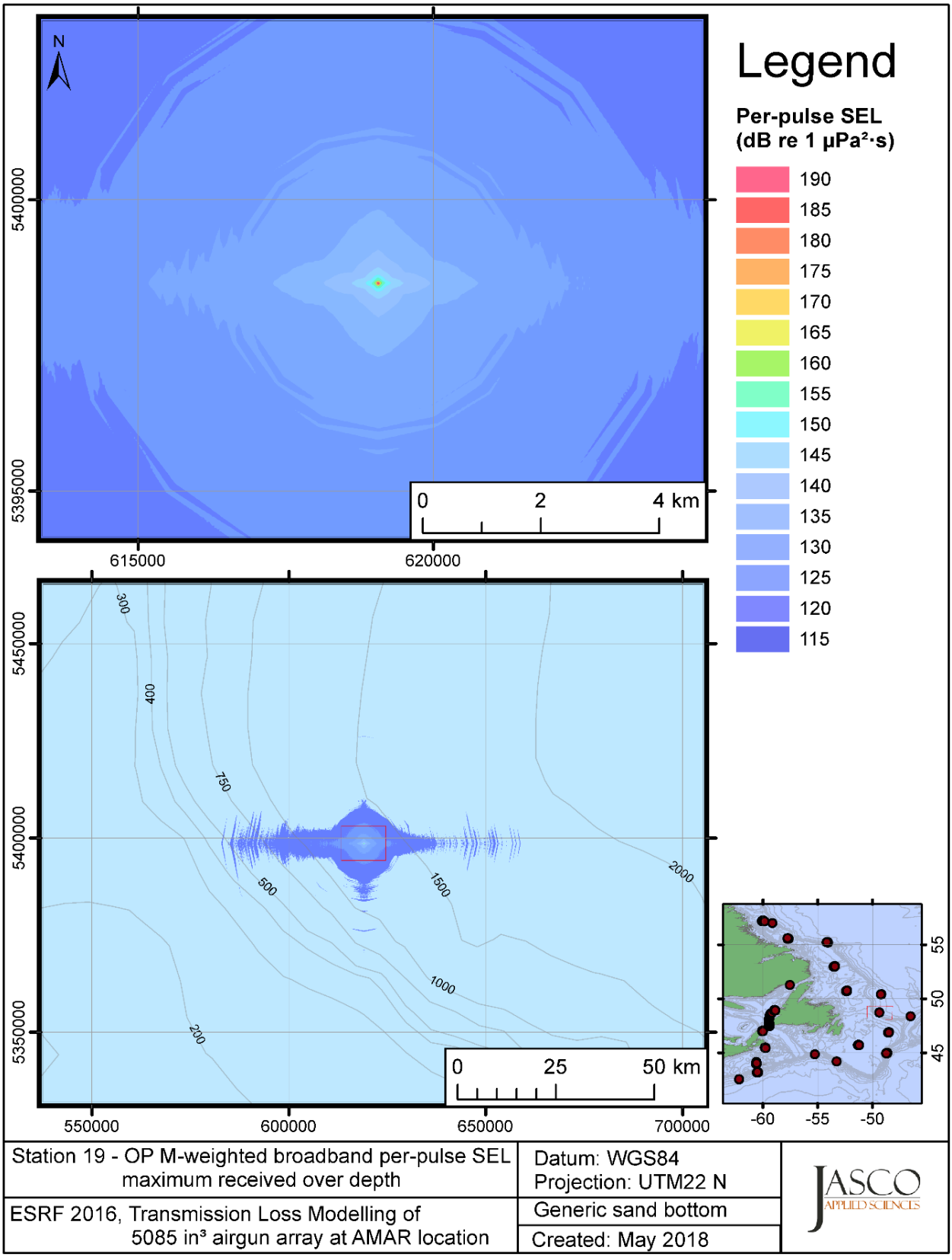

Figure C-402. Stn 19, OP M-weighted maximum-over-depth SEL received at any location on the map, modelled using a generic sand bottom, with the airgun array at the AMAR location and in-situ July SSP.

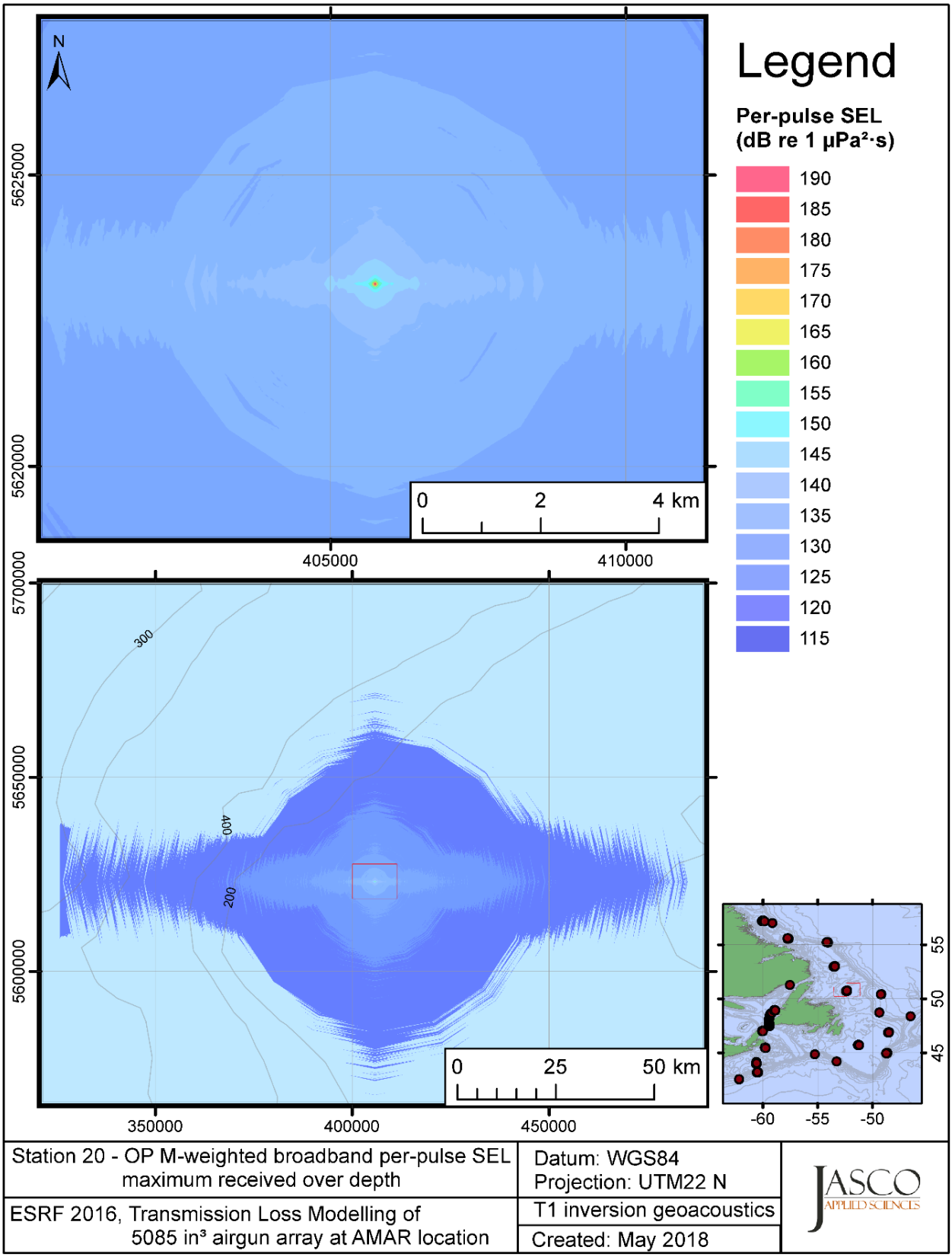

Figure C-403. Stn 20, OP M-weighted maximum-over-depth SEL received at any location on the map, modelled using the track 1 inversion geoacoustic bottom, with the airgun array at the AMAR location and in-situ July SSP.

C.12. Modelling PP M-weighted Max-over-depth Received Level at Distant Locations - Summer

This section presents the results of modelling the maximum-over-depth per-pulse sound exposure level (SEL) received at distant receiver locations (varied in range and azimuth) for the source held fixed at the AMAR location. The modelling uses the geoacoustic inversion bottom parameters at the 14 sites where they are available and only uses a generic sand bottom at the other six sites. The modelling results are presented in the form of coloured maps where the colour at any map location represents the predicted maximum-over-depth received level at that spot on the map. This section includes only the phocid pinnipeds in water (OP) marine-mammal-weighted per-pulse SEL results; additional maps for other marine mammal received level auditory weightings are presented in adjoining sections. The sound speed profiles (SSP) used are detailed in Appendix B.1.

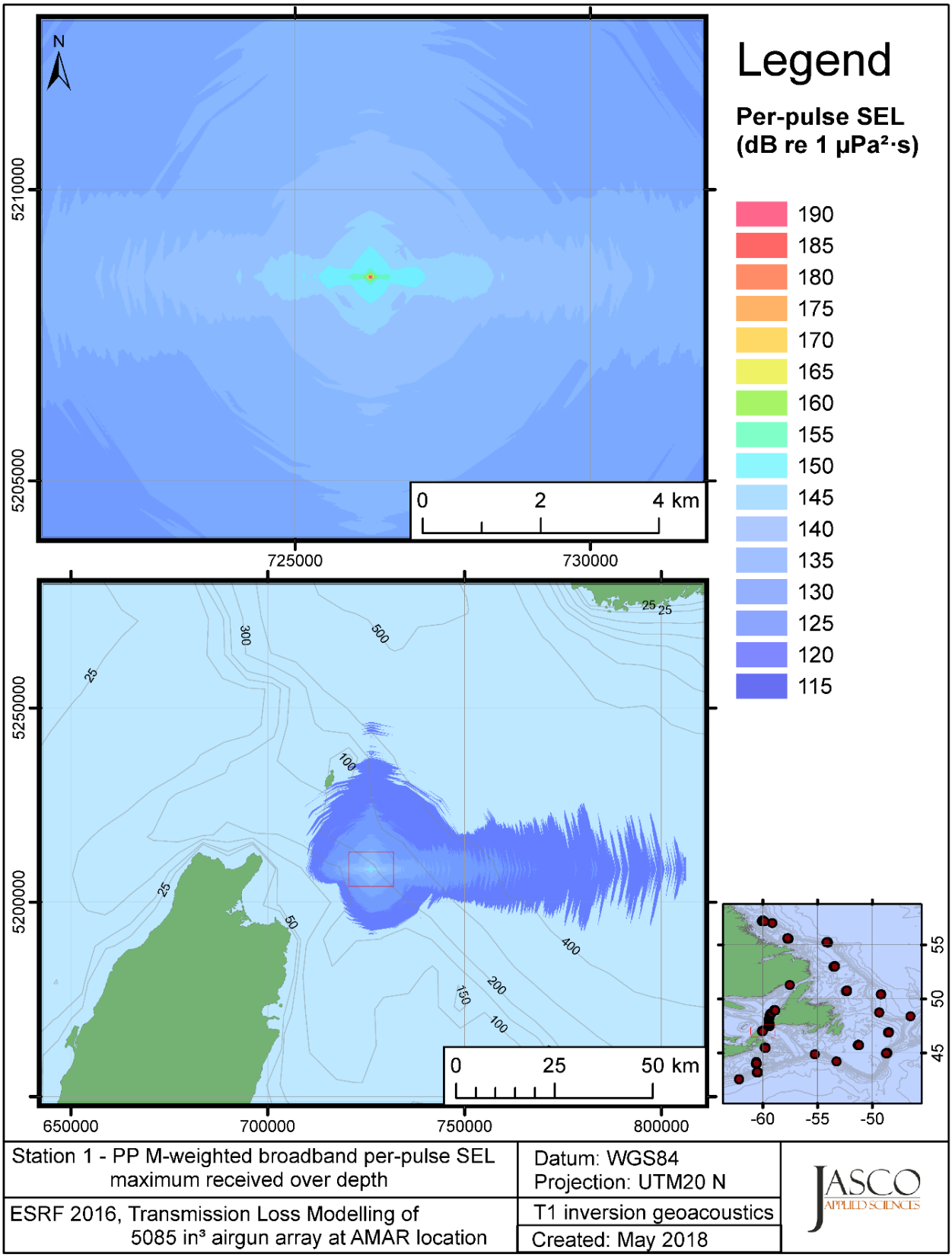

Figure C-404. Stn 1, PP M-weighted maximum-over-depth SEL received at any location on the map, modelled using the track 1 inversion geoacoustic bottom, with the airgun array at the AMAR location and in-situ July SSP.

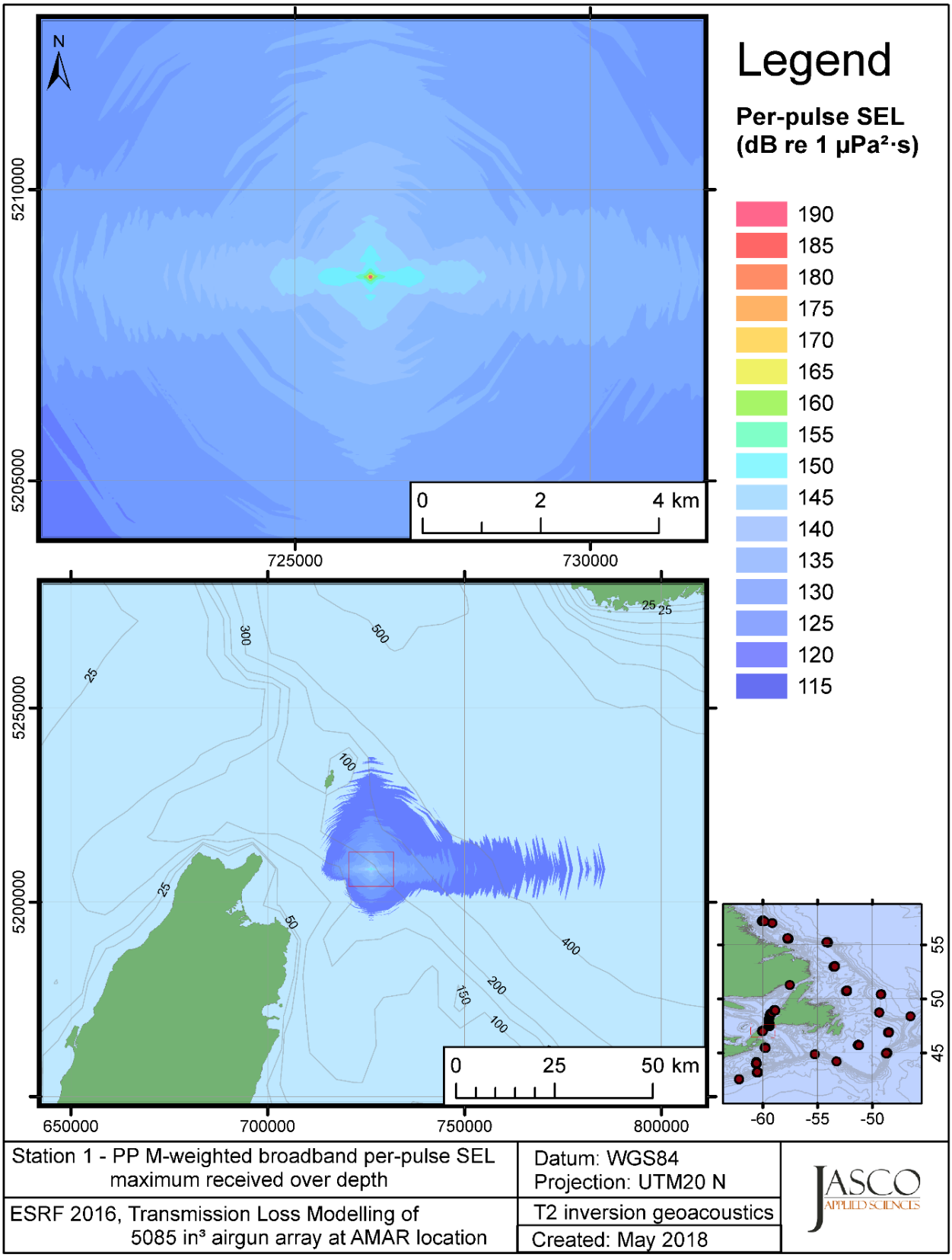

Figure C-405. Stn 1, PP M-weighted maximum-over-depth SEL received at any location on the map, modelled using the track 2 inversion geoacoustic bottom, with the airgun array at the AMAR location and in-situ July SSP.

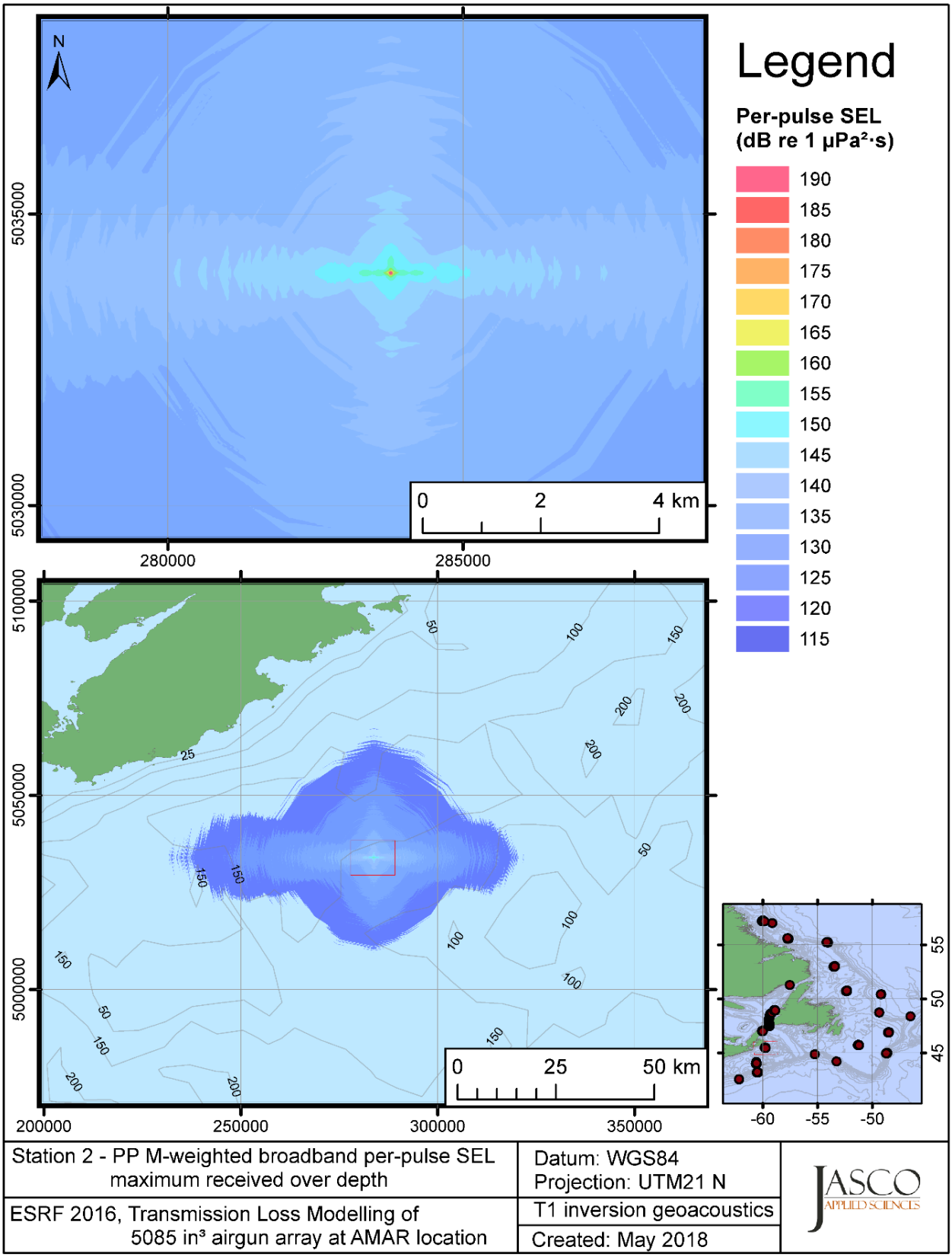

Figure C-406. Stn 2, PP M-weighted maximum-over-depth SEL received at any location on the map, modelled using the track 1 inversion geoacoustic bottom, with the airgun array at the AMAR location and in-situ July SSP.

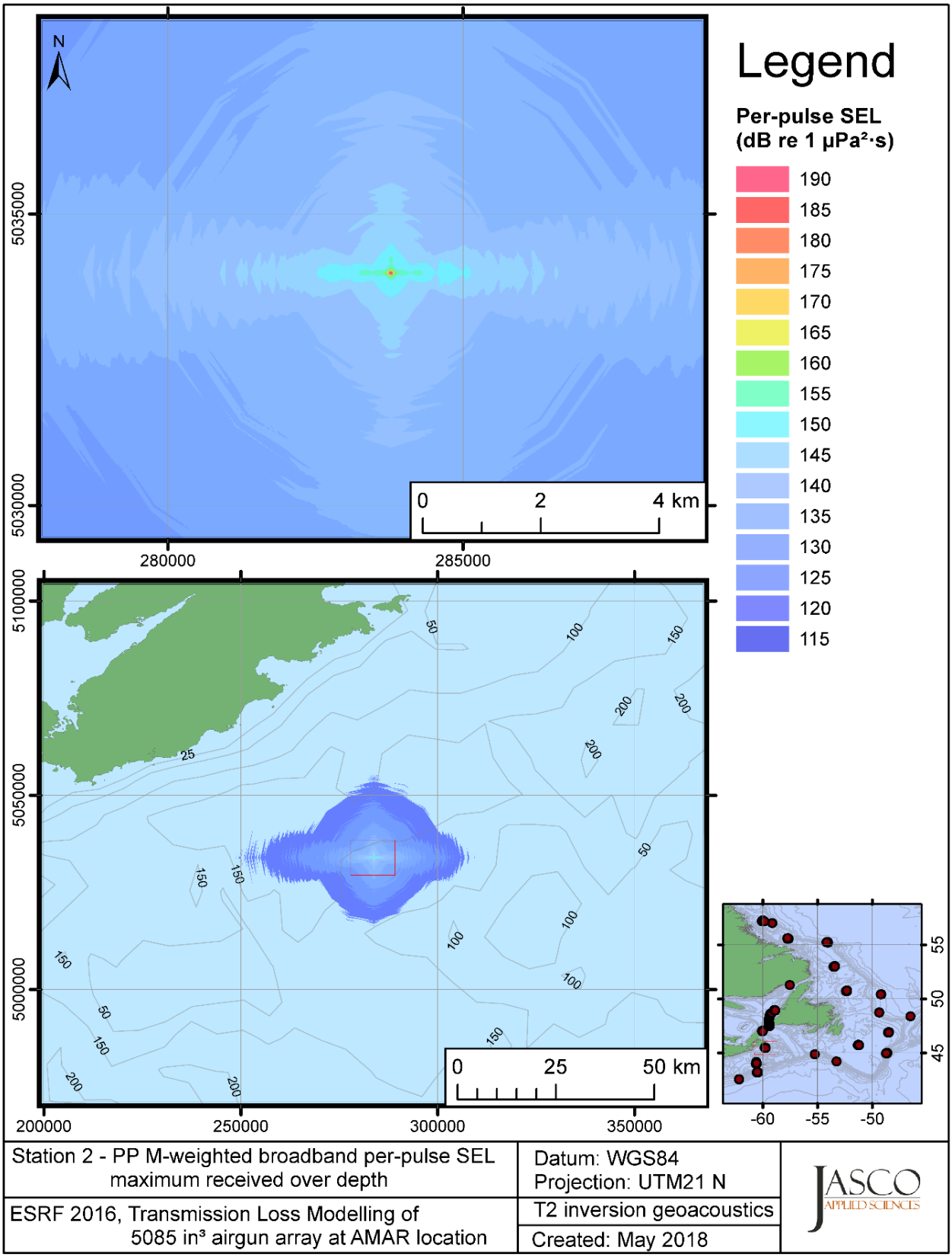

Figure C-407. Stn 2, PP M-weighted maximum-over-depth SEL received at any location on the map, modelled using the track 2 inversion geoacoustic bottom, with the airgun array at the AMAR location and in-situ July SSP.

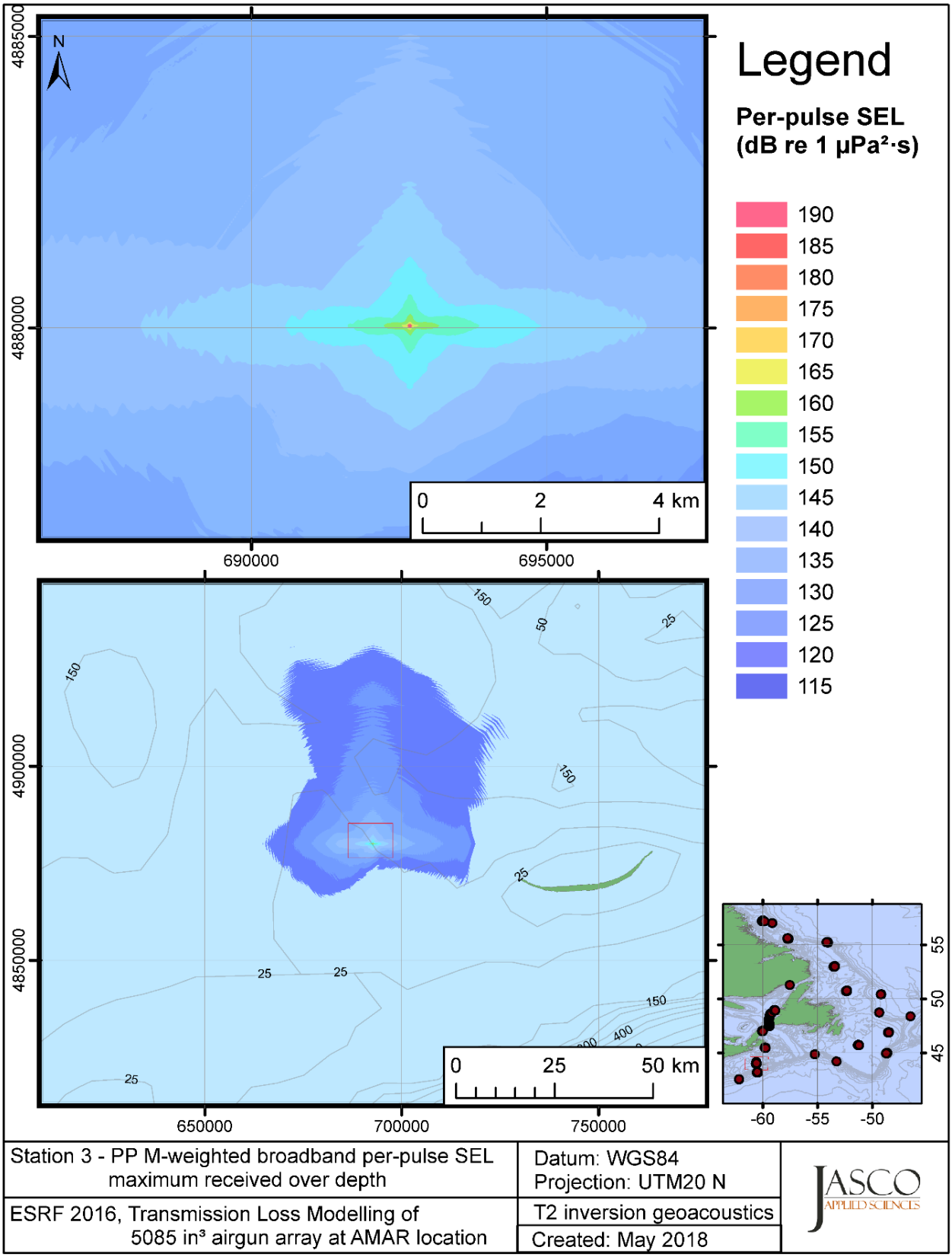

Figure C-408. Stn 3, PP M-weighted maximum-over-depth SEL received at any location on the map, modelled using the track 2 inversion geoacoustic bottom, with the airgun array at the AMAR location and in-situ July SSP.

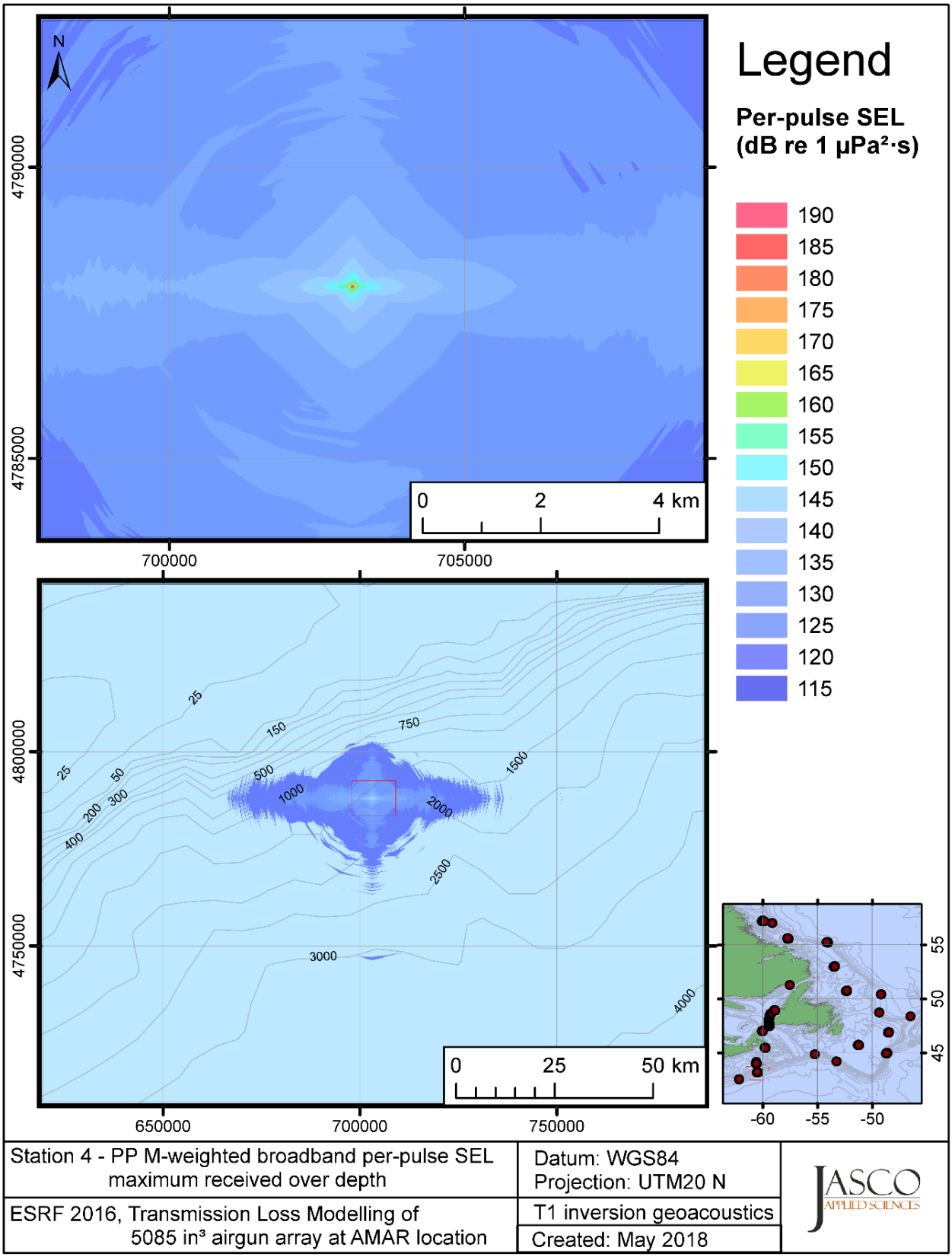

Figure C-409. Stn 4, PP M-weighted maximum-over-depth SEL received at any location on the map, modelled using the track 1 inversion geoacoustic bottom, with the airgun array at the AMAR location and in-situ July SSP.

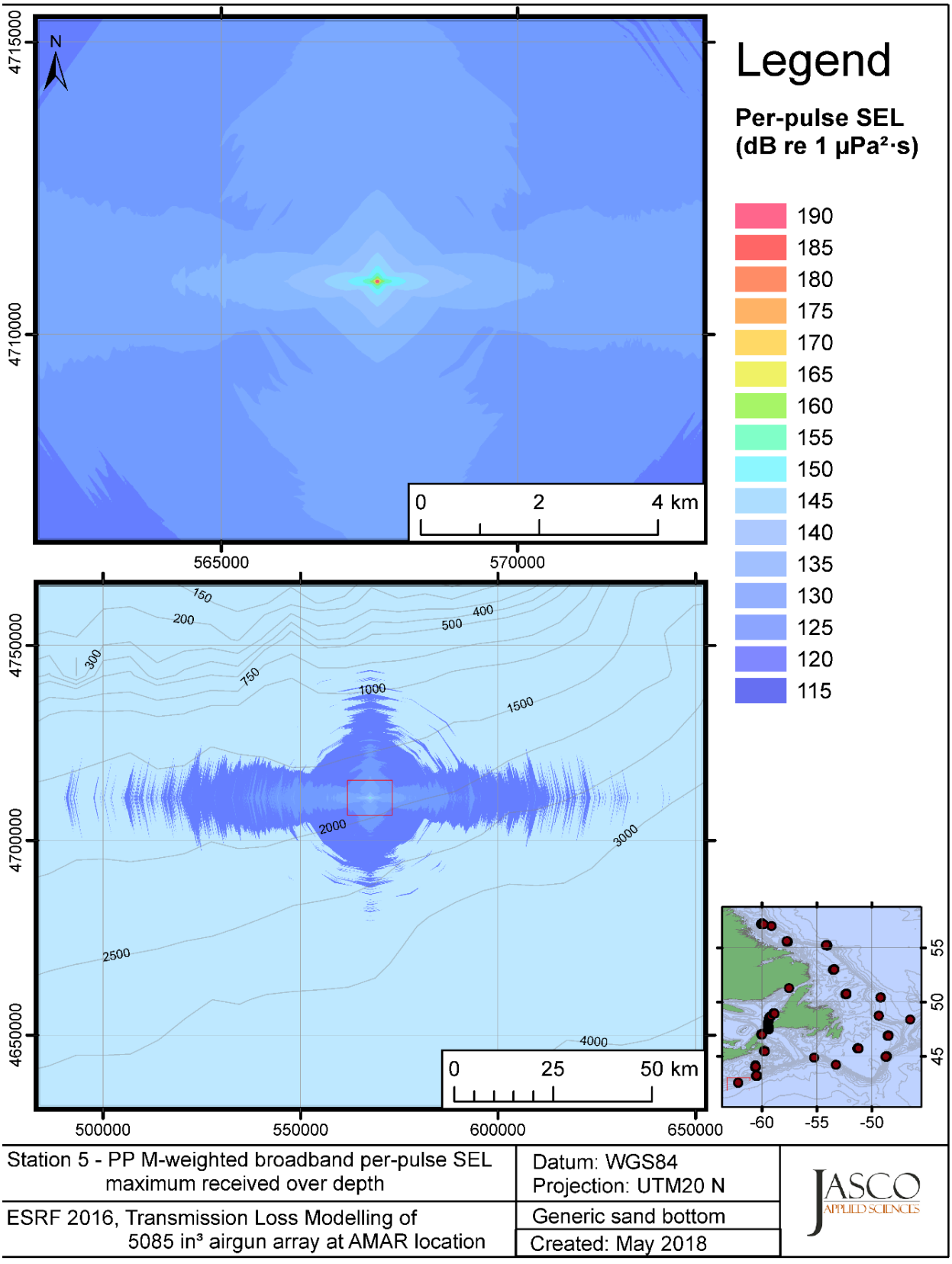

Figure C-410. Stn 5, PP M-weighted maximum-over-depth SEL received at any location on the map, modelled using a generic sand bottom, with the airgun array at the AMAR location and in-situ July SSP.

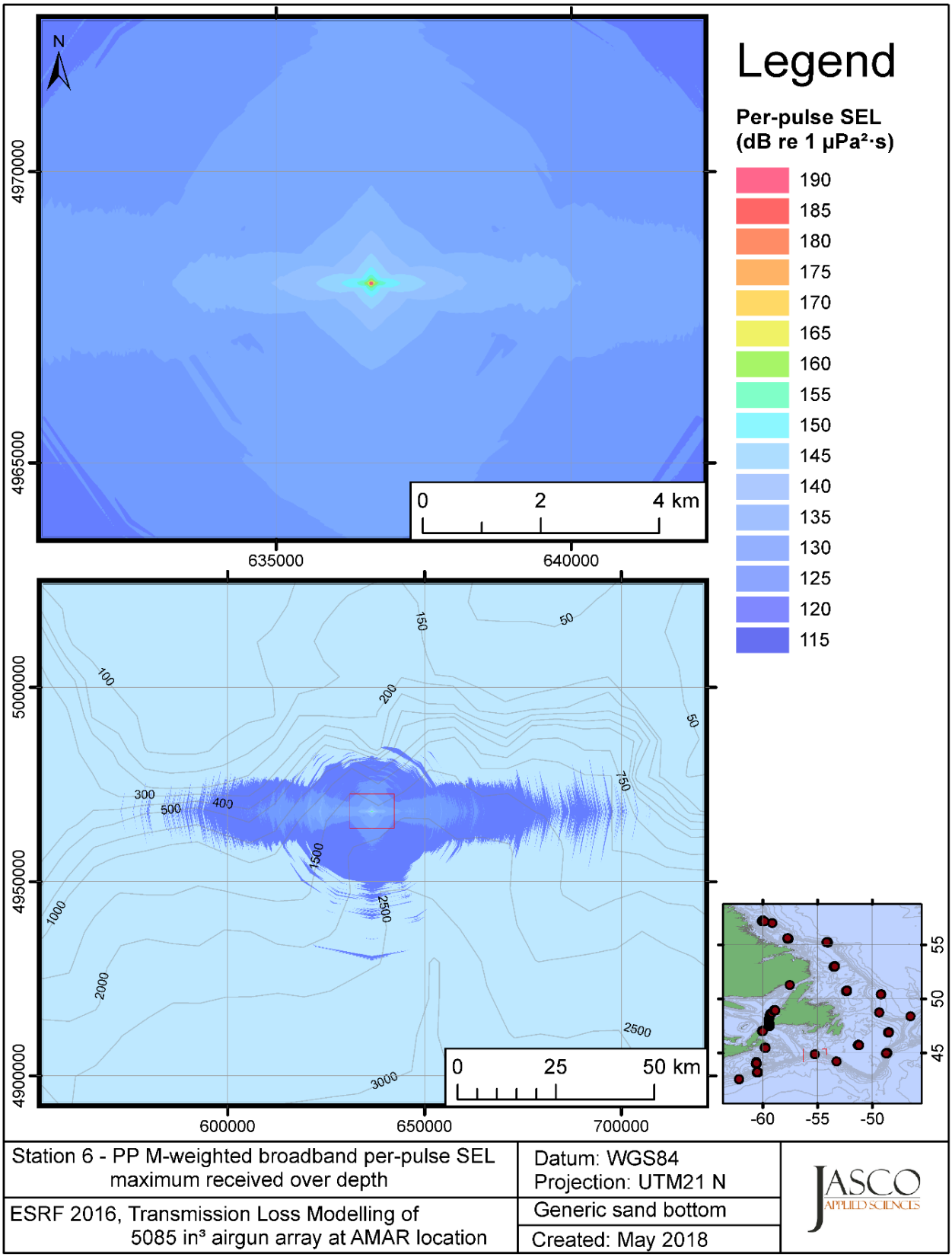

Figure C-411. Stn 6, PP M-weighted maximum-over-depth SEL received at any location on the map, modelled using a generic sand bottom, with the airgun array at the AMAR location and in-situ July SSP.

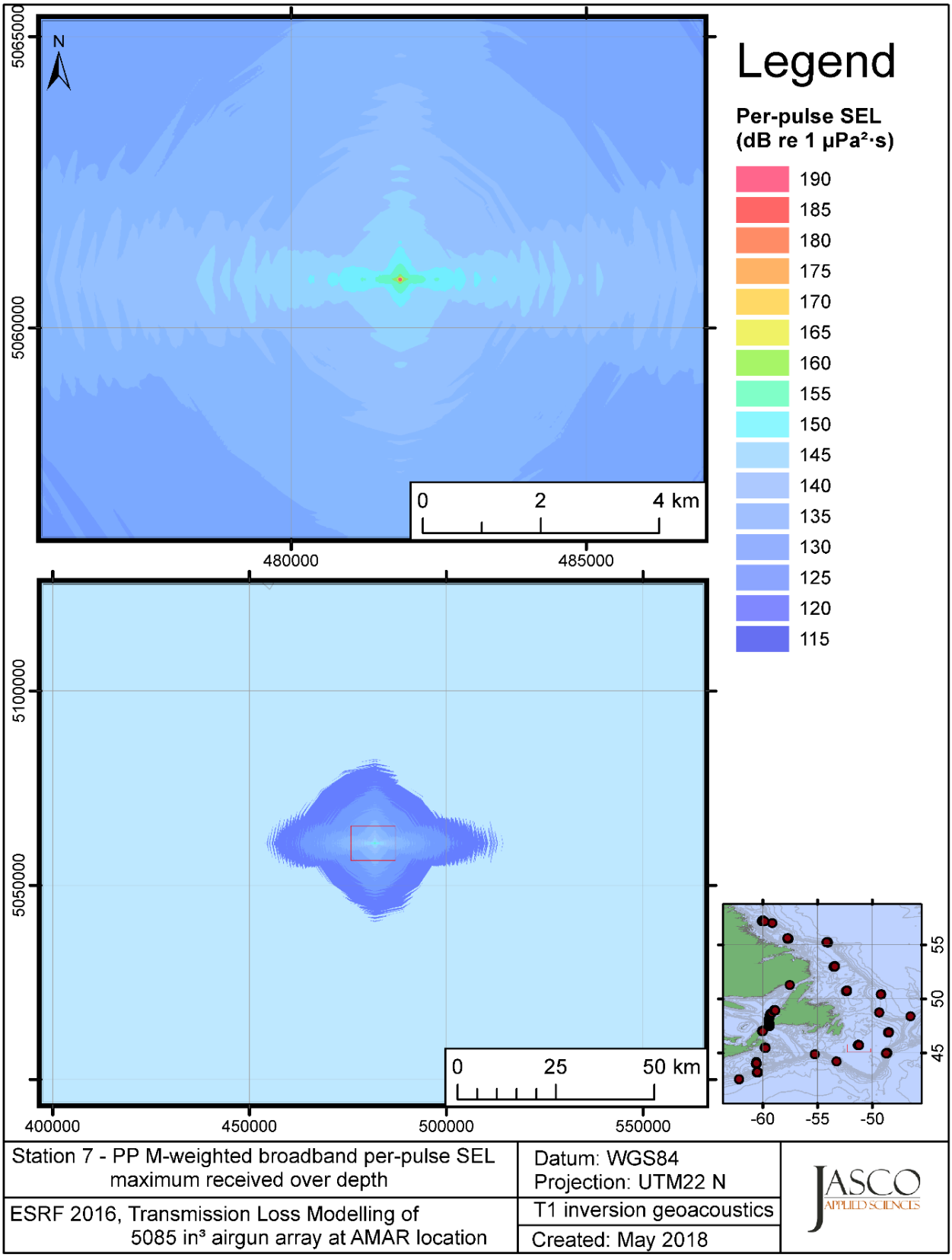

Figure C-412. Stn 7, PP M-weighted maximum-over-depth SEL received at any location on the map, modelled using the track 1 inversion geoacoustic bottom, with the airgun array at the AMAR location and in-situ July SSP.

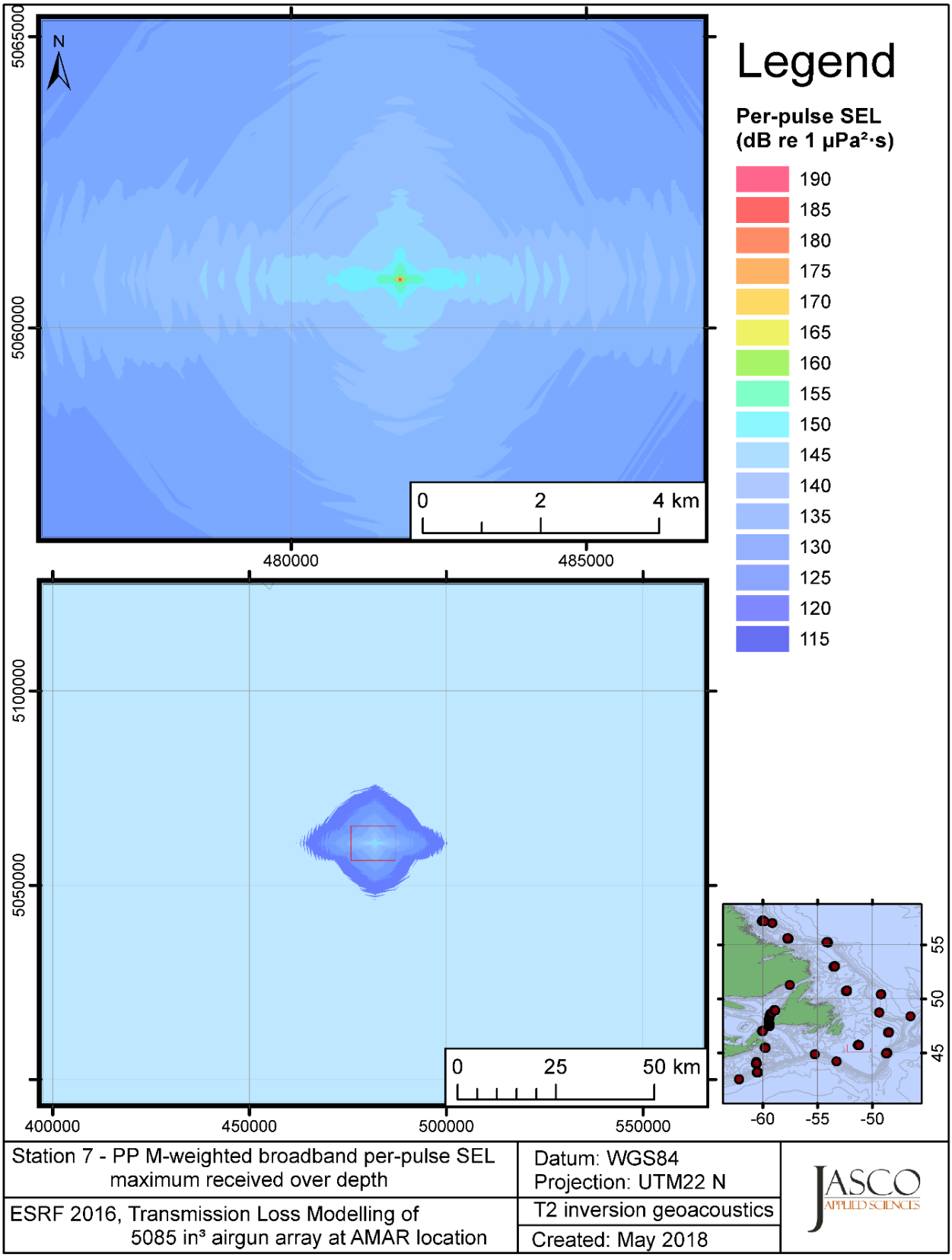

Figure C-413. Stn 7, PP M-weighted maximum-over-depth SEL received at any location on the map, modelled using the track 2 inversion geoacoustic bottom, with the airgun array at the AMAR location and in-situ July SSP.

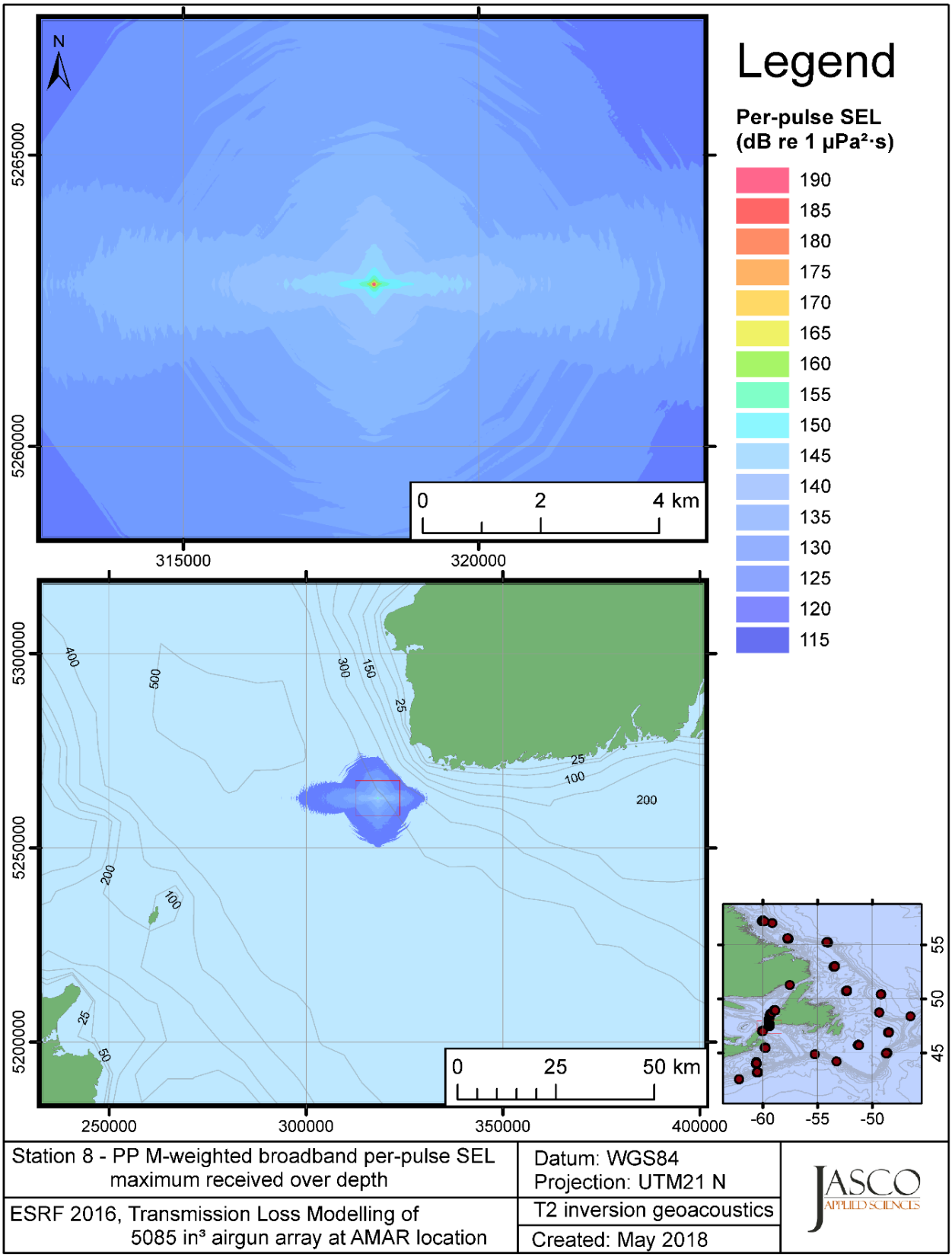

Figure C-414. Stn 8, PP M-weighted maximum-over-depth SEL received at any location on the map, modelled using the track 2 inversion geoacoustic bottom, with the airgun array at the AMAR location and GDEM July SSP.

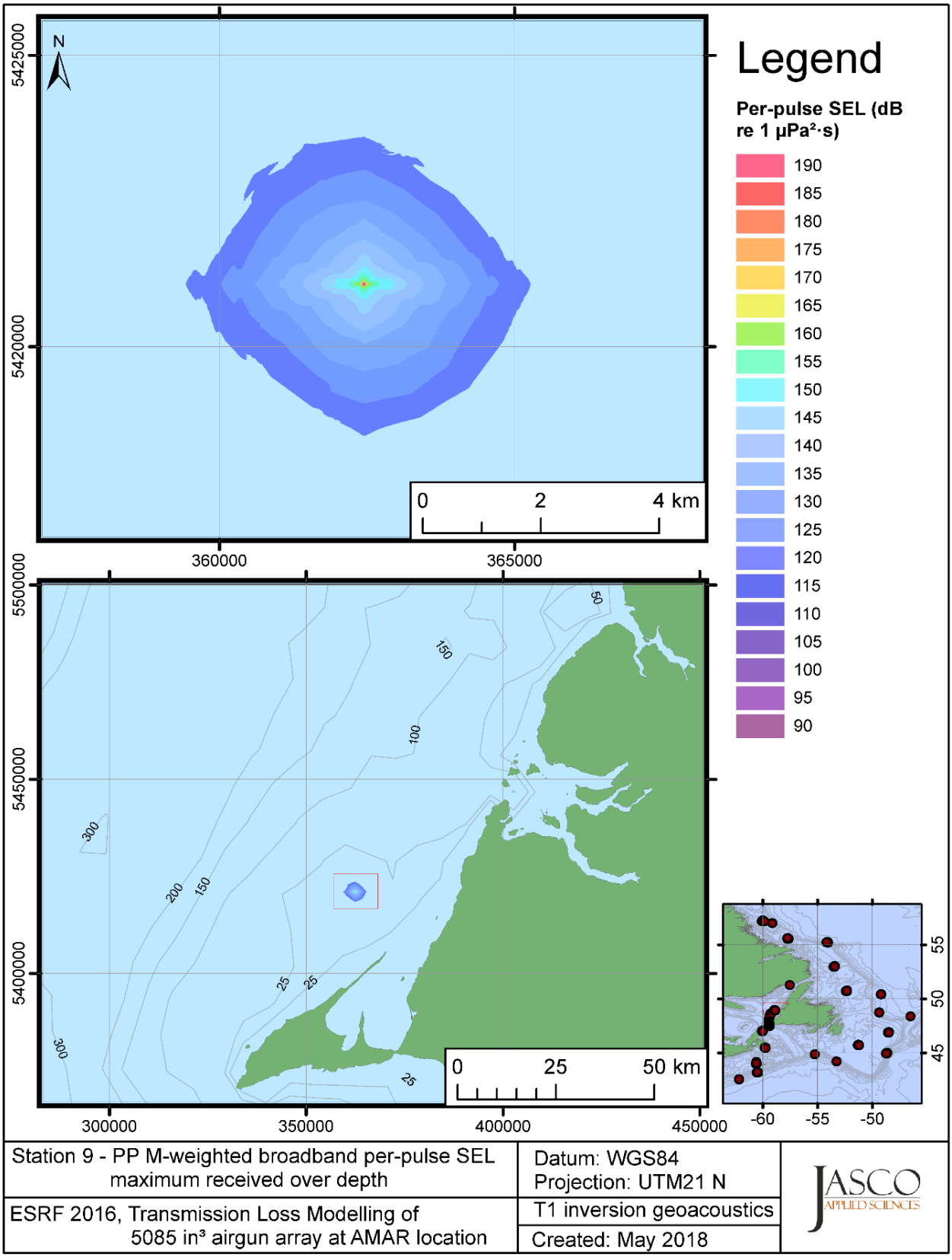

Figure C-415. Stn 9, PP M-weighted maximum-over-depth SEL received at any location on the map, modelled using the track 1 inversion geoacoustic bottom, with the airgun array at the AMAR location and GDEM July SSP.

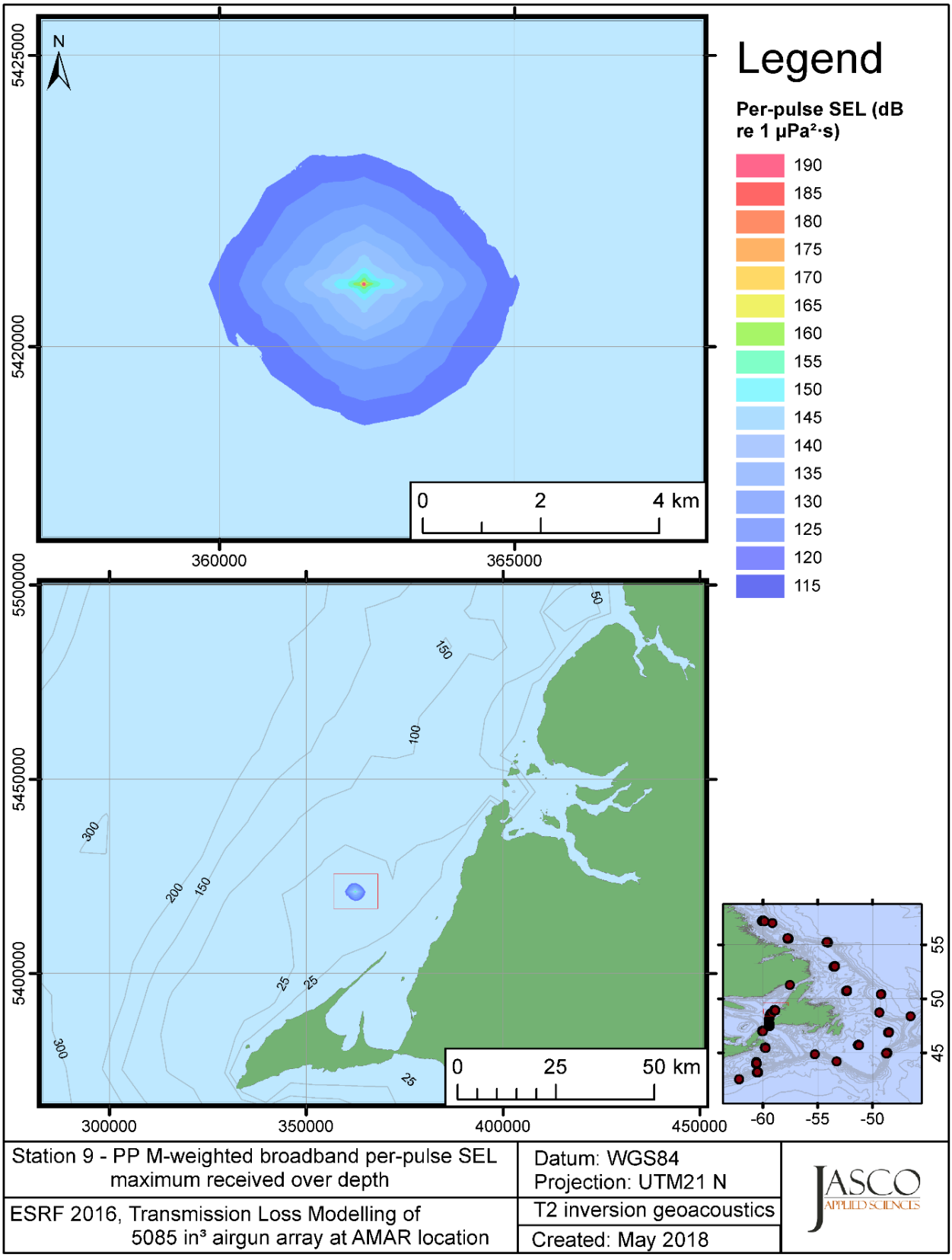

Figure C-416. Stn 9, PP M-weighted maximum-over-depth SEL received at any location on the map, modelled using the track 2 inversion geoacoustic bottom, with the airgun array at the AMAR location and GDEM July SSP.

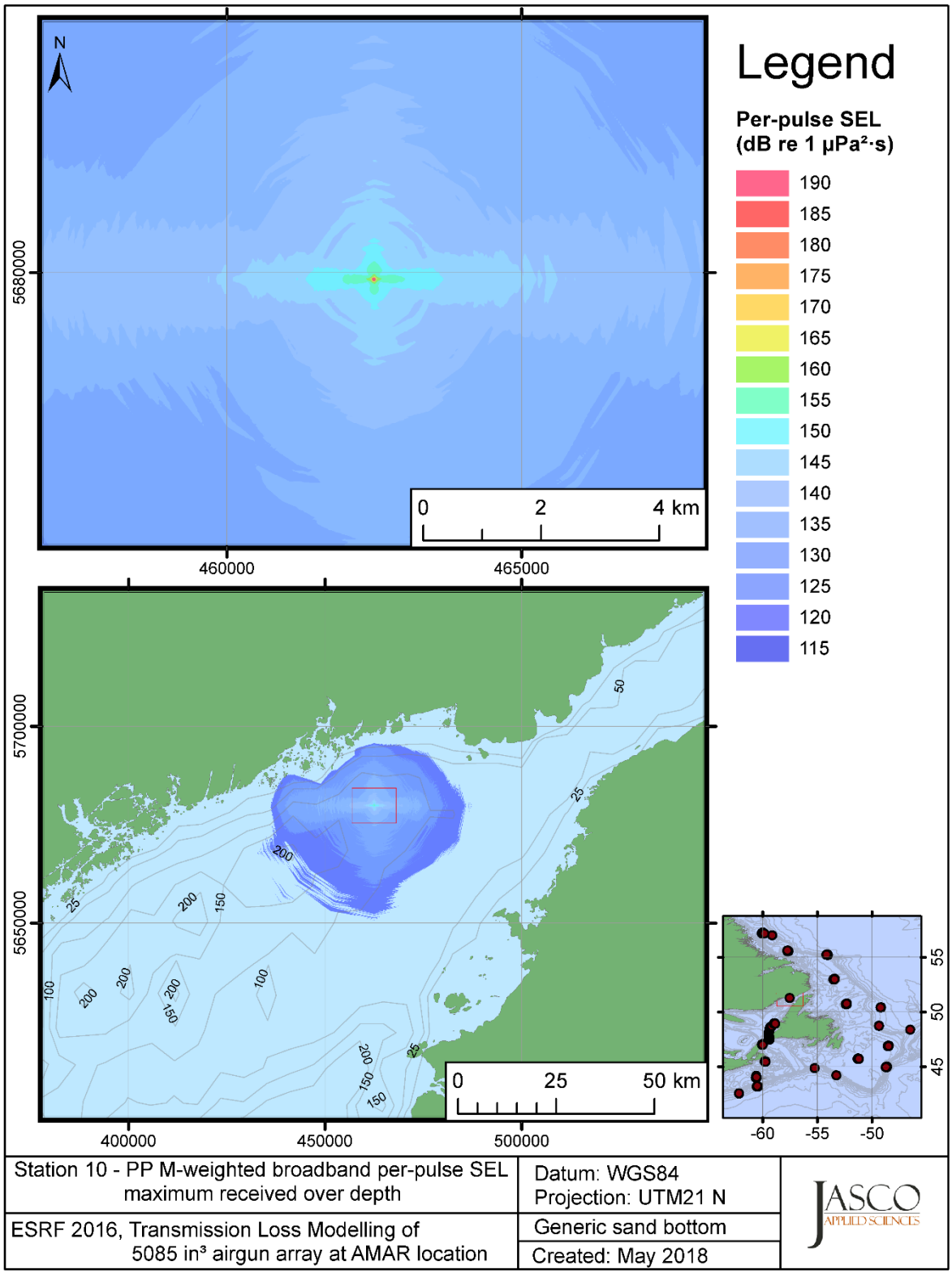

Figure C-417. Stn 10, PP M-weighted maximum-over-depth SEL received at any location on the map, modelled using a generic sand bottom, with the airgun array at the AMAR location and in-situ July SSP.

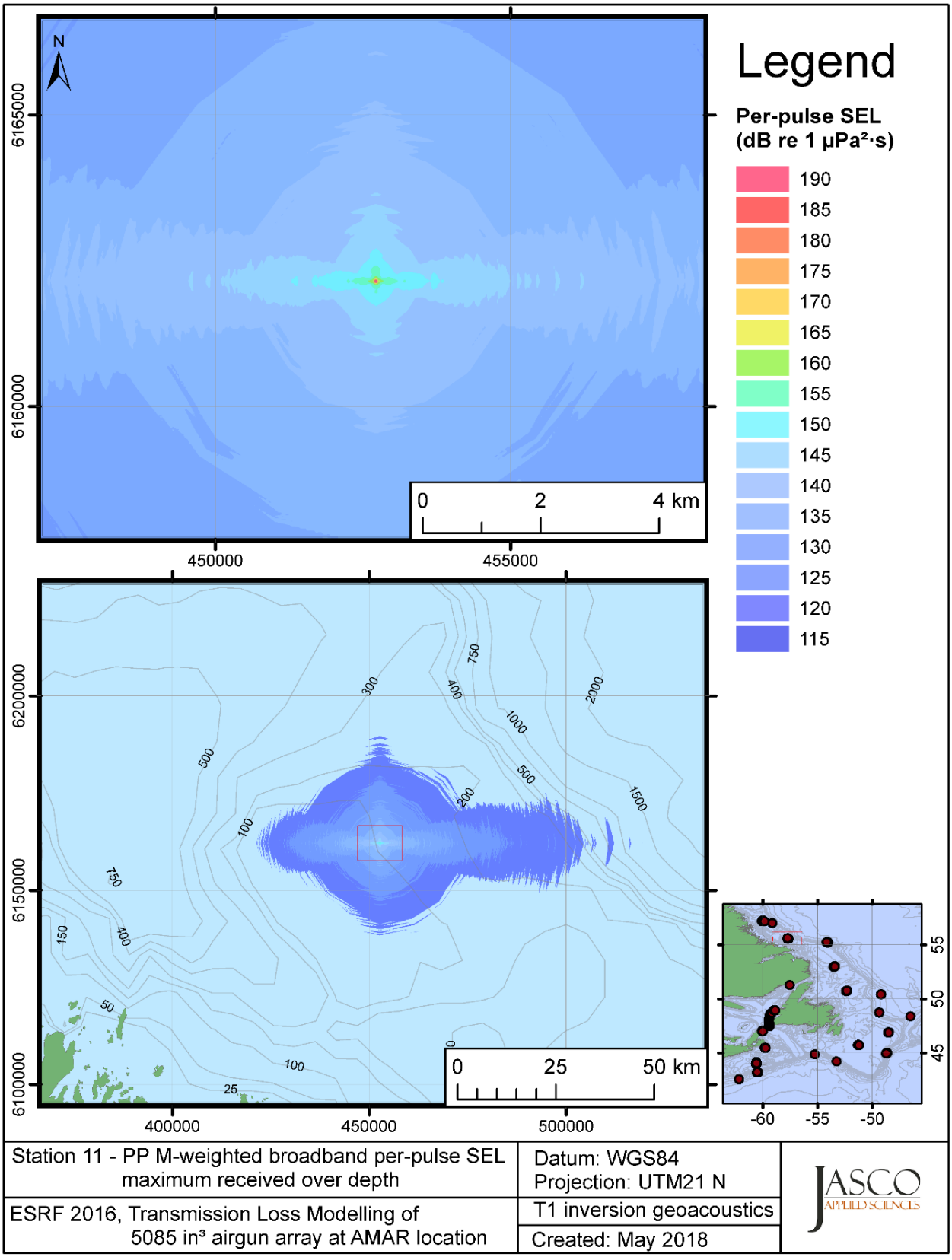

Figure C-418. Stn 11, PP M-weighted maximum-over-depth SEL received at any location on the map, modelled using the track 1 inversion geoacoustic bottom, with the airgun array at the AMAR location and in-situ July SSP.

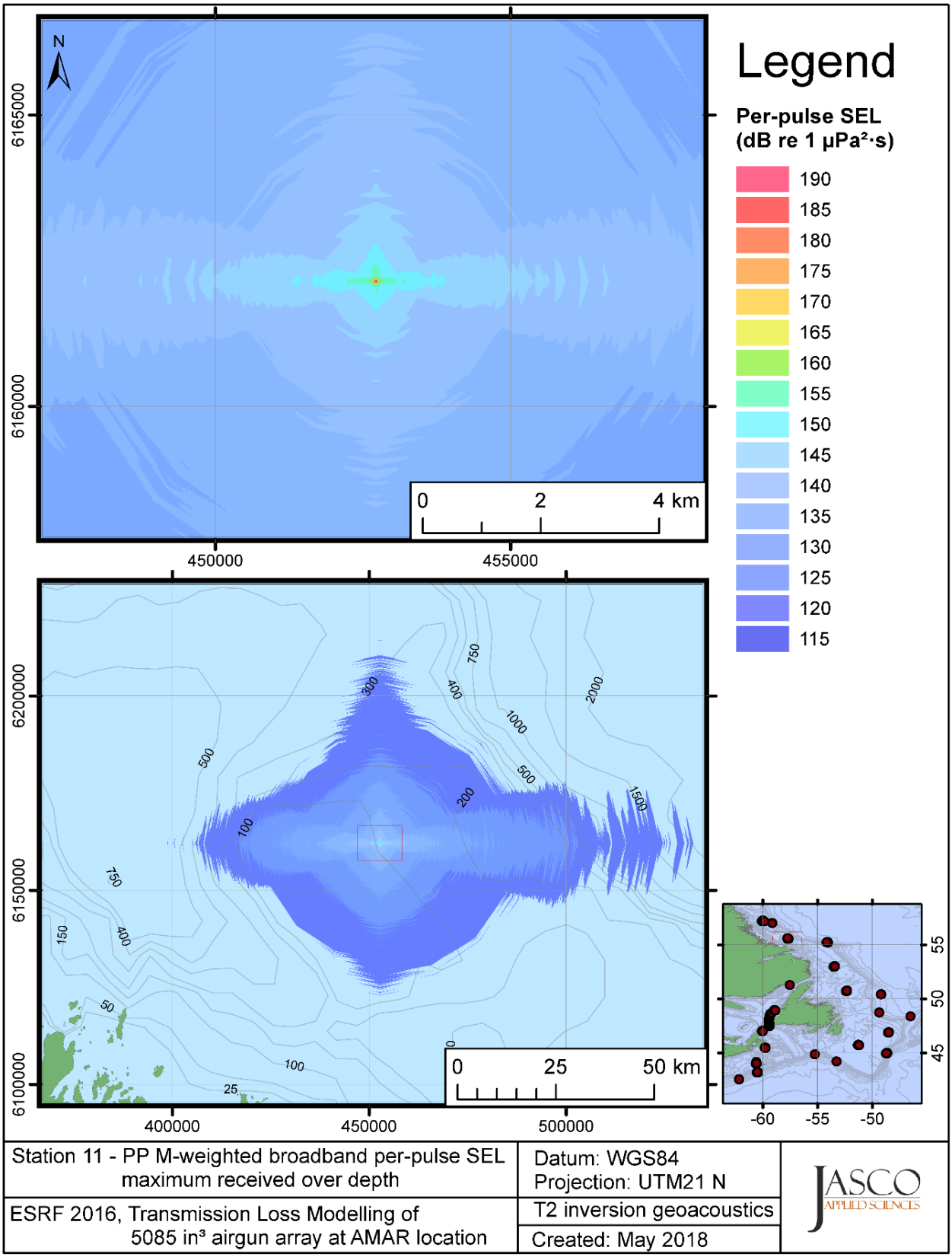

Figure C-419. Stn 11, PP M-weighted maximum-over-depth SEL received at any location on the map, modelled using the track 2 inversion geoacoustic bottom, with the airgun array at the AMAR location and in-situ July SSP.

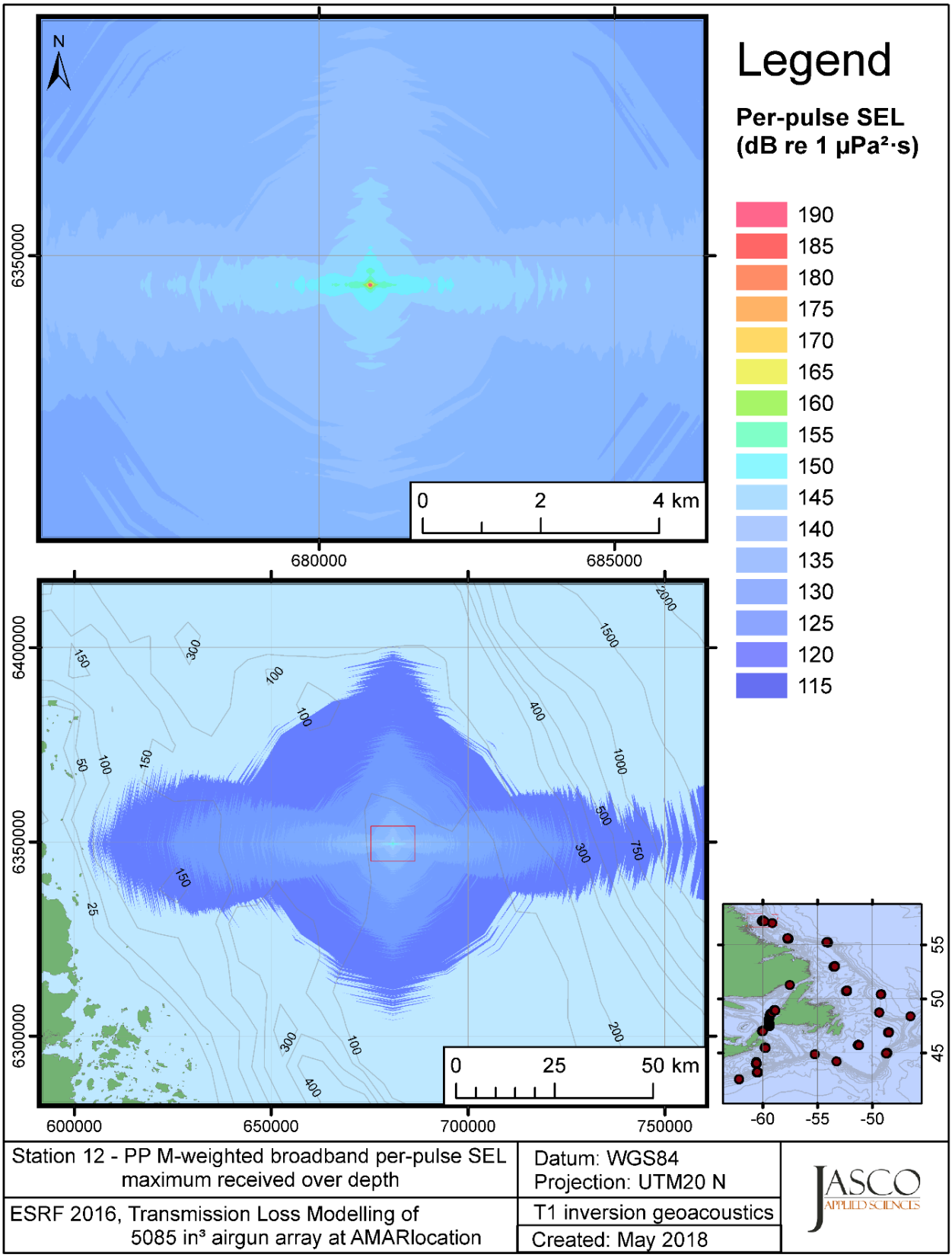

Figure C-420. Stn 12, PP M-weighted maximum-over-depth SEL received at any location on the map, modelled using the track 1 inversion geoacoustic bottom, with the airgun array at the AMAR location and in-situ July SSP.

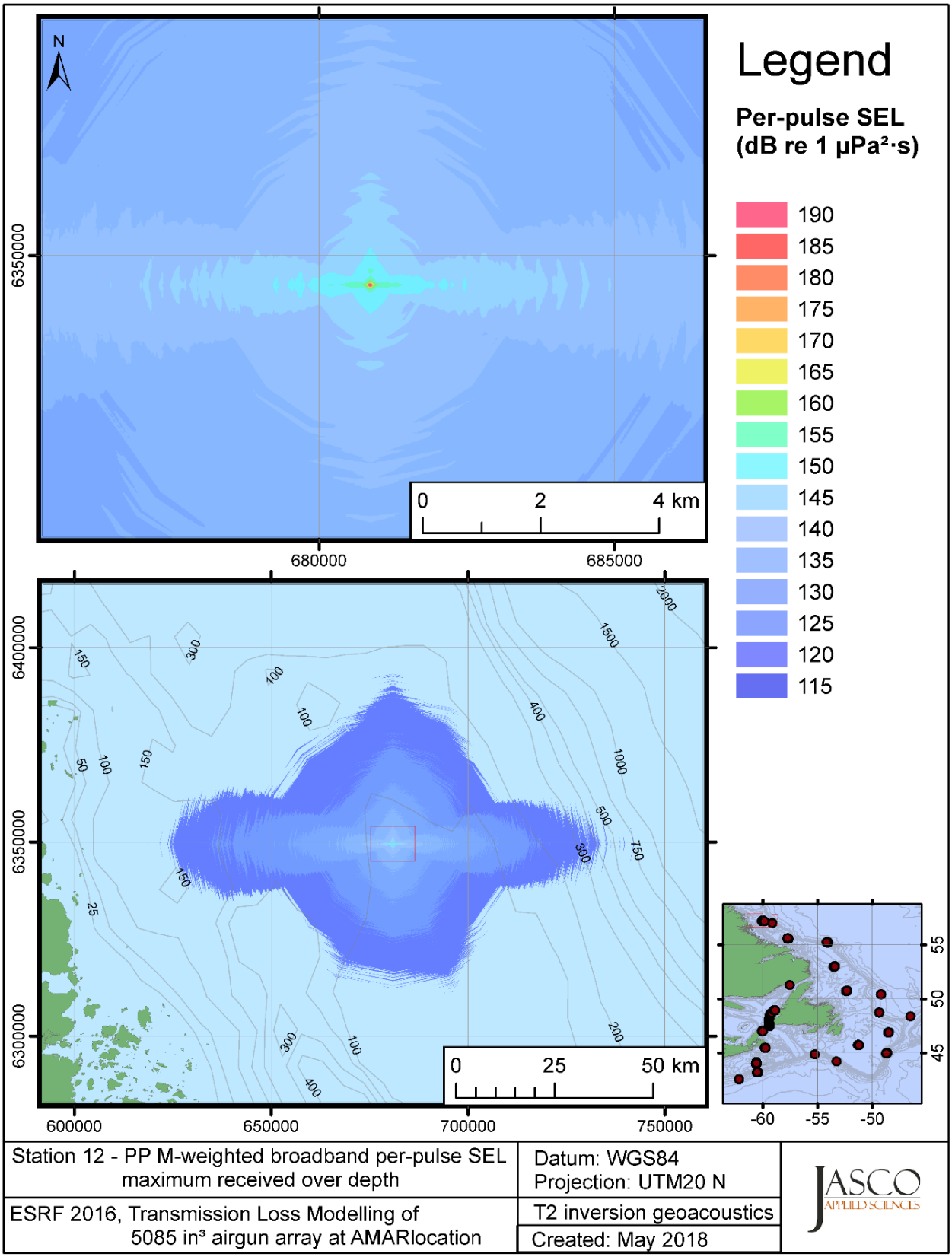

Figure C-421. Stn 12, PP M-weighted maximum-over-depth SEL received at any location on the map, modelled using the track 2 inversion geoacoustic bottom, with the airgun array at the AMAR location and in-situ July SSP.

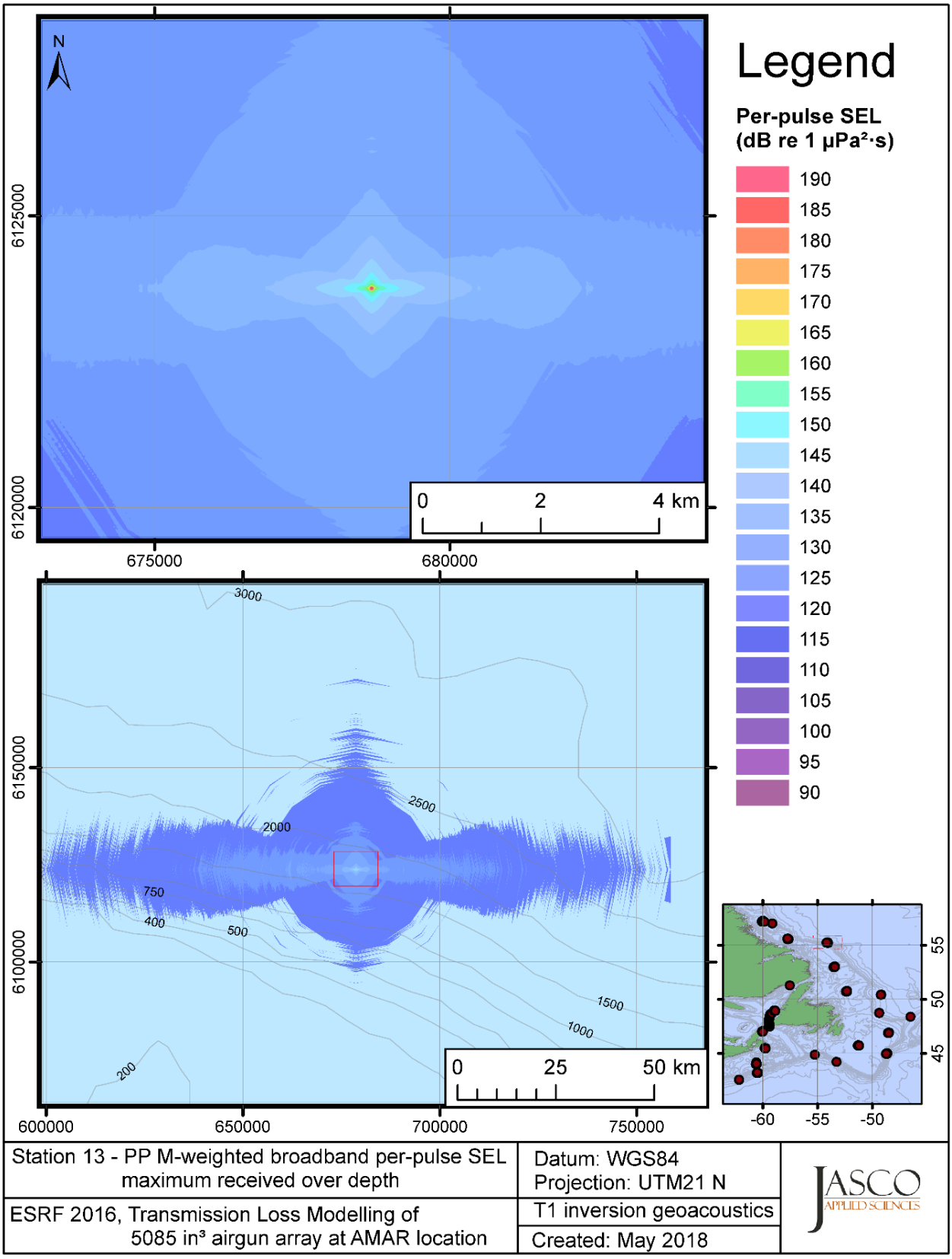

Figure C-422. Stn 13, PP M-weighted maximum-over-depth SEL received at any location on the map, modelled using the track 1 inversion geoacoustic bottom, with the airgun array at the AMAR location and in-situ July SSP.

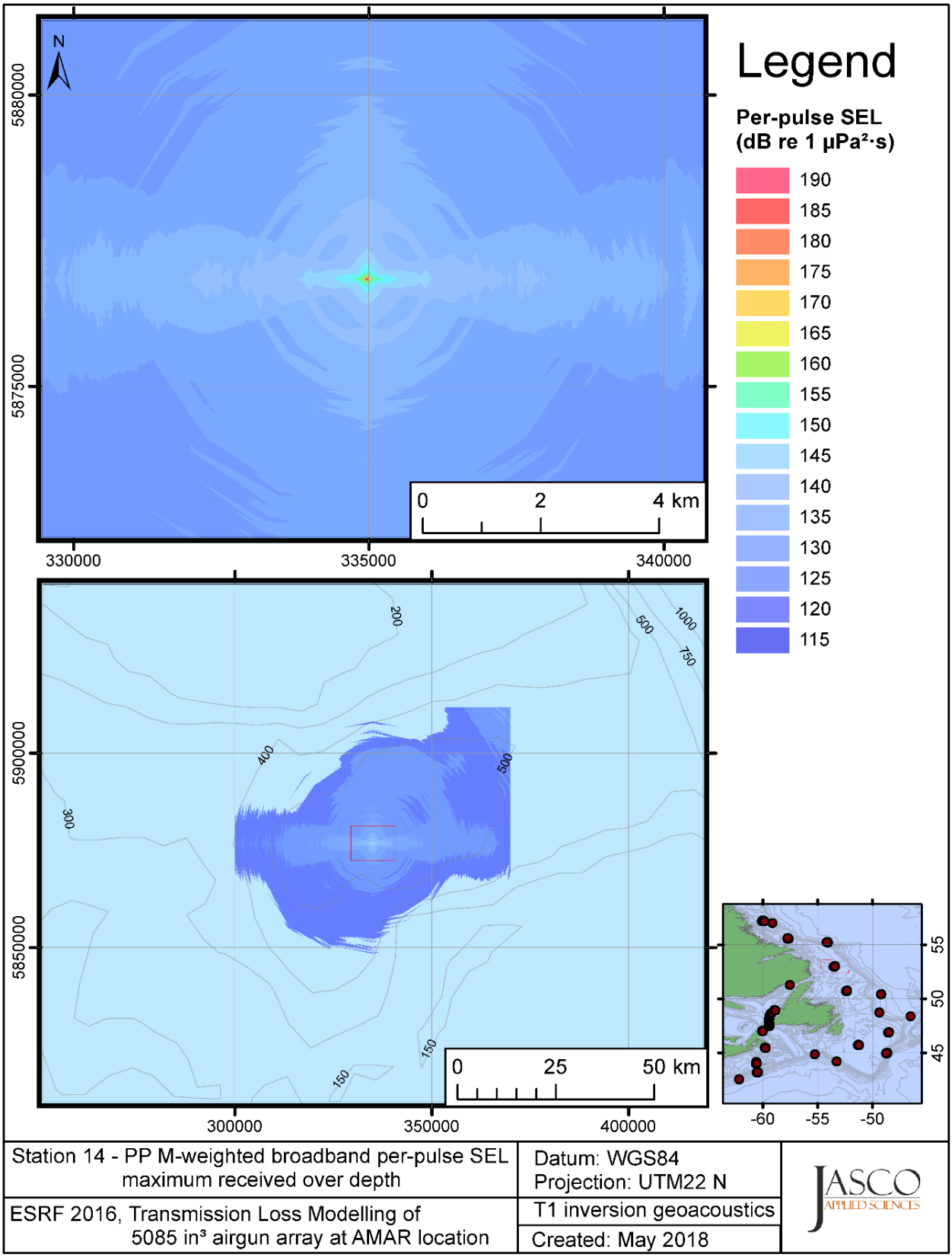

Figure C-423. Stn 14, PP M-weighted maximum-over-depth SEL received at any location on the map, modelled using the track 1 inversion geoacoustic bottom, with the airgun array at the AMAR location and in-situ July SSP.

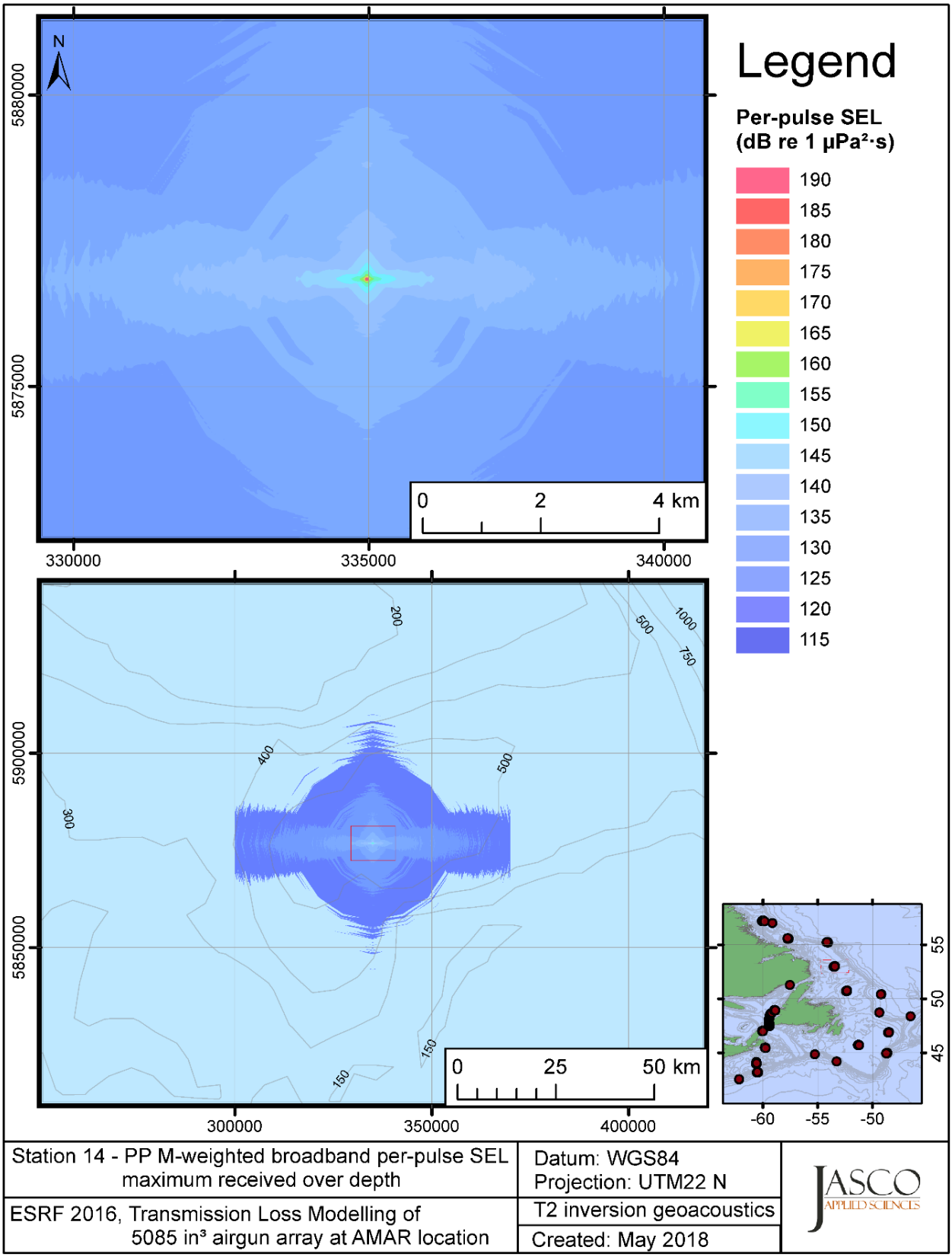

Figure C-424. Stn 14, PP M-weighted maximum-over-depth SEL received at any location on the map, modelled using the track 2 inversion geoacoustic bottom, with the airgun array at the AMAR location and in-situ July SSP.

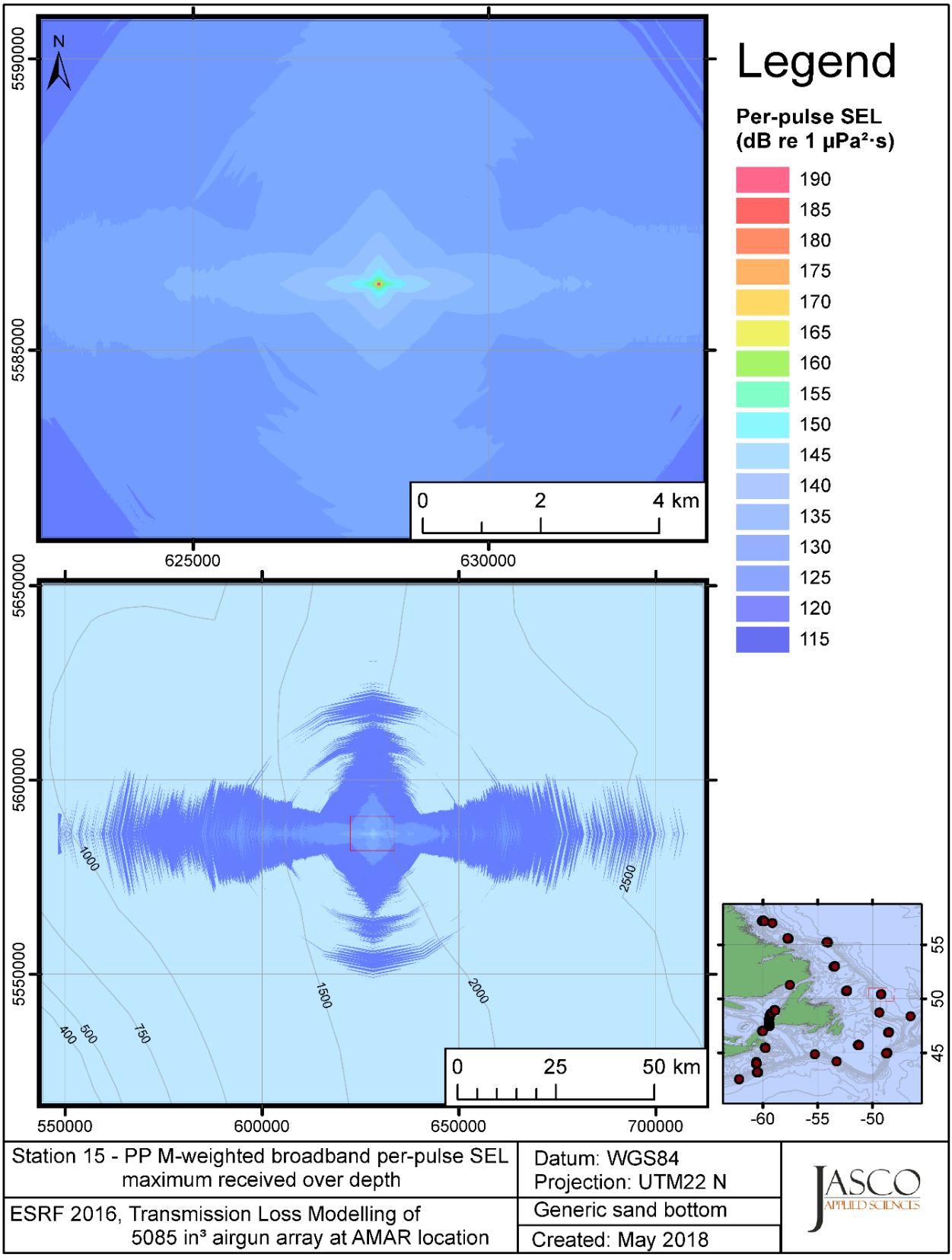

Figure C-425. Stn 15, PP M-weighted maximum-over-depth SEL received at any location on the map, modelled using a generic sand bottom, with the airgun array at the AMAR location and in-situ July SSP.

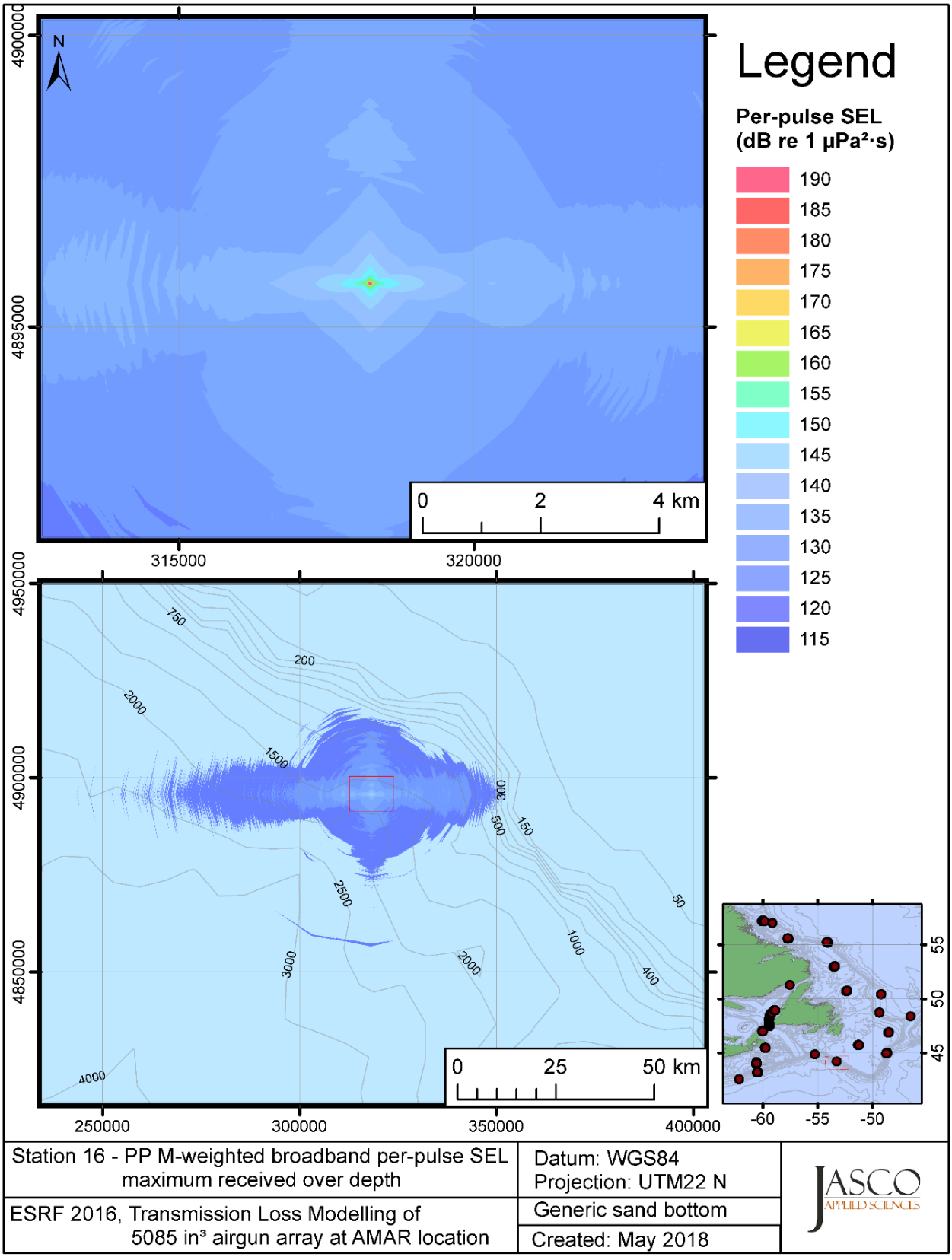

Figure C-426. Stn 16, PP M-weighted maximum-over-depth SEL received at any location on the map, modelled using a generic sand bottom, with the airgun array at the AMAR location and in-situ July SSP.

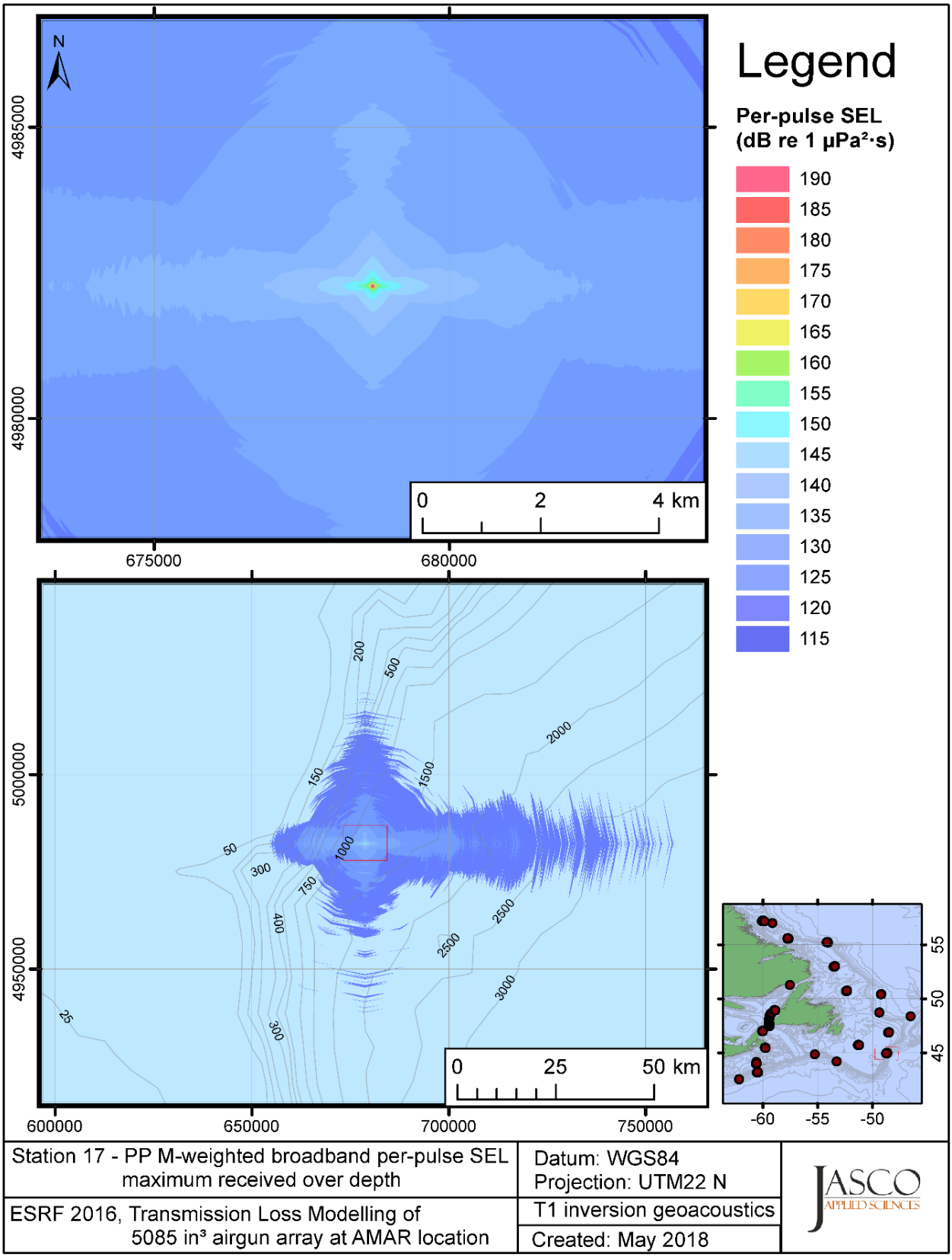

Figure C-427. Stn 17, PP M-weighted maximum-over-depth SEL received at any location on the map, modelled using the track 1 inversion geoacoustic bottom, with the airgun array at the AMAR location and in-situ July SSP.

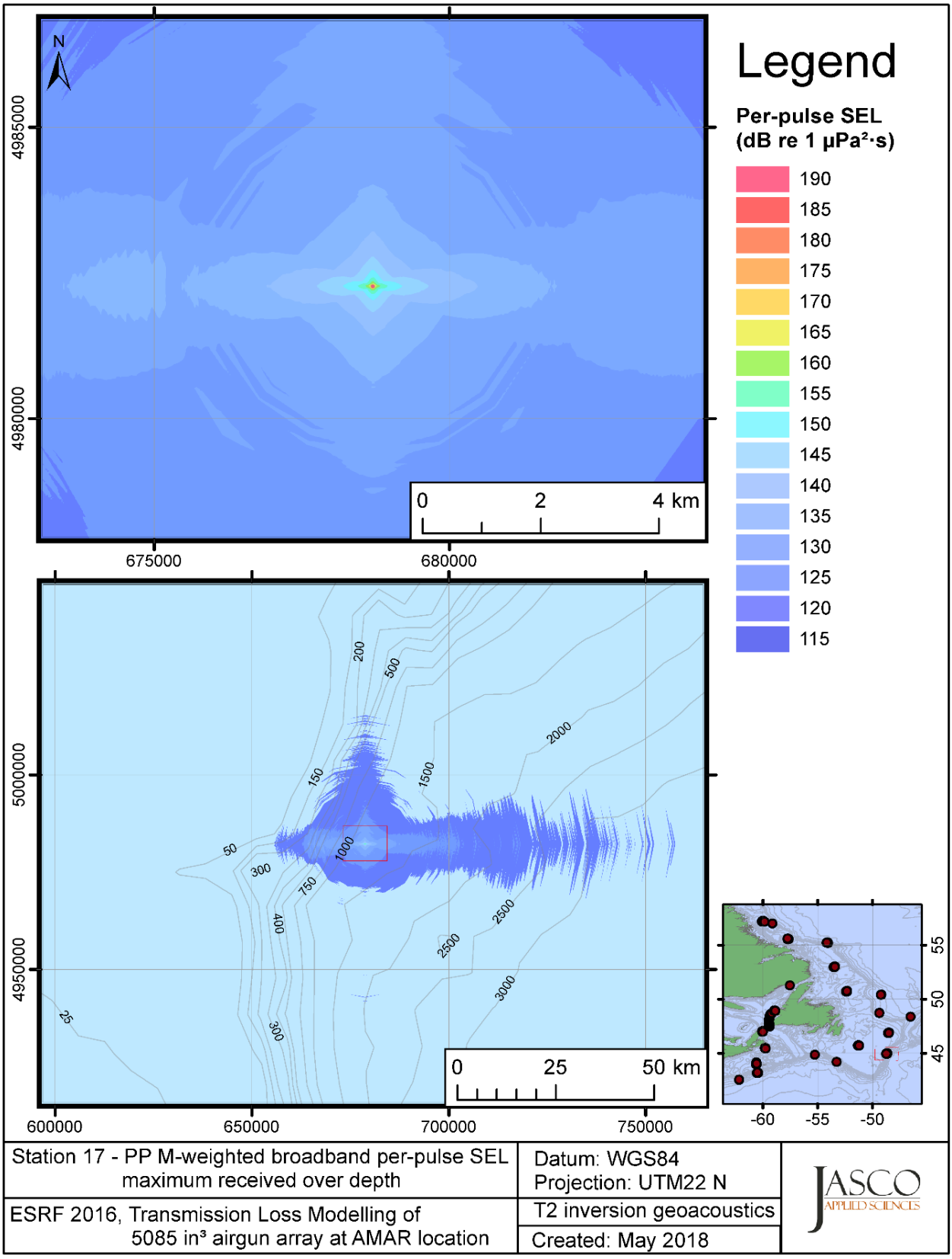

Figure C-428. Stn 17, PP M-weighted maximum-over-depth SEL received at any location on the map, modelled using the track 2 inversion geoacoustic bottom, with the airgun array at the AMAR location and in-situ July SSP.

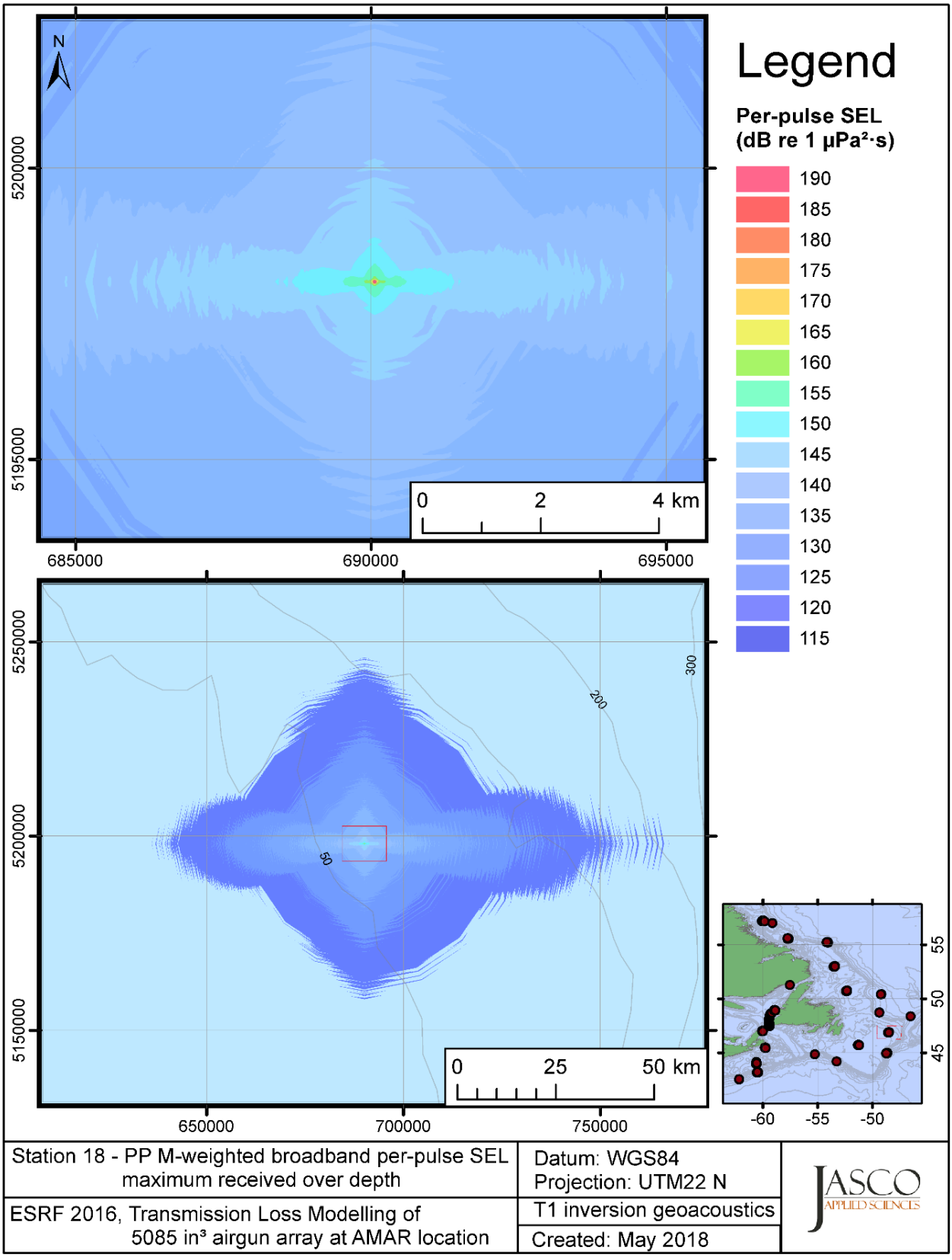

Figure C-429. Stn 18, PP M-weighted maximum-over-depth SEL received at any location on the map, modelled using the track 1 inversion geoacoustic bottom, with the airgun array at the AMAR location and in-situ July SSP.

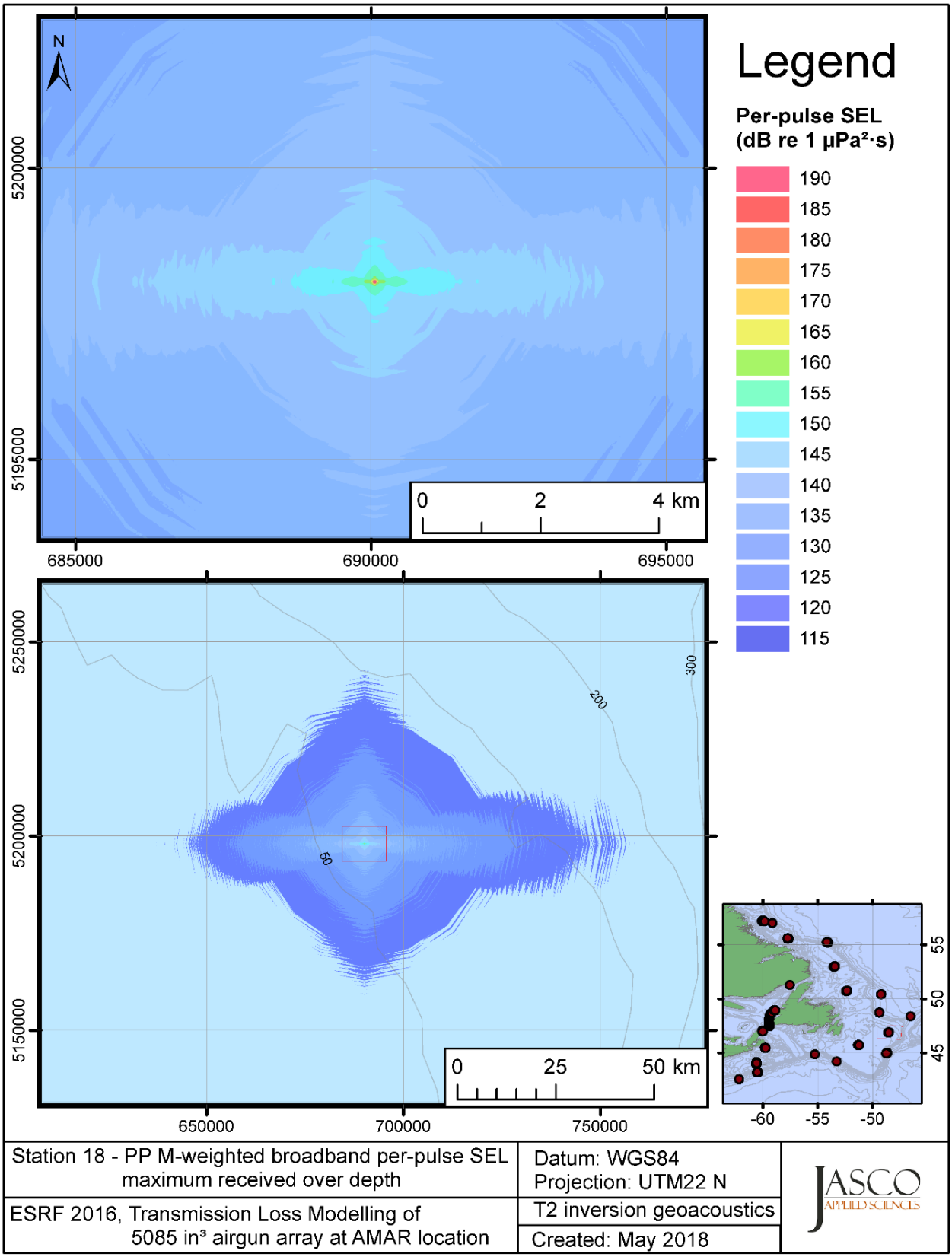

Figure C-430. Stn 18, PP M-weighted maximum-over-depth SEL received at any location on the map, modelled using the track 2 inversion geoacoustic bottom, with the airgun array at the AMAR location and in-situ July SSP.

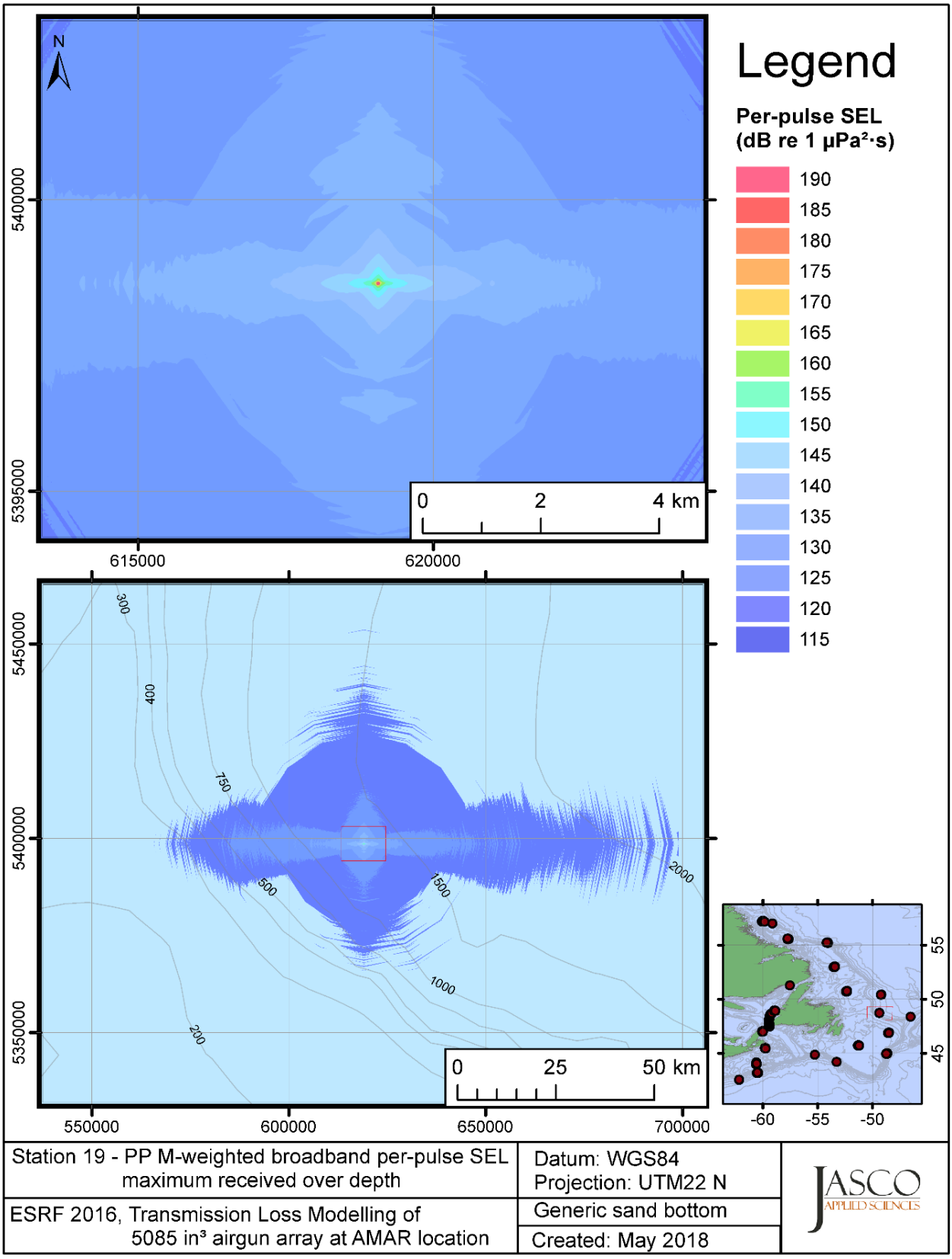

Figure C-431. Stn 19, PP M-weighted maximum-over-depth SEL received at any location on the map, modelled using a generic sand bottom, with the airgun array at the AMAR location and in-situ July SSP.

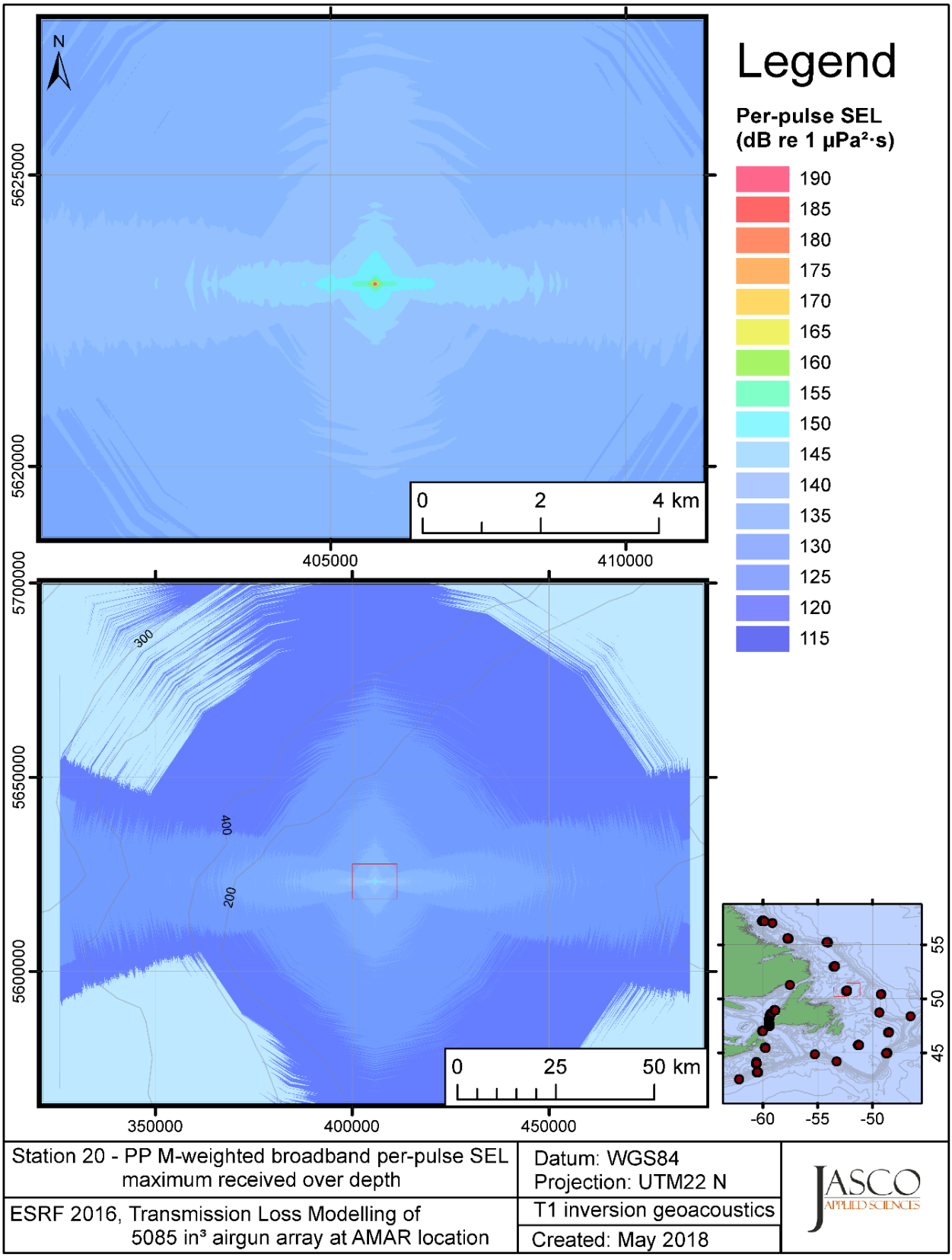

Figure C-432. Stn 20, PP M-weighted maximum-over-depth SEL received at any location on the map, modelled using the track 1 inversion geoacoustic bottom, with the airgun array at the AMAR location and in-situ July SSP.

C.13. Modelling Unweighted Max-over-depth Received Level at Distant Locations - Winter

This section presents the results of modelling the maximum-over-depth per-pulse sound exposure level (SEL) received at distant receiver locations (varied in range and azimuth) for the source held fixed at the AMAR location. The modelling uses the geoacoustic inversion bottom parameters at the 14 sites where they are available and only uses a generic sand bottom at the other six sites. The modelling results are presented in the form of coloured maps where the colour at any map location represents the predicted maximum-over-depth received level at that spot on the map. This section includes only the unweighted per-pulse SEL results; additional maps for marine mammal received level auditory weightings are presented in adjoining sections. The sound speed profiles (SSP) used are detailed in Appendix B.2.

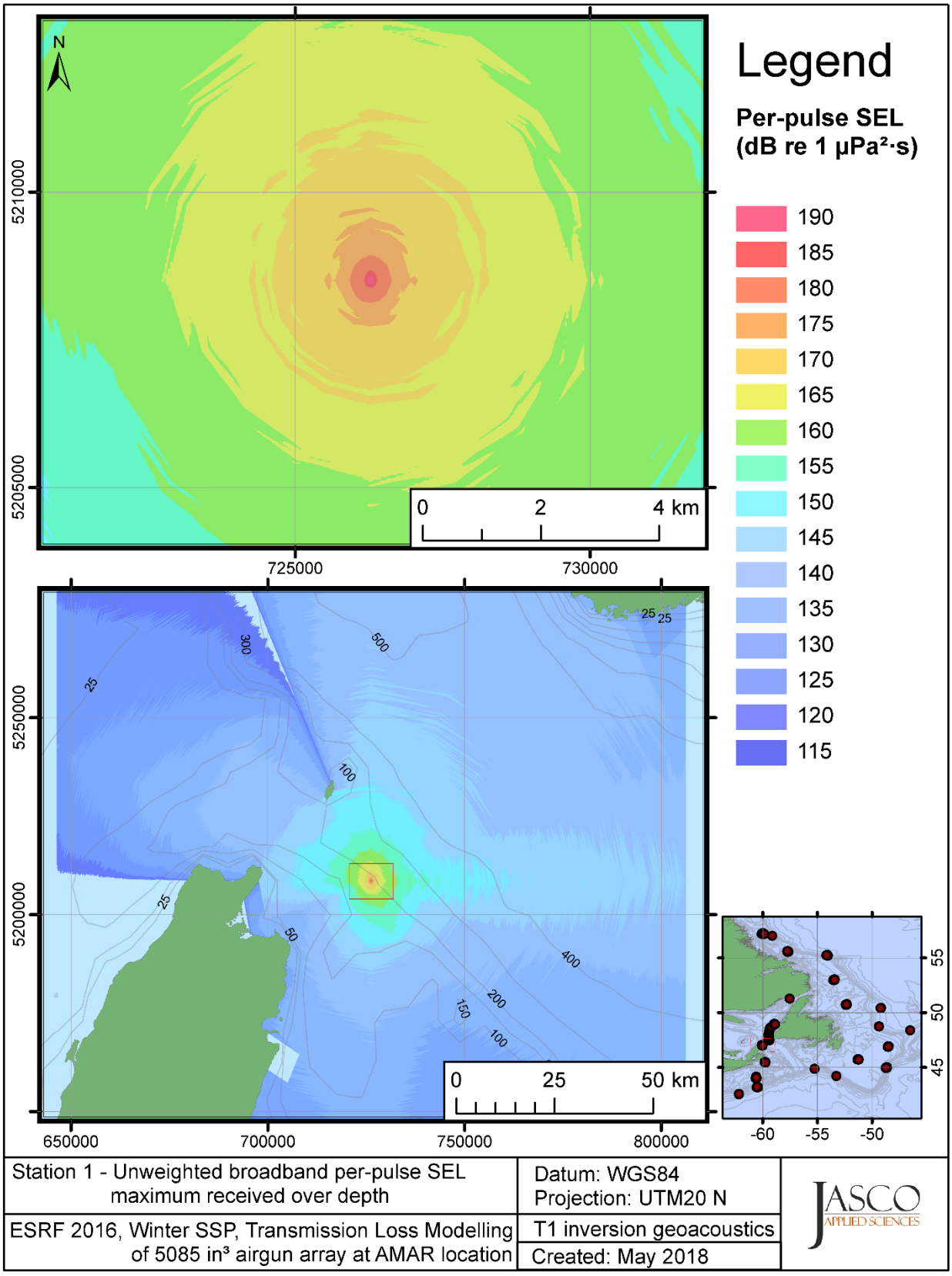

Figure C-433. Stn 1, unweighted maximum-over-depth SEL received at any location on the map, modelled using the track 1 inversion geoacoustic bottom, with the airgun array at the AMAR location and GDEM February SSP.

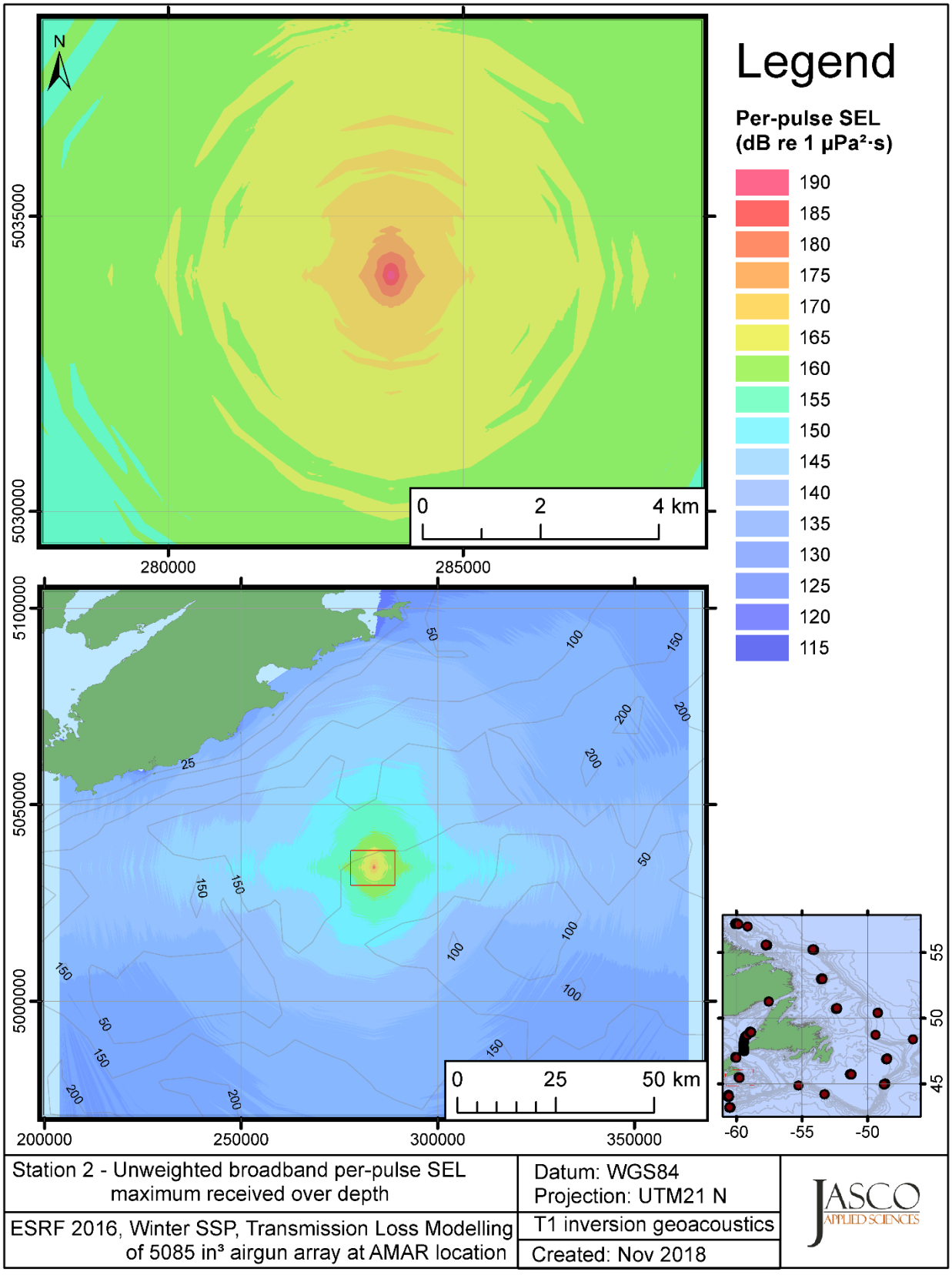

Figure C-434. Stn 2, unweighted maximum-over-depth SEL received at any location on the map, modelled using the track 1 inversion geoacoustic bottom, with the airgun array at the AMAR location and GDEM February SSP.

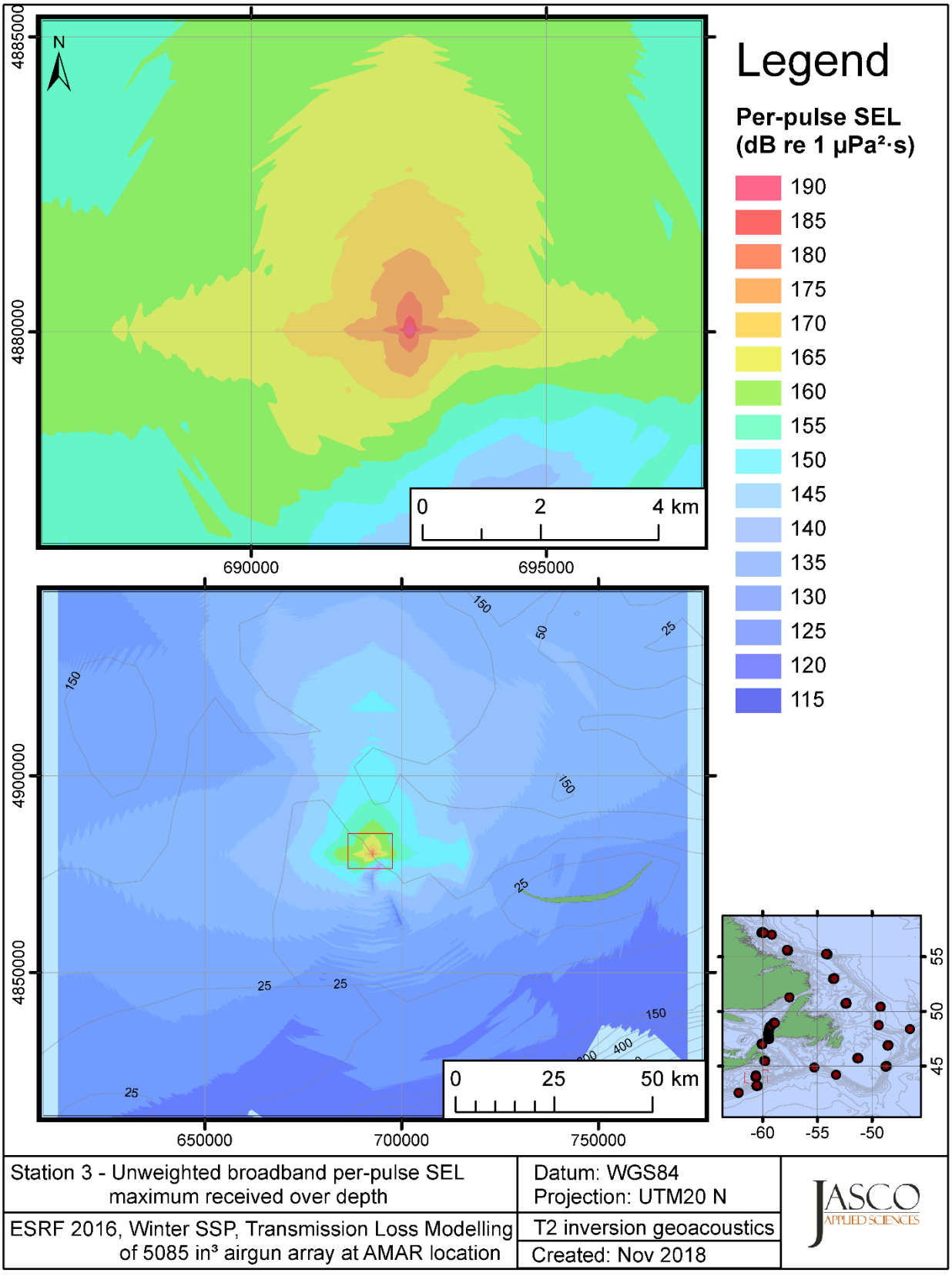

Figure C-435. Stn 3, unweighted maximum-over-depth SEL received at any location on the map, modelled using the track 2 inversion geoacoustic bottom, with the airgun array at the AMAR location and GDEM February SSP.

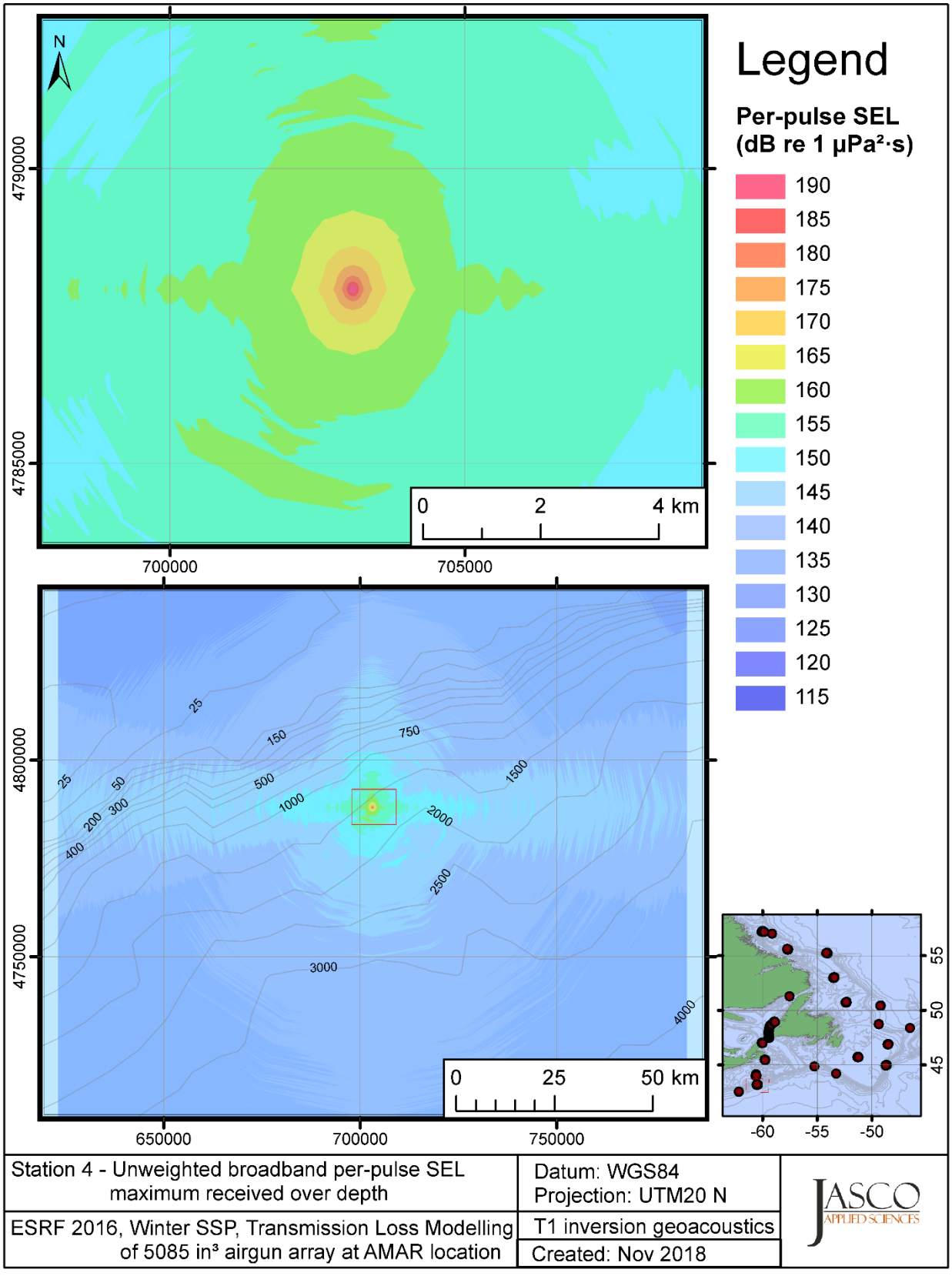

Figure C-436. Stn 4, unweighted maximum-over-depth SEL received at any location on the map, modelled using the track 1 inversion geoacoustic bottom, with the airgun array at the AMAR location and GDEM February SSP.

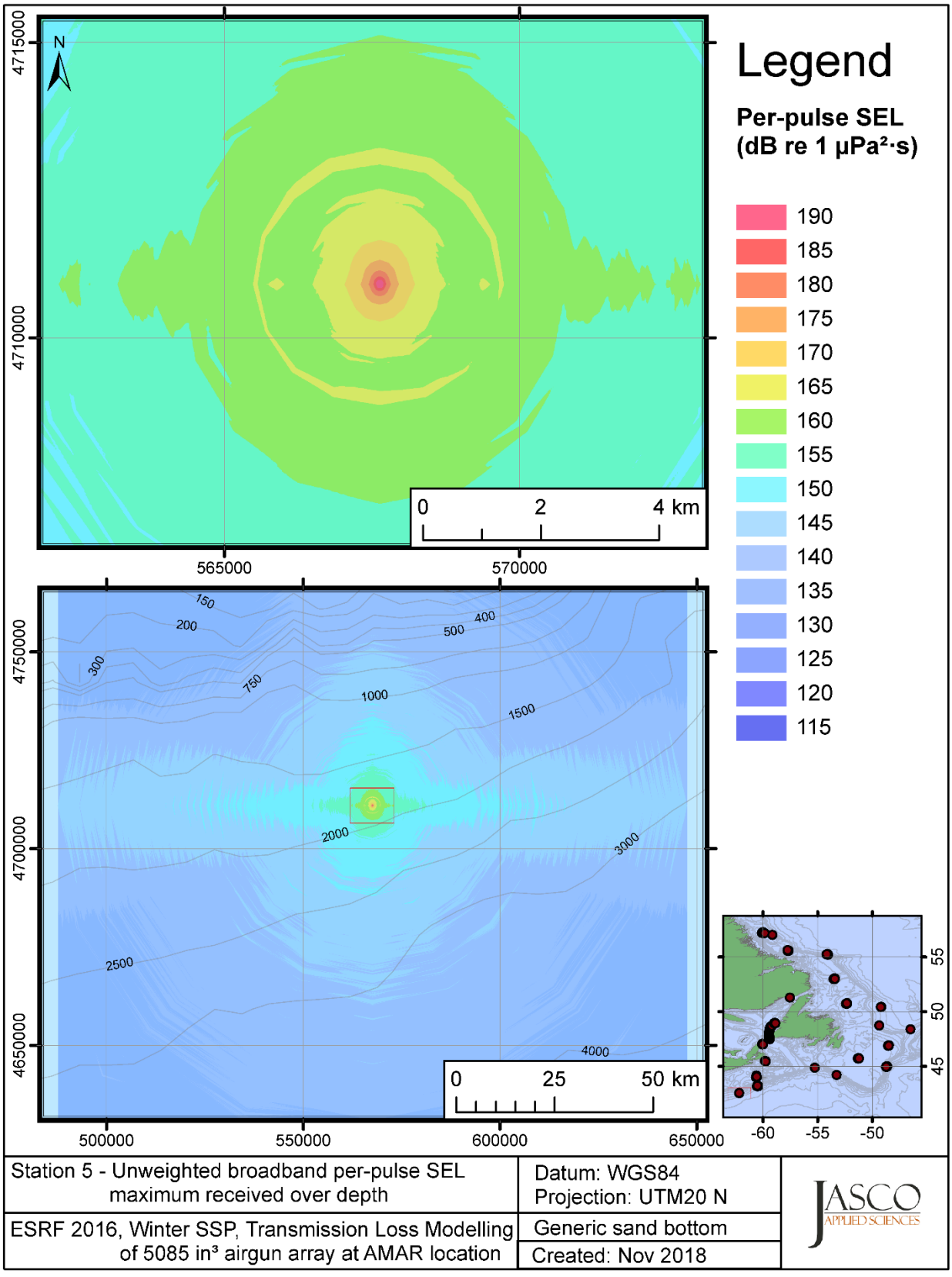

Figure C-437. Stn 5, unweighted maximum-over-depth SEL received at any location on the map, modelled using a generic sand bottom, with the airgun array at the AMAR location and GDEM February SSP.

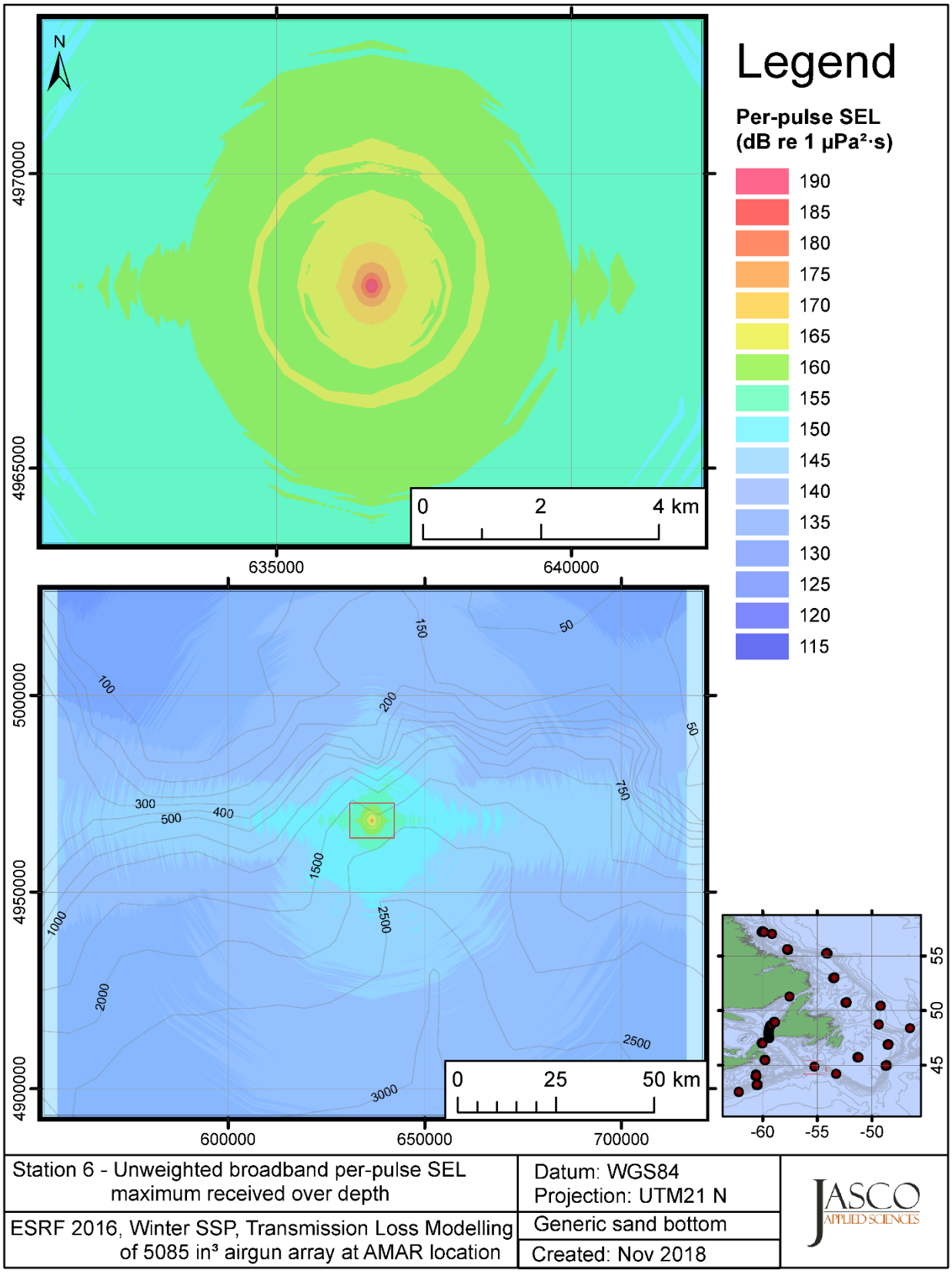

Figure C-438. Stn 6, unweighted maximum-over-depth SEL received at any location on the map, modelled using a generic sand bottom, with the airgun array at the AMAR location and GDEM February SSP.

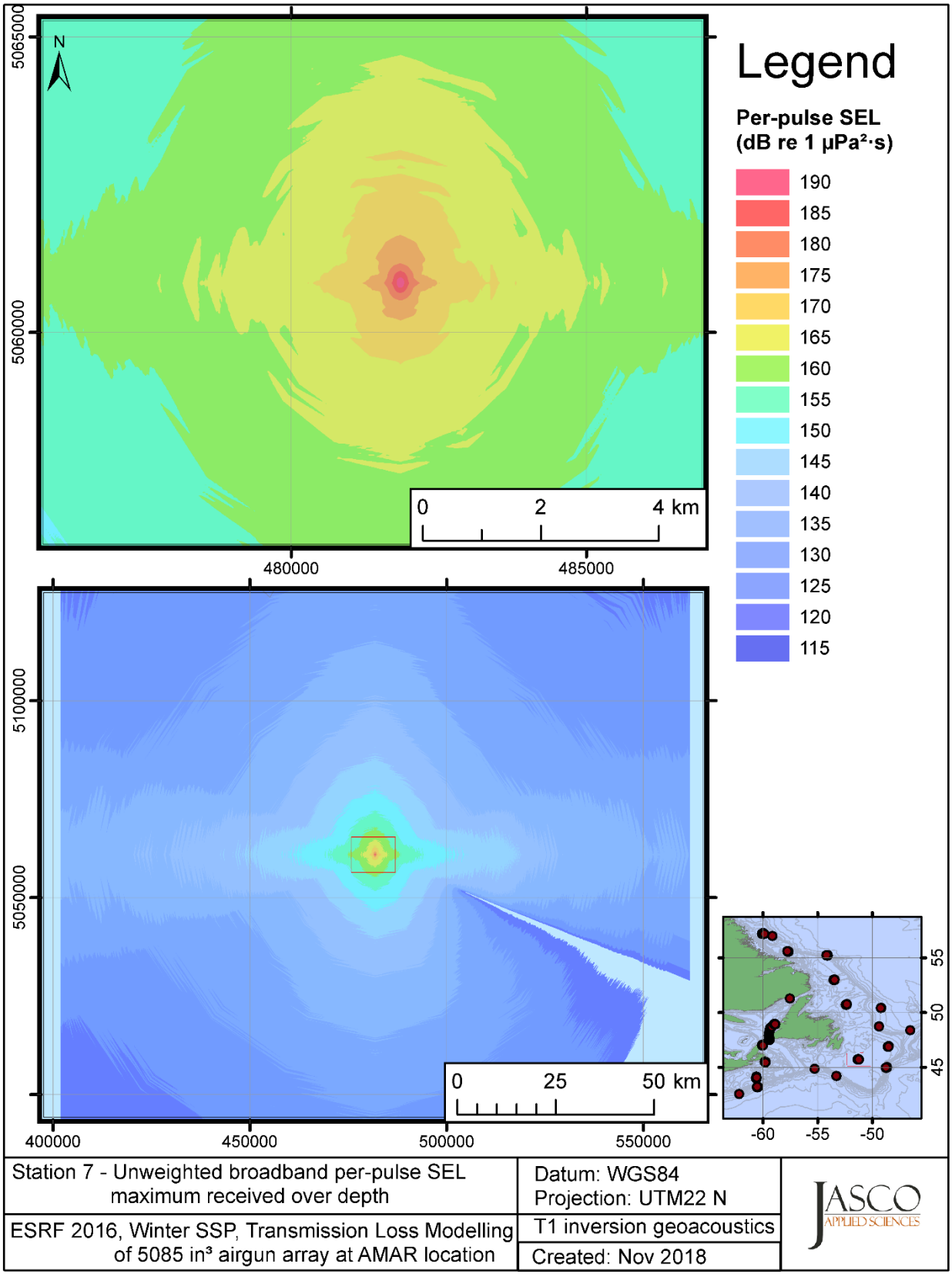

Figure C-439. Stn 7, unweighted maximum-over-depth SEL received at any location on the map, modelled using the track 1 inversion geoacoustic bottom, with the airgun array at the AMAR location and GDEM February SSP.

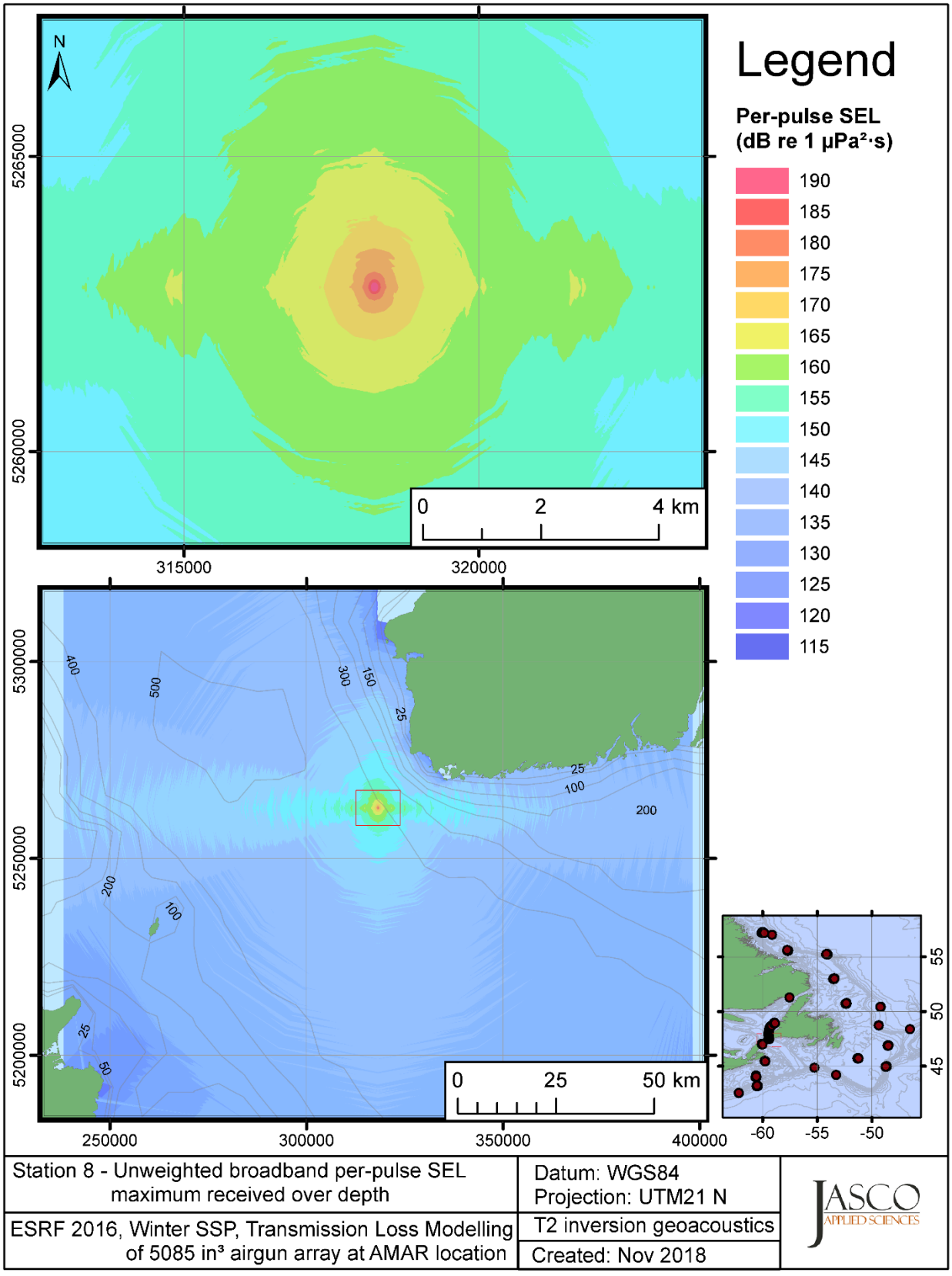

Figure C-440. Stn 8, unweighted maximum-over-depth SEL received at any location on the map, modelled using the track 2 inversion geoacoustic bottom, with the airgun array at the AMAR location and GDEM February SSP.

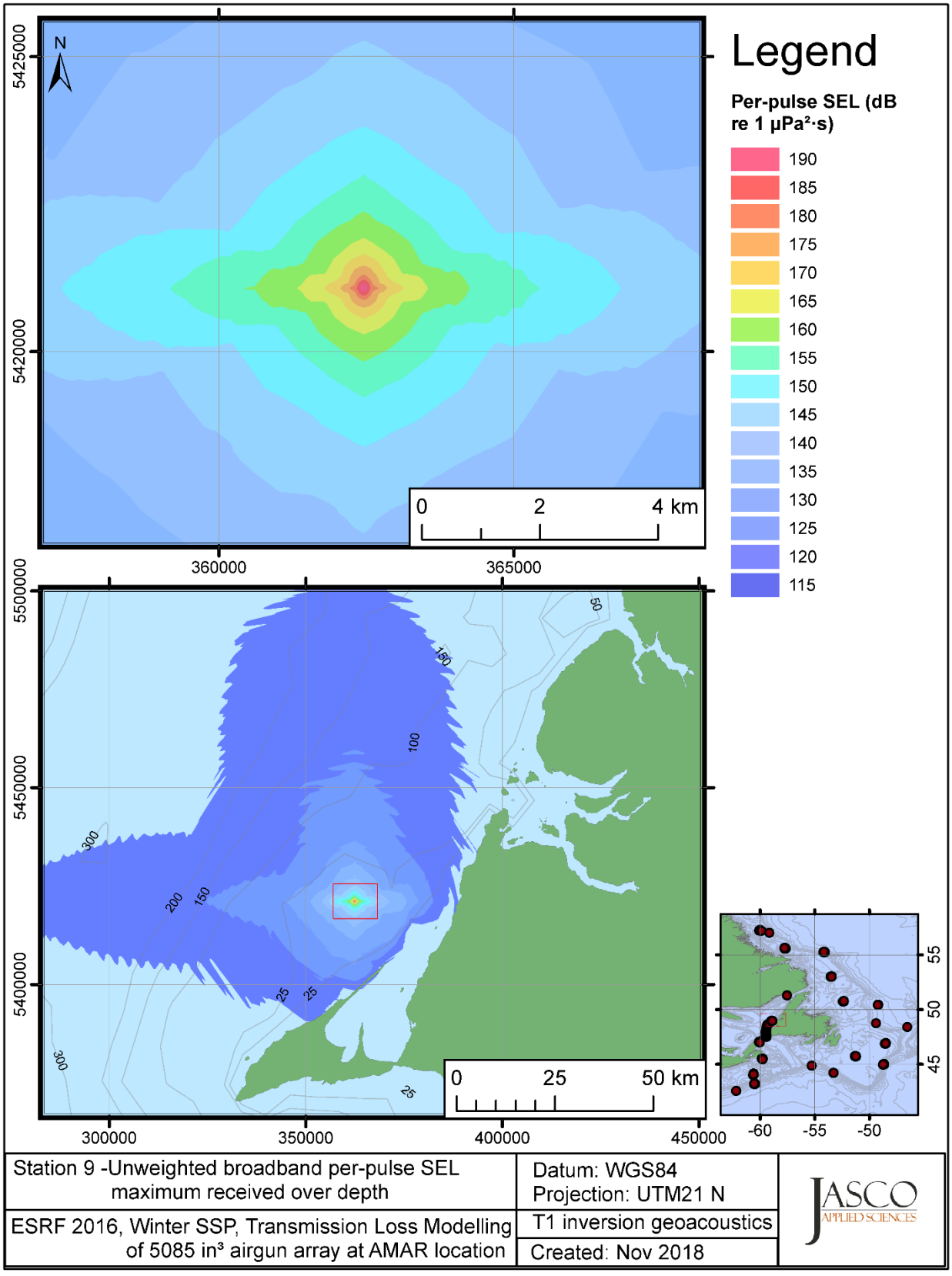

Figure C-441. Stn 9, unweighted maximum-over-depth SEL received at any location on the map, modelled using the track 1 inversion geoacoustic bottom, with the airgun array at the AMAR location and GDEM February SSP.

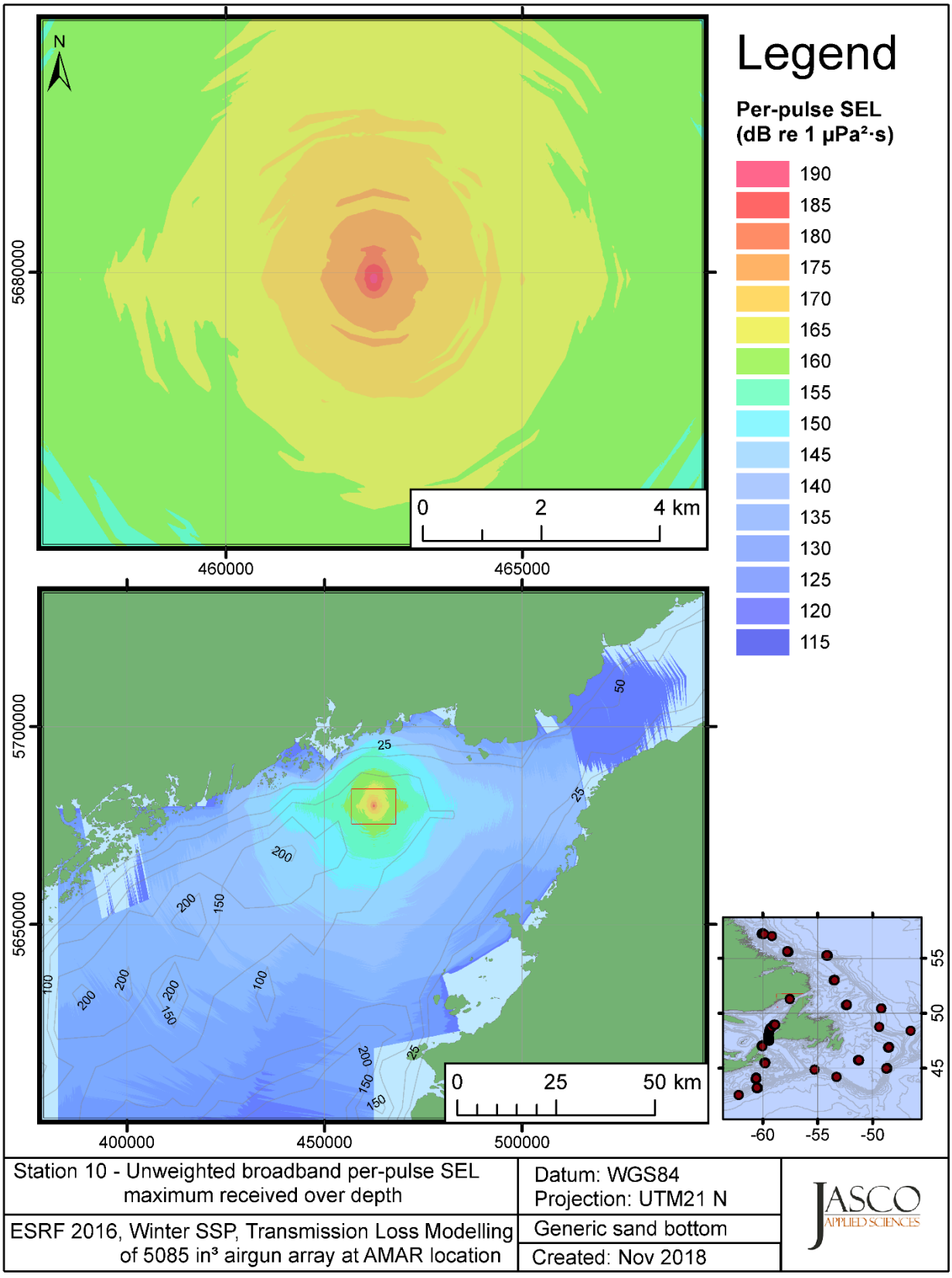

Figure C-442. Stn 10, unweighted maximum-over-depth SEL received at any location on the map, modelled using a generic sand bottom, with the airgun array at the AMAR location and GDEM February SSP.

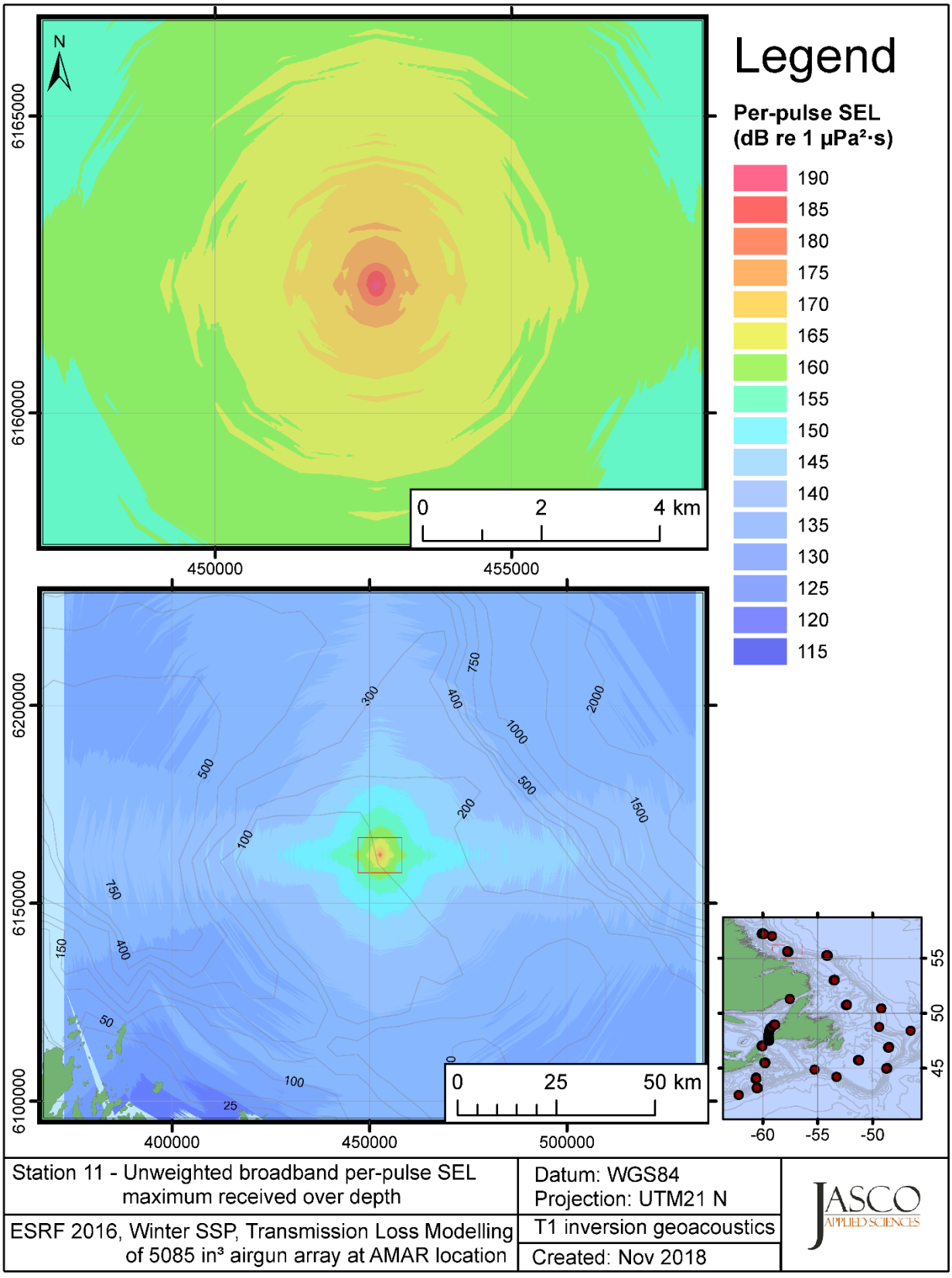

Figure C-443. Stn 11, unweighted maximum-over-depth SEL received at any location on the map, modelled using the track 1 inversion geoacoustic bottom, with the airgun array at the AMAR location and GDEM February SSP.

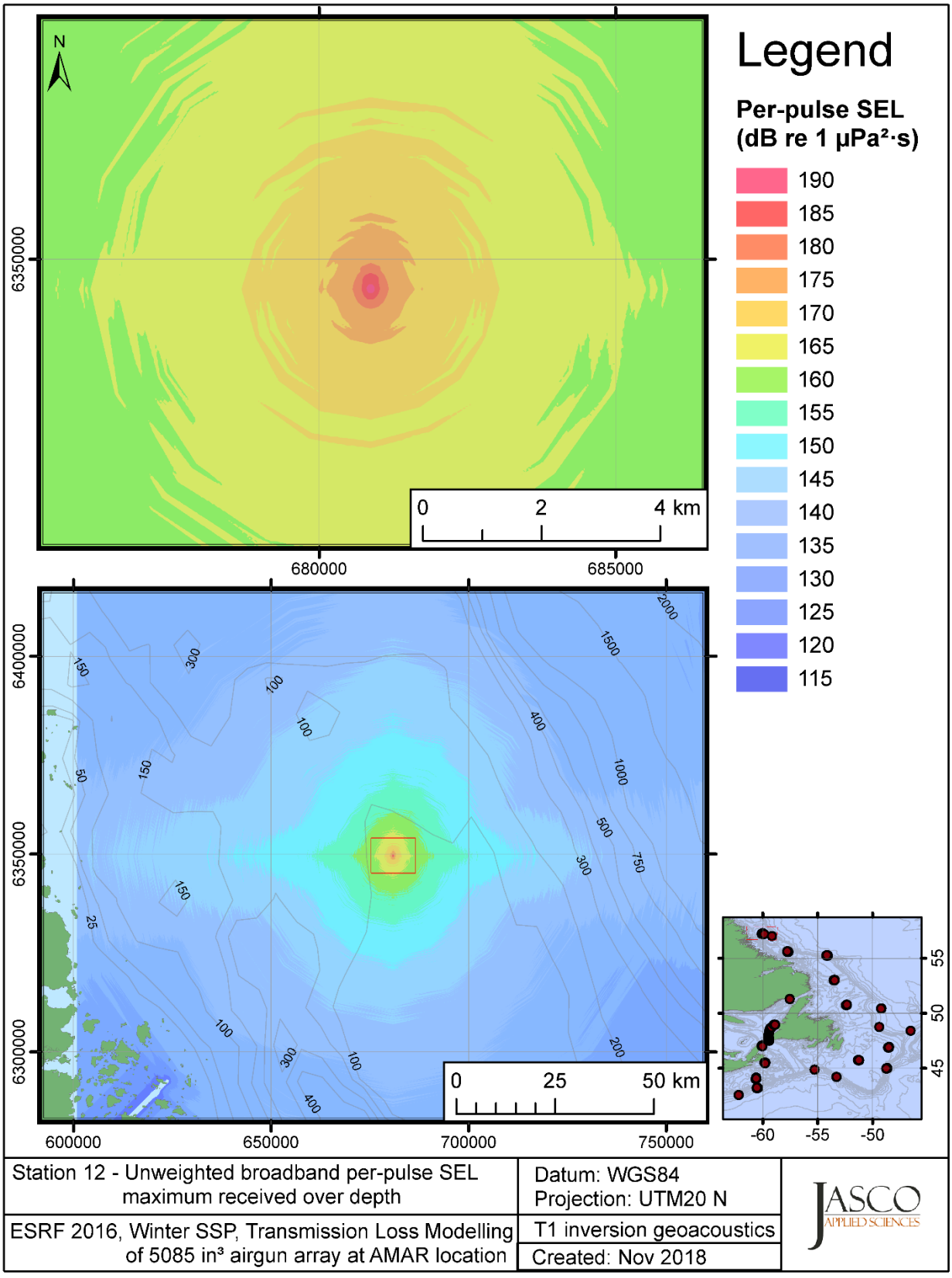

Figure C-444. Stn 12, unweighted maximum-over-depth SEL received at any location on the map, modelled using the track 1 inversion geoacoustic bottom, with the airgun array at the AMAR location and GDEM February SSP.

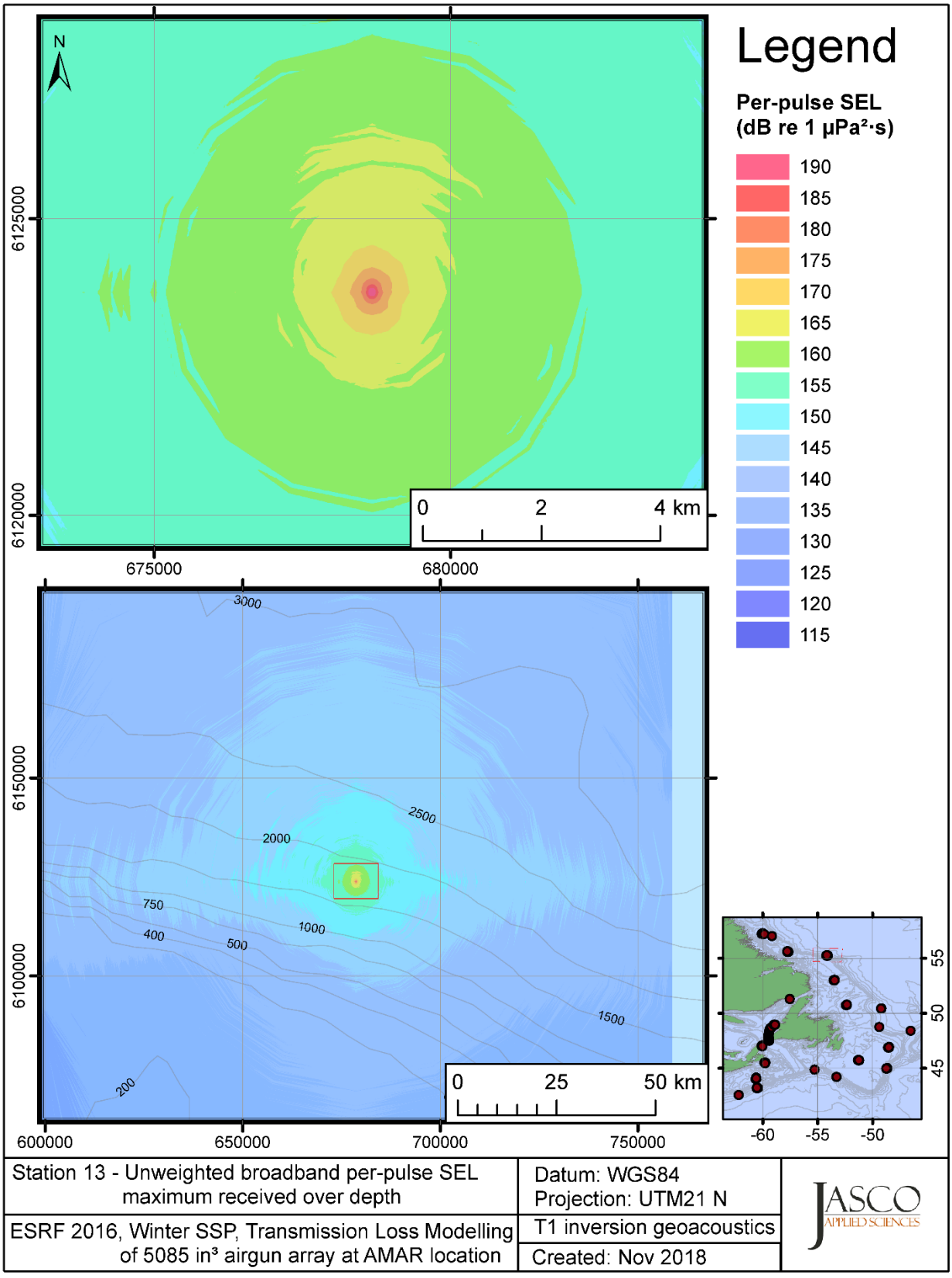

Figure C-445. Stn 13, unweighted maximum-over-depth SEL received at any location on the map, modelled using the track 1 inversion geoacoustic bottom, with the airgun array at the AMAR location and GDEM February SSP.

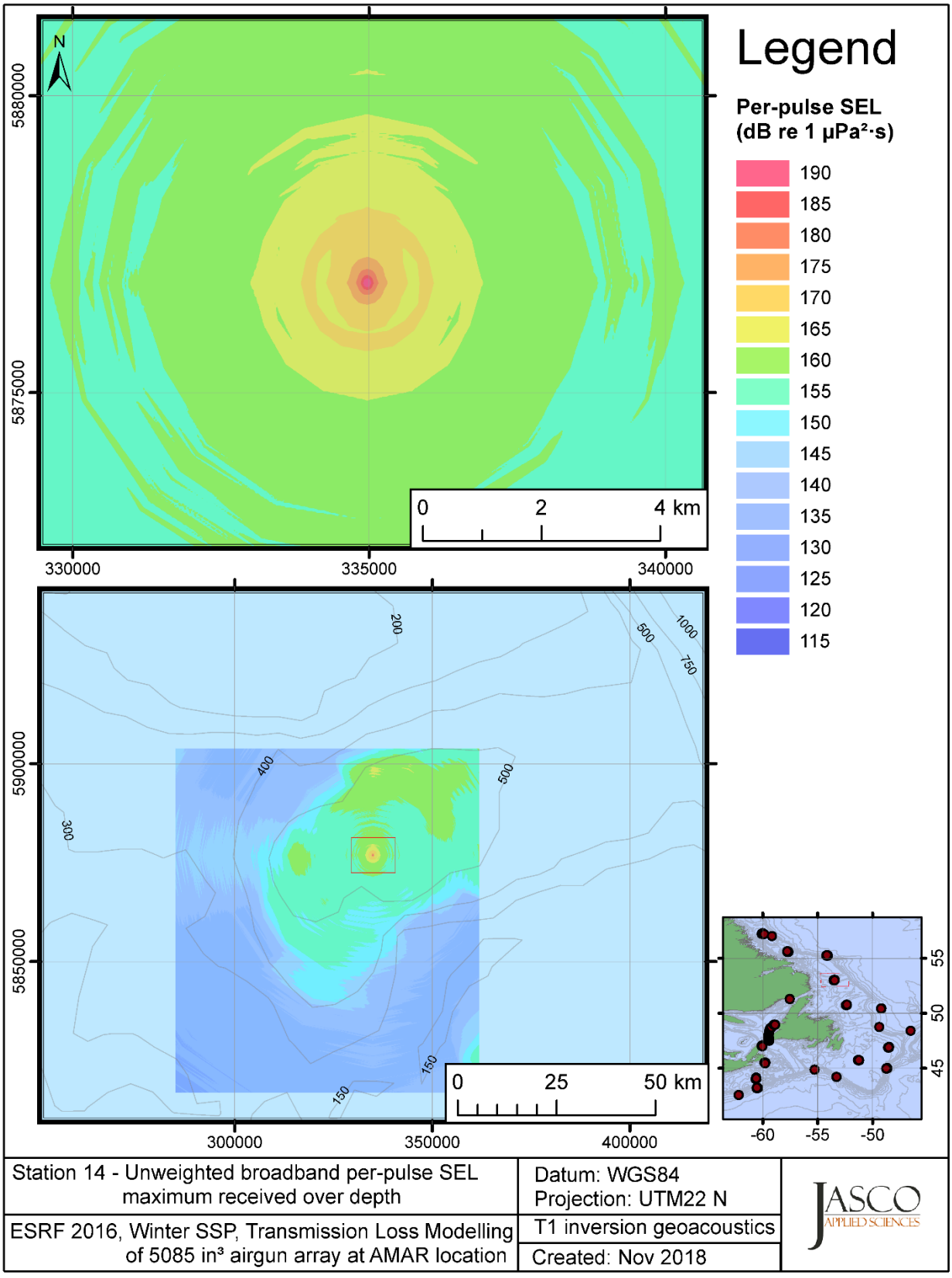

Figure C-446. Stn 14, unweighted maximum-over-depth SEL received at any location on the map, modelled using the track 1 inversion geoacoustic bottom, with the airgun array at the AMAR location and GDEM February SSP.

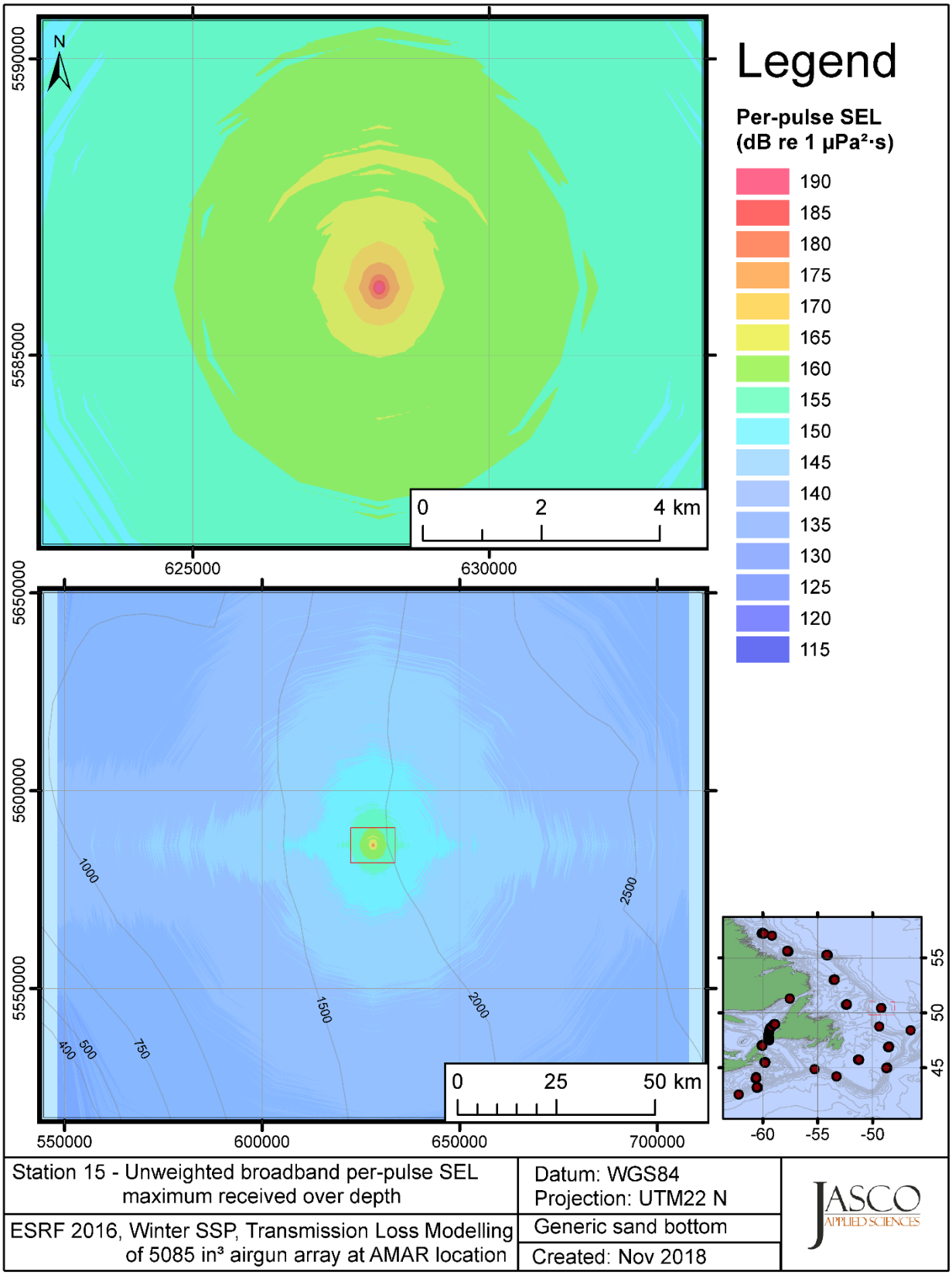

Figure C-447. Stn 15, unweighted maximum-over-depth SEL received at any location on the map, modelled using a generic sand bottom, with the airgun array at the AMAR location and GDEM February SSP.

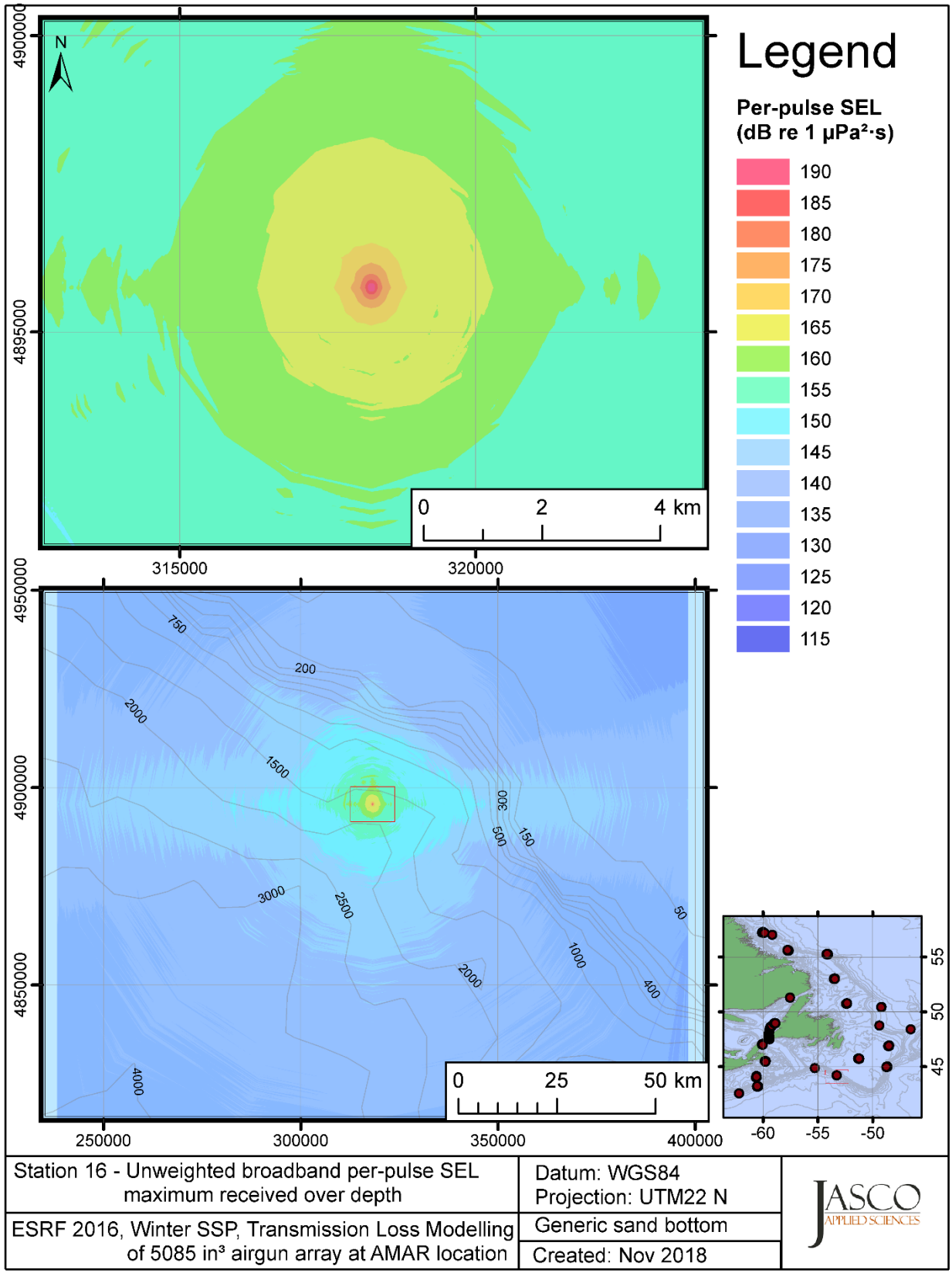

Figure C-448. Stn 16, unweighted maximum-over-depth SEL received at any location on the map, modelled using a generic sand bottom, with the airgun array at the AMAR location and GDEM February SSP.

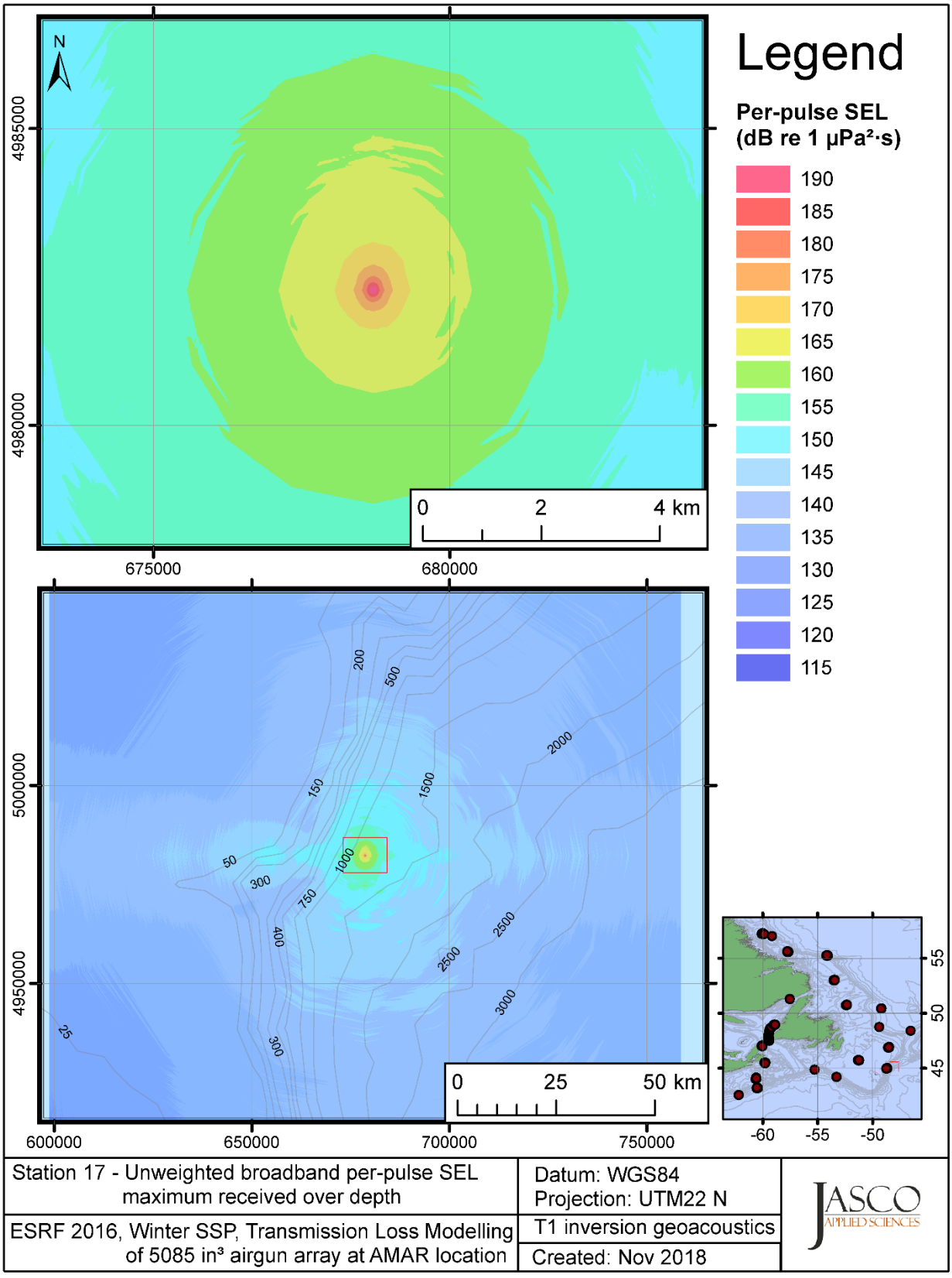

Figure C-449. Stn 17, unweighted maximum-over-depth SEL received at any location on the map, modelled using the track 1 inversion geoacoustic bottom, with the airgun array at the AMAR location and GDEM February SSP.

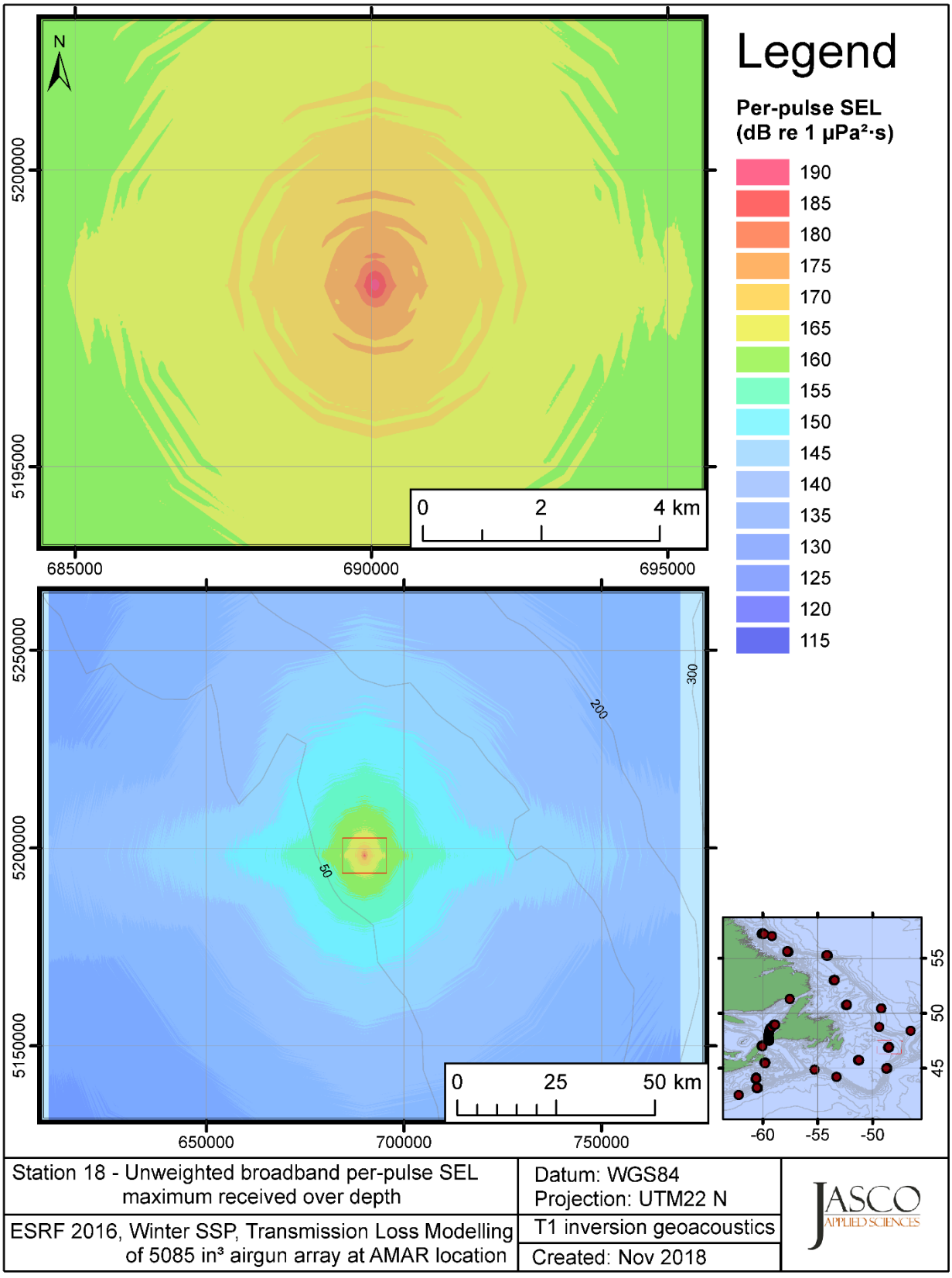

Figure C-450. Stn 18, unweighted maximum-over-depth SEL received at any location on the map, modelled using the track 1 inversion geoacoustic bottom, with the airgun array at the AMAR location and GDEM February SSP.

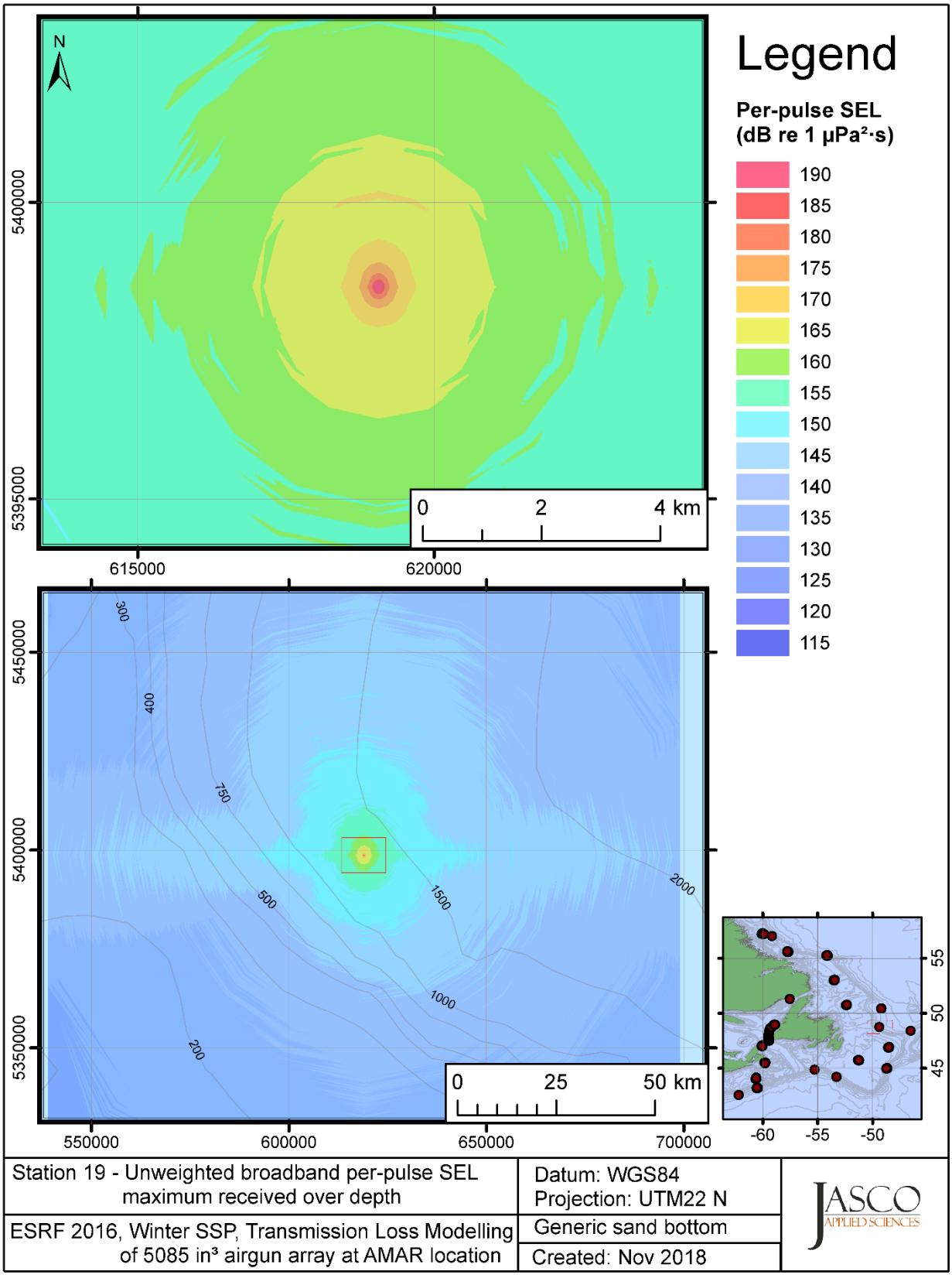

Figure C-451. Stn 19, unweighted maximum-over-depth SEL received at any location on the map, modelled using a generic sand bottom, with the airgun array at the AMAR location and GDEM February SSP.

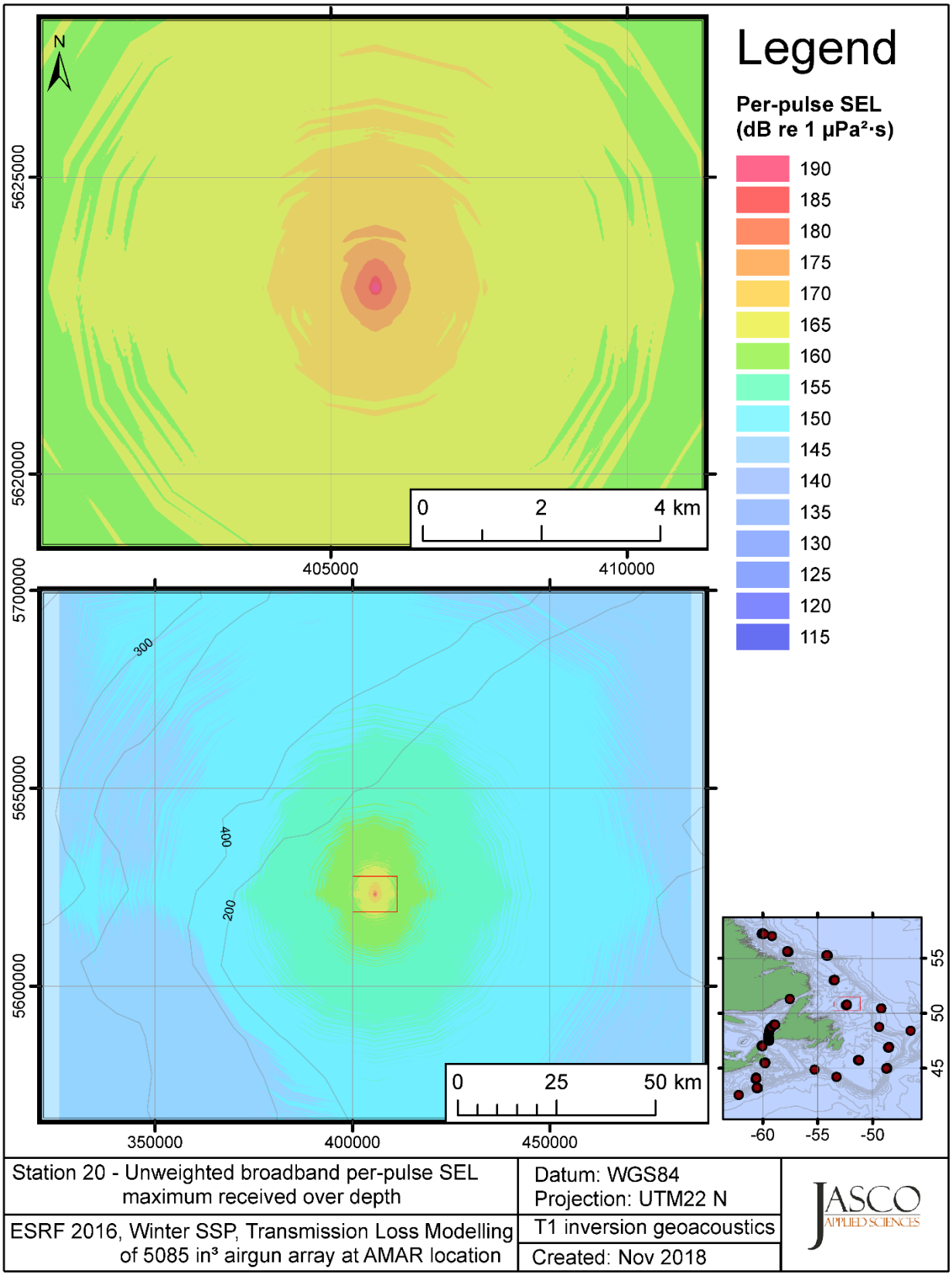

Figure C-452. Stn 20, unweighted maximum-over-depth SEL received at any location on the map, modelled using the track 1 inversion geoacoustic bottom, with the airgun array at the AMAR location and GDEM February SSP.

C.14. Modelling LF M-weighted Max-over-depth Received Level at Distant Locations - Winter

This section presents the results of modelling the maximum-over-depth per-pulse sound exposure level (SEL) received at distant receiver locations (varied in range and azimuth) for the source held fixed at the AMAR location. The modelling uses the geoacoustic inversion bottom parameters at the 14 sites where they are available and only uses a generic sand bottom at the other six sites. The modelling results are presented in the form of coloured maps where the colour at any map location represents the predicted maximum-over-depth received level at that spot on the map. This section includes only the low-frequency cetaceans (LF) marine-mammal-weighted per-pulse SEL results; additional maps for other marine mammal received level auditory weightings are presented in adjoining sections. The sound speed profiles (SSP) used are detailed in Appendix B.2.

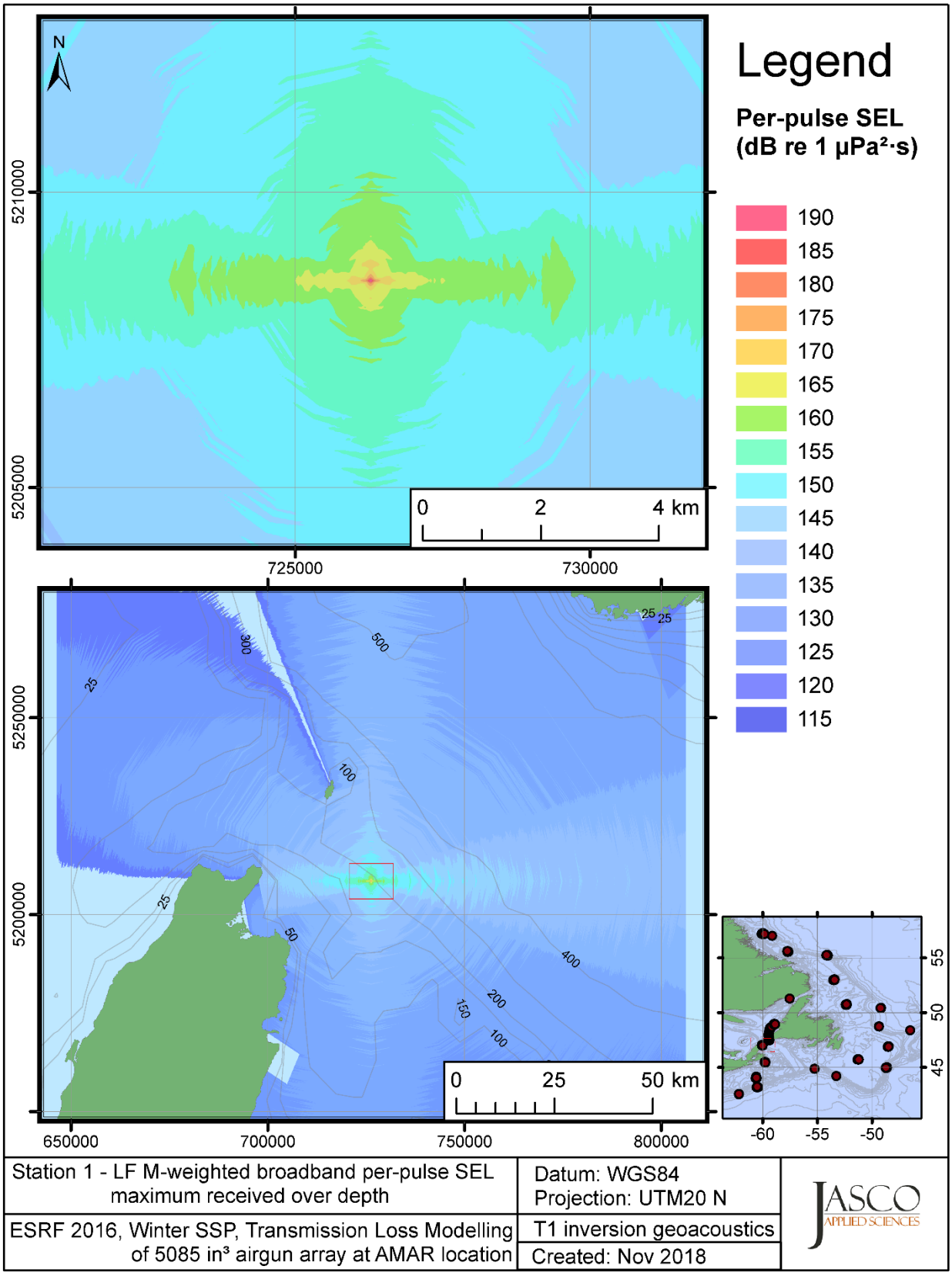

Figure C-453. Stn 1, LF M-weighted maximum-over-depth SEL received at any location on the map, modelled using the track 1 inversion geoacoustic bottom, with the airgun array at the AMAR location and GDEM February SSP.

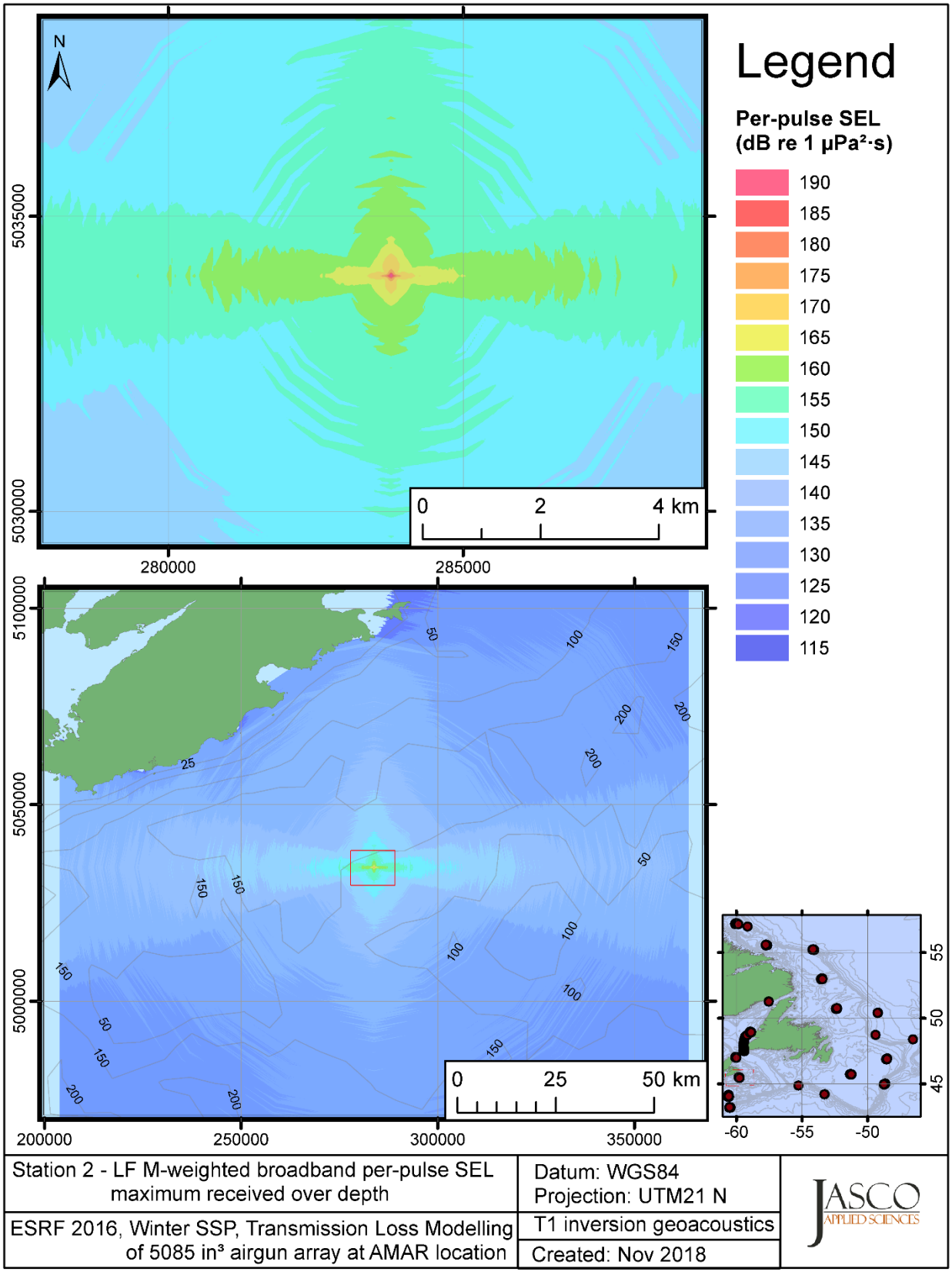

Figure C-454. Stn 2, LF M-weighted maximum-over-depth SEL received at any location on the map, modelled using the track 1 inversion geoacoustic bottom, with the airgun array at the AMAR location and GDEM February SSP.

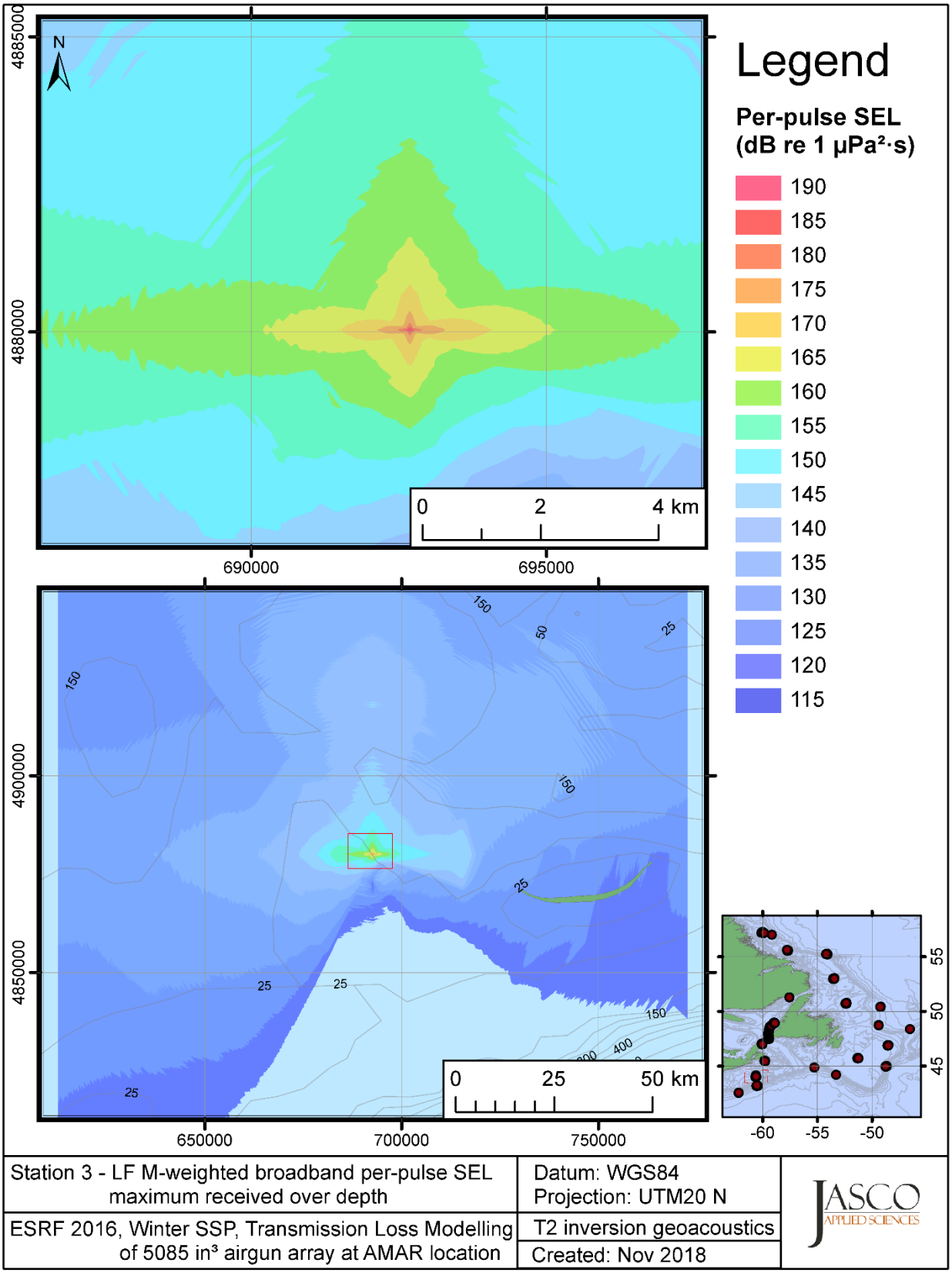

Figure C-455. Stn 3, LF M-weighted maximum-over-depth SEL received at any location on the map, modelled using the track 2 inversion geoacoustic bottom, with the airgun array at the AMAR location and GDEM February SSP.

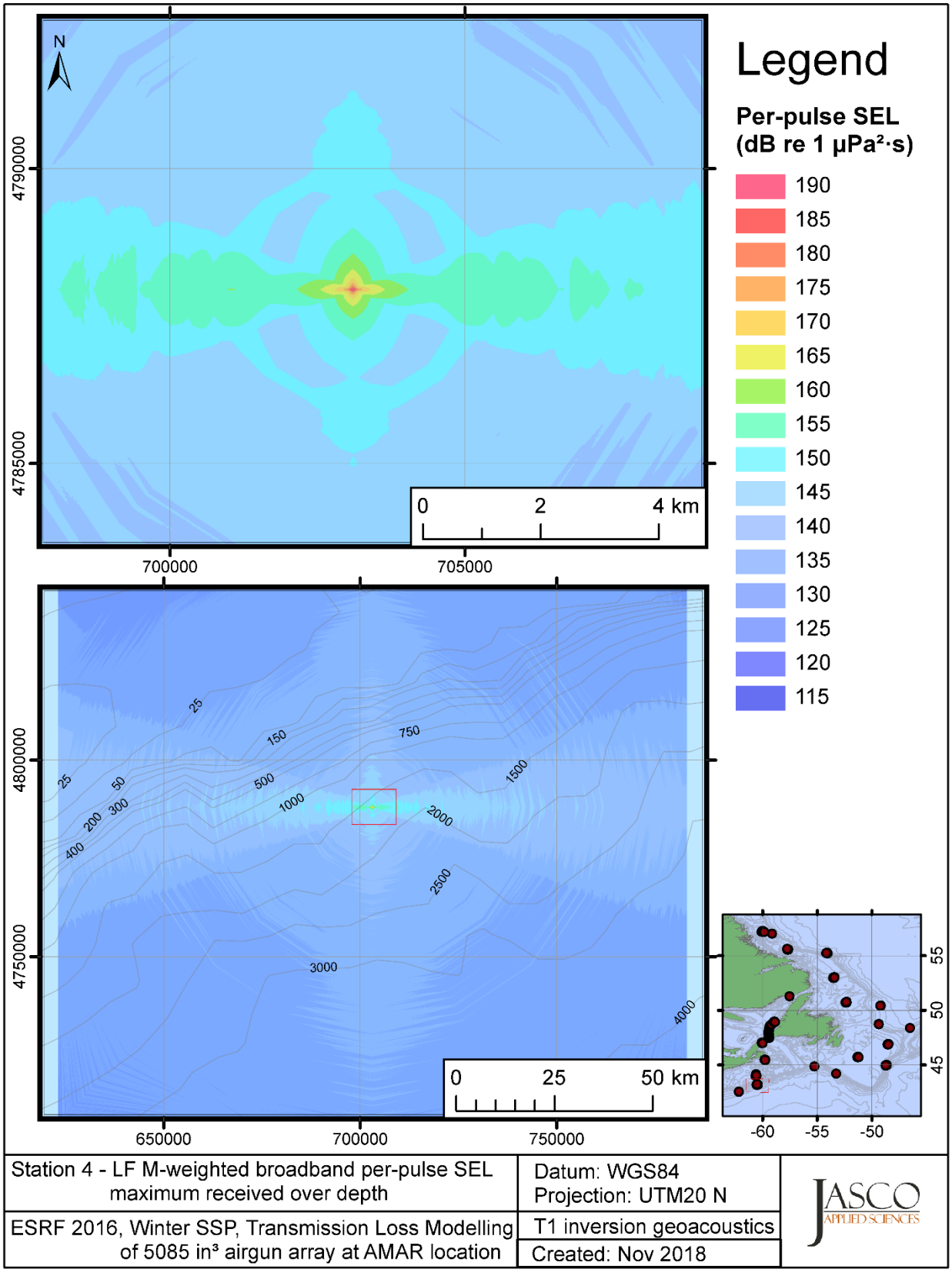

Figure C-456. Stn 4, LF M-weighted maximum-over-depth SEL received at any location on the map, modelled using the track 1 inversion geoacoustic bottom, with the airgun array at the AMAR location and GDEM February SSP.

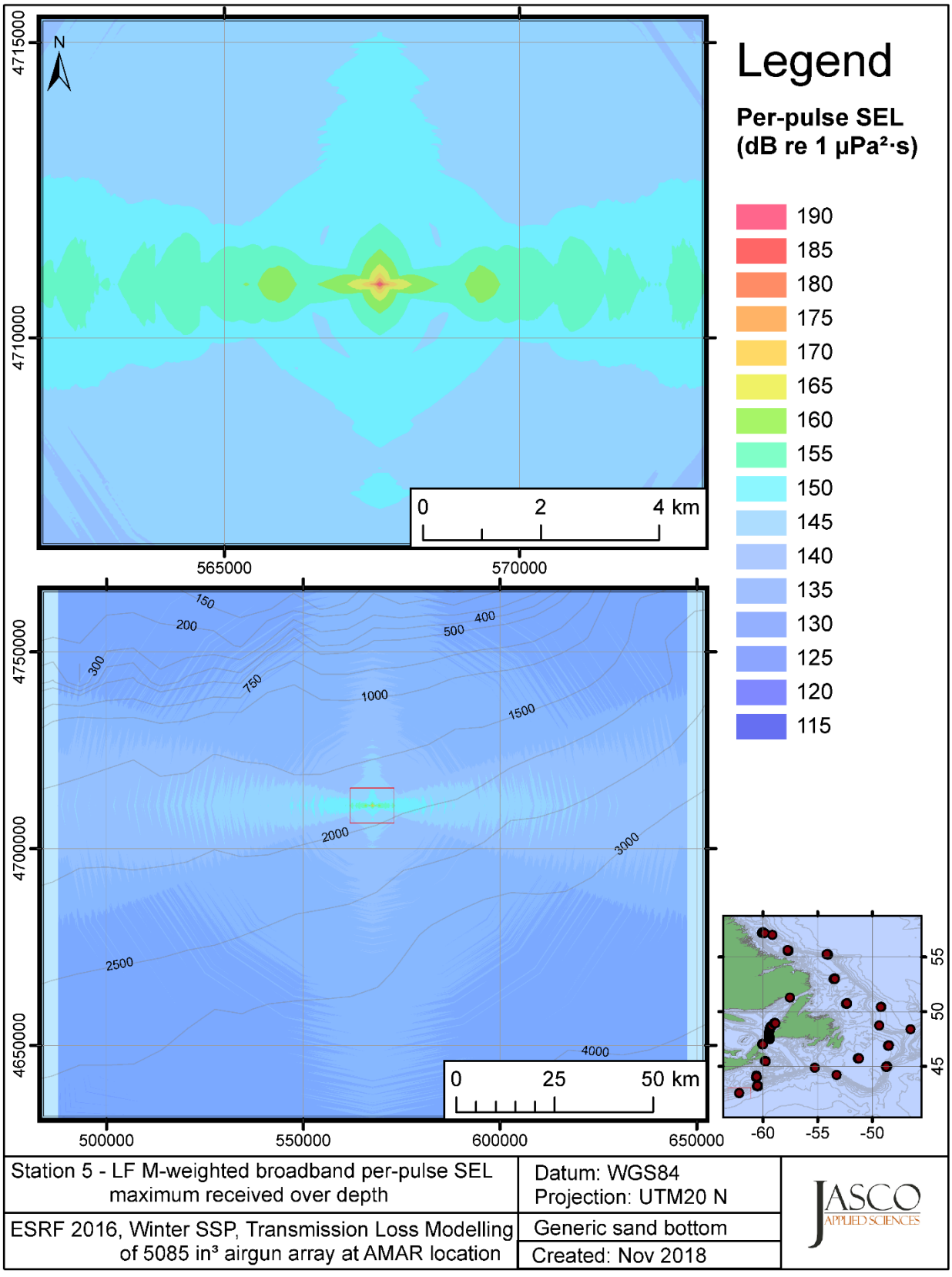

Figure C-457. Stn 5, LF M-weighted maximum-over-depth SEL received at any location on the map, modelled using a generic sand bottom, with the airgun array at the AMAR location and GDEM February SSP.

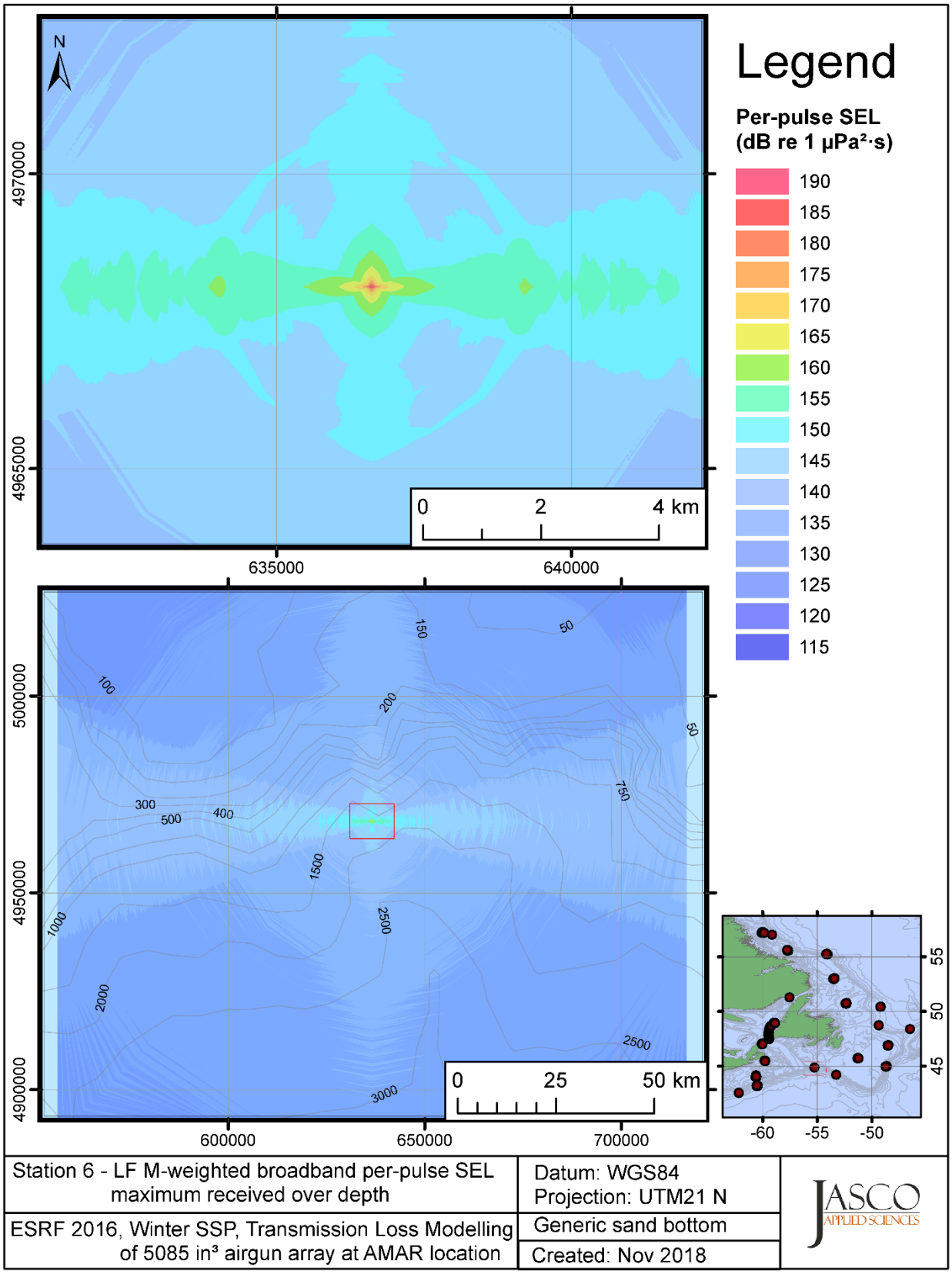

Figure C-458. Stn 6, LF M-weighted maximum-over-depth SEL received at any location on the map, modelled using a generic sand bottom, with the airgun array at the AMAR location and GDEM February SSP.

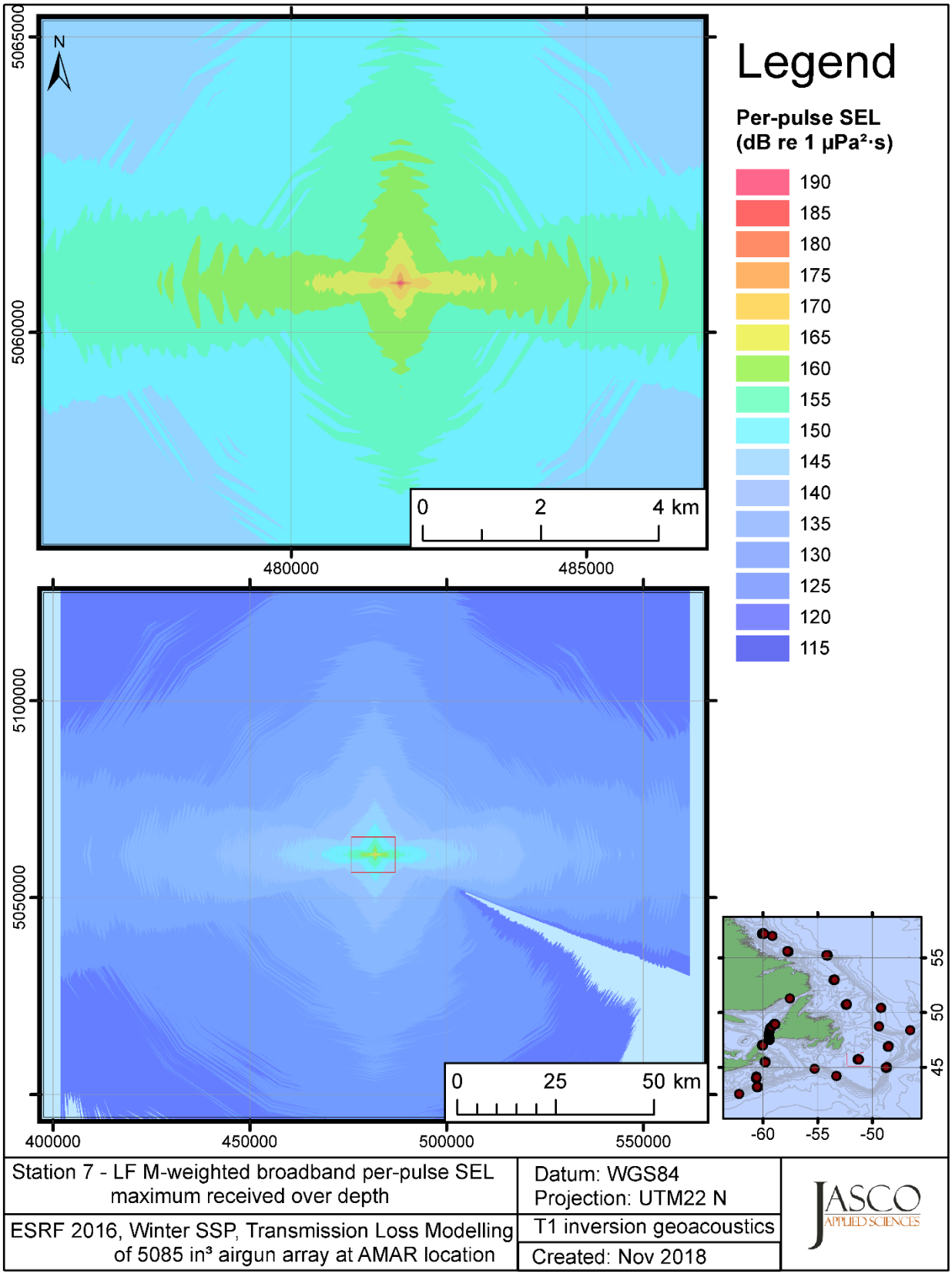

Figure C-459. Stn 7, LF M-weighted maximum-over-depth SEL received at any location on the map, modelled using the track 1 inversion geoacoustic bottom, with the airgun array at the AMAR location and GDEM February SSP.

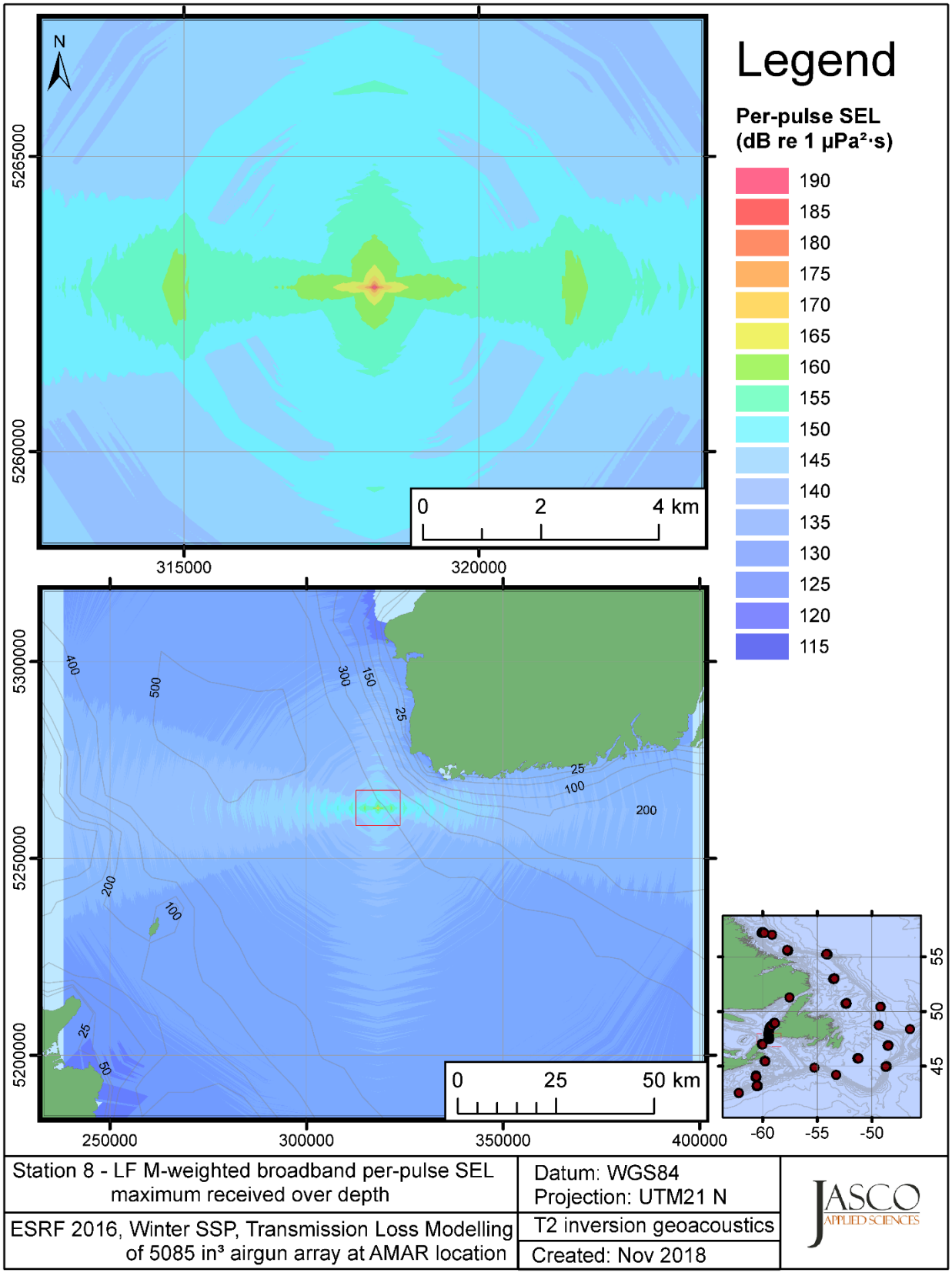

Figure C-460. Stn 8, LF M-weighted maximum-over-depth SEL received at any location on the map, modelled using the track 2 inversion geoacoustic bottom, with the airgun array at the AMAR location and GDEM February SSP.

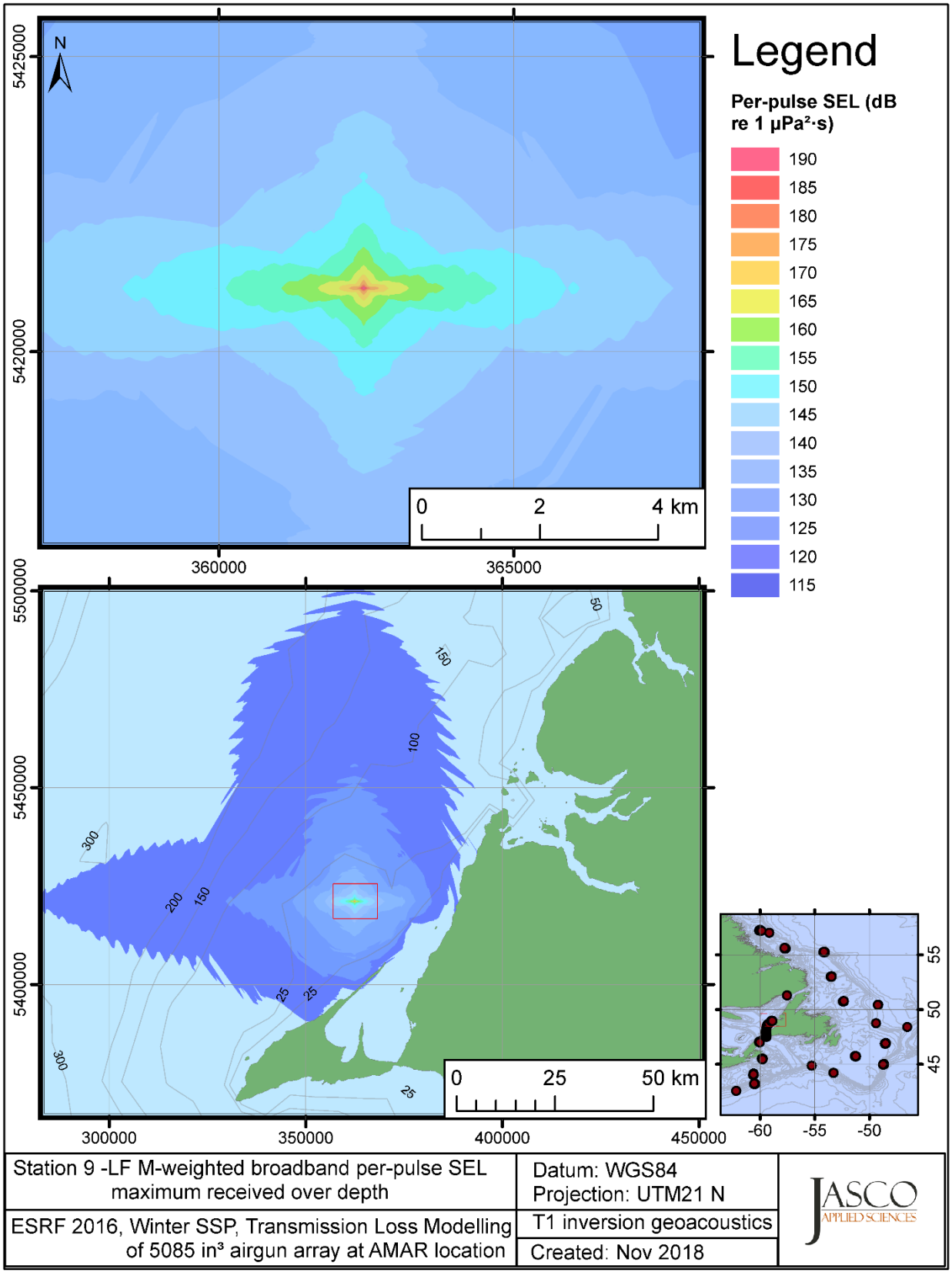

Figure C-461. Stn 9, LF M-weighted maximum-over-depth SEL received at any location on the map, modelled using the track 1 inversion geoacoustic bottom, with the airgun array at the AMAR location and GDEM February SSP.

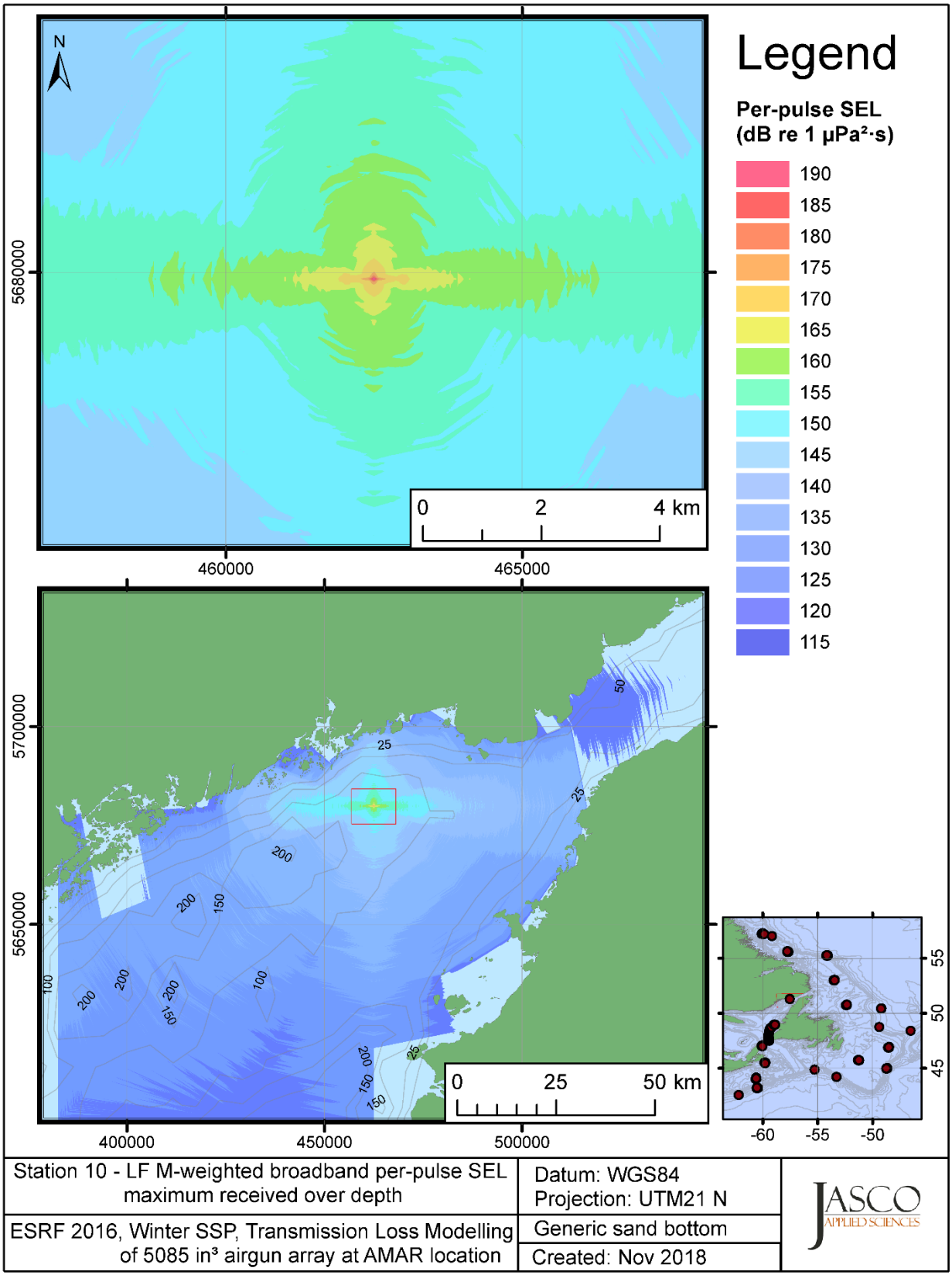

Figure C-462. Stn 10, LF M-weighted maximum-over-depth SEL received at any location on the map, modelled using a generic sand bottom, with the airgun array at the AMAR location and GDEM February SSP.

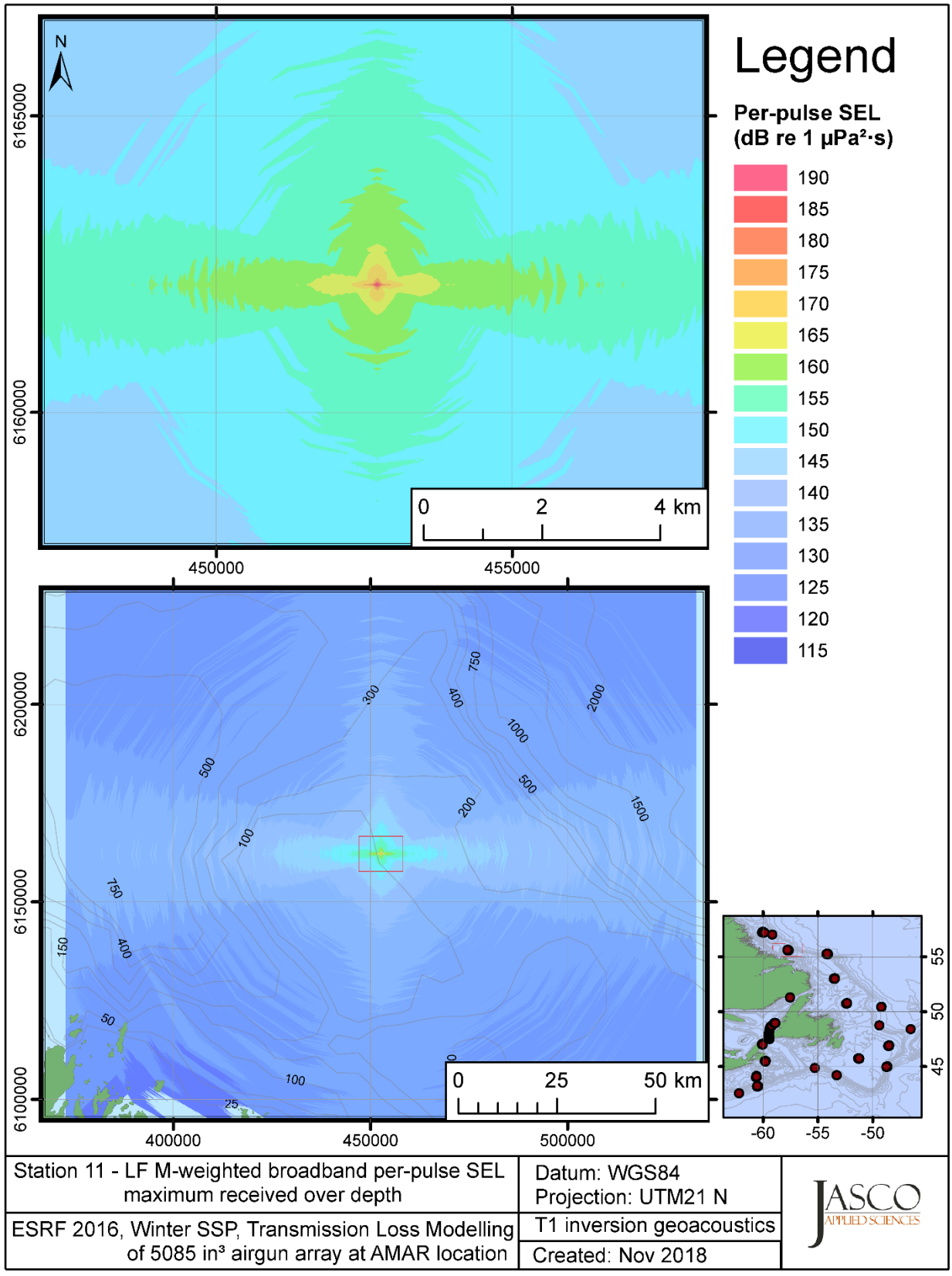

Figure C-463. Stn 11, LF M-weighted maximum-over-depth SEL received at any location on the map, modelled using the track 1 inversion geoacoustic bottom, with the airgun array at the AMAR location and GDEM February SSP.

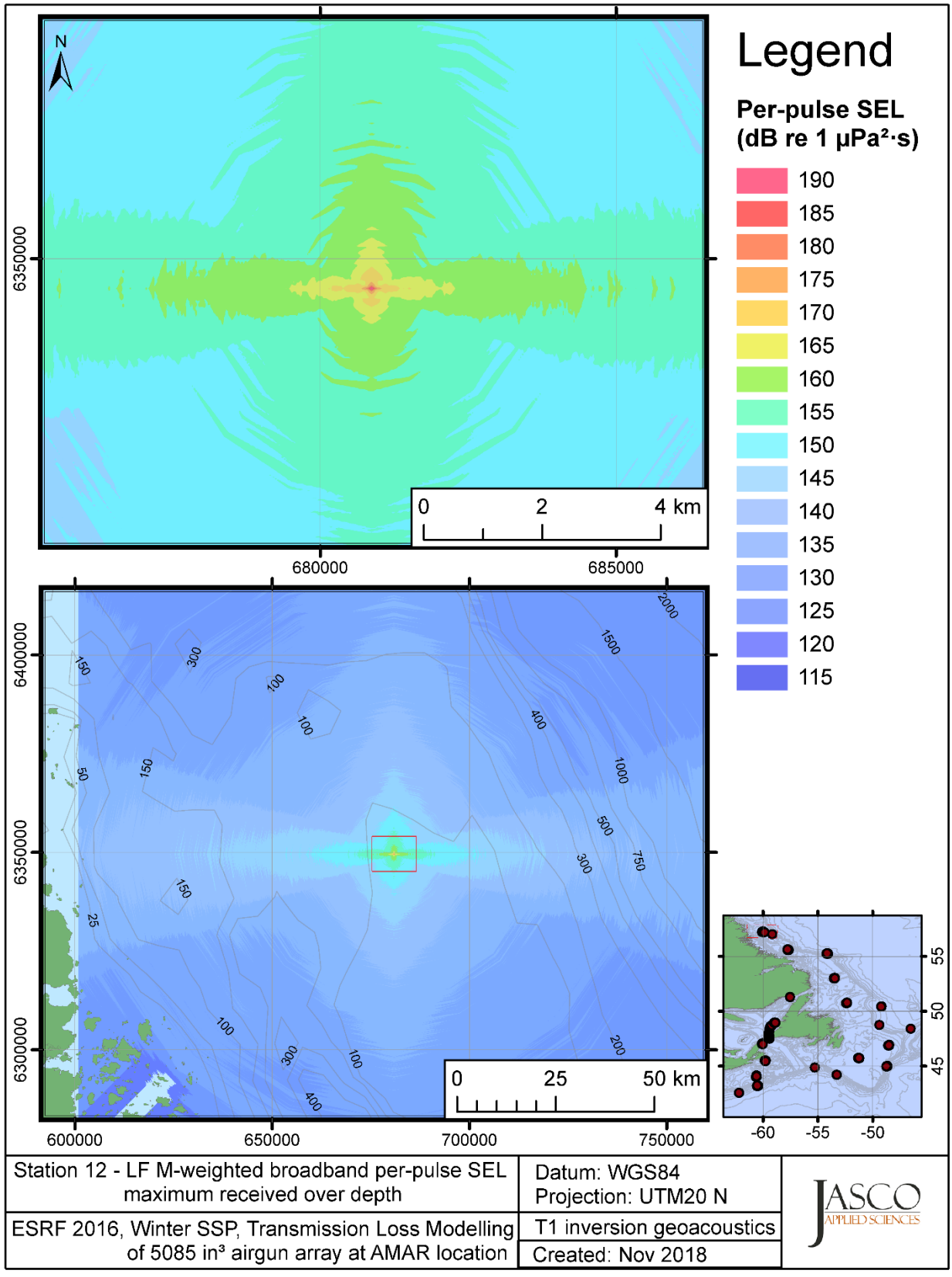

Figure C-464. Stn 12, LF M-weighted maximum-over-depth SEL received at any location on the map, modelled using the track 1 inversion geoacoustic bottom, with the airgun array at the AMAR location and GDEM February SSP.

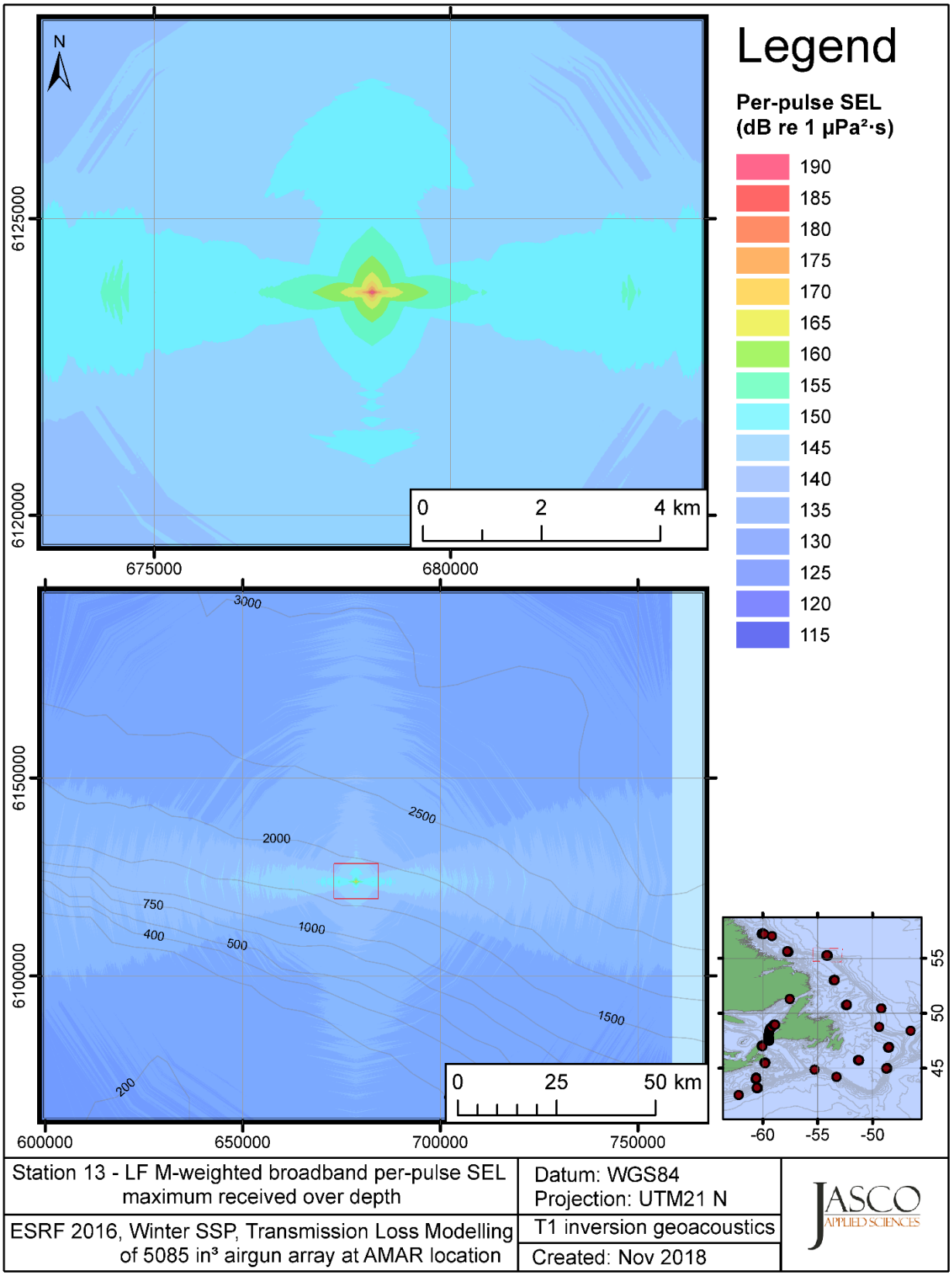

Figure C-465. Stn 13, LF M-weighted maximum-over-depth SEL received at any location on the map, modelled using the track 1 inversion geoacoustic bottom, with the airgun array at the AMAR location and GDEM February SSP.

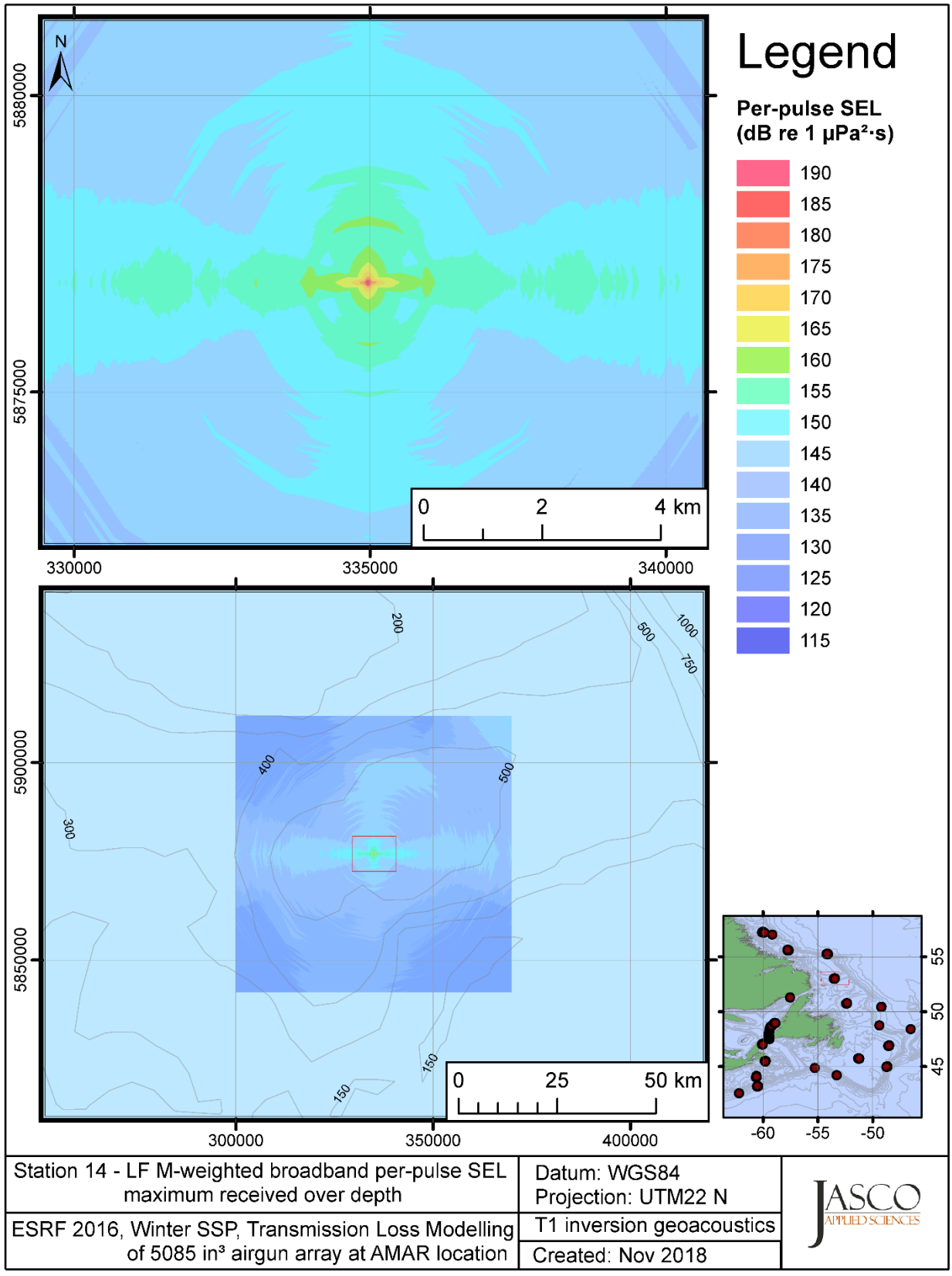

Figure C-466. Stn 14, LF M-weighted maximum-over-depth SEL received at any location on the map, modelled using the track 1 inversion geoacoustic bottom, with the airgun array at the AMAR location and GDEM February SSP.

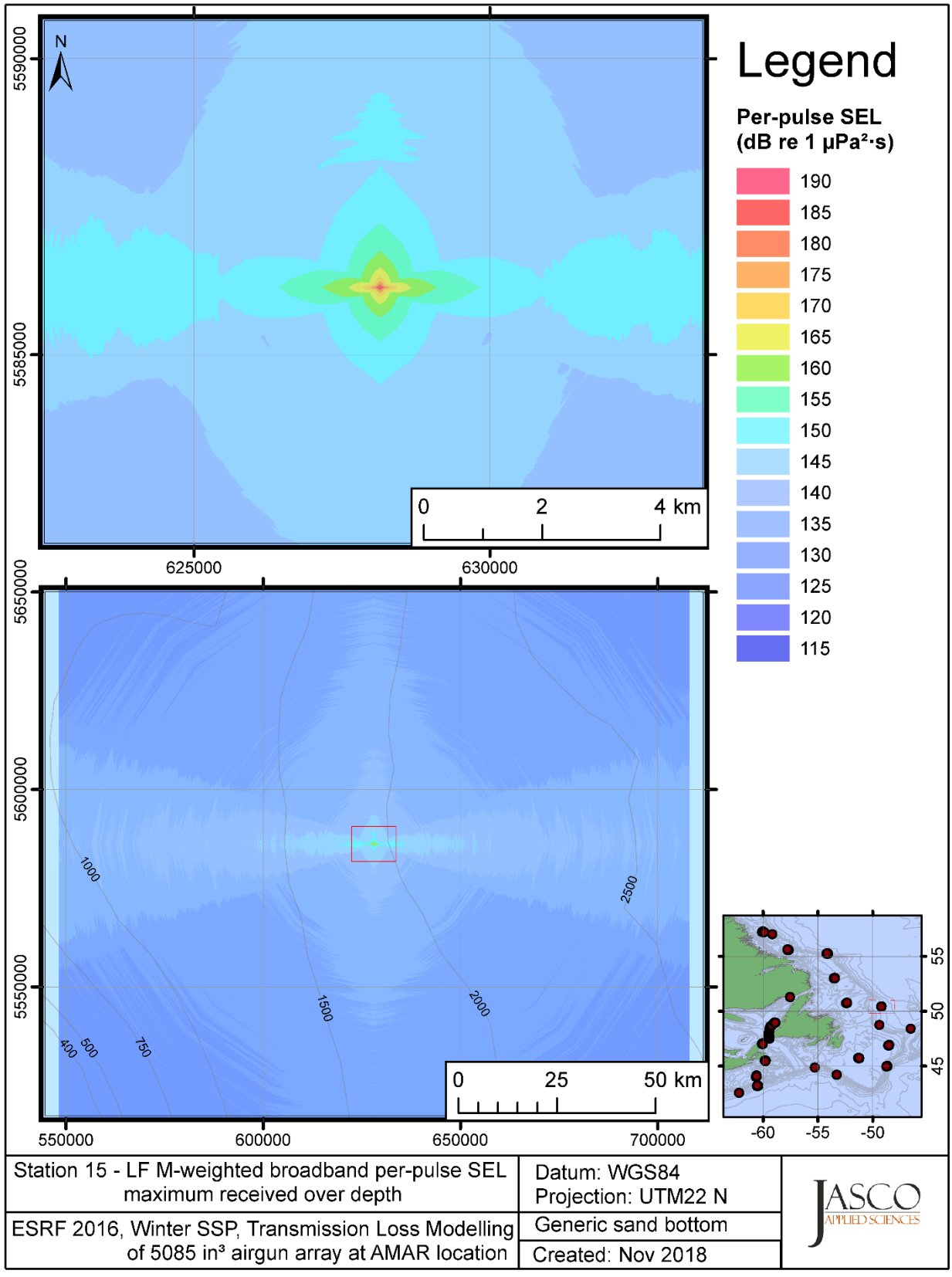

Figure C-467. Stn 15, LF M-weighted maximum-over-depth SEL received at any location on the map, modelled using a generic sand bottom, with the airgun array at the AMAR location and GDEM February SSP.

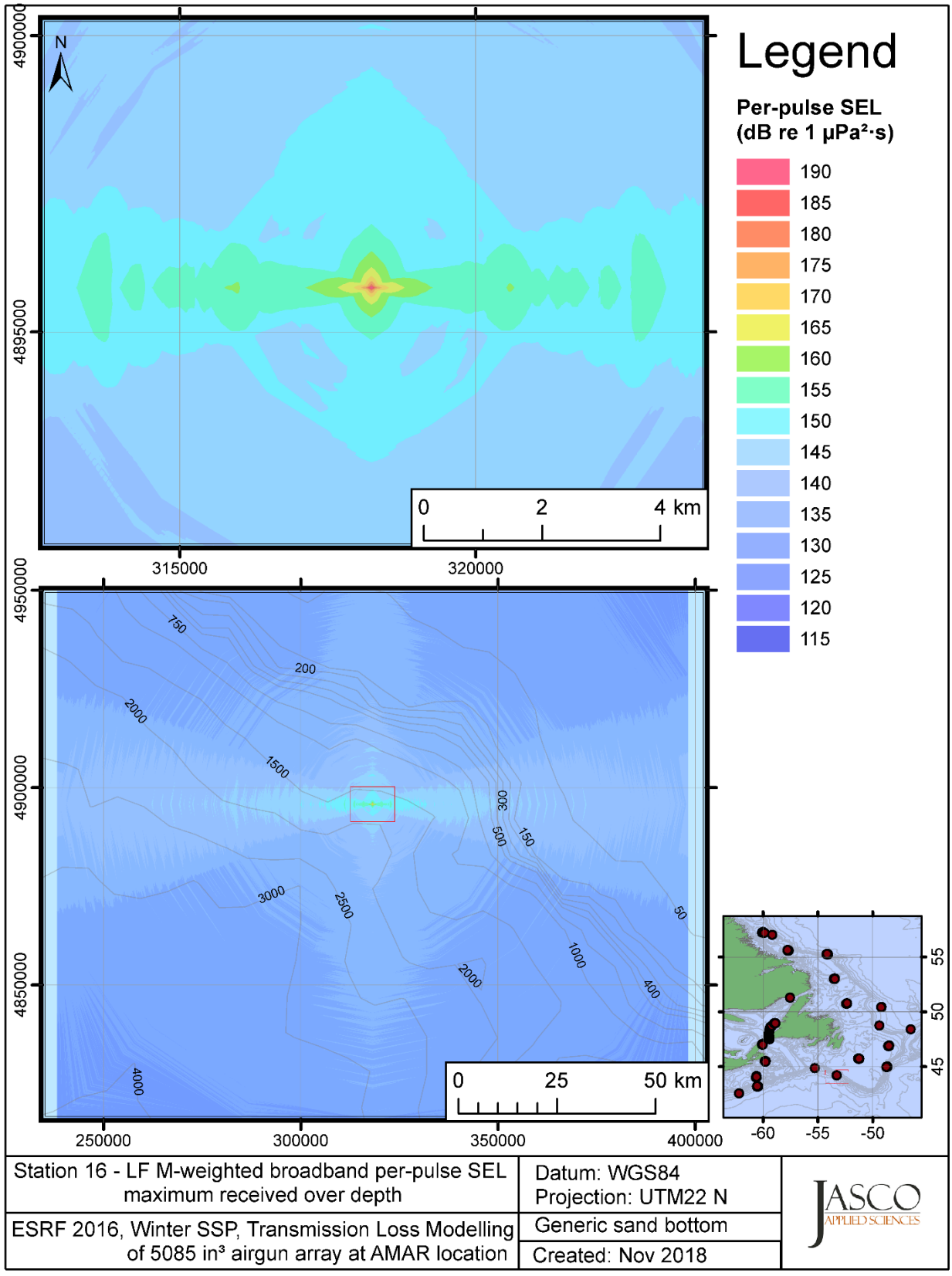

Figure C-468. Stn 16, LF M-weighted maximum-over-depth SEL received at any location on the map, modelled using a generic sand bottom, with the airgun array at the AMAR location and GDEM February SSP.

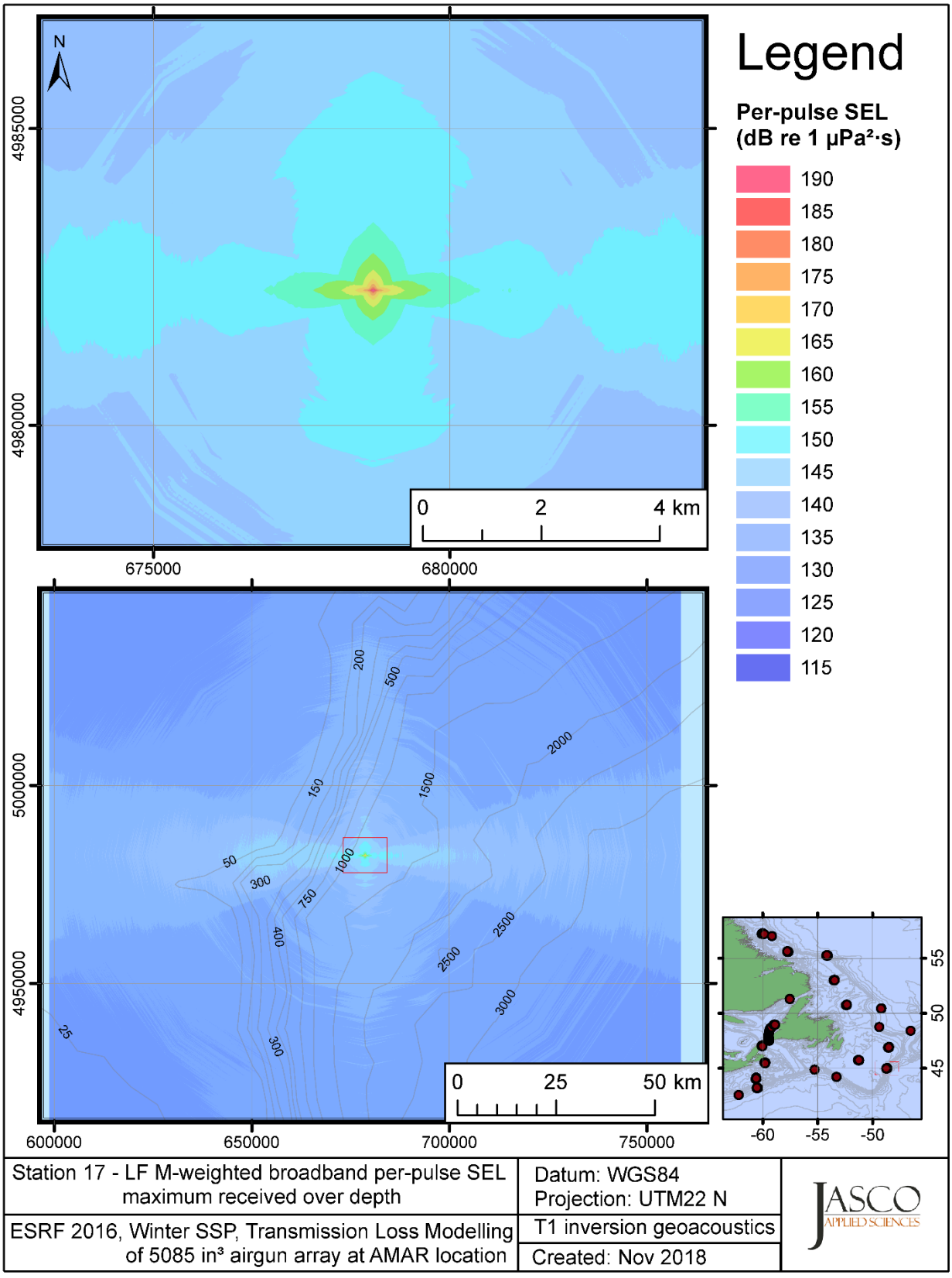

Figure C-469. Stn 17, LF M-weighted maximum-over-depth SEL received at any location on the map, modelled using the track 1 inversion geoacoustic bottom, with the airgun array at the AMAR location and GDEM February SSP.

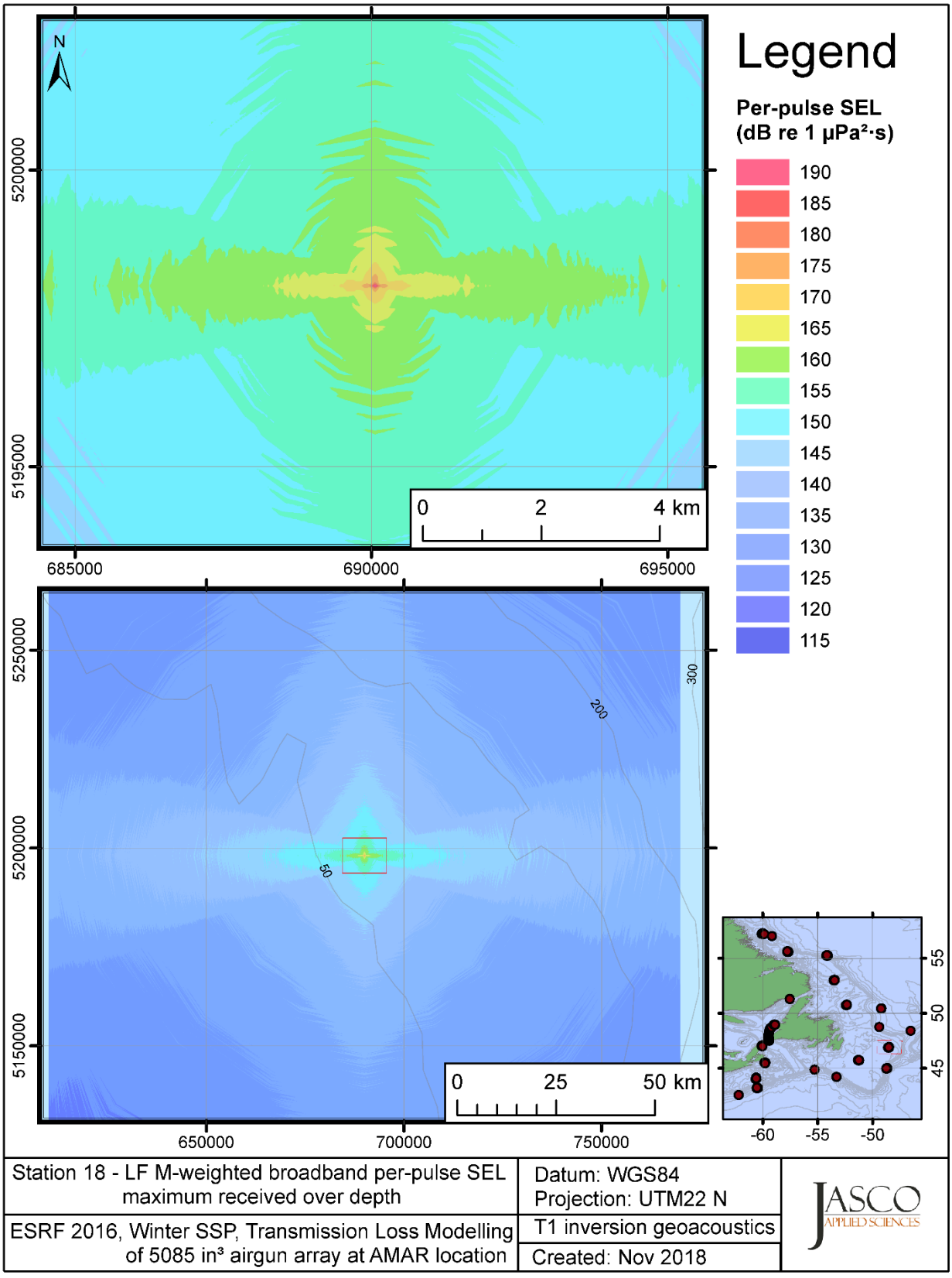

Figure C-470. Stn 18, LF M-weighted maximum-over-depth SEL received at any location on the map, modelled using the track 1 inversion geoacoustic bottom, with the airgun array at the AMAR location and GDEM February SSP.

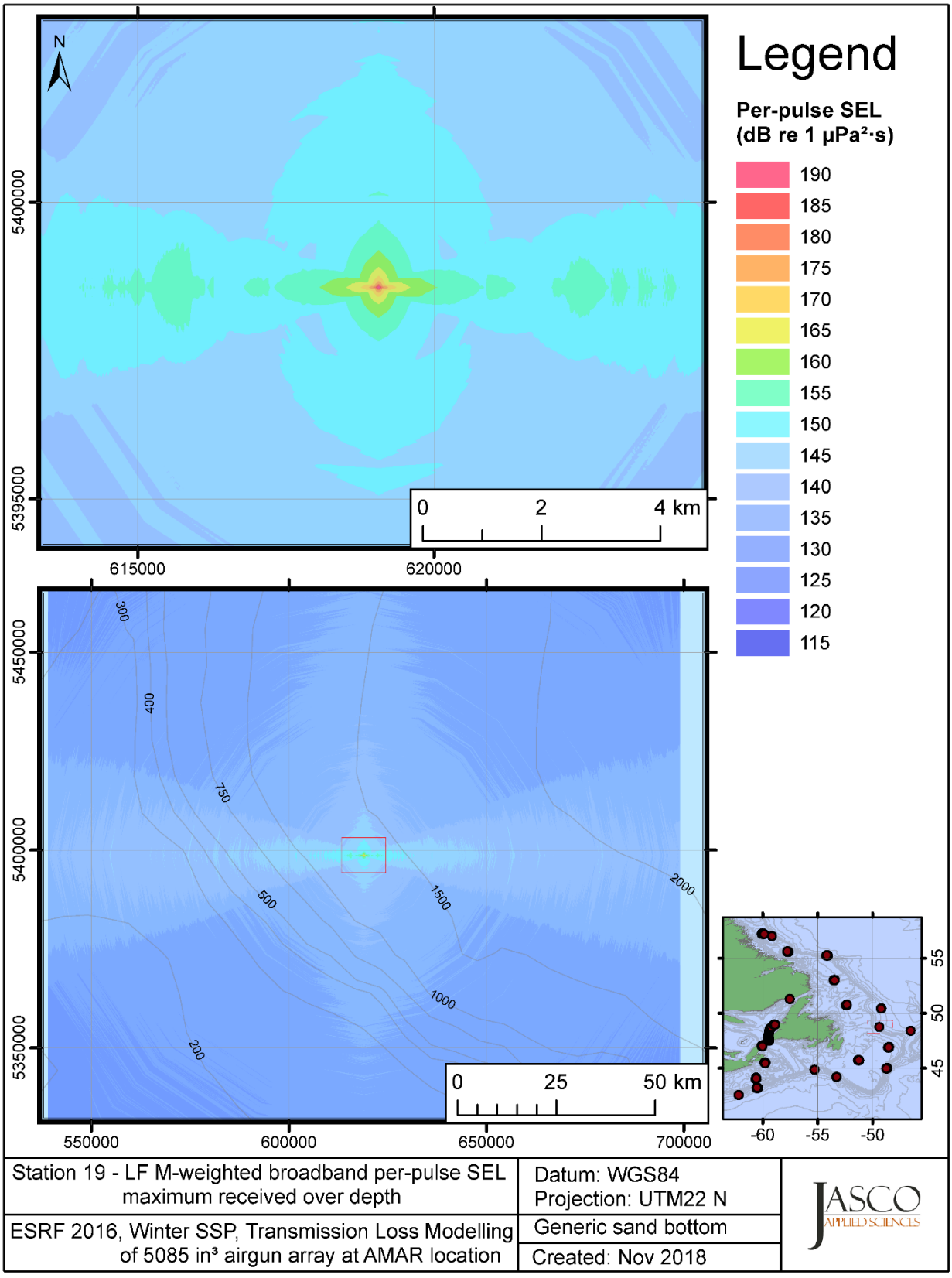

Figure C-471. Stn 19, LF M-weighted maximum-over-depth SEL received at any location on the map, modelled using a generic sand bottom, with the airgun array at the AMAR location and GDEM February SSP.

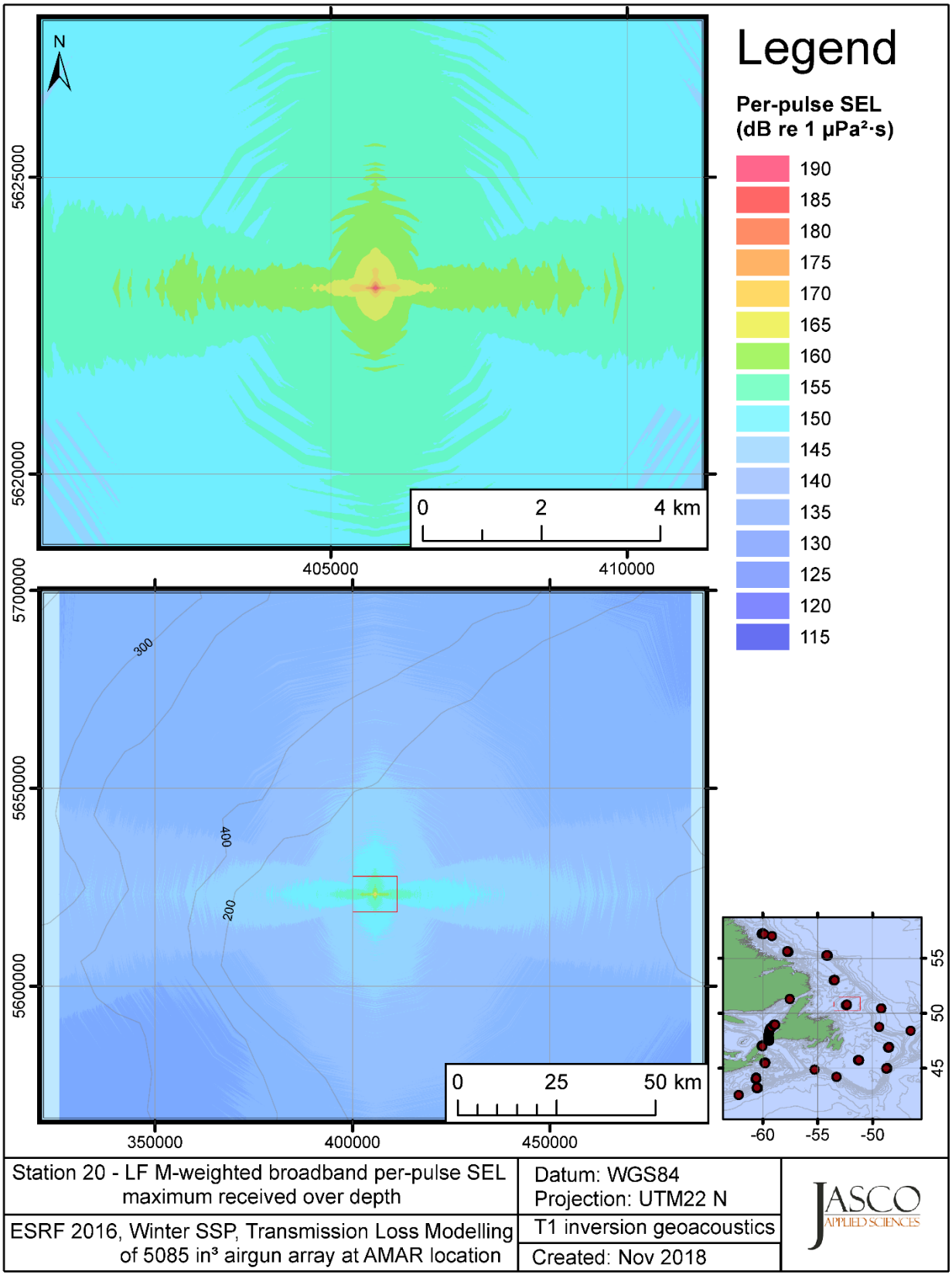

Figure C-472. Stn 20, LF M-weighted maximum-over-depth SEL received at any location on the map, modelled using the track 1 inversion geoacoustic bottom, with the airgun array at the AMAR location and GDEM February SSP.

C.15. Modelling MF M-weighted Max-over-depth Received Level at Distant Locations - Winter

This section presents the results of modelling the maximum-over-depth per-pulse sound exposure level (SEL) received at distant receiver locations (varied in range and azimuth) for the source held fixed at the AMAR location. The modelling uses the geoacoustic inversion bottom parameters at the 14 sites where they are available and only uses a generic sand bottom at the other six sites. The modelling results are presented in the form of coloured maps where the colour at any map location represents the predicted maximum-over-depth received level at that spot on the map. This section includes only the medium-frequency cetaceans (MF) marine-mammal-weighted per-pulse SEL results; additional maps for other marine mammal received level auditory weightings are presented in adjoining sections. The sound speed profiles (SSP) used are detailed in Appendix B.2.

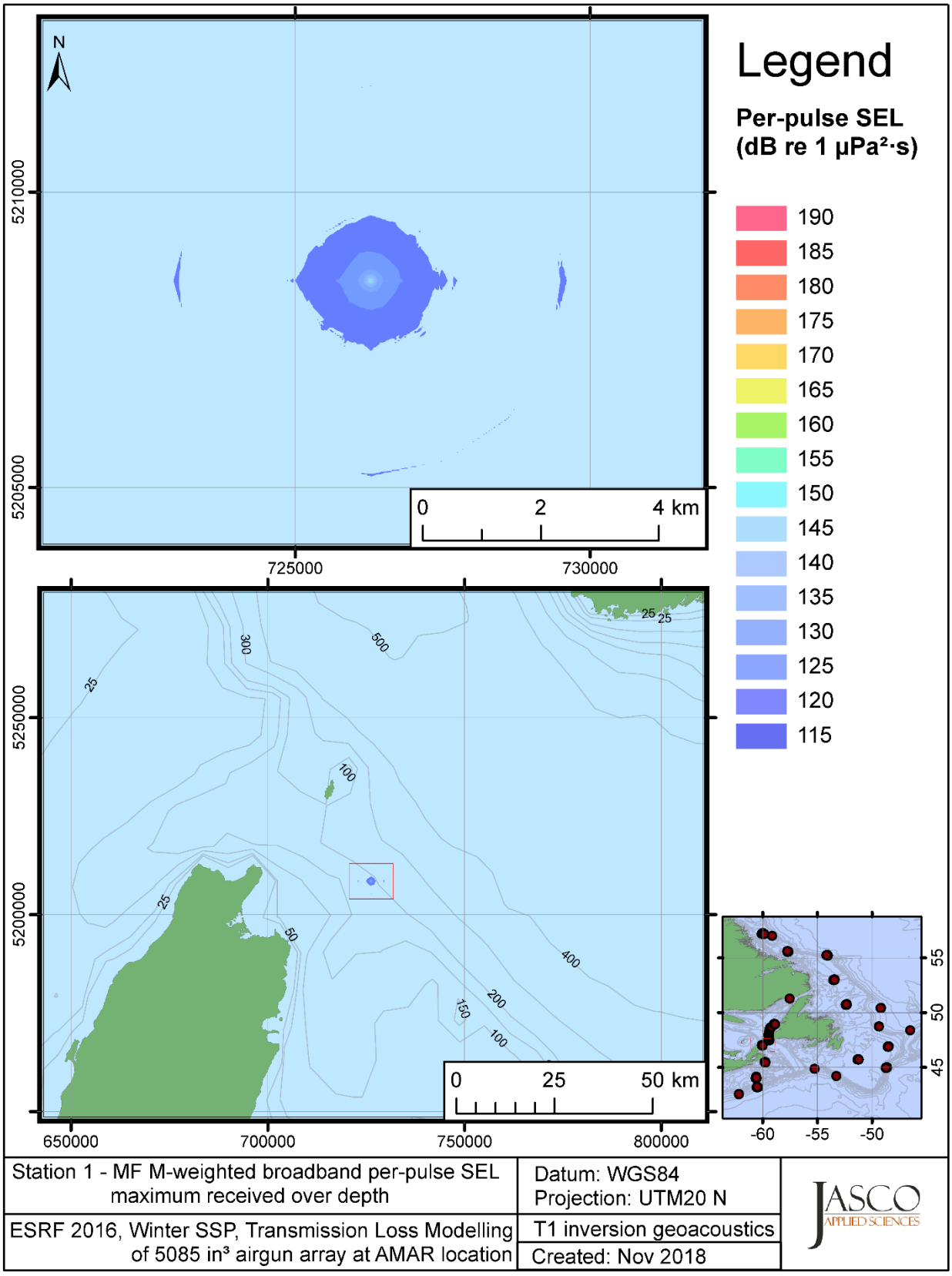

Figure C-473. Stn 1, MF M-weighted maximum-over-depth SEL received at any location on the map, modelled using the track 1 inversion geoacoustic bottom, with the airgun array at the AMAR location and GDEM February SSP.

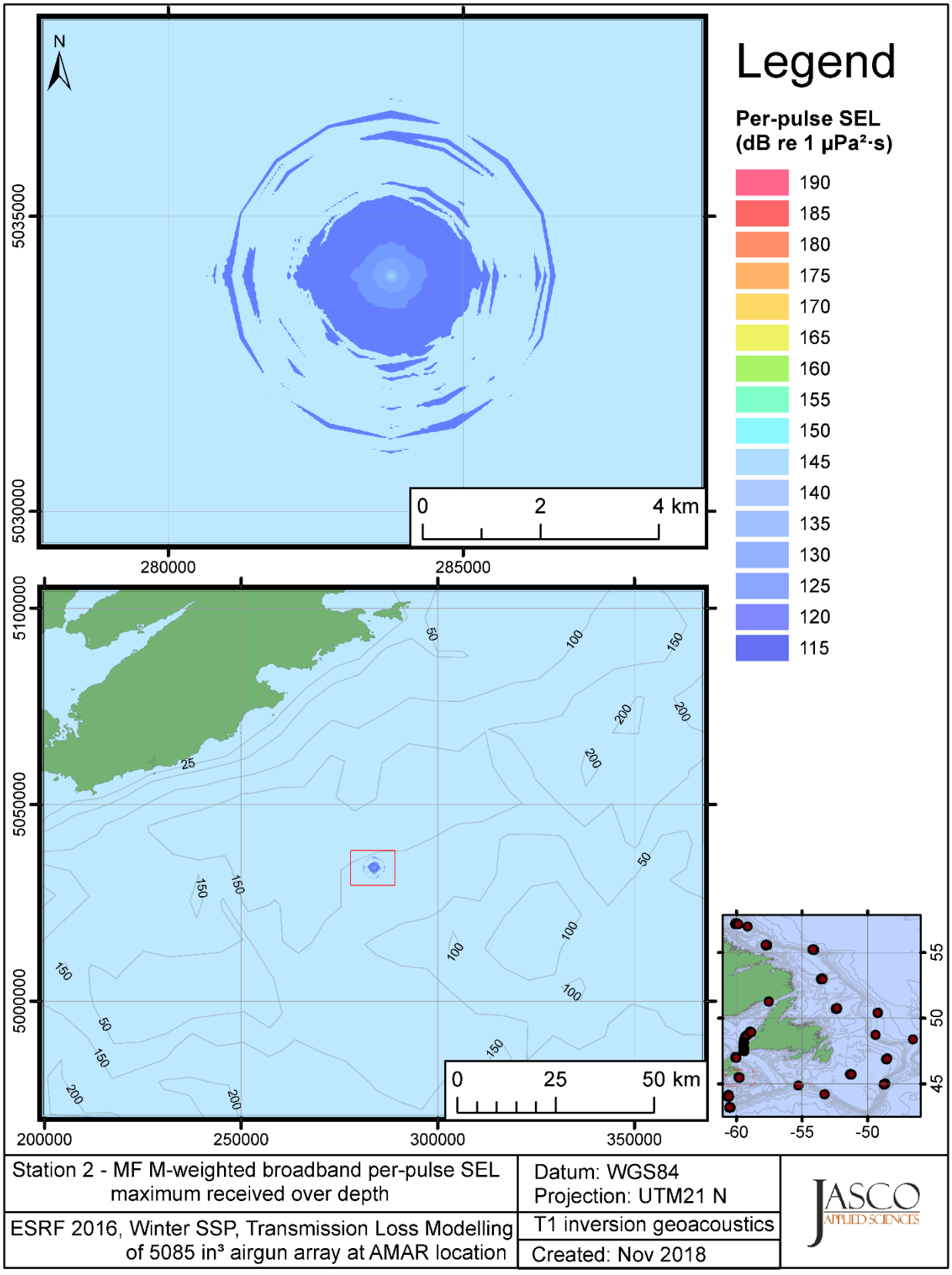

Figure C-474. Stn 2, MF M-weighted maximum-over-depth SEL received at any location on the map, modelled using the track 1 inversion geoacoustic bottom, with the airgun array at the AMAR location and GDEM February SSP.

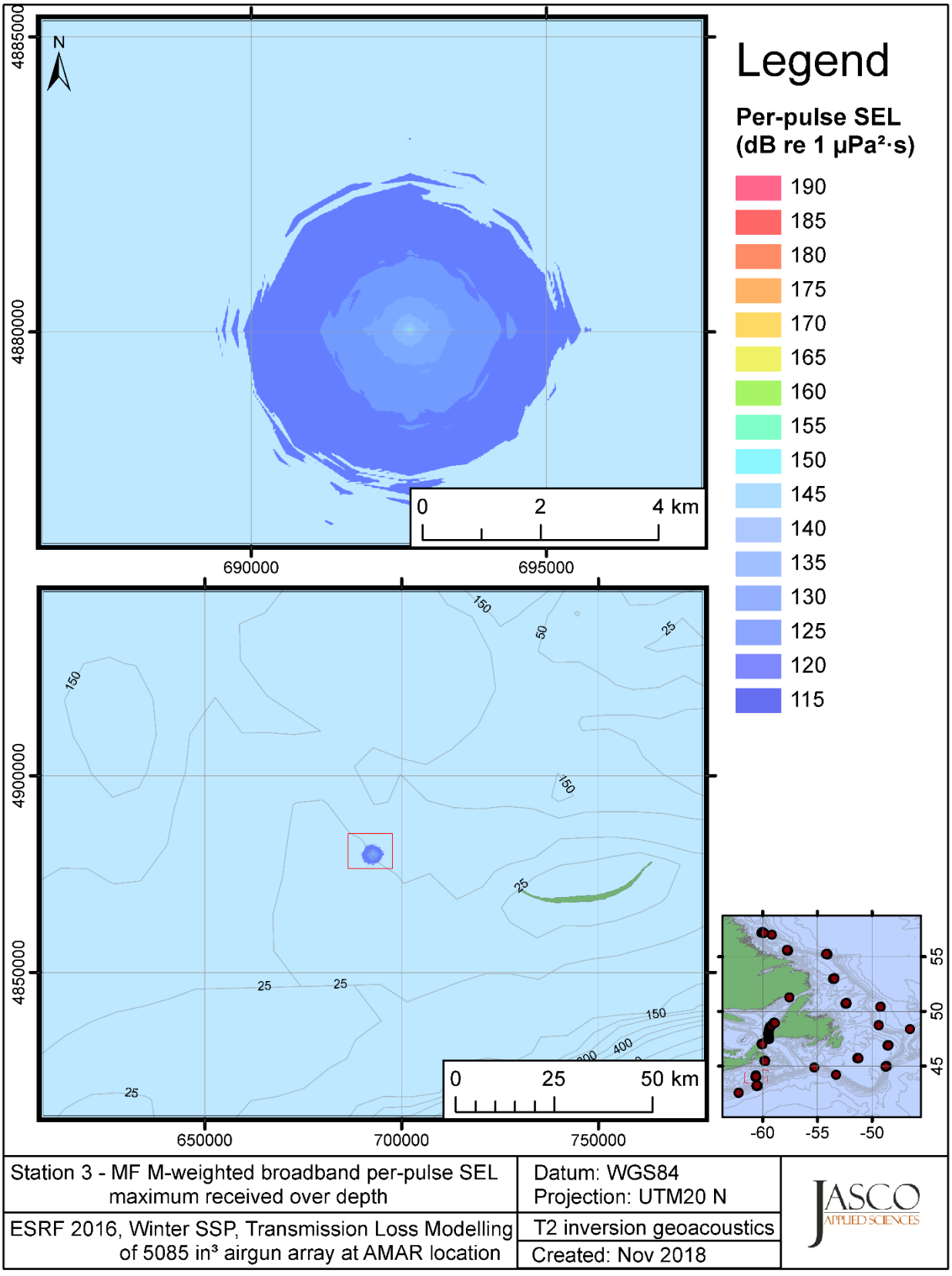

Figure C-475. Stn 3, MF M-weighted maximum-over-depth SEL received at any location on the map, modelled using the track 2 inversion geoacoustic bottom, with the airgun array at the AMAR location and GDEM February SSP.

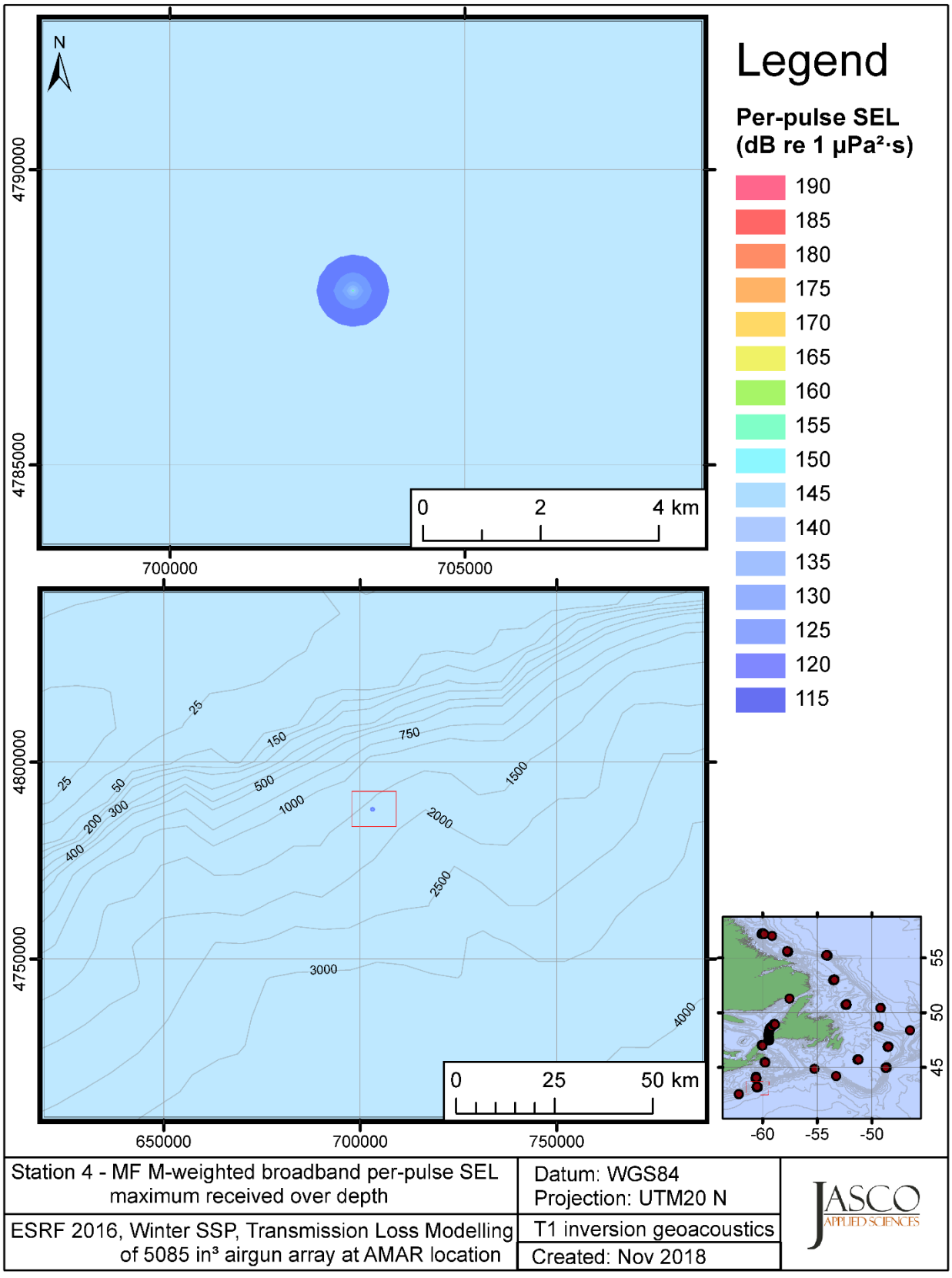

Figure C-476. Stn 4, MF M-weighted maximum-over-depth SEL received at any location on the map, modelled using the track 1 inversion geoacoustic bottom, with the airgun array at the AMAR location and GDEM February SSP.

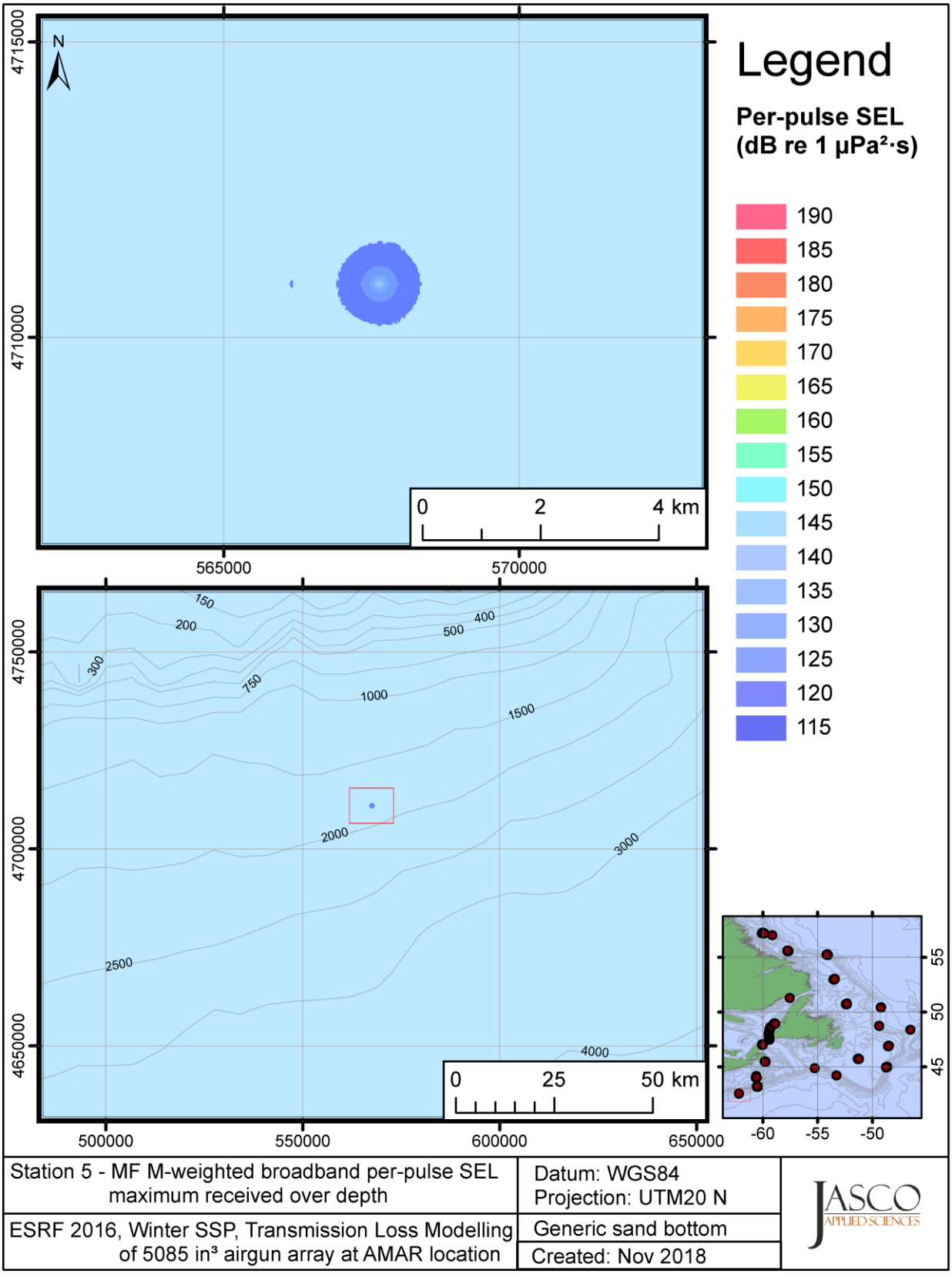

Figure C-477. Stn 5, MF M-weighted maximum-over-depth SEL received at any location on the map, modelled using a generic sand bottom, with the airgun array at the AMAR location and GDEM February SSP.

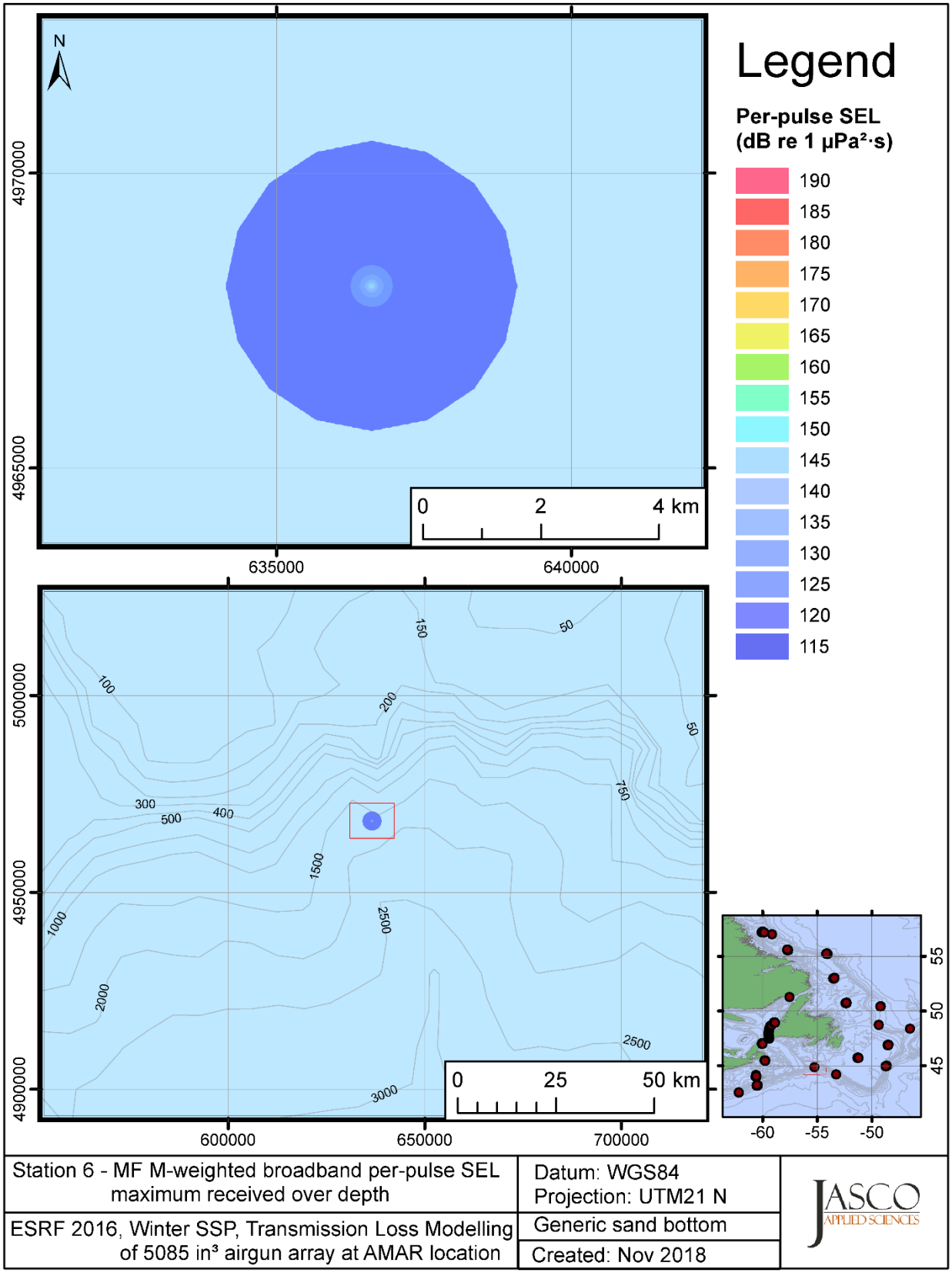

Figure C-478. Stn 6, MF M-weighted maximum-over-depth SEL received at any location on the map, modelled using a generic sand bottom, with the airgun array at the AMAR location and GDEM February SSP.

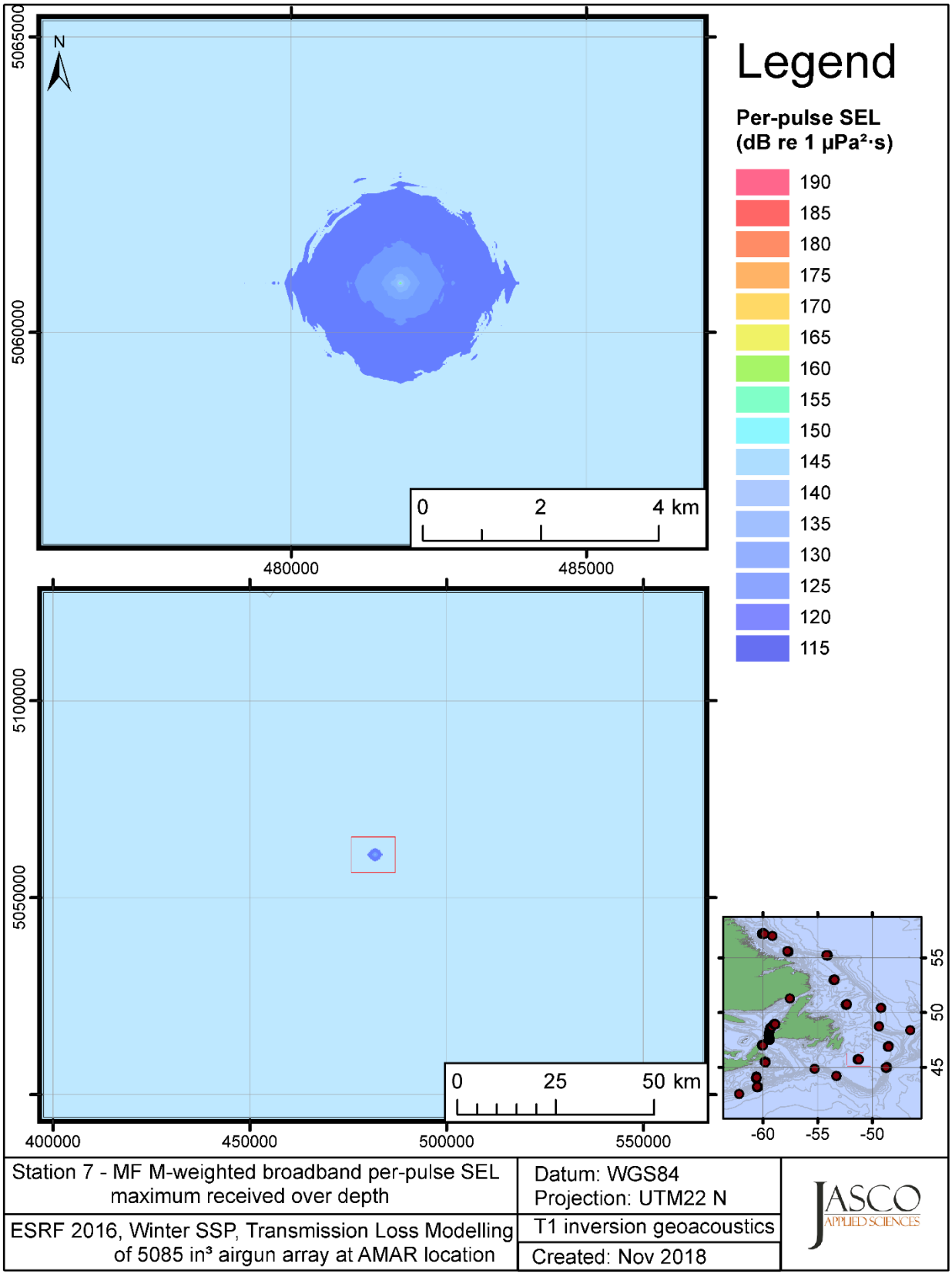

Figure C-479. Stn 7, MF M-weighted maximum-over-depth SEL received at any location on the map, modelled using the track 1 inversion geoacoustic bottom, with the airgun array at the AMAR location and GDEM February SSP.

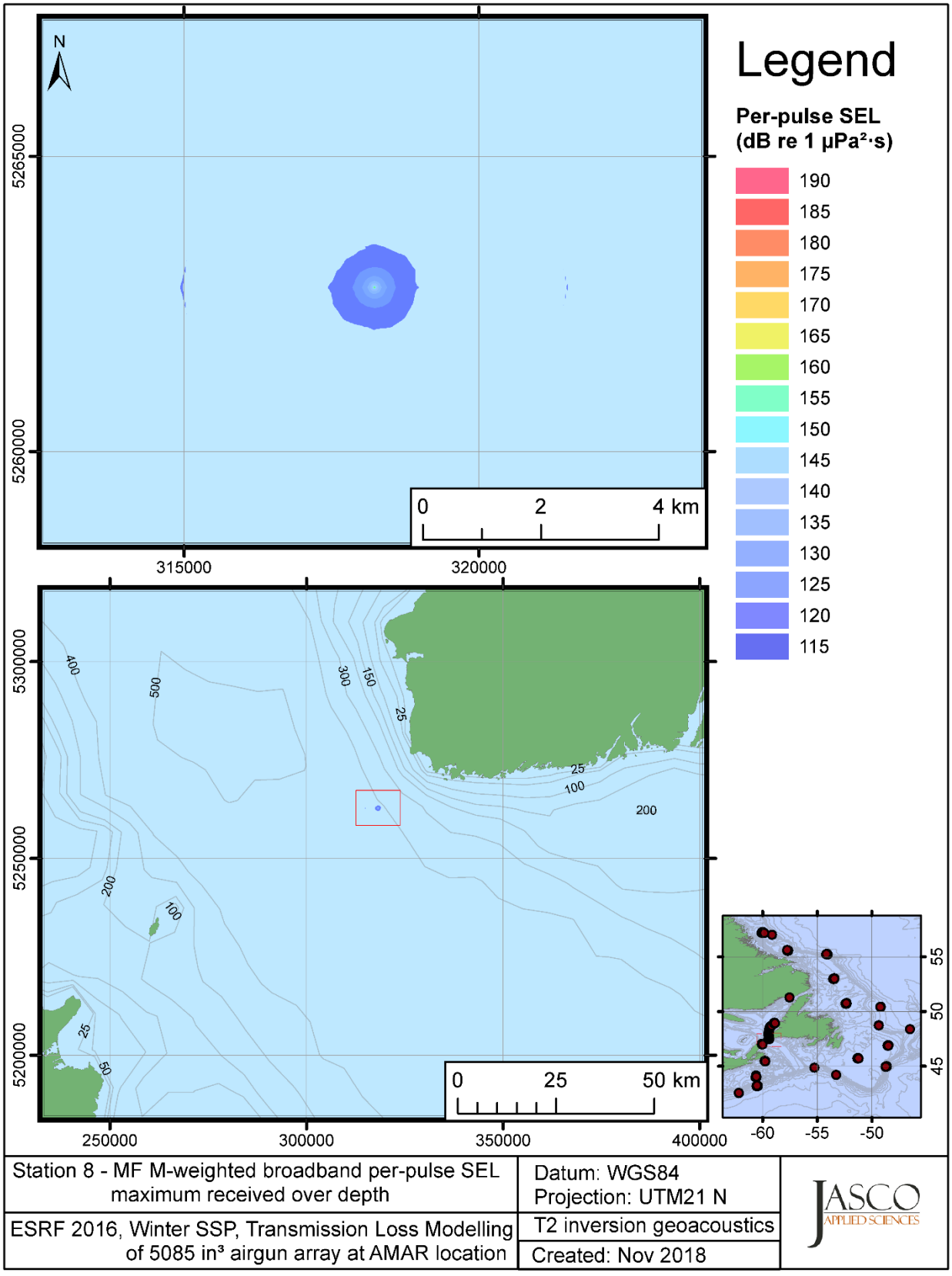

Figure C-480. Stn 8, MF M-weighted maximum-over-depth SEL received at any location on the map, modelled using the track 2 inversion geoacoustic bottom, with the airgun array at the AMAR location and GDEM February SSP.

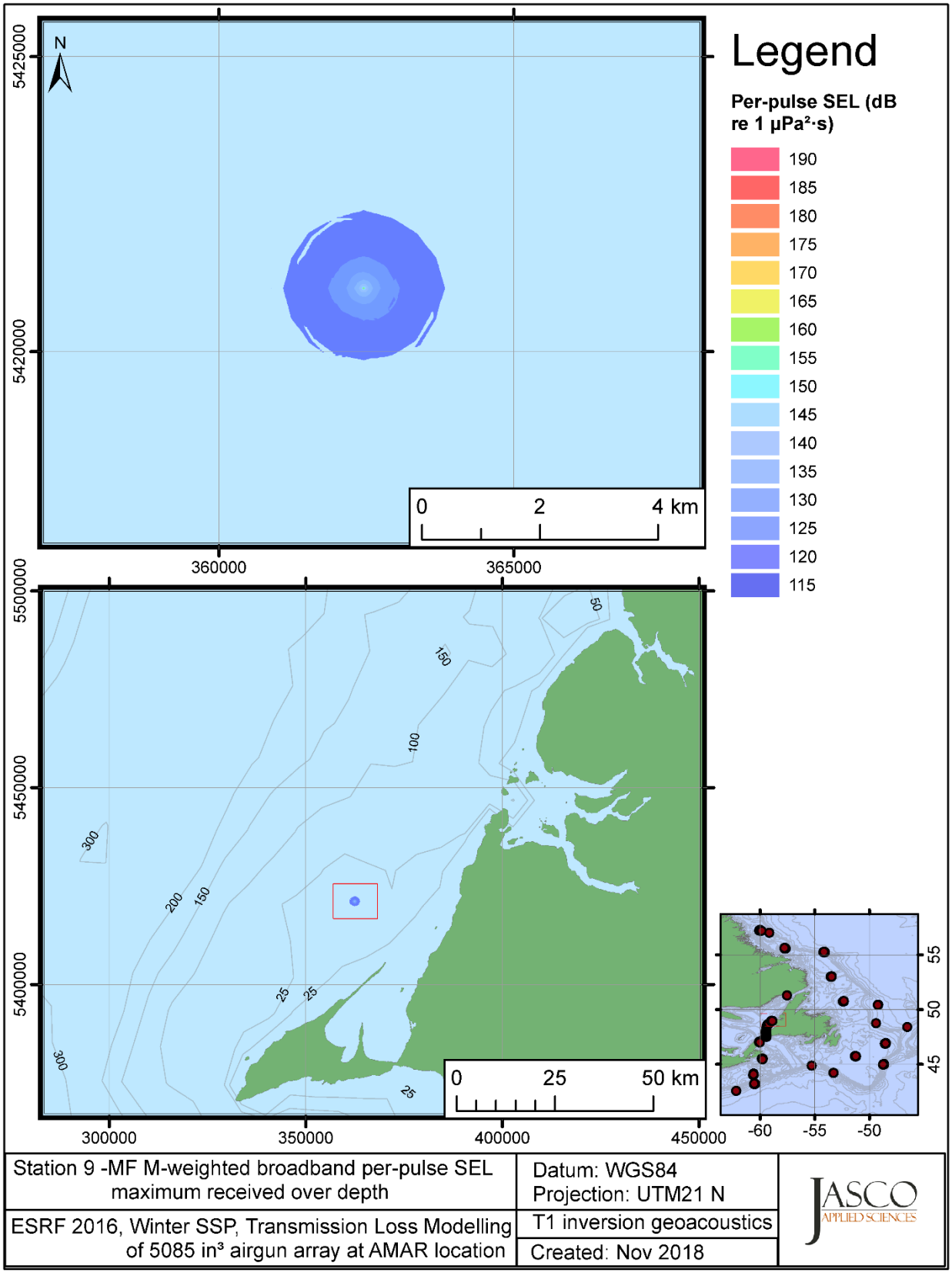

Figure C-481. Stn 9, MF M-weighted maximum-over-depth SEL received at any location on the map, modelled using the track 1 inversion geoacoustic bottom, with the airgun array at the AMAR location and GDEM February SSP.

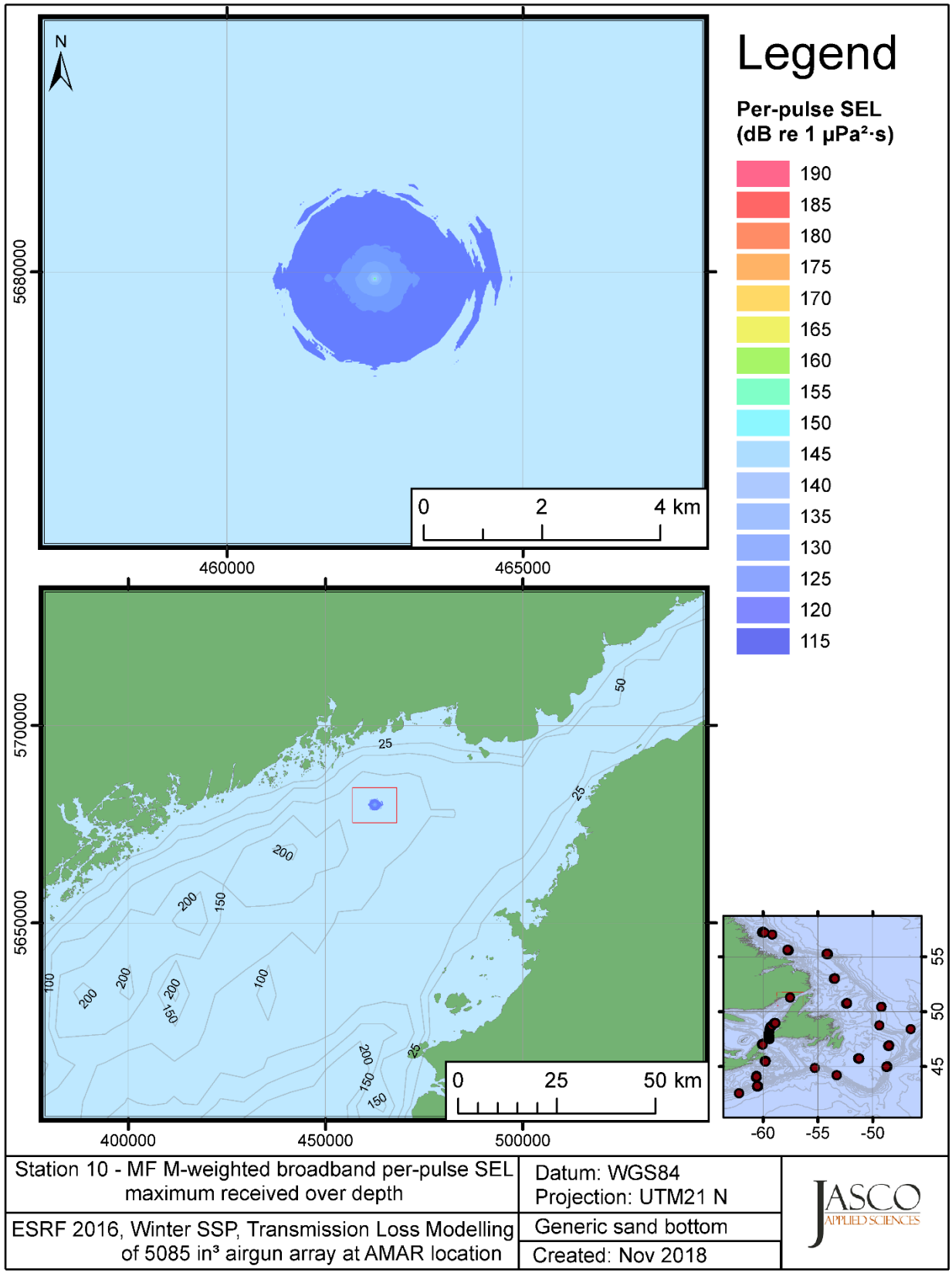

Figure C-482. Stn 10, MF M-weighted maximum-over-depth SEL received at any location on the map, modelled using a generic sand bottom, with the airgun array at the AMAR location and GDEM February SSP.

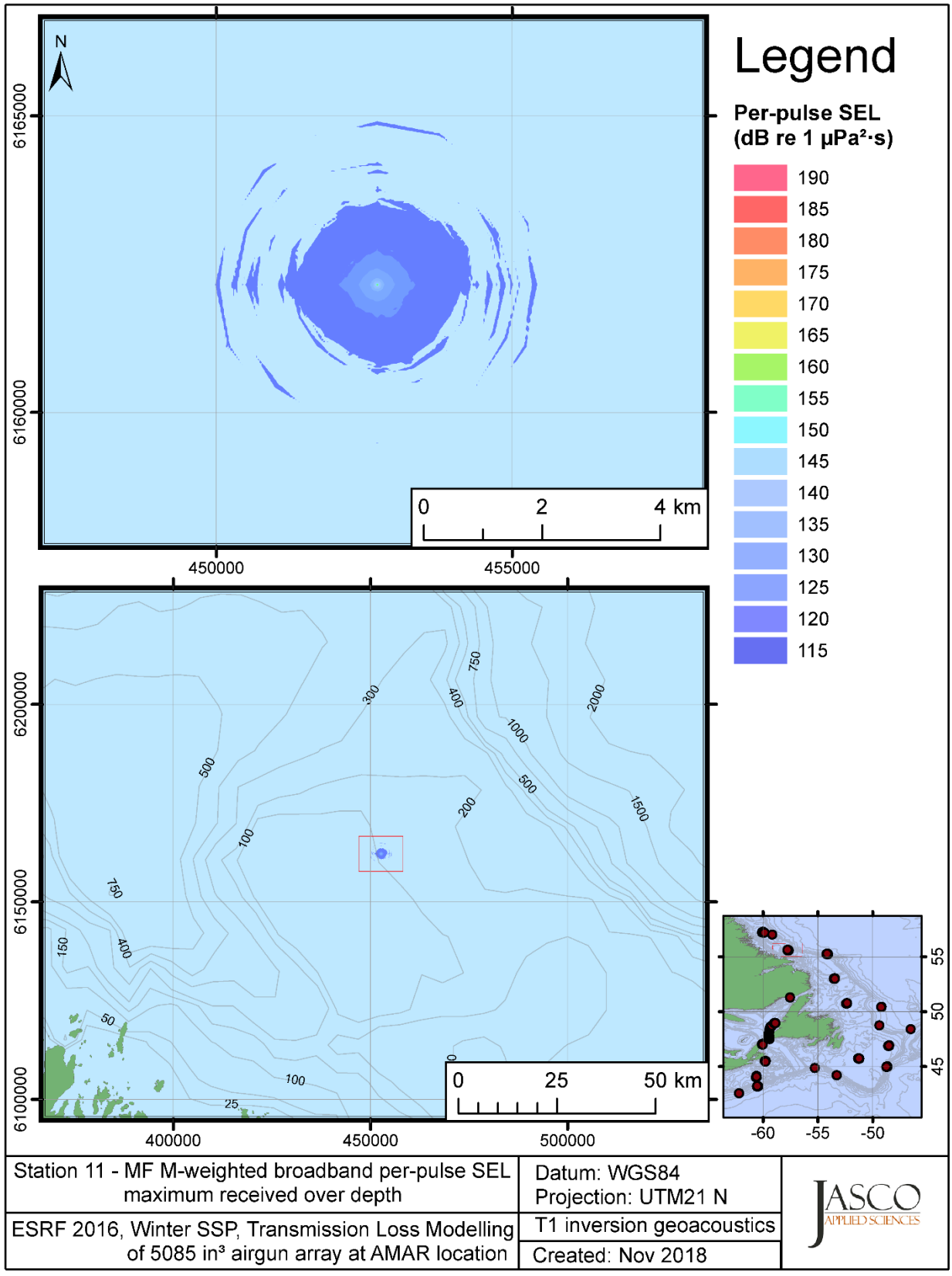

Figure C-483. Stn 11, MF M-weighted maximum-over-depth SEL received at any location on the map, modelled using the track 1 inversion geoacoustic bottom, with the airgun array at the AMAR location and GDEM February SSP.

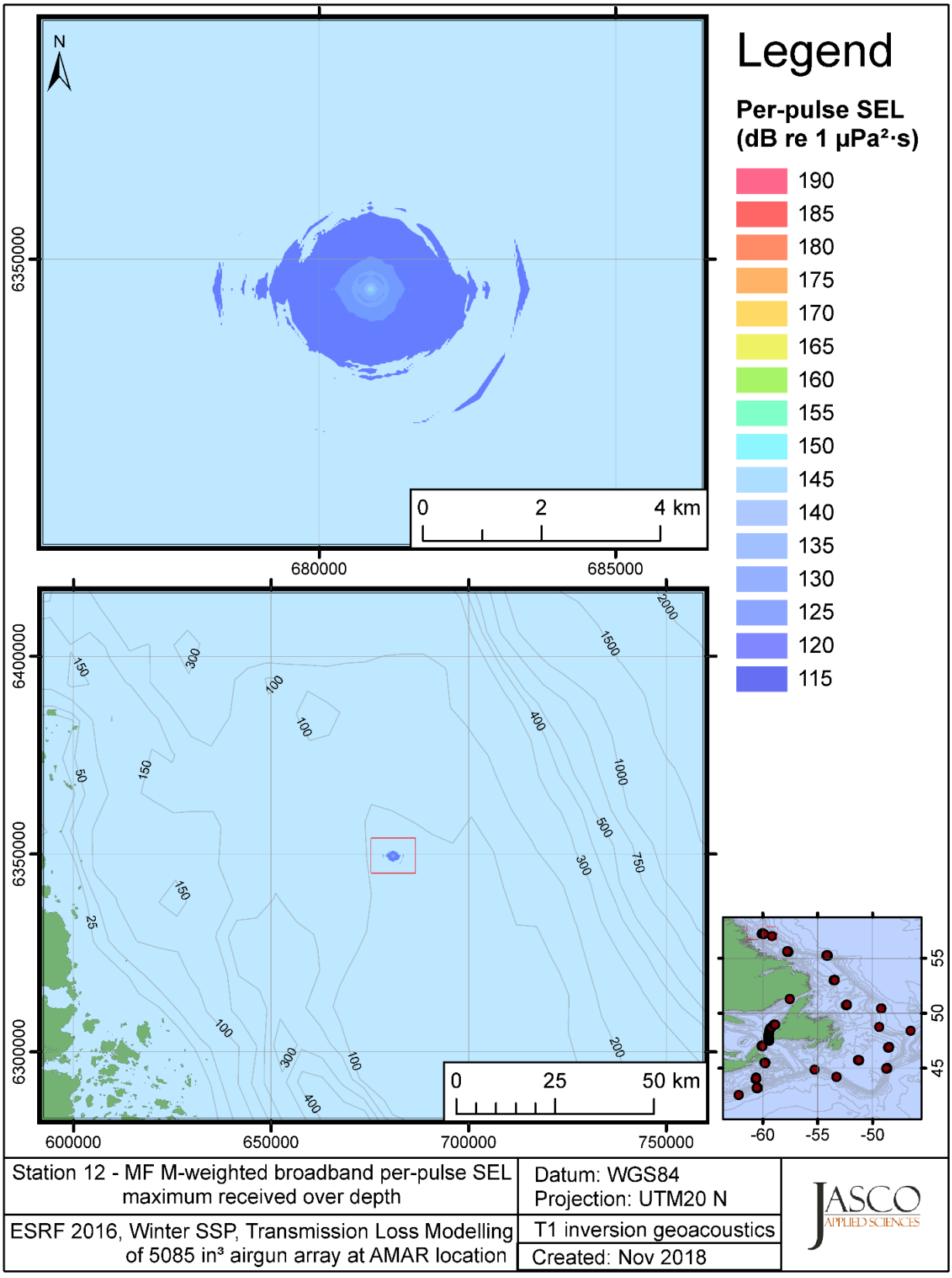

Figure C-484. Stn 12, MF M-weighted maximum-over-depth SEL received at any location on the map, modelled using the track 1 inversion geoacoustic bottom, with the airgun array at the AMAR location and GDEM February SSP.

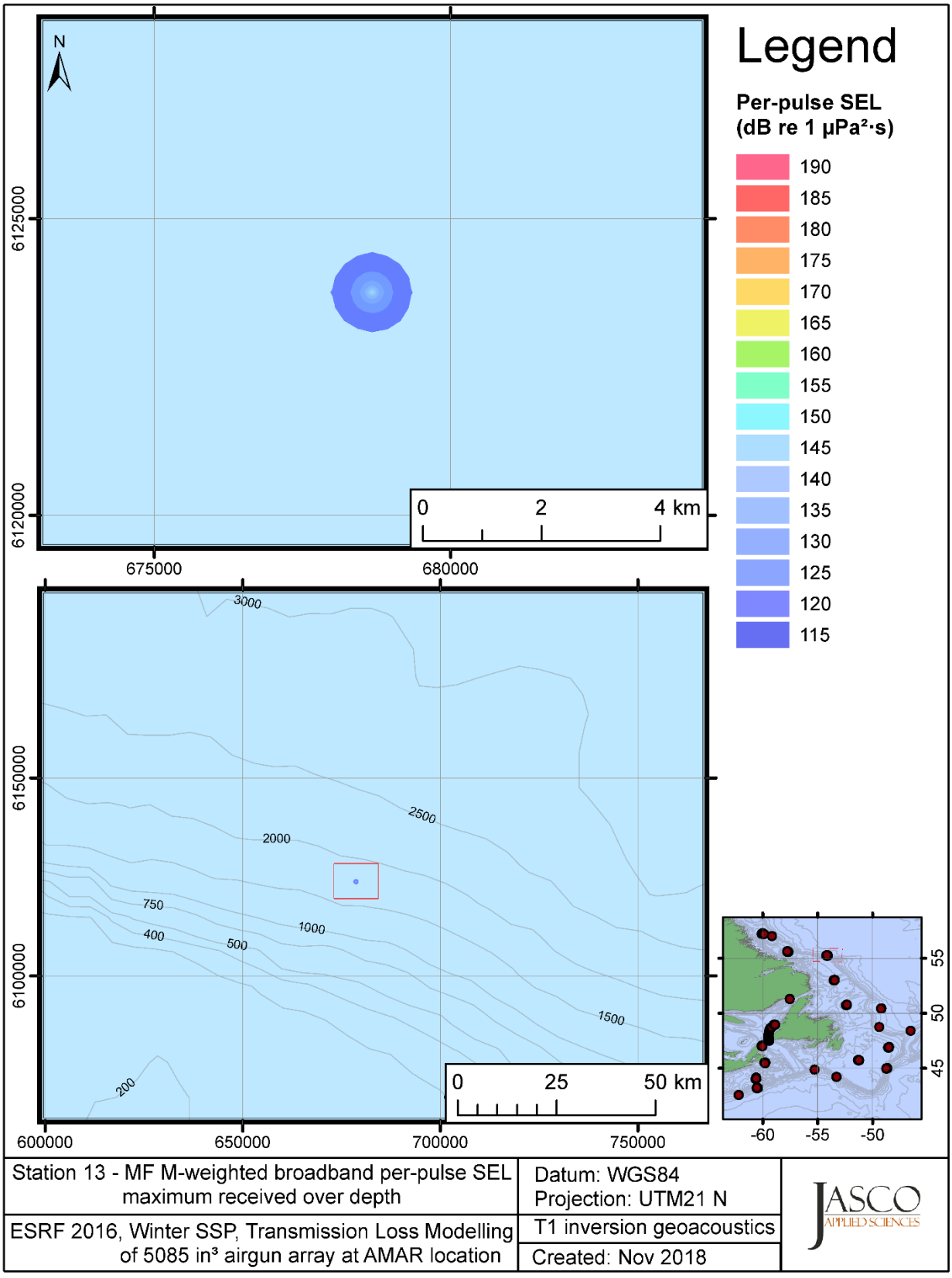

Figure C-485. Stn 13, MF M-weighted maximum-over-depth SEL received at any location on the map, modelled using the track 1 inversion geoacoustic bottom, with the airgun array at the AMAR location and GDEM February SSP.

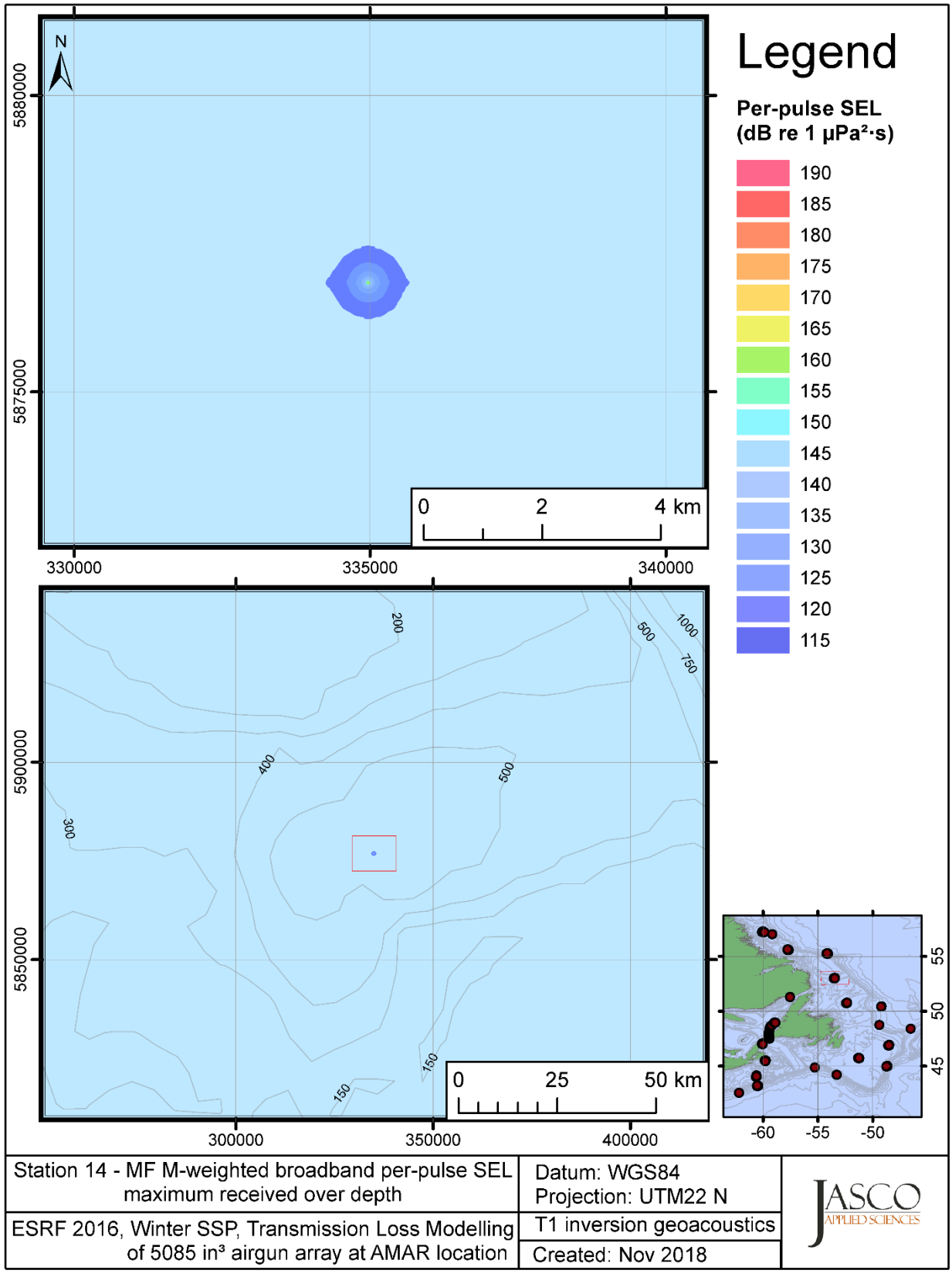

Figure C-486. Stn 14, MF M-weighted maximum-over-depth SEL received at any location on the map, modelled using the track 1 inversion geoacoustic bottom, with the airgun array at the AMAR location and GDEM February SSP.

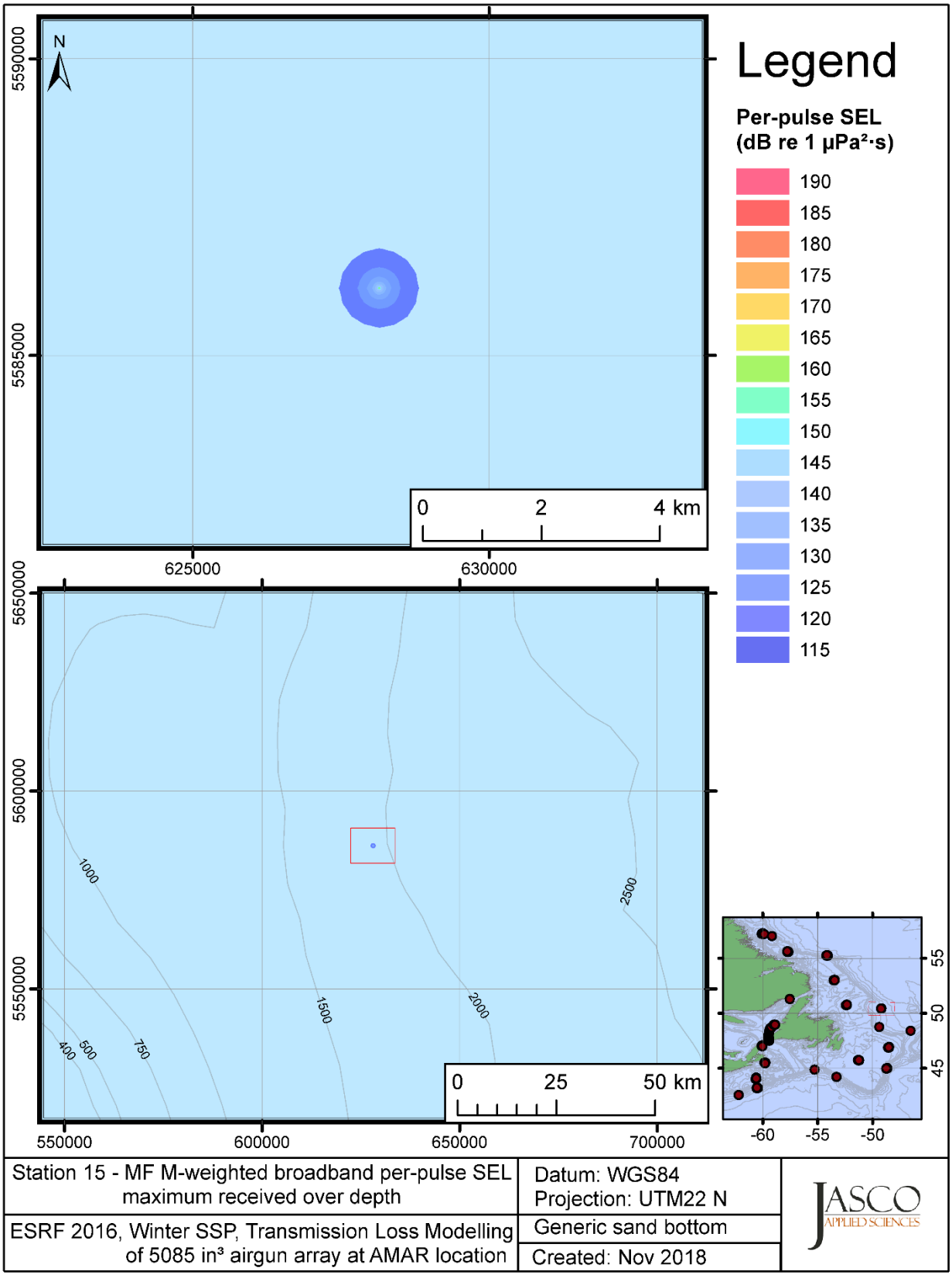

Figure C-487. Stn 15, MF M-weighted maximum-over-depth SEL received at any location on the map, modelled using a generic sand bottom, with the airgun array at the AMAR location and GDEM February SSP.

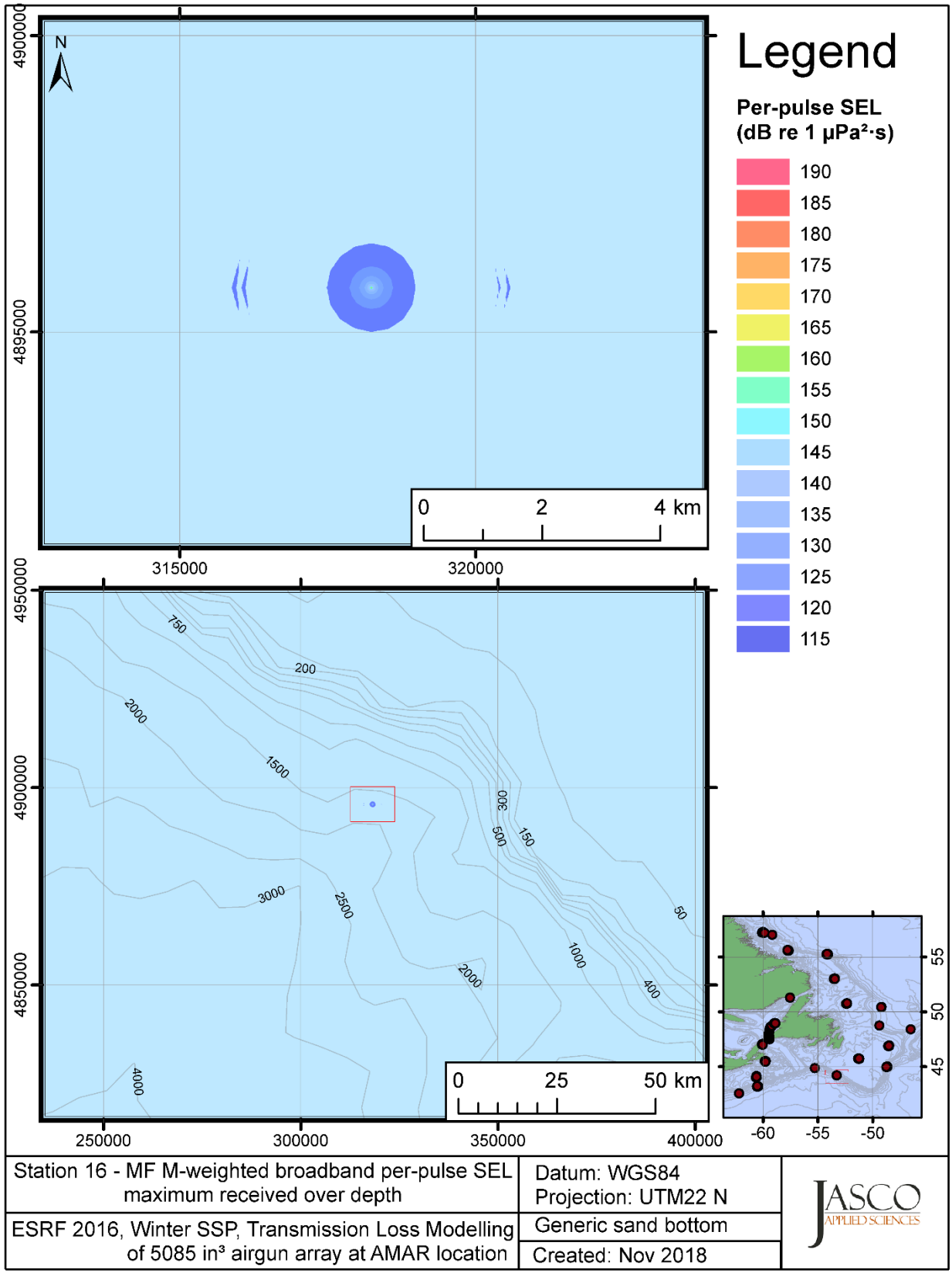

Figure C-488. Stn 16, MF M-weighted maximum-over-depth SEL received at any location on the map, modelled using a generic sand bottom, with the airgun array at the AMAR location and GDEM February SSP.

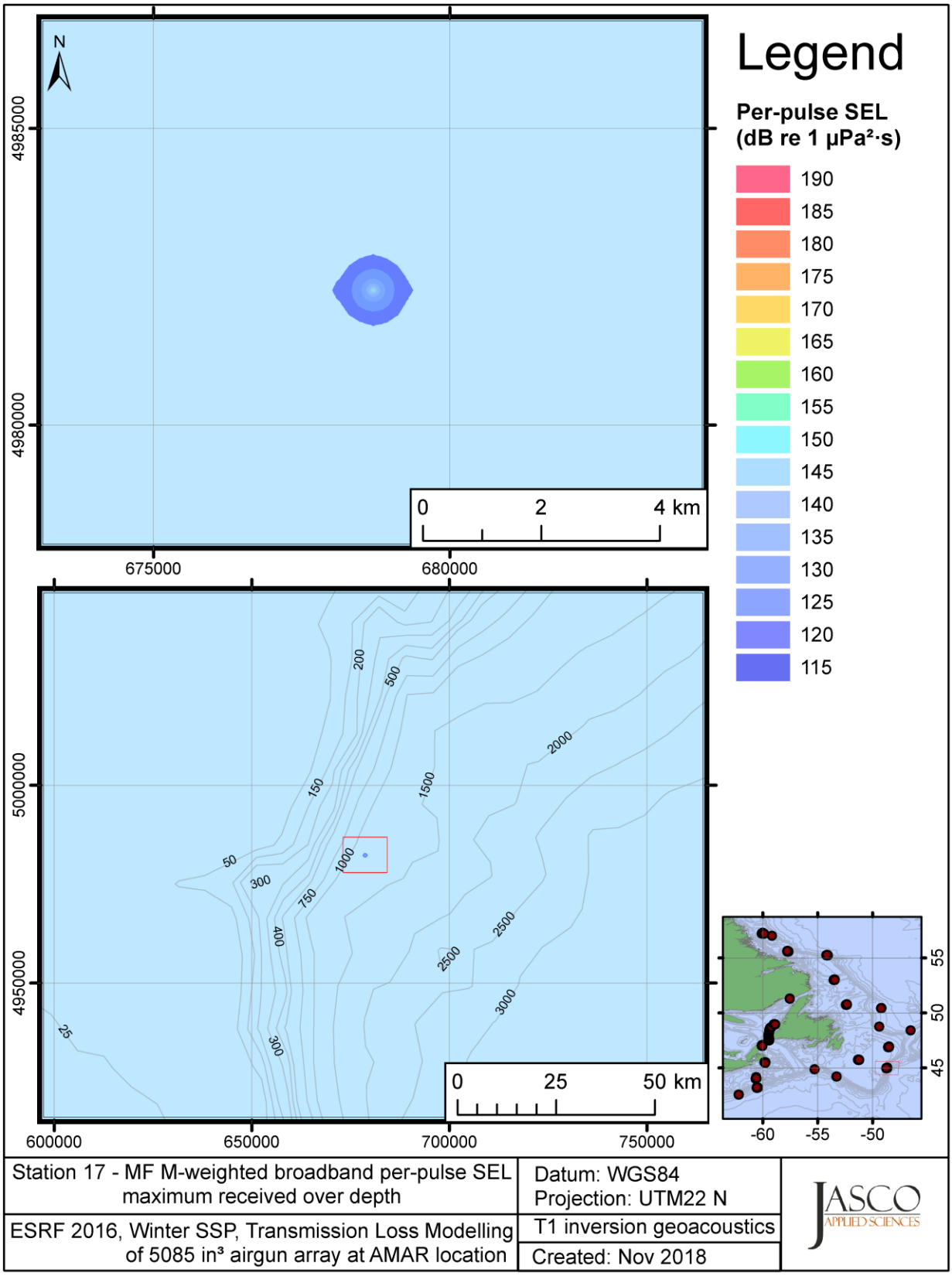

Figure C-489. Stn 17, MF M-weighted maximum-over-depth SEL received at any location on the map, modelled using the track 1 inversion geoacoustic bottom, with the airgun array at the AMAR location and GDEM February SSP.

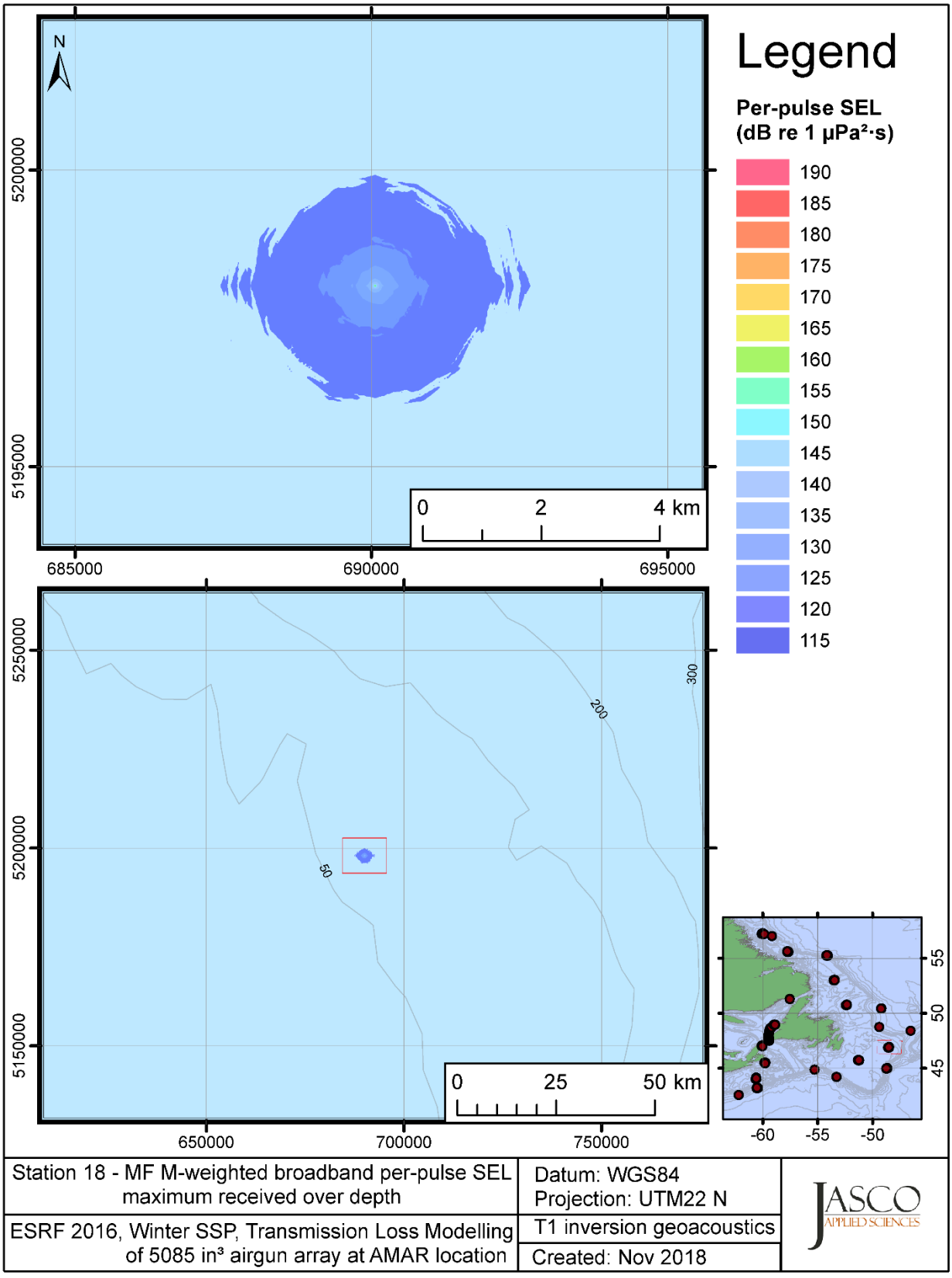

Figure C-490. Stn 18, MF M-weighted maximum-over-depth SEL received at any location on the map, modelled using the track 1 inversion geoacoustic bottom, with the airgun array at the AMAR location and GDEM February SSP.

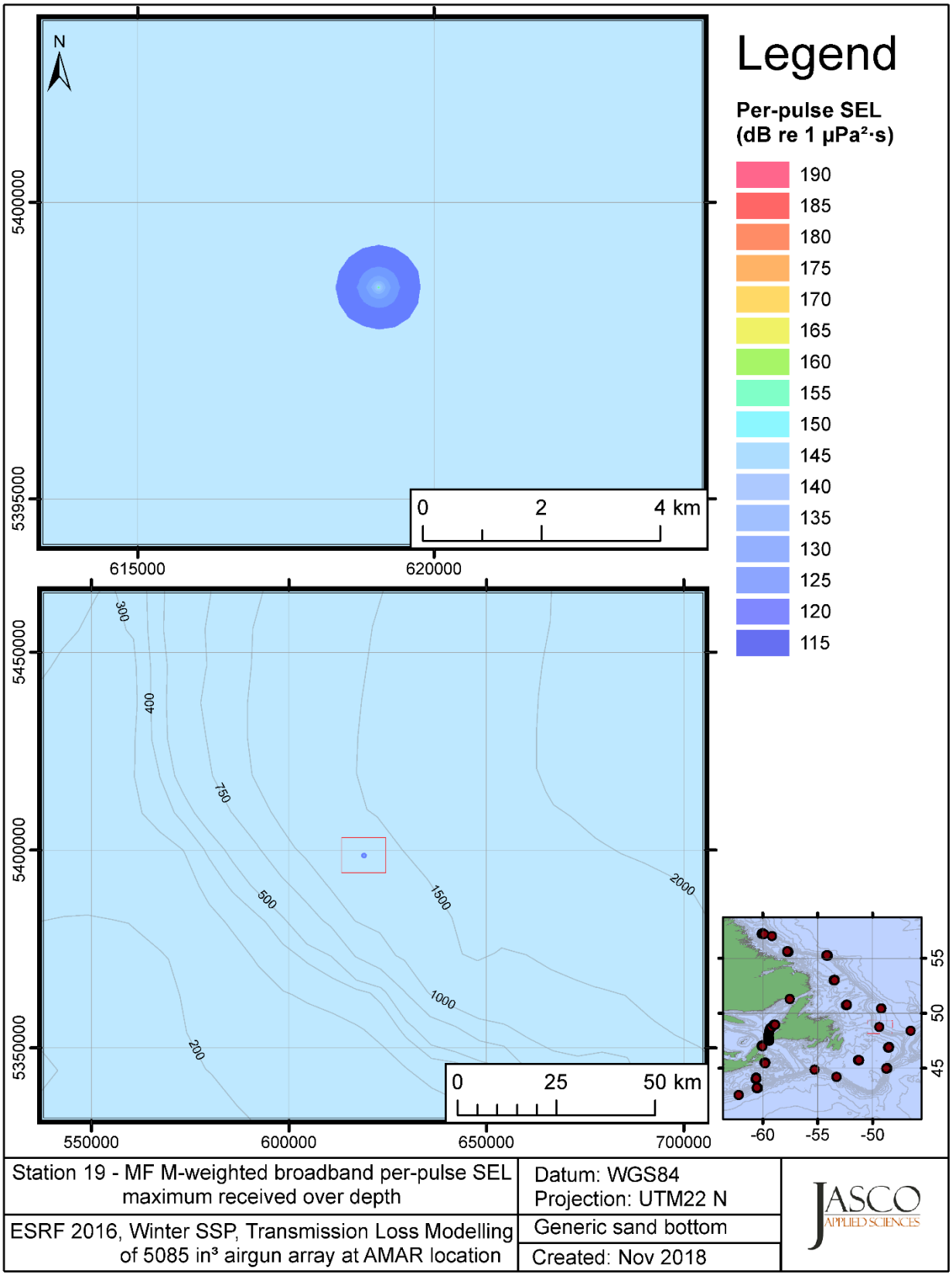

Figure C-491. Stn 19, MF M-weighted maximum-over-depth SEL received at any location on the map, modelled using a generic sand bottom, with the airgun array at the AMAR location and GDEM February SSP.

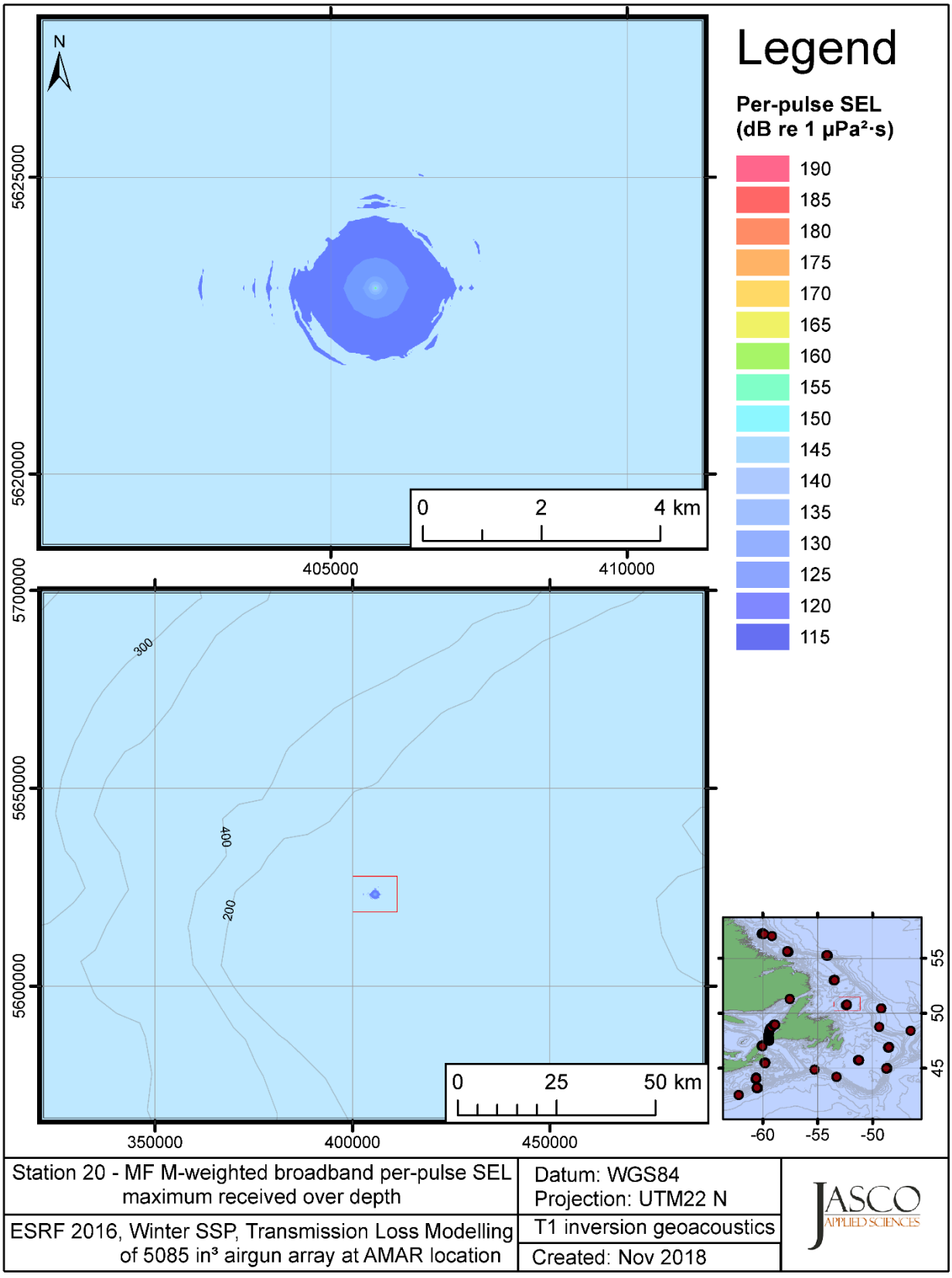

Figure C-492. Stn 20, MF M-weighted maximum-over-depth SEL received at any location on the map, modelled using the track 1 inversion geoacoustic bottom, with the airgun array at the AMAR location and GDEM February SSP.

C.16. Modelling HF M-weighted Max-over-depth Received Level at Distant Locations - Winter

This section presents the results of modelling the maximum-over-depth per-pulse sound exposure level (SEL) received at distant receiver locations (varied in range and azimuth) for the source held fixed at the AMAR location. The modelling uses the geoacoustic inversion bottom parameters at the 14 sites where they are available and only uses a generic sand bottom at the other six sites. The modelling results are presented in the form of coloured maps where the colour at any map location represents the predicted maximum-over-depth received level at that spot on the map. This section includes only the high-frequency cetaceans (HF) marine-mammal-weighted per-pulse SEL results; additional maps for other marine mammal received level auditory weightings are presented in adjoining sections. The sound speed profiles (SSP) used are detailed in Appendix B.2.

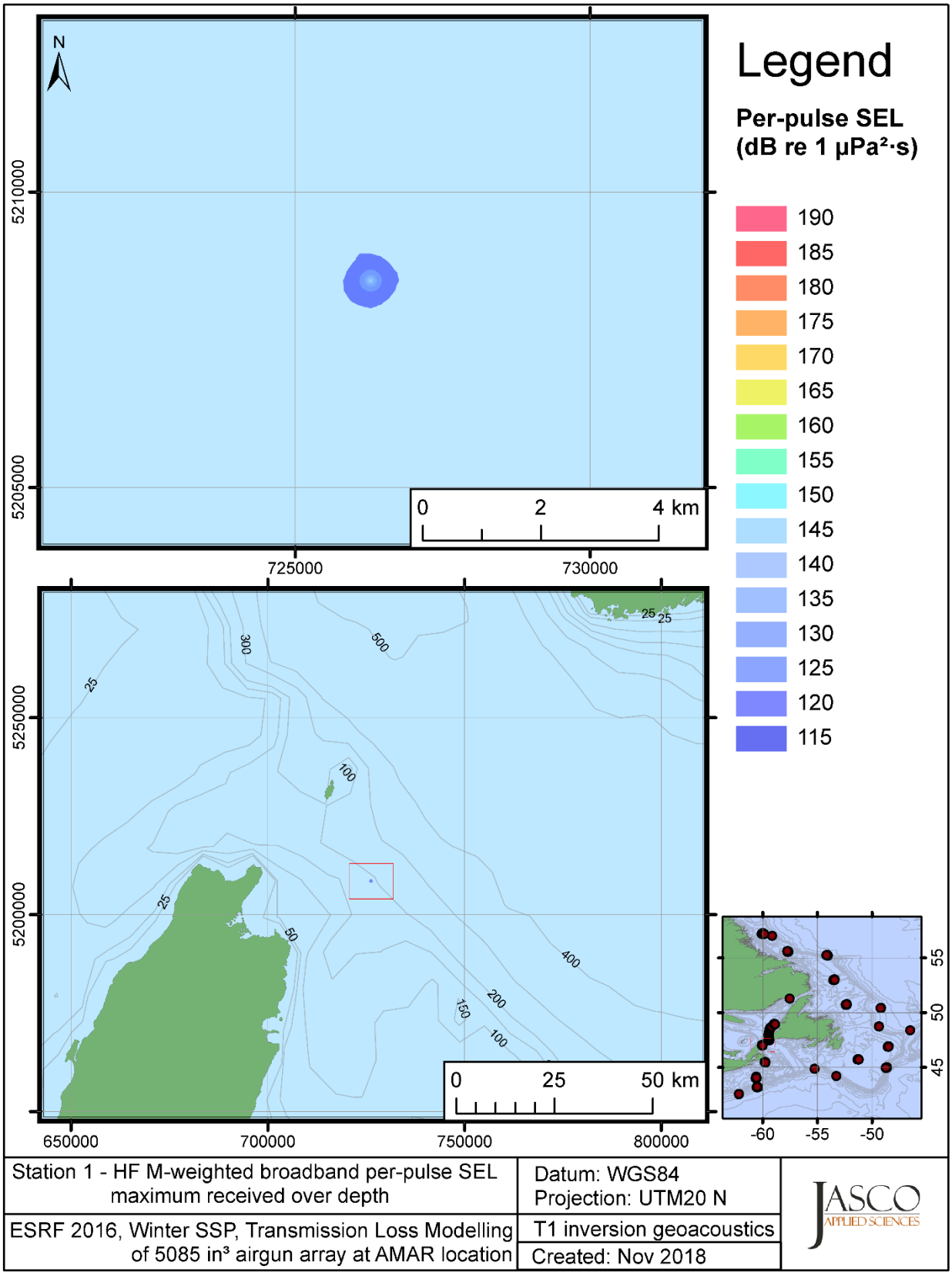

Figure C-493. Stn 1, HF M-weighted maximum-over-depth SEL received at any location on the map, modelled using the track 1 inversion geoacoustic bottom, with the airgun array at the AMAR location and GDEM February SSP.

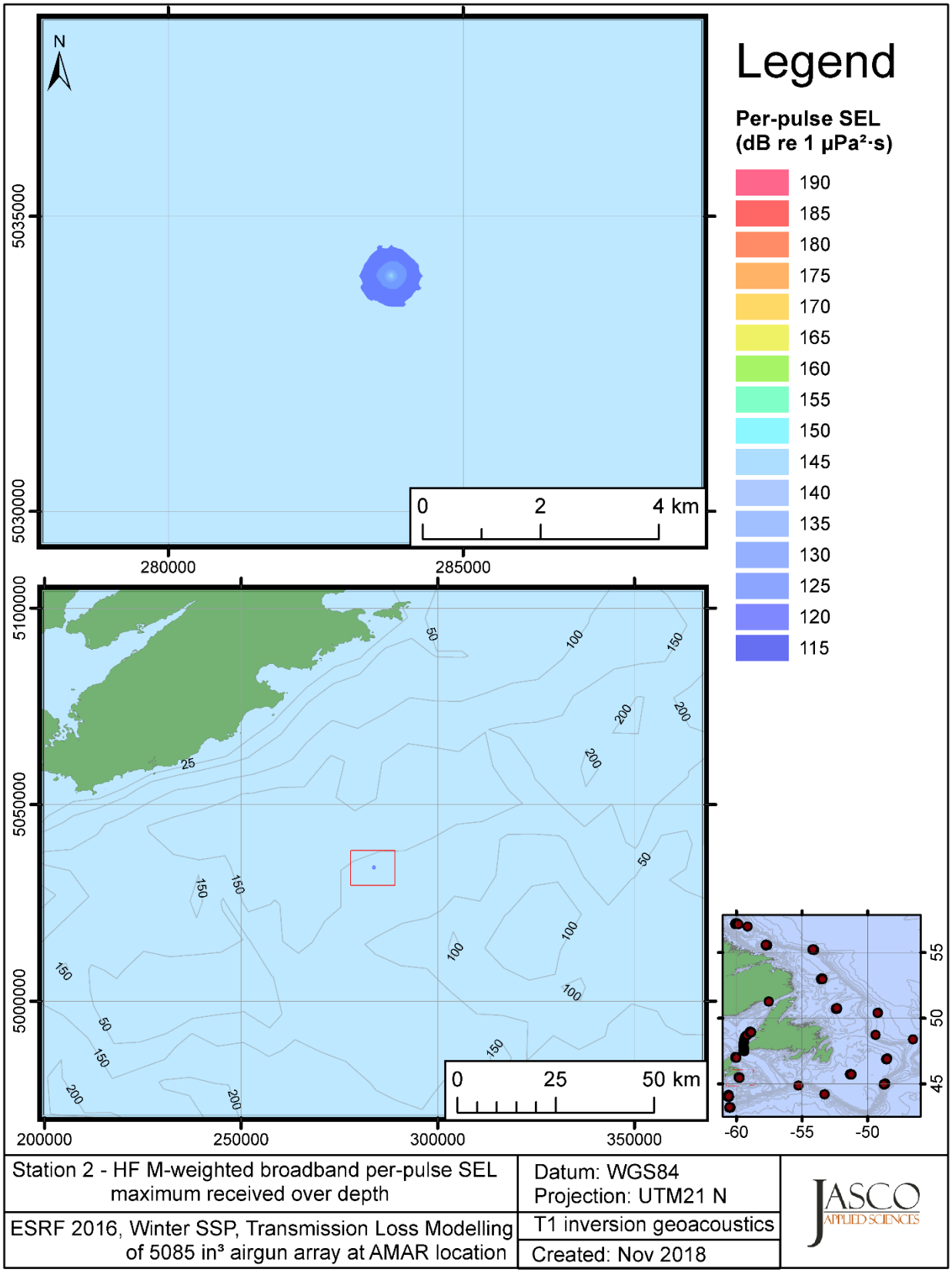

Figure C-494. Stn 2, HF M-weighted maximum-over-depth SEL received at any location on the map, modelled using the track 1 inversion geoacoustic bottom, with the airgun array at the AMAR location and GDEM February SSP.

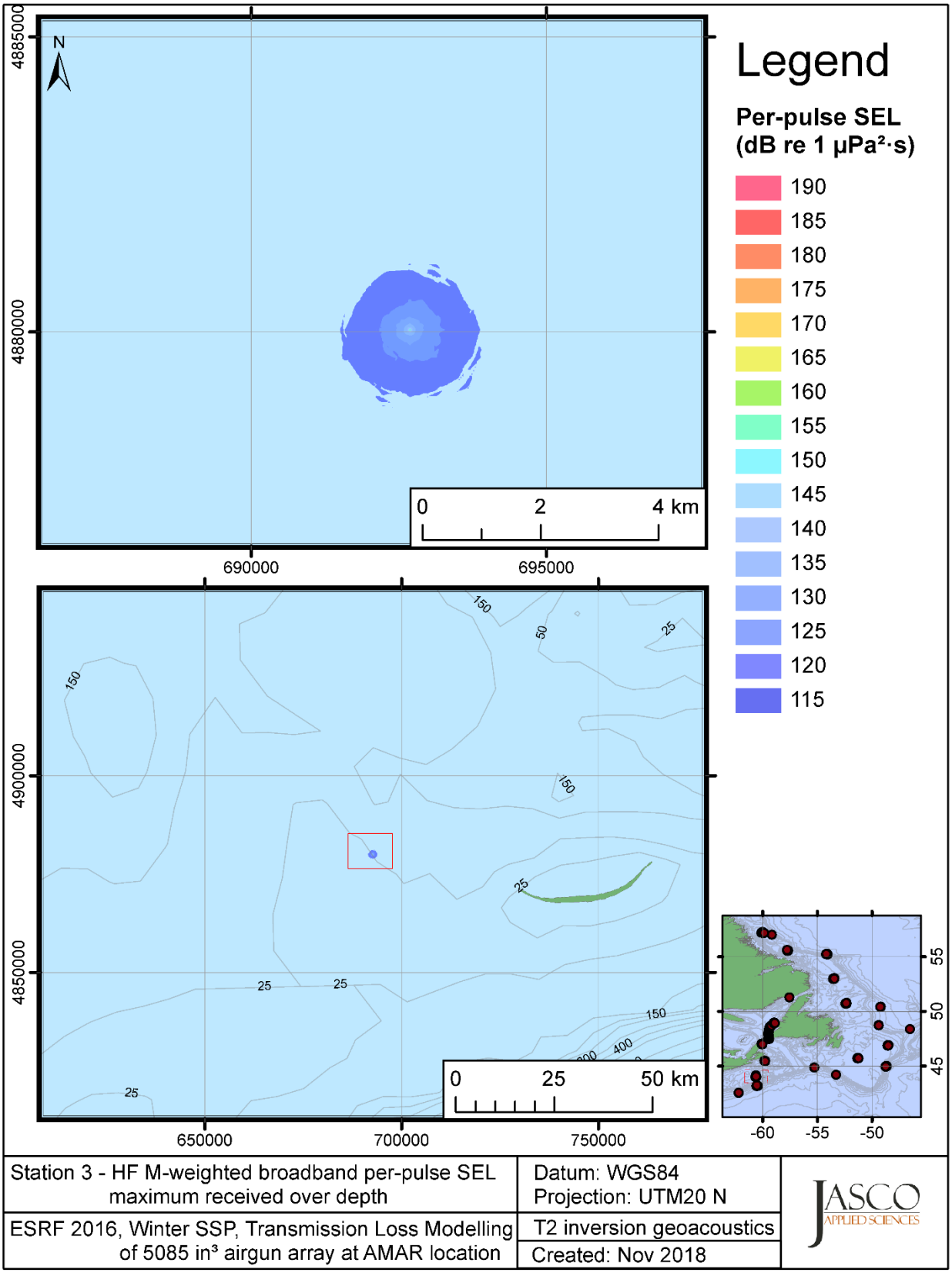

Figure C-495. Stn 3, HF M-weighted maximum-over-depth SEL received at any location on the map, modelled using the track 2 inversion geoacoustic bottom, with the airgun array at the AMAR location and GDEM February SSP.

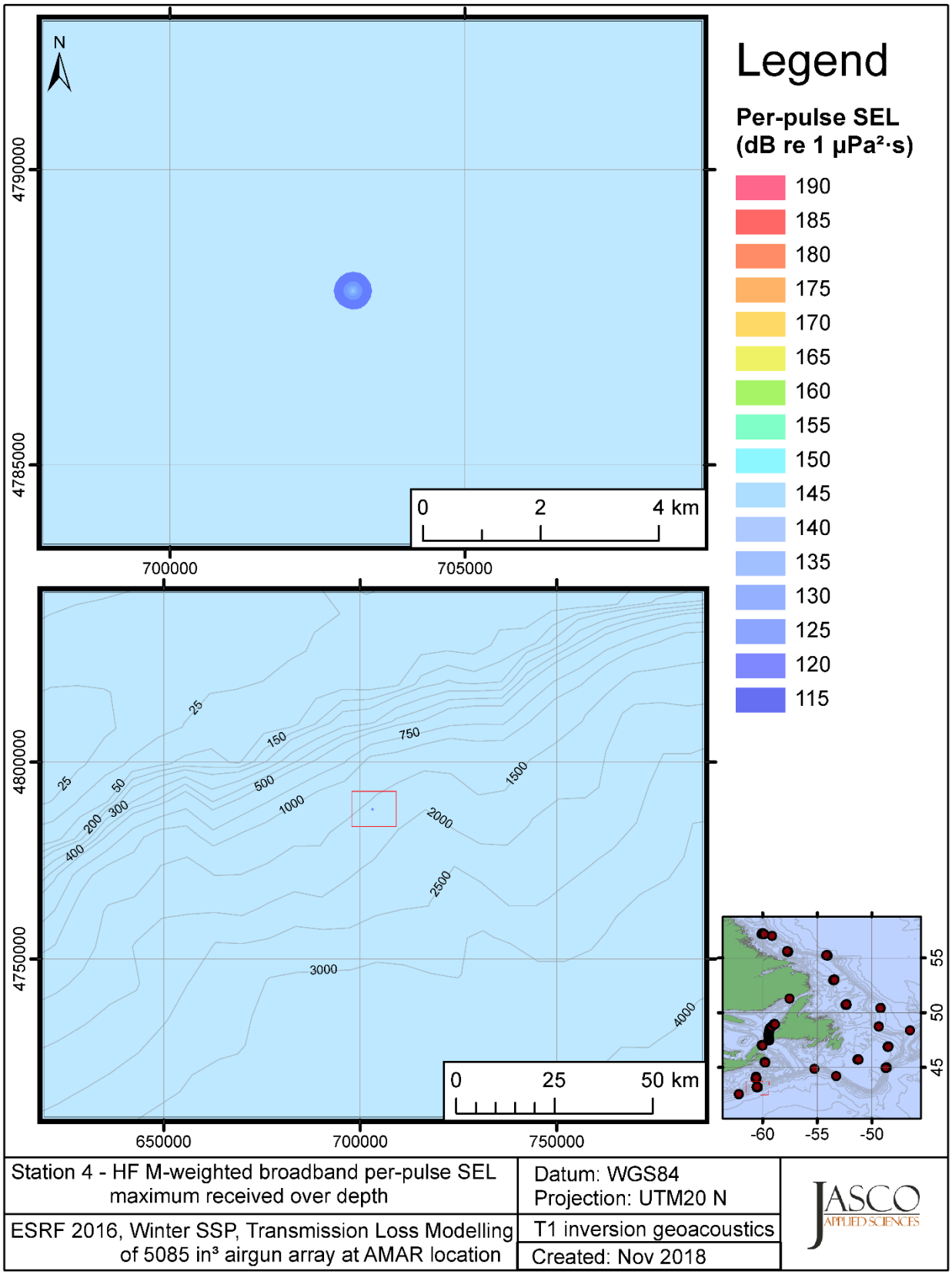

Figure C-496. Stn 4, HF M-weighted maximum-over-depth SEL received at any location on the map, modelled using the track 1 inversion geoacoustic bottom, with the airgun array at the AMAR location and GDEM February SSP.

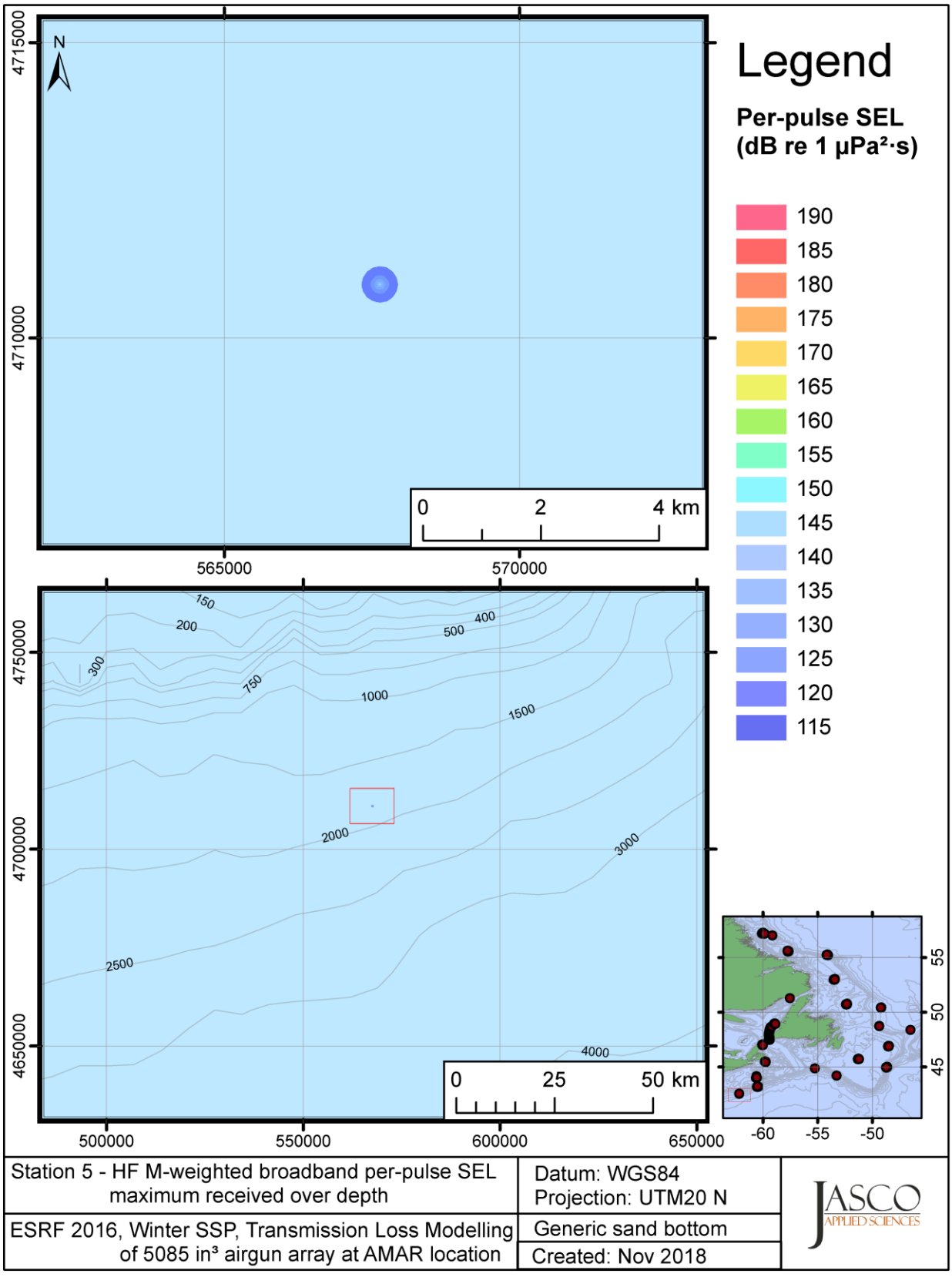

Figure C-497. Stn 5, HF M-weighted maximum-over-depth SEL received at any location on the map, modelled using a generic sand bottom, with the airgun array at the AMAR location and GDEM February SSP.

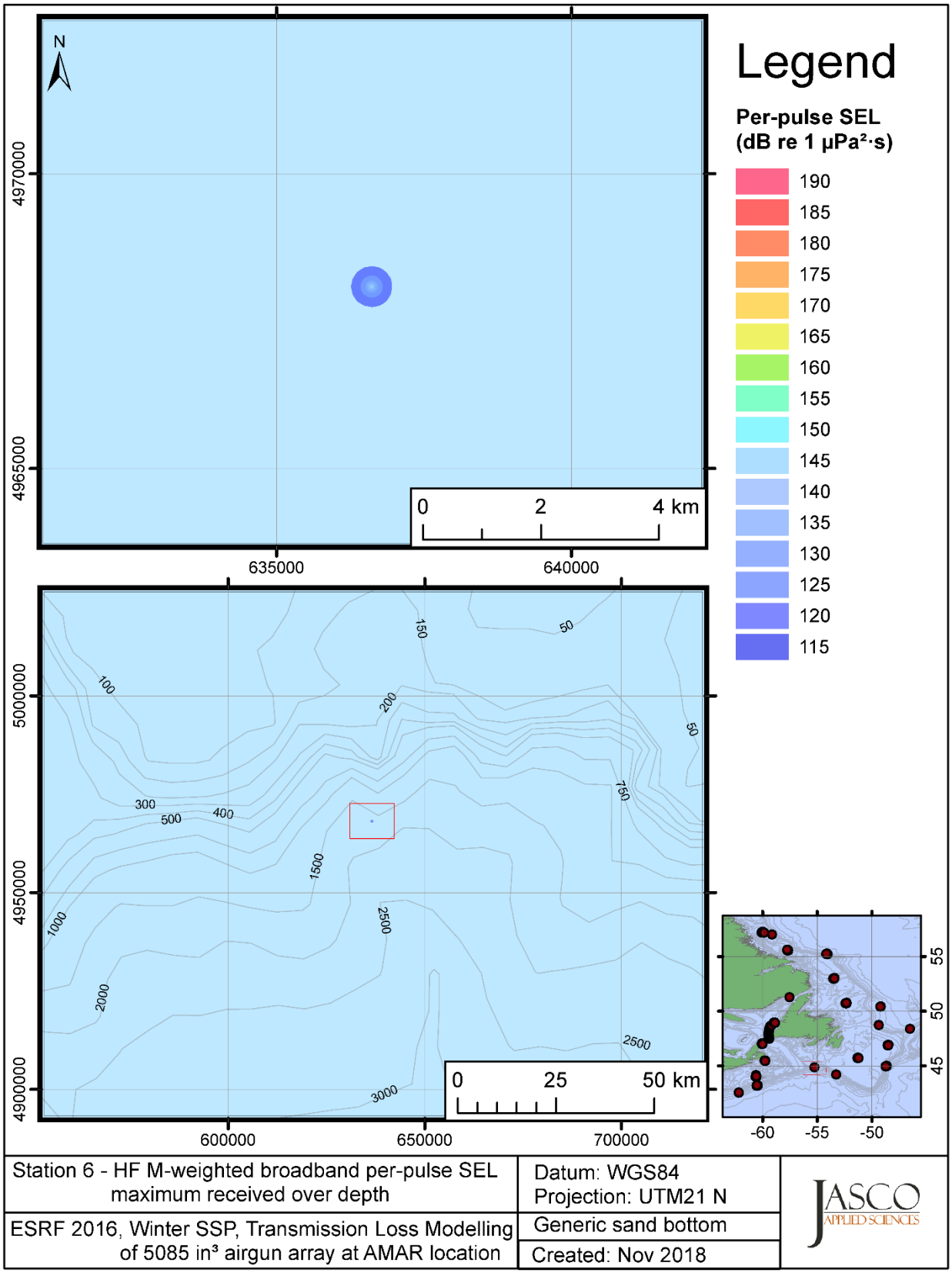

Figure C-498. Stn 6, HF M-weighted maximum-over-depth SEL received at any location on the map, modelled using a generic sand bottom, with the airgun array at the AMAR location and GDEM February SSP.

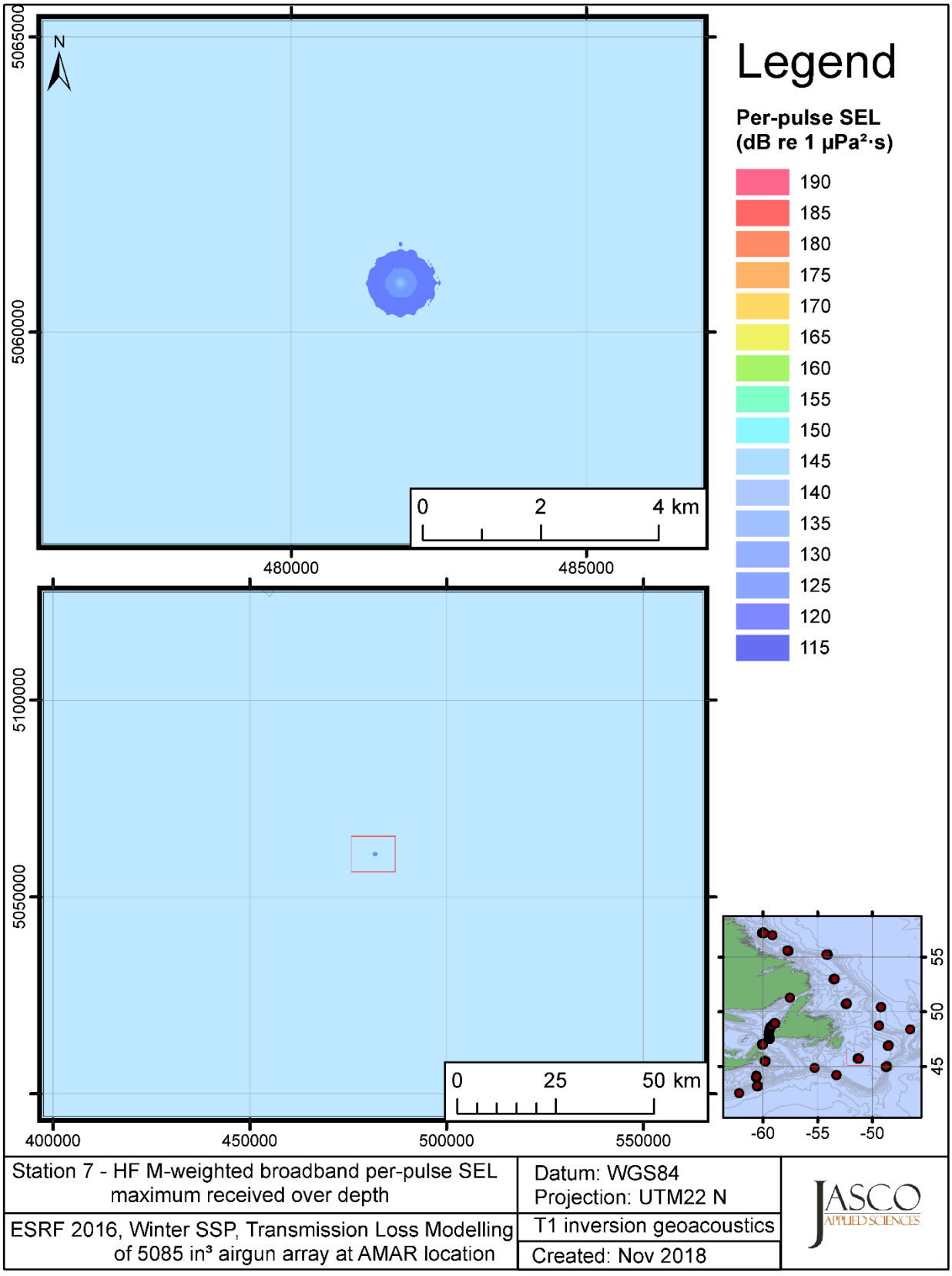

Figure C-499. Stn 7, HF M-weighted maximum-over-depth SEL received at any location on the map, modelled using the track 1 inversion geoacoustic bottom, with the airgun array at the AMAR location and GDEM February SSP.

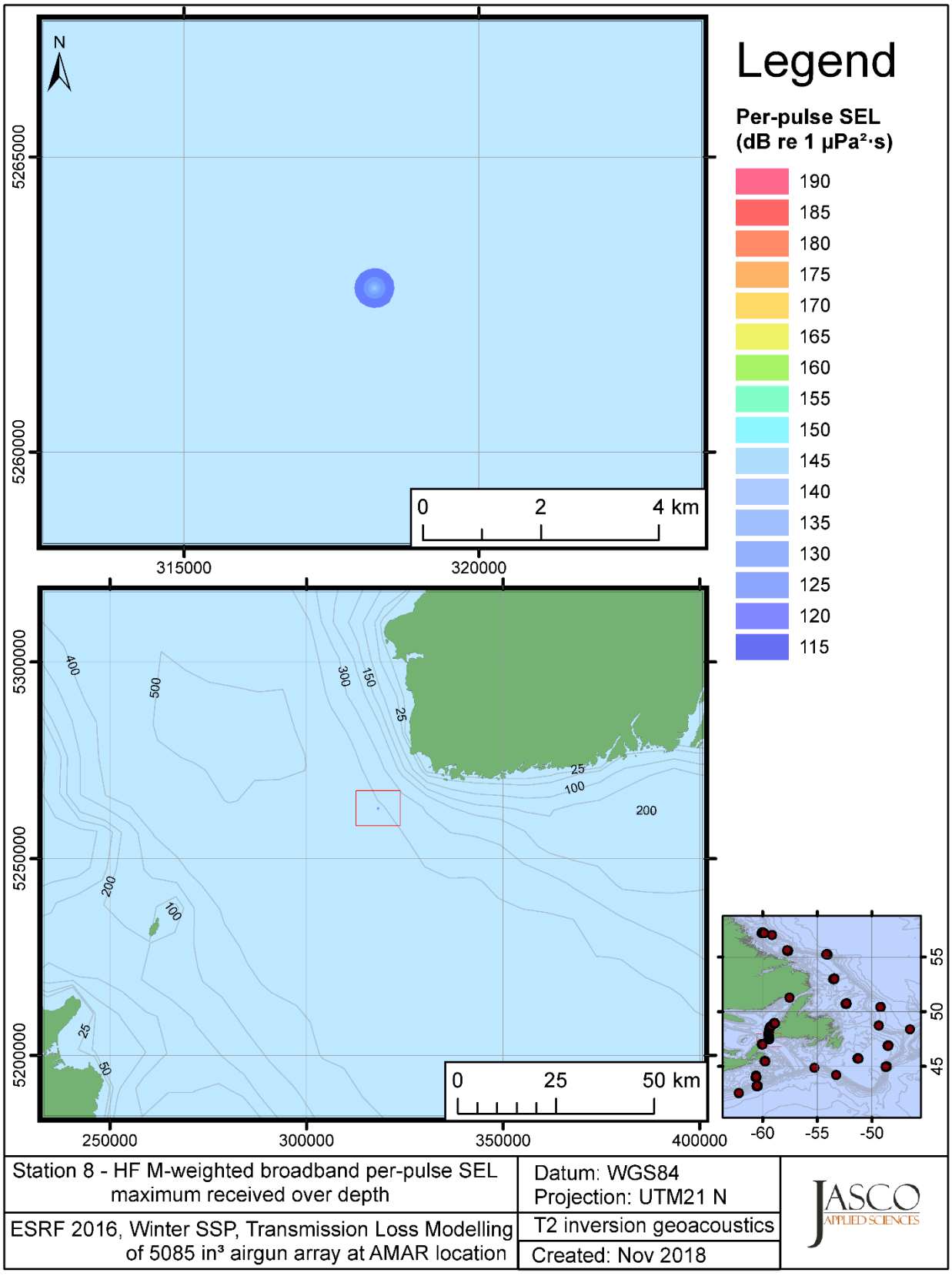

Figure C-500. Stn 8, HF M-weighted maximum-over-depth SEL received at any location on the map, modelled using the track 2 inversion geoacoustic bottom, with the airgun array at the AMAR location and GDEM February SSP.

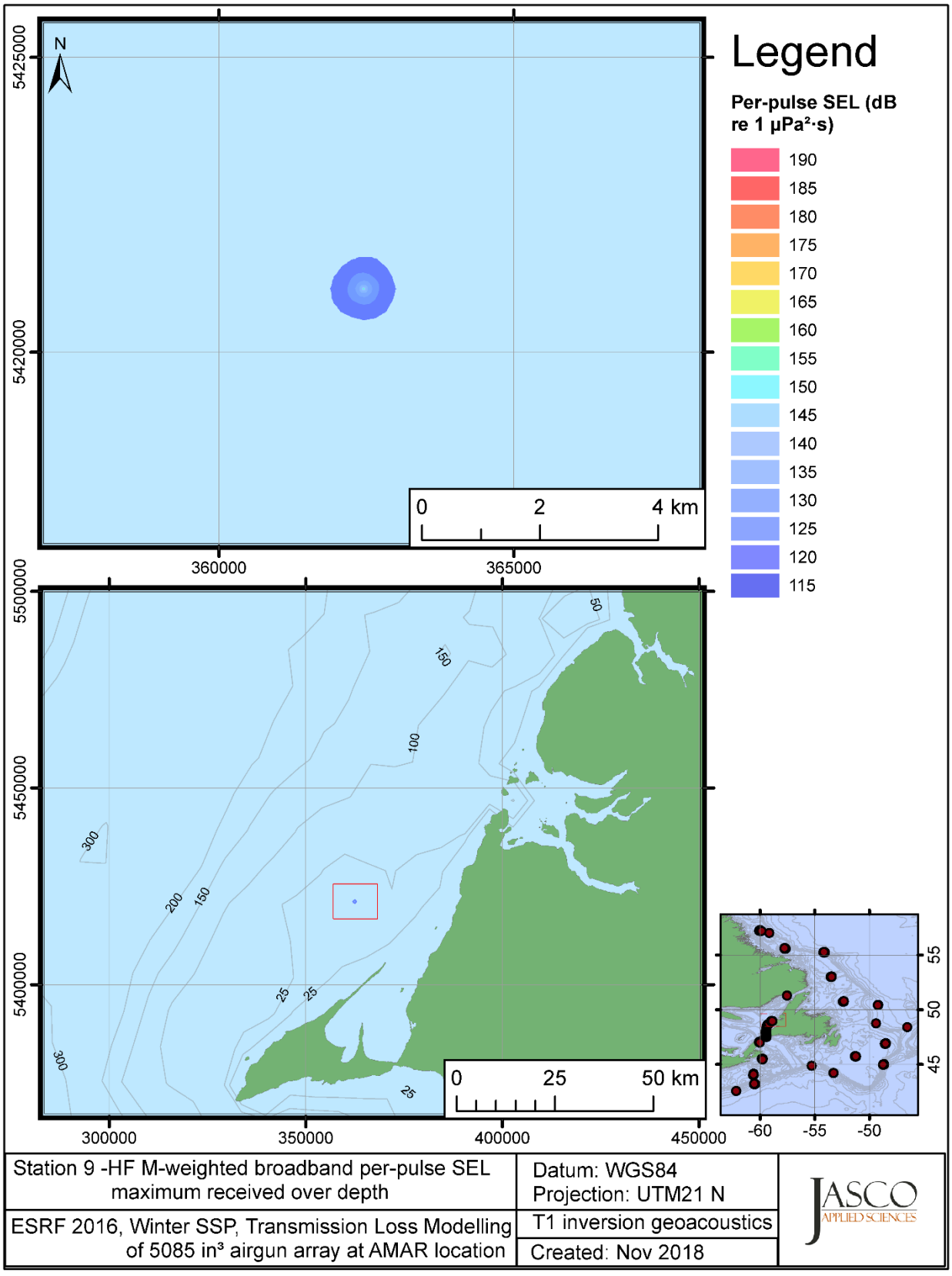

Figure C-501. Stn 9, HF M-weighted maximum-over-depth SEL received at any location on the map, modelled using the track 1 inversion geoacoustic bottom, with the airgun array at the AMAR location and GDEM February SSP.

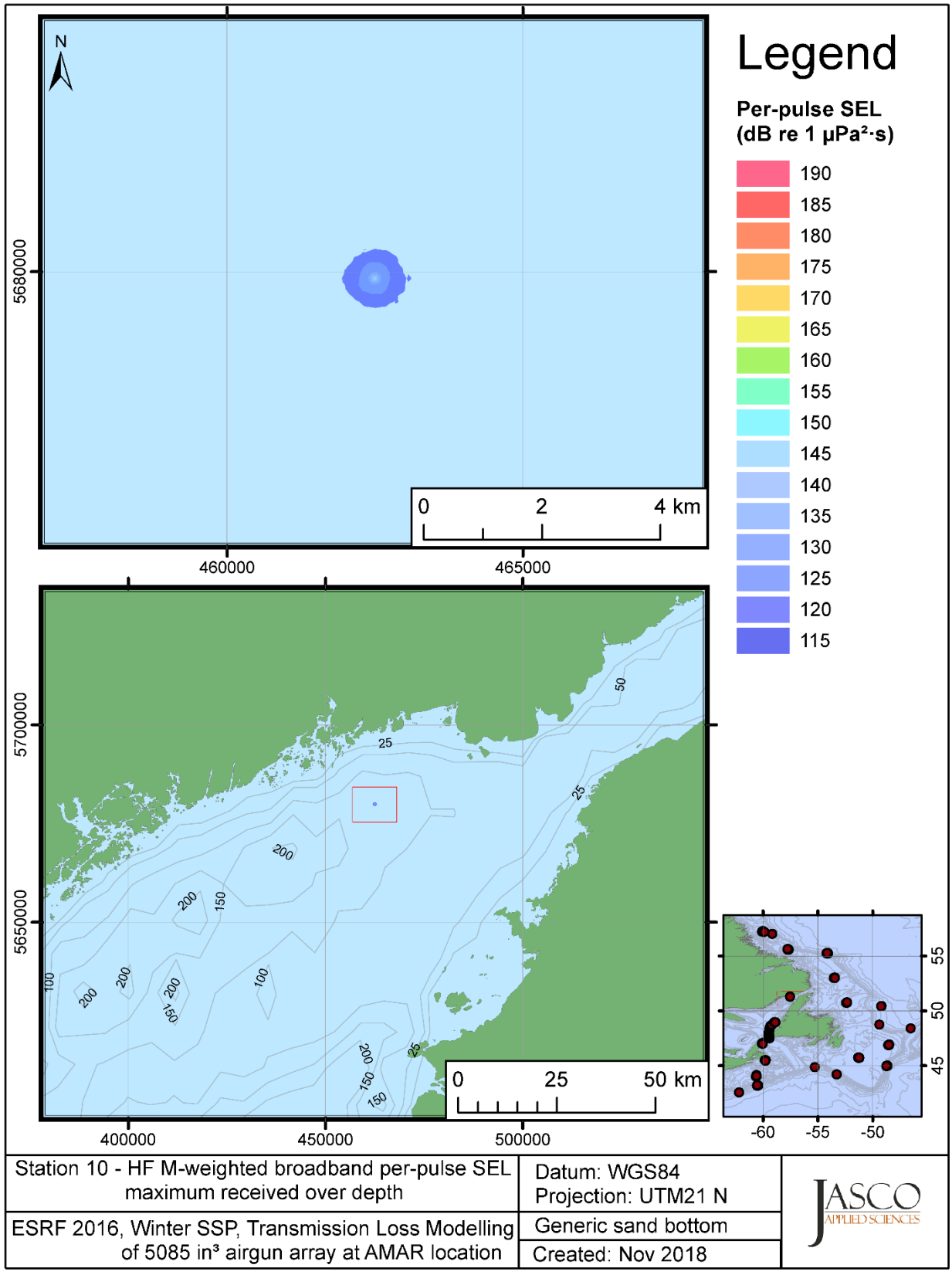

Figure C-502. Stn 10, HF M-weighted maximum-over-depth SEL received at any location on the map, modelled using a generic sand bottom, with the airgun array at the AMAR location and GDEM February SSP.

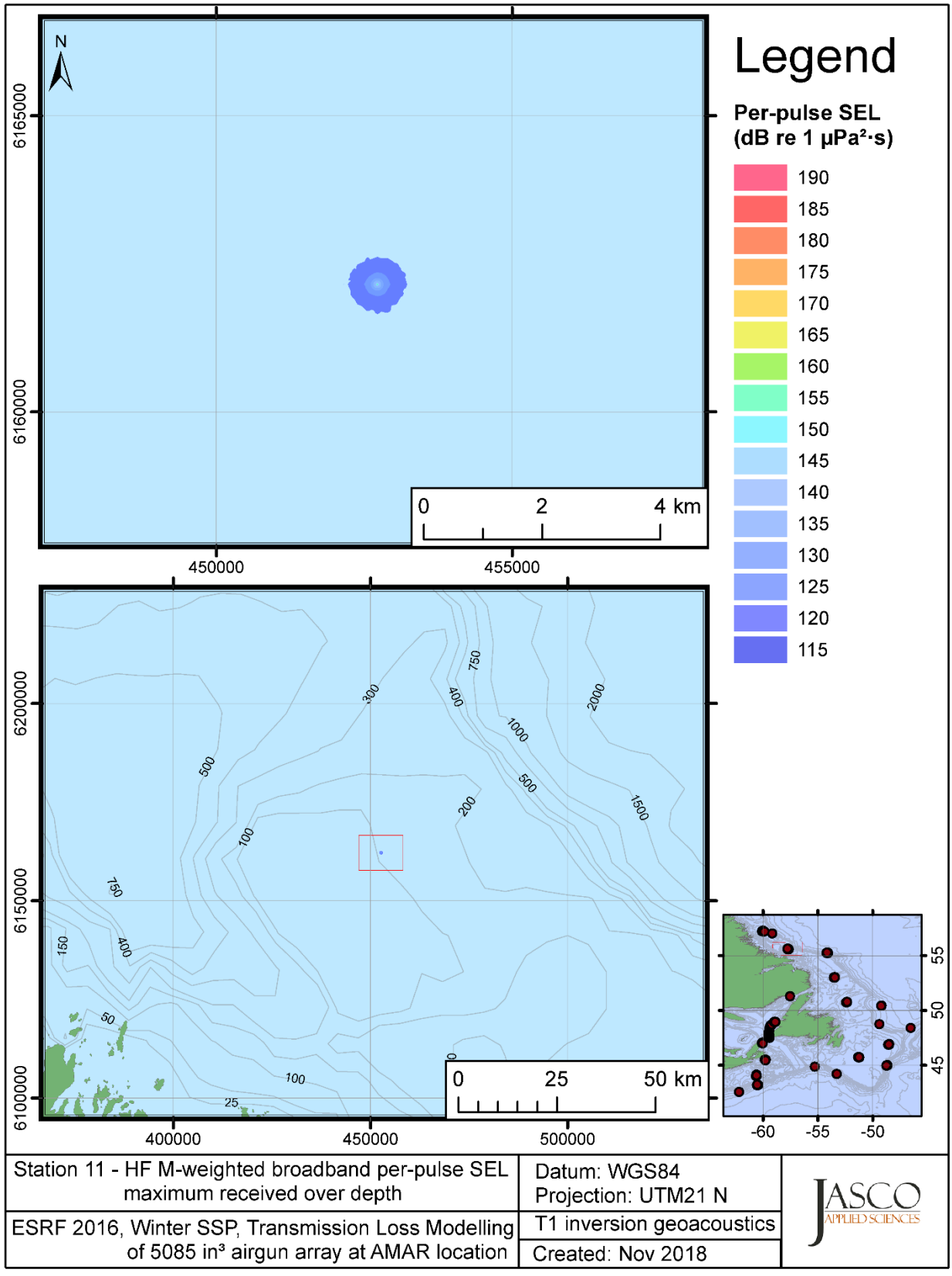

Figure C-503. Stn 11, HF M-weighted maximum-over-depth SEL received at any location on the map, modelled using the track 1 inversion geoacoustic bottom, with the airgun array at the AMAR location and GDEM February SSP.

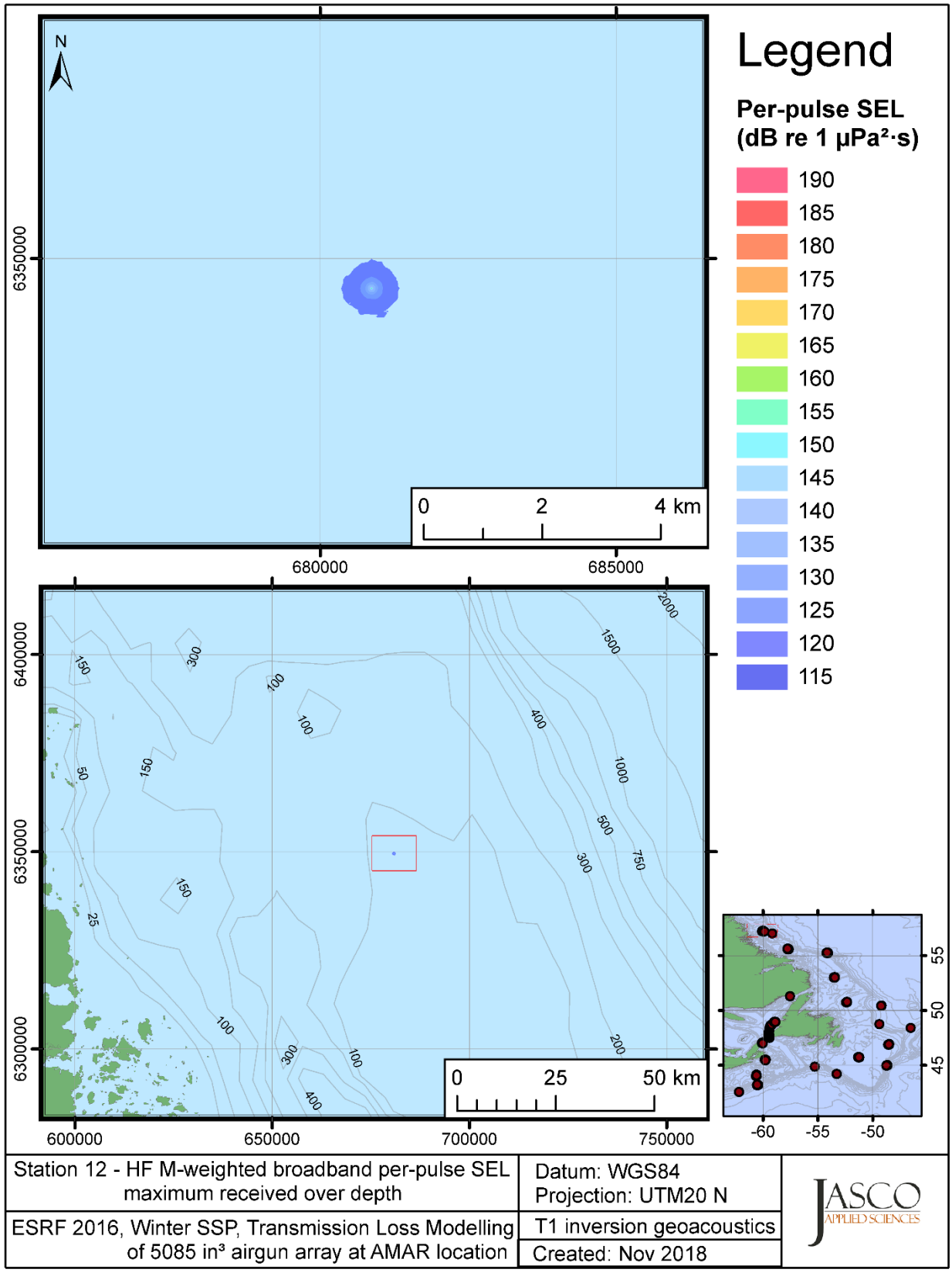

Figure C-504. Stn 12, HF M-weighted maximum-over-depth SEL received at any location on the map, modelled using the track 1 inversion geoacoustic bottom, with the airgun array at the AMAR location and GDEM February SSP.

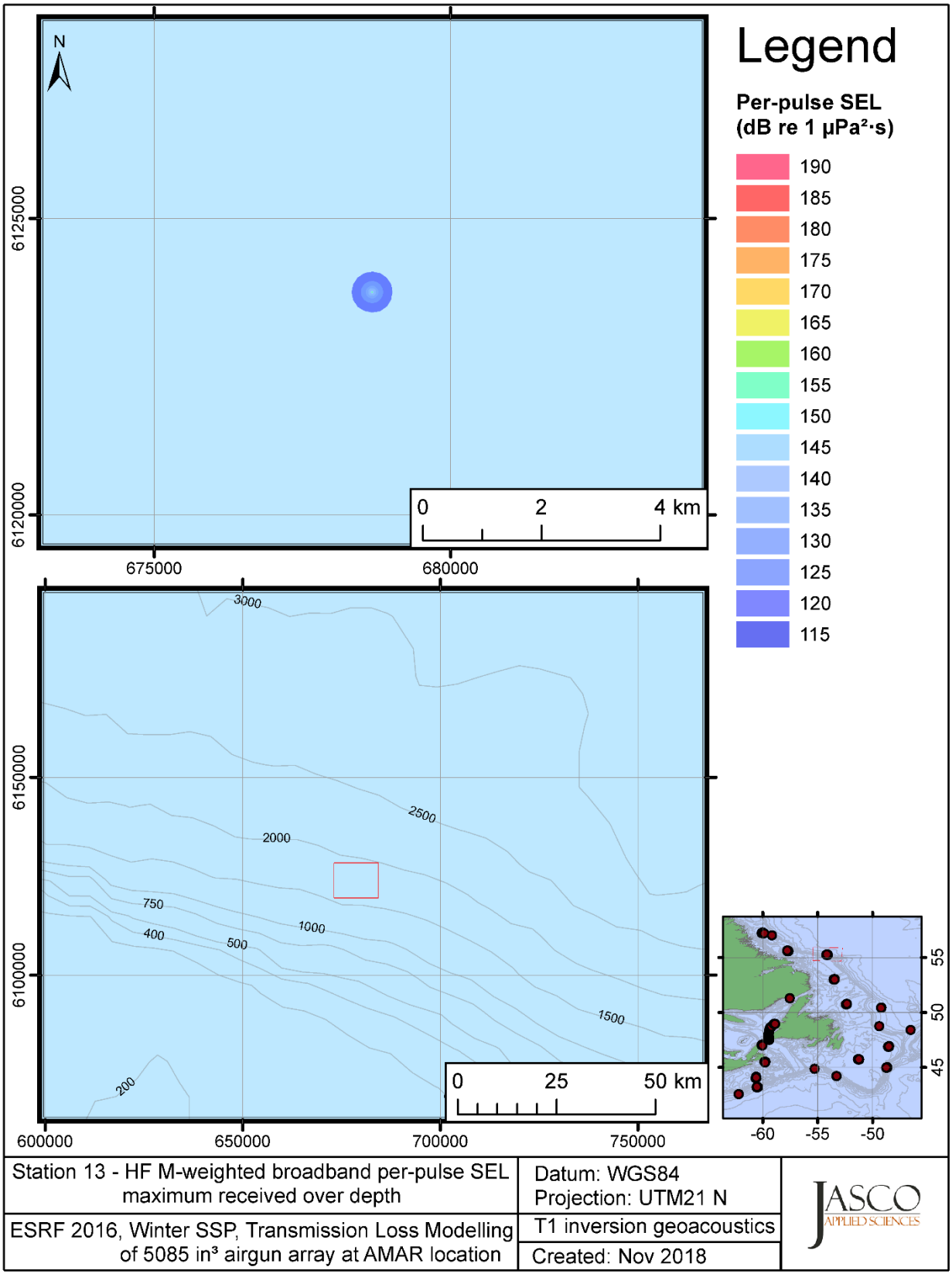

Figure C-505. Stn 13, HF M-weighted maximum-over-depth SEL received at any location on the map, modelled using the track 1 inversion geoacoustic bottom, with the airgun array at the AMAR location and GDEM February SSP.

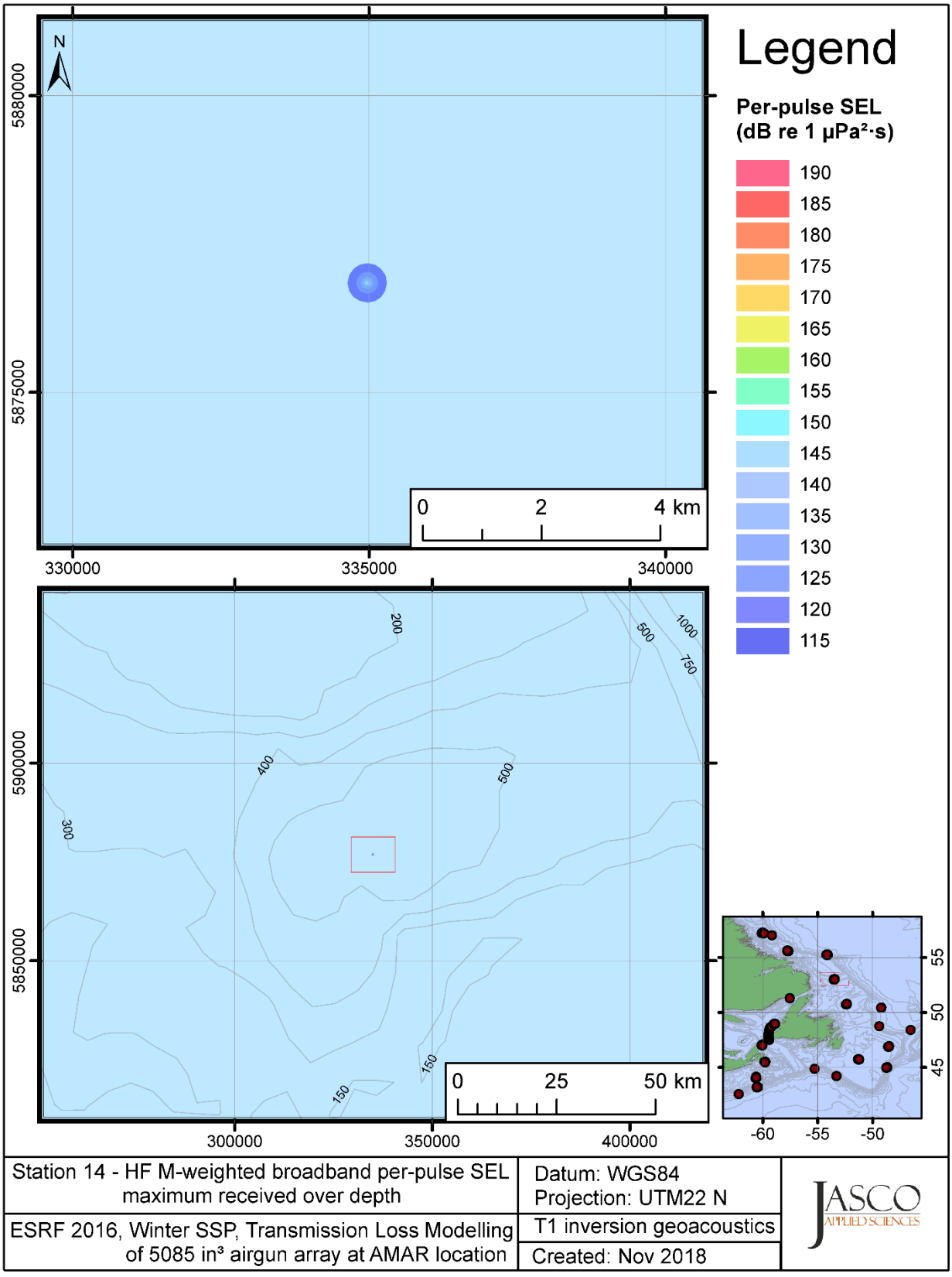

Figure C-506. Stn 14, HF M-weighted maximum-over-depth SEL received at any location on the map, modelled using the track 1 inversion geoacoustic bottom, with the airgun array at the AMAR location and GDEM February SSP.

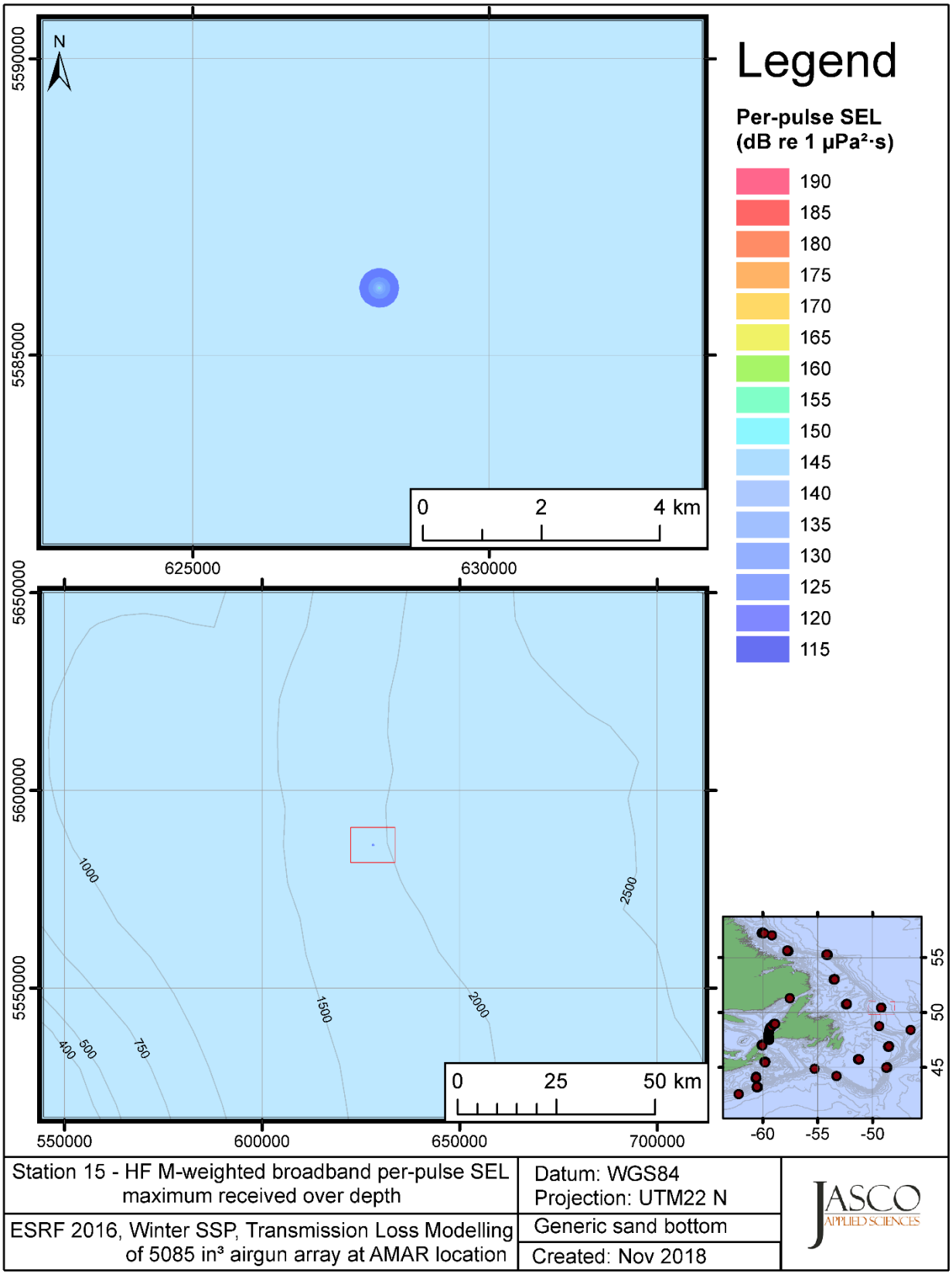

Figure C-507. Stn 15, HF M-weighted maximum-over-depth SEL received at any location on the map, modelled using a generic sand bottom, with the airgun array at the AMAR location and GDEM February SSP.

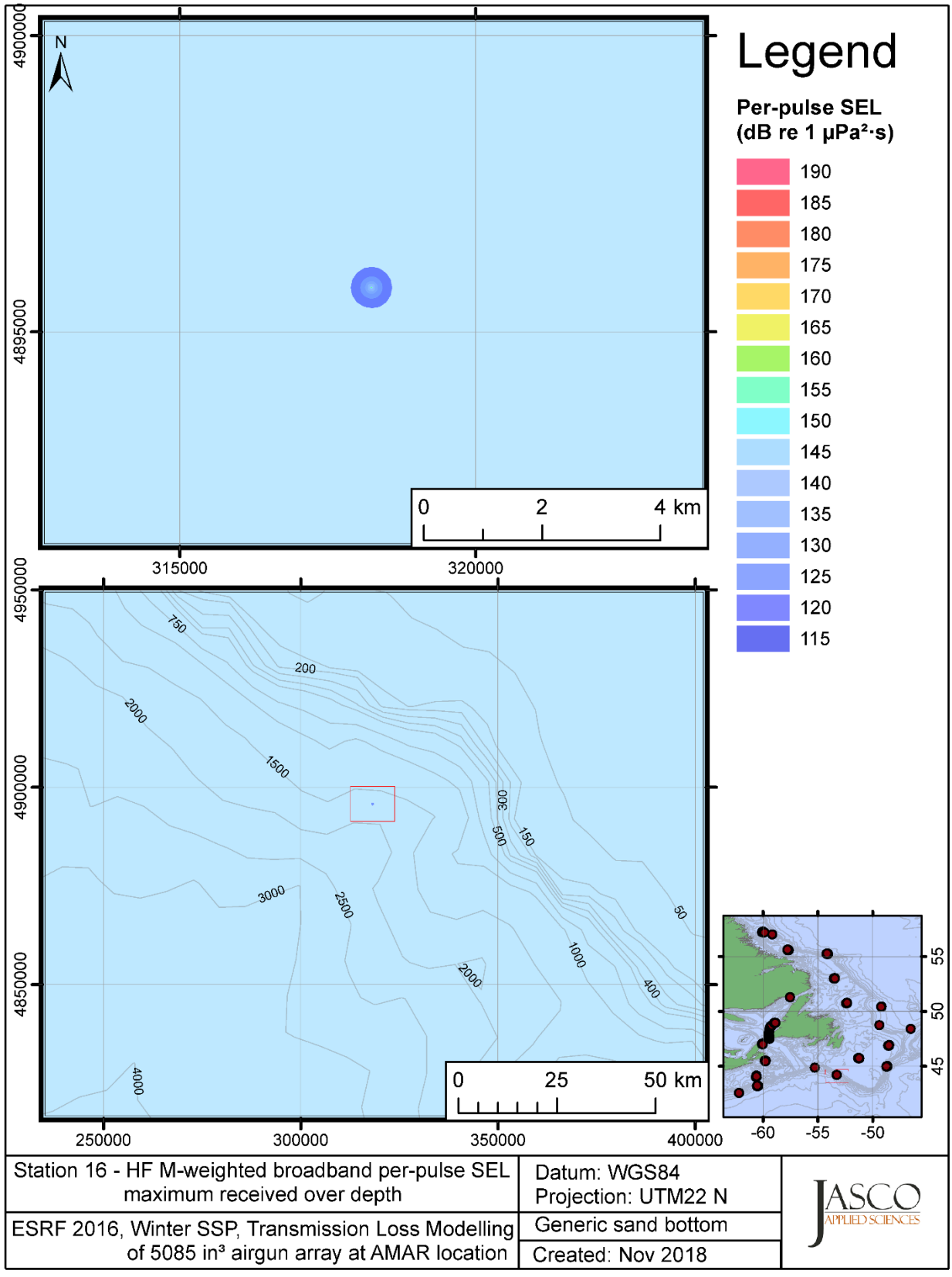

Figure C-508. Stn 16, HF M-weighted maximum-over-depth SEL received at any location on the map, modelled using a generic sand bottom, with the airgun array at the AMAR location and GDEM February SSP.

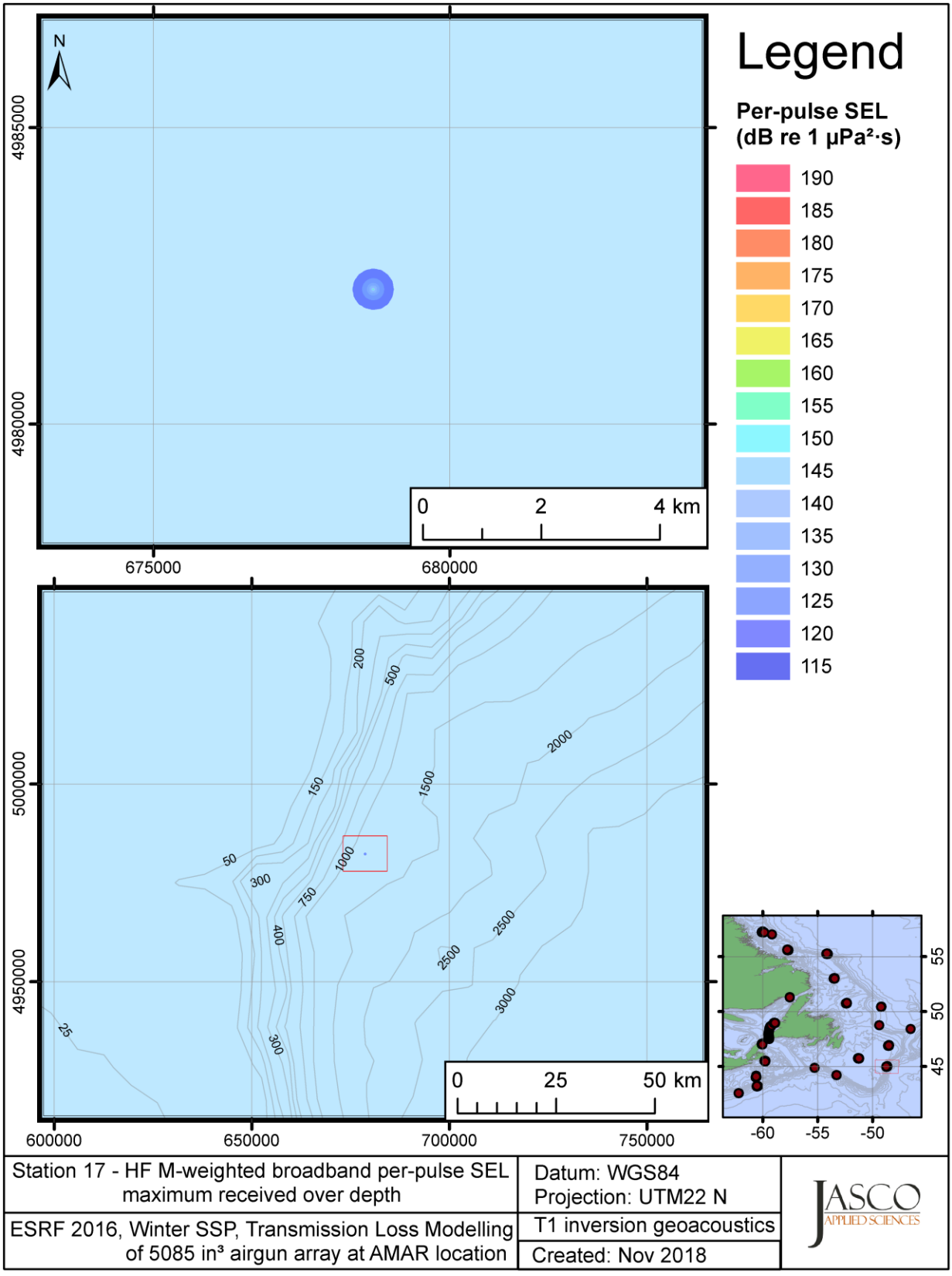

Figure C-509. Stn 17, HF M-weighted maximum-over-depth SEL received at any location on the map, modelled using the track 1 inversion geoacoustic bottom, with the airgun array at the AMAR location and GDEM February SSP.

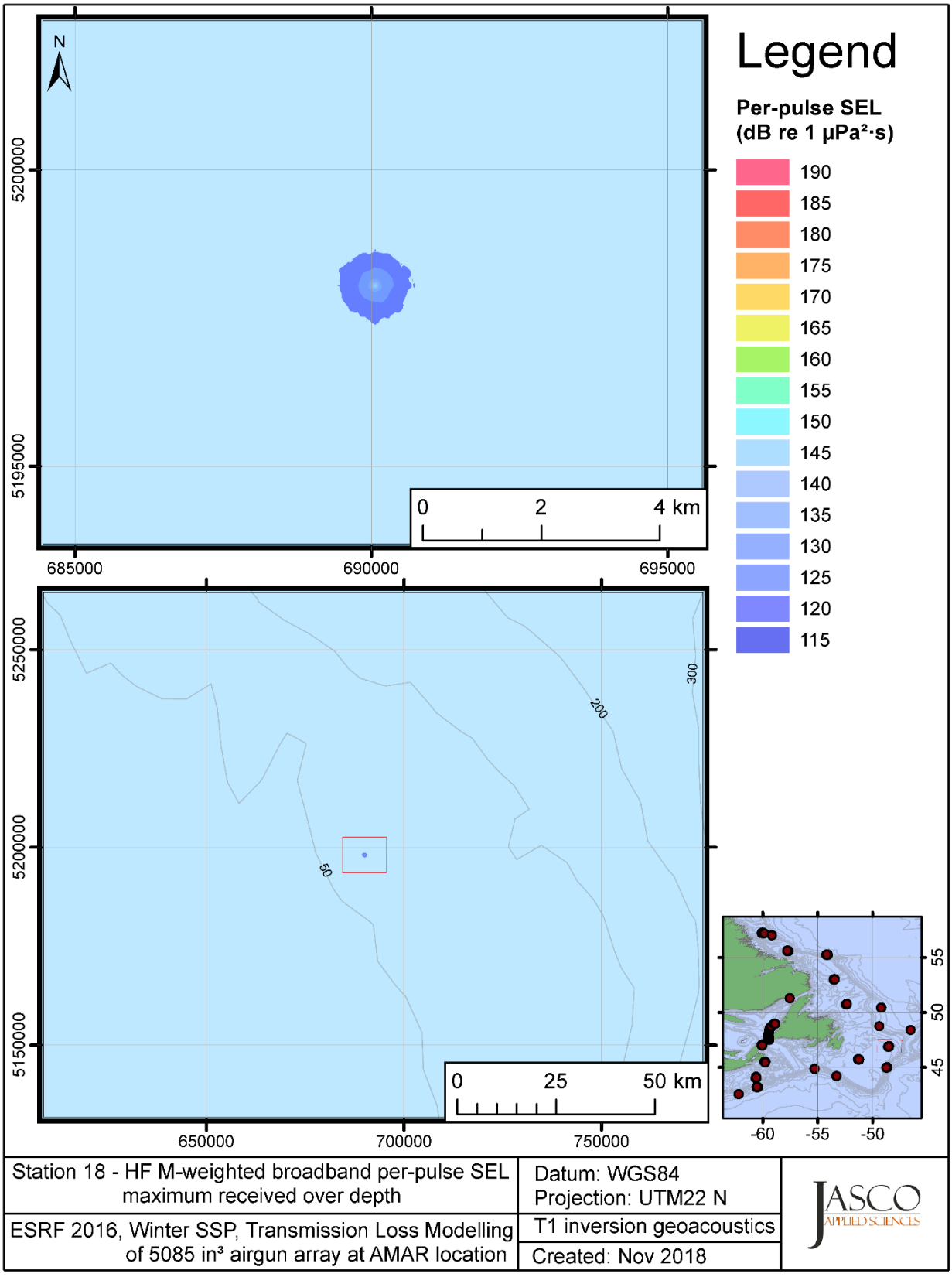

Figure C-510. Stn 18, HF M-weighted maximum-over-depth SEL received at any location on the map, modelled using the track 1 inversion geoacoustic bottom, with the airgun array at the AMAR location and GDEM February SSP.

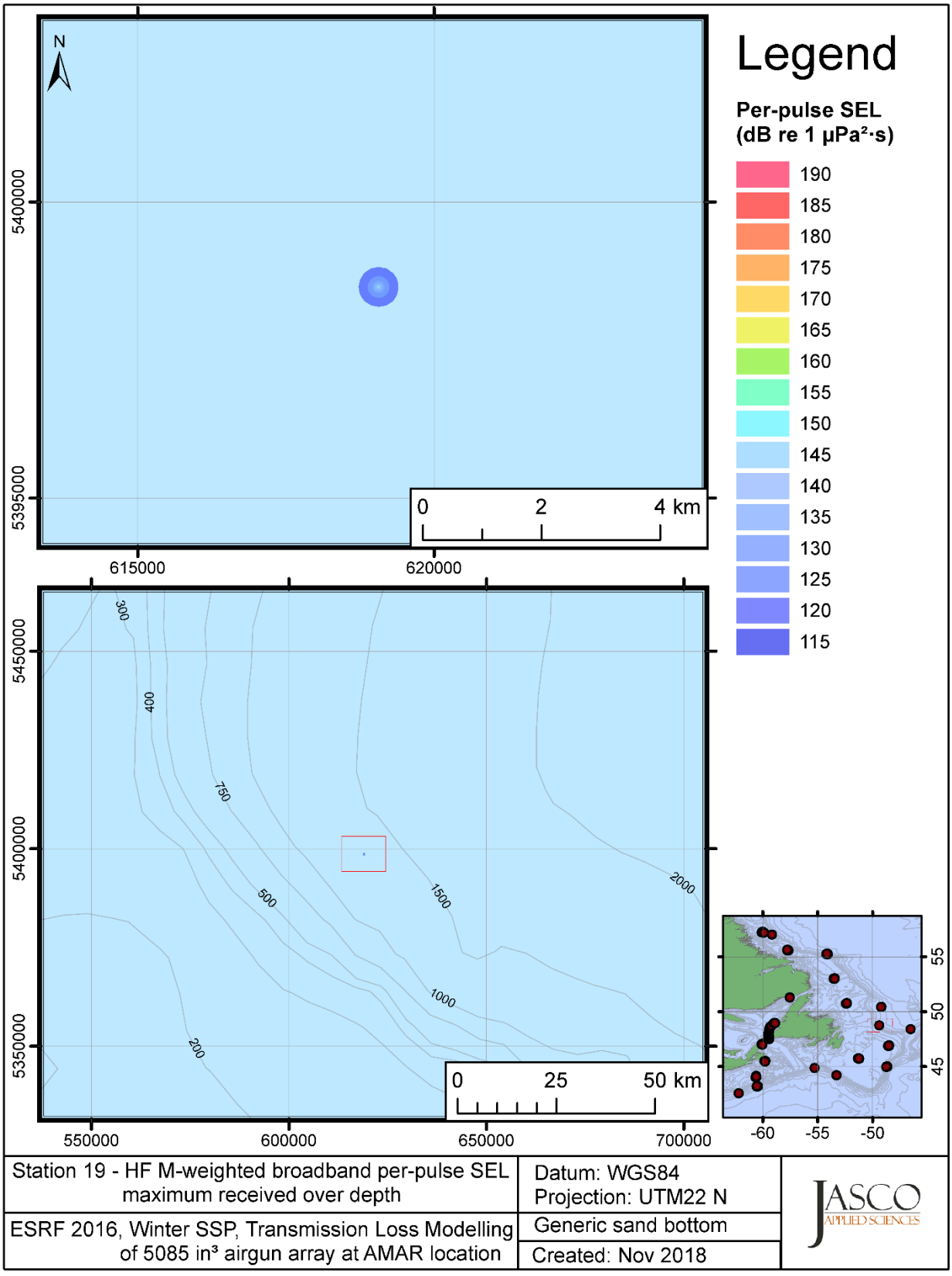

Figure C-511. Stn 19, HF M-weighted maximum-over-depth SEL received at any location on the map, modelled using a generic sand bottom, with the airgun array at the AMAR location and GDEM February SSP.

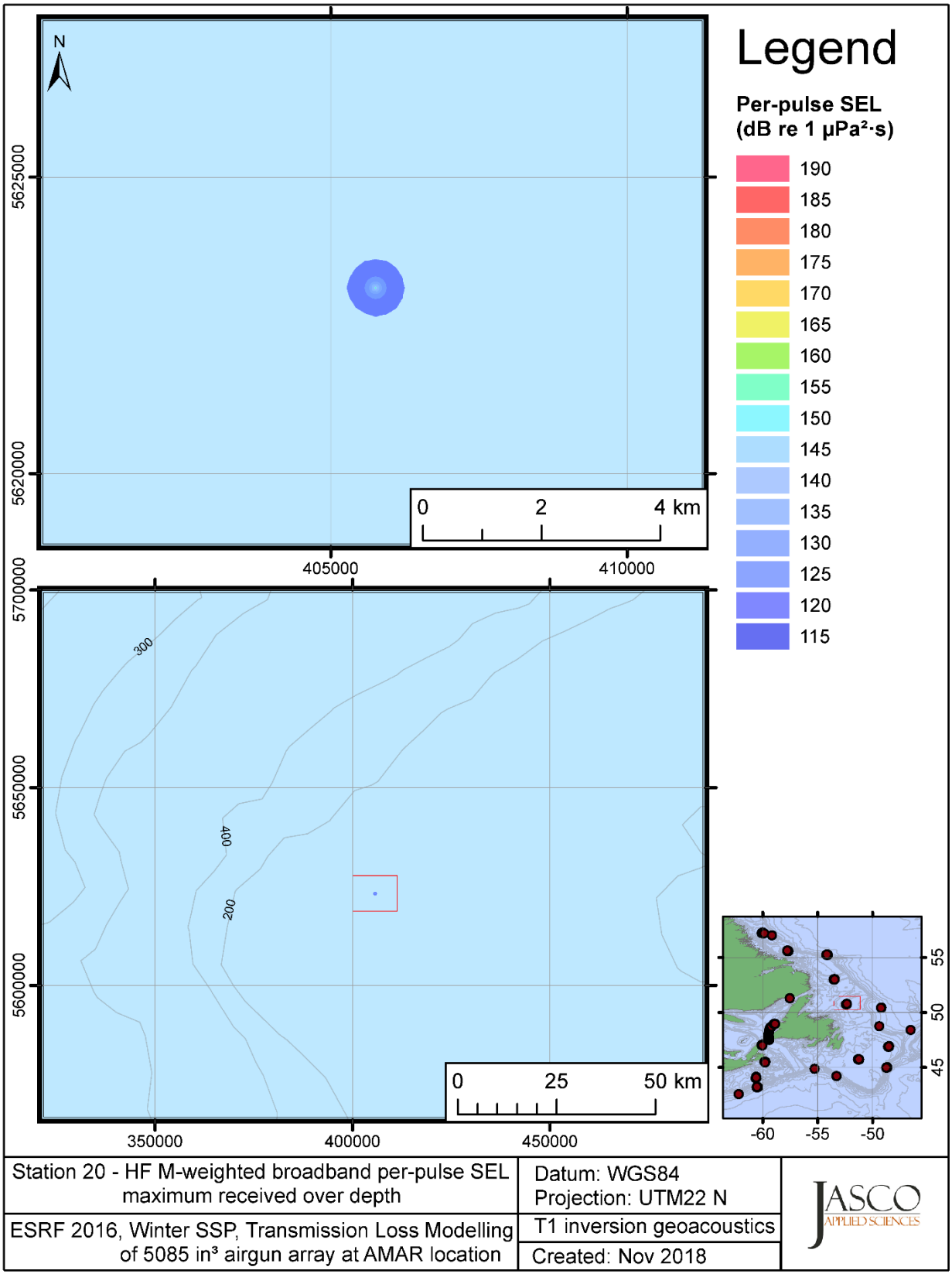

Figure C-512. Stn 20, HF M-weighted maximum-over-depth SEL received at any location on the map, modelled using the track 1 inversion geoacoustic bottom, with the airgun array at the AMAR location and GDEM February SSP.

C.17. Modelling OP M-weighted Max-over-depth Received Level at Distant Locations - Winter

This section presents the results of modelling the maximum-over-depth per-pulse sound exposure level (SEL) received at distant receiver locations (varied in range and azimuth) for the source held fixed at the AMAR location. The modelling uses the geoacoustic inversion bottom parameters at the 14 sites where they are available and only uses a generic sand bottom at the other six sites. The modelling results are presented in the form of coloured maps where the colour at any map location represents the predicted maximum-over-depth received level at that spot on the map. This section includes only the otariid pinnipeds in water (OP) marine-mammal-weighted per-pulse SEL results; additional maps for other marine mammal received level auditory weightings are presented in adjoining sections. The sound speed profiles (SSP) used are detailed in Appendix B.2.

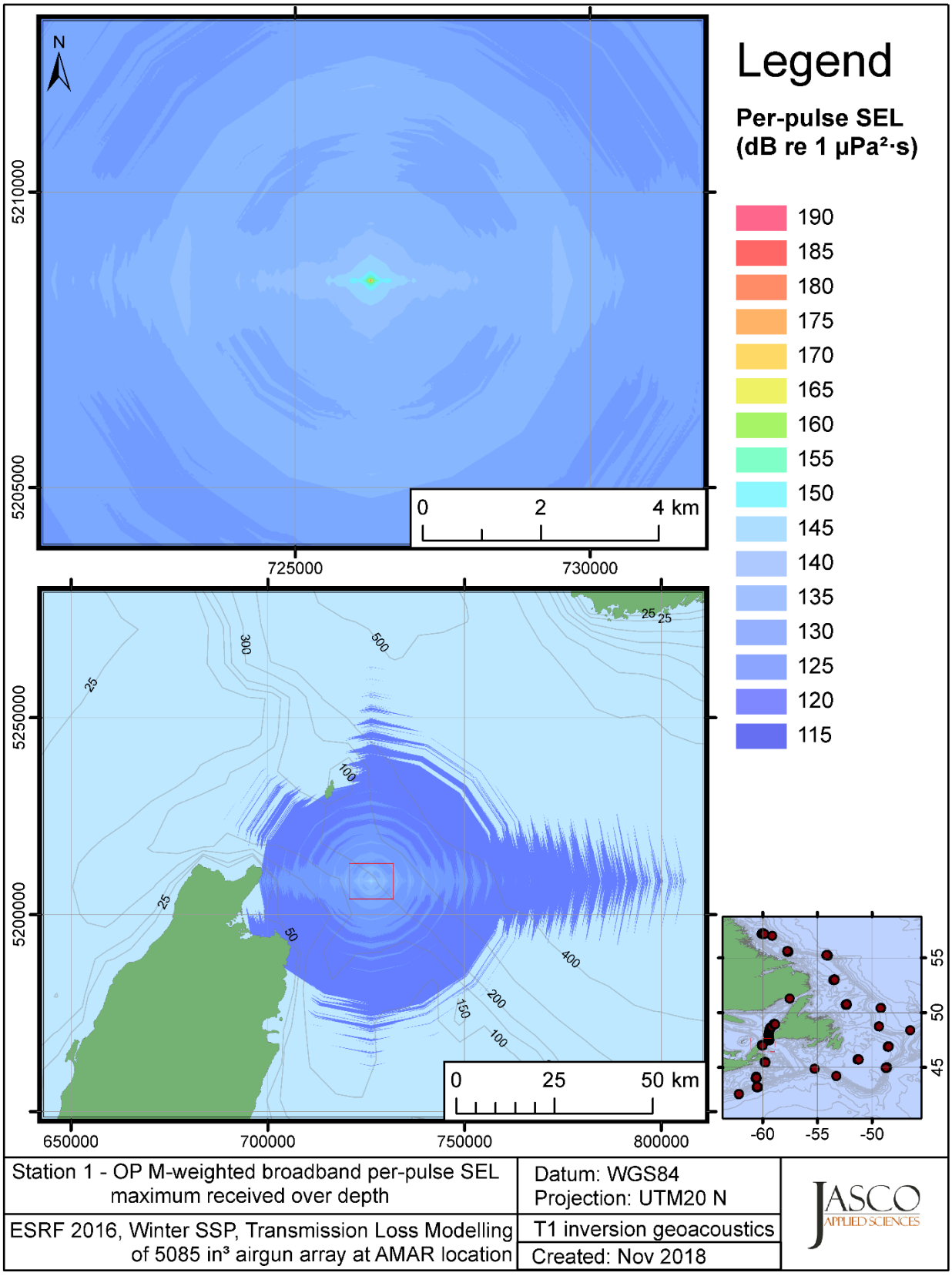

Figure C-513. Stn 1, OP M-weighted maximum-over-depth SEL received at any location on the map, modelled using the track 1 inversion geoacoustic bottom, with the airgun array at the AMAR location and GDEM February SSP.

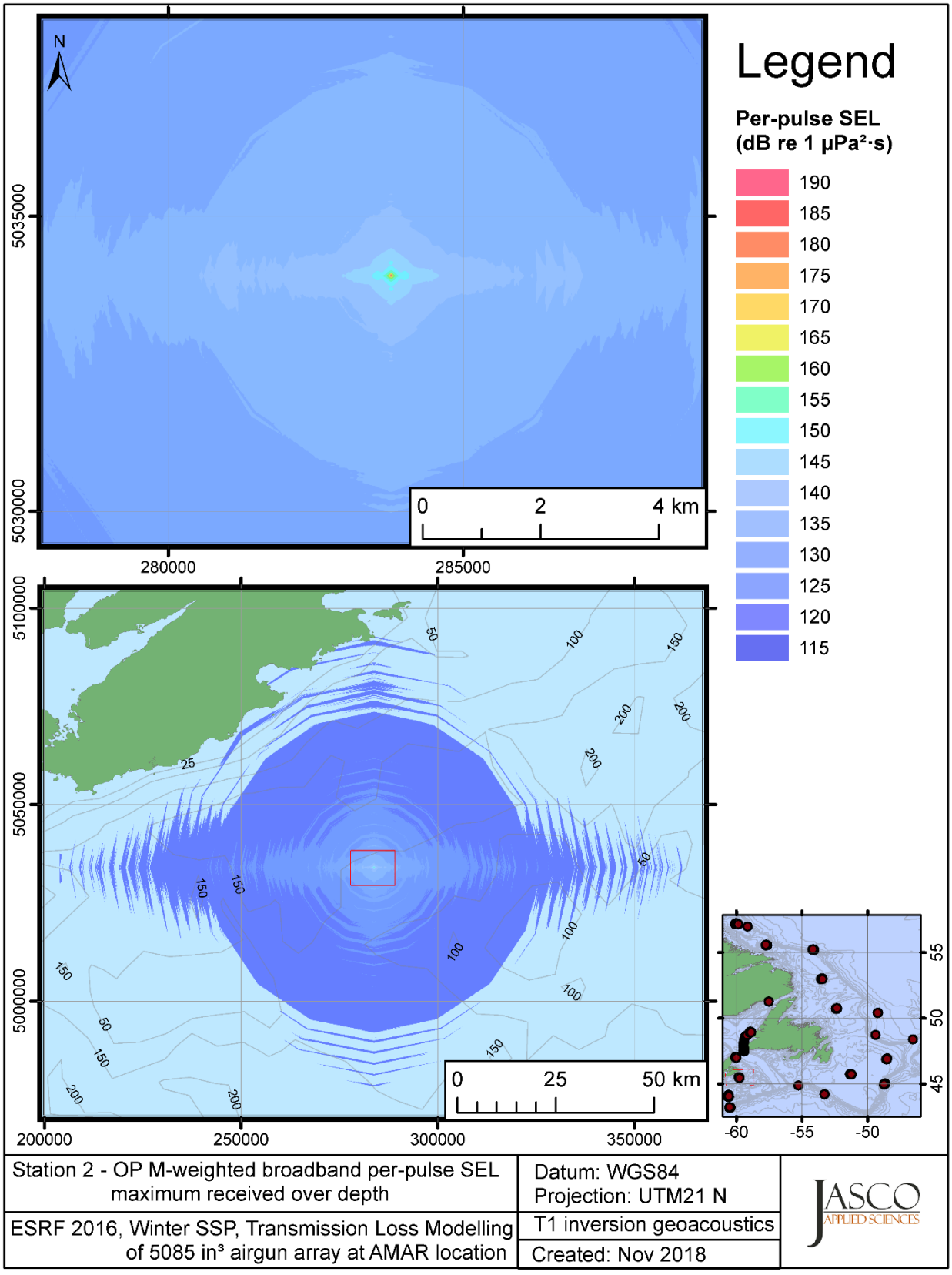

Figure C-514. Stn 2, OP M-weighted maximum-over-depth SEL received at any location on the map, modelled using the track 1 inversion geoacoustic bottom, with the airgun array at the AMAR location and GDEM February SSP.

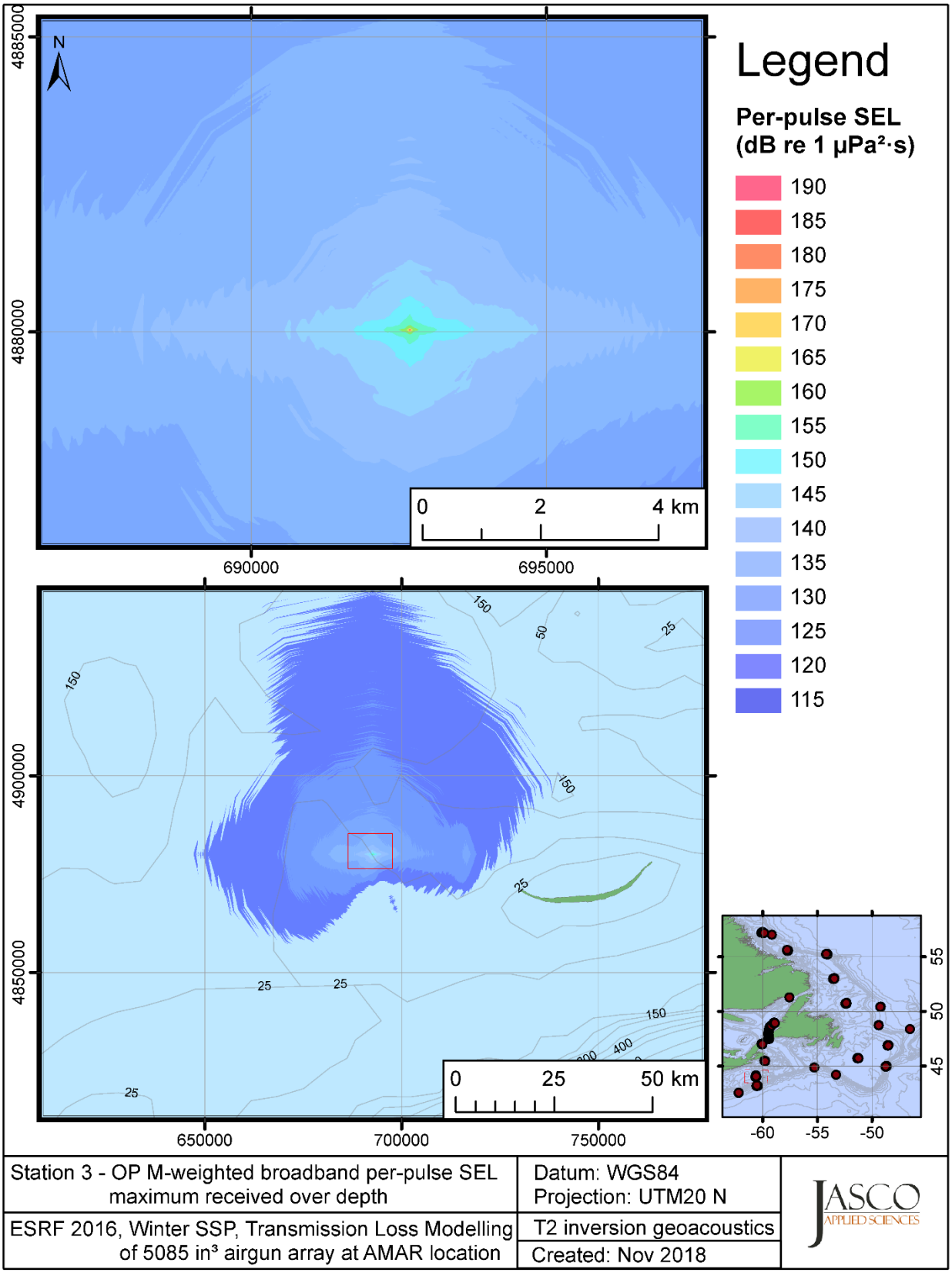

Figure C-515. Stn 3, OP M-weighted maximum-over-depth SEL received at any location on the map, modelled using the track 2 inversion geoacoustic bottom, with the airgun array at the AMAR location and GDEM February SSP.

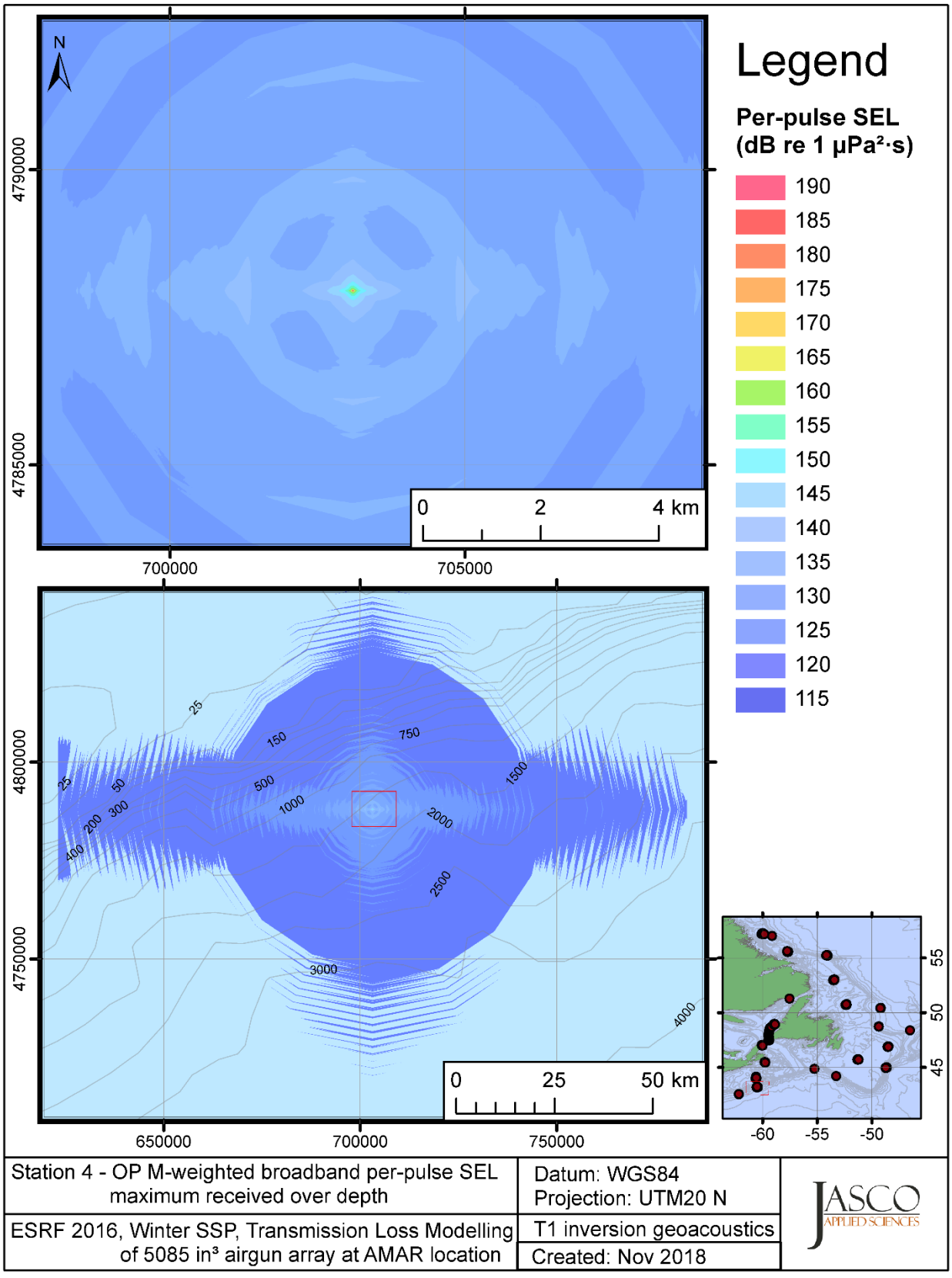

Figure C-516. Stn 4, OP M-weighted maximum-over-depth SEL received at any location on the map, modelled using the track 1 inversion geoacoustic bottom, with the airgun array at the AMAR location and GDEM February SSP.

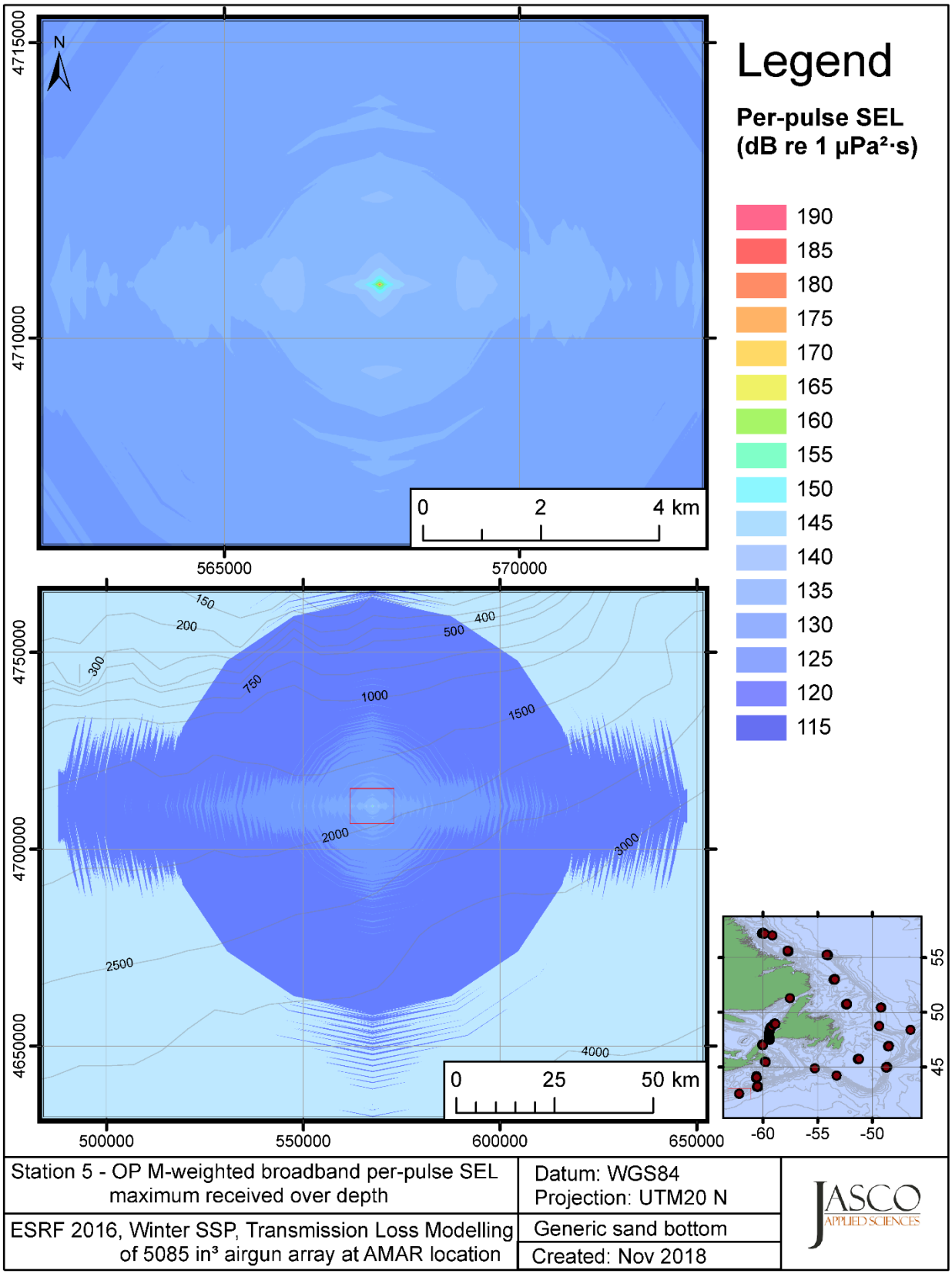

Figure C-517. Stn 5, OP M-weighted maximum-over-depth SEL received at any location on the map, modelled using a generic sand bottom, with the airgun array at the AMAR location and GDEM February SSP.

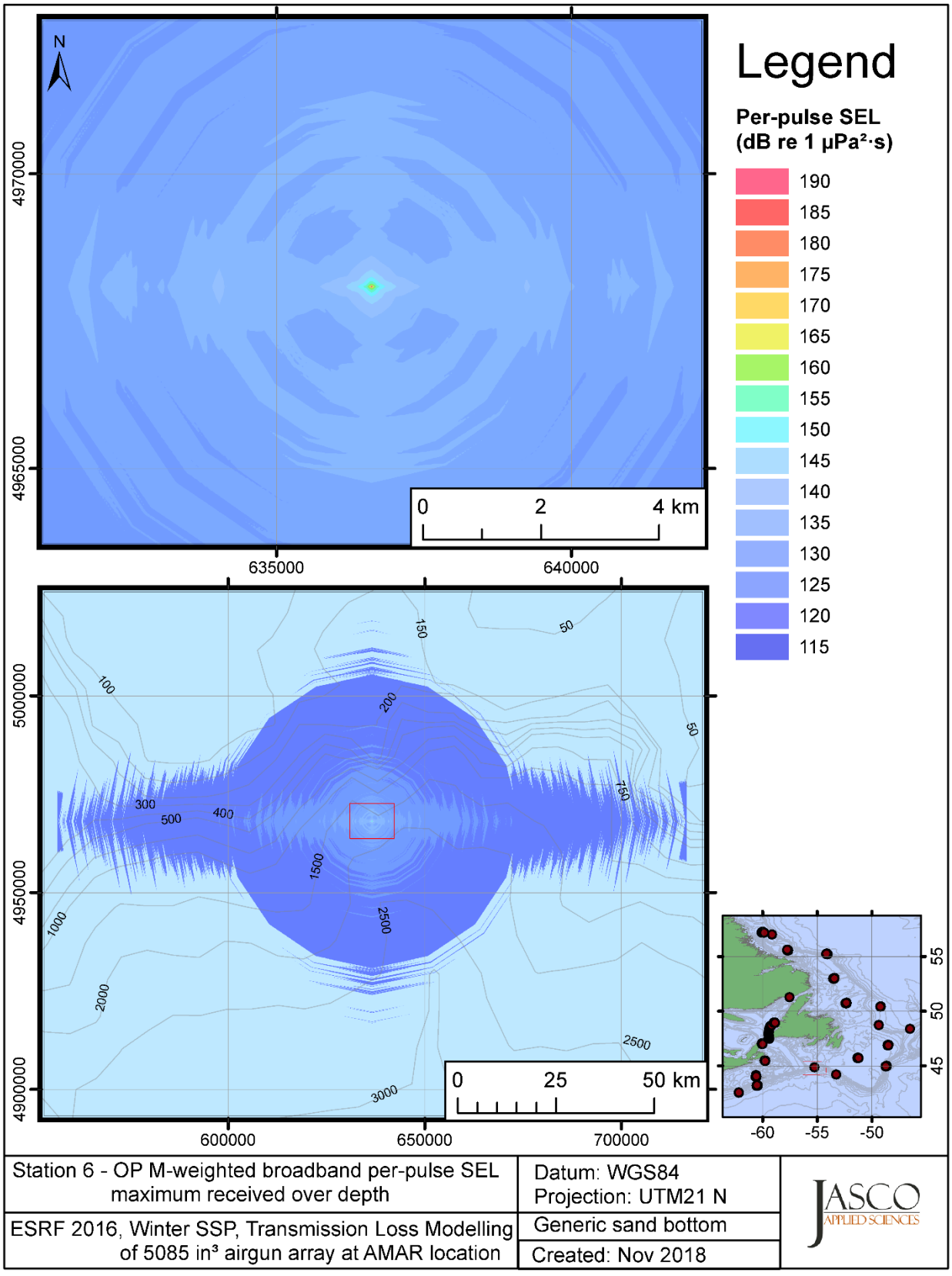

Figure C-518. Stn 6, OP M-weighted maximum-over-depth SEL received at any location on the map, modelled using a generic sand bottom, with the airgun array at the AMAR location and GDEM February SSP.

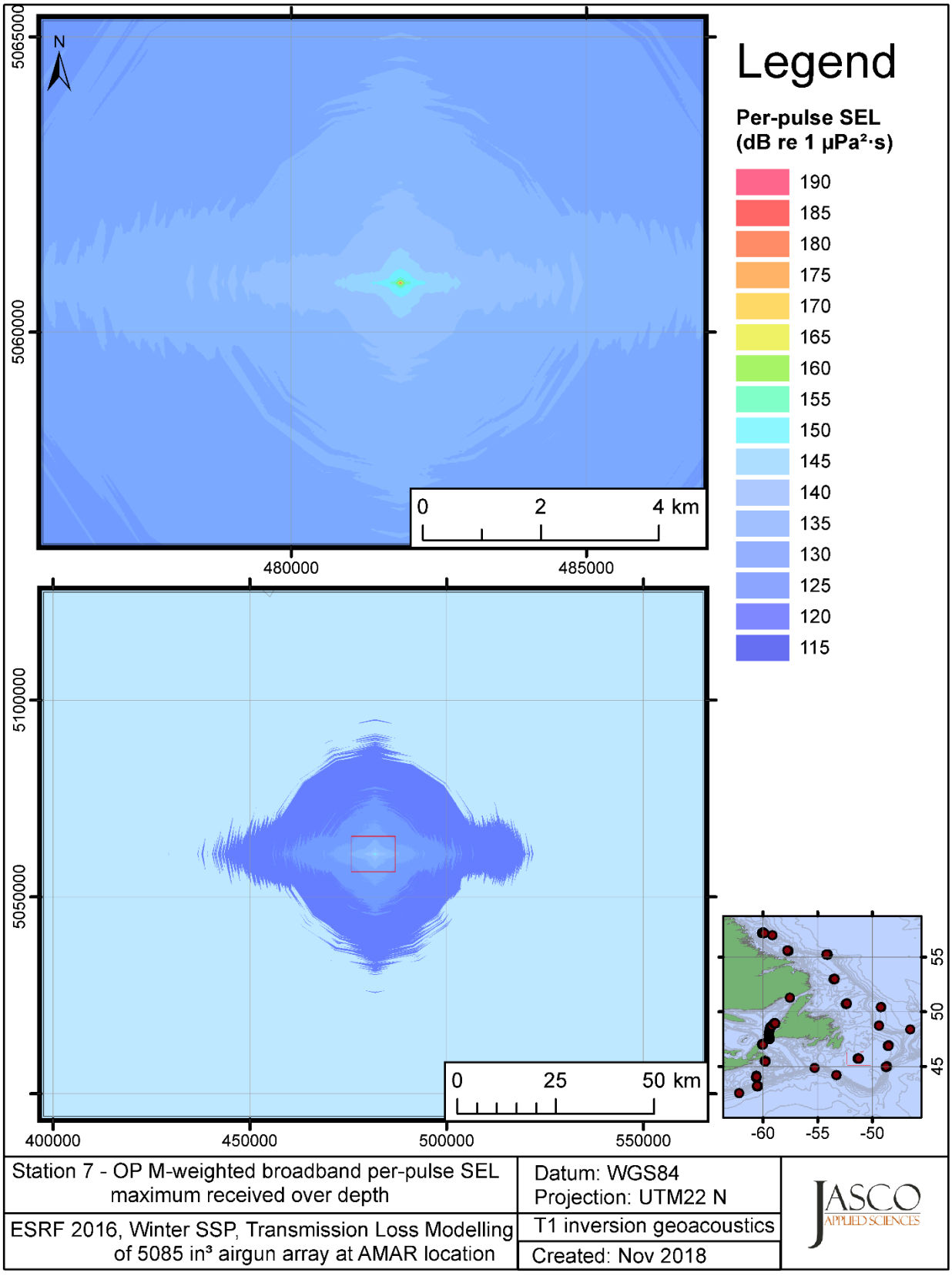

Figure C-519. Stn 7, OP M-weighted maximum-over-depth SEL received at any location on the map, modelled using the track 1 inversion geoacoustic bottom, with the airgun array at the AMAR location and GDEM February SSP.

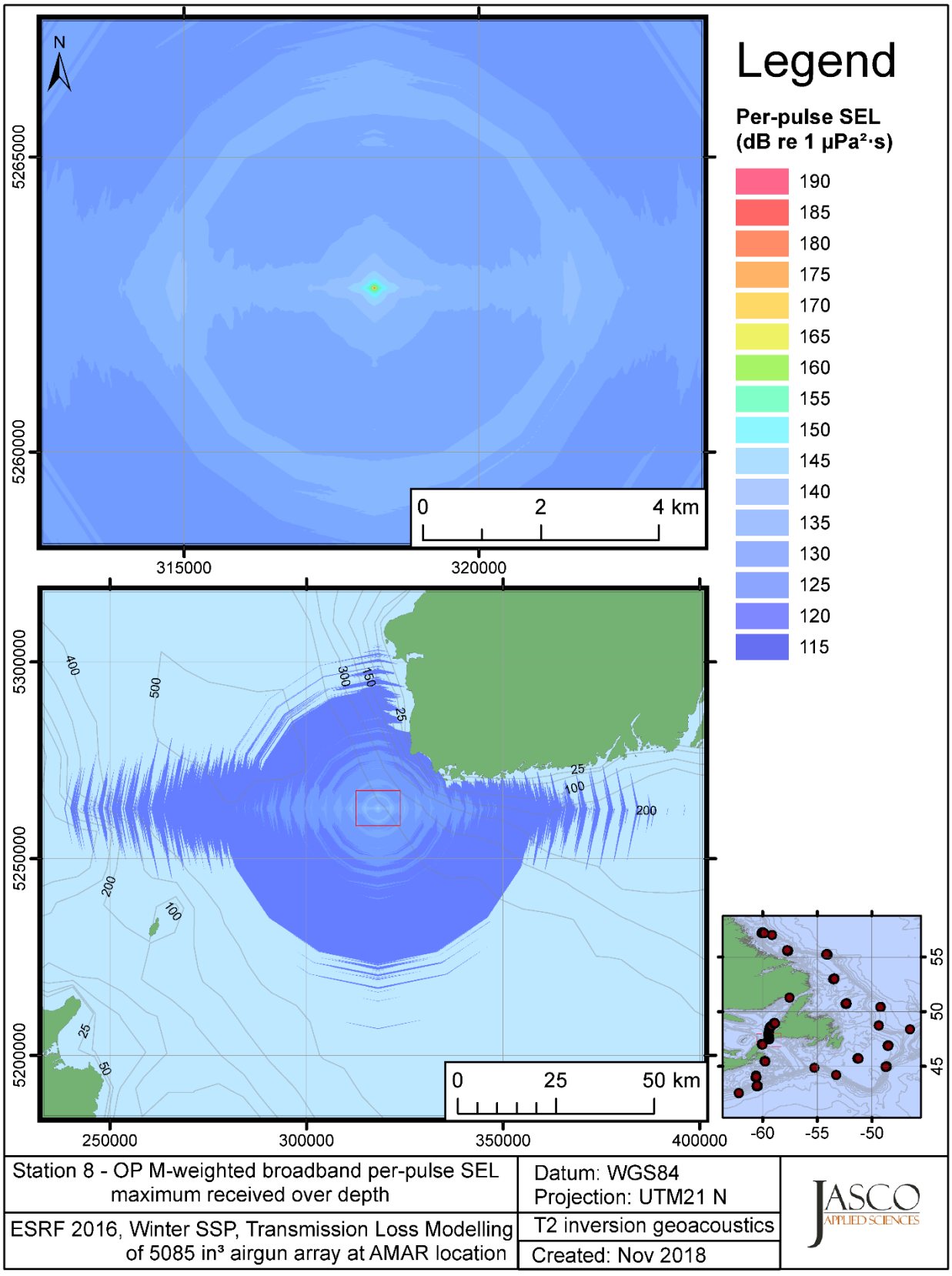

Figure C-520. Stn 8, OP M-weighted maximum-over-depth SEL received at any location on the map, modelled using the track 2 inversion geoacoustic bottom, with the airgun array at the AMAR location and GDEM February SSP.

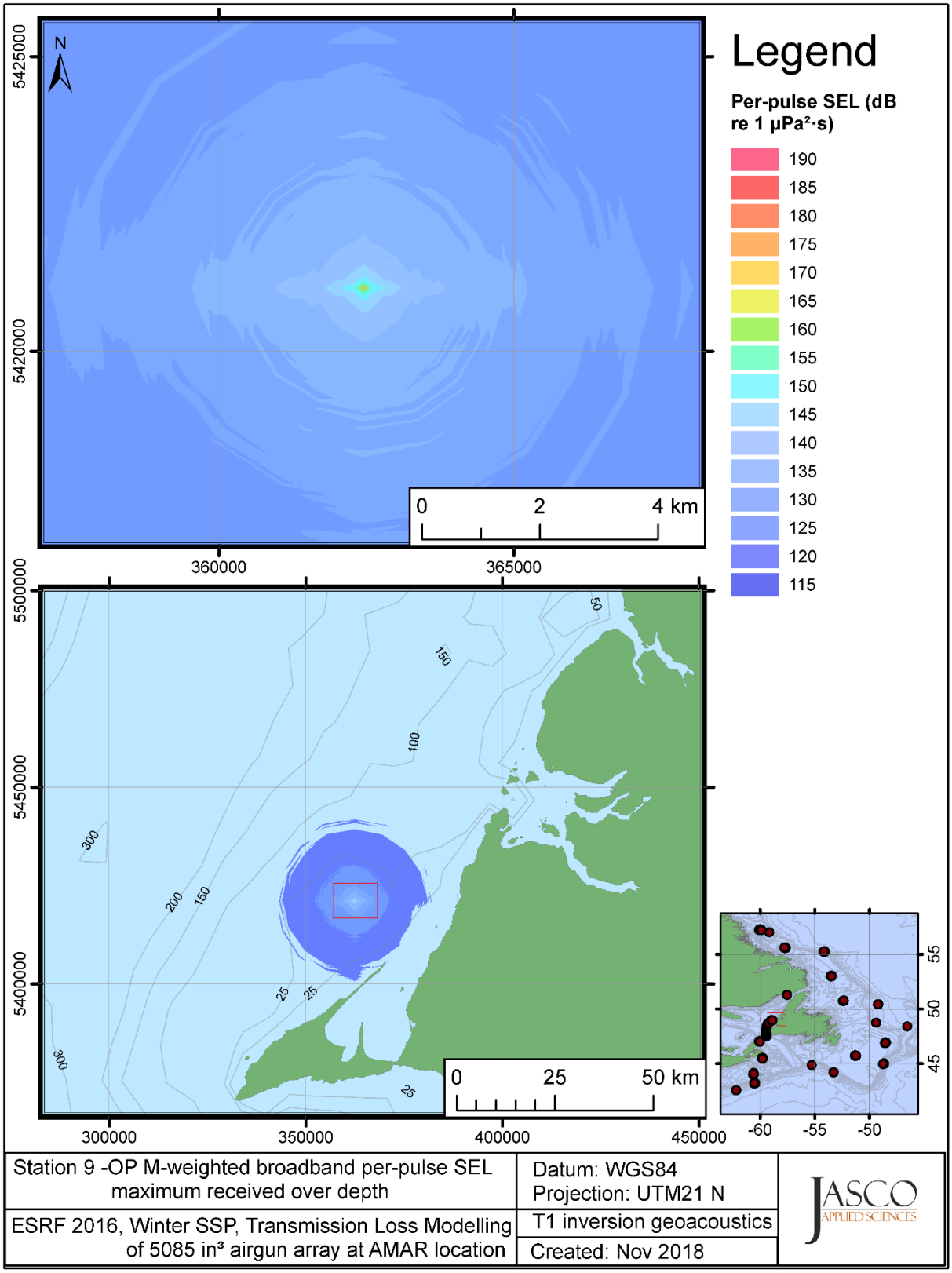

Figure C-521. Stn 9, OP M-weighted maximum-over-depth SEL received at any location on the map, modelled using the track 1 inversion geoacoustic bottom, with the airgun array at the AMAR location and GDEM February SSP.

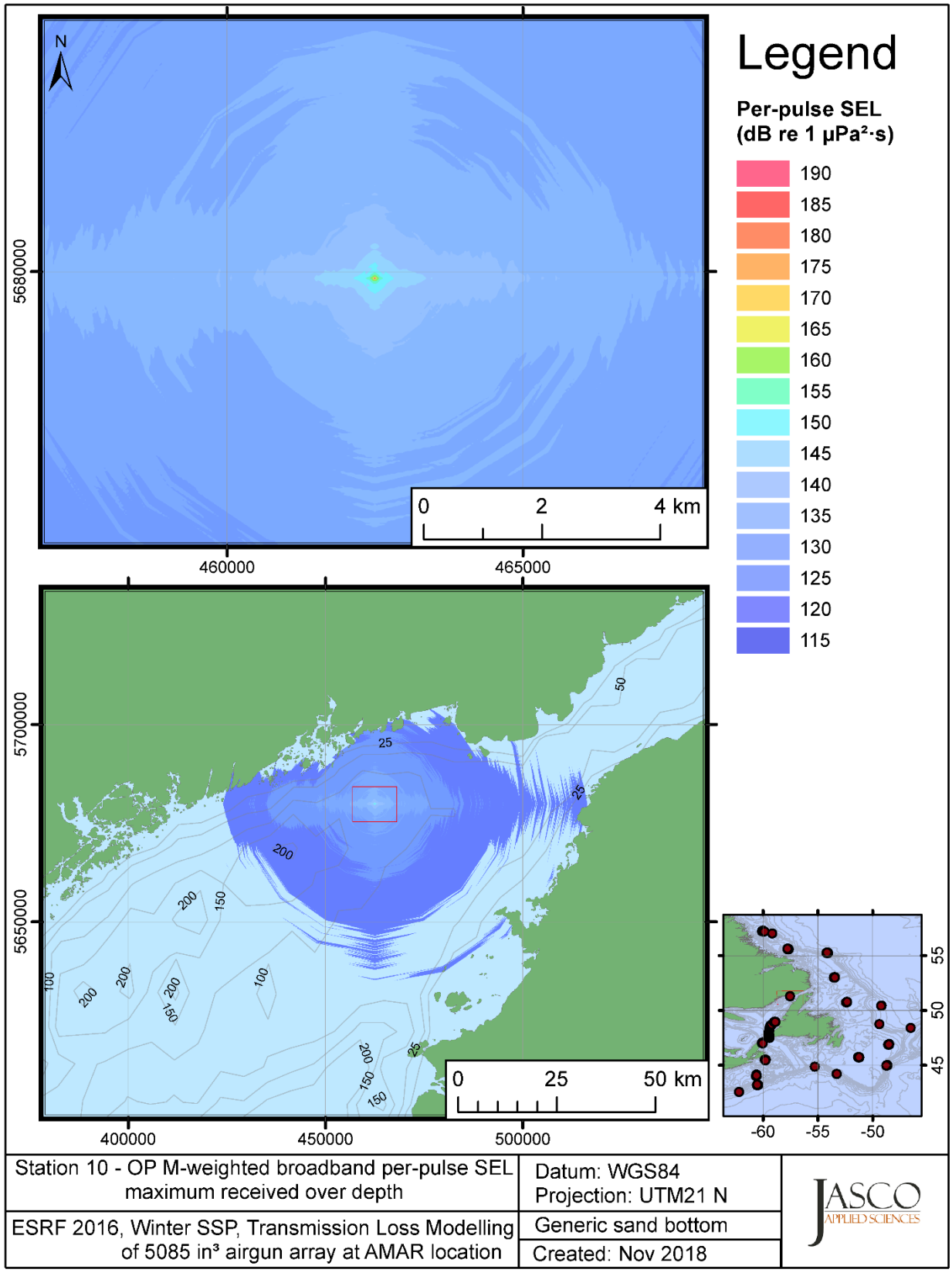

Figure C-522. Stn 10, OP M-weighted maximum-over-depth SEL received at any location on the map, modelled using a generic sand bottom, with the airgun array at the AMAR location and GDEM February SSP.

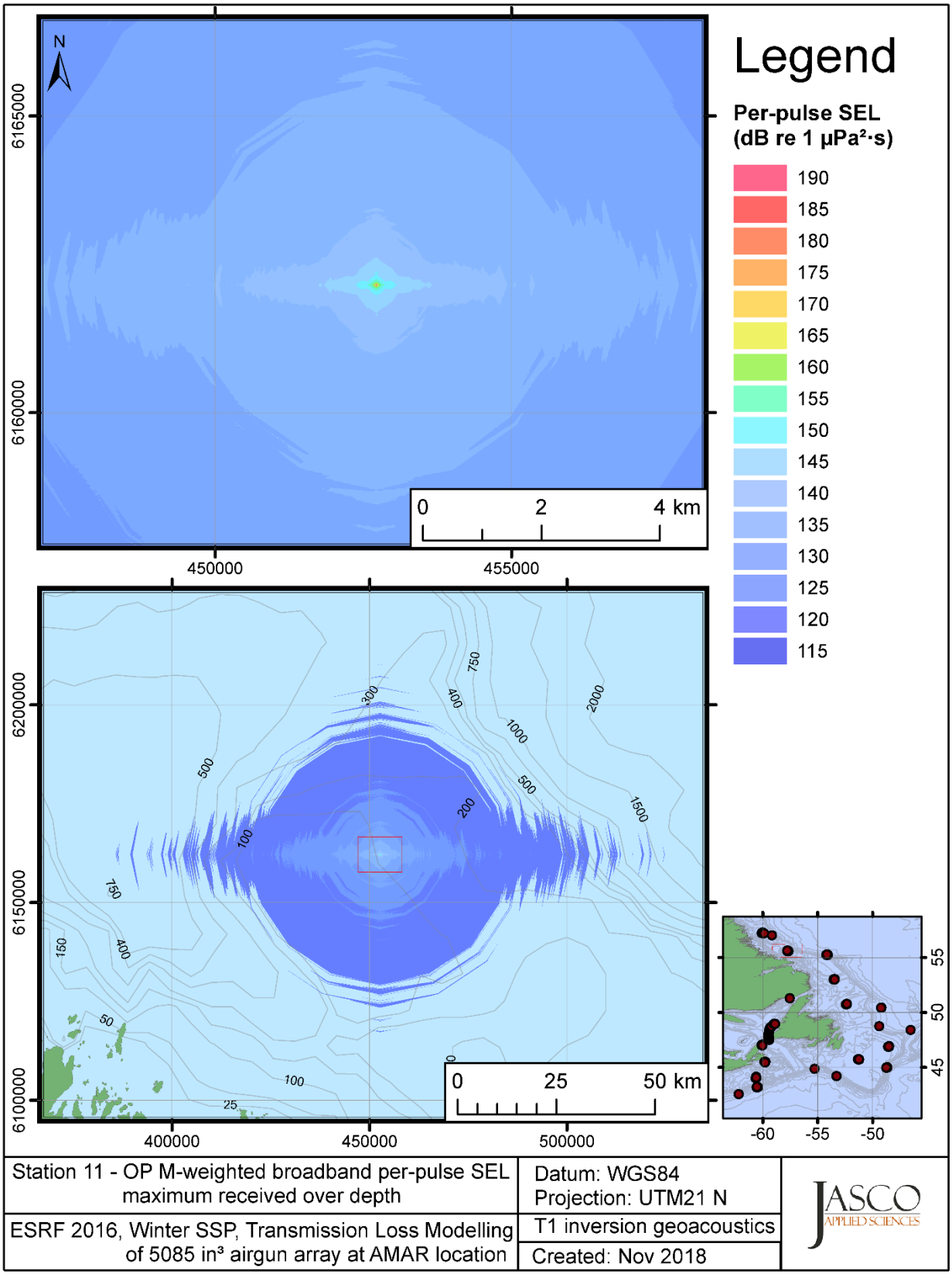

Figure C-523. Stn 11, OP M-weighted maximum-over-depth SEL received at any location on the map, modelled using the track 1 inversion geoacoustic bottom, with the airgun array at the AMAR location and GDEM February SSP.

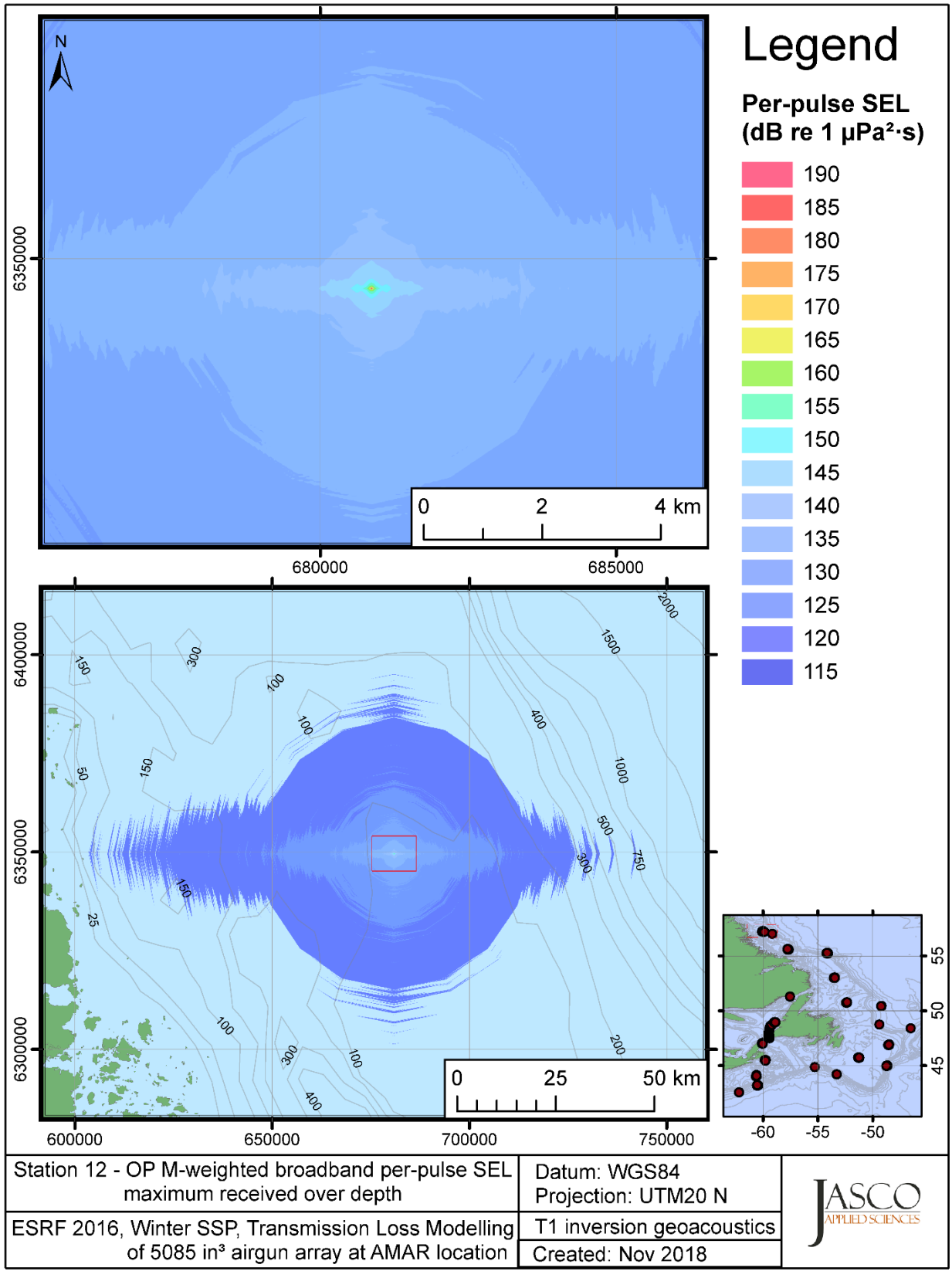

Figure C-524. Stn 12, OP M-weighted maximum-over-depth SEL received at any location on the map, modelled using the track 1 inversion geoacoustic bottom, with the airgun array at the AMAR location and GDEM February SSP.

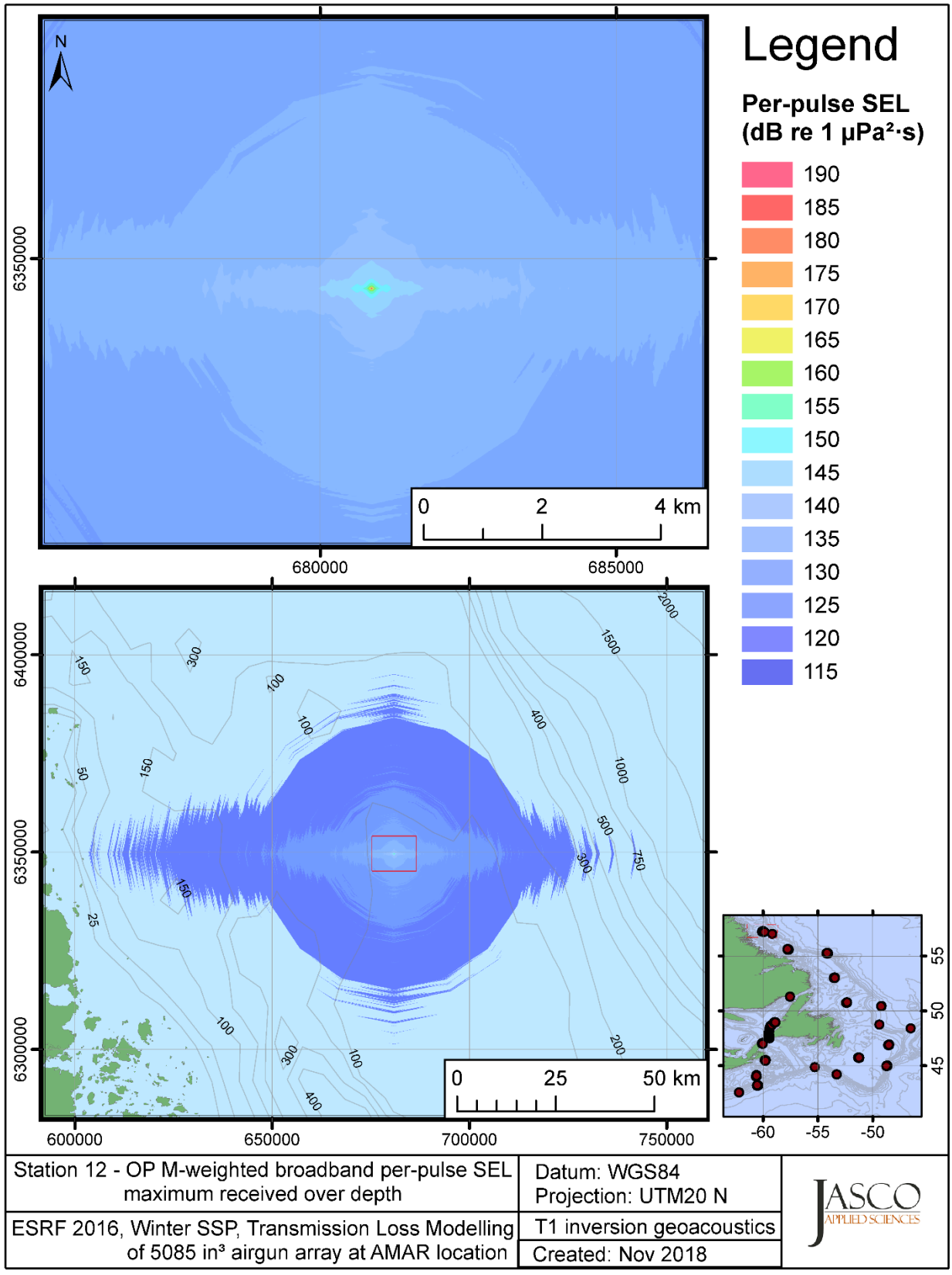

Figure C-525. Stn 13, OP M-weighted maximum-over-depth SEL received at any location on the map, modelled using the track 1 inversion geoacoustic bottom, with the airgun array at the AMAR location and GDEM February SSP.

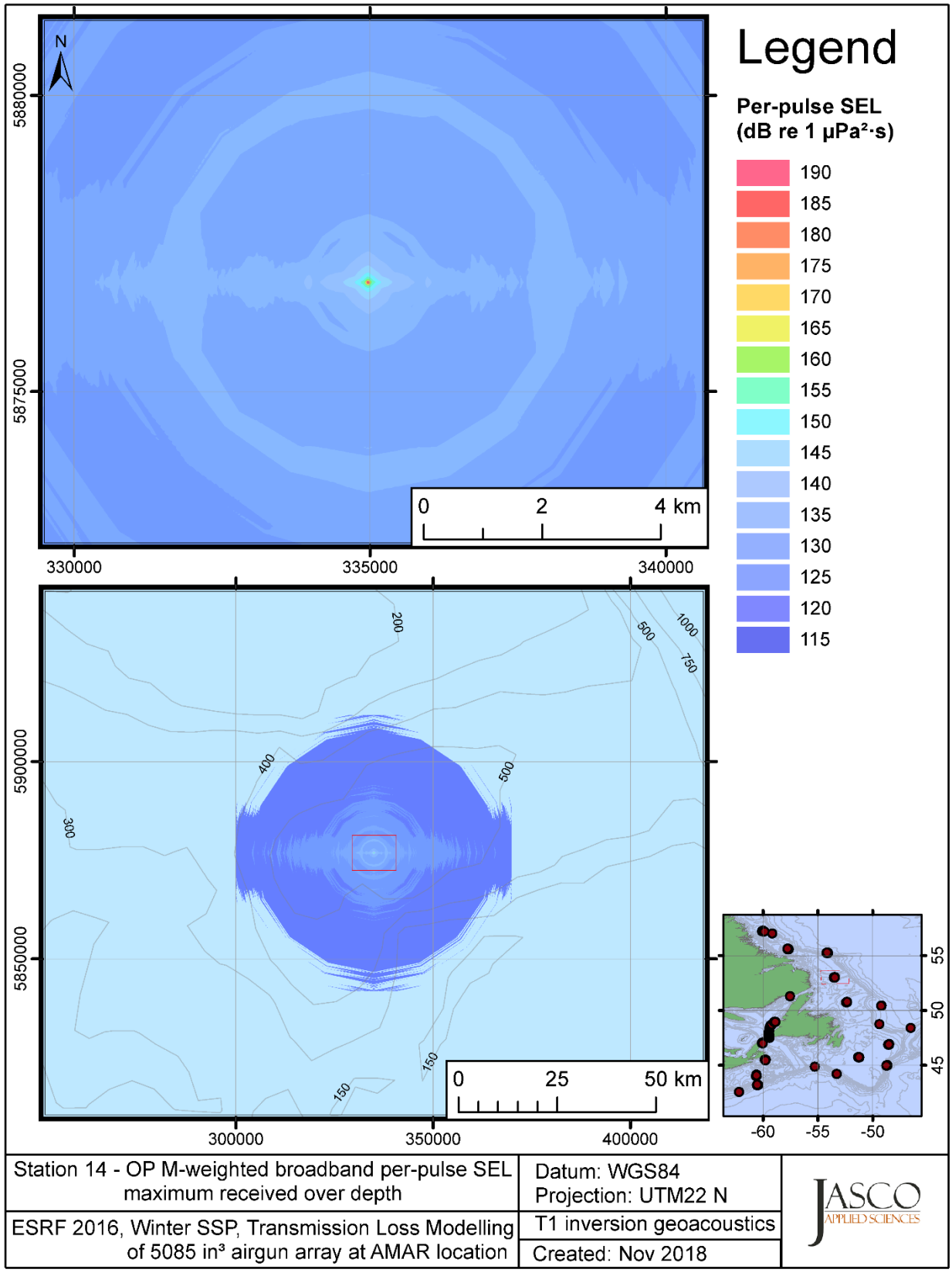

Figure C-526. Stn 14, OP M-weighted maximum-over-depth SEL received at any location on the map, modelled using the track 1 inversion geoacoustic bottom, with the airgun array at the AMAR location and GDEM February SSP.

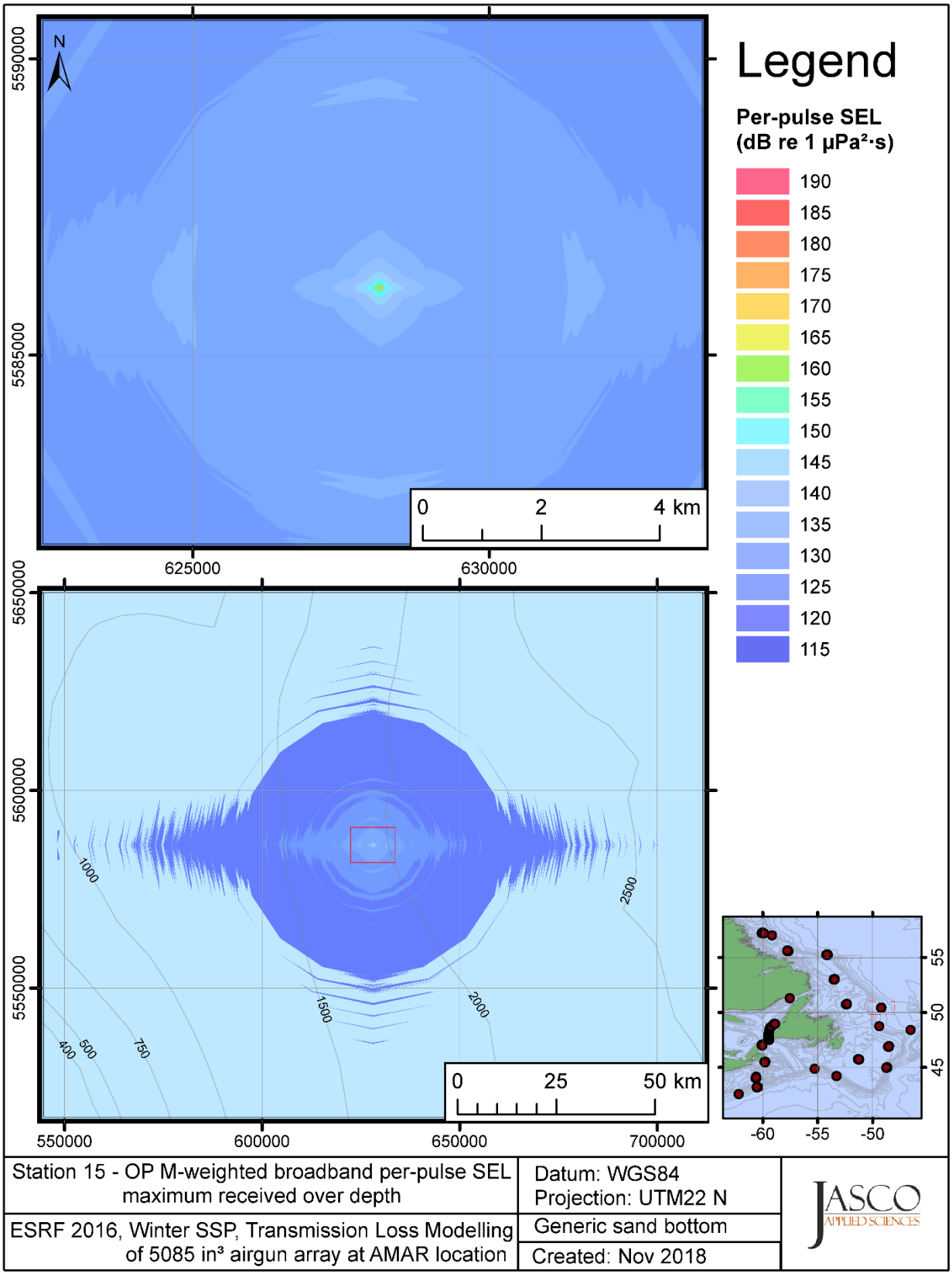

Figure C-527. Stn 15, OP M-weighted maximum-over-depth SEL received at any location on the map, modelled using a generic sand bottom, with the airgun array at the AMAR location and GDEM February SSP.

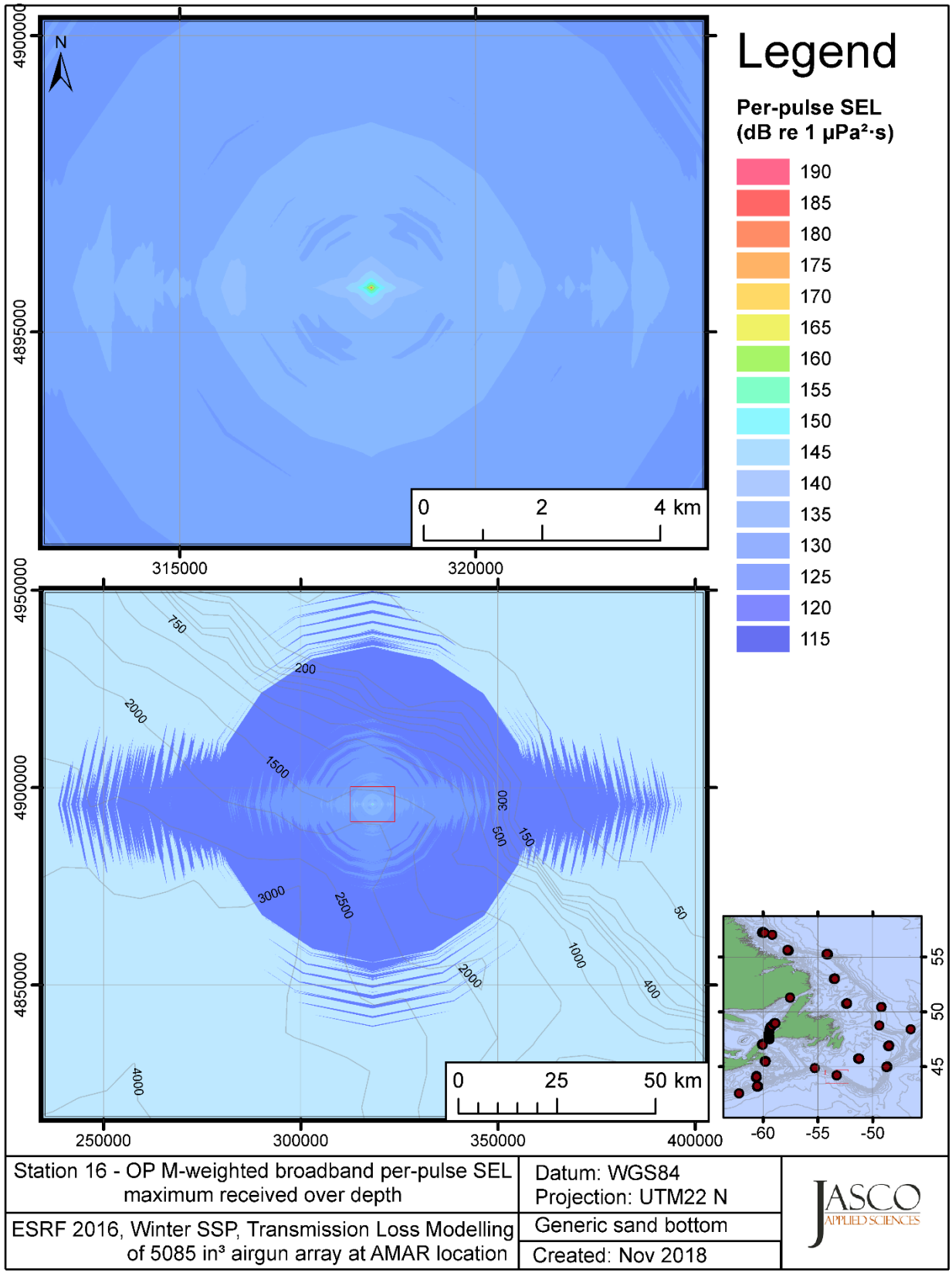

Figure C-528. Stn 16, OP M-weighted maximum-over-depth SEL received at any location on the map, modelled using a generic sand bottom, with the airgun array at the AMAR location and GDEM February SSP.

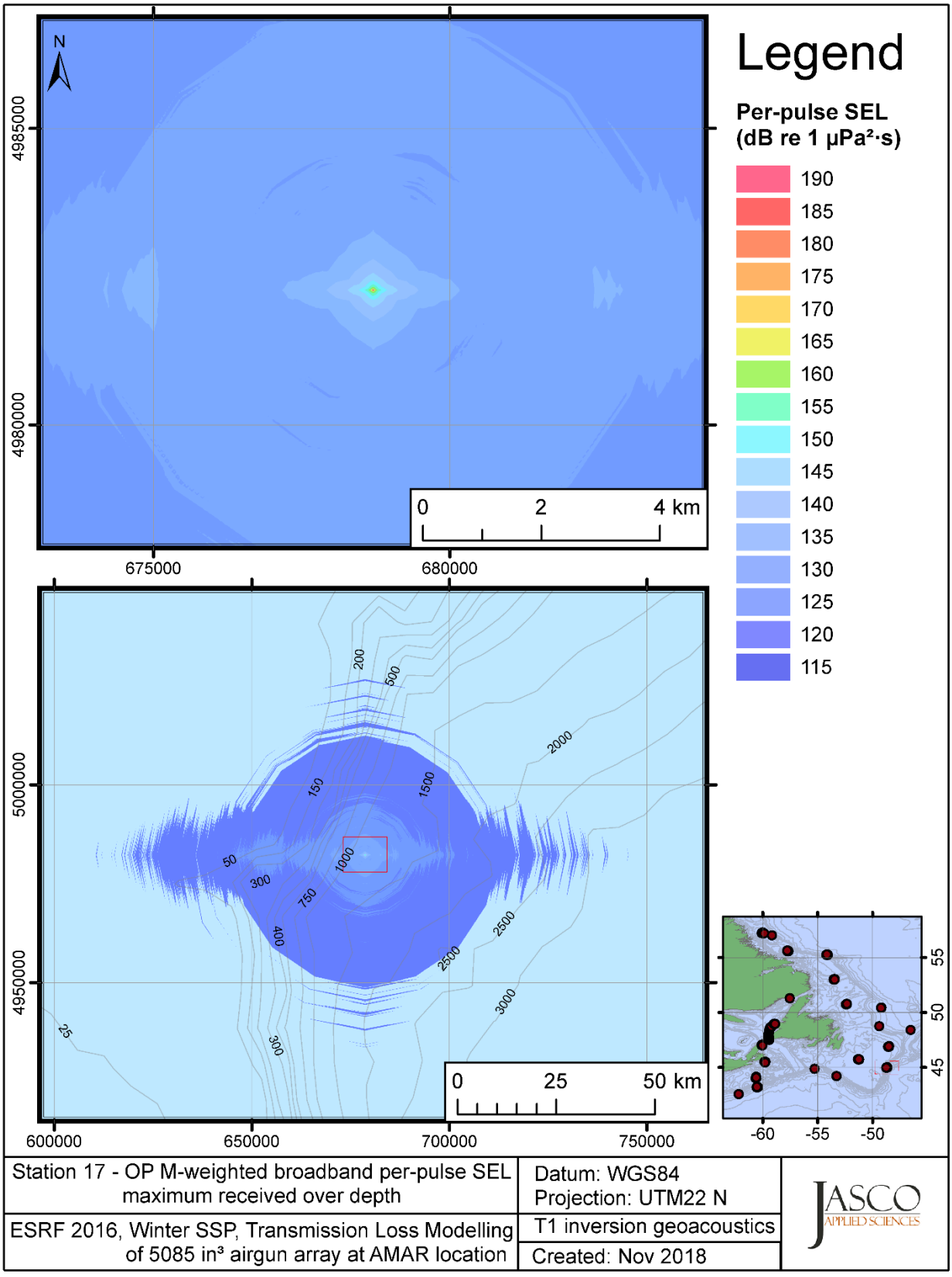

Figure C-529. Stn 17, OP M-weighted maximum-over-depth SEL received at any location on the map, modelled using the track 1 inversion geoacoustic bottom, with the airgun array at the AMAR location and GDEM February SSP.

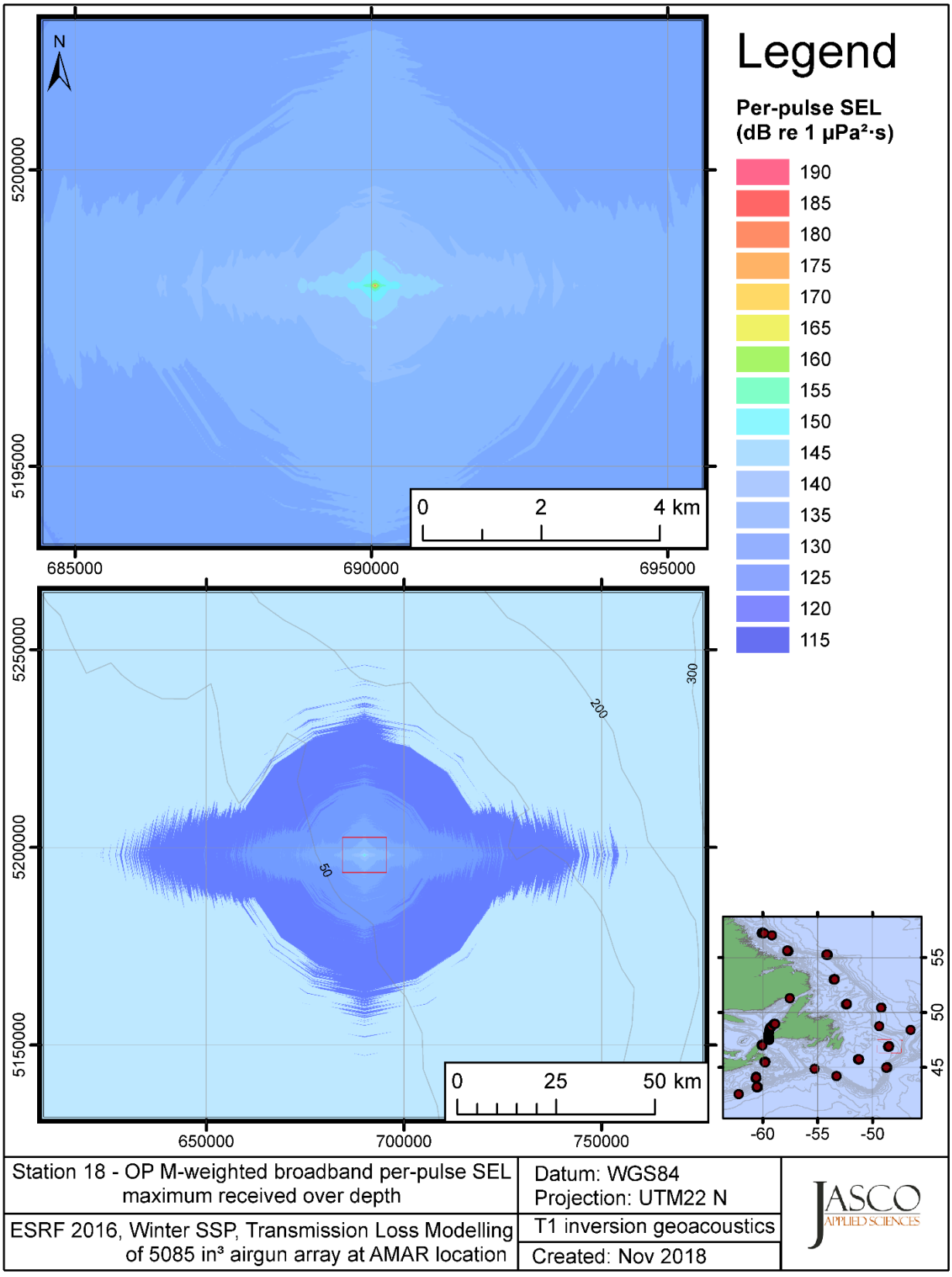

Figure C-530. Stn 18, OP M-weighted maximum-over-depth SEL received at any location on the map, modelled using the track 1 inversion geoacoustic bottom, with the airgun array at the AMAR location and GDEM February SSP.

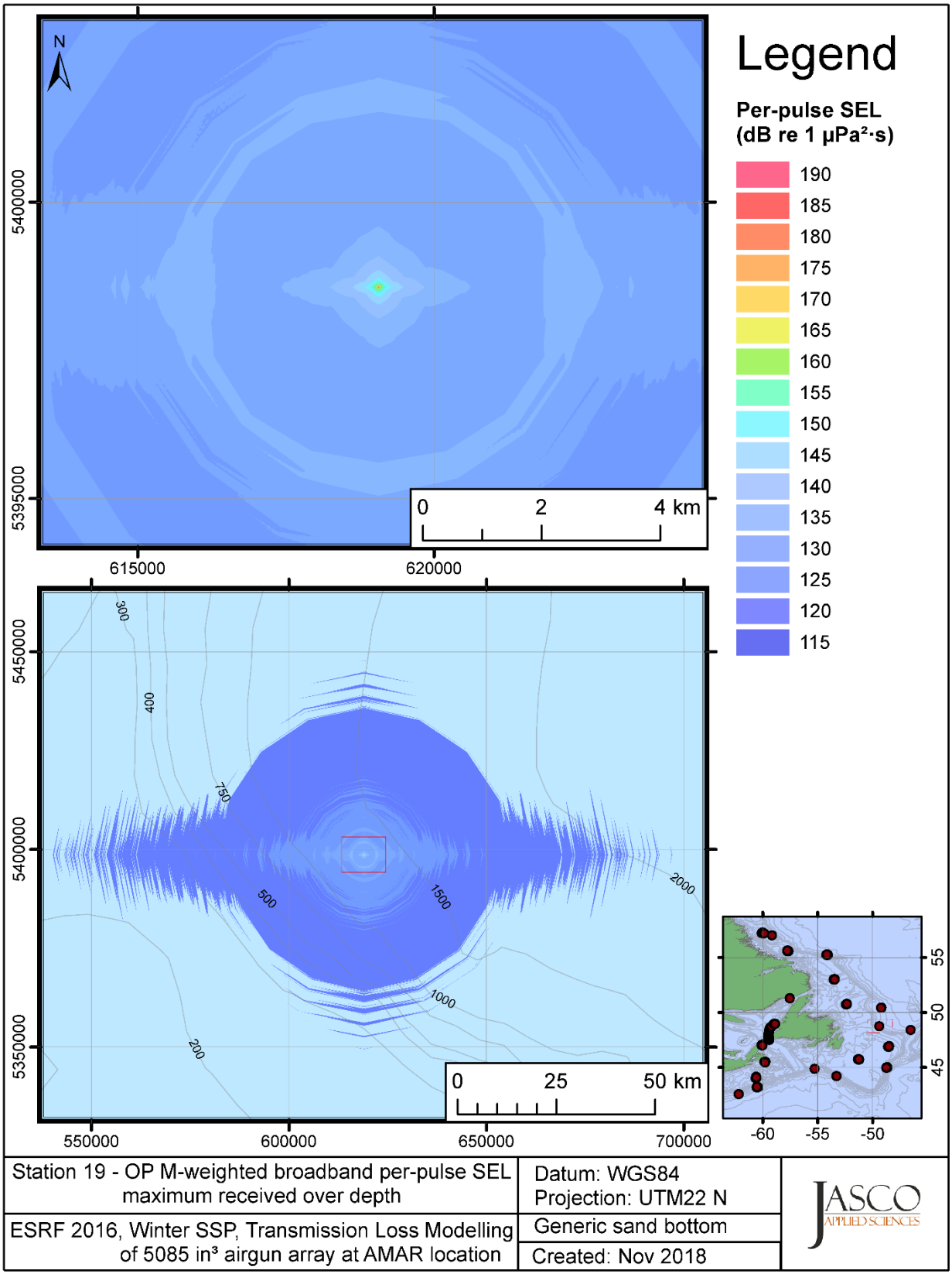

Figure C-531. Stn 19, OP M-weighted maximum-over-depth SEL received at any location on the map, modelled using a generic sand bottom, with the airgun array at the AMAR location and GDEM February SSP.

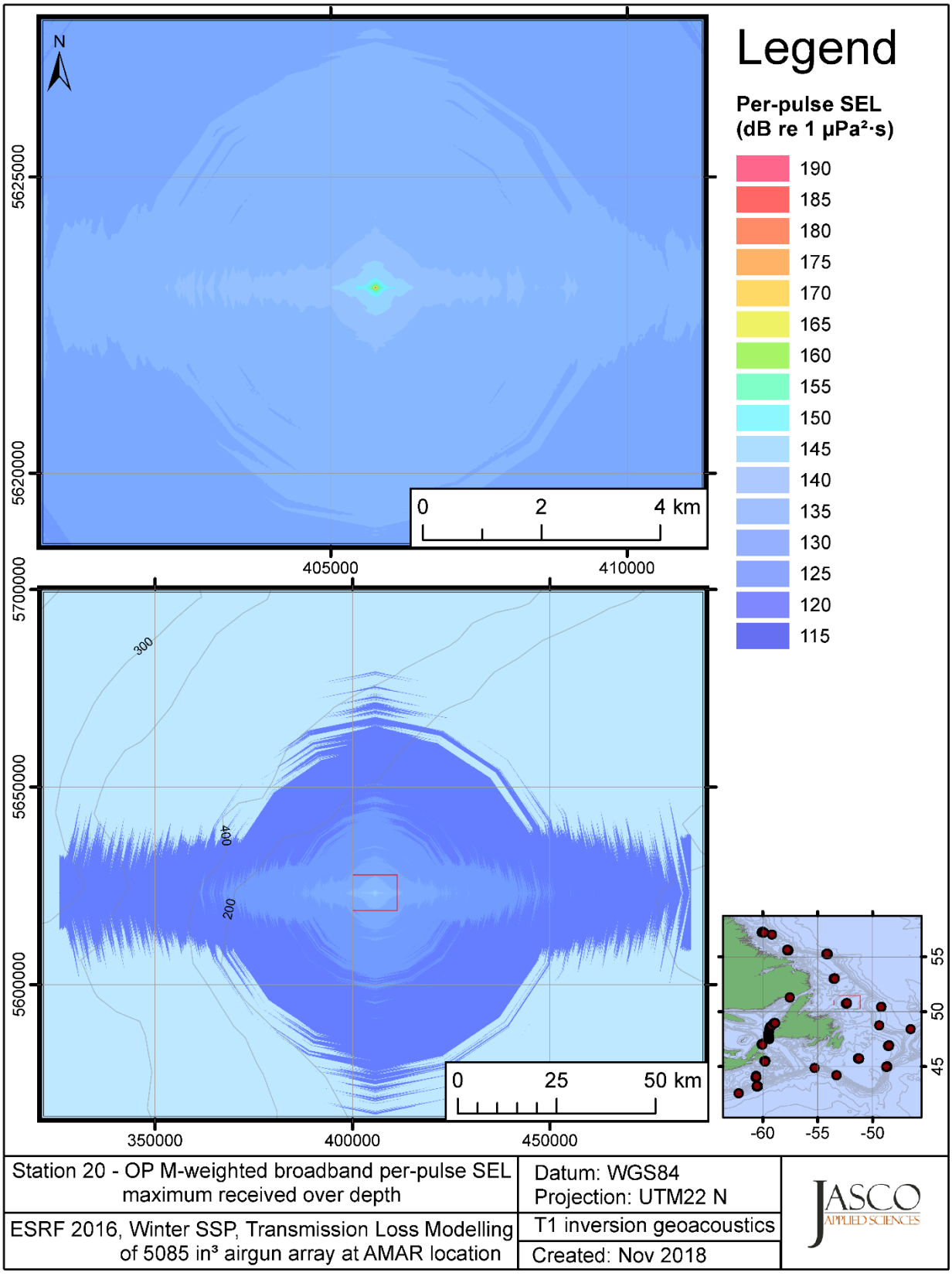

Figure C-532. Stn 20, OP M-weighted maximum-over-depth SEL received at any location on the map, modelled using the track 1 inversion geoacoustic bottom, with the airgun array at the AMAR location and GDEM February SSP.

C.18. Modelling PP M-weighted Max-over-depth Received Level at Distant Locations - Winter

This section presents the results of modelling the maximum-over-depth per-pulse sound exposure level (SEL) received at distant receiver locations (varied in range and azimuth) for the source held fixed at the AMAR location. The modelling uses the geoacoustic inversion bottom parameters at the 14 sites where they are available and only uses a generic sand bottom at the other six sites. The modelling results are presented in the form of coloured maps where the colour at any map location represents the predicted maximum-over-depth received level at that spot on the map. This section includes only the phocid pinnipeds in water (OP) marine-mammal-weighted per-pulse SEL results; additional maps for other marine mammal received level auditory weightings are presented in adjoining sections. The sound speed profiles (SSP) used are detailed in Appendix B.2.

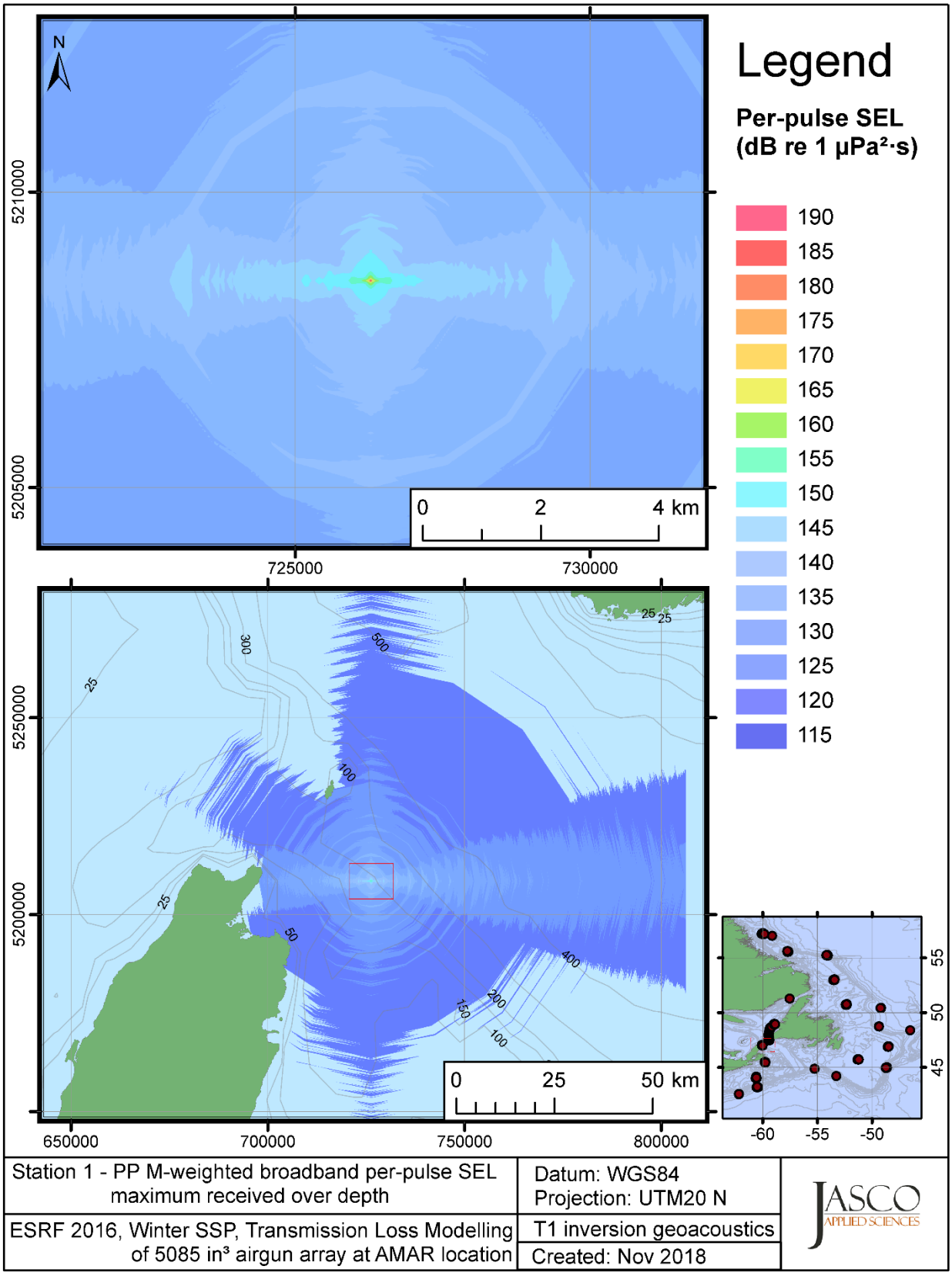

Figure C-533. Stn 1, PP M-weighted maximum-over-depth SEL received at any location on the map, modelled using the track 1 inversion geoacoustic bottom, with the airgun array at the AMAR location and GDEM February SSP.

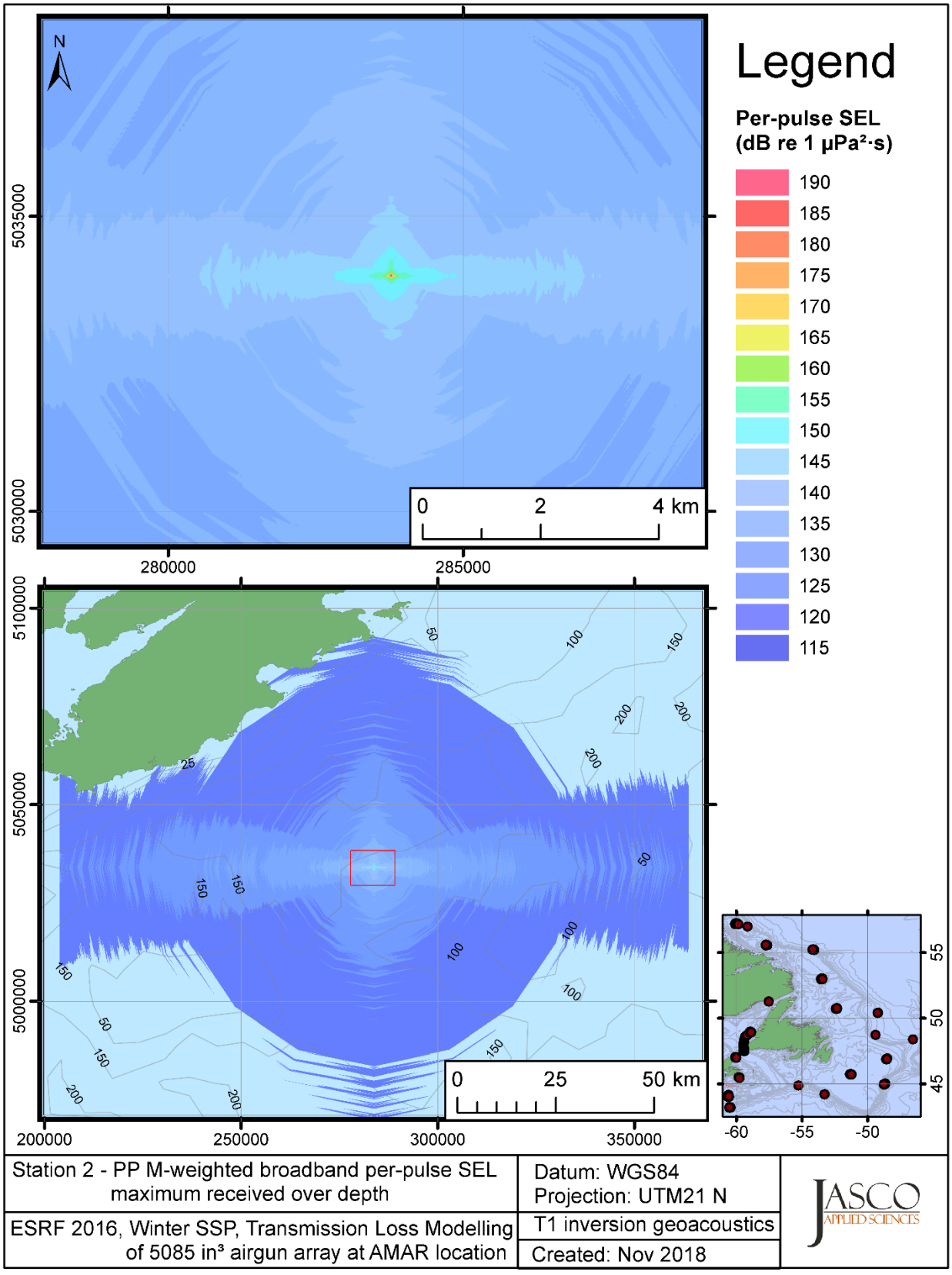

Figure C-534. Stn 2, PP M-weighted maximum-over-depth SEL received at any location on the map, modelled using the track 1 inversion geoacoustic bottom, with the airgun array at the AMAR location and GDEM February SSP.

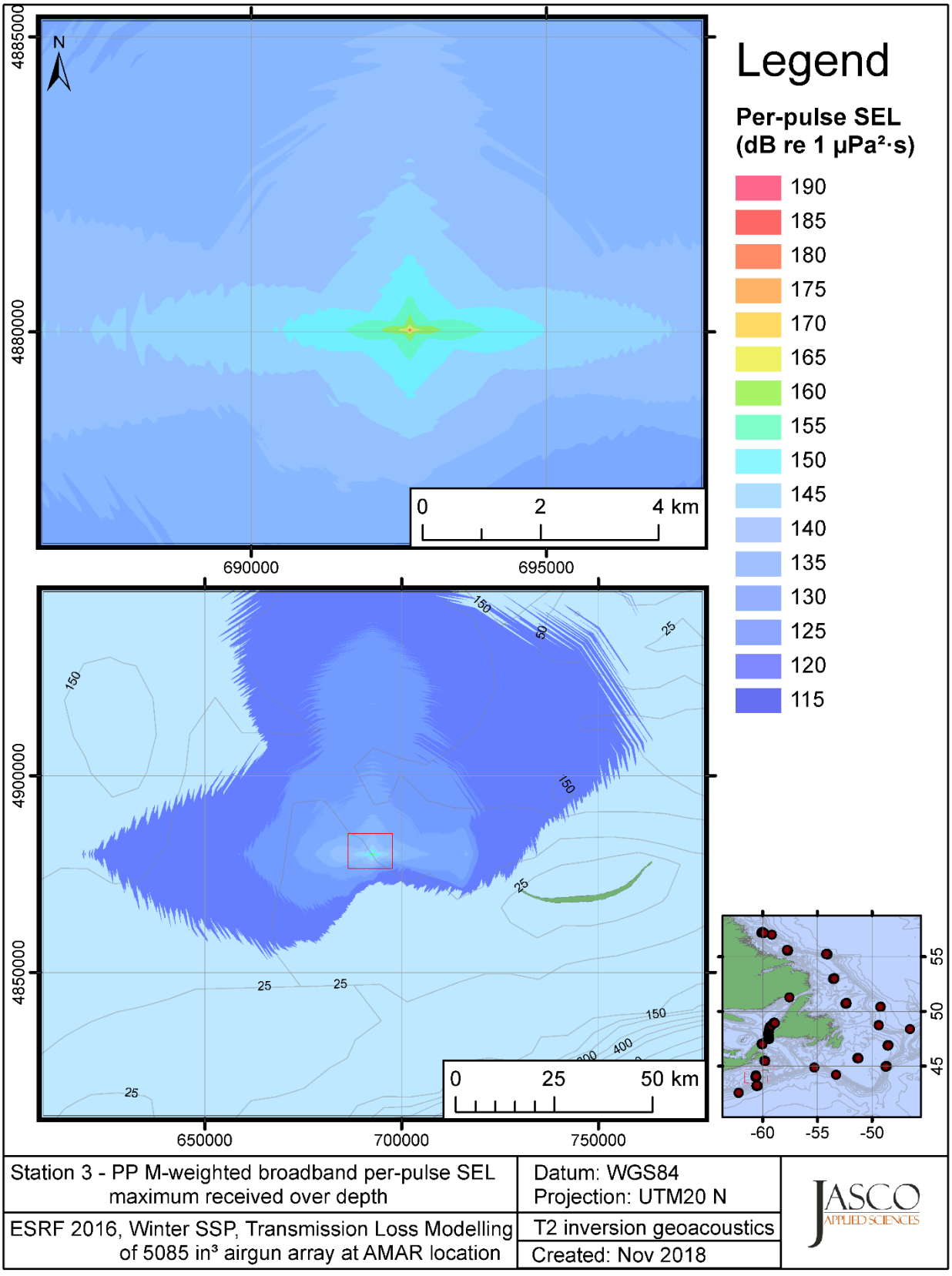

Figure C-535. Stn 3, PP M-weighted maximum-over-depth SEL received at any location on the map, modelled using the track 2 inversion geoacoustic bottom, with the airgun array at the AMAR location and GDEM February SSP.

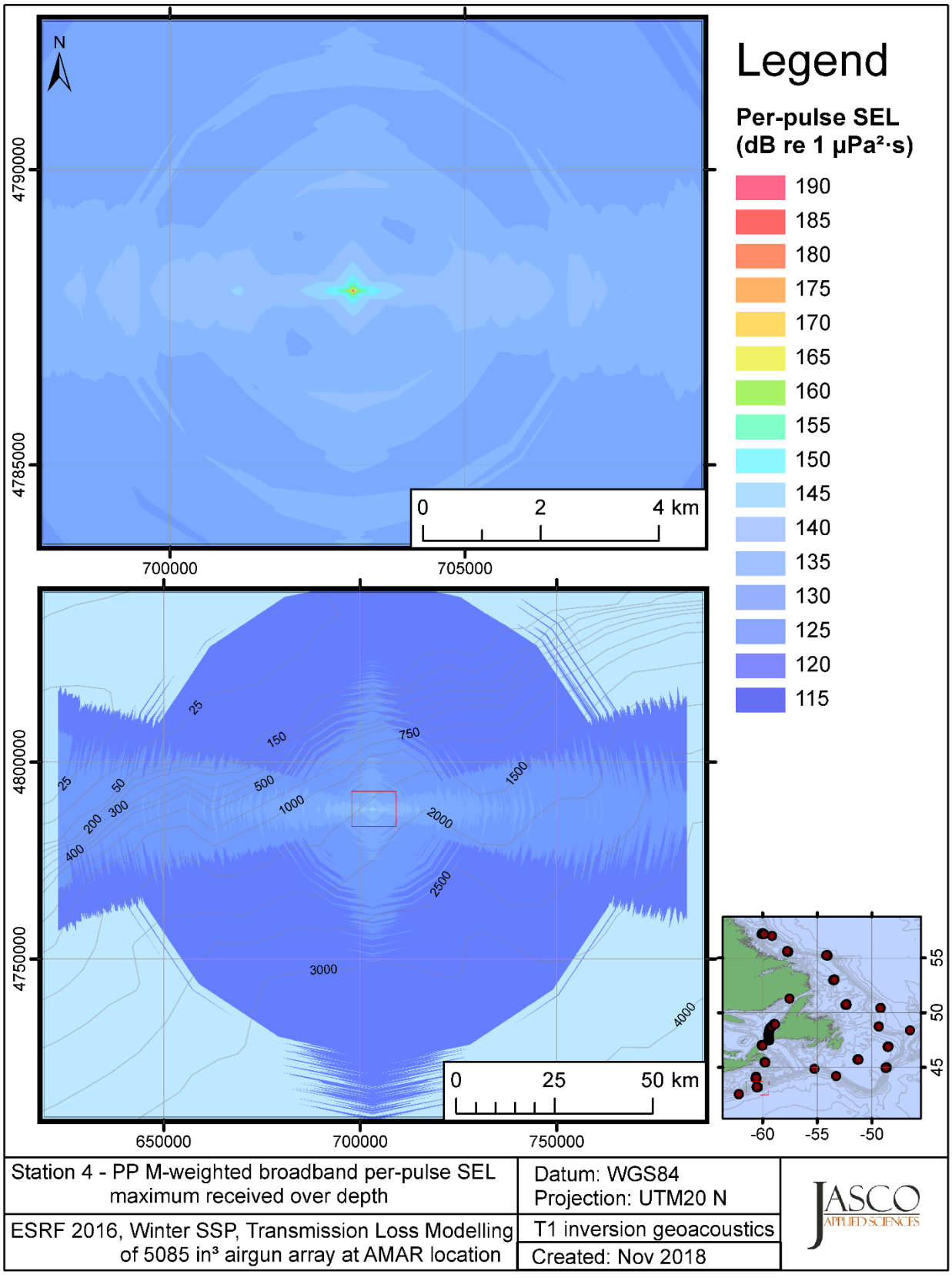

Figure C-536. Stn 4, PP M-weighted maximum-over-depth SEL received at any location on the map, modelled using the track 1 inversion geoacoustic bottom, with the airgun array at the AMAR location and GDEM February SSP.

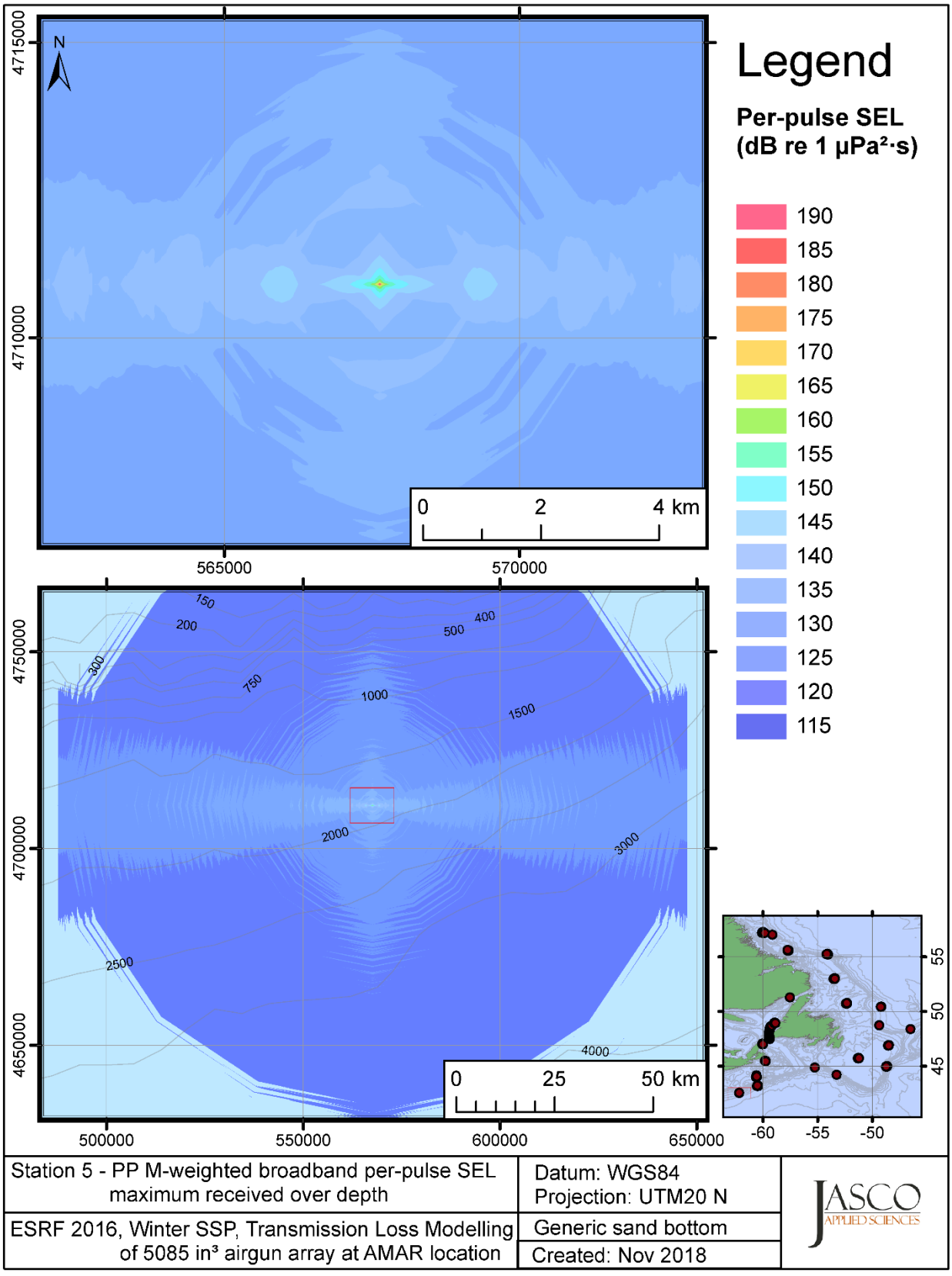

Figure C-537. Stn 5, PP M-weighted maximum-over-depth SEL received at any location on the map, modelled using a generic sand bottom, with the airgun array at the AMAR location and GDEM February SSP.

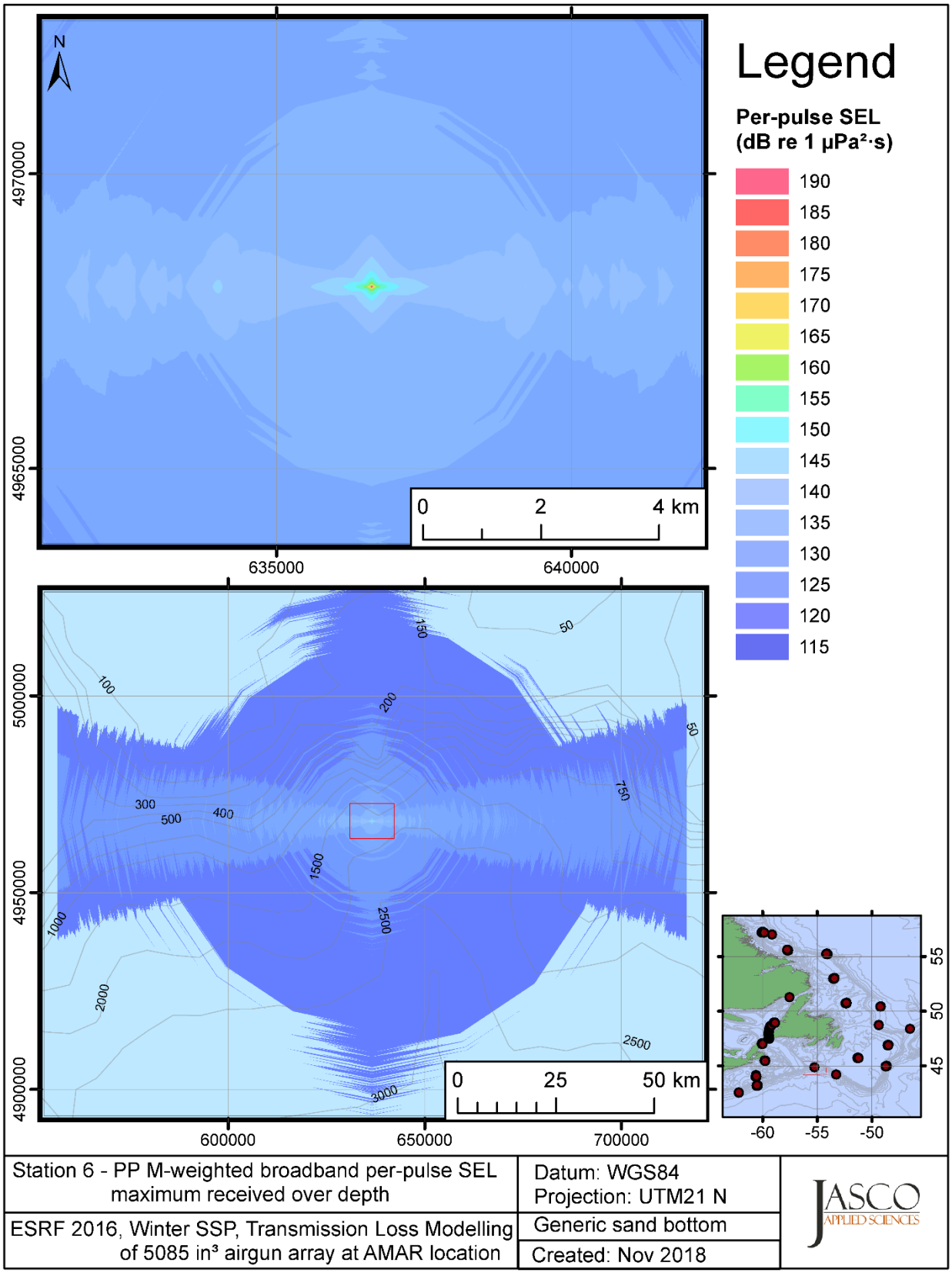

Figure C-538. Stn 6, PP M-weighted maximum-over-depth SEL received at any location on the map, modelled using a generic sand bottom, with the airgun array at the AMAR location and GDEM February SSP.

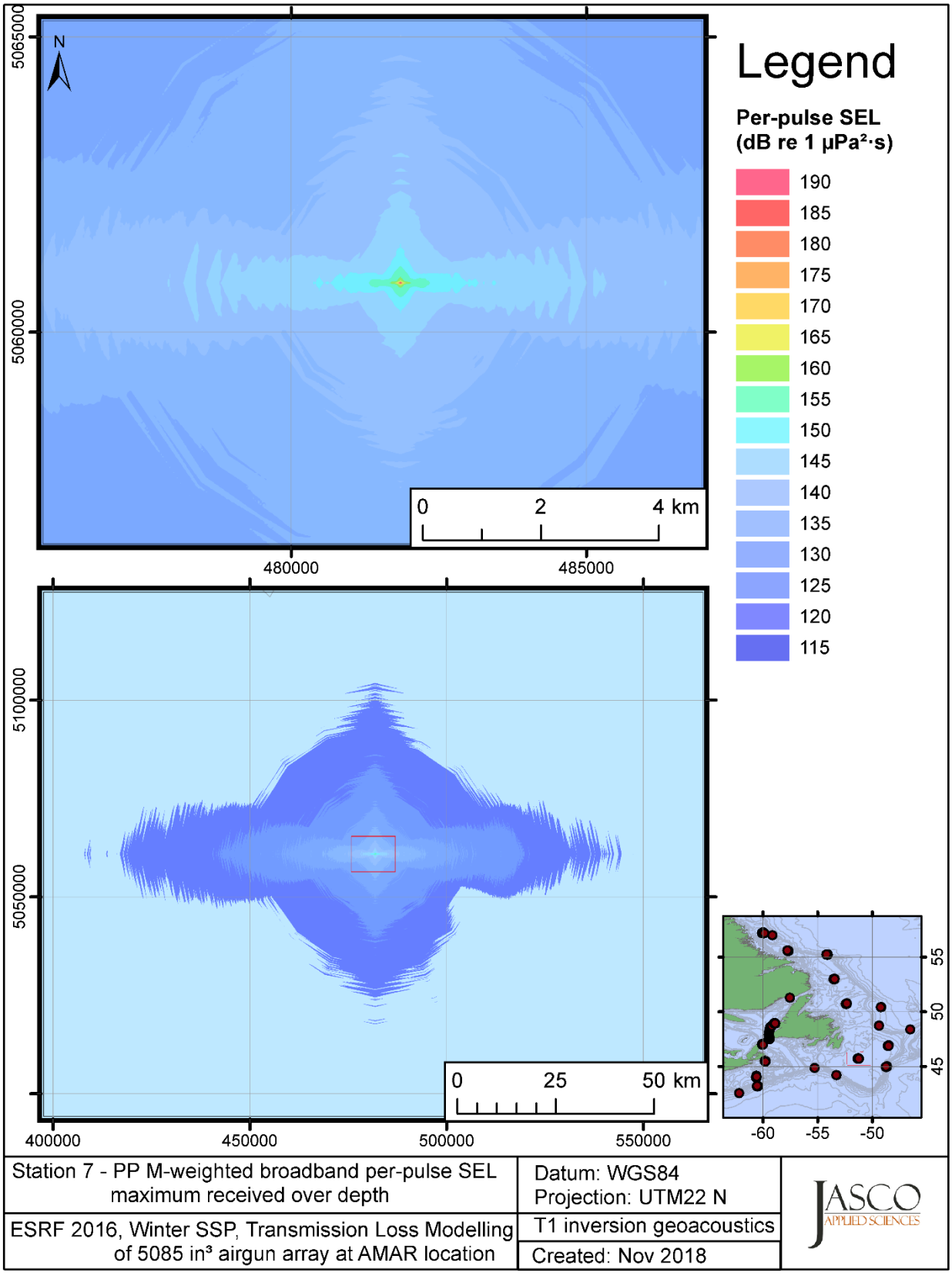

Figure C-539. Stn 7, PP M-weighted maximum-over-depth SEL received at any location on the map, modelled using the track 1 inversion geoacoustic bottom, with the airgun array at the AMAR location and GDEM February SSP.

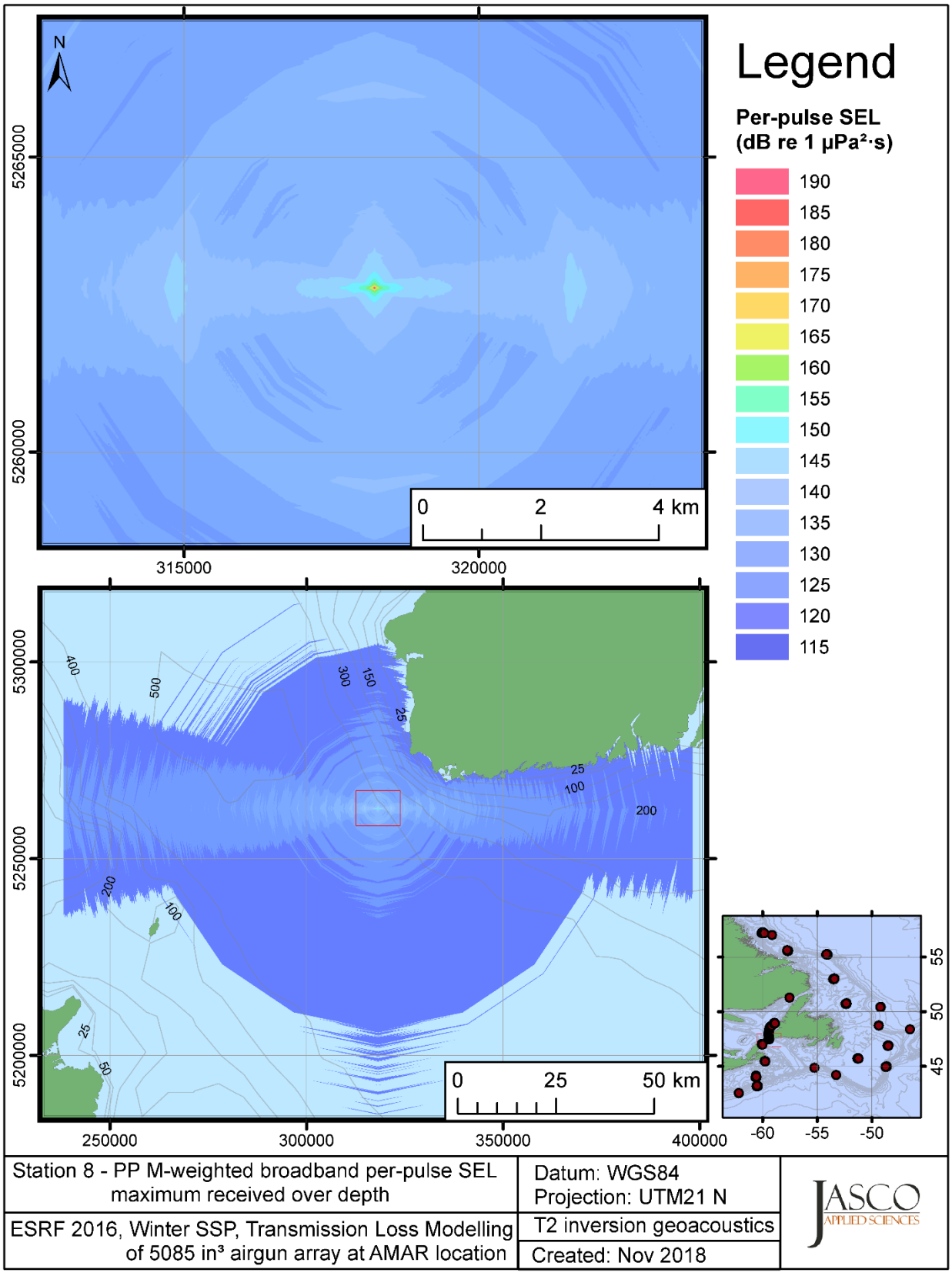

Figure C-540. Stn 8, PP M-weighted maximum-over-depth SEL received at any location on the map, modelled using the track 2 inversion geoacoustic bottom, with the airgun array at the AMAR location and GDEM February SSP.

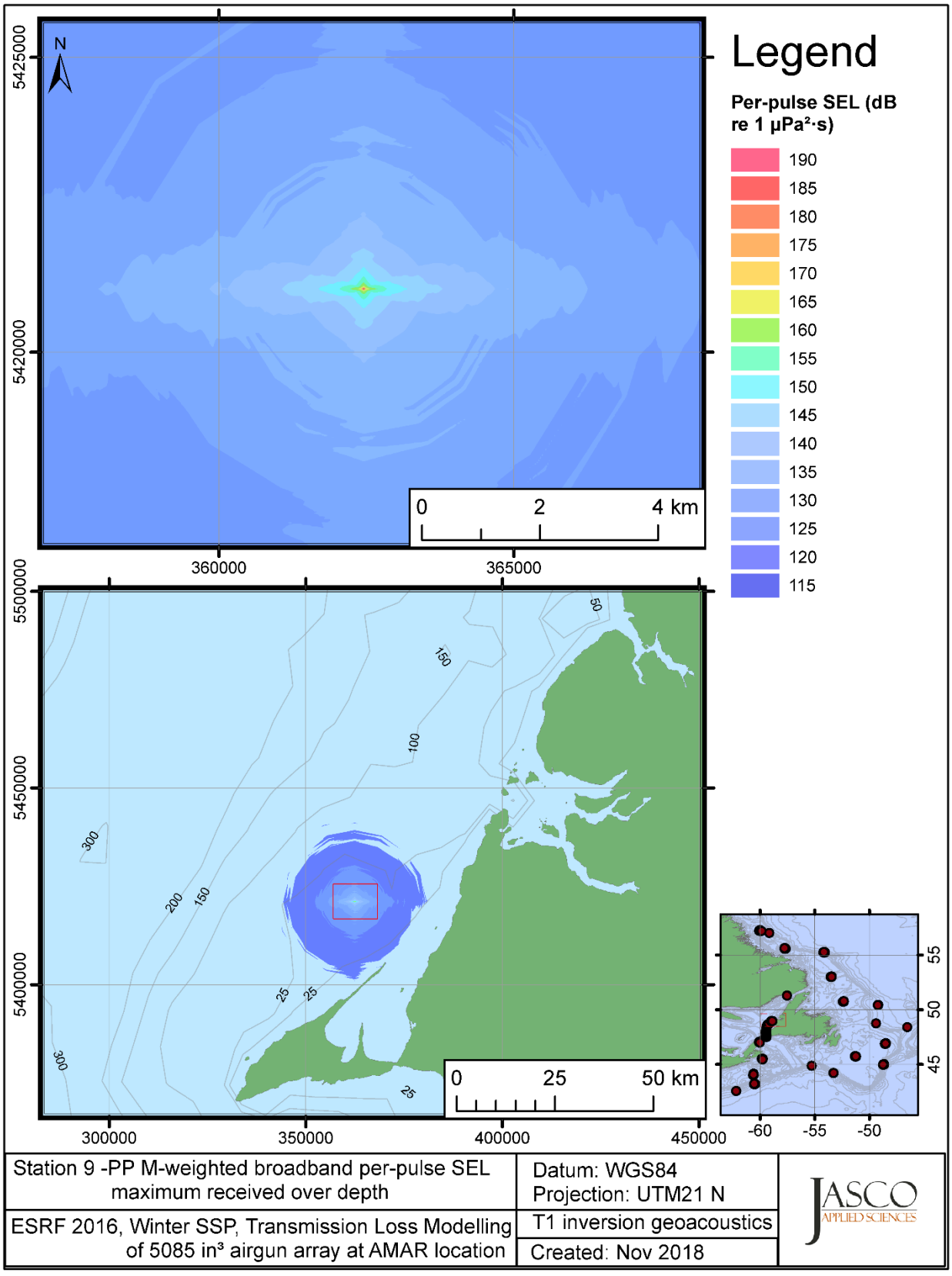

Figure C-541. Stn 9, PP M-weighted maximum-over-depth SEL received at any location on the map, modelled using the track 1 inversion geoacoustic bottom, with the airgun array at the AMAR location and GDEM February SSP.

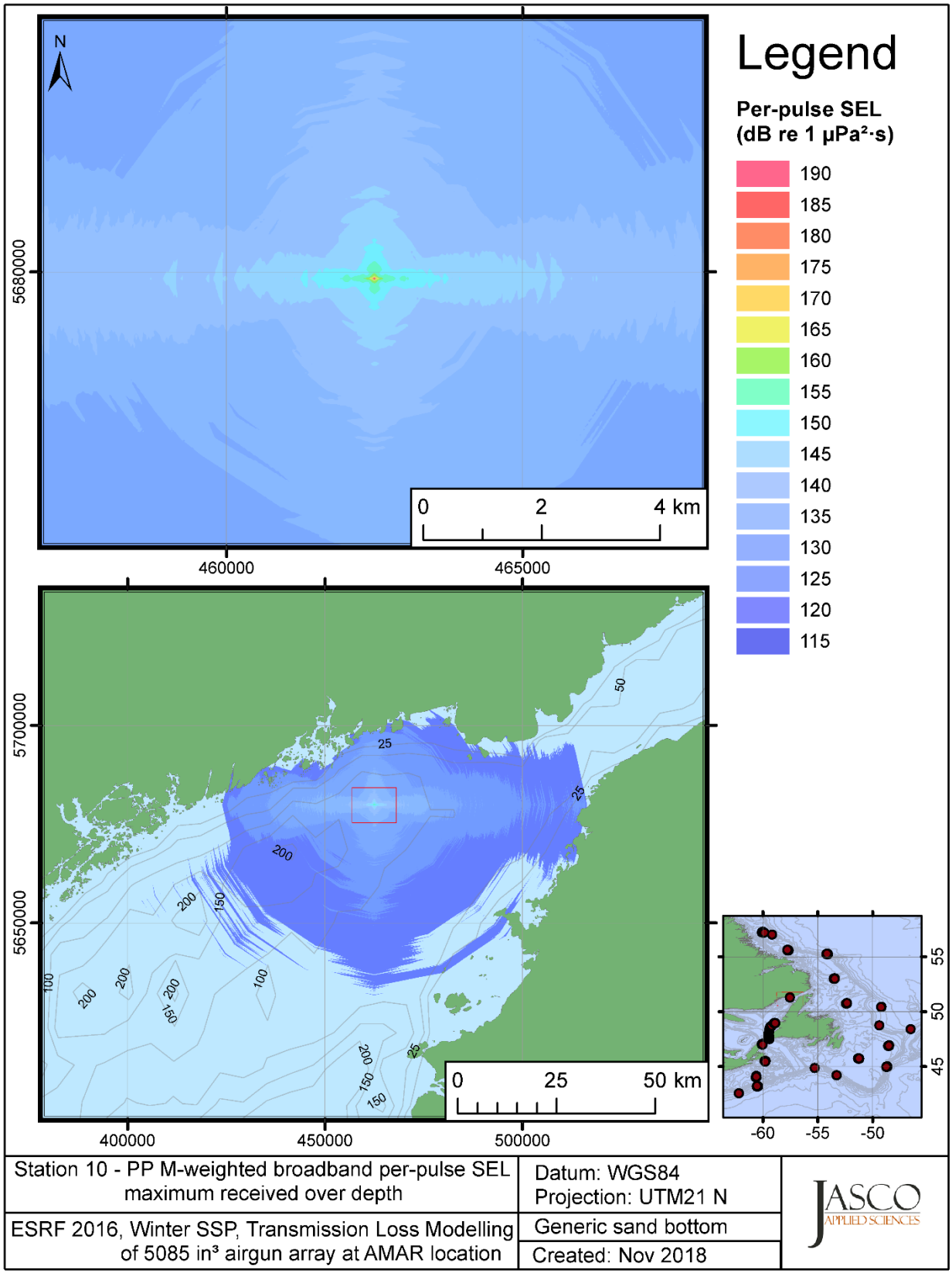

Figure C-542. Stn 10, PP M-weighted maximum-over-depth SEL received at any location on the map, modelled using a generic sand bottom, with the airgun array at the AMAR location and GDEM February SSP.

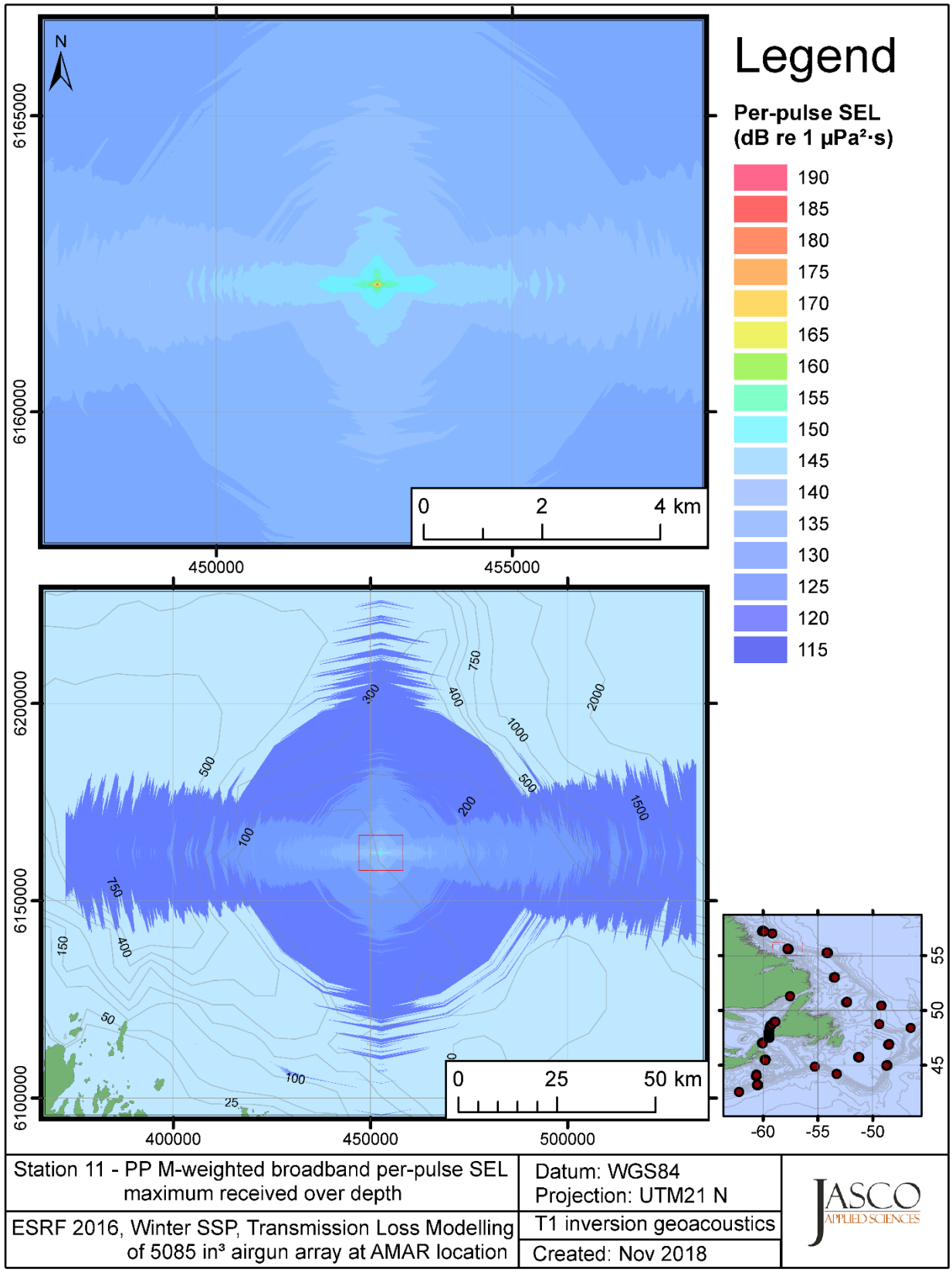

Figure C-543. Stn 11, PP M-weighted maximum-over-depth SEL received at any location on the map, modelled using the track 1 inversion geoacoustic bottom, with the airgun array at the AMAR location and GDEM February SSP.

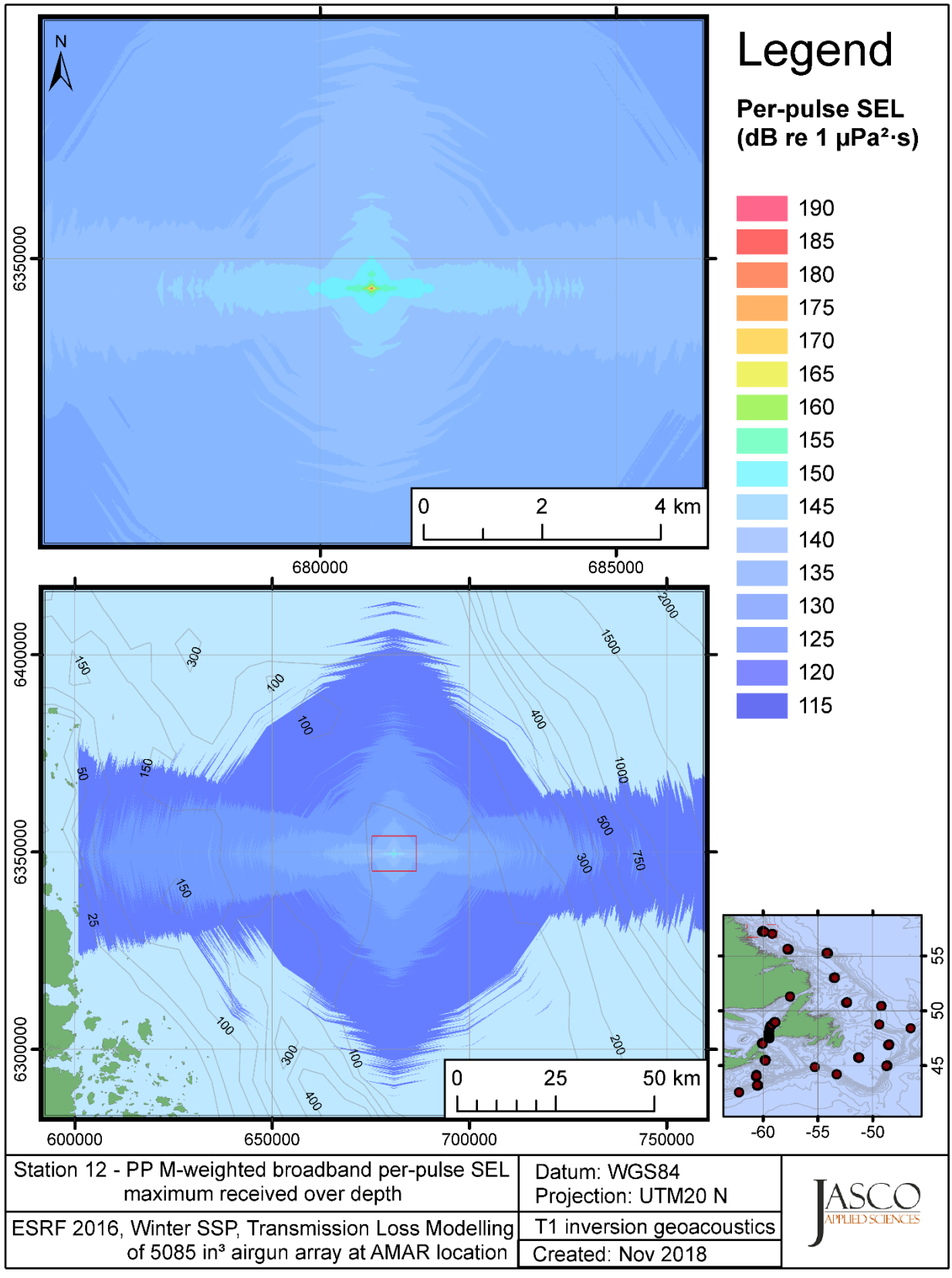

Figure C-544. Stn 12, PP M-weighted maximum-over-depth SEL received at any location on the map, modelled using the track 1 inversion geoacoustic bottom, with the airgun array at the AMAR location and GDEM February SSP.

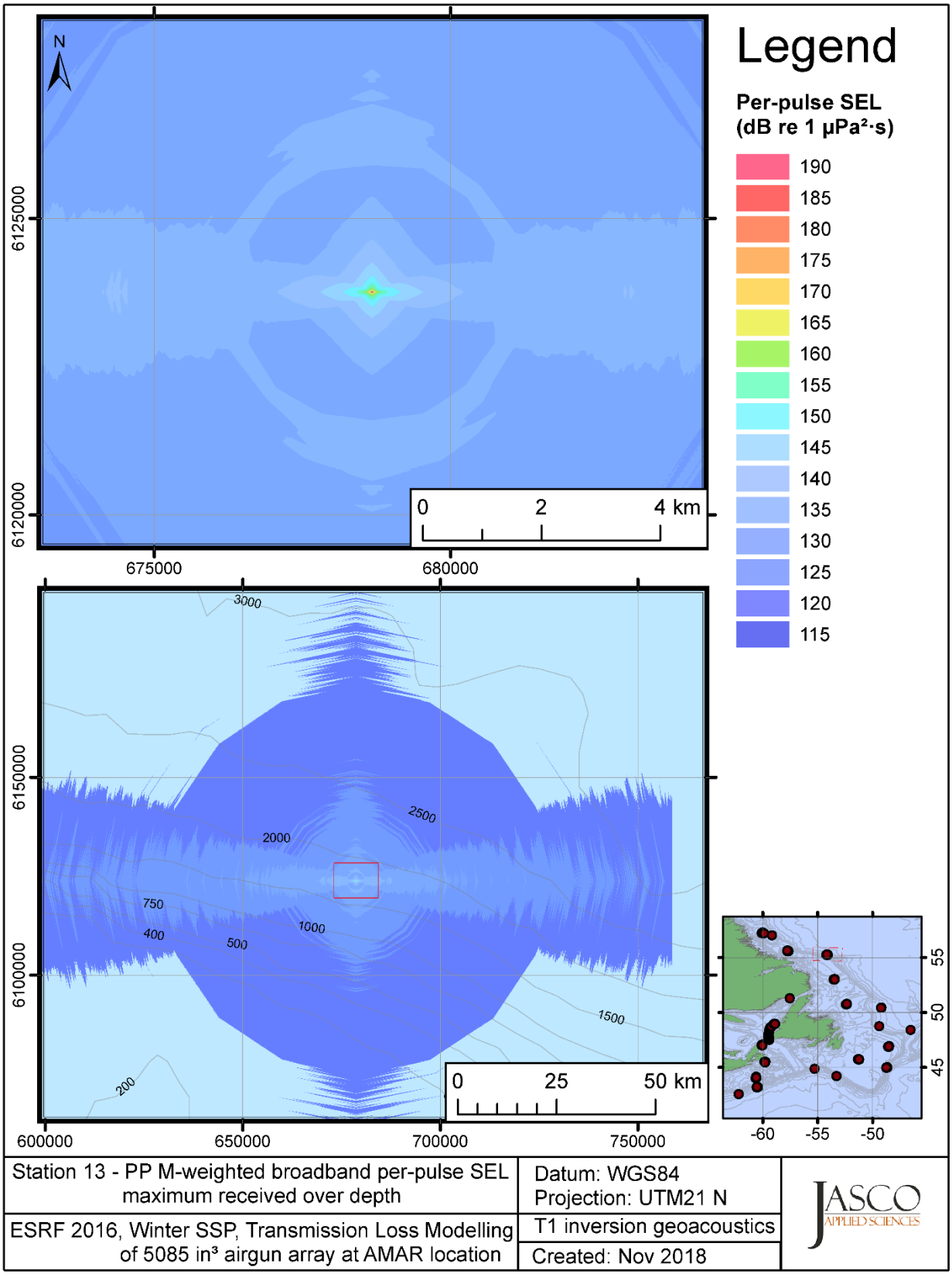

Figure C-545. Stn 13, PP M-weighted maximum-over-depth SEL received at any location on the map, modelled using the track 1 inversion geoacoustic bottom, with the airgun array at the AMAR location and GDEM February SSP.

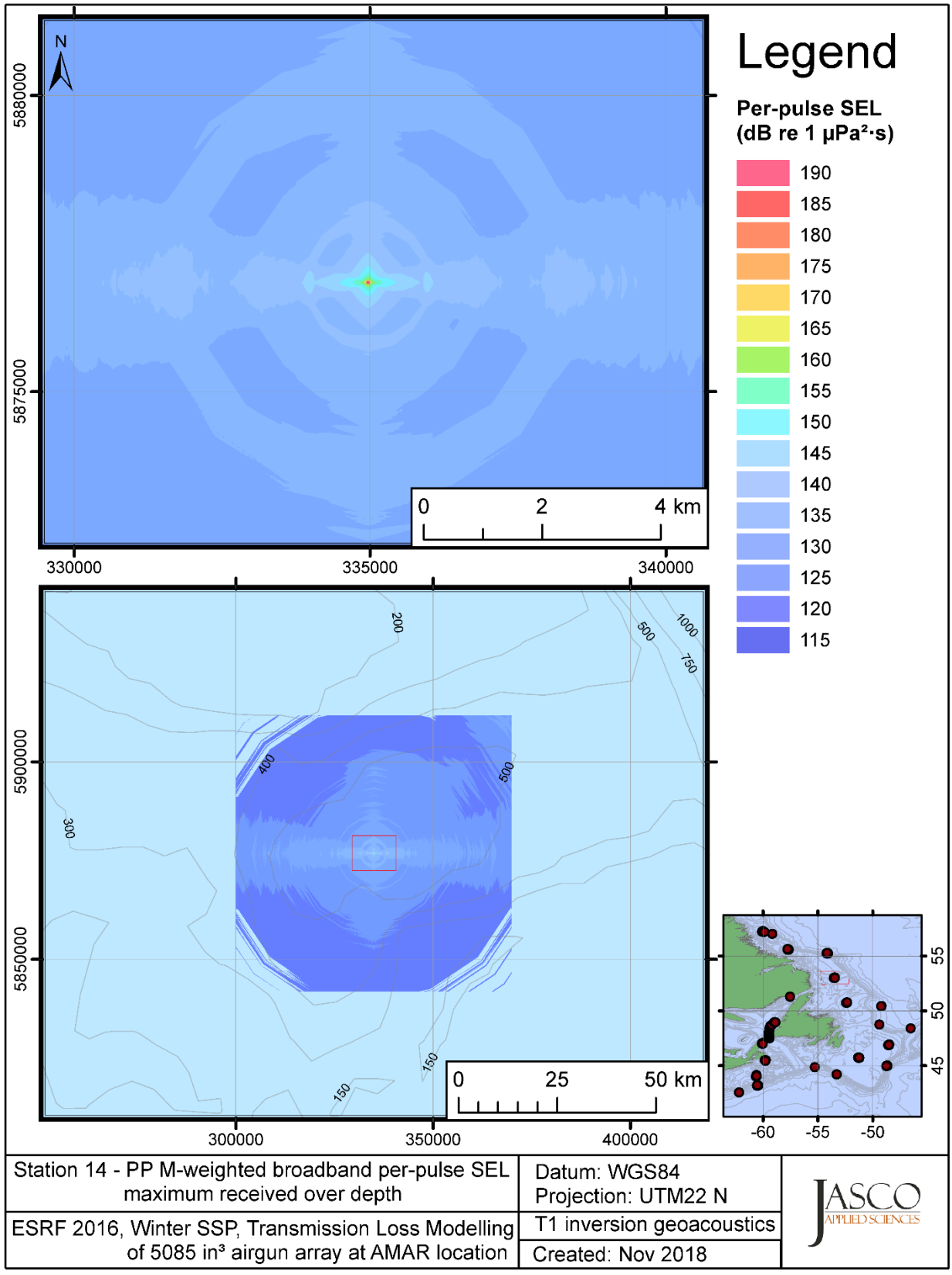

Figure C-546. Stn 14, PP M-weighted maximum-over-depth SEL received at any location on the map, modelled using the track 1 inversion geoacoustic bottom, with the airgun array at the AMAR location and GDEM February SSP.

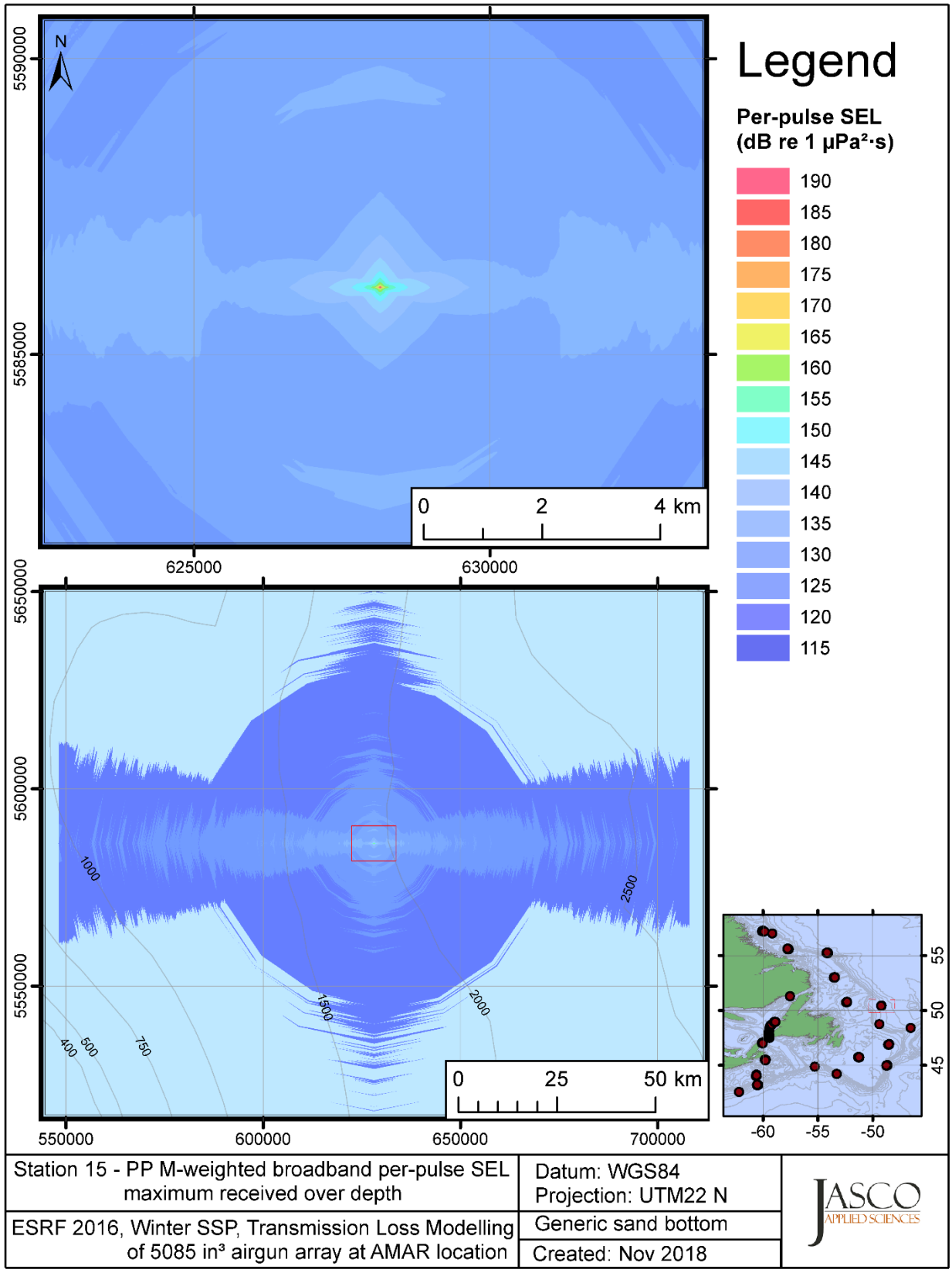

Figure C-547. Stn 15, PP M-weighted maximum-over-depth SEL received at any location on the map, modelled using a generic sand bottom, with the airgun array at the AMAR location and GDEM February SSP.

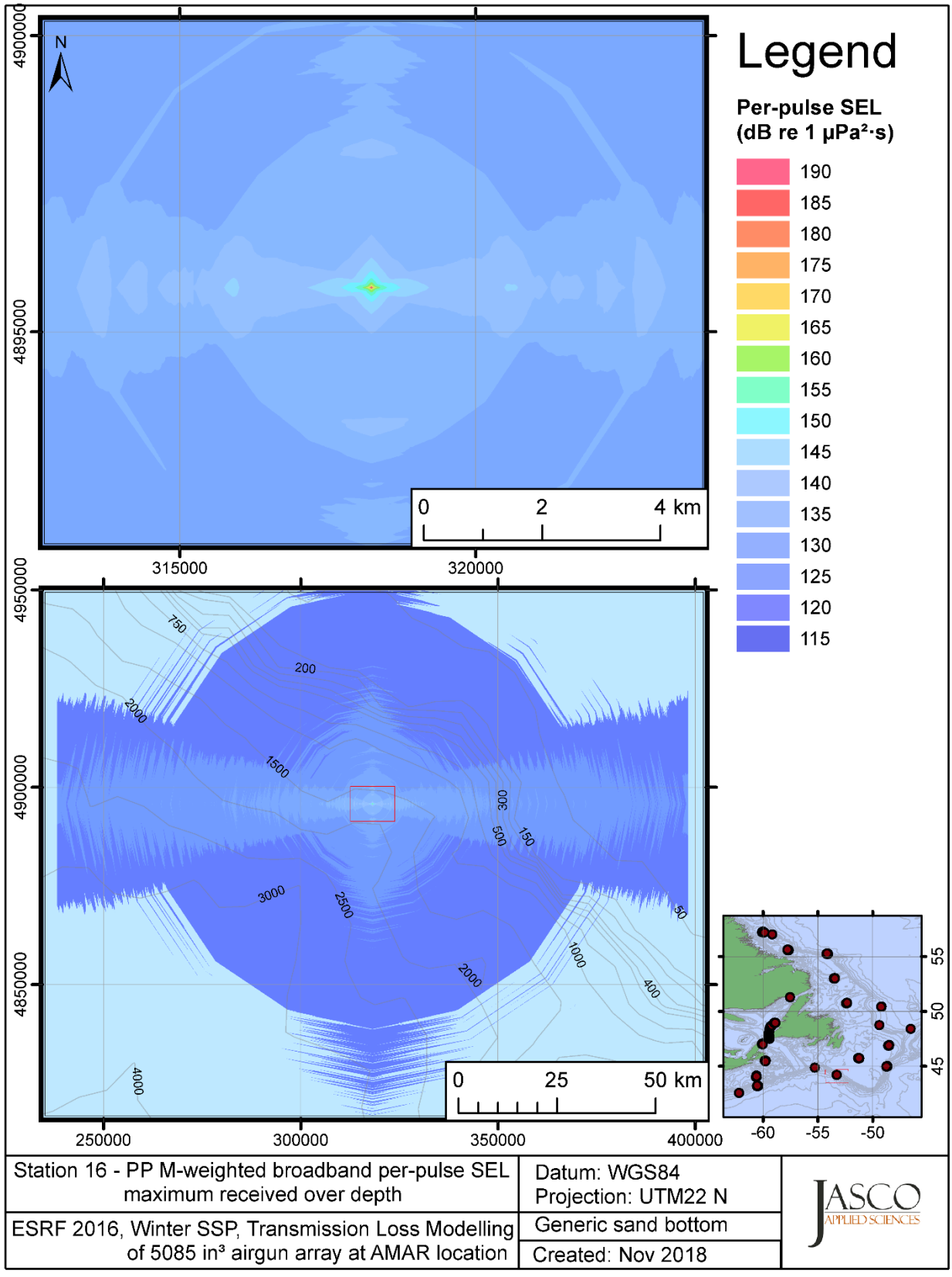

Figure C-548. Stn 16, PP M-weighted maximum-over-depth SEL received at any location on the map, modelled using a generic sand bottom, with the airgun array at the AMAR location and GDEM February SSP.

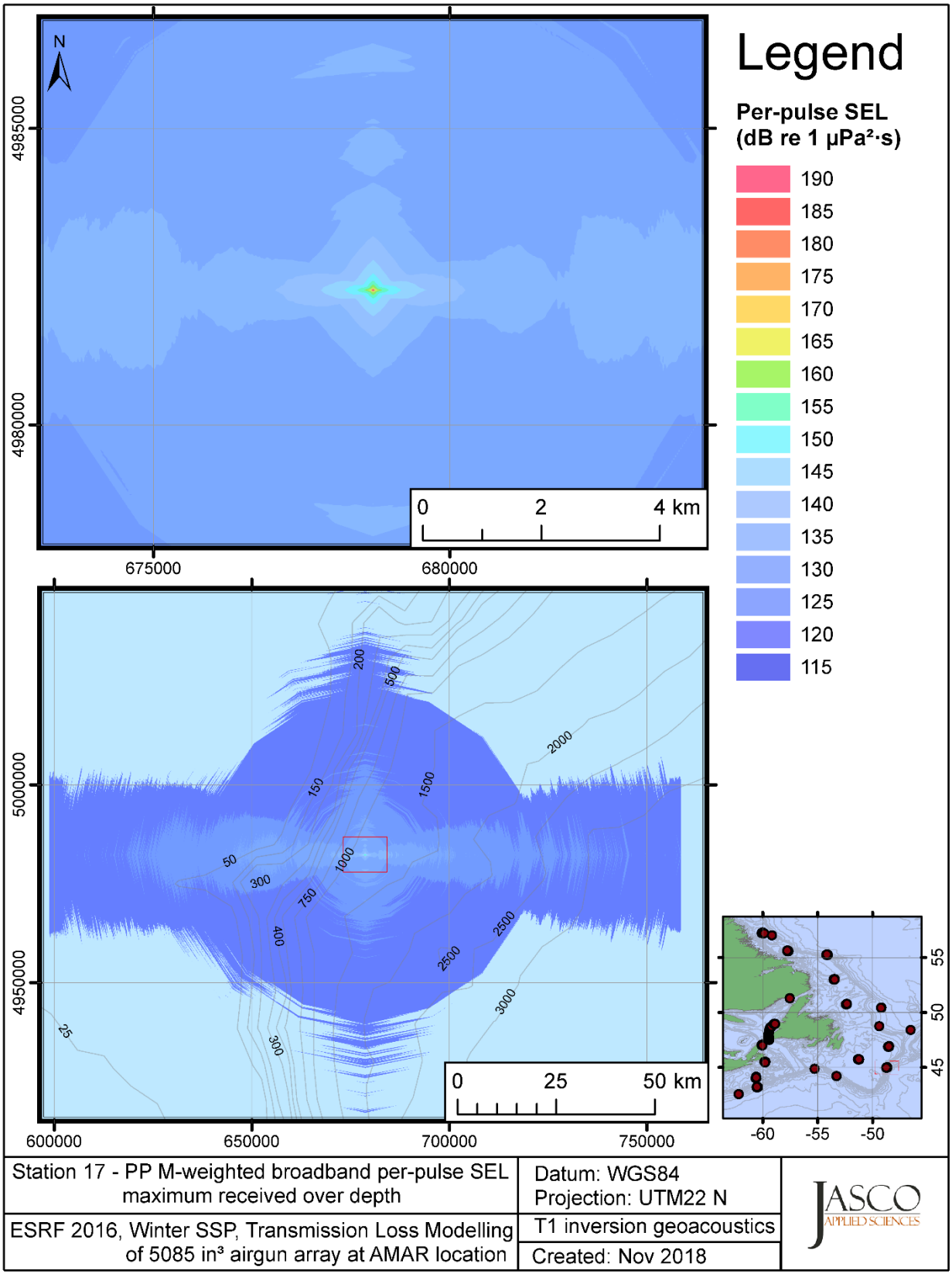

Figure C-549. Stn 17, PP M-weighted maximum-over-depth SEL received at any location on the map, modelled using the track 1 inversion geoacoustic bottom, with the airgun array at the AMAR location and GDEM February SSP.

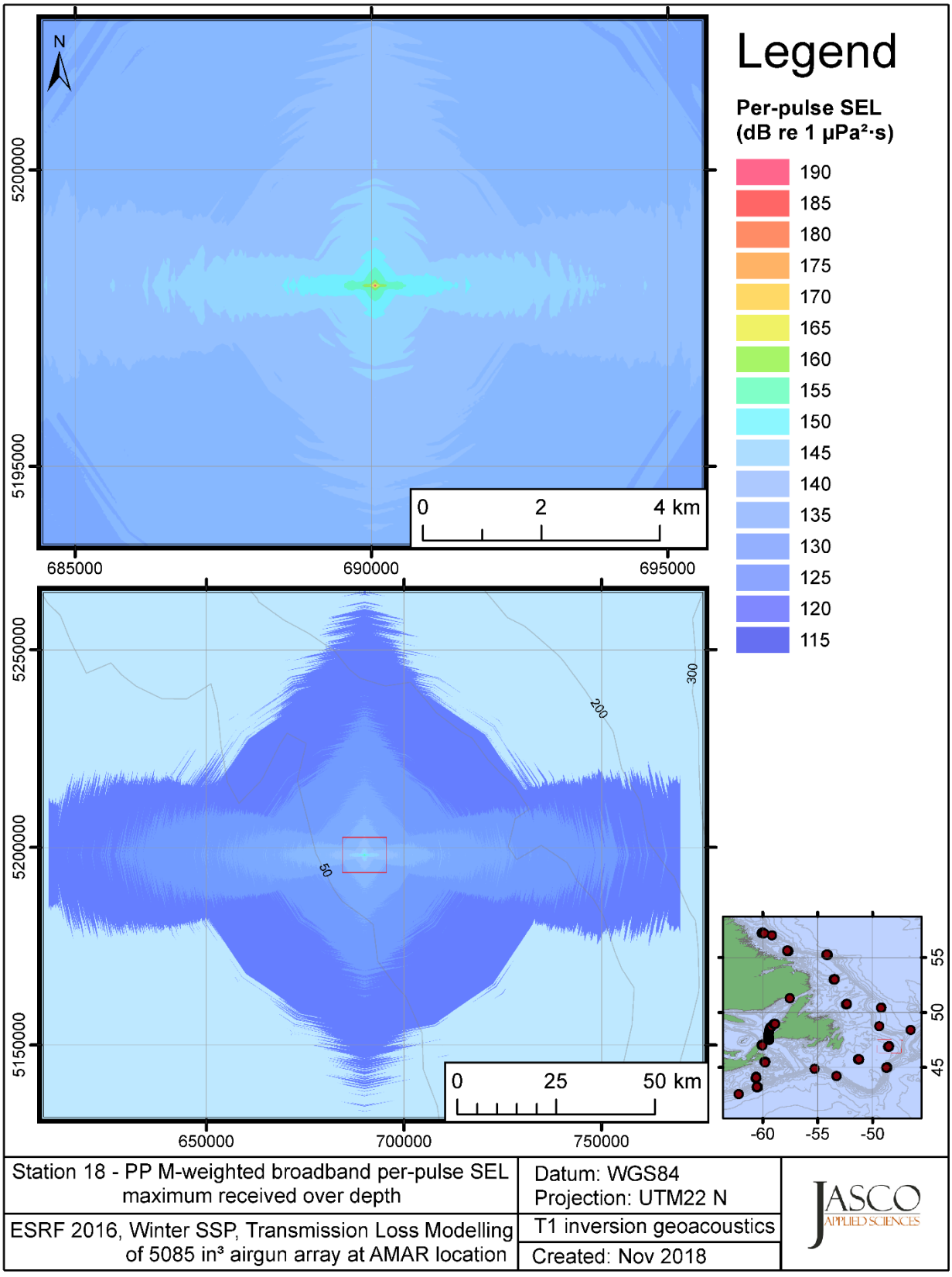

Figure C-550. Stn 18, PP M-weighted maximum-over-depth SEL received at any location on the map, modelled using the track 1 inversion geoacoustic bottom, with the airgun array at the AMAR location and GDEM February SSP.

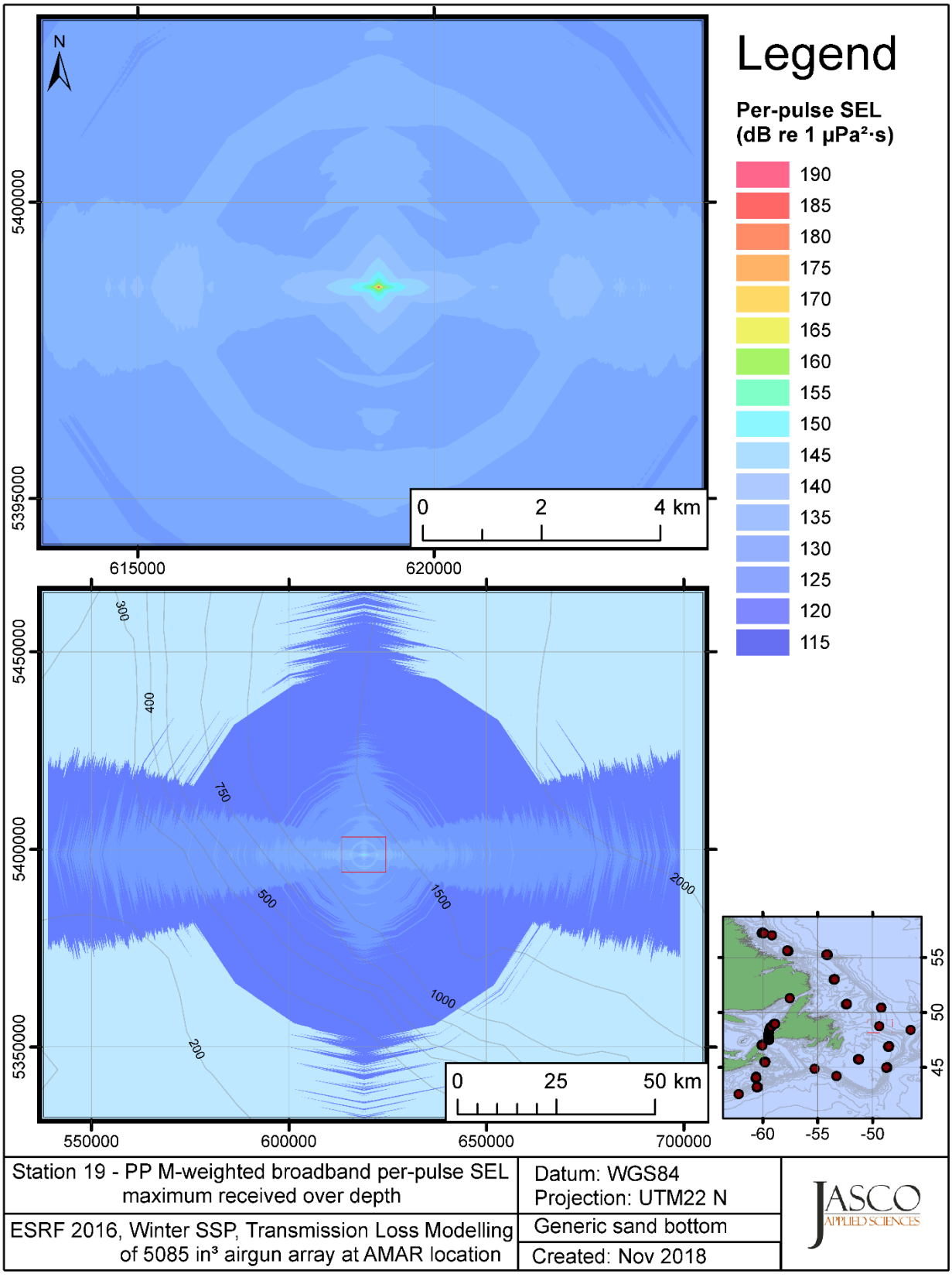

Figure C-551. Stn 19, PP M-weighted maximum-over-depth SEL received at any location on the map, modelled using a generic sand bottom, with the airgun array at the AMAR location and GDEM February SSP.

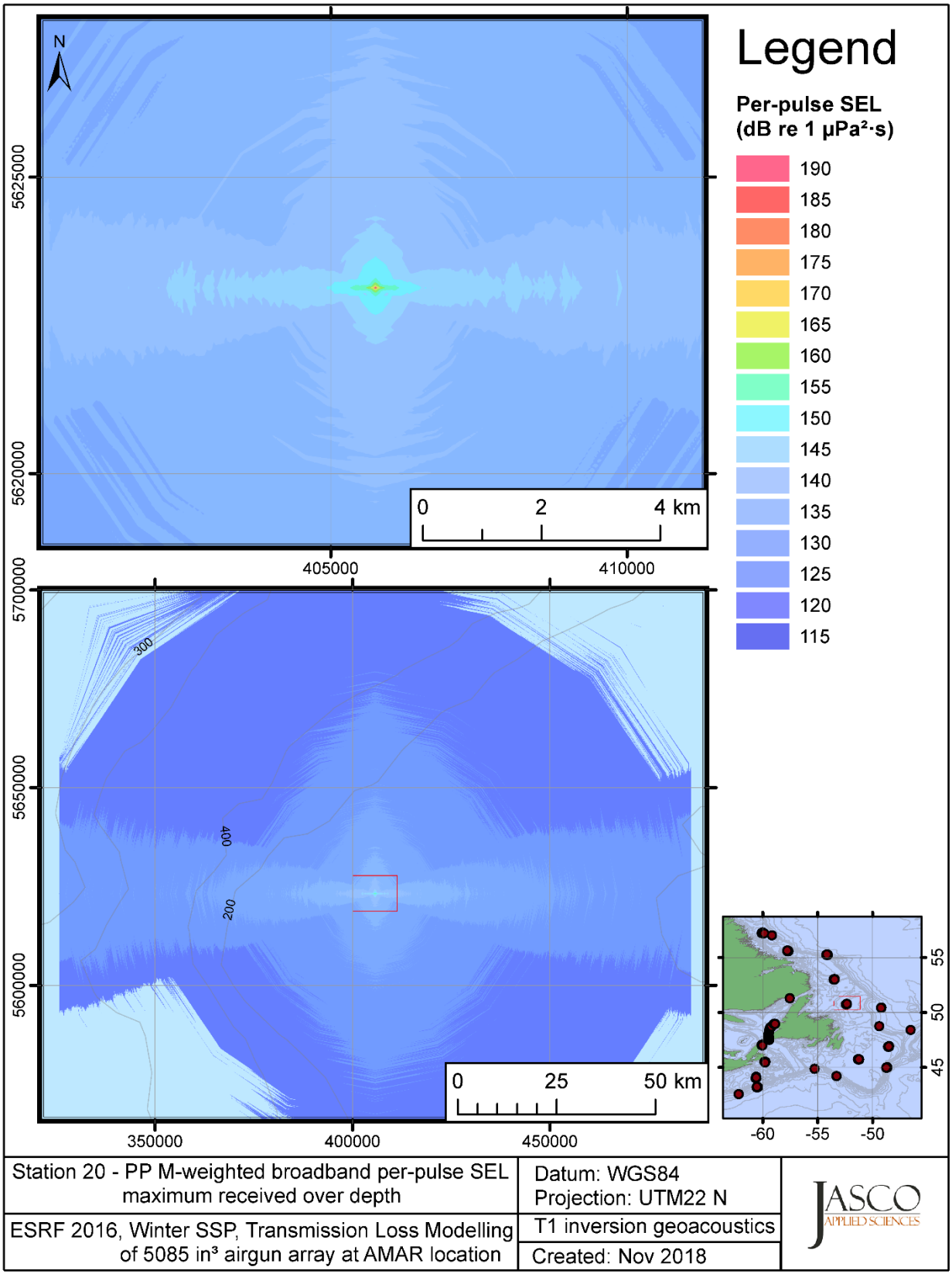

Figure C-552. Stn 20, PP M-weighted maximum-over-depth SEL received at any location on the map, modelled using the track 1 inversion geoacoustic bottom, with the airgun array at the AMAR location and GDEM February SSP.

[HESS] High Energy Seismic Survey. 1999. *High Energy Seismic Survey Review Process and Interim Operational Guidelines for Marine Surveys Offshore Southern California*. Prepared for the California State Lands Commission and the United States Minerals Management Service Pacific Outer Continental Shelf Region by the High Energy Seismic Survey Team, Camarillo, CA. 98 pp.

[ISO] International Organization for Standardization. 2016. *ISO/DIS 18405.2:2017. Underwater acoustics—Terminology*. Geneva. https://www.iso.org/standard/62406.html.

[NMFS] National Marine Fisheries Service. 1998. *Acoustic Criteria Workshop*. Dr. Roger Gentry and Dr. Jeanette Thomas Co-Chairs.

[NMFS] National Marine Fisheries Service. 2018. *2018 Revision to: Technical Guidance for Assessing the Effects of Anthropogenic Sound on Marine Mammal Hearing (Version 2.0): Underwater Thresholds for Onset of Permanent and Temporary Threshold Shifts*. U.S. Department of Commerce, NOAA. NOAA Technical Memorandum NMFS-OPR-59. 167 pp. https://www.fisheries.noaa.gov/webdam/download/75962998.

[NOAA] National Oceanic and Atmospheric Administration. 2013. *Draft guidance for assessing the effects of anthropogenic sound on marine mammals: Acoustic threshold levels for onset of permanent and temporary threshold shifts*. National Oceanic and Atmospheric Administration, U.S. Department of Commerce, and NMFS Office of Protected Resources, Silver Spring, MD, USA. 76 pp. http://www.nmfs.noaa.gov/pr/acoustics/draft_acoustic_guidance_2013.pdf.

[NOAA] National Oceanic and Atmospheric Administration. 2015. *Draft guidance for assessing the effects of anthropogenic sound on marine mammal hearing: Underwater acoustic threshold levels for onset of permanent and temporary threshold shifts*. NMFS Office of Protected Resources, Silver Spring, MD, USA. 180 pp. http://www.nmfs.noaa.gov/pr/acoustics/draft%20acoustic%20guidance%20July%202015.pdf.

[NOAA] National Oceanic and Atmospheric Administration. 2016. *Document Containing Proposed Changes to the NOAA Draft Guidance for Assessing the Effects of Anthropogenic Sound on Marine Mammal Hearing: Underwater Acoustic Threshold Levels for Onset of Permanent and Temporary Threshold Shifts*, p. 24. http://www.nmfs.noaa.gov/pr/acoustics/draft_guidance_march_2016_.pdf.

[ONR] Office of Naval Research. 1998. *ONR Workshop on the Effect of Anthropogenic Noise in the Marine Environment*. Dr. R. Gisiner Chair.

Aerts, L., M. Blees, S.B. Blackwell, C.R. Greene, Jr., K.H. Kim, D.E. Hannay, and M.E. Austin. 2008. *Marine mammal monitoring and mitigation during BP Liberty OBC seismic survey in Foggy Island Bay, Beaufort Sea, July-August 2008: 90-day report*. Document Number LGL Report P1011-1. Report by LGL Alaska Research Associates Inc., LGL Ltd., Greeneridge Sciences Inc. and JASCO Applied Sciences for BP Exploration Alaska. 199 pp. http://www.nmfs.noaa.gov/pr/pdfs/permits/bp_liberty_monitoring.pdf.

ANSI S12.7-1986. R2006. *American National Standard Methods for Measurements of Impulsive Noise*. American National Standards Institute, New York.

ANSI S1.1-1994. R2004. *American National Standard Acoustical Terminology*. American National Standards Institute, New York.

ANSI S1.1-2013. R2013. *American National Standard Acoustical Terminology*. American National Standards Institute, New York.

ANSI/ASA S1.13-2005. R2010. *American National Standard Measurement of Sound Pressure Levels in Air*. American National Standards Institute and Acoustical Society of America, New York.

Babushina, Y.S., G.L. Zaslavskii, and L.I. Yurkevich. 1991. Air and underwater hearing characteristics of the northern fur seal: Audiograms, frequency and differential thresholds. *Biophysics* 36(5): 909-913.

Becker, J.J., D.T. Sandwell, W.H.F. Smith, J. Braud, B. Binder, J. Depner, D. Fabre, J. Factor, S. Ingalls, et al. 2009. Global Bathymetry and Elevation Data at 30 Arc Seconds Resolution: SRTM30_PLUS. *Marine Geodesy* 32(4): 355-371.

Collins, M.D. 1993. A split-step Padé solution for the parabolic equation method. *Journal of the Acoustical Society of America* 93(4): 1736-1742. https://doi.org/10.1121/1.406739.

Collins, M.D., R.J. Cederberg, D.B. King, and S. Chin-Bing. 1996. Comparison of algorithms for solving parabolic wave equations. *Journal of the Acoustical Society of America* 100(1): 178-182. https://doi.org/10.1121/1.415921.

Dragoset, W.H. 1984. A comprehensive method for evaluating the design of airguns and airgun arrays. *16th Annual Proc. Offshore Tech. Conf.* Volume 3. pp 75–84.

Ellison, W.T. and P.J. Stein. 1999. *SURTASS LFA High Frequency Marine Mammal Monitoring (HF/M3) Sonar: Sustem Description and Test & Evaluation*. Under U.S. Navy Contract N66604-98-D-5725.

Finneran, J.J. and C.E. Schlundt. 2010. Frequency-dependent and longitudinal changes in noise-induced hearing loss in a bottlenose dolphin (*Tursiops truncatus*). *Journal of the Acoustical Society of America* 128(2): 567-570. https://doi.org/10.1121/1.3458814.

Finneran, J.J. and A.K. Jenkins. 2012. *Criteria and thresholds for U.S. Navy acoustic and explosive effects analysis*. SPAWAR Systems Center Pacific, San Diego, CA. 64 pp.

Finneran, J.J. 2015. *Auditory weighting functions and TTS/PTS exposure functions for cetaceans and marine carnivores*. Technical report by SSC Pacific, San Diego, CA.

Finneran, J.J. 2016. *Auditory weighting functions and TTS/PTS exposure functions for marine mammals exposed to underwater noise*. Technical Report for Space and Naval Warfare Systems Center Pacific, San Diego, CA. 49 pp. http://www.dtic.mil/dtic/tr/fulltext/u2/1026445.pdf.

Fisher, F.H. and V.P. Simmons. 1977. Sound absorption in sea water. *Journal of the Acoustical Society of America* 62(3): 558-564. https://doi.org/10.1121/1.381574.

Funk, D., D.E. Hannay, D.S. Ireland, R. Rodrigues, and W.R. Koski (eds.). 2008. *Marine mammal monitoring and mitigation during open water seismic exploration by Shell Offshore Inc. in the Chukchi and Beaufort Seas, July–November 2007: 90-day report*. LGL Report P969-1. Prepared by LGL Alaska Research Associates Inc., LGL Ltd., and JASCO Research Ltd. for Shell Offshore Inc., National Marine Fisheries Service (U.S.), and U.S. Fish and Wildlife Service. 218 pp.

Hannay, D.E. and R.G. Racca. 2005. *Acoustic Model Validation*. Document Number 0000-S-90-04-T-7006-00-E, Revision 02. Technical report by JASCO Research Ltd. for Sakhalin Energy Investment Company Ltd. 34 pp.

Ireland, D.S., R. Rodrigues, D. Funk, W.R. Koski, and D.E. Hannay. 2009. *Marine mammal monitoring and mitigation during open water seismic exploration by Shell Offshore Inc. in the Chukchi and Beaufort Seas, July–October 2008: 90-Day Report*. Document Number LGL Report P1049-1. 277 pp.

Kastak, D. and R.J. Schusterman. 1998. Low-frequency amphibious hearing in pinnipeds: Methods, measurements, noise, and ecology. *Journal of the Acoustical Society of America* 103(4): 2216-2228. https://doi.org/10.1121/1.421367.

Kastelein, R.A., R. van Schie, W.C. Verboom, and D. de Haan. 2005. Underwater hearing sensitivity of a male and a female Steller sea lion (*Eumetopias jubatus*). *Journal of the Acoustical Society of America* 118(3): 1820-1829. http://dx.doi.org/10.1121/1.1992650.

Landro, M. 1992. Modeling of GI gun signatures. *Geophysical Prospecting* 40: 721–747. https://doi.org/10.1111/j.1365-2478.1992.tb00549.x

Laws, M., L. Hatton, and M. Haartsen. 1990. Computer modeling of clustered airguns. *First Break* 8: 331–338.

Lucke, K., U. Siebert, P. Lepper, A., and M.-A. Blanchet. 2009. Temporary shift in masked hearing thresholds in a harbor porpoise (*Phocoena phocoena*) after exposure to seismic airgun stimuli. *Journal of the Acoustical Society of America* 125(6): 4060-4070. https://asa.scitation.org/doi/10.1121/1.3117443.

Lurton, X. 2002. *An Introduction to Underwater Acoustics: Principles and Applications.* Springer, Chichester, U.K.

Malme, C.I., P.R. Miles, C.W. Clark, P. Tyak, and J.E. Bird. 1983. *Investigations of the Potential Effects of Underwater Noise from Petroleum Industry Activities on Migrating Gray Whale Behavior*. Report Number 5366. http://www.boem.gov/BOEM-Newsroom/Library/Publications/1983/rpt5366.aspx.

Malme, C.I., P.R. Miles, C.W. Clark, P.L. Tyack, and J.E. Bird. 1984. *Investigations of the Potential Effects of Underwater Noise from Petroleum Industry Activities on Migrating Gray Whale Behavior. Phase II: January 1984 migration*. Report Number 5586. Report prepared by Bolt, Beranek and Newman Inc. for the U.S. Department of the Interior, Minerals Management Service, Cambridge, MA (USA). 357 pp. https://www.boem.gov/BOEM-Newsroom/Library/Publications/1983/rpt5586.aspx.

Martin, B., K. Broker, M.-N.R. Matthews, J. MacDonnell, and L. Bailey. 2015. *Comparison of measured and modeled air-gun array sound levels in Baffin Bay, West Greenland. OceanNoise 2015*, 11-15 May, Barcelona, Spain.

Martin, B.S., E. Maxner, M. Wood, L. Horwich, and K. Kowarski. 2017a. *Soundscape Characterization and Marine Mammal Presence on the Eastern Grand Banks, NF: September to October 2017*. Document Number 01305. Version 1.0. Technical report by JASCO Applied Sciences for DFO Newfoundland.

Martin, S.B., M.-N.R. Matthews, J.T. MacDonnell, and K. Bröker. 2017b. Characteristics of seismic survey pulses and the ambient soundscape in Baffin Bay and Melville Bay, West Greenland. *Journal of the Acoustical Society of America* 142(6): 3331-3346. https://doi.org/10.1121/1.5014049.

Mattsson, A. and M. Jenkerson. 2008. *Single Airgun and Cluster Measurement Project*. *Joint Industry Programme (JIP) on Exploration and Production Sound and Marine Life Proramme Review*, October 28-30. International Association of Oil and Gas Producers, Houston, TX.

Moore, P.W.B. and R.J. Schusterman. 1987. Audiometric assessment of northern fur seals, *Callorhinus ursinus*. *Marine Mammal Science* 3: 31-53.

Mulsow, J. and C. Reichmuth. 2007. Electrophysiological assessment of temporal resolution in pinnipeds. *Aquatic Mammals* 33: 122-131.

Mulsow, J., J.J. Finneran, and D.S. Houser. 2011a. California sea lion (*Zalophus californianus*) aerial hearing sensitivity measured using auditory steady-state response and psychophysical methods. *Journal of the Acoustical Society of America* 129: 2298-2306. https://asa.scitation.org/doi/10.1121/1.3552882.

Mulsow, J., C. Reichmuth, F.M.D. Gulland, D.A.S. Rosen, and J.J. Finneran. 2011b. Aerial audiograms of several California sea lions (*Zalophus californianus*) and Steller sea lions (*Eumetopias jubatus*) measured using single and multiple simultaneous auditory steady-state response methods. *Journal of Experimental Biology* 214: 1138-1147. http://jeb.biologists.org/content/jexbio/214/7/1138.full.pdf.

Nedwell, J.R. and A.W. Turnpenny. 1998. The use of a generic frequency weighting scale in estimating environmental effect. *Workshop on Seismics and Marine Mammals*. 23–25 Jun 1998, London, U.K.

Nedwell, J.R., A.W. Turnpenny, J. Lovell, S.J. Parvin, R. Workman, and J.A.L. Spinks. 2007. *A validation of the dB_{ht} as a measure of the behavioural and auditory effects of underwater noise*. Document Number 534R1231 Report prepared by Subacoustech Ltd. for the UK Department of Business, Enterprise and Regulatory Reform under Project No. RDCZ/011/0004. http://www.subacoustech.com/wp-content/uploads/534R1231.pdf.

O'Neill, C., D. Leary, and A. McCrodan. 2010. Sound Source Verification. (Chapter 3) *In* Blees, M.K., K.G. Hartin, D.S. Ireland, and D.E. Hannay (eds.). *Marine mammal monitoring and mitigation during open water seismic exploration by Statoil USA E&P Inc. in the Chukchi Sea, August-October 2010: 90-day report*. LGL Report P1119. Prepared by LGL Alaska Research Associates Inc., LGL Ltd., and JASCO Applied Sciences Ltd. for Statoil USA E&P Inc., National Marine Fisheries Service (U.S.), and U.S. Fish and Wildlife Service. pp 1-34.

Payne, R. and D. Webb. 1971. Orientation by means of long range acoustic signaling in baleen whales. *Annals of the New York Academy of Sciences* 188: 110-142. https://doi.org/10.1111/j.1749-6632.1971.tb13093.x.

Porter, M.B. and Y.-C. Liu. 1994. Finite-element ray tracing. *In*: Lee, D. and M.H. Schultz (eds.). *Proceedings of the International Conference on Theoretical and Computational Acoustics*. Volume 2. World Scientific Publishing Co. pp 947-956.

Racca, R.G., A. Rutenko, K. Bröker, and M.E. Austin. 2012a. A line in the water - design and enactment of a closed loop, model based sound level boundary estimation strategy for mitigation of behavioural impacts from a seismic survey. *11th European Conference on Underwater Acoustics 2012*. Volume 34(3), Edinburgh, United Kingdom.

Racca, R.G., A. Rutenko, K. Bröker, and G. Gailey. 2012b. *Model based sound level estimation and in-field adjustment for real-time mitigation of behavioural impacts from a seismic survey and post-event evaluation of sound exposure for individual whales*. *Acoustics 2012 Fremantle: Acoustics, Development and the Environment*, Fremantle, Australia. http://www.acoustics.asn.au/conference_proceedings/AAS2012/papers/p92.pdf.

Richardson, W.J., B. Würsig, and C.R. Greene, Jr. 1986. Reactions of bowhead whales, *Balaena mysticetus*, to seismic exploration in the Canadian Beaufort Sea. *Journal of the Acoustical Society of America* 79(4): 1117-1128. https://doi.org/10.1121/1.393384.

Richardson, W.J., B. Würsig, and C.R. Greene, Jr. 1990. Reactions of bowhead whales, *Balaena mysticetus*, to drilling and dredging noise in the Canadian Beaufort Sea. *Marine Environmental Research* 29(2): 135-160. https://doi.org/10.1016/0141-1136(90)90032-J.

Schusterman, R.J., R.F. Balliet, and J. Nixon. 1972. Underwater audiogram of the California sea lion by the conditioned vocalization technique. *Journal of the Experimental Analysis of Behavior* 17: 339-350. https://www.ncbi.nlm.nih.gov/pmc/articles/PMC1333909/pdf/jeabehav00130-0042.pdf.

Smith, W.H.F. and D.T. Sandwell. 1997. Global sea floor topography from satellite altimetry and ship depth soundings. *Science* 277(5334): 1956-1962.

Southall, B.L., A.E. Bowles, W.T. Ellison, J.J. Finneran, R.L. Gentry, C.R. Greene, Jr., D. Kastak, D.R. Ketten, J.H. Miller, et al. 2007. Marine Mammal Noise Exposure Criteria: Initial Scientific Recommendations. *Aquatic Mammals* 33(4): 411-521. https://doi.org/10.1080/09524622.2008.9753846.

Warner, G. and A.O. MacGillivray. 2018. *Analysis of Acoustic Particle Motion Data from the Svein Vaage Airgun Study: Final Report*. Document Number 01656. Version 1.0. Technical report by JASCO Applied Sciences for Environmental Studies Research Fund.

Warner, G.A., C. Erbe, and D.E. Hannay. 2010. Underwater Sound Measurements. (Chapter 3) *In* Reiser, C.M., D. Funk, R. Rodrigues, and D.E. Hannay (eds.). *Marine Mammal Monitoring and Mitigation during Open Water Shallow Hazards and Site Clearance Surveys by Shell Offshore Inc. in the Alaskan Chukchi Sea, July-October 2009: 90-Day Report*. LGL Report P1112-1. Report by LGL Alaska Research Associates Inc. and JASCO Applied Sciences for Shell Offshore Inc., National Marine Fisheries Service (U.S.), and U.S. Fish and Wildlife Service. pp 1-54.

Wood, J., B.L. Southall, and D.J. Tollit. 2012. *PG&E offshore 3-D Seismic Survey Project Environmental Impact Report–Marine Mammal Technical Draft Report*. SMRU Ltd. 121 pp. https://www.coastal.ca.gov/energy/seismic/mm-technical-report-EIR.pdf.

Zhang, Z.Y. and C.T. Tindle. 1995. Improved equivalent fluid approximations for a low shear speed ocean bottom. *Journal of the Acoustical Society of America* 98(6): 3391-3396. https://doi.org/10.1121/1.413789.

Ziolkowski, A. 1970. A method for calculating the output pressure waveform from an air gun. *Geophysical Journal of the Royal Astronomical Society* 21(2): 137-161.